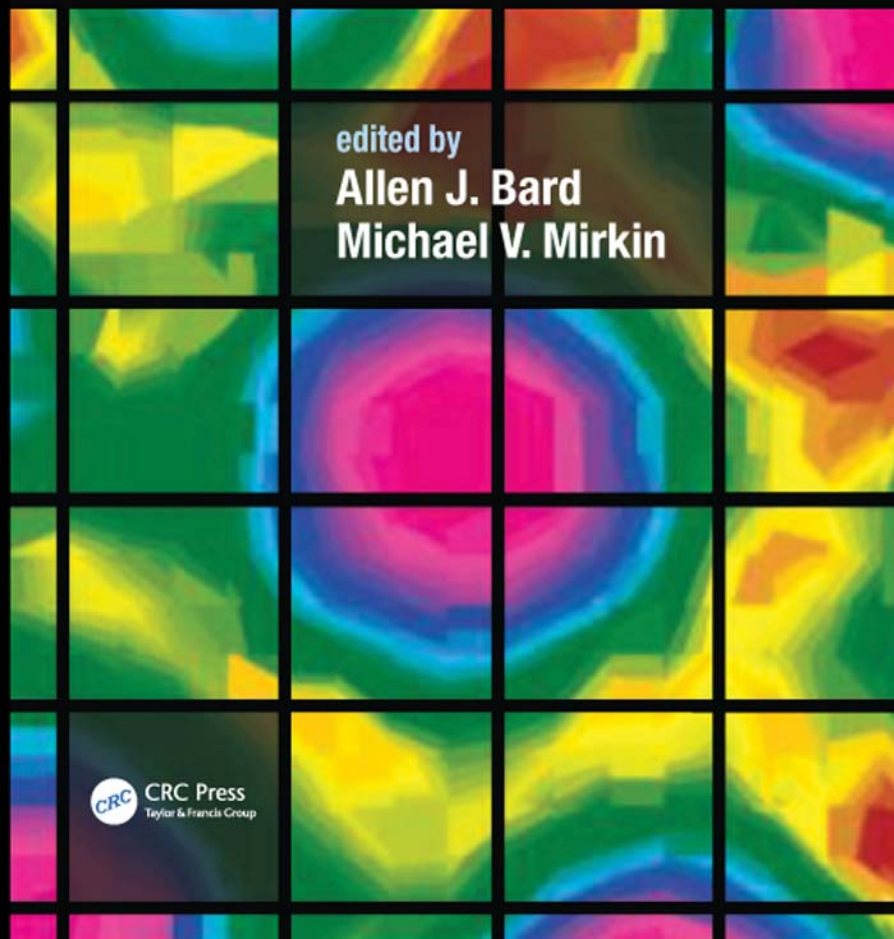
Scanning Electrochemical Microscopy

Second Edition



Scanning Electrochemical Microscopy Second Edition

Scanning Electrochemical Microscopy Second Edition

edited by
Allen J. Bard
Michael V. Mirkin

CRC Press
Taylor & Francis Group
Boca Raton London New York

CRC Press is an imprint of the
Taylor & Francis Group, an **informa** business

CRC Press
Taylor & Francis Group
6000 Broken Sound Parkway NW, Suite 300
Boca Raton, FL 33487-2742

© 2012 by Taylor & Francis Group, LLC
CRC Press is an imprint of Taylor & Francis Group, an Informa business

No claim to original U.S. Government works
Version Date: 20120215

International Standard Book Number-13: 978-1-4398-3113-7 (eBook - PDF)

This book contains information obtained from authentic and highly regarded sources. Reasonable efforts have been made to publish reliable data and information, but the author and publisher cannot assume responsibility for the validity of all materials or the consequences of their use. The authors and publishers have attempted to trace the copyright holders of all material reproduced in this publication and apologize to copyright holders if permission to publish in this form has not been obtained. If any copyright material has not been acknowledged please write and let us know so we may rectify in any future reprint.

Except as permitted under U.S. Copyright Law, no part of this book may be reprinted, reproduced, transmitted, or utilized in any form by any electronic, mechanical, or other means, now known or hereafter invented, including photocopying, microfilming, and recording, or in any information storage or retrieval system, without written permission from the publishers.

For permission to photocopy or use material electronically from this work, please access www.copyright.com (http://www.copyright.com/) or contact the Copyright Clearance Center, Inc. (CCC), 222 Rosewood Drive, Danvers, MA 01923, 978-750-8400. CCC is a not-for-profit organization that provides licenses and registration for a variety of users. For organizations that have been granted a photocopy license by the CCC, a separate system of payment has been arranged.

Trademark Notice: Product or corporate names may be trademarks or registered trademarks, and are used only for identification and explanation without intent to infringe.

Visit the Taylor & Francis Web site at
http://www.taylorandfrancis.com

and the CRC Press Web site at
http://www.crcpress.com

Contents

Preface vii
Contributors ix

Chapter 1 Introduction and Principles 1
Allen J. Bard

Chapter 2 Instrumentation 15
Fu-Ren F. Fan, Allen J. Bard, and Peixin He

Chapter 3 Preparation of Tips for Scanning Electrochemical Microscopy 25
Fu-Ren F. Fan and Christophe Demaille

Chapter 4 Scanning Electrochemical Microscopic Imaging 53
Fu-Ren F. Fan

Chapter 5 Theory 75
Michael V. Mirkin and Yixian Wang

Chapter 6 Heterogeneous Electron Transfer Reactions 127
Shigeru Amemiya

Chapter 7 Visualizing and Quantifying Homogeneous Chemical Reactions in Electrochemical Processes 157
Patrick R. Unwin

Chapter 8 Charge Transfer Processes at the Liquid–Liquid Interface 191
Michael V. Mirkin and Michael Tsionsky

Chapter 9 Imaging Molecular Transport across Membranes 233
Henry S. White and Frederic Kanoufi

Chapter 10 Potentiometric Probes 275
Guy Denuault, Geza Nagy, and Klara Toth

Chapter 11 Biotechnological Applications 317
Benjamin R. Horrocks and Gunther Wittstock

Chapter 12 Scanning Electrochemical Microscopy of Living Cells 379
Janine Mauzeroll and Steen B. Schougaard

Chapter 13 Localized Flux Measurements and Kinetic Imaging at Interfaces 417
Patrick R. Unwin and Julie V. Macpherson

Chapter 14 Applications of Scanning Electrochemical Microscopy in Corrosion Research 451
Dennis E. Tallman and Mark B. Jensen

Chapter 15 Micro- and Nanopatterning Using Scanning Electrochemical Microscopy 489
Daniel Mandler

Chapter 16 Application to Electrocatalysis and Photocatalysis and Surface Interrogation 525
Joaquín Rodríguez López, Cynthia G. Zoski, and Allen J. Bard

Chapter 17 Hybrid Scanning Electrochemical Techniques: Methods and Applications 569
Julie V. Macpherson and Christophe Demaille

Chapter 18 Additional Recent Applications and Prospects 635
Allen J. Bard, Fernando Cortés Salazar, and Hubert H. Girault

Preface

During the 10 years that have passed since the publication of the first edition of this book, scanning electrochemical microscopy (SECM) has evolved substantially. The number of publications in this field has greatly increased, and their focus has changed from proof-of-concept experiments to real-world applications. SECM has been employed as an electrochemical tool to study heterogeneous and homogeneous reactions, for high-resolution imaging of various substrates, including biological cells, and for microfabrication. This technique is now used by a number of research groups in many different countries. We think the time has come for a new edition of this book that will provide up-to-date comprehensive reviews of different aspects of SECM.

All chapters in this edition are either new or thoroughly updated. Chapters 1 through 5 contain experimental and theoretical background, which is essential for everyone working in this field. Chapter 1 covers the principles of SECM measurements, Chapter 2 deals with instrumentation, Chapter 3 describes the preparation of SECM probes, Chapter 4 covers imaging methodologies, and Chapter 5 deals with theory. Other chapters are dedicated to specific applications and are self-contained. Although some knowledge of electrochemistry and physical chemistry is assumed, the key ideas discussed are at a level suitable for beginning graduate students.

SECM has proved useful for a broad range of interdisciplinary research. Various applications discussed in this book range from studies of biological systems to sensors to probing reactions at the liquid–liquid interface. Although we did not intend to present even a brief survey of these diverse areas of research, each chapter provides sufficient details to allow a specialist to evaluate the applicability of SECM for solving a specific problem. We hope it will be useful to all interested in learning about this technique and applying it.

Four new chapters in this book describe recent advances of SECM in several areas of current interest, i.e., studies of single biological cells (Chapter 12), corrosion (Chapter 14), electrocatalysis (Chapter 16), and hybrid techniques (Chapter 17). Another major development covered throughout the book is the ongoing shift from micrometer-scale experiments to the nanoscale. Recent methodological advances have greatly increased the capacity of SECM to characterize interfaces at the nanoscale and to obtain molecular-level chemical information. To keep this new edition to a manageable size, it was felt necessary to omit some material from the first edition (e.g., in Chapter 2). Interested readers should still be able to access this material from the first edition of this book.

In closing, we thank our students, coworkers, and colleagues who have done so much to develop SECM. The future for this technique, which is unique among scanning probe methods in its quantitative rigor and in its ability to study with ease samples in liquid environments, continues to be a bright one.

Allen J. Bard

Michael V. Mirkin

Contributors

Shigeru Amemiya
Department of Chemistry
University of Pittsburgh
Pittsburgh, Pennsylvania

Allen J. Bard
Department of Chemistry and Biochemistry
The University of Texas at Austin
Austin, Texas

Christophe Demaille
Centre National de la Recherche Scientifique
University Paris Diderot-Paris 7
Paris, France

and

Department of Chemistry and Biochemistry
The University of Texas at Austin
Austin, Texas

Guy Denuault
School of Chemistry
University of Southampton
Southampton, United Kingdom

Fu-Ren F. Fan
Department of Chemistry and Biochemistry
The University of Texas at Austin
Austin, Texas

Hubert H. Girault
Ecole Polytechnique Federale de Lausanne
Lausanne, Switzerland

Peixin He
CH Instruments, Inc.
Austin, Texas

Benjamin R. Horrocks
School of Chemistry
Newcastle University
Newcastle upon Tyne, United Kingdom

Mark B. Jensen
Department of Chemistry
Concordia College
Moorhead, Minnesota

Frederic Kanoufi
Centre National de la Recherche Scientifique
Ecole Supérieure de Physique et de Chimie Industrielles ParisTech
Paris, France

Joaquín Rodríguez López
The University of Texas at Austin
Austin, Texas

Julie V. Macpherson
Department of Chemistry
University of Warwick
Coventry, United Kingdom

Daniel Mandler
Institute of Chemistry
The Hebrew University of Jerusalem
Jerusalem, Israel

Janine Mauzeroll
Department of Chemistry
Laboratory for Electrochemical Reactive Imaging and Detection for Biological Systems
Université du Québec à Montréal
Montréal, Québec, Canada

Michael V. Mirkin
Department of Chemistry and Biochemistry
Queens College
The City University of New York
Flushing, New York

Geza Nagy
Department of General and Physical Chemistry
University of Pécs
Pécs, Hungary

Fernando Cortés Salazar
Ecole Polytechnique Federale de Lausanne
Lausanne, Switzerland

Steen B. Schougaard
Department of Chemistry
Laboratory for Functional Materials
Université du Québec à Montréal
Montréal, Québec, Canada

Dennis E. Tallman
Department of Coatings and Polymeric Materials
and
Department of Chemistry and Biochemistry
North Dakota State University
Fargo, North Dakota

Klara Toth
Technical Analytical Research Group
Hungarian Academy of Sciences
Budapest, Hungary

Michael Tsionsky
Derwood, Maryland

Patrick R. Unwin
Department of Chemistry
University of Warwick
Coventry, United Kingdom

Yixian Wang
Department of Chemistry and Biochemistry
Queens College
The City University of New York
Flushing, New York

Henry S. White
Department of Chemistry
University of Utah
Salt Lake City, Utah

Gunther Wittstock
Faculty of Mathematics and Natural Sciences
Department of Pure and Applied Chemistry
Center of Interface Science
Carl von Ossietzky University of Oldenburg
Oldenburg, Germany

Cynthia G. Zoski
New Mexico State University
Las Cruces, New Mexico

1 Introduction and Principles

Allen J. Bard

CONTENTS

1.1 Background of Scanning Electrochemical Microscopy 1
1.2 Principles of SECM 2
1.2.1 Ultramicroelectrodes 2
1.2.2 Feedback Mode 3
1.2.3 Collection–Generation Modes 6
1.2.4 Transient Methods 6
1.2.5 Fabrication 6
1.3 Mediators 7
1.4 Applications of SECM 7
References 12

1.1 BACKGROUND OF SCANNING ELECTROCHEMICAL MICROSCOPY

This book is devoted to a complete and up-to-date treatment of scanning electrochemical microscopy (SECM). In this introductory chapter, we cover the historical background of the technique, the basic principles of SECM, and an overview of some of its applications (covered in more depth in the later chapters). A number of general reviews of this field have also been published.[1–11] More focused reviews to particular topics are indicated in the following chapters.

SECM involves the measurement of the current through an ultramicroelectrode (UME) (an electrode with a radius, a, of the order of a few nm to 25 μm) when it is held or moved in a solution in the vicinity of a substrate. Substrates, which can be solid surfaces of different types (e.g., glass, metal, polymer, biological material) or liquids (e.g., mercury, immiscible oil), perturb the electrochemical response of the tip and this perturbation provides information about the nature and properties of the substrate. The development of SECM depended on previous work on the use of UMEs in electrochemistry and the application of piezoelectric elements to position a tip, as in scanning tunneling microscopy (STM). Certain aspects of SECM behavior also have analogies in electrochemical thin-layer cells and arrays of interdigitated electrodes.

The movement of the tip is usually carried out by drivers based on piezoelectric elements, similar to those used in STM, as described in Chapter 2. Often inchworm drivers (Burleigh Instruments, Fishers, NY) are used, since they can move larger distances than simple piezoelectric tube scanners. However, where higher resolution is needed, piezoelectric pushers can be added, so that the inchworms or stepping motors provide "coarse" drives and the pushers nanometer-resolution drives. Generally, the direction normal to the substrate is taken as the Z-direction, while X and Y are those in the plane of the substrate.

There are several modes of operation of the SECM. In the tip generation/substrate collection (TG/SC) mode, the tip is used to generate a reactant that is detected at a substrate electrode. For example, the reaction $O + ne \rightarrow R$ occurs at the tip and the reverse reaction occurs at the substrate. This mode of operation is similar to that at the rotating ring-disk electrode.[12] Similar behavior is observed for a pair of side-by-side microband electrodes[13,14] and in thin-layer cells.[15] In the SECM,

TG/SC is usually used in the studies of homogeneous chemical reactions, where the reaction of species R as it transits between tip and substrate causes a decrease in the substrate current (see Chapters 7 and 16). An alternative mode, where the substrate is the generator and tip the collector (SG/TC mode), can also be employed and is used in the studies of reactions at a substrate surface (Chapters 6, 9, 11, and 13). The SG/TC mode was first used to study concentration profiles near an electrode surface without scanning and imaging.[16–18]

The most frequent mode of operation of the SECM is the feedback mode, where only the tip current is monitored. As discussed in the next section, the tip current is perturbed by the presence of a substrate at close proximity by blockage of the diffusion of solution species to the tip (negative feedback) and by regeneration of O at the substrate (positive feedback). This effect allows investigation of both electrically insulating and conducting surfaces and makes possible imaging of surfaces and the reactions that occur there. This mode of operation with surface imaging was first described, along with the apparatus and theory, in a series of papers in 1989.[19–21] It is also possible to carry out the same electrode reaction at the tip and substrate, called the shielding or competitive mode.[22]

1.2 PRINCIPLES OF SECM

1.2.1 Ultramicroelectrodes

An understanding of the operation of the SECM and an appreciation of the quantitative aspects of measurements with this instrument depend upon an understanding of electrochemistry at small electrodes. The behavior of UMEs in bulk solution (far from a substrate) has been the subject of a number of reviews.[23–28] A simplified experimental setup for an electrochemical experiment is shown in Figure 1.1. The solution contains a species, O, at a concentration, c, and usually contains supporting electrolyte to decrease the solution resistance and insure that transport of O to the electrode occurs predominantly by diffusion. The electrochemical cell also contains an auxiliary electrode that completes the circuit via the power supply. As the power supply voltage is increased, a reduction reaction $O + ne \rightarrow R$ occurs at the tip, resulting in a current flow. An oxidation reaction will occur at the auxiliary electrode, but this reaction is usually not of interest in SECM, since this electrode is placed sufficiently far from the UME that products formed at the auxiliary electrode do not reach the tip during the experiment. The potential of the tip electrode is monitored against a stable reference electrode, such as a silver/silver chloride electrode. A plot of the current flowing as a function of the potential of the UME is called a voltammogram; a typical one is shown in

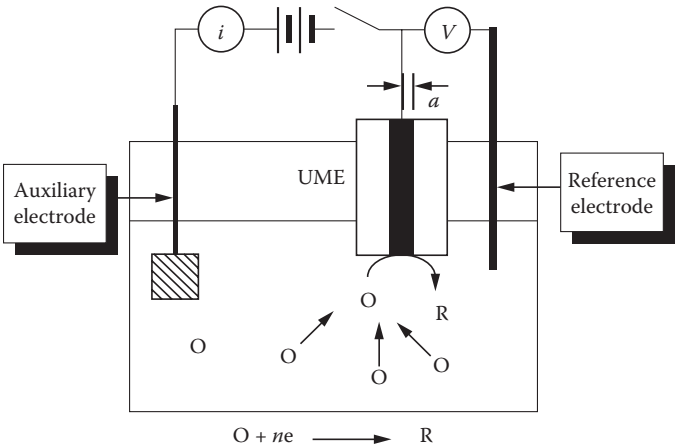


FIGURE 1.1 Schematic diagram of a cell for ultramicroelectrode voltammetry.

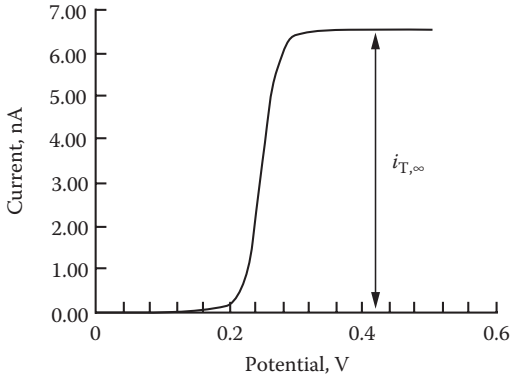


FIGURE 1.2 Typical voltammogram for an ultramicroelectrode.

Figure 1.2. As shown, an S-shaped curve is produced. The current eventually limits to a value that is completely controlled by the rate of mass transfer by diffusion of O from the bulk solution to the electrode surface, where the electrochemical reaction has decreased its concentration to essentially zero. For a conductive disk of radius a in an insulating sheath, this steady-state diffusion-controlled current when the tip is far from a surface is given by

$$i_{T,\infty} = 4nFDca \tag{1.1}$$

where

D is the diffusion coefficient of species O
F is the Faraday

The current at electrodes with other shapes, for example, hemispheres or cones, can be expressed in a similar way, as discussed in Chapter 3, but almost all SECM experiments are carried out with disk-shaped electrodes, because they show the best sensitivity. The current is also relatively independent of the radius of the insulating sheath, r_g, often expressed in the SECM literature as $RG = r_g/a$. Moreover, because the flux of O to a small disk by diffusion, which is $\sim Dc/a$, is quite large, the current is relatively immune to convective effects like stirring in the solution. The current at a small disk also reaches steady state in a relatively short time ($\sim a^2/D$). For example, a 10 μm radius disk will attain steady state in a fraction of a second. These characteristics imply that an UME used as a scanning tip and moved in a solution can be treated as a steady-state system. Finally, because of the small currents that characterize most experiments with UME tips, generally pA to nA, resistive drops in the solution during passage of current are generally negligible.

1.2.2 Feedback Mode

The general principles of the feedback mode are shown in Figure 1.3. As shown in Equation 1.1, the current, $i_{T,\infty}$, is measured at the UME tip when it is far from any surface (A), the subscript, ∞, implying this long distance. In fact, as we shall see, this distance only has to be a few tip diameters. The current under these conditions is driven by the hemispherical flux of species O from the bulk solution to the tip (Figure 1.3A). When the tip is brought near an electrically insulating substrate, like a piece of glass or plastic (Figure 1.3C), the substrate blocks some of the diffusion of O to the tip and the current will decrease compared to $i_{T,\infty}$. The closer the tip gets to the substrate, the smaller i_T becomes. At the limit when the distance between tip and substrate, d, approaches zero, i_T also

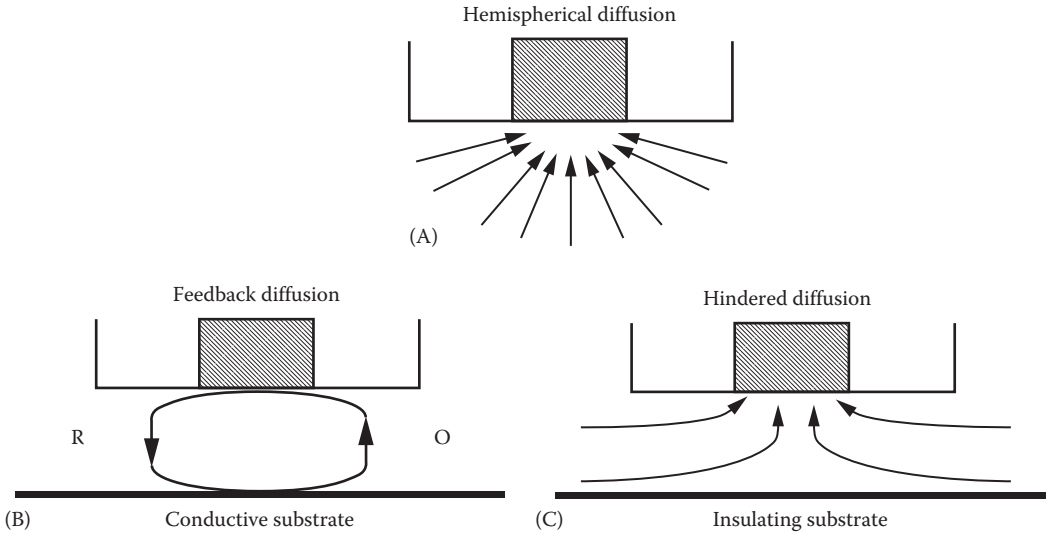


FIGURE 1.3 Basic principles of scanning electrochemical microscopy (SECM): (A) far from the substrate, diffusion leads to a steady-state current, $i_{T,\infty}$; (B) near a conductive substrate, feedback diffusion leads to $i_T > i_{T,\infty}$; and (C) near an insulating substrate, hindered diffusion leads to $i_T < i_{T,\infty}$. (Reprinted from Bard, A.J., Denuault, G., Lee, C., Mandler, D., and Wipf, D.O., *Acc. Chem. Res*., 23, 357, 1990. Copyright 1990 American Chemical Society.)

approaches zero. This decrease in current with distance is called *negative feedback*. When the tip is brought near an electrically conductive substrate, like a platinum electrode, while there is still blockage of diffusion of O to the tip by the substrate, there is also the oxidation of the product R back to O. This O generated at the substrate diffuses to the tip and causes an increase in the flux of O compared with $i_{T,\infty}$. Thus with a conductive substrate $i_T > i_{T,\infty}$. In the limit as d approaches zero, the tip will move into a regime where electron tunneling can occur and the tip current will get very large. This increase of current with distance is called *positive feedback*. A plot of i_T vs. d, as a tip is moved in the Z-direction, is called an *approach curve*.

A quantitative description of approach curves can be obtained by solving the diffusion equations for the situation of a disk electrode and a planar substrate,[16] as discussed in Chapter 5. Typical approach curves for a conductive substrate (essentially infinite rate of regeneration of O from R) and an insulating substrate (zero rate of regeneration of O) are shown in Figure 1.4. These curves are given in dimensionless form by plotting $I_T = i_T/i_{T,\infty}$ (the tip current normalized by the current far from substrate) vs. $L = d/a$ (the tip–substrate separation normalized by the tip radius). Since this plot involves only dimensionless variables, it does not depend upon the concentration or diffusion coefficient of O. From these curves, one can readily find d from the measured I_T and a knowledge of a. The approach curves for an insulator actually depend upon r_g, since the sheath around the conducting portion of the electrode also blocks diffusion, but this effect is not usually important with most practical tips. If the rate constant for electron transfer at the substrate to species O is $k_{b,s}$, the limiting curves represent $k_{b,s} \rightarrow 0$ (insulator) and $k_{b,s} \rightarrow \infty$ (conductor). The approach curves for intermediate values of $k_{b,s}$ can be found (Chapter 5) (Figure 1.5). These are very useful in finding the rate of heterogeneous charge transfer at an interface (see Chapters 6 and 8). In the shielding mode, with the substrate at the same potential as the tip, the current falls away at decreasing distance even faster than pure negative feedback, that is, lies below the curve in Figure 1.4B.[21] General curves for different potentials at the substrate vs. the tip can be given with the behavior changing from shielding to mass transfer controlled positive feedback.

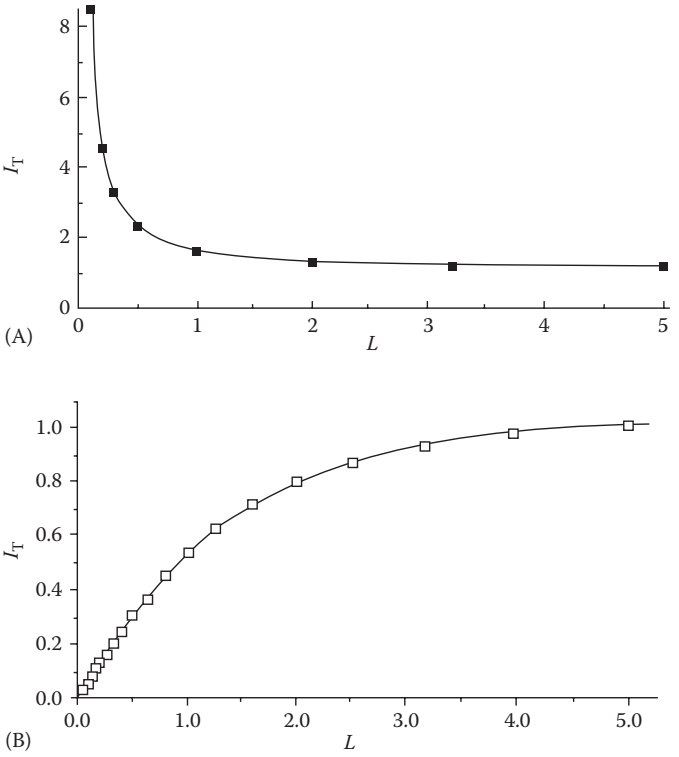


FIGURE 1.4 Diffusion-controlled steady-state tip current as a function of tip–substrate separation. (A) Substrate is a conductor and (B) substrate is an insulator. (From Bard, A.J., Fan, F.-R.F., Mirkin, M.V., *Electroanalytical Chemistry*, Bard, A.J. (Ed.). Marcel Dekker, New York, 1993, 18, pp. 243–373.)

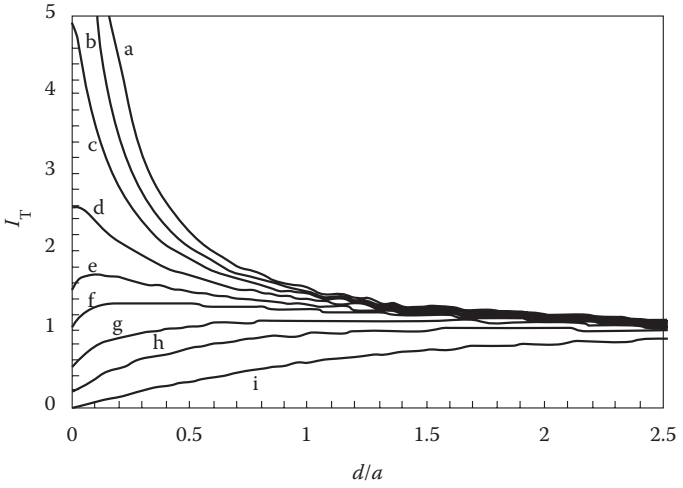


FIGURE 1.5 Approach curves as a function of the heterogeneous reaction rate constant for electron transfer at the substrate, k, $I_T = i_T/i_{T,\infty}$. From top to bottom, k (cm/s) is (a) 1, (b) 0.5, (c) 0.1, (d) 0.025, (e) 0.015, (f) 0.01, (g) 0.005, (h) 0.002, and (i) 0.0001. Curve (a) is identical to that for mass transfer control and curve (i) for an insulating substrate.

1.2.3 Collection–Generation Modes

As discussed earlier, there are two modes of this type. In the TG/SC, the tip is held at a potential where an electrode reaction occurs and the substrate at a different potential where a product of the tip reaction will react and thus be "collected." In most cases, the substrate is considerably larger than the tip, so that the collection efficiency, given by i_S/i_T, where i_S is the substrate current, is essentially 1 (100%) for a stable tip-generated species R. If R reacts on transit from tip to substrate, i_S/i_T becomes smaller, and its change with separation, d, allows determination of the rate constant of the homogeneous reaction (Chapter 7). The TG/SC mode is particularly useful in scanning arrays for screening electrocatalysts. For example, in studying the oxygen reduction reaction, one can generate oxygen at the tip at a constant current and measure how large the substrate current for oxygen reduction (i.e., how much of the oxygen is collected) as a function of substrate potential (Chapter 16).

The alternative mode is the SG/TC mode. In this case, the tip probes the reactions that are occurring on a substrate. For example, a scan in the Z-direction can produce the concentration profile, while a scan over the surface can identify "hot spots" where reactions occur at a higher rate. This can also be used to examine electrocatalysts. Usually in the SG/TC mode, the collection efficiency by the tip is smaller than 1, so the system has to be calibrated with a known mediator couple.

A related method involves the use of the tip reaction to perturb a reaction at a surface; an example of this approach is SECM-induced desorption (SECMID).[29] For example, the adsorption/desorption kinetics of proton on a hydrous metal oxide surface can be studied in an unbuffered solution by bringing the tip near the surface and reducing proton (to hydrogen) at the tip. This causes a local change in pH that results in proton desorption from the surface. The tip current can be used to study the kinetics of proton desorption and diffusion on the surface (Chapter 13).

1.2.4 Transient Methods

Most SECM measurements involve steady-state current measurements. This can be a significant convenience in the measurement of kinetics, even for rapid processes, under conditions where factors like double layer charging and adsorption do not contribute to the observed currents. However, one can also carry out transient measurements, recording i_T as a function of time. This can be of use in measurements of homogeneous kinetics (Chapter 7) and for systems that are changing with time. It can also be used to determine the diffusion coefficient, D, of a species without the knowledge of the solution concentration or number of electrons transferred in the electrode reaction.[30]

Another powerful use of transients involves cyclic voltammetric (potential scans) (CV) at the tip during SECM investigations.[31] CV is also used during the surface interrogation (SI) mode of SECM[32] for studying adsorbed species, such as reaction intermediates, as discussed in Chapter 16.

1.2.5 Fabrication

The SECM can also be used as a tool for modification of surfaces. For example, metals or semiconductors can be etched or metals can be deposited on a surface by passing the tip close to the surface and carrying out an appropriate electrochemical reaction. Two different modes are possible. In the *direct mode*, the tip acts as the counter electrode and the desired electrochemical reaction occurs on the substrate; for example, the etching of Cu occurs on the Cu substrate. Spatial resolution is determined by the current density distribution between tip and substrate. In the *feedback mode*, a reactant is generated at the tip that promotes the reaction on the substrate. For example, Cu can be etched by bromine electrogenerated at the tip. In this case, resolution is determined by the lateral (x–y) diffusion of reactant as it diffuses from tip to substrate. Details of fabrication using SECM are covered in Chapter 15.

1.3 MEDIATORS

The choice of solvent and mediator is based on the chemistry that is being probed. Basically, for interface studies, one form of the mediator, O or R, is a titrant that reacts with the species of interest and selectivity depends on the mediator selected. Water is the usual solvent in SECM, but several studies involve others like acetonitrile or dichloromethane. The mediator couple selected is almost always one with a one-electron Nernstian or kinetically rapid half reaction, and both O and R in the mediator couple should be stable. Choice is usually based on the redox potential and the pH conditions needed. Table 1.1 shows a list of mediator couples in water that span a wide potential range. Because oxygen is reduced at electrodes over a wide potential region, the solutions used are often deaerated before measurements and the cells are maintained under a blanket of inert gas (e.g., Ar). In some studies, for example, of biological systems, oxygen can serve as the tip-reduced species under conditions where negative feedback is expected. In some studies, for example, where ferrocene methanol is used as a mediator, deaeration is not necessary.

1.4 APPLICATIONS OF SECM

The chapters that follow illustrate a wide range of applications of SECM that have appeared. The following is an overview and some examples that might help put the technique in perspective before the detailed treatments:

1. *Imaging*: By scanning the tip in the *x–y* plane and measuring current changes (the *constant height mode*) (or, less frequently, by maintaining a constant current and measuring the changes in *d* in a *constant current mode*), one can obtain topographic images of conducting and insulating substrates (Chapter 4). The resolution of such images is governed by the tip radius, *a*, and *d*. However, by working in the thin film of water that condenses on a mica surface in humid air, it is possible to obtain higher resolution with a conical tip that is only slightly immersed in the water film. Of particular interest is the use of SECM to perform "chemical imaging" and note differences in reaction rates at different locations on a surface. This mode is useful, for example, in studying biological materials (e.g., enzyme sites) (Chapter 11) and in corrosion studies (Chapter 14) where surfaces have active and passive sites. It is also important when scanning arrays of electrocatalysts or photocatalysts and judging their relative activities (Chapter 16).
2. *UME shape characterization*: It is frequently difficult to determine the actual shape of an UME, for example, by the examination by an optical or scanning electron microscope. For example, the conducting portion may be slightly recessed inside the glass mantle or the shape may be that of a cone protruding from the insulator. Electrodes with radii of the order of 1 μm or less are particularly difficult to characterize. Simply determining a voltammogram with the tip in bulk solution is usually not useful in this regard, since almost all UMEs will produce a steady-state wave-shaped voltammogram characteristic of roughly hemispherical diffusion. However by recording an approach curve, i_T vs. d, one can frequently identify recessed tips (where i_T does not increase at small d when the insulator hits the substrate) or tips with shapes different than disks, which show different approach behaviors (Chapter 5).
3. *Heterogeneous kinetics measurements*: As suggested earlier, by recording an approach curve or voltammogram with the tip close to a substrate, one can study the rates of electron transfer reactions at electrode surfaces (Chapter 6). Because mass transfer rates at the small tip electrodes are high, measurements of fast reactions without interference of mass transfer are possible. As a rule of thumb, one can measure k^o values (cm/s) that are of the order of D/d, where D is the diffusion coefficient (cm^2/s). For example, k^o for ferrocene oxidation at a Pt electrode in acetonitrile solution was measured at a 1-μm radius tip at a

TABLE 1.1
Selected Oxidation–Reduction Mediators for Aqueous Solution[a]

Mediator Half Reaction	Formal or Standard Potential (V vs. NHE)
$Ru(bpy)_3^{3+/2+}$	1.27
$Ru(phen)_3^{3+/2+}$	1.22
Br_2/Br^-	1.09
$Fe(phen)_3^{3+/2+}$	1.07
$Fe(bpy)_3^{3+/2+}$	1.07
$IrCl_6^{2-/3-}$	1.00
$Ru(bpy)_2(NH_3)_2^{3+/2+}$	0.88
$Ru(CN)_6^{3-/4-}$	0.86
$Os(bpy)_3^{3+/2+}$	0.84
$Mo(CN)_8^{3-/4-}$	0.77
1,1-Dicarboxylic acid ferrocene	0.64
$Co(oxalate)_3^{3-/4-}$	0.57
$W(CN)_8^{3-/4-}$	0.49
Ferrocene methanol$^{+/0}$	0.44
$Co(phen)_3^{3+/2+}$	0.38
$CoEDTA^{-/2-}$	0.38
$Fe(CN)_6^{3-/4-}$	0.36
$Co(bpy)_3^{3+/2+}$	0.32
1,4-Benzoquinone/hydroquinone	0.28
N,*N*,*N*′,*N*′-Tetramethyl-*p*-phenylenediamine (TMPD)	0.27
$Ru(en)_3^{3+/2+}$	0.18
1,2-Naphthoquinone/napthohydroquinone	0.14
$FeEDTA^{-/2-}$	0.12
$Ru(NH_3)_6^{3+/2+}$	0.05
Methylene blue	0.01
$Co(en)_3^{3+/2+}$	–0.22
Anthraquinone-2-sulfonate/anthrahydroquinone	–0.22
Methyl viologen$^{2+/1+}$	–0.45
Co(sepulchrate)$^{3+/2+}$	–0.54
4,4′-Dimethyl-1,1′-trimethylene-2,2′-bipyridyl	–0.69
$Fe(TEA)_2^{3+/2+}$ (TEA = triethanolamine) (1 M NaOH)	–0.82

Sources: Adapted from Bard, A.J. et al., *The Handbook of Surface Imaging and Visualization*, Hubbard, A.T. (Ed.), CRC Press, Boca Raton, FL, 1995, pp. 667–679. Other listings of potential mediator compounds are listed in this reference and also in Zoski, C.G. (Ed.), *Handbook of Electrochemistry*, Elsevier, Amsterdam, the Netherlands, 2007, Chap. 18.

[a] pH ~ 7, unless otherwise noted, but many of these can be used at more acidic pH as well.

"*d*" of about 0.1 µm yielded a value of 3.7 cm/s.[33] The use of small tips and small currents decreases any interferences from uncompensated resistance effects.

4. *Measurements of homogeneous kinetics*: Rate constants for homogeneous reactions of tip-generated species as they transit between tip and conducting substrate can be determined from steady-state feedback current or TG/SC experiments or by transient measurements (Chapter 7). Generally, rate constants can be measured if the lifetime of the species of

interest is of the order of the diffusion time between tip and substrate, $d^2/2D$. Thus first-order reaction rate constants up to about 10^5 s^{-1} and second-order reaction rate constants up to about 108 M^{-1} s^{-1} are accessible.

5. *Biological systems*: There have been a number of applications of SECM to biological systems (Chapters 11 and 12). These include imaging of living cells, studies of enzymatic reactions, and oxygen evolution on leaf surfaces. SECM has also been applied in investigations of the transport of species through skin (Chapter 9). Because SECM is capable of monitoring a wide range of chemical species with good specificity and high spatial resolution, it finds wide application in studies of living organisms (e.g., bacteria, yeast) and isolated tissues and cells (e.g., mammalian HeLa). Potential applications include toxicological studies, quorum sensing, and antibiotic resistance mechanisms.
6. *Liquid–liquid interfaces*: There is considerable interest in ion and electron transfer processes at the interface between two immiscible electrolyte solutions (ITIES), for example, water and 1,2-dichloroethane. SECM can be used to monitor such processes (Chapter 8). It allows one to separate ion transport from electron transfer and is relatively insensitive to the resistance effects often found with more conventional (four-electrode) electrochemical measurements.
7. *Membranes and thin films*: Different types of films on solid surfaces (e.g., polymers, AgBr) and membranes separating solutions have been examined by SECM (Chapters 6 and 9). SECM is a powerful technique for examining transport through membranes, with the ability to scan the surface to locate positions of different permeabilities. It has also been used with polymer films, for example, polyelectrolytes or electronically conductive polymers, to probe the counter ion (dopant) flux during redox processes. SECM can be particularly useful in probing film thickness as a film is grown on a surface.[34] SECM is unique in its ability to probe inside some thin films and study species and electrochemical processes within the films.[35,36] For example, consider the tip current vs. z-displacement curve as a conical tip (30 nm radius, 30 nm height) is moved from a solution of 40 mM $NaClO_4$ into a nominally 2000 Å thick Nafion film containing $Os(bpy)_3^{2+}$ on a glass/ITO substrate (Figure 1.6).[26] The tip was held at 0.80 V vs. SCE where $Os(bpy)_3^{2+}$ is oxidized to the 3+ form at a diffusion-controlled rate. The different stages of penetration of the tip into the film from initial contact to tunneling at the ITO can clearly be seen and the film thickness can be established. Moreover, with the tip at position c, a voltammogram can be recorded (Figure 1.7). From such a voltammogram, one can determine the diffusion coefficient of $Os(bpy)_3^{2+}$ and information about the kinetics and thermodynamics of the reaction occurring in the film. SECM is also useful in examining the behavior of self-assembled monolayers (SAMs).
8. *Surface reactions*: Measurements of the rates of surface reactions on insulator surfaces, such as dissolution, adsorption, and surface diffusion, are possible (Chapter 13). For example, proton adsorption on an oxide surface could be studied by using the tip to reduce proton and induce a pH increase near the surface.[29] Then, by following the tip current with time, information about proton desorption kinetics could be obtained. Studies of corrosion reactions are also possible (Chapter 14). Indeed, work has been reported where a tip-generated species has initiated localized corrosion and then SECM feedback imaging has been used to study it.[37] Thus in these types of studies, the tip is used both to perturb a surface and then follow changes with time.
9. *Electrocatalysts*: One can screen arrays for electrochemical activity using SECM. This rapid screening along with rapid array preparation is an excellent way to test very rapidly a large number of compositions. As described in Chapter 16, several different SECM modes can be employed. This approach has been used, for example, with oxygen reduction, water oxidation, and methanol oxidation electrocatalysts.
10. *Semiconductor surfaces*: SECM has been used to probe heterogeneous electron transfer reaction kinetics on a number of semiconductor electrodes. In these studies, as in studies

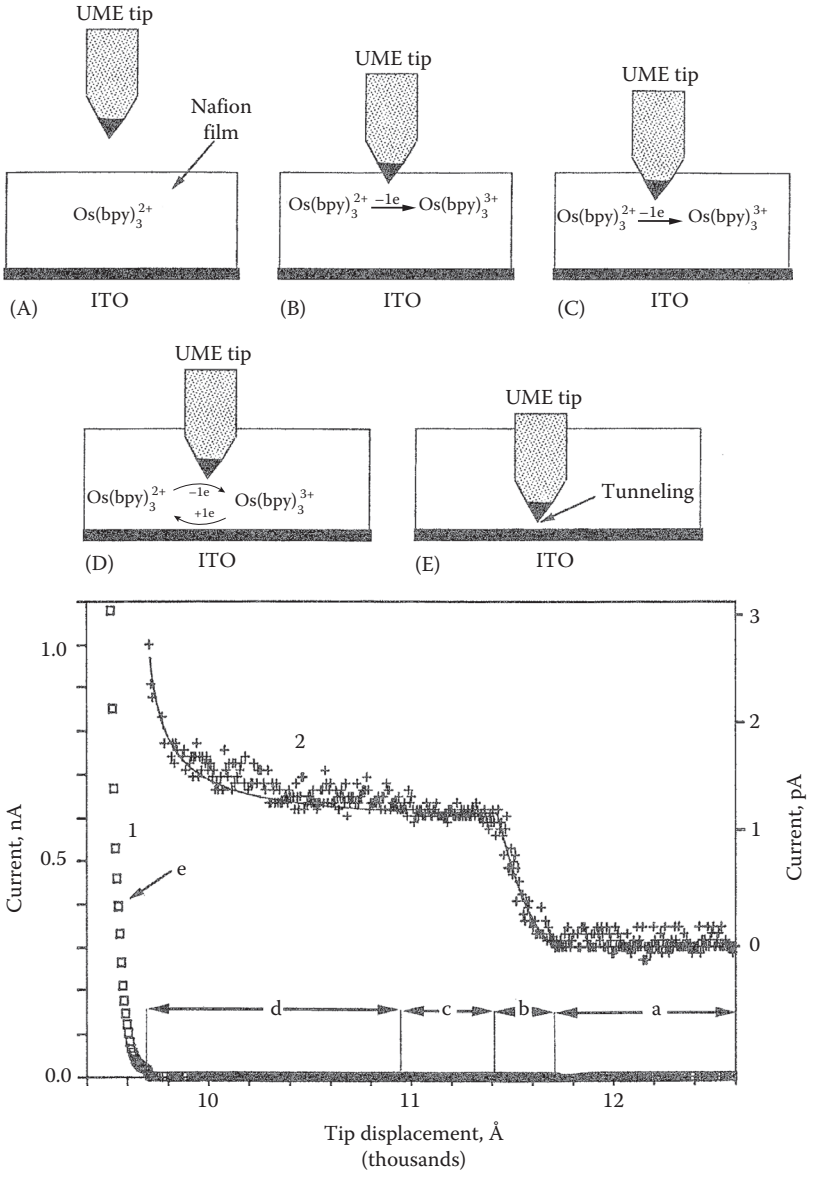


FIGURE 1.6 (Top) Scheme representing five stages of the SECM current–distance experiment. (A) The tip is positioned in the solution close to the Nafion coating. (B) The tip has penetrated partially into Nafion and the oxidation of $Os(bpy)_3^{2+}$ occurs. The effective tip surface grows with penetration. (C) The entire tip electrode is in the film but is not close to the ITO substrate. (D) The tip is sufficiently close to the substrate to observe positive SECM feedback. (E) The tunneling region. (Bottom) Dependence of the tip current vs. distance. The letters a–e correspond to the five stages A–E described earlier. The displacement values are given with respect to an arbitrary zero point. The current observed during the stages a–d is much smaller than the tunneling current and therefore cannot be seen on the scale of curve 1 (the left-hand scale). Curve 2 is at higher current sensitivity to show the current–distance curve corresponding to stages a–d (the right-hand current scale). The solid line is computed for a conically shaped electrode with a height, $h = 30\,\text{nm}$, and a radius, $r_0 = 30\,\text{nm}$ for zones a–c, and SECM theory for zone d. The tip was biased at 0.80 V vs. SCE, and the substrate at 0.20 V vs. SCE. The tip moved at a rate of 30 Å/s. (From Mirkin, M.V., Fan, F.-R.F., Bard, A.J., *Science*, 257, 364, 1992.)

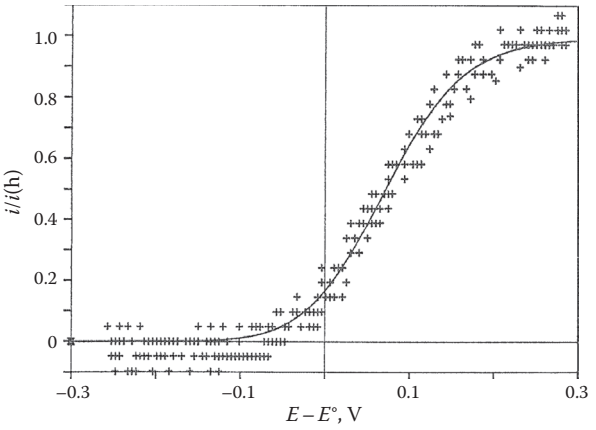


FIGURE 1.7 Voltammogram at a microtip electrode partially penetrating a Nafion film containing 0.57 M $Os(bpy)_3^{2+}$. Scan rate, $v = 5$ mV/s. The substrate was biased at 0.2 V vs. SCE. The solid line is computed with a heterogeneous rate constant, $k^\circ = 1.6 \times 10^{-4}$ cm/s and $D = 1.2 \times 10^{-9}$ cm^2/s. (From Mirkin, M.V., Fan, F.-R.F., Bard, A.J., *Science*, 257, 364, 1992.)

at the liquid–liquid interface, the use of a separate metal probe electrode is useful in freeing the measured response from resistance effects. It also allows one to examine differences in behavior at different points on a surface. These are described in Chapter 16, as well as studies of arrays of photocatalysts for finding optimal compositions for photoelectrochemical reactions. As discussed in Chapter 15 on applications to fabrication, SECM has also been used to etch semiconductor surfaces and study the nature of the etching reactions.

11. *Electrochemistry in small volumes of solution*: Because of its ability to position an electrode tip with high spatial resolution in three dimensions, SECM can be used to probe electrochemistry in a small volume of liquid (e.g., on a conductive substrate that serves as a counter/reference electrode). For example, a 3–20 μL volume of solution was used to probe the adsorption isotherms on a mineral surface.[38] Probing even smaller volumes, for example, of liquids contained in pores, should be possible. Since electrochemical generation is an ideal method of producing small, controlled, amounts of reactants, studies where one wants to probe chemistry with very limited amounts of sample appear to be a good application. In such studies, means to maintain the sample volume and prevent evaporation, for example, by close control of the humidity or using an overlayer of an immiscible liquid, will be required. Volumes in picoliter (pL) can also be examined by positioning two tips. This configuration allows, for example, studies of reaction kinetics of two different species, electrogenerated at each tip in the gap.[39]
12. *Thin liquid layers*: The SECM has been used to form thin liquid layers and probe electrochemical reactions in them. When the tip is pushed through the interface between two immiscible liquids, for example, through an aqueous layer above a layer of mercury or a layer of benzene above an aqueous layer, a thin film (several hundred nm to a few μm) of the top liquid layer is trapped on the surface of the tip.[40–42] Electrochemical measurements can be used to probe reactions in this layer. This approach is useful, with the water–Hg interface, to form and trap very small volumes (zL) of solution with small amounts, down to single molecules, of an electroactive species.[43] Another type of thin layer that has been studied is the one that forms on a surface when exposed to humid air. In this case, a water layer that can be as thin as a few nm forms on a hydrophilic surface (e.g., mica). The SECM tip can probe into this layer, although studies have mainly been aimed so far at imaging rather than investigating the properties of the layer (Chapter 4).

13. *Potentiometry*: While most SECM studies are carried out with amperometric tips that drive a Faradaic (electron transfer) reaction, it is also possible to use potentiometric tips that produce a potential change in response to concentration changes of species. These are usually typical ion-selective electrode tips, although other types, such as Sb tips for pH detection have been described.[44] Probes of this type and their applications are discussed in Chapter 10. They are particularly useful for studies of species that do not show electroactivity, like Na^+, K^+, and Ca^{2+}. Note, however, that ions of this type can alternatively be determined in an amperometric mode by the use of micropipette electrodes that respond to the transport of ions across an interface between two immiscible liquids.[45,46]
14. *Fabrication*: A variety of studies have now been done that demonstrate that the SECM can carry out metal deposition, metal and semiconductor etching, polymer formation, and other surface modifications with high resolution. Such processes are discussed in Chapter 15. These SECM approaches have the advantage over analogous STM procedures in that the conditions of deposition or etching are usually known and well-defined, based on electrochemical studies at larger electrodes.

REFERENCES

1. Bard, A. J., Fan, F.-R. F., Pierce, D. T., Unwin, P. R., Wipf, D. O., Zhou, F. Chemical imaging of surfaces with the scanning electrochemical microscope. *Science* 1991, 254, 68–74.
2. Bard, A. J., Fan, F.-R. F., Mirkin, M. V. Scanning electrochemical microscopy. In *Electroanalytical Chemistry*, Bard, A. J. (Ed.). Marcel Dekker, New York, 1993, Vol. 18, pp. 243–373.
3. Arca, M., Bard, A. J., Horrocks, B. R., Richards, T. C., Treichel, D. A. Advances in scanning electrochemical microscopy. *Analyst* 1994, 119, 719–726.
4. Mirkin, M. V. High resolution studies of heterogeneous processes with the scanning electrochemical microscope. *Mikrochim. Acta* 1999, 130, 127–153.
5. Bard, A. J., Fan, F.-R. F., Mirkin, M. V. Scanning electrochemical microscopy. In *The Handbook of Surface Imaging and Visualization*, Hubbard, A. T. (Ed.). CRC Press, Boca Raton, FL, 1995, pp. 667–679.
6. Bard, A. J., Fan, F.-R. F., Mirkin, M. V. Scanning electrochemical microscopy. In *Physical Electrochemistry: Principles, Methods and Applications*, Rubinstein, I. (Ed.). Marcel Dekker, New York, 1995, pp. 209–242.
7. Amemiya, S., Bard, A. J., Fan, F.-R. F., Mirkin, M. V., Unwin, P. R. Scanning electrochemical microscopy. In *Annual Review of Analytical Chemistry*, Yeung, E. S., Zare, R. N. (Eds.). Annual Reviews, Palo Alto, CA, 2008, pp. 95–131.
8. Laforge, F. O., Sun, P., Mirkin, M. V. Physicochemical applications of scanning electrochemical microscopy. *Adv. Chem. Phys*. 2008, 139, 177–244.
9. Sun, P., Laforge, F. O., Mirkin, M. V. Scanning electrochemical microscopy in the 21st century. *Phys. Chem. Chem. Phys*. 2007, 9, 802–823.
10. Wipf, D. O. Scanning electrochemical microscopy. *Charact. Mater*. 2003, 1, 636–652.
11. Fan, F.-R. F., Fernandez, J., Liu, B., Mauzeroll, J. Scanning electrochemical microscopy. In *Handbook of Electrochemistry*, Zoski, C. G. (Ed.). Elsevier, Amsterdam, the Netherlands, 2007, Chap. 12, pp. 471–540.
12. Bard, A. J., Faulkner, L. R. *Electrochemical Methods*. Wiley, New York, 1980, p. 298.
13. Amatore, C. Electrochemistry at ultramicroelectrodes. In *Physical Electrochemistry: Principles, Methods and Applications*, Rubinstein, I. (Ed.). Marcel Dekker, New York, 1995, Chap. 4.
14. Bard, A. J., Crayston, J. A., Kittlesen, G. P., Shea, T. V., Wrighton, M. S. Digital simulation of the measured electrochemical response of reversible redox couples at microelectrode arrays: Consequences arising from closely spaced ultramicroelectrodes. *Anal. Chem*. 1986, 58, 2321.
15. Hubbard, A. T., Anson, F. C. The theory and practice of electrochemistry with thin layer cells. In *Electroanalytical Chemistry*, Bard, A. J. (Ed.). Marcel Dekker, New York, 1970, Vol. 4, pp. 129–214.
16. Engstrom, R. C., Weber, M., Wunder, D. J., Burgess, R., Winquist, S. Measurements within the diffusion layer using a microelectrode probe. *Anal. Chem*. 1986, 58, 844.
17. Engstrom, R. C., Meaney, T., Tople, R., Wightman, R. M. Spatiotemporal description of the diffusion layer with a microelectrode probe. *Anal. Chem*. 1987, 59, 2005.

18. Engstrom, R. C., Wightman, R. M., Kristensen, E. W. Diffusional distortion in the monitoring of dynamic events. *Anal. Chem*. 1988, 60, 652.
19. Bard, A. J., Fan, F.-R. F., Kwak, J., Lev, O. Scanning electrochemical microscopy. 1. Introduction and principles. *Anal. Chem*. 1989, 61, 132.
20. Kwak, J., Bard, A. J. Scanning electrochemical microscopy. 2. Theory of the feedback mode. *Anal. Chem*. 1989, 61, 1221.
21. Kwak, J., Bard, A. J. Scanning electrochemical microscopy. 4. Apparatus and two-dimensional scans of conductive and insulating substrates. *Anal. Chem*. 1989, 61, 1794.
22. Zoski, C. G., Aguilar, J. C., Bard, A. J. Scanning electrochemical microscopy. 46. Shielding effects on reversible and quasireversible reactions. *Anal. Chem*. 2003, 75(13), 2959–2966.
23. Wightman, R. M., Wipf, D. O. Electrochemistry at ultramicroelectrodes. In *Electroanalytical Chemistry*, Bard, A. J. (Ed.). Marcel Dekker, New York, 1989, Vol. 15, pp. 267–353.
24. Montenegro, M. I., Queirós, M. A., Daschbach, J. L. (Eds.). *Microelectrodes: Theory and Applications*. Kluwer Academic Publishers, Dordrecht, the Netherlands, 1991.
25. Heinze, J. Ultramicroelectrodes in electrochemistry. *Angew. Chem. Int. Ed*. 1993, 32, 1268–1288.
26. Forster, R. J. Microelectrodes: New dimensions in electrochemistry. *Chem. Soc. Rev*. 1994, 23, 289–297.
27. Zoski, C. G. Steady-state voltammetry. In *Modern Techniques in Electroanalysis*, Vanysek, P. (Ed.). Wiley-Interscience, New York, 1996, Chap. 6.
28. Zoski, C. G. Ultramicroelectrodes: Design, characterization, fabrication. *Electroanalysis* 2002, 14, 1041–1051.
29. Unwin, P. R., Bard, A. J. Scanning electrochemical microscopy. 14. Scanning electrochemical microscope induced desorption: A new technique for the measurement of adsorption/desorption kinetics and surface diffusion rates at the solid/liquid interface. *J. Phys. Chem*. 1992, 96, 5035.
30. Denuault, G., Mirkin, M. V., Bard, A. J. Direct determination of diffusion coefficients by chronoamperometry at microdisk electrodes. *J. Electroanal. Chem. Interfacial Electrochem*. 1991, 308, 27.
31. Schrock, D. S., Wipf, D. O., Baur, J. E. Feedback effects in combined fast-scan cyclic voltammetry-scanning electrochemical microscopy. *Anal. Chem*. 2007, 79, 4931–4941.
32. Rodríguez-López, J., Alpuche-Avilés, M. A., Bard, A. J. Interrogation of surfaces for the quantification of adsorbed species on electrodes: Oxygen on gold and platinum in neutral media. *J. Am. Chem. Soc*. 2008, 130, 16985–16995.
33. Mirkin, M. V., Richards, T. C., Bard, A. J. Scanning electrochemical microscopy. 20. Steady-state measurements of the fast heterogeneous kinetics in the ferrocene/acetonitrile system. *J. Phys. Chem*. 1993, 97, 7672.
34. Wei, C., Bard, A. J. Scanning electrochemical microscopy. 29. In situ monitoring of thickness changes of thin films on electrodes. *J. Electrochem. Soc*. 1995, 142, 2523.
35. Mirkin, M. V., Fan, F.-R. F., Bard, A. J. Direct electrochemical measurements inside a 2000 Angstrom thick polymer film by scanning electrochemical microscopy. *Science* 1992, 257, 364.
36. Pyo, M., Bard, A. J. Scanning electrochemical microscopy. 35. Determination of diffusion coefficients and concentrations of $Ru(NH_3)_6^{3+}$ and methylene blue in polyacrylamide films by chronoamperometry at ultramicrodisk electrodes. *Electrochim. Acta* 1997, 42, 3077.
37. Wipf, D. Initiation and study of localized corrosion by scanning electrochemical microscopy. *Colloids Surf. A* 1994, 93, 251.
38. Unwin, P. R., Bard, A. J. Ultramicroelectrode voltammetry in a drop of solution: A new approach to the measurement of adsorption isotherms at the solid–liquid interface. *Anal. Chem*. 1992, 64, 113.
39. Wang, Q., Rodríguez-López, J., Bard, A. J. Evaluation of the chemical reactions from two electrogenerated species in picoliter volumes by scanning electrochemical microscopy. *ChemPhysChem* 2010, 11, 2969–2978.
40. Mirkin, M. V., Bard, A. J. Scanning electrochemical microscopy. 18. Thin layer cell formation with a mercury pool substrate. *J. Electrochem. Soc*. 1992, 139, 3535.
41. Wei, C., Bard, A. J., Mirkin, M. V. Scanning electrochemical microscopy. 31. Application of SECM to the study of charge transfer processes at the liquid/liquid interface. *J. Phys. Chem*. 1995, 99, 16033.
42. Tsionsky, M., Bard, A. J., Mirkin, M. V. Scanning electrochemical microscopy. 34. Potential dependence of the electron-transfer rate and film formation at the liquid/liquid interface. *J. Phys. Chem*. 1996, 100, 17881.
43. Sun, P., Mirkin, M. V. Electrochemistry of individual molecules in zeptoliter volumes. *J. Am. Chem. Soc*. 2008, 130, 8241–8250.

44. Horrocks, B. R., Mirkin, M. V., Pierce, D. T., Bard, A. J., Nagy, G., Toth, K. Scanning electrochemical microscopy. 19. Ion-selective potentiometric microscopy. *Anal. Chem*. 1993, 65, 1213.
45. Solomon, T., Bard, A. J. Scanning electrochemical microscopy. 30. The application of glass micropipet tips and electron transfer at the ITIES for SECM imaging. *Anal. Chem*. 1995, 67, 2787.
46. Shao, Y., Mirkin, M. V. Voltammetry at micropipet electrodes. *Anal. Chem*. 1998, 70, 3155.
47. Bard, A. J., Denuault, G., Lee, C., Mandler, D., Wipf, D. O. Scanning electrochemical microscopy: A new technique for the characterization and modification of surfaces. *Acc. Chem. Res*. 1990, 23, 357.
48. Zoski, C. G. (Ed.). Electrode potentials. *Handbook of Electrochemistry*, Elsevier, Amsterdam, the Netherlands, 2007, Chap. 18.

2 Instrumentation

Fu-Ren F. Fan, Allen J. Bard, and Peixin He

CONTENTS

2.1 Basic SECM Apparatus 15
2.2 SECM Cells and Electrode Setup 18
2.3 Methods and Operation Modes 19
2.3.1 Amperometric Methods 19
2.3.2 Potentiometric Methods 20
2.3.3 AC Impedance Method 21
2.A Appendix: Typical SECM Modes in CH Series 900 SECM 21
2.A.1 Probe Scan Curve 21
2.A.2 Probe Approach Curve 22
2.A.3 Surface Patterned Condition 22
2.A.4 SECM (Imaging) 22
References 23

With scanning electrochemical microscopy (SECM) becoming a widely used and mature technique, with a wide range of applications, many in fields outside of fundamental or applied electrochemistry, relatively few researchers construct their own instruments. Thus, we will not deal with homebuilt instruments in this chapter. Those interested in constructing an SECM are referred to a chapter that goes into details about the basics of this in the first edition of this book.[1] A number of companies have commercialized SECM instrumentation (Table 2.1). Thus in this chapter we will discuss, as an example, the operation of a commercial SECM, the CH Instruments model series 900, which is the most frequently used instrument. Information about the other instruments can be obtained from the manufacturers or their websites. Some practical aspects of cell construction and using a commercial SECM are also addressed.

2.1 BASIC SECM APPARATUS

A diagram of the SECM instrument is shown in Figure 2.1. The SECM positioning system includes the positioning elements, translation stages, and motor controllers. The data acquisition system, which starts with the bipotentiostat to control the tip and substrate potentials, measures and amplifies the tip current and converts it to a voltage. After amplification, the signal is acquired with an analog-to-digital converter (ADC) and stored in the computer, which is also used to send out (through the interface modules) the controlling signals for the potentiostat and controllers for positioning elements and translation motors. Computer software is required to control the positioning and data acquisition system as well as to display and analyze the SECM data. Other important accessories of an SECM are the probe mount system and electrochemical cells, which will be described in the following sections for different experiments. No special antivibration table is required when the tip size and image resolution are above a few 100 nm. However, a vibration isolation system is required for high-resolution ($d < 100$ nm) SECM experiments. Various vibration isolation systems are described in the scanning probe literature. A simple one consists of

TABLE 2.1
Commercial SECM Instruments

Company	Resolution Positioning System (nm)	Current Range	Accessories
CH Instruments http://www.chinstruments.com/chi900.shtml	1.6	1 pA–0.25 A	Jet dispensing device
Sensolytics http://silverstripe.sensolytics.de/secm/	20	10 pA–10 mA	Shear force
HEKA http://www.heka.com/chem/equipment/elpro_possystem.html	10	100 pA–2 A	Shear force, inverted microscope
Princeton Applied Research http://www.princetonappliedresearch.com/Our-Products/Surface-Imaging-and-Scanning-Instruments/SECM370-Scanning-Electrochemical-Microscope-System.aspx	8	1 nA–10 mA	Scanning droplet system, noncontact surface profiling
Uniscan http://www.uniscan. com/electrochemistry-instruments/scanning_electrochemical_microscope/	8	1 nA–10 mA	Scanning droplet system, noncontact surface profiling
Windsor Scientific Limited http://www.windsorscientific.co.uk/index.php?main_id=54 &page_id=62	<1	1 pA–10 mA	SECM-AFM

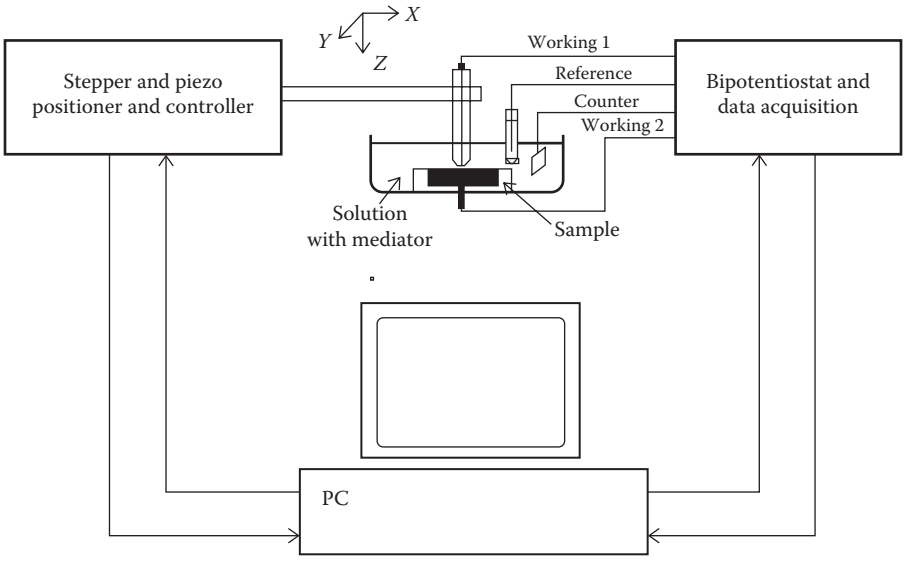


FIGURE 2.1 Diagram of the scanning electrochemical microscope.

a concrete slab supported on a stand by three elastic (bungee) cords. A piece of soft plastic on the slab under the SECM stand is often also used. For experiments sensitive to oxygen or moisture, for example, in nonaqueous solutions, the entire SECM can be set up in a controlled inert gas chamber.

An illustration showing translators, tip, cell, and cell mount for the commercially available CH Instruments model 920C SECM is shown in Figure 2.2 as an example.

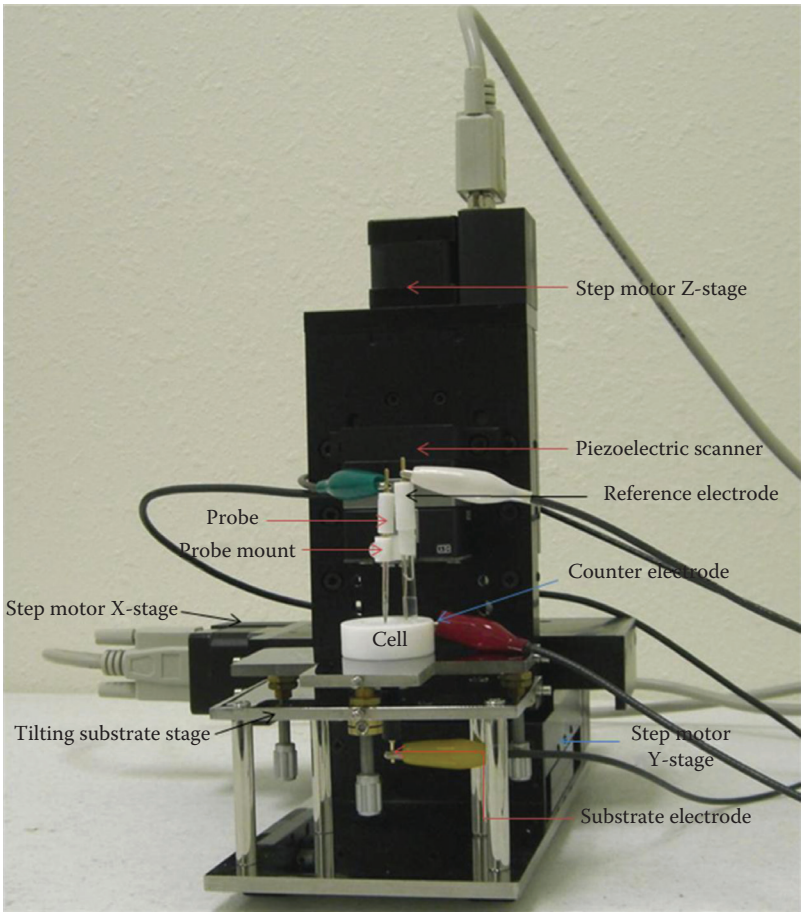


FIGURE 2.2 Illustration showing translators, tip, cell, and cell mount for the commercially available CH Instruments model 920C SECM.

The CH Instruments model 920C SECM includes the cell and the probe positioner as well as a computer, a motor controller, and a bipotentiostat/galvanostat. Lateral probe scans as large as 5.0 cm (8 nm resolution) are accomplished by two stepper motors driving crossed-roller-bearing translator stages. Vertical motion is provided by mounting the probe directly onto the tip holder on a three-axis piezoelectric scanner (for model 900B, 910B, or 920C), which is mounted on the Z-stage driven by the third motor. A three-axis piezoelectric scanner can be used for fine positioning and scanning (total range 85–100 μm; 1.8 nm resolution); this eliminates the effect of the step movement of the stepper motor and thus provides smooth movement. The electrochemical cell is stationary and mounted on an adjustable tilting platform, which can compensate for the substrate tilt. Open-loop motor control is used, and software calibration corrects scan rate, axis, and direction-dependent effects on the probe motion.

The data acquisition system and bipotentiostat/galvanostat of the CH series 900 SECM are microprocessor based and communicate with the PC controller via a serial data link. The bipotentiostat/galvanostat is suitable for analytical voltammetry with tip and substrate potentials up to ±10 V and a compliance voltage of ±12 V and potentiostat rise time of 0.6 μs. The current measurement sensitivity is in the pA range (resolution <0.01 pA). Adjustable second-order Bessel filters provide noise reduction and prevent aliasing by the ADC, which has at least 16 bits of resolution. The software for the model series 900 SECM runs on the Windows operating system and provides

all the controls necessary for positioning the probe in three dimensions and setting parameters for various electrochemical techniques. The software also supports a wide range of different electrochemical experiments (e.g., square wave voltammetry (SWV), differential pulse voltammetry (DPV), AC impedance (IMP), open circuit potential–time (OCP-t), and others), graphical displays, and data processing.

During probe scanning, either amperometric or potentiometric signal can be recorded. Other software features include a probe approach curve routine that automatically stops the probe when the current reaches a set level and that automatically slows the speed of approach as the probe approaches the substrate surface, helping to prevent crashing the tip.

SECM imaging is normally operated at constant height mode, but imaging at potentiometric, constant current and impedance modes are also possible. Graphics output during imaging and post scan is by gray-scale plots, color-coded plots, or interactive 3D plots. Further data and graphical manipulation must be done outside the main program with commercially available software packages. Closed-loop or shear force–based positioning systems are also available in almost all commercially available apparatus. Some specialized terms used in its techniques are listed and explained in the appendix.

2.2 SECM CELLS AND ELECTRODE SETUP

Figure 2.3A is a versatile cell used in CH series 900 SECM, which can easily be dissembled for cleaning and substrate polishing or replacement. The cell is circular in cross section and machined out of a Teflon rod. The bottom section seats into an adjustable 1/4 in. thick stainless steel or aluminum tilting platform to compensate for the substrate tilt. Cylindrical substrates are introduced into the cell via a circular hole in the cell bottom. By press-fitting the sample into the cell hole, the lubricity of the Teflon is often sufficient to provide a leak-free seal. If required, a better seal is achieved by wrapping the substrate with Teflon tape before insertion. The substrate for use in this cell can be machined to fit into the bottom opening. Commercially available electrodes are also accommodated in this cell by changing the bottom hole size to accept the

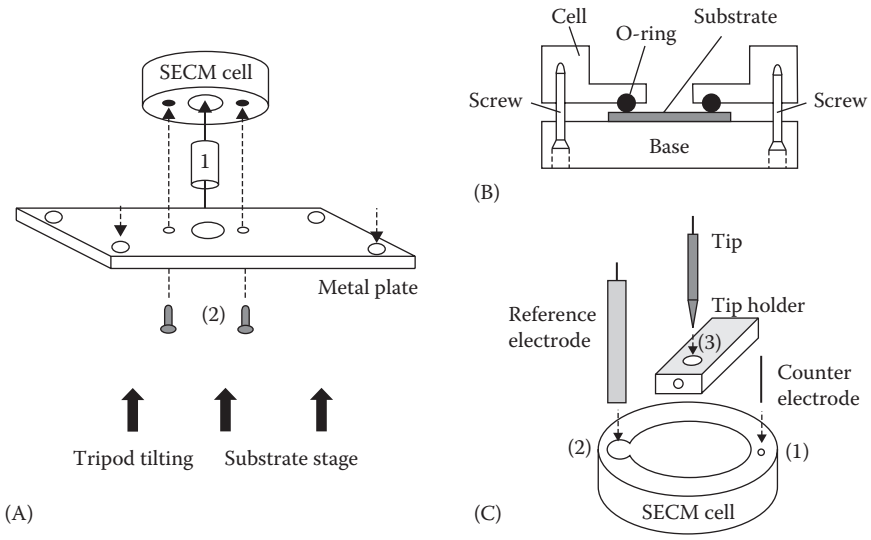


FIGURE 2.3 (A) Schematic of the SECM cell assembly: (1) inserting the substrate electrode in the SECM cell and (2) screwing the cell onto the SECM metal plate. (B) SECM cell for flat substrate. (C) Schematic of electrode setup.

electrode. Alternately, several different diameters of substrate can be accommodated by using Teflon or Viton O-rings to fit the cell and substrate. Irregular substrates can be potted in epoxy to cast cylindrical rods for insertion into the hole; however, the epoxy should be checked for chemical attack in extreme pH or nonaqueous solution. Figure 2.3B shows a SECM cell for flat substrate. Special cells and stands can be constructed for mounting on an optical microscope or for illumination from below.

2.3 METHODS AND OPERATION MODES

Only several commonly used SECM methods and operation modes are briefly described in the following sections. Different methods are listed and available in commercially available SECMs. The operational principles and practical procedures for each technique are described in the other chapters.

2.3.1 Amperometric Methods

SECM amperometric methods are based on the measurement of electrode currents (tip and substrate, i_T and i_S, respectively) as a function of various parameters, including tip–substrate distance (d) and tip or substrate potentials (E_T or E_S). With any system studied (e.g., an electrode, an inert surface, a catalyst, or a living organism), the probe tip is a necessary component to perform any SECM experiment. In all cases, the amperometric tip is an ultramicroelectrode (UME) that can be positioned in close proximity to another surface. Technically, there are two major steady-state amperometric techniques: feedback and generation/collection modes. Unlike the feedback mode where only the tip current is monitored, it is also possible to carry out the same electrode reaction at the tip and substrate, called the shielding or competitive mode.[2] In the feedback mode, under steady-state conditions, the i_T as a function of d is called the approach curve (one of the most commonly used SECM techniques) that allows one to get a precise value of d when the electrode reactions are diffusion controlled. Both positive and negative feedback effects have been theoretically treated and it is possible to correlate the experimental approach curves to analytical equations to determine accurately the position of the tip with respect to the substrate surface. Furthermore, approach curves recorded over a conducting substrate provide an additional measurement of the effective radius of the UME tip, while those recorded over insulators provide information about the effective outer radius of the insulating sheath of the tip with respect to its radius. Thus, this type of experiment is very useful for the characterization of SECM tips. The approach curve can also provide information about the actual shape of the electrode (i.e., disk, hemisphere, and cone) and also signal when the electrode is recessed in the insulating sheet.

Most SECM measurements involve steady-state current measurements, for example, steady-state cyclic voltammetry (CV). However, one can also carry out transient measurements, recording the i_T as a function of time at a fixed E_T, for example, chronoamperometry or with fast scan CV. Another interesting and powerful SECM operation mode involving transient measurements is the surface interrogation (SI) mode (discussed in detail in Section 16.4).[3] In SI-SECM mode, a SECM tip generates a titrant from a reversible redox mediator that reacts chemically with an electrogenerated or chemically adsorbed species at a substrate of about the same size as the tip, which is positioned at a short distance from it (ca.1 μm). The reaction between the titrant and the adsorbate provides a transient positive feedback loop until the adsorbate is consumed completely. As shown schematically in Figure 2.4, the sensing mechanism is provided by the contrast between positive and negative feedbacks, which allows a direct quantification of the charge neutralized at the substrate.

Another useful feature for an SECM is provision for a potential program that can allow one to clean the tip before a scan, for example, by steps to very positive potentials, followed by steps to negative potentials, and finally to the starting potential.

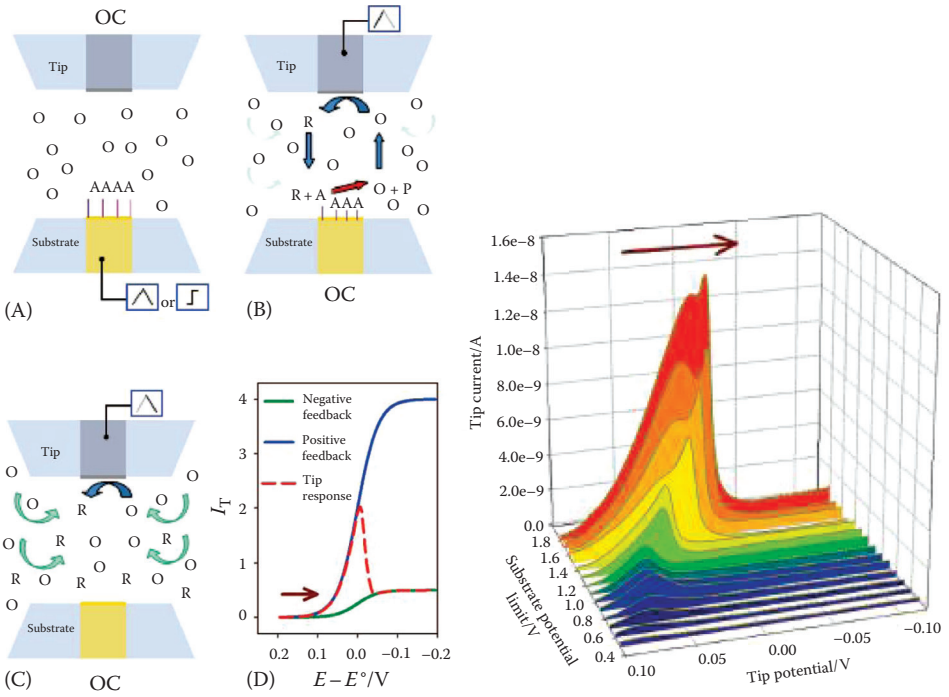


FIGURE 2.4 Left: Schematics of the proposed mechanism and the experimental sequence for the surface interrogation. (A) A reactive species is chemically or electrochemically adsorbed at the substrate upon a potential scan or step while the tip is at open circuit. (B) The substrate is taken to open circuit, and the tip generates the titrant, which reacts at the surface of the substrate to support positive feedback at the same tip. (C) Upon consumption of the adsorbate at the substrate, the tip experiences negative feedback. (D) Expected current response at the tip following the events depicted in panels (A)–(C) for an arbitrary electrode setup. Right: Typical results of the quantification of adsorbed oxygen on gold at neutral pH at different potentials of operation of the substrate electrode. The tip interrogates producing the titrant through CV.

2.3.2 Potentiometric Methods

A standard one-electrode configuration for potentiometric measurements consists of the potentiometric electrode connected to a voltage follower and the reference electrode connected to electrical ground. To improve noise level and drift, a differential potentiometric mode can be employed in a three-electrode configuration consisting of the SECM potentiometric probe and two independent external references. For example, the potential difference between the potentiometric probe and a large inert Pt electrode (ΔE_{tip}) is compared to the potential difference between a large reference electrode of the same nature as the potentiometric probe and the Pt electrode (ΔE_{ref}). The Pt wire is connected to the electrical ground of the electronic circuit. The resulting output ($\Delta E_T = \Delta E_{tip} - \Delta E_{ref}$) can then be measured with a precision unit-gain differential amplifier.

Analogous to SECM amperometric methods, SECM potentiometric methods are based on the measurement of electrode potentials (tip and substrate, ΔE_T and ΔE_S, respectively) as a function of various parameters, including tip–substrate distance (d), XY location, and time. Again, a potentiometric tip responsive to the desired solution component is necessary to perform any SECM potentiometric experiment. To use potentiometric probes in SECM, it must be possible to exactly evaluate the tip-to-substrate distance. Different electrochemical methods to evaluate the potential–distance dependence have been investigated, for example, utilization of metal/metal oxide electrodes as both amperometric and potentiometric tips for pH measurement,[4] double barrel tips having one

amperometric UME and one potentiometric probe,[5] or an AC impedance technique.[6] Potentiometric SECM is discussed in detail in Chapter 10.

2.3.3 AC Impedance Method

Besides the DC or transient amperometric techniques described earlier, several research groups[7] have also explored and shown that AC impedance measurements at solid–liquid interfaces with SECM (AC-SECM or IMP-SECM) could provide information on topography and conductivity of substrates. The distance dependence of the AC feedback signal can be employed for constant distance imaging of insulating substrates immersed in dilute electrolyte solutions[7b] and of live cells in a growth medium.[8]

Both negative and positive AC feedback have been observed above conductive substrates, depending on the experimental conditions, such as AC frequency, supporting electrolyte concentration, tip-to-sample separation, and the tip diameter.[7d] Diakowski and Ding[9] have shown that identical AC current responses can be obtained above a conductor and an insulator at optimized low AC frequency. This finding has been utilized to perform constant distance AC-SECM imaging experiments that provided information on sample topography not affected by the reactivity of the sample. Thus AC-SECM can potentially present a valuable supplementary technique to the "classical" DC-SECM measurements. This approach is particularly useful when sample surfaces are rough, which do not allow for constant height imaging. Currently, this method is only applicable in the case of unbiased substrates. Furthermore, AC and DC measurements can be performed simultaneously and information on the topography and reactivity can be obtained by separating the AC and DC signals.

2.A APPENDIX: TYPICAL SECM MODES IN CH SERIES 900 SECM

2.A.1 Probe Scan Curve

Probe scan curve is for probe scan in *X*-, *Y*-, or *Z*-direction with current recording of probe or both probe and substrate electrodes. It allows independent probe and substrate electrode potential control and current sensitivity setting. The probe electrode potential can also be pulsed for electrochemical cleaning before data sampling. The pulse potential and duration can be programmed. The substrate electrode can be turned on or off.

The scan distance, the increment distance, and increment time (sampling time) can be specified. The probe scan can be aborted manually if the current is either greater or less than a specified level, for probe protection.

There are several measurement modes: amperometry, potentiometry, constant current, and impedance. The amperometry mode measures the probe current–position curve. The potentiometry mode measures the probe potential-position curve. The constant current mode will adjust the *Z*-position of the probe to maintain the current constant. A probe height–position curve is recorded. If the sample or substrate is an insulator, the curve can be translated to the topographic information. The impedance mode measures the probe impedance–position curve. If the probe scan is in the *X*- or *Y*-direction, amperometry, potentiometry, and impedance are under a constant height mode.

For the constant current mode, the current value and tolerance need to be specified. For the impedance mode, the frequency and the amplitude need to be specified. When the impedance mode is used for a *Z*-direction scan, the impedance will increase sharply when approaching the surface. It can therefore be used to approach the surface without a redox mediator in solution. The impedance is also more sensitive to the distance to the surface compared with the DC current-distance response. It is possible to adjust the probe *Z*-position to maintain a constant impedance and measure the DC current response, which could be essentially a current-position curve at the constant distance mode.

2.A.2 Probe Approach Curve

Probe approach curve moves the probe toward the surface of the sample of substrate, while the current response is recorded. It uses PID control for the probe to approach the surface. At a distance far from the surface, the probe increment distance is relatively large; the increment distance will get smaller as the probe gets closer to the surface. This allows a rapid surface approach without causing the probe to crash at the sample surface. The approach will be stopped once the current ratio is reached to a level compared with the current at infinitive distance. This ratio is greater than 1 if the substrate is a conductor electrode, or smaller than 1 if the substrate is an insulator. The probe approach will stop when either current ratio is reached. Typically a first scan is taken, setting the limit as $0.8i_{T,\infty}$ for an insulator or $1.2i_{T,\infty}$ for a conductor. This allows estimation of the tip–substrate distance and permits slower scans to closer distances in subsequent scans.

Current recording of probe or both probe and substrate electrodes is supported. The probe and substrate electrode potential and the current sensitivity setting can be independently specified or controlled. The probe electrode potential can also be pulsed for electrochemical cleaning before data sampling. The pulse potential and duration can be programmed. The substrate electrode can be turned on or off.

The maximum increment distance, the increment time (sampling time), the probe current ratio, or absolute current level for the approach to stop can be specified.

2.A.3 Surface Patterned Condition

The surface patterned condition mode is used to condition the surface with a pattern or for micromachining. First, a bitmap pattern of the *XY* plane is created. The pattern size can be specified. Initially, all pixels are dark. By pressing down the left mouse button and moving the mouse, a bright trace or pixel appears. The dark pixel represents "0"; it controls the probe and substrate (if it is turned on) at the first potential for the first hold time. A bright pixel represents "1." It controls the probe and substrate (if it is turned on) at the second potentials for the second hold time. If the first potential is set where no reaction will occur, but the second potential is set where reaction will occur, depending on the electrode connection, one can deposit or etch the substrate surface. A maximum of 512×512 points pattern is allowed. The distance between the pixels can be specified.

2.A.4 SECM (Imaging)

SECM scans the probe on the *XY* plane and records the probe response. When the probe response is plotted as function of *XY* position, an SECM image is formed.

SECM allows independent probe and substrate electrode potential control and current sensitivity setting. Usually the image from the probe electrode response will be given, but the image from the substrate electrode response can also be given in amperometry mode if selected.

The scan distance, the increment distance, and increment time (sampling time) can be specified. There are several SECM image modes: amperometry, potentiometry, constant current, and impedance. Amperometry mode measures the current response versus the *XY* position when the probe is held at the constant height. Potentiometry mode measures the probe potential response versus the *XY* position while the probe is maintained at a constant height. Constant current mode will adjust the *Z*-position of the probe to maintain the current constant when the *XY* position is scanned. The probe height–position response is then recorded. If the sample or substrate is an insulator, the image can be translated to topographic information. Impedance mode measures the probe impedance–position response when the probe is held at the constant height.

For constant current mode, the current value and tolerance need to be specified. For impedance mode, the frequency and the amplitude need to be specified.

It is possible to adjust the probe *Z*-position to maintain the constant impedance at each *XY* position and measure the DC current response, which could generate an SECM image essentially at the constant distance mode.

During SECM imaging, gray-scale or color-coded two-dimensional plot will be displayed on the real-time basis. Interactive three dimensional plots can be generated post run.

REFERENCES

1. Wipf, D. Instrumentation. In *Scanning Electrochemical Microscopy*, A. J. Bard, M. V. Mirkin (eds.), 1st edn., Marcel Dekker, New York, 2001, Chapter 2.
2. Zoski, C. G., Aguilar, J. C., Bard, A. J. Scanning electrochemical microscopy. 46. Shielding effects on reversible and quasireversible reactions, *Anal. Chem*. 2003, 75, 2959–2966.
3. Rodríguez-López, J., Alpuche-Avilés, M. A., Bard, A. J. Interrogation of surfaces for the quantification of adsorbed species on electrodes: Oxygen on gold and platinum in neutral media, *J. Am. Chem. Soc*. 2008, 130, 16985–16995.
4. Horrocks, B. R., Mirkin, M. V., Pierce, D. T., Bard, A. J., Nagy, G., Toth, K. Scanning electrochemical microscopy. 19. Ion-selective potentiometric microscopy, *Anal. Chem*. 1993, 65, 1213–1224.
5. Wei, C., Bard, A. J., Nagy, G., Tóth, K. Scanning electrochemical microscopy. 28. Ion-selective neutral carrier-based microelectrode potentiometry, *Anal. Chem*. 1995, 67, 1346–1356.
6. Horrocks, B. R., Schmidtke, D., Heller, A., Bard, A. J. Scanning electrochemical microscopy. 24. Enzyme ultramicroelectrodes for the measurement of hydrogen peroxide at surfaces, *Anal. Chem*. 1993, 65, 3605–3614.
7. (a) Alpuche-Aviles, M., Wipf, D. Impedance feedback control for scanning electrochemical microscopy, *Anal. Chem*. 2001, 73, 4873–4881; (b) Baranski, A. S., Diakowski, P. M. Application of AC impedance techniques to scanning electrochemical microscopy, *J. Solid State Electrochem*. 2004, 8, 683–692; (c) Gabrielli, C., Keddam, M., Portail, N., Rousseau, P., Takenouti, H., Vivier, V. Electrochemical impedance spectroscopy investigations of a microelectrode behavior in a thin-layer cell: Experimental and theoretical studies, *J. Phys. Chem. B* 2006, 110, 20478–20485; (d) Diakowski, P. M., Baranski, A. S. Positive and negative AC impedance feedback observed above conductive substrates under SECM conditions, *Electrochim. Acta* 2006, 52, 854–862.
8. Kurulugama, R., Wipf, D. O., Takacs, S., Pongmayteegul, S., Garris, P., Baur, J. E. Scanning electrochemical microscopy of model neurons: Constant distance imaging, *Anal. Chem*. 2005, 77, 1111–1117.
9. Diakowski, P. M., Ding, Z. Novel strategy for constant-distance imaging using alternating current scanning electrochemical microscopy, *Electrochem. Commun*. 2007, 9, 2617–2621.

3 Preparation of Tips for Scanning Electrochemical Microscopy

Fu-Ren F. Fan and Christophe Demaille

CONTENTS

3.1 Introduction 25
3.2 Preparation Techniques 26
3.2.1 Metal Microelectrodes 26
3.2.1.1 Disk-in-Glass Microelectrodes 26
3.2.1.2 Submicrometer Glass-Encapsulated Microelectrodes 27
3.2.1.3 Electrochemical Etching of Metal Wires 28
3.2.1.4 Self-Assembled Spherical Gold Microelectrodes 30
3.2.1.5 Mercury Microelectrodes 36
3.2.2 Carbon Microelectrodes 37
3.2.2.1 Carbon Fiber Microelectrodes 37
3.2.2.2 Pyrolytic Carbon Microelectrodes 39
3.2.2.3 Diamond SECM Microelectrodes 41
3.2.3 Development of Other Sealing Techniques 41
3.2.3.1 Deposition of an Organic Insulating Polymer 42
3.2.3.2 Other Sealing Materials 44
3.2.4 Micropipette and Other Tips 44
3.3 Non-Disk Tips and Tip Shape Characterization 45
3.4 Conclusions 46
Acknowledgments 47
References 47

3.1 INTRODUCTION

In this chapter, several methods for the fabrication of different types of amperometric tips suitable for scanning electrochemical microscopy (SECM) are described. We have also suggested some microelectrode fabrication techniques that have not been yet tested for SECM but may provide alternative ways for its tip preparation. Section 3.2.1 describes the techniques for the preparation of various metallic microelectrodes, including Pt, Pt–Ir, Au, Hg, W, and so on. The manufacture of carbon microelectrodes is presented in Section 3.2.2. Most of these tips are encapsulated in or supported with glass capillaries. Other coating materials and techniques are treated in Section 3.2.3.

While most of the SECM work has been carried out with amperometric tips for measuring feedback current or for use in the generation/collection mode, other types of tips such as potentiometric and enzymatic tips are also possible but are only briefly described in Section 3.2.4. The readers who are interested in these tips are encouraged to refer to the appropriate chapters in this book. Finally,

Section 3.3 deals with an approach to determining the shape of an ultramicroelectrode (UME) from its SECM response.

3.2 PREPARATION TECHNIQUES

3.2.1 Metal Microelectrodes

3.2.1.1 Disk-in-Glass Microelectrodes

The conventional technique frequently used for the preparation of SECM tips is largely based on the fabrication technique for disk-shaped microelectrodes, which has been described in the literature [1–3]. The procedures for the manufacture of this type of SECM tips have been described in detail previously [4] and are only presented briefly here.

A fine wire of Pt, Au, or a carbon fiber of the desired radius ($\geq$5 μm, commercially available) is placed in a 10 cm long, 1 mm i.d. Pyrex (or soft glass for Au) tube sealed at one end. The open end of the tube is connected to a vacuum line and heated with a helix nichrome wire for approximately half an hour to desorb any impurity or moisture on the wire and glass tube. One end of the wire is then sealed in the glass at the closed end of the tube by increasing the heating coil temperature. The glass should melt around the wire for at least 1–2 mm at the tip of assembly. The whole glass tube, including the part that seals the wire, should be straight. After the glass has cooled, the electrode is inspected under a microscope to see whether the wire is completely sealed at the tip and to make sure that there are no trapped air bubbles. The sealed end is polished with coarse sandpaper, until the cross section of the wire is exposed, and then successively with 15, 6, 3, 1, and 0.25 μm diamond paste (Buehler, Lake Bluff, IL). Electrical connection to the unsealed end of the wire is made with silver paint (Ekote, No. 3030, Acme Chemicals and insulation Co., New Haven, CT) or colloidal silver (Cat. No. 16031, Ted Pella, Inc., Tustin, CA) to a Cu wire. After this, a small amount of Torr Seal Epoxy (Varian Associates, Palo Alto, CA) is packed into the open end of the glass capillary. This seals the barrel and provides strain relief for the contact wire. The glass wall surrounding the conducting disk is conically sharpened with emery paper (grit 600) and 6 μm diamond paste, with frequent checking with an optical microscope until the diameter of the flat glass section is 10 times less than that of the conducting disk (i.e., RG < 10). Small RG decreases the possibility of contact between glass and substrate because of any slight deviation in the axial alignment of the tip as the tip approaches the substrate. So far, technique for the sharpening of the glass sheath remains to be improved. This technique has been successfully used to prepared tips of diameter larger than 1 μm. The manufacture of smaller tips from Wollaston wire (Goodfellow Metals, Cambridge, United Kingdom) based on this technique is also possible, but it takes a lot of practice and patience [4]. Very sturdy, polishable and long lifetime tips can be prepared by this technique although the procedures are tedious and time consuming. Preparation of submicron SECM tips by this technique is very challenging.

Reduction of the size of SECM probes is important, since the resolution of SECM depends strongly on the size of tip used. In order to achieve this goal, one has to thin down the diameter of commercially available metal wires by electrochemical etching or by pulling in glass capillary as described later. Further coating and exposing steps are then necessary, as in the case of unetched wires, to expose only the electrode surface. One method for the preparation of submicron Pt disks in glass was developed by Lee et al. [5]. A 1–2 cm long Pt wire (25 μm diameter) is sharpened by electrochemical etching in a solution containing saturated $CaCl_2$ (60% by volume), H_2O (36%), and concentrated HCl (4%) at 2 V rms ac applied with a Variac transformer [6,7] as described later. A Pyrex capillary with a tip diameter greater than 100 μm is drawn from a piece of Pyrex tubing (2 mm o.d. and 1 mm i.d.) by using a microelectrode puller (Cat. No. 51217, Stoelting Co., Chicago, IL), having heat setting at 65 and pull setting at 100. The tip of the capillary is sealed by heating for 1 s in a gas flame. The sharpened wire is transferred inside the glass capillary, and the open end of the tube is connected to a vacuum line. The capillary tip is then heated with four

loops (1/4 in. i.d.) of nichrome wire (1.3 mm thick) at an ac voltage of 3.8 V (temperature ca. 800°C). Excess glass near the tip of the Pt wire is removed by heating the electrode in the resistive heating coil, which pulls the glass toward the Pt wire. Heating is halted just before the Pt wire is exposed. The diameter of the exposed Pt disk could be controlled from 0.2 to 25 μm by controlling the extent of the final polishing. Further heating for 0.5–1 min causes the glass to pull away from the Pt wire so that the small exposed Pt disk protrudes from the sealed glass. Electrical connection to the unsealed end of the wire and the packing of Torr Seal Epoxy into the open end of the glass capillary are made as described earlier.

3.2.1.2 Submicrometer Glass-Encapsulated Microelectrodes

3.2.1.2.1 Sealing Etched Wires into Glass

The previously described method, consisting in embedding an etched metal wire into a glass capillary to produce submicron-sized microelectrodes, has been recently improved by White's group, allowing nanometer-sized disk-in-glass microelectrodes to be fabricated. Pt and Au wires, 25–100 μm and 50 μm in diameter, respectively, were electrochemically etched in 6 M NaCN/0.1 M NaOH using a 180 Hz ac voltage (3.6 V amplitude for Pt and 4.5 V for Au). The applied voltage was removed immediately upon cessation of bubbling and the etched wires were washed with water. This method produces very sharp conical tips displaying a ~20 nm radius of curvature for gold and ~50 nm for platinum. Platinum tips can be further sharpened by applying to the Pt wire, immersed in a 0.1 M H_2SO_4 solution, a 4 kHz, 15 V, 16 μs pulse waveform for 1 s. A dc voltage of −1.1 V is then applied to the sharpened Pt wire in order to reduce any platinum oxide formed on its surface. Conical Pt tips with a radius of curvature as small as 2 nm can be produced in this way. Obtaining very sharp tips is critical since the radius of curvature of the etched wire ultimately limits the diameter of the disk-in-glass electrode to be fabricated. Another key step is sealing the etched Pt and Au wires in glass capillaries without damaging the ultrasharp tip apex. This requires using capillaries with thermal coefficients equal to greater than that of the metal wire. Pb-doped glass capillaries were shown to be a good choice for sealing both Au- and Pt-sharpened wires. The wires were sealed into the glass tube by slowly softening the capillary in a H_2–O_2 flame. The sealing temperature must be kept much lower than the melting point of the metal. The most critical step in this tip preparation technique is polishing the glass capillary until a nanometer-sized metal disk is exposed. Due to the conical shape of the sharpened metal tips, even slight overpolishing results in electrodes with radii much larger than desired. To overcome this problem, a transistor-based circuit was used to monitor the radius of the disk electrode *during* polishing. This device alerts the experimentalist in real time when a preselected disk radius is obtained. Polishing is carried out using a Buehler Microcloth pad wetted with a slurry of 50 nm alumina particles and 0.02 M KCl. Disk-in-glass Au and Pt microelectrodes ~20 and ~10 nm in radii, respectively, were produced using this method that also allows nanopore electrodes to be fabricated [6b,6c].

This tip preparation technique is one of the rare benchtop methods allowing nanometer-sized microelectrodes having a disk-in-glass geometry to be reproducibly fabricated. These nanoelectrodes could be used as sensitive SECM probes provided the very large glass sheath surrounding the microelectrode disk can be thinned down in some way to yield acceptable RG values.

3.2.1.2.2 Pulling Metal Wires in Glass Capillaries

An alternative preparation procedure for submicron glass-encapsulated SECM tips involved pulling metal wires with the help of a pipette puller [8,9]. This quite attractive technique has been introduced by Pendley and Abruna [8], was further developed by Fish et al. [10], and has since been successfully used and improved by several groups. Platinum, gold, or silver microwire (25–80 μm diameter) and borosilicate tubes (1.2 mm o.d.) were used as starting materials. Several different parameters of the pulling program can be varied in order to control the shape and size of the micropipette. A more detailed description of the pulling procedure can be found elsewhere [9h].

Immediately after pulling, the metal core is entirely covered with glass, and the next step is to expose the tip of the wire. This is typically done by micropolishing with a micropipette beveler (e.g., Model BV-10, Sutter Instrument Company, Novato, CA) equipped with a micromanipulator and a working distance stereomicroscope. The micromanipulator was used to move the pipette toward the slowly rotating abrasive disk covered with 0.05 μm alumina (Sutter Instrument Company), a lapping tape can also be used (Precision Surfaces International, Houston, Texas). Alternatively, the polishing disk can be stationary and the pipette rotated along its axis. One has to ensure that the axis of the pipette is perpendicular to the polishing surface. This can be done by using a plumb bob to check the verticality of the tip and a two axis bubble level to make sure that the polishing plane is horizontal. When the pipette touches the disk, the small change in the angle can be detected microscopically. The size of the prepared tip increases with the length of polishing. It has been reported that only a fraction of the complete turn of the polishing wheel is required to produce a nanometer-sized polished electrode. The electrode resistance between the tip and an InGa alloy liquid was used to estimate the surface area of the electrode during preparation. When the tip is completely covered with glass, the resistance is extremely high, and it decreases sharply when the tip becomes exposed to solution by polishing. By this technique, electrodes with an effective radius as small as 2 nm and as large as a few micrometers can be manufactured.

Figure 3.1A shows a steady-state voltammogram of 10 mM $Ru(NH_3)_6^{3+}$ at a polished Pt electrode whose effective radius appears to be 84 nm. At a scan rate of 20 mV/s, the voltammogram is well shaped with a flat plateau. At a higher scan rate, for example, 2 V/s, no peaks characteristic for non-steady-state diffusion could be detected, and the limiting current plateau remained flat. This indicates that the size of the electrode is significantly smaller than 1 μm. A modest contribution of the charging current to the total current was consistent with the apparent radius of about 100 nm. The response of a smaller tip (radius ca. 22 nm, thick line in Figure 3.1B) is in good agreement with the theory (thin line). The current at an even smaller (radius ca. 2 nm) electrode (Figure 3.1C) is slightly noisy but its voltammogram remains sigmoidal and retraceable at scan rates as high as several volts per second. This indicates that the true area of the electrode is very small. The low background currents observed at these polished electrodes indicate that there is no apparent solution leakage through the cracks in the glass insulator.

An SECM approach curve under favorable condition for a polished Pt tip to a Pt substrate showed good agreement between the experimental data and the theoretical curve for a microdisk electrode and a relatively large maximum value of the normalized tip current suggested that the tip was a planar electrode with an effective radius of ca. 380 nm. As shown in Figure 3.2, even smaller SECM tips, with effective radii from 50 to 100 nm, giving rise to large normalized feedback currents, were recently reported [9d]. The RG value for these tips can vary from <5 and up to 20 depending on the pulling conditions. They were successfully used for fast kinetic measurements and for high-resolution imaging applications [9d,9g].

3.2.1.3 Electrochemical Etching of Metal Wires

The electrochemical etching procedures usually involve the anodic dissolution of the metals. There are two ways in which this can be done: an ac etch or a dc etch according to the applied potential. Each procedure gives a different tip shape; the ac-etched tips have a conical shape and much larger cone angles than the dc-etched tips. The dc-etched tips, on the other hand, have the shape of a hyperboloid and are much sharper than ac-etched tips. The etching procedures used for several metal wires are described as following.

3.2.1.3.1 Pt, Ir, or Pt–Ir Alloy

A 1–2 cm long Pt or Pt–Ir (80%–20%) wire (125 or 250 μm diameter) is sharpened by electrochemical etching in a solution containing saturated $CaCl_2$ (60% by volume), H_2O (36%), and concentrated HCl (4%) at ca. 20 V rms ac applied with a Variac transformer [6,7]. Lower voltage (e.g., 2 V rms ac) is used for thinner wires (e.g., 25 μm diameter). A carbon rod or plate serves as the counter electrode

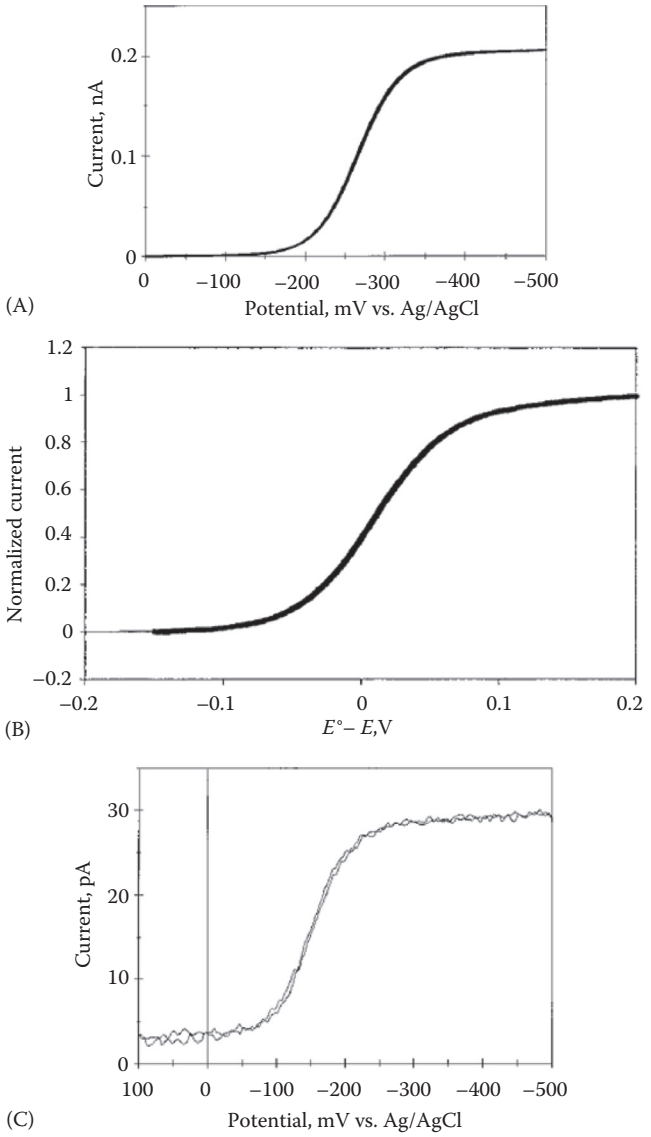


FIGURE 3.1 Steady-state voltammograms of $Ru(NH_3)_6Cl_3$ at polished Pt electrodes. Solution contained (A) 10 mM $Ru(NH_3)_6Cl_3$ and 1 M KCl, (B) 10 mM $Ru(NH_3)_6Cl_3$ and 0.5 M KNO_3, and (C) 50 mM $Ru(NH_3)_6Cl_3$ and 0.5 M KCl. The effective electrode radius (assuming disk geometry) and the potential sweep rate were (A) $a = 84$ nm, $v = 20$ mV/s; (B) $a = 22$ nm, $v = 5$ mV/s; and (C) $a = 2$ nm, $v = 20$ mV/s. The thin line in (B) is the theory for a 22 nm microdisk. (Reprinted with permission from Shao, Y., Mirkin, M.V., Fish, G., Kokotov, S., Palanker, D., and Lewis, A., Nanometer-sized electrochemical sensors, *Anal. Chem.*, 69, 1627–1634, 1997. Copyright 1997 American Chemical Society.)

in a two-electrode etching cell. The etching current, which depends on the area of immersed wire and the applied voltage, was adjusted to an initial value of ca. 0.5 A (for 250 μm diameter Pt–Ir rod) by varying the immersed depth of the metal wire. The etching proceeds uniformly over the immersed wire except at the extreme lower end and the air–solution interface where the etching rate is faster. This process produces a neck shape near the interface. As the etching proceeds, the neck-like region becomes thinner and thinner, and eventually the lower portion falls off. The current shows a uniform decrease during etching. However, it decreases abruptly as the lower portion falls

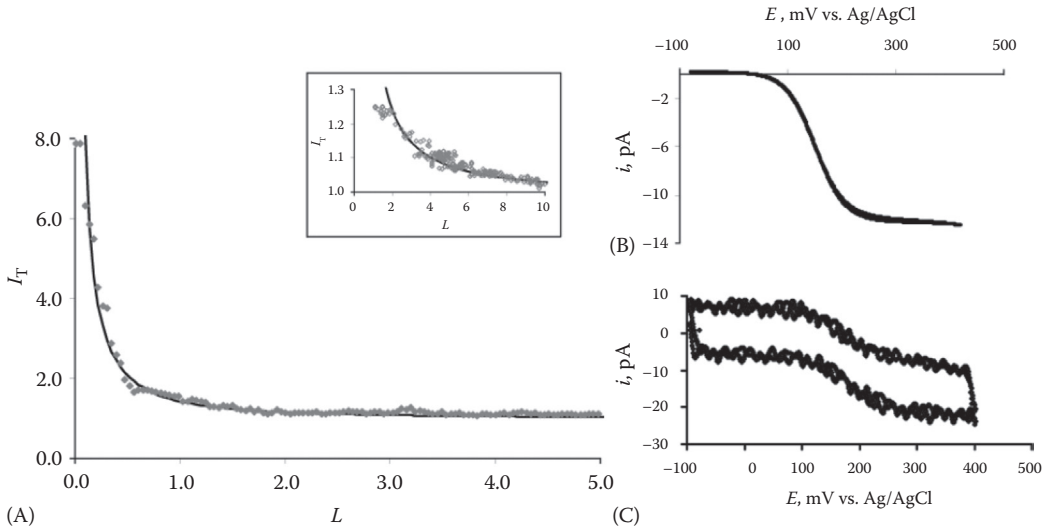


FIGURE 3.2 (A) SECM current vs. distance curve, (B) steady-state voltammogram, and (C) two successive fast-scan cyclic voltammograms obtained with a 46 nm radius polished Pt electrode. Aqueous solution contained 1 mM $FcCH_2OH$ and 0.2 M NaCl. (A) Theoretical curve (solid line) for diffusion-controlled positive feedback. Symbols are experimental data. The tip approached the unbiased Au film substrate with a 5 nm/s speed. (B) 50 mV/s and (C) 10 V/s. The inset in (A) shows an approach curve for a 13 nm tip. (Reprinted with permission from Sun, P. and Mirkin, M.V., Kinetics of electron-transfer reactions at nanoelectrodes, *Anal. Chem*., 78, 6526–6534, 2006. Copyright 2006 American Chemical Society.)

off. To get a very sharp tip with a small protrusion at the end, one needs to switch off the circuit as soon as the current abruptly drops. Failing to switch off the circuit as soon as the lower portion falls off, the upper part of the wire will continue to etch as long as it remains in the electrolyte under an applied potential and will end up a much rounded tip. The switching-off can be best achieved by means of an electronic circuit. Several circuits have been designed to supervise these electrochemical etching or polishing processes [11–13]. It has been found that the cutoff time of the etch circuit has a significant effect on the radius of curvature and cone angle of the etched tip; that is, the faster the cutoff time, the sharper the tip [13].

3.2.1.3.2 Au, Ag, or W

These metals are etched by similar technique but with different etching solutions. The commonly used etching solution for Au and Ag is 3 M NaCN in 1 M NaOH, while 3 M NaOH solution is used for W wire etching. The cyanide facilitated the complexation and dissolution of metal from the immersed wire, and the NaOH inhibited the formation of the toxic HCN. All electrochemical etching processes were performed in a fume hood. It should be mentioned that placing the tungsten tip in an aqueous solution or exposing it to air will result in the formation of a surface oxide. There are several cleaning procedures for the removal of the surface oxide [14–19]. The easiness of oxide formation prevent W from being a useful electrode material for SECM amperometric tips in aqueous solutions. However, it could be beneficial as a tip used for imaging in humid air as described in Chapter 4.

3.2.1.4 Self-Assembled Spherical Gold Microelectrodes

3.2.1.4.1 Nanogold Particle Self-Assembly Process

This technique, developed by Bard and coworkers [20], relies on the finding of Schiffrin and coworkers who reported that nanometer-sized gold nanoparticles could be self-assembled, using thiols cross-linkers, to form conductive bulk materials [21] and multilayer thin films [22]. The

fabrication technique itself originated from the idea of confining the dithiol linker (1,9-nonane dithiol) inside the micron-sized tip of a pulled capillary that was then immersed into a solution of octyl-ammonium-protected 8 nm gold nanoparticles [20], forcing the encounter of the gold nanoparticles and of the dithiol linker to occur only at the very end of the tip. Smooth spherical shiny structures were observed to form at the end of the tip (Figure 3.3). The growth of such spherical structures raised numerous questions about their growth mechanism. The growth process was, however, qualitatively represented as shown in Figure 3.4. Nanoparticles diffused toward the tip where they were cross-linked by dithiol molecules. A diffusion-limited growth would have, however, resulted in a dendritic structure. The fact that smooth spherical structures were obtained was indicative of a certain mobility of the individual particles within the assembly. The particles can accommodate themselves into a sphere, which is the most favorable geometry to minimize the surface energy. That the nanoparticles maintained their individualities inside the material was demonstrated by growing a similar material out of porous glass and studying it by x-ray diffraction [23]. Not only the diffraction peak width showed an average domain size corresponding to the nanoparticle size but the high degree of self-organization of the particles within the self-assembled structure was suggested by the presence of a peak at low diffraction angle corresponding to a lattice parameter of the order of the nanoparticle. This is consistent with previous TEM observations that solutions of similar nanoparticles, when reacted with dithiols, form ordered globular aggregates on the 100 nm scale rather than random dendritic structures [21]. Similar preparations were also observed to lead to the formation of two-dimensional superlattices of gold nanoparticles [24]. The fact that the spheres have diameters greater than the capillary tip size indicates that the sphere growth continues even though the tip opening is already closed by numerous layers of cross-linked nanoparticles. This indicates that the dithiol molecules are able to move within the growing spheres possibly, as shown in Figure 3.4, probably by replacement reactions. The sphere then grows until all

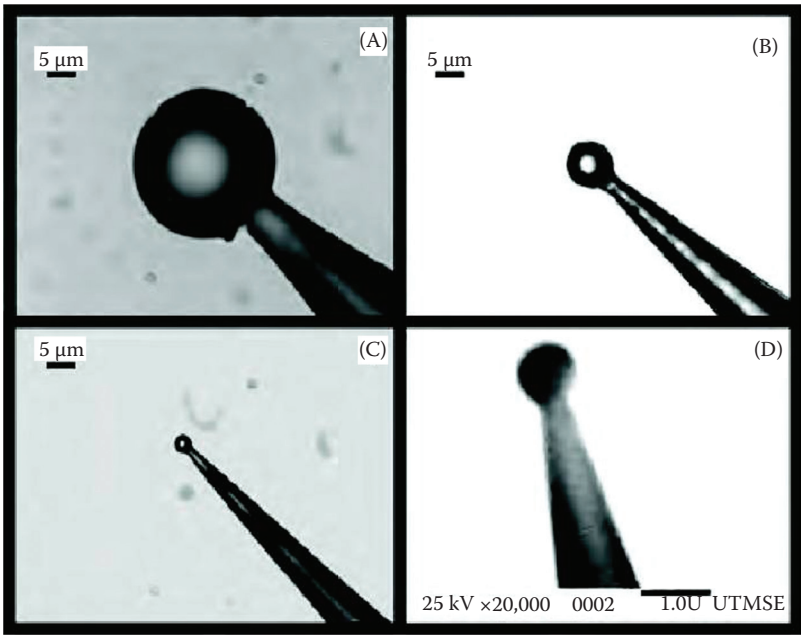


FIGURE 3.3 Optical (A–C) and SEM (D) pictures of the self-assembled spherical gold microelectrodes. The horizontal bar at the lower corner of (D) represents 1 µm. Electrode diameter: (A) 26, (B) 8, (C) 3, and (D) 0.9 µm. (Reprinted with permission from Demaille, C., Brust, M., Tsionsky, M., and Bard, A.J., Fabrication and characterization of self-assembled spherical gold ultramicroelectrodes, *Anal. Chem.*, 69, 2323–2328, 1997. Copyright 1997 American Chemical Society.)

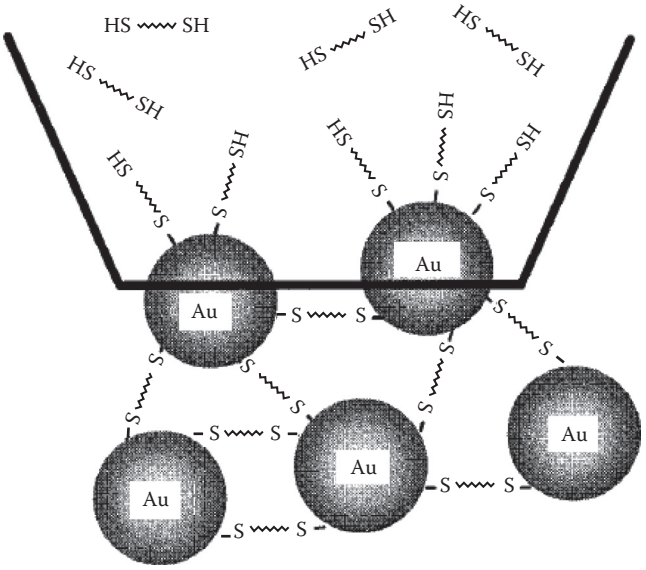


FIGURE 3.4 Schematic picture of the self-assembly process leading to the formation of gold microspheres at the end of the micropipette tip. (Reprinted with permission from Demaille, C., Brust, M., Tsionsky, M., and Bard, A.J., Fabrication and characterization of self-assembled spherical gold ultramicroelectrodes, *Anal. Chem*., 69, 2323–2328, 1997. Copyright 1997 American Chemical Society.)

the dithiol is consumed. By varying the capillary size, spherical electrodes having diameters from 1 to 30 μm could be easily obtained. The sphere diameter was ranging from 2 to 20 times the capillary tip diameter depending on the amount of dithiol inside the tip.

The well-defined spherical shape of these structures and their smoothness made them very attractive to be used as microelectrodes and as SECM tips. In order to establish an electrical contact with these spherical assemblies, the quartz capillary carbonization technique described later was used. This time it was desirable not to close the capillary but to still obtain a conductive carbon coverage on the inner walls of the capillary. This could be achieved using the described carbonizing setup and introducing the capillary into the heated zone only once. This carbon-coated capillary was then used for the preparation of spherical gold microelectrode based on the procedures as summarized in Figure 3.5 and resulted in self-assembled spherical gold microelectrodes such as those presented in Figure 3.3.

3.2.1.4.2 Electrochemical Behavior of Self-Assembled Spherical Gold Microelectrodes

The electrochemical behavior of these spherical microelectrodes was first characterized by recording the gold oxide film formation/reduction in acidic conditions. The voltammogram obtained was as expected for a gold surface. Moreover, the electrode surface as deduced from the area under the oxide peak [25] was found to correspond to the geometrical surface as calculated from that measured optically. This was indicative of the high smoothness and the absence of porosity in the self-assembled structures. The use of the self-assembled spherical structures as microelectrodes was further tested by cyclic voltammetry both in aqueous (Figure 3.6A) and in nonaqueous media (Figure 3.6B). In every case, a Nernstian behavior was observed. The steady-state current corresponded well with the one expected from the size of the electrode measured optically [26]. This ideal behavior was maintained even at high scan rates (up to 10 V/s), especially in nonaqueous solvents. As the scan rate was raised, any porosity or a bad seal between the glass and the sphere would cause a thin-layer cell behavior in the voltammograms (as observed in the case of pyrolytic

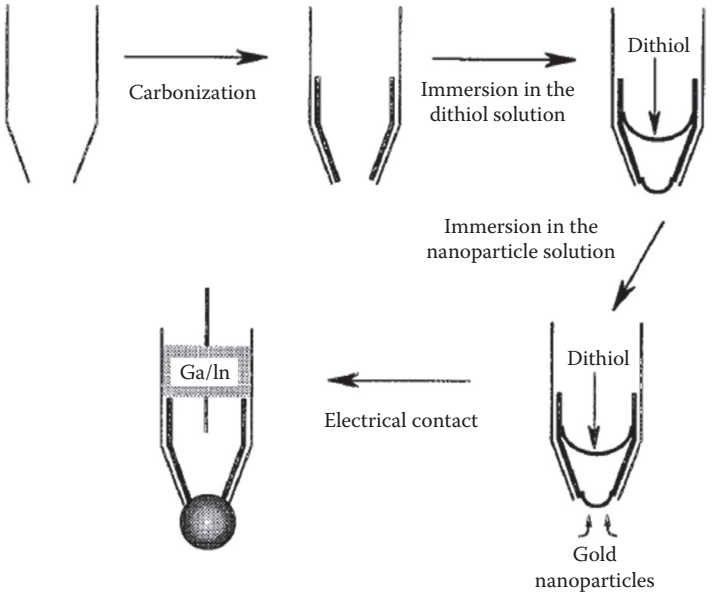


FIGURE 3.5 Schematic diagram for the preparation of the self-assembled spherical gold microelectrodes. (Reprinted with permission from Demaille, C., Brust, M., Tsionsky, M., and Bard, A.J., Fabrication and characterization of self-assembled spherical gold ultramicroelectrodes, *Anal. Chem*., 69, 2323–2328, 1997. Copyright 1997 American Chemical Society.)

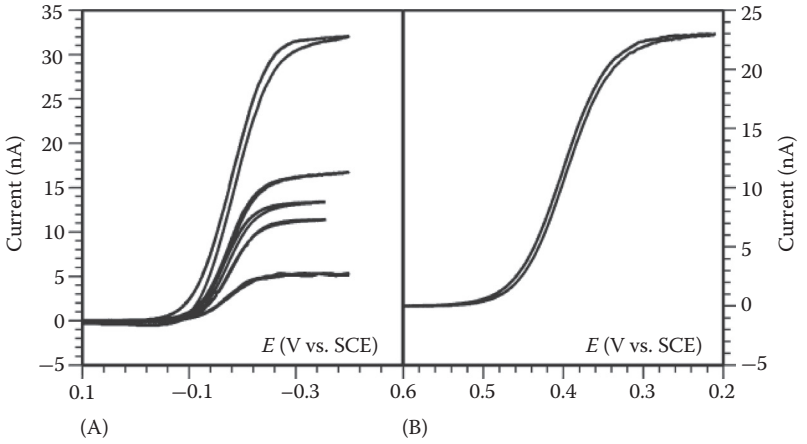


FIGURE 3.6 Cyclic voltammogram of a self-assembled spherical gold microelectrode. (A) In a 7.5 mM aqueous solution of hexaaminеruthenium(III) chloride and 1 M KCl electrolyte. Electrode diameters, from top to bottom, 10, 5, 4, 3, and 1.7 µm. Scan rate 0.1 V/s. (B) In a 6.5 mM solution of tetracyanoquinodimethane in acetonitrile. Supporting electrolyte: tetrabutylammonium tetrafluoroborate (0.1 M). Electrode diameter: 6 µm. Scan rate 0.1 V/s. (Reprinted with permission from Demaille, C., Brust, M., Tsionsky, M., and Bard, A.J., Fabrication and characterization of self-assembled spherical gold ultramicroelectrodes, *Anal. Chem*., 69, 2323–2328, 1997. Copyright 1997 American Chemical Society.)

carbon microelectrodes described later). It was therefore concluded that the self-assembled spherical gold microelectrodes, although consisting of individual gold nanoparticles, have an electrochemical behavior very similar to that of bulk gold microelectrodes. Although the resistivity of the material is expected to be higher than that of bulk gold, it is still too small to have any consequences on the voltammetric behavior, since the currents flowing through microelectrodes are usually very small.

3.2.1.4.3 Size Limitations

The size of the spherical electrodes prepared by this technique could be controlled by the dithiol concentration or by the size of the pulled capillary. These two parameters determined the amount of dithiol present in the pipette tip. In order to obtain fully developed spheres, the self-assembly process was left to proceed until completion. It was observed that spheres having a diameter greater than 15–20 μm were very fragile and had a tendency to split open. Although it was possible to grow spherical structures of a few hundreds of nanometers in diameter from capillary tips of a few tens of nanometers, the growth of such submicron structures was more difficult than micron-sized tips. The making of submicron self-assembled spherical electrodes was possible but somehow difficult to reproduce.

3.2.1.4.4 Use of Self-Assembled Spherical Gold Microelectrodes as SECM Tips

The great smoothness, well-defined spherical shape, and good voltammetric behavior of the self-assembled electrodes made them very attractive to be used as SECM tips. One of the major advantages of these electrodes was their accessibility to the substrate surface. The approach of disk-shaped SECM tips to a planar substrate is mainly limited by the tip misalignment that results in an early contact between the insulating sheath of the probe and the substrate. The spherical shape and the absence of an insulating sheath render self-assembled microelectrodes much less sensitive to such alignment errors. At much shorter distance, the tip roughness might become the limiting factor for the approach. The smoothness of the surface of the self-assembled microelectrodes may therefore allow very small tip–substrate separation to be obtained. Not only the shape of the very end of a SECM tip has to be compatible for a close approach to the substrate but its geometry has to be well defined in order to extract information from the approach curves. The theoretical approach curve corresponding to the tip geometry has also to be known. The theoretical approach curves for a spherical electrode was derived from the curve calculated for a hemispherical electrode [27] by assuming that the upper part of the spherical electrode does not participate in the feedback process (see also Section 3.4 for the SECM approach curves for non-disk tips). Thus, it only contributes to the tip current by a constant current corresponding to the unperturbed diffusion of the mediator to the upper half of the spherical electrode (see Figure 3.7). This constant current therefore equals half the current measured at infinite tip–substrate separation. This assumption results in a simple expression that relates the feedback current for a spherical probe (I_s) to the one for a hemispherical probe (I_h): $I_s = (I_h + 1)/2$. Experimental approach curves for a conducting or an insulating substrate were reasonably well fitted by this expression (see Figure 3.8).

When a self-assembled spherical electrode approaches to a conducting substrate (Figure 3.8, curve (a)), the current rise due to the positive feedback process is expectedly not as sharp as the one for a disk-shaped electrode but is sufficiently high to sense the surface. An interesting feature of the experimental approach curve obtained in this case was that a very small normalized distance (L ca. 0.05) could easily be achieved when a disk-shaped SECM tip only allows for L ca. 4 times greater. When a self-assembled spherical electrode approaches to an insulating substrate (Figure 3.8, curve (b)), only a small current decrease is observed, as expected for spherical electrodes. Thus, spherical electrodes have a reduced ability to sense an insulating substrate. The agreement between the theoretical and experimental results in this case is not as good as in the case of conducting substrate. This can be explained by the fact that the original model for the hemispherical electrode

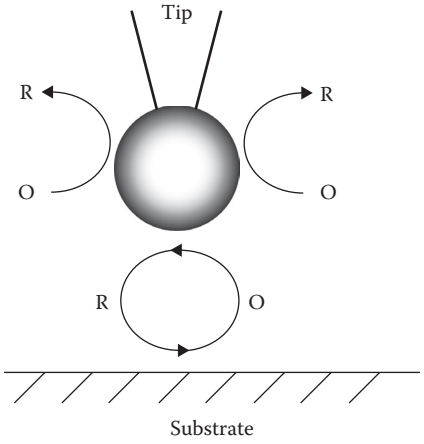


FIGURE 3.7 Schematic picture of the diffusional processes taking place at a spherical electrode approaching a conductive substrate. Illustration of how positive feedback occurs at the lower hemisphere while the contribution of the upper hemisphere to the tip current remains constant. (Reprinted with permission from Demaille, C., Brust, M., Tsionsky, M., and Bard, A.J., Fabrication and characterization of self-assembled spherical gold ultramicroelectrodes, *Anal. Chem*., 69, 2323–2328, 1997. Copyright 1997 American Chemical Society.)

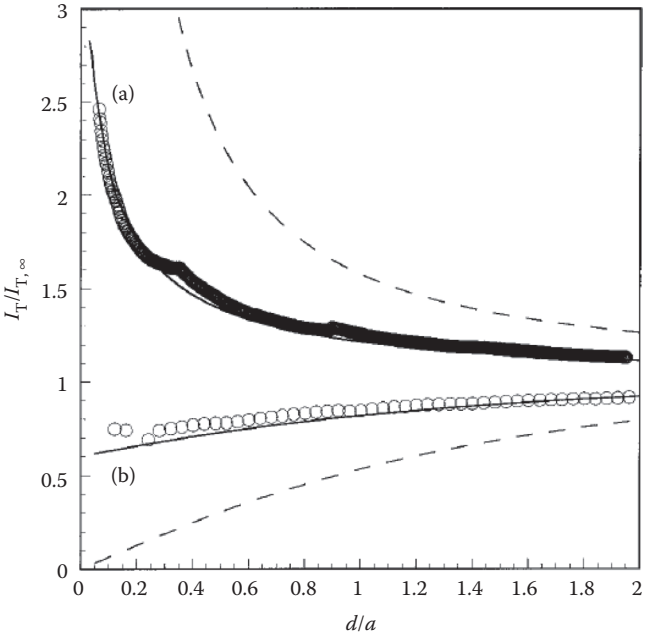


FIGURE 3.8 Experimental approach curve obtained with a 4 μm diameter spherical self-assembled ultramicroelectrode: variation of the normalized current with the dimensionless tip–substrate separation d/a (d is the tip–substrate separation, a is the electrode effective radius). ——: Theoretical approach curve for a spherical electrode calculated as described in the text. - - - -: Theoretical approach curve for a disk electrode. (a) Conductive platinum substrate. (b) Insulating glass substrate. Aqueous solution of hexaaammineruthenium(III) chloride and 1 M KCl electrolyte. (Reprinted with permission from Demaille, C., Brust, M., Tsionsky, M., and Bard, A.J., Fabrication and characterization of self-assembled spherical gold ultramicroelectrodes, *Anal. Chem*., 69, 2323–2328, 1997. Copyright 1997 American Chemical Society.)

was calculated from data corresponding to planar electrodes having an insulating sheath, whose influence is negligibly small for positive feedback but significant for negative feedback. The closest distance attained in the negative feedback mode seems greater than that obtained in the positive feedback mode, which might also be limited by an early contact due to the roughness of the glass slide used as the insulating substrate.

It can be concluded from the earlier discussion that the improvements gained by utilizing self-assembled spherical microelectrodes as SECM probes strongly depend on the operational mode of the SECM used. For surface imaging, the use of a small electrode has the obvious advantage of increasing the lateral resolution. In this mode, the improvement brought by the self-assembly technique is simply the easiness of making relatively small probes as compared to conventional techniques. The main drawback of the self-assembled electrodes for surface imaging comes from their reduced sensitivity to insulating substrates. When SECM is used as a tool for the kinetic studies of fast homogeneous reactions following electron transfer [28], the capability to bring a self-assembled spherical electrode very close to the substrate surface can be a major improvement. In this kinetic mode, short-lived intermediates generated at the tip can be collected and detected at the substrate if the tip-to-substrate distance can be made small enough that the intermediates can reach the substrate before being consumed by the fast chemical reactions. In other words, the diffusional tip-to-substrate transit time, $\tau \sim d^2/D$ (d is the tip–substrate separation and D is the diffusion coefficient of the species), must be in the order of the lifetime of the intermediate. This would mean that for a 1 μm diameter spherical electrode that could be approached 25 nm away from the substrate, intermediates having lifetimes less than microseconds can be detected and characterized.

As explained earlier, the upper part of a spherical tip always gives rise to a permanent and distance-independent component of the tip current. In the feedback mode, this feature can limit the sensitivity of the feedback detection of small amounts of intermediate species. However, in the tip generation/substrate collection (TG/SC) mode, no current would theoretically flow through the substrate until it ultimately detects the intermediate species. This characteristic allows for the measurement of a very small substrate current due to the redox reaction of intermediate species. However, this would require minimizing the background current flowing through the substrate by limiting its size to an upper limit of an order of magnitude greater than the probe size. As mentioned earlier, for the probe to be able to approach closely to the substrate, one also requires using smooth substrates. Good candidates for the required small and smooth substrates would be the biggest self-assembled spherical electrodes obtainable if one can solve the problem associated with the alignment of 2 μm size spheres.

3.2.1.5 Mercury Microelectrodes

Together with carbon, mercury is one of the most attractive electrode materials. It has high proton reduction overpotential and possesses a very well-defined and smooth surface. For these reasons, it has been widely used as electrode material in organic electrochemistry. The preparation of mercury microelectrodes has thus been an interesting and challenging problem that was addressed by several groups [29–31]. Following these initial reports, SECM mercury tips have been successfully fabricated and used [32]. The technique of making mercury microelectrode typically consists in the reduction of mercury ions at the surface of a disk-shaped metallic or carbon microelectrodes, albeit Hg microelectrodes can also be formed by simple contact to a mercury pool. The choice of substrate material for mercury deposition is critical. Mercury should wet the substrate surface properly but not form amalgam with it. It was initially reported that iridium was the most suitable material, albeit Hg SECM tips are mostly fabricated from Pt microelectrodes. Carbon is relatively acceptable but a worse substrate for mercury deposition. Mercury is electrodeposited from a 10 mM $Hg_2(NO_3)_2$ solution in 0.1 M KNO_3 acidified to 0.5% with HNO_3. A potential of −0.1 V vs. Ag/AgCl is applied to the microelectrode for 300 s. The growth of the mercury electrodes can be monitored by recording the variation in the reduction current of the mercury ions with time. From the amount of mercury deposited, assuming a hemispherical growth, the radius of the microelectrode can be calculated.

It was found that the radius corresponded quite well with that deduced from the diffusion-limited current expected for the reduction of an electroactive species at the same microelectrode, assuming a hemispherical shape. From these observations, it was suggested that mercury microelectrodes are shaped like hemispheres having a few microns in diameter [29]. In some cases, the growth of a mercury microelectrode of a few tens of microns in size was followed by optical microscopy. It was observed to grow to an almost hemispherical microelectrode [32d]. Apparently in all cases, the radii of the mercury microelectrodes are equal to or larger than that of the supporting disk-shaped electrode. SECM characterization of Hg microelectrodes, carried out by comparing theoretical and experimental feedback approach curves, confirmed their sphere-cap geometry [32].

Even though it was stated that mercury microelectrodes having radii much larger than the supporting disk-shaped surface would in fact more resemble to shielded spheres than to actual hemispheres [31], all these microelectrodes share an interesting feature: they behave as very smooth, hemispherical microelectrodes. As mentioned previously and discussed in Section 3.3, although the approach curves of spherical-segment-shaped microelectrodes are not as steep as a microdisk, they are still quite suitable for SECM applications. Another merit of such mercury probes is their inherent smoothness. Moreover, it has been shown that spherical Hg SECM tips are robust enough to withstand physical contact with insulating, or even metallic, substrate surfaces [33]. One should finally mention that besides spherical-cap Hg microelectrodes, Au/Hg and Pt/Hg amalgam microelectrodes, consisting of a thin film of Hg deposited onto disk-shaped microelectrode, have also been fabricated and successfully used as SECM tips [34]. In such a case, the tip geometry remains essentially disk shaped, while the electrochemical behavior of the tip is comparable to one of the Hg electrodes.

3.2.2 Carbon Microelectrodes

In the last 20 years, a lot of work has been done on the design of carbon microelectrodes and several reviews have been devoted to this large amount of work [35,36]. The purpose of this chapter is therefore only to review the techniques that might be useful for the preparation of SECM tips based on the criteria presented earlier defining a good SECM tip. Some of our own work about the use of pyrolytic carbon electrodes as SECM probes will also be discussed.

3.2.2.1 Carbon Fiber Microelectrodes

3.2.2.1.1 Glass Encapsulation of Carbon Fiber Microelectrodes

The electrochemical behavior of carbon electrodes makes carbon a very interesting substitute for metals as microelectrode material. Unlike metallic electrodes, carbon electrodes do not form oxide films. They also have much higher proton reduction overpotential than most metallic electrodes. As a result, they allow the exploration of a larger potential window. These characteristics have made carbon a versatile electrode material widely used in organic electrochemistry. Neurobiologists also took advantage of this versatility to use carbon as the electrode material for the detection of neurotransmitters such as dopamine. Their requirement of ultimately working in vivo, that is, in a confined environment, led to the initial development of amperometric micron-sized carbon fiber microelectrodes [37]. These early carbon fiber microelectrodes consisted of short bare fibers held by an insulting support. This cylindrical geometry was not ideal for purely electrochemical investigations and is even less suitable for SECM experiments. More interesting for this purpose is the development of disk-shaped carbon microelectrodes that followed the initial papers by Wightman et al. [38,39]. In these early reports and many of the following ones, the fabrication of disk-shaped carbon microelectrodes consisted in sealing the carbon fiber into a glass tube either by pulling and melting the glass around the fiber or by filling the space between the fiber and the glass taper with very fluid epoxy resins that were brought to the electrode end by capillary. Mercury or conducting epoxy was used as the electrical contact to the fiber. The surface of the disk-shaped electrode was then exposed by cutting the end of the electrode with a scalpel. Depending on the initial capillary tip size, this

resulted in a disk-shaped electrode having a diameter of a few microns located somewhere in the plane of a larger (or much larger) insulating disk. With small glass capillaries, microelectrodes having an RG (the ratio of the total microelectrode tip diameter over the diameter of the active carbon electrode) as small as 10 could be obtained. Microelectrodes to be useful as SECM probes should not have an RG exceeding 10 in order to be able to approach closely to the surface of the substrate. Exposing the surface of a disk-shaped electrode by cutting the end of the capillary was, however, shown to result in fragile electrodes having quite rough, slightly protruding electrode surfaces. In spite of this drawback, this fabrication technique could still be useful for making SECM tips as it is fast and can directly produce electrodes with a small RG, although one needs to consider how to cut the electrodes perpendicularly to their axes.

Tips of smaller RGs were produced later in order to be beveled [40]. The beveling technique consisted in using a microelectrode beveller, that is, a polishing setup consisting of a slowly rotating abrasive wheel to which a microelectrode mounted on a micromanipulator is approached at a certain angle (e.g., 45°). This resulted in carbon fiber microelectrodes having small RGs and much smoother electrode surfaces. The beveled tips were well suited for their intended use, that is, an easy penetration of the biological tissues. However, since the surface of a beveled electrode in most cases is not a disk but an ellipse and also the electroactive plane is not perpendicular to the tip axis, these tips are unsuitable for SECM. However, by placing these tips perpendicularly to the polishing wheel instead of using a 45° angle one could make disk-shaped smooth carbon microelectrodes that would be usable as SECM probes. A few attempts of using a beveling apparatus in such a way to polish the very end of glass-capillary-based SECM probes have been reported [9,41] with somewhat success.

When the diameter of the capillary used to seal the carbon fiber is in the order of a few millimeters, much more robust disk-shaped electrodes were produced [3]. The active electrode surface can then be easily exposed and smoothen by a regular polishing procedure. This kind of microelectrodes can then be changed into a SECM tip by following the glass-sheath grinding procedure described earlier. Most of the carbon fiber SECM probes reported in the literature were made by this technique [28f,42]. As a result, these carbon tips present the same limitations encountered in the metallic ones: a tedious and time-consuming preparation procedure and a minimum size of a few microns, corresponding to the smallest carbon fiber tips available. One could think of addressing these two drawbacks, respectively, by using other sealing techniques and by thinning down those existing carbon fibers with different etching techniques. Several techniques allowing such improvements are reported in the literature and are examined in the following.

3.2.2.1.2 Carbon Fiber Etching

It is worth examining various different techniques that were developed in order to make carbon microelectrodes smaller than the lower limit imposed by the diameter of the commercially available carbon fibers (a few microns). In order to achieve this goal, the diameter of commercial carbon fibers was decreased by different etching procedures. These techniques generally result in the etched part of the fiber having the shape of a truncated cone. The tip diameter and its length depend on the etching conditions. Further coating and exposing steps are then necessary, as in the case of unetched fibers, in order to expose only the electrode surface.

By taking advantage of the fact that carbon fibers can be etched down to a size of ~100 nm by passing the fiber through a flame, Strein and Ewing [43] constructed polymer-coated submicron disk electrodes from flame-etched carbon fibers. Electrodes with an apparent diameter as small as 124 nm were obtained. The flame-etched fibers had however a very rough aspect. Another technique based on electrochemical etching a carbon fiber in a half-saturated solution of sodium nitrite with an alternating current (50 Hz 2–6 V) was proposed earlier [44]. Even though the final conically etched carbon fiber diameter was ca. 0.4–1.5 μm, it had the advantage of being imbedded in glass. The embedding technique consisted in introducing the etched tip in a capillary that was later pulled

and melted around the etched conical carbon fiber end. This resulted in a microelectrode having an overall conical shape. Although it was not clear how well the very tip of the electrode was characterized, further cutting or micropolishing of the produced electrode could have led to an interesting SECM probe.

By using a different electrochemical etching technique, a 480 nm diameter carbon microelectrode was fabricated [45]. A carbon fiber was first etched by applying on it with a 2 V amplitude and 1–50 Hz square wave in a 3 M KOH solution. The etched fiber was initially insulated with a very thin layer of sputtered SiO_2 and then embedded in epoxy glue. More recently, a technique of carbon fiber etching by an argon ion beam thinner was proposed [46]. The unetched part of the fiber was then imbedded in glass, thus resulting in a very long conical microelectrode. This geometry is unsuitable for SECM applications. However, this technique could provide etched carbon fibers having a diameter as small as 50 nm, which is produced in much milder conditions than the flame etching technique. The surfaces of these fibers were also much smoother than those flame-etched ones.

All these etched fibers have submicron diameters, making them attractive to be used as SECM probes. However, they share the same constraints as the unetched fibers in terms of designing a coating technique that would make them suitable for SECM probes. But, in the case of etched tips an extra problem arises. If disk-shaped electrodes are desired, the etched part has to be long enough so that the technique used to expose the carbon disk surface (e.g., micropolishing or cutting) exposes only the very end of the fiber. Alternatively, one can also use these conically shaped etched carbon fibers to make *conical* SECM probes. This requires coating the conical fiber down to its very end, leaving only a very short cone exposed at the end as described in other sections. Such type of conical microelectrodes have been fabricated from carbon fibers etched in a 0.01 M NaOH solution, using a 50 Hz square wave voltage (4–5 V in aptitude) and insulated by deposition of an electrophoretic cathodic paint (see Section 3.2.3.1.2) [47]. To avoid insulation of the tip apex, the etched carbon fiber was immersed in the paint solution in an "inverted position," that is, with the tip of the microelectrode oriented upward and the tip just breaking through the solution surface. Microelectrodes with an effective radius as small as 1 nm were thus fabricated. Fabrication of nanometer-sized etched carbon fiber SECM tips, insulated by a thin phenol/allylphenol coating, and having disk or conical geometry has also been reported [48]. The initially insulated apex of these probes was exposed by electrochemical etching. These probes were used for SECM imaging and patterning of horseradish peroxidase (HRP)-covered surfaces. Micron-sized, etched carbon fiber-based SECM tips, insulated by deposition of anodic electrophoretic paint, were fabricated and used to study individual living cells [49]. The disk-shaped apex of these probes was exposed by mechanical cutting.

3.2.2.2 Pyrolytic Carbon Microelectrodes

3.2.2.2.1 Survey of Previously Reported Carbonization Techniques

The use of pyrolytic carbon deposited as a thin film resulting from the pyrolysis of methane as an electrode material has been reported by Blaedel and Mabbot [50]. The pyrolysis of methane on a heated quartz cylinder under an inert atmosphere resulted in the deposition of a carbon film onto the quartz cylinder. The reasonably good electrochemical behavior of this pyrolytic carbon film was demonstrated. This technique was later applied for the deposition of carbon inside heated quartz capillaries. At first, the deposition of a thin carbon film on the inside walls of micrometer-sized capillaries was reported [51]. In order to be usable, the capillary had then to be backfilled with epoxy glue and cut with a razor blade. This procedure resulted in ring-shaped carbon microelectrodes of a few microns in size. More recently, it was reported that this technique could also result in disk-shaped carbon microelectrodes if the carbonization time was increased, and the end of the capillary was then supposedly ultimately closed by a carbon cap [52]. The resulting electrodes displayed, at least at slow scan rates reported, a remarkably good electrochemical behavior, both in water and

in organic solutions. Carbon microelectrodes of an apparent size of a few tenth of micron could be obtained. This microelectrode-making technique consisted of introducing an open quartz capillary filled by methane under high pressure (about 130 psi) into a larger heated quartz tube in which an inert gas flows. A high methane pressure is required in order to insure the presence of methane at the very end of the capillary. The inert gas flow avoids the combustion of the carbon film deposited. The temperatures required for the deposition being around 1000°C, the use of quartz capillaries is required. Since commercially available laser-based pullers allow for quartz capillaries having a tip diameter of a few tens of nanometers to be pulled, this carbonization technique seems particularly attractive for the preparation of submicron-sized carbon microelectrodes.

3.2.2.2.2 Modification of Carbonization Techniques

The feasibility of using these pyrolytic carbon-filled capillary microelectrodes as SECM tips was explored by Bard et al. [53]. Quartz capillaries of 0.5 mm i.d. and 1 mm o.d. were pulled using a laser puller in order to obtain capillaries of a tip size ranging from a few microns down to a few tens of nanometers. The sizes of samples of capillaries were estimated by scanning electron microscopy or by conductivity measurements [54]. In order to acquire a better control on the carbonization conditions, the setup presented in Figure 3.9 was built. This setup was modified from the ones previously used in the literature [50–52]. In order to have a better control of the carbonizing temperature, the heat source consists of a nichrome wire coil instead of an unstable Bunsen burner flame. The introduction of the capillary into the heated quartz tube is controlled via the use of a Langmuir balance Z-positioner. By mounting the pulled capillary to the positioner's arm, this setup allows for a perfect control of the introduction and the withdrawing rate of the capillary from the heated zone. The carbonization time of the tip inside the hot zone can also be well controlled. The carbonizing temperature used was typically ca. 1000°C. The methane pressure was ranging from 240 psi for the largest capillaries to 500 psi for the smallest ones. The use of a gas chromatography line and a ferrule-based capillary holder allowed for the flow of high-pressure methane. For a given size of pulled capillary, the minimum pressure required was determined as the one at which bubbles were starting to come out from the capillary through a water bubbler. However, the methane flux had to be kept below a certain level, because an excessive flux always resulted in the absence of carbonization. It was observed that removal of the traces of oxygen remaining inside the system greatly improved the apparent quality of the carbon film. This was achieved by connecting the methane line to vacuum before introducing the methane. Once the interior of the tip was carbonized, electrical contact to the carbon film was established by introducing liquid gallium indium eutectic from the back of the capillary.

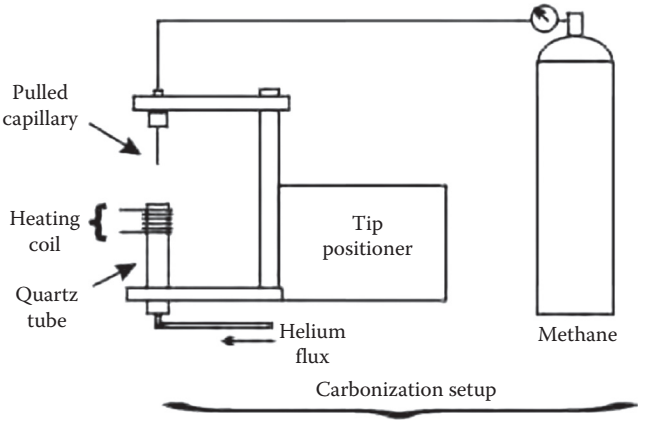


FIGURE 3.9 Schematic diagram of the capillary carbonization setup.

The voltammetric characteristics of the fabricated pyrolytic carbon microelectrodes in water can be very good at slow scan rates. However, at high scan rates and/or in organic solvents, they show thin-layer cell behavior, indicating that the tips are widely open. A longer carbonization time does not help to close the opening. The only way to close the end was by slowly introducing the capillary back and forth into the heated zone several times. By this technique, pyrolytic carbon microelectrodes of a size ranging from a few tens to a few hundreds of nanometer, showing a nice voltammetric behavior in both water and organic solvent at various scan rates, could be obtained.

3.2.2.2.3 SECM Behavior of Pyrolytic Carbon Microelectrodes

The biggest pyrolytic carbon microelectrodes obtained from this technique have a diameter of a few microns. Their exact size could be measured using an optical microscope and compared with the apparent size derived from the steady-state current obtained by cyclic voltammetry. This apparent size is expected to decrease with the recessed depth of the electrode [55]. In the case of pyrolytic carbon microelectrodes, the sizes of electrodes measured optically and by cyclic voltammetry were very close, indicating that the recessed depth was less than one- or two-electrode diameter. A very thin conducting carbon film is deposited on the inside of the capillary walls down to the very end of the tip and the capillary is eventually closed by carbon a few electrode diameters away from the capillary tip. We therefore conclude that the carbonization technique can easily produce slightly recessed submicron carbon tips; however, their recessed nature renders them not useful as SECM tips if the recessed depth is larger than the effective tip radius. Attempts to polish the very end of the micron-sized tip using a pipette beveller were unsuccessful due to the very small thickness of the carbon film closing the tip. However, the carbonization technique allows one to coat the inside walls of very small capillaries with a stable conducting carbon film, which can be used as an electrical contact to the macroscopic end of the electrode as described previously.

3.2.2.3 Diamond SECM Microelectrodes

Besides amorphous carbon-based tips, diamond SECM tips were also fabricated [56]. Boron-doped diamond (BDD) UMEs were fabricated by the growth of BDD films by chemical vapor deposition onto sharpened tungsten wires. The diamond-coated wires were then insulated with nail varnish, electrophoretic paint, or fast-setting epoxy to form disk-shaped UME tips 1–25 μm in size. The tip apex was exposed by abrading on fine mesh wet and dry paper. The use of BDD UMEs as SECM tips was validated by recording approach curves to insulating and conducting surfaces. BDD tips were used to obtain SECM images of immobilized bacterium *E. coli*. The specific interest of these tips arises from the very good properties of BDD as an electrode material. BDD has a wide potential window in aqueous solution, a low background current and, unlike amorphous carbon is not prone to oxide formation. BDD also exhibits a good resistance to fouling, making BDD SECM tips very attractive for electrochemical imaging in biological media.

3.2.3 Development of Other Sealing Techniques

As mentioned earlier, the radius of the insulating sheath surrounding the electrode surface is a parameter needed to be considered if a microelectrode is used as an SECM probe. Microelectrodes with large RGs are very robust but can only be useful as SECM probes after a tedious and delicate grinding procedure. On the other hand, the use of tips with too small RGs may result in deviation from the theoretical behavior especially when an insulating substrate is used. A large insulating sheath, resulting in a large overall diameter of the microelectrode tip, is also detrimental when the microelectrode is used in a confined biological environment. Thus, a lot of efforts were devoted to develop alternative coating techniques that would produce microelectrodes having smaller overall diameters than the ones obtained from the conventional glass-encapsulating technique. Several alternative methods are described as follows.

3.2.3.1 Deposition of an Organic Insulating Polymer

3.2.3.1.1 Electropolymerization

One coating method consists in the oxidative electropolymerization onto the surface of the electrodes. Films of poly(oxyphenylene) were initially deposited from an 1:1 (by volume) water:methanol solution containing 0.25 M 2-allylphenol, 0.2 M 2-butoxyethanol, and 0.4 M ammonium hydroxide or allylamine by biasing the wires at a constant voltage of 4 V for half an hour [57]. Under these conditions, the phenolic groups of the monomers are oxidized, generating a free radical that initiates the growth of polymer. Later, a phenol–allylphenol copolymer was preferred to the simple allylphenol polymer [58]. In all cases, the deposited thin polymer film was cured at 150°C for 1/2–1 h. This technique resulted in a fiber coated by a few microns of insulating polymer film. The disk-shaped microelectrode was then exposed either by cutting the insulated wire with a sharp scalpel or razor blade or by inducing an arc of current at the very end of the electrode, which locally desorbed the polymer. The thickness of the coating could be varied from 0.1 to a few microns by changing the deposition conditions such as the electrodeposition time and the concentration of the monomer solution. Phenol-allylphenol-isolated carbon fiber microelectrodes were notably used as SECM tips for imaging model neurons [58].

3.2.3.1.2 Electrophoretic Deposition

An alternative approach consisting in the anodic electrophoretic deposition of paint was initially proposed for insulating carbon fibers by organic polymers [59] and later extended to the insulation of etched metal wires. In this technique, negatively charged micelles of poly(acrylic-carboxylic acid) are electrophoretically attracted toward the anodically biased fiber (or wire). Hydrolysis at the fiber surface decreases the pH locally, resulting in the precipitation of the micelles as a thin and uniform film on the fiber surface. Heat curing is then necessary to obtain carbon fibers or metal wires covered with a few microns of thick insulating films. Disk or conical microelectrodes can then be fabricated from the insulated fibers or wires, depending on the technique used to expose their apex. Disk-shaped microelectrodes are produced by cutting the extremity of the insulated fiber/wire. An interesting aspect of this simple exposing technique is that it results in disk-shaped electrode surfaces located exactly at the center of the insulating polymer plane. Moreover, the small RG of these electrodes is useful for SECM applications. However, the electroactive surface exposed by the cutting procedure can be quite rough. Polish of the electrode surface for submicron wires, if possible, may be difficult. If conical microelectrodes are sought then one relies on the shrinking of the paint film, which happens during heat curing, to expose the very apex of the etched fiber/wire. Submicron-sized conical microelectrodes [60], SECM tips [61], and even atomic force microscope (AFM)-SECM combined probes [62] were fabricated in this way. Cathodically deposited electrophoretic (cathaphoretic) paints were also used to insulate SECM and AFM-SECM tips [63]. Using cathaphoretic paints instead of anaphoretic paints is particularly recommended for insulating metal wires since anodic corrosion of the wires during painting is avoided. The wires are typically biased at potentials equal to, or more negative than, −5 V vs. a sacrificial counter electrode. The paint consists of positively charged micelles of quaternary-amine-bearing polymer chains that precipitate upon H^+ reduction and ensuing local pH rise [64]. Isocyanide-bearing chains are also present in the paint and cross-link with the amine-bearing chains during curing. The resulting film is highly cross-linked and insulation is therefore very good. However, paint films deposited from cathaphoretic paints shrink to a very moderate extent during heat curing, and it often happens that the apex of the etched wire is not exposed at this step. Selectively exposing the tip apex can nevertheless be achieved by applying a high-voltage pulse to the microwire, which results in blowing away the film covering the apex [63b,65]. One problem with using unsupported wire or fiber-based electrodes is that they tend to remain so slender and flexible that it may be difficult to align its surface with the substrate. However, the high aspect ratio of these polymer-coated electrodes could be beneficial as an SECM probe for imaging rough surfaces.

3.2.3.1.3 Coating with Molten Polymers or Apiezon Wax

The use of poly(α-methylstyrene) as an insulating material has previously been reported [66]. Other promising insulating materials appear to be Apiezon wax and low-melting-point polyethylene [67,68], although they are unstable and tend to dissolve or swell in most organic solvents. For insulation based on the procedures reported [68], the sharp-etched fibers are mounted on a manipulator. A copper plate (1.5 mm thick), held as shown in Figure 3.10, is heated using a soldering iron element and is used to melt the polymers or Apiezon wax. A 1 mm wide rectangular slit extends from one side to the center of the copper plate, providing a temperature gradient (colder at the open end and hotter at the closed end) for the melted polymer or wax. The tip is raised through the molten wax or polymer and allowed to break the top surface of the melt. If the tip breaks the surface at a too hot region, it is mostly bare. If the tip breaks the surface at the colder region of the melt, it raises a bulb of wax or polymer above it and the tip must be reentered into a hot region to remove the excess wax or polymer. Between these two regions exists an optimum zone where the wax or polymer coats the tip well. The insulated tip is moved sideways out of the groove so as to leave the very end of the tip unperturbed. Several coatings are usually required to insulate the tip completely or nearly completely. The degree of insulation of a tip can be checked by carrying out cyclic voltammetry in a solution containing a redox species. A completely insulated tip will not show detectable voltammetric waves. For a completely insulated tip, the very end of the tip is exposed by placing it in a scanning tunneling microscope (STM) with bias potentials on the tip and a conductive substrate (e.g., a Pt disk or an indium tin oxide (ITO) plate) and the STM set in the constant current mode. The onset of current flow (e.g., 0.1 nA) produces a hole in the tip insulation at the point of closest approach of tip to substrate, while leaving most of the tip still insulated. The amount of exposed area of the tip can be controlled by the bias voltage and the onset current flow. A further treatment of "micropolishing" these tips, by continuously scanning them over the substrate surface, can enlarge

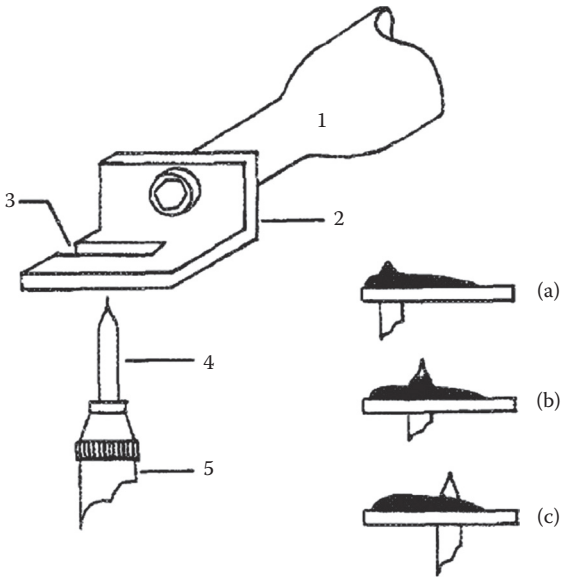


FIGURE 3.10 Illustration of the apparatus/technique used for tip insulation. (1) Soldering iron, (2) copper plate, (3) 1 mm wide slit, (4) STM tip, and (5) pin socket for the tip. (a) At too cold a region, the tip is completely covered with polymer or Apiezon wax. (b) Optimum point allows only the extreme end of the tip to be exposed. (c) At too hot a region, the tip receives little insulation and is thus mostly bare. (Reprinted with permission from Nagahara, L.A., Thundat, T., and Lindsay, S.M., Preparation and characterization of STM tips for electrochemical studies, *Rev. Sci. Instrum.*, 60, 3128–3130, 1989. Copyright 1989, American Institute of Physics.)

the exposed area relative to that of tips not receiving this treatment. These electrodes are very fragile and much more difficult, if possible, to repolish as compared to the glass-encapsulated ones and are discarded after 1 or 2 days of experiments.

Penner et al. used a similar coating technique for polystyrene and its derivatives [66]. A procedure utilizing a soldering iron with an "omega"-shaped wire (diameter = 4 mm) was employed. The polymer bead was supported by this wire and was heated by the soldering iron. It was found that the rate of tip translation during the polymer-coating step did not appear to be an important variable in determining the final coating morphology. The quantity of exposed metal at the coated tip varied reproducibly with the polymer melt temperature. During coating, the polymer melt was adjusted to a temperature of 190°C–205°C. Within this temperature range, the cone/hemisphere radius decreased from 10 to 0.5 μm as the temperature was increased.

3.2.3.1.4 Other Polymer-Coating Techniques

Nanometer-sized disk-shaped SECM tips were prepared from etched Pt wires insulated with a polyimide layer [69]. Polymerization of the polyimide insulating film was thermally triggered: the etched Pt wire was immersed into a *N*,*N*-dimethylacetamide solution containing 1,2,4,5-benzenetetracarboxylic anhydride and 4,4′-diaminodiphenyl ether and the electrode body was heated up until an insulating film formed. The apex of the electrode was exposed by dipping the coated wire in 0.01 M NaOH for a few minutes.

Micrometer-sized conical SECM tips were also fabricated from etched Pt and Au wires insulated by a "Teflon-like" thin film coating [70]. The insulating film was formed by repeatedly dipping the wire (treated with octadecanethiol) into a solution of a highly fluorinated perfluoroether followed by curing under UV light. Three coating/curing cycles were required for a good insulation of the tip. The major interest of this technique is that the tips can be used in nonaqueous solvents including acetonitrile, *N*,*N*-dimethylformamide, and 1,2-dichloroethane. This of course is a benefit of the good chemical resistance of the Teflon-like coating. Indeed most of the other organic thin film coatings typically swell or deteriorate in nonaqueous solvents, largely restricting the use of microelectrodes insulated with organic coatings to aqueous medium. Finally, let us mention that a comparative study of the techniques of thin film insulation coating of microelectrodes can be found in literature [71].

3.2.3.2 Other Sealing Materials

Other sealing materials recommended previously include Torr Seal (Varian Associates, Palo Alto, CA) [72], EPON 828 (Miller-Stephenson Chemical Co., Danbury, CT) [73], and Epoxylite 6001 varnish (Epoxylite Corp., Irvine, CA) [7]. Various sealing materials reported early for electrochemical STM [74] may also be interesting for SECM. The proper choice of the sealing materials depends on the intended use of the microelectrodes. For example, one should pay attention to the solubility, chemical stability, and swelling effect of a sealant in organic solvents if a long-term exposure is required.

3.2.4 Micropipette and Other Tips

Pipette-based electrodes have been used for a wide range of applications, for example, micropipette ion-selective electrodes (ISEs) for potentiometric determination of intracellular and extracellular activities of different ions in living cells [75]. Several scanning probe techniques based on micropipette electrodes have been developed to obtain topographic and chemical information about a sample substrate. For example, scanning ion conductance microscopy [76], which uses an electrolyte-filled Ag/AgCl micropipette electrode as the probe, was used to image the topography of surfaces, and scanning ion-selective potentiometric microscopy [48,77] was developed to map local concentration profiles of various ions. A micropipette tip has also been utilized to form a

micro-ITIES to study ion-transfer and electron-transfer processes and also for SECM imaging [78]. Miniaturization of the electrode body has made possible the fabrication of pipette-based ISEs with tip diameters of micrometer and submicrometer dimensions. Nanometer-sized pipettes can be fabricated by the use of microprocessor-controlled pipette pullers (Laser puller Model P-2000, Sutter Instrument Company) with laser heating of quartz tubes to produce orifice diameters of a few tens of nanometers, and nanopipette electrodes can be constructed using these and an electrolyte filling [77].

3.3 NON-DISK TIPS AND TIP SHAPE CHARACTERIZATION

Two aspects of the use of non-disk microtips in SECM experiments are the evaluation of the shape of microelectrodes and the utilization of advantages associated with a specific tip geometry. For very small electrodes (nanometer-sized electrodes), one cannot obtain good images by electron microscopic techniques and SECM approach curves rather than the voltammetric measurements are used to evaluate UME geometry. In an early report for the steady-state current in a thin-layer cell formed by two electrodes, it was shown that the normalized steady-state diffusion-limited current is fairly sensitive to the geometry of the electrodes [79]. However, the thin-layer theory does not describe accurately the steady-state current between a small tip and a larger planar substrate because the tip steady-state current, $I_{T,\infty}$, was not included in that approximate model. A more realistic approximate theory for SECM with a tip shaped as a cone or spherical segment vs. a planar substrate was later presented [27] and discussed [32,80]. The surface of the nonplanar electrode was considered to be a series of thin circular strips, each of which is parallel to the planar electrode (Figure 3.11). The diffusional flux to each strip was calculated from Equation 3.1 for a conductive substrate or Equation 3.2 for an insulating substrate:

$$I_{\text{disk}}(\Im) = 0.68 + 0.78377/\Im + 0.3315\exp(-1.0672/\Im) \tag{3.1}$$

$$I_{\text{disk}}(\Im) = 1/\left[0.15 + 1.5385/\Im + 0.58\exp(-1.14/\Im) + 0.0908\exp\left\{(\Im - 6.3)/(1.017\Im)\right\}\right] \tag{3.2}$$

in which $\Im = z$ for a spherical tip or x for a conical tip. The normalized current to the whole surface of the segment can be expressed as

$$I_{\text{sp}}(L) = [2/\sin^2\alpha_0]\int_{\cos\alpha_0}^{1} I_{\text{disk}}(z)y\,dy \tag{3.3}$$

for a spherical tip and

$$I_{\text{cone}}(L) = [2/k^2]\int_{0}^{k} I_{\text{disk}}(x)y\,dy \tag{3.4}$$

for a conical one, where L is the distance between the substrate and the point of tip closest to it normalized by the tip radius (i.e., $L = d_0/a_0$), $z = L + (1 - y)/\sin\alpha_0$, $x = L + y$, $I_{\text{disk}}(z)$ is the SECM current function given by Equation 3.1 or 3.2, and k is the ratio of the cone height to its base radius; other parameters are explained in Figure 3.11

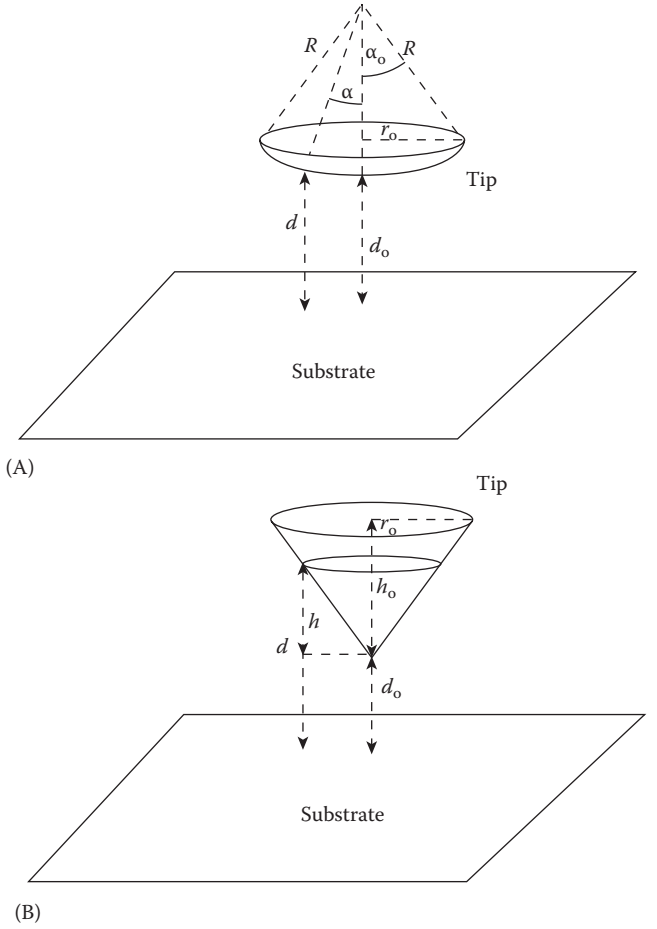


FIGURE 3.11 Schematic diagrams of thin-layer cells formed by a spherical segment tip and a planar substrate (A) and by a conical tip and a planar substrate (B). (Reprinted from *J. Electroanal. Chem.*, 328, Mirkin, M.V., Fan, F.-R.F., and Bard, A.J., Scanning electrochemical microscopy: Part 13. Evaluation of the tip shapes of nanometer size microelectrodes, 47–62, Copyright 1992, with permission from Elsevier.)

The families of working curves, as shown in Figure 3.12, for conductive and insulating substrates were computed from Equations 3.1 through 3.4 for spherical and conical tip shapes, respectively. One can see that the different working curves have substantially different curvatures, thus a unique curve can be found to obtain the best fit with the experimental data. One can also see that the current for a conical tip tends to reach some limiting values as $L \rightarrow 0$ and as $k \rightarrow 0$ the working curves for a conical tip approach that computed for a disk-shaped tip.

3.4 CONCLUSIONS

Since the resolution of SECM depends strongly on the size of tip, future work on tip preparation will probably be directed toward the fabrication of sturdy nanometer-sized tips. It would also be useful to devise a broader range of tip materials, including carbon nanotube and synthetic tips such as chemically modified ones, and to develop multiple tips for both sensing and detection, for example, SECM/ECL (electrogenerated chemiluminescence), SECM/AFM, and SECM/NSOM (near-field scanning optical microscope) tips. The fabrication of potentiometric and enzymatic tips with ultra-high resolution and fast response would also be very valuable. Those combined tips will find useful applications and are described in detail in the appropriate chapters.

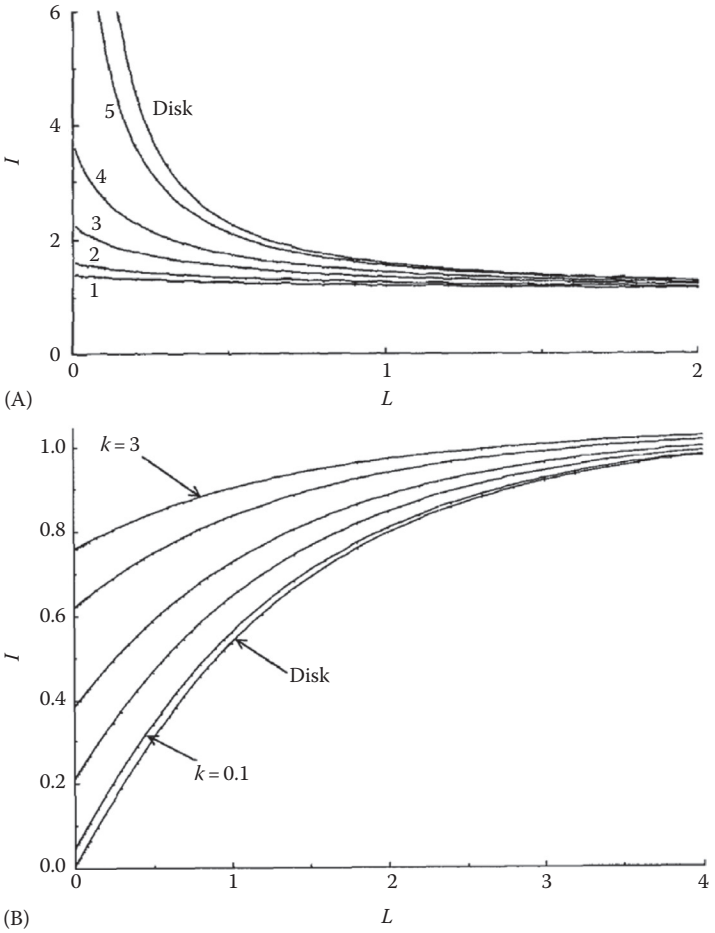


FIGURE 3.12 Steady-state current–distance curve for a conical tip over conductive (A) and insulating (B) substrates corresponding to different values of the parameter $k = h_0/a_0$. (A) $k = 3$ (curve 1), 2 (curve 2), 1 (curve 3), 0.5 (curve 4), and 0.1 (curve 5). The upper curve was computed for a disk-shaped tip from Equation 3.1. (B) From top to bottom, $k = 3$, 2, 0.5, and 0.1. The lower curve was computed for a disk-shaped tip from Equation 3.2. (Reprinted from *J. Electroanal. Chem.*, 328, Mirkin, M.V., Fan, F.-R.F., and Bard, A.J., Scanning electrochemical microscopy: Part 13. Evaluation of the tip shapes of nanometer size microelectrodes, 47–62, Copyright 1992, with permission from Elsevier.)

ACKNOWLEDGMENTS

Fu-Ren F. Fan thanks his colleagues for their inputs and discussions during the development of SECM. The support of the research in SECM by the Robert A. Welch Foundation, the National Science Foundation, and the Texas Advanced Research Program is also gratefully acknowledged.

REFERENCES

1. Fleischmann, M., Pons, S., Rolison, D. R., Schmidt, P. P. *Ultramicroelectrodes*, Datatech Systems, Morgantown, NC, 1987.
2. Kwak, J. Scanning electrochemical microscopy-Experiments and theory, PhD dissertation, The University of Texas at Austin, Austin, TX, 1989.

3. Wightman, R. M., Wipf, D. O. Voltammetry at ultramicroelectrodes. In *Electroanalytical Chemistry*, Vol. 15, A. J. Bard (ed.), Marcel Dekker, New York, 1988, p. 267.
4. (a) Bard, A. J., Fan, F.-R. F., Mirkin, M. V. Scanning electrochemical microscopy. In *Electroanalytical Chemistry*, Vol. 18, A. J. Bard (ed.), Marcel Dekker, New York, 1994, pp. 243–373. (b) Fan, F.-R. F., Fernandez, J., Liu, B., Mauzeroll, J., Zoski, C. G. Platinum and gold inlaid disks. In *Handbook of Electrochemistry*, C. G. Zoski (ed.), Elsevier, Amsterdam, the Netherlands, 2006, pp. 189–197.
5. Lee, C., Miller, C. J., Bard, A. J. Scanning electrochemical microscopy: Preparation of submicrometer electrodes, *Anal. Chem*. 1991, 63, 78–83.
6. (a) Liu, H.-Y., Fan, F.-R. F., Lin, C. W., Bard, A. J. Scanning electrochemical and tunneling ultramicroelectrode microscope for high-resolution examination of electrode surfaces in solution, *J. Am. Chem. Soc*. 1986, 108, 3838–3839. (b) White, H. S. Private communications. (c) Zhang, B., Wang, G., White, H. S. Glass nanopore electrodes. In *Handbook of Electrochemistry*, C. G. Zoski (ed.), Elsevier, Amsterdam, the Netherlands, 2006, pp. 254–260.
7. Gewirth, A. A., Craston, D. H., Bard, A. J. Fabrication and characterization of microtips for in situ scanning tunneling microscopy, *J. Electroanal. Chem*. 1989, 261, 477–482.
8. Pendley, B. D., Abruna, H. D. Construction of submicrometer voltammetric electrodes, *Anal. Chem*. 1990, 62, 782–784.
9. (a) Shao, Y., Mirkin, M. V., Fish, G., Kokotov, S., Palanker, D., Lewis, A. Nanometer-sized electrochemical sensors, *Anal. Chem*. 1997, 69, 1627–1634. (b) Katerlann, B. B., Schuhmann, W. Fabrication and characterization of needle-type Pt-disk nanoelectrodes, *Electroanalysis* 2002, 14, 22–28. (c) Ufheil, J., Hess, C., Borgwarth, K., Heinze, J. Nanostructuring and nanoanalysis by scanning electrochemical microscopy (SECM), *Phys. Chem. Chem. Phys*. 2005, 7, 3185–3190. (d) Sun, P., Mirkin, M. V. Kinetics of electron-transfer reactions at nanoelectrodes, *Anal. Chem*. 2006, 78, 6526–6534. (e) Velmurugan, J., Sun, P., Mirkin, M. V. Scanning electrochemical microscopy with gold nanotips: The effect of electrode material on electron transfer rates, *J. Phys. Chem. C* 2009, 113, 459–464. (f) Li, Y., Berman, D., Zhang, B. Preparation and electrochemical response of 1–3 nm Pt disk electrodes, *Anal. Chem*. 2009, 81, 5496–5502. (g) Laforge, F. O., Velmurugan, J., Wang, Y., Mirkin, M. V. Nanoscale imaging of surface topography and reactivity with the scanning electrochemical microscope, *Anal. Chem*. 2009, 81, 3143–3150. (h) Mauzeroll, J., LeSuer, R. J. Laser-pulled ultramicroelectrodes. In *Handbook of Electrochemistry*, C. G. Zoski (ed.), Elsevier, Amsterdam, the Netherlands, 2006, pp. 199–211.
10. Fish, G., Bouevitch, O., Kokotov, S., Lieberman, K., Palanker, D., Turovets, I., Lewis, A. Ultrafast response micropipette-based submicrometer thermocouple, *Rev. Sci. Instrum*. 1995, 66, 3300–3306.
11. Morgan, R. An automatic electropolishing supervisor for preparing field ion microscope specimens, *J. Sci. Instrum*. 1967, 4, 808–809.
12. Chen, Y., Xu, W., Huang, J. A simple new technique for preparing STM tips, *J. Phys. E* 1989, 22, 455–457.
13. Ibe, J. P., Bey, P. P., Jr., Brandow, S. L., Brizzolara, R. A., Burnham, N. A., DiLella, D. P., Lee, K. P., Marrian, C. R. K., Colton, R. J. On the electrochemical etching of tips for scanning tunneling microscopy, *J. Vac. Sci. Technol. A* 1990, 8, 3570–3575.
14. Hansma, P. K., Tersoff, J. Scanning tunneling microscopy, *J. Appl. Phys*. 1987, 61, R1–R23.
15. Stroscio, J. A., Feenstra, R. M., Fein, A. P. Local state density and long-range screening of adsorbed oxygen atoms on the GaAs(110) surface, *Phys. Rev. Lett*. 1987, 58, 1668–1671.
16. Neddermeyer, H., Drechsler, M. Electric field-induced changes of tungsten(110) and tungsten(111) tips, *J. Microsc*. 1988, 152, 459–466.
17. Binh, V. T. In situ fabrication and regeneration of microtips for scanning tunneling microscope, *J. Microsc*. 1988, 152, 355–360.
18. Biegelsen, D. K., Ponce, F. A., Tramontana, J. C., Koch, S. M. Ion mined tips for scanning tunneling microscopy, *Appl. Phys. Lett*. 1987, 50, 696–698.
19. Biegelsen, D. K., Ponce, F. A., Tramontana, J. C. Simple ion mining preparation of (111) tungsten tips, *Appl. Phys. Lett*. 1989, 54, 1223–1225.
20. Demaille, C., Brust, M., Tsionsky, M., Bard, A. J. Fabrication and characterization of self-assembled spherical gold ultramicroelectrodes, *Anal. Chem*. 1997, 69, 2323–2328.
21. Brust, M., Bethell, D., Schiffrin, D. J., Kiely, C. J. Novel gold-dithiol nano-networks with non-metallic electronic properties, *Adv. Mater*. 1995, 7, 795–797.
22. Bethell, D., Brust, M., Schiffrin, D. J., Kiely, C. J. From monolayers to nanostructured materials: An organic chemist's view of self-assembly, *J. Electroanal. Chem*. 1996, 409, 137–143.
23. Demaille, C., Brust, M., Tsionsky, M., Bard, A. J. Unpublished results.
24. (a) Whetten, R. L., Khoury, J. T., Alvarez, M. M., Murthy, S., Vezmar, I., Wang, Z. L., Stephens, P. W., Cleveland, C. L., Luedtke, W. D., Landman, U. Nanocrystal gold molecules, *Adv. Mater*. 1996, 8,

428–433. (b) Andres, R. P., Bielefeld, J. D., Henderson, J. I., Janes, D. B., Kolagunta, V. R., Kubiak, C. P., Mahoney, W. J., Osifchin, R. G. Self-assembly of a two-dimensional superlattice of molecularly linked metal clusters, *Science* 1996, 273, 1690–1693.

25. Rand, D. A. J., Woods, R. The nature of adsorbed oxygen on rhodium, palladium and gold electrodes, *J. Electroanal. Chem*. 1971, 31, 29–38.
26. Montenegro, M. I., Queiros, M. A., Daschbach, J. L. (eds.). *Microelectrodes: Theory and Applications*, NATO ASI Ser. Appl. Sci., Vol. 197, Kluwer Academic Publishers, Dordrecht, the Netherlands, 1991.
27. Mirkin, M. V., Fan, F.-R. F., Bard, A. J. Scanning electrochemical microscopy: Part 13. Evaluation of the tip shapes of nanometer size microelectrodes, *J. Electroanal. Chem*. 1992, 328, 47–62.
28. (a) Unwin, P. R., Bard, A. J. Scanning electrochemical microscopy. 9. Theory and application of the feedback mode to the measurement of following chemical reaction rates in electrode processes, *J. Phys. Chem*. 1991, 95, 7814–7824. (b) Zhou, F., Unwin, P. R., Bard, A. J. Scanning electrochemical microscopy. 16. Study of second-order homogeneous chemical reactions via the feedback and generation/collection modes, *J. Phys. Chem*. 1992, 96, 4317–4324. (c) Unwin, P. R., Bard, A. J. Scanning electrochemical microscopy. 14. Scanning electrochemical microscope induced desorption: A new technique for the measurement of adsorption/desorption kinetics and surface diffusion rates at the solid/liquid interface, *J. Phys. Chem*. 1992, 96, 5035–5045. (d) Treichel, D. A., Mirkin, M. V., Bard, A. J. Scanning electrochemical microscopy. 27. Application of a simplified treatment of an irreversible homogeneous reaction following electron transfer to the oxidative dimerization of 4-nitrophenolate in acetonitrile, *J. Phys. Chem*. 1994, 98, 5751–5757. (e) Zhou, F., Bard, A. J. Detection of the electrohydrodimerization intermediate acrylonitrile radical anion by scanning electrochemical microscopy, *J. Am. Chem. Soc*. 1994, 116, 393–394. (f) Demaille, C., Unwin, P. R., Bard, A. J. Scanning electrochemical microscopy. 33. Application to the study of ECE/DISP reactions, *J. Phys. Chem*. 1996, 100, 14137–14143.
29. Wehmeyer, K. R., Wightman, R. M. Cyclic voltammetry and anodic stripping voltammetry with mercury ultramicroelectrodes, *Anal. Chem*. 1985, 57, 1989–1993.
30. Golas, J., Galus, Z., Osteryoung, J. Iridium-based small mercury electrodes, *Anal. Chem*. 1987, 59, 389–392.
31. Stojek, Z., Osteryoung, J. Experimental determination of the coefficient in the steady state current equation for spherical segment microelectrodes, *Anal. Chem*. 1989, 61, 1305–1308.
32. (a) Selzer, Y., Mandler, D. Scanning electrochemical microscopy. Theory of the feedback mode for hemispherical ultramicroelectrodes: Steady-state and transient behavior, *Anal. Chem*. 2000, 72, 2383–2390. (b) Daniele, S., Bragato, C., Ciani, I., Baldo, M. Sphere-cap mercury microelectrodes for scanning electrochemical microscopy above an insulating substrate, *Electroanalysis* 2003, 15, 621–628. (c) Mauzeroll, J., Buda, M., Bard, A. J. Detection of Tl(I) transport through a gramicidin-dioleoylphosphatidylcholine monolayer using the substrate generation–tip collection mode of scanning electrochemical microscopy, *Langmuir* 2002, 18, 9452–9461. (d) Mauzeroll, J., Hueske, E. A., Bard, A. J. Scanning electrochemical microscopy. 48. Hg/Pt hemispherical ultramicroelectrodes: Fabrication and characterization, *Anal. Chem*. 2003, 75, 3880–3889. (e) Lindsey, G., Abercrombie, S., Denuault, G., Daniele, S., De Faberi, E. Scanning electrochemical microscopy: Approach curves for sphere-cap scanning electrochemical microscopy tips, *Anal. Chem*. 2007, 79, 2952–2956.
33. Ciani, H., Daniele, S., Bragato, C., Baldo, M. Stability of mercury-coated platinum microelectrodes upon touching a solid surface in scanning electrochemical microscopy (SECM) experiments, *Electrochem. Commun*. 2003, 5, 354–358.
34. (a) Rudolph, D., Neuhuber, S., Kranz, C., Taillefert, M., Mizaikoff, B. Scanning electrochemical microscopy imaging of rhodochrosite dissolution using gold amalgam microelectrodes, *Analyst* 2004, 129, 443–448. (b) Alpuche-Aviles, M. A., Baur, J. E., Wipf, D. O. Imaging of metal ion dissolution and electrodeposition by anodic stripping voltammetry–scanning electrochemical microscopy, *Anal. Chem*. 2008, 80, 3612–3621. (c) Jung, C., Sánchez-Sánchez, C. M., Lin, C.-L., Rodríguez-López, J., Bard, A. J. Electrocatalytic activity of Pd–Co bimetallic mixtures for formic acid oxidation studied by scanning electrochemical microscopy, *Anal. Chem*. 2009, 81, 7003–7008.
35. Edmonds, T. E. Electroanalytical applications of carbon fibre electrodes, *Anal. Chim. Acta* 1985, 175, 1–22.
36. Besenhard, J. O., Schulte, A., Schur, K., Jannakoudakis, P. P. Preparation of voltammetric and potentiometric carbon fiber microelectrodes. In *Microelectrodes: Theory and Applications*, NATO ASI Ser. A001. Sci., Vol. 197, M. I. Montenegro, M. A. Queiros, and J. L. Daschbach (eds.), Kluwer Academic Publishers, Dordrecht, the Netherlands, 1991.
37. Ponchon, J. L., Cespuglio, R., Conon, F., Jouvet, M., Pujol, J.-F. Normal pulse polarography with carbon fiber electrodes for in vitro and in vivo determination of catecholamines, *Anal. Chem*. 1979, 51, 1483–1486.

38. Dayton, M. A., Brown, J. C., Stutts, K. J., Wightman, R. M. Faradaic electrochemistry at microvoltammetric electrodes, *Anal. Chem*. 1980, 52, 946–950.
39. Wightman, R. M. Microvoltammetric electrodes, *Anal. Chem*. 1981, 53, 1125A–1134A.
40. Kelly, R. S., Wightman, R. M. Bevelled carbon-fiber ultramicroelectrodes, *Anal. Chim. Acta* 1986, 187, 79–87.
41. (a) Miles, D. T., Knedlik, A., Wipf, D. O. Construction of gold microbead ultramicroelectrodes, *Anal. Chem*. 1997, 69, 1240–1243. (b) Tsionsky, M., Demaille, C., Bard, A. J. Unpublished results.
42. (a) Bard, A. J., Fan, F.-R. F., Kwak, J., Lev, O. Scanning electrochemical microscopy. Introduction and principles, *Anal. Chem*. 1989, 61, 132–138. (b) Pierce, D. T., Unwin, P. R., Bard, A. J. Scanning electrochemical microscopy. 17. Studies of enzyme–mediator kinetics for membrane and surface-immobilized glucose oxidase, *Anal. Chem*. 1992, 64, 1795–1804.
43. Strein, T. G., Ewing, A. G. Characterization of submicron-sized carbon electrodes insulated with a phenol–allylphenol copolymer, *Anal. Chem*. 1992, 64, 1368–1373.
44. Meulemans, A., Poulain, B., Baux, G., Tau, L., Henzel, D. Micro carbon electrode for intracellular voltammetry, *Anal. Chem*. 1986, 58, 2088–2091.
45. Abe, T., Itaya, K., Uchida, I. An electrochemical fabrication method for gold and carbon ultramicroelectrodes, *Chem. Lett*. 1988, 399–402.
46. Zhang, X., Zhang, W., Zhou, X., Ogorevc, B. Fabrication, characterization, and potential application of carbon fiber cone nanometer-size electrodes, *Anal. Chem*. 1996, 68, 3338–3343.
47. Che, S., Kucernak, A. Fabrication of carbon microelectrodes with an effective radius of 1 nm, *Electrochem. Commun*. 2002, 4, 80–85.
48. Li, X., Geng, Q., Wang, Y., Si, Z., Jiang, W., Zhang, X., Jin, W. Micropatterning of active enzyme with a high-resolution by scanning electrochemical microscopy coupled with a nanometer-sized carbon fiber disk tip, *Electrochim. Acta* 2007, 53, 2016–2024.
49. Bauermann, L. P., Schuhmann, W., Schulte, A. An advanced biological scanning electrochemical microscope (Bio-SECM) for studying individual living cells, *Phys. Chem. Chem. Phys*. 2004, 6, 4003–4008.
50. Blaedel, W. J., Mabbot, G. A. Pyrolytic carbon film electrode, *Anal. Chem*. 1978, 50, 933–936.
51. Kim, Y.-T., Scanulis, D. M., Ewing, A. G. Carbon-ring electrodes with 1-μm tip diameter, *Anal. Chem*. 1986, 58, 1782–1786.
52. Wong, D. K. Y., Xu, L. Y. F. Voltammetric studies of carbon disk electrodes with submicrometer-sized structural diameters, *Anal. Chem*. 1995, 67, 4086–4090.
53. Bard, A. J., Demaille, C., Tsionsky, M. Unpublished results.
54. Wei, C., Bard, A. J., Nagy, G., Toth, K. Scanning electrochemical microscopy. 28. Ion-selective neutral carrier-based microelectrode potentiometry, *Anal. Chem*. 1995, 67, 1346–1356.
55. Fan, F.-R. F., Kwak, J., Bard, A. J. Single molecule electrochemistry, *J. Am. Chem. Soc*. 1996, 118, 9669–9675.
56. Holt, K. B., Hu, J., Foord, J. S. Fabrication of boron-doped diamond ultramicroelectrodes for use in scanning electrochemical microscopy experiments, *Anal. Chem*. 2007, 79, 2556–2561.
57. Pojte-Kamloth, K., Janata, J., Josowicz, M. Electrochemically prepared insulation for carbon fiber microelectrodes, *Ber. Bunsen. Phys. Chem*. 1989, 93, 1480–1485.
58. Liebetrau, J. M., Miller, H. M., Baur, J. E., Takacs, S. A., Anupunpisit, V., Garris, P. A., Wipf, D. O. Scanning electrochemical microscopy of model neurons: Imaging and real-time detection of morphological changes, *Anal. Chem*. 2003, 75, 563–571.
59. (a) Schulte, A., Chow, R. H. A simple method for insulating carbon-fiber microelectrodes using anodic electrophoretic deposition of paint, *Anal. Chem*. 1996, 68, 3054–3058. (b) Schulte, A., Chow, R. H. Cylindrically etched carbon–fiber microelectrodes for low-noise amperometric recording of cellular secretion, *Anal. Chem*. 1998, 70, 985–990. (c) Bach, C. E., Nichols, R. J., Meyer, H. I., Besenhard, J. O. An electropainting method for coating STM tips for electrochemical measurements, *Surf. Coat*. 1994, 67, 139–144. (d) Bach, C. E., Nichols, R. J., Beckman, W., Meyer, H., Schulte, A., Besenhard, J. O. Effective insulation of scanning tunneling microscopy tips for electrochemical studies using an electropainting method, *J. Electrochem. Soc*. 1993, 140, 1281–1284. (e) Slevin, C. J., Gray, N. J., Macpherson, J. V., Webb, M. A., Unwin, P. R. Fabrication and characterisation of nanometer-sized platinum electrodes for voltammetric analysis and imaging, *Electrochem. Commun*. 1999, 1, 282–288.
60. Conyers, J. L., White, H. S., Electrochemical characterization of electrodes with submicrometer dimensions, *Anal. Chem*. 2000, 72, 4441–4446.
61. Zu, Y., Ding, Z., Lee, Y., Bard, A. J., Scanning optical microscopy with an electrogenerated chemiluminescent light source at a nanometer tip, *Anal. Chem*. 2001, 73, 2153–2156.

62. Macpherson, J. V., Unwin, P. R. Combined scanning electrochemical-atomic force microscopy, *Anal. Chem*. 2000, 72, 276–285.
63. (a) Gray, N. J., Unwin, P. R. Simple procedure for the fabrication of silver/silver chloride potentiometric electrodes with micrometre and smaller dimensions: Application to scanning electrochemical microscopy, *Analyst* 2000, 125, 889–893. (b) Abbou, J., Demaille, C., Druet, M., Moiroux, J. Fabrication of submicrometer-sized gold electrodes of controlled geometry for scanning electrochemical-atomic force microscopy, *Anal. Chem*. 2002, 74, 6355–6363.
64. Zhu, L., Claude-Montigny, B., Gattrell, M. Insulating method using cataphoretic paint for tungsten tips for electrochemical scanning tunnelling microscopy (ECSTM), *Appl. Surf. Sci*. 2005, 252, 1833–1845.
65. Demaille, C. Gold spherical microelectrodes. In *Handbook of Electrochemistry*, C. G. Zoski (ed.), Elsevier, Amsterdam, the Netherlands, 2006, pp. 230–235.
66. Penner, R. M., Heben, M. J., Lewis, N. S. Preparation and electrochemical characterization of conical and hemispherical ultramicroelectrodes, *Anal. Chem*. 1989, 61, 1630–1636.
67. Wiechers, J., Toomey, T., Kolb, D. M., Behm, R. J. An in-situ scanning tunneling microscopy study of Au(111) with atomic scale resolution, *J. Electroanal. Chem*. 1988, 248, 451–460.
68. Nagahara, L. A., Thundat, T., Lindsay, S. M. Preparation and characterization of STM tips for electrochemical studies, *Rev. Sci. Instrum*. 1989, 60, 3128–3130.
69. Sun, P., Zhang, Z., Guo, J., Shao, Y. Fabrication of nanometer-sized electrodes and tips for scanning electrochemical microscopy, *Anal. Chem*. 2001, 73, 5346–5351.
70. Liu, B., Rolland, J. P., DeSimone, J. M., Bard, A. J. Fabrication of ultramicroelectrodes using a "Teflon-like" coating material, *Anal. Chem*. 2005, 77, 3013–3017.
71. Lindsay, A. E., O'Hare, D. A comparative study of thin film insulation techniques for gold electrodes, *Electrochim. Acta* 2006, 51, 6572–6579.
72. Thormann, W., Bond, A. M. Application of transient electrochemical techniques to inlaid ultra-microelectrodes: Assessment of fabrication quality, *J. Electroanal. Chem*. 1987, 218, 187–196.
73. Kovach, P. M., Deakin, M. R., Wightman, R. M. Electrochemistry at partially blocked carbon–fiber microcylinder electrodes, *J. Phys. Chem*. 1986, 90, 4612–4617.
74. Bard, A. J., Fan, F.-R. F. Applications in electrochemistry. In *Scanning Tunneling Microscopy and Spectroscopy: Theory, Techniques, and Applications*, D. A. Bonnell (ed.), 2nd edn., Wiley-VCH Publishers, Inc., New York, 2001.
75. Ammann, D. *Ion Selective Microelectrodes: Principles, Design and Application*, Springer-Verlag, New York, 1986.
76. (a) Hansma, P. K., Marti, O., Gould, S. A. C., Prater, C. B. The scanning ion-conductance microscope, *Science* 1989, 243, 641–643. (b) Prater, C. B., Hansma, P. K., Tortonese, M., Quate, C. F. Improved scanning ion-conductance microscope using microfabricated probes, *Rev. Sci. Instrum*. 1991, 62, 2634–2638.
77. (a) Toth, K., Nagy, N., Wei, C., Bard, A. J. Novel application of potentiometric microelectrodes: Scanning potentiometric microscopy, *Electroanalysis* 1995, 7, 801–810. (b) Horrocks, B. R., Mirkin, M. V., Pierce, D. T., Bard, A. J., Nagy, N., Toth, K. Scanning electrochemical microscopy. 19. Ion-selective potentiometric microscopy, *Anal. Chem*. 1993, 65, 1213–1224.
78. (a) Stewart, A. A., Taylor, G., Girault, H. H. J. Voltammetry at microITIES supported at the tip of a micropipette: Part I. Linear sweep voltammetry, *J. Electroanal. Chem*. 1990, 296, 491–515. (b) Solomon, T., Bard, A. J. Scanning electrochemical microscopy. 30. The application of glass micropipet tips and electron transfer at the ITIES for SECM imaging, *Anal. Chem*. 1995, 67, 2787–2790. (c) Shao, Y., Mirkin, M. V. Fast kinetic measurements with nanometer-sized pipets-transfer of potassium ion from water into dichloroethane facilitated by dibenzo-18-crown-6, *J. Am. Chem. Soc*. 1997, 119, 8103–8104. (d) Zhan, D., Li, X., Zhan, W., Fan, F.-R. F., Bard, A. J. Scanning electrochemical microscopy. 58. Application of a micropipet-supported ITIES tip to detect Ag^+ and study its effect on fibroblast cells, *Anal. Chem*. 2007, 79, 5225–5231. (e) Zhan, D., Fan, F.-R. F., Bard, A. J. The Kv channel blocker 4-aminopyridine enhances Ag^+ uptake: A scanning electrochemical microscopy study of single living cells, *Proc. Natl. Acad. Sci. USA* 2008, 105, 12118–12122.
79. Davis, J. M., Fan, F.-R. F., Bard, A. J. Currents in thin layer electrochemical cells with spherical and conical electrodes, *J. Electroanal. Chem*. 1987, 238, 9–31.
80. Zoski, C. G., Liu, B., Bard, A. J. Scanning electrochemical microscopy: Theory and characterization of electrodes of finite conical geometry, *Anal. Chem*. 2004, 76, 3646–3654.

4 Scanning Electrochemical Microscopic Imaging

Fu-Ren F. Fan

CONTENTS

4.1 Introduction 53
4.2 Principle and Methodology of SECM Imaging 53
4.3 Imaging in Solutions 55
4.3.1 Membranes 55
4.3.2 Leaves and Single Cells 56
4.3.3 Artificially Patterned Biological Systems 60
4.3.4 Thin Films and Corrosion Systems 61
4.3.5 Other Systems and Potentiometric Imaging 62
4.4 Imaging in Humid Air 63
4.4.1 Instrumentation and Sample Preparation 63
4.4.2 Electrochemical Behavior 63
4.4.3 SECM Behavior and Imaging 66
4.5 Conclusions 72
Acknowledgments 72
References 72

4.1 INTRODUCTION

In this chapter, it is intended to provide the readers with an up-to-date account of scanning electrochemical microscopic (SECM) imaging in chemical and biological applications. Some examples of SECM imaging in bulk liquid environments are demonstrated in Section 4.2, which include membranes, leaves, single biological cells, artificially patterned biological systems, and corrosion systems. In Section 4.3, an imaging technique involving an ultrathin liquid layer on a mica substrate is described. The images of an ionic conductive polymer, for example, Nafion, and several macrobiological molecules are shown to demonstrate the applicability of this technique for imaging. Since the main focus of this chapter is on the developments related to imaging, other applications of SECM and detailed account of the development in instrumentation will not be given here. Interested readers are recommended to consult individual chapters presented in this book.

4.2 PRINCIPLE AND METHODOLOGY OF SECM IMAGING

A three-dimensional SECM image is obtained by scanning the tip in the x–y plane and monitoring the tip current, i_T, as a function of tip location, the so-called constant height mode. The image can be converted to a plot of z-height (distance between tip and substrate), d, vs. x–y position via an i_T vs. d calibration plot or can be plotted as a gray-scale image, where high values of i_T are shown in light colors and small values as dark colors. Figure 4.1A shows a constant height SECM image of a

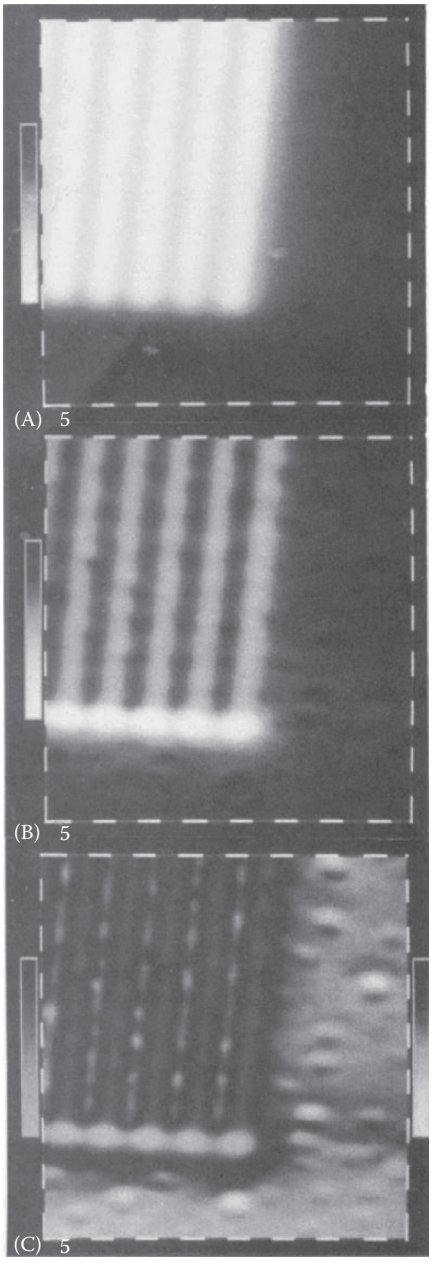


FIGURE 4.1 (A) Constant height SECM image of a 80 μm × 80 μm portion of an IDA in a solution containing 1.5 mM $Ru(NH_3)_6^{3+}$ in pH 4.0 buffer. The IDA structure consists of 3 μm wide bands of Pt separated by 5 μm of SiO_2. For this image, a 1 μm radius Pt disk served as the tip. The imaging tip current was 200–850 pA and $i_{T,\infty} = 470$ pA, $d \sim 0.9$ μm. (B) and (C) show the SECM images of the same IDA structure as used in (A) acquired by TPM technique. Modulation frequency = 160 Hz. (B) TPM SECM image, scale −7 to 15 pA_{rms}. (C) Absolute value TPM SECM image, left scale = 0–15; right scale = 0–7 pA_{rms}. (Reprinted with permission from Wipf, D.O. and Bard, A.J., Scanning electrochemical microscopy. 15. Improvements in imaging via tip-position modulation and lock-in detection, *Anal. Chem*., 64, 1362–1367, 1992. Copyright 1992 American Chemical Society.)

80 μm × 80 μm portion of an interdigitated electrode array (IDA), which consists of 3 μm wide bands of Pt separated by 5 μm of SiO_2. For this image, a 1 μm radius Pt disk served as the tip, and this tip and the IDA were immersed in a solution containing 1.5 mM $Ru(NH_3)_6^{3+}$ in pH 4.0 buffer. The imaging tip current was 200–850 pA and $i_{T,\infty} = 470$ pA.

The resolution attainable with the SECM is largely governed by the tip size and the distance between tip and sample. With a very small diameter tip (e.g., diameter <100 nm), scanning the tip in close proximity to the substrate surface (e.g., 100 nm above the surface) and measuring the tip current become very difficult because stray vibrations, irregularities in the sample surface, or tilt of the sample can cause a "tip crash." Thus, for high resolution, the SECM must be operated in the constant current (or alternatively, constant impedance) mode, as is often used with the scanning tunneling microscope (STM) [1], where the distance is adjusted by a feedback loop to the *z*-piezo to maintain i_T constant. This is straightforward when the sample is either all conductive or all insulating, since the piezo feedback can be set to counter a decrease or increase in tip current by either moving the tip closer (conductor) or farther away (insulator).

For the samples that contain both types of regions, a method of recognizing the nature of the substrate must be available for the designing feedback loop. One approach is to modulate the motion of the tip normal to the sample surface and record di_T/dz, the so-called tip position modulation (TPM) technique [2]. The use of TPM technique can substantially improve the sensitivity and resolution of the SECM image and provide a method of distinguishing between conductive and insulating areas on the substrate surface being examined. Figure 4.1B and C shows the SECM images of the same IDA structure as used in Figure 4.1A acquired by TPM technique. As shown, the images acquired with the TPM signal are significantly more detailed than the dc image (Figure 4.1A). In particular, note the improved detail in the insulating region of the image due to the better sensitivity of the TPM signal at insulators. Another interesting topography feedback mechanism for SECM imaging is the one based on hydrodynamic force modulation developed by Ludwig et al. [3], in which a microelectrode is vibrated laterally and the damping of the tip vibration amplitude upon its approach to the sample surface is measured. Such an approach allows for controlling the vertical position of the electrode independently from electrochemical parameters. Other related combined SECM imaging techniques are discussed in more detail in appropriate chapters.

4.3 IMAGING IN SOLUTIONS

Because the SECM response is a function of the rate of the heterogeneous reaction at the substrate, it can be used to image the local chemical and electrochemical reactivity of surface features. A technique called reaction-rate imaging, which is unique to SECM, is particularly useful in imaging the areas on a surface where reactions occur. Membranes [4–6], leaves [7–9], polymers [10,11], surface films [12–16], artificially patterned biological systems [6,17–19], and single biological cells have been imaged with SECM.

4.3.1 Membranes

Images of the molecular flux across porous membranes, for example, track-etched mica membranes [4] and excised mouse skins [5] have been obtained by monitoring the iontophoretic current through the pores. The ability to detect ca. 1 μm radius pores separated by 50–100 μm has been demonstrated. The contribution of the electrophoretic flux of individual types of ions to the total conductivity through individual pores was also studied. Figure 4.2 shows a series of constant height SECM images of polycarbonate filtration membranes having a nominal average pore size of ca. 14 μm. These images were taken at Pt disk tips immersed in a KCl solution containing $K_4Fe(CN)_6$. As shown in images A–C for a 10 μm diameter Pt disk, the resolution of SECM images can be improved by decreasing the height at which the tip is rastered above the surface.

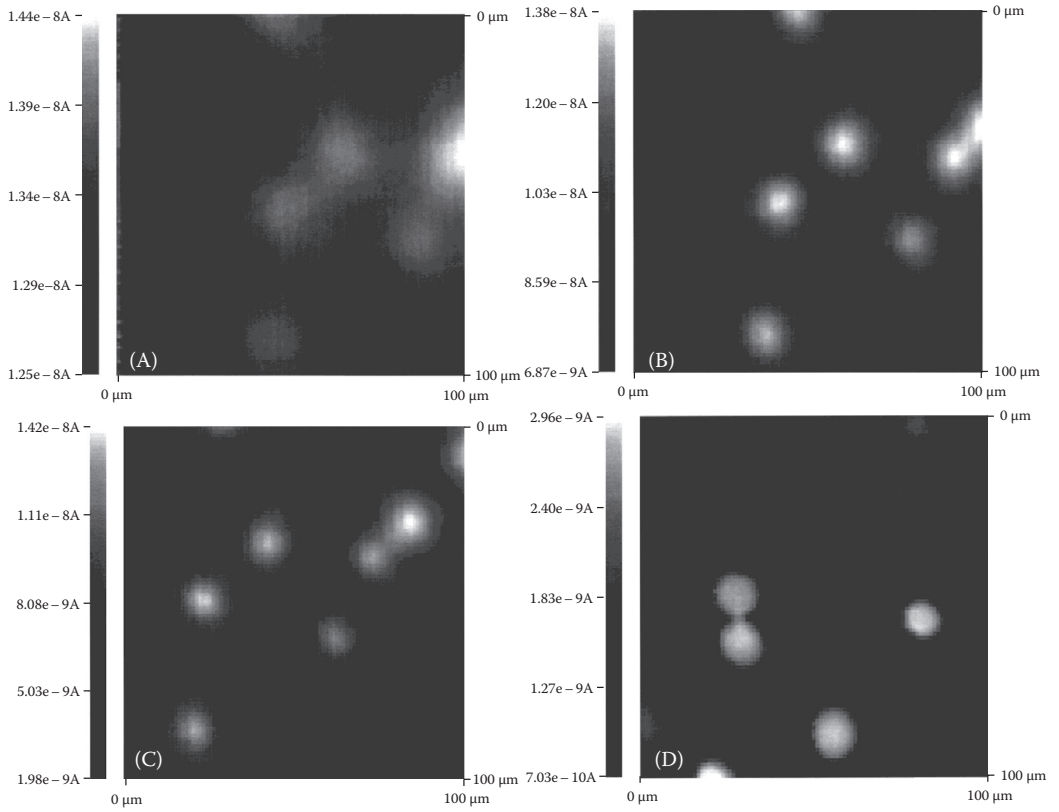


FIGURE 4.2 Series of constant height SECM images of polycarbonate filtration membranes having a nominal average pore size of ca. 14 µm. The scan size of each image is 100 µm × 100 µm. These images were taken with a commercially available SECM unit at Pt disk tips immersed in a solution containing $K_4Fe(CN)_6$ as the redox mediator and KCl as the supporting electrolyte. Images A–C for a 10 µm diameter Pt disk were taken at different normalized distances, L. (A) $L = 2.4$, (B) 1.0, and (C) 0.25. Image (D) shows one SECM image at a different location of the same membrane taken with a smaller tip (2 µm diameter) at a normalized distance of 1.

The image taken at a normalized distance of 2.4 (image A) shows significant overlap between the diffusion fields of the electroactive mediator around individual pores. Decrease the tip height to a normalized distance of 0.25 (image C) resolves almost completely individual pores, although the apparent pore size is substantially larger than the nominal value. Figure 4.2D shows one SECM image of the same membrane with a smaller tip (2 µm diameter) at a normalized distance of 1. As can be seen, not only individual pores are well resolved but the apparent pore size is fairly close to the nominal value.

4.3.2 Leaves and Single Cells

In one of the previous works, SECM has been used to obtain topographic information about biological samples immersed in an electrolyte solution, either by using the feedback mode or by detecting a substrate-generated electroactive species (e.g., oxygen in the photosynthesis process) at the tip [7]. For example, the upper surface of a *Ligustrum sinense* leaf that was immersed in an aqueous solution of $Fe(CN)_6^{4-}$ could be imaged by SECM (Figure 4.3A). The image in gray scale shows the parallel venation pattern characteristic of monocot leaves. An SECM image over the bottom surface of the leave is shown in Figure 4.3B. Several open stomata structures can be seen,

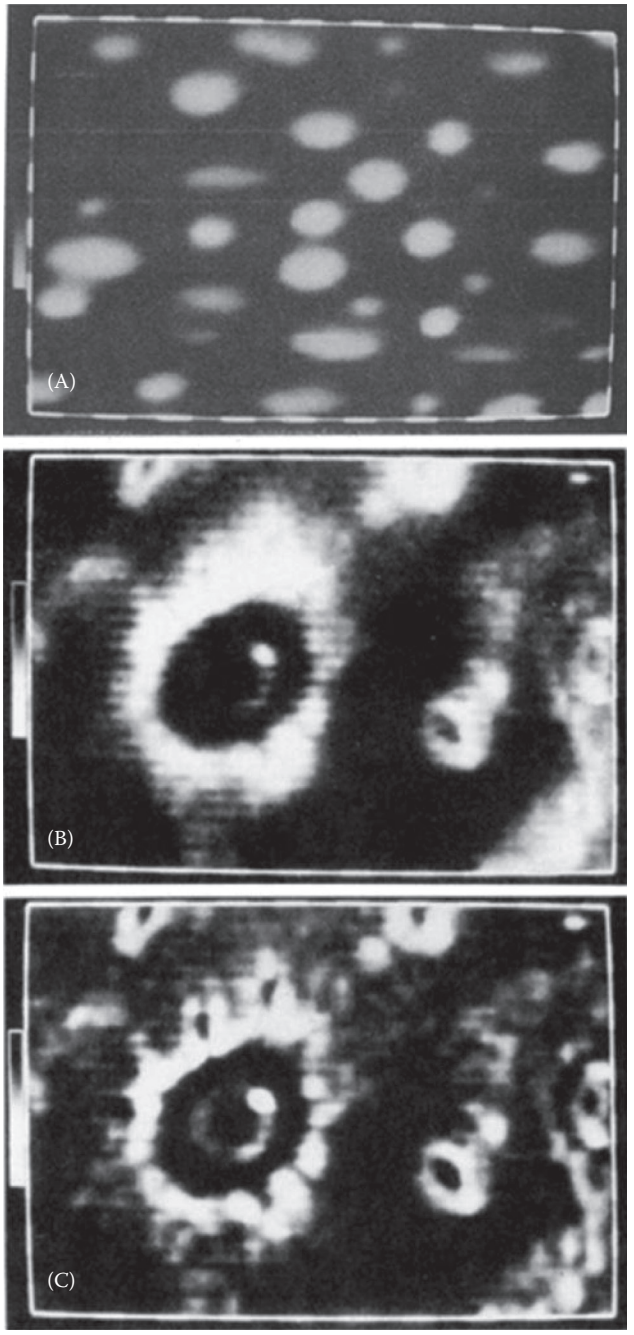


FIGURE 4.3 Gray-scale images of leaves in a 20 mM $K_4Fe(CN)_6$ and 0.1 M KCl solution scanned with a 1 μm radius Pt tip: scan area 188 μm × 142 μm (white markers around edges = 10 μm). (A) Top surface of a grass leaf. (B) Bottom surface of a *L. sinense* leaf. (A and B: Reprinted with permission from Lee, C.M., Kwak, J.Y., and Bard, A.J., Application of scanning electrochemical microscopy to biological samples, *Proc. Natl. Acad. Sci. USA*, 87, 1740–1743, 1990. Copyright 1990 National Academy of Science, USA.) (C) The image in (B) after image processing by the use of the Laplacian of Gaussian (LOG) filter. (Lee, C.M., Wipf, D.O., Bard, A.J., Bartels, K., and Bovik, A.C., Scanning electrochemical microscopy. 11. Improvement of image resolution by digital processing techniques, *Anal. Chem*., 63, 2442–2447, 1991. Copyright 1991 American Chemical Society.)

showing that the guard cells (pairs of specialized epidermal cells surrounding each stomata) are swollen and protrude above the surrounding epidermal cells. The image of Figure 4.3B after image processing by the use of the Laplacian of Gaussian (LOG) filter [20] is shown in Figure 4.3C. A large, crater-like feature at middle left shows finer structure and some stomata at the upper-right and middle-right edges show their structures more clearly. The tip can also be used to detect electroactive products generated at a biological substrate. For example, the detection of oxygen during illumination of an Elodea leaf has been carried out in a 10 mM NaCl solution saturated with CO_2 [7].

SECM has also been used to examine in vivo topography and photosynthetic electron transport of individual guard cells in *Tradescantia fluminensis* [9]. A topographic image by SECM of a 200 μm × 200 μm leaf area shows three stomata complexes (Figure 4.4). Prior to making the image, the stomata were opened by applying 0.1 M KCl, and SECM clearly detects the open stomata pores. Figure 4.4A shows the current image; the dark areas represent bulges on the leaf surface and correspond to low tip current. Figure 4.4B shows the proper topographic image by converting the tip current to distance. As shown, a typical *T. fluminensis* stomata complex protrudes ~4 μm from the surrounding epidermal region of the leaf. In addition to topographic images, SECM has also been used to monitor oxygen evolution from an illuminated leaf for an individual stomata region. Figure 4.5A shows three peaks in the tip current corresponding to oxygen evolution from three stomata. i_T values for these peaks are at least twice background i_T for the leaf surface as a whole.

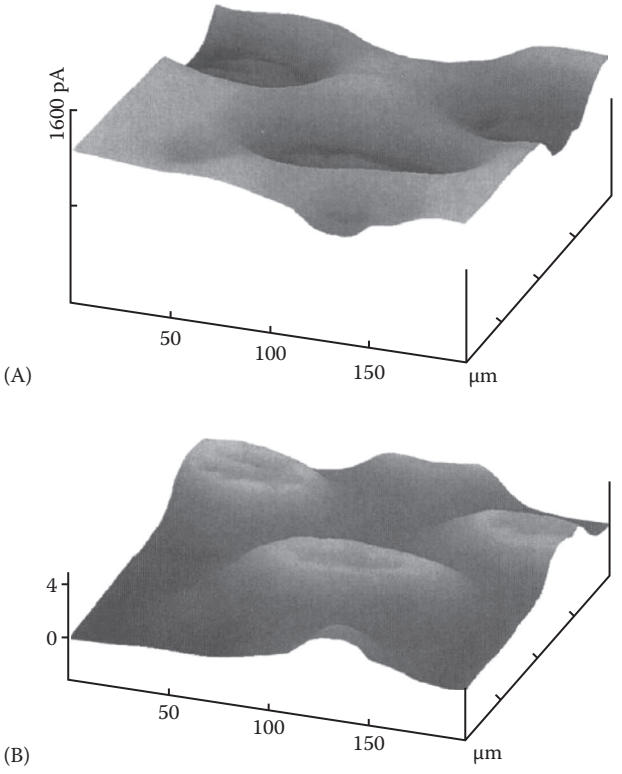


FIGURE 4.4 SECM images of a green portion of a *T. fluminensis* leaf obtained with a 7 μm diameter carbon tip in an air-saturated solution in the dark. (A) i_T across the leaf surface. The image is inverted, that is, the dark areas represent bulges on the surface and correspond to low i_T. (B) The image in (A) returned to the proper physical orientation (y-axis in μm). The images were obtained 30 min after the addition of 0.1 M KCl to the buffer solution to open stomata. (Reprinted from Tsionsky, M. et al., *Plant Physiol.*, 113, 895, 1997. With permission. Copyright 1997 American Society of Plant Physiologists.)

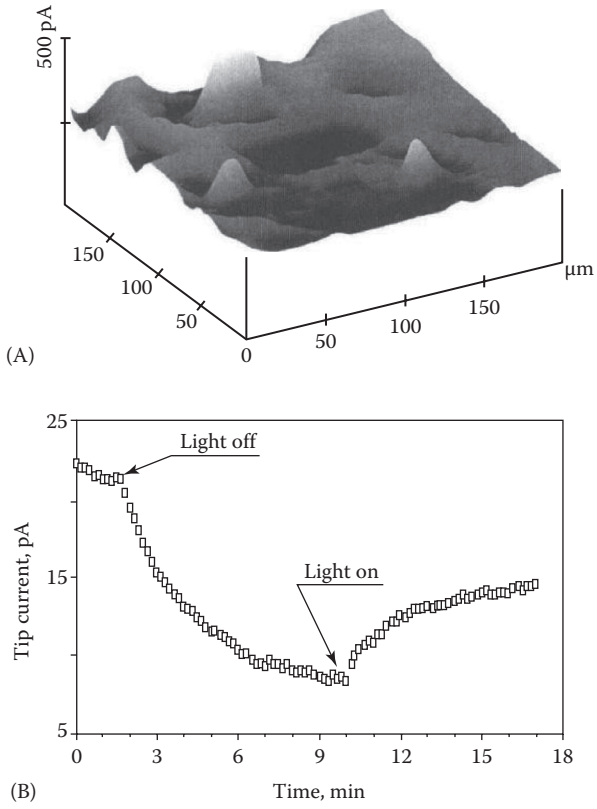


FIGURE 4.5 (A) O_2 evolution from three stomata of an illuminated green leaf region (200 μm × 200 μm). The *x*- and *y*-axes represent position on the leaf; the *z*-axis is i_T measured in feedback mode. (B) The response of i_T to step changes in light availability when held over a stoma in a green leaf region. Measured current tracks O_2 diffusion and decreases after the leaf is placed in the dark and increases after reillumination (800 μE/m²/s). Measurements for (A) and (B) were made with a 7 μm diameter carbon microelectrode. (Reprinted from Tsionsky, M. et al., *Plant Physiol*., 113, 895, 1997. With permission. Copyright 1997 American Society of Plant Physiologists.)

If the tip is held in position above individual stomata, the response of the tip current to the change in light intensity can be examined. As shown in Figure 4.5B, when the light source is eliminated, i_T decreases as oxygen evolution from the stomata slows. When the light source is restored, i_T increases as photosynthesis and O_2 evolution recommence.

In recent years, SECM has been extensively applied to image a variety of biological cells [21]. In these new biological applications of SECM, a chemical substance that participates in a cellular process or a redox mediator is monitored selectively and sensitively to obtain both qualitative and quantitative information of biological significance. SECM was first used to image (with constant height mode) and to probe the redox activity of individual living nonmetastatic and metastatic human breast cells [21b]. SECM was also applied to investigate menadione metabolism by monitoring the export of a menadione–glutathione conjugate, that is, thiodione, by an ATP-dependent pump. Exposure of yeast cells to menadione was immediately followed by the active export of thiodione [21e]. The active thiodione export was also investigated for hepatoblastoma [21f]. Successive constant height SECM images of a single Hep G2 cell were obtained to demonstrate that a thiodione efflux decreased gradually to fall below detectable limits after 1 h.

Figure 4.6 shows a representative topographical image of undifferentiated (i.e., no treatment of nerve growth factor, NGF) and differentiated (NGF-treated) PC12 cells (model neurons) recorded

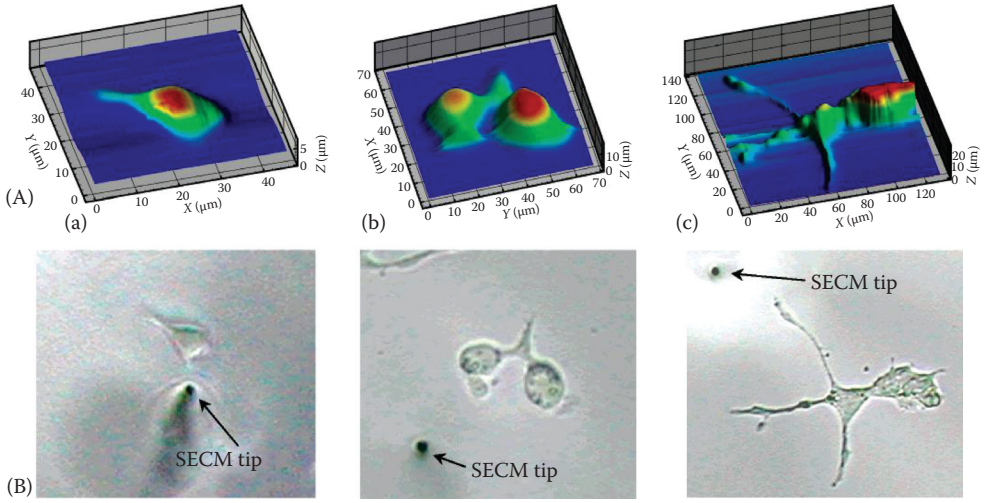


FIGURE 4.6 (A) Topographic images acquired using constant current imaging with a ~1 μm diameter carbon ring electrode. (a) Undifferentiated PC12 cell, (b) PC12 cells in the early stage of neurite development following exposure to NGF, and (c) differentiated PC12 cell. Conditions: 1.0 mM $Ru(NH_3)_6^{3+}$ mediator in HBSS, $E_T = -0.4$ V, scan rate 5 μm/s for (a) and 6 μm/s for (b) and (c). (B) The corresponding optical micrographs. (Adapted from Kurulugama, R. et al., *Anal. Chem*., 77, 1111, 2005. With permission.)

with carbon ring electrodes (~1 μm diameter) using the constant current imaging mode [21g]. These data were collected in Hank's balanced salt solution (HBSS) using $Ru(NH_3)_6^{3+}$ as the mediator. In contrast to the previous images recorded in the constant height mode [21d], the constant current mode is capable of providing more detailed topographical images of the entire cell, which demonstrate the height differences at the cell body and neutrites. The SECM image of Figure 4.6A shows the elongation of an undifferentiated PC12 cell and a short process emitted by the cell. In Figure 4.6B, the processes of two closely spaced cells have formed a connection that is reproduced by the SECM topographical image. Figure 4.6C shows a wider-field image of a typical differentiated PC12 cell. Although most regions of the differentiated cell's morphology are accurately obtained, there are some regions that suggest significant tip–substrate interaction, as manifested by the streaking lines shown in the image.

Besides the constant current mode, the constant impedance mode can also be used for distance control. In the latter mode, no mediator is required and thus the imaging can take place, in principle, directly in the cell growth media. Although the highest resolution was achieved using carbon ring electrodes with the constant current mode, it has been suggested that the constant impedance mode has some important advantages over the constant height mode that topography and faradaic current can be measured simultaneously.

4.3.3 Artificially Patterned Biological Systems

As stated earlier, SECM can be used to image the reactivity of surface features. A feedback detection scheme was used to observe the localized reaction of glucose oxidase (GOD) and mitochondria-bound NADH–cytochrome c reductase [6]. The spatial resolution of the imaging is high for enzymatic systems with a fast catalytic turnover. For slower reactions, however, sensitivity constraints need to be considered and image resolution must be sacrificed in favor of adequate detection level.

The enzyme-linked immunosorbent assay (ELISA) method [22] has recently been used for the preparation of ultrasmall biological structures for SECM measurements. For example, microspots

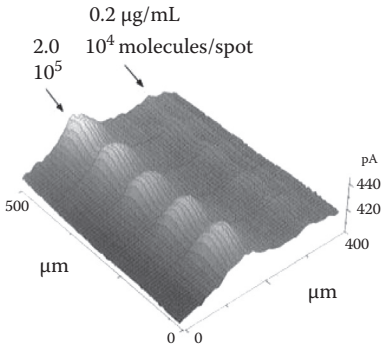


FIGURE 4.7 SECM image of a series of antigen–antibody immobilized spots in a 1.0 mM ferrocenyl methanol/0.5 mM H_2O_2/0.1 M phosphate buffer solution (pH 7.0). Carcinoembryonic antigen concentration of the solution for making spots, 2.0 (left) and 0.2 μg/mL (right); distance, $d = 10$ μm. (Reprinted with permission from Shiku, H., Matsue, T., and Uchida, I., Detection of microspotted carcinoembryonic antigen on a glass substrate by scanning electrochemical microscopy, *Anal. Chem*., 68, 1276–1278, 1996. Copyright 1996 American Chemical Society.)

of carcinoembryonic antigen (CEA) on glass substrates were imaged by SECM [19]. CEA was immobilized via a sandwich method using horseradish peroxidase (HRP)-labeled anti-CEA. The reduction current of the oxidized form of ferrocene methanol generated by the HRP reaction was monitored to view SECM images. Figure 4.7 shows an SECM image of the substrate with CEA/HRP-labeled anti-CEA spots. The appearance of circular spots with large reduction currents is attributed to the HRP-catalyzed reactions at the spots, which indicates the localized presence of CEA. The reduction currents depend on the CEA concentration of the solution for making a CEA spot. In this figure, the five spots on the left side of the figure were made using a 2.0 μg/mL CEA solution, while the five spots on the right were for a 0.2 μg/mL CEA solution. The number of CEA molecules in a single spot (ca. 20 μm radius) on the right was ca. 10^4. Wittstock et al. [18] also demonstrated the imaging of immobilized antibody layers. The readers who are interesting in detailed discussions on the bioanalytical applications of SECM are recommended to consult the proper chapters in this book.

4.3.4 Thin Films and Corrosion Systems

Using SECM, Casillas et al. [14] demonstrated the first direct experimental observation of precursor sites for pitting on the surface of a TiO_2-covered Ti substrate. Figure 4.8 shows the voltammetric response of a Ti/TiO_2 (5 nm thick oxide) electrode immersed in a 1 M KBr/0.05 M H_2SO_4 solution open to the ambient atmosphere. The broad wave between 1.1 and 2.0 V corresponds to Br^- oxidation. The anodic wave decays to a background current level when the potential is more positive than ca. 1.6 V vs. SCE due to the passivation of the surface sites. The sudden and large increase in current at 3.0 V is due to the onset of pitting corrosion, as readily verified by visual inspection of the electrode surface. The images shown in the insets of Figure 4.8 are constant height (ca. 20 μm) SECM images of a 400 μm × 400 μm region of the Ti/TiO_2 surface recorded at the tip potential of 0.6 V vs. SCE, where Br_2 generated at the Ti/TiO_2 surface is reduced to Br^-.

When the Ti/TiO_2 surface was poised at potentials below 1.0 V, SECM images of the surface were essentially featureless and the current was small (ca. 0.1 nA). At potentials between 1.0 and 2.0 V, SECM images revealed a few microscopic sites, such as the one shown in Figure 4.8, where intense Br_2 generation occurred. The maximum current measured at the tip above an electroactive site was typically between 0.2 and 2 nA. SECM images were stable and reproducible at Ti/TiO_2 potentials between 1.0 and 1.5 V. At slightly more positive potentials, the current at the tip decayed

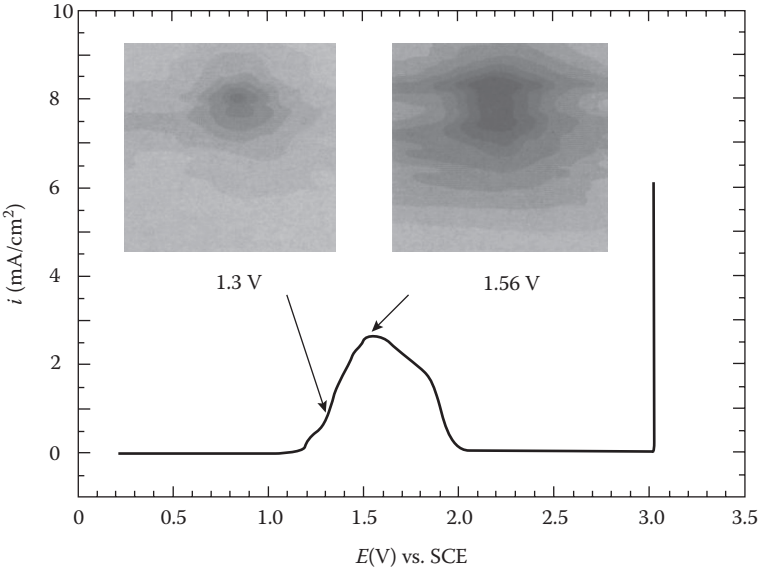


FIGURE 4.8 Voltammetric response of a Ti/TiO_2 electrode in 1 M KBr/0.05 M H_2SO_4 at 1 mV/s. Insets: SECM images of a 400 μm × 400 μm region of the Ti/TiO_2 surface at 1.3 and 1.56 V vs. SCE. SECM tip potential: 0.6 V vs. SCE. (Reprinted from Casillas, N. et al., *J. Electrochem. Soc*., 140, L142, 1993. With permission. Copyright 1993 The Electrochemical Society, Inc.)

to background levels over a period of a few minutes as a result of the passivation of the active sites. The number density of active sites for Br_2 electrogeneration on the Ti/TiO_2 surface is estimated to be on the order of 30 sites/cm^2. The dimensions of the surface active sites varied considerably from site to site but appear to be on the order of 10–100 μm. As depicted in the SECM images of Figure 4.8, the apparent electrochemical activity of the surface sites at any particular potential correlates very well with the magnitude of the faradaic current observed in the voltammogram. The intensity of Br_2 generation in the image taken at 1.56 V is clearly much greater than that at 1.3 V. Other examples of electrochemically active sites are inclusions on aluminum alloy surfaces [23] and stainless steel [24].

Related to the corrosion problems was a recent SECM study, which demonstrated the possibility of eliminating typical experimental problems, encountered in the measurements of heterogeneous electron transfer at semiconductor electrodes [25]. In this experiment, the redox reaction of interest (e.g., reduction of $Ru(NH_3)_6^{3+}$) is driven at a diffusion-controlled rate at the tip. The rate of reaction at the semiconductor substrate is probed by measuring the feedback current as a function of substrate potential. By holding the substrate at a potential where no species other than that tip generated would react at the substrate, most irreversible parasitic processes, such as corrosion, did not contribute to the tip current. Thus, separation of the redox reaction of interest from parallel processes at the semiconductor electrode was achieved.

4.3.5 Other Systems and Potentiometric Imaging

SECM images of other systems, including mixed metal–insulator surfaces [26] and substrates composed of two conductors with different reactivities (e.g., gold and glassy carbon [27] or Pt and carbon [28]), have been reviewed recently [29]. Imaging of Prussian blue films in the constant current mode has also been described [30]. Here, the SECM feedback occurred inside the solid phase. The resulting image depended strongly on the substrate potential, which in turn governed the film reactivity. SECM imaging can also be carried out with potentiometric probes instead of

amperometric tips [29]. For example, Horrocks et al. [31] used antimony tips as pH sensors to image local pH changes around a disk of immobilized urease hydrolyzing urea and a disk of immobilized yeast cells in glucose solution. Other types of potentiometric imaging are also possible. The readers who are interested in detailed information on this imaging mode should refer to the proper chapter in this book.

4.4 IMAGING IN HUMID AIR

Most SECM measurements were carried out with the sample under a thick liquid layer; thus, the tip must be sheathed in an insulator in order to achieve high resolution. SECM measurements can also be carried out within a thin layer of water that forms on the surface of a sample in air. In this case, very high resolution can be attained using tips without insulation (i.e., the usual W or Pt–Ir STM-type tips) because the tip area is defined by the small part of the tip that touches the liquid layer [32]. Studies of mica surfaces, polymer films, and some biological samples as described later are possible by this technique. High-resolution electrochemical deposition of silver nanostructures on mica surfaces in humid air was also achieved [33]. With this mode, it is also possible to fabricate small metal structures in polymer films as demonstrated previously [34]. For detailed information on SECM applications for fabrication, the readers are encouraged to refer to the relevant chapter in this book.

4.4.1 Instrumentation and Sample Preparation

The instrument employed in the following studies was capable of both SECM and STM measurements with a current sensitivity <0.1 pA [35]. Electrochemically etched tips were prepared from either 250 μm diameter Pt–Ir (80%–20%) (Etchant, saturated $CaCl_2$:concentrated HCl:water [60%:4%:36% by volume]) or 500 μm W wire (etchant, 3 M NaOH). The SECM/STM scanning head was contained in a Faraday cage and a Plexiglas box in which the relative humidity (RH) of the atmosphere was controlled by various humidity-limiting solutions [36,37]. A constant humidity within the box was usually attained within 1 h as determined by monitoring the surface conductance of the mica sample or by measuring the RH with a humidity probe (Model 6517-RH, Keithley Instruments, Inc., Cleveland, OH). The tip–sample arrangement is shown in Figure 4.9.

Freshly cleaved mica substrates (Spruce Pine Mica Co., Spruce Pine, NC) were vacuum coated with about a 500 Å thick layer of gold at one end; this served as the reference/counter electrode contact. In all experiments, the tip was positioned 1–2 mm from the Au contact, as shown. If not otherwise mentioned, the mica sample was treated with one small drop (~10 μL) of a solution containing the specimen in solution A (10 mM Tris buffer and 1 mM ethylenediaminetetraacetic acid [EDTA] [disodium salt], pH 7) for 5 min. The sample was then dipped (1 s) in water, dried for 5 min in air, and dipped again for 1 s in water. Excess water on the surface was carefully removed with filter paper and the sample was mounted on the SECM/STM and allowed to equilibrate with the atmosphere within the box before the experiments were carried out.

4.4.2 Electrochemical Behavior

Information about the mechanism of current flow was obtained from current–voltage (i–V) curves under different conditions. In these experiments, a rather blunt tip (radius of curvature ~10 μm) was brought into contact with the sample and the piezo feedback was switched off to avoid changes in the tip–substrate gap during the potential scan. Typical i–V curves are shown in Figure 4.10. The curve for a Nafion film with a Pt–Ir tip (Figure 4.10A) shows some hysteria in the range of +1 and −1 V where pA currents flow. Outside this range, the curves become linear and are largely independent of scan direction. The shape of the curves is consistent with an electrochemical reaction, presumably mainly water electrolysis, at the tip and Au contact. Above this

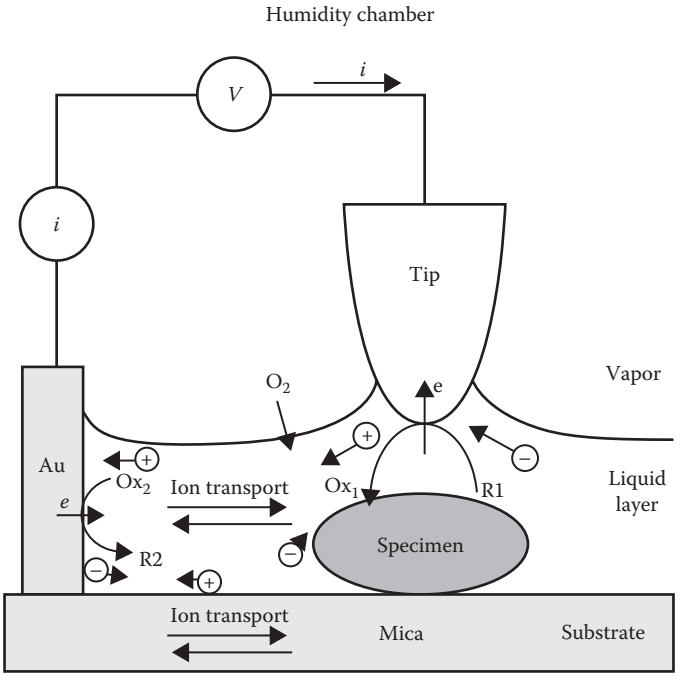


FIGURE 4.9 Schematic diagram for the SECM chamber with controlled humidity and the electrochemical processes that control the current. The tip was located ~1–2 mm from the Au contact. *V*: voltage bias between the tip and Au contact. *i*: current flow through the tip. R and Ox represent the reduced and oxidized forms of an electroactive species. ⊕ and θ represent cations and anions in the water film. (From Fan, F.-R.F. and Bard, A.J., STM on wet insulators: Electrochemistry or tunneling? *Science*, 270, 1849–1851, 1995. Adapted with permission of American Association for the Advancement of Science.)

region, the current is limited by the resistance of the thin film (~7.5×10^{11} Ω). The *i*–*V* curves with a blunt Pt–Ir tip on a mica substrate treated with solution A are more complex and depend upon scan history (Figure 4.10B). Thus, for scans from 0 V to negative tip potential (C1–C3), the *i*–*V* relation is fairly linear with the current increasing slightly on each scan. An initial scan of the tip toward positive potentials following these scans is also almost linear (A1). However, on successive scans (A2–A4), a definite peak appears; the current decreases and the peak shifts to less positive potentials on each scan. The voltammetric scan is restored if the tip is biased to negative potentials for about 2 min, suggesting that a species, probably H_2, builds up around the tip at negative bias that is depleted during successive anodic tip scans. After a series of scans of the tip to positive potentials, an initial cathodic tip scan shows decreased current (C4), but gradually attains the linear behavior shown in successive cathodic scans. For purposes of imaging with a Pt–Ir tip, the current is fairly stable for negative tip bias values; with positive tip bias, oscillations frequently occurred.

As expected for an electrochemical process, the *i*–*V* curves also depend upon the tip material. For a blunt W tip on mica treated with solution A (Figure 4.10C), the current is stable and increases almost linearly for positive tip bias, but tends to saturate and shows considerable hysteria on scan reversal in the negative tip bias region. Thus with a W tip, imaging at positive bias is appropriate. The observed electrochemical behavior also depends on the pretreatment of the insulating substrate like mica. For example, the voltammetric behavior is very different when the mica is simply immersed in water for a few hours rather than treated with solution A. Here, an *i*–*V* curve at 100% RH at a W tip (Figure 4.10D) shows only very small currents across a region of ±5 V. The current at a Pt–Ir tip at 100% RH is at least one order of magnitude smaller for a water-treated

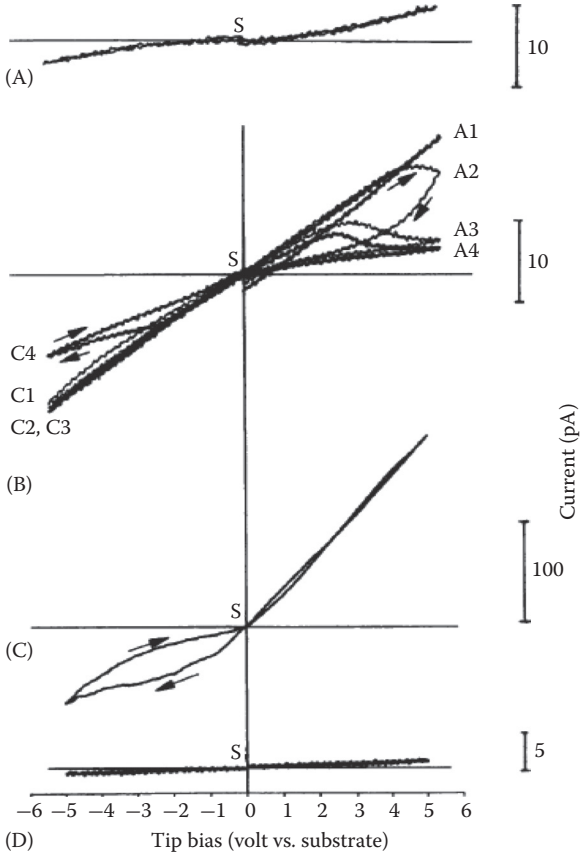


FIGURE 4.10 Typical voltammetric curves in the humidity chamber at 100% RH, 25°C. Radius of tip curvature = 10 μm. In all cases, the voltage was scanned from 0 V (point S) in either direction and then returned to 0 V; the scan rate was 0.2 V/s. (A) Pt–Ir tip, Nafion film (~200 nm thick) on mica. (B) Pt–Ir tip, mica substrate treated with solution A. Curves C1–C3: first, second, and third negative scans. Curves A1–A4: first, third, fourth, and fifth positive scans after C3. Curve C4: first negative scan after A4. (C) W tip, mica substrate treated with solution A. (D) W tip, mica substrate treated only with water. (From Fan, F.-R.F. and Bard, A.J., STM on wet insulators: Electrochemistry or tunneling? *Science*, 270, 1849–1851, 1995. Reprinted with permission of American Association for the Advancement of Science.)

sample compared to the one treated with solution A. The current under these conditions, however, was steady and showed little hysteria. At low RH (e.g., 33%), no appreciable current (<0.1 pA) was observed in the region of ±5 V. Thus, pretreatment of the insulating substrate to provide ions in the water layer, thus increasing its conductivity appears to be useful. Presumably following treatment with solution A, sufficient ions remain adsorbed on the mica surface, even after washing, to yield some conductance in the water film that forms on exposure to humid air.

The electrochemical signal observed here could arise from both capacitive charging and faradaic processes. However, charging processes are transient and cannot sustain a steady direct current. Because the observed *i–V* curves are perturbed by resistive drops in the solution, one cannot identify with certainty the nature of the faradaic processes at the tip and Au contact. At Pt–Ir, candidate reactions are oxidation of water to O_2, reduction of water or protons to H_2, reduction of dissolved O_2, and processes involving adsorbed species, for example, oxidation of EDTA or adventitious impurities. At W, in addition to these processes, oxidation of W to form the oxide (WO_3), and transiently, reduction of native or electrochemically generated oxide are possible. The large and stable currents with a W tip at positive tip bias compared to Pt–Ir (see also the following discussion) suggest that

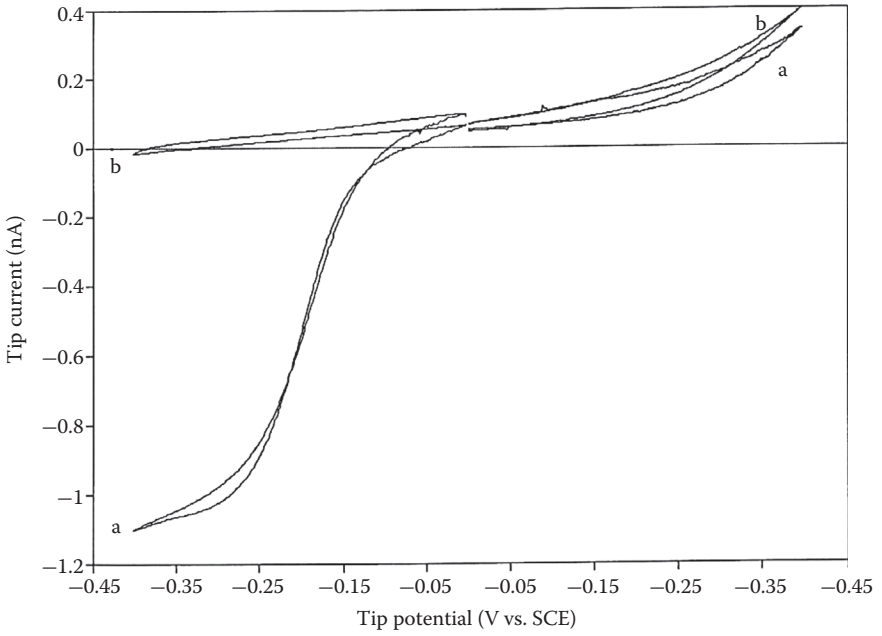


FIGURE 4.11 Cyclic voltammograms of a polyurethane-coated W tip in 1 mM $Ru(NH_3)_6^{3+}$/10 mM $NaClO_4$ solution (curve a) and 10 mM $NaClO_4$ only (curve b). Potential scan rate is 5 mV/s. (Reprinted with permission from Fan, F.-R.F. and Bard, A.J., Imaging of biological macromolecules on mica in humid air by scanning electrochemical microscopy, *Proc. Natl. Acad. Sci. USA*, 96, 14222–14227, 1999. Copyright 1999 National Academy of Science, USA.)

the W oxidation reaction occurs at the tip. Note that the faradaic processes also generate ions that can contribute to the solution conductivity. Ions in the water layer also play an important role in establishing the double layers at both electrodes and providing charge compensation for electrogenerated species. They may also affect the hydrophilicity of the substrate surface and the thickness and structure of the water layer that forms on it.

It is interesting to estimate the effective tip radius immersed in the water layer, which is responsible for a tip current of ca. 1 pA at 1 V bias. As shown in Figure 4.11, a polyurethane-coated W tip behaves as a microelectrode. A sigmoidal diffusion-limited current superimposed on the linear background current was obtained for the reduction of 1 mM $Ru(NH_3)_6^{3+}$ in 10 mM $NaClO_4$ solution. An effective radius estimated from the nearly steady-state current is ca. 3 μm. If one assumes that similar tip area is responsible for both cathodic and anodic redox processes, an estimated effective contact radius of ca. 3 nm is obtained for a current flow of 1 pA in similar concentration of an electroactive species having comparable diffusion coefficient. Since the concentrations of the electroactive species could be considerably higher than 1 mM and the detectable current can be much less than 1 pA at a bias voltage higher than 1 V, an effective contact radius less than 1 nm (and a comparable lateral resolution) is possible to achieve. Also shown in Figure 4.11 is the anodic background current due to the oxidation of W at potentials positive of ca. 0.4 V vs. SCE (curve b).

4.4.3 SECM Behavior and Imaging

When a W or Pt–Ir tip (biased at +3 V) approached the sample at 3 nm/s, the current remained at zero until it contacted the liquid layer where it increased sharply, showing several orders of magnitude increase over a distance of a few nanometers. Accompanying with this sharp increase in the tip current when it contacted the liquid layer, both parallel tip conductance and parallel tip capacitance also increased very rapidly (see Figure 4.12). This is characteristic of the occurrence

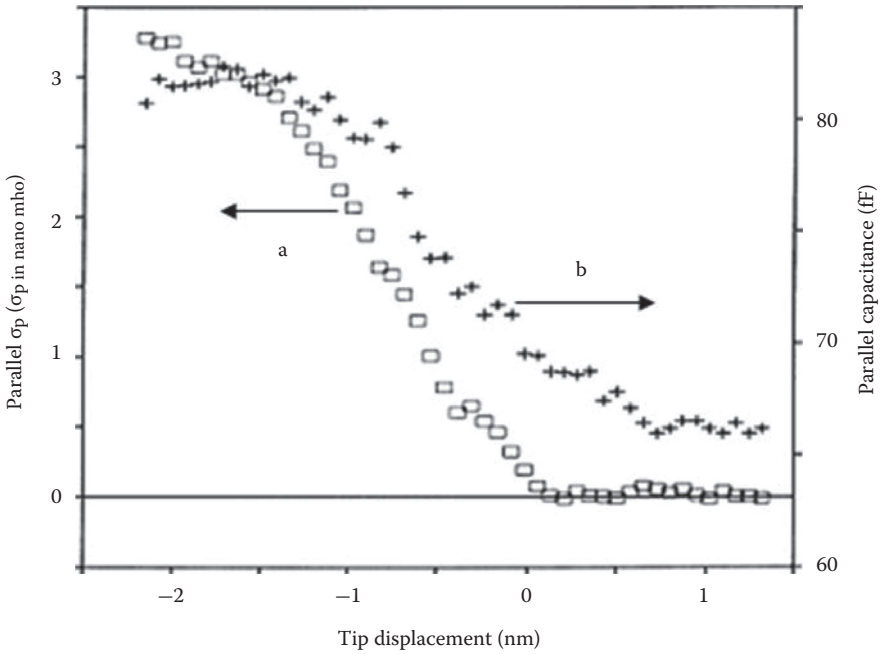


FIGURE 4.12 Typical parallel conductance, σ_p (a) and parallel capacitance (b) vs. tip displacement curves for a blunt W tip at 100% RH and 25°C for a mica substrate treated with solution A. Tip bias is 3 V with respect to the Au counter electrode. The tip approaches the substrate surface at a rate of 3 nm/s. (Reprinted with permission from Fan, F.-R.F. and Bard, A.J., Imaging of biological macromolecules on mica in humid air by scanning electrochemical microscopy, *Proc. Natl. Acad. Sci. USA*, 96, 14222–14227, 1999. Copyright 1999 National Academy of Science, USA.)

of a faradaic process. As reported previously, this arrangement can be used for imaging [32] and fabrication [33,34,38].

Figure 4.13A shows the image of the mica surface obtained in the constant current mode at a reference tip current of 0.3 pA. The step running diagonally from the lower left corner represents a cleavage plane for a single mica layer, ca. 1 nm high, and the small pieces seen on the lower plane probably represent salt residue or debris left after cleavage. A thin film (~200 nm) of Nafion could also be imaged by this technique. The film was prepared on the mica substrate by spin coating at 3000 rpm with a photoresist spinner (Headway Research, Garland, TX) from an isopropanol–ethanol (4:1 by volume) solution containing 5% Nafion. The image of this film (Figure 4.13B) shows smaller circular domain structures, 1–2 nm diameter, consisting of a more conductive central zone surrounded by a less conductive region. These structures correspond to those proposed in Gierke's cluster model (Figure 4.13C) for a Nafion membrane [39] in which a central hydrophilic domain consisting of backbone ions and water is surrounded by a Teflon-like hydrophobic zone. This image demonstrates that SECM can distinguish between zones of different ionic conductivity in a sample. It also suggests that such an imaging mode does not pose serious limitation on the specimen thickness as long as the surface water film provides a closed circuit for ion conduction.

As first reported by Guckenberger et al. [40], images of DNA on mica could also be obtained in this configuration. DNA on mica was prepared as follows: A small drop (10 μL) of the DNA specimen ("Bluescript," 2.96 kbp, 21.75 μg/mL) in solution A was placed on mica to cover ca. 1 cm^2 and left to adsorb for ca. 5 min. The sample was then dipped (1 s) in water, dried for 5 min in air, and dipped again for 1 s in water. Excess water on the surface was carefully removed with filter paper and the sample was mounted on the SECM/STM and allowed to equilibrate with the

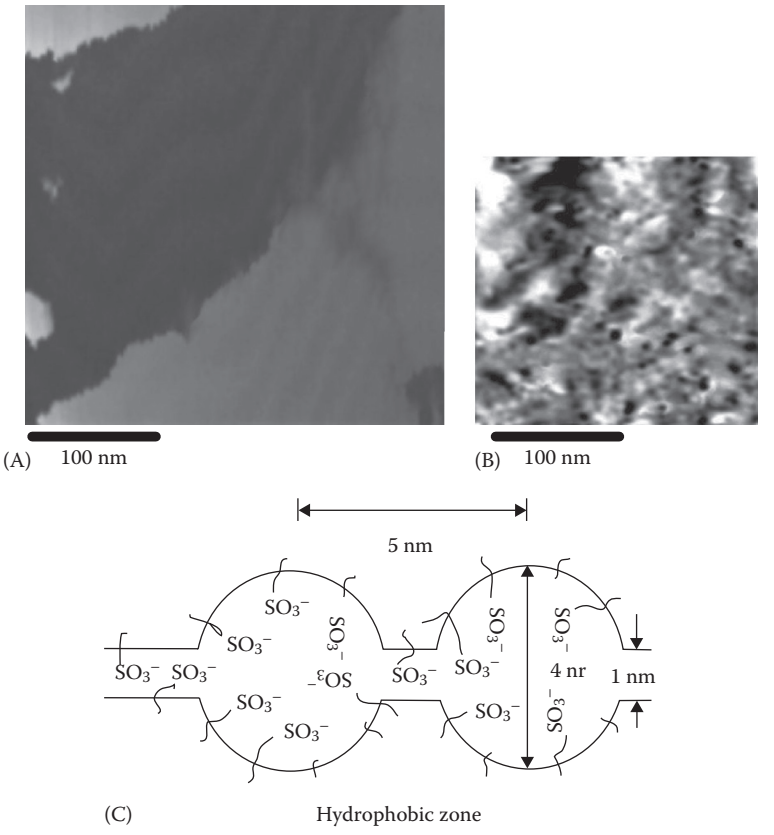


FIGURE 4.13 (A) Image of a mica surface treated with solution A taken in humid air (80% RH at 25°C) with a sharp W tip at a reference current of 0.3 pA and a tip bias of 3 V. The tip rastering rate was 0.25 Hz. The total *z*-range is 3 nm. (B) Image of a Nafion film on mica taken in humid air (100% RH at 25°C) with a sharp Pt–Ir tip at a reference current of 3 pA and a tip bias of 3 V with respect to the Au counter electrode. The tip rastering rate was 0.25 Hz. The image is inverted to enhance the visual effect of the domain structure; the dark region has a higher transient current than the lighter region and is corresponding to the hydrophilic domain. (A and B: From Fan, F.-R.F. and Bard, A.J., STM on wet insulators: Electrochemistry or tunneling? *Science*, 270, 1849–1851, 1995. Reprinted with permission of American Association for the Advancement of Science.) (C) Gierke's cluster model for Nafion membrane. (From Hsu, W.Y. and Gierke, T.D., *J. Membr. Sci*., 13, 307, 1983.)

atmosphere within the box before the imaging was carried out. Figure 4.14 shows corresponding images of several DNA molecules on mica. In general, imaging is more stable at positive tip bias if a W tip is used. There is a tendency to lose the image after repeated scans at the same area, presumably due to the depletion of electroactive species at or near the tip and the non-negligible tip–sample interaction. The magnitude of the signal can be recovered by imaging at different areas. As shown in Figure 4.14, the lateral resolution obtained (4–8 nm) is considerably larger than the expected diameter of DNA (~2.5 nm). Information in the *z*-axis is limited, due to the lack of a quantitative relationship between the charge transfer rate and the tip–sample distance for this system.

Besides DNA, antibody (e.g., a mouse monoclonal IgG), enzyme (e.g., glucose oxidase), and hemocyanin (e.g., keyhole limpet hemocyanin [KLH]) molecules were also possibly imaged by the same technique. All of these protein molecules have characteristic three-dimensional structures, and the majority of their surfaces are hydrophilic, and so the molecules allow one to test the applicability of this technique for imaging. A small drop of 10 μL protein solution to cover ca. 1 cm^2 of the mica surface was used for the experiment. The stock solutions of IgG (15 μg/mL) and GOD

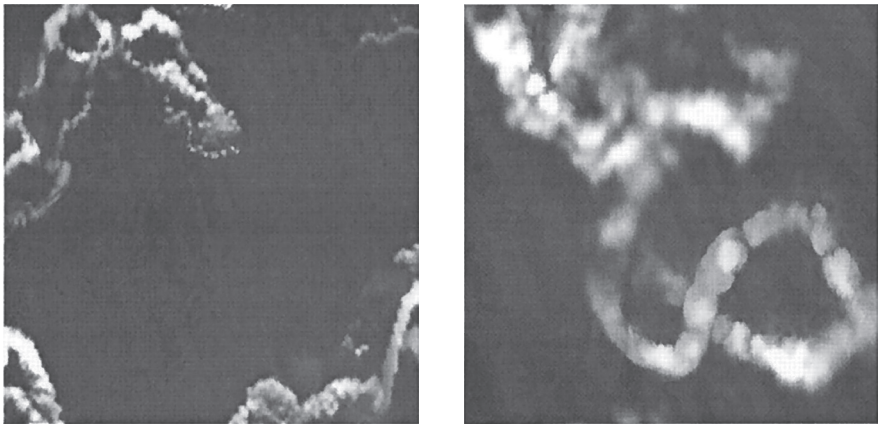


FIGURE 4.14 Constant current images of fragments of DNA specimen [(A) supercoiled; (B) "Bluescript," 2.96 kbp] on mica substrates in humid air (80% RH at 25°C). Images were taken with a sharp W tip at a reference current of 0.3 pA and a tip bias of 3 V. The tip rastering rate was 0.25 Hz. (Reprinted with permission from Fan, F.-R.F. and Bard, A.J., Imaging of biological macromolecules on mica in humid air by scanning electrochemical microscopy, *Proc. Natl. Acad. Sci. USA*, 96, 14222–14227, 1999. Copyright 1999 National Academy of Science, USA.)

(22.5 μg/mL) were prepared from a buffer solution containing 24 μM KH_2PO_4, 170 μM NaCl, and 10 μM NaN_3. It is important to use low concentrations of protein to minimize aggregate formation. However, for imaging purpose the protein concentration should be high enough to have a proper coverage of protein molecules on the mica surface. The images were recorded using a W tip. The reference current was 1 pA at a tip bias of 1.5 V (vs. the Au contact). Figure 4.15 shows a region of the mica surface that contains several mouse IgG (MW = 150,000 Da) molecules. All the molecules were of similar size and had a very characteristic quaternary structure (two arms and one body corresponding to two Fab and one Fc fragments of the IgG molecule [41]). The image of native IgG obtained by this technique is remarkably similar to the data from x-ray crystallography [42,43] and TEM [44]. However, the apparent dimensions (~12 nm × 9 nm) are significantly larger than those (8.5 nm × 6 nm) determined from x-ray crystallographic studies. Information in the *z*-axis is limited, due to the lack of a quantitative relationship between the charge transfer rate and the tip–sample distance for this system, but the approximate height of the molecule is ca. 4.5 nm, which is somewhat higher than the TEM and x-ray data (~4 nm).

Figure 4.16 shows the image of a group of GOD (MW = 160,000 Da, from *Aspergillus niger*) molecules on a mica surface at 81% RH. All of them were of similar size. Most of the molecules show a dimeric structure corresponding to the folded form of the two identical polypeptide chains of the GOD molecules. The monomeric unit is apparently a compact spheroid with approximate dimensions 8 nm × 4 nm. The top-view images of some of the molecules are observed as nearly as circles with diameters of ca. 7 nm, which might represent the third dimension of the spheroidal monomeric unit. Contacts between two monomeric units forming the dimer are confined to a long, narrow stretch. The overall dimensions of the GOD molecules are thus approximately 8 nm × 7 nm × 8 nm, which are significantly larger than those (6.0 nm × 5.2 nm × 7.7 nm) determined from x-ray crystallographic data on the partially deglycosylated enzyme [45].

Finally, we chose hemocyanin molecules from gastropods (e.g., KLH) as a testing specimen for this imaging technique, since they have a distinctive cylindrical profile, having 6, 9, 12, and so on parallel rows, depending on their sizes [46]. Images for KLH molecules (MW ~7–8 × 10^6) were taken at 65% RH with a W tip biased at 1.7 V with a reference current of 1 pA. Figure 4.17

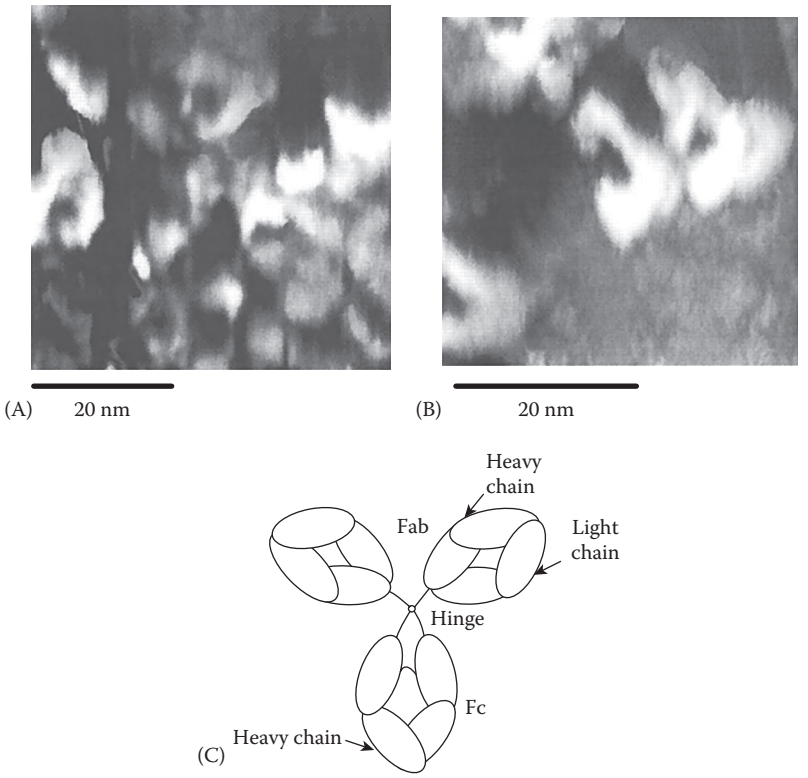


FIGURE 4.15 (A) and (B) Constant current images showing several mouse IgG (MW = 150,000 Da) molecules on mica substrates. The images were recorded using a W tip in humid air (80% RH at 25°C). The reference current was 1 pA at a tip bias of 1.5 V (vs. the Au contact). (A and B: Reprinted with permission from Fan, F.-R.F. and Bard, A.J., Imaging of biological macromolecules on mica in humid air by scanning electrochemical microscopy, *Proc. Natl. Acad. Sci. USA*, 96, 14222–14227, 1999. Copyright 1999 National Academy of Science, USA.) (C) Schematic drawing of an IgG molecule showing two Fab arms and the Fc portion. (From Burton, D.R., In *Molecular Genetics of Immunoglobulin*, F. Calabi and M.S. Neuberger, eds., Elsevier, Amsterdam, the Netherlands, 1987.)

shows a cylindrically shaped molecule having nine parallel sections. It has a rectangular profile with one dimension of 30–35 nm and the other dimension of 45–50 nm, which are quite close to those observed by TEM. The shape of the molecule is remarkably similar to the model for the structure of a six-parallel-row gastropod hemocyanin proposed in 1972 by Mellema and Klug [47] based on a computer processed three-dimensional reconstruction of the TEM data. The reconstruction showed a hollow cylindrical molecule partly closed at both ends by a collar and possibly a central cap. The walls are made from 60 morphological units of similar size, shape, and orientation, which were correlated with 120 oxygen-binding sites. This result again suggests that such an imaging mode does not pose serious limitation on the specimen thickness as long as the surface water film provides a closed circuit for ion conduction.

The significant increases in size of the DNA and small protein molecules determined by this technique as compared with other techniques are most likely due to the presence of water and salt around the molecules, and the convolution of the non-negligible tip size. They could also be caused by the deformation of the molecules by the tip during imaging, as frequently encountered in AFM or STM images for biological samples [48–52]. It is conceivable that when the dimensions of the specimen are large as compared with the tip curvature, the relative deviation due to tip geometry is small. It is also possible to deconvolute the images if one knows the exact tip dimensions and the

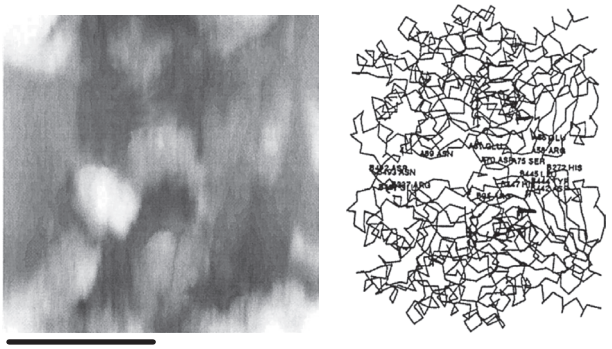


FIGURE 4.16 (A) Constant current image showing several glucose oxidase (MW = 160,000 Da, from *A. niger*) molecules on mica substrates. The images were recorded using a W tip in humid air (80% RH at 25°C). The reference current was 1 pA at a tip bias of 1.5 V vs. the Au counter electrode. (Reprinted with permission from Fan, F.-R.F. and Bard, A.J., Imaging of biological macromolecules on mica in humid air by scanning electrochemical microscopy, *Proc. Natl. Acad. Sci. USA*, 96, 14222–14227, 1999. Copyright 1999 National Academy of Science, USA.) (B) C^{α} tracing of the dimer structure of a glucose oxidase molecule (From Hecht, H.J. et al., *J. Mol. Biol.*, 229, 153, 1993.). Contacts between molecules forming the dimer are confined to a long, narrow stretch.

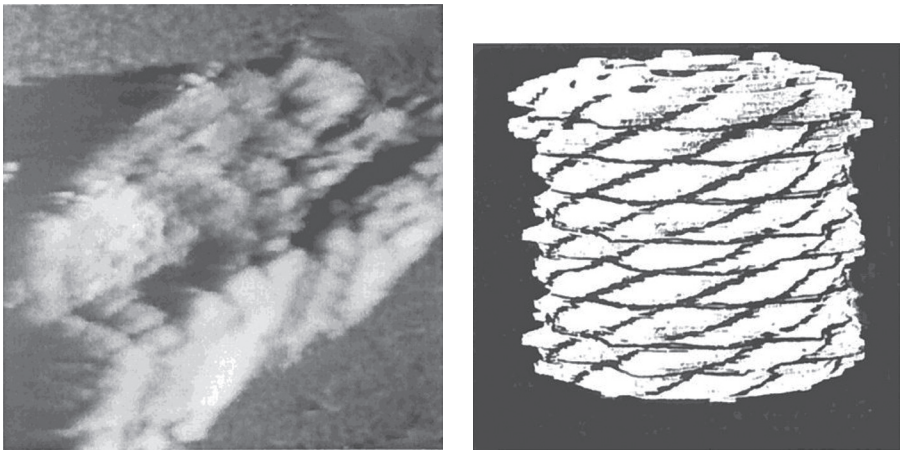


FIGURE 4.17 (A) Constant current image (A) of a keyhole limpet hemocyanin (MW ~7–8 × 10^6 Da) molecule on a mica surface. The image was taken at 65% RH with a W tip biased at 1.7 V with a reference current of 1 pA. (Reprinted with permission from Fan, F.-R.F. and Bard, A.J., Imaging of biological macromolecules on mica in humid air by scanning electrochemical microscopy, *Proc. Natl. Acad. Sci. USA*, 96, 14222–14227, 1999. Copyright 1999 National Academy of Science, USA.) (B) An analogous Mellema and Klug's model for a nine parallel rows gastropod hemocyanin. (From Mellema, J.E. and Klug, A., *Nature*, 239, 146, 1972.)

detailed mechanisms of imaging. One can also minimize the size deviation by optimizing the RH and the salt concentration. In spite of this discrepancy, the overall shapes of the DNA and protein molecules are well reproduced in this experiment and are remarkably similar to those determined from other more established techniques. These results give us confidence that this technique is accurately reflecting the native conformation of the DNA and protein molecules. They further indicate that the use of a mica surface, which is atomically flat and can easily be chemically modified, is a suitable substrate for studying protein samples.

4.5 CONCLUSIONS

Complementary with other imaging techniques, such as electron microscopy and other scanning probe microscopies (SPMs), the SECM routinely offers micrometer resolution of the surface structures in bulk electrolyte solutions. The SECM also provides the local chemical and electrochemical reactivity of surface features. The latter application is unique to SECM and is particularly useful in identifying and understanding the functional aspects of these surface structures. As stated earlier, the spatial resolution of the SECM is governed by the tip radius. By applying both constant height and constant current modes, Laforge et al. [53] have most recently been able to use nanometer-sized probes to attain a lateral resolution in the range of tens of nanometers for ordered "hard" materials. The smallest feature size in the employed samples (~200 nm) was significantly larger than the spatial resolution attainable with nanometer-sized tips.

Those images of biomacromolecules taken in humid air further demonstrate that the resolution can reach a few nanometers, although it is still not as high as that seen in STM of ordered conductive surfaces. Improved resolution should result from lower RH conditions to decrease the thickness of the water film but still keep the ionic conductivity of the mica substrate and the individual molecules high enough for detection. As stated earlier, the resolution is also a function of the exposed tip area and perhaps could be improved by treatment of the tip except at the very end with a hydrophobic agent to decrease the wetted area above the contact point. The potential of this technique for ultrahigh resolution chemical imaging, as successfully applied in bulk liquid phase studies, is very attractive. Yet the problems of getting better control of the electrochemical reactions within the film have not been resolved. But one must realize that these problems are not fundamental and they may be solvable.

ACKNOWLEDGMENTS

I thank Prof. B.L. Iverson and Dr. G. Chen for their generous donation of DNA and hemocyanin samples. I also thank Drs. X.-H. Xu and C. Demaille for their helpful technical assistance, suggestions, and discussions. The support of the research in SECM by the Robert A. Welch Foundation, the National Science Foundation, and the Texas Advanced Research Program is also gratefully acknowledged.

REFERENCES

1. Binnig, G., Rohrer, H. Vacuum tunnel microscope, *Helv. Phys. Acta* 1982, 55, 726.
2. Wipf, D. O., Bard, A. J. Scanning electrochemical microscopy. 15. Improvements in imaging via tip-position modulation and lock-in detection, *Anal. Chem*. 1992, 64, 1362–1367.
3. Ludwig, M., Kranz, C., Schuhmann, W., Gaub, H. E. Topography feedback mechanism for the scanning electrochemical microscope based on hydrodynamic forces between tip and sample, *Rev. Sci. Instrum*. 1995, 66, 2857–2860.
4. Scott, E. R., White, H. S., Phipps, J. B. Scanning electrochemical microscopy of a porous membrane, *J. Membr. Sci*. 1991, 58, 71–87.
5. Scott, E. R., White, H. S., Phipps, J. B. Direct imaging of ionic pathways in stratum corneum using scanning electrochemical microscopy, *Solid State Ionics* 1992, 53, 176–183.
6. Pierce, D. T., Bard, A. J. Scanning electrochemical microscopy. 23. Reaction localization of artificially patterned and tissue-bound enzymes, *Anal. Chem*. 1993, 65, 3598–3604.
7. Lee, C. M., Kwak, J. Y., Bard, A. J. Application of scanning electrochemical microscopy to biological samples, *Proc. Natl. Acad. Sci. USA* 1990, 87, 1740–1743.
8. Jackson, R. B., Tsionsky, M., Cardon, Z. G., Bard, A. J. Unpublished results.
9. Tsionsky, M., Cardon, Z. G., Bard, A. J., Jackson, R. B. Photosynthetic electron transport in single guard cells as measured by scanning electrochemical microscopy, *Plant Physiol*. 1997, 113, 895–901.
10. Lee, C. M., Anson, F. C. Use of electrochemical microscopy to examine counterion ejection from Nafion coatings on electrodes, *Anal. Chem*. 1992, 64, 528–533.

11. Jeon, I. C., Anson, F. C. Application of scanning electrochemical microscopy to studies of charge propagation within polyelectrolyte coatings on electrodes, *Anal. Chem*. 1992, 64, 2021–2028.
12. Kwak, J. Y., Lee, C. M., Bard, A. J. Scanning electrochemical microscopy. V. A study of the conductivity of a polypyrrole film, *J. Electrochem. Soc*. 1990, 137, 1481–1484.
13. Lee, C. M., Bard, A. J. Scanning electrochemical microscopy. Application to polymer and thin metal oxide films, *Anal. Chem*. 1990, 62, 1906–1913.
14. Casillas, N., Charlebois, S., Smyrl, W., White, H. S. Scanning electrochemical microscopy of precursor sites for pitting corrosion on titanium, *J. Electrochem. Soc*. 1993, 140, L142–L145.
15. Casillas, N., Charlebois, S., Smyrl, W., White, H. S. Pitting corrosion of titanium, *J. Electrochem. Soc*. 1994, 141, 636–642.
16. James, P., Casillas, N., Smyrl, W. Simultaneous scanning electrochemical and photoelectrochemical microscopy by use of a metallized optical fiber, *J. Electrochem. Soc*. 1996, 143, 3853–3865.
17. Shiku, H., Takeda, T., Yamoda, H., Matsue, T., Uchida, I. Microfabrication and characterization of diaphorase-patterned surfaces by scanning electrochemical microscopy, *Anal. Chem*. 1995, 67, 312–317.
18. Wittstock, G., Yu, K.-J., Halsall, H. B., Ridgway, T. H., Heineman, W. R. Imaging of immobilized antibody layers with scanning electrochemical microscopy, *Anal. Chem*. 1995, 67, 3578–3582.
19. Shiku, H., Matsue, T., Uchida, I. Detection of microspotted carcinoembryonic antigen on a glass substrate by scanning electrochemical microscopy, *Anal. Chem*. 1996, 68, 1276–1278.
20. Lee, C. M., Wipf, D. O., Bard, A. J., Bartels, K., Bovik, A. C. Scanning electrochemical microscopy. 11. Improvement of image resolution by digital processing techniques, *Anal. Chem*. 1991, 63, 2442–2447.
21. (a) Yasukawa, T., Kaya, T., Matsue, T. Characterization and imaging of single cells with scanning electrochemical microscopy, *Electroanalysis* 2000, 12, 653–659. (b) Liu, B., Rotenberg, S., Mirkin, M. V. Scanning electrochemical microscopy of living cells: Different redox activities of nonmetastatic and metastatic human breast cells, *Proc. Natl. Acad. Sci. USA* 2000, 97, 9855–9860. (c) Hengstenberg, A., Blöchl, A., Dietzel, I., Schuhmann, W. Spatially resolved detection of neurotransmitter secretion from individual cells by means of scanning electrochemical microscopy, *Angew. Chem. Int. Ed*. 2001, 40, 905–908. (d) Liebetrau, J. M., Miller, H. M., Baur, J. E., Takacs, S. A., Anupunpisit, V., Garris, P. A., Wipf, D. O. Scanning electrochemical microscopy of model neurons: Imaging and real-time detection of morphological changes, *Anal. Chem*. 2003, 75, 563–571. (e) Mauzeroll, J., Bard, A. J. Scanning electrochemical microscopy of menadione–glutathione conjugate export from yeast cells, *Proc. Natl. Acad. Sci. USA* 2004, 101, 7862–7867. (f) Mauzeroll, J., Bard, A. J., Owhadian, O., Monks, T. Menadione metabolism to thiodione in hepatoblastoma by scanning electrochemical microscopy, *Proc. Natl. Acad. Sci. USA* 2004, 101, 17582–17587. (g) Kurulugama, R., Wipf, D. O., Takacs, S., Pongmayteegul, S., Garris, P., Baur, J. E. Scanning electrochemical microscopy of model neurons: Constant distance imaging, *Anal. Chem*. 2005, 77, 1111–1117. (h) Bard, A. J., Li, X., Zhan, W. Chemically imaging living cells by scanning electrochemical microscopy, *Biosens. Bioelectron*. 2006, 22, 461–472. (i) Amemiya, S., Guo, J., Xiong, H., Gross, D. Biological applications of scanning electrochemical microscopy: Chemical imaging of single living cell and beyond, *Anal. Bioanal. Chem*. 2006, 386, 458–471. (j) Sun, P., Laforge, F. O., Abeyweera, T. P., Rotenberg, S. A., Carpino, J., Mirkin, M. V. Nanoelectrochemistry of mammalian cells, *Proc. Natl. Acad. Sci. USA* 2008, 105, 443–448.
22. Hage, D. S. Immunoassays, *Anal. Chem*. 1995, 67, 455–462.
23. Sukamto, J. P. H., Smyrl, W. H., Casillas, N., Al-Odan, M., James, P., Jin, W., Douglas, L. Microvisualization of corrosion, *Mater. Sci. Eng. A* 1995, 198, 177–196.
24. Zhu, Y. Y., Williams, D. E. Scanning electrochemical microscopic observation of a precursor state to pitting corrosion of stainless steel, *J. Electrochem. Soc*. 1997, 144, L43–L45.
25. Horrocks, B. R., Mirkin, M. V., Bard, A. J. Scanning electrochemical microscopy. 25. Application to investigation of the kinetics of heterogeneous electron transfer at semiconductor (WSe_2 and Si) electrodes, *J. Phys. Chem*. 1994, 98, 9106–9114.
26. Engstrom, R. C., Weber, M., Wunder, D. J., Burgess, R., Winquist, S. Measurements within the diffusion layer using a microelectrode probe, *Anal. Chem*. 1986, 58, 844–848.
27. Wipf, D. O., Bard, A. J. Scanning electrochemical microscopy. X. High resolution imaging of active sites on an electrode surface, *J. Electrochem. Soc*. 1991, 138, L4–L6.
28. Engstrom, R. C., Small, B., Kattan, L. Observation of microscopically local electron-transfer kinetics with scanning electrochemical microscopy, *Anal. Chem*. 1992, 64, 241–244.
29. Bard, A. J., Fan, F.-R. F., Mirkin, M. V. Scanning electrochemical microscopy. In *Electroanalytical Chemistry*, Vol. 18 (A. J. Bard, ed.), Marcel Dekker, New York, 1994, p. 243.
30. Sugimura, H., Shimo, N., Kitamura, N., Masuhara, H. Topographical imaging of Prussian Blue surfaces by direct-mode scanning electrochemical microscopy, *J. Electroanal. Chem*. 1993, 346, 146–160.

31. Horrocks, B. R., Mirkin, M. V., Pierce, D. T., Bard, A. J., Nagy, G., Toth, K. Scanning electrochemical microscopy. 19. Ion-selective potentiometric microscopy, *Anal. Chem*. 1993, 65, 1213–1224.
32. (a) Fan, F.-R. F., Bard, A. J. STM on wet insulators: Electrochemistry or tunneling? *Science* 1995, 270, 1849–1851. (b) Fan, F.-R. F., Bard, A. J. Imaging of biological macromolecules on mica in humid air by scanning electrochemical microscopy, *Proc. Natl. Acad. Sci. USA* 1999, 96, 14222–14227.
33. Forouzan, F., Bard, A. J. Evidence for Faradaic processes in scanning probe microscopy on mica in humid air, *J. Phys. Chem. B*. 1997, 101, 10876–10879.
34. Craston, D. H., Lin, C. W., Bard, A. J. High resolution deposition of silver in Nafion films with the scanning tunneling microscope, *J. Electrochem. Soc*. 1988, 135, 785–786.
35. Fan, F.-R. F., Bard, A. J. In situ scanning tunneling microscopy of polycrystalline platinum electrodes under potential control. Copper electrodeposition and pyrrole electropolymerization, *J. Electrochem. Soc*. 1989, 136, 3216–3222.
36. Dean, J. A. ed. *Lange's Handbook of Chemistry*, 13th edn., McGraw-Hill, New York, 1985.
37. Kirgintsev, A. N., Luk'yanov, A. V. *Zh. Neor. Khim*. 1967, 12, 2032.
38. McCarley, R. L., Hendricks, S. A., Bard, A. J. Controlled nanofabrication of highly oriented pyrolytic graphite with the scanning tunneling microscope, *J. Phys. Chem*. 1992, 96, 10089–10092.
39. Hsu, W. Y., Gierke, T. D. Ion transport and clustering in Nafion perfluorinated membranes, *J. Membr. Sci*. 1983, 13, 307–326.
40. Guckenberger, R., Heim, M., Ceve, G., Knapp, H., Wiegräbe, W., Hillebrand, A. Scanning tunneling microscopy of insulators and biological specimens based on lateral conductivity of ultrathin water films, *Science* 1994, 266, 1538–1540.
41. Burton, D. R. Structure and function of antibodies. In *Molecular Genetics of Immunoglobulin* (F. Calabi and M. S. Neuberger, eds.), Elsevier, Amsterdam, the Netherlands, 1987.
42. Wells, T. N. C., Stedman, M., Leatherbarrow, R. J. Imaging of proteins by scanning tunnelling microscopy, *Ultramicroscopy* 1992, 42–44, 1200–1203.
43. Marquart, M., Deisenhofer, J., Huber, R., Palm, W. Crystallographic refinement and atomic models of the intact immunoglobulin molecule Kol and its antigen-binding fragment at 3.0 Å and 1.9 Å resolution, *J. Mol. Biol*. 1980, 141, 369–391.
44. Valentine, R. C., Green, N. M. Electron microscopy of an antibody–hapten complex, *J. Mol. Biol*. 1967, 27, 615–616.
45. Hecht, H. J., Kalisz, H. M., Handel, J., Schmid, R. D., Schomburg, D. Crystal structure of glucose oxidase from *Aspergillus niger* refined at 2.3 Å resolution, *J. Mol. Biol*. 1993, 229, 153–172.
46. Van Bruggen, E. F. J. An electron microscopist's view of the quaternary structure of arthropodan and molluscan hemocyanins. In *Structure and Function of Invertebrate Respiratory Proteins* (E. J. Wood, ed.), Harwood Academic Publishers, London, U.K., 1982.
47. Mellema, J. E., Klug, A. Quaternary structure of gastropod haemocyanin, *Nature* 1972, 239, 146–150.
48. Leatherbarrow, R. J., Stedman, M., Wells, T. N. C. Structure of immunoglobulin G by scanning tunnelling microscopy, *J. Mol. Biol*. 1991, 221, 361–365.
49. Leggett, G. J., Davies, M. C., Jackson, D. E., Roberts, C. J., Tendler, S. J. B., Williams, P. M. Studies of covalently immobilized protein molecules by scanning tunneling microscopy: The role of water in image contrast formation, *J. Phys. Chem*. 1993, 97, 8852–8854.
50. Lin, J. N., Drake, B., Lea, A. S., Hansma, P. K., Andrade, J. D. Direct observation of immunoglobulin adsorption dynamics using the atomic force microscope, *Langmuir* 1990, 6, 509–511.
51. Chi, Q., Zhang, J., Dong, S., Wang, E. Direct observation of native and unfolded glucose oxidase structures by scanning tunnelling microscopy, *J. Chem. Soc. Faraday Trans*. 1994, 90, 2057–2060.
52. Tang, S. L., McGhie, A. J. Imaging individual chaperonin and immunoglobulin G molecules with scanning tunneling microscopy, *Langmuir* 1996, 12, 1088–1093.
53. Laforge, F. O., Velmurugan, J., Wang, Y., Mirkin, M. V. Nanoscale imaging of surface topography and reactivity with the scanning electrochemical microscope, *Anal. Chem*. 2009, 81, 3143–3150.

5 Theory

Michael V. Mirkin and Yixian Wang

CONTENTS

5.1 Introduction 75
5.2 Feedback Mode of SECM Operation 76
5.2.1 General Theory of SECM Feedback for a First-Order Heterogeneous Reaction at the Tip/Substrate 76
5.2.2 Steady-State Conditions 80
5.2.2.1 Diffusion-Controlled and Nernstian Steady-State Processes 81
5.2.2.2 Irreversible Substrate Kinetics 86
5.2.2.3 Quasireversible Processes 87
5.2.2.4 Electron Transfer at Self-Assembled Monolayers 88
5.2.3 Microscopic or Partially Blocked Substrates 91
5.2.4 Nondisk Tips and Tip Shape Characterization 92
5.3 Generation/Collection Mode of SECM Operation 96
5.3.1 Potentiometric G/C Mode 97
5.3.2 Amperometric G/C Modes 98
5.3.2.1 Substrate Generation/Tip Collection Mode 98
5.3.2.2 Tip Generation/Substrate Collection Mode 99
5.4 SECM of More Complicated Chemical Systems 100
5.4.1 Processes Involving Homogeneous Reactions 100
5.4.1.1 First-Order Following Reaction 100
5.4.1.2 Second-Order Following Reaction 104
5.4.1.3 ECE and DISP1 Mechanisms 104
5.4.2 Surface Reactions and Interfacial Transfer Processes 106
5.4.2.1 Adsorption/Desorption Processes and Lateral Mass/Charge Transfer 106
5.4.2.2 Dissolution of Ionic Crystals 108
5.4.2.3 Charge Transfer Processes at the Liquid–Liquid Interface 108
5.4.2.4 Finite Enzyme Kinetics at the Substrate 110
5.4.3 3D Simulations and Nonideal Conditions 111
5.5 Numerical Solution of SECM Diffusion Problems Using COMSOL Multiphysics 113
5.5.1 Diffusion to an Embedded Microdisk 113
5.5.2 Diffusion-Controlled SECM Feedback 115
5.5.3. E_rC_i Mechanism 117
Acknowledgment 120
References 120

5.1 INTRODUCTION

The quantitative scanning electrochemical microscopic (SECM) theory has been developed for various regimes of measurements and electrochemical mechanisms. Different operating modes of the SECM, for example, feedback and generation/collection (G/C) modes, steady-state and transient

measurements, require significantly different theoretical descriptions. Quantitative treatments are available for both diffusion-controlled processes and finite kinetics as well as for more complicated mechanisms involving adsorption and homogeneous reactions in the gap. The focus of this chapter is on fundamentals of the SECM theory, that is, steady-state and transient measurements, feedback mode, and G/C experiments. While the theory for a one-step heterogeneous reaction is covered in detail, only a brief discussion of other processes is included to avoid overlap with other chapters. SECM responses for more complicated processes and geometries can be simulated using commercially available software packages. An example of SECM simulations using popular COMSOL Multiphysics software is given in the last section of this chapter.

5.2 FEEDBACK MODE OF SECM OPERATION

Feedback theory has been the basis for most quantitative SECM applications reported to date. Historically, the first theoretical treatment of the feedback response was the finite element simulation of a diffusion-controlled process by Kwak and Bard [1], but we will start from a more general formulation for a quasireversible process under non-steady-state conditions and then consider some important special cases.

5.2.1 General Theory of SECM Feedback for a First-Order Heterogeneous Reaction at the Tip/Substrate

In the feedback mode experiment, both the tip and the substrate are immersed in a solution containing an electrolyte and a redox species (e.g., a reducible species, O). This species is reduced at the microdisk tip electrode, and the product, R, can be reoxidized at the substrate:

$$\mathrm{O} + n\mathrm{e}^- \rightarrow \mathrm{R} \quad \text{(tip electrode)} \tag{5.1}$$

$$\mathrm{R} - n\mathrm{e}^- \rightarrow \mathrm{O} \quad \text{(substrate)} \tag{5.2}$$

A considerable complexity of SECM theory is due to the combination of a cylindrical diffusion to the ultramicroelectrode (UME) tip and a thin-layer-type diffusion space. The time-dependent diffusion problem for a simple quasireversible reaction in cylindrical coordinates is as follows [2,3]:

$$\frac{\partial C_\mathrm{i}}{\partial T} = \frac{\partial^2 C_\mathrm{i}}{\partial Z^2} + \frac{\partial^2 C_\mathrm{i}}{\partial R^2} + \frac{1}{R}\frac{\partial C_\mathrm{i}}{\partial R} \quad 0 < T, \quad 0 \le R, \quad 0 < Z < L \tag{5.3}$$

where L is the normalized tip/substrate distance (d/a) and other dimensionless variables are

$$R = \frac{r}{a} \tag{5.4}$$

$$Z = \frac{z}{a} \tag{5.5}$$

$$C_\mathrm{i} = \frac{c_\mathrm{i}}{c_\mathrm{O}^\mathrm{o}} \tag{5.6}$$

$$T = \frac{tD_O}{a^2} \tag{5.7}$$

where

r and z are, respectively, the coordinates in the directions radial and normal to the electrode surface

D_i and c_i are the diffusion coefficient and concentration of the species i ($i = O$, $D_i = D_O$)

c_O^o is the bulk concentration of O

a is the tip electrode radius

t is the time

The assumption of equal diffusion coefficients ($D_O = D_R = D$) allows the problem to be described in terms of a single species (O). The boundary conditions are of the form
$0 < T$, $0 \le R < 1$, $Z = 0$ (tip electrode surface):

$$\frac{\partial C_O}{\partial Z} = K_{f,T} C_O - K_{b,T}(1 - C_O) = J_T \tag{5.8}$$

$$0 < T, \quad 1 \le R \le RG, \quad Z = 0 \quad \text{(glass insulating sheath)} : \frac{\partial C_O}{\partial Z} = 0 \tag{5.9}$$

$0 < T$, $0 \le R \le h$, $Z = L$ (substrate surface):

$$\frac{\partial C_O}{\partial Z} = K_{b,S} C_O - K_{f,S}(1 - C_O) = J_S \tag{5.10}$$

$$R > RG, \quad 0 \le Z \le L : \quad C_O = 1 \tag{5.11}$$

where J_T and J_S are the normalized fluxes of species at the tip and the substrate

$$K_{f/b,S} = \frac{k_{f/b,S} a}{D} \tag{5.12}$$

$$K_{f/b,T} = \frac{k_{f/b,T} a}{D} \tag{5.13}$$

$$RG = \frac{r_g}{a} \tag{5.14}$$

$$h = \frac{a_S}{a} \tag{5.15}$$

where

r_g is the radius of the tip-insulating material

a_S is the substrate radius

The initial condition, completing the definition of the problem, is

$$T = 0, \quad 0 \le R, \quad 0 \le Z \le L; \quad C_O = 1 \tag{5.16}$$

If the substrate is an insulator, $J_S \equiv 0$. If both tip and substrate reactions are electrochemical processes, the rate constants for reduction (k_f) and oxidation (k_b) are given by the Butler–Volmer relations:

$$k_f = k^o \exp\left[-\alpha n f(E - E^{\circ\prime})\right] \tag{5.17}$$

$$k_b = k^\circ \exp\left[(1-\alpha) n f(E - E^{\circ\prime})\right] \tag{5.18}$$

where
- k° is the standard rate constant
- E is the electrode potential
- $E^{\circ\prime}$ is the formal potential
- α is the transfer coefficient
- n is the number of electrons transferred per redox event
- $f = F/RT$ (here, F is the Faraday, R is the gas constant, and T is the temperature)

The solution of the problem can be obtained in terms of the dimensionless currents $I_T(T)$ and $I_S(T)$:

$$I_T(T) = -\frac{\pi}{2}\int_0^1 J_T(T,R) R\, dR; \quad I_S(T) = -\frac{\pi}{2}\int_0^h J_S(T,R) R\, dR \tag{5.19}$$

where I_T and I_S are equal to the physical currents normalized by the limiting diffusion tip current, $I = i/i_{T,\infty}$, where

$$i_{T,\infty} = 4nFDc^\circ a \tag{5.20}$$

The aforementioned formulation is somewhat overly general, since it includes the possibility of mixed diffusion/kinetic control of both the tip and substrate processes. In practice, at least one of those electrodes is held under diffusion control, so either Equation 5.21a

$$0 < T, \quad 0 \le R < 1, \quad Z = 0; \quad C_O = 0 \tag{5.21a}$$

can be used instead of Equation 5.8, or Equation 5.10 can be replaced with a much simpler boundary condition

$$0 < T, \quad 0 \le R \le h, \quad Z = L; \quad C_O = 1 \tag{5.21b}$$

This problem was solved semianalytically in terms of two-dimensional (2D) integral equations [2,3] and numerically by using Krylov integrator [4] and the alternating direction implicit (ADI) finite difference method [3,5]. Potentiostatic transients were computed for two limiting cases: a diffusion-controlled process and totally irreversible kinetics [3–5]. The analysis of the simulation

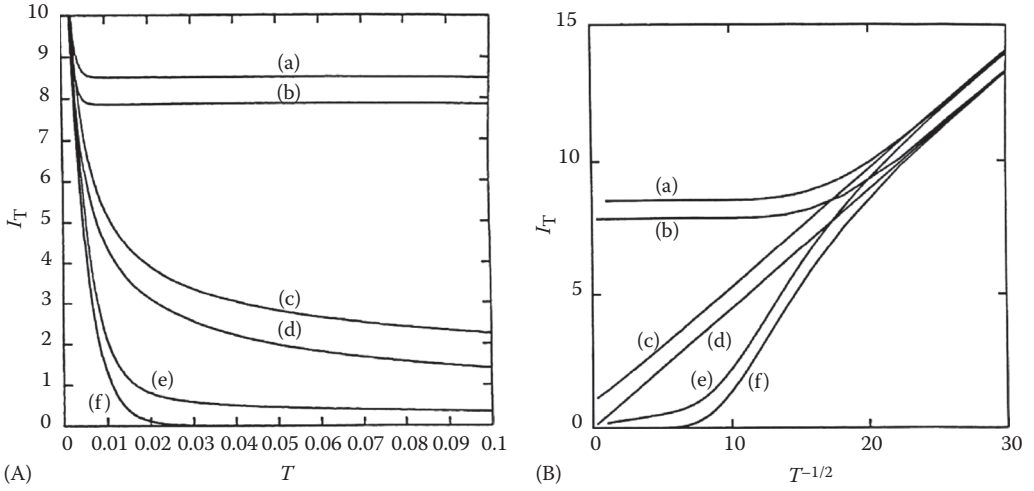


FIGURE 5.1 Comparison of (A) simulated SECM transients with (B) transients corresponding to different electrode geometries (all processes are diffusion controlled). (a) SECM transient for a conductive substrate, (b) two-electrode thin-layer cell, (c) microdisk, (d) planar electrode, (e) SECM with an insulating substrate, and (f) one-electrode thin-layer cell. Curves A, B, E, and F were computed with $L = d/a = 0.1$. (Adapted from Bard, A.J., Denuault, G., Friesner, R.A., Dornblaser, B.C., and Tuckerman, L.S., Scanning electrochemical microscopy: Theory and application of the transient (chronoamperometric) SECM response, *Anal. Chem*., 63, 1282–1288, 1991. Copyright 1991 American Chemical Society.)

results [4] revealed several time regions typical for SECM transients (Figure 5.1). In the short-time region ($T \leq 0.001$), an SECM tip current follows closely the microdisk transient, and then it starts to deviate and finally levels at a constant value of i_T. For a conductive substrate, $i_T \geq i_{T,\infty}$, and it is always larger than the value calculated for the same time from thin-layer cell (TLC) theory. For an insulating substrate, $i_T < i_{T,\infty}$. The smaller the tip/substrate separation, the earlier the deviations between the SECM and microdisk transients occur. The time when the SECM undergoes a transition from the microdisk regime to the TLC regime is related to the time needed by the species to diffuse across the gap between the tip and the substrate. This time can be determined experimentally and can be used to evaluate the diffusion coefficient [4]. The transients computed for different rates of an irreversible heterogeneous reaction [5] also showed a microdisk-type behavior at short times. The current magnitude at longer times and its eventual steady-state value are determined by the value of the dimensionless heterogeneous rate constant, $K_{b,S}$ (Figure 5.2). The substrate behaves as a conductor as $K_{b,S} \to \infty$, and as an insulator as $K_{b,S} \to 0$. A few transients and non-steady-state CVs for a quasireversible process were computed for both insulating and conducting substrates [2].

Martin and Unwin simulated chronoamperometric feedback allowing for unequal diffusion coefficients of the oxidized and reduced forms of the redox mediator [6]. Unlike steady-state SECM response, the shape of the tip current transients is sensitive to the ratio of the diffusion coefficients, $\gamma = D_O/D_R$ (Figure 5.3). When $D_O = D_R$, the tip current attains a steady-state value much faster than for any $\gamma \neq 1$. At $\gamma < 1$, a characteristic minimum appears in the short-time region, which is quite unusual for potentiostatic transients. Ghilane et al. [7] carried out similar simulations for a very broad range of γ ($0.001 < \gamma < 1000$). This extension of the model was necessary to describe the SECM experiments in ionic liquids, where the D_O and D_R values may be strikingly different.

One should notice that Equation 5.11 implies that concentration of the mediator is equal to its bulk value everywhere beyond the limits of the tip-insulating sheath ($R \geq RG$). This approximation is applicable only if $RG \gg 1$, and even for $RG = 10$ it leads to about 2% error [8,9].

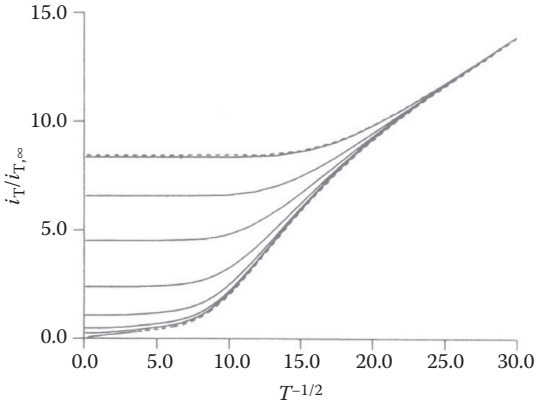


FIGURE 5.2 Simulated feedback SECM transients with various rate constants for an irreversible heterogeneous process at the substrate. The upper and lower dashed curves correspond, respectively, to the limits $K_{b,S} \rightarrow \infty$ and $K_{b,S}=0$. The solid curves (from top to bottom) represent log $K_{b,S}=3.0$, 1.5, 1.0, 0.5, 0, −0.5, and −1.0. RG = 10. (Reprinted with permission from Bard, A.J., Mirkin, M.V., Unwin, P.R., and Wipf, D.O., Scanning electrochemical microscopy. 12. Theory and experiment of the feedback mode with finite heterogeneous electron-transfer kinetics and arbitrary substrate size, *J. Phys. Chem*., 96, 1861–1868, 1992. Copyright 1992 American Chemical Society.)

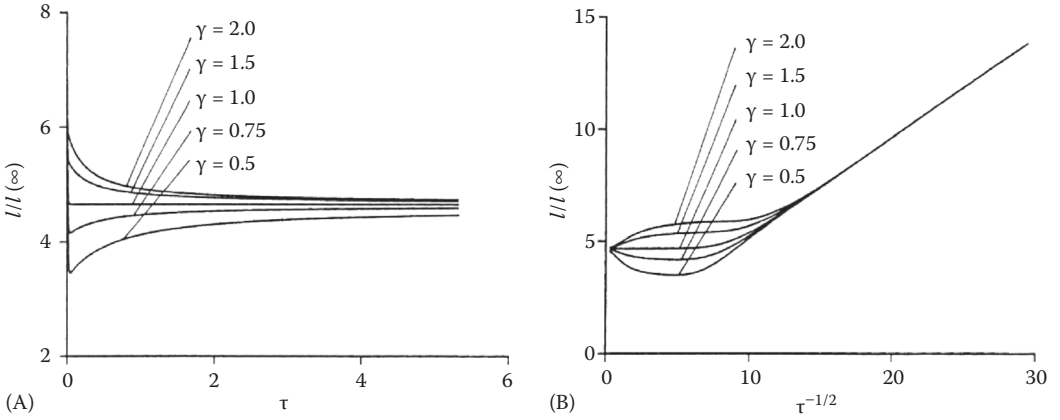


FIGURE 5.3 Effect of γ on the chronoamperometric characteristics for the positive feedback process at a tip/substrate separation, $L=0.2$. The reduced form initially present in solution is oxidized at the tip and regenerated at the substrate. Normalized tip current is plotted as a function of dimensionless time, $\tau = tD_R/a^2$. (Reprinted from *J. Electroanal. Chem*., 439, Martin, R.D. and Unwin, P.R., Scanning electrochemical microscopy: Theory and experiment for the positive feedback mode with unequal diffusion coefficients of the redox mediator couple, 123–136, Copyright 1997, with permission from Elsevier Science S.A.)

5.2.2 Steady-State Conditions

The formulation of the steady-state SECM problem is significantly simpler [10]. It includes a single Laplace equation

$$\frac{\partial^2 C}{\partial Z^2} + \frac{\partial^2 C}{\partial R^2} + \frac{1}{R}\frac{\partial C}{\partial R} = 0 \tag{5.22}$$

for oxidized (or reduced) form of the mediator with boundary conditions (5.9) and (5.11) and one of two pairs of boundary conditions for the tip and substrate surfaces, that is, either Equations 5.10

and 5.21a (diffusion-controlled tip reaction and quasireversible substrate kinetics) or Equations 5.8 and 5.21b (diffusion-controlled substrate reaction and finite kinetics tip at the tip). All variables in these equations are now time independent. The assumption of equal diffusion coefficients is unnecessary under steady state, because the concentrations of O and R at steady state are interrelated as follows:

$$c_{\mathrm{O}} + \frac{c_{\mathrm{R}} D_{\mathrm{R}}}{D_{\mathrm{O}}} = c_{\mathrm{O}}^{\mathrm{o}} + \frac{c_{\mathrm{R}}^{\mathrm{o}} D_{\mathrm{R}}}{D_{\mathrm{O}}} \tag{5.23}$$

The solution for the finite kinetics at the tip and diffusion-limited substrate reaction is [10]

$$\frac{1 - \pi J_{\mathrm{T}}(R)/4\kappa'}{\theta} = \int_0^1 u J_{\mathrm{T}}(u)\,du \int_0^\infty J_0(pR) J_0(pu) \tanh(pL)\,dp \tag{5.24}$$

where J_0 is the Bessel function of the first kind of order zero

$$\kappa' = \frac{\pi a k^{\mathrm{o}} \exp[-\alpha n f(E - E^{\mathrm{o}\prime})]}{4 D_{\mathrm{O}}} \tag{5.25a}$$

and

$$\theta = 1 + \frac{\exp\left[n f(E - E^{\mathrm{o}\prime})\right] D_{\mathrm{O}}}{D_{\mathrm{R}}} \tag{5.25b}$$

However, Equation 5.24 has not been utilized in any calculations. Most published computational results represent the long-time limit of the data obtained by solving time-dependent equations. By fitting these results, several analytical approximations have been obtained for different situations including diffusion-controlled, irreversible, and quasireversible reactions at both tip and substrate surfaces.

5.2.2.1 Diffusion-Controlled and Nernstian Steady-State Processes

The knowledge of the shape of the I_{T}–L curve for a diffusion-controlled process is critical for both imaging and quantitative kinetic measurements because it allows one to establish the distance scale. The equations describing a diffusion-controlled SECM process represent two limiting cases of the general steady-state problem discussed earlier, that is, (i) "pure positive feedback" produced by rapid regeneration of the reactant species at the substrate and (ii) "pure negative feedback" observed when no mediator regeneration occurs at the substrate. Both problems were treated numerically by Kwak and Bard [1]. The dimensionless current–distance curves were tabulated for both insulating and conductive substrates, assuming the equality of the diffusion coefficients and an infinitely large substrate. Later [11], analytical approximations were obtained for both working curves. Both numerical results in Ref. [1] and analytical expressions in Ref. [11] are suitable only for large values of RG (i.e., RG ≥ 10). However, the tips with much thinner insulating sheath have often been employed because they allow one to obtain closer tip/substrate separation. A typical RG for a pipette-based tip is ~1.1 [8].

More recent treatments of this problem [8,9] are suitable for 1.1 ≤ RG ≤ 10. The diffusion problem in dimensionless form is

$$\frac{\partial^2 C}{\partial Z^2} + \frac{\partial^2 C}{\partial R^2} + \frac{1}{R}\frac{\partial C}{\partial R} = 0 \quad 0 \le R, \quad L1 < Z < L \tag{5.26}$$

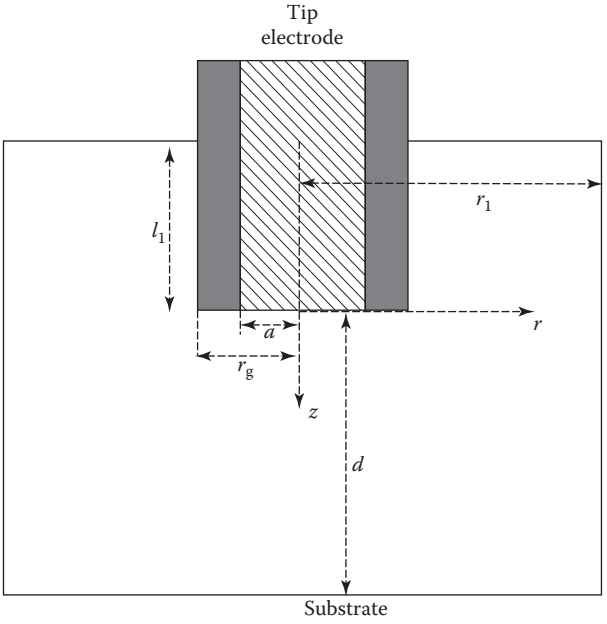


FIGURE 5.4 Geometry of the simulation domain and the parameters defining the diffusion problem for SECM. (Adapted from Shao, Y. and Mirkin, M.V., Probing ion transfer at the liquid/liquid interface by scanning electrochemical microscopy (SECM), *J. Phys. Chem. B*, 102, 9915–9921, 1998. Copyright 1998 American Chemical Society.)

where $L1 = \ell 1/a$ shows how far behind the tip surface ($Z = 0$) the simulation goes (Figure 5.4); other dimensionless variables are defined earlier. The boundary conditions are

$$0 \le R < 1, \quad Z = 0 \quad \text{(tip surface)}: \quad C = 0 \tag{5.27a}$$

$$1 \le R \le \text{RG}, \quad Z = 0 \quad \text{and} \quad R = \text{RG}, \; L1 < Z < 0 \; \text{(insulating glass)}:$$

$$\frac{\partial C}{\partial n} = 0 \tag{5.27b}$$

where $\dfrac{\partial C}{\partial n}$ is the normal derivative on the surface of insulating glass surrounding the conductive core of the tip.

$0 \le R \le \text{RMAX}$, $Z = L$ (substrate):

$$C = 1 \quad \text{(positive feedback)} \tag{5.28a}$$

$$\text{or} \quad \frac{\partial C}{\partial Z} = 0 \quad \text{(negative feedback)} \tag{5.28b}$$

$\text{RG} \le R < \text{RMAX}$, $Z = L1$ or $R = \text{RMAX}$, $L1 < Z < L$ (simulation space limits):

$$C = 1 \tag{5.29}$$

The main difference between Equations 5.26 through 5.29 and the previous simulation [1] is in problem geometry. The values of $L1 = 0$ and RMAX = RG were used in Ref. [1], that is, the concentration of the mediator was assumed to equal its bulk value everywhere beyond the limits of the tip-insulating sheath ($R \geq$ RG). However, for RG << 10 satisfactory simulation accuracy can only be achieved by taking into account mediator diffusion from behind the shield and extending the simulation domain much further than $R =$ RG. The values of $L1 \leq -20$ and $R1 = 100$ were sufficient to ensure the relative error of <1% for all L and RG values [8].

Several normalized current vs. distance curves for pure positive (A) and negative (B) feedback and different RG values are presented in Figure 5.5. To fit an experimental approach curve to the theory, one usually normalizes the measured tip current by the experimental $i_{T,\infty}$ value. For RG ≈ 10, the experimental $i_{T,\infty}$ is close to the $4nFaDc$ value given by Equation 5.20. In earlier SECM studies, the tip current was normalized by this quantity. But at RG << 10, $i_{T,\infty}$ becomes larger than $4nFaDc$ due to the mediator diffusion from the back of the tip [12]. The correction for the finite insulator thickness can be introduced by replacing the factor "4" in Equation 5.20 by one suitable for a given RG, for example, 4.06 (RG = 10), 4.43 (RG = 2), 4.64 (RG = 1.5), and 5.14 (RG = 1.1). All tip current values in Figure 5.5 are normalized by the $i_{T,\infty}$ corresponding to a specified RG.

For positive SECM feedback, the effect of the RG on the shape of the current–distance curve is relatively small. But when the substrate is an insulator, a smaller RG results in a significantly higher current at any tip/substrate separation. Analytical approximations can be obtained for both positive and negative feedback working curves (solid lines in Figure 5.5). Equation 5.30 with the parameter

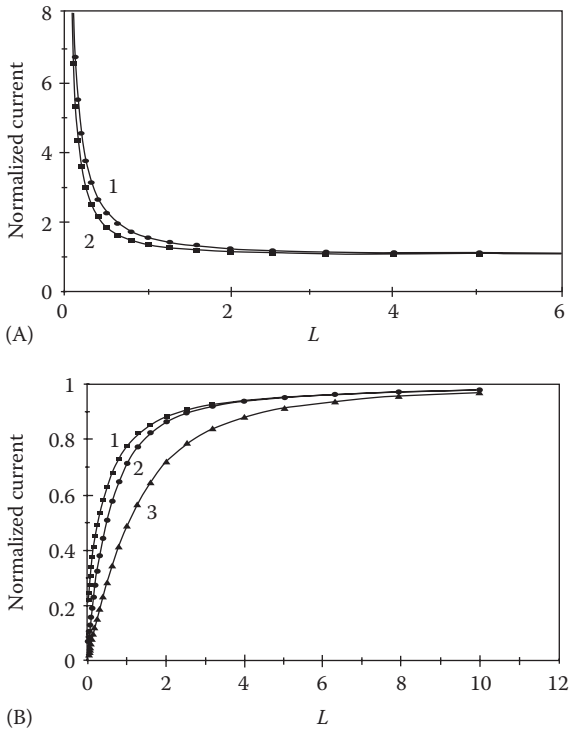


FIGURE 5.5 Simulated SECM current vs. distance curves for a pure (A) positive and (B) negative feedback and different RG values. Symbols, simulation; solid line in (A), Equation 5.30; solid line in (B), Equation 5.31. (A) RG = (1) 10 and (2) 1.1. (B) RG = (1) 1.1, (2) 2, and (3) 10. (Reprinted from Shao, Y. and Mirkin, M.V., Probing ion transfer at the liquid/liquid interface by scanning electrochemical microscopy (SECM), *J. Phys. Chem. B*, 102, 9915–9921, 1998. Copyright 1998 American Chemical Society.)

values listed in Table 5.1 fits within 1% of the simulated I_T–L data for a conductive substrate over the L interval from 0.04 to 10 and for RG values between 1.1 and 10:

$$I_T^c(L) = A + B/L + C\exp(D/L) \tag{5.30}$$

For an insulating substrate, Equation 5.31 with the parameter values listed in Table 5.2 is similarly accurate over the same ranges of L and RG values:

$$I_T^{ins}(L) = \frac{1}{\left[A + B/L + C\exp(D/L)\right]} + \frac{E \times L}{(F + L)} \tag{5.31}$$

Amphlett and Denuault [9] have formulated a time-dependent SECM problem based on the same ideas (i.e., the simulation space is expanded beyond the edge of the insulting sheath and diffusion from behind the shield is taken into account). The steady-state responses were calculated as a long-time limit of the tip transient currents. These authors also obtained two equations describing SECM approach curves for a pure positive and negative feedback. The equation for a diffusion-controlled positive feedback is identical to Equation 5.30. The approximate expression for the negative feedback in Ref. [9] is of the same form as an approximation for RG = 10 in Ref. [11]:

$$I_T^{ins}(L) = \frac{1}{\left[k_1 + k_2/L + k_3\exp(k_4/L)\right]} \tag{5.32}$$

with the parameter values listed in Table 5.3. Although Equation 5.32 is not valid for small tip/substrate distances ($L \geq 0.2$ for all RG values, and $L \geq 2$ for RG = 1.11), it can be useful for $2 < RG < 10$, and for larger RG values unavailable in Table 5.2.

TABLE 5.1
Parameter Values for Equation 5.30

RG	A	B	C	D
1.1	0.5882629	0.6007009	0.3872741	–0.869822
1.5	0.6368360	0.6677381	0.3581836	–1.496865
2.0	0.6686604	0.6973984	0.3218171	–1.744691
5.1	0.72035	0.75128	0.26651	–1.62091
10	0.7449932	0.7582943	0.2353042	–1.683087

TABLE 5.2
Parameter Values for Equation 5.31

RG	A	B	C	D	E	F
1.1	1.1675164	1.0309985	0.3800855	–1.701797	0.3463761	0.0367416
1.5	1.0035959	0.9294275	0.4022603	–1.788572	0.2832628	0.1401598
2.0	0.7838573	0.877792	0.4248416	–1.743799	0.1638432	0.1993907
10	0.4571825	1.4604238	0.4312735	–2.350667	–0.145437	5.5768952

TABLE 5.3
Parameter Values for Equation 5.32

RG	k_1	k_2	k_3	k_4	% Error	Validity Range
1002	0.13219	3.37167	0.8218	−2.34719	<1	0.3–20
100	0.27997	3.05419	0.68612	−2.7596	<1	0.4–20
50.9	0.30512	2.6208	0.66724	−2.6698	<1	0.4–20
20.1	0.35541	2.0259	0.62832	−2.55622	<1	0.4–20
15.2	0.37377	1.85113	0.61385	−2.49554	<1	0.4–20
10.2	0.40472	1.60185	0.58819	−2.37294	<1	0.4–20
8.13	0.42676	1.46081	0.56874	−2.28548	<1	0.4–20
5.09	0.48678	1.17706	0.51241	−2.07873	<1	0.2–20
3.04	0.60478	0.86083	0.39569	−1.89455	<0.2	0.2–20
2.03	0.76179	0.60983	0.23866	−2.03267	<0.15	0.2–20
1.51	0.90404	0.42761	0.09743	−3.23064	<0.7	0.2–20
1.11	−1.46539	0.27293	2.45648	8.995E−7	<1	2–20

The reversible (Nernstian) steady-state voltammogram for any electrode geometry can be calculated from the following equation:

$$i(E) = \frac{i_{\text{dif}}}{\theta} \tag{5.33a}$$

where
i_{dif} is the diffusion limiting current
θ was defined in Equation 5.25b

Thus, for the SECM,

$$i_{\text{T}}(E, L) = \frac{I_{\text{T}}(L)}{\theta} \tag{5.33b}$$

where $I_{\text{T}}(L)$ is given by Equations 5.30 and 5.31 for a conductive and an insulating substrates, respectively.

Lefrou and Cornut reported different analytical approximations for approach curves under pure positive [13a] and negative [13b] feedback conditions. Both expressions explicitly include the RG parameter, thus making them suitable for any RG value. In the case of positive feedback, where the tip current dependence on RG is relatively weak, a more complicated approximation [13a] does not offer significant advantages in comparison with Equation 5.30. One may wish to use it only if the RG is very small, exactly known, and significantly different from the values in Table 5.1. In contrast, Equation 5.34 derived for pure negative feedback [13b] can be useful for determining RG from approach curves, especially for pipette-based tips with RG < 3:

$$I_{\text{T}}(L) = \frac{\dfrac{2.08}{\text{RG}^{0.358}}\left(L - \dfrac{0.145}{\text{RG}}\right) + 1.585}{\dfrac{2.08}{\text{RG}^{0.358}}(L + 0.0023\text{RG}) + 1.57 + \dfrac{\ln \text{RG}}{L} + \dfrac{2}{\pi \text{RG}} \ln\left(1 + \dfrac{\pi \text{RG}}{2L}\right)} \tag{5.34}$$

(to preserve the consistency of symbols used throughout this chapter, we had to modify the unusual notation introduced in [13b]). Other closed form expressions for diffusion-controlled SECM approach curves have been reported (see, e.g., Ref. [14]).

5.2.2.2 Irreversible Substrate Kinetics

A special case of totally irreversible substrate kinetics ($K_{f,S}=0$) was treated numerically [3]. Later, the entire family of theoretical working curves (I_T vs. $K_{b,S}$) calculated for various L was fit to Equation 5.35 [15]:

$$I_T(L) = I_S\left(1 - \frac{I_T^{ins}}{I_T^C}\right) + I_T^{ins} \tag{5.35a}$$

$$I_S = \frac{0.78377}{L(1+1/\Lambda)} + \frac{\left[0.68 + 0.3315\exp(-1.0672/L)\right]}{\left[1 + F(L,\Lambda)\right]} \tag{5.35b}$$

where

I_T^C and I_T^{ins} are given by Equations 5.30 and 5.31 with RG = 10
I_S is the kinetically controlled substrate current
$F(L,\Lambda) = (11/\Lambda + 7.3)/(110 - 40L)$
$\Lambda = K_{b,S}d/a$

Figure 5.6 shows a family of working curves for different values of L along with the simulated data from Ref. [3]. The numerical results (triangles) fit Equation 5.34 (squares) over an L interval from 0.1 to 1.5 and $-2 \le \log \Lambda \le 3$ within ~1%–2%. These working curves were calculated for RG = 10 and should not be used for the analysis of data obtained with very sharp tips (e.g., RG < 3). A closed form expression suitable for small RG values was derived by Cornut and Lefrou [16].

The radius of the portion of the substrate surface participating in the SECM feedback loop can be evaluated as $h^\infty \cong 1 + 1.5L$ [3]. Thus at small tip/substrate separations (e.g., $L \le 2$), a large substrate behaves as a virtual UME of a size comparable with that of the tip electrode. The SECM allows probing local kinetics at a small portion of the macroscopic substrate with all of the advantages of microelectrode measurements.

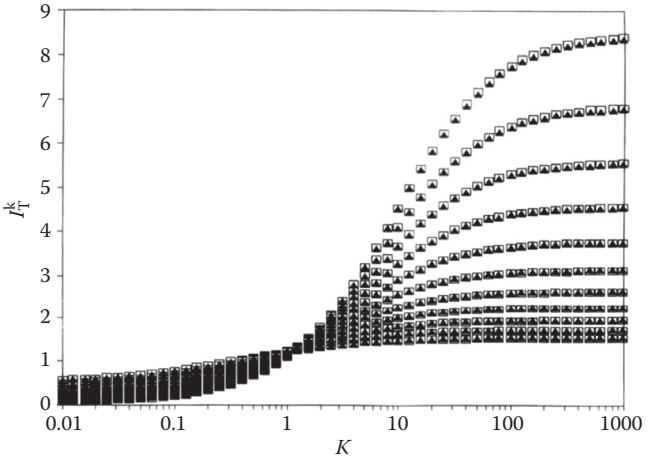


FIGURE 5.6 Working curves of I_T vs. $K_{b,S}$ for different values of L. Open squares, Equation 5.34; filled triangles, simulation in Ref. [3]. From top to bottom, $\log(d/a) = -1.0, -0.9, -0.8, -0.7, -0.6, -0.5, -0.4, -0.3, -0.2, -0.1$, and 0.0. (Reprinted with permission from Wei, C., Bard, A.J., and Mirkin, M.V., Scanning electrochemical microscopy. 31. Application of SECM to the study of charge transfer processes at the liquid/liquid interface, *J. Phys. Chem.*, 99, 16033–16042, 1995. Copyright 1995 American Chemical Society.)

Equation 5.35 is equally applicable to finite electrochemical and chemical kinetics at the substrate. The only difference is that an electrochemical rate constant is a function of electrode potential, while for a one-step chemical process $\left(\mathrm{R} \xrightarrow{k_b} \mathrm{O}\right)$, k_b is potential independent. For more complicated surface reactions, the theory has to be modified.

5.2.2.3 Quasireversible Processes

For quasireversible (Butler–Volmer) kinetics at the tip and a diffusion-controlled mediator regeneration at the substrate, one can obtain an approximate equation for the tip current at any potential assuming uniform accessibility of the tip surface (i.e., the current density is uniform over the tip surface) [17]:

$$I_T(E,L) = \frac{\left[0.68 + 0.78377/L + 0.3315\,\exp(-1.0672/L)\right]}{(\theta + 1/\kappa)} \tag{5.36}$$

where $\kappa = k^\circ \exp[-\alpha nf\,(E - E^{\circ\prime})/m_O$, θ is defined in Equation 5.25b, and the effective mass transfer coefficient for SECM is

$$m_O = \frac{4D_O[0.68 + 0.78377/L + 0.3315\,\exp(-1.0672/L)]}{(\pi a)} = \frac{i_T(L)}{\pi a^2 nFc} \tag{5.37}$$

One can see from Equation 5.37 that at $L \gg 1$, $m_O \sim D/a$ (as for a microdisk electrode alone), but at $L \ll 1$, $m_O \sim D/d$, that is, a TLC-type behavior. This suggests that the SECM should be useful for studying rapid heterogeneous electron transfer (ET) kinetics. By decreasing the tip/substrate distance, the mass transport rate can be increased sufficiently for quantitative characterization of the ET kinetics, preserving the advantages of steady-state methods, that is, the absence of problems associated with ohmic drop, adsorption, and charging current.

At constant L, Equation 5.36 describes a quasireversible steady-state tip voltammogram. Such a curve can be obtained by scanning the potential of the tip while the substrate potential is held constant. An equation not relying on the assumption of uniform accessibility of the tip surface was presented in Ref. [18]. Later [19], a more accurate modification of that Equation 5.38 was derived and verified by numerical simulations:

$$I_T(E,L) = \frac{0.78377}{L(\theta + 1/\kappa)} + \frac{0.68 + 0.3315\exp(-1.0672/L)}{\theta\left[1 + \dfrac{\pi}{\kappa\theta}\dfrac{2\kappa\theta + 3\pi}{4\kappa\theta + 3\pi^2}\right]} \tag{5.38}$$

The computational results in Ref. [2] (cyclic voltammograms) and Ref. [3] (steady-state current–distance curves) illustrate the essential features of the SECM response when substrate reaction is quasireversible. In this case, the assumption of uniformly accessible substrate surface is inaccurate, and no simple approximation similar to Equation 5.36 is available. The non-steady-state response depends on too many parameters to allow presentation of a complete set of working curves. Although an extensive table in Ref. [3] contains values of the normalized steady-state current for various values of the dimensionless rate constant and L, it may be hard to use for analysis of experimental results. Zoski et al. [20a] addressed this problem by developing an approximate

analytical treatment for the approach curves. Equation 5.39 allows one to calculate the approach curves for the whole range of the kinetic parameter $\Lambda = ak_s^{\circ}/D$. The discussion was focused on "SECM shielding experiments," in which the substrate potential is controlled so that the same ET reaction (e.g., O → R) occurs at both substrate and tip. By keeping the substrate potential in the "shielding" region, the kinetics of the substrate reaction can be effectively slowed and thus more easily measured. Further,

$$i_T = \frac{nFADC_O^*}{d\left(\frac{D}{k^{\circ}d\theta^{1-\alpha}} + \frac{1+\theta}{\theta}\right)} = \frac{i_{T,\infty}\pi a}{4d\frac{1+\theta}{\theta}\left(\frac{D\theta^{\alpha}}{k^{\circ}d(1+\theta)} + 1\right)} = \frac{i_{T,\infty}\pi}{4L\frac{1+\theta}{\theta}\left(\frac{\theta^{\alpha}}{\Lambda L(1+\theta)} + 1\right)} \tag{5.39}$$

theoretical treatment for shielding conditions was developed in Ref. [20b] to describe a series of steady-state tip voltammograms that can be obtained by slowly scanning E_T while the substrate is held at a fixed potential, and then repeating the experiment at a different E_S value. Simulations were carried out and approximate equations derived for both steady-state and quasi-steady-state tip voltammograms were obtained in such experiments.

5.2.2.4 Electron Transfer at Self-Assembled Monolayers

The SECM feedback current can be produced by ET across a molecular monolayer adsorbed on the substrate surface [21]. The theory was developed for three possible pathways: mediated ET (Figure 5.7A), direct electron tunneling through the monolayer (Figure 5.7B), and ET through pinholes (Figure 5.7C). Despite higher complexity of the mediator regeneration process, it was shown that the shape of an approach curve is described by Equation 5.35 that is generally applicable to finite substrate kinetics. By fitting an experimental I_T–L curve to Equation 5.35, one can obtain the Λ value and calculate the effective heterogeneous rate constant, $k_{eff} = \Lambda D/d$. The kinetic parameters of the substrate reaction can be obtained from the analysis of k_{eff}, as discussed later [21].

If a self-assembled monolayer (SAM) contains an electroactive group, M, the regeneration of the mediator can occur via a bimolecular reaction with these surface-bound redox centers (Figure 5.7A):

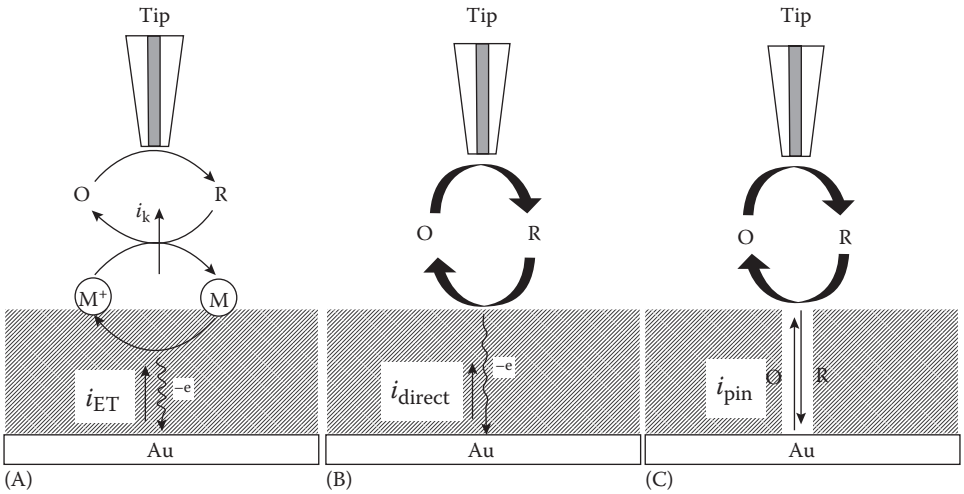


FIGURE 5.7 Schematic view of the processes involved in the SECM measurements of ET across an electroactive SAM. (A) Mediated ET, (B) direct electron tunneling through monolayer, and (C) ET through pinholes. (Adapted from Liu, B., Bard, A.J., Mirkin, M.V., and Creager, S.E., Electron transfer at self-assembled monolayers measured by scanning electrochemical microscopy, *J. Am. Chem. Soc.*, 126, 1485–1492, 2004. Copyright 2004 American Chemical Society.)

$$R + M^+ \underset{k_{Red}}{\overset{k_{Ox}}{\rightleftharpoons}} O + M \quad \text{(bimolecular ET at the film/solution interface)} \tag{5.40}$$

$$M - e^- \underset{k_f}{\overset{k_b}{\rightleftharpoons}} M^+ \text{ (electron tunneling through the monolayer)} \tag{5.41}$$

The overall SECM process includes the following consecutive steps: (i) mass transfer in the tip/substrate gap (the diffusion-limiting current for this step is given by Equation 5.30), (ii) bimolecular ET between the mediator species and the monolayer-bound redox centers (Equation 5.40), and (iii) the electron tunneling through the monolayer (Equation 5.41). The rates of steps (ii) and (iii) are given by Equations 5.42 and 5.43, respectively,

$$i_K = nFA\left(k_{Ox}\Gamma_{M^+}c_R^s - k_{Red}\Gamma_M c_O^s\right) \quad \text{(quasireversible reaction)} \tag{5.42a}$$

or

$$i_K = nFAk_{Ox}\Gamma_{M^+}c_R^s \quad \text{(irreversible reaction)} \tag{5.42b}$$

$$i_{ET} = nFA\left(k_b\Gamma_M - k_f\Gamma_{M^+}\right) \quad \text{(quasireversible reaction)} \tag{5.43}$$

where

A is the surface area

k_{Ox} and k_{Red} are the bimolecular oxidation–reduction rate constants ($mol^{-1}cm^3s^{-1}$)

k_b and k_f are the electron tunneling rate constants (s^{-1})

Γ_{M^+} and Γ_M are the surface concentrations (mol/cm^2) of oxidized and reduced forms of redox centers in the monolayer (the total coverage $\Gamma^* = \Gamma_M + \Gamma_{M^+}$)

c_R^s and c_O^s are the concentrations of reduced and oxidized forms of redox mediator at the substrate surface (mol/cm^3)

The treatment developed in Ref. [21] for the combination of irreversible reaction (5.40) with either quasireversible or irreversible reaction (5.41). It was shown that in general

$$k_{eff} = \frac{k_{Ox}k_b\Gamma^*}{k_{Ox}c^\circ + k_b + k_f} \tag{5.44}$$

There are two limiting cases for which the analysis of k_{eff} can be simplified: (a) $k_{Ox}c^\circ >> k_b + k_f$ (i.e., $E_{ads}^{\circ'} >> E_{med}^{\circ'}$, c° is not very small, and E_S is not much more positive than $E_{ads}^{\circ'}$). Under these conditions, Equation 5.44 is reduced to

$$k_{eff} \cong \frac{k_b\Gamma^*}{c^\circ} \tag{5.45}$$

and the k_b value can be extracted from the slope of the linear dependence of k_{eff} vs. $1/c^\circ$. (b) $k_{Ox}c^\circ << k_b + k_f$ (i.e., either $E_{ads}^{\circ'} \approx E_{med}^{\circ'}$ and c° is small, or $E_S >> E_{ads}^{\circ'}$). In this case, Equation 5.44 becomes

$$k_{eff} \cong \frac{k_{Ox}k_b\Gamma^*}{k_b + k_f} \tag{5.46}$$

so that k_{eff} is concentration independent. Moreover, if $E_S >> E^{\circ'}_{ads}$,

$$k_{eff} \cong \frac{k_{Ox} k_b \Gamma^*}{k_b} = k_{Ox} \Gamma^* \tag{5.47}$$

that is, k_{eff} is also potential independent, and the k_{Ox} value can be obtained from Equation 5.47.

When the monolayer is blocking (i.e., it contains no redox centers capable of reacting with the mediator species), the mediator regeneration can occur via direct tunneling through the film (Figure 5.7B). The characteristic current for this reaction is

$$i_{direct} = nFAk_{direct} c^\circ \tag{5.48}$$

where k_{direct} is the rate constant of direct electron tunneling.

In the presence of pinhole defects in a blocking monolayer, they provide an additional pathway for ET (Figure 5.7C) with a characteristic current

$$i_{pin} = nFA'' k_{pin} c^\circ \tag{5.49}$$

where

k_{pin} is the rate constant of the ET through pinholes

$A'' = A \times \theta_{pin}$ and θ_{pin} is the fractional area of the pinholes in the SAM

If a SAM is composed of a mixture of electroactive and non-electroactive components, all three pathways discussed earlier can contribute to the ET through the film. The total current across the monolayer in this case is

$$i_{e,total} = i_e + i_{direct} + i_{pin} \tag{5.50}$$

and

$$k_{eff} = \frac{k_{Ox} k_b \Gamma^*}{k_{Ox} c^\circ + k_b + k_f} + k' \tag{5.51}$$

where $k' = (1 - \theta_M) k_{direct} + \theta_{pin} k_{pin}$. k' represents the contribution from direct tunneling and ET through defects. Again, there are two limiting cases:

(a) $k_{Ox} c^\circ >> k_b + k_f$, which yields

$$k_{eff} \cong \frac{k_b \Gamma^*}{c^\circ} + k' \tag{5.52}$$

Despite the direct tunneling effect, the plot of k_{eff} vs. $1/c^\circ$ is linear, and the k_b value can be extracted from its slope. The nonzero intercept of the k_{eff} vs. $1/c^\circ$ dependence gives the k' value.

(b) $k_{Ox} c^\circ << k_b + k_f$, when k_{eff} becomes concentration independent

$$k_{eff} \cong \frac{k_{Ox} k_b \Gamma^*}{k_b + k_f} + k' \tag{5.53}$$

Moreover, if $E_S >> E_{ads}^{\circ'}$,

$$k_{eff} \cong \frac{k_{Ox}k_b\Gamma^*}{k_b} + k' = k_{Ox}\Gamma^* + k' \tag{5.54}$$

Thus, the k_{Ox} value can be obtained from the slope of the k_{eff} vs. Γ^* plot.

5.2.3 Microscopic or Partially Blocked Substrates

The discussion in the previous sections was based on assumption of a macroscopic (i.e., infinitely large compared to the tip) uniformly reactive substrate. This assumption works well for most kinetic SECM experiments, but it is not appropriate when the substrate is small (e.g., another microdisk electrode [3]), or when a macroscopic substrate surface consists of small patches of different reactivities. The magnitude of either positive or negative feedback produced by a microscopic substrate is lower than the effect that would be produced under the same conditions by the large substrate. The current–distance curves in Figure 5.8 were computed for various values of h using both numerical solution of integral equations and the ADI simulations [3]. Apparently, the size of the substrate is most important when $h \leq 1$.

At $h \geq h^{\infty} = 1 + 1.5L$, the substrate behaves essentially as an infinite one. The value of h^{∞} defines the surface area that is actually seen in an SECM feedback experiment and, thus, has important implications in terms of the resolution of SECM images (see Ref. [22] for detailed discussion). The difference between the steady-state feedback current for a finite conductive substrate and that for an insulating one becomes small at $h < 0.05$–0.1. Thus, it should be possible to identify particles (or other objects) 10–20 times smaller than the tip by SECM (if these particles are sufficiently well separated).

Particular caution is necessary for interpretation of images containing small conductive spots ($0 < h < h^{\infty}$); from Figure 5.8, one can see that such features may appear as conductors at smaller L and as insulators at larger L. These are typical for surfaces modified with SAMs. The theory

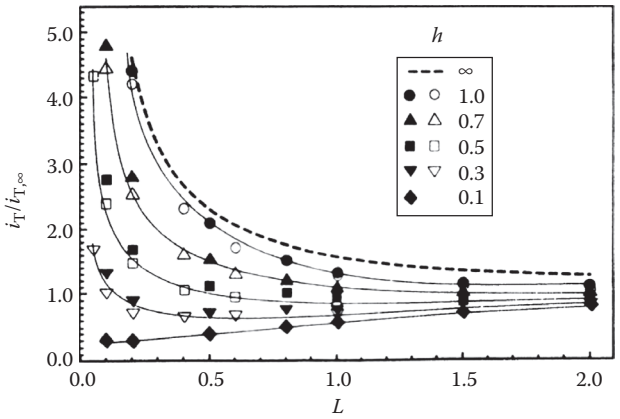


FIGURE 5.8 I_T vs. L curves for finite disk-shaped substrates. Both tip and substrate reactions are diffusion controlled. Filled symbols are calculated using multidimensional integral equations, open symbols are from ADI simulation. The h values are as indicated. Dashed line is simulation for $h = \infty$ from Ref. [1]. The lines through the symbols are drawn as a guide. (Reprinted with permission from Bard, A.J., Mirkin, M.V., Unwin, P.R., and Wipf, D.O., Scanning electrochemical microscopy. 12. Theory and experiment of the feedback mode with finite heterogeneous electron-transfer kinetics and arbitrary substrate size, *J. Phys. Chem.*, 96, 1861–1868, 1992. Copyright 1992 American Chemical Society.)

was developed for a substrate covered with a blocking film that contains microscopic conductive disk-shaped defects [23]. The use was made of the effective medium approach developed by Zwanzig and Szabo [24b]. It was shown that the steady-state diffusion limiting current to a uniformly accessible (e.g., spherical) inert surface partially covered by randomly distributed active disks is equivalent to kinetically controlled current at the same surface with an effective rate constant:

$$k_{\text{eff}} = \frac{4(1-\theta)D}{\pi R_{\text{d}}} \tag{5.55}$$

where

θ is the fraction of surface that is insulating, that is, free from active disk-shaped defects
R_{d} is the defect radius

Thus, the SECM current–distance curve at a partially covered substrate should have the same shape as the kinetically controlled i_{T}–d curve at an uncovered substrate described by Equation 5.35 with the rate constant given by Equation 5.55.

To investigate electrochemical or catalytic properties of nanoparticles and metal clusters, one may need to probe the reactivity of an unbiased microscopic conductive spot on the insulating surface. This situation was treated numerically by Xiong et al. [25]. Similarly to the case of a biased finite substrate [3], a slower rate of heterogeneous ET at an unbiased substrate results in lower feedback current. The most important difference between these two cases is that the potential of an unbiased substrate (E_{s}) is not controlled by the applied voltage. On the contrary, E_{s} depends on the separation distance, tip potential, and other experimental factors. The total substrate current, which is the sum of the mediator regeneration current flowing at the substrate portion facing the tip and the current produced by the opposite redox reaction occurring at the substrate periphery, must equal zero at any given moment. Thus, E_{s} continuously adjusts in the course of the feedback experiment to keep $i_{\text{s}} = 0$. This makes the feedback response at an unbiased substrate extremely sensitive to the geometry of the tip/substrate arrangement.

The Amemiya group developed theory for a different type of microscopic substrates—a one-dimensional nanostructure [26]. The model for this arrangement included a disk-shaped tip above an infinitely long planar band electrode [26a]. The corresponding three-dimensional (3D) diffusion problem was solved using the commercial program FEMLAB (the latter versions of this simulation package were named COMSOL Multiphysics). An interesting finding was that the feedback current from the band can be detected even if the band width (w) is much smaller than the tip diameter, for example, $w/2a = 0.003$ in Figure 5.9. This means that a very thin conductive "wire" (e.g., a carbon nanotube) can be detected and probed with a much larger (micrometer-sized) SECM tip. In contrast, a disk-shaped, biased conductive spot on the insulating substrate surface can only be detected if its radius is $\geq 0.1a$ [3]. High sensitivity of the SECM response to finite dimensions of the unbiased band substrate, that is, its length, width, and height from the insulating surface, has been demonstrated [26b]. More recently [26c], the developed theory was expanded to an unbiased finite band substrate containing a nanometer-sized gap. A surprising theoretical prediction that a peak current response should be obtained when the tip is scanned laterally above an insulating nanogap was confirmed experimentally. The thickness of the smallest gap detectable by SECM was shown to be $\sim 0.005a$.

5.2.4 Nondisk Tips and Tip Shape Characterization

Several advantages of the inlaid disk-shaped tips (e.g., well-defined thin-layer geometry and high feedback at short tip/substrate distances) make them most useful for SECM measurements. However, the preparation of submicrometer-sized disk-shaped tips is difficult, and also some applications may

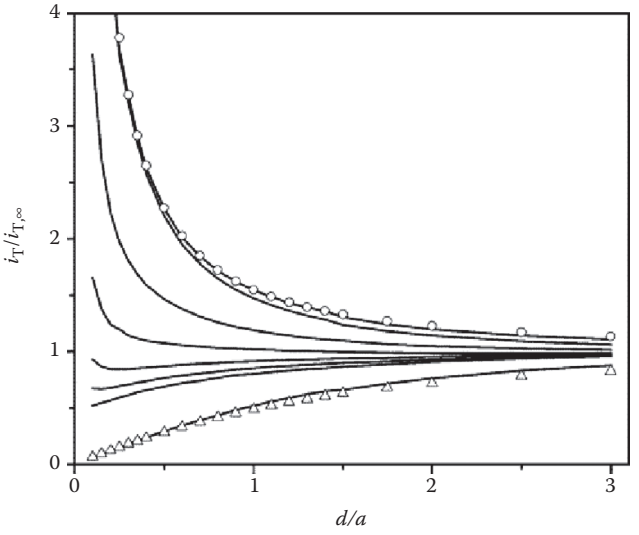


FIGURE 5.9 Simulated approach curves with a disk UME probe above band substrate electrodes with different widths. The solid lines are for $w/2a = 10$ (a conductive substrate), 1, 0.3, 0.1, 0.03, 0.01, 0.003, and 0 (an insulating substrate) from the top. The circles and triangles represent theoretical approach curves with conductive and insulating substrates, respectively. (Reprinted with permission from Xiong, H., Gross, D.A., Guo, J., and Amemiya, S., Local feedback mode of scanning electrochemical microscopy for electrochemical characterization of one-dimensional nanostructure: Theory and experiment with nanoband electrode as model substrate, *Anal. Chem.*, 78, 1946–1957, 2006. Copyright 2006 American Chemical Society.)

require nondisk microprobes (e.g., conical tips are useful for penetrating thin polymer films [27]). Two aspects of the related theory are the calculation of the current–distance curves for a specific tip geometry and the evaluation of the UME shape. Approximate expressions were obtained for the steady-state current in a TLC formed by two electrodes, for example, one a plane, and the second a cone or hemisphere [28]. It was shown that the normalized steady-state, diffusion-limited current, as a function of the normalized separation for thin-layer electrochemical cells, is fairly sensitive to the geometry of the electrodes. However, the thin-layer theory does not describe accurately the steady-state current between a small disk tip and a planar substrate because the tip steady-state current $i_{T,\infty}$ was not included in the approximate model [28].

A more realistic approximate theory for the SECM with a tip shaped as a cone or spherical segment was presented in Ref. [11]. The surface of the nonplanar tip electrode was considered to be a series of thin circular strips, each of which is parallel to the planar substrate. The diffusional flux to each strip was calculated using approximate equations for a disk-shaped tip over a conductive or an insulating substrate. The normalized current to the nonplanar tip was obtained by integrating the current over the entire tip surface. The families of working curves calculated for conical and sphere-cap tips over conductive and insulating substrates illustrated the effect of the tip geometry: the larger the ratio of a cone (or a spherical cap) height to its radius ($H = h/a$), the lower both positive and negative feedback responses obtained with such a tip. The working curves calculated for different h/a values possess substantially different curvatures, and thus a unique curve could be found to obtain the best fit with the experimental data and characterize the tip geometry.

More exact theory for sphere-cap tips was developed by using digital simulations [29,30]. Selzer and Mandler solved numerically a time-dependent 2D axisymmetric diffusion problem for a sphere-cap electrode [29a]. They used the same approach to develop comprehensive time-dependent and steady-state SECM theory for a hemispherical tip approaching either a conductive or an insulating substrate [29b]. Daniele and coworkers [30] focused on diffusion-controlled steady-state responses and calculated approach curves for a broad range of H and various RG values. For RG = 10, the

numerical results obtained for conductive and insulating substrates were fitted to two analytical approximations. Current–distance curves for negative feedback were fitted to Equation 5.32 (the same equation with a different set of parameters is also applicable to a disk-shaped tip approaching an insulating substrate). One should notice that the separation distance, d (and the normalized distance, $L = d/a$) in this case was defined as the distance between the substrate and the base plane of the sphere-cap tip. For pure positive feedback, the corresponding equation is

$$I_T(L) = \frac{k_1 + k_2}{L - H/3} + \frac{k_3}{L - 2H/3} + \frac{k_4}{L - H} \tag{5.56}$$

With the parameter values listed in Table 5.4, both approximations are accurate within 1% for the range $H + 0.1 \le L \le 20$.

The numerical solutions of the diffusion problem for a conical electrode approaching either a conductive or an insulating substrate [31,32] yielded current–distance curves significantly more accurate than those reported earlier in Ref. [11]. Several families of I_T vs. L curves were computed for different H and RG values. Figure 5.10 shows two families of such curves calculated for tips with RG = 2 approaching either a perfect conductor (A) or a perfect insulator (B). It can be seen that the magnitude of either positive or negative feedback decreases with increasing ratio of the cone height to its base radius (H). For $H = 1$, the maximum I_T^c is only ~2, and the minimum $I_T^{ins} \cong 0.65$. These working curves can be used to determine the geometry of the electrode for H up to ~3, but because of the dramatically lower feedback at $H > 1$, conical tips are not very useful for feedback mode experiments. The same is true for spherical microprobes [29,30] that also exhibit significantly lower feedback responses than disk-shaped tips.

When a submicrometer-sized UME is used as an SECM tip, it is essential to distinguish between planar and recessed geometries. In the latter case, the metal core of an UME is recessed into the

TABLE 5.4
Coefficients for Equations 5.32 and 5.56 Describing Approach Curves for Sphere-Cap Tips with Different *H*

H	k_1	k_2	k_3	k_4
		Negative feedback (Equation 5.32)		
0.1	0.5242	1.5277	0.4754	−2.9363
0.2	0.5053	1.5919	0.4949	−2.9518
0.48	0.4367	1.8196	0.5641	−2.9927
0.5	0.4249	1.8440	0.5753	−2.9625
0.78	0.3081	2.1772	0.6931	−2.9374
1	0.1725	2.5203	0.8293	−2.8574
1.03	0.1536	2.5690	0.8482	−2.8472
1.41	−0.2430	3.3956	1.2451	−2.5772
1.88	−0.9720	4.7528	1.9753	−2.2981
2	−1.277	5.2349	2.2808	−2.2026
		Positive feedback (Equation 5.56)		
0.1	0.9758	−3.4734	5.6423	−1.6517
0.2	0.9774	−1.0965	1.9023	−0.2882
0.5	0.9808	−0.2723	0.7916	0.01694
1	0.981	−0.14	0.7133	0.0499
2	0.9828	−0.4871	1.2261	0.0589

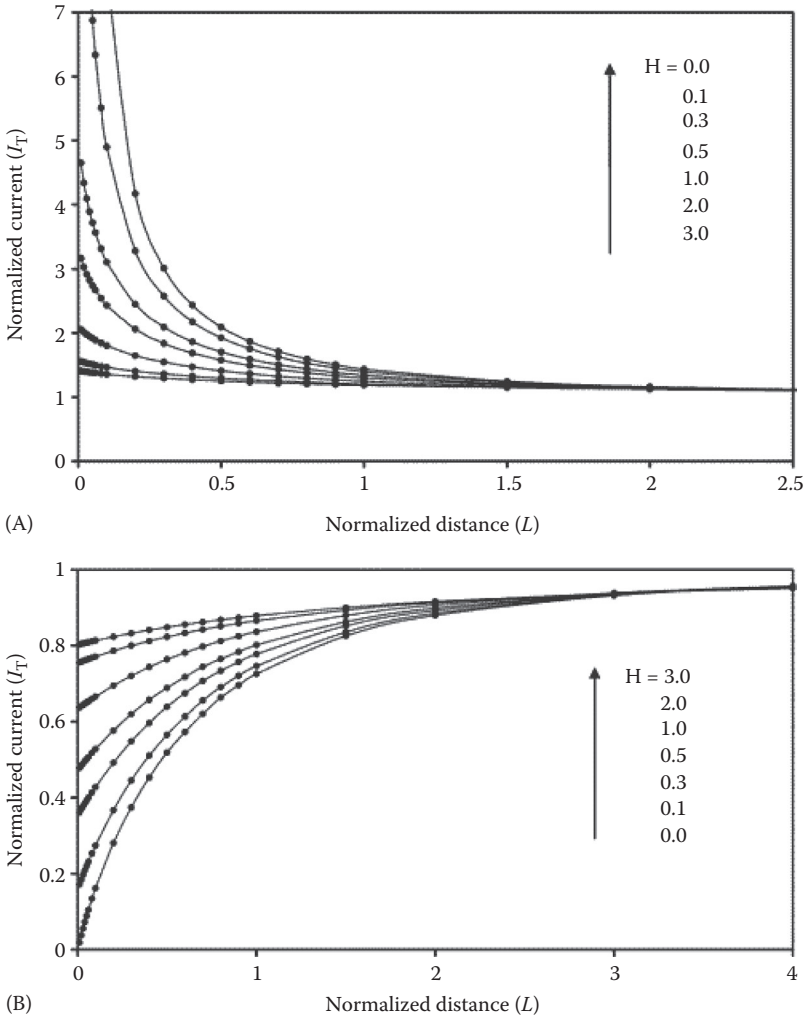


FIGURE 5.10 Steady-state current–distance curves for a conical tip over conductive (A) and insulating (B) substrates corresponding to the values of the parameter $H = h/a$ shown in the figure. L is the distance between the substrate and the point of tip closest to it normalized by the base radius. The upper curve in (A) and the lower curve in (B) were computed for a disk-shaped tip. (Adapted from Zoski, C.G., Liu, B., and Bard, A.J., Scanning electrochemical microscopy: Theory and characterization of electrodes of finite conical geometry, *Anal. Chem*., 76, 3646–3654, 2004. Copyright 2004 American Chemical Society.)

solution-filled microcavity inside the glass insulator. Such electrodes are usually unsuitable for kinetic measurements [33]. On the other hand, a nanometer-thick solution layer trapped between such a nanometer-sized recessed tip and the substrate can be used for single-molecule detection [34] or TLC-type experiments [35a]. Fan et al. [34b] simulated the feedback experiment with a recessed tip for a special case. A more extensive set of simulated approach curves for "slightly recessed" tips (i.e., $H = l/a \leq 2$, where l is the recess depth) approaching either a conductive or an insulating substrates was reported in Ref. [35b]. The simulations were carried out for RG = 10 using COMSOL Multiphysics 3.3a commercial software and assuming cylindrical geometry of the solution-filled cavity inside the insulating sheath of a recessed electrode. As expected, the approach curves for recessed tips show positive and negative feedback responses lower than those obtained with a conductive disk tip flush with the surrounding insulator. Moreover, the deeper the recess, the less pronounced the SECM feedback.

TABLE 5.5
Parameter Values for Equation 5.58

a	b	c	d	e	f	g	h	i	j	k
1.79862	0.40135	0.16349	0.01994	1.79815	0.38238	0.67767	0.17304	0.015745	2.01384	0.33559

Several approximations were obtained by fitting the numerical results. Equation 5.57 yields the $I_{T,\infty}$ values for $0.01 \leq H \leq 5$ that fit the simulated data within 0.4% [35b]

$$I_{T,\infty} = \frac{i_{T,\infty}}{4nFDc^* a} = 1/(1.0354 + 1.2621H + 0.01155\ln(H)) \tag{5.57}$$

The inverse of this equation (Eq. 9B in Ref. [35b]) allows one to evaluate the recess depth from the measured $i_{T,\infty}$ value. In the case of pure positive feedback, the family of SECM working curves calculated for $0.01 \leq L \leq 3$ and $0.01 \leq H \leq 2$ fits within <2% (Equation 5.58) [35b]

$$I_T = \frac{a + b\ln H + c(\ln H)^2 + d(\ln H)^3 + eL + fL^2}{1 + g\ln H + h(\ln H)^2 + i(\ln H)^3 + jL + kL^2} \tag{5.58}$$

with the parameter values listed in Table 5.5.

Since the shape of a nonplanar tip is typically imperfect, quantitative kinetic experiments with such probes may be problematic. Thus, no theory has been developed for finite kinetics at either tip or substrate electrode.

An example of a better-defined nondisk geometry is a ring-shaped tip. A ring electrode typically surrounds some other functional component of probe; for example, it can be formed by metallization of an optical fiber to enable simultaneous optical measurements [36]. The theory for a ring-shaped tip was developed by Lee et al. [37] who used PDEase2D commercial program to carry out finite element simulations. For pure positive feedback, the shape of the calculated i_T vs. L curves was shown to be largely determined by the ratio of the inner/outer ring radii, while RG was a major factor determining the negative feedback response. The magnitude of the positive feedback with a ring microelectrode is less than that with a disk-shaped tip; moreover, as the ring becomes thinner, the extent of positive feedback decreases. It was shown that the geometry of ring electrodes can be determined from SECM approach curves [37].

Another axisymmetric SECM probe—a micro ring-disk tip—was used by Liljeroth et al. [38] for G/C experiments. The theory developed for the disk generation/ring collection mode includes the dependences of the ring and disk currents and their ratio (i.e., collection efficiency) vs. L for both conductive and insulating substrates. The complete quantitative description of this system is somewhat complicated because of a large number of geometric parameters (the disk and ring radii, the ring thickness, and RG).

Nann and Heinze [39] developed and used an adaptive finite element (AFE) algorithm to carry out simulations of steady-state, chronoamperometric, and voltammetric SECM responses for various nondisk tip geometries, for example, hemispherical, conical, and "capillary" electrodes.

5.3 GENERATION/COLLECTION MODE OF SECM OPERATION

In different publications, the term "G/C mode" has been applied to several substantially different SECM experiments. The two main types are tip generation/substrate collection (TG/SC) and substrate generation/tip collection (SG/TC) modes. The modifications of the latter type of G/C

experiments include potentiometric G/C mode, where the tip is a potentiometric sensor, and two amperometric modes. In the first of them, the tip/substrate separation is so large that no feedback effect is observed, and the amperometric tip only detects the species produced at the substrate. At much shorter distances, the species reoxidized (or rereduced) at the tip can return to the substrate producing a feedback effect.

5.3.1 Potentiometric G/C Mode

Unlike the feedback mode of the SECM operation, where the overall redox process is essentially confined to the thin layer between the tip and the substrate, in SG/TC experiments the tip travels within a thick diffusion layer produced by a larger substrate. The theoretical treatment is easier when the tip is a potentiometric sensor. Such a passive sensor does not change the concentration profile of electroactive species generated (or consumed) chemically or electrochemically at the substrate. Still a consistent theoretical treatment was proposed only for a steady-state situation when a small substrate (a microdisk or a spherical cap) generates stable species. The concentration of such species can be measured by an ion-selective microtip as a function of the tip position. The concentration at any point can be related to that at the source surface. For a microdisk substrate, the dimensionless expression is [40,41]

$$\frac{c(R,Z)}{c(0,L)} = \frac{2}{\pi}\tan^{-1}\left[\frac{2}{R^2+Z^2-1+\sqrt{(R^2+Z^2-1)^2+4Z^2}}\right]^{1/2} \tag{5.59}$$

(a somewhat similar expression was derived for a disk-shaped sink [42]). Sometimes, it is more useful to relate the concentration distribution in the diffusion layer to the flux at the source surface. This relation was obtained in Ref. [43]

$$C(R,Z) = \frac{2}{\pi}\int_0^1 \sqrt{u/RJ_S(u)pk(p)du} \tag{5.60}$$

for a disk-shaped substrate, where $k(p)$ is the complete elliptic integral of the first kind [44], and $p = 2\sqrt{Ru}\Big/\sqrt{Z^2+(R+u)^2}$. Note that R and Z in Equations 5.59 and 5.60 are normalized by the substrate radius a_S, rather than the tip radius, a. The flux at the substrate, $J_S(R)$, can be defined using either a constant current or a constant concentration approximation [45]. Both assumptions lead to fairly complicated integral expressions. The dimensionless concentration profiles were obtained numerically from those expressions and tabulated [43].

The potentiometric SECM experiment yields the potential of the tip electrode, E, as a function of the tip position. To establish the correspondence between these data and the aforementioned theory, one needs to use a calibration curve, that is, a Nernstian E vs. c plot. Using such a calibration, one can transform the experimental results to the c vs. (z, r) dependence and fit them to the theory in order to find J_S and establish the distance scale. The earlier discussion implies that the products generated on the substrate do not participate in any chemical reaction in solution. Otherwise, a more complicated treatment may be necessary (e.g., when the tip is a pH sensor used to monitor proton concentration in a buffered aqueous solution [43]).

One can also evaluate the relative change in rate of heterogeneous reaction at the substrate by measuring concentration of the reaction product at the tip. In this setup, the tip is positioned at fixed distance from the substrate, and the time dependence of concentration is measured. This simpler approach is based on the proportionality between the heterogeneous reaction rate and the product concentration. It is most useful when the substrate flux cannot be measured directly (e.g., the substrate reaction is not an electrochemical process) [46,47].

5.3.2 Amperometric G/C Modes

5.3.2.1 Substrate Generation/Tip Collection Mode

In a SG/TC experiment, there are two different distance scales: one scale is determined by the tip size and another one by the substrate size. If $a_S/a \gg 1$, the diffusion layer generated by the substrate is much thicker than that at the tip electrode. The theory assuming no feedback (i.e., the substrate current unaffected by the tip process) is applicable either at $d/a \gg 1$ or when the product of the tip process does not react at the substrate. The rigorous theoretical description is difficult because (i) the moving tip stirs the substrate diffusion layer; disturbances are especially significant when the tip is an amperometric sensor and has its own diffusion layer; (ii) when the substrate is large, no true steady state can be achieved; and (iii) the tip blocks the diffusion to the substrate surface, and this screening effect is hard to take into account.

The SG/TC mode with an amperometric tip was historically the first SECM-type measurement performed [48]. The aim of such experiments was to probe the diffusion layer generated by the large substrate electrode with a much smaller amperometric sensor. A simple approximate theory [48a,b] using the well-known $c(z, t)$ function for a potentiostatic transient at a planar electrode [49] was developed to predict the evolution of the concentration profile following the substrate potential perturbation. A more complicated theory was based on the concept of the "impulse response function" [48c]. While these theories have been successful in calculating concentration profiles, the prediction of the time-dependent tip current response is not straightforward because it is a complex function of the concentration distribution. Moreover, these theories do not account for distortions caused by interference of the tip and substrate diffusion layers and feedback effects.

When the separation distance is sufficiently large to eliminate feedback to the substrate, the diffusion of species between two electrodes can be probed by transient SG/TC measurements. The tip current transient following the application of a short potential pulse to the substrate electrode is peak shaped. The time corresponding to the maximum tip current, t_{max}, is independent of the tip size and can be expressed as [50]

$$t_{max} = \frac{0.11d^2}{D} \tag{5.61}$$

If the tip/substrate distance, d, is known, one can use Equation 5.61 to evaluate the diffusion coefficient. Alternatively, using a mediator with an established D value, one can evaluate d [51].

Few amperometric SG/TC experiments with the separation distance of the same order of magnitude as the tip radius have been reported. The applications of this mode have been limited by the shortcomings listed in the beginning of this section, and also by low collection efficiency (i_T/i_S), significant IR-drop caused by a large substrate current, and the lack of adequate theoretical treatments. Martin and Unwin developed the first quantitative treatment for amperometric SG/TC experiments [52]. Although a chronoamperometric current at a macroscopic substrate does not exhibit any steady state, the collection current at the tip electrode at long times reaches a stable, time-independent value. The time-dependent theory for a diffusion-controlled process was illustrated by a number of 3D concentration profiles and working curves covering a range of experimental conditions.

The steady-state SG/TC measurements were shown to be complimentary to the feedback mode experiment in the same solution [52]. In a feedback experiment (assuming that only oxidized form, O, is initially present in solution), the tip and the substrate reactions are given by Equations 5.1 and 5.2, respectively. In a SG/TC experiment, the tip and the substrate reactions are transposed:

$$O + ne^- = R \quad \text{(substrate)} \tag{5.62}$$

$$R - ne^- = O \quad \text{(tip electrode)} \tag{5.63}$$

At long times, the O form becomes depleted within the thick diffusion layer of the substrate electrode. The tip probes only a micrometer-thick layer adjacent to the substrate surface, in which $c_O \cong 0$ and $c_R = \gamma c_O^o$ according to Equation 5.23. When the tip is a few radii away from the substrate, the feedback effects are negligible and the tip current is

$$i_{\text{collection},\infty} = 4nFDc_O^o a\gamma = \gamma i_{T,\infty} \tag{5.64}$$

The shape of the SG/TC current–distance curves is very similar to that of the feedback mode $i-d$ curves, and the ratio of the collection current to the corresponding feedback current is the same at any separation distance:

$$\frac{i_{\text{collection}}}{i_{\text{feedback}}} = \gamma \tag{5.65}$$

Thus the diffusion coefficient ratio of the oxidized and reduced forms (γ) can be found by measuring the ratio of the feedback and collection currents at the same d [52]. No prior knowledge of a or d is required for this determination. One should also notice that the transient current flowing at the macroscopic substrate electrode vanishes at long times. The steady-state current is confined to the microscopic area of the substrate surface facing the tip. This largely eliminates the IR-drop problem.

Sanchez-Sanchez et al. [53] performed COMSOL-based simulations to show that collection efficiency in SG/TC mode with a small (e.g., 100 μm diameter) substrate depends on the tip radius, the separation distance (d), and RG. They quantitatively calibrated the SG/TC mode of SECM and determined the maximum collection efficiency for different values of the aforementioned geometric parameters. The developed steady-state model assumes the diffusion-controlled ET with no heterogeneous or homogeneous kinetic complications and allows quantitative determination of the number of transferred electrons.

5.3.2.2 Tip Generation/Substrate Collection Mode

The earliest version of the TG/SC mode [54] was somewhat similar to the feedback mode of the SECM. In both cases, an electroactive species is generated at the tip and collected at the substrate. The TG/SC experiment includes simultaneous measurements of both tip and substrate currents. Immediately after the application of a potential step to the tip electrode, the substrate current is close to zero. The i_S grows with time while the tip current decreases. For an uncomplicated process, the difference between i_T and i_S vanishes gradually. At steady state, these quantities are almost identical, if L is not very large [54,55] (the collection efficiency, i_S/i_T, is more than 0.99 at $L \leq 2$, and $i_S/i_T \cong 0.8$ at $L = 5$ [54]). Under these conditions, the tip-generated species predominantly diffuse to the large substrate rather than escaping from the tip/substrate gap. For a process with a coupled chemical reaction, the collection efficiency may be much less than one, and important kinetic information can be extracted from the i_S/i_T vs. L dependencies (see Section 5.4.1).

Another approach to TG/SC experiments does not rely on the mediator feedback [56]. The reactant galvanostatically electrogenerated at the tip diffuses to the substrate and undergoes the reaction of interest at its surface. The substrate current is recorded as a function of either time or the tip/substrate separation distance (approach curves). The theory for transient responses, steady-state TG/SC approach curves, and polarization curves (i.e., I_S vs. E_S) was generated solving the diffusion problem numerically (an explicit finite difference method was used). The substrate process was treated as a first-order irreversible reaction, and the effects of its rate constant and the experimental parameters were illustrated by families of the dimensionless working curves (Figure 5.11).

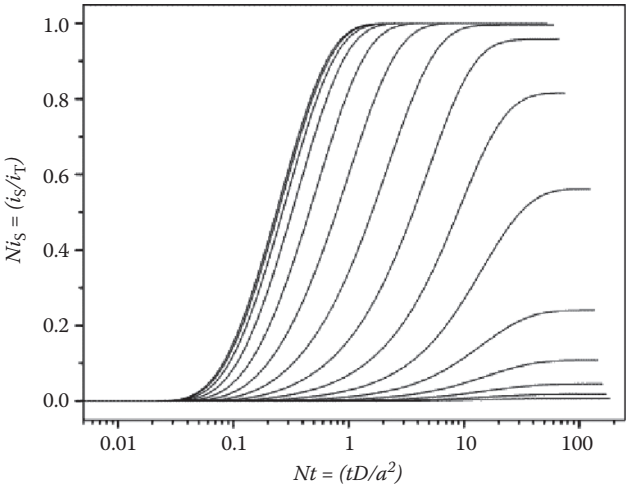


FIGURE 5.11 Dependence of the normalized substrate current on the normalized time in simulated TG/SC experiments with different rate constants at the substrate. $L = 0.8$, RG = 10. From top to bottom, normalized rate constant, $ka/D = 100$, 40, 16, 6.4, 2.56, 1.024, 0.4096, 0.1638, 6.554×10^{-2}, 2.621×10^{-2}, 1.05×10^{-2}, 4.19×10^{-3}, 1.68×10^{-3}, 6.71×10^{-4}, and 2.68×10^{-4}. (Reprinted with permission from Fernández, J.L. and Bard, A.J., Scanning electrochemical microscopy. 50. Kinetic study of electrode reactions by the tip generation–substrate collection mode, *Anal. Chem*., 76, 2281–2289, 2004. Copyright 2004 American Chemical Society.)

5.4 SECM OF MORE COMPLICATED CHEMICAL SYSTEMS

5.4.1 Processes Involving Homogeneous Reactions

A homogeneous chemical reaction occurring in the gap between the tip and substrate electrodes causes a change in i_T; therefore, its rate can be determined from SECM measurements. If both heterogeneous processes at the tip and substrate electrodes are rapid (at extreme potentials of both working electrodes) and the chemical reaction (rate constant, k_c) is irreversible, the SECM response is a function of a single kinetic parameter $K = \text{const} \times k_c/D$, and its value can be extracted from I_T vs. L dependencies.

SECM theory has been developed for four mechanisms with homogeneous chemical reactions coupled with ET, that is, a first-order irreversible reaction (E_rC_i mechanism) [5], a second-order irreversible dimerization (E_rC_{2i} mechanism) [54], and ECE and DISP1 reactions [57]. (The solution obtained for a E_qC_r mechanism in terms of multidimensional integral equations [2] has not been utilized in any calculations.) While for E_rC_i and E_rC_{2i} mechanisms analytical approximations are available [58], only numerical solutions have been reported for more complicated ECE and DISP1 reactions [57].

Three approaches to kinetic analysis were proposed: (i) steady-state measurements in a feedback mode, (ii) G/C experiments, and (iii) analysis of the chronoamperometric SECM response. Unlike the feedback mode, the G/C measurements included simultaneous analysis of both I_T–L and I_S–L curves or the use of the collection efficiency parameter (I_S/I_T when the tip is a generator and the substrate is a collector). The chronoamperometric measurements were found less reliable [5], so only steady-state theory will be discussed here.

5.4.1.1 First-Order Following Reaction

For the E_rC_i mechanism,

$$O + e^- \rightarrow R \quad \text{(tip)} \tag{5.66a}$$

$$R \xrightarrow{k_c} \text{products} \quad \text{(gap)} \tag{5.66b}$$

$$R - e^- \rightarrow O \quad \text{(substrate)} \tag{5.66c}$$

The SECM diffusion problem is represented by the system of differential equations

$$\frac{\partial c_O}{\partial t} = D_O \left[\frac{\partial^2 c_O}{\partial z^2} + \frac{\partial^2 c_O}{\partial r^2} + \frac{1}{r} \frac{\partial c_O}{\partial r} \right] \tag{5.67a}$$

$$\frac{\partial c_R}{\partial t} = D_R \left[\frac{\partial^2 c_R}{\partial z^2} + \frac{\partial^2 c_R}{\partial r^2} + \frac{1}{r} \frac{\partial c_R}{\partial r} \right] - k_c c_R \tag{5.67b}$$

with initial and boundary conditions

$$t = 0, \quad 0 \le r, \quad 0 < z < d; \quad c_O = c_O^o; \quad c_R = 0 \tag{5.68}$$

$$0 \le r \le a, \quad z = 0; \quad c_O = 0; \quad D_O \left[\frac{\partial c_O}{\partial z} \right] = -D_R \left[\frac{\partial c_R}{\partial z} \right] \tag{5.69}$$

$$a \le r \le r_g, \quad z = 0; \quad D_O \left[\frac{\partial c_O}{\partial z} \right] = D_R \left[\frac{\partial c_R}{\partial z} \right] = 0 \tag{5.70}$$

$$0 \le r \le r_g, \quad z = d; \quad c_R = 0; \quad D_O \left[\frac{\partial c_O}{\partial z} \right] = -D_R \left[\frac{\partial c_R}{\partial z} \right] \tag{5.71}$$

$$r_g < r, \quad 0 < z < d; \quad c_O = c_O^o; \quad c_R = 0 \tag{5.72}$$

$$r = 0, \quad 0 < z < d; \quad D_O \left[\frac{\partial c_O}{\partial z} \right] = D_R \left[\frac{\partial c_R}{\partial z} \right] = 0 \tag{5.73}$$

It was solved numerically using the ADI finite difference method [5]. The steady-state results were obtained as a long-time limit and presented in the form of two-parameter families of working curves [5]. These represent steady-state tip current or collection efficiency as functions of $K = ak_c/D$ and L.

It was shown later [58] that the theory for E_rC_i process under SECM conditions can be reduced to a single working curve. To understand this approach, it is useful to first consider a positive feedback situation with a simple redox mediator (i.e., without homogeneous chemistry involved) and with both tip and substrate processes under diffusion control. The normalized steady-state tip current can be presented as the sum of two terms:

$$I_T = I_f + I_T^{ins} \tag{5.74}$$

where

I_f is the feedback current coming from the substrate

I_T^{ins} is the current due to the hindered diffusion of the electroactive species to the tip from the bulk of solution given by Equation 5.31

All variables are normalized by $i_{T,\infty}$

The substrate current is

$$I_S = I_f + I_d \tag{5.75}$$

where

I_f is the same quantity as in Equation 5.74, representing the oxidized species that eventually arrive at the tip as a feedback current

I_d is the dissipation current, that is, the flux of species not reaching the tip

It was shown in Ref. [54] that I_S/I_T is >0.99 at $0 < L \leq 2$, that is, for any L within this interval the tip and the substrate currents are essentially equal to each other. Thus from Equations 5.74 and 5.75,

$$I_d = I_T^{ins} \tag{5.76}$$

or

$$I_d/I_S = \frac{I_T^{ins}}{I_T} = f(L) \tag{5.77}$$

where $f(L)$ can be computed for any L as the ratio of the right-hand side of Equation 5.31 to that of Equation 5.30 assuming RG = 10.

Analogously, for an electrochemical process followed by an irreversible homogeneous reaction of any order one can write

$$I_T' = I_f' + I_T^{ins} \tag{5.78}$$

$$I_S' = I_f' + I_d' \tag{5.79}$$

where the variables labeled with the prime are analogous to unlabeled variables in Equations 5.74 and 5.75, and I_T^{ins} is unaffected by the occurrence of the homogeneous reaction in Equation 5.66b. Since the species O are stable, the fraction of these species arriving at the tip from the substrate should also be unaffected by the reaction in Equation 5.66b, that is, the relation $I_d'/I_S' = f(L)$ holds true. Consequently,

$$\begin{aligned} I_T' &= I_T^{ins} + I_S' - I_d' \\ &= I_T^{ins} + I_S'(1 - f(L)) \end{aligned} \tag{5.80}$$

that is, for an SECM process with a following homogeneous chemical reaction of any order, the dependence I_T' vs. I_S' at any given L should be linear with a slope equal to $1 - f(L)$ and an intercept equal to $I_T^{ins}(L)$. Thus, the G/C mode of the SECM (with the tip electrode serving as a generator)

for these mechanisms is completely equivalent to the feedback mode, and any quantity, $I_T^{\square}$, $I_S^{\square}$, or $I_S^{\square}/I_T^{\square}$, can be calculated from Equation 5.80 for a given L, if any other of these quantities is known.

For mechanisms with following irreversible reactions, one can expect the collection efficiency, $I_S^{\square}/I_T^{\square}$, to be a function a single kinetic parameter κ. If this parameter is known, the SECM theory for this mechanism can be reduced to a single working curve. After the function $\kappa = F\left(I_S'/I_T'\right)$ is specified, one can immediately evaluate the rate constant from $I_S^{\square}/I_T^{[}$ vs. L or $I_T^{\square}$ vs. L experimental curves. If only tip current has been measured, the collection efficiency can be calculated as

$$I_S'/I_T' = \frac{1 - I_T^{ins}/I_T'}{1 - f(L)} \tag{5.81}$$

For the E_rC_i mechanism, $\kappa = k_c d^2/D$. Figure 5.12A represents the working curve, κ vs. $I_S^{\square}/I_T^{\square}$, along with the simulated data from Ref. [5]. The numerical results fit the analytical approximation

$$\kappa = F(x) = 5.608 + 9.347\exp(-7.527x) - 7.616\exp\left(\frac{-0.307}{x}\right) \tag{5.82}$$

(solid curve in Figure 5.12A), where $x = I_S'/I_T'$, within about 1%. The first-order rate constants in excess of 2×10^4 s^{-1} should be accessible to SECM measurements under steady-state conditions.

The latest contribution to the theory of the EC processes in SECM was the modeling of the SG/TC situation by Martin and Unwin [59]. Both the tip and substrate chronoamperometric responses to the potential step applied to the substrate were calculated. From the tip current transient, one can extract the value of the first-order homogeneous rate constant and (if necessary) determine the tip/

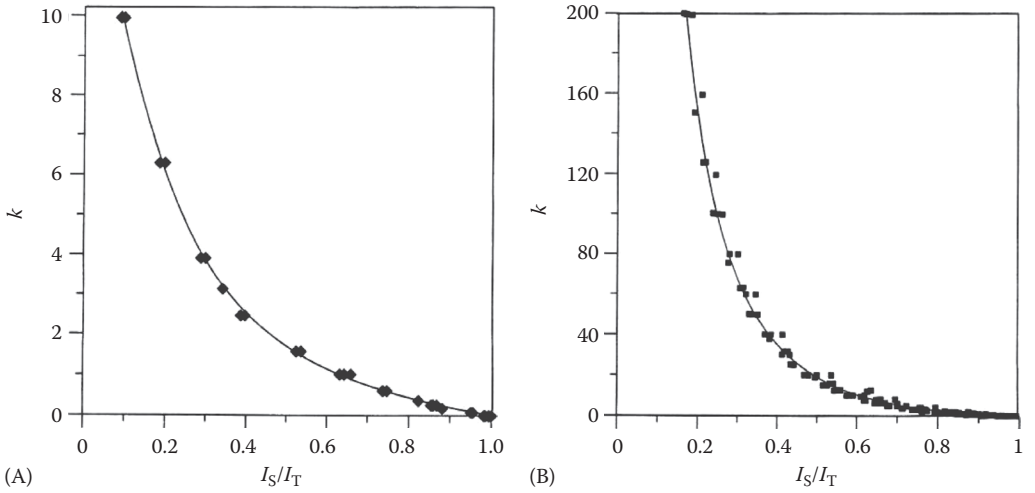


FIGURE 5.12 Kinetic parameter κ as a function of the collection efficiency ($I_S^{\square}/I_T^{\square}$). (A) E_rC_i mechanism; $\kappa = k_c d^2/D$, solid line was computed from Equation 5.85, diamonds are simulated data taken from Ref. [5]. (B) E_rC_{2i} mechanism; $\kappa' = c^{\circ}\ k_c d^3/aD$, solid line was computed from Equation 5.88, squares are simulated data taken from Ref. [54]. (Reprinted with permission from Treichel, D.A., Mirkin, M.V., and Bard, A.J., Scanning electrochemical microscopy. 27. Application of a simplified treatment of an irreversible homogeneous reaction following electron transfer to the oxidative dimerization of 4-nitrophenolate in acetonitrile, *J. Phys. Chem.*, 98, 5751–5757, 1994. Copyright 1994 American Chemical Society.)

substrate distance. However, according to the authors, this technique is unlikely to match the TG/SC mode with its high collection efficiency under steady-state conditions.

5.4.1.2 Second-Order Following Reaction

The detailed TG/SC theory was developed for an electrode process with a following dimerization reaction (E_rC_{2i} mechanism) [54]:

$$\text{Tip}: \quad \text{O} + n\text{e}^- \rightarrow \text{R} \tag{5.83a}$$

$$\text{Gap}: \quad 2\text{R} \xrightarrow{k_c'} \text{products} \tag{5.83b}$$

$$\text{Substrate}: \quad \text{R} - n\text{e}^- \rightarrow \text{O} \tag{5.83c}$$

This diffusion problem is similar to one for E_rC_i mechanism (Equation 5.66) except for the different Fick's equation for c_R:

$$\frac{\partial c_R}{\partial t} = D_R \left[\frac{\partial^2 c_R}{\partial z^2} + \frac{\partial^2 c_R}{\partial r^2} + \frac{1}{r} \frac{\partial c_R}{\partial r} \right] - k_c' {c_R}^2 \tag{5.84}$$

Both chronoamperometric and steady-state responses were calculated by solving the related equations numerically. An analytical approach discussed in the previous section is equally applicable to E_rC_{2i} mechanism under steady-state conditions. Equation 5.80 was verified using the data simulated from Ref. [54], and $I_T^{\square}$ vs. $I_S^{\square}$ dependences were plotted for different values of L [58]. Although for the E_rC_{2i} mechanism, the choice of κ is less straightforward than for E_rC_i, an acceptable fit for all the data points computed in Ref. [54] was obtained using $\kappa' = c^\circ k_C' d_3/aD$ (Figure 5.12B). These data were fited to Equation 5.85:

$$\kappa' = 104.87 - 9.948x - 185.89/\sqrt{x} + 90.199/x + 0.389/x^2 \tag{5.85}$$

Although this approximation is less accurate than Equation 5.82, its use would not lead to an error of more than about 5%–10%, which is within the usual range of experimental error. The invariability of $k_c^{\square}$ computed from different experimental points would assure the validity of the results. The upper limit for the rate constant accessible to steady-state TG/SC SECM measurements is about 5×10^8 M^{-1}.

5.4.1.3 ECE and DISP1 Mechanisms

These reactions involving two ET steps are shown schematically in Figure 5.13 [57]. The product of homogeneous chemical reaction (C) often is easier to reduce than A. This second reduction can either occur at the tip electrode (ECE mechanism in Figure 5.13A) or via the disproportionation (DISP1 mechanism in Figure 5.13B):

$$\text{C} + \text{B} \xrightarrow{k} \text{A} + \text{D} \tag{5.86}$$

With the substrate biased at a potential slightly more positive than E° of A–B couple, B is oxidized to form A for both DISP1 and ECE mechanisms. However, in the latter case, the reduction of C

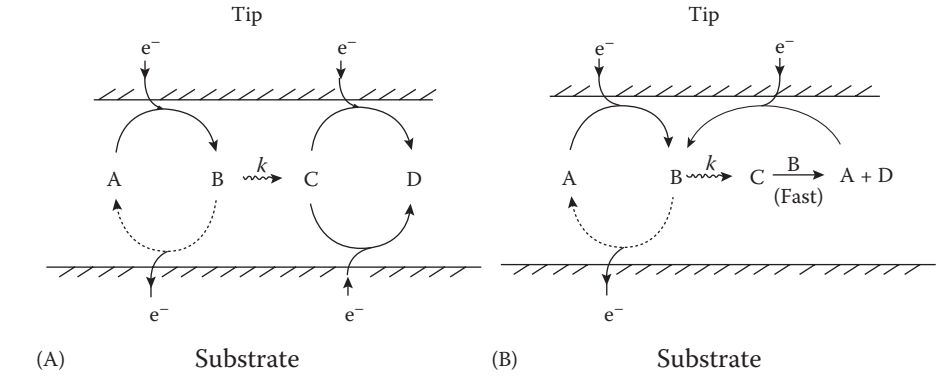


FIGURE 5.13 Diffusional and chemical processes occurring within the tip/substrate domain in the case of (A) an ECE pathway and (B) a DISP1 pathway. (Reprinted with permission from Demaille, C., Unwin, P.R., and Bard, A.J., Scanning electrochemical microscopy. 33. Application to the study of ECE/DISP reactions, *J. Phys. Chem*., 100, 14137–14143, 1996. Copyright 1996 American Chemical Society.)

also occurs at the substrate. The numerical solution of corresponding diffusion problems (see Ref. [57] for problem formulations) yielded several families of working curves shown in Figure 5.14 (DISP1 pathway) and Figure 5.15 (ECE pathway). In both cases, the tip and the substrate currents are functions of the dimensionless kinetic parameter, $K = ka^2/D$. The normalization of the i_T and i_S for two-electron processes is somewhat problematic. In Ref. [57], both quantities are normalized with respect to the one-electrode steady-state current that flows at infinite tip/substrate separation ($i_{T,1e,\infty} = 4FDac_a^o$). However, this value is not equal to experimentally measured tip current at $d \to \infty$, which also includes the contribution from the second ET. Nevertheless, by comparing

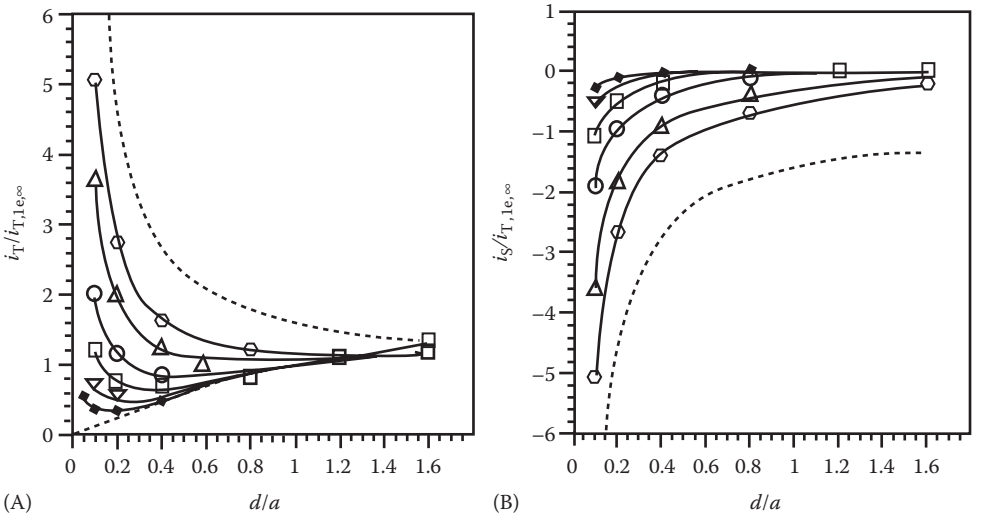


FIGURE 5.14 DISP1 pathway. Theoretical current–distance curves for several values of $K = ka^2/D$: 1 (◇), 2 (△), 5 (○), 10 (□), 20 (▽), and 50 (♦). The upper dashed line in part (A) represents the one-electron pure positive feedback ($K = 0$). The lower dashed line is the two-electron pure negative feedback ($K = \infty$). In part (B), the dashed line represents the one-electron pure positive feedback. (Reprinted with permission from Demaille, C., Unwin, P.R., and Bard, A.J., Scanning electrochemical microscopy. 33. Application to the study of ECE/DISP reactions, *J. Phys. Chem*., 100, 14137–14143, 1996. Copyright 1996 American Chemical Society.)

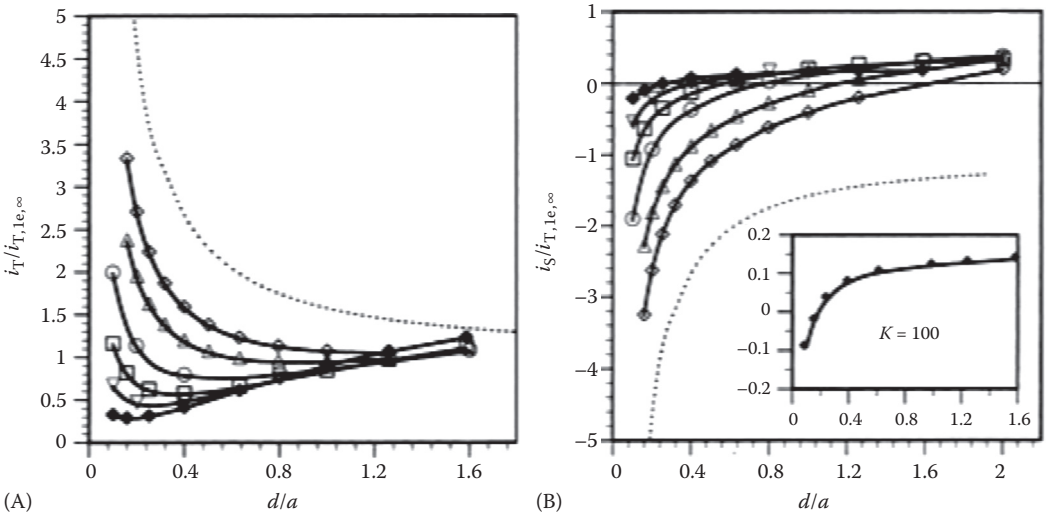


FIGURE 5.15 ECE pathway. Theoretical current–distance curves for several values of $K = ka^2/D$: 1 (◇), 2 (Δ), 5 (○), 10 (□), 20 (▽), and 50 (♦). The upper dashed line in part (A) represents the one-electron pure positive feedback ($K = 0$). In part (B), the dashed line represents the one-electron pure positive feedback. The inset shows the substrate current for $K = 100$. (Reprinted with permission from Demaille, C., Unwin, P.R., and Bard, A.J., Scanning electrochemical microscopy. 33. Application to the study of ECE/DISP reactions, *J. Phys. Chem*., 100, 14137–14143, 1996. Copyright 1996 American Chemical Society.)

experimental current–distance curves to the theory one can distinguish between DISP1 and ECE pathways and evaluate the *k* value [57].

5.4.2 Surface Reactions and Interfacial Transfer Processes

The use of the SECM for studies of surface reactions and phase transfer processes is based on its abilities to perturb the local equilibrium and measure the resulting flux of species across the phase boundary. This may be a flux of electrons or ions across the liquid–liquid interface, a flux of species desorbing from the substrate surface, and so on. Furthermore, as long as the mediator is regenerated by a first-order irreversible heterogeneous reaction at the substrate, the current–distance curves are described by the same Equation 5.35 regardless of the nature of the interfacial process. When the regeneration kinetics are more complicated, the theory has to be modified. A rather complete discussion of the theory of adsorption/desorption reactions, crystal dissolution by SECM, and the description of the liquid–liquid interface under SECM conditions can be found in other chapters of this book. In this section, we only consider some basic ideas and list the key references.

5.4.2.1 Adsorption/Desorption Processes and Lateral Mass/Charge Transfer

Two opposite reactions, adsorption on and desorption from the substrate surface, can be probed by the SECM microtip [60]. In the former case, the SECM functioned only as a micromanipulator aimed to bring the microtip electrode inside the small drop of liquid (3.5–20 μL volume). The adsorption was determined through the decrease in the tip current caused by decreasing concentration of adsorbing species in a liquid phase. To study desorption process, the UME tip is positioned close to the surface of the substrate covered with an adsorbate [61]. Following the application of the potential step to the tip electrode, the reduction (or oxidation) begins leading to the depletion of adsorbing species in the tip/substrate gap. The depletion in turn results in two competing processes:

the desorption from the substrate and surface diffusion driven by the surface concentration gradient. The desorbed species can diffuse to the tip and react at its surface, thus contributing to the measured tip current. The rates of both desorption and surface diffusion processes can be deduced from the chronoamperometric SECM response [61].

One should notice that only small amount of species is adsorbed on a microscopic portion of the substrate facing the tip. Thus, the desorption kinetics can be obtained from the short-time transient behavior when the effect of surface diffusion is negligible. At times sufficiently long for a true steady state to prevail, I_T always attains the value for an inert insulating substrate, and the adsorption/desorption kinetics are not accessible.

Surface diffusion provides an additional path for the transport of the adsorbed mediator into the tip/substrate domain. Its main effect is to increase the magnitude of the current flowing in the longer time region of the transient and, in particular, to enhance the final steady-state current as compared to that at an inert substrate. The adsorption/desorption process is at equilibrium, and thus, the tip current depends on the solution and surface diffusion rates. The larger the surface diffusion coefficient, as compared to that in solution, the larger the steady-state current at the tip UME. The steady-state current becomes increasingly sensitive to the surface diffusion process as L is minimized. The related theory is complicated and involves a large number of empirical parameters. Several families of chronoamperometric transients and steady-state approach curves can be found in Ref. [61] (see also Chapter 13).

Building on the results of Ref. [61], the Unwin group proposed a family of equilibrium perturbation-based approaches to study lateral surface diffusion [62]. The theory based on numerical solution of a time-dependent diffusion problem was developed to describe a triple potential step transient experiments [62a], chronoamperometric experiments, and steady-state approach curves [62b]. An approximate analytical expression for the approach curves produced by the combination of bulk diffusion in the tip/substrate gap with heterogeneous ET and lateral charge transport on the substrate surface is also available [63].

Somewhat similar approaches were developed for surface conductivity measurements by SECM [64]. The electrochemical mass transport equation in this case was

$$\frac{\partial^2 \tilde{\mu}}{\partial R^2} + \frac{1}{R}\frac{\partial \tilde{\mu}}{\partial R} - \frac{K^o}{\Sigma}\left((1 - C_{Z=L})e^{\tilde{\mu}/2} - C_{Z=L}e^{-\tilde{\mu}/2}\right) = 0 \tag{5.87}$$

where

$\tilde{\mu} = (\mu - \mu^o)/kT$ is the dimensionless electrochemical potential of the electrons in the conductive film

K^o is the normalized standard rate constant of the ET between the solution redox species and the film

$C_{Z=L}$ is the dimensionless concentration of the solution redox species at the film surface

Σ is the dimensionless conductivity of the film given by Equation 5.88

$$\Sigma = \frac{\sigma kT\Delta z}{e^2 a D c^{\text{bulk}} N_A} \tag{5.88}$$

where

σ is the conductivity

k is the Boltzmann constant

T is the absolute temperature

Δz is the thickness of the film

e is the elementary charge
D and c^{bulk} are the diffusion coefficient and the bulk concentration of the redox species
N_A is the Avogadro constant.

A more detailed model for the treatment of steady-state feedback data from which the conductivity of thin films can be extracted was reported in Ref. [65]. It was shown that an accurate determination of κ can be achieved by using an approximate method for processing multiple data sets and including a constant calibration factor.

5.4.2.2 Dissolution of Ionic Crystals

Macpherson and Unwin [66] developed the theory for dissolution processes at the substrate induced by depletion of electroactive species at the SECM tip. The UME tip can oxidize or reduce the species of interest in solution at the crystal surface. If this species is one of the crystal components, the depletion of its concentration in the solution gap between the tip and substrate induces crystal dissolution. This process produces additional flux of electroactive species to the tip similarly to positive feedback situation discussed in previous sections. Unlike desorption reaction, where only small amount of adsorbed species can contribute to the tip current, the dissolution of a macroscopic crystal is not limited by surface diffusion. Accordingly, the developed theory is somewhat similar to that for finite heterogeneous kinetics at the substrate. Several models developed in Refs. [66a–d] use different forms of the dissolution rate law applicable to different experimental systems. In general, the rate of the substrate process is [66a]

$$j = k_n \sigma^n \tag{5.89}$$

where
j is the flux of dissolving species
k_n is the rate constant
n is the reaction order
σ is the undersaturation produced by the tip reaction

The SECM theory for the first-order process was developed [66a] and applied to dissolution of the (100) face of copper sulfate single crystal, while the second-order kinetic model was shown to describe well the dissolution of potassium ferrocyanide trihydrate [66c]. By considering a dislocation-free crystal surface on which dissolution sites are only nucleated above a certain critical value of the undersaturation, one can also model an oscillatory dissolution process [66b]. In all cases, the change in geometry caused by dissolution of the substrate and electrodeposition at the tip was neglected.

The developed theory was extended to the case of salt dissolution in solution containing no supporting electrolyte [66e]. Although the theory describing mass transport via diffusion/migration in such systems is more complicated, it was possible to fit the experimental current–distance curves for AgCl dissolution and to demonstrate the applicability of the second-order rate law to this process. A more complete discussion of the theory of the SECM-induced dissolution can be found in Chapter 13.

5.4.2.3 Charge Transfer Processes at the Liquid–Liquid Interface

With regard to SECM theory, the main difference between charge transfers at the liquid–liquid boundary and heterogeneous ET reactions considered in previous sections is in the presence of the second liquid phase. Different charge transfer reactions occurring at the interfacial boundary include ET between redox species confined to different liquid phases and ion transfer (IT) reactions (see Chapter 8 for more detailed discussion). All these processes can be studied by the

SECM [8,15,67,68]. ET can be probed using a feedback mode of the SECM. A tip UME is placed in the upper liquid phase (e.g., organic solvent) containing one form of the redox species (e.g., the reduced form, R). When the tip is held at a positive potential, R reacts at the tip surface to produce the oxidized form of the species, O. When the tip approaches the ITIES, the mediator can be regenerated at the interface via the bimolecular redox reaction between O in the organic phase and a reduced form of aqueous redox species (Figure 5.16A). In addition to the ET step, the overall interfacial process includes the transfer of a common ion between two liquid phases and the mass transfer in the bottom phase. If these steps are rapid, the current–distance curves are described by Equation 5.35. Otherwise, a more complicated theory may be required [15,68].

IT at the liquid–liquid interface can be probed using a micropipette tip [8,69]. Two types of IT processes, that is, facilitated and simple IT, require different treatments. In the first case, an aqueous solution in the pipette contains some ions, for example, a metal cation (M^+). The micropipette is immersed in organic solvent containing dissolved ionophore, R, capable of complexing the ion of interest. The facilitated IT reaction at the micropipette tip is

$$M^+(w) + R(o) = MR^+(o) \quad \text{(at the pipette tip)} \tag{5.90a}$$

When the tip approaches the bottom (aqueous) layer, M^+ is released from the complex and transferred to the aqueous solution, and R, which serves as a mediator, is regenerated (Figure 5.16B):

$$MR^+(o) = M^+(w) + R(o) \quad \text{(at the liquid – liquid interface)} \tag{5.90b}$$

It was shown in Ref. [69] that the overall process in Equations 5.90a and b is mathematically equivalent to conventional feedback situation. If regeneration of the mediator at the interface [Reaction (5.90b)] is rapid, the SECM theory for a conductive substrate is applicable; with no regeneration, the insulating behavior is observed.

Unlike conventional feedback mode and facilitated IT experiments (in which R acts as a mediator), no mediator species is involved in a simple IT process (Figure 5.16C):

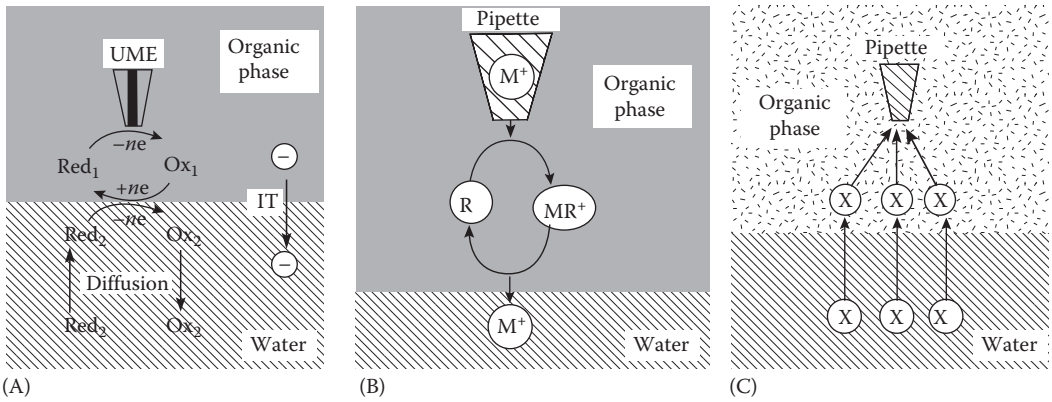


FIGURE 5.16 Studying charge transfer processes at the liquid–liquid interface by SECM. (A) Probing interfacial electron transfer. The SECM operates in the feedback mode with a reversible redox mediator. (B) Probing facilitated IT with the SECM operating in the feedback mode. A cation is transferred from the aqueous solution inside the pipette into the organic phase by interfacial complexation and from organic phase into the bottom aqueous layer by interfacial dissociation mechanism. (C) Probing simple IT with the SECM. The tip depletes the concentration of species X at the phase boundary inducing the transfer of X across the ITIES or the liquid–membrane interface.

$$M^+(o) = M^+(w) \quad \text{(at the pipette tip)} \tag{5.91a}$$

$$M^+(w) = M^+(o) \quad \text{(at the liquid–liquid interface)} \tag{5.91b}$$

In this case, the top and the bottom liquid phases contain the same ion M^+ at equilibrium. A micropipette tip is used to deplete concentration of this ion in the top solvent near the phase boundary. This depletion results in IT across the liquid–liquid interface. Reaction (5.91b) can produce positive feedback if concentration of M^+ in the bottom phase is sufficiently high. Any solid surface (or a liquid phase containing no specific ion) acts as an insulator in this experiment. The interface between the top and the bottom layers is nonpolarizable, and the potential drop is determined by the ratio of concentrations of the common ion (i.e., M^+) in two phases.

Unlike interfacial ET and facilitated IT, the simple IT reaction (5.3) is initially at equilibrium and has to be treated as a quasireversible process [8]. The theory for interfacial transfer processes in two-phase systems developed in Refs. [68a,b] is applicable to both steady-state conditions and transient experiments. The model accounts for reversibility of the transfer reaction and allows for diffusion limitations in both liquid phases. The possibility of different diffusion coefficients in two phases is also included. The steady-state situation is defined by three dimensionless parameters, that is, $K_e = c_O/c_w$ (the ratio of bulk concentrations in organic and aqueous phases), $\gamma = D_O/D_w$ (the ratio of diffusion coefficients), and $K = k^o a/D_O$ (normalized rate constant for the transfer from organic to water). The tip current (at a given distance) increases strongly with both K and γK_e values, but is largely independent of individual values of K_e and γ as long as their product is constant. The diffusion limitations in the second phase (i.e., the liquid phase containing no electrodes) are noticeable only at $\gamma K_e \lesssim 10$. Separating the effects of all three parameters on the shape of current–distance curves may be difficult.

Partitioning of a neutral solute across the liquid–liquid phase boundary is independent of the interfacial voltage; also, unlike ET and IT reactions, this process does not produce electric current across the interface. Building on an earlier model [68a], Barker and Unwin developed theory for double potential step chronoamperometry (SECM-DPSC) that can be used to investigate solute partitioning [70]. The species of interest is generated at the tip in the first potential step; then, it diffuses to the liquid–liquid boundary and partitions to the second phase during a given time period. This species is then collected back at the tip by reversing the potential step. Because of the non-steady-state nature of the DPSC experiment and a large number of related parameters, the theory presented in the form of dimensionless current transients is fairly complicated.

Laforge et al. [71] considered the case when solute partitioning and interfacial bimolecular ET simultaneously contribute to the positive feedback current. It was shown that the contributions of these two processes can be quantitatively separated by analysis of the i_T–d curves. A simple approximate theory for the concentration profile of the partitioning solute in one of two liquid phases was also developed and used to extract the partition coefficient (K) value from the SECM approach curves under quasi-steady-state conditions [71b]. An advantage of this approach is that K can be determined without waiting for the complete equilibration of the solute, which can be very slow if one of the liquid phases (e.g., ionic liquid) is viscous.

5.4.2.4 Finite Enzyme Kinetics at the Substrate

Enzymatic reactions and patterning substrate with enzymes have been the subject of many SECM studies. Original simulations of enzyme kinetics at the substrate were carried out by Pierce et al. [72]. A more extensive set of simulations and the analysis of limitations of the earlier treatment were presented later by Burchardt et al. [73]. The most comprehensive treatment to date is by Lefrou et al. [74] who visualized different experimental situations in the form of a zone diagram, derived analytical approximations for approach curves, and proposed strategies for the extraction of kinetic

parameters from current–distance curves in the presence of large excess of enzyme substrate. A more detailed discussion of these results can be found in Chapter 11.

5.4.3 3D Simulations and Nonideal Conditions

Most of the SECM theory discussed earlier was developed by solving numerically either time-dependent or steady-state 2D axisymmetric diffusion problems. Such a treatment is suitable only for an idealized situation—a flat, planar substrate, strictly perpendicular to the axis of the well-shaped disk tip. The availability of more sophisticated numerical methods and faster personal computers enabled 3D SECM simulations that can address more complicated situations. In this way, one can evaluate the effects of imperfect tip and/or substrate geometry and alignment on the experimental results and data analysis. 3D simulations are also required to describe the responses when the substrate topography is complicated and/or its surface reactivity is highly nonuniform. Unfortunately, a generalized presentation of such theoretical results is almost impossible because of the large number of geometric parameters; thus, we can only give a brief summary of reported simulations.

Fulian et al. [75] introduced the boundary element method (BEM) for the numerical solution of SECM diffusion problems and showed that it is more suitable for problems with regions of complex or rapidly changing geometries than finite difference methods employed in earlier SECM publications. The BEM was used to simulate current responses for a nondisk tip approaching a flat substrate; a disk-shaped tip over a hemispherical or a sphere-cap substrate, or a tilted substrate; a lateral scan of a disk-shaped tip over an insulating/conductive boundary.

Sklyar and Wittstock [76a] used a different version of the BEM method to improve the computational accuracy for several systems simulated in Ref. [75]. Their "exterior Laplace formulation" assigns no geometrical boundaries to the solution, and therefore it does not require any assumption about the extension of the diffusion layer at long times. A number of steady-state simulations were presented to investigate the effect of the tip tilt on approach curves and analyze different distance control modes used in SECM instruments. It was concluded that for an RG ≈ 5, the tilt of the probe of ≤8° does not significantly affect the shapes of the i_T–d curves when d is measured from the center of the electroactive area. However, if d is assumed to be the distance between the substrate and the part of the probe closest to it (i.e., the glass edge), the shapes of i_T–d curves change dramatically, and the attainable maximum positive (or negative) feedback is much lower. This observation becomes significant when one uses the shear force mode to control the tip/substrate separation distance because in such experiments the distance is measured between the glass edge and the substrate.

The next reported advance was the development of a BEM-based approach to solving diffusion problems involving two different redox species [76b]. This extension allowed the authors to simulate G/C SECM experiments. An impressive computational example (Figure 5.17) represents a SG/TC experiment for two sphere-cap beads coated with an enzyme. The enzyme reaction produces redox species that get oxidized the tip surface. The four line scans of the tip over the center of the beads (Figure 5.17B) correspond to different arrangements of the beads shown in Figure 5.17A. Such a simulation allows one to predict the features of the SG/TC images that can be expected for different combinations of geometric, transport, and kinetic parameters, and to evaluate the extent of the overlap of the diffusion fields and its effect on the SECM data analysis.

Sklyar et al. [76c] used BEM to model the response of an integrated AFM-SECM probe consisting of a nonconducting AFM tip surrounded by the electroactive gold square frame. The feedback current and the substrate topography were mapped simultaneously when such a tip was scanned over the substrate. The data from the topographic image were used to calculate the simulated current response, and the simulation results were compared to experimentally recorded SECM images. Numerical simulations quantitatively reproduced the experimental results.

Most recently, the Wittstock group extended their approach to include nonlinear boundary conditions [73]. The approach curves were simulated for Michaelis–Menten kinetics at the enzyme-coated substrate. It was found that approximating enzyme kinetics by first-order models is likely to yield

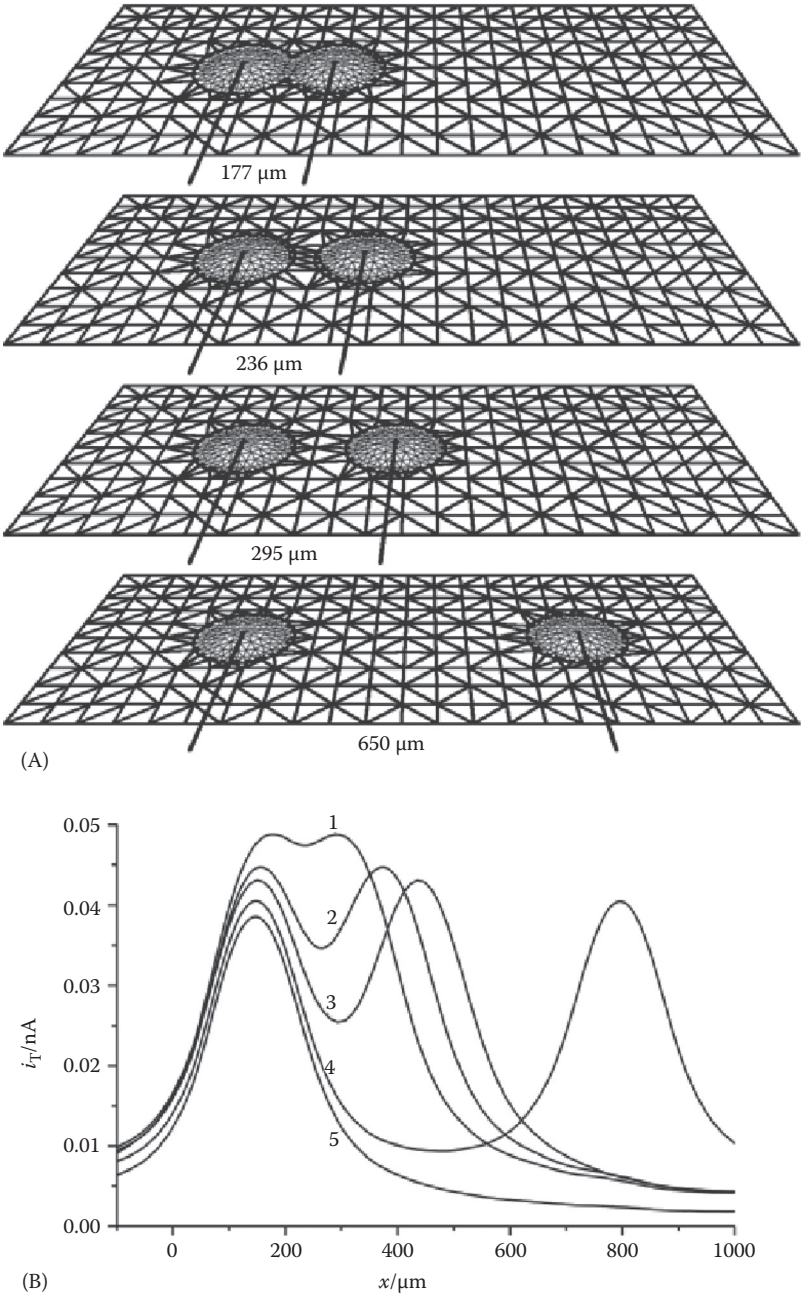


FIGURE 5.17 Simulation of SG/TC experiments for two sphere-cap beads placed on the same support. (A) Layout of the spots; midpoint–midpoint distances (µm) are (1) 177, (2) 236, (3) 296, and (4) 650 and (B) corresponding line scans over the center of the bead spots for layouts 1–4. (Reprinted with permission from Sklyar, O., Träuble, M., Zhao, C., and Wittstock, G., Modeling steady-state experiments with a scanning electrochemical microscope involving several independent diffusing species using the boundary element method, *J. Phys. Chem. B*, 110, 15869–15877, 2006. Copyright 2006 American Chemical Society.)

misleading results. The use of a linear approximation is marginally acceptable (expected errors ≤10%) only if the ratio of the mediator concentration to the Michaelis–Menten constant is ≤0.1.

The results of 3D simulations of feedback mode experiments with a nanoband substrate [26] are summarized in Section 5.2.3.

5.5 NUMERICAL SOLUTION OF SECM DIFFUSION PROBLEMS USING COMSOL MULTIPHYSICS

The SECM theory for most systems reviewed in previous sections is rather complicated. Analytical approximations are only available for a limiting number of relatively simple processes. The generation of theoretical data requires numerical solution of partial differential equations, which makes it harder for an experimentalist to carry out quantitative SECM studies. COMSOL Multiphysics (formerly FEMLAB) is a finite element software package for various physics and engineering applications, especially suitable for modeling coupled processes, or "multiphysics" [77]. The examples of simulations given in this section illustrate the solution of three progressively more complicated steady-state problems, that is, diffusion to an embedded microdisk, pure positive (or negative) feedback at the SECM tip, and E_rC_i mechanism.

5.5.1 Diffusion to an Embedded Microdisk

During the modeling process, one has to specify the physics that describe the system, its geometry, the initial and boundary conditions, perform the meshing of the simulation space, and select the solver. Variables, expressions, and physical constants are selected for spatial domains, boundaries, edges, and points. COMSOL Multiphysics internally compiles a set of equations representing the entire model [77].

A library model for a axisymmetric 2D diffusion transport can be used for solving most SECM problems, in which the coordinates are r and z. The normalized variables are defined by Equations 5.4 through 5.6 and 5.14. The computed diffusion-limited current is normalized by $i_{T,\infty}$ (Equation 5.20). The steps of the modeling process are as follows.

Parameters

(predefined, used though the whole model)

Name	Expression	Value	Description
RG	100	100	Maximum value of r; thick insulating sheath
zmax	100	100	The extent of the system in z-direction

Geometry

(Geometry can be set by choosing "Add Bezier Polygon" to draw the boundaries of the problem, and the domains are automatically formed by Multiphysics. The polygon is defined by (R, Z) pairs)

$$(0,0) \rightarrow (1,0) \rightarrow (\mathrm{RG},0) \rightarrow (\mathrm{RG},\mathrm{zmax}) \rightarrow (0,\mathrm{zmax}) \rightarrow (0,0)$$

Physics: Transport of Diluted Species (chds)

Dependent variables

Number of species: 1

Concentrations: c

Domain

Diffusion coefficient: $D = 1$; isotropic
Initial values: $c = 1$

Boundaries

No.	Expression	Description
1	—	Axial symmetry
2	$c = 0$	Tip surface
3	$c = 1$	Far from the disk, simulation space limit
4	$\partial c/\partial n = 0$	Insulator surface surround the dick
5	$c = 1$	Outer boundary of domain, simulation space limit

Mesh

(The mesh should be highly refined where the concentration and/or flux of redox species change sharply. One can either specify the mesh size of certain domain or boundaries or points, or refine a certain area manually.)

Domain: Normal mesh

Add free triangular:

Choose boundary 2, make maximum element size as low as possible

Refine:

Specify bounding box r (0–10), z (0–10)
Specify bounding box r (0.995–1.005), z (0–0.005) several times

Study: Stationary

Results:

(The results analysis and visualization include several groups of operations: *data sets*, *plots and plot groups*, *derived values and tables*, and *reports*. Using the data sets, one can choose the source of data for plotting, then display a *plot group*, for example, the concentration distribution, or flux distribution in the graphics window. To calculate the current, one can use the *derived values* to do integration over the disk surface.)

2D plot group

Add surface
Expression: c

1D plot group

Choose boundary 2, 4
Y: chds.ndflux_c (normal diffusive flux of c)
X: r

Derived values

Line integration boundary 2
Expression: chds.ndflux_c

Integration settings

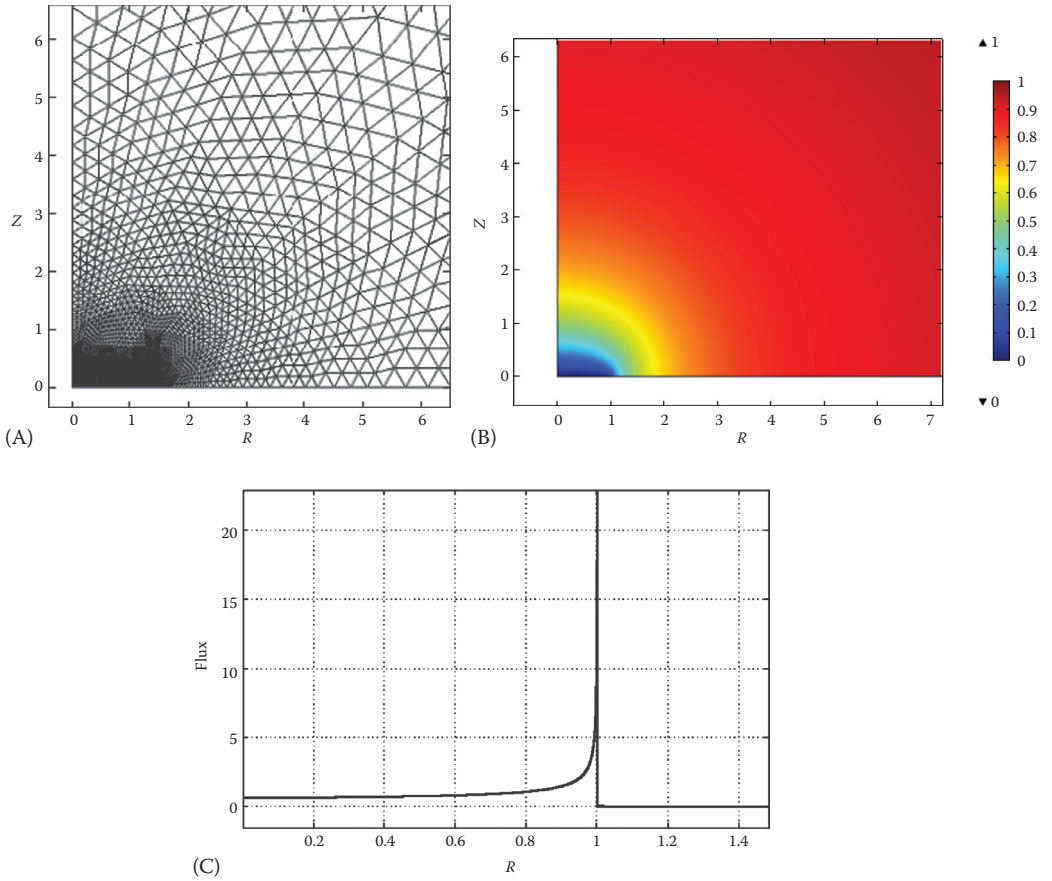


FIGURE 5.18 Simulation of steady-state diffusion-limited current at an embedded microdisk electrode by COMSOL 4.0a. (A) The mesh generated by the program. (B) The concentration profile of redox species. (C) The flux distribution over the disk surface.

Check the "compute surface integral" box for axial symmetry.

Figure 5.18 contains some graphical output. The triangular mesh grid generated by the program (Figure 5.18A) is dense near the electrode surface (especially at the edge of the disk where the current density is very large), and sparse far from it. The corresponding concentration profile (Figure 5.18B) shows how the concentration of redox species changes from zero at the disk to one in the bulk solution. The flux distribution over the disk surface is shown in Figure 5.18C. The normalized current computed by integration of the flux ($i/4nFac^{\circ}D = 0.998$) is within 0.2% from the exact value (1.000). If required, the accuracy can be improved by further refining the mesh at the expense of longer computation time.

5.5.2 Diffusion-Controlled SECM Feedback

The modeling sequence of the SECM problem is similar to that used above for a microdisk. Additional changes are required to take into account mediator diffusion from behind the shield. The following Multiphysics model can be used to simulate negative feedback mode (insulating substrate) by solving the diffusion problem from Section 5.2.2.1, that is, Equation 5.26 with boundary conditions given by Equations 5.27, 5.28b, and 5.29.

Parameters

Name	Expression	Description
RG	1.1	Thin insulating sheath
L	1	Distance between substrate and tip
$L1$	20	How far behind the tip surface the simulation goes
RMAX	100	The extent of the system in r-direction

Geometry
Bezier polygon:

$$(0,0) \rightarrow (1,0) \rightarrow (\mathrm{RG},0) \rightarrow (\mathrm{RG},-L1) \rightarrow (\mathrm{RMAX},-L1) \rightarrow (\mathrm{RMAX},L) \rightarrow (0,L) \rightarrow (0,0)$$

Physics: Transport of Diluted Species (chds)

Dependent variables

Number of species: 1
Concentrations: c

Domain

Diffusion coefficient: $D_c = 1$, isotropic
Initial values: $c = 1$

Boundaries

No.	Expression	Description
1	—	Axial symmetry
2	$c = 0$	Disk surface
3	No flux	Substrate, negative feedback
4	No flux	Insulator plane surround the disk
5	No flux	Cylindrical inert surface surrounding the tip
6	$c = 1$	Far from the disk, bulk concentration
7	$c = 1$	Outer boundary of domain, bulk concentration

Mesh
Domain: Normal mesh
Add free triangular:
Choose boundary 2 and 4, make maximum element size as low as possible

Refine:
Specify bounding box r (0–2), z (−0.05 to 1), 1 refinement
Specify bounding box r (0–2), z (0.8 to 1), 5 refinements
Specify bounding box r (1–2), z (−0.05 to 0.05), 2 refinements

Study: Stationary

Results

2D plot group
Add surface
Expression: c

(Here we create a 2D cross-sectional plot by using a cut line data set, which visualizes a quantity in one line along a parameter range.)

Cut line 2D data set: (0, 0) to (10, 0)

1D plot group 1

(Distribution of concentration of redox species over *r*-axis)
Data set: cut line 2D

Y: *c*
X: *r*

(Another cut line was selected for the (0.0) to (1,0) data set)

1D plot group 2

(Distribution of flux over *r*-axis)

Data set: Cut line 2D
Y: chds.dfluxz_c
X: *r*

Derived values

Line integration boundary 2
Expression: chds.ndflux_c

Integration settings: check the "compute surface integral" box

Figure 5.19 shows the distributions of concentration of redox species over *R*- and over *Z*-axes (A) and the flux distribution over the tip surface (B). One should notice the "negative" flux from the back of the tip.

To simulate positive feedback situation, one has to replace the "no flux" condition for boundary 3 representing the substrate surface with "$c = 1$." Minor modifications in the input file allow the simulation of the SECM responses for recessed or protruding tips, and finite heterogeneous kinetics at the tip and/or substrate.

5.5.3. E_rC_i Mechanism

The diffusion problem solved in this section is a steady-state version of Equations 5.67 through 5.73, in which $\partial c_i/\partial t = 0$, all variables are time independent, and the initial condition (Equation 5.68) is omitted. The normalized variables employed are defined earlier including the dimensionless homogeneous rate constant, $K = k_c a^2/D_R$. The main difference between this model and the ones described earlier is that concentrations of both forms of redox species (c_O and c_R) have to be computed by solving two partial differential equations. To save space, the diffusion from behind the shield has been neglected; it can be taken into account by introducing additional boundary segments as discussed in Section 5.5.2. An implicit assumption of equal diffusion coefficients ($D_O = D_R$) is not essential and can easily be eliminated.

Parameters

Name	Expression	Description
RG	10	Insulating sheath
L	0.25	Tip/substrate distance
K	1	Dimensionless homogeneous rate constant

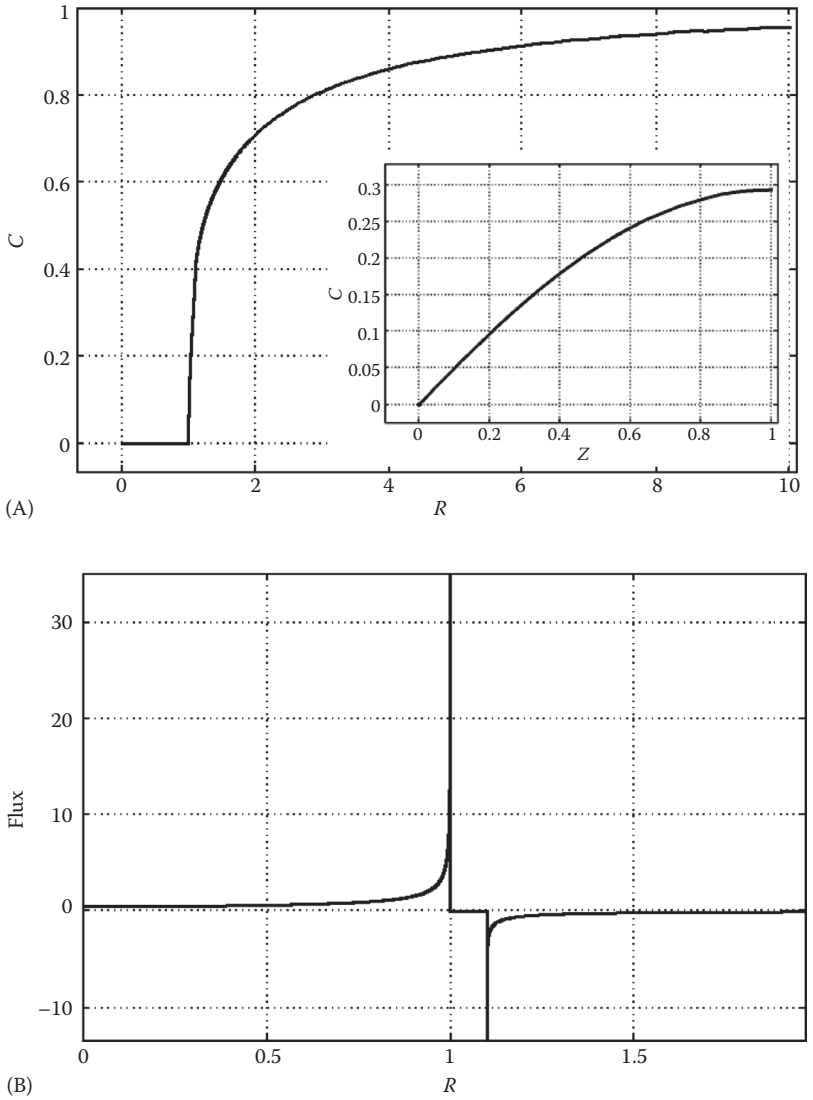


FIGURE 5.19 Simulation of the diffusion-controlled SECM process at an insulting substrate by COMSOL 4.0a. (A) Distribution of concentration of redox species over *R*-axis and over *Z*-axis (inset). (B) Distribution of the flux over the tip surface.

Geometry

Bezier polygon:

$$(0,0) \rightarrow (1,0) \rightarrow (\mathrm{RG},0) \rightarrow (\mathrm{RG},L) \rightarrow (2,L) \rightarrow (0,L) \rightarrow (0,0)$$

Physics: Transport of Diluted Species (chds)

Dependent variables

Number of species: 2
Concentrations: c_{O}, c_{R}

Domain

Diffusion coefficient: $D_O = 1$, $D_R = 1$; isotropic
Initial values: $c_O = 1$, $c_R = 0$

Reactions: Rate $= -K^* c_R$ ($\nabla(-\nabla c_R) =$ Rate)

Boundaries

No.	Expression	Description
1	—	Axial symmetry
2	$c_O = 0$	Disk surface
	$N_{0,c}$R = chds.ndflux_cO	Flux of R at the tip = flux of O
3, 5	$c_R = 0$	Substrate
	$N_{0,c}$O = chds.ndflux_cR	Flux of O at the substrate = flux of R
4	No flux	Insulator plane surround the disk
6	$c = 1$	Far from the disk, bulk concentration

Mesh

Domain: Normal mesh
Add free triangular:
Choose boundary 2 and 3, make maximum element size 0.0005, and element growth rate 1.15
Refine:
Specify bounding box r (0.9–1.2), z (0–0.1), 1 refinement
Specify bounding box r (1–1.2), z (0–0.0.02), 3 refinements

Study: Stationary

Results

2D plot group

Add surface
Expression: cO

1D plot group 1 (distribution of the flux of O across the tip surface)

Choose boundary 2, 4
Y: chds.ndflux_cO
X: r

1D plot group 2 (distribution of the flux of R over the substrate surface)

Choose boundary 3,5
Y: chds.ndflux_cR
X: r

Derived values

Line integration 1 (tip current)
Boundary 2
Expression: chds.ndflux_cO

Integration settings: check the “compute surface integral” box
The computed dimensionless tip current ($i/4nFacD$) was 2.066

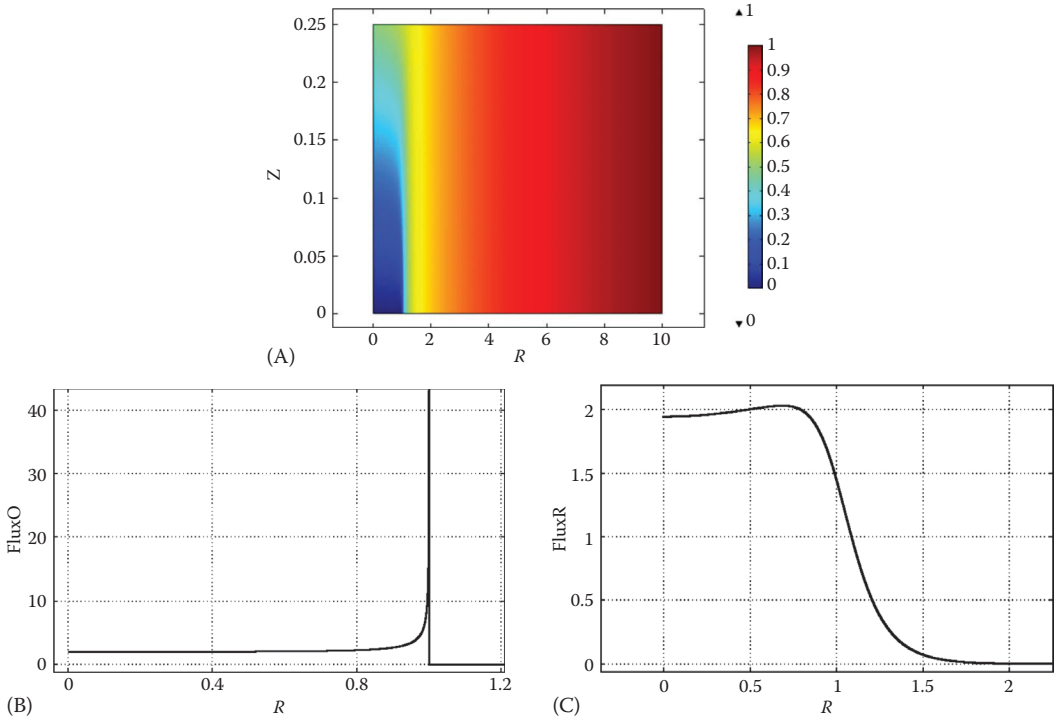


FIGURE 5.20 Simulation of the E_rC_i mechanism by COMSOL 4.0a. (A) The concentration profile of oxidized species. (B) Distribution of the flux of O over the tip surface. (C) Distribution of the flux of R over the substrate surface.

Line integration 2 (substrate current)

Boundary 3,5
Expression: chds.ndflux_cR

Integration settings: check the "compute surface integral" box

Computational results in Figure 5.20 include the concentration profile of O (A) and the distributions of fluxes of O across the tip surface (B) and R over the substrate surface (C) obtained with $L = 0.25$, $K = 1$, and RG = 10. The computed dimensionless substrate current ($i/4nFacD$) was 2.003. The substrate current was slightly smaller than the tip current because a small amount of R was consumed by homogeneous reaction.

ACKNOWLEDGMENT

The support of our research in SECM by the National Science Foundation (CHE-0957313 and CHE-1026582) and Petroleum Research Fund administrated by the American Chemical Society is gratefully acknowledged.

REFERENCES

1. Kwak, J., Bard, A. J. 1989. Scanning electrochemical microscopy. Theory of the feedback mode. *Anal Chem* 61:1221–1227.
2. Mirkin, M. V., Bard, A. J. 1992. Multidimensional integral equations: A new approach to solving microelectrode diffusion problems: Part 2. Applications to microband electrodes and the scanning electrochemical microscope. *J Electroanal Chem* 323:29–51.

3. Bard, A. J., Mirkin, M. V., Unwin, P. R., Wipf, D. O. 1992. Scanning electrochemical microscopy. 12. Theory and experiment of the feedback mode with finite heterogeneous electron-transfer kinetics and arbitrary substrate size. *J Phys Chem* 96:1861–1868.
4. Bard, A. J., Denuault, G., Friesner, R. A., Dornblaser, B. C., Tuckerman, L. S. 1991. Scanning electrochemical microscopy: Theory and application of the transient (chronoamperometric) SECM response. *Anal Chem* 63:1282–1288.
5. Unwin, P. R., Bard, A. J. 1991. Scanning electrochemical microscopy. 9. Theory and application of the feedback mode to the measurement of following chemical reaction rates in electrode processes. *J Phys Chem* 95:7814–7824.
6. Martin, R. D., Unwin, P. R. 1997. Scanning electrochemical microscopy: Theory and experiment for the positive feedback mode with unequal diffusion coefficients of the redox mediator couple. *J Electroanal Chem* 439:123–136.
7. Ghilane, J., Lagrost, C., Hapiot, P. 2007. Scanning electrochemical microscopy in nonusual solvents: Inequality of diffusion coefficients problem. *Anal Chem* 79:7383–7391.
8. Shao, Y., Mirkin, M. V. 1998. Probing ion transfer at the liquid/liquid interface by scanning electrochemical microscopy (SECM). *J Phys Chem B* 102:9915–9921.
9. Amphlett, J. L., Denuault, G. 1998. Scanning electrochemical microscopy (SECM): An investigation of the effects of tip geometry on amperometric tip response. *J Phys Chem B* 102:9946–9951.
10. Bard, A. J., Fan, F.-R. F., Mirkin, M. V. 1993. *Electroanalytical Chemistry*, A. J. Bard, ed., Marcel Dekker, New York, pp. 243–373.
11. Mirkin, M. V., Fan, F.-R. F., Bard, A. J. 1992. Scanning electrochemical microscopy. Part 13. Evaluation of the tip shapes of nanometer size microelectrodes. *J Electroanal Chem* 328:47–62.
12. (a) Shoup, D., Szabo, A. 1984. Influence of insulation geometry on the current at microdisk electrodes. *J Electroanal Chem* 160:27–31. (b) Fang, Y., Leddy, J. 1995. Cyclic voltammetric responses for inlaid microdisks with shields of thickness comparable to the electrode radius: A simulation of reversible electrode kinetics. *Anal Chem* 67:1259–1270.
13. (a) Lefrou, C. 2006. A unified new analytical-approximation for positive feedback currents with a microdisk SECM tip. *J Electroanal Chem* 592:103–112. (b) Cornut, R., Lefrou, C. 2007. Unified new analytical approximation for negative feedback currents with a microdisk SECM tip. *J Electroanal Chem* 608:59–66.
14. Galceran, J., Cecilia, J., Companys, E., Salvador, J., Puy, J. 2000. Analytical expressions for feedback currents at the scanning electrochemical microscope. *J Phys Chem B* 104:7993–8000.
15. Wei, C., Bard, A. J., Mirkin, M. V. 1995. Scanning electrochemical microscopy. 31. Application of SECM to the study of charge transfer processes at the liquid/liquid interface. *J Phys Chem* 99:16033–16042.
16. Cornut, R., Lefrou, C. 2008. New analytical approximation of feedback approach curves with a microdisk SECM tip and irreversible kinetic reaction at the substrate. *J Electroanal Chem* 621:178–184.
17. Mirkin, M. V., Bard, A. J. 1992. Simple analysis of quasi-reversible steady-state voltammograms. *Anal Chem* 64:2293–2302.
18. Mirkin, M. V., Richards, T. C., Bard, A. J. 1993. Scanning electrochemical microscopy. 20. Steady-state measurements of the fast heterogeneous kinetics in the ferrocene/acetonitrile system. *J Phys Chem* 97:7672–7677.
19. Sun, P., Mirkin, M. V. 2006. Kinetics of electron-transfer reactions at nanoelectrodes. *Anal Chem* 78:6526–6534.
20. (a) Zoski, C. G., Aguilar, J. C., Bard, A. J. 2003. Scanning electrochemical microscopy. 46. Shielding effects on reversible and quasireversible reactions. *Anal Chem* 75:2959–2966. (b) Zoski, C. G., Luman, C. R., Fernandez, J. L., Bard, A. J. 2007. Scanning electrochemical microscopy. 57. SECM tip voltammetry at different substrate potentials under quasi-steady-state and steady-state conditions. *Anal Chem* 79:4957–4966.
21. Liu, B., Bard, A. J., Mirkin, M. V., Creager, S. E. 2004. Electron transfer at self-assembled monolayers measured by scanning electrochemical microscopy. *J Am Chem Soc* 126:1485–1492.
22. Borgwarth, K., Ricken, C., Ebling, D. G., Heinze, J. 1996. Surface analysis by scanning electrochemical microscopy. Resolution studies and applications to polymer samples. *Fresenius J Anal Chem* 356:288–294.
23. Forouzan, F., Bard, A. J., Mirkin, M. V. 1997. Voltammetric and scanning electrochemical microscopic studies of the adsorption kinetics and self-assembly of *n*-alkanethiol monolayers on gold. *Isr J Chem* 37:155–163.

24. (a) Zwanzig, R. 1990. Diffusion-controlled ligand binding to spheres partially covered by receptors: An effective medium treatment. *Proc Natl Acad Sci USA* 87:5856–5857. (b) Zwanzig, R., Szabo, A. 1991. Time dependent rate of diffusion-influenced ligand binding to receptors on cell surfaces. *Biophys J* 60:671–678. (c) Szabo, A., Zwanzig, R. 1991. Chronoamperometric current at a random ensemble of microdisk electrodes. *J Electroanal Chem* 314:307–311.
25. Xiong, H., Guo, J., Amemiya, S. 2007. Probing heterogeneous electron transfer at an unbiased conductor by scanning electrochemical microscopy in the feedback mode. *Anal Chem* 79:2735–2744.
26. (a) Xiong, H., Gross, D. A., Guo, J., Amemiya, S. 2006. Local feedback mode of scanning electrochemical microscopy for electrochemical characterization of one-dimensional nanostructure: Theory and experiment with nanoband electrode as model substrate. *Anal Chem* 78:1946–1957. (b) Xiong, H., Kim, J., Kim, E., Amemiya, S. 2009. Scanning electrochemical microscopy of one-dimensional nanostructure: Effects of nanostructure dimensions on the tip feedback current under unbiased conditions. *J Electroanal Chem* 629:78–86. (c) Kim, E., Kim, J., Amemiya, S. 2009. Spatially resolved detection of a nanometer-scale gap by scanning electrochemical microscopy. *Anal Chem* 81:4788–4791.
27. (a) Mirkin, M. V., Fan, F.-R. F., Bard, A. J. 1992. Direct electrochemical measurements inside a 2000 angstrom thick polymer film by scanning electrochemical microscopy. *Science* 257:364–366. (b) Fan, F.-R. F., Mirkin, M. V., Bard, A. J. 1994. Polymer films on electrodes. 25. Effect of polymer resistance on the electrochemistry of poly(vinylferrocene): Scanning electrochemical microscopic, chronoamperometric, and cyclic voltammetric studies. *J Phys Chem* 98:1475–1481.
28. Davis, J. M., Fan, F.-R. F., Bard, A. J. 1987. Currents in thin layer electrochemical cells with spherical and conical electrodes. *J Electroanal Chem* 238:9–31.
29. (a) Selzer, Y., Mandler, D. 1999. Comprehensive treatment of sphere-cap microelectrodes (SCMS) using digital simulations. *Electrochem Commun* 1:569–575. (b) Selzer, Y., Mandler, D. 2000. Scanning electrochemical microscopy. Theory of the feedback mode for hemispherical ultramicroelectrodes: Steady-state and transient behavior. *Anal Chem* 72:2383–2390.
30. (a) Daniele, S., Bragato, C., Ciani, I., Baldo, M. A. 2003. Sphere-cap mercury microelectrodes for scanning electrochemical microscopy above an insulating substrate. *Electroanalysis* 15:621–628. (b) Lindsey, G., Abercrombie, S., Denuault, G., Daniele, S., De Faveri, E. 2007. Scanning electrochemical microscopy: Approach curves for sphere-cap scanning electrochemical microscopy tips. *Anal Chem* 79:2952–2956. (c) Daniele, S., Ciani, I., Battistel, D. 2008. Effect of the insulating shield thickness on the steady-state diffusion-limiting current of sphere cap microelectrodes. *Anal Chem* 80:253–259.
31. Zoski, C. G., Liu, B., Bard, A. J. 2004. Scanning electrochemical microscopy: Theory and characterization of electrodes of finite conical geometry. *Anal Chem* 76:3646–3654.
32. Xiong, H., Guo, J. D., Kurihara, K., Amemiya, S. 2004. Fabrication and characterization of conical microelectrode probes templated by selectively etched optical fibers for scanning electrochemical microscopy. *Electrochem Commun* 6:615–620.
33. (a) Baranski, A. S. 1991. On possible systematic errors in determinations of charge transfer kinetics at very small electrodes. *J Electroanal Chem* 307:287–292. (b) Oldham, K. B. 1992. A hole can serve as a microelectrode. *Anal Chem* 64:46–51.
34. (a) Fan, F.-R. F., Bard, A. J. 1995. Electrochemical detection of single molecules. *Science* 267:871–874. (b) Fan, F.-R. F., Kwak, J., Bard, A. J. 1996. Single molecule electrochemistry. *J Am Chem Soc* 118:9669–9675.
35. (a) Sun, P., Mirkin, M. V. 2008. Electrochemistry of individual molecules in zeptoliter volumes. *J Am Chem Soc* 130:8241–8250. (b) Sun, P., Mirkin, M. V. 2007. Scanning electrochemical microscopy with slightly recessed nanotips. *Anal Chem* 79:5809–5816. DOI: 10.1021/ac202917r.
36. James, P., Casillas, N., Smyrl, W. H. 1996. Simultaneous scanning electrochemical and photoelectrochemical microscopy by use of a metallized optical-fiber. *J Electrochem Soc* 143:3853–3865.
37. Lee, Y., Amemiya, S., Bard, A. J. 2001. Scanning electrochemical microscopy. 41. Theory and characterization of ring electrodes. *Anal Chem* 73:2261–2267.
38. (a) Liljeroth, P., Johans, C., Slevin, C. J., Quinn, B. M., Kontturi, K. 2002. Micro ring-disk electrode probes for scanning electrochemical microscopy. *Electrochem Commun* 4:67–71. (b) Liljeroth, P., Johans, C., Slevin, C. J., Quinn, B. M., Kontturi, K. 2002. Disk-generation/ring-collection scanning electrochemical microscopy: Theory and application. *Anal Chem* 74:1972–1978.
39. Nann, T., Heinze, J. 2003. Simulation in electrochemistry using the finite element method. Part 2: Scanning electrochemical microscopy. *Electrochim Acta* 48:3975–3980.
40. Saito, Y. 1968. Theoretical study on the diffusion current at the stationary electrodes of circular and narrow band types. *Rev Polarogr* 15:177–187.

41. (a) Scott, E. R., White, H. S., Phipps, J. B. 1993. Iontophoretic transport through porous membranes using scanning electrochemical microscopy: Application to in vitro studies of ion fluxes through skin. *Anal Chem* 65:1537–1545. (b) Bath, B. D., Lee, R. D., White, H. S., Scott, E. R. 1998. Imaging molecular transport in porous membranes. Observation and analysis of electroosmotic flow in individual pores using the scanning electrochemical microscope. *Anal Chem* 70:1047–1058.
42. Bond, A. M., Oldham, K. B., Zoski, C. G. 1988. Theory of electrochemical processes at an inlaid disc microelectrode under steady-state conditions. *J Electroanal Chem* 245:71–104.
43. Horrocks, B. R., Mirkin, M. V., Pierce, D. T., Bard, A. J., Nagy, G., Toth, K. 1993. Scanning electrochemical microscopy. 19. Ion-selective potentiometric microscopy. *Anal Chem* 65:1213–1224.
44. Abramowitz, M., Stegun, I., Eds. 1965. *Handbook of Mathematical Functions*, Dover, New York.
45. Fleischmann, M., Pons, S. 1988. The behavior of microdisk and microring electrodes. Mass transport to the disk in the unsteady state: Chronopotentiometry. *J Electroanal Chem* 250:257–267.
46. (a) Troise Frank, M. H., Denuault, G. 1993. Scanning electrochemical microscopy: Probing the ingress and egress of protons from a polyaniline film. *J Electroanal Chem* 354:331–339. (b) Troise Frank, M. H., Denuault, G. 1994. Scanning electrochemical microscope (SECM) study of the relationship between proton concentration and electronic charge as a function of ionic strength during the oxidation of polyaniline. *J Electroanal Chem* 379:399–406.
47. Horrocks, B. R., Mirkin, M. V. 1998. Evidence for a potential-dependent reversible inactivation of urease adsorbed on a gold electrode. *J Chem Soc Faraday Trans* 94:1115–1118.
48. (a) Engstrom, R. C., Weber, M., Wunder, D. J., Burgess, R., Winquist, S. 1986. Measurements within the diffusion layer using a microelectrode probe. *Anal Chem* 58:844–848. (b) Engstrom, R. C., Meaney, T., Tople, R., Wightman, R. M. 1987. Spatiotemporal description of the diffusion layer with a microelectrode probe. *Anal Chem* 59:2005–2010. (c) Engstrom, R. C., Wightman, R. M., Kristensen, E. W. 1988. Diffusional distortion in the monitoring of dynamic events. *Anal Chem* 60:652–656.
49. Bard, A. J., Faulkner, L. R. 1980. *Electrochemical Methods, Fundamentals and Applications*, Wiley, New York.
50. Mirkin, M. V., Arca, M., Bard, A. J. 1993. Scanning electrochemical microscopy. 22. Examination of thin solid silver(I) bromide films: Ion diffusion in the film and heterogeneous kinetics at the film/solution interface. *J Phys Chem* 97:10790–10795.
51. Shao, Y., Mirkin, M. V., Fish, G., Kokotov, S., Palanker, D., Lewis, A. 1997. Nanometer-sized electrochemical sensors. *Anal Chem* 69:1627–1634.
52. Martin, R. D., Unwin, P. R. 1998. Theory and experiment for the substrate generation/tip collection mode of the scanning electrochemical microscope: Application as an approach for measuring the diffusion coefficient ratio of a redox couple. *Anal Chem* 70:76–84.
53. Sanchez-Sanchez, C. M., Rodriguez-Lopez, J., Bard, A. J., 2008. Scanning electrochemical microscopy. 60. Quantitative calibration of the SECM substrate generation/tip collection mode and its use for the study of the oxygen reduction mechanism. *Anal Chem* 80:3254–3260.
54. Zhou, F., Unwin, P. R., Bard, A. J. 1992. Scanning electrochemical microscopy. 16. Study of second-order homogeneous chemical reactions via the feedback and generation/collection modes. *J Phys Chem* 96:4917–4924.
55. Lee, C., Kwak, J., Anson, F. C. 1991. Application of scanning electrochemical microscopy to generation/collection experiments with high collection efficiency. *Anal Chem* 63:1501–1504.
56. Fernández, J. L., Bard, A. J. 2004. Scanning electrochemical microscopy 50. Kinetic study of electrode reactions by the tip generation–substrate collection mode. *Anal Chem* 76:2281–2289.
57. Demaille, C., Unwin, P. R., Bard, A. J. 1996. Scanning electrochemical microscopy. 33. Application to the study of ECE/DISP reactions. *J Phys Chem* 100:14137–14143.
58. Treichel, D. A., Mirkin, M. V., Bard, A. J. 1994. Scanning electrochemical microscopy. 27. Application of a simplified treatment of an irreversible homogeneous reaction following electron transfer to the oxidative dimerization of 4-nitrophenolate in acetonitrile. *J Phys Chem* 98:5751–5757.
59. Martin, R. D., Unwin, P. R. 1998. Scanning electrochemical microscopy. Kinetics of chemical reactions following electron-transfer measured with the substrate-generation–tip-collection mode. *J Chem Soc Faraday Trans* 94:753–759.
60. Unwin, P. R., Bard, A. J. 1992. Ultramicroelectrode voltammetry in a drop of solution: A new approach to the measurement of adsorption isotherms at the solid–liquid interface. *Anal Chem* 64:113–119.
61. Unwin, P. R., Bard, A. J. 1992. Scanning electrochemical microscopy. 14. Scanning electrochemical microscope induced desorption: A new technique for the measurement of adsorption/desorption kinetics and surface diffusion rates at the solid/liquid interface. *J Phys Chem* 96:5035–5045.

62. (a) Zhang, J., Slevin, C. J., Morton, C., Scott, P., Walton, D. J., Unwin, P. R. 2001. New approach for measuring lateral diffusion in Langmuir monolayers by scanning electrochemical microscopy (SECM): Theory and application. *J Phys Chem B* 105:11120–11130. (b) Zhang, J., Unwin, P. R. 2002. Scanning electrochemical microscopy (SECM) feedback approach for measuring lateral proton diffusion in Langmuir monolayers: Theory and application. *Phys Chem Chem Phys* 4:3814–3819.
63. Lie, L. H., Mirkin, M. V., Hakkarainen, S., Houlton, A., Horrocks, B. R. 2007. Lateral charge transport in metal complex-DNA films synthesized on Si(111) surfaces. *J Electroanal Chem* 603:67–80.
64. Liljeroth, P., Vanmaekelbergh, D., Ruiz, V., Kontturi, K., Jiang, H., Kauppinen, E., Quinn, B. M. 2004. Electron transport in two-dimensional arrays of gold nanocrystals investigated by scanning electrochemical microscopy. *J Am Chem Soc* 126:7126–7132.
65. (a) Zhang, J., Barker, A. L., Mandler, D., Unwin, P. R. 2003. Effect of surface pressure on the insulator to metal transition of a Langmuir polyaniline monolayer. *J Am Chem Soc* 125:9312–9313. (b) Whitworth, A. L., Mandler, D., Unwin, P. R. 2005. Theory of scanning electrochemical microscopy (SECM) as a probe of surface conductivity. *Phys Chem Chem Phys* 7:356–365.
66. (a) Macpherson, J. V., Unwin, P. R. 1994. A novel approach to the study of dissolution kinetics using the scanning electrochemical microscope: Theory and application to copper sulfate pentahydrate dissolution in aqueous sulfuric acid solutions. *J Phys Chem* 98:1704–1713. (b) Macpherson, J. V., Unwin, P. R. 1994. Oscillatory dissolution of an ionic single crystal surface observed with the scanning electrochemical microscope. *J Phys Chem* 98:11764–11770. (c) Macpherson, J. V., Unwin, P. R. 1995. Scanning electrochemical microscope induced dissolution: Rate law and reaction rate imaging for dissolution of the (010) face of potassium ferrocyanide trihydrate in nonstoichiometric aqueous solutions of the lattice ions. *J Phys Chem* 99:3338–3351. (d) Macpherson, J. V., Unwin, P. R. 1995. Scanning electrochemical microscopy as a probe of silver chloride dissolution kinetics in aqueous solutions. *J Phys Chem* 99:14824–14831. (e) Macpherson, J. V., Unwin, P. R. 1996. Scanning electrochemical microscope-induced dissolution: Theory and experiment for silver chloride dissolution kinetics in aqueous solution without supporting electrolyte. *J Phys Chem* 100:19475–19483.
67. (a) Tsionsky, M., Bard, A. J., Mirkin, M. V. 1996. Scanning electrochemical microscopy. 34. Potential dependence of the electron-transfer rate and film formation at the liquid/liquid interface. *J Phys Chem* 100:17881–17888. (b) Tsionsky, M., Bard, A. J., Mirkin, M. V. 1997. Long-range electron transfer through a lipid monolayer at the liquid/liquid interface. *J Am Chem Soc* 119:10785–10792.
68. (a) Slevin, C. J., Macpherson, J. V., Unwin, P. R. 1997. Measurement of local reactivity at liquid/solid, liquid/liquid, and liquid/gas interfaces with the scanning electrochemical microscope: Principles, theory, and applications of the double potential step chronoamperometric mode. *J Phys Chem B* 101:10851–10859. (b) Barker, A. L., Macpherson, J. V., Slevin, C. J., Unwin, P. R. 1998. Scanning electrochemical microscopy (SECM) as a probe of transfer processes in two-phase systems: Theory and experimental applications of SECM-induced transfer with arbitrary partition coefficients, diffusion coefficients, and interfacial kinetics. *J Phys Chem B* 102:1586–1598.
69. Shao, Y., Mirkin, M. V. 1997. Scanning electrochemical microscopy (SECM) of facilitated ion transfer at the liquid/liquid interface. *J Electroanal Chem* 439:137–143.
70. Barker, A. L., Unwin, P. R. 2001. Measurement of solute partitioning across liquid/liquid interfaces using scanning electrochemical microscopy-double potential step chronoamperometry (SECM-DPSC): Principles, theory, and application to ferrocenium ion transfer across the 1,2-dichloroethane/aqueous interface. *J Phys Chem B* 105:12019–12031.
71. (a) Laforge, F. O., Kakiuchi, T., Shigematsu, F., Mirkin, M. V. 2004. Comparative study of electron transfer reactions at the ionic liquid/water and organic/water interfaces. *J Am Chem Soc* 126:15380–15381. (b) Laforge, F. O., Kakiuchi, T., Shigematsu, F., Mirkin, M. V. 2006. SECM study of solute partitioning and electron transfer at the ionic liquid/water interface. *Langmuir* 22:10705–10710.
72. Pierce, D. T., Unwin, P. R., Bard, A. J. 1992. Scanning electrochemical microscopy. 17. Studies of enzyme mediator kinetics for membrane-immobilized and surface-immobilized glucose-oxidase. *Anal Chem* 64:1795–1804.
73. Burchardt, M., Traeuble, M., Wittstock, G. 2009. Digital simulation of scanning electrochemical microscopy approach curves to enzyme films with Michaelis–Menten kinetics. *Anal Chem* 81:4857–4863.
74. Lefrou, C., Hapiot, P., Cornut, R. 2009. Enzyme–mediator kinetics studies with SECM: Numerical results and procedures to determine kinetics constants. *J Electroanal Chem* 633:221–227.
75. (a) Fulian, Q., Fisher, A. C., Denuault, G. 1999. Applications of the boundary-element method in electrochemistry—Scanning electrochemical microscopy. *J Phys Chem B* 103:4387–4392. (b) Fulian, Q., Fisher, A. C., Denault, G. 1999. Applications of the boundary-element method in electrochemistry—Scanning electrochemical microscopy, Part 2. *J Phys Chem B* 103:4393–4398.

76. (a) Sklyar, O., Wittstock, G. 2002. Numerical simulations of complex nonsymmetrical 3D systems for scanning electrochemical microscopy using the boundary element method. *J Phys Chem B* 106:7499–7508. (b) Sklyar, O., Träuble, M., Zhao, C., Wittstock, G. 2006. Modeling steady-state experiments with a scanning electrochemical microscope involving several independent diffusing species using the boundary element method. *J Phys Chem B* 110:15869–15877. (c) Sklyar, O., Kueng, A., Kranz, C., Mizaikoff, B., Lugstein, A., Bertagnolli, E., Wittscock, G. 2005. Numerical simulation of scanning electrochemical microscopy experiments with frame-shaped integrated atomic force microscopy–SECM probes using the boundary element method. *Anal Chem* 77:764–771.
77. *COMSOL Multiphysics User's Guide*, Copyright 1998–2010, COMSOL AB.

6 Heterogeneous Electron Transfer Reactions

Shigeru Amemiya

CONTENTS

6.1 Introduction 127
6.2 SECM Tip Voltammetry of Heterogeneous ET Reactions 128
6.2.1 Principle 128
6.2.2 Applications 130
6.2.2.1 Nanotip Voltammetry of Rapid ET Reactions 130
6.2.2.2 Room Temperature Ionic Liquid 131
6.3 SECM of Heterogeneous ET Reactions at Various Substrates 132
6.3.1 Principle 132
6.3.1.1 Feedback and SG/TC Modes 132
6.3.1.2 Irreversible Substrate Reactions 133
6.3.1.3 Reversible and Quasireversible Substrate Reactions 135
6.3.1.4 Unbiased Substrates 136
6.3.1.5 Reaction-Rate Imaging 137
6.3.2 Applications 139
6.3.2.1 Single-Walled Carbon Nanotube Network 139
6.3.2.2 Individual One-Dimensional Nanostructures 141
6.3.2.3 Boron-Doped Diamond Electrode 144
6.3.2.4 Monolayer-Mediated ET 146
6.3.2.5 Electroactive Polymer Film 149
6.4 Conclusions and Future Perspectives 153
Acknowledgments 153
References 153

6.1 INTRODUCTION

Scanning electrochemical microscopy (SECM) is a powerful electrochemical tool to investigate heterogeneous electron transfer (ET) reactions at interfaces. The major advantages of SECM against other electrochemical methods reside in its high time and spatial resolutions as well as the wide range of its applicability to various interfaces. Subsequently, SECM enables more advanced assessment of ET theories and mechanisms and more detailed evaluation of diverse electroactive interfaces. For instance, the extremely rapid kinetics of a heterogeneous ET reaction can be probed without a diffusion limitation under steady states by employing high mass transport conditions achieved in the SECM-based thin-layer cell with the short separation distance, d, between the substrate and the inlaid disk ultramicroelectrode (UME) tip (Figure 6.1). Moreover, the laterally heterogeneous electroactivity of the substrate surface can be probed by scanning the tip to obtain an electrochemical image with high spatial resolution determined by the small tip radius, a. In standard SECM kinetic

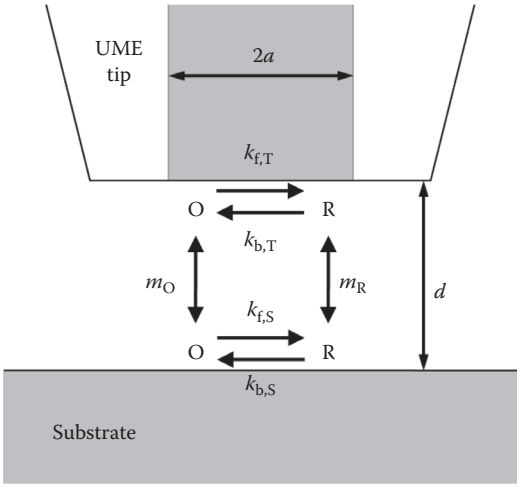


FIGURE 6.1 Schematic diagram of a SECM-based thin-layer cell with heterogeneous ET reactions at the tip and substrate electrodes coupled by the mass transport of redox mediators.

measurements, both tip and substrate are biased externally using a bipotentiostat to independently control ET rates at the respective interfaces. Alternatively, a SECM tip can drive and monitor a heterogeneous ET reaction at a substrate without a bias from an external circuit to characterize an electroactive substrate material in a pristine state or on an insulating support.

This chapter is focused on recent progresses in the SECM studies of heterogeneous ET reactions at various interfaces. The modes of SECM operation, that is, feedback and substrate generation/tip collection (SG/TC) modes, are briefly introduced for tip voltammetry of outer-sphere ET reactions at noble metal tips in aqueous, organic, and ionic liquid media. The same operation modes serve also as the principle of SECM approach curve and imaging experiments to probe heterogeneous ET reactions at advanced (nano)materials, molecular monolayers, and polymer films. The major experimental goal of these SECM studies is to determine rate constants for a heterogeneous ET reaction (e.g., $O + e \rightleftharpoons R$ in Figure 6.1) either at the tip or substrate, $k_{f,T}$ and $k_{b,T}$ or $k_{f,S}$ and $k_{b,S}$, respectively, by the quantitative analysis of the tip current (or occasionally the substrate current). The tip and substrate reactions are coupled by the efficient mass transport of redox mediators (O and R) in the narrow tip–substrate gap. The corresponding mass transport rates, m_O and m_R, respectively, are well defined and maximized in quantitative kinetic measurements by employing an inlaid disk UME as a tip.

6.2 SECM TIP VOLTAMMETRY OF HETEROGENEOUS ET REACTIONS

6.2.1 Principle

The experimental assessment of the ET theory [1] has been the central theme in the SECM study of tip reactions. Kinetic parameters for a heterogeneous ET reaction at the UME tip are determined by tip voltammetry. The tip reaction of a redox mediator that is initially present in the bulk solution (i.e., the oxidized form of a redox couple, O, in Figure 6.2) is monitored as tip current at various tip potentials to obtain a steady-state voltammogram. In tip voltammetry based on the total positive feedback current (Figure 6.2a), the tip-generated species, R, is electrolyzed at the surface of an electroactive substrate so that the original mediator is regenerated at a diffusion-limited rate. When the tip is positioned within a tip diameter away from the substrate, the redox molecules efficiently diffuse between the tip–substrate gap to enhance the tip current in comparison to its

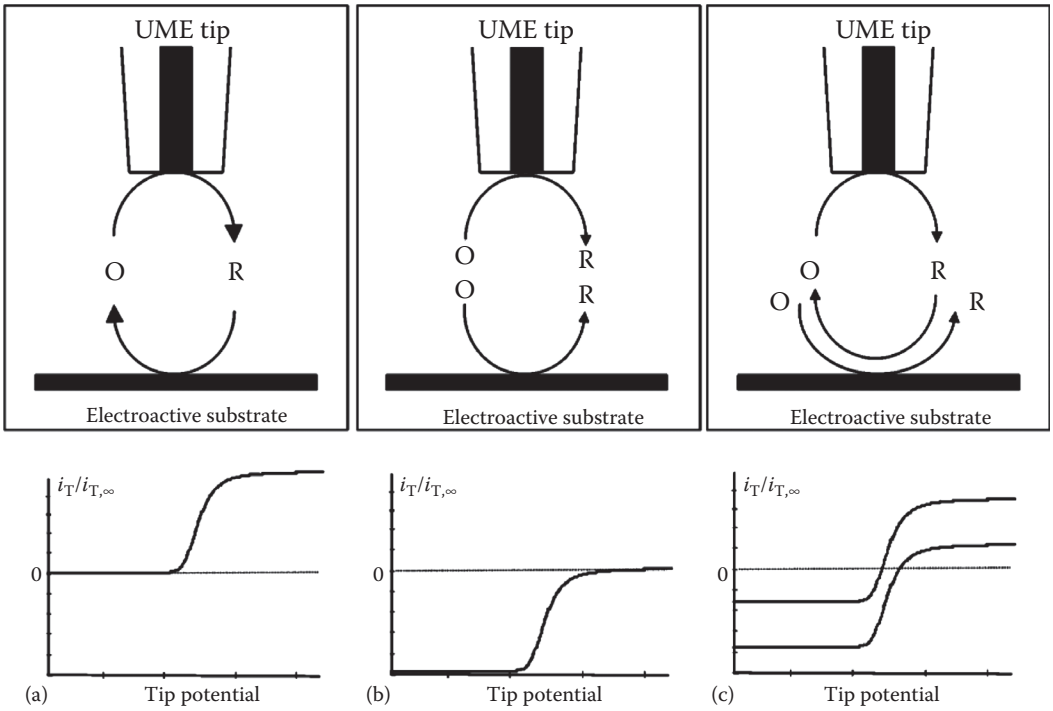


FIGURE 6.2 Schematic diagram of different SECM cases and the resulting tip voltammograms. (a) total positive feedback (tpf), (b) total shielding (ts), and (c) partial positive feedback–partial shielding (pf–ps). (Reprinted with permission from Zoski, C.G., Luman, C.R., Fernandez, J.L., and Bard, A.J., Scanning electrochemical microscopy. 57. SECM tip voltammetry at different substrate potentials under quasi-steady-state and steady-state conditions, *Anal. Chem*., 79, 4957–4966, 2007. Copyright 2007 American Chemical Society.)

steady-state value in the bulk solution, $i_{T,\infty}$. A mass transport rate for a redox mediator increases from $\sim D/a$ in the bulk solution to $\sim D/d$ with the narrow tip–substrate gap (D is the diffusion coefficient of the redox mediator) to render the tip current more sensitive to the kinetics of the tip reaction. When the tip reaction is quasireversible and also follows the classical Butler–Volmer model [2], both thermodynamic and kinetic parameters for the tip reaction, that is, the formal potential of a redox couple, $E^{0'}$, standard rate constant, k^0, and transfer coefficient, α, are determined from a set of the half-wave potential and two quartile potentials of the corresponding tip voltammogram [3] or more precisely by fitting the whole voltammogram with an approximate formula obtained from simulation results [4]. For instance, tip voltammetry was employed in the recent study of ferrocene methanol (FcMeOH) at a Pt tip in dimethyl sulfoxide–water mixtures to find the good linear dependences of $\ln k^0$ on the logarithms of solvent viscosity and longitudinal relaxation time [5].

Tip voltammetry was generalized by considering the effect of substrate potential on the tip current [6]. The total positive feedback current is obtained when the substrate potential is sufficiently anodic for the diffusion-limited regeneration of an original mediator, O (Figure 6.2a). In contrast, the substrate potential can be cathodic enough to completely deplete the original mediator from the tip–substrate gap (Figure 6.2b). Under this total shielding condition, no current response to the original mediator is obtained at the tip while a voltammetric tip response to the substrate-generated species, R, is seen at anodic tip potentials. This anodic tip response is rather based on the SG/TC mode. Intermediate substrate potentials result in a series of tip voltammograms based on partial positive feedback/partial shielding effects (Figure 6.2c). Interestingly, both experiment and numerical simulation with a reversible substrate reaction demonstrated that a quasi-steady-state or a

steady-state tip voltammogram can be obtained even under transient shielding conditions at a macroscopic substrate after the substrate is held at the corresponding potential for a sufficient length of time (for a quiet time of ~5 s under typical experimental conditions). Reversible tip voltammograms thus obtained at various substrate potentials can be analyzed numerically or by using approximate equations to give the formal potential of a redox couple and its diffusion coefficients in both oxidized and reduced forms. Also, tip voltammetry under shielding conditions is potentially useful for obtaining information about the short-lived intermediate product of a substrate reaction.

6.2.2 Applications

6.2.2.1 Nanotip Voltammetry of Rapid ET Reactions

The kinetics of rapid ET reactions at nanometer-sized tips was investigated voltammetrically under total positive feedback conditions to check the predictions of the ET theory. Disk-type, polished Pt nanoelectrodes with 3.7–400 nm radii were developed to reproducibly obtain well-defined tip voltammograms for various redox mediators with rapid kinetics such as FcMeOH (Figure 6.3) [4]. Both k^0 and α values (Table 6.1 [7]) determined from quasireversible nanotip voltammograms were independent of the tip–substrate distance and, subsequently, mass transport rates, thereby confirming the reliability of the kinetic measurements. Most strikingly, an extremely large k^0 value of 17.0 ± 0.9 cm/s was obtained for the $Ru(NH_3)_6^{3+/2+}$ couple while the upper limit of the k^0 value measurable by nanotip voltammetry was estimated to be much higher (up to ~200 cm/s). Such large electrochemical rate constants are expected for simple outer-sphere ET reactions. Nevertheless, the

TABLE 6.1
Electrochemical Kinetic Parameters, α and k^0, as Determined by Nanotip Voltammetry, Self-Exchange Rate Constants, k_{ex}, and Calculated Standard Rate Constants, k^0_{calc}

Mediator	Electrode	Solvent	α	k^0 (cm/s)	k_{ex} (M^{-1} s^{-1})	k^0_{calc} (cm/s)[a]
$Ru(NH_3)_6^{3+}$	Pt[b]	Water[c]	0.45 ± 0.03	17 ± 0.9	800–4300	0.9–2.1
	Au[d]	Water[c]	0.45 ± 0.09	13.5 ± 2		
	Pt[d]	Water[e]	0.40 ± 0.05	11.9 ± 0.5		
	Au[d]	Water[e]	0.42 ± 0.03	9.3 ± 0.4		
Ferrocene	Pt[b]	Acetonitrile	0.47 ± 0.02	8.4 ± 0.2	9×10^6	95
	Au[d]	Acetonitrile	0.44 ± 0.03	8.0 ± 0.5		
FcMeOH	Pt[b]	Water	0.42 ± 0.03	6.8 ± 0.7		
	Au[d]	Water	0.42 ± 0.06	8 ± 1		
TCNQ[f]	Pt[b]	Acetonitrile	0.42 ± 0.02	1.1 ± 0.4	4×10^9	2×10^3
TTF[g]	Pt[d]	1,2-DCE[h]	0.375 ± 0.02	8.8 ± 0.4	6.6×10^{9}[i]	2.6×10^3
	Au[d]	1,2-DCE[h]	0.395 ± 0.02	9.0 ± 0.4		

[a] Calculated using Equation 6.1.
[b] Data from Ref. [4].
[c] 0.5 M KCl.
[d] Data from Ref. [9].
[e] 1 M KF.
[f] 7,7′,8,8′-Tetracyanoquinodimethane.
[g] Tetrathiafulvalene.
[h] 1,2-Dichloroethane.
[i] Data from Ref. [7].

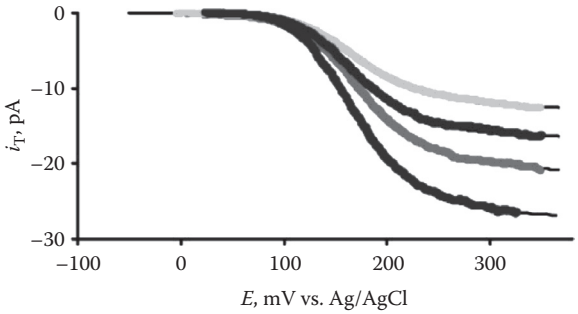


FIGURE 6.3 Experimental (symbols) and theoretical (solid lines) steady-state voltammograms of 1 mM FcMeOH obtained at different separation distances between the 36 nm Pt tip and Au substrate. $d = \infty$, 54, 29, and 18 nm from the top to the bottom. Scan rate, 50 mV/s. (Reprinted with permission from Sun, P. and Mirkin, M.V., Kinetics of electron-transfer reactions at nanoelectrodes, *Anal. Chem*., 78, 6526–6534, 2006. Copyright 2006 American Chemical Society.)

comparison of the heterogeneous ET rate constants with the corresponding self-exchange rate constants, k_{ex}, did not show the simple correlation predicted by the Marcus theory [8] as

$$k^0 = Z_{het}\sqrt{k_{ex}/Z_{bi}} \tag{6.1}$$

where $Z_{het} \sim 10^4$ cm/s and $Z_{bi} \sim 10^{11}$ M^{-1} s^{-1} are heterogeneous and bimolecular collision frequencies, respectively (see Table 6.1 for experimental and calculated k^0 values).

Tip voltammetrically was also applied to the feedback study of rapid ET reactions at polished Au nanotips with disk radii of 43–153 nm (Table 6.1) [9]. The kinetic parameters for FcMeOH, ferrocene, and tetrathiafulvalene (TTF) at Pt and Au nanotips were independent of electrode material. In contrast, a smaller k^0 value of 13.5 ± 2 cm/s was obtained for the $Ru(NH_3)_6^{3+/2+}$ couple using Au nanotips. The metal-dependent k^0 values suggest some degree of nonadiabaticity of this ET reaction, which has been considered as an adiabatic reaction [10].

6.2.2.2 Room Temperature Ionic Liquid

Room temperature ionic liquid (RTIL) has received increasing attention as an electrolyte material with unique physicochemical features [11]. The kinetics of heterogeneous ET reactions in RTIL media was investigated by tip voltammetry under total positive feedback conditions. A series of steady-state voltammograms at a micrometer-sized Pt tip with various tip–substrate distances was measured for a ferrocene-modified RTIL as a redox mediator in a solvent-free RTIL (Figure 6.4a) to observe a Butler–Volmer type response with $\alpha = 0.56 \pm 0.08$ and $k^0 = 7.6 \pm 0.85 \times 10^{-3}$ cm/s [12]. Moreover, tip voltammetry of ferrocene in the RTILs of various 1-alkyl-3-imidazolium cations revealed that k^0 decreases as RTIL viscosity increases (Figure 6.4b) [13]. These k^0 values in the RTILs are much smaller than the corresponding value of 8.4 ± 0.2 cm/s for ferrocene in less viscous acetonitrile as measured by nanotip voltammetry (Table 6.1) [4]. The dependence of ET kinetics on RTIL viscosity is qualitatively consistent with the prediction of the ET theory. Noticeably, the viscosity effect in the solvent-free RTIL media is partially due to interactions of redox mediators with purely ionic environment rather than with electrically neutral polar solvent environment. It was suggested that ET in the highly viscous RTILs may be controlled by the slow diffusive motion of counter ions that are ion paired with charged redox mediators [14].

The aforementioned SECM studies of RTILs [12,13] also demonstrated that tip voltammograms and approach curves can be obtained under steady states despite slow mediator diffusion [14,15] and significant convection caused by tip movement [13] in highly viscous RTIL media. Interestingly,

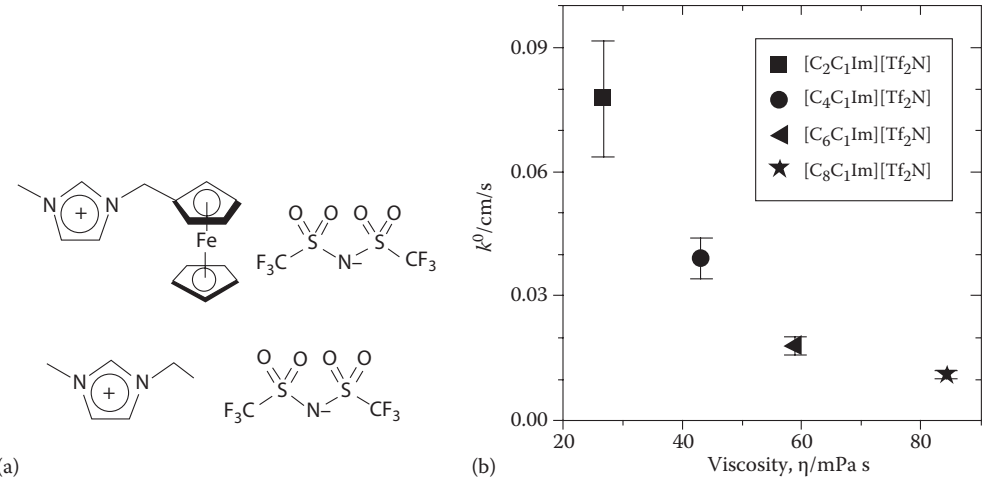


FIGURE 6.4 (a) Structures of the bis(trifluoromethylsulfonyl)imide (Tf_2N)-based RTILs of 1-ferrocenylmethyl-3-methylimidazolium (top) and 1-ethyl-3-methylimidazolium (C_nC_1Im with $n=2$) (bottom). (b) Plot of k^0 vs. the viscosity of [C_nC_1Im][Tf_2N] RTILs ($n=2$, 4, 6, and 8). (Reprinted with permission from Lovelock, K.R.J., Cowling, F.N., Taylor, A.W., Licence, P., and Walsh, D.A., Effect of viscosity on steady-state voltammetry and scanning electrochemical microscopy in room temperature ionic liquids, *J. Phys. Chem. B*, 114, 4442–4450, 2010. Copyright 2010 American Chemical Society.)

steady-state SECM images were also obtained in RTIL using nanometer-sized tips [16]. In addition, a chronoamperometric tip response in the total positive feedback mode was studied to determine the unequal diffusion coefficients of the oxidized and reduced forms of redox couples in RTILs, for example, the $O_2/O_2^{\bullet-}$ couple [17,18] and a series of nitro-derivative compounds [19]. The smaller diffusion coefficients of the radical anions generated from neutral oxidants were ascribed to electrostatic interactions with RTIL cations.

6.3 SECM OF HETEROGENEOUS ET REACTIONS AT VARIOUS SUBSTRATES

6.3.1 Principle

6.3.1.1 Feedback and SG/TC Modes

A heterogeneous ET reaction at the substrate surface can be probed by SECM using either feedback or SG/TC mode (Figure 6.5) [20]. A common mode, however, is the feedback mode where the amperometric tip current based on the diffusion-limited electrolysis of an original mediator ($O + e \rightarrow R$) is measured in the presence of an electroactive substrate at close proximity. In the typical feedback measurement of a substrate reaction, the substrate potential is set to drive electrochemically irreversible mediator regeneration ($R \rightarrow O + e$) at the local surface of the substrate under the tip without any electrolysis at the exterior substrate surface (Figure 6.5a). This irreversible condition has been traditionally employed to ensure the advantageous steady-state measurement of the feedback tip current [21]. Importantly, such a positive feedback effect is expected also from an unbiased electroactive substrate, where mediator regeneration is driven by its reverse reaction ($O + e \rightarrow R$) at the exterior surface (Figure 6.5b). The opposite reactions at the two different regions of the substrate surface are coupled by lateral electron transport along the substrate so that any of these three processes can limit the feedback effect from an unbiased electroactive substrate.

The SG/TC mode of SECM requires the external bias of an electroactive substrate to initiate the substrate reaction of the original mediator, O. The species thus generated at the substrate, R, is

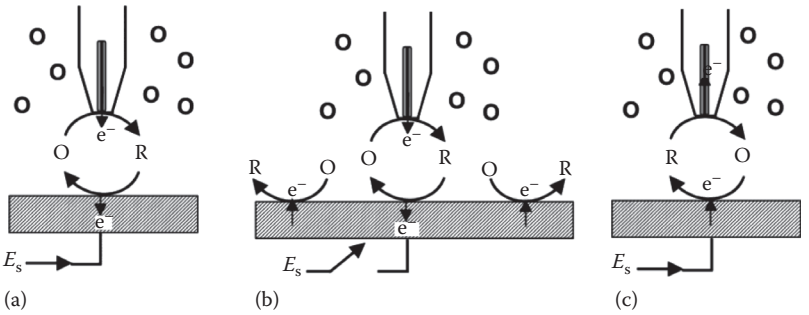


FIGURE 6.5 SECM feedback mode at (a) biased and (b) unbiased substrates and (c) SG/TC mode at a biased substrate. (Reprinted with permission from Zoski, C.G., Simjee, N., Guenat, O., and Koudelka-Hep, M., Addressable microelectrode arrays: Characterization by imaging with scanning electrochemical microscopy, *Anal. Chem.*, 76, 62–72, 2004. Copyright 2004 American Chemical Society.)

amperometrically detected at the tip at a diffusion-limited rate. The tip current in the SG/TC mode is also enhanced at short tip–substrate distances by the efficient diffusion of the substrate-generated species to the tip across the narrow gap (Figure 6.5c). This mechanism, however, has not been used in traditional SG/TC experiments, where a tip is positioned far enough from the substrate to amperometrically monitor the concentration profile of the substrate-generated species without the interaction of the tip diffusion layer with the substrate surface [22].

6.3.1.2 Irreversible Substrate Reactions

Typically, the kinetics of a heterogeneous ET reaction at a substrate is determined from an approach curve as measured under an electrochemically irreversible condition at the substrate. For instance, this experimental protocol was recently employed to investigate the effect of mechanical stress on the ET kinetics at a stainless steel substrate using $Ru(NH_3)_6^{3+}$ as a redox mediator [23]. A more positive approach curve at a more anodic substrate potential (Figure 6.6a) corresponds to faster mediator regeneration at the substrate surface. Potential-dependent rate constants for the anodic substrate reaction, k_b (equivalent to $k_{b,S}$ in Figure 6.1), were determined by fitting the experimental approach curves with an approximate formula based on the results of the numerical simulation of totally irreversible substrate reactions [24]. The linear Tafel plot of k_b vs. E_S (Figure 6.6b) confirms the irreversible conditions expected from the Butler–Volmer relationship, thereby yielding α (0.15) from the slope and k^0 (~10^{-3} cm/s) from the intercept at $E_S = E^{0\prime}$. Interestingly, k^0 decreased with increasing tensile stress applied to the stainless steel sample up to 27 MPa while α remained essentially constant. The rather small α and k^0 values, which contribute to the maintenance of the irreversible conditions over the wide range of the substrate potential, were ascribed to the presence of a passive oxide film on the substrate surface. It should be noted that the determination of an effective rate constant, k_{eff} (= $k_{f,S}$ or $k_{b,S}$ in Figure 6.1), from an irreversible approach curve does not require any kinetic model, for example, the Butler–Volmer model, which may not be valid for some substrate reactions [25]. Various microscopic models have been successfully applied to interpret the dependence of k_{eff} on substrate properties and experimental conditions (see Section 6.3.2).

An electrochemically irreversible condition at a substrate electrode necessitates setting the substrate potential far from the formal potential of a redox couple and, subsequently, limits the kinetic study of a rapid substrate reaction. These issues were seen in the study of catalytic H_2 oxidation at a macroscopic Pt substrate with H^+ as a redox mediator [26] (see Chapter 16 for the SECM study of electrocatalysis). The H_2 oxidation rate, k, increased with the increase of substrate potential in the range of $-0.4\,V < E_S < -0.3\,V$ to obtain $\alpha = 0.5$ and $k^0 = 0.42$ cm/s from the linear Tafel plot in this potential range (Figure 6.7). This rather moderate k^0 value is the largest value that has

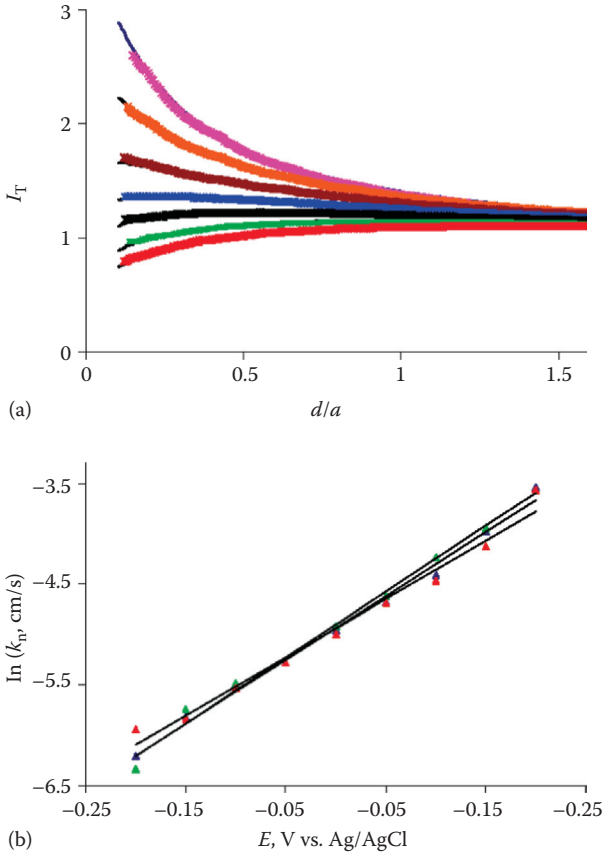


FIGURE 6.6 (a) Approach curves to a T316 stainless steel sample as obtained with an 11.5 μm radius Pt tip in 1 mM $Ru(NH_3)_6Cl_3$ and 0.2 M KNO_3. The substrate potentials (mV vs. Ag/AgCl) are 200 (pink), 150 (orange), 100 (brown), 50 (blue), 0 (black), −50 (green), and −150 (red). Symbols are experimental data; solid lines represent the theory for finite substrate kinetics. The tip current is normalized by $i_{T,\infty} = 3.58$ nA. (b) Tafel plots obtained from three different families of approach curves. (Reprinted with permission from Sun, P., Liu, Z., Yu, H.H., and Mirkin, M.V., Effect of mechanical stress on the kinetics of heterogeneous electron transfer, *Langmuir*, 24, 9941–9944, 2008. Copyright 2008 American Chemical Society.)

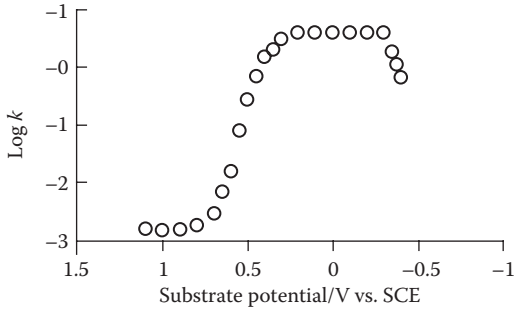


FIGURE 6.7 Heterogeneous reaction rate constant, k, of hydrogen oxidation at a Pt substrate with different potentials in 0.01 M $HClO_4$ and 0.1 M $NaClO_4$. The k values were obtained by fitting the experimental approach curves with the theoretical ones. Approach speed, 3 μm/s. (Reprinted from Zhou, J., Zu, Y., Bard, A.J., *J Electroanal. Chem.* 491, 22, 2000, with permission from Elsevier.)

been determined for a substrate reaction by SECM so far. In fact, the kinetic effect was barely observed within the narrow range of the substrate potential, which is limited not only by diffusion at $E_S > -0.3$ V but also by transient proton reduction at the Pt substrate at $E_S < -0.4$ V. Shielding of the tip by the substrate under the latter condition results in the semitransient tip current (see Section 6.3.1.3). Noticeably, the H_2 oxidation was slowed at $E_S > 0.3$ V until the Pt substrate lost its electrocatalytic activity at $E_S > 0.7$ V, corresponding to the potential-dependent formation of a passive PtO layer on the substrate surface.

6.3.1.3 Reversible and Quasireversible Substrate Reactions

The feedback mode under shielding conditions was developed to investigate reversible and quasireversible ET reactions at substrates [27]. As discussed for tip voltammetry (Figure 6.2b and c), the shielding effect is observed when an original mediator, O, is depleted at the whole substrate surface ($O + e \rightleftharpoons R$) by setting the substrate potential around $E^{0\prime}$ while the original mediator is consumed at the tip at a diffusion-limited rate ($O + e \rightarrow R$). When the tip and substrate electrodes are far from each other, shielding of the tip by the substrate decreases the amperometric tip current below the value found over an insulator (Figure 6.8). In contrast, a positive feedback response becomes dominant as the tip approaches within the feedback distance from the electroactive substrate. The semitransient tip current is obtained with a macroscopic substrate under a shielding condition, where the linear concentration profile of the potentiostatically consumed original mediator changes during tip approach. Moreover, this concentration profile is affected by natural convection due to the long experimental time (~45 s) and also by the tip movement. Nevertheless, an approximate theory based on the diffusional transport of a redox mediator under shielding conditions fits reasonably well with

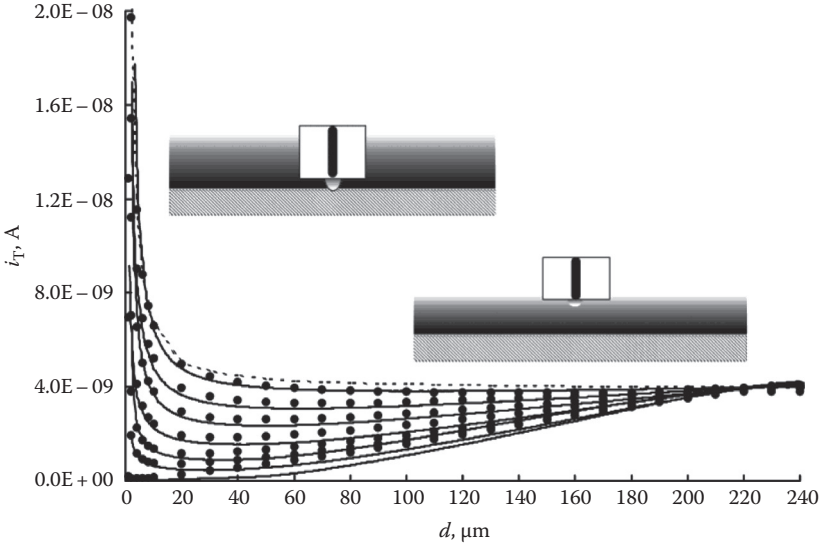


FIGURE 6.8 Experimental (solid lines) and theoretical (solid dots) approach curves for 1.1 mM FcMeOH solution in 0.1 M NaCl with a 12.5 μm radius Au tip at an approach speed of 6 μm/s to a 1 mm radius Au disk after a quiet time of 5 s and an initial distance of 250 μm. The tip potential was set at 0.4 V vs. Ag/AgCl. Values of $D = 7.1 \times 10^{-6}$ cm²/s and $E^0 = 0.218$ V vs. Ag/AgCl were used in calculating the theoretical approach curves. The dotted approach curve is that for a conductor. Substrate potentials (vs. Ag/AgCl) from top to bottom correspond to 0.160, 0.200, 0.220, 0.240, 0.260, 0.280, and 0.360 V. Inset shows the schematic diagram of tip and substrate diffusion layers at different separations, d: (top) substrate senses tip diffusion layer at a short separation; (bottom) tip enters substrate diffusion layer at a large separation. (Adapted from Zoski, C.G., Aguilar, J.C., and Bard, A.J., Scanning electrochemical microscopy. 46. Shielding effects on reversible and quasireversible reactions, *Anal. Chem.*, 75, 2959–2966, 2003. Copyright 2003 American Chemical Society.)

experimental approach curves as confirmed for the reversible reaction of FcMeOH at a Pt substrate in the wide range of the substrate potential around $E^{0\prime}$ (Figure 6.8). Such a reversible approach curve under a shielding condition gives the diffusion coefficient of a redox mediator without the knowledge of other experimental parameters. Also, shielding conditions were successfully applied to obtain a k^0 value of 0.20 cm/s for H_2 oxidation at an Ir substrate from the corresponding quasireversible semitransient approach curves. A similar k^0 value at an Ir substrate was also determined by employing the feedback mode under electrochemically irreversible conditions [28], thereby validating the shielding approach. It, however, was suggested that the kinetics of a fast ET reaction at a substrate should be measurable by moving the substrate potential to a shielding region to render the substrate reaction quasireversible when this reaction is diffusion-limited under electrochemically irreversible conditions.

The SG/TC mode can also be operated under reversible or quasireversible conditions for a substrate reaction at the substrate potential around $E^{0\prime}$. The resulting tip current is semitransient with a macroscopic substrate. In contrast, steady-state tip current is expected in the SG/TC mode when a UME serves as a substrate to develop the steady-state concentration profile of a substrate-generated species near the surface. In a steady-state SG/TC experiment, either tip or substrate current is monitored during the linear sweep of the substrate potential maintaining a constant tip–substrate distance. This voltammetric SG/TC approach was applied to the quantitative study of the H_2O_2 production in the oxygen reduction reaction at noble metal UMEs [29] and also the kinetic study of a UME based on a single-walled carbon nanotube (SWNT) network (see Section 6.3.2.1). The quantitative analysis of the steady-state current response requires the careful calibration of the corresponding collection efficiency, which depends on experimental geometry including the collector tip radius, the tip–substrate distance, and the size of the insulating glass sheath surrounding the collector tip with respect to the size of the UME substrate [29].

6.3.1.4 Unbiased Substrates

The feedback mode of SECM allows for the investigation of a substrate reaction under an unbiased condition, which is advantageous when the substrate cannot be conveniently connected to an external circuit or when the application of a potential causes an undesirable effect on the substrate. An unbiased condition is also useful for the characterization of a pristine electrode material and an electroactive film coated on an insulating support. An ET reaction at an unbiased conductive substrate, however, is practically diffusion limited when the area of the substrate is semi-infinitely large with respect to the tip area [30]. In this case, the sufficiently large exterior surface of the unbiased substrate is exposed to the bulk solution containing only an original mediator to set the open-circuit potential of the substrate for diffusion-limited mediator regeneration, thereby yielding the total positive feedback effect.

The feedback measurement of a heterogeneous ET reaction at an unbiased electroactive substrate can be performed under reversible or quasireversible conditions when the dimensions of the substrate are finite with respect to the tip size [31]. The resulting approach curve to the unbiased finite substrate can be even negative and becomes more negative with a larger tip. This theoretical prediction was confirmed experimentally for the reversible reaction of 1,1′-ferrocene dimethanol at a carbon fiber UME as an unbiased substrate by using Pt tips with comparable sizes (Figure 6.9a). Eventually, the totally negative feedback effect is expected from the unbiased conductive substrate at short tip–substrate distances when the outer radius of a tip, r_g, is large enough to completely screen the exterior surface of the substrate from the original mediator in the bulk solution. This screening effect was confirmed as the origin of the negative feedback tip current because a tip with a smaller outer radius, that is, $RG = r_g/a = 2.0$ in Figure 6.9b, gave a positive approach curve for this reversible redox couple. In contrast, the approach curve for $Co(phen)_3^{2+}$ (phen = 1,10-phenanthroline) with the identical experimental geometry is negative (Figure 6.9b), which indicates that the regeneration of this mediator at the unbiased carbon fiber substrate is kinetically limited. In fact, the experimental approach curve fits well with a simulated curve to

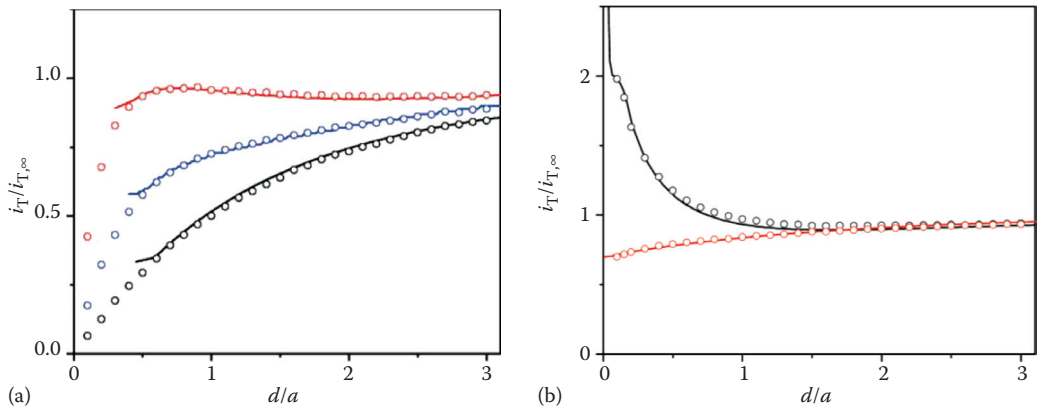


FIGURE 6.9 (a) Approach curves to an unbiased disk carbon fiber substrate as obtained using disk Pt probes with 1 mM 1,1′-ferrocene dimethanol in 0.1 M KCl. The solid lines and circle lines represent the experimental and theoretical curves, respectively. (a, b/a, RG) = (12.5 μm, 1.29, 10.0), (5.0 μm, 3.65, 8.0), and (3.0 μm, 5.61, 7.5) were used for the data in black, blue, and red, where b is the substrate radius. Tip potential, 0.4 V vs. Ag/AgCl. Probe scan rates, 1.5 μm/s for a = 12.5 μm, and 0.6 μm/s for a = 5.0 and 3.0 μm. (b) Approach curves to the unbiased carbon fiber substrate with 1 mM 1,1′-ferrocene dimethanol (black) and 2 mM $Co(phen)_3^{2+}$ (red) in 0.1 M KCl as obtained using a 5 μm radius Pt disk probe with RG = 2.0. Tip potential, 0.3 V vs. Ag/AgCl for $Co(phen)_3^{2+}$. (Reprinted with permission from Xiong, H., Guo, J., and Amemiya, S., Probing heterogeneous electron transfer at an unbiased conductor by scanning electrochemical microscopy in the feedback mode, *Anal. Chem*., 79, 2735–2744, 2007. Copyright 2007 American Chemical Society.)

obtain $k^0 = 3.7 \times 10^{-3}$ cm/s and $\alpha = 0.5$. Moreover, both experiment and simulation demonstrate that the open-circuit potential of the substrate was around $E^{0\prime}$ during tip approach, which confirms that the substrate reaction was quasireversible.

Quasireversible conditions were also achieved at a Au nanoband isolated on a SiO_2 surface to measure a much larger k^0 value of 0.19 cm/s for the $Ru(NH_3)_6^{3+/2+}$ couple [32]. In this case, the intrinsically faster substrate reaction became quasireversible because of more efficient mass transport of the redox mediators at the narrow band. The nanoscale dimensions of the 50 μm long Au nanoband were controlled by electron-beam lithography, that is, 100 nm in width and 47 nm in height. The geometry and dimensions of both nanoband and tip were quantitatively treated using three-dimensional finite element simulation to determine the intrinsic rate constant and open-circuit potential of the nanoband from an approach curve. The simulation confirmed quasireversible conditions, where the substrate potential, which was immeasurable directly, varied with the tip–substrate distance around $E^{0\prime}$.

6.3.1.5 Reaction-Rate Imaging

High-resolution SECM imaging in the feedback mode is useful for finding "hot spots" at the laterally heterogeneous surface of an electroactive substrate. This reaction-rate imaging, however, is challenging when a tip is scanned at a constant height over a substrate with a rough surface because the feedback tip current depends not only on the electroactivity of the substrate surface but also on the tip–substrate distance. Qualitatively, these two effects on the feedback tip current in the constant-height imaging mode can be investigated separately by externally adjusting the substrate potential. This approach was nicely demonstrated in constant-height imaging of the defect-rich surface of a glassy carbon electrode [33]. When the substrate potential is set for total positive feedback, the contrast of a constant-height image over a rough substrate surface represents only its topography without a kinetic effect. The topographic image of a glassy carbon electrode thus obtained using Fe^{2+} as a redox mediator (Figure 6.10a) shows surface defects as lighter regions around $X = Y = 125$ μm, where higher feedback tip current is due to shorter

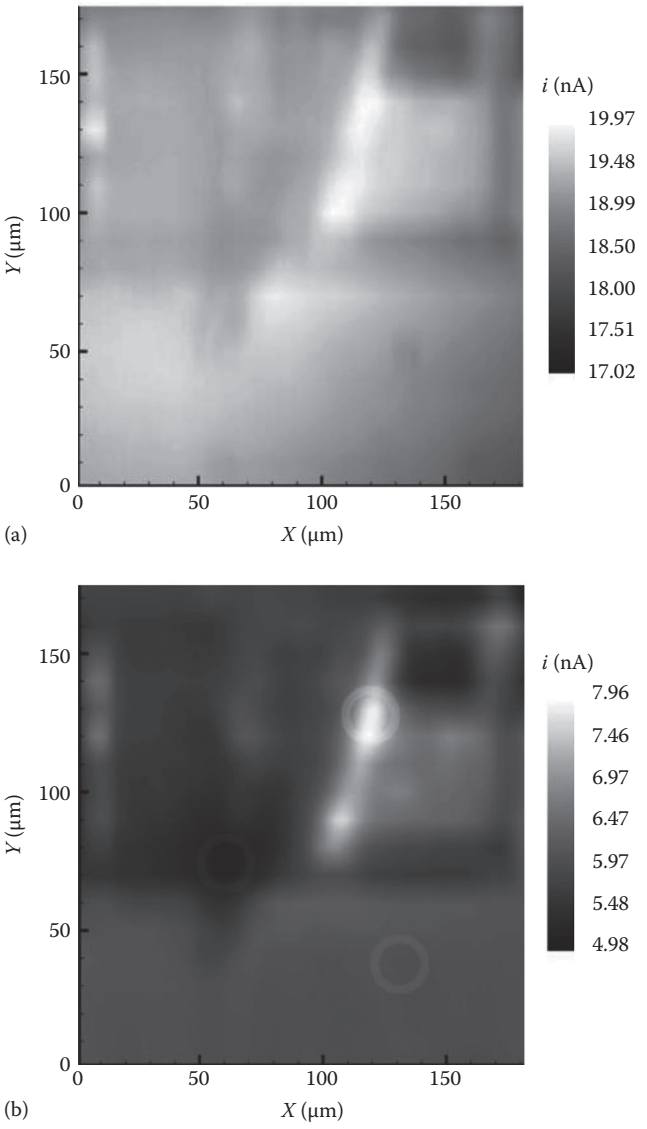


FIGURE 6.10 (a) Topographic and (b) reaction-rate images of a defect-rich surface of a glassy carbon electrode held at −1.0 and −0.4 V, respectively, as collected with a 5 μm radius Pt tip biased at 0.8 V in the solution of 2.0 mM $Fe(ClO_4)_2$ in 1 M H_2SO_4. The potentials are given with respect to a Hg/Hg_2SO_4 reference electrode. (With kind permission from Springer Science: Tenent, R.C. and Wipf, D.O., *J. Solid State Electrochem.,* 13, 583–590, 2009.)

tip–substrate separation. In contrast, an image with less negative substrate potential mainly reflects differences in ET rate although variations in the tip–substrate distance also contribute to the contrast. The corresponding reaction-rate image of the glassy carbon surface (Figure 6.10b) indicates that the defect regions are more electroactive than the other regions as expected for a carbon surface. Importantly, electroactivity differences can be evaluated much less ambiguously as rate differences from approach curves. In fact, approach curves at three different locations with highest (whitest), medium, and lowest tip current in the reaction-rate image (labeled by the transparent rings in Figure 6.10b) give k^0 values of $2.79 \times 10^{-5} > 1.86 \times 10^{-5} > 9.10 \times 10^{-6}$ cm/s, respectively.

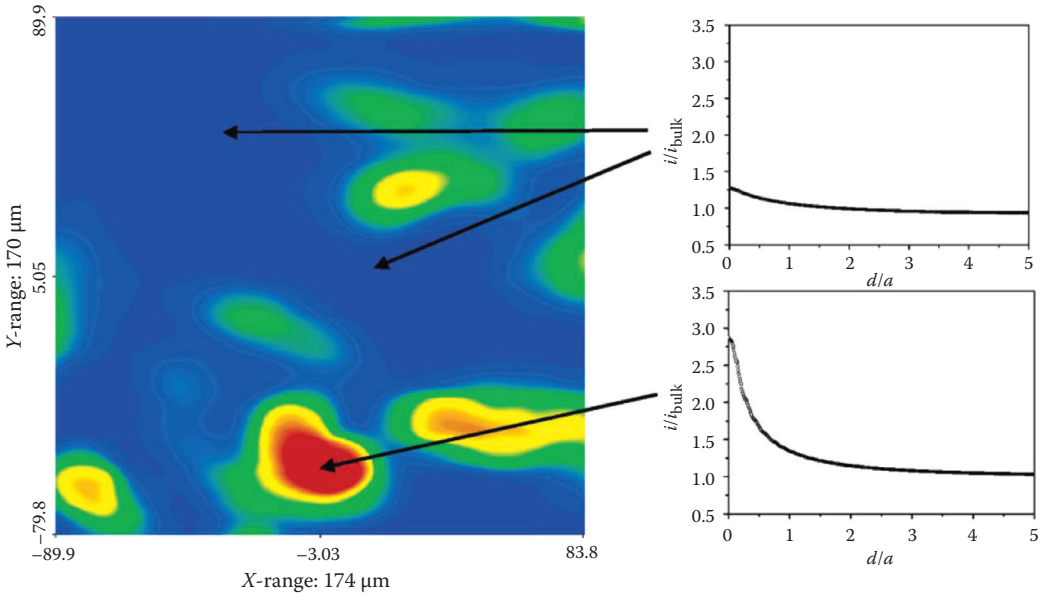


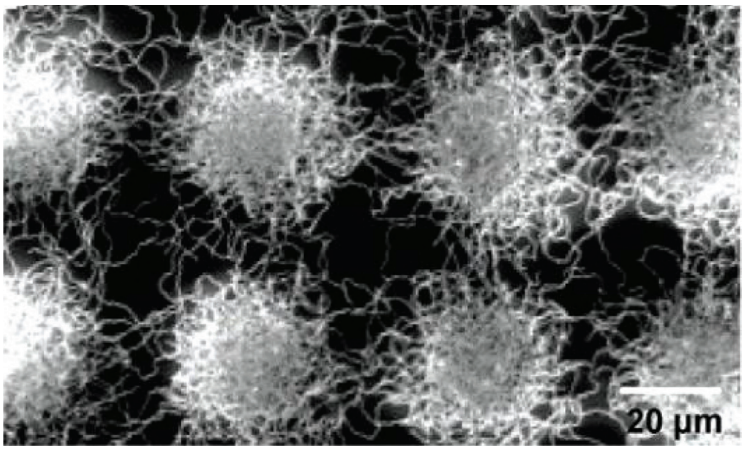
FIGURE 6.11 Normalized current contour plot (false color range 1.0–2.7) from SECM mapping and approach curves on a mixed-phase film of CuTCNQ. (Reprinted with permission from O'Mullane, A.P., Neufeld, A.K., and Bond, A.M., Distinction of the two phases of CuTCNQ by scanning electrochemical microscopy, *Anal. Chem*., 77, 5447–5452, 2005. Copyright 2005 American Chemical Society.)

The combination of SECM imaging with approach curve measurement is also useful for the quantitative study of an unbiased electroactive substrate with laterally heterogeneous surface activity. The feedback image of an unbiased semiconductive material, CuTCNQ, shows high tip current spots in low tip current regions (Figure 6.11) [34]. Approach curves to the respective regions confirm different local electroactivities of $k_{eff} = 0.025$ and 0.006 cm/s as obtained with the approximation of electrochemically irreversible substrate reactions. The different electroactivities were ascribed to the existence of two CuTCNQ phases with different conductivities, which result from the different types of the coordination of TCNQ molecules to a copper atom.

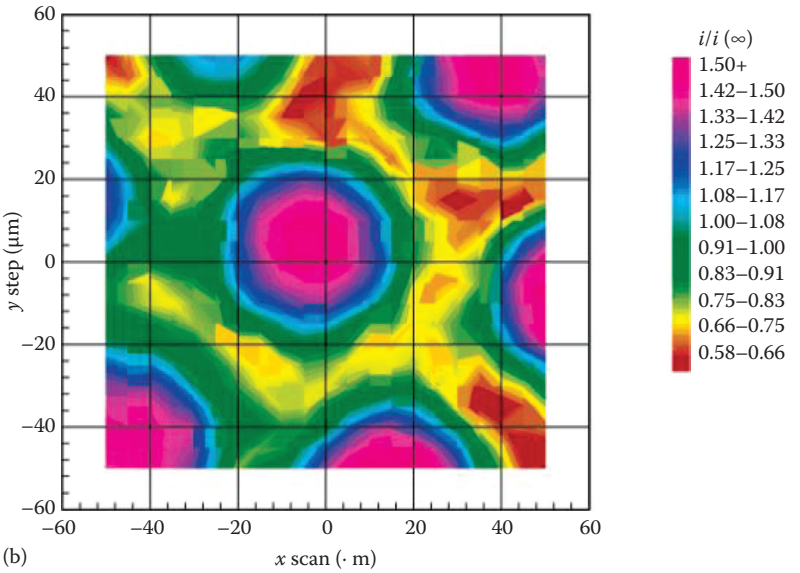
6.3.2 Applications

6.3.2.1 Single-Walled Carbon Nanotube Network

Carbon nanotube is an emerging class of nanoscale electrode materials with well-defined, structure-dependent electrical properties. The origins of their electroactivity, however, have been poorly understood and often associated with defects and contaminants [35,36]. Recently, the intrinsically high electrochemical activity of pristine SWNT films was revealed by employing the SECM feedback mode under unbiased conditions [37]. The uniform film or patterned sample (Figure 6.12a) of a two-dimensional random SWNT network was directly grown on a SiO_2-covered Si wafer using chemical vapor deposition technique with iron nanoparticles as catalysts. SECM imaging of a patterned, as-grown sample gave positive feedback responses over high-density SWNTs separated by lower-density region (Figure 6.12b). The tip current that was diminished over the lower-density area was higher than the total negative feedback current over an insulating surface, indicating the significant electroactivity of the sparse SWNT network. The effect of SWNT density on the feedback response was also confirmed by approach curves. The total positive feedback effect was obtained from a SWNT film, which covers only ~1% of the underlying SiO_2 surface. The electrochemical behavior of the low-density SWNT network as a uniformly active film is due to diffusional overlap between neighboring SWNTs as predicted by simulations. Also, the SWNTs must be highly



(a)



(b)

FIGURE 6.12 (a) FE-SEM image of a patterned SWNT surface and (b) SECM feedback image of the same sample taken with the tip biased at a potential to reduce $Ru(NH_3)_6^{3+}$ (2 mM in 0.1 M KNO_3 supporting electrolyte) at a diffusion-controlled rate at a tip–substrate separation of ~1 μm. The tip current, i, has been normalized with respect to $i(\infty)$ (= $i_{T,\infty}$). (Reprinted with permission from Wilson, N.R., Guille, M., Dumitrescu, I., Fernandez, V.R., Rudd, N.C., Williams, C.G., Unwin, P.R., and Macpherson, J.V., Assessment of the electrochemical behavior of two-dimensional networks of single-walled carbon nanotubes, *Anal. Chem*., 78, 7006–7015, 2006. Copyright 2006 American Chemical Society.)

electroactive because individual SWNTs in the sparse film need to support the extremely high fluxes that correspond to >100 times the flux at a uniformly active surface. High mass transport conditions in SECM imaging and approach curve experiments were also useful to confirm the significant electrochemical activities of multiwalled carbon nanotubes covalently patterned on Si(111) surfaces [38].

The high electroactivity of a SWNT network was voltammetrically measured by using the SG/TC mode of SECM [39]. In this work, a SWNT network was connected to an external circuit

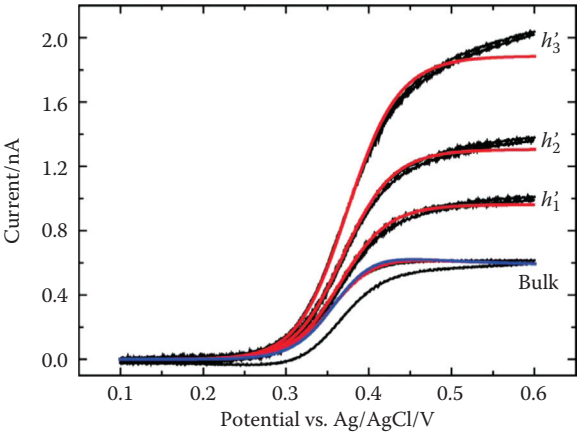


FIGURE 6.13 Experimental current vs. voltage curves (black lines) for the oxidation of 0.1 mM $FcTMA^+$ in 0.1 M NaCl at a 25 μm radius SWNT electrode at three different tip–substrate separations, $h_1' = 18$ μm, $h_2' = 12$ μm, and $h_3' = 7$ μm, and corresponding simulations based on Butler–Volmer ET with $k^0 = 0.010$ cm/s and $\alpha = 0.31$ (red lines). Scan rate, 20 mV/s. The blue line represents the simulated bulk wave for reversible ET. (Reprinted with permission from Dumitrescu, I., Dudin, P.V., Edgeworth, J.P., Macpherson, J.V., and Unwin, P.R., Electron transfer kinetics at single-walled carbon nanotube electrodes using scanning electrochemical microscopy, *J. Phys. Chem. C*, 114, 2633–2639, 2010. Copyright 2010 American Chemical Society.)

and the 25 μm radius disk-shaped surface of the network was exposed from an insulating photoresist to serve as a UME. Quasi-steady-state cyclic voltammograms for ferrocenylmethyltrimethylammonium ($FcTMA^+$) were obtained at the SWNT network UME as a substrate positioned under a 50 μm radius disk Pt tip held at a potential of 0.0 V for the diffusion-limited regeneration of $FcTMA^+$ (Figure 6.13). The substrate voltammograms were quasireversible at short tip–substrate distances of 7–18 μm and carefully analyzed using kinetic indicator plots simulated for the given experimental geometry to obtain $k^0 = 0.010$ cm/s and $\alpha = 0.31$. This apparent k^0 value was estimated to be 1% of an average k^0 value at individual SWNTs, which cover <1% of the 25 μm radius substrate surface. A minimum average k^0 value of 1 cm/s thus assigned to SWNTs is comparable to the large k^0 values of the same redox couple as obtained at individual SWNTs (7.6 cm/s) [40] and at Pt nanoelectrodes (4.8 cm/s) [41]. The large k^0 values at SWNTs suggest that the whole sidewall of SWNTs is highly electroactive despite its sp^2-carbon character. If only defects on the sidewall are active, unprecedentedly large k^0 values of 100–4000 cm/s are assigned to each defect because of the low defect density (0.25–10 per μm) of SWNTs grown by chemical vapor deposition.

6.3.2.2 Individual One-Dimensional Nanostructures

Understanding of how small electroactive substrates can be investigated by SECM is important for the SECM study of nanomaterials and nanostructured electrode surfaces. The high sensitivity of the SECM feedback mode to electroactive one-dimensional (1D) nanostructures was recently demonstrated using SWNTs [42] and metal nanobands without [43] and with [44] a nanometer-wide gap. Interestingly, these anisotropic nanomaterials as well as the nanogap can be readily detected at individual structure levels using micrometer-sized SECM tips while a disk-shaped conductive spot must be as large as at least 10%–20% of a tip diameter for the SECM feedback detection [21].

SECM feedback imaging was employed to directly assess the electroactivity of an individual SWNT [42]. A pristine SWNT (~1.6 nm in diameter and ~2 mm in length) was grown horizontally on a SiO_2 surface by chemical vapor deposition (Figure 6.14a) and imaged by SECM using $FcTMA^+$ as a redox mediator. The resulting SECM image (Figure 6.14b) shows higher tip current

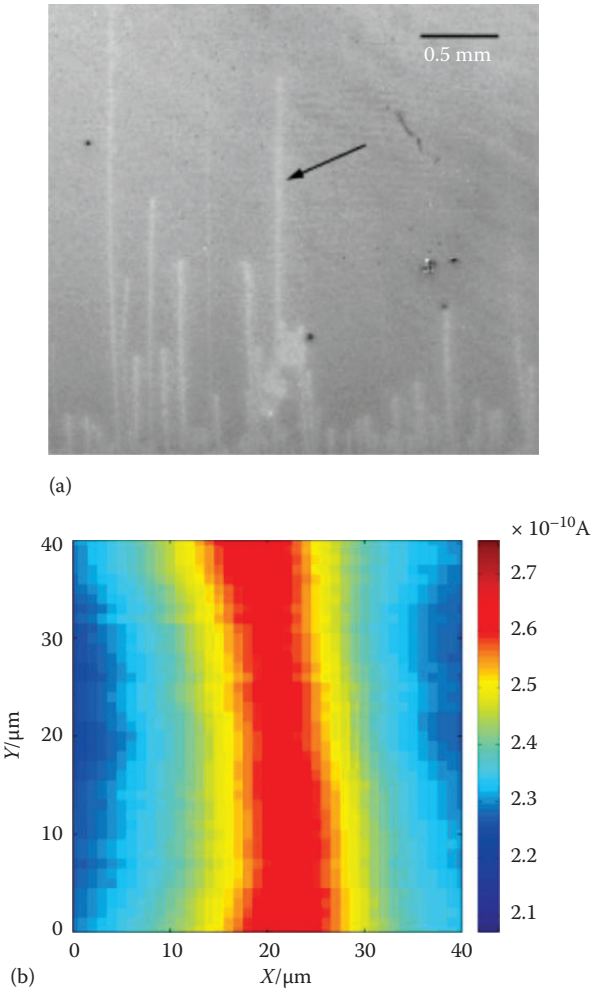


FIGURE 6.14 (a) FE-SEM image of long SWNTs grown on a SiO_2/Si wafer at low density. The arrow indicates the region of the SWNT imaged by SECM. (b) SECM image of the individual SWNT as obtained using a 5 μm radius disk Pt probe at a tip height of 5.2 μm in a solution containing 0.3 mM $FcTMA^+$ and 0.1 M KNO_3. Probe scan rate, 15 μm/s. (Reprinted with permission from Kim, J., Xiong, H., Hofmann, M., Kong, J., and Amemiya, S., Scanning electrochemical microscopy of individual single-walled carbon nanotubes, *Anal. Chem*., 82, 1605–1607, 2010. Copyright 2010 American Chemical Society.)

due to a feedback effect exerted from the individual SWNT. The micrometer-scale resolution of the SECM image is determined by the radius of a disk-shaped tip (5 μm) rather than by the nanotube diameter (~1.6 nm). Interestingly, the SWNT is readily detectable using the tip with the diameter that is ~6000 times larger than the nanotube diameter. This high sensitivity of the SECM feedback method is ascribed to efficient mass transport and facile ET at the nanotube sidewall under the tip. An intrinsically high electroactivity of $k_{eff} > 4$ cm/s was estimated for the sidewall of the individual pristine SWNT from the feedback tip current as obtained under a high mass transport condition at the 1.6 nm diameter nanotube. Noticeably, the rapid mediator regeneration at the unbiased SWNT is coupled with the reverse reaction at the exterior surface of the ultralong nanotube by efficient electron transport along the sidewall.

The feasibility of the SECM-based detection of an individual SWNT was originally predicted in the study of nanoband substrate electrodes [43]. Nanoband electrodes are important not only as

the first example of nanoelectrodes, that is, the electrodes of dimensions in the smaller numbers of nanometers [45], but also as the geometrical model of 1D nanostructures, that is, the new class of anisotropic nanomaterials as represented by nanotubes and nanowires based on various conductive and semiconductive materials [46]. The SECM images of a 100 nm wide Pt nanoband inlaid in an insulating matrix were obtained using $Ru(NH_3)_6^{3+}$ as a redox mediator to detect the continuous and damaged regions of the polished nanoband surface (Figure 6.15a and b, respectively). The apparent width of the high current region in the image of the continuous nanoband is determined by

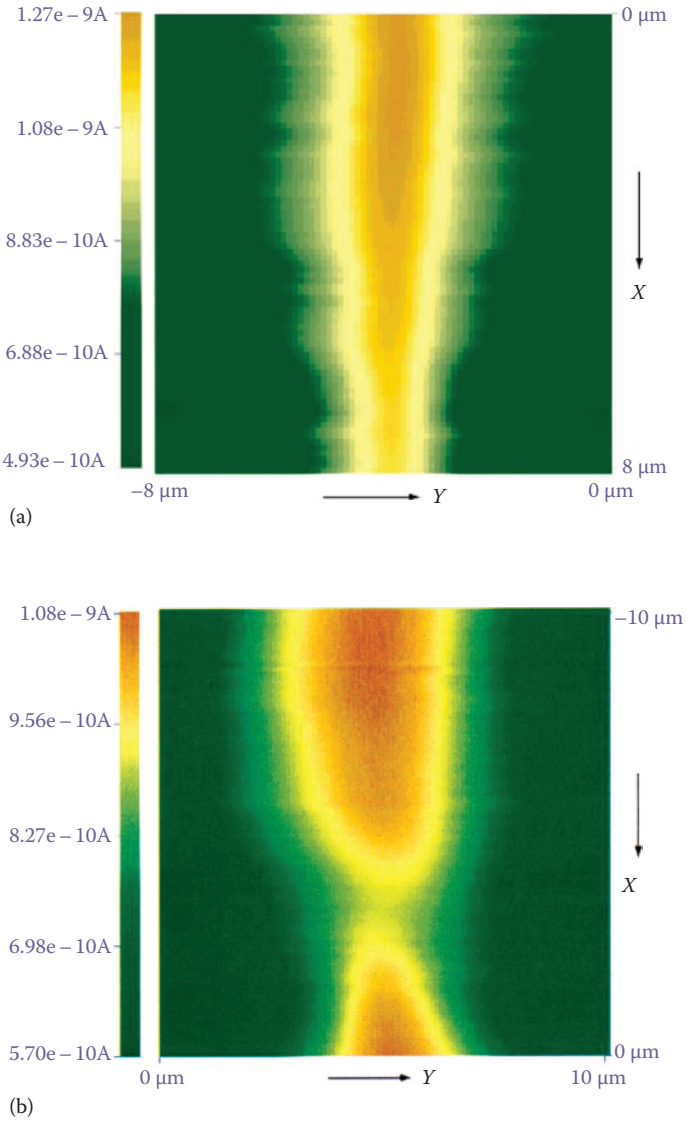


FIGURE 6.15 SECM images of (a) defect-free and (b) defect regions of a 100 nm wide and 2.6 cm long Pt band electrode as obtained using a 0.9 μm radius Pt tip with $Ru(NH_3)_6^{3+}$ as a redox mediator. Tip potential, –0.4 V vs. Ag/AgCl. Probe scan rate, 1.1 μm/s. The band electrode was unbiased. (Reprinted with permission from Xiong, H., Gross, D.A., Guo, J., and Amemiya, S., Local feedback mode of scanning electrochemical microscopy for electrochemical characterization of one-dimensional nanostructure: Theory and experiment with nanoband electrode as model substrate, *Anal. Chem.*, 78, 1946–1957, 2006. Copyright 2006 American Chemical Society.)

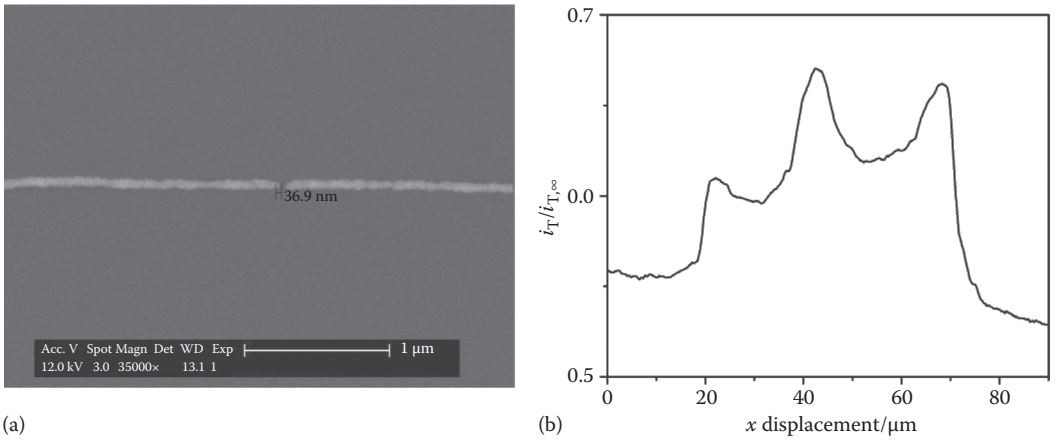


FIGURE 6.16 (a) FE-SEM image of a 37 nm wide gap in a 50 μm long Au nanoband lithographically fabricated on a SiO_2/Si wafer. (b) SECM line scan over the gapped nanoband along its length as obtained using a 1.0 μm radius Pt tip scanned at a constant height of 1.1 μm from the nanoband surface. Scan rate, 3 μm/s. (Reprinted with permission from Kim, E., Kim, J., and Amemiya, S., Spatially resolved detection of a nanometer-scale gap by scanning electrochemical microscopy, *Anal. Chem*., 81, 4788–4791. Copyright 2009 American Chemical Society.)

the tip radius (1 μm) rather than by the width of the nanoband as confirmed by three-dimensional numerical simulations. This quantitative theory demonstrates that a feedback effect from a nanoband substrate electrode weakly depends on its nanometer width because of a unique hemicylindrical diffusion pattern at the nanoband surface. Subsequently, SECM maintains its sensitivity to a 1D material with small nanoscale dimensions, thereby enabling the detection of an individual SWNT using micrometer-radius tips (see Section 6.3.2.2). In contrast, the tip current response over the damaged region is broader than expected from the tip radius and also smaller, which corresponds to lower electroactivity (Figure 6.15b).

The feedback mode of SECM allows for the spatially resolved detection of the nanometer-wide gap formed in a conductive 1D nanostructure [44]. This unique capability of SECM is potentially useful for the characterization of a nanogap introduced as a defect in SWNTs [47] or formed in a nanowire by employing high-throughput and low-cost chemical methods for electronics and optics applications [48]. Interestingly, a peak-shaped tip current response was obtained over a 37 nm wide gap in an isolated Au nanoband although the exposed SiO_2 surface under the gap was insulating (see Figure 6.16a and b for the field-emission scanning electron microscopy (FE-SEM) image and SECM line scan of the gapped nanoband, respectively). This enhanced tip response to the inactive nanogap region was confirmed theoretically by using three-dimensional finite element simulation and was ascribed to a unique feedback effect from a gap in a finitely long nanoband under an unbiased condition. Only when the tip is positioned above the nanogap, both fragments of the unbiased gapped nanoband participate in the feedback process to maximize the tip current. Noticeably, smaller peak current responses were also seen when the tip was positioned over the outer edges of the gapped nanoband. Such an edge response is also unique to an unbiased conductive substrate with finite dimensions as observed also with a gap-free nanoband [44] and a disk UME [31].

6.3.2.3 Boron-Doped Diamond Electrode

Doping of diamond with impurities such as boron turns this intrinsically superb insulator into sufficiently conducting material for a number of electrochemical technologies [49]. Recently, the laterally heterogeneous electroactivity of the boron-doped diamond (BDD) surface was revealed by

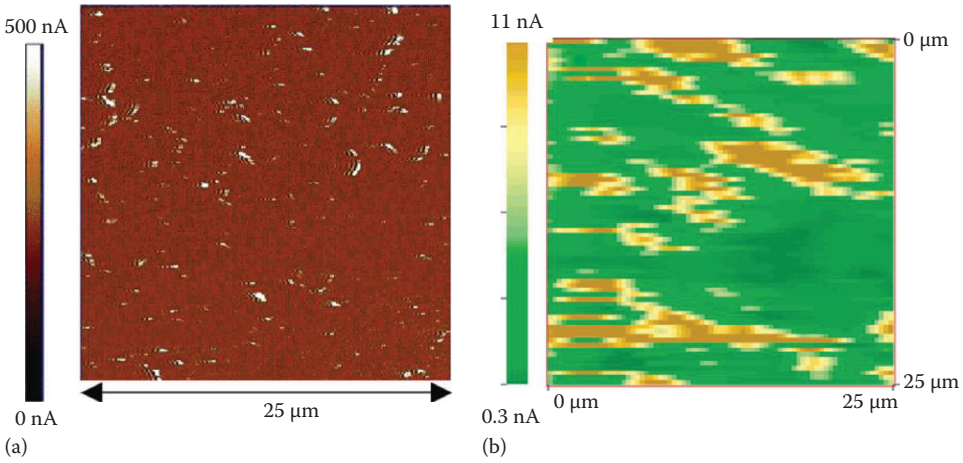


FIGURE 6.17 (a) Conductive AFM image of a BDD sample doped with 10 ppm B_2H_6 with a bias of −200 mV applied between sample and tip. (b) SECM image of a 10 ppm doped BDD substrate as obtained with a 1 μm radius Pt tip in a solution containing 1.3 mM $Ru(NH_3)_6^{3+}$ and 0.1 M KCl. Tip and substrate potentials were −0.4 and 0 V vs. Ag/AgCl, respectively. Scan rate, 10 μm/s. (Reprinted with permission from Holt, K.B., Bard, A.J., Show, Y., and Swain, G.M., Scanning electrochemical microscopy and conductive probe atomic force microscopy studies of hydrogen-terminated boron-doped diamond electrodes with different doping levels, *J. Phys. Chem. B*, 108, 15117–15127, 2004. Copyright 2004 American Chemical Society.)

high-resolution SECM imaging to obtain greater understanding of its structure–reactivity relationship [50]. The pattern of conductivity at a BDD surface is clearly seen by conductive probe atomic force microscopy (CP-AFM), where the conductive areas with diameters of 0.5–2 μm randomly and nonuniformly distribute over the surface of an insulating diamond matrix (Figure 6.17a). The density of high conductivity sites increases as the surface is doped with a higher concentration of gas phase B_2H_6 in the range of 0–10 ppm. SECM imaging with $Ru(NH_3)_6^{3+}$ as a redox mediator confirms the corresponding lateral heterogeneity of the BDD surface with electrochemically active areas within an insulating, less active matrix (Figure 6.17b). The density of electrochemically active sites is also greater with higher doping level. In addition, a more positive approach curve to an electrochemical "hot spot" at more highly doped BDD corresponds to a larger k_{eff} value of up to 0.15 cm/s. A hot spot with a finite k_{eff} value was modeled as an inactive surface partially covered by randomly distributed conductive disks, that is,

$$k_{eff} = 4(1-\theta)D/\pi R_d \tag{6.2}$$

where

θ is the fraction of the surface that is insulating
R_d is the radius of the conductive areas

The accumulation of boron dopant is likely to result in the formation of conductive disks. Moreover, the conductive sites, which are smaller than the tip, must be biased to exert a positive feedback effect, indicating that these sites are connected to the underlying *p*-type silicon wafer through conductive pathways across a 1–10 μm thick diamond film. It was suggested that such sites are formed at the grain boundaries of polycrystalline BDD. In addition, the recent SECM study of microcrystalline and nanocrystalline BDD films revealed that the locations of highly electroactive regions depend on redox mediators [51]. Mediator-dependent local electroactivity was also observed by SECM for BDD under unbiased conditions [52] and for the films and particles of undoped nanodiamonds at various potentials [53].

Multidimensional information about the spatially heterogeneous surface of oxygen-terminated BDD was obtained by using SECM in combination with other imaging techniques [54]. The well-defined array of 75 disk-shaped BDD UMEs (~53 μm in diameter and ~250 μm in center-to-center separation) was developed as a substrate electrode to be imaged under quasi-steady-state conditions in the SG/TC mode using $Ru(NH_3)_6^{3+}$ as a mediator. As the substrate potential was changed from the anodic side of the formal potential to the cathodic side, mediator reduction at the substrate surface was accelerated to give larger tip current (Figure 6.18). The tip current enhancement, however, depends on the tip position, which indicates spatial variations in ET rates on the flat BDD surface. The sizes of the domains with different electroactivities are consistent with the sizes of individual grains with various levels of conductivity as observed by CP-AFM. Grain-dependent electroactivities were also seen for silver electrodeposition by FE-SEM and for oxygen reduction by fluorescence laser-scanning confocal microscopy. In a more recent study, the spatially heterogeneous electroactivity of an oxygen-terminated BDD surface was ascribed to nonuniform boron uptake across the surface as quantified using cathodoluminescence mapping, which detected metal-like zones with degenerative doping and less electroactive regions with less doping [55]. Different regions with metallic and semiconducting properties were also observed on a BDD surface by Raman microscopy while the corresponding local variations in electroactivity were confirmed by SECM [56]. Moreover, oxygen-terminated BDD at low doping level was investigated as the model of a semiconductive region to assess its electroactivity experimentally by SECM and theoretically by employing the Marcus–Gerischer–Morrison theory of ET at a semiconductor–electrolyte interface [57].

6.3.2.4 Monolayer-Mediated ET

During the past two decades, long-range ET mediated across redox-active self-assembled monolayers (SAMs) of thiolates on metal electrodes have been extensively investigated because of their fundamental and technological importance [58]. In comparison to conventional electrochemical methods such as cyclic voltammetry, the feedback mode of SECM offers several advantages, that is, steady-state measurement, the elimination of double-layer charging current, and the reduction of iR drop, to determine higher ET rates across redox-active SAMs (Figure 6.19a) [59]. In this SECM feedback measurement, an effective ET rate constant, k_{eff}, is determined by the rate constant, k_{ir}, for irreversible bimolecular ET between the redox moiety and redox mediator at the monolayer–solution interface ($R + M^+ \rightarrow O + M$, where M^+ and M are the oxidized and reduced forms of an electroactive SAM) and the forward and reverse rate constants, k_f and k_b, for quasireversible electron tunneling through the monolayer ($M^+ + e \rightleftharpoons M$) as

$$k_{eff} = k_{ir}k_b\Gamma^* / (k_{ir}c^0 + k_f + k_b) \tag{6.3}$$

where

Γ^* is the total coverage of the redox-active SAM
c^0 is the bulk concentration of a redox mediator

It was estimated that the largest rate constants of $k_{ir} = 5 \times 10^{11}$ mol^{-1} cm^3 s^{-1} and $k_b = \sim 10^8$ s^{-1} are measurable from SECM approach curves. For instance, a relatively large k_b value of 1.2×10^5 s^{-1} was obtained for electron tunneling across short-chain ferrocenyl-thiol SAMs ($FcCONH(CH_2)_7SH$) using $Ru(NH_3)_6^{3+}$ as a mediator (Figure 6.19d). Moreover, a large k_{ir} value of 1.6×10^{10} mol^{-1} cm^3 s^{-1} was determined for an ET reaction between tip-generated $IrCl_6^{2-}$ and monolayer-bound ferrocene. This rate constant, however, is somewhat smaller than the value of 3×10^{11} mol^{-1} cm^3 s^{-1} predicted by the Marcus theory for a homogeneous ET reaction between freely diffusing ferrocene and $IrCl_6^{2-}$ (Equation 6.1), indicating that the reactivity of monolayer-bound ferrocene is lower than that of freely diffusing ferrocene.

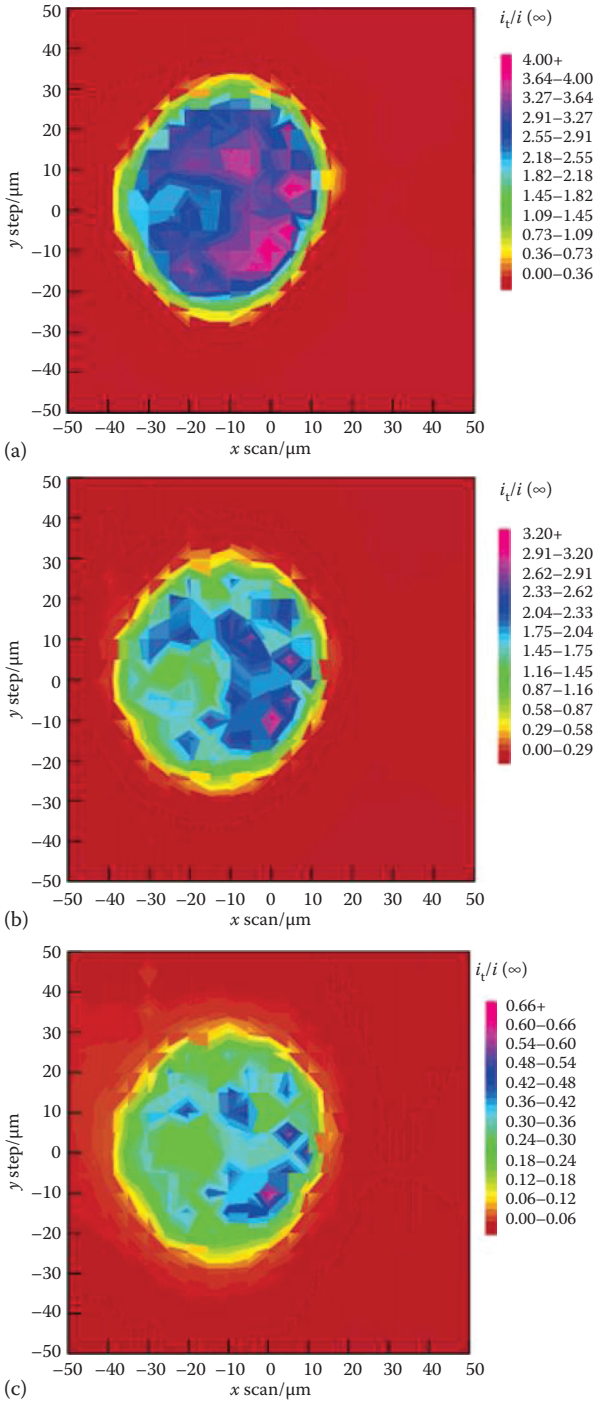


FIGURE 6.18 SG/TC images of a BDD UME at (a) −0.4, (b) −0.3, and (c) −0.2 V. The 2.5 μm radius disk Pt tip was held at 0.0 V vs. Ag/AgCl, enabling the collection of surface-generated $Ru(NH_3)_6^{2+}$ (from 5 mM $Ru(NH_3)_6^{3+}$ in 0.2 M KNO_3) at a diffusion-controlled rate. A tip–substrate imaging height of ~0.6 μm was employed. (Reprinted with permission from Colley, A.L., Williams, C.G., Johansson, U.D., Newton, M.E., Unwin, P.R., Wilson, N.R., and Macpherson, J.V., Examination of the spatially heterogeneous electroactivity of boron-doped diamond microarray electrodes, *Anal. Chem.*, 78, 2539–2548, 2006. Copyright 2006 American Chemical Society.)

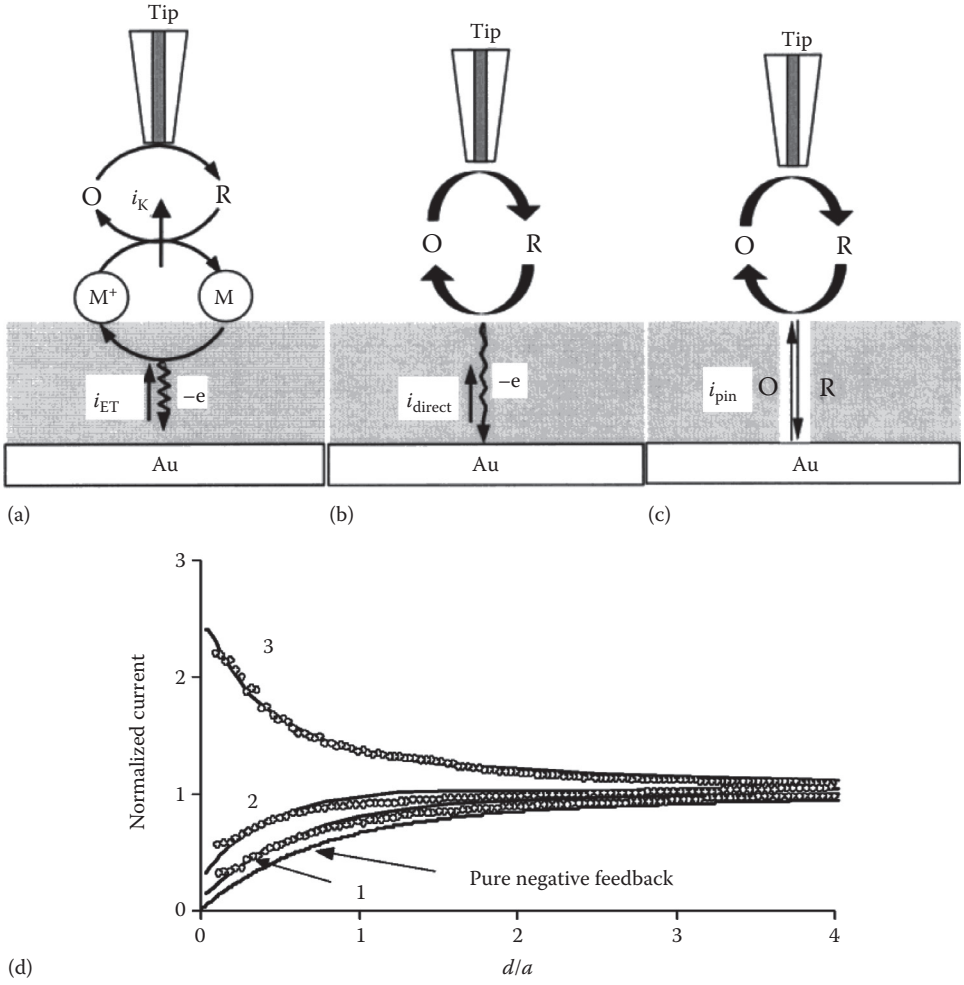


FIGURE 6.19 Schematic view of the processes involved in the SECM measurements of ET across an electroactive SAM: (a) mediated ET, (b) direct electron tunneling through monolayer, (c) ET through pinholes. (d) SECM approach curves (open circles) obtained on gold coated by (1, 3) the mixed monolayer of $FcCONH(CH_2)_7SH$ and $CH_3(CH_2)_8SH$ or (2) the monolayer of $CH_3(CH_2)_8SH$ in a solution containing 1 mM $Ru(NH_3)_6Cl_3$ and 0.05 M $NaClO_4$ (pH 3). The tip was a 1 μm radius Pt disk. Substrate potential, (1) 0.2 and (2, 3) 0.5 V vs. Ag/AgCl. The approaching speed was 0.2 μm/s. The solid lines are theoretical SECM curves. (Reprinted with permission from Liu, B., Bard, A.J., Mirkin, M.V., and Creager, S.E., Electron transfer at self-assembled monolayers measured by scanning electrochemical microscopy, *J. Am. Chem. Soc.*, 126, 1485–1492, 2004. Copyright 2004 American Chemical Society.)

SECM allows for more accurate measurement of rate constants for direct electron tunneling through nonelectroactive blocking monolayers (Figure 6.19b) with the compensation of contributions from ET through pinholes (Figure 6.19c) [60]. The pinhole contributions lead to not only overestimated k^0 but also anomalously small α of <0.2. A model was proposed and validated to determine a k^0 value for monolayer-mediated electron tunneling by subtracting a constant pinhole current from SECM data such that a normal α value of 0.5 is obtained. The corrected k^0 values for different chain lengths follow the expected exponential decay to yield a tunneling decay constant, β, of 0.9 $Å^{-1}$, which is in reasonable agreement with the reported β value of ~1 for saturated chains. Moreover, the corrected k^0 values are several orders of magnitude smaller than those previously reported in the literature. The literature values are likely to be overestimated due to pinhole contributions.

The corrected k^0 value for the $Ru(NH_3)_6^{3+/2+}$ couple at a blocking SAM thus determined by SECM is three orders of magnitude smaller than the rate constant for a very similar redox couple covalently bound to a monolayer with the equivalent chain length, confirming the theoretical expectation that tunneling via bonded contacts is more efficient than tunneling to nonbonded contacts.

The feedback mode of SECM also enables the quantitative investigation of the heterogeneous ET and lateral diffusion of a redox-active lipid in the monolayer formed at the air–water interface [61]. The corresponding effective ET rate constant, k_{eff}, and lateral diffusion coefficient, D_{surf}, were measured by employing a triple potential step method based on the transient feedback tip current. Specifically, the 1:1 mixed monolayer of *N*-octadecylferrocenecarboxamide and 1-octadecanol was formed in a Langmuir trough while $Ru(bipy)_3^{2+}$ was electrolyzed at a submarine SECM tip placed in the water phase close to the monolayer (Figure 6.20a). This first potential step initiates the diffusion-limited generation of $Ru(bipy)_3^{3+}$ at the tip. The tip-generated species diffuses to and reacts with the ferrocene-attached lipid at the air–water interface, thereby regenerating the original mediator to exert a positive feedback effect on the tip current. A k_{eff} value for this heterogeneous bimolecular ET reaction can be determined by the numerical analysis of the resulting chronoamperometric tip current (top curve in Figure 6.20b), which decays toward zero as the ferrocene-attached lipid is depleted under the tip. After this "bleaching" step, the potential step is reverted to convert the tip-generated species to its initial form. During this period, the depleted region of the monolayer under the tip recovers toward the initial condition because of the lateral diffusion of redox lipids while the reverse ET reaction between $Ru(bipy)_3^{2+}$ and the ferrocenium moiety of an amphiphile is too unfavorable thermodynamically to contribute to the recovery of the monolayer. Finally, the tip potential is stepped to generate $Ru(bipy)_3^{2+}$ again so that a feedback effect is obtained from the partially recovered interfacial region. The resulting chronoamperogram (middle curve) depends on the D_{surf} value of the ferrocene-attached amphiphile, which determines the degree of the monolayer recovery. Furthermore, a chronoamperogram after a very short recovery step (bottom curve) is useful for the determination of the tip–substrate distance, which is required for the analysis of the aforementioned chronoamperograms.

This elaborate triple potential step method was employed to determine k_{eff} and D_{surf} values at various monolayer densities. As the mean area occupied by each lipid molecule decreased from 50 to 30 Å^2, k_{eff} increased from 0.035 to 0.06 cm/s. These rate constants, however, are several orders of magnitude lower than expected from the Marcus theory for bimolecular ET reactions either in solution or at a liquid–liquid interface. The slow ET kinetics was ascribed to highly constrained local environment in the compressed monolayer at the air–water interface. Moreover, D_{surf} decreased from 1.0×10^{-6} to $<1.0 \times 10^{-7}$ cm^2/s at the more compressed monolayer. These diffusion coefficients agree with values determined previously by the microline electrode technique [62], thereby validating the SECM method.

6.3.2.5 Electroactive Polymer Film

The modification of an electrode surface with an electroactive polymer film is a powerful approach to control the electrode surface functionality for various electrochemical applications [63]. SECM provides detailed insights into complicated charge transport at polymer-modified electrodes. For instance, SECM was used to probe the potential-driven transition of a highly conjugated polymer between the insulating and conductive states (Figure 6.21a) [64]. A conductive polymer film coated on an electrode surface gives the total positive feedback tip current when the regeneration of a redox mediator at the film–solution interface is fast enough to be diffusion limited. In contrast, the total negative feedback current is expected when a film is not only insulating but also impermeable to a redox mediator to completely block its access to the underlying electrode. Namely, the permeability of a polymer film on an electrode can also be assessed by SECM using a redox mediator that does not react with the film [65]. In practice, an intermediate feedback effect is exerted from a conducting polymer film, which, as the first approximation, mediates the irreversible ET reaction of a redox mediator at the surface. The k_{eff} values for poly(benzobisim

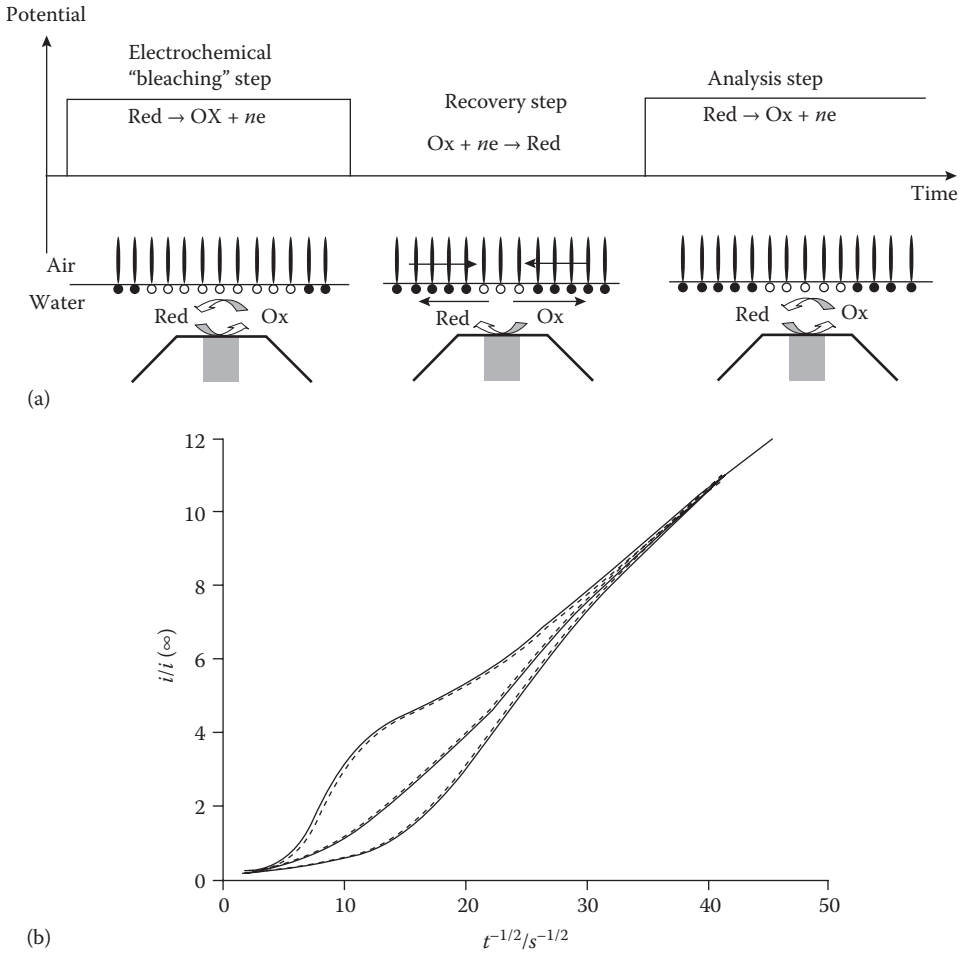


FIGURE 6.20 (a) Schematic diagram (not to scale) of the potential step profile and corresponding processes for SECM triple potential step experiment at the air–water interface and (b) the corresponding experimental results (solid lines) for the first step transient (top), and the third step transient obtained with $t_1 = 0.4$ s and $t_2 = 2.4$ s (middle), or $t_1 = 0.4$ s and $t_2 = 0.44$ s (bottom), where the second and third steps occur at t_1 and t_2, respectively. The dashed lines are the best fits to the theoretical model with log $d/a = -1.0$ and $D = 4.8 \times 10^{-6}$ cm^2/s as determined from bottom curve. In addition, the top and middle dashed lines fit to $k_{eff} = 0.045$ cm/s and $D_{surf} = 4.8 \times 10^{-7}$ cm^2/s. (Reprinted with permission from Zhang, J., Slevin, C.J., Morton, C., Scott, P., Walton, D.J., and Unwin, P.R., New approach for measuring lateral diffusion in Langmuir monolayers by scanning electrochemical microscopy (SECM): Theory and application, *J. Phys. Chem. B.*, 105, 11120–11130, 2001. Copyright 2001 American Chemical Society.)

idazobenzophenanthroline) ladder polymer on an indium–tin oxide electrode were determined from approach curves using this approximation to find that the dramatic change in k_{eff} between the substrate potentials of −0.3 and −0.4 V (Figure 6.21b) agrees with a change in the polymer conductivity [66]. Noticeably, a potential-driven change in polymer conductivity is coupled with a change in the oxidation state of the polymer, which drives ion transport at the film–solution interface to maintain electroneutrality in the film. The voltammetric transport of a target ion near the interface can be selectively monitored in real time by SECM when various ions are transported across the interface [67]. More recently, SECM was also applied to probe the deposition of a conducting polyaniline film on an insulating and blocking thin layer of diphenylamine grafted on a carbon electrode [68].

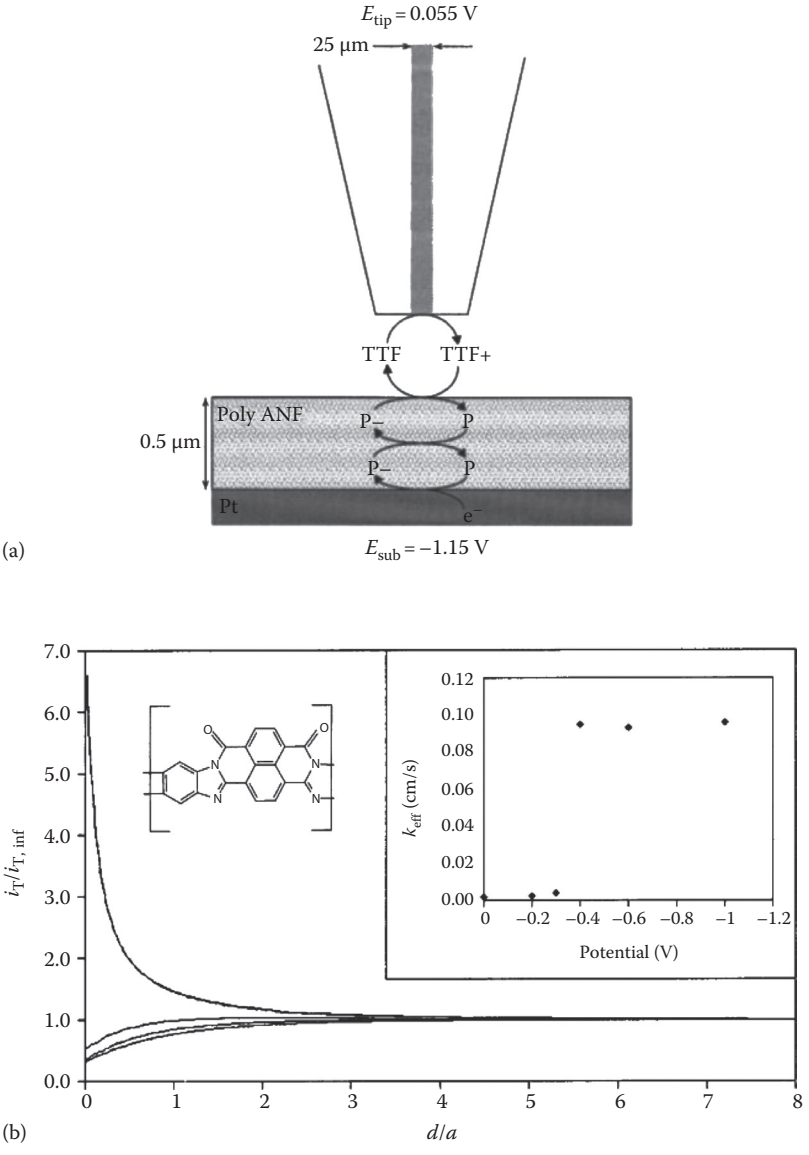


FIGURE 6.21 (a) Schematic of the processes involved in an SECM experiment at a Pt substrate modified with poly(7,14-diphenylacenaphtho[1,2-*k*]fluoranthene) (ANF) in a solution containing a redox mediator, TTF. (Reprinted from *J. Electroanal. Chem*., 498, Quinto, M. and Bard, A.J., Polymer films on electrodes. Part 29. Electropolymerized poly(7,14-diphenylacenaphtho[1,2-*k*]fluoranthene): Electrochemistry and conductance of a novel electrochromic hydrocarbon ladder polymer film, 67–74, Copyright 2001, with permission from Elsevier.) (b) SECM tip ($a = 12.5\,\mu m$) approach curves with 5 mM TTF as redox mediator on poly(benzobi simidazobenzophenanthroline) (BBL) at potentials of 0.0, −0.2, −0.3, −0.4, −0.6, and −0.8 V from the bottom to the top (last three curves are superimposed). Insets: Scheme of BBL (left) and variation of k_{eff} with the potential applied to the film (right). (Adapted from Quinto, M., Jenekhe, S.A., and Bard, A.J., Polymer films on electrodes. 30. Electrochemistry and scanning electrochemical microscopy characterization of benzimidazolebenzophenanthroline-type ladder (BBL) and semiladder (BBB) polymer films, *Chem. Mater*., 13, 2824–2832, 2001. Copyright 2001 American Chemical Society.)

An SECM feedback response to an electroactive polymer film can be controlled either by ET kinetics at the film–solution interface or by film conductivity. The contribution of lateral film conductivity to the effective ET rate measured by SECM was addressed in the recent study of polyaryl multilayers attached with ferrocenes [65] or ferrocene-terminated dendrimers [69] on unbiased carbon electrodes. In the latter study, the dependence of apparent ET rate constant, k_{el}, on the generation of dendrimers (Table 6.2) was ascribed to the different efficiencies of electron transport inside and between dendrimers (Figure 6.22). Interestingly, the theory of the aforementioned triple potential step method predicts its potential to separately determine heterogeneous ET rate and lateral conductivity for a thin polymer film coated on an insulating surface [70].

TABLE 6.2
Apparent Electron Transfer Rate Constants k_{el} for the Adsorbed Dendrimers G0, G1, and G2 with the Four Mediators

		k_{el} (10^{-2} cm/s)		
Mediator	E^{o}_{med}[a]	**G0**	**G1**	**G2**
Tris(*p*-tolyl)amine	0.35	5.5±0.2	>16±2	2.7±0.1
Ethynyl-Fc	0.18	4.2±0.1	7.5±0.2	3.2±0.2
Fc	0.00	5.0±0.2	5.1±0.2	2.3±0.1
Decamethyl-Fc	–0.45	Insulating	Insulating	Insulating

[a] Redox potential of the mediator (V vs. Fc).

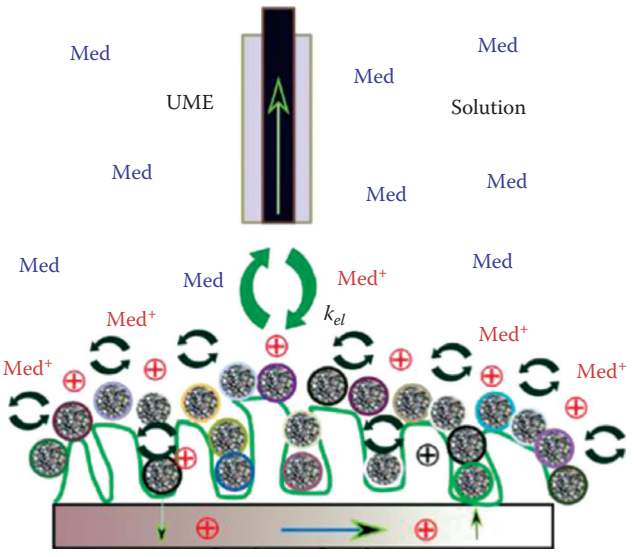


FIGURE 6.22 Schematic diagram of local reduction and charge transport in SECM experiments on dendrimer-adsorbed surfaces. (Reprinted with permission from Wang, A., Ornelas, C., Astruc, D., and Hapiot, P., Electronic communication between immobilized ferrocenyl-terminated dendrimers, *J. Am. Chem. Soc.*, 131, 6652–6653, 2009. Copyright 2009 American Chemical Society.)

6.4 CONCLUSIONS AND FUTURE PERSPECTIVES

The past decade has seen exciting and important progresses in the SECM study of heterogeneous ET reactions. The experimental and theoretical reinforcement of SECM into a more sophisticated electrochemical method enables the study of heterogeneous ET reactions at various interfaces with higher spatial and time resolutions. The applications of SECM broadly extend from the fundamental study of ET to the characterization of diverse electrode materials. The latter direction will continue to grow as (nano)material sciences have been directed toward electrochemical applications. High-resolution SECM imaging compliments other high-resolution imaging techniques to obtain multidimensional information about a target interface. Three-dimensional simulation has enabled the quantitative analysis of SECM data with complicated experimental geometry and will become more efficient to directly determine the heterogeneous electroactivity of a substrate from its SECM image.

Both spatial and time resolutions of SECM have been continuously improved by the applications of smaller tips, which can be as small as several nanometers. In particular, nanotip voltammetry has been highly successful for more reliable measurement of extremely rapid heterogeneous ET reactions to address the predictions of the ET theory [4,9]. The applications of such tiny tips to the kinetic study of substrate ET reactions will be also important for the assessment of ET theories including recent ones [71,72] because the materials, surface properties, geometries, and dimensions of a substrate can be more freely altered in comparison to those of a nanometer-sized tip. The nanoscale SECM measurement of substrate reactions, however, is more challenging and requires experimental protocols for efficiently positioning nanotips at nanometer distances from substrate surfaces [16], which usually possess ill-defined topography at this distance scale. More generalized SECM theory for substrate ET reactions will also be useful and complement the recent general theory of tip voltammetry [6].

ACKNOWLEDGMENTS

This work was supported by grants from the NIH (GM073439) and the NSF (CAREER award, CHE-0645623).

REFERENCES

1. Marcus, R. A. Tutorial on rate constants and reorganization energies. *J. Electroanal. Chem*. 2000, 483, 2–6 and references cited therein.
2. Bard, A. J., Faulkner, L. R. *Electrochemical Methods: Fundamentals and Applications*, 2nd ed., John Wiley & Sons, New York, 2001, pp. 92–107.
3. Mirkin, M. V., Bard, A. J. Simple analysis of quasi-reversible steady-state voltammograms. *Anal. Chem*. 1992, 64, 2293–2302.
4. Sun, P., Mirkin, M. V. Kinetics of electron-transfer reactions at nanoelectrodes. *Anal. Chem*. 2006, 78, 6526–6534.
5. Miao, W., Ding, Z., Bard, A. J. Solution viscosity effects on the heterogeneous electron transfer kinetics of ferrocenemethanol in dimethyl sulfoxide–water mixtures. *J. Phys. Chem. B* 2002, 106, 1392–1398.
6. Zoski, C. G., Luman, C. R., Fernandez, J. L., Bard, A. J. Scanning electrochemical microscopy. 57. SECM tip voltammetry at different substrate potentials under quasi-steady-state and steady-state conditions. *Anal. Chem*. 2007, 79, 4957–4966.
7. Nelsen, S. F., Ismagilov, R. F., Gentile, K. E., Nagy, M. A., Tran, H. Q., Qu, Q. L., Halfen, D. T., Odegard, A. L., Pladziewicz, J. R. Indirect determination of self-exchange electron transfer rate constants. *J. Am. Chem. Soc*. 1998, 120, 8230–8240.
8. Marcus, R. A. On the theory of electron-transfer reactions. VI. Unified treatment for homogeneous and electrode reactions. *J. Chem. Phys*. 1965, 43, 679–701.
9. Velmurugan, J., Sun, P., Mirkin, M. V. Scanning electrochemical microscopy with gold nanotips: The effect of electrode material on electron transfer rates. *J. Phys. Chem. C* 2008, 113, 459–464.
10. Schmickler, W. *Interfacial Electrochemistry*, Oxford University Press, Oxford, U.K., 1996, pp. 98–99.

11. Hapiot, P., Lagrost, C. Electrochemical reactivity in room-temperature ionic liquids. *Chem. Rev*. 2008, 108, 2238–2264.
12. Taylor, A. W., Qiu, F. L., Hu, J. P., Licence, P., Walsh, D. A. Heterogeneous electron transfer kinetics at the ionic liquid/metal interface studied using cyclic voltammetry and scanning electrochemical microscopy. *J. Phys. Chem. B* 2008, 112, 13292–13299.
13. Lovelock, K. R. J., Cowling, F. N., Taylor, A. W., Licence, P., Walsh, D. A. Effect of viscosity on steady-state voltammetry and scanning electrochemical microscopy in room temperature ionic liquids. *J. Phys. Chem. B* 2010, 114, 4442–4450.
14. Fontaine, O., Lagrost, C., Ghilane, J., Martin, P., Trippe, G., Fave, C., Lacroix, J. C., Hapiot, P., Randriamahazaka, H. N. Mass transport and heterogeneous electron transfer of a ferrocene derivative in a room-temperature ionic liquid. *J. Electroanal. Chem*. 2009, 632, 88–96.
15. Carano, M., Bond, A. M. Prospects for the application of scanning electrochemical microscopy in ionic liquids. *Aust. J. Chem*. 2007, 60, 29–34.
16. Laforge, F. O., Velmurugan, J., Wang, Y., Mirkin, M. V. Nanoscale imaging of surface topography and reactivity with the scanning electrochemical microscope. *Anal. Chem*. 2009, 81, 3143–3150.
17. Ghilane, J., Lagrost, C., Hapiot, P. Scanning electrochemical microscopy in nonusual solvents: Inequality of diffusion coefficients problem. *Anal. Chem*. 2007, 79, 7383–7391.
18. Zigah, D., Wang, A. F., Lagrost, C., Hapiot, P. Diffusion of molecules in ionic liquids/organic solvent mixtures. Example of the reversible reduction of O_2 to superoxide. *J. Phys. Chem. B* 2009, 113, 2019–2023.
19. Zigah, D., Ghilane, J., Lagrost, C., Hapiot, P. Variations of diffusion coefficients of redox active molecules in room temperature ionic liquids upon electron transfer. *J. Phys. Chem. B* 2008, 112, 14952–14958.
20. Zoski, C. G., Simjee, N., Guenat, O., Koudelka-Hep, M. Addressable microelectrode arrays: Characterization by imaging with scanning electrochemical microscopy. *Anal. Chem*. 2004, 76, 62–72.
21. Bard, A. J., Mirkin, M. V., Unwin, P. R., Wipf, D. O. Scanning electrochemical microscopy. 12. Theory and experiment of the feedback mode with finite heterogeneous electron-transfer kinetics and arbitrary substrate size. *J. Phys. Chem*. 1992, 96, 1861–1868.
22. Baltes, N., Thouin, L., Amatore, C., Heinze, J. Imaging concentration profiles of redox-active species with nanometric amperometric probes: Effect of natural convection on transport at microdisk electrodes. *Angew. Chem. Int. Ed. Engl*. 2004, 43, 1431–1435.
23. Sun, P., Liu, Z., Yu, H. H., Mirkin, M. V. Effect of mechanical stress on the kinetics of heterogeneous electron transfer. *Langmuir* 2008, 24, 9941–9944.
24. Wei, C., Bard, A. J., Mirkin, M. V. Scanning electrochemical microscopy. 31. Application of SECM to the study of charge transfer processes at the liquid/liquid interface. *J. Phys. Chem*. 1995, 99, 16033–16042.
25. Turyan, I., Orel, B., Reisfeld, R., Mandler, D. Studying electron transfer at electrochromic tungsten oxide sol–gel films with scanning electrochemical microscopy (SECM). *Phys. Chem. Chem. Phys*. 2003, 5, 3212–3219.
26. Zhou, J., Zu, Y., Bard, A. J. Scanning electrochemical microscopy part 39. The proton/hydrogen mediator system and its application to the study of the electrocatalysis of hydrogen oxidation. *J. Electroanal. Chem*. 2000, 491, 22–29.
27. Zoski, C. G., Aguilar, J. C., Bard, A. J. Scanning electrochemical microscopy. 46. Shielding effects on reversible and quasireversible reactions. *Anal. Chem*. 2003, 75, 2959–2966.
28. Zoski, C. G. Scanning electrochemical microscopy: Investigation of hydrogen oxidation at polycrystalline noble metal electrodes. *J. Phys. Chem. B* 2003, 107, 6401–6405.
29. Sanchez-Sanchez, C. M., Rodriguez-Lopez, J., Bard, A. J. Scanning electrochemical microscopy. 60. Quantitative calibration of the SECM substrate generation/tip collection mode and its use for the study of the oxygen reduction mechanism. *Anal. Chem*. 2008, 80, 3254–3260.
30. Wipf, D. O., Bard, A. J. Scanning electrochemical microscopy. 7. Effect of heterogeneous electron-transfer rate at the substrate on the tip feedback current. *J. Electrochem. Soc*. 1991, 138, 469–474.
31. Xiong, H., Guo, J., Amemiya, S. Probing heterogeneous electron transfer at an unbiased conductor by scanning electrochemical microscopy in the feedback mode. *Anal. Chem*. 2007, 79, 2735–2744.
32. Xiong, H., Kim, J., Kim, E., Amemiya, S. Scanning electrochemical microscopy of one-dimensional nanostructure: Effects of nanostructure dimensions on the tip feedback current under unbiased conditions. *J. Electroanal. Chem*. 2009, 629, 78–86.
33. Tenent, R. C., Wipf, D. O. Local electron transfer rate measurements on modified and unmodified glassy carbon electrodes. *J. Solid State Electrochem*. 2009, 13, 583–590.

34. O'Mullane, A. P., Neufeld, A. K., Bond, A. M. Distinction of the two phases of CuTCNQ by scanning electrochemical microscopy. *Anal. Chem*. 2005, 77, 5447–5452.
35. McCreery, R. L. Advanced carbon electrode materials for molecular electrochemistry. *Chem. Rev*. 2008, 108, 2646–2687.
36. Dumitrescu, I., Unwin, P. R., Macpherson, J. V. Electrochemistry at carbon nanotubes: Perspective and issues. *Chem. Commun*. 2009, 6886–6901.
37. Wilson, N. R., Guille, M., Dumitrescu, I., Fernandez, V. R., Rudd, N. C., Williams, C. G., Unwin, P. R., Macpherson, J. V. Assessment of the electrochemical behavior of two-dimensional networks of single-walled carbon nanotubes. *Anal. Chem*. 2006, 78, 7006–7015.
38. Fabre, B., Hauquier, F., Herrier, C., Pastorin, G., Wu, W., Bianco, A., Prato, M., Hapiot, P., Zigah, D., Prasciolu, M., Vaccari, L. Covalent assembly and micropatterning of functionalized multiwalled carbon nanotubes to monolayer-modified Si(111) surfaces. *Langmuir* 2008, 24, 6595–6602.
39. Dumitrescu, I., Dudin, P. V., Edgeworth, J. P., Macpherson, J. V., Unwin, P. R. Electron transfer kinetics at single-walled carbon nanotube electrodes using scanning electrochemical microscopy. *J. Phys. Chem. C* 2010, 114, 2633–2639.
40. Heller, I., Kong, J., Heering, H. A., Williams, K. A., Lemay, S. G., Dekker, C. Individual single-walled carbon nanotubes as nanoelectrodes for electrochemistry. *Nano Lett*. 2005, 5, 137–142.
41. Watkins, J. J., Chen, J., White, H. S., Abruna, H. D., Maisonhaute, E., Amatore, C. Zeptomole voltammetric detection and electron-transfer rate measurements using platinum electrodes of nanometer dimensions. *Anal. Chem*. 2003, 75, 3962–3971.
42. Kim, J., Xiong, H., Hofmann, M., Kong, J., Amemiya, S. Scanning electrochemical microscopy of individual single-walled carbon nanotubes. *Anal. Chem*. 2010, 82, 1605–1607.
43. Xiong, H., Gross, D. A., Guo, J., Amemiya, S. Local feedback mode of scanning electrochemical microscopy for electrochemical characterization of one-dimensional nanostructure: Theory and experiment with nanoband electrode as model substrate. *Anal. Chem*. 2006, 78, 1946–1957.
44. Kim, E., Kim, J., Amemiya, S. Spatially resolved detection of a nanometer-scale gap by scanning electrochemical microscopy. *Anal. Chem*. 2009, 81, 4788–4791.
45. Murray, R. W. Nanoelectrochemistry: Metal nanoparticles, nanoelectrodes, and nanopores. *Chem. Rev*. 2008, 108, 2688–2720.
46. Xia, Y., Yang, P., Sun, Y., Wu, Y., Mayers, B., Gates, B., Yin, Y., Kim, F., Yan, H. One-dimensional nanostructures: Synthesis, characterization, and applications. *Adv. Mater*. 2003, 15, 353–389.
47. Goldsmith, B. R., Coroneus, J. G., Khalap, V. R., Kane, A. A., Weiss, G. A., Collins, P. G. Conductance-controlled point functionalization of single-walled carbon nanotubes. *Science* 2007, 315, 77–81.
48. Hurst, S. J., Payne, E. K., Qin, L. D., Mirkin, C. A. Multisegmented one-dimensional nanorods prepared by hard-template synthetic methods. *Angew. Chem. Int. Ed*. 2006, 45, 2672–2692.
49. Swain, G. M. Electrically conducting diamond thin films: Advanced electrode materials for electrochemical technologies, in *Electroanalytical Chemistry*, Vol. 22 (A. J. Bard and I. Rubinstein, eds.), Marcel Dekker, New York, 2004, pp. 181–277.
50. Holt, K. B., Bard, A. J., Show, Y., Swain, G. M. Scanning electrochemical microscopy and conductive probe atomic force microscopy studies of hydrogen-terminated boron-doped diamond electrodes with different doping levels. *J. Phys. Chem. B* 2004, 108, 15117–15127.
51. Wang, S. H., Swain, G. M. Spatially heterogeneous electrical and electrochemical properties of hydrogen-terminated boron-doped nanocrystalline diamond thin film deposited from an argon-rich CH_4/H_2/Ar/B_2H_6 source gas mixture. *J. Phys. Chem. C* 2007, 111, 3986–3995.
52. Neufeld, A. K., O'Mullane, A. P. Effect of the mediator in feedback mode-based SECM interrogation of indium tin-oxide and boron-doped diamond electrodes. *J. Solid State Electrochem*. 2006, 10, 808–816.
53. Holt, K. B., Ziegler, C., Zang, J. B., Hu, J. P., Foord, J. S. Scanning electrochemical microscopy studies of redox processes at undoped nanodiamond surfaces. *J. Phys. Chem. C* 2009, 113, 2761–2770.
54. Colley, A. L., Williams, C. G., Johansson, U. D., Newton, M. E., Unwin, P. R., Wilson, N. R., Macpherson, J. V. Examination of the spatially heterogeneous electroactivity of boron-doped diamond microarray electrodes. *Anal. Chem*. 2006, 78, 2539–2548.
55. Wilson, N. R., Clewes, S. L., Newton, M. E., Unwin, P. R., Macpherson, J. V. Impact of grain-dependent boron uptake on the electrochemical and electrical properties of polycrystalline boron doped diamond electrodes. *J. Phys. Chem. B* 2006, 110, 5639–5646.
56. Szunerits, S., Mermoux, M., Crisci, A., Marcus, B., Bouvier, P., Delabouglise, D., Petit, J. P., Janel, S., Boukherroub, R., Tay, L. Raman imaging and Kelvin probe microscopy for the examination of the heterogeneity of doping in polycrystalline boron-doped diamond electrodes. *J. Phys. Chem. B* 2006, 110, 23888–23897.

57. Chane-Tune, J., Petit, J.-P., Szunerits, S., Bouvier, P., Delabouglise, D., Marcus, B., Mermoux, M. Using scanning electrochemical microscopy to determine the doping level and the flatband potential of boron-doped diamond electrodes. *ChemPhysChem* 2006, 7, 89–93.
58. Finklea, H. O. Electrochemistry of organized monolayers of thiols and related molecules on electrodes, in *Electroanalytical Chemistry*, Vol. 19 (A. J. Bard, ed.), Marcel Dekker, New York, 1996, pp. 109–335.
59. Liu, B., Bard, A. J., Mirkin, M. V., Creager, S. E. Electron transfer at self-assembled monolayers measured by scanning electrochemical microscopy. *J. Am. Chem. Soc*. 2004, 126, 1485–1492.
60. Kiani, A., Alpuche-Aviles, M. A., Eggers, P. K., Jones, M., Gooding, J. J., Paddon-Row, M. N., Bard, A. J. Scanning electrochemical microscopy. 59. Effect of defects and structure on electron transfer through self-assembled monolayers. *Langmuir* 2008, 24, 2841–2849.
61. Zhang, J., Slevin, C. J., Morton, C., Scott, P., Walton, D. J., Unwin, P. R. New approach for measuring lateral diffusion in Langmuir monolayers by scanning electrochemical microscopy (SECM): Theory and application. *J. Phys. Chem. B* 2001, 105, 11120–11130.
62. Charych, D. H., Landau, E. M., Majda, M. Electrochemistry at the air/water interface. Lateral diffusion of an octadecylferrocene amphiphile in Langmuir monolayers. *J. Am. Chem. Soc*. 1991, 113, 3340–3346.
63. Chidsey, C. E. D., Murray, R. W. Electroactive polymers and macromolecular electronics. *Science* 1986, 231, 25–31.
64. Quinto, M., Bard, A. J. Polymer films on electrodes part 29. Electropolymerized poly(7,14-diphenylacenaphtho[1,2-*k*]fluoranthene): Electrochemistry and conductance of a novel electrochromic hydrocarbon ladder polymer film. *J. Electroanal. Chem*. 2001, 498, 67–74.
65. Zigah, D., Noel, J. M., Lagrost, C., Hapiot, P. Charge transfer between electroactive species immobilized on carbon surfaces by aryl diazonium reduction. SECM investigations. *J. Phys. Chem. C* 2010, 114, 3075–3081.
66. Quinto, M., Jenekhe, S. A., Bard, A. J. Polymer films on electrodes. 30. Electrochemistry and scanning electrochemical microscopy characterization of benzimidazolebenzophenanthroline-type ladder (BBL) and semiladder (BBB) polymer films. *Chem. Mater*. 2001, 13, 2824–2832.
67. Yang, N. J., Zoski, C. G. Polymer films on electrodes: Investigation of ion transport at poly(3,4-ethylenedioxythiophene) films by scanning electrochemical microscopy. *Langmuir* 2006, 22, 10338–10347.
68. Santos, L. M., Ghilane, J., Fave, C., Lacaze, P. C., Randriamahazaka, H., Abrantes, L. M., Lacroix, J. C. Electrografting polyaniline on carbon through the electroreduction of diazonium salts and the electrochemical polymerization of aniline. *J. Phys. Chem. C* 2008, 112, 16103–16109.
69. Wang, A., Ornelas, C., Astruc, D., Hapiot, P. Electronic communication between immobilized ferrocenyl-terminated dendrimers. *J. Am. Chem. Soc*. 2009, 131, 6652–6653.
70. O'Mullane, A. P., Macpherson, J. V., Unwin, P. R., Cervera-Montesinos, J., Manzanares, J. A., Frehill, F., Vos, J. G. Measurement of lateral charge propagation in $[Os(bpy)_2(PVP)_nCl]Cl$ thin films: A scanning electrochemical microscopy approach. *J. Phys. Chem. B* 2004, 108, 7219–7227.
71. White, R. J., White, H. S. Electrochemistry in nanometer-wide electrochemical cells. *Langmuir* 2008, 24, 2850–2855.
72. Feldberg, S. W. Implications of Marcus–Hush theory for steady-state heterogeneous electron transfer at an inlaid disk electrode. *Anal. Chem*. 2010, 82, 5176–5183.

7 Visualizing and Quantifying Homogeneous Chemical Reactions in Electrochemical Processes

Patrick R. Unwin

CONTENTS

7.1 Introduction and Principles 158
7.2 EC_i Processes 160
7.2.1 Tip Generation/Substrate Collection and Feedback Mode Characteristics 161
7.2.2 Substrate Generation/Tip Collection Mode 165
7.2.3 Applications 166
7.2.3.1 Oxidation of *N,N*,-Dimethyl-*p*-Phenylenediamine in Basic Aqueous Solution 166
7.2.3.2 Reduction of $[Cp^*Re(CO)_2(p\text{-}N_2C_6H_4OMe)][BF_4]$ in Acetonitrile 171
7.2.3.3 Oxidation of Di-tert-Butyl Nitroxide in Acetonitrile 173
7.2.3.4 Identification of Intermediates in the Oxidation of Borohydride 173
7.2.3.5 Probing Ligand Reorganization 175
7.3 EC_{2i} Processes 175
7.3.1 Principles and Theoretical Framework 175
7.3.2 Applications 176
7.3.2.1 Reductive Dimerization of Dimethyl Fumarate and Fumaronitrile in *N,N*-Dimethylformamide 176
7.3.2.2 Detection of Acrylonitrile Radical Anion 177
7.3.2.3 Oxidative Dimerization of 4-Nitrophenolate in Acetonitrile 178
7.3.2.4 Detection of Nicotinamide Adenine Dinucleotide Radical 179
7.3.2.5 Dimerization of Nitro Radical Anions 179
7.3.2.6 Superoxide Generation and Its Interaction with 1,4-Dihydropyridines 179
7.4 ECE/DISP Processes 179
7.4.1 Principles and Theoretical Characteristics 179
7.4.2 Applications 180
7.4.2.1 Anthracene Reduction in the Presence of a Proton Donor 180
7.4.2.2 Lifetime of Guanosine Radical Cation 182
7.4.2.3 Oxidation of Epinephrine 182
7.5 Catalytic EC′ Processes 182
7.5.1 Principles and Theoretical Characteristics 183

7.5.2 Applications 183
7.5.2.1 Oxidation of Amidopyrine by Electrogenerated $Fe(CN)_6^{3-}$ 183
7.5.2.2 Catalytic Reduction of Aromatic Halides 185
7.5.2.3 Temporal–Spatial Mapping of Concentration Profiles within a Working Glucose Biosensor 186
7.6 Conclusions and Future Perspectives 187
Acknowledgments 187
References 187

7.1 INTRODUCTION AND PRINCIPLES

Scanning electrochemical microscopy (SECM) and related ultramicroelectrode (UME) methods have proven powerful for measuring the kinetics of homogeneous reactions coupled to heterogeneous electron transfer. For this type of investigation, the tip and substrate are both electrodes and one can usefully consider the tip/substrate electrode configuration as a variable gap ultrathin layer cell. In essence, the gap thickness determines the diffusional transit time of chemical species between the tip and substrate and hence the range of timescales that can be studied.

The main classes of electrochemical reaction have been investigated using SECM, including irreversible chemical reactions of electrogenerated species,[1–6] catalytic reactions following electron transfer,[7] and chemical reactions sandwiched between successive electron transfers, as in the ECE/DISP scheme.[8] It should also be pointed out that homogeneous reactions coupled to electron transfer have also been exploited to create electrogenerated chemiluminescence in SECM,[9,10] but the focus of these studies is essentially to turn the tip into a light source, rather than to investigate homogeneous kinetics. Similarly, follow-up chemical reactions to tip electron transfer have been exploited as a means of enhancing the spatial resolution of SECM, via the so-called chemical lens.[11] These aspects will not be considered further in this chapter, which focuses on kinetic measurements.

The use of SECM to probe homogeneous reaction kinetics can be traced to the earliest applications of UMEs to profile concentration gradients at macroscopic (millimeter-sized) electrodes.[1,2] There has been considerable progress subsequently, such that short-lived intermediates, in electrode reactions, can readily be identified by SECM under steady-state conditions, that would be difficult to characterize by alternative transient UME methods, such as fast scan cyclic voltammetry (FSCV).[12]

The principal modes of SECM used to characterize and measure homogeneous reactions of the type identified earlier are the feedback mode, the tip generation/substrate collection (TG/SC) mode, and the substrate generation/tip collection (SG/TC) mode. For illustrative purposes, these modes are compared schematically in Figure 7.1 for the case where a species B, produced by reduction of a species A at a generator electrode, undergoes a first-order chemical reaction in solution (rate constant, k_1). In both of these modes, and as drawn, there is significant diffusional coupling (feedback) of redox species between the tip and substrate. However, it should also be pointed out that SG/TC measurements have also been carried out under conditions where this feature is negated, by employing a very small tip size compared with the tip/substrate separation. In this case, the tip serves as a passive probe of the concentration boundary layer at the larger substrate electrode and can be used to map the concentration profiles of reactants, products, and intermediates.[7,13–16] This type of approach has also been used to probe the extent of chemical reactions coupled to electron transfer at freely reacting liquid–liquid interfaces.[17]

To consider how SECM may be used to measure coupled chemical kinetics, let us examine briefly the case of an irreversible chemical reaction (C_i) following heterogeneous electron transfer at an electrode (E step). In the closely related feedback and TG/SC modes, the heterogeneous electron transfer process is driven at a diffusion-controlled rate, usually at a disk-shaped tip UME (radius *a*). A larger collector (substrate) electrode, positioned directly below the tip, typically at a tip/substrate

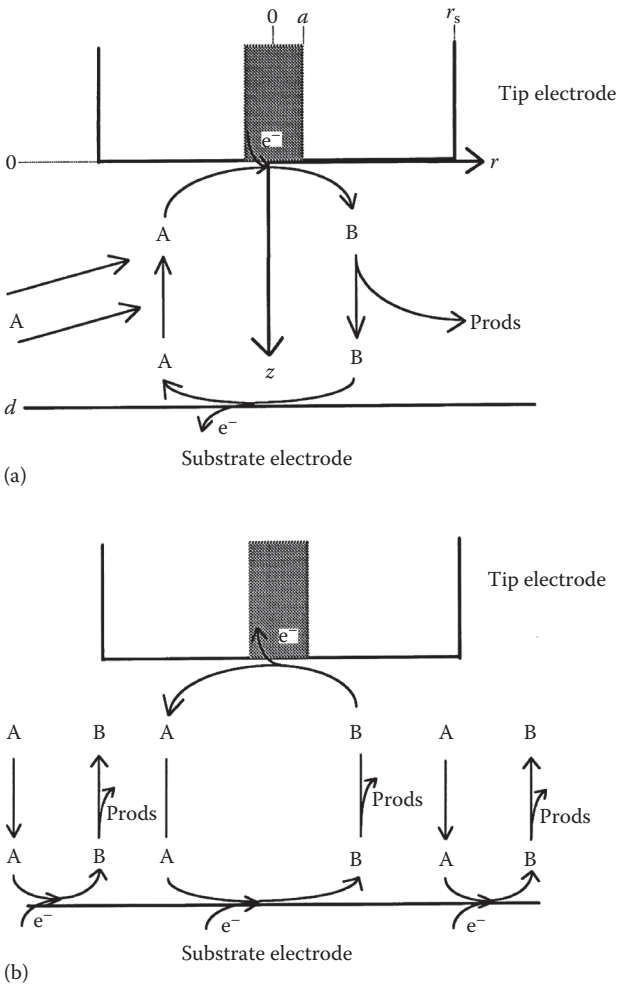


FIGURE 7.1 Principles of (a) the feedback (TG/SC) modes and (b) the SG/TC mode for measuring follow-up chemical reactions of electrogenerated species. Species B, produced from a solution precursor species, A, at a generator electrode undergoes decomposition during transit to a collector electrode. Note that in the case of the feedback and SG/TC mode, only the tip current is generally measured, whereas for the TG/SC mode, the tip and substrate currents are of interest. The coordinate system and notation for the SECM geometry is shown. The schematic is not to scale; typically, $r_S \geq a$ and $d \geq a$.

distance $d \leq 2a$, is held at a potential where the oxidation of B back to A is diffusion controlled. With this electrode configuration, a competition is established between (i) the diffusion of B from the tip to the substrate, with the consequent regeneration and feedback diffusion of A and (ii) the chemical decomposition of B to products (generally considered to be electroinactive at the potentials of interest). The kinetics of the chemical reaction are probed by varying the tip/substrate distance, and thus the diffusion time of B to the substrate, while measuring the tip current, i_T (in the feedback mode) or i_T and the substrate current, i_S (TG/SC mode). When the tip/substrate diffusion time, of the order d^2/D (where d is the tip/substrate separation and D is the diffusion coefficient of B), is short compared to the lifetime of B, most of B generated reaches the substrate electrode for conversion to A, with the result that i_T and i_S approach values expected for positive feedback in the absence of homogeneous kinetics. In the fast kinetic limit, the tip response is similar to that for negative

feedback and i_S tends to zero, since little B survives the passage across the gap. Between these two limits, kinetic measurements are possible.

From a practical viewpoint, feedback measurements are the easiest to implement, in terms of both the electrochemical and positioning instrumentation required, because it may be unnecessary to bias the substrate externally,[18] allowing the use of a simple two- or three-electrode arrangement in which the tip UME is the sole working electrode. A bipotentiostat is required for experimental investigations if substrate currents are also to be measured, as in the TG/SC mode. For this mode, the substrate electrode is shrunk to a size where background noise is minimized, but all B reaching the substrate is still collected. The factors governing the minimum substrate size for this type of measurement are outlined in Section 7.2.1. For this case, it is necessary to align the tip and a substrate UME with good precision, typically demanding the use of high-resolution remote-controlled positioners on all three axes of the SECM. For feedback mode experiments, it is only necessary to accurately control the position of the tip in the direction normal to a large substrate electrode, which greatly simplifies the instrumentation requirements. As will become clear from Section 7.2.1, the TG/SC mode offers significant advantages over the feedback mode in the study of rapid follow-up chemical reactions, because one uses the substrate to collect a transient species under conditions where no other electrochemical processes contribute to the signal measured at that electrode.

In the SG/TC mode (Figure 7.1b), species B is electrogenerated at the substrate electrode and the reverse process, in which B is oxidized to A, occurs at the tip. In experiments hitherto, the substrate electrode has generally,[1,2,6,13–16,19] but not exclusively,[4,7,20] been macroscopic (millimeter dimensions) with a disk of micrometer dimensions serving as the collector electrode. As with the feedback and TG/SC modes, discussed earlier, the tip/substrate separation is a key experimental variable. If the substrate electrode is large, as is often the case, high-resolution positioning is only required in the direction perpendicular to the surfaces of the tip and substrate.

A further recent mode uses both the tip and substrate to generate each of two reactants that undergo a homogeneous redox reaction.[21] This configuration[22] requires high-resolution positioning to align the two electrodes, but offers the opportunity of essentially studying homogeneous reactions of electrogenerated species in a picoliter volume cell.

7.2 EC_i PROCESSES

The EC_i process is perhaps the simplest example of an electrochemical reaction mechanism involving a homogeneous reaction coupled to heterogeneous electron transfer at an electrode. Dual electrode methods have proven especially useful for studying the kinetics of the C_i step, including the rotating ring-disk electrode (RRDE),[23] twin electrodes in a thin layer cell,[24] double channel or tubular electrodes,[25] interdigitated channel array electrodes,[26] and paired microband electrodes.[27] Common to all of these methods is the use of a second (collector) electrode to measure the fraction of an electrogenerated species that survives the transit from a nearby generator electrode. Overall, considering the E step to involve the reduction of A to B, the following processes occur:

$$\text{Generator electrode} : \mathrm{A} + n\mathrm{e}^- \rightarrow \mathrm{B} \tag{7.1}$$

$$\text{Solution} : \mathrm{B} \xrightarrow{k_1} \text{Products} \tag{7.2}$$

$$\text{Collector electrode} : \mathrm{B} - n\mathrm{e}^- \rightarrow \mathrm{A} \tag{7.3}$$

Although SECM operates on broadly similar principles to other double electrode methods, the SECM geometry offers several major advantages, in terms of the kinetic range that can be studied and the precision with which measurements can be made, as discussed later.

7.2.1 Tip Generation/Substrate Collection and Feedback Mode Characteristics

In order to understand and explain the effects of irreversible follow-up chemical reactions on the SECM response, it is first useful to briefly explain the feedback and TG/SC characteristics under diffusion-controlled conditions, without complications from homogeneous kinetics. Consider the situation where the tip potential is stepped from a value where no reactions occur to one where the conversion of A to B is diffusion limited. Typical theoretical characteristics for the chronoamperometric tip and substrate responses vs. normalized time, $\tau = tD/a^2$ (where t is time) are shown in Figure 7.2 for several different tip/substrate separations. These particular data, for the case where the diffusion coefficients of A and B are equal, were obtained numerically with the alternating direction implicit finite difference method (ADIFDM),[4,28] and are equivalent to earlier simulations using a Krylov integrator.[29] Treatments for the case of unequal diffusion coefficients of A and B have also been given.[30,31] At the shortest time, the tip current i_T (normalized by the steady-state tip current in bulk solution, $i_{T,\infty}$) is independent of d/a, since the diffusion field adjacent to the UME is small compared to the size of the tip/substrate gap and the tip shows the behavior predicted for a simple disk UME under chronoamperometric control.[32] With time, the diffusion field extends toward, and ultimately intercepts, the substrate (collector) electrode causing a current flow. Since the tip/substrate diffusion time is of the order d^2/D, the smaller the value of d/a, the sooner the substrate current begins to flow and the more rapidly the currents at the tip and substrate attain steady-state values. Moreover, the closer the two electrodes are positioned together, the greater is the extent of positive feedback, reflected by increases in i_T and i_S as d/a is decreased.[3,4]

For all of the tip–substrate separations shown in Figure 7.2, steady-state (denoted by the subscript SS) collection efficiencies

$$N_{SS} = \left(\frac{i_S}{i_T}\right)_{SS} \tag{7.4}$$

of essentially 100% are apparent. The high collection efficiency (CE) (with the tip and substrate currents further enhanced by feedback)[33] makes TG/SC measurements particularly sensitive for kinetic measurements, compared to alternative dual electrode configurations, such as those mentioned in Section 7.2.

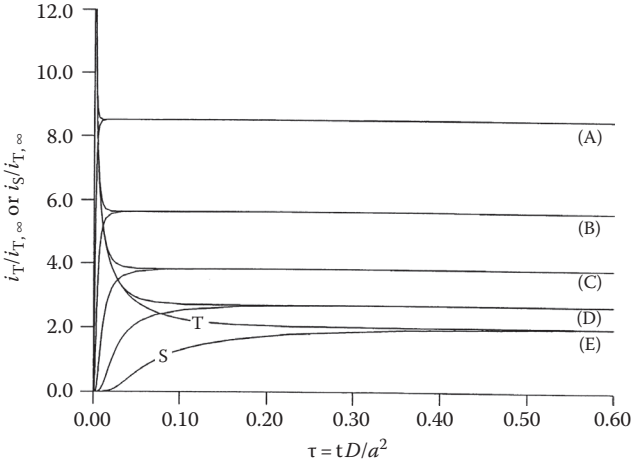


FIGURE 7.2 Tip and substrate chronoamperometric characteristics (presented as normalized current magnitudes) for the TG/SC mode for diffusion-controlled positive feedback with no homogeneous kinetic complications. The data are for $\log(d/a)$ = (A) −1.0, (B) −0.8, (C) −0.6, (D) −0.4, and (E) −0.2. The tip and substrate currents are denoted by T and S on curve (e).

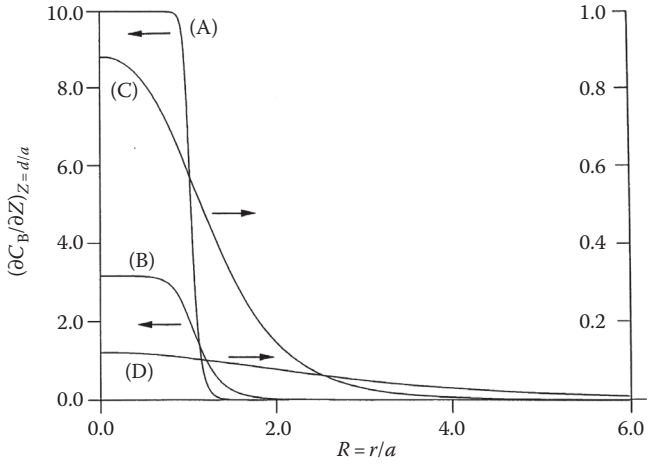


FIGURE 7.3 Normalized flux of the tip-generated species, B, over the substrate (collector) electrode for diffusion-controlled kinetically uncomplicated conditions. The data are for $\log(d/a)$ = (A) −1.0, (B), −0.5, (C) 0.0, and (D) 0.5. Note that (A) and (B) refer to left hand *y*-ordinate and (C) and (D) to the right hand *y*-ordinate.

The portion of the substrate electrode that collects the intermediate species B depends on the normalized tip/substrate separation, d/a. This point is illustrated in Figure 7.3, which shows the flux of tip-generated species B over the surface of the substrate electrode. As $d/a \rightarrow 0$, the domain of the substrate that collects the tip-generated species approaches the size of the tip, but increases as the tip is moved away from the substrate. Empirically, the minimum dimensionless substrate size, h/a, where h is the radius of the substrate required for a steady-state CE of effectively 100%, is given by[34]

$$h/a = 1 + 1.5\left(\frac{d}{a}\right) \tag{7.5}$$

Equation 7.5 has important experimental implications, since the noise, in the form of residual current, associated with a steady-state current signal is typically proportional to the area of the electrode. This equation thus serves as a useful guide of the minimum substrate size that can be employed experimentally, to maximize the signal-to-noise ratio in TG/SC measurements. This aspect is well illustrated, for example, by the studies reported in Section 7.4.2.2.

To illustrate the effect of an irreversible follow-up chemical reaction on the feedback tip response, Figure 7.4 shows calculated chronoamperometric behavior for $\log(d/a)$ values of −1.0 and −0.4, for a range of values of the dimensionless kinetic constant, $K = k_1 a^2/D$. To emphasize the short-time behavior, data are presented as normalized current vs. the inverse square root of normalized time. At the shortest time (largest $\tau^{-1/2}$), the i_T response is the same as for the simple electron transfer case discussed earlier, showing no dependence on K or d/a. On this timescale, the current is governed by the diffusion of species A to the electrode, which results in a Cotrellian response. As K increases, the behavior shifts from a limit where the response is essentially that for positive feedback to a situation where, as $K \rightarrow \infty$, the behavior tends to that for negative feedback with an inert substrate. In this latter case, the lifetime and reaction layer thickness of B approaches zero, so that the tip current is governed entirely by the hindered diffusion of A.

For intermediate values of K, the current–time behavior initially follows that for positive diffusion-controlled feedback, without kinetic complications, that is, a quasi-steady-state current is rapidly attained, resulting in plateau regions in the $i_T - \tau^{-1/2}$ plots. Under these conditions, the rates of diffusion between the tip and the substrate electrode are sufficiently rapid for the follow-up chemical reaction to be outrun. At times comparable to the lifetime of B, deviations from pure positive feedback behavior are observed, as the homogeneous chemical process begins to consume

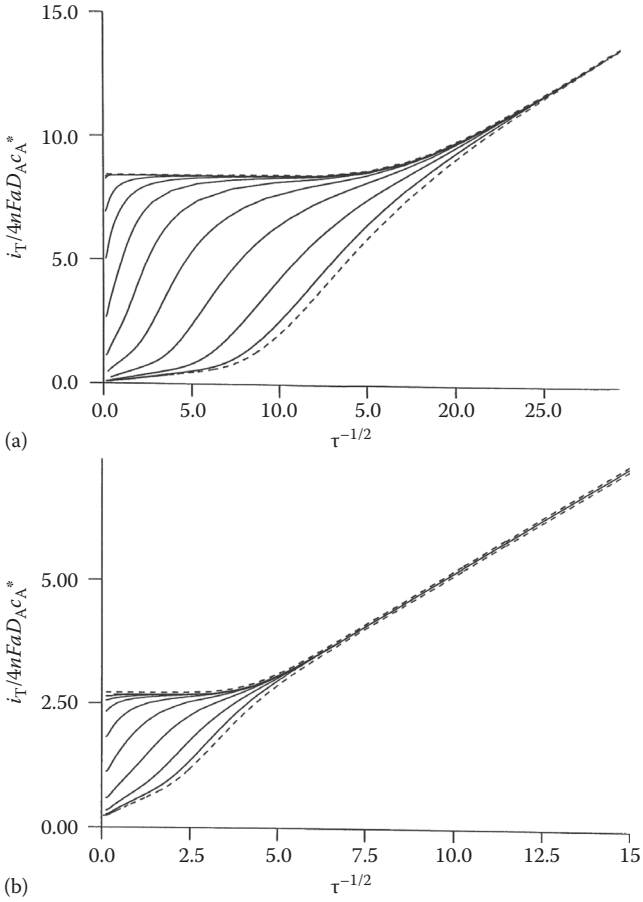


FIGURE 7.4 Calculated tip feedback current transients for an EC_i process, displayed as a function of $\tau^{-1/2}$, for $\log(d/a) =$ (a) −1.0 and (b) −0.4. The upper and lower dashed curves in each diagram are, respectively, the behavior for diffusion-controlled positive and negative feedback. The curves between these extremes are for (a) $\log K = 3.0$ (lower solid curve), 2.5, 2.0, 1.5, 1.0, 0.5, 0.0, −0.5, −1.5, and −2.0 (upper solid curve) and (b) $\log K = 1.8$ (lower solid curve), 1.3, 0.8, 0.3, −0.2, −0.7, −1.2, −1.7, and −2.2 (upper solid curve).

the tip-generated species. In general, the larger the K value: the earlier is the deviation from positive feedback, the more rapid is the current decay, and the smaller is the final steady-state current.

A discussion of the chronoamperometric feedback response is valuable, as potential step measurements have been used to obtain homogeneous kinetic parameters.[3] Calculations of the chronoamperometric response also provide valuable information on the time taken to reach a true steady state, which is particularly important for approach curve measurements. It has been demonstrated that values of τ in excess of 100 may be necessary to achieve steady-state conditions (within a few percent).[3] For typical tip disk electrode radii of 12.5 and 2.5 μm, and a typical diffusion coefficient of 1×10^{-5} cm^2 s^{-1}, this corresponds to real times that are greater than 15 and 0.6 s, respectively. For the larger disk size, the time is longer than required for many other steady-state measurements with SECM. Furthermore, it is important to point out that this analysis is for the situation where A and B have the same diffusion coefficient. It has been demonstrated comprehensively that unequal diffusion coefficients of A and B greatly increase the time to true steady state even for simple electron transfer without homogeneous kinetics.[30]

Steady-state working curves of the tip feedback response as a function of K for different tip/substrate separations are given in Ref. [3], and a set of curves for several distances is shown in

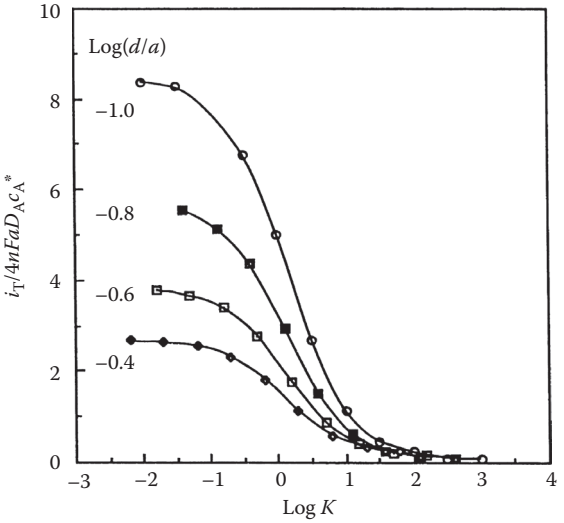


FIGURE 7.5 Steady-state normalized tip feedback current–K working curves for several values of log(d/a).

Figure 7.5. As with many kinetic applications of SECM, this figure illustrates that the range of kinetics open to characterization can be expanded by decreasing the interelectrode separation. Moreover, under conditions of close tip/substrate separation, the feedback current varies most sharply with K, in principle, allowing measurements to be made with the greatest precision.

For TG/SC (feedback) measurements, a formalism is available that relates the steady-state substrate current to the steady-state tip generator current:[5]

$$i_S = i_T^{con}\left(\frac{i_T - i_T^{ins}}{i_T^{con} - i_T}\right) \tag{7.6}$$

where i_T^{con} and i_T^{ins} are the steady-state tip currents for the limits of pure diffusion-controlled positive ($K=0$) and negative ($K\rightarrow\infty$) feedback, respectively. These currents are given by[5,35]

$$\frac{i_T^{con}}{i_{T,\infty}} = \frac{0.78377}{L} + 0.3315\exp\left(\frac{-1.0672}{L}\right) + 0.68 \tag{7.7}$$

$$\frac{i_T^{ins}}{i_{T,\infty}} = \left(0.15 + \frac{1.5358}{L} + 0.58\exp\left(\frac{-1.14}{L}\right) + 0.0908\exp\left[\frac{(L-6.3)}{(1.017L)}\right]\right)^{-1} \tag{7.8}$$

It has further been shown that, under steady-state conditions, the CE, N_{SS}, depends on a single-valued dimensionless parameter:

$$\kappa = \frac{k_1 d^2}{D} \tag{7.9}$$

with the following empirical equation describing the relationship within about 1%

$$\kappa = 5.608 + 9.347\exp(-7.527N_{SS}) - 7.616\exp\left(\frac{-0.307}{N_{SS}}\right) \tag{7.10}$$

The determination of kinetic parameters from CE measurements is most suitable when values lie between 0.1 and 0.8,[5] which corresponds to κ values in the range ca. 0.5–10. Assuming $d = 200$ nm as the closest distance that is achievable reliably with disk-shaped UMEs of the type used for SECM kinetic measurements, this translates to an upper range for k_1 values of 1.25×10^4 to 2.5×10^5 s^{-1}, for a typical D value of 10^{-5} cm^2 s^{-1}. Lower values of k_1 are, of course, accessible by employing larger d values.

7.2.2 Substrate Generation/Tip Collection Mode

In this mode, Equations 7.1 through 7.3 are applicable, but Equation 7.1 is driven at a substrate electrode, while the collection process occurs at the tip UME. In initial investigations using this mode,[1,2] for various types of follow-up, and intermediate, chemical reactions, it was assumed that the tip UME was a passive sensor, acting as a local noninvasive probe of a time-dependent planar diffusion field at a larger substrate electrode. Although this approach gave interesting semiquantitative insights into reaction kinetics and mechanisms, a more rigorous model, taking account of possible feedback effects between the substrate and tip, was later developed for the EC_i mechanism[6] and will be discussed here.

Typical tip current transients are shown in Figure 7.6 for the case where the substrate is switched on to drive Equation 7.1 at a diffusion-limited rate and Equation 7.3 occurs at the tip. Two different distances, $\log(d/a) = -0.7$ (a) and -0.2 (b), are shown for a range of kinetic constants. Considering first the $K = 0$ case, it can be seen that after an initial lag period, the tip current rises from zero to a steady-state value. The magnitude of the steady-state current and the rise time depend on the tip/substrate separation,[6,19] such that the closer the tip and substrate, the more rapid the current rise, and the sooner a steady state is established.

In contrast, for finite values of K, the current does not reach a steady state; rather it rises to a peak value and then decreases at longer times. The values of both K and d/a have a marked effect on the overall shape of the transient tip current and the magnitude of the peak current. For a given tip/substrate separation, the larger the value of K, the smaller is the peak current, the shorter the time to reach the peak, and the steeper the decay curve following the peak. In essence, by increasing the rate of the following chemical reaction, the fraction of substrate-generated B that reaches the tip in the first pass decreases, thereby diminishing the peak current. The importance of diffusional feedback between the substrate and tip decreases with increasing rate constant, causing the rapid decay in the current and the appearance of the peak at shorter times.

As for feedback and TG/SC measurements, discussed in Section 7.2.1.1, it can be seen from Figure 7.6 that the tip collector current response ($i_{T,C}$) becomes less sensitive to solution kinetics, the greater the spacing between the tip and substrate electrodes. For a given value of K, the peak current can be increased by decreasing the tip/substrate separation, but this also pushes the peak to shorter times. Thus, although close tip/substrate separations lead to high sensitivity in terms of tip current, the tip response has to be measured with the highest time resolution in this situation.

The characteristic features of the tip current transients in Figure 7.6 are the peak current, peak time, and post-half-peak time. These features show interesting dependences on the tip/substrate separation and K (Figure 7.7). The magnitude of the normalized peak current (Figure 7.7a) increases as the values of both K and d/a are decreased, whereas the time taken to reach the peak increases as the value of d/a is increased and K is decreased (Figure 7.7b). This contrasting behavior allows both K and d/a to be determined from a single transient measurement with good precision. In particular, kinetics are determinable from SG/TC measurements with no prior knowledge of the tip/substrate separation.[6] The post-half-peak time has a yet different dependence on d/a and K. This increases as K decreases but shows only a minimal dependence on the normalized interelectrode separation (Figure 7.7c).

The range of k_1 measurable with the SG/TC mode is largely governed by the timescale on which tip currents can be recorded. For example, toward the fast kinetic limit, a normalized peak current in excess of unity results for $\log K = 2.5$, with tip/substrate separations closer than $\log(d/a) < -0.8$ (Figure 7.7). The normalized time at which the peak occurs is, however, smaller than 0.01. For a tip

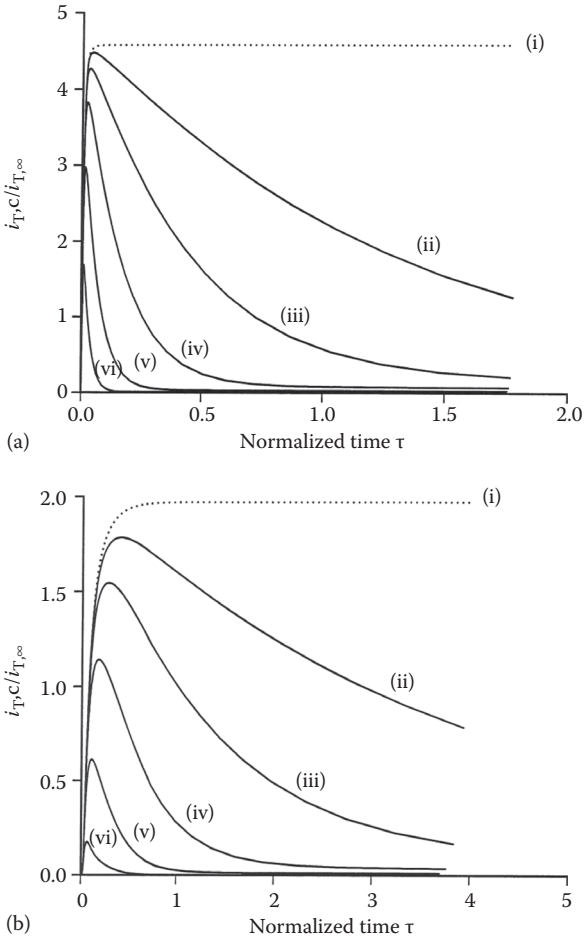


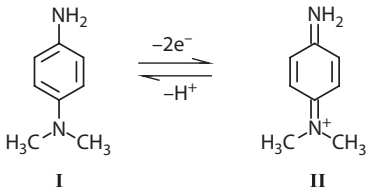
FIGURE 7.6 SG/TC tip chronoamperometric characteristics for an EC_i process at normalized tip/substrate separations of $\log(d/a) =$ (a) −0.7 and (b) −0.2. The dashed lines (i) show the behavior for $K = 0$, while the solid lines are for log K values of (ii) −0.5, (iii) 0.0, (iv) 0.5, (v) 1.0, and (vi) 1.5.

UME with a radius of 10 µm and a typical diffusion coefficient of 10^{-5} cm^2 s^{-1}, these figures relate to a rate constant in excess of 3000 s^{-1} and a corresponding peak time less than 10^{-3} s.

7.2.3 Applications

7.2.3.1 Oxidation of *N,N,*-Dimethyl-*p*-Phenylenediamine in Basic Aqueous Solution

The oxidation of dimethyl-*p*-phenylenediamine (DMPPD) is a model EC_i process,[36] which has been used to determine the capabilities of SECM as a probe of follow-up chemical kinetics.[3,6] A fast two-electron oxidation, with the loss of a proton, constitutes the E step (Equation 7.11), which may be followed by a pH-dependent deamination (C) step (Equation 7.12):



(7.11)

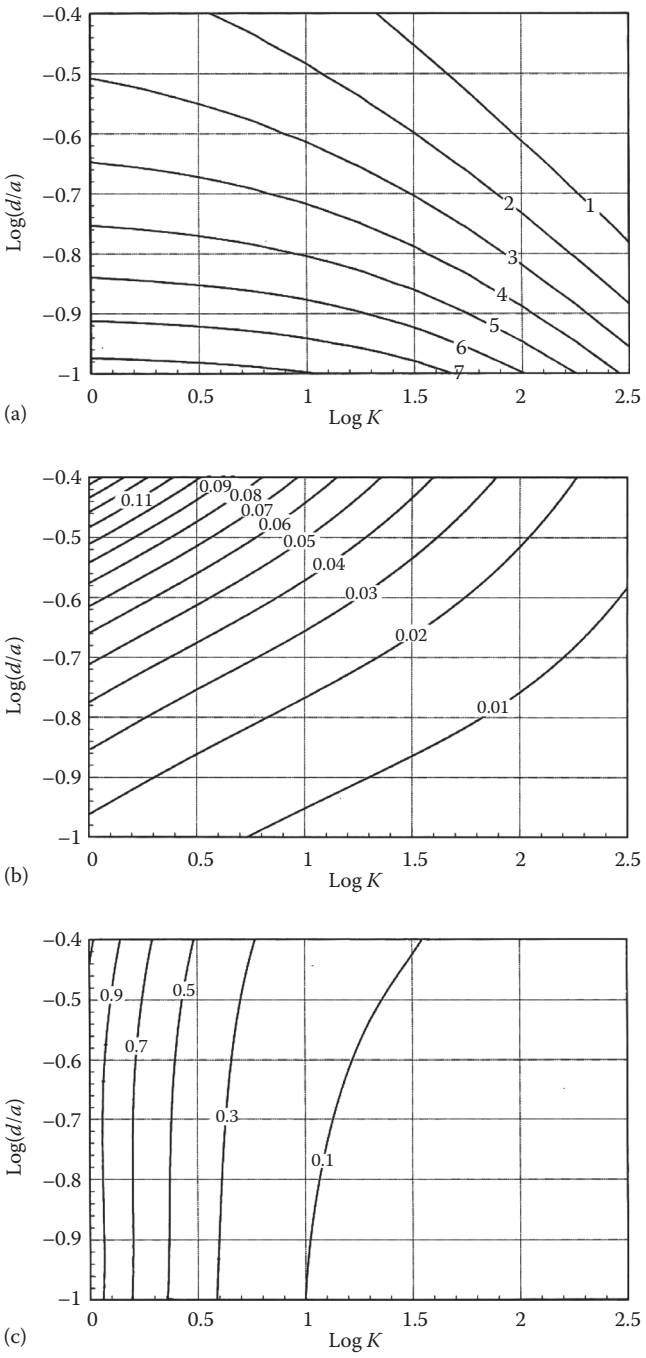
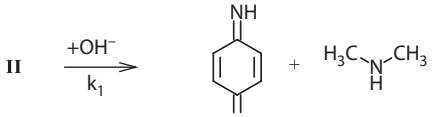


FIGURE 7.7 Theoretical contour plots showing the variation of (a) peak current, (b) peak time, and (c) post-half-peak time with tip/substrate separation and normalized rate constant. The labels on the contours are values of the normalized current ratio ($i_{T,C}/i_{T,\infty}$) in (a) and normalized time (τ) in (b) and (c).



(7.12)

The first SECM studies of this scheme employed chronoamperometric and steady-state feedback measurements with a 25 μm diameter Pt UME tip and an unbiased macroscopic Pt disk substrate. Given the relatively large size of the probe employed for the DMPPD system, measurements were made pointwise at a series of distances to ensure a steady state was attained.[3]

Typical feedback approach curves for DMPPD oxidation in solutions of pH 10.20, 10.78, and 11.24 are shown in Figure 7.8, along with the behavior for diffusion-controlled positive and negative feedback. The tip electrode process was defined by Equation 7.11, while the unbiased macroscopic substrate was poised at a potential where the reverse reaction occurred at a diffusion-controlled rate:

$$\mathbf{II} + 2e^- + H^+ \rightarrow \mathbf{I} \tag{7.13}$$

Evidently as the pH is raised, the current at any particular distance shifts away from the positive feedback response, toward the behavior predicted for negative feedback, due to the consumption of **II** in solution, according to Equation 7.12.

Experimental data analyzed well in terms of EC_i theory.[3] Using i_T–K working curves for each of the distances in Figure 7.8, the tip currents were converted to values of K and then κ. It is evident from Equation 7.9 that, for a given pH, a plot of κ values vs. d^2 should be linear and intercept the origin. Figure 7.9 shows that this is the case; k_1 of 19 s^{-1} (pH 11.24), 5.8 s^{-1} (pH 10.78), and 1.4 s^{-1} (pH 10.20) were obtained from the slopes of the lines.[3] The corresponding second-order rate constants (approximating the measured activity of OH^- by concentration), $k_2 = k_1/[OH^-]$, were found to be reasonably consistent: 1.1×10^4, 9.5×10^3, and 9.0×10^3 mol^{-1} dm^3 s^{-1}, respectively.

Chronoamperometric measurements of the oxidation of DMPPD were made over a range of pH from 7.80 to 12.42, with a fixed tip/substrate separation of 6.5 μm. Typical experimental data are shown in Figure 7.10, alongside theoretical transients based on the mean rate constant derived from the steady-state measurements described earlier. For pH 7.80, the deamination process was assumed to proceed to a negligible extent, while for the other pH, the rate constants used to fit the data were $k_1 = 7.8$ s^{-1} (pH 10.90), 24 s^{-1} (pH 11.38), 42 s^{-1} (pH 11.63), and 260 s^{-1} (pH 12.42). Even with the large UME and tip/substrate separation employed for this study, the ability of transient chronoamperometric measurements to probe follow-up chemical reactions over a wide dynamic range (almost two orders of magnitude in k_1) and relatively fast kinetics is clearly evident from Figure 7.10.

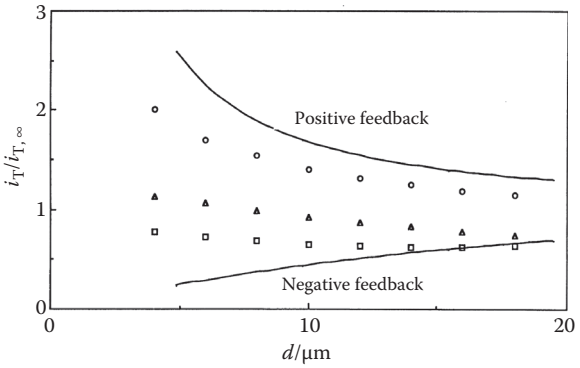


FIGURE 7.8 Steady-state feedback i_T–d characteristics for the oxidation of 5×10^{-4} M DMPPD at pH 10.20 (○), 10.78 (Δ), and 11.24 (□). The solid lines represent the theoretical behavior for diffusion-controlled positive feedback ($K = 0$) and negative feedback ($K \rightarrow \infty$).

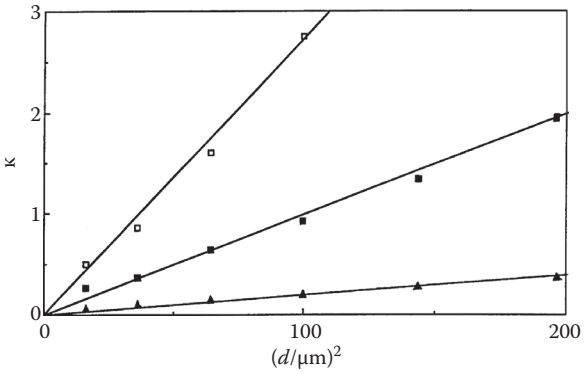


FIGURE 7.9 Kinetic analysis of the data in Figure 7.8 using Equation 7.9 [pH 10.20 (Δ), 10.78 (■), and 11.24 (□)].

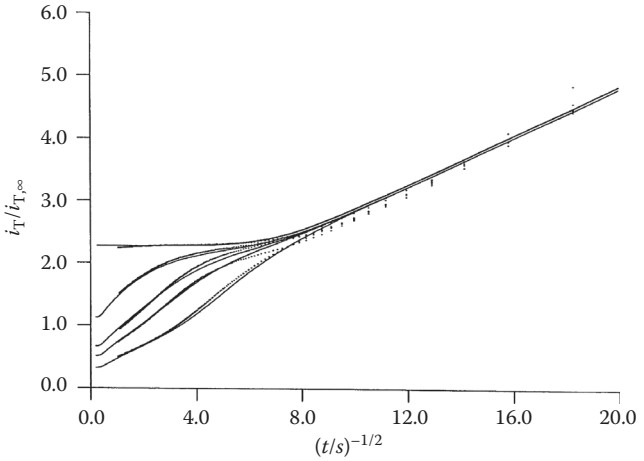


FIGURE 7.10 Potential step chronoamperometric feedback characteristics (···) with a 25 μm diameter Pt tip at a tip/substrate separation of 6.5 μm, for the oxidation of DMPPD at pH 7.80 (upper curve), 10.90, 11.38, 11.63, and 12.42 (lower curve). The solid lines show the corresponding theoretical behavior for each pH using the rate constants defined in the text.

As discussed in Sections 7.2.1 and 7.2.2, the analysis of SECM chemical kinetic data assumes that the electroactive precursor (A in the terminology of our example case) and the electrogenerated species (B) have the same diffusion coefficient. A simple approach for confirming this is to measure the tip currents at a fixed (close) tip/substrate separation, under positive feedback and then SG/TC control. For a chemically stable redox couple, the ratio of the tip feedback and collector currents under steady-state conditions reveals the diffusion coefficient ratio, β, directly[19]

$$\beta = \frac{i_{T,c}}{i_T^{con}} \tag{7.14}$$

without any prior knowledge of the tip/substrate separation, the electrode sizes, or the concentration of the species of interest. Figure 7.11 shows typical tip transients in the feedback and SG/TC modes for the oxidation of DMPPD at pH 7.65, where the follow-up chemical reaction (Equation 7.11) was negligible on the SECM timescale. The tip/substrate separation was ca. 5 μm, as inferred from the steady-state feedback current, which is β-independent[10] (although this information is not needed for

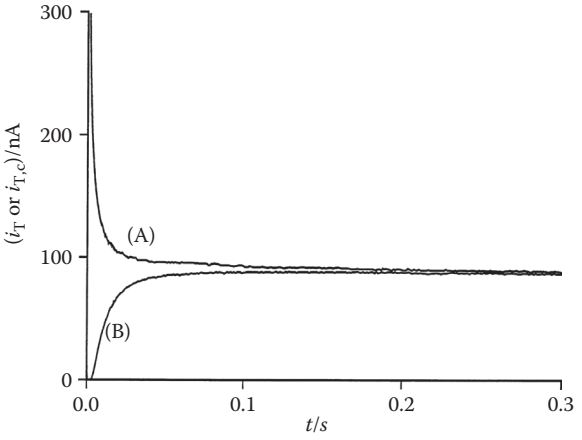


FIGURE 7.11 (A) Tip feedback and (B) SG/TC tip collector chronoamperometric characteristics for the oxidation of 4 mM DMPPD at pH 7.65, with a fixed tip/substrate separation of 5.0 μm. The transients reach similar steady-state values indicating that the ratio of diffusion coefficients (β) of the electrode reactant and product is close to unity.

the analysis). For the I/II couple, it was found that $\beta = 0.98 \pm 0.02$, indicating that the diffusion coefficients of I and II were effectively the same.[19]

The kinetics of the deamination step (Equation 7.12) of oxidized DMPPD have also been investigated with the SG/TC mode, with a 2 mm^2 substrate generator electrode and a 25 μm diameter Pt disk UME collector electrode. Figure 7.12 shows a selection of typical tip current responses for the oxidation of I at the substrate electrode and the collection of II at the tip, with three pH values (10.94, 11.36, and 11.54) to promote the deamination process. For these measurements, the substrate potential was stepped to drive the oxidation of DMPPD at a diffusion-controlled rate and the tip UME potential was such that Equation 7.13 was driven at a diffusion-controlled rate.

The shapes of the experimental tip transients were found to be consistent with the theoretical predictions for an EC_i process (Section 7.2.2), with the collector current initially rising to a peak value and then decaying at longer times. In each case, the interelectrode separation and diffusion coefficient of DMPPD were known, and thus the rate constant was the only variable in the fitting procedure. The transients at different pH yield a consistent rate constant for the deamination step, with values for k_1 of 8.8 s^{-1} [(a), pH 10.94], 23 s^{-1} [(b), pH 11.36], and 33 s^{-1} [(c) pH 11.54]. For comparative purposes, these values yielded a second-order rate constant, $k_2 = k_1/[OH^-] = 1.0(\pm 0.1) \times 10^4$ mol^{-1} dm^3 s^{-1}, in good agreement with the feedback measurements discussed earlier.

Although the interelectrode separations were known with good precision in this set of experiments,[6] the extent to which SG/TC transients could determine both the rate constant and interelectrode separation was also examined. Figure 7.13 shows the sets of interelectrode spacings and rate constants that are consistent with the peak currents and peak times derived from the transients in Figure 7.12. The intersection of the two contours on each plot yields the following values of d and k_1, respectively: (a) 2.7 μm and 9.2 s^{-1} (pH 10.94), (b) 1.9 μm and 30 s^{-1} (pH 11.36), and (c) 2.6 μm and 37 s^{-1} (pH 11.54). The values of interelectrode separation are close to those assumed in fitting the entire transients mentioned earlier, while the rate constants are in good agreement with those obtained by fitting the full tip transients, yielding $k_2 = 1.15(\pm 0.15) \times 10^4$ mol^{-1} dm^3 s^{-1}. These results clearly illustrate that both chemical reaction rate constants and interelectrode separations can be determined with good precision and accuracy from the measurement of the peak current and peak time from tip collector transient measurements in the SG/TC mode.

Along with several other examples, the oxidation of DMPPD in basic solution was used as a model system to illustrate the potential of multispecies measurements via FSCV-SECM.[37] The idea

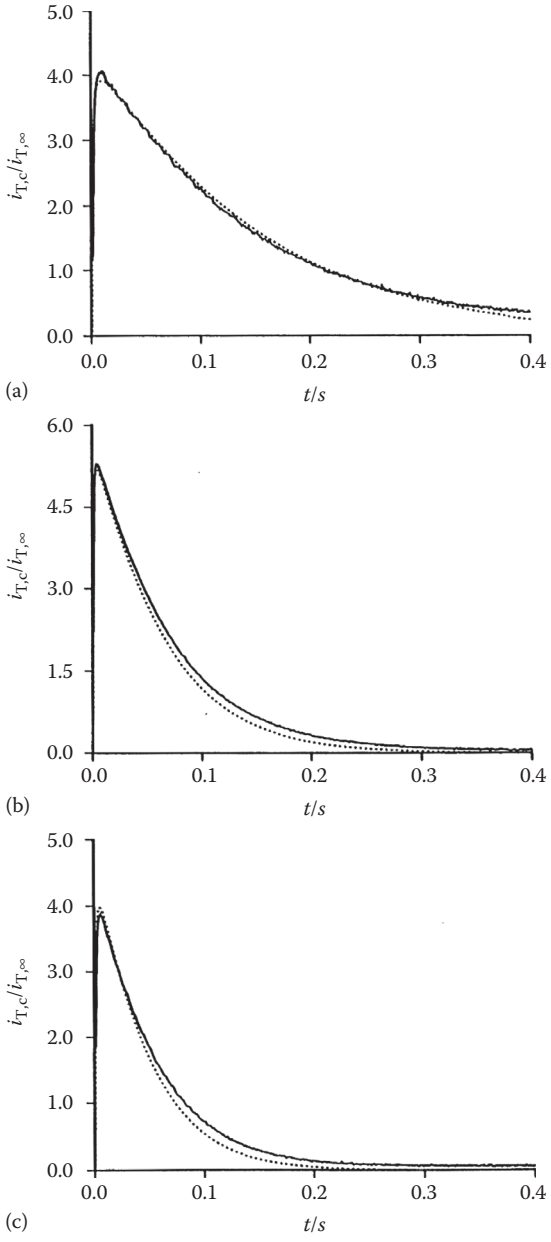


FIGURE 7.12 Tip collector chronoamperometric responses for the oxidation of 4 mM DMPPD in the SG/TC mode, under the following conditions: (a) pH 10.54, $d = 2.75\,\mu m$; (b) pH 11.36, $d = 2.0\,\mu m$; and (c) pH 11.54, $d = 2.5\,\mu m$. The experimental data (—) have been fitted to theoretical responses using the values of k_1 cited in the text.

of this technique is to run CVs at every point during the acquisition of an SECM image thereby enhancing the information content. One can then construct current images (either parallel or normal to the substrate electrode, which is typically held at a fixed potential) at any desired tip potential and, in so doing, obtain information on the local concentration of a particular species.

7.2.3.2 Reduction of $[Cp^*Re(CO)_2(p\text{-}N_2C_6H_4OMe)][BF_4]$ in Acetonitrile

SECM feedback measurements have been applied, together with cyclic voltammetry and controlled potential electrolysis,[38] to the reduction of the rhenium aryldiazenido complex

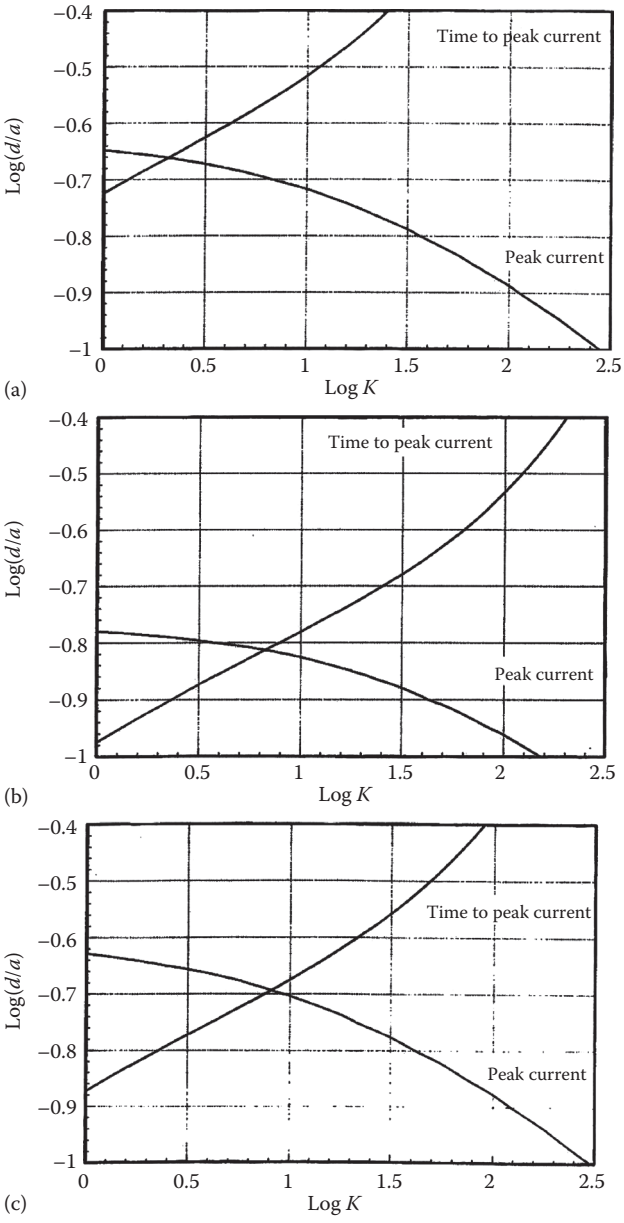


FIGURE 7.13 Contours showing the sets of values of log (*d/a*) and log *K* derived from the measurements of the peak current and peak time from the transients in Figure 7.12. Data are for pH (a) 10.94, (b) 11.36, and (c) 11.54.

$[Cp^*Re(CO)_2(p\text{-}N_2C_6H_4OMe)][BF_4]$ (**III**(BF_4); $Cp^* = \eta\text{-}C_5Me_5$; $Me = CH_3$). A one-electron reduction results in the 19-electron complex, **IV** (Equation 7.15), which then decomposes to give products (Equation 7.16):

$$\underset{\textbf{III}}{\left[Cp^*Re(CO)_2(p\text{-}N_2C_6H_4OMe)\right]^+} + e^- \rightarrow \underset{\textbf{IV}}{Cp^*Re(CO)_2(p\text{-}N_2C_6H_4OMe)} \tag{7.15}$$

$$\textbf{IV} \xrightarrow{k_1} Cp^*Re(CO)_2(N_2) \tag{7.16}$$

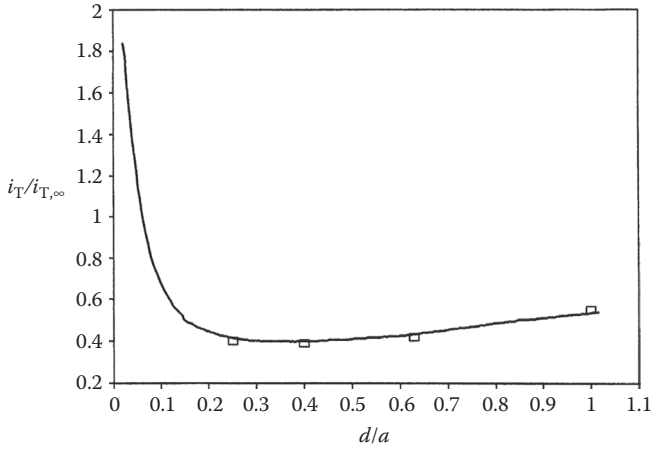


FIGURE 7.14 Tip feedback approach curve (solid line) for the reduction of 1.0 mM $[Cp^*Re(CO)_2(p\text{-}N_2C_6H_4OMe)][BF_4]$ in acetonitrile at a 25 μm diameter Pt UME translated toward a Pt substrate at 0.05 μm s^{-1}. The remaining experimental details are given in the text. The squares are theoretical values for $k_1 = 145\ s^{-1}$.

A normalized steady-state approach curve of tip current vs. tip/substrate separation for the reduction of III(BF_4) is shown in Figure 7.14. This was obtained with a 25 μm diameter Pt UME, biased to promote the diffusion-controlled reduction of III, as the probe was translated toward a 1 mm diameter Pt disk substrate, biased to promote the diffusion-controlled oxidation of IV. The approach curve yielded a value $k_1 = 145\ s^{-1}$, which was in excellent agreement with that determined by cyclic voltammetry at sweep rates between 10 and 50 V s^{-1}.

7.2.3.3 Oxidation of Di-tert-Butyl Nitroxide in Acetonitrile

The oxidation of di-*tert*-butyl nitroxide (DTBN) in acetonitrile has been shown to involve an irreversible follow-up reaction that has proven difficult to characterize by conventional voltammetry because the CVs are often distorted. Using steady-state SECM TG/SC measurements, the follow-up reaction was measured clearly and convincingly as having a rate constant of 21 s^{-1}.[39] CE and tip/substrate separation plots were analyzed using Equations 7.9 and 7.10 over a wide range of DTBN concentrations (5–50 mM) to prove that the follow-up reaction was first order in DTBN.

7.2.3.4 Identification of Intermediates in the Oxidation of Borohydride

The oxidation of borohydride at gold electrodes in aqueous alkaline solution is a highly complex multistage process.[20,40] On relatively long voltammetric timescales, either slow scan speed (100 mV s^{-1}) experiments at large electrodes, or steady-state measurements at moderate-sized microdisk electrodes ($a = 25$ μm), voltammograms have been found to be irreversible, with close to eight electrons involved in the oxidation process. This is attributable to the following overall reaction:

$$BH_4^- + 8\ OH^- \rightarrow BO_2^- + 6\ H_2O + 8\ e^- \tag{7.17}$$

With FSCV, a new two-electron anodic peak was detected, at more negative potentials, for the first stage of the oxidation process, with an accompanying cathodic peak on the reverse scan.[20] The ratio of the forward to the reverse peak currents increased toward unity as the scan rate was raised to ~200 V s^{-1} (Figure 7.15). This behavior was attributed to the initial two-electron process accompanied by a fairly rapid follow-up chemical reaction, and was successfully analyzed in terms of an E_qC_i process (quasireversible electron transfer followed by a first-order irreversible chemical process), with a rate constant for the chemical step, $k_1 = 250\ s^{-1}$.

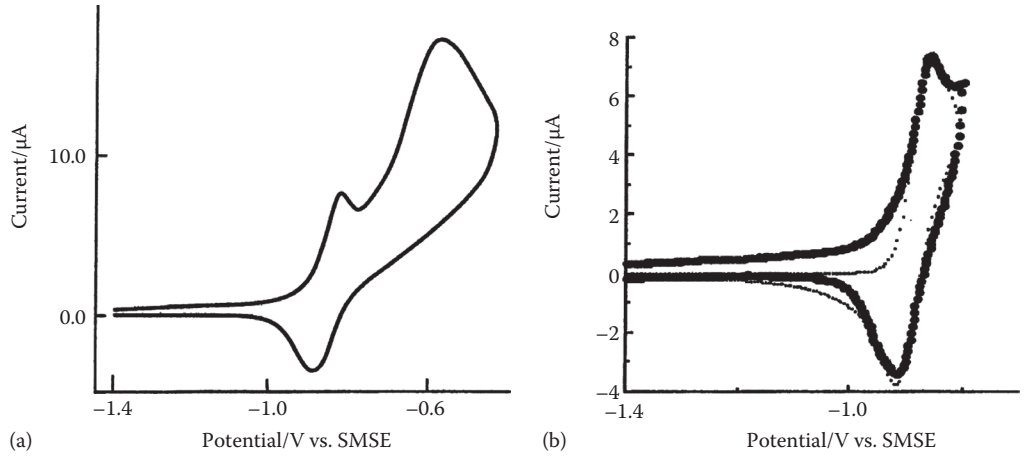


FIGURE 7.15 (a) Cyclic voltammogram (sweep rate 200 V/s) at a 50 μm diameter Au microdisk for the oxidation of 10 mM sodium borohydride in 1 M aqueous NaOH. (b) Cyclic voltammogram as (a), but with a reversal potential of −0.8 V. The fine points are the experimental data, and the bold points represent the behavior computed for an E_qC_i mechanism for a two-electron process with $D = 1.6 \times 10^{-5}$ cm^2 s^{-1}, a standard rate constant of 0.3 cm s^{-1} and a transfer coefficient of 0.5.

SECM SG/TC experiments were carried out to prove that the product of the initial two-electron oxidation process diffused into the solution, where it would react homogeneously and irreversibly. For these measurements, a 10 μm diameter Au tip UME was stationed ~1 μm above a 100 μm diameter Au substrate electrode. With the tip held at a potential of −1.3 V vs. saturated mercurous sulfate electrode (SMSE), to collect substrate-generated species by reduction, the substrate electrode was scanned through the range of potentials to promote the oxidation of borohydride. The substrate and tip electrode responses for this experiment are shown in Figure 7.16. The fact that a cathodic current flowed at the tip, when the substrate was at a potential where borohydride oxidation occurred, proved that the intermediate formed in the initial two-electron transfer process (presumed to be monoborane) diffused into the solution. An upper limit of 500 s^{-1} was estimated for the rate constant describing the reaction of this species (with water or OH^-), based on the diffusion time in the experimental configuration. This was consistent with the results of the cyclic voltammetry experiments.[20]

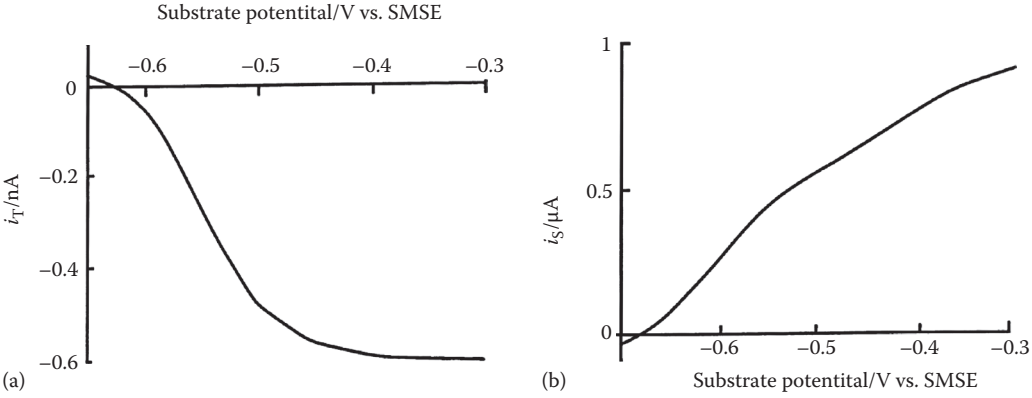


FIGURE 7.16 Steady-state tip (a) and substrate (b) currents as a function of substrate potential for SG/TC measurements of the borohydride oxidation process. A 10 μm diameter Au tip, biased at −1.3 V vs. SMSE was positioned ca. 1 μm above a 100 μm diameter substrate electrode, which was swept through the range of potentials indicated.

7.2.3.5 Probing Ligand Reorganization

The redox chemistry of Cu(I/II) complexes of *N*,*N*-bis(2-quinilylmethyl)-L-methionine in acetonitrile involves a complex scheme of squares: reduction of the Cu(II) complex to Cu(I) is followed by ligand reorganization (chemical step) to give a Cu(I) complex that is oxidized rapidly followed by another reorganization. SECM feedback (TG/SC) measurements focused on the reduction and first chemical step (essentially an EC_i process) that allowed the kinetics of the first ligand rearrangement to be characterized as occurring on the 25 ms timescale.[41]

7.3 EC_{2i} PROCESSES

7.3.1 Principles and Theoretical Framework

In the EC_{2i} process, an initial electron transfer step is followed by a second-order irreversible chemical reaction (typically a dimerization process or adduct formation, as considered in the practical examples in Section 7.3.2). The SECM approaches to characterizing the kinetics of second-order chemical reactions follow the same principles as for the EC_i case, discussed in Section 7.2, with a generator electrode employed to electrogenerate the species of interest (B; see Equation 7.1), which is collected at a second electrode (Equation 7.3). The main features of this technique can be illustrated by considering the following second-order process involving the consumption of B to form electroinactive products, in the gap between the two electrodes:

$$\text{Solution:} \qquad 2\,\text{B} \xrightarrow{k_2} \text{Products} \tag{7.18}$$

Rigorous theoretical treatments for this mechanism have been developed for the feedback and TG/SC modes.[4,5] The normalized kinetic parameter in this case is

$$K_2 = \frac{k_2 a^2 c_A^*}{D} \tag{7.19}$$

Theoretical results have been presented for both chronoamperometric and steady-state conditions.[4] The following empirical relationship between the steady-state CE and a generalized parameter, κ_2, allows the measurement of rate constants with an error of no greater than 5%–10%, provided $0.3 \le N_{SS} \le 0.9$[5]:

$$\kappa_2 = 104.87 - 9.948N_{SS} - \frac{185.89}{N_{SS}^{1/2}} + \frac{90.199}{N_{SS}} + \frac{0.389}{N_{SS}^2} \tag{7.20}$$

where

$$\kappa_2 = \frac{k_2 d^3 c_A^*}{D_A a} \tag{7.21}$$

From Equation 7.20, $N_{SS} \sim 0.3$ corresponds to $\kappa_2 \sim 70$. Assuming $d = 200\,\text{nm}$ is the closest attainable tip/substrate separation and a typical value of $D = 10^{-5}\ \text{cm}^2\ \text{s}^{-1}$, the upper limit on the range of measurable rate constants is estimated as $k_2 \le (8.75 \times 10^{10}\,\text{cm}^{-1}\text{s}^{-1}) a / c_A^*$. The absolute value of k_2 then depends on the value of a and c_A^*, with a large value of the former parameter and small value of the latter, favoring the measurement of rapid kinetics. Even for moderate values of $a = 2.5\,\mu\text{m}$ and $c_A^* = 10^{-3}$ mol dm^{-3}, diffusion-controlled solution reactions are potentially accessible from TG/SC measurements.

7.3.2 Applications

7.3.2.1 Reductive Dimerization of Dimethyl Fumarate and Fumaronitrile in *N,N*-Dimethylformamide

The reductive hydrodimerization of activated olefins was considered as a good test system for initial SECM studies, due to the fact that the dimerization rate constant could be tuned via the substituent activating the olefinic double bond.[42,43] For the relatively slow dimerization of the dimethyl fumarate (DF) radical anion, a large UME (25 μm diameter Pt electrode) was employed so that the value of K_2 (Equation 7.19) was in the range where the SECM response would be sensitive to the kinetics. Experiments were carried out with solutions of 5.15 and 11.5 mM DF in dimethylformamide (DMF), containing 0.1 M tetrabutylammoniumtetrafluoroborate as a supporting electrolyte. The oxidation of *N,N,N′,N′*-tetramethyl-1,4-phenylenediamine (TMPD), included in solutions at a concentration of ca. 4 mM, was used as a calibrant of the tip/substrate separation, through positive feedback measurements.

Normalized steady-state feedback current–distance approach curves for the diffusion-controlled reduction of DF and the one-electron oxidation of TMPD are shown in Figure 7.17. The experimental approach curves of normalized tip current vs. log(*d*/*a*) for the reduction of DF lie just below the response for the oxidation of TMPD, diagnostic of a follow-up chemical reaction in the reduction of DF, albeit rather slow on the SECM timescale. The reaction is clearly not first order, as the deviation from positive feedback increases as the concentration of DF is increased. Analysis of the data in terms of EC_{2i} theory yielded values of $K_2 = 0.14$ (5.15 mM) and 0.27 (11.5 mM), and thus fairly consistent k_2 values of 180 and 160 M^{-1} s^{-1}, respectively.

Typical steady-state tip and substrate electrode responses for TG/SC voltammetric measurements, on the reduction of 28.2 mM fumaronitrile (FN), with a tip ($a = 5$ μm)–substrate ($r_S = 50$ μm) separation of 1.8 μm are shown in Figure 7.18. These were obtained by scanning the tip (generator) potential at 100 mV s^{-1} through the $FN/FN^{\cdot-}$ wave, while holding the substrate (collector) electrode at a potential to detect $FN^{\cdot-}$ by diffusion-controlled oxidation to FN. The substrate current is much smaller than the tip current, because $FN^{\cdot-}$ is lost by dimerization in solution during transit from the tip to the substrate. The voltammograms provide a clear

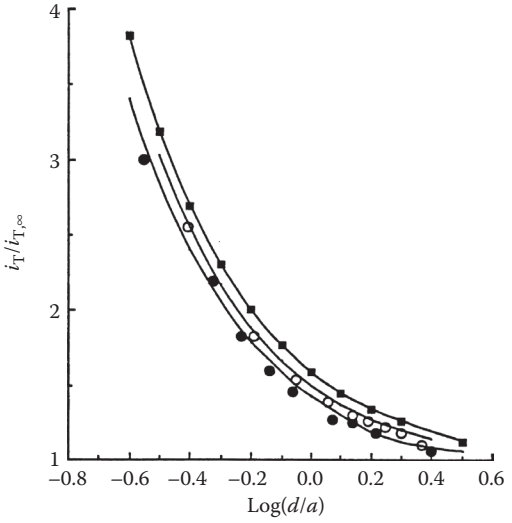


FIGURE 7.17 Normalized steady-state tip feedback current–distance behavior for the reduction of DF at concentrations of 5.15 mM (○) and 11.5 mM (●), along with the best theoretical fits (solid lines) for $K_2 = 0.14$ and 0.27, respectively. The behavior obtained for simple diffusion-controlled positive feedback measurements on the oxidation of TMPD is also shown (■).

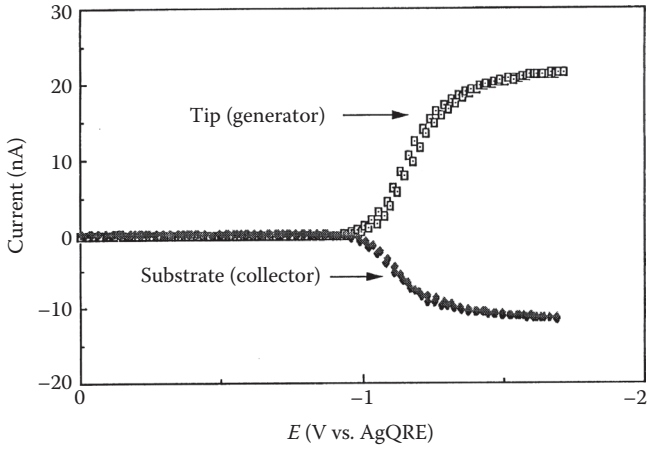


FIGURE 7.18 Voltammograms for the reduction of 28.2 mM FN in the TG/SC mode at a tip/substrate separation, $d = 1.8\,\mu m$. The tip was scanned at 100 mV s^{-1} over the potential range shown, while the substrate potential was maintained at 0.0 V vs. AgQRE (Ag quasi-reference electrode).

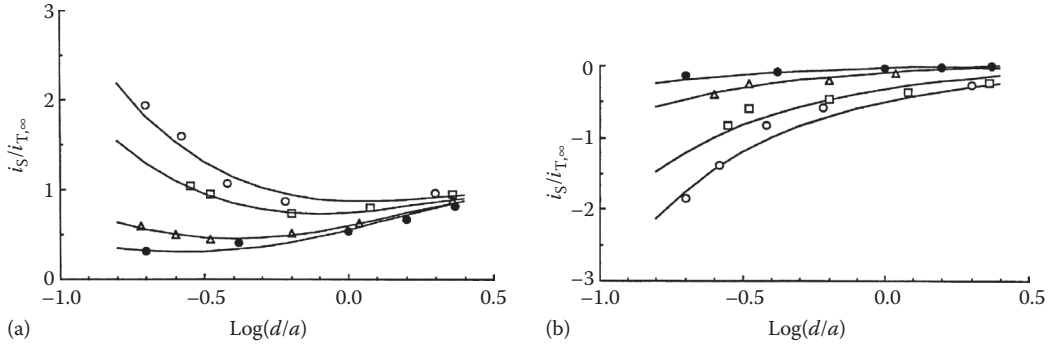


FIGURE 7.19 Tip (a) and substrate (b) current–distance behavior for the reduction of FN at the tip and collection of $FN^{\cdot-}$ at the substrate (TG/SC mode). The data relate to [FN] = 1.5 mM (○), 4.12 mM (□), 28.2 mM (Δ), and 121 mM (●). The solid lines are the best theoretical fits with the values of K_2 cited in the text.

illustration of the ability of SECM TG/SC to detect relatively unstable intermediates with good sensitivity.

Tip and substrate steady-state approach curves for TG/SC measurements with four different FN concentrations are shown in Figure 7.19, along with theoretical analyses obtained with $K_2 = 10$ (1.5 mM), 25 (4.1 mM), 200 (28.2 mM), and 1000 (121 mM). Together, these measurements—over almost two orders of magnitude in [FN]—yielded a consistent dimerization rate constant of 2.0 $(\pm 0.4) \times 10^5$ M^{-1} s^{-1}. This was in reasonable agreement with the rate constant of 6 $(\pm 3) \times 10^5$ M^{-1} s^{-1} estimated from earlier simultaneous electrochemical electron spin resonance studies,[43] but considerably lower than that determined by RRDE measurements.[43] The SECM data were considered to be more reliable than those obtained in the RRDE configuration, due to the higher sensitivity of CE measurements in the SECM geometry.[4]

7.3.2.2 Detection of Acrylonitrile Radical Anion

One of the most powerful illustrations of the ability of steady-state TG/SC measurements to identify short-lived intermediates in electrode processes comes from studies in which the radical anion of

acrylonitrile (AN) was detected in the electrohydrodimerization reaction.[12] Prior to these investigations, the mechanism of the AN electrohydrodimerization process was unclear. On the basis of SECM measurements, it was shown that the reaction involved the electrogeneration of the radical anion, $R^{\cdot -}$, followed by dimerization and then protonation to yield the hydrodimer:

$$R + e^- \rightarrow R^{\cdot -} \tag{7.22}$$

$$2\,R^{\cdot -} \xrightarrow{k_2} R_2^{2-} \tag{7.23}$$

$$R_2^{2-} \xrightarrow{H^+} R_2H^- \xrightarrow{H^+} R_2H_2 \tag{7.24}$$

SECM measurements were carried out in dry DMF at low AN concentration to minimize possible complications from side reactions. The tip was scanned through the range of potentials corresponding to the reduction of AN, while the substrate electrode was held at a potential where any $AN^{\cdot -}$ reaching its surface would be detected by diffusion-controlled oxidation back to AN. The dimerization kinetics of $AN^{\cdot -}$ were determined by measuring collection efficiencies, as a function of interelectrode separation for three different AN concentrations (Figure 7.20). There was reasonable agreement between experiment and EC_{2i} theory in all three cases, with the closest results obtained with the lowest AN concentration, where contributions from competing polymerization side reactions were less important. Taking account of all data sets, a dimerization rate constant of $k_2 = (6 \pm 3) \times 10^7\ M^{-1}\ s^{-1}$ was deduced.[12]

7.3.2.3 Oxidative Dimerization of 4-Nitrophenolate in Acetonitrile

A further powerful illustration of the capability of TG/SC measurements was the determination of the rate constant for the rapid oxidative dimerization of 4-nitrophenolate (ArO^-) in acetonitrile solutions[5]:

$$\text{Tip}: \quad ArO^- - e^- \rightarrow ArO^{\cdot} \tag{7.25}$$

$$\text{Gap}: \quad 2ArO^{\cdot} \rightarrow (ArO)_2 \tag{7.26}$$

$$\text{Substrate}: \quad ArO^{\cdot} + e^- \rightarrow ArO^- \tag{7.27}$$

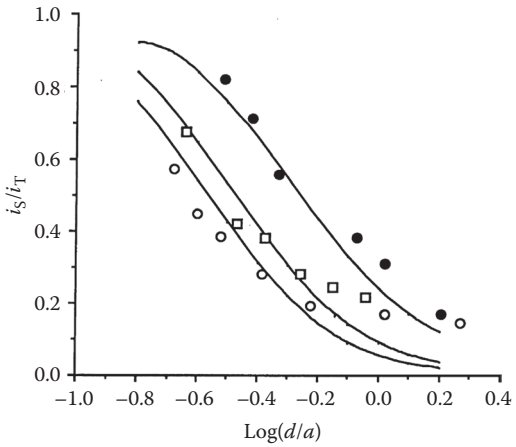


FIGURE 7.20 Steady-state TG/SC collection efficiencies as a function of tip/substrate separation for AN reduction at the tips for [AN] = 0.58 mM (●), 1.50 mM (□), and 1.91 mM (○). The solid lines through each set of experimental data are the best theoretical fits obtained with $K_2 = 100$ (0.58 mM), 500 (1.50 mM), and 1000 (1.91 mM).

A radical dimerization rate constant of 1.2 (± 0.3) $\times 10^8$ M^{-1} s^{-1} was determined,[5] which was in reasonable agreement with that determined earlier using FSCV.[32]

7.3.2.4 Detection of Nicotinamide Adenine Dinucleotide Radical

The initial stage in the reduction of the oxidized form of nicotinamide adenine dinucleotide (NAD^+) in aqueous solution results in the formation of a radical ($NAD^{\cdot}$), which rapidly dimerizes. Through investigations with the SG/TC mode, Engstrom et al.[1] provided clear evidence that $NAD^{\cdot}$, electrogenerated at a glassy carbon substrate, could be detected by oxidation to NAD^+ at a 25 μm diameter Pt tip UME positioned as close to the substrate as possible. Although no quantitative information was obtained on the rate constant for the dimerization process, this early work provided a good illustration of the ability of SECM to detect short-lived intermediates in electrode reactions.

7.3.2.5 Dimerization of Nitro Radical Anions

Both SECM and CV were used to study the dimerization kinetics of nitro radical anions electrogenerated by the one-electron reduction of nitro compounds of biological relevance. Specifically, the reduction of an antituberculosis agent and a bactericidal agent in dimethylsulfoxide was considered.[44] The rate constants obtained by the two techniques were similar.

7.3.2.6 Superoxide Generation and Its Interaction with 1,4-Dihydropyridines

The short tip/substrate diffusion times in SECM allowed the one-electron electrogeneration and collection (by oxidation) of superoxide in DMSO on a timescale where superoxide was stable. This enabled the standard rate constant of the quasireversible $O_2/O_2^{\cdot -}$ couple to be determined. Subsequent studies investigated the irreversible interaction of electrogenerated $O_2^{\cdot -}$ with various 1,4-dihydropyridines present in bulk solution.[45] It should be pointed out that the data obtained were analyzed using EC_{2i} theory that is not applicable to this situation.

7.4 ECE/DISP PROCESSES

7.4.1 Principles and Theoretical Characteristics

The ECE/DISP framework covers many two-electron oxidation and reduction processes. Using a cathodic process as an example, the reduction of an initial species, A, producing B, is followed by a first-order homogeneous reaction, yielding an intermediate (C) that is often more easily electrolyzed at the electrode (to give D) than the starting material. With this proviso, the second-electron transfer can occur in the solution, by disproportionation of B and C, so that overall the following steps have to be considered:

$$\text{Electrode}: \quad A + e^- \rightarrow B \quad (E^{\circ}_{A/B}) \tag{7.28}$$

$$\text{Solution}: \quad B \xrightarrow{k_1} C \tag{7.29}$$

$$\text{Electrode}: \quad C + e^- \rightarrow D \quad (E^{\circ}_{C/D}) \tag{7.30}$$

$$\text{Solution}: \quad B + C \xrightarrow{k_d} A + D \tag{7.31}$$

The limiting ECE situation applies when Equations 7.28 through 7.30 are important, while the DISP scenario involves Equations 7.28, 7.29, and 7.31. The terminology DISP1 is used when the first-order decomposition of B to C is rate-limiting, while DISP2 defines the case where Equation 7.31 is rate limiting. The difference in the reduction potentials for the A/B and C/D couples is often so great

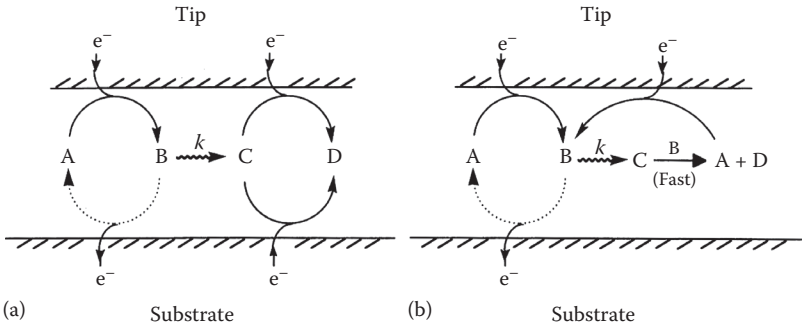


FIGURE 7.21 Diffusional and chemical processes occurring within the tip–substrate domain for the TG/SC mode with (a) an ECE pathway and (b) a DISP1 pathway.

that the disproportionation reaction is usually driven at a diffusion-controlled rate, so that the problem reduces to considering the competition between ECE and DISP1 processes.

Distinguishing between ECE and DISP1 mechanisms by many conventional electrochemical methods is difficult. However, in common with generation–collection measurements at other double electrode geometries,[46] and earlier applications of double potential step transient methods,[47,48] generation–collection and feedback measurements with SECM have been shown to allow an unequivocal mechanistic assignment.[8] Moreover, SECM allows the measurement of larger rate constants, for Equation 7.29, than these other techniques.

With reference to the aforementioned scheme, the study of ECE/DISP1 processes by the feedback and TG/SC modes involves reducing A at a diffusion-controlled rate at the tip UME, with the substrate held at a potential where the oxidation of B is diffusion-controlled. Provided that the substrate potential is not too positive of $E^{o}_{A/B}$, the ECE mechanism involves the reduction of C at the substrate, as well as the tip. The resulting diffusional and chemical processes within the tip/substrate domain, for ECE and DISP1 pathways, are shown schematically in Figure 7.21. As for the EC_i and EC_{2i} processes, considered in Sections 7.2 and 7.3, the route to measuring the rate constant for the conversion of B to C is to establish a competition between the diffusion of B to the substrate and the solution decomposition step. Mechanistic resolution comes from measuring the substrate current simultaneously with the tip current, since the conversion of C to D at the substrate in the ECE reaction causes a (partial) cathodic current to flow, whereas the DISP1 reaction only involves an anodic current at the substrate for the oxidation of B to A.

7.4.2 Applications

7.4.2.1 Anthracene Reduction in the Presence of a Proton Donor

The reduction of anthracene (A) in DMF in the presence of phenol (PhOH) was studied, as an example of a DISP1 process, yielding 9,10-dihydroanthracene (AH_2):[40,41]

$$A + e^- \rightarrow A^{\cdot -} \tag{7.32}$$

$$A^{\cdot -} + PhOH \xrightarrow{k_1} AH^{\cdot} + PhO^- \tag{7.33}$$

$$AH^{\cdot} + A^{\cdot -} \xrightarrow{k_d} AH^- + A \tag{7.34}$$

$$AH^- + PhOH \xrightarrow{fast} AH_2 + PhO^- \tag{7.35}$$

Equation 7.33 has been shown to be rate limiting, and this can be considered as pseudo first order in the presence of excess PhOH.

Experiments were carried out in DMF with 4 mM A, and PhOH at concentrations in the range 0.1–0.43 M, with tetrabutylammonium tetrafluoroborate as a supporting electrolyte. Distances were established using the positive feedback response for the oxidation of decamethylferrocene, which was added to solutions at millimolar levels. A 7 μm diameter C fiber UME was employed as the tip, while the substrate was a 60 μm diameter Au disk electrode. Typical steady-state tip and substrate approach curves for the diffusion-limited reduction of A at the tip and the oxidation of A^{-} at the substrate are shown in Figure 7.22. The tip and substrate currents are normalized by the steady-state tip current for the one-electron reduction of A (without any chemical reaction, i.e., with no PhoH) in bulk solution, denoted by $i_{T,1e,\infty}$. The tip current showed the features predicted for ECE/DISP1 processes, while the substrate current—always of opposite sign to the tip current—indicated a DISP1 pathway unambiguously.

A series of tip feedback current–distance curves for a range of PhOH concentrations is shown in Figure 7.23. As PhOH increases, the current decreases due to the consumption of A^{-} in the gap

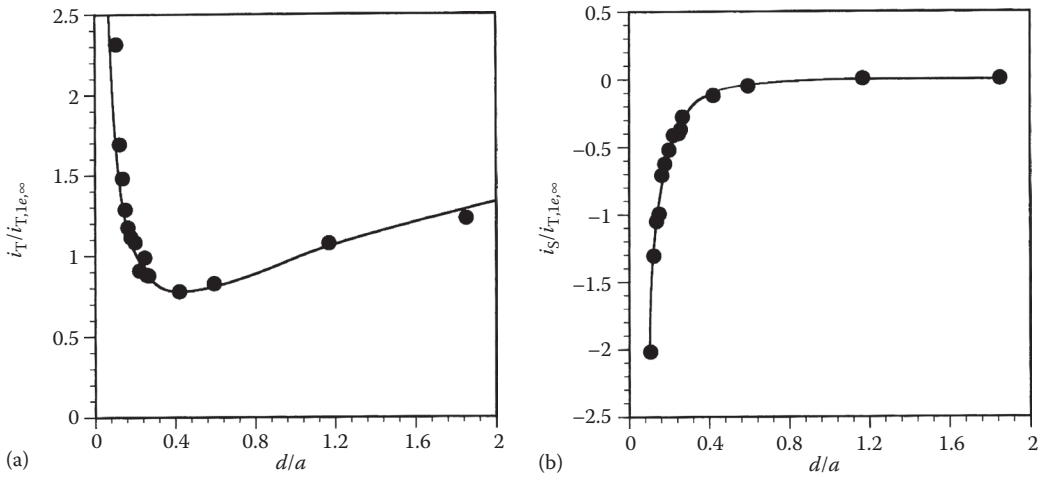


FIGURE 7.22 Steady-state tip (a) and substrate (b) approach curves for the reduction of 4.1 mM anthracene (A) at the tip, in the presence of PhOH, and the collection of A^{-} at the substrate.

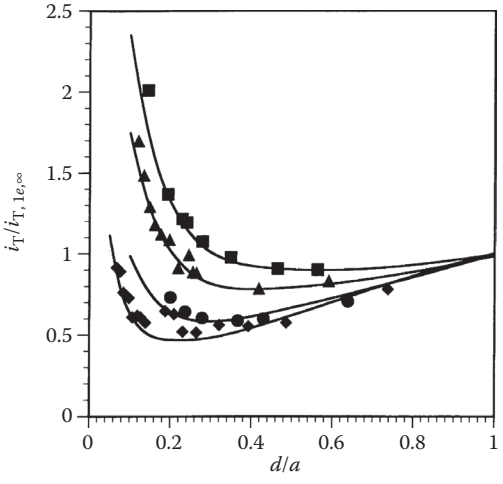


FIGURE 7.23 Normalized steady-state tip approach curves for the reduction of 4 mM A, with PhOH present at concentrations of 0.1 (■), 0.154 (▲), 0.23 (●), and 0.43 (♦) M. The solid lines through each data set correspond to $K = 4$, 6, 12.5, and 22 (from top to bottom).

between the tip and substrate electrodes, causing a diminution in the extent of positive feedback for the A/A^{-} couple. Analysis of all datasets allowed the effective first-order rate constants to be determined, from which the second-order rate constant $k_2 = k_1/[PhOH] = (4.4 \pm 0.4) \times 10^3\ M^{-1}\ s^{-1}$ was deduced. This value was in good agreement with that measured by double potential step chronoamperometry,[47] confirming the applicability of SECM in the study of ECE/DISP1 processes.

7.4.2.2 Lifetime of Guanosine Radical Cation

SECM has been used to study the oxidation of guanosine (G) in DMF, illustrating how TG/SC measurements can be used to estimate the lifetime of an important radical cation (implicated in the transfer of charge and in radiative damage of DNA),[49] and to estimate the oxidation potential. The overall electrooxidation of G in DMF is considered to be an ECE process, where the radical cation, $G^{\cdot+}$, generated in a one-electron oxidation step, undergoes rapid deprotonation followed by fast loss of a second electron and subsequent hydration. The experimental measurements involved scanning the tip (generator) electrode potential through a range of values to promote the oxidation of G under steady-state conditions, while holding the substrate electrode potential at a value to reduce any $G^{\cdot+}$ reaching its surface. Because the flux of $G^{\cdot+}$ reaching the collector electrode was small, it was necessary to minimize background current contributions by employing 10 μm diameter carbon fiber UMEs as both the tip and the substrate. Analysis of the data yielded an estimate of the lifetime of $G^{\cdot+}$ of ≤40 μs and a standard electrode potential of 1.55 V (vs. normal hydrogen electrode).

7.4.2.3 Oxidation of Epinephrine

A further example of the application of SECM to investigate DISP processes comes from studies of the oxidation of epinephrine, which proceeds via an initial rapid two electron–two proton process to yield the corresponding quinone (Q). Considering this as an E step, Q undergoes deprotonation and cyclization (C step), producing leukoadrenochrome (L) that is easily oxidized at the electrode in a two electron–two proton process, forming adrenochrome (A). This second group of electron transfers, which can be considered as an E step, can also occur in solution by disproportionation of Q and L. Although this latter mechanistic pathway was termed ECC,[2] it is, in fact, a DISP process.[50] By identifying the intermediate Q and product A, using the SG/TC mode, a second-order DISP2 process was considered to provide the best fit to tip current–distance curves. The possibility of feedback processes (in the detection of Q), modifying the apparent concentration profiles was not, however, considered in this early work.[2]

7.5 CATALYTIC EC′ PROCESSES

In the catalytic EC′ process, the product of an initial heterogeneous electron transfer step, for example, B in Equation 7.36, reacts with a species Y, presents in the solution, to regenerate A, the starting material (Equation 7.37), while Y is converted to products. It is usually assumed that Y is electroinactive at the electrode over the same potential range:

$$A + ne^{-} \rightarrow B \tag{7.36}$$

$$B + Y \rightarrow A + \text{Products} \tag{7.37}$$

The EC′ mechanism is central to the concept of homogeneous redox catalysis,[51] which is used to promote a redox reaction between an electrogenerated mediator and soluble reactant, under conditions where heterogeneous electron transfer to the reactant is restricted on kinetic grounds. Many redox processes between soluble mediators and oxidoreductase enzymes have also been shown to reduce to the simple EC′ mechanism under limiting conditions.[52]

As highlighted in the following, SECM has been used in several ways to investigate this mechanism, ranging from TG/SC (feedback) measurements[7] to imaging measurements at large[16] and

small[7] electrodes. Small electrodes have also been used to profile reactant and product concentrations in working glucose biosensors, which operate with this type of mechanism.[53]

7.5.1 Principles and Theoretical Characteristics

A comprehensive analysis of the TG/SC (feedback mode) approach to kinetic resolution has been presented.[7] In this situation, Equation 7.36 is driven at a tip generator electrode and the reverse redox reaction takes place at a collector electrode, regenerating species A in the process, which diffuses back to the tip. The theory developed was for cases where Y was in sufficient excess for the process to be first order, and also where Y was depleted by the reaction in solution so that its diffusion had to be taken into account.

To highlight the main features of the theoretical results, it is useful to focus on pseudo-first-order conditions, where the normalized kinetic parameter is

$$K' = \frac{k'a^2}{D} \tag{7.38}$$

where k' is the pseudo first kinetic constant for Equation 7.37.

Figure 7.24 shows simulated normalized steady-state current responses of the tip (a) and substrate (b), and the CE $= i_S/i_T$ (c) as a function of $\log(d/a)$ for various values of K' in the range 0.5–50. As for the EC_i case considered in Section 7.2.1, the behavior is governed primarily by the relative magnitudes of the tip–substrate diffusion time, compared to the lifetime of species B.

For most of the K' values considered, the tip response is similar to that in bulk solution for the largest separation shown ($\log(d/a) = 0.3$ in Figure 7.24a), even though there is a finite tip/substrate separation. This is because the catalytic solution process (Equation 7.37) thins the reaction layer at the UME. For the fastest kinetics (short lifetime of species B), the concentration boundary (reaction) layer is small compared to the largest tip/substrate separation considered. This effect is also evident in the substrate current data for $K' = 50$ (Figure 7.24b), where an essentially zero normalized substrate current can be seen for $\log(d/a) > 0$, indicating that the flux of B reaching the substrate is vanishingly small. As the rate constant for the catalytic step decreases, the timescale for the conversion of B to A in solution increases (reaction layer thickens), so that there is increasing conversion of B to A heterogeneously at the substrate electrode. Consequently, the current at the substrate (at a particular distance) increases, while the tip current decreases.

The CE is the most sensitive parameter for the determination of kinetics, as is evident from Figure 7.24c. It is clear that the decrease in the CE from unity at close tip–substrate separation (indicating essentially no reaction of B in solution) to zero (effectively no B reaching the substrate electrode) at larger tip–substrate separation occurs over closer tip–substrate separations the higher the value of K'. Clearly, to implement CE measurements, it is essential that d is known with high precision. This can be achieved by measuring the SECM positive feedback current for the redox (A/B) couple without the coreactant (Y) present.

In the SG/TC mode, the heterogeneous electron transfer process, defined by Equation 7.36, is carried out at a substrate electrode and a small tip (generally considered to be noninvasive) is used to detect species B by reduction to A (and may also be used to detect species Y). Analysis then involves matching the experimental profiles to theory, using the kinetic constant in solution as the variable.

7.5.2 Applications

7.5.2.1 Oxidation of Amidopyrine by Electrogenerated $Fe(CN)_6^{3-}$

Both TG/SC and SG/TC (imaging) experiments have been carried out on a system that involves the one-electron oxidation of $Fe(CN)_6^{4-}$ to $Fe(CN)_6^{3-}$, which goes on to oxidize amidopyrine (1-phenyl-2,3-dimethyl-4-dimethylamino-5-pyrazalone), being converted back to $Fe(CN)_6^{4-}$ in

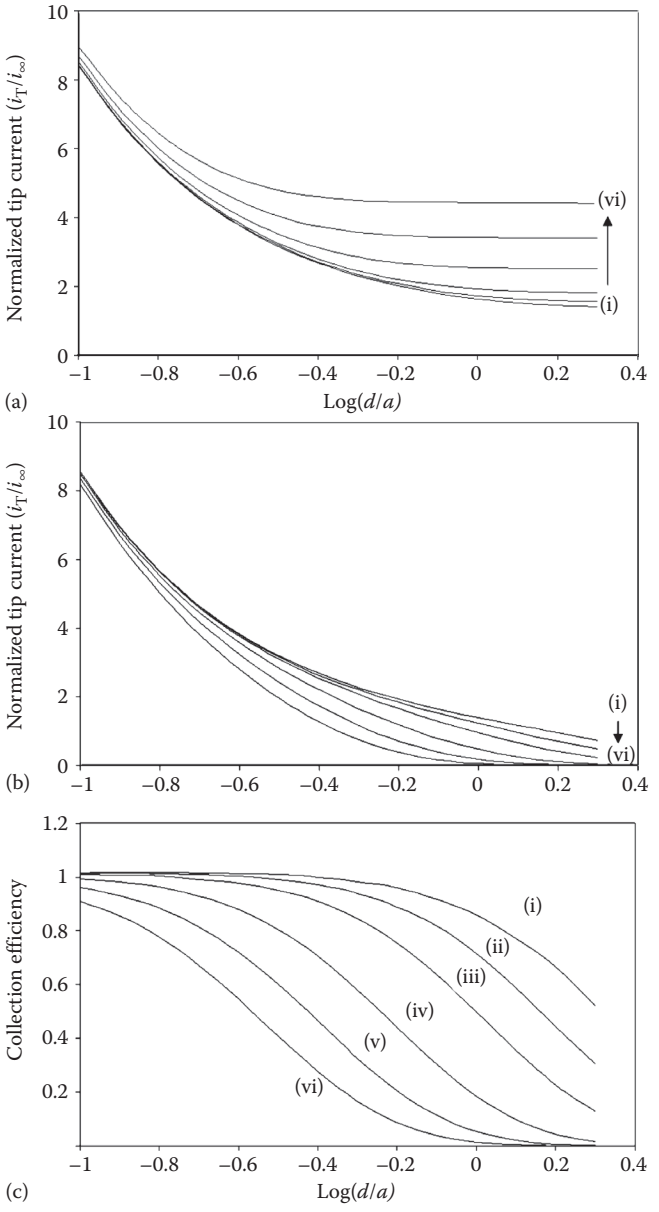


FIGURE 7.24 (a) Tip current, (b) substrate current, and (c) collection efficiency as a function of log(*d*/*a*) for an EC′ mechanism with *K*′ values of: (i) 0.5, (ii) 1, (iii) 2.5, (iv) 10, (v) 25, and (vi) 50. Note that in the case i_∞ refers to the steady-state-current for the reduction of A to B in bulk solution, with no homogeneous catalytic reaction.

the process.[7] The collector electrode in both methods was used to detect $Fe(CN)_6^{3-}$ (and regenerate $Fe(CN)_6^{4-}$). Figure 7.25 shows typical plots of TG/SC CE as a function of log(*d*/*a*), for 1 mM $Fe(CN)_6^{4-}$ in bulk solution at two different concentrations of amidopyrine (10 and 30 mM). These data were analyzed using the rate constant for the solution oxidation reaction as the only adjustable parameter. From the best fit data, the effective second-order rate constant for the reaction was determined as $390 \pm 30\ M^{-1}\ s^{-1}$ (30 mM amidopyrine) and $390 \pm 80\ M^{-1}\ s^{-1}$ (10 mM amidopyrine). An interesting outcome of the SECM studies was that much better voltammetry was observed in the

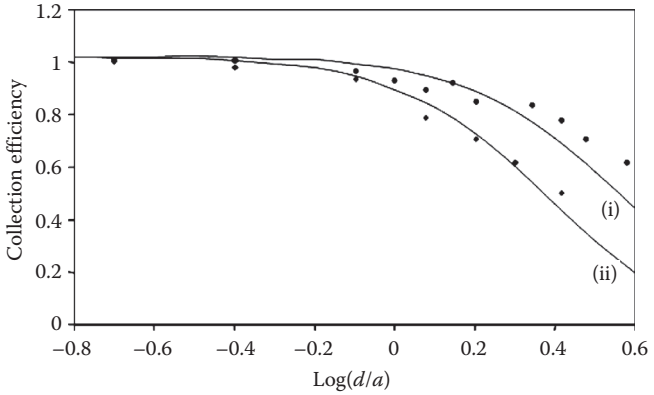


FIGURE 7.25 TG/SC collection efficiency as a function of log(*d*/*a*) for the oxidation of 1×10^{-3} mol dm^{-3} $Fe(CN)_6^{4-}$ in 0.5 mol dm^{-3} KOH with 1×10^{-2} mol dm^{-3} amidopyrine (●) and 3×10^{-2} mol dm^{-3} amidopyrine (◆). The best fits of the TG/SC experimental data were for a second-order rate constant of 390 mol^{-1} dm^3 s^{-1} (solid lines).[7]

TG/SC mode than for voltammetry at a single UME, because recycling of the redox mediator in the tip/substrate gap enhances the voltammetric signal compared to background electrode processes, whereas at the single electrode the simultaneous direct oxidation of amidopyrine (although representing a minor contribution) distorts the voltammetry.[7]

In the SG/TC imaging mode, the substrate electrode (50 μm diameter disk) was held at a potential to promote the diffusion-limited oxidation of $Fe(CN)_6^{4-}$ to $Fe(CN)_6^{3-}$ while the imaging tip UME (1 μm diameter) was held at a potential to intercept substrate-generated $Fe(CN)_6^{4-}$. Images in the plane normal to the substrate (*x*–*z*) were recorded with the tip located on the *y*-axis so that it bisected the center of the substrate UME. Figure 7.26 shows tip current images obtained in a solution of alkaline $Fe(CN)_6^{4-}$ alone (0.5 M KOH) (a), and then with amidopyrine present at concentrations of 10 mM (b) and 60 mM (c). For these measurements, the tip was deliberately positioned 15 μm or more from the substrate electrode, to prevent feedback coupling between the tip and the substrate. Thus, the tip response is a direct indication of the local concentration of $Fe(CN)_6^{3-}$.

In Figure 7.26a, the current image reflects the expected hemispherical concentration profile of $Fe(CN)_6^{3-}$ that extends well beyond the limits of the scan size. The addition of amidopyrine to the solution diminishes the tip current because $Fe(CN)_6^{3-}$ is converted to $Fe(CN)_6^{4-}$ locally due to its reaction with amidopyrine in the solution. The images in Figure 7.26b and c clearly show that the homogeneous reaction compresses the concentration profile of $Fe(CN)_6^{3-}$ closer to the UME surface, as expected for an EC′ process.[52] With 60 mM amidopyrine, the solution reaction is so fast that almost all of the $Fe(CN)_6^{3-}$ is depleted in the area of the scan and only a small current signal (pA levels) is detected at the tip.

7.5.2.2 Catalytic Reduction of Aromatic Halides

UMEs have been used to measure the concentration profiles of redox couples, under conditions where a reductant is electrogenerated at a macroscopic electrode that goes on to carry out a catalytic reduction of an aromatic halide in the solution, regenerating the oxidized form of the couple.[16] Because these measurements were made at large planar electrodes, it was only necessary to map the concentration profiles normal to the surface of the substrate (generator) electrode. A trend similar to that identified in Section 7.5.2.1 was observed, namely that as the concentration of the aromatic halide increased the concentration profile of the redox couple, which was largely linear, became compressed closer to the macroscopic electrode.

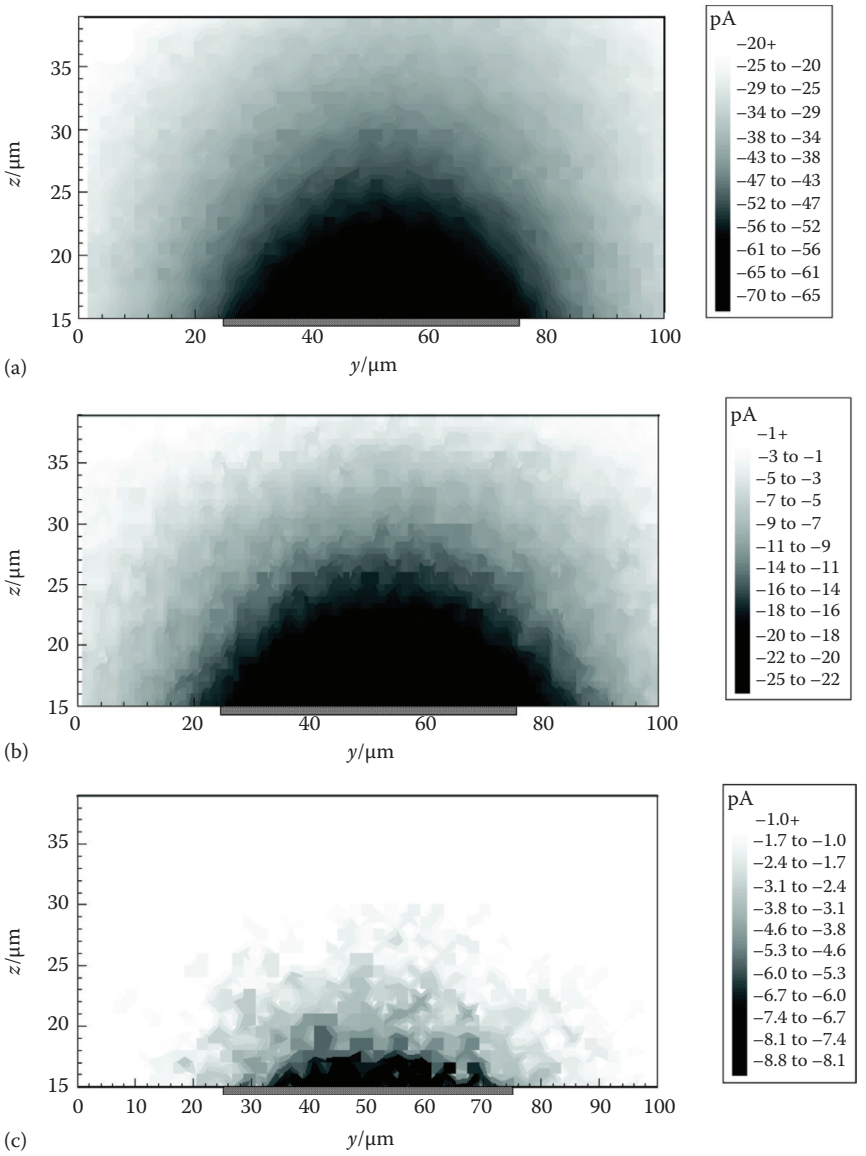


FIGURE 7.26 SG/TC visualization of $Fe(CN)_6^{3-}$ generated above a 50 μm diameter Pt UME by the diffusion-limited oxidation of 1 mM $Fe(CN)_6^{4-}$ (0.5 M aqueous KOH). A 1 μm diameter Pt tip UME (located at $z = 15–40$ μm above the generator electrode to avoid diffusional feedback) was used to detect $Fe(CN)_6^{3-}$ at a diffusion-limited rate in solutions of: (a) $Fe(CN)_6^{4-}$ alone, and then with (b) 1×10^{-2} mol dm^{-3} amidopyrine added and (c) 6×10^{-2} mol dm^{-3} amidopyrine added. The addition of amidopyrine depletes the concentration of $Fe(CN)_6^{3-}$ detected locally, regenerating $Fe(CN)_6^{4-}$ in this EC′ catalytic reaction. Note the different tip current scales for each of the images. The position of the substrate electrode is indicated on each of the images.

7.5.2.3 Temporal–Spatial Mapping of Concentration Profiles within a Working Glucose Biosensor

As a final example, we briefly highlight the application of a carbon fiber UME (with a thin coating) that was deployed within a working glucose biosensor to inform on the spatial and temporal distribution of $Fe(CN)_6^{4-}$ that is detected by the sensor as a product of the catalytic reaction with

glucose oxidase and glucose after a defined reaction period. Knowledge of the local concentration is important toward understanding diffusion and reactions in such devices. The concentration of $Fe(CN)_6^{4-}$ was monitored as a function of distance from the sensor surface and time in order to extract time-dependent concentration profiles.[53]

7.6 CONCLUSIONS AND FUTURE PERSPECTIVES

This chapter has illustrated how SECM can be used to quantitatively study electrode reaction mechanisms involving coupled chemical reactions. The main advantages of SECM are that a wide range of variable and calculable mass transport rates can be achieved with high reproducibility, simply by changing the interelectrode separation and the tip size. Crucially, high mass transfer rates can be obtained through the employment of small electrodes at close tip/substrate separations, facilitating the study of rapid reactions. Alternatively, the UME tip of the SECM can be used to visualize and quantify concentration profiles at larger electrodes.

Of the three SECM modes that have mainly been used to study electrode reaction mechanisms—the TG/SC, feedback, and SG/TC modes—the former has proven the most powerful for measuring rapid kinetics. With this approach, fast follow-up and sandwiched chemical reactions can be characterized *under steady-state conditions* that are difficult to study even with *rapid transient techniques* such as FSCV or double potential step chronoamperometry, where extensive corrections for background currents are often mandatory.[54] Alternative SECM electrode configurations, such as coaxially aligned UMEs,[22] allow the analysis of small volumes of material and fast kinetics of reagents electrogenerated at each of the electrodes.[21] At present, first- and second-order rate constants up to ca. 10^5 s^{-1} and 10^{10} M^{-1} s^{-1}, respectively, are measurable with SECM. As such, SECM is undoubtedly the best electrochemical method for quantifying homogeneous reactions coupled to electron transfer, and deserves to be used much more widely. Furthermore, with reliable methods reported for the fabrication[55–57] and positioning[58,59] of nanoscale electrodes, the detection and characterization of electrogenerated species with submicrosecond lifetimes should be realizable.

This chapter has also considered the use of UMEs to measure concentration profiles at larger electrodes. This approach is powerful for understanding voltammetry and diffusion at conventional electrodes and working sensor devices; the ability to probe the profiles of particular species has proven particularly useful in providing mechanistic information to which conventional voltammetry measurements may be blind.

In addition to SECM visualization, it should be mentioned that high-resolution confocal techniques, based on fluorescence[60–62] and Raman spectroscopy,[63] have proven effective for local chemical visualization, on a rapid timescale in the case of fluorescence. These techniques provide complementary information to SECM and, when combined with SECM, constitute powerful approaches for chemical mapping of electrode and interfacial processes.

ACKNOWLEDGMENTS

The author thanks Dr. Massimo Peruffo for advice and assistance in the preparation of this chapter and the European Research Council for an Advanced Investigator Grant (QUANTIF).

REFERENCES

1. R.C. Engstrom, M. Weber, D.J. Wunder, R. Burgess, S. Winquist. Measurements within the diffusion layer using a microelectrode probe. *Anal Chem*. 58:844 (1986).
2. R.C. Engstrom, T. Meaney, R. Tople, R.M. Wightman. Spatiotemporal description of the diffusion layer with a microelectrode probe. *Anal Chem*. 59:2005 (1987).
3. P.R. Unwin, A.J. Bard. Scanning electrochemical microscopy. 9. Theory and application of the feedback mode to the measurement of following chemical-reaction rates in electrode processes. *J Phys Chem*. 95:7814 (1991).

4. F. Zhou, P.R. Unwin, A.J. Bard. Scanning electrochemical microscopy. 16. Study of 2nd-order homogeneous chemical-reactions via the feedback and generation collection modes. *J Phys Chem*. 96:4917 (1992).
5. D.A. Treichel, M.V. Mirkin, A.J. Bard. Scanning electrochemical microscopy. 27. Application of a simplified treatment of an irreversible homogeneous reaction following electron-transfer to the oxidative dimerization of 4-nitrophenolate in acetonitrile. *J Phys Chem*. 98:5751 (1994).
6. R.D. Martin, P.R. Unwin. Scanning electrochemical microscopy—Kinetics of chemical reactions following electron-transfer measured with the substrate-generation–tip-collection mode. *J Chem Soc Faraday Trans*. 94:753 (1998).
7. S. Cannan, J. Cervera, R.J. Steliaros Née Haskins, E. Bitziou, A.L. Whitworth, P.R. Unwin. Scanning electrochemical microscopy (SECM) studies of catalytic EC′ processes: Theory and experiment for feedback, generation/collection and imaging measurements. *Phys Chem Chem Phys*. 13:5403–5412 (2011).
8. C. Demaille, P.R. Unwin, A.J. Bard. Scanning electrochemical microscopy. 33. Application to the study of ECE/DISP reactions. *J Phys Chem*. 100:14137 (1996).
9. F.R.F. Fan, D. Cliffel, A.J. Bard. Scanning electrochemical microscopy. 37. Light emission by electrogenerated chemiluminescence at SECM tips and their application to scanning optical microscopy. *Anal Chem*. 70:2941 (1998).
10. R. Lei, L. Stratmann, D. Schafer, T. Erichsen, S. Neugebauer, N. Li, W. Schuhmann. Imaging biocatalytic activity of enzyme–polymer spots by means of combined scanning electrochemical microscopy/electrogenerated chemiluminescence. *Anal Chem*. 81:5070 (2009).
11. K. Borgwarth, J. Heinze. Increasing the resolution of the scanning electrochemical microscope using a chemical lens: Application to silver deposition. *J Electrochem Soc*. 146:3285 (1999).
12. F.M. Zhou, A.J. Bard. Detection of the electrohydrodimerization intermediate acrylonitrile radical-anion by scanning electrochemical microscopy. *J Am Chem Soc*. 116:393 (1994).
13. C. Amatore, S. Szunerits, L. Thouin. Mapping concentration profiles within the diffusion layer of an electrode Part II. Potentiometric measurements with an ultramicroelectrode. *Electrochem Commun*. 2:248 (2000).
14. C. Amatore, S. Szunerits, L. Thouin, J.S. Warkocz. Mapping concentration profiles within the diffusion layer of an electrode. Part III. Steady-state and time-dependent profiles via amperometric measurements with an ultramicroelectrode probe. *Electrochem Commun*. 2:353 (2000).
15. C. Amatore, S. Szunerits, L. Thouin, J.S. Warkocz. Monitoring concentration profiles in situ with an ultramicroelectrode probe. *Electroanalysis.* 13:646 (2001).
16. C. Amatore, C. Pebay, O. Scialdone, S. Szunerits, L. Thouin. Mapping concentration profiles within the diffusion layer of an electrode: Application to redox catalysis. *Chem Eur J*. 7:2933 (2001).
17. C.J. Slevin, J. Zhang, P.R. Unwin. Oxidation of 4-methylanisole by aqueous cerium(IV) in a two-phase immiscible liquid/liquid system: Interfacial versus homogeneous control. *J Phys Chem*. 106:3025 (2002).
18. D.O. Wipf, A.J. Bard. Scanning electrochemical microscopy. 7. Effect of heterogeneous electron-transfer rate at the substrate on the tip feedback current. *J Electrochem Soc*. 138:469 (1991).
19. R.D. Martin, P.R. Unwin. Theory and experiment for the substrate generation–tip collection mode of the scanning electrochemical microscope: Application as an approach for measuring the diffusion coefficient ratio of a redox couple. *Anal Chem*. 70:276 (1998).
20. M.V. Mirkin, H.J. Yang, A.J. Bard. Borohydride oxidation at a gold electrode. *J Electrochem Soc*. 139:2212 (1992).
21. Q.A. Wang, J. Rodriguez-Lopez, A.J. Bard. Evaluation of the chemical reactions from two electrogenerated species in picoliter volumes by scanning electrochemical microscopy. *Chem Phys Chem*. 11:2969 (2010).
22. J.V. Macpherson, C.J. Slevin, P.R. Unwin. Probing the oxidative etching kinetics of metals with the feedback mode of the scanning electrochemical microscope. *J Chem Soc Faraday Trans*. 92:3799 (1996).
23. W.J. Albery, M.L. Hitchman. *Ring Disc Electrodes*. Clarendon Press, Oxford, U.K. (1971).
24. L.B. Anderson, C.N. Reilley. Thin-layer electrochemistry: Steady-state methods of studying rate processes. *J Electroanal Chem*. 10:295 (1965).
25. P.R. Unwin, R.G. Compton. The use of channel electrodes in the investigation of interfacial reaction mechanisms. *Compr Chem Kinet*. 29:173 (1989).
26. T.Y. Ou, S. Moldoveanu, J.L. Anderson. Hydrodynamic voltammetry at an interdigitated electrode array in a flow channel. 2. Chemical-reaction succeeding electron-transfer. *J Electroanal Chem*. 247:1 (1988).
27. T.V. Shea, A.J. Bard. Digital-simulation of homogeneous chemical-reactions coupled to heterogeneous electron-transfer and applications at platinum mica platinum ultramicroband electrodes. *Anal Chem*. 59:2101 (1987).

28. D.W. Peaceman, H.H. Rachford. The numerical solution of parabolic and elliptic differential equations. *J Soc Ind Appl Math*. 3:28 (1955).
29. A.J. Bard, G. Denault, R.A. Friesner, B.C. Dornblaser, L.S. Tuckerman. Scanning electrochemical microscopy—Theory and application of the transient (chronoamperometric) SECM response. *Anal Chem*. 63:1282 (1991).
30. R.D. Martin, P.R. Unwin. Scanning electrochemical microscopy: Theory and experiment for the positive feedback mode with unequal diffusion coefficients of the redox mediator couple. *J Electroanal Chem*. 439:123 (1997).
31. D. Zigah, J. Ghilane, C. Lagrost, P. Hapiot. Variations of diffusion coefficients of redox active molecules in room temperature ionic liquids upon electron transfer. *J Phys Chem*. 112:14952 (2008).
32. D. Shoup, A. Szabo. Chronoamperometric current at finite disk electrodes. *J Electroanal Chem*. 140:237 (1982).
33. C. Lee, J.Y. Kwak, F.C. Anson. Application of scanning electrochemical microscopy to generation/collection experiments with high collection efficiency. *Anal Chem*. 63:1501 (1991).
34. A.J. Bard, M.V. Mirkin, P.R. Uiwin, D.O. Wipf. Scanning electrochemical microscopy. 12. Theory and experiment of the feedback mode with finite heterogeneous electron-transfer kinetics and arbitrary substrate size. *J Phys Chem*. 96:1861 (1992).
35. M.V. Mirkin, F.R.F. Fan, A.J. Bard. Scanning electrochemical microscopy. 13. Evaluation of the tip shapes of nanometer size microelectrodes. *J Electroanal Chem*. 328:47 (1992).
36. K. Aoki, H. Matsuda. Hydrodynamic voltammetry at channel electrodes. 6. Experimental-verification of theory of collection efficiencies. *J Electroanal Chem*. 94:157 (1978).
37. L. Diaz-Ballote, M. Alpuche-Aviles, D.O. Wipf. Fast-scan cyclic voltammetry-scanning electrochemical microscopy. *J Electroanal Chem*. 604:17 (2007).
38. T.C. Richards, A.J. Bard, A. Cusanelli, S. Sutton. Investigation of the electrochemical reduction of $[Cp^*Re(CO)_2(p\text{-}N_2C_6H_4OME)][BF_4]$ by scanning electrochemical microscopy. *Organometallics.* 13:757 (1994).
39. L. Mckay, R.J. Le Suer. A mechanistic investigation of di-*tert*-butyl nitroxide using scanning electrochemical microscopy (SECM). *Electrochim Acta.* 53:8305 (2008).
40. M.V. Mirkin, A.J. Bard. Voltammetric method for the determination of borohydride concentration in alkaline aqueous-solutions. *Anal Chem*. 63:532 (1991).
41. H.S. Barcena, B. Liu, M.V. Mirkin, J.W. Canary. An electrochiroptical molecular switch: Mechanistic and kinetic studies. *Inorg Chem*. 44:7652 (2005).
42. L.S.R. Yeh, A.J. Bard. Electrocarboxylation reactions—Rotating-ring-disk electrode, voltammetric, and electron-spin resonance studies of dialkylfumarates and maleates. *J Electroanal Chem*. 124:355 (1977).
43. I.B. Goldberg, D. Boyd, R. Hirasawa, A.J. Bard. Simultaneous electrochemical-electron spin-resonance measurements. 3. Determination of rate constants for second-order radical-anion dimerization. *J Phys Chem*. 78:295 (1974).
44. S. Bollo, L. Nunez-Vergara, J.A. Squella. Electrogenerated nitro radical anions—A comparative kinetic study using scanning electrochemical microscopy. *J Electrochem Soc*. 151:E322 (2004).
45. S. Bollo, P. Jara-Ulloa, S. Finger, L.J. Nunez-Vergara, J.A. Squella. Scanning electrochemical microscopy (SECM) study of superoxide generation and its reactivity with 1,4-dihydropyridines. *J Electroanal Chem*. 577:235 (2005).
46. P.R. Unwin. The ECE-DISP1 problem—General resolution via double channel electrode collection efficiency measurements. *J Electroanal Chem*. 297:103 (1991).
47. C. Amatore, J.M. Saveant. Electrochemical hydrogenation of aromatic-hydrocarbons—Discrimination between ECE and disproportionation mechanisms by double potential step chronoamperometry. *J Electroanal Chem*. 107:353 (1980).
48. C. Amatore, M. Gareil, J.M. Saveant. Homogeneous vs heterogeneous electron-transfer in electrochemical reactions—Application to the electrohydrogenation of anthracene and related reactions. *J Electroanal Chem*. 147:1 (1983).
49. S.P. Bi, B. Liu, F.R.F. Fan, A.J. Bard. Electrochemical studies of guanosine in DMF and detection of its radical cation in a scanning electrochemical microscopy nanogap experiment. *J Am Chem Soc*. 127:3690 (2005).
50. M.D. Hawley, S.V. Tatawawadi, S. Piekarski, R.N. Adams. Electrochemical studies of the oxidation pathways of catecholamines. *J Am Chem Soc*. 89:447 (1967).
51. H. Lund, K. Daasbjerg, T. Lund, S.U. Pedersen. On electron transfer in aliphatic nucleophilic substitution. *Acc Chem Res*. 28:313 (1995).

52. P.N. Bartlett, K.F.E. Pratt. Theoretical treatment of diffusion and kinetics in amperometric immobilized enzyme electrodes. 1. Redox mediator entrapped within the film. *J Electroanal Chem*. 397:61 (1995).
53. D.P. Burt, P.R. Unwin. Minimally invasive spatial and temporal concentration profiling within working glucose biosensors. *Electrochem Commun*. 10:934 (2008).
54. R.M. Wightman, D.O. Wipf. Voltammetry at ultramicroelectrodes. *Electroanal Chem*. 15:267 (1989).
55. J. Velmurugan, P. Sun, M.V. Mirkin. Scanning electrochemical microscopy with gold nanotips: The effect of electrode material on electron transfer rates. *J Phys Chem C* 113:459 (2009).
56. B.B. Katemann, A. Schulte, W. Schuhmann. Constant-distance mode scanning electrochemical microscopy. Part II: High-resolution SECM imaging employing Pt nanoelectrodes as miniaturized scanning probes. *Electroanalysis* 16:60 (2004).
57. M.A. Mezour, M. Morin, J. Mauzeroll. Fabrication and characterization of laser pulled platinum microelectrodes with controlled geometry. *Anal Chem*. 83:2378 (2011).
58. K. McKelvey, M.A. Edwards, P.R. Unwin. Intermittent contact-scanning electrochemical microscopy (IC-SECM): A new approach for tip positioning and simultaneous imaging of interfacial topography and activity. *Anal Chem*. 82:6334 (2010).
59. D.J. Comstock, J.W. Elam, M.J. Pellin, M.C. Hersam. Integrated ultramicroelectrode-nanopipet probe for concurrent scanning electrochemical microscopy and scanning ion conductance microscopy. *Anal Chem*. 82:1270 (2010).
60. S. Cannan, I.D. Macklam, P.R. Unwin. Three-dimensional imaging of proton gradients at microelectrode surfaces using confocal laser scanning microscopy. *Electrochem Commun*. 4:886 (2002).
61. N.C. Rudd, S. Cannan, E. Bitziou, L. Ciani, A.L. Whitworth, P.R. Unwin. Fluorescence confocal laser scanning microscopy as a probe of pH gradients in electrode reactions and surface activity. *Anal Chem*. 77:6205 (2005).
62. A. Rutkowska, T.M. Bawazeer, J.V. Macpherson, P.R. Unwin. Visualisation of electrochemical processes at optically transparent carbon nanotube ultramicroelectrodes (OT-CNT-UMEs). *Phys Chem Chem Phys*. 13:5223–5226 (2011).
63. C. Amatore, F. Bonhomme, J.L. Bruneel, L. Servant, L. Thouin. Mapping dynamic concentration profiles with micrometric resolution near an active microscopic surface by confocal resonance Raman microscopy. Application to diffusion near ultramicroelectrodes: First direct evidence for a conproportionation reaction. *J Electroanal Chem*. 484:1 (2000).

8 Charge Transfer Processes at the Liquid–Liquid Interface

Michael V. Mirkin and Michael Tsionsky

CONTENTS

8.1 Introduction 191
8.2 Electron Transfer 192
8.2.1 Electron Transfer at the Clear ITIES 192
8.2.1.1 Principles of SECM/ITIES Measurements 192
8.2.1.2 SECM Apparatus and Procedure 195
8.2.1.3 Separation of ET from IT and Solute Partitioning Processes 196
8.2.1.4 Potential Drop across a Nonpolarized ITIES 198
8.2.1.5 Potential Dependence of Heterogeneous Rate Constant of ET at the ITIES 199
8.2.1.6 ET Rate as a Function of the Standard Potential Difference 202
8.2.2 Electron Transfer across Molecular Monolayer 203
8.2.2.1 Adsorption of Phospholipids at the ITIES 204
8.2.2.2 Driving Force Dependence of the ET Rate across a Lipid Monolayer 206
8.2.2.3 Distance Dependence of ET 207
8.2.2.4 Effect of the Lipid Monolayer Structure on the ET Rate 208
8.2.2.5 Temperature Dependence of ET Rate across Lipid Monolayers Adsorbed at the ITIES 211
8.3 Transfer of Ions and Neutral Species 212
8.3.1 Facilitated Ion Transfer 212
8.3.2 Simple Ion Transfer 214
8.3.3 Micro- and Nanopipette Probes 219
8.3.4 Transfer of Neutral Species 221
8.4 More Complicated Heterogeneous Processes 221
8.4.1 Processes with Coupled Homogeneous Reactions 221
8.4.2 Nucleation/Growth of Metal at the ITIES 225
Acknowledgment 226
References 226

8.1 INTRODUCTION

The structure and dynamics of the liquid–liquid interface have been the focus of considerable research activity [1]. In addition to fundamental interest, the charge transfer (CT) reactions occurring at the liquid–liquid interface, that is, electron transfer (ET), simple ion transfer (IT), and facilitated IT, are relevant to important technological systems from chemical sensors to drug delivery in pharmacology to solvent extraction in hydrometallurgy [1,2]. At the interface between two immiscible electrolyte solutions (ITIES), one can conduct reactions that cannot occur at solid electrodes,

for example, reactions involving species of very different polarities. These reactions find applications in electrochemical catalysis and syntheses [3]. The liquid–liquid interface has been suggested as a simple model for biological and artificial membranes [4].

The state of knowledge in the field of CT at the liquid–liquid interface is different from homogeneous ET and ET at the metal–solution interface where the well-established theory has been validated by a number of experiments [5]. Several conflicting models have been proposed for CT processes at the ITIES, and experimental data necessary for testing these models have yet to be obtained. For example, Marcus suggested that classical ET theory should be applicable to the ITIES and proposed expressions for reorganization energy and rate constant [6]. Other authors argued that Marcus model may not correctly describe ET at the ITIES [7]. Schiffrin and coworkers [8] studied interfacial ET implicitly assuming that the potential dependence of the rate constant obeys Butler–Volmer equation. At the same time, the apparent potential dependence of the ET rate can be attributed to the change in concentrations of the reactants at the interface rather than to activation control [1b,9]. Similarly, the kinetic data reported for IT reactions at the ITIES does not allow one to choose between the activation mechanism [10] and slow diffusion through the boundary layer proposed as the rate-determining step [11,12].

The information available about the structure of the ITIES is also sparse. Despite recent progress in spectroscopic studies [13] and molecular dynamics simulations [1e,14], questions remain about the nature and properties of the boundary (mixed solvent) layer that is supposed to separate two liquid phases [1]. Since the thickness of the interface and physical localization of the ET reaction are largely unknown, the microscopic description of this process remains problematic.

There are two fundamentally different ways of studying CT reactions at the ITIES by electrochemical methods. A more conventional approach is based on the application of external voltage across a polarizable interface, that is, the ITIES formed by two liquid phases containing no common ion. The applied voltage provides the driving force for an ET or IT reaction. The thermodynamics and kinetics of such a reaction can be evaluated from the current vs. voltage curves (e.g., cyclic voltammograms) as one does at a solid electrode. The applicability of this approach is limited by severe experimental problems caused by uncompensated *i*R-drop in highly resistive nonaqueous solvents and double-layer charging current. Unlike the metal–liquid interface, faradaic and non-faradaic processes occurring at the ITIES are less directly accessible by electrochemical measurements, and the extraction of mechanistic information from the measured current is not straightforward [1]. In most cases, the discrimination between ET and IT is difficult.

An alternative approach is to probe CT reactions at a nonpolarizable ITIES where two immiscible liquids contain a common ion. The interfacial potential drop ($\Delta_w^o\varphi$) in this case is governed by the ratio of common ion concentration in water and in organic phase. By changing local chemical composition in the interfacial region, one can selectively induce the desired ET or IT reaction without applying any external voltage across the ITIES. This approach is easy to implement using the scanning electrochemical microscopy (SECM), which is capable of probing CT reactions at the ITIES in the same way as ET at a solid substrate. The interfaces between water and various organic solvents were found to be mechanically stable and sharp on a submicrometer scale [15]. With the SECM, one can quantitatively separate interfacial ET from IT processes and minimize resistive potential drop and double-layer charging effects. In this chapter, we discuss SECM studies of a broad range of heterogeneous reactions including ET, IT, electrochemical catalysis, nucleation and growth of metals, and reactions involving monolayer-protected clusters at the liquid–liquid interface.

8.2 ELECTRON TRANSFER

8.2.1 Electron Transfer at the Clear ITIES

8.2.1.1 Principles of SECM/ITIES Measurements

Conventional electrochemical experiments at the ITIES are based on a four-electrode configuration with a reference and an auxiliary electrode positioned in each liquid phase [16,17]. A four-electrode

potentiostat is used to apply a voltage between the reference electrodes and to measure the current flowing between the auxiliary electrodes. The interfacial CT is assumed to be rate limiting, and the whole potential drop occurs mostly within a thin interfacial layer. However, the ITIES in such an experiment is not microscopically probed directly, and the nature of CT reaction (i.e., ET vs. IT) typically remains uncertain.

Slow ET between redox species, confined to two immiscible solvents, was first observed by Guainazzi et al. [18], and a number of theoretical and experimental studies of such reactions have been reported [6–8,15,19–21]. Severe experimental problems complicate extraction of the kinetic parameters by conventional electrochemical measurements at the ITIES (e.g., by cyclic voltammetry). Besides the difficulty of discrimination between ET and IT, there are also distortions from the double-layer charging current and *i*R-drop in the highly resistive nonaqueous solvents, and the limited potential window for studying ET in the absence of currents controlled by IT [1,16].

Unlike conventional electrochemical techniques, in most reported SECM experiments, the ITIES was poised by concentrations of the potential-determining ions, providing a constant driving force for the ET process. This eliminated some of the problems mentioned earlier. In a typical SECM/ITIES experiment (Figure 8.1A), a tip ultramicroelectrode (UME) with a radius a is placed in the upper liquid phase containing reduced form of redox species, R_1. The tip is held at a positive potential, and R_1 reacts at its surface to produce the oxidized form of the mediator species, O_1. When the tip approaches the ITIES, the mediator can be regenerated at the interface via bimolecular redox reaction between O_1 in the upper phase and R_2 in the bottom phase:

$$R_1 - e^- \rightarrow O_1 \quad \text{(tip)} \tag{8.1}$$

$$O_1 + R_2 \rightarrow R_1 + O_2 \quad \text{(liquid–liquid interface)} \tag{8.2}$$

In these reactions, electrons are transferred from the bottom liquid phase into the upper phase. To maintain electroneutrality in both phases, the transfer of common ions (anions, cations, or both) occurs simultaneously with ET reaction.

Thus, the overall CT reaction at the ITIES consists of several steps shown in Figure 8.1A:

- Diffusion of organic mediator species in the tip UME/ITIES gap
- Diffusion of aqueous mediator to and from the interface
- ET between organic and aqueous mediators
- Transfer of the common ion (negative charge in Figure 8.1A)

In principle, any of these steps can limit the rate of the overall reaction occurring at the ITIES. Unlike previous measurements at the polarized ITIES, the SECM/ITIES technique allows one to distinguish between slow IT, ET, and diffusion-controlled processes.

The electric current across the ITIES (i_s) caused by a multistep serial process can be expressed as [22]

$$1/i_s = 1/i_T^c + 1/i_{ET} + 1/i_d + 1/i_{IT} \tag{8.3}$$

where i_T^c, i_{ET}, i_d, and i_{IT} are the characteristic limiting currents for the aforementioned four stages. When IT and mediator diffusion in the bottom phase are not rate limiting, the following equations can be used to extract the first-order effective heterogeneous ET rate constant from approach curves [15]:

$$I_T^k = I_S^k(1 - I_T^{ins}/I_T^c) + I_T^{ins} \tag{8.4}$$

$$I_S^k = 0.78377/L(1+1/\Lambda) + \left[0.68 + 0.3315\exp(-1.0672/L)\right]/[1+F(L,\Lambda)] \tag{8.5}$$

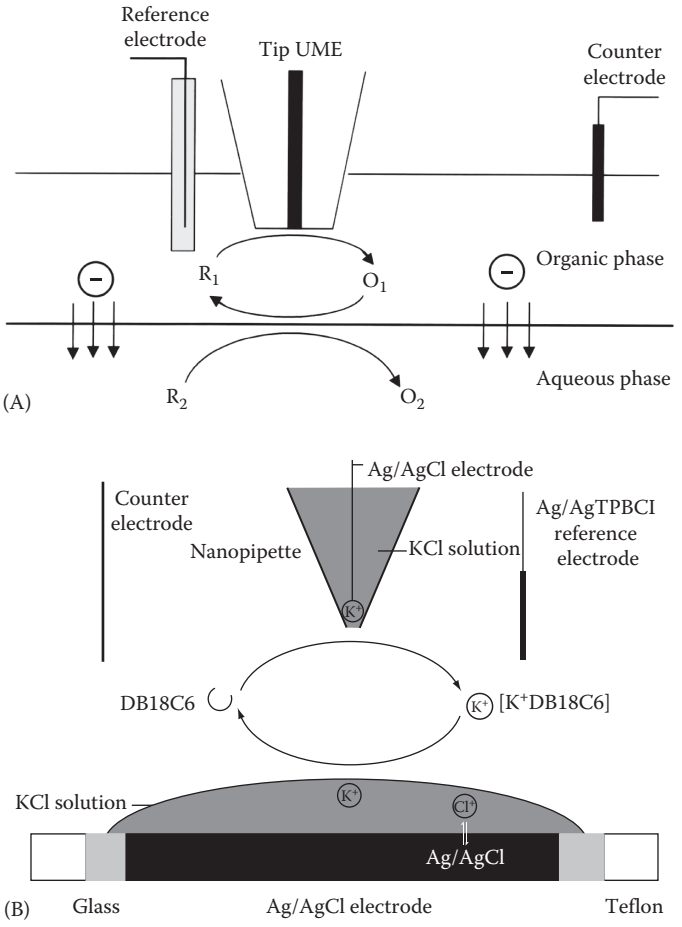


FIGURE 8.1 (A) Schematic diagram of the feedback mode SECM measurement of the ET kinetics between organic and aqueous redox species. Electroneutrality was maintained by the transfer of common ions shown as negative charges. (B) Schematic diagram of the application of SECM to probe facilitated IT at an externally polarized liquid–liquid interface. TPBCl = tetrakis(4-chlorophenyl)borate. (Reprinted with permission from Sun, P., Zhang, Z., Gao, Z., and Shao, Y., Probing fast facilitated ion transfer across an externally polarized liquid-liquid interface by scanning electrochemical microscopy, *Angew. Chem. Int. Ed.*, 41, 3445–3448, 2002. Copyright 2002 American Chemical Society.)

where I_T^c, I_T^k, and I_T^{ins} represent the normalized currents for diffusion-controlled regeneration of redox mediator, finite substrate kinetics, and insulating substrate (i.e., no mediator regeneration), respectively, at a normalized tip–substrate separation, $L = d/a$, I_S^k is the kinetically controlled substrate current; $\Lambda = k_f d/D_R$, where k_f is the apparent heterogeneous rate constant (cm/s) and D_R is the diffusion coefficient of the reduced mediator in the top phase; and $F(L,\Lambda) = (11 + 2.3\Lambda)/[\Lambda(110 - 40L)]$. These currents are normalized by the tip current at an infinite tip–substrate separation, $i_{T,\infty} = 4nFaD_R c_R$. The analytical approximations for I_T^c and I_T^{ins} are

$$I_T^c = 0.78377/L + 0.3315 \exp(-1.0672/L) + 0.68 \tag{8.6}$$

$$I_T^{ins} = 1/(0.15 + 1.5358/L + 0.58\exp(-1.14/L) + 0.0908 \exp[(L - 6.3)/(1.017L)]) \tag{8.7}$$

One can avoid complications caused by slow diffusion in the bottom phase by keeping the concentration of redox species there significantly (e.g., >20 times) higher than that in the top phase [23]. Barker et al. [24] developed a more comprehensive model to take into account diffusion limitations in the bottom solvent. This approach has extended the upper limit for accessible bimolecular rate constants.

8.2.1.2 SECM Apparatus and Procedure

The basic apparatus used for the SECM/ITIES experiments is essentially the same as for any other SECM measurements (see Chapter 2). Before SECM measurements, the tip UME is positioned in the top phase near the interface and biased at a potential where the tip process is diffusion controlled. Typically, both liquid phases are placed into a small (e.g., 2 mL) beaker. In this arrangement, the less dense phase forms the top layer. If one wants the less dense phase to be the bottom phase, a small (10–50 μL) volume of it can be stabilized at the end of glass capillary inside the other phase [23]. Alternatively, an inverted "submarine" SECM tip can be placed in the bottom liquid phase [25,26] and approach the interface from beneath. This setup makes possible SECM measurements not only at the liquid–liquid interface, but also at the air–liquid interface [26]. The list of liquid–liquid systems used for ET studies by SECM is shown in Table 8.1.

The mechanical stability of the liquid–liquid boundary, and the accuracy and reproducibility of measurements were demonstrated in earlier SECM/ITIES experiments. For instance, an SECM approach curve (i_T vs. d) in Figure 8.2 was obtained with a 5 μm radius tip immersed in the aqueous solution (top phase) containing 5 mM $FcCOO^-$ (ferrocene carboxylic acid) and 0.1 M KCl, and approaching nitrobenzene (NB; bottom phase) containing no electroactive species [15]. In this configuration, the NB layer acts as an electrical insulator, and the UME current shows negative feedback in good agreement with the related theory [38]. The tip current for micrometer-sized SECM tips as well as for a 25-nm Pt UME [15] was oscillation free. It was concluded that the interface is sharp on the nanometer scale and z-coordinate corresponding to the zero-distance point can be easily determined. This is essential for any quantitative SECM measurements. In later SECM/ITIES publications, the shape of the approach curve to insulating ITIES served as a test for a proper tip geometry and stability of the liquid–liquid boundary. The measurements are reliable only if the experimental data fits the theory at small tip/ITIES distances (i.e., $d/a \leq 0.1$). The reliability of measurements can also be verified by fitting experimental i_T vs. d curves to the theory for conductive substrate. The maximum normalized feedback current for such a process should be at least 6.

In earlier SECM work, the potential drop across the ITIES was controlled by changing the concentration ratio of the common ion in both liquid phases. The potential window accessible in such experiments was about ±120 mV with respect to the standard transfer potential of the common ion. Studying ET processes by SECM at an externally polarized ITIES [39,40] enabled measurements over a significantly wider potential range (up to ~0.6 V). A typical SECM experiment at the externally polarized ITIES (Figure 8.1B) is done in a three-electrode setup [39]. A millimeter-sized reference electrode coated with a small (μL) droplet of aqueous solution was immersed in the organic phase. A glass capillary filled with aqueous solution and containing a Ag/AgCl electrode could also be used as substrate for SECM measurements at the externally polarized ITIES [41]. Either a metal UME [41,42] or a nanopipette-filled aqueous solution [39,43] was employed as a tip.

In earlier SECM studies of the nonpolarizable ITIES modified with adsorbed lipids, which were carried out using the aforementioned setup, the state of the monolayer could be neither controlled nor extensively characterized [28,29]. The combination of SECM with Langmuir trough described by the Unwin group [25,26] allowed precise control of coverage and state of monodispersed lipids absorbed on liquid–liquid or air–liquid interface. These experiments are discussed in Section 8.3.4.

TABLE 8.1
Redox Systems Studied by SECM/ITIES Technique

Interface	Redox System	Transferred Ion	References
Water/nitrobenzene	$Ru(bpy)_3^{3+}$/Fc	Fc^+	[15]
	FcCOO/Fc	TEA^+, ClO_4^-, Fc^+	[15]
	$IrCl_6^{2-}$/Fc	Fc^+	[27]
	$Fe(phen)_3^{3+}$/Fc	Fc^+	[27]
	$Mo(CN)_8^{3-}$/Fc	Fc^+	[27]
	$Fe(CN)_6^{3-}$/Fc	Fc^+	[27]
Benzene/water	$ZnPor^+/Ru(CN)_6^{4-}$	ClO_4^-	[23]
	$ZnPor^+/Mo(CN)_8^{4-}$	ClO_4^-	[28]
	$ZnPor^+/Fe(CN)_6^{4-}$	ClO_4^-	[28,29]
	$ZnPor^+/Fe^{2+}$	ClO_4^-	[28]
	$ZnPor^+/V^{2+}$	ClO_4^-	[28]
	$ZnPor^+$/Co(II) sepulchrate	ClO_4^-	[28]
Water/dichloroethane	$Fe(CN)_6^{4-}$/TCNQ	$TPAs^+$	[30]
Water/benzonitrile	B_{12}/dibromocyclohexane	ClO_4^-	[31]
Water/nitrobenzene or 1,2-dichloroethane	$ZnPor^+/Ru(CN)_6^4$	PF_6^- ClO_4^-	[32]
Water/nitrobenzene	ZnTPP$^+$, ZnTPP(OH) and $ZnTPP(OCH_3)^+/Fe(CN)_6^4$	ClO_4^-	[33]
Water/benzonitrile, benzene or 1,2-dichloroethane	$ZnPor^+/Ru(CN)_6^{4-}$	ClO_4^-	[34]
	$ZnPor^+/Fe(CN)_6^{4-}$	PF_6^-	
	$ZnPor^+/Mo(CN)_8^{4-}$		
	$ZnPor^+/W(CN)_8^{4-}$		
	$ZnPor^+/Fe(EDTA)^{2-}$		
	$ZnPor^+/Ru(NH_3)_6^{2+}$		
	$ZnPor^+/V^{2+}$		
	$ZnPor^+/Co(Sep)^{2+}$		
Water/ionic liquid	$Fe(CN)_6^{3-}$/Fc	$C_8mimC_1C_1N^-$ C8mim$^+$	[35]
Water/1,2-dichloroethane	Au monolayer-protected clusters/Ce^{4+}, $Fe(CN)_6^{4-}$,$Ru(NH_3)_6^{3+}$,$Ru(CN)_6^{4-}$,$IrCl_6^{2-}$	Clo_4^-, $TPAs^+$, TBA^+, TMA^+	[36,37]

8.2.1.3 Separation of ET from IT and Solute Partitioning Processes

In most conventional electrochemical studies carried out at either macro- or micro-ITIES, the same interfacial area was available for both ET and IT processes. In contrast, the ET process in SECM experiments occurs at a micrometer-sized area of the ITIES confronting the tip, while charge-compensating IT can occur at any point of the large (e.g., cm^2) phase boundary. Thus, the interfacial ET can be probed without complications caused by IT. This assumption was checked for the ET between aqueous $Ru(bpy)_3^{3+}$ and ferrocene (Fc) dissolved in NB:

$$Fc^{o}_{(NB)} + Ru\left(bpy\right)_3^{3+}{}_{(w)} \rightarrow Fc^{+}_{(NB)} + Ru\left(bpy\right)_3^{2+}{}_{(w)} \tag{8.8}$$

A very large difference of standard potentials of these redox couples (~1 V) suggested that the interfacial process should be rapid. However, in the absence of supporting electrolyte in NB, the

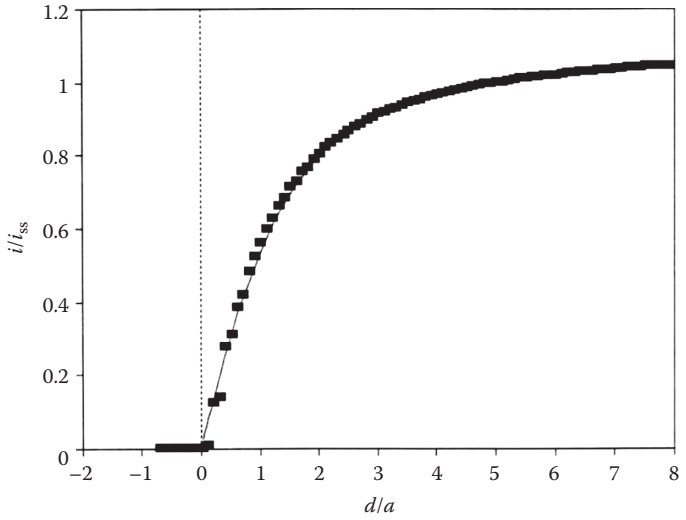


FIGURE 8.2 SECM current–distance curve for a 5 μm radius Pt tip UME approaching NB from an aqueous solution containing 5 mM FcCOONa and 0.1 M NaCl. Positive distances correspond to the tip in water; negative distances correspond to tip penetration into NB. The tip potential was held at +400 mV vs. Ag/AgCl, that is, sufficiently positive for the oxidation of $FcCOO^-$ to be diffusion controlled. The NB phase contained no electroactive species. Solid line represents SECM theory for an insulating substrate (Equation 8.7). (Reprinted with permission from Wei, C., Bard, A.J., and Mirkin, M.V., Scanning electrochemical microscopy. 31. Application of SECM to the study of charge transfer processes at the liquid/liquid interface, *J. Phys. Chem*., 99, 16033–16042, 1995. Copyright 1995 American Chemical Society.)

overall process rate was limited by charge-compensating IT. Using the slower ET reaction between FcCOOH and Fc,

$$Fc^{o}_{(NB)} + FcCOO_{(w)} \rightarrow Fc^{+}_{(NB)} + FcCOO^{-}_{(w)} \tag{8.9}$$

the transition from slow IT to slow ET was observed when the concentration of supporting electrolyte in NB (tetraethylammonium perchlorate) increased from 0 to 10 mM. It was found that IT limitations can be avoided by keeping the concentration of common ion in both phases at least 10 times higher than the redox mediator concentration in the top phase.

A shallow minimum is typically present in the approach curve when the interfacial process is partially limited by common ion transport. This characteristic feature was never observed for an ET-controlled processes, and it can be used to detect IT limitations.

Another interfacial process that can complicate ET kinetics measurements at liquid interfaces is partitioning of a neutral redox species. While partitioning does not contribute to the current flowing across the ITIES, the oxidation (or reduction) of the extracted species at the tip has to be taken into account. Normally, this problem can be minimized by selecting a sufficiently hydrophobic organic (and sufficiently hydrophilic aqueous) mediator; however, in some systems (e.g., ionic liquid/water [35]) preventing the partitioning may not be feasible because of the limited choice of mediators. In ref. [35b], the tip current comprised two components, that is, positive feedback from the ET between aqueous ferricyanide and Fc dissolved in ionic liquid (I_{ET}) and direct oxidation of Fc whose partitioning to the aqueous phase was not negligible (I_{part}). It was shown that the contributions of these processes to the tip current are mutually independent, and the I_{ET} was evaluated by subtracting the I_{part} component from the measured I_T.

8.2.1.4 Potential Drop across a Nonpolarized ITIES

The ET process at the ITIES is a very interesting intermediate case linking homogeneous and heterogeneous ET. The interpretation of experimental results depends on the adopted model of the liquid interface. One of the questions is about potential profile in the interfacial region. Only the potential drop that exists between the two reacting molecules can contribute to the driving force for ET reaction; however, it is not clear what fraction of the total Galvani potential difference ($\Delta_w^o\varphi$) at the liquid junction actually drops between the reacting molecules. In most experimental studies, it was implicitly assumed that the potential dependence of the rate constant obeys Butler–Volmer equation. This should be the case if the reactants are separated by the sharp phase boundary [6a] (Figure 8.3A) or a thin ion-free layer (Figure 8.3B). If the reactants can penetrate the phase boundary [6b,c], or if ET reaction occurs within a fairly thick mixed solvent layer (Figure 8.3C), the fraction of the interfacial voltage contributing to the ET-driving force should be negligible or at least much smaller than the total $\Delta_w^o\varphi$ value.

Girault [1b] pointed out that the apparent potential dependence of the ET rate may be attributed to the change in concentration of the reactants near the interface rather than to activation control. This model, further developed by Schmickler [9], postulates that the rate constant is essentially potential-independent because the potential drop across the compact part of the double layer at the ITIES is small. In this model, the ET rate dependence on the interfacial potential drop is only due to the diffuse layer effect similar to Frumkin effect at metal electrodes.

Some of these questions were addressed by studying the potential dependence of the ET rate at the ITIES with the SECM. The potential drop across the ITIES ($\Delta_w^o\varphi$) can be quantitatively controlled and varied by changing the ratio of concentrations of the potential-determining ions in the two liquid phases. If only one type of ion (e.g., ClO_4^- anion) partitions between two solvents, then

$$\Delta_w^o\varphi = \Delta_w^o\varphi^o_{ClO_4^-} - 0.059 \log\left(\left[ClO_4^-\right]_w / \left[ClO_4^-\right]_o\right) \tag{8.10}$$

This way of controlling the interracial voltage was used to study the potential dependence of the rate constant for ET with no external potential applied across the ITIES [23]. The heterogeneous rate constant of the ET between $ZnPor^+$ in benzene and aqueous $Ru(CN)_6^{4-}$ was measured with NaCl and $NaClO_4$ dissolved in water and tetrahexylammonium perchlorate ($THAClO_4$) in benzene. Perchlorate was the only ion common to both phases. The transfer of this ion between the two phases maintained the electroneutrality.

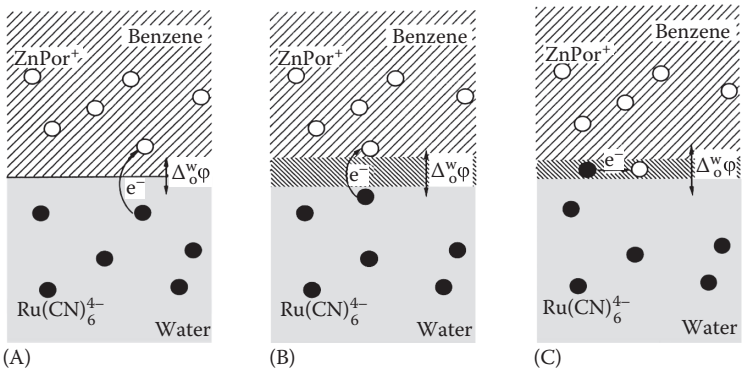


FIGURE 8.3 Different models of interfacial ET. (A) Aqueous and organic redox species are separated by the sharp interfacial boundary. (B) Interfacial potential drop across a thin ion-free layer between redox reactants. (C) ET reaction occurs within a nanometer-thick mixed solvent layer. No potential drops between reactant molecules.

With the perchlorate concentration in organic phase kept constant (e.g., $[ClO_4^-] = 0.25\,M$) in all experiments [23,28], $\Delta_w^o\varphi$ was a linear function of $\log[ClO_4^-]_w$ with the slope close to 60 mV per decade:

$$\Delta_w^o\varphi = \text{const} - 0.06 \log\left[ClO_4^-\right]_w \tag{8.11}$$

Equation 8.11 was verified experimentally by measuring steady-state voltammograms of different oxidation reactions in the following cell:

$$\text{Ag / AgCl / } H_2O,\ \text{KCl(sat'd) / } H_2O,\ 0.1\ \text{M NaCl},\ 0.01 - 2\ \text{M } NaClO_4\ //$$

$$\text{benzene},\ 0.25\ \text{M } THAClO_4,\ 5\ \text{mM ZnPor (or Fc) / Pt} \tag{8.12}$$

Reversible half-wave potentials ($E_{1/2}$) of Fc and ZnPor oxidation in benzene at a 25-μm electrode were measured with respect to the aqueous Ag/AgCl reference. The dependencies of $E_{1/2}$ vs. $\log[ClO_4^-]_w$ were linear with a ~60 mV/decade slope in agreement with Equation 8.11 [23].

Equation 8.11 gives the relative values of the potential drop across the ITIES, which is one of two components of the total driving force for ET reaction [28]:

$$\Delta G^\circ = -F(\Delta E^\circ + \Delta_w^o\varphi) \tag{8.13}$$

where ΔE° is the difference between the formal potentials of the organic and the aqueous redox couples [28]. Because the diffusion coefficients of oxidized and reduced forms are usually similar, one can assume that the formal potential is approximately equal to the reversible half-wave potential. As the $E_{1/2}$ values for both aqueous and organic redox species were measured with respect to the same aqueous reference electrode, the difference of these values is

$$\Delta E_{1/2} \approx \Delta E^\circ + \Delta_w^o\varphi \tag{8.14}$$

Although the absolute value of $\Delta_w^o\varphi$ cannot be found without an extra thermodynamic assumption [1], $\Delta E_{1/2}$ gives the absolute value of the driving force.

Two groups studied interfacial ET reactions between monolayer-protected gold clusters (MPCs) dissolved in 1,2-dichloroethane (DCE) and aqueous redox species by SECM [36,37]. The Au cluster cores, protected with phenylethylthiolate ligands, were sufficiently small (~1 nm diameter) to exhibit molecule-like redox activity. Accordingly, the evaluation of the rate constant at the nonpolarizable liquid–liquid interface was accomplished using the approach discussed earlier, which was originally developed for bimolecular ET reactions between conventional redox entities. The heterogeneous rate constant was measured for ET between organic soluble Au_{38} clusters and an aqueous $[IrCl_6]^{2-}$ oxidant [37]. As can be expected from Marcus theory, this process was found to be faster than similar ET reactions between conventional aqueous and organic redox species at the liquid–liquid interface.

8.2.1.5 Potential Dependence of Heterogeneous Rate Constant of ET at the ITIES

The scheme of SECM measurements of the rate of the ET between $ZnPor^+$ in benzene and aqueous $Ru(CN)_6^{4-}$ [23] was analogous to the one in Figure 8.1A. The tip electrode generates $ZnPor^+$ ions by oxidation of ZnPor. $ZnPor^+$ diffuses to the ITIES, where it is reduced back to ZnPor by $Ru(CN)_6^{4-}$:

$$\text{ZnPor} - e^- \rightarrow \text{ZnPor}^+ \quad \text{(tip)} \tag{8.15}$$

$$\text{ZnPor}^+ + Ru(CN)_6^{4-} \rightarrow \text{ZnPor} + Ru(CN)_6^{3-} \quad \text{(ITIES)} \tag{8.16}$$

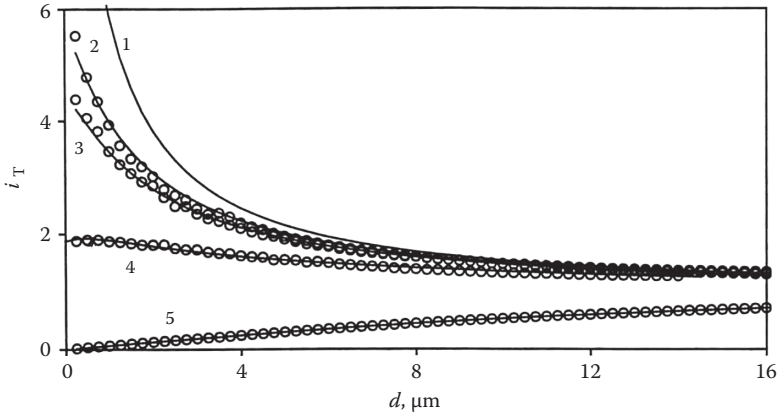


FIGURE 8.4 SECM current–distance curves for a 12.5 μm radius Pt tip UME in benzene solution approaching the water–benzene interface. Benzene contained 0.5 mM ZnPor and 0.25 M $THAClO_4$. The aqueous phase contained 0.1 M NaCl, 0.01 M $NaClO_4$, and (curve 2) 50, (curve 3) 5, (curve 4) 0.5, or (curve 5) 0 mM $Ru(CN)_6^{4-}$. Curve 1 is the theoretical curve for a diffusion-controlled process obtained from Equation 8.6. The tip potential was held at 0.95 V vs. Ag/AgCl, corresponding to the plateau current of first oxidation of ZnPor. The tip was scanned at 0.5 μm/s. Circles are experimental data and lines represent the theoretical fit obtained from Equations 8.4 and 8.5. (Reprinted with permission from Tsionsky, M., Bard, A.J., and Mirkin, M.V., Scanning electrochemical microscopy 34. Potential dependence of the electron-transfer rate and film formation at the liquid/liquid interface, *J. Phys. Chem.*, 100, 17881–17888, 1996. Copyright 1996 American Chemical Society.)

The rate of the mediator regeneration via reaction (8.16) was evaluated from the tip current. When no oxidizable species was present in the aqueous phase, i_T vs. d dependence followed the SECM theory for an insulator (curve 5 in Figure 8.4). In the presence of $Ru(CN)_6^{4-}$, the tip current increased with the decrease in d; at higher $[Ru(CN)_6^{4-}]$, the closer i_T vs. d dependencies approached the diffusion limit given by curve 1 in Figure 8.4.

The values of the effective heterogeneous rate constant for reaction (8.16) were found by fitting the families of approach curves obtained at different concentrations of $Ru(CN)_6^{4-}$ and $NaClO_4$ in water phase to Equations 8.4 and 8.5 (Figure 8.4). At low concentrations of $Ru(CN)_6^{4-}$, k_f was proportional to $[Ru(CN)_6^{4-}]$ for any given value of $[ClO_4^-]_w$ (Figure 8.5), as expected for reaction (8.16), which is the first order in $Ru(CN)_6^{4-}$:

$$k_f = \text{const} \left[Ru(CN)_6^{4-}\right] \exp(-\Delta G^{\#}/RT) \tag{8.17}$$

where $\Delta G^{\#}$ is the free energy barrier. For lower overvoltages, a Butler–Volmer type approximation can be used:

$$\Delta G^{\#} = \alpha \Delta G^{\circ} = -\alpha F(\Delta E^{\circ} + \Delta_w^o \varphi) \tag{8.18}$$

where

ΔE° is the difference of standard potentials of two redox couples
α is the transfer coefficient

At a given concentration of $Ru(CN)_6^{4-}$, the apparent rate constant depends on the potential drop across the ITIES, which increases with a decrease in $NaClO_4$ concentration:

$$k_f = \text{const}\,[Ru(CN)_6^{4-}] \exp(-0.06\alpha F \log[ClO_4^-]_w / RT) \tag{8.19a}$$

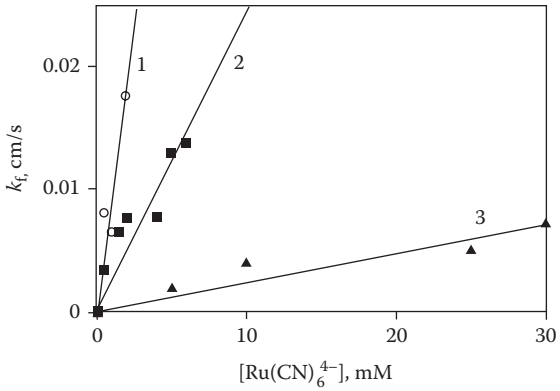


FIGURE 8.5 Dependence of the effective heterogeneous rate constant on $[Ru(CN)_6^{4-}]$ at different concentrations of $NaClO_4$ in water. $[ClO_4^-]_w$ was (1) 0.01, (2) 0.1, and (3) 1 M. (Reprinted with permission from Tsionsky, M., Bard, A.J., and Mirkin, M.V., Scanning electrochemical microscopy 34. Potential dependence of the electron-transfer rate and film formation at the liquid/liquid interface, *J. Phys. Chem*., 100, 17881–17888, 1996. Copyright 1996 American Chemical Society.)

or

$$\log k_f = \text{const} + \log[Ru(CN)_6^{4-}] - \alpha \log[ClO_4^-]_w \tag{8.19b}$$

In agreement with Equation 8.19b, the $\log k_f$ vs. $\log\left[ClO_4^-\right]_w$ dependencies at different concentrations of $Ru(CN)_6^{4-}$ were linear (Figure 8.6A). At lower $[ClO_4^-]$, corresponding to a more positive $\Delta_w^o\varphi$, the ET rate approached the diffusion limit and $\log k_f$ vs. $\log[ClO_4^-]$ curves leveled off. Clearly, this effect is more significant at higher concentration of $Ru(CN)_6^{4-}$ (curve 1 in Figure 8.6A), for which the k_f values (at the same $\Delta_w^o\varphi$) are higher. Two similar transfer coefficient values were found from the linear portions of the Tafel plots, that is, $\alpha = 0.49 \pm 0.1$ for 50 mM $Ru(CN)_6^{4-}$ and $\alpha = 0.56 \pm 0.05$ for 5 mM $Ru(CN)_6^{4-}$. The potential dependence of bimolecular rate constant $\left(k = k_f / \left[Ru(CN)_6^{4-}\right]\right)$ presented in Figure 8.6B shows similar slope of Tafel dependence over >1.5 orders of magnitude in k.

The following conclusions about the mechanism of ET process and the ITIES structure were made from the obtained potential dependencies of the ET rate constant:

- The linear Tafel plots and α values close to 0.5 indicate that conventional ET theory, for example, Butler–Volmer model is applicable to heterogeneous reactions at the ITIES.
- The participants of the ET reaction are separated by a thin interfacial boundary which they do not significantly penetrate (Figure 8.3A). Otherwise, the potential drop between two redox molecules would be much smaller than the total $\Delta_w^o\varphi$, and α would be much smaller than 0.5. Similarly, the experimental results do not support a picture of ET occurring within a fairly thick mixed solvent layer (Figure 8.3C). This does not exclude the possibility of a thin ion-free layer at the interface separating participants of the redox reaction (Figure 8.3B). Such a layer would result in the smaller ET rate constant, but would not affect the α value.

Similar dependencies of the ET rate on the interfacial voltage were reported by several groups (Table 8.1). The transfer coefficient values close to 0.5 were obtained at nonpolarizable water–organic

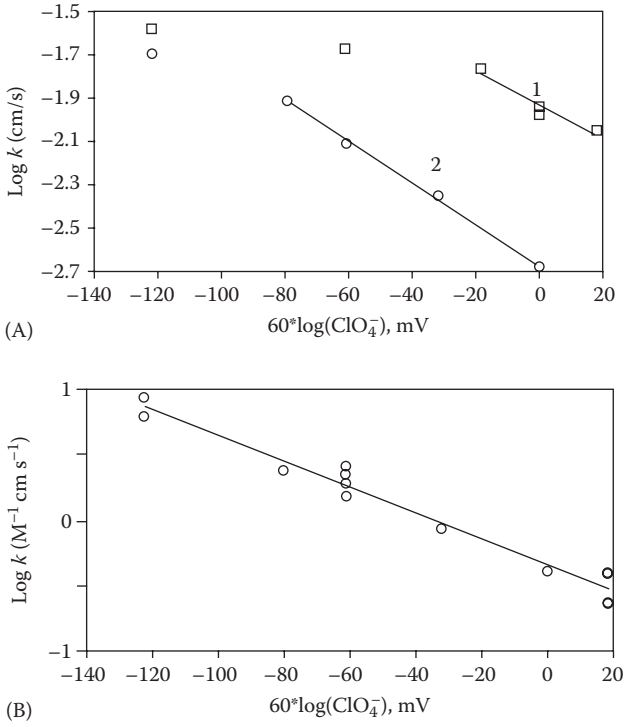


FIGURE 8.6 (A) Dependencies of the effective heterogeneous rate constant on potential drop across the ITIES at (1) 50 and (2) 5 mM concentrations of $Ru(CN)_6^{4-}$. For other experimental parameters, see Figure 8.4. $\Delta_w^o\varphi$ is expressed in terms of $[ClO_4^-]_w$ according to Equation 8.11. (B) Potential dependence of the effective bimolecular rate constant. (Reprinted with permission from Tsionsky, M., Bard, A.J., and Mirkin, M.V., Scanning electrochemical microscopy 34. Potential dependence of the electron-transfer rate and film formation at the liquid/liquid interface, *J. Phys. Chem*., 100, 17881–17888, 1996. Copyright 1996 American Chemical Society.)

solvent [32–34] and water–ionic liquid [35] interfaces by changing the concentration of the common ion. Similar behavior was also observed in absence of common ion at polarizable ITIES, where the potential drop was controlled externally using a three-electrode setup [41]. The unusual α values obtained in some studies (e.g., 1.62 [41]) may be due to specific adsorption [44], ion partitioning [45], and double-layer effects [46a]. In contrast, the authors of an SECM study of the oxidation of ascorbic and chlorogenic acids by the radical cation of 5,10,15,20-tetraphenylporphyrinato zinc(II) at the nonpolarizable ITIES suggested that this process involves interfacial IT reaction and ET occurring homogeneously in the organic phase [47].

Essentially potential-independent rate was measured for the reaction between ZnPor and $Ru(CN)_6^{3-}$ at the interfaces between water and three organic solvents of different polarities [48]. The finding was attributed to the use of neutral organic species, whose interfacial concentration is not affected by the $\Delta_w^o\varphi$. However, no similar observation was reported for any other ET reaction at the ITIES, and the origin of this behavior has yet to be understood.

8.2.1.6 ET Rate as a Function of the Standard Potential Difference

The driving force for an ET reaction at the ITIES consists of two components, that is, the difference of standard potentials of redox mediators and the interfacial potential drop (Equation 8.14). The dependence of k_f on ΔE° was studied for reactions between $ZnPor^+$ in benzene and the series of similar cyanide complexes in water [28]:

$$ZnPor^{+} + R_w \rightarrow ZnPor + O_w \quad (8.20)$$

where $R_w = Ru(CN)_6^{4-}$, $Mo(CN)_8^{4-}$, or $Fe(CN)_6^{4-}$.

Assuming that standard rate constants (i.e., k_f at $\Delta G^\circ = 0$) are similar, the differences in ET rates for these reactants can be attributed to the different ΔE° values. The formal potentials of $Ru(CN)_6^{4-}$, $Mo(CN)_8^{4-}$, and $Fe(CN)_6^{4-}$ couples measured by cyclic voltammetry are 750, 590, and 235 mV vs. Ag/AgCl, respectively. Accordingly, the feedback current obtained with $Mo(CN)_8^{4-}$ in water was higher than with $Ru(CN)_6^{4-}$. With $Fe(CN)_6^{4-}$, the ET rate is much higher, and the overall process was diffusion-controlled at any $[ClO_4^-]_w$.

At relatively low overpotentials, Tafel-like driving force dependencies of the rate constant were obtained for several reactions at different ITIES [24,33,34,49]. The transfer coefficient values estimated from these measurements varied between 0.3 and 0.8. The Marcus inverted behavior [6], that is, the rate constant decreasing with increasing driving force, was reported for redox pairs with large standard potential differences. In earlier SECM/ITIES experiments [28,29], a lipid monolayer was formed on water–organic solvent interface to decrease the ET rate and enable the observation of the inverted region (see Section 8.2.2). Later, the inverted driving force dependence was observed at unmodified ITIES for several redox couples with $\Delta E^\circ > \sim 0.8$ V [34,50,51]. Additional experimental evidence for Marcus inverted region ET was obtained from the investigation of electrogenerated chemiluminescence (ECL) reactions occurring at the ITIES [52].

8.2.2 Electron Transfer across Molecular Monolayer

Similar to the earlier studies at metal electrodes, molecular monolayers of long-chain saturated phospholipids assembled at the ITIES have been used as spacers to check the predictions of Marcus theory (Figure 8.7) [28,29].

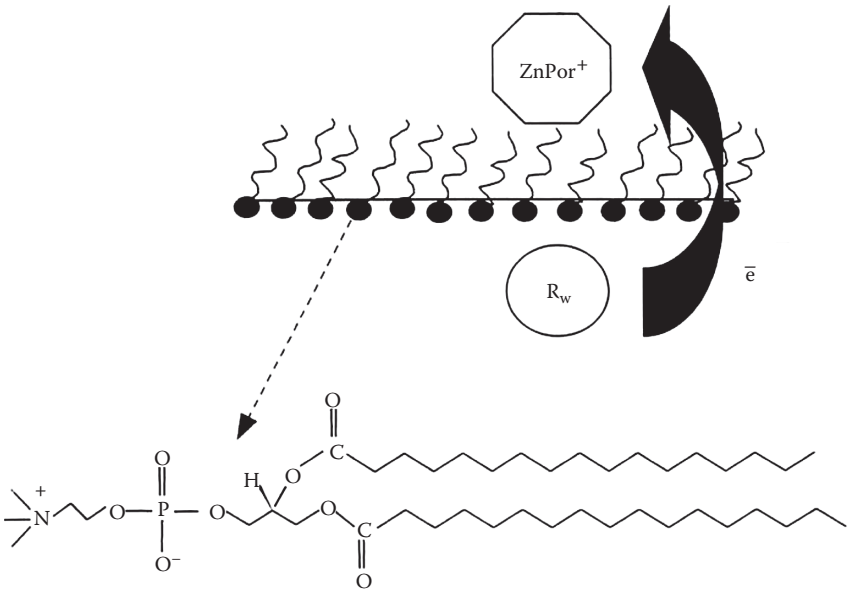


FIGURE 8.7 The ITIES modified with a monolayer of phospholipid. The insert shows the structure of synthetic saturated phosphatidylcholine lipid. (Reprinted with permission from Tsionsky, M., Bard, A.J., and Mirkin, M.V., Long-range electron-transfer through a lipid monolayer at the liquid/liquid interface, *J. Am. Chem. Soc.*, 119, 10785–10792, 1997. Copyright 1997 American Chemical Society.)

8.2.2.1 Adsorption of Phospholipids at the ITIES

Amphiphilic lipid molecules dissolved in an organic solvent spontaneously form a monolayer film at the water–organic solvent interface. The orientation of the monolayer is such that the hydrophilic head group is immersed in water, while the hydrophobic tail remains in the organic phase. The first attempt to probe ET across a phospholipid monolayer adsorbed at the ITIES was reported by Cheng and Schiffrin, who found that a monolayer makes the ET rate immeasurably slow [53].

SECM measurements of the interfacial ET between $ZnPor^+$ in benzene and aqueous $Fe(CN)_6^{4-}$ also showed a strong blocking effect of phospholipids adsorbed at the ITIES [28,29,32]. In the presence of the monolayer of 1,2-diacyl-*sn*-glycero-3-phosphocholine (PC) [28,29] or 1,2-diacyl-*sn*-glycero-3-phospho-L-serine (PS) [32] with 10 methylene groups in a hydrocarbon chain (C-10; the abbreviations C-10, C-12, C-14, etc. are used in this section to designate different PC and PS with the corresponding numbers of methylene groups in the hydrocarbon chain), the k_f value, which was immeasurably high at a clear ITIES, decreased and became accessible by SECM measurements.

The blocking effect of the lipid film can be attributed to the decrease in either the ET or IT rate. Kakiuchi and coworkers [54] and Schiffrin and coworkers [55] extensively studied the effect of different lipid monolayers on transfer rates of various ions, including ClO_4^-. The largest decrease in IT rate caused by the presence of a compact phospholipid monolayer at the ITIES was by a factor of 5. The effects observed in Ref. [28] were orders of magnitude larger. This observation and also the characteristic shape of approach curves discussed in Section 8.2.1.3 allowed the authors to rule out the possibility of the slow IT effect.

A typical set of SECM current–distance curves for different concentrations of C-10 under equilibrium conditions is shown in Figure 8.8 for $Ru(CN)_6^{4-}$ species in the aqueous solution and ZnPor in benzene [28]. The ET rate decreases monotonically as the lipid concentration increases from 0 (curve 2) to 48 μM (curve 6) due to increasing coverage of the interface. The ET, both at clear ITIES and that covered with lipid, contributed to the obtained effective rate constant values. The adsorption isotherms (dependencies of k_f vs. lipid concentration) were obtained for two different

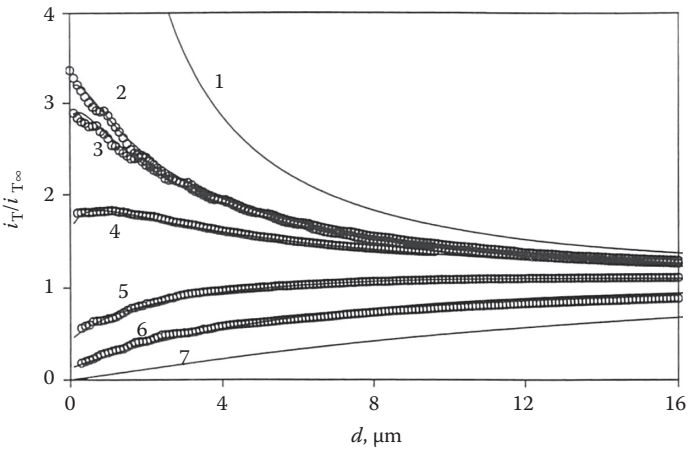


FIGURE 8.8 Effect of lipid concentration on the shape of the SECM current–distance curves. The aqueous solution was 0.1 M NaCl, 0.1 M $NaClO_4$, and 7 mM $Na_4Ru(CN)_6$. The concentration of C-10 lipid in benzene was (2) 0, (3) 1.12, (4) 3.54, (5) 12.4, and (6) 47.8 μM. Circles are experimental data. Solid lines represent the theory for the following k_f values (cm/s): (1) ∞ (diffusion-controlled process), (2) 0.0145, (3) 0.013, (4) 0.0075, (5) 0.002, (6) 0.0006, and (7) 0 (pure negative feedback). The tip was scanned at 1 μm/s. (Reprinted with permission from Tsionsky, M., Bard, A.J., and Mirkin, M.V., Long-range electron-transfer through a lipid monolayer at the liquid/liquid interface, *J. Am. Chem. Soc.*, 119, 10785–10792, 1997. Copyright 1997 American Chemical Society.)

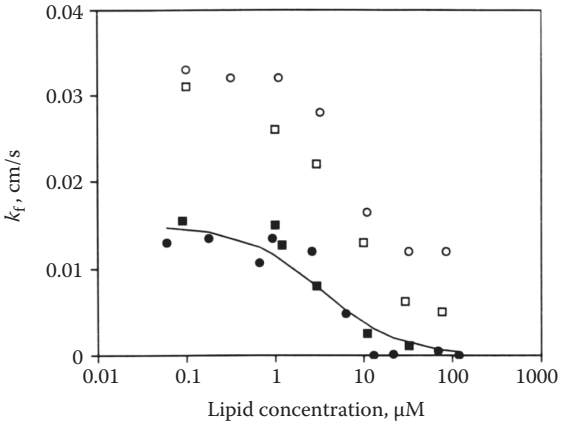


FIGURE 8.9 Dependence of the rate constant of ET between $ZnPor^+$ and $Ru(CN)_6^{4-}$ (■ and ●) or $Fe(CN)_6^{4-}$ (□ and ○) on lipid concentration in benzene. The number of methylene groups in the lipid hydrocarbon chain was 10 (■ and ○), 12 (□), and 20 (●). The organic phase contained 0.25 M $THAClO_4$, 0.5 mM ZnPor, and lipid. The water phase was 0.1 M NaCl, 0.1 M $NaClO_4$, and 7 mM $Na_4Ru(CN)_6$ (■ and ●) or $Na_4Fe(CN)_6$ (□ and ○). ET rate constants were obtained by fitting experimental approach curves (Figure 8.8) to the theory (Equations 8.4 and 8.5). The solid line represents Frumkin isotherm (Equation 8.21) with $B = 2 \times 10^5$ M^{-1} and $a = 0.25$. (Reprinted with permission from Tsionsky, M., Bard, A.J., and Mirkin, M.V., Long-range electron-transfer through a lipid monolayer at the liquid/liquid interface, *J. Am. Chem. Soc.*, 119, 10785–10792, 1997. Copyright 1997 American Chemical Society.)

aqueous redox species, $Ru(CN)_6^{4-}$ and $Fe(CN)_6^{4-}$, and several different lipids (Figure 8.9). At high concentration of any lipid (i.e., >50 μM), the ET rate between $Ru(CN)_6^{4-}$ and $ZnPor^+$ becomes immeasurably slow.

The k_f vs. [lipid] dependencies for $Fe(CN)_6^{4-}$ are different. Although the ET rate decreases markedly with increasing concentration of lipid, it does not approach zero at higher concentrations, but reaches the limiting value at about 50 μM. This saturation suggests the formation of a complete phospholipid monolayer at the ITIES. The formation of compact phospholipid monolayers at similar lipid concentrations was observed at water–NB [56a] and water–DCE [56b] interfaces.

The presence of defects and pinholes is always a concern in experimental work with monolayers. The following findings indicated that the defect density in the lipid film is too low to affect ITIES/SECM measurements [28]:

- The extent of the blocking effect apparently depends on the driving force for ET. When the driving force is small (e.g., $\Delta E^\circ \sim 100$ mV for $Ru(CN)_6^{4-}$ and $ZnPor^+$), the formation of any long-chain phospholipid monolayer (i.e., PC with C-10 to C-20) resulted in the ET rate below the lower limit for SECM measurements. This shows that the density of the possible defects in the monolayer was too low to produce detectable feedback current under experimental condition of Ref. [28].
- The ET between $Fe(CN)_6^{4-}$ and $ZnPor^+$, for which ΔE° is about 0.5 V larger, occurred at a measurable rate via tunneling through the monolayer. If the electrons were transferred through pinholes rather than across the lipid monolayer, one would expect the ET rate to be independent of the spacer length. In contrast, the longer lipid (i.e., C-12; open squares in Figure 8.9) inhibits ET stronger than C-10 at the same concentration (open circles).
- The time dependencies [28] showed that the adsorption of lipids at the ITIES is fully reversible. The lipid adsorption on and desorption from the ITIES occur at about the same timescale. The monolayer self-assembled at the ITIES is in dynamic equilibrium with

dissolved lipid molecules that allow any pinhole defects to be healed. In contrast, self-assembly on the solid–liquid interface often involves irreversible adsorption and requires high purity of chemicals, complex pretreatment, and preparation protocols to obtain a low-defect density molecular monolayer.

The equilibrium adsorption of phospholipids at the ITIES was shown to follow Frumkin isotherm [54–59]:

$$B[\text{lipid}] = \theta \exp(-2a\theta) / (1 - \theta) \tag{8.21}$$

where
- a is a small lateral interaction parameter
- θ is the coverage of the ITIES with lipid

The standard Gibbs energy of adsorption, $\Delta G^{\circ}_{ads} = -RT \ln B$, is about 35–40 kJ/mol [57,59c]. The best fit to experimental data (solid line in Figure 8.9) was obtained with $a = 0.25$ and $B = 2 \times 10^5$. Similar dependencies of the ET rate constant on lipid length and concentrations were obtained for PS lipids [32]. However, the absolute values of k_f across PS monolayers turned out to be significantly lower than the rate constants across PC lipids with the same numbers of methylene groups. Unlike phosphatidylcholines, which are neutral, phosphatidylserine lipids are negatively charged at pH 7 and neutral at pH < 5 [46b]. The difference between ET rates across PC and PS films was explained by repulsion of anionic $Fe(CN)_6^-$ species by negatively charged heads of PS lipids. Such repulsion may result in both the decreased interfacial concentration of $Fe(CN)_6^{4-}$ and larger separation of redox reactants. The authors did not find strong pH effect on ET rate across PS layers, which was attributed to counterbalancing of the two effects, that is, the formation of the more compact film due to lower electrostatic repulsion between lipid molecules and the elimination of $Fe(CN)_6^{4-}$ repulsion discussed earlier.

8.2.2.2 Driving Force Dependence of the ET Rate across a Lipid Monolayer

The potential dependence of the ET rate across a lipid monolayer was measured using the methodology developed for a clear ITIES [23,28]. The driving force for ET reaction was evaluated as a difference between the two half-wave potentials measured with respect to the same aqueous Ag/AgCl reference. The decrease in $[ClO_4^-]_w$ corresponded to the increase in driving force for ET (Reaction 8.20). Figure 8.10 illustrates the driving force dependence of the ET rate across a C-10 lipid monolayer adsorbed on the water–benzene interface for $ZnPor^+$ and three different aqueous redox species. For the $Fe(CN)_6^{4-}/ZnPor^+$ reaction, the $\left(\Delta E^{\circ} + \Delta^{\circ}_{w}\varphi\right)$ values were within the range of 570–700 mV. At lower overpotentials $\left(\Delta E^{\circ} + \Delta^{\circ}_{w}\varphi \le 630 \text{ mV}\right)$, the Tafel plot was linear with a slope corresponding to $\alpha = 0.59$. At higher overpotentials, this curve leveled off, as predicted by Marcus theory [5a]:

$$\Delta G^{\neq} = (\lambda_o / 4)(1 + \Delta G^{\circ} / \lambda_o)^2 \tag{8.22}$$

where
- λ_o is the reorganization energy
- ΔG° is given by Equation 8.18

At higher overpotentials (i.e., $\Delta G^{\circ} > \lambda_o$), Equation 8.22 predicts the existence of the inverted region, in which the increasing driving force results in a decrease in the ET rate [5]. This effect cannot be observed at metal electrodes, where a continuum of electronic states exists in the metal below Fermi level. In contrast, the concentrations of redox species in both liquid phases are finite, and one can expect to see the inverted behavior when ΔG° is sufficiently large. Accordingly, the

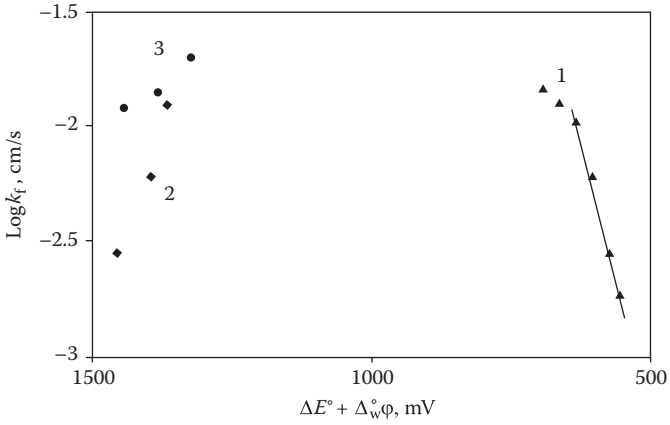


FIGURE 8.10 Driving force dependence of the ET rate between $ZnPor^+$ in benzene and various aqueous redox species across a monolayer of C-10 lipid. The organic phase contained 0.25 M $THAClO_4$, 0.5 mM ZnPor, and 100 μM C-10. The aqueous phase contained 7 mM of $Fe(CN)_6^{4-}$ (1), Co(II) sepulchrate (2), and V^{2+} (3). For other parameters, see Figure 8.7. (Reprinted with permission from Tsionsky, M., Bard, A.J., and Mirkin, M.V., Long-range electron-transfer through a lipid monolayer at the liquid/liquid interface, *J. Am. Chem. Soc*., 119, 10785–10792, 1997. Copyright 1997 American Chemical Society.)

rate constant of the $ZnPor^+/V^{2+}$ reaction decreased significantly when the driving force increased by 120 mV (filled circles in Figure 8.10). A large decrease in the ET rate with increasing ΔG° was also observed for the $ZnPor^+/CoSep^{2+}$ system (diamonds in Figure 8.10). One might try to explain the observed behavior by a diffuse layer effect. Unlike $Ru(CN)_6^{4-}$, $Mo(CN)_8^{4-}$, and $Fe(CN)_6^{4-}$ species, both V^{2+} and $CoSep^{2+}$ are cationic. The decrease in interfacial concentrations of such species may result in the lower ET rate. However, according to the theory in Ref. [9], the diffuse layer effect should be significant mostly for species residing in organic phase. Besides, the rate of ET between cationic (but significantly more positive) Fe^{2+} species and $ZnPor^+$ increased with the increase in driving force [28]. No inverted behavior was observed for this reaction because of a much lower driving force (i.e., 270–400 mV).

8.2.2.3 Distance Dependence of ET

To probe the distance dependence of ET, the k_f was measured for the reaction between $Fe(CN)_6^{4-}$ and $ZnPor^+$ at the ITIES modified with monolayers of different saturated phospholipids (C-10, C-12, C-14, and C-16) [28,29]. The feedback current decreased markedly with increasing number of methylene groups (n) in a hydrocarbon chain at any concentration of ClO_4^- in the aqueous phase (Figure 8.11). With the C-16 lipid, the results were less reproducible, and the k_f vs. n dependence tends to level off. This may be due to the partial penetration of $ZnPor^+$ into the lipid monolayer. The unknown depth of $ZnPor^+$ penetration impaired quantitative analysis of k_f vs. n results in terms of the distance dependence of ET. Even for C-10 to C-14 lipids fitting the experimental points to Equation 8.23

$$k_f(n) = k_f(0)\exp(-\beta n) \tag{8.23}$$

yielded the β value about one-half of that usually reported for saturated hydrocarbon spacers [60]. However, the penetration depth must be significantly less than the length of the hydrocarbon tail in C-10; otherwise, the ET rate would not decrease by several orders of magnitude in the presence of C-10 monolayer, and the lengthening of the hydrocarbon chain from C-10 to C-14 would not cause further decrease in k_f.

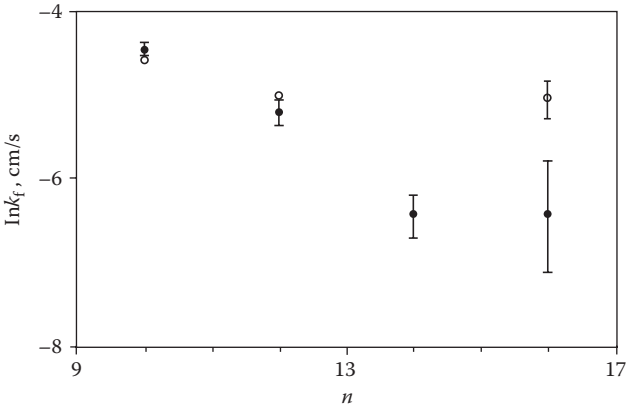


FIGURE 8.11 Distance dependence of the ET rate between $ZnPor^+$ and $Fe(CN)_6^{4-}$. The abscissa plots the number of the methylene groups in the lipid hydrocarbon chain. The concentration of $NaClO_4$ was 0.1 M, corresponding to a 635 mV driving force for the ET reaction. For other parameters, see Figure 8.7. (Reprinted with permission from Tsionsky, M., Bard, A.J., and Mirkin, M.V., Long-range electron-transfer through a lipid monolayer at the liquid/liquid interface, *J. Am. Chem. Soc*., 119, 10785–10792, 1997. Copyright 1997 American Chemical Society.)

8.2.2.4 Effect of the Lipid Monolayer Structure on the ET Rate

The studies at solid electrodes showed that the introduction of delocalized conjugated units and aromatic groups in a molecular monolayer affects the ET rate. The SECM has been used to compare the ET rate across C-16 and similarly sized dipalmitoyl phosphocholine (DPHC). The latter phospholipid has a *trans*, *trans*, *trans*-1,6-diphenyl-1,3,5,-hexatriene chain. This prototype of polyene systems has been previously used as a fluorescent probe [61]. In addition to its conjugated chain, DPHC also contains one saturated C-16 alkyl chain that is easily incorporated into C-16 monolayer.

Similarly by to saturated lipids, increasing concentration of DPHC in benzene resulted in the formation of a compact film and stronger blocking of the interfacial ET [29]. The limiting ET rate across the complete monolayer of DPHC was 2.4 times higher than that obtained with C-16 (Figure 8.12). A possible interpretation of this result is that ET occurs more readily through the delocalized conjugated chain of the DPHC. If so, this pathway should be quite efficient given that only half of the chains contain a more conductive conjugated assembly. Alternatively, the structure of the DPHC layer might be less compact and allow greater penetration of $ZnPor^+$ into lipid film. The ET rate constant across DPHC layer is similar to the k_f for a much shorter saturated lipid (C-10) (Figure 8.11).

The aforementioned approach was used to probe the distribution of molecules in mixed phospholipid monolayers [29]. It was shown that a lipid can embed itself into the preexisting monolayer of another lipid. First, a complete monolayer of C-16 was formed at the benzene–water interface. The ET at this interface was slow ($k_f = 0.005$ cm/s). The addition of DPHC to the organic phase caused an increase in the apparent rate constant (Figure 8.13, curve b). The increase in k value was observed only with the mole fraction of DPHC (x_{DPHC}) in solution ≥0.3. The k_f reached a constant value and ceased to increase at $x_{DPHC} \approx 0.55$. The opposite effect was induced by increasing the mole fraction of C-16 ($x_{C\text{-}16}$) in organic phase in the presence of monolayer of DPHC (Figure 8.13, curve a), that is, the sharp decrease in k_f was observed at $x_{C\text{-}16} > 0.4$.

While the approach curves for monolayers of pure C-16 and DPHC lipids were reproducible, the k_f obtained at mixed monolayers of lipids showed larger variations. Some k_f values obtained from different approach curves were very close to those for pure C-16 and DPHC monolayers. This was explained by segregation of lipids in the monolayer into separate domains composed

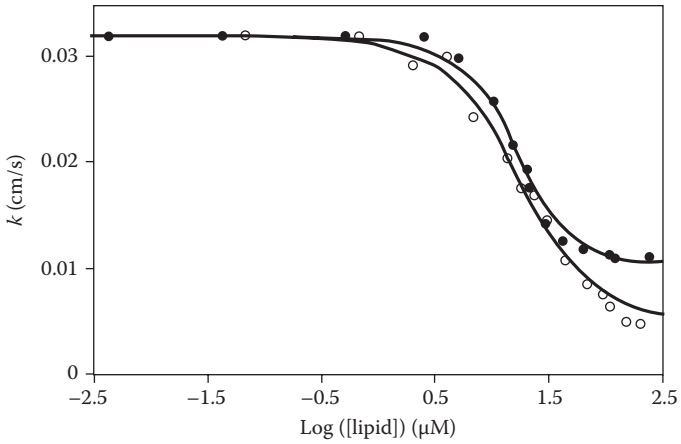


FIGURE 8.12 Heterogeneous ET rate constant, k_f, as a function of the DPHC (●) and C-16 (○) concentrations in the organic phase. The organic phase contained 0.25 M $THAClO_4$, 0.5 mM ZnPor, and lipid. The aqueous phase was 0.1 M NaCl, 0.1 M $NaClO_4$, and 7 mM $Na_4Fe(CN)_6$. The 25 μm Pt tip was scanned at 1 μm/s. (Reprinted with permission from Delville, M.-H., Tsionsky, M., and Bard, A.J., Scanning electrochemical microscopy studies of electron-transfer through monolayers containing conjugated species at the liquid-liquid interface, *Langmuir*, 14, 2774–2779, 1998. Copyright 1998 American Chemical Society.)

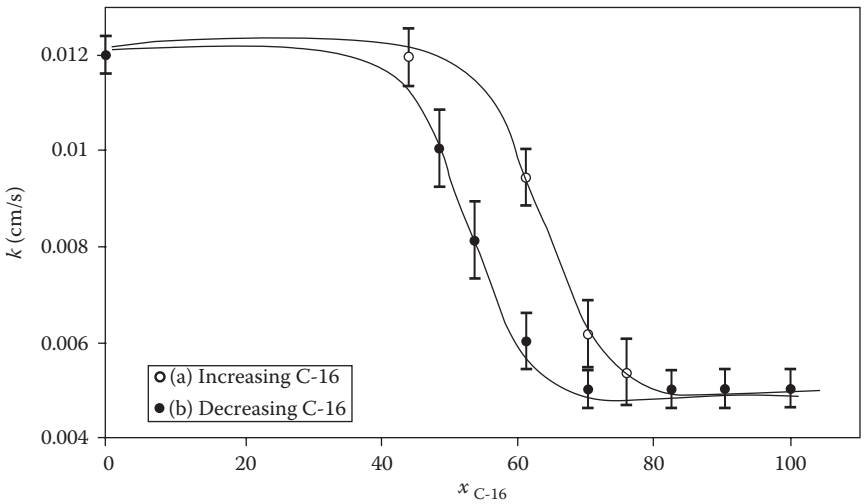


FIGURE 8.13 Variation of the rate constant of ET across mixed lipid monolayer adsorbed at the ITIES. (a) Incorporation of C-16 into preexisting monolayer of DPHC. (b) Incorporation of DPHC into preexisting monolayer of C-16. (Reprinted with permission from Delville, M.-H., Tsionsky, M., and Bard, A.J., Scanning electrochemical microscopy studies of electron-transfer through monolayers containing conjugated species at the liquid-liquid interface, *Langmuir*, 14, 2774–2779, 1998. Copyright 1998 American Chemical Society.)

mostly of pure C-16 or DPHC. The apparent k_f value depends on the nature of the domain facing the UME tip.

To prove the existence of separate domains in the mixed monolayer, the tip was scanned laterally above the interface. At a clear ITIES or the interface covered with a monolayer of a single phospholipid (either DPHC or C-16), the current fluctuations during the lateral scan did not exceed

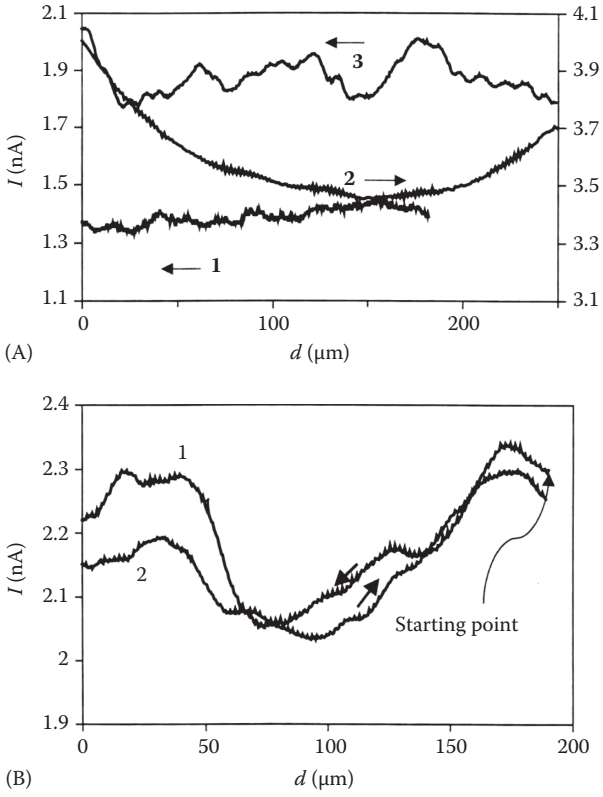


FIGURE 8.14 (A) Images of the ITIES obtained by lateral scanning of the tip UME: (1) the tip is far ($d \approx 250\,\mu m$) from the interface, (2) a clear ITIES without adsorbed lipid ($d \approx 3–5\,\mu m$), and (3) ITIES covered with mixed lipid monolayer ($d \approx 3–5\,\mu m$). The mole fractions of DPHC and C-16 in organic phase were 0.7 and 0.3, respectively. The total lipid concentration in the organic phase was 62 μM. (B) Forward (1) and backward (2) lateral scans of the tip UME above the mixed lipid monolayer adsorbed at the ITIES. Curves 1 and 2 were recorded within 2 min time interval. The composition of the monolayer was the same as for curve 3 in Figure 8.8. (Reprinted with permission from Delville, M.-H., Tsionsky, M., and Bard, A.J., Scanning electrochemical microscopy studies of electron-transfer through monolayers containing conjugated species at the liquid-liquid interface, *Langmuir*, 14, 2774–2779, 1998. Copyright 1998 American Chemical Society.)

5%–10% (Figure 8.14A, curves 1 and 2). Much stronger fluctuations of the tip current were observed at mixed lipid films (Figure 8.14A, curve 3). The lateral movement of the UME along the interface revealed the existence of 10–30 μm size domains composed of different lipids. These numbers are in a good agreement with domain sizes found from fluorescent probe microscopy of DPHC adsorbed at the air–water interface [62]. As expected, the forward and reverse lateral scans of the same portion of the interface separated by ~2 min interval showed similar current responses (Figure 8.14B). So it was concluded that only small changes in domain structure of the monolayer occur on this timescale.

Two different kinds of micrometer-sized domains were observed in monolayers of PS with 10 methylene groups when the aqueous phase contained 20 μM Ca^{2+} prior to the film formation [32]. One type of domains produced lower feedback current compared to the feedback in the absence of Ca^{2+}. The stronger blocking effect was attributed to solidification of the lipid film in the presence of Ca^{2+} ions. Another type of domains exhibited lower blocking effect as compared to Ca^{2+}-free lipid films, which was explained by clustering of pinhole defects. Stable SECM images of two types

of domains were recorded. The addition of Ca^{2+} to the aqueous phase after the formation of a PS monolayer resulted in a decreased blocking of the ET, but no domain structure was detected in such experiments.

8.2.2.5 Temperature Dependence of ET Rate across Lipid Monolayers Adsorbed at the ITIES

Lipid monolayers adsorbed at the air–water interface can undergo phase transitions at certain values of pressure and temperature [54c,56,58,63]. Different phases detected in lipid monolayer, that is, gas, liquid-flexible, liquid-extended, solid-tilted, and solid-vertical [58], have been characterized with respect to typical values of area per lipid molecule, conformation, and tilt angle of hydrocarbon chain. Such transitions may change the separation distance between aqueous and organic redox species and hence the ET rate.

The SECM has been used to measure temperature dependence of the ET rate and detect phase transitions occurring in phospholipid monolayers adsorbed on the ITIES [29]. The temperature dependencies of the ET rate between $ZnPor^+$ and $Fe(CN)_6^{4-}$ across monolayers of C-10 and C-16 are shown in Figure 8.15 for the temperature range from 5°C to 25°C. The ET rate across a C-10 monolayer slightly decreased when the temperature was changed from 25°C to 15°C (Figure 8.15, curve A). However, there was a sharp drop in k_f for the temperature decrease between 15°C and 10°C. The further decrease in the temperature had a small effect on k_f value, and the slope of the $\ln k_f - 1/T$ dependence was about the same as that for the 15°C–25°C range. The sharp decrease in the ET rate between 15°C and 10°C may have been caused by a phase transition in the C-10 monolayer. The 10°C–15°C temperature range agrees well with the results of the phase transition study by impedance technique [54c]. In comparison, no sharp decrease in k_f was observed for a monolayer of C-16 (Figure 8.15, curve B) which does not undergo phase transitions in the temperature range 5°C–25°C [53].

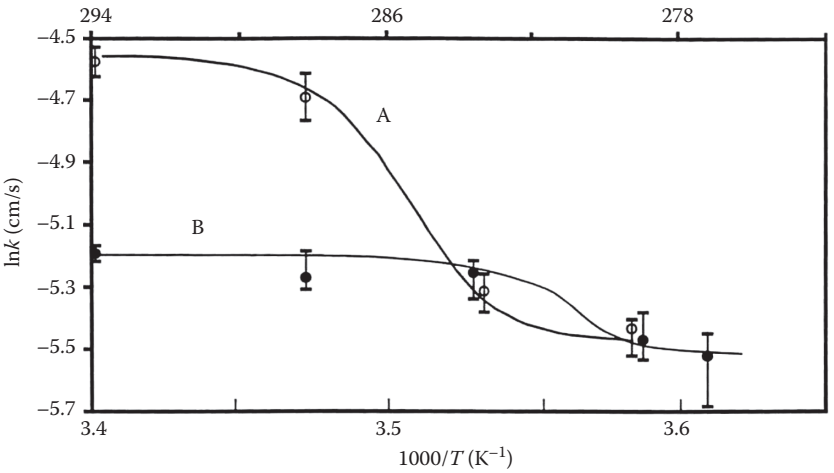


FIGURE 8.15 Temperature dependence of ET rate between $ZnPor^+$ and $Fe(CN)_6^{4-}$ across the ITIES with adsorbed monolayer of (A) C-10 and (B) C-16. The organic phase contained 0.25 M $THAClO_4$, 0.5 mM ZnPor, and 60 μM C-10 or 110 μM C-16. The water phase was 0.1 M NaCl, 0.1 M $NaClO_4$, and 7 mM $Fe(CN)_6^{4-}$. The temperature was controlled within ±0.01°C. The standard deviations were calculated using at least four different data points. (Reprinted with permission from Delville, M.-H., Tsionsky, M., and Bard, A.J., Scanning electrochemical microscopy studies of electron-transfer through monolayers containing conjugated species at the liquid-liquid interface, *Langmuir*, 14, 2774–2779, 1998. Copyright 1998 American Chemical Society.)

8.3 TRANSFER OF IONS AND NEUTRAL SPECIES

Historically, the first IT reactions studied by SECM were ion-exchange processes at ionically and electronically conductive polymer films [64]. The ions of interest were electrochemically active (e.g., $Fe(CN)_6^{3-}$ or Br^-) to enable amperometric detection at the tip. It was shown more recently that the tip process can be an IT reaction rather than ET if a micropipette electrode is used as an amperometric probe [65]. In this section, we consider two different types of IT reactions employed in SECM studies, that is, facilitated IT and simple IT.

8.3.1 Facilitated Ion Transfer

In a typical facilitated IT reaction, an ion (most often, a cation, M^+) is transferred from aqueous solution into the organic phase. A complex species formed by this ion and a ligand (L, initially present in organic phase) is easier to transfer than M^+ itself. Reactions of this type are widely used in chemical sensors (ion-selective electrodes, liquid ion-exchangers [66]). For SECM experiments, an aqueous solution of M^+ is placed inside a micropipette that serves as a tip electrode. The facilitated IT reaction at the micropipette tip is

$$M^+_{(w)} + L_{(o)} \rightarrow ML^+_{(o)} \quad \text{(at the pipette tip)} \tag{8.24}$$

With the tip biased at a sufficiently positive potential and the concentration of M^+ inside a pipette much higher than concentration of L in the outer solvent, the tip current is limited by diffusion of L to the pipette orifice. When the tip approaches the bottom (aqueous) layer, M^+ is released from the complex and transferred to the aqueous solution, and L is regenerated (Figure 8.16A):

$$ML^+_{(o)} \rightarrow M^+_{(w)} + L_{(o)} \quad \text{(at the ITIES)} \tag{8.25}$$

The ITIES formed at the pipette tip is polarizable, and the voltage applied between the micropipette and the reference electrode in organic phase provides the driving force for the facilitated IT reaction. The interface between organic (top) and water (bottom) layers can be either nonpolarizable or polarizable. In the former case, the potential drop, $\Delta^o_w\varphi$, is governed by the ratio of concentrations of the common ion (e.g., ClO_4^-) in two phases [65]. The $\Delta^o_w\varphi$ value determines the rate of reaction (8.25). The species L serves as a mediator in reactions (8.24) and (8.25), and its consumption at the tip and regeneration via a heterogeneous IT at the ITIES are mathematically equivalent to the conventional (i.e., ET-based) SECM feedback scheme. The tip current enhancement (positive feedback) is observed when reaction (8.25) is rapid, and the negative feedback occurs if L is not regenerated at the ITIES. In the first SECM study of facilitated IT at externally polarized ITIES reported by the Shao group [39], a three-electrode SECM setup was used (see Section 8.2.1.2).

Six stages of the overall process can affect the tip current, that is, (i) diffusion of M^+ inside the pipette, (ii) facilitated IT at the pipette tip, (iii) diffusion of L in organic solvent, (iv) IT at the water–organic solvent interface, (v) diffusion of M^+ in the bottom aqueous phase, and (vi) in the case of a nonpolarizable ITIES, charge compensation by transfer of supporting electrolyte between water and organic phase. In principle, any of these stages can be rate-limiting, and a careful choice of experimental conditions is essential for meaningful kinetic analysis. Typically, step (v) is fast and the charge-compensating IT (stage vi) does not affect the overall process rate because both concentrations of the common ion in organic and aqueous layers are much higher than concentration of L. The concentration of M^+ should be sufficiently high to exclude the possibility of diffusion limitations inside the pipette (stage i). The rate of the IT reaction at the pipette–solution interface can be made rapid by biasing the tip at a sufficiently positive potential. Under these conditions, only

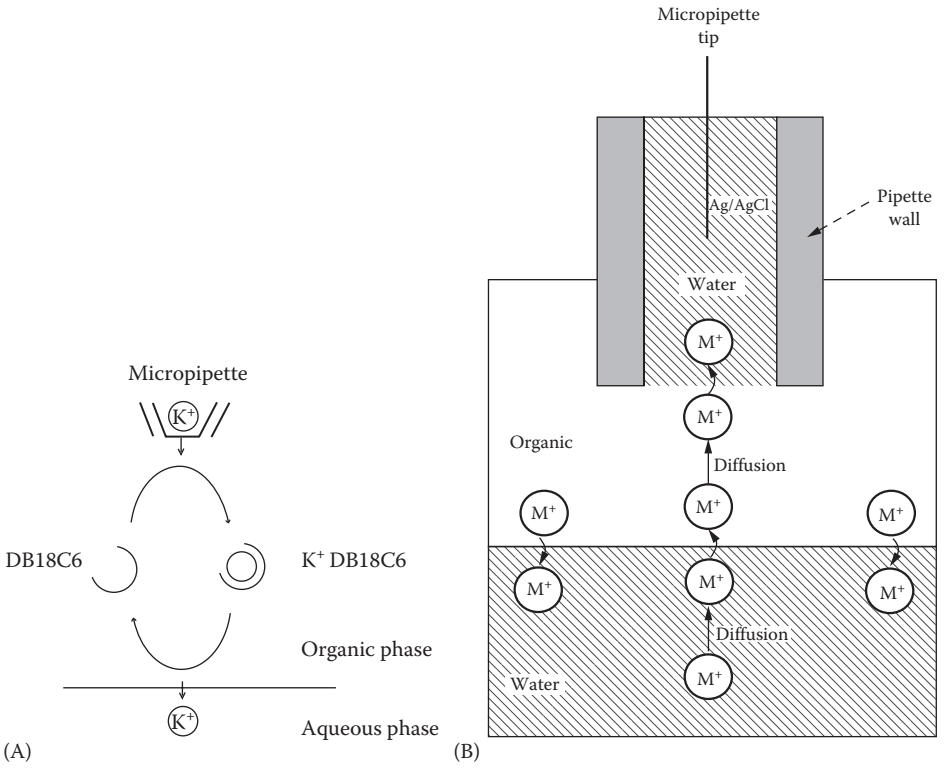


FIGURE 8.16 Schematic representation of the SECM operating in the facilitated (A) and simple (B) IT feedback mode. (A) Potassium ions are transferred from the pipette into DCE by interfacial complexation with DB18C6 (Equation 8.26) and from DCE to the bottom aqueous layer by interfacial dissociation mechanism (Equation 8.27). (Reprinted from *J. Electroanal. Chem*., 439, Shao, Y. and Mirkin, M.V., Scanning electrochemical microscopy (SECM) of facilitated ion transfer at the liquid/liquid interface, 137–143, Copyright 1997, with permission from Elsevier Science S.A.) (B) Positive feedback is due to IT from the bottom (aqueous) layer into the organic phase. Electroneutrality in the bottom layer is maintained by reverse transfer of the common ion across the ITIES beyond the close proximity of the pipette where its concentration is depleted.

diffusion of the L in organic phase and/or interfacial dissociation reaction may control the overall process rate. If Reaction (8.25) is rapid, the SECM theory for a conductive substrate is applicable; otherwise, finite IT kinetics should be observed.

The first facilitated IT process used in SECM experiments, that is, the transfer of K^+ from the aqueous solution inside the pipette to DCE assisted by dibenzo-18-crown-6 (DB18C6) [65]

$$K^+_{(w)} + DB18C6_{(DCE)} \rightarrow \left[K^+DB18C6\right]_{(DCE)} \text{ (at the pipette tip)} \tag{8.26}$$

has been extensively studied and shown to be a mechanistically simple one-step interfacial complexation reaction [1b]. With the concentration of K^+ inside a pipette at least 50 times higher than the concentration of DB18C6 in DCE, the tip current was limited by diffusion of DB18C6 to the pipette orifice. When the tip approached the bottom aqueous layer, the regeneration of DB18C6 occurred via interfacial dissociation:

$$[K^+DB18C6]_{(DCE)} \rightarrow K^+_{(w)} + DB18C6_{(DCE)} \text{ (at the ITIES)} \tag{8.27}$$

Thus, a positive feedback current was observed when the tip approached the water–DCE interface. The negative feedback was observed when the tip approached glass insulator.

Since the SECM response depends on rates of both heterogeneous reactions (8.26) and (8.27), their kinetics can be measured using methodologies developed previously for ET processes. The mass transfer rate for IT measurements by SECM is similar to that for heterogeneous ET measurements, and the standard rate constants of the order of 1 cm/s should be measurable. With relatively large pipette probes used in Ref. [65] (i.e., $a \geq 10\,\mu m$), the mass transfer coefficient was <0.01 cm/s, that is, too low to measure the standard rate constant of potassium transfer (1.3 cm/s [67]), and the SECM response was diffusion controlled. Kinetically controlled regeneration of the mediator was observed at a nonpolarizable ITIES for a slower reaction of proton transfer assisted by 1,10-phenanthroline.

In experiments at the externally polarized interface with submicrometer-sized pipette probes (200–600 nm) [39,43], SECM approach curves exhibited kinetically controlled response. At a lower driving force, the potential dependence of the IT rate constant exhibited Tafel-like behavior and followed classical Butler–Volmer kinetics. The standard rate constant and transfer coefficient values for facilitated transfer of K^+ to organic phase extracted from SECM approach curves (using the theory developed for RG = 10) recorded at different potentials were 0.7 ± 0.3 cm/s and 0.56 ± 0.08 [39], respectively. More surprising results were obtained for the transfer of Li^+ and Na^+ facilitated by DB18C6 [43]. At lower driving force, the transfer coefficient of ~0.3 was measured for the Na^+ transfer. The transfer of Li^+ was investigated over the wider range of interfacial voltages than that of Na^+, and the observed driving force dependence of the IT rate constant was parabolic. The authors attempted to explain this very unusual "inverted behavior" using Marcus theory.

The accuracy of the IT kinetic measurements performed with micropipette tips may have been affected by their small RG, that is, the ratio of the outer glass radius to the aperture radius, which is normally ≤2 [68]. In earlier SECM literature, the theory was developed for RG = 10 that is typical for metal-in-glass tips. Because of this issue, no satisfactory theoretical fit could be obtained for approach curves of facilitated potassium transfer either for the diffusion-controlled positive feedback or pure negative feedback [65]. Both conductive and insulting curves were fitted later to the theory developed for small RG values [69] (see Chapter 5). However, the SECM theory for finite substrate kinetics and small RG was developed much later [70], and to our knowledge has not yet been used in any study of IT at the ITIES.

8.3.2 Simple Ion Transfer

Simple IT reactions are numerous and of great importance for biological systems [4c]. Unlike both ET and facilitated IT processes, no mediator species is involved in a simple IT reaction. IT can be induced in two different ways: either by applying external voltage across the interface or by depleting the concentration of the common ion in one of two liquid phases near the ITIES. White and coworkers used the first approach to probe localized iontophoretic fluxes of electroactive species (e.g., Fe^{2+}) through artificial membranes and hairless mouse skin [71]. The tip scanned over the membrane surface detected the species driven through pores by applied voltage. In addition to flux profile maps, such measurements allow quantitative determination of the rates of mass transport in membrane pores. Matsue et al. [72a] probed the transfer of ions through alamethicin channels in a bilayer lipid membrane (BLM) induced by voltage applied across the membrane. The flux of electroactive ions (e.g., I^-) was monitored with a Pt UME positioned near BLM. Different permselectivity values were measured for several cations and anions. Unlike typical SECM experiments, CT in that work occurred at a large interface. Such measurements are likely to suffer from resistive and capacitive effects.

The second approach is based on using a microprobe to perturb equilibrium in one of the phases near the interfacial boundary. The transfer of electrochemically active ions and neutral molecules across the liquid–liquid interface can be studied with a metal tip positioned near the phase boundary

[73]. The interfacial flux was induced by using a disk-shaped UME to deplete the concentration of transferred species in one of two phases. The transfer processes at an air–water and hydrogel–solution interfaces can be studied similarly [73].

A rather general theory of double potential step chronoamperometry coupled with SECM (SECM/DPSC) developed for such processes in Refs. [73b,c] is applicable to both steady-state and transient conditions. The model accounts for reversibility of the transfer reaction and allows for diffusion limitations in both liquid phases. The possibility of different diffusion coefficients in two phases was also included. The steady-state situation was defined by three dimensionless parameters, that is, $K_e = c_o/c_w$ (the ratio of bulk concentrations in organic and aqueous phases), $\gamma = D_o/D_w$ (the ratio of diffusion coefficients), and $K = k_o a/D_o$ (normalized rate constant for the transfer from organic phase to water). The effects of these parameters on the shape of current–distance curves are shown in Figure 8.17. The tip current (at a given distance) increases strongly with both K and

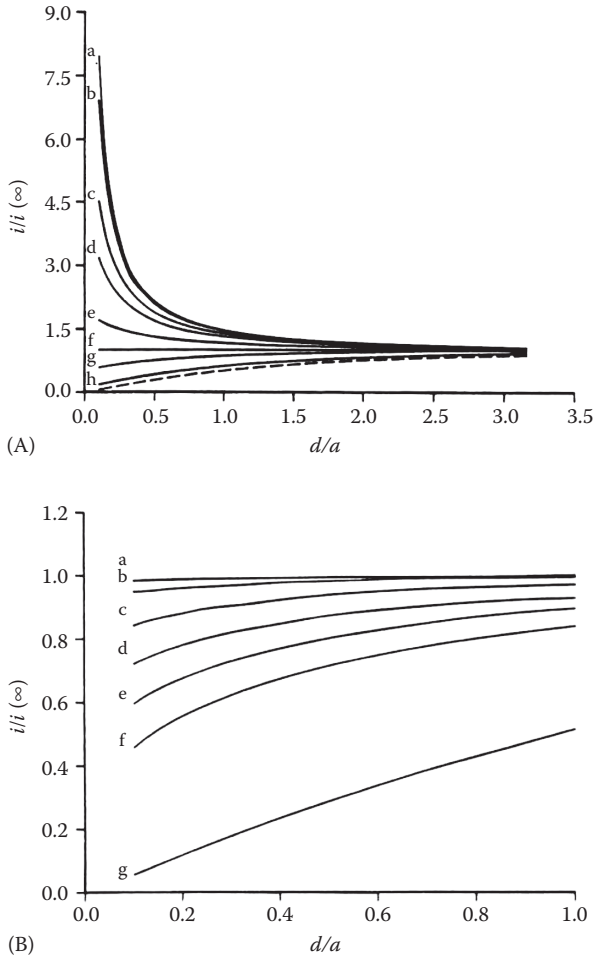


FIGURE 8.17 Simulated normalized steady-state current as a function of normalized tip–interface distance for (A) $K = 10^5$, $\gamma = 1$, and $K_e =$ (a) 1000, (b) 50, (c) 10, (d) 5, (e) 2, (f) 1, (g) 0.5, and (h) 0.1. The dashed line is the theory for the blocking interface. (B) $K_e = 1$, $\gamma = 1$, and $K =$ (a) 1000, (b) 20, (c) 5, (d) 2, (e) 1, (f) 0.5, and (g) 0.0. (Reprinted with permission from Barker, A.L., Macpherson, J.V., Slevin, C.J., and Unwin, P.R., Scanning electrochemical microscopy (SECM) as a probe of transfer processes in 2-phase systems-theory and experimental applications of SECM-induced transfer with arbitrary partition-coefficients, diffusion-coefficients, and interfacial kinetics, *J. Phys. Chem.*, 102, 1586–1598, 1998. Copyright 1998 American Chemical Society.)

γK_e values, but is largely independent of individual values of K_e and γ as long as their product is constant. The diffusion in the bottom phase significantly affects the SECM response at $\gamma K_e \lesssim 10$. While this theory provides a very general description of transfer of neutral species, in the case of IT some modifications may be necessary to include potential dependence of the rate constant and ensure electroneutrality in the bottom phase.

Interestingly, this approach allows the determination of the diffusion coefficient and concentration of species in the bottom phase with the tip positioned in the top phase. The microprobe does not have to enter or contact the second phase which may allow measurements in the media unsuitable for electrochemical experiments (e.g., very nonpolar solvents) [73c].

In a more recent article [74], Barker and Unwin extended the SECM/DPSC approach to probe the transfer of an electrogenerated species across the ITIES without restriction on the partition coefficient of the solute between the two phases. Partitioning of ferrocenium (Fc^+) ion between DCE and water was probed by this technique. A Pt tip was located in organic solution in a close proximity of the liquid–liquid interface. During the first (forward) step of the cycle, the UME was biased at potential of Fc oxidation and generated Fc^+ ions, which could cross the phase boundary. During the second (reverse) step, a negative potential was applied to the tip to collect back Fc^+. It was shown that SECM/DPSC can be used to measure both the partition coefficient and the IT rate constant; however, the rate constant of the transfer of Fc^+ across the DCE–water interface was found to be too fast to measure (>0.5 cm/s).

IT of electroactive species was also studied using a three-phase junction formed at the carbon ceramic electrode (CCE) modified by a thin layer of decamethylferrocene (DMFc) solution in 2-nitrophenyloctyl ether and immersed in the aqueous phase [75]. CCE was formed by intercalation of graphite microparticles into porous hydrophobic silica gel material [76] and impregnated with hydrophobic redox species and organic solvent. $DMFc^+$ was generated by CCE at the graphite–organic solvent interface. IT of $DMFc^+$ was detected in the substrate generation/tip collection mode by the Pt tip positioned in the aqueous phase close to CCE. This three-phase junction system is an interesting alternative to the three-electrode setup for studies of externally polarized ITIES (see Section 8.2.1.2). However, quantitative interpretation of the experimental data is difficult because the tip has to be positioned above a small patch of organic solvent on the CCE surface and to be sufficiently far from any bare graphite zone to avoid interferences.

An important advantage of the replacement of the metal tip with a micropipette in IT measurements is the possibility of probing numerous processes involving redox-inactive ionic reactants. One should also notice that a mechanistic study of interfacial transfer of reducible (or oxidizable) ions is problematic because it is hard to distinguish between the IT and ET pathways (see, e.g., [72b]). A scheme of the simple IT-based SECM process is shown in Figure 8.16B. A cation (M^+) is transferred from organic phase into the aqueous filling solution inside a pipette:

$$M^+_{(o)} \rightarrow M^+_{(w)} \quad \text{(at the pipette tip)} \tag{8.28}$$

In this case, the top and the bottom liquid phases contain the same ion at equilibrium. A micropipette tip is used to deplete the concentration of this ion in the top solvent near the ITIES. This depletion results in the IT across the ITIES:

$$M^+_{(w)} \rightarrow M^+_{(o)} \quad \text{(at the ITIES)} \tag{8.29}$$

Reaction (8.29) can produce positive feedback if the concentration of M^+ in the bottom phase is sufficiently high. Any solid surface (or a liquid phase containing no specific ion) acts as an insulator in this experiment. The interface between the top and the bottom layers is nonpolarizable, and the potential drop is determined by the ratio of concentrations of the common ion (i.e., M^+) in two phases.

Two different arrangements were used to probe the transfer of tetraethylammonium cation (TEA^+) between water and DCE [69]. Cell 1 includes a pipette filled with an aqueous solution containing supporting electrolyte (LiCl) and immersed in a DCE solution containing TEA^+:

$$\underset{\text{outer DCE solution}}{\text{Ag / AgTPB / 0.4 mM TEATPBCl + 0.01 M BTPPATPB / /}} \underset{\text{pipette}}{\text{10 mM LiCl / AgCl / Ag}} \qquad \text{(Cell 1)}$$

where

BTPPATPB is bis(triphenylphosphoranylidene)ammonium tetraphenylborate
TEATPBCl is tetraethylammonium tetrakis[4-chlorophenyl]borate)

When the pipette is biased at a sufficiently positive potential, the steady-state diffusion-limiting current is observed due to essentially spherical diffusion of TEA^+ to the pipette orifice. A family of approach curves in Figure 8.18 was obtained by moving such a pipette toward the aqueous bottom layer containing different concentrations of TEACl. With no TEA^+ in the bottom layer (curve 1), the ITIES blocks the diffusion to the pipette, and a pure negative feedback is observed. The experimental approach curve fits well the theory for an insulating substrate with RG = 1.1.

The current–distance curve obtained with equal concentrations of TEA^+ in the top and bottom phases (curve 2) is essentially flat, that is, $I_T \approx 1$ at any L. This can be expected [73c] because the diffusion coefficients of TEA^+ in water and DCE are similar and interfacial IT is quite fast. The overall process rate is limited by diffusion of TEA^+ in the bottom aqueous layer. When $c_{TEA^+,w}$ is higher than $c_{TEA^+,o}$, an increase in the I_T at closer distances is observed (curve 3). The feedback current increases with $c_{TEA^+,w}$ due to the faster diffusion in the bottom layer.

At $c_{TEA^+,w} \gtrsim 15 c_{TEA^+,o}$ diffusion in the bottom layer cannot be rate limiting, and either a pure positive feedback or finite heterogeneous kinetics should be observed [23], but the measured $I_T - L$ curve remained significantly lower than the theoretical curve for a pure positive feedback (curve 4) even at high $c_{TEA^+,w}/c_{TEA^+,o}$ ratios (e.g., $c_{TEA^+,w}/c_{TEA^+,o} = 25$ in curve 3). This finding was attributed to

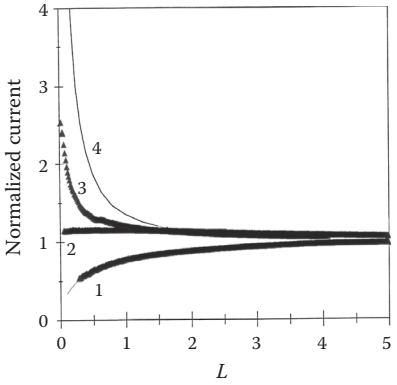


FIGURE 8.18 Current–distance curves obtained with different concentrations of TEACl in the bottom aqueous layer and constant composition of the organic phase (0.4 mM TEATPBCl + 10 mM BTPPATPB in DCE). The filling aqueous solution contained 10 mM LiCl. The concentration of TEACl in the bottom aqueous phase was (1) 0, (2) 0.4, and (3) 10 mM. Aqueous phase also contained 10 mM LiCl. Solid lines represent SECM theory for an insulating substrate (curve 1) and pure positive feedback (curve 4). The radius of the pipette orifice was (1) 18, (2) 10, and (3) 12 μm. The tip was scanned at 1 μm/s. (Reprinted with permission from Shao, Y. and Mirkin, M.V., Probing ion transfer at the liquid/liquid interface by scanning electrochemical microscopy (SECM), *J. Phys. Chem. B*, 102, 9915–9921, 1998. Copyright 1998 American Chemical Society.)

the finite rate of the interfacial IT reaction (i.e., $TEA^+_{(w)} \rightarrow TEA^+_{(o)}$), which is somewhat surprising because of a large standard rate constant (e.g., $k^\circ \geq 0.1$ cm/s [77]) measured for this reaction at a polarized ITIES. One of the possible reasons for slow kinetics is that the common ion concentration in the bottom layer affects the heterogeneous IT rate constant, k_f. The k_f was shown to follow Butler–Volmer equation (8.1):

$$k_f = k^\circ \exp\left(-\frac{\alpha F}{RT}(\Delta^o_w\varphi - \Delta^o_w\varphi^\circ)\right) \tag{8.30}$$

where

F is the Faraday constant
$\alpha \approx 0.5$ is the transfer coefficient
$\Delta^o_w\varphi^o$ is the standard potential of TEA^+ transfer

The interfacial potential drop, $\Delta^o_w\varphi$, is governed by the ratio of TEA^+ concentration in water and the organic phase [1a]:

$$\Delta^o_w\varphi = \Delta^o_w\varphi^\circ + (RT/F)\ln\left(c_{TEA^+,w}/c_{TEA^+,o}\right) \tag{8.31}$$

The combination of Equations 8.30 and 8.31 gives

$$k_f = k^\circ\left(c_{TEA^+,w}/c_{TEA^+,o}\right)^{-\alpha} \tag{8.32}$$

The decrease in the rate constant with increasing $c_{TEA^+,w}/c_{TEA^+,o}$ ratio may allow probing faster IT reactions with no complications associated with slow diffusion in the bottom phase. One should also notice that unlike previously studied ET processes at the ITIES, the rate of the reverse reaction cannot be neglected. The difference is that in the former experiments no ET equilibrium existed at the interface because only one (reduced) form of redox species was initially present in each liquid phase [15,23]. In contrast, reaction (8.29) is initially at equilibrium and has to be treated as a quasireversible process [73c]. Probing kinetics of simple IT reactions at a nonpolarizable ITIES under steady-state conditions with the pipette SECM tips should be as advantageous as analogous ET measurements [23], but the required theory has not been published to date.

The pipettes filled with an organic solvent are suitable for quantitative voltammetric measurements in aqueous media [68] (see also Section 8.3.3). Using such a pipette as an SECM tip, one can probe IT from organic phase to water and perform imaging in aqueous solutions. The $I_T - d$ curves obtained with organic-solvent-filled pipettes immersed in an aqueous solution and approaching the ITIES were similar to those in Figure 8.18 [69]. The change from the negative to positive feedback occurs with increasing concentration of TEA^+ in the bottom (organic) phase, but the pure positive feedback could not be observed, as discussed earlier.

The IT feedback mode of the SECM can also be used for imaging of solid–liquid and liquid–liquid interfaces. The topography of a solid substrate can be imaged in the same way as insulators are imaged in conventional SECM experiments. For membrane–solution and liquid–liquid interfaces, the maps of IT reactivity of the interfacial boundary can be obtained. A high stability of the pipette response is required for SECM imaging. The diffusion-limiting current at a pipette should remain practically constant during ≥10 min (an approximate time required to scan one SECM image). The response instabilities are usually caused by transfer of supporting electrolyte into the pipette, which results in precipitation and clogging of the pipette tip. It can be minimized by proper choice of both

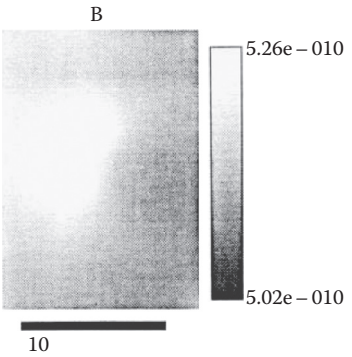


FIGURE 8.19 Constant height mode gray-scale image of a 5 μm pore in a polycarbonate membrane obtained with a 3 μm pipette tip. The filling DCE solution contained 10 mM TBATPBCl. The aqueous phase contained 0.4 mM TEACl + 10 mM LiCl. The scale bar corresponds to 10 μm. The tip scan speed was 10 μm/s. (Reprinted with permission from Shao, Y. and Mirkin, M.V., Probing ion transfer at the liquid/liquid interface by scanning electrochemical microscopy (SECM), *J. Phys. Chem. B*, 102, 9915–9921, 1998. Copyright 1998 American Chemical Society.)

aqueous and organic supporting electrolytes and by keeping the pipette potential within the potential window limits.

Figure 8.19 shows a constant height mode gray-scale image of a 5-μm pore in the 10-μm thick polycarbonate membrane obtained with a 3 μm diameter pipette tip. The fluxes of electroactive species through porous membranes have previously been imaged using generation/collection mode of the SECM operation [71]. In contrast, the feedback mode image in Figure 8.19 was obtained without any current flowing across the interface and is free from diffusion broadening; hence a significantly higher lateral resolution. Such an image represents the distribution of IT reactivity on the interfacial boundary. Filling a pipette with an organic solvent was essential for experiments with polycarbonate membranes that are soluble in organic media. The same setup can be employed to map ITs occurring at a polymer–solution interface and in living cells. A water-filled micropipette should be used as a SECM tip for imaging in organic media.

The spatial resolution of the feedback mode SECM imaging is governed by the size of the microprobe (Chapter 4) [78]. Although the earlier SECM experiments employed relatively large pipettes (i.e., 3–50 μm diameter), the nanopipette electrodes as small as 5 nm radius have been fabricated and can be used as SECM tips [67,79a]. Thus, a high-resolution image of the 1.8 μm × 1.8 μm portion of an IBM wafer was obtained recently [79b] using a 106 nm radius pipette as a tip and the transfer of TEA^+ from water to the DCE filling solution as the source of negative feedback. Another advantage of this approach is the possibility to work without redox mediator in solution. This technique should be most useful for probing IT rates in biological systems.

8.3.3 Micro- and Nanopipette Probes

Important advantages of micropipettes for electrochemical studies of the ITIES have been demonstrated by Girault's group [80]. The pipettes as small as a few nanometer radius have recently been prepared and used for voltammetric and SECM experiments [67,79a,81–83]. Such pipettes are easier to make than similarly sized metal nanoelectrodes. However, a careful surface pretreatment is necessary to ensure reproducibility of the response and avoid major deviations from the theory [68]. When a glass pipette is immersed in an organic solvent, a small amount of the filling aqueous solution flows out of the pipette and forms a submicrometer-thick layer on the hydrophilic outer wall. This makes the effective area of the ITIES much larger than geometrical area of the pipette orifice. The diffusion current to such a pipette is significantly (more than twice) higher than the theoretical

prediction based on the orifice radius [68]. This effect is equally important for any CT process at a micropipette (i.e., simple and facilitated IT, and ET) as long as its rate is controlled by diffusion of species in the external solution to the pipette orifice.

The aqueous layer can be eliminated by silanizing the outer pipette wall to render it hydrophobic. To silanize only the outer surface of the pipette, the flow of argon should be passed through the pipette from the back while its tip is immersed in a solution of trimethylchlorosilane. It is crucial to avoid silanization of the inner wall if the pipette is going to be filled with an aqueous solution; otherwise, the outer organic solvent gets drawn inside a pipette whose inner surface is hydrophobic. This procedure allows one to achieve quantitative agreement between experimental and theoretical values of diffusion current to the pipette by taking into account small thickness of the pipette wall [68] (see also Chapter 5). Experimental SECM approach curves obtained with thin-wall pipettes approaching an insulating substrate were in a good agreement with the theory for both IT [69,82] and ET [84] reactions occurring at the nanopipette-supported ITIES.

A pipette with a silanized inner wall can be filled with an organic solvent and used for measurements in aqueous solutions. The inner wall has to be silanized to prevent penetration of aqueous solution into the pipette. This can be done by holding the pipette 1–2 cm above the liquid surface of chlorotrimethylsilane for ~1 min. Silanized pipettes retain their hydrophobic properties for about 1 week after preparation. To reduce the roughness of the glass edge, a nanopipette can be polished using the protocol that was previously developed for glass-sealed metal electrodes [85]. Voltammograms, SEM images, and SECM approach curves showed that pipettes with a radius as small as <10 nm can be polished without breaking the tip or plugging the orifice with polishing material [79a]. A smoother glass surface and a more stable diffusion current produced by polishing made possible quantitative SECM experiments with very small pipette probes (e.g., 8 nm radius) and at separation $d \approx 1$ nm.

A considerable ohmic resistance of a pipette may impair kinetic measurements. When the filling solution is aqueous, the resistive potential drop in it is typically negligible even for nanopipettes [67]. For organic-solvent-filled pipettes, the resistive effect is more important. For example, the resistance of a typical 10 μm radius pipette filled with DCE and containing 0.01 M of supporting electrolyte was found to be about 10 MΩ, and it is approximately inversely proportional to the pipette radius. This corresponds to ~15 mV iR-drop when 0.5 mM TEA^+ is transferred from the outer aqueous phase into a 10 μm radius pipette. The resistive potential drop can be minimized by using higher concentrations of supporting electrolyte inside a pipette and by improving pulling programs to produce shorter (patch-type) pipettes. Fortunately, the ohmic resistance of a pipette is less important for SECM setup than for voltammetric measurements because the pipette tip is biased at a potential corresponding to the diffusion current plateau.

A novel experimental setup employing a micropipette tip was described by Walsh et al. [86]. The outer wall of a borosilicate pipette was coated with Au and insulated by applying electrophoretic paint so that only a ring of gold at the very tip of the micropipette remained exposed to external solution. Experimental approach curves to conductive and insulating substrates fitted well the theory for a ring-shaped tip. Thus, the ring could be used for the distance control and/or feedback-type measurements. Unlike aforementioned SECM/ITIES experiments, in Ref. [86] both the filling solution inside the pipette and the other liquid phase were aqueous. Moreover, no metal wire was inserted into the pipette, which, therefore, could not be biased. Redox species (ferrocene methanol [FcMeOH]) dissolved in the filling solution (but not present in the external solution) were delivered to the substrate surface by diffusion. Two SECM images were obtained by recording the substrate current produced by oxidation of FcMeOH at the 100 μm Pt disk and the tip current (due to the reduction of ferrocenium at the ring) as the pipette tip was scanned over the disk surface.

Micropipette delivery approach can be useful for probing substrate catalytic activity when the electroactive species cannot be generated electrochemically in situ. A micropipette-supported ITIES was used to deliver species of interest to the SECM substrate [87]. A neutral species (FcMeOH) partitioned from the organic phase inside the micropipette tip to the external aqueous phase. The

conductive substrate was biased at a suitable potential to oxidize FcMeOH delivered by the micropipette. This approach was successfully employed for imaging of Pt microelectrode using different neutral redox mediators. Mapping electrocatalytic activity was demonstrated for methanol oxidation of Pt–Ce and Pt–Pb substrates with different metal atomic ratios.

The reagent delivery from the micropipette was also used for surface patterning [88]. The pipette was filled with aqueous solution of silver ions and immersed into organic solution containing a macrocyclic ligand to facilitate the transfer of Ag^+ across the ITIES. The formation of well-defined Ag pattern on the Au substrate was reported. The size and structure of Ag deposits can be controlled by varying the Ag^+ flux and the tip–substrate separation distance.

8.3.4 Transfer of Neutral Species

Oxygen transfer at unmodified liquid–liquid and air–liquid interfaces and those covered with a phospholipid monolayer was studied by the Unwin group [25,26] using an inverted U-shaped microelectrode and a Langmuir trough (Figure 8.20A). Unlike earlier SECM studies [28,29], the combination of SECM with a Langmuir trough allowed precise control of the state of the lipid monolayer absorbed on either liquid–liquid or air–liquid interface. A U-shaped tip was positioned in the bottom (aqueous) phase, while the lighter organic solvent (e.g., decane) or air served as a top phase. At the air–water interface, the lipid monolayer was formed by applying a known volume of phospholipid solution in a highly volatile organic solvent, which was allowed to evaporate. To form the ITIES, a layer of organic solvent was introduced on top of a preformed lipid monolayer. Oxygen transfer across the monolayer was studied as a function of surface pressure, which was controlled using movable barriers of the Langmuir trough.

The approach curves obtained at unmodified liquid–liquid or air–liquid interface were fitted to the theory for diffusion-controlled transfer of oxygen. In the liquid-expanded state, the monolayer did not appreciably impede the oxygen flux across the interface. At surface pressures >5 mN/m, the monolayer adsorbed at the air–liquid interface became liquid condensed, that is, more compact and ordered. Significantly higher pressures were required for the formation of liquid-condensed films at the liquid–liquid interface. This was explained by the presence of organic solvent molecules in the lipid monolayer. The extrapolation of oxygen transfer rate vs. surface pressure dependencies to ~0.065 N/m pressure produced similar values at the air–liquid and liquid–liquid interfaces, indicating that at this pressure the monolayer structure is similar in both systems (Figure 8.20B). To our knowledge, the combination of SECM with a Langmuir trough has not yet been used for quantitative studies of either ET or IT across molecular monolayers adsorbed at the ITIES.

8.4 MORE COMPLICATED HETEROGENEOUS PROCESSES

8.4.1 Processes with Coupled Homogeneous Reactions

Many interesting processes occurring at the liquid–liquid interface involve coupled homogeneous chemical reactions. In principle, electrochemical methods used for probing complicated mechanisms at metal electrodes [89] can be employed at the ITIES. However, many of these techniques (e.g., rotating ring-disk electrode or fast scan cyclic voltammetry) are hard to adapt to liquid–liquid measurements. Due to technical problems, few studies of multistep processes at the ITIES have been reported to date [1,90].

The SECM/ITIES setup offers a number of ways to study complicated mechanisms which cannot be realized with a metal electrode. The ITIES can serve as a controllable source (or sink) of reagents and charges. Utilizing preferential solubilities of different species in either aqueous or organic medium, one may be able to simplify the analysis of different mechanisms by probing successive steps of a complex process independently. For example, consider a hypothetical ECE

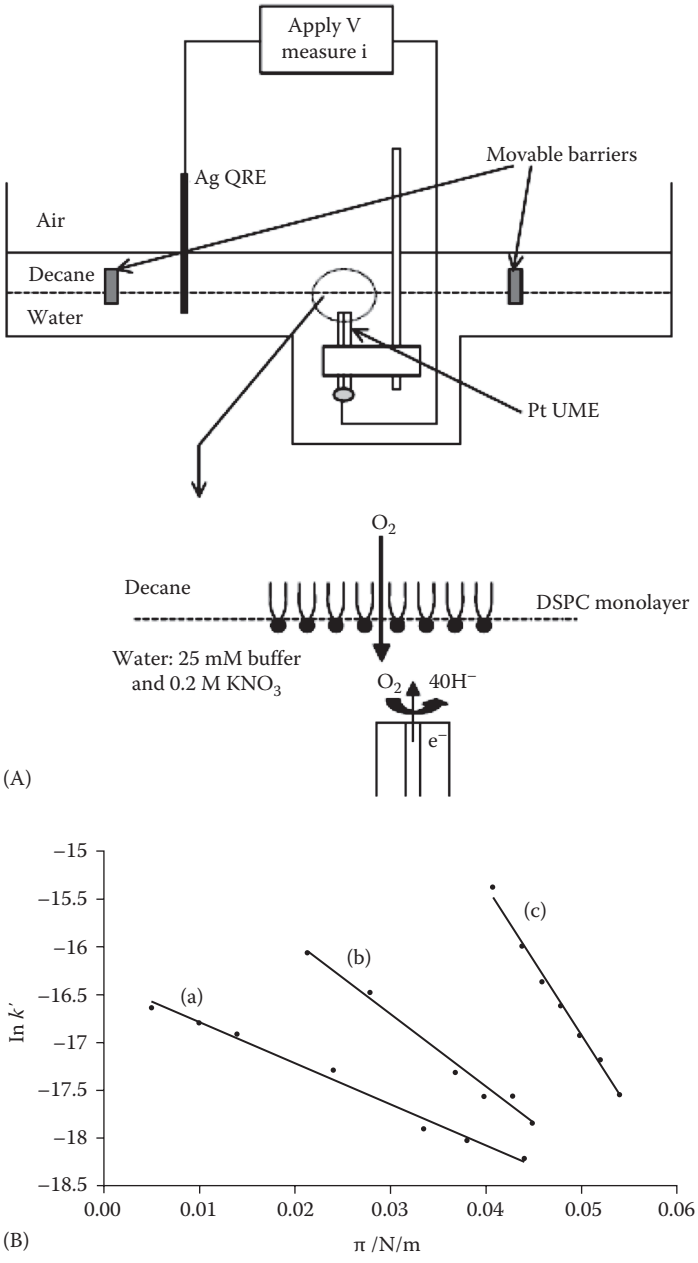


FIGURE 8.20 (A) Schematic of the SECM/Langmuir trough technique for the study of interfacial oxygen transfer. (Reprinted with permission from Zhang, J., Strutwolf, J., Cannan, S., and Unwin, P.R., Combined scanning electrochemical microscopy-Langmuir trough technique for investigating phase transfer kinetics across liquid/liquid interfaces modified by a molecular monolayer, *Electrochem. Commun.*, 5, 105–110, 2003. Copyright 2004 American Chemical Society.) (B) Plot of ln k' vs. surface pressure for the transfer of oxygen across a L-α-phosphatidylethanolamine distearoyl monolayer adsorbed at the interface between (a) air/water, (b) thin decane film/water, and (c) thick decane/water. (Reprinted with permission from Cannan, S., Zhang, J., Grunfeld, F., and Unwin, P.R., Scanning electrochemical microscopy (SECM) Studies of oxygen transfer across phospholipid monolayers under surface pressure control: Comparison of monolayers at air/water and oil/water interfaces, *Langmuir*, 20, 701–707, 2004. Copyright 2004 American Chemical Society.)

mechanism involving water-soluble species A and X, and species B confined to organic phase. Under SECM conditions, the following reactions occur:

$$A + 1e^- \rightarrow A^- \quad \text{(tip)} \tag{8.33a}$$

$$A^- + B \rightarrow X \quad \text{(ITIES)} \tag{8.33b}$$

$$X + 1e^- \rightarrow X^- \quad \text{(tip)} \tag{8.33c}$$

At a sufficiently negative tip potential, both ET reactions are diffusion controlled, and the rate of the overall process is limited by heterogeneous reaction (8.33b). Its rate constant can be determined from the current–distance curves as discussed in Section 8.2. The kinetic analysis of a more complicated ECE mechanism can be reduced to the measurement of an effective heterogeneous rate constant at the ITIES.

An SECM study of electrochemical catalysis at the ITIES was based on a similar concept [31]. The ITIES was used as a model system to study catalytic electrochemical reactions in microemulsions. Microemulsions, that is, microheterogeneous mixtures of oil, water, and surfactant, appear attractive for electrochemical synthesis and other applications [91]. The ITIES with a monolayer of adsorbed surfactant is of the same nature as the boundary between microphases in a microemulsion. The latter interface is not, however, directly accessible to electrochemical measurements. While interfacial area in a microemulsion can be uncertain, the ITIES is well-defined. A better control of the ITIES was achieved by using the SECM to study kinetics of electrochemical catalytic reduction of *trans*-1,2-dibromocyclohexane (DBCH) by Co(I)L (the Co(I) form of vitamin B_{12}):

$$\left[\text{Co(II)L} - \text{H}\right]^+ + e^- \rightarrow \text{Co(I)L} - \text{H} \quad \text{(tip)} \tag{8.34}$$

$$2\text{Co(I)L} - \text{H} + RBr_2 \rightarrow 2\left[\text{Co(II)L} - \text{H}\right]^+ + 2Br^- + \text{olefin(ITIES)} \tag{8.35}$$

Reactions (8.34) and (8.35) together represent electrochemical catalysis of the reduction of DBCH. From earlier voltammetric studies, the elementary rate-determining step was thought to be [92]

$$\text{Co(I)L} - \text{H} + RBr_2 \rightarrow \left[\text{Co(II)L} - \text{H}\right]^+ + RBr^{\cdot} + Br^- \tag{8.36}$$

Under SECM conditions, Reaction (8.35) is mathematically equivalent to kinetically controlled regeneration of the mediator at a solid substrate and can be characterized by the value of the effective heterogeneous rate constant. This greatly simplifies the analysis of the SECM current–distance curves, which can be fit to Equations 8.4 and 8.5. The dependencies of the rate of reaction (8.35) on various experimental parameters, that is, reactant concentrations, interfacial potential drop, and the presence of adsorbed surfactant, were investigated. Unlike uncomplicated ET processes discussed earlier, the overall rate of reaction (8.35) was independent of the interfacial potential drop, and the apparent second-order rate constant depended on the concentration of vitamin B_{12}. The rate of DBCH reduction was only slightly affected by adsorbed long-chain surfactants. These results suggest that bimolecular ET reaction (8.36) is not the rate-limiting step of the process, and the interfacial reaction is not fully described by a simple second-order rate law, as it was found previously. Thus, the use of SECM/ITIES technique allowed uncovering details of interfacial complexity in a reaction that may not be obvious from conventional voltammetric studies in microemulsions.

An important example of an ET process with coupled homogeneous reactions is reduction oxygen with DMFc at the water–DCE interface [93]. The substrate generation/tip collection mode of

SECM was used to monitor in situ the formation of hydrogen peroxide at a polarized water–DCE interface via proton-coupled ET. The tip current produced by H_2O_2 oxidation depended strongly on the Galvani potential drop across the ITIES.

Kanoufi et al. obtained "anomalous" approach curves for oxalate oxidation by a ruthenium(III) coordination complex at the benzonitrile–water interface [94]. This process is complicated by homogeneous chemical degradation of the Ru(III) form of the mediator species. It was described as a heterogeneous ET in competition with a first-order homogeneous reaction, and a zone diagram was constructed showing pure ET heterogeneous kinetic control, pure homogeneous kinetic control, and mixed control. The developed quantitative treatment was used to obtain interfacial ET rate constants and investigate the activation–driving force relationship. The experimental results were in a better agreement with the Marcus model assuming a 2 nm thick mixed solvent layer than with a sharp boundary model [6].

A novel approach to studying chemical reactions at the ITIES was described by Slevin and Unwin [95]. They combined the SECM operating in the potentiometric collection mode with a previously developed dropping electrolyte electrode [96]. The Ag/AgCl microelectrode tip was used to measure the concentration profile of Cl^- produced by hydrolysis of triphenylmethyl chloride (TPMCl)

$$TPMCl_{(org)} + H_2O \rightarrow TPMOH_{(org)} + Cl^-_{(aq)} \tag{8.37}$$

which occurred at the interface between the growing DCE droplet and water (Figure 8.21). The rate constant for this reaction was obtained by fitting experimental concentration profiles to the

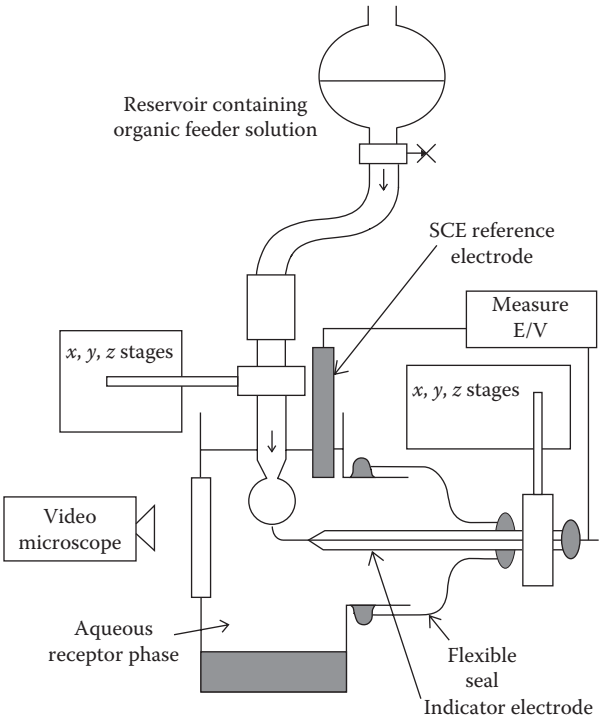


FIGURE 8.21 Schematic diagram of the SECM apparatus employed for probing interfacial reactions at the ITIES. An UME tip is used to measure the local concentration of a reactant or product in the near-interface region of an expanding droplet. (Reprinted with permission from Slevin, C.J. and Unwin, P.R., Measurement of liquid/liquid interfacial kinetics by directly probing the concentration profiles at expanding droplets, *Langmuir*, 13, 4799–4803, 1997. Copyright 1997 American Chemical Society.)

numerical solution of convective diffusion equation. The main advantage of this technique over conventional SECM setup is in a predictable flux of a reactant delivered to the continuously renewable interface. In contrast to feedback and GC modes of the SECM operation, this approach is useful when all reactants are initially present in the system rather than being generated at a tip or a substrate electrode. The precise tip/drop alignment and accuracy in distance determination are critical for quantitative applications of this method.

8.4.2 Nucleation/Growth of Metal at the ITIES

Unique properties of the ITIES, such as the defect-free phase boundary, different ways of controlling interfacial voltage drop, and confinement of redox species to separate phases, make it an interesting system for studying heterogeneous nucleation/growth. The deposition of metal on externally polarized ITIES was observed and studied by several groups [18,97]. An externally polarized liquid–liquid interface supported by the tip of a micropipette was used to study the deposition of individual silver particles [98].

Li et al. used an SECM tip to induce and monitor nucleation and growth of silver particles at the nonpolarizable water–DCE interface [99]. A Ag UME was positioned in the aqueous phase in a close proximity of the interface, and an anodic potential step was applied to it to induce the dissolution of silver. DCE phase contained DMFc, which reduced silver ions at the ITIES, and tetrabutylammonium perchlorate. The interfacial voltage was determined by concentrations of the common ion (perchlorate) in two liquid phases, thus providing controllable driving force for silver reduction by DMFc (Figure 8.22A). The formation of Ag particles at the liquid–liquid interface was confirmed by confocal microscopy (Figure 8.22B). The theory was developed to extract the rate constants for Ag particle growth at the water–DCE interface and estimate the particle density from the UME chronoamperometric response to nucleation and growth of silver particles at the ITIES. The apparent particle density increased with an increasing flux of silver ions generated at the tip. The nucleation of silver at the ITIES was found to be coupled with adsorption of Ag^+, and its rate—unlike nucleation processes at the metal–solution interface—did not depend strongly on Galvani potential drop across the phase boundary.

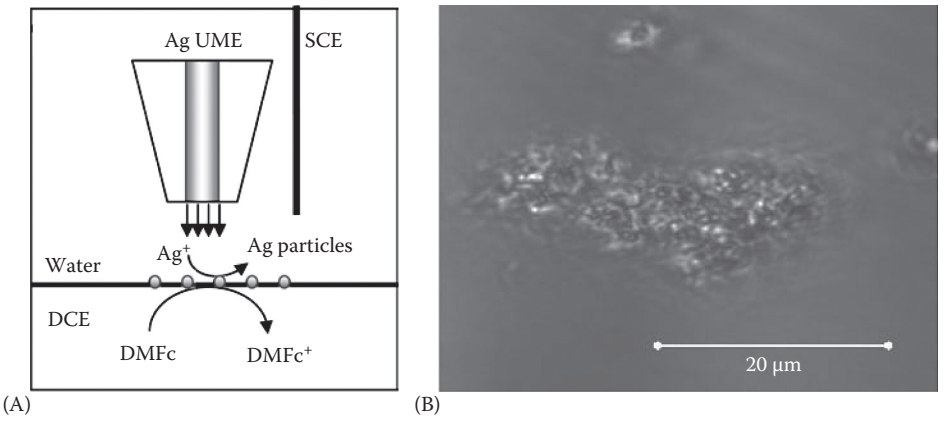


FIGURE 8.22 (A) Schematic of the SECM setup for Ag particle nucleation at the water–DCE interface and (B) transmission mode confocal micrograph of formed Ag particles. (Adapted with permission from Li, F., Edwards, M., Guo, J., and Unwin, P.R., Silver particle nucleation and growth at liquid/liquid interfaces: A scanning electrochemical microscopy approach, *J. Phys. Chem. C*, 113, 3553–3565, 2009. Copyright 2009 American Chemical Society.)

ACKNOWLEDGMENT

Michael V. Mirkin gratefully acknowledges the support by the National Science Foundation (CHE-0957313 and CHE-1026582).

REFERENCES

1. (a) Girault, H. H., Schiffrin, D. J. In *Electroanalytical Chemistry*, Vol. 15, Bard, A. J., Ed., Marcel Dekker, New York, 1989, p. 1. (b) Girault, H. H. In *Modern Aspects of Electrochemistry*, Vol. 25, Bockris, J. O'M., Conway, B. E., White, R. E., Eds., Plenum Press, New York, 1993, p. 1. (c) Samec, Z., Kakiuchi, T. In *Advances in Electrochemical Science and Electrochemical Engineering*, Vol. 4, Gerischer, H., Tobias, C. W., Eds., VCH, New York, 1995, p. 297. (d) Volkov, A. G., Deamer D. W., Eds., *Liquid–Liquid Interfaces. Theory and Methods*, CRC Press, Boca Raton, FL, 1996. (e) Benjamin, I. Chemical reactions and solvation at liquid interfaces: A microscopic perspective. *Chem. Rev*. 1996, 96, 1449–1476. (f) Liu, B., Mirkin, M. V. Electrochemistry at microscopic liquid-liquid interfaces, *Electroanalysis* 2000, 12, 1433–1446. (g) Dryfe, R. A. W. In *Advances in Chemical Physics*, Vol. 141, Wiley-Interscience, New York, 2009, p. 153. (h) Girault, H. H. In *Electroanalytical Chemistry*, Vol. 23, Bard, A. J., Zoski, C. G., Eds., CRC Press, New York, 2010, p. 1.
2. (a) Arai, K., Ohasawa, M., Kusu, F., Takamura, K. Drug ion transfer across an oil–water interface and pharmacological activity. *Bioelectrochem. Bioenerg*. 1993, 31, 65–76. (b) Lo, T. C., Baird, M. H. I., Hanson, C., Eds., *Handbook of Solvent Extraction*, John Wiley & Sons, New York, 1994. (c) Vanysek, P. Analytical applications of electrified interfaces between two immiscible solutions. *Trends Anal. Chem*. 1993, 12, 357.
3. (a) Rusling, J. F. Controlling electrochemical catalysis with surfactant microstructures. *Acc. Chem. Res*. 1991, 24, 75–81. (b) Cunnane, V. J., Murtomaki, L. In *Liquid–Liquid Interfaces. Theory and Methods*, Volkov, A. G., Deamer, D. W., Eds., CRC Press, Boca Raton, FL, 1996, p. 401. (c) Jung, Y., Marcus, R. A. On the theory of organic catalysis "on water." *J. Am. Chem. Soc*. 2007, 129, 5492–5502. (d) Su, B., Hatay, I., Trojnek, A., Samec, Z., Khoury, T., Gros, C. P., Barbe, J.-M., Daina, A., Carrupt, P.-A., Girault, H. H. Molecular electrocatalysis for oxygen reduction by cobalt porphyrins adsorbed at liquid/liquid interfaces. *J. Am. Chem. Soc*. 2010, 132, 2655–2662. (e) Crossley, S., Faria, J., Shen, M., Resasco, D. E. Solid nanoparticles that catalyze biofuel upgrade reactions at the water/oil interface. *Science* 2010, 327, 68–72.
4. (a) Girault, H. H., Schiffrin, D. J. In *Charge and Field Effects in Biosystems*, Allen, M. J., Usherwood, P. N. R., Eds., Abacus Press, Turnbridge Wells, England, 1984, p. 171. (b) Ohkouchi, T., Kakutani, T., Senda, M. Electrochemical study of the transfer of uncouplers across the organic/aqueous interface. *Bioelectrochem. Bioenerg*. 1991, 25, 71–80. (c) Gennis, R. B. *Biomembranes*, Springer, New York, 1995.
5. (a) Marcus, R. A., Sutin, N. Electron transfers in chemistry and biology. *Biochim. Biophys. Acta* 1985, 811, 265–322. (b) Barbara, P. F., Meyer, T. J., Ratner, M. A. Contemporary issues in electron transfer research. *J. Phys. Chem*. 1996, 100, 13148–13168.
6. (a) Marcus, R. A. Reorganization free energy for electron transfers at liquid–liquid and dielectric semiconductor–liquid interface. *J. Phys. Chem*. 1990, 94, 1050–1055. (b) Marcus, R. A. Theory of electron-transfer rates across liquid–liquid interfaces. *J. Phys. Chem*. 1990, 94, 4152–4155; addendum, *J. Phys. Chem*. 1990, 94, 7742. (c) Marcus, R. A. Theory of electron-transfer rates across liquid–liquid interfaces. 2. Relationships and application. *J. Phys. Chem*. 1991, 95, 2010–2013; addendum, *J. Phys. Chem*. 1995, 99, 5742.
7. Smith, B. B., Halley, J. W., Nozik, A. J. On the Marcus model of electron transfer at immiscible liquid interfaces and its application to the semiconductor/liquid interface. *Chem. Phys*. 1996, 205, 245–267.
8. (a) Geblewicz, G., Schiffrin, D. J. Electron transfer between immiscible solutions: The hexacyanoferrate–lutetium biphthalocyanine system. *J. Electroanal. Chem*. 1988, 244, 27–37. (b) Cheng, Y., Schiffrin, D. J. Electron transfer between bis(pyridine)meso-tetraphenylporphyrinato iron(II) and ruthenium(III) and the hexacyanoferrate couple at the 1,2-dichloroethane/water interface. *J. Electroanal. Chem*. 1991, 314, 153–163.
9. Schmickler, W. Electron-transfer reactions across liquid/liquid interfaces. *J. Electroanal. Chem*. 1997, 428, 123–127.
10. (a) Gurevich, Y. Y., Kharkats, Y. I. Ion transfer through a phase boundary: A stochastic approach. *J. Electroanal. Chem*. 1986, 200, 3–16. (b) Shao, Y., Girault, H. H. Kinetics of the transfer of acetylcholine

across the water+sucrose/1,2-dichloroethane interface: A comparison between ion transport and ion transfer. *J. Electroanal. Chem*. 1900, 282, 59–72.
11. Kakiuchi, T. Current–potential characteristic of ion transfer across the interface between two immiscible electrolyte solutions based on the Nernst–Planck equation. *J. Electroanal. Chem*. 1992, 322, 55–61.
12. Kontturi, K., Manzanares, J. A., Murtomaki, L., Schiffrin, D. J. Rate constant for ion transfer in inhomogeneous media at the interface of immiscible electrolytes. *J. Phys. Chem*. 1997, 101, 10801–10806.
13. (a) Eisenthal, K. B. Liquid interfaces probed by second-harmonic and sum-frequency spectroscopy. *Chem. Rev*. 1996, 96, 1343–1360. (b) Conboy, J. C., Messmer, M. C., Richmond, G. L. Investigation of surfactant conformation and order at the liquid–liquid interface by total internal reflection sum-frequency vibrational spectroscopy. *J. Phys. Chem*. 1996, 100, 7617–7622. (c) Luo, G., Malkova, S., Yoon, J., Schultz, D. G., Lin, B., Meron, M., Benjamin, I., Vanysek, P., Schlossman, M. Ion distributions near a liquid–liquid interface. *Science* 2006, 311, 216–218.
14. (a) Benjamin, I. Theory and computer simulations of solvation and chemical reactions at liquid interfaces. *Acc. Chem. Res*. 1995, 28, 233–239. (b) Benjamin, I. Mechanism and dynamics of ion transfer across a liquid–liquid interface. *Science* 1993, 261, 1559–1560. (c) Schweighofer, K. J., Benjamin, I. Electric field effects on the structure and dynamics at a liquid/liquid interface. *J. Electroanal. Chem*. 1995, 391, 1–10. (d) Wilson, M. A., Pohorille, A. Mechanism of unassisted ion transport across membrane bilayers. *J. Am. Chem. Soc*. 1996, 118, 6580–6587.
15. Wei, C., Bard, A. J., Mirkin, M. V. Scanning electrochemical microscopy. 31. Application of SECM to the study of charge transfer processes at the liquid/liquid interface. *J. Phys. Chem*. 1995, 99, 16033–16042.
16. Senda, M., Kakiuchi, T., Osakai, T. Electrochemistry at the interface between two immiscible electrolyte solutions. *Electrochim. Acta* 1991, 36, 253–262.
17. Samec, Z., Marecek, V. Charge transfer between two immiscible electrolyte solutions: Part X. Kinetics of tetraalkylammonium ion transfer across the water/nitrobenzene interface. *J. Electroanal. Chem*. 1986, 200, 17–33.
18. Guainazzi, M., Silvestry, G., Survalle, G. Electrochemical metallization at the liquid–liquid interfaces of non-miscible electrolytic solutions. *J. Chem. Soc. Chem. Commun*. 1975, 200–201.
19. (a) Kharkats, Yu. I., Volkov, A. G. Interfacial catalysis: Multielectron reactions at the liquid–liquid interface. *J. Electroanal. Chem*. 1985, 184, 435–442. (b) Kharkats, Yu. I., Ulstrup, J. The electrostatic Gibbs energy of finite-size ions near a planar boundary between two dielectric media. *J. Electroanal. Chem*. 1991, 308, 17–26.
20. Girault, H. H. Solvent reorganization energy for heterogeneous electron-transfer reactions at liquid/liquid interfaces. *J. Electroanal. Chem*. 1995, 388, 93–100.
21. (a) Senda, M. Theory of the double-layer effect on the rate of ion transfer across an oil–water interface. *Anal. Sci*. 1994, 10, 649–650. (b) Senda, M. Theory of the double-layer effect on the rate of charge transfer across an electrolyte/electrolyte interface. *Electrochim. Acta* 1995, 40, 2993–2997. (c) Katano, H., Maeda, K., Senda, M. Effect of diffuse layer on the rate of electron transfer across an electrolyte vs. electrolyte solution interface. *J. Electroanal. Chem*. 1995, 396, 391–396.
22. Andrieux, C. P., Saveant, J.-M. In *Molecular Design of Surfaces*, Murray, R. W., Ed., John Wiley & Sons, New York, 1992, pp. 207–270.
23. Tsionsky, M., Bard, A. J., Mirkin, M. V. Scanning electrochemical microscopy. 34. Potential dependence of the electron-transfer rate and film formation at the liquid/liquid interface. *J. Phys. Chem*. 1996, 100, 17881–17888.
24. Barker, A. L., Unwin, P. R., Amemiya, S., Zhou, J., Bard, A. J. Scanning electrochemistry microscopy (SECM) in the study of electron transfer kinetics at liquid/liquid interfaces: Beyond the constant composition approximation. *J. Phys. Chem. B* 1999, 103, 7260–7269.
25. Zhang, J., Strutwolf, J., Cannan, S., Unwin, P. R. Combined scanning electrochemical microscopy–Langmuir trough technique for investigating phase transfer kinetics across liquid/liquid interfaces modified by a molecular monolayer. *Electrochem. Commun*. 2003, 5, 105–110.
26. Cannan, S., Zhang, J., Grunfeld, F., Unwin, P. R. Scanning electrochemical microscopy (SECM) studies of oxygen transfer across phospholipid monolayers under surface pressure control: Comparison of monolayers at air/water and oil/water interfaces. *Langmuir* 2004, 20, 701–707.
27. Selzer, Y., Mandler, D. J. A novel-approach for studying charge-transfer across an interface of 2 immiscible solutions using the scanning electrochemical microscope (SECM). *J. Electroanal. Chem*. 1996, 409, 15–17.

28. Tsionsky, M., Bard, A. J., Mirkin, M. V. Long-range electron-transfer through a lipid monolayer at the liquid/liquid interface. *J. Am. Chem. Soc*. 1997, 119, 10785–10792.
29. Delville, M.-H., Tsionsky, M., Bard, A. J. Scanning electrochemical microscopy studies of electron-transfer through monolayers containing conjugated species at the liquid–liquid interface. *Langmuir* 1998, 14, 2774–2779.
30. Solomon, T., Bard, A. J. Reverse (Uphill) electron-transfer at the liquid/liquid interface. *J. Phys. Chem*. 1995, 99, 17487–17489.
31. Shao, Y., Mirkin, M. V., Rusling, J. F. Liquid/liquid interface as a model system for studying electrochemical catalysis in microemulsions—Reduction of trans-1,2-dibromocyclohexane with vitamin-B-12. *J. Phys. Chem. B* 1997, 101, 3202–3208.
32. Liu, B., Mirkin, M. V. Electron transfer at liquid/liquid interfaces. The effects of ionic adsorption, electrolyte concentration, and spacer length on the reaction rate. *J. Phys. Chem. B* 2002, 106, 3933–3940.
33. Lu, X., Zhang, H., Hu, L., Zhao, C., Zhang, L., Liu, X. Investigation of the effects of metalloporphyrin species containing different substitutes on electron transfer at the liquid/liquid interface. *Electrochem. Commun*. 2006, 8/6, 1027–1034.
34. Ding, Z., Quinn, B. M., Bard, A. J. Kinetics of heterogeneous electron transfer at liquid/liquid interfaces as studied by SECM. *J. Phys. Chem. B* 2001, 105, 6367–6374.
35. (a) Laforge, F. O., Kakiuchi, T., Shigematsu, F., Mirkin, M. V. Comparative study of electron transfer reactions at the ionic liquid/water and organic/water interfaces. *J. Am. Chem. Soc*. 2004, 126, 15380–15381. (b) Laforge, F. O., Kakiuchi, T., Shigematsu, F., Mirkin, M. V. SECM study of solute partitioning and electron transfer at the ionic liquid/water interface. *Langmuir* 2006, 22, 10705–10710.
36. Quinn, B. M., Liljeroth, P., Kontturi, K. Interfacial reactivity of monolayer-protected clusters studied by scanning electrochemical microscopy. *J. Amer. Chem. Soc*. 2002, 124, 12915–12921.
37. Georganopoulou, D. G., Mirkin, M. V., Murray, R. W. SECM measurement of the fast electron transfer dynamics between Au_{38}^{1+} nanoparticles and aqueous redox species at a liquid/liquid interface. *Nano Lett*. 2004, 4, 1763–1767.
38. Kwak, J., Bard, A. J. Scanning electrochemical microscopy. Theory of the feedback mode. *Anal. Chem*. 1989, 61, 1221–1227.
39. Sun, P., Zhang, Z., Gao, Z., Shao, Y. Probing fast facilitated ion transfer across an externally polarized liquid–liquid interface by scanning electrochemical microscopy. *Angew. Chem. Int. Ed*. 2002, 41, 3445–3448.
40. (a) Ulmeanu, S., Lee, H. J., Fermin, D. J., Girault, H. H., Shao, Y. Voltammetry at a liquid–liquid interface supported on a metallic electrode. *Electrochem. Commun*. 2001, 3, 219–223. (b) Gobry, V., Ulmeanu, S., Reymond, F., Bouchard, G., Carrupt, P., Testa, B., Girault, H. H. Generalization of ionic partition diagrams to lipophilic compounds and to biphasic systems with variable phase volume ratios. *J. Am. Chem. Soc*. 2001, 123, 10684–10690. (c) Zhang, Z., Yuan, Y., Sun, P., Su, J., Guo, Y., Shao, Y., Girault, H. H. Study of electron-transfer reactions across an externally polarized water/1,2-dichloroethane interface by scanning electrochemical microscopy. *J. Phys. Chem. B*, 2002, 106, 6713–6717.
41. Xie, S., Meng, X., Liang, Z., Li, B., Chen, Z., Zhu, Z., Li, M., Shao, Y. Kinetics of heterogeneous electron transfer reactions at the externally polarized water/*o*-nitrophenyl octyl ether interface. *J. Phys. Chem. C* 2008, 112, 18117–18124.
42. Zhang, Z., Yuan, Y., Sun, P., Su, B., Guo, J., Shao, Y. Study of electron-transfer reactions across an externally polarized water/1,2-dichloroethane interface by scanning electrochemical microscopy. *J. Phys. Chem. B* 2002, 106, 6713–6717.
43. Li, F., Chen, Y., Sun, P., Zhang, M., Gao, Z., Zhan, D., Shao, Y. Investigation of facilitated ion-transfer reactions at high driving force by scanning electrochemical microscopy. *J. Phys. Chem. B* 2004, 108, 3295–3302.
44. Cheng, Y., Schiffrin, D. J. A.C. impedance study of rate constants for two-phase electron-transfer reactions. *J. Chem. Soc. Faraday Trans*. 1993, 89, 199–205.
45. Kakiuchi, T. In *Liquid-Liquid Interfaces: Theory and Methods*, Volkov, A. G., Deamer, D. W., Eds., CRC Press, Boca Raton, FL, 1996, pp. 1–18.
46. (a) Kakiuchi, T., Senda, M. Structure of the electrical double layer at the interface between nitrobenzene solution of tetrabutylammonium tetraphenylborate and aqueous solution of lithium chloride. *Bull. Chem. Soc. Jpn*. 1983, 56, 1753–1760. (b) Seimiya, T., Ohki, S. Ionic structure of phospholipid membranes and binding of calcium ions. *Biochim. Biophys. Acta* 1973, 298, 546–561.
47. Sugihara, T., Kinioshita, T., Aoyagi, S., Tsujino, Y., Osakai, T. A mechanistic study of the oxidation of natural antioxidants at the oil/water interface using scanning electrochemical microscopy. *J. Electroanal. Chem*. 2008, 612, 241–246.

48. Liu, B., Mirkin, M. V. Potential-independent electron transfer rate at the liquid/liquid interface. *J. Am. Chem. Soc*. 1999, 121, 8352–8355.
49. Osakai, T., Okamoto, M., Sugihara, T., Nakatani, K. Bimolecular-reaction effect on the rate constant of electron transfer at the oil/water interface as studied by scanning electrochemical microscopy. *J. Electroanal. Chem*. 2009, 628, 27–34.
50. Zhang, J., Unwin, P. R. Investigation of the kinetics of electron transfer process involving fullerenes at liquid–liquid interfaces using scanning electrochemical microscopy: Evidence of Marcus inverted region behaviour. *J. Chem. Soc. Perkin Tran*. 2001, 2, 1608–1612.
51. Sun, P., Li, F., Chen, Y., Zhang, M., Zhang, Z., Gao, Z., Shao, Y. Observation of the Marcus inverted region of electron transfer reactions at a liquid/liquid interface. *J. Am. Chem. Soc*. 2003, 125, 9600–9601.
52. Zu, Y., Fan, F.-R, F., Bard, A. J. Inverted region electron-transfer demonstrated by electrogenerated chemiluminescence at the liquid/liquid interface. *J. Phys. Chem. B* 1999, 103, 6272–6276.
53. Cheng, Y., Schiffrin, D. J. Redox electrocatalysis by tetracyanoquinodimethane in phospholipid monolayers adsorbed at a liquid/liquid interface. *J. Chem. Soc. Faraday Trans*. 1994, 90, 2517–2523.
54. (a) Kakiuchi, T., Kondo, T., Senda, M. Divalent cation-induced phase transition of phosphatidylserine monolayer at the polarized oil–water interface and its influence on the ion-transfer processes. *Bull. Chem. Soc. Jpn*. 1990, 63, 3270–3276. (b) Kakiuchi, T., Kondo, T., Kotani, M., Senda, M. Ion permeability of dilauroylphosphatidylethanolamine monolayer at the polarized nitrobenzene/water interface. *Langmuir* 1992, 8, 169–175. (c) Kakiuchi, T., Kotani, M., Noguchi, J., Nakanishi, M., Senda, M. Phase transition and ion permeability of phosphatidylcholine monolayers at the polarized oil/water interface. *J. Colloid Interf. Sci*. 1992, 149, 279–289.
55. Cunnane, V. J., Schiffrin, D. J., Fleischman, M., Geblewicz, G., Williams, D. The kinetics of ionic transfer across adsorbed phospholipid layers. *J. Electroanal. Chem*. 1988, 243, 455–464.
56. (a) Kakiuchi, T., Yamane, M., Osakai, T., Senda, M. Monolayer formation of dilauroylphosphatidylcholine at the polarized nitrobenzene–water interface. *Bull. Chem. Soc. Jpn*. 1987, 60, 4223–4228. (b) Girault, H. H., Schiffrin, D. J. Adsorption of phosphatidylcholine and phosphatidyl-ethanolamine at the polarised water/1,2-dichloroethane interface. *J. Electroanal. Chem*. 1984, 179, 277–284.
57. Kakiuchi, T., Nakanishi, M., Senda, M. The electrocapillary curves of the phosphatidylcholine monolayer at the polarized oil–water interface. I. Measurement of interfacial tension using a computer-aided pendant-drop method. *Bull. Chem. Soc. Jpn*. 1988, 61, 1845–1851.
58. Larsson, K., Quinn, P. J. In *The Lipid Handbook*, Gunstone, F. D., Harwood, J. L., Padley, F. B., Eds., Chapman & Hall, London, U.K., 1994, pp. 401–486.
59. (a) Girault, H. H., Schiffrin, D. J. Charge effects on phospholipid monolayers in relation to cell motility. *Biochim. Biophys. Acta* 1986, 857, 251–258. (b) Wandlowski, T., Marecek, V., Samec, Z. Adsorption of phospholipids at the interface between two immiscible electrolyte solutions: Part I. Equilibrium adsorption of phosphatidylcholines at the water/nitrobenzene interface. *J. Electroanal. Chem*. 1988, 242, 277–290. (c) Kakiuchi, T., Nakanishi, M., Senda, M. The electrocapillary curves of the phosphatidylcholine monolayer at the polarized oil–water interface. II. Double layer structure of dilauroylphosphatidylcholine monolayer at the nitrobenzene–water interface. *Bull. Chem. Soc. Jpn*. 1989, 62, 403–409.
60. (a) Becka, A. N., Miller, C. J. Electrochemistry at omega-hydroxy thiol coated electrodes. 3. Voltage independence of the electron tunneling barrier and measurements of redox kinetics at large overpotentials. *J. Phys. Chem*. 1992, 96, 2657–2668. (b) Smalley, J. F., Feldberg, S. W., Chidsey, C. E. D., Linford, M. R., Newton, M. D., Liu, Y.-P. The kinetics of electron transfer through ferrocene-terminated alkanethiol monolayers on gold. *J. Phys. Chem*. 1995, 99, 13141–13149.
61. (a) Piknova, B., Marsh, D., Thompson, T. E. Fluorescence-quenching study of percolation and compartmentalization in two-phase lipid bilayers. *Biophys. J*. 1996, 71, 892–897. (b) Wu, J. R., Lentz, B. R. A method for quantitative interpretation of fluorescence detection of poly(ethylene glycol)-mediated 1-palmitoyl-2-[[[2-[4-(phenyl-trans-1,3,5-hexatrienyl) phenyl]ethyl]oxyl]carbonyl]3-*sn*-phosphatidylcholine (DPHpPC) transfer and fusion between phospholipid vesicles in the dehydrated state. *J. Floresc*. 1994, 4, 153–163. (c) Allen, M. T., Miola, L., Whitten, D. G. Host–guest interactions: A fluorescence investigation of the solubilization of diphenylpolyene solute molecules in lipid bilayers. *J. Am. Chem. Soc*. 1988, 110, 3198–3206.
62. (a) Walker, R. A., Conboy, J. C., Richmond, G. L. Molecular structure and ordering of phospholipids at a liquid–liquid interface. *Langmuir* 1997, 13, 3070–3073. (b) Mingins, J., Taylor, J. A. G., Pethica, B. A., Jackson, C. M., Yue, B. Y. T. Phospholipid monolayers at non-polar oil/water interfaces. Part 3. Effect of chain length on phase transitions in saturated di-acyl lecithins at the *n*-heptane/aqueous sodium chloride interface. *J. Chem. Soc. Faraday Trans. 1* 1982, 78, 323–329. (c) Taylor, J. A. G., Mingins, J.,

Pethica, B. A. Phospholipid monolayers at the *n*-heptane/water interface. Part 2. Dilute monolayers of saturated 1,2-diacyl-lecithins and -cephalins. *J. Chem. Soc. Faraday Trans. 1* 1976, 72, 2694–2702. (d) Yue, B. Y. T., Jackson, C. M., Taylor, J. A. G., Mingins, J., Pethica, B. A. Phospholipid monolayers at non-polar oil/water interfaces. Part 1. Phase transitions in distearoyl-lecithin films at the *n*-heptane aqueous sodium chloride interface. *J. Chem. Soc. Faraday Trans. 1* 1976, 72, 2685–2693.

63. Miller, A., Mohwald, H. Fractal growth of crystalline phospholipid domains in monomolecular layers. *Phys. Rev. Lett*. 1986, 56, 2633–2636.
64. (a) Kwak, J., Anson, F. C. Monitoring the ejection and incorporation of $Fe(CN)_6^{3-}$ and $Fe(CN)_6^{4-}$ counterions at protonated poly(4-vinylpyridine) coatings on electrodes with the scanning electrochemical microscope. *Anal. Chem*. 1992, 64, 250–256. (b) Lee, C., Anson, F. C. Use of electrochemical microscopy to examine counterion ejection from Nafion coatings on electrodes. *Anal. Chem*. 1992, 64, 528–533. (c) Denuault, G., Troise Frank, M. H., Peter, L. M. Scanning electrochemical microscopy—Potentiometric probing of ion fluxes. *Faraday Discuss*. 1992, 94, 23–35. (d) Troise Frank, M. H., Denuault, G. Scanning electrochemical microscope (SECM) study of the relationship between proton concentration and electronic charge as a function of ionic-strength during the oxidation of polyaniline. *J. Electroanal. Chem*. 1994, 379, 399–406. (e) Arca, M., Mirkin, M. V., Bard, A. J. Polymer-films on electrodes. 26. Study of ion-transport and electron-transfer at polypyrrole films by scanning electrochemical microscopy. *J. Phys. Chem*. 1995, 99, 5040–5050.
65. Shao, Y., Mirkin, M. V. Scanning electrochemical microscopy (SECM) of facilitated ion transfer at the liquid/liquid interface. *J. Electroanal. Chem*. 1997, 439, 137–143.
66. (a) Buhlmann, P., Pretch, E., Bakker, E. Carrier-based ion-selective electrodes and bulk optodes. 2. Ionophores for potentiometric and optical sensors. *Chem. Rev*. 1998, 98, 1593–1688. (b) Bradshaw, J. S., Izatt, R. M. Crown ethers: The search for selective ion ligating agents. *Acc. Chem. Res*. 1997, 30, 338–345.
67. Shao, Y., Mirkin, M. V. Fast kinetic measurements with nanometer-sized pipettes—Transfer of potassium-ion from water into dichloroethane facilitated by dibenzo-18-crown-6. *J. Am. Chem. Soc*. 1997, 119, 8103–8104.
68. Shao, Y., Mirkin, M. V. Voltammetry at micropipet electrodes. *Anal. Chem*. 1998, 70, 3155–3161.
69. Shao, Y., Mirkin, M. V. Probing ion transfer at the liquid/liquid interface by scanning electrochemical microscopy (SECM). *J. Phys. Chem. B* 1998, 102, 9915–9921.
70. Cornut, R., Lefrou, C. New analytical approximation of feedback approach curves with a microdisk SECM tip and irreversible kinetic reaction at the substrate. *J. Electroanal. Chem*. 2008, 621, 178–184.
71. (a) Scott, E. R., White, H. S., Phipps, J. B. Scanning electrochemical microscopy of a porous membrane. *J. Membr. Sci*. 1991, 58, 71–87. (b) Scott, E. R., White, H. S., Phipps, J. B. Iontophoretic transport through porous membranes using scanning electrochemical microscopy: Application to in vitro studies of ion fluxes through skin. *Anal. Chem*. 1993, 65, 1537–1545. (c) Bath, B. D., Lee, R. D., White, H. S., Scott, E. R. Imaging molecular transport in porous membranes. Observation and analysis of electroosmotic flow in individual pores using the scanning electrochemical microscope. *Anal. Chem*. 1998, 70, 1047–1058.
72. (a) Matsue, T., Shiku, H., Yamada, H., Uchida, I. Permselectivity of voltage-gated alamethicin ion-channel studied by microamperometry. *J. Phys. Chem*. 1994, 98, 11001–11003. (b) Yamada, H., Akiyama, S., Inoue, T., Koike, T., Matsue, T., Uchida, I. A microvoltammetric study of transport process through a nitrobenzene/water interface. *Chem. Lett*. 1998, 2, 147–148.
73. (a) Slevin, C. J., Umbers, J. A., Atherton, J. H., Unwin, P. R. A new approach to the measurement of transfer rates across immiscible liquid/liquid interfaces. *J. Chem. Soc. Faraday Trans*. 1996, 92, 5177–5180. (b) Slevin, C. J., Macpherson, J. V., Unwin, P. R. Measurement of local reactivity at liquid/solid, liquid/ liquid, and liquid/gas interfaces with the scanning electrochemical microscope—Principles, theory, and applications of the double potential step chronoamperometric mode. *J. Phys. Chem*. 1997, 101, 10851–10859. (c) Barker, A. L., Macpherson, J. V., Slevin, C. J., Unwin, P. R. Scanning electrochemical microscopy (SECM) as a probe of transfer processes in 2-phase systems—Theory and experimental applications of SECM-induced transfer with arbitrary partition-coefficients, diffusion-coefficients, and interfacial kinetics. *J. Phys. Chem*. 1998, 102, 1586–1598.
74. Barker, A. L., Unwin, P. R. Measurement of solute partitioning across liquid/liquid interfaces using scanning electrochemical microscopy-double potential step chronoamperometry (SECM-DPSC): Principles, theory, and application to ferrocenium ion transfer across the 1,2-dichloroethane/aqueous interface. *J. Phys. Chem. B* 2001, 105, 12019–12031.
75. Shul, G., Nogala, W., Zakorchemna, I., Niedziolka, J., Opallo, M. Scanning electrochemical microscopy study of ion transfer process across water/2-nitophenyloctylether interface supported by hydrophobic carbon ceramic electrode. *J. Solid State Electrochem*. 2008, 12, 1285–1291.

76. Tsionsky, M., Gun, G., Glezer, V., Lev, O. Sol–gel-derived ceramic-carbon composite electrodes: Introduction and scope of applications. *Anal. Chem*. 1994, 66, 1747–1753.
77. (a) Marecek, V., Lhotsky, A., Racinsky, S. Fluctuation analysis and Faradaic impedance at micro liquid/liquid interface—I. *Electrochim. Acta* 1995, 40, 2905–2908. (b) Beattie, P. D., Delay, A., Girault, H. H. Investigation of the kinetics of ion and assisted ion transfer by the technique of ac impedance of the micro-ITIES. *Electrochim. Acta* 1995, 40, 2961–2969.
78. (a) Fan, F.-R. F., Chapter 4 in this book. (b) Borgwarth, K., Ricken, C., Ebling, D. G., Heinze, J. Surface analysis by scanning electrochemical microscopy: Resolution studies and applications to polymer samples. *Fresenius J. Anal. Chem*. 1996, 356, 288–294.
79. (a) Elsamadisi, P., Wang, Y., Velmurugan, J., Mirkin, M. V. Polished nanopipets: New probes for high-resolution scanning electrochemical microscopy. *Anal. Chem*. 2011, 83, 671–673. (b) Laforge, F. O., Velmurugan, J., Wang, Y., Mirkin, M. V. Nanoscale imaging of surface topography and reactivity with the scanning electrochemical microscope (SECM). *Anal. Chem*. 2009, 81, 3143–3150.
80. (a) Taylor, G., Girault, H. H. Ion transfer reactions across a liquid–liquid interface supported on a micropipette tip. *J. Electroanal. Chem*. 1986, 208, 179–183. (b) Campell, J. A., Girault, H. H. Steady state current for ion transfer reactions at a micro liquid/liquid interface. *J. Electroanal. Chem*. 1989, 266, 465–469. (c) Campbell, J. A., Stewart, A. A., Girault, H. H. Determination of the kinetics of facilitated ion transfer reactions across the micro interface between two immiscible electrolyte solutions. *J. Chem. Soc. Faraday Trans. 1* 1989, 85, 843–853. (d) Stewart, A. A., Shao, Y., Pereira, C. M., Girault, H. H. Micropipette as a tool for the determination of the ionic species limiting the potential window at liquid/liquid interfaces. *J. Electroanal. Chem*. 1991, 305, 135–139.
81. Wei, C., Bard, A. J., Feldberg, S. W. Current rectification at quartz nanopipet electrodes. *Anal. Chem*. 1997, 119, 4627–4633.
82. Cai, C., Tong, Y., Mirkin, M. V. Probing rapid ion transfer across a nanoscopic liquid–liquid interface. *J. Phys. Chem. B* 2004, 108, 17872–17878.
83. Li, Q., Xie, S., Liang, Z., Meng, X., Liu, S., Girault, H. H., Shao, Y. Fast ion-transfer processes at nanoscopic liquid/liquid interfaces. *Angew. Chem. Int. Ed*. 2009, 48, 8010–8013.
84. Cai, C., Mirkin, M. V. Electron transfer kinetics at polarized nanoscopic liquid/liquid interfaces. *J. Am. Chem. Soc*. 2006, 128, 171–179.
85. Sun, P., Mirkin, M. V. Kinetics of electron transfer reactions at nanoelectrodes. *Anal. Chem*. 2006, 78, 6526–6534.
86. Walsh, D. A., Fernandez, J. L., Mauzeroll, J., Bard, A. J. Scanning electrochemical microscopy. 55. Fabrication and characterization of micropipet probes. *Anal. Chem*. 2005, 77, 5182–5188.
87. Lin, C. L., Rodriguez-Lopez, J., Bard, A. J. Micropipet delivery-substrate collection mode of scanning electrochemical microscopy for the imaging of electrochemical reactions and the screening of methanol oxidation electrocatalysis. *Anal. Chem*. 2009, 81, 8868–8877.
88. Turyan, I., Etienne, M., Mandler, D., Schuhmann, W. Improved resolution of local metal deposition by means of constant distance mode scanning electrochemical microscopy. *Electroanalysis* 2007, 17, 538–542.
89. Bard, A. J., Faulkner, L. R. *Electrochemical Methods*, 2nd edn., Wiley, New York, 2001, Chapter 11.
90. Kong, Y.-T., Imabayashi, S.-I., Kakiuchi, T. Electrochemical study of the SN2 reaction of 1-*p*-toluenesulfonyl-2,4-dinitronaphthalene with hydroxide ions at the nitrobenzene–water interface. *Anal. Sci*. 1998, 14, 121–126.
91. (a) Rusling, J. F. In *Electroanalytical Chemistry*, Vol. 18, Bard, A. J., Ed., Marcel Dekker, New York, 1994, p. 1. (b) Rusling, J. F. In *Modern Aspects of Electrochemistry*, Vol. 26, Bockris, J. O. M., Conway, B. E., White, R. E., Eds., Plenum Press, New York, 1994, p. 44.
92. Connors, T. F., Arena, J. V., Rusling, J. F. Electrocatalytic reduction of vicinal dibromides by vitamin B12. *J. Phys. Chem*. 1988, 92, 2810–2816.
93. Li, F., Su, B., Salazar, F. C., Nia, R. P., Girault, H. H. Detection of hydrogen peroxide produced at a liquid/liquid interface using scanning electrochemical microscopy. *Electrochem. Commun*. 2009, 11, 473–476.
94. Kanoufi, F., Cannes, C., Zu, Y., Bard, A. J. Scanning electrochemical microscopy. 43. Investigation of oxalate oxidation and ECL across the liquid–liquid interface. *J. Phys. Chem. B* 2001, 105, 8951–8962.
95. Slevin, C. J., Unwin, P. R. Measurement of liquid/liquid interfacial kinetics by directly probing the concentration profiles at expanding droplets. *Langmuir* 1997, 13, 4799–4803.
96. Koryta, J., Vanysek, P., Brezina, M. Electrolysis with an electrolyte dropping electrode. *J. Electroanal. Chem*. 1976, 67, 263–266.

97. Cheng, Y. F., Schiffrin, D. J. Electrodeposition of metallic gold clusters at the water/1,2-dichloroethane interface. *J. Chem. Soc. Farad. Trans*. 1996, 92, 3865–3871.
98. Yatziv, Y., Turyan, I., Mandler, D. A new approach to micropatterning: Application of potential-assisted ion transfer at the liquid–liquid interface for the local metal deposition. *J. Am. Chem. Soc*. 2002, 124, 5618–5619.
99. Li, F., Edwards, M., Guo, J., Unwin, P. R. Silver particle nucleation and growth at liquid/liquid interfaces: A scanning electrochemical microscopy approach. *J. Phys. Chem. C* 2009, 113, 3553–3565.

9 Imaging Molecular Transport across Membranes

Henry S. White and Frederic Kanoufi

CONTENTS

9.1 Introduction 234
9.2 Principles of Imaging Porous Membranes 236
9.2.1 Concentration Distribution above a Pore Opening 236
9.2.2 Relationship between Tip Current and Pore Transport Rate 239
9.2.3 Image Shape 240
9.2.4 Quantitative Measurement of Pore Flux and Radius 242
9.2.5 Enforced Mass Transport across Porous Membranes 243
9.2.6 Resolution Issues 244
9.2.7 Imaging Strategies 245
9.2.7.1 Tip Collection Mode 246
9.2.7.2 Reverse Imaging Mode 247
9.2.7.3 Negative Feedback Mode 247
9.2.7.4 Combined Tip Collection and Negative Feedback Mode 247
9.2.8 Tip Perturbations 248
9.3 Applications 248
9.3.1 Synthetic Membranes 248
9.3.1.1 Diffusion and Migration across Porous Mica and Polycarbonate Membranes 248
9.3.1.2 Electroosmosis across Membranes 251
9.3.1.3 Access to Transport Dynamics: Detection of Single Nanoparticle Capture 255
9.3.2 Biomaterials 256
9.3.2.1 Diffusion and Convection in Dentine and Laryngeal Cartilage 256
9.3.2.2 Iontophoresis across Skin 260
9.3.3 Imaging Transport of Non-Electroactive Species 262
9.3.3.1 Use of Potentiometric Probes 263
9.3.3.2 Selective Amperometric Probes 263
9.3.3.3 Alternating Current Impedance Imaging 265
9.3.4 Imaging Single Nanopores 267
9.3.4.1 Nanopore Images in Air 267
9.3.4.2 Nanopore Imaging in Solution 268
9.4 Future Directions 269
References 270

9.1 INTRODUCTION

Traditional models of molecular transport in porous membranes are based on measurements of spatially averaged fluxes, incorporating details of the membrane structure obtained from independent experimentation and theory.[1] While such transport models are successful in predicting the overall flux across a membrane, the microscopic features incorporated within the models are often left untested by direct measurements. In this chapter, we describe spatially resolved measurements of the transport of molecular species across porous membranes using scanning electrochemical microscopy (SECM).[2–6] Absolute values of the rate of transport of a chemical species through a *single* pore can be directly measured using SECM, and "images of the molecular flux" across a porous membrane can be obtained with submicrometer resolution. SECM provides a means to identify submicroscopic structures in the membrane that are associated with molecular transport paths and mechanisms.

In a typical application, the SECM tip is rastered at constant height across the surface of a membrane mounted in a diffusion cell (Figure 9.1). An electroactive species is dissolved in the lower (donor) compartment and is either allowed to freely diffuse across the membrane or driven across the membrane by an applied force. The SECM tip in the upper (receptor) compartment is poised at a potential such that the electroactive species is oxidized or reduced at the mass-transport-limited rate as it emerges from the pores in the membrane. The magnitude of the Faradaic current, i_t (measured as the SECM tip is rastered across the membrane surface), is proportional to the local concentration of the electroactive species. Since the concentration above the membrane surface is greater at regions where the transmembrane flux is large, the resulting SECM image directly reflects the local transport pathways in the membrane. For example, Figure 9.2 shows an image of the iontophoretic transport of $Fe(CN)_6^{4-}$ through a 1 mm^2 section of mouse skin.[7] The bright region in the SECM image corresponds to a localized region where the flux of $Fe(CN)_6^{4-}$ through the skin sample is very high. The contrast in this SECM image reflects differences in the local rate of mass transport across the membrane, rather than topographical features on the surface.

SECM has been used to investigate transport across both synthetic model porous membranes[7–10] and biological membranes.[7,9,11–16] The flux across the membrane usually results from a concentration gradient that is established by a difference in the concentration of electroactive species in the receptor and donor compartments of the diffusion cell. The flux may also be a function of an external force (electric field[10] or pressure[11,12]) applied across the membrane. The general goal of these

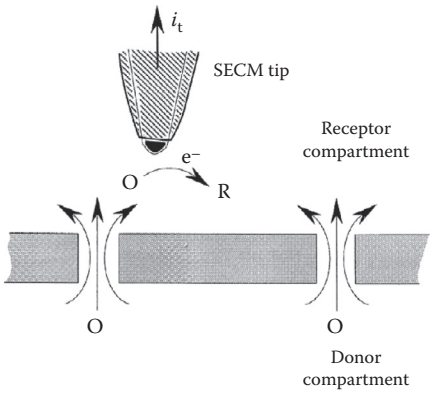


FIGURE 9.1 SECM measurement of localized molecular flux through a porous membrane. The SECM tip current, i_t, resulting from the redox reaction, $O + e^- \rightarrow R$, is largest when the tip is directly above a pore.

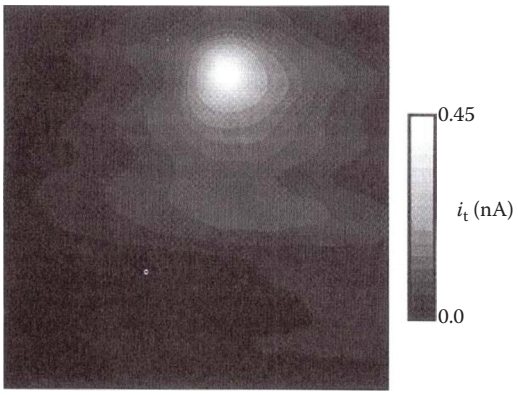


FIGURE 9.2 SECM image of $Fe(CN)_6^{4-}$ transport across a 1 mm^2 region of hairless mouse skin. Donor solution: 0.1 M $K_6Fe(CN)_6$ in 0.1 M NaCl. Receptor solution: 0.1 M NaCl. (Reprinted from Scott, E.R. et al., *Anal. Chem*., 65, 1537, 1993. With permission.)

studies is to determine the paths and mechanisms of transport *within* the membrane. However, once the molecule emerges from the membrane it is transported solely by diffusion into the bulk solution of the receptor compartment. As discussed in detail later, this simplifies the analysis of SECM data, as straightforward analytical expressions based on Fick's laws of diffusion can be used to relate the measured tip current to the local flux of molecules within the membrane. In a reverse imaging mode (RIM), one may also describe how molecules enter the pore membrane in the donor compartment.[17,18] These capabilities are key to fully characterizing transport across heterogeneous biological membranes, where the molecular flux may vary significantly as a function of spatial position.

Membrane imaging techniques based on the measurement of the local solution conductivity using scanning ion conductance microscopes (SICM) have also been reported by Burnette and Ongpipattanakul,[19] by Hansma et al.,[20] and more quantitatively by Baker group.[21] A unique advantage of SECM relative to SICM is that the individual fluxes of different chemical species in a multicomponent solution may be determined by adjusting the electrochemical potential of the SECM tip to a value where the electroactive species of interest is reduced or oxidized. Since different chemical species have different electrochemical reduction potentials, it is possible to analyze for the individual membrane fluxes of several electroactive species in the same experiment.[14] In addition, the use of selective SECM tips extends the SECM capabilities to the detection of fluxes of nonelectroactive species.[22–26]

SECM has also been used to measure transport dynamics in membranes.[10,27,28] In this application, the current at the tip is recorded as a function of time following a chemical or physical perturbation that alters the rate of transport across the membrane (e.g., a change in the electric field across the membrane and obstruction of the pore by a nanoparticle[27,28]). No other analytical technique or microscopy provides a comparable level of direct information about the pathways and dynamics of molecular transport in membranes.

Finally, these capabilities have been scaled down to the imaging of membranes with high density of nanopores thanks to the development of submicrometric probes and the combination of SECM with scanning force microscopy.

The basic principles, methodology, and theory employed in SECM imaging of porous membranes are presented in this chapter. Many of the experimental procedures (e.g., tip preparation), as well as the basic SECM instrumentation, employed in imaging porous membranes are similar to that described in Chapters 2 (*Instrumentation*) and 3 (*Tips*). The interested reader should consult these chapters or the original literature for complete details.

9.2 PRINCIPLES OF IMAGING POROUS MEMBRANES

SECM images of porous membranes represent contour maps of the concentration of a redox species in the vicinity of the membrane pore *after* it has emerged from, or, in the RIM, *before* it has entered, the membrane pore. Thus, the interpretation of SECM images requires consideration of the flux of the species away from the pore. This is a relatively straightforward problem for transport from a single pore; however, the situation becomes very complex in the case of a membrane in which the spacing between pores is small, and the diffusional fields of the pores overlap. The following sections outline the basic mathematical description of the shape of the SECM image in the receptor solution (Figure 9.1) at the exit of a single pore, and the procedure for determining the absolute value of the flux through the pore, as well as the pore radius. The RIM is briefly described in Section 9.3.1.2. The single pore model is very useful in the analysis of SECM images of real membranes.

9.2.1 Concentration Distribution above a Pore Opening

Transport within a pore can result from diffusion, migration, convection, or some combination of these mechanisms. For a relatively large (>1 μm radius) unobstructed pore, the composition of the solution within the pore is essentially identical to that of the donor/receptor solutions that are in contact with the pore; the mechanism of transport inside the pore is generally well understood in this case. In the absence of an applied field or a pressure gradient, transport of a molecule in such a pore occurs by diffusion, with the same molecular diffusivity inside the pore and in the bulk solution outside the pore. For complex biological samples, such as skin, or for membranes with very small pores (i.e., radius <10 nm), the composition of the solution inside the pores may be significantly different from that of the donor/receptor solutions, preventing, a priori, knowledge of the transport mechanism within the pore. Electroosmotic flow may also occur in pores that are permselective toward either anions or cations.[10,29–33] Fortunately, in the following theoretical description of the SECM experiment, it is only necessary to consider the flux *after* the molecules have emerged from the pore (Figure 9.1). In essence, the pore opening is treated as a source of the molecular species, without regard to the transport processes that occur within the pore. Information concerning transport phenomena occurring inside the membrane pores (e.g., electroosmotic velocity) is extracted from the SECM data once the flux in the pore has been determined (see Section 9.3).

In the following discussion, we consider an ideal situation where the flux of a molecular species is localized to a single pore; the membrane is otherwise impermeable to the molecule. Although this model is only an approximation of real samples, the resulting theory remains useful in the quantitative analysis of porous membranes, provided that the pores are not too closely spaced. The membrane separates donor and receptor solutions; the donor solution contains an electroactive molecule that is transported across the membrane and detected by the SECM tip on the receptor side of the membrane (Figure 9.1).

In the presence of an excess concentration of supporting electrolyte in the receptor compartment, and in the absence of convective flow, the flux of the species away from the opening of a small pore is dominated by radial diffusion. Assuming, for simplicity, that the pore opening is hemispherical with radius r_o, the rate of transport from the pore opening, Ω (mol/s), can be readily obtained from the solution of the continuity equation, $\nabla^2 C(r) = 0$, where $C(r)$ is the concentration at radial distance, r, measured from the center of the pore opening. Using Fick's law and employing the appropriate boundary conditions for the experiment ($C(r) = 0$ as $r \to \infty$ and $C(r) = C_s$ at $r = r_o$) yield[1,34,35]

$$\Omega = 2\pi D C_s r_o \tag{9.1}$$

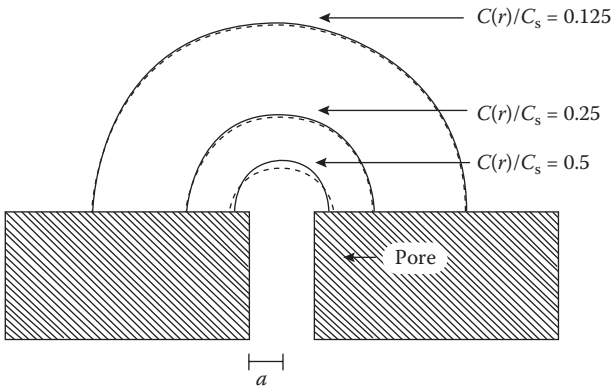


FIGURE 9.3 Steady-state isoconcentration contours projected in the x–z plane corresponding to semi-infinite diffusion from hemispherical (solid lines) and disk-shaped (dashed lines) pore openings. Contours are plotted for $C_s/2$, $C_s/4$, and $C_s/8$, where C_s is the concentration at the surface of the pore. The disk-shaped pore drawn in the figure has a radius a; the radius of the corresponding hemispherical pore opening (not shown), r_o, is equal to $2a/\pi$.

where

D is the diffusion coefficient for the electroactive species *after* it has entered the receptor compartment

C_s is the concentration of the molecule at the surface of the pore opening

The concentration profile above the pore opening, $C(r)$, is given by the following:

$$C(r) = \left(\frac{r_o}{r}\right) C_s \tag{9.2}$$

Figure 9.3 shows several isoconcentration contours (solid curves) surrounding a hemispherical-shaped pore opening.

Pore openings on real membrane surfaces rarely have a hemispherical shape but rather present disk-shaped or a flat, irregular opening. However, the flux of molecules from a microscopic pore diverges rapidly in a radial pattern, resulting in approximately hemispherical-shaped isoconcentration contours. The rate of mass transport and concentration distribution associated with a disk-shaped pore of radius a are given by[34,36]

$$\Omega = 4DC_s a \tag{9.3}$$

and

$$C(r,z) = \frac{2C_s}{\pi} \tan^{-1} \frac{a\sqrt{2}}{\left((r^2 + z^2 - a^2) + \left((r^2 + z^2 - a^2) + 4z^2a^2\right)^{1/2}\right)^{1/2}} \tag{9.4}$$

Here r and z are the radial and axial coordinates, respectively, in the two-dimensional cylindrical coordinate system. Comparison of (9.1) and (9.3) shows that the rate of mass transport from a disk is equivalent to that of a hemisphere with an effective radius, r_{eff}, given by

$$r_{\text{eff}} = \frac{2a}{\pi} \tag{9.5}$$

Theoretical isoconcentration contours corresponding to a disk-shaped pore opening (Equation 9.4) are plotted in Figure 9.3 (dashed lines) for comparison with contour lines corresponding to a hemispherical pore opening. While the two-dimensional projections of the contours for the hemispherical pore are perfect semicircles, the contours resulting from diffusion from a disk-shaped source are flattened in the center because of planar diffusion. This is most evident in the contour for $C(r)/C_s = 0.5$. However, at larger distances, for example, $5a$, the contours for the disk and hemispherical geometry are indistinguishable.

The isoconcentration contours above a pore can be experimentally evaluated by SECM.[7] In this experiment, an electroactive molecule placed in the donor solution is allowed to freely diffuse across the membrane. The concentration of the permeant emerging into the receptor solution is measured throughout the solution volume adjacent to the pore opening. Concentration is determined by measuring the voltammetric limiting current, i_t, at the SECM tip that corresponds to the oxidation or reduction of the redox molecule. Assuming a hemispherical tip geometry, the relationship between i_t and $C(r)$ is given by[35]

$$i_t = 2\pi nFDC(r)r_t \tag{9.6}$$

where

r_t is the SECM tip radius
F is the Faraday
n is the number of electrons transferred per molecule

Once $C(r)$ is determined in the volume above the pore, isoconcentration contours (e.g., a semicircular line) above the opening are constructed by choosing an arbitrary value of $C(r)$ and finding the locus of points above the pore opening that corresponds to that value. The radius of this semicircular line can be determined by fitting the resulting isoconcentration contour to the equation of a semicircle.

Figure 9.4A shows isoconcentration contours around a single 7 μm radius track-etched pore in mica, measured during the diffusional transport of $Fe(CN)_6^{3-}$ through the pore.[7] Best fit semicircular isocontour lines are plotted for comparison assuming a hemispherical pore opening (Equation 9.2). The isoconcentration contours are nearly semicircular in shape, except at distances close to the electrode surface where planar diffusion becomes significant. These results demonstrate that the radial divergence of the diffusive flux from a microscopic pore, regardless of its real shape, results in the pore appearing as if it were hemispherical in shape. The opening of the track-etched pore, in fact, is neither hemispherical nor disk shaped; instead, its cross section has a rhomboidal shape (Figure 9.4B).[8] The true shape of the pore could be revealed by scanning the tip at distances from the membrane smaller than the pore size.

As a side note, the aforementioned procedure for determining the isoconcentration contours also provides the steady-state rate of mass transfer through the pore, Ω. From mass continuity $rC(r) = r_oC_s$ (see Equation 9.2), the measurement of r and $C(r)$ for any arbitrary isoconcentration contour is then equivalent to determining the value of the product r_oC_s. In turn, substituted into Equation 9.1 one obtains Ω. Similarly, for a disk-shaped opening, $rC(r) = r_{\text{eff}}C_s = (2a/\pi)C_s$; Ω is then obtained from aC_s and Equation 9.3. Although relatively precise and accurate values of Ω can be determined by this method,[7] the sampling of $C(r)$ in the solution volume above the pore is time consuming. A more rapid method for measuring Ω is described in Section 9.2.4.

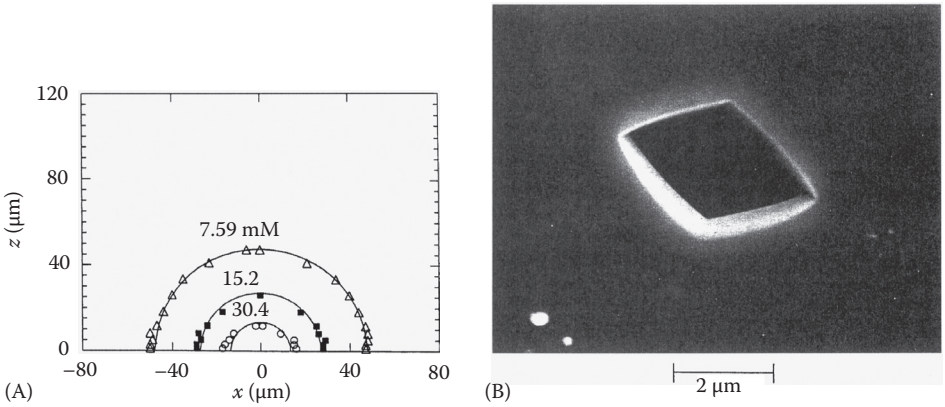


FIGURE 9.4 (A) $Fe(CN)_6^{3-}$ isoconcentration contours above a $7 \pm 1\,\mu m$ radius pore in a $10\,\mu m$ thick mica membrane. (Reprinted from Scott, E.R. et al., *Anal. Chem*., 65, 1537, 1993.) Concentrations corresponding to each contour are shown in the figure. Donor solution: 0.1 M $K_3Fe(CN)_6$ in 10 mM NaCl; receptor solution: 10 mM NaCl. (B) Scanning electron micrograph of a typical pore in the mica membrane. (Reprinted from Scott, E.R. et al., *J. Membr. Sci*., 58, 71, 1991.) Although the pore opening has a rhomboid-shaped opening, the isoconcentration contours are hemispherical, a result of radial diffusion away from the pore.

9.2.2 Relationship between Tip Current and Pore Transport Rate

The current measured at the SECM tip, when the tip is positioned above the pore opening, is proportional to the rate of transport of the redox molecule inside the pore. Transport of the molecule from the opening of a disk-shaped pore into the bulk solution occurs by diffusion and is given by Equation 9.3. When the tip is positioned directly at the surface of the pore opening ($z=0$), the tip current, $i_t(z=0)$, is proportional to the concentration at the surface of the pore opening, C_s, and Equation 9.6 is rewritten as

$$i_t(z = 0) = 2\pi nFDC_s r_t \tag{9.7}$$

Combining Equations 9.3 and 9.7 yields a proportional relationship between the SECM tip current, $i_t(z=0)$, and the transport rate, whatever its mechanism, within the pore, Ω[10]:

$$i_t(z = 0) = \left(\frac{\pi nFr_t}{2a}\right)\Omega \tag{9.8}$$

At steady state, mass continuity requires that the rate of transport from the pore into the receptor compartment be equal to the rate of transport within the pore, N (mol/cm^2·s), obtained by dividing Ω by the cross-sectional area of the pore. *Thus, $i_t(z=0)$ is proportional to the flux at any point within the pore, independent of whether the flux is due to diffusion, migration, or convection*. Hence, the tip current at any arbitrary separation distance, z, is also proportional to the flux in the pore.

In principle, Equation 9.8 can be used to compute Ω in a single pore if the pore radius, a, is known. Implicitly in Equation 9.8, the tip does not interfere with the molecular diffusion from the pore. This is a reasonable approximation when the tip radius is very small compared with the pore radius, that is, $r_t \ll a$. However, in many experiments, r_t is comparable to or even larger than a, and the tip cannot be treated as a noninterfering probe when it is placed directly at the pore opening. Thus, Equation 9.8 is useful only as an approximate relationship between the tip current and Ω. Furthermore, the radius of the pore, a, may not be known a priori in real samples. A quantitative method of analysis that circumvents both of these problems is presented in Section 9.2.4. Regardless

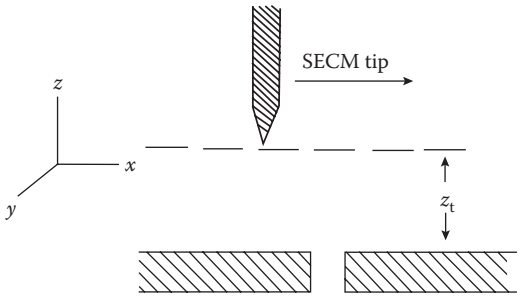


FIGURE 9.5 Schematic diagram showing the SECM tip scanned in the x–y plane at constant membrane-to-tip separation, z_t.

of tip interference effects, the key result here is that the magnitude of the SECM tip current is proportional to the molecular flux in the pore.

9.2.3 Image Shape

It is relatively straightforward to compute the shape of the SECM image that corresponds to the transport of a molecule from an individual pore. Consider a typical experiment in which the SECM tip is rastered in the x–y plane across a flat membrane at a constant height, z_t. A schematic of this experiment with the coordinate system is shown in Figure 9.5. The current measured at the SECM tip is proportional to the concentration of the electroactive species at tip position (x, y, z); thus, computing the shape of the image requires knowledge of how the concentration varies as the tip is moved in either the x- or y-direction (while keeping z at z_t). The concentration distribution above a pore with hemispherical opening is given by Equation 9.2, which is expressed, for convenience, in Cartesian coordinates as

$$C(x, y, z) = \frac{C_s r_0}{(x^2 + y^2 + z^2)^{1/2}} \tag{9.9}$$

Since the SECM tip current is proportional to $C(x, y, z)$, a plot of Equation 9.9 with $z = z_t$ is equivalent to the shape of an SECM image in which the tip current is plotted as a function of (x, y). Figure 9.6 shows examples of theoretical $C(x, y, z)$ curves (normalized to C_s) for different tip-to-substrate distances, z_t. The curves are obtained by setting $y = 0$ and allowing x to vary, corresponding to a scan across the middle of the pore at height z_t. The SECM image reaches a maximum directly above the pore opening.

Similarly, for a disk-shaped pore, Equation 9.4 describes the two-dimensional concentration distribution above the pore. Using $r = (x^2 + y^2)^{1/2}$, the image of $C(x, y, z)/C_s$ is readily computed for the constant height experiment and compared with a hemispherical pore opening (Figure 9.6). In calculating $C(x, y, z)/C_s$, Equation 9.5 is used to scale the radius of the disk-shaped pore opening to that of a hemispherical opening so that the rate of mass transport is identical in both cases. The curves in Figure 9.6 demonstrate that the SECM images of disk and hemispherical openings are indistinguishable when the tip is scanned at a distance greater than a few pore radii from the surface. A significant difference in the concentration profiles can be resolved only at very small separations.

Experimental confirmation of this Lorentzian shape of the SECM image is shown in Figure 9.7 for experiments involving the diffusive transport of $Fe(CN)_6^{4-}$ through a small pore in mica.[8] Figure 9.4 shows a comparison of the experimental i_t profile (points) with the profile (solid line) calculated from Equation 9.9. The tip-to-substrate separation, z_t, in this experiment is ca. 9.0 μm. It is

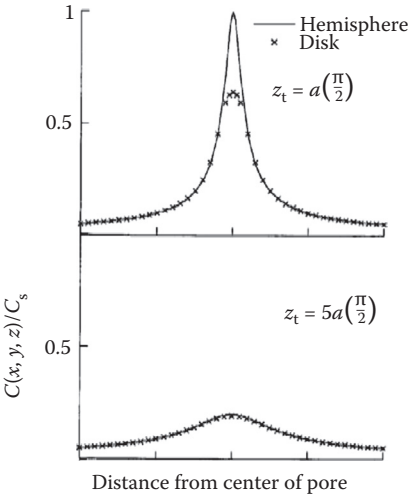


FIGURE 9.6 Normalized concentration above a pore at constant membrane-to-tip separations, z_t. Values of z_t (in units of pore radius, a) are indicated in the figure. Solid lines correspond to a hemispherical pore opening; crosses (x) correspond to a disk-shaped pore opening.

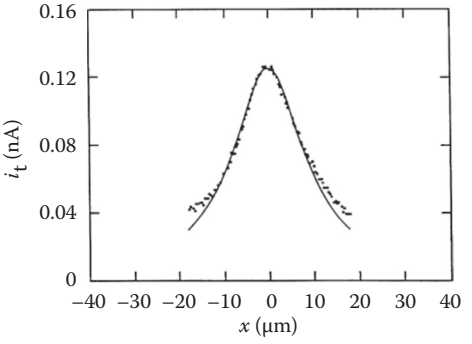


FIGURE 9.7 Plot of experimental SECM tip current (points) measured above a track-etched pore in mica. The solid line corresponds to Equation 9.9 with $z_t = 9\,\mu m$, after converting $C(x, y, z)$ to tip current, i_t, using Equation 9.6. The image corresponds to the diffusion of $Fe(CN)_6^{4-}$ through the membrane. (Reprinted from Scott, E.R. et al., *J. Membr. Sci*., 58, 71, 1991. With permission.)

clear from these results that the theoretical expression and experimental data are in good agreement within ±10 μm of the center of the pore. At greater lateral distances, the theory underestimates the experimental values. This is probably due to a slight overlap of diffusion fields from neighboring pores and the noncircular shape of the pore opening (Figure 9.4B). However, the agreement between theory and experiment is very good, validating the assumption of diffusional transport away from the pore opening.

From inspection of Figure 9.6 and Equation 9.9, it is clearly advantageous to scan the SECM tip as close as possible to the membrane surface (i.e., small z_t) to optimize both resolution and sensitivity. Indeed, first, for a scan across the center of a hemispherical pore opening, the SECM tip current is proportional to $(z_t^2 + x^2)^{-1/2}$. Thus, the lower limit of detection of species emerging from the pore increases as z_t decreases. Second, Equation 9.9 and Figure 9.6 show that the SECM peak width above a pore decreases with decreasing z_t—the peak width at half of the maximum current is equal to $z_t\sqrt{12}$.

9.2.4 Quantitative Measurement of Pore Flux and Radius

In addition to providing images of localized transport, SECM measurements provide sufficient information to quantify the absolute flux of a molecular permeant through an individual pore, a particularly important parameter in characterizing transport across membranes. As discussed in Section 9.2.1, one method of doing this is based on mapping the isoconcentration contours to obtain the product of the pore radius and surface concentration, $r_o C_s$ or aC_s. A considerably simpler and faster method is described here.

Diffusive transport of a species from a disk-shaped pore into the receptor solution yields a concentration profile given by Equation 9.4. As shown in Figure 9.8, the distribution profile is uniquely determined by two parameters: the surface concentration, C_s, and the pore radius, a. These parameters are also the two unknowns in Equation 9.3 that are required to compute the rate of mass transport through the pore.

To evaluate C_s and a, the SECM tip current can be measured as a function of r and z and used to establish the concentration profile $C(r, z)$ near the pore opening. The analysis is greatly simplified by measuring only the concentration profile along the hypothetical centerline axis of the pore that extends away from the pore surface into the receptor compartment.[10] In the cylindrical coordinate system, this axis corresponds to $r=0$. From Equation 9.4, the concentration profile along this axis is given by the following equation:

$$C(z) = \frac{2C_s}{\pi} \tan^{-1}\left(\frac{a}{z}\right) \tag{9.10}$$

Equation 9.10 computed in Figure 9.8, indicates that $C(z)$ is also uniquely determined by C_s and a. Values of these parameters are obtained by fitting Equation 9.10 to the experimental $C(z)$ profiles (see Section 9.3.1.2). Once C_s and a are determined, they are used in Equation 9.3 to compute Ω.

It can be shown straightforwardly from Equation 9.10 that the $C(z)$ profile is sensitive to a for values less than ~200 μm. For values of a greater than ~200 μm, the concentration profiles approach the expected profile for diffusion from a planar surface. In this limiting case, $C(z)$ is independent of a, and the analysis is no longer useful.

The aforementioned method of determining Ω has proved very successful in analyzing transport through both synthetic and biological membranes and is illustrated in different examples in Section 9.3.

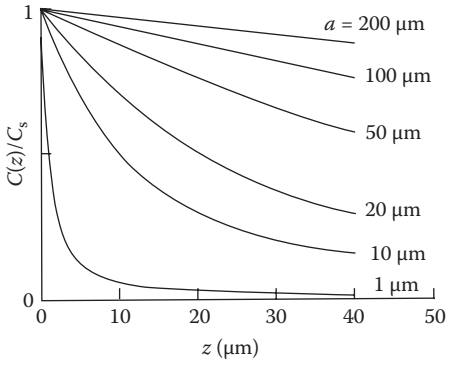


FIGURE 9.8 Theoretical normalized concentration profiles above a disk-shaped pore opening as a function of the pore radius (Equation 9.10). C_s is the concentration at the pore surface.

9.2.5 Enforced Mass Transport across Porous Membranes

In order to optimize image resolution, it is sometimes useful to enhance the mass transport of the solute across the pores. This can be achieved by application of a pressure or of an electric field across the porous membrane. When an electric field or equivalently an iontophoretic current, i_{app}, is applied between the donor and receptor compartments, the transport of a species may occur by diffusion and electroosmotic flow (and migration if the species is charged). In the most general situation of chemical systems involving such enforced mass transport, the flux, $N(z)$, of a charged permeant, of charge z' and local concentration C_p at position z, is described by the Nernst–Planck equation (9.11) that accounts, respectively, for concentration gradient, convective flow, and electric field (or migration):

$$N(z) = -D_p \nabla C_p(z) + C_p(z)v - \frac{z'F}{RT} D_p C_p(z) \nabla \phi \tag{9.11}$$

where the convective transport term is associated with a solution velocity v and ϕ is the electric potential at the position z. The effective solvent flow may originate from a pressure gradient, electroosmosis (for charged pores), etc., and is illustrated in different examples in Section 9.3. In the case of convective transport generated by the application of an iontophoretic current, i_{app}, across the membrane, the value of the electroosmotic velocity v_{eo} depends on both i_{app} and the ion-selective properties of the pore interior. The resolution of the pore transport problem has been presented and used in these different contexts. In the most general case, assuming a constant potential gradient in the pore ($\nabla\phi = cst = \Delta\phi/l$ with l the pore length), the substitution of the flux $N(z)$ (Equation 9.11) into the mass conservation law ($\nabla.N(z) = 0$), and integration over the length of the pore, yield the steady-state flux between the donor and receptor compartments that takes into account all the transport contributions[33]

$$N = \kappa(\mathrm{Pe} - Q)\frac{D_p}{l}\frac{C_s^D - C_s^R \exp(Q - \mathrm{Pe})}{1 - \exp(Q - \mathrm{Pe})} \tag{9.12}$$

where

- κ is the equilibrium coefficient describing the partitioning of the redox molecule between the pore interior and the aqueous solutions (e.g., when the pore is filled by Nafion)
- Q is the dimensionless parameter describing the solute migration ($Q = z'F\Delta\phi/RT$)
- Pe is the Peclet number characterizing the convective flow ($\mathrm{Pe} = vl/D_p$)
- C_s^D and C_s^R represent the concentrations of the solute at the pore exit in the donor and receptor solutions, respectively

Equation 9.12 relates the pore flux, N, to the different transport modes of the solute within the pore. For electric-field-driven transport, it also represents the relationship between the SECM tip current i_t and the iontophoretic current i_{app}, since the SECM tip current is proportional to the flux inside the pore ($i_t \propto N$), and since $\mathrm{Pe}(v_{eo})$ and Q depend on i_{app}. Thus, a quantitative analysis of the contribution of the different transport modes is made by examining the dependence of i_t on i_{app}.

1. As i_{app} and thus $\mathrm{Pe}(v_{eo})$ and $Q(\Delta\phi)$ approach 0, $N_{diff} = \kappa(D_p C_s^D/l)$

This limit is simply the diffusion-limited flux of the permeant.
At large i_{app}, the flux N depends on the sign of $Q - \mathrm{Pe}$, and the effective mobility of the solute.

2. $N \to \kappa(D_p C_s^D/l)(\mathrm{Pe} - Q)$ in the limit $Q - \mathrm{Pe} \to -\infty$

In this limit, the flux of the redox-active solute molecule from the donor compartment to the receptor compartment is due entirely to the electroosmotic (convection) and the electrophoretic (migration) contributions. Thus, i_t should increase linearly with i_{app}.

3. $N \rightarrow 0$ in the limit $Q - \mathrm{Pe} \rightarrow +\infty$

In this limit, convective flow and migration from the receptor to the donor compartment oppose diffusion, driving the net flux of solute molecules to zero. One expects i_t to approach zero as i_{app} is made increasingly more negative.

9.2.6 Resolution Issues

The analysis presented in the preceding sections is based on the model of a single pore in an otherwise impermeable membrane. Of course, real membranes deviate in one or more ways from this highly idealized model.

Figure 9.9 shows isoconcentration contours above the surfaces of three membranes, each having slightly different structural or transport characteristics. Membrane I contains two pores in an otherwise impermeable phase. The spacing between the two pores is large compared with the pore radii, resulting in little overlap between the concentration profiles. In this case, the pores can be analyzed separately using the analysis presented earlier for a single ideal pore. Widely spaced track-etched pores in mica are representative of this limiting case.

Membrane II depicts a membrane that contains many closely spaced pores, such that overlap occurs between the diffusional fields of each pore. Far away from the pore openings, the isoconcentration contours no longer have a hemispherical shape, because of overlapping fluxes from neighboring pores. This case is frequently encountered in real membranes, including examples discussed later in Section 9.3. Clearly, the ability to resolve individual pores depends on how close the tip is positioned above the surface, and the size of the tip. If the SECM tip radius, r_t, is significantly smaller than the spacing between two pores and is positioned at a tip-to-membrane distance smaller

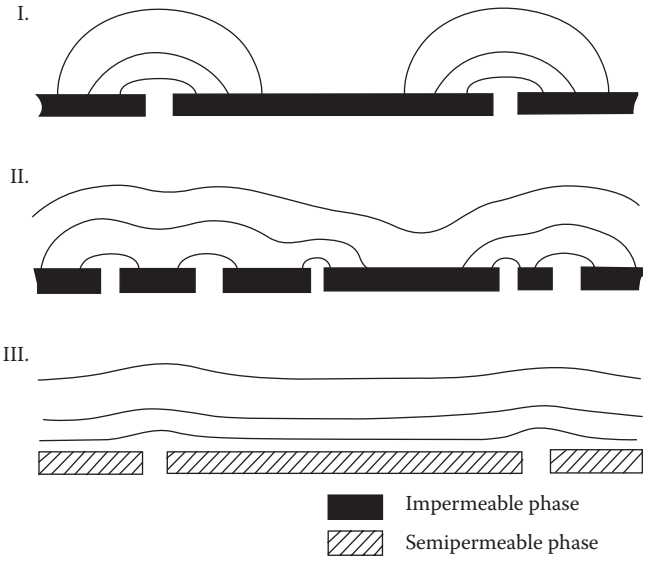


FIGURE 9.9 Isoconcentration contours above porous membranes. Transport in membranes I and II occurs exclusively through pores in an otherwise impermeable phase. In membrane III, transport occurs through both pores and the semipermeable phase.

than the pore radius ($z_t \ll a$), then the individual pores in the membrane can be readily resolved. These conditions are often difficult to achieve, especially on rough surfaces where z_t is necessarily large in order to prevent the tip from crashing into the surface. In such instances, the flux of molecules from two adjacent pores cannot be completely resolved unless using instruments with nanometer-resolution imaging capability, for example, a combined SECM-AFM microscope.

Quantitative measurement of the rate of mass transfer, Ω, from a pore whose diffusional field overlaps that of a neighboring pore can also be accessed from positioning the tip above the pore opening instead of rastering it across the surface. When the tip is very close to the pore opening, the current is dominated by the flux of molecules from that pore, with very little interference from neighboring pores. Analysis of i_t as a function of z_t, as described in Section 9.2.4, yields the rate of mass transport. At larger z_t, i_t is more affected by overlapping profiles; thus, the range of z_t for measuring i_t may be significantly reduced.

Membrane III in Figure 9.9 depicts another nonideal behavior encountered in imaging membranes. Here, discrete pores are surrounded by a homogeneous phase that is moderately permeable to the species of interest. For instance, the homogeneous phase may contain many pores that are too small to be resolved by SECM. Transport across the homogeneous phase presents several difficulties in the SECM analysis. First, it is more difficult to resolve the discrete pores in the membrane. There are two reasons for this: (i) the flux in the pore is reduced because of competitive transport through the neighboring homogeneous regions, and (ii) the isoconcentration contours on the receptor side are a combination of radial diffusion from the pores and planar diffusion from the homogeneous region; the increase in planar diffusion reduces the ability to resolve the flux from a pore. Second, it is difficult to quantify the flux across the homogeneous region by SECM, since the flux in this region is frequently very small and thus i_t is also small. Compounding the problem is the fact that the rate of mass transport, Ω, from the semipermeable region is often large since this region occupies the largest fraction of exposed surface area (frequently >95% of the surface). Thus, it is difficult to quantify the overall mass transport rate for such a membrane using SECM alone. In this situation, one must measure the total transmembrane flux by an independent method. This usually involves more classical transport measurements, such as sampling the bulk concentration of the molecular permeant in the receptor compartment as a function of time. The mass transport rate through the pores can still be measured as before using SECM and subtracted from the total rate to estimate the flux through the homogeneous region. This procedure has been reported for analysis of transport across skin, where ~75% of the flux is associated through a handful of discrete pores, and the remainder is associated with the more homogeneous tissues of skin.[15]

Using smaller tips or a combined topographical and SECM imaging (SECM-AFM) should allow to resolve, with nanometric resolution, permeant fluxes across smaller pores in more dense membranes. This technique resolved ~200 nm individual nanopores in a membrane containing ~5 pores/μm^2.[26] It has not yet been tested in more stringent resolution conditions such as those required for the imaging of biological or nanoporous structures presenting ~50 nanopores of 15 nm diameter per μm^2. For such membranes, the determination of average pore size and transport rates have been provided by SECM inspection, from classical approach curves[37,38] interpreted in terms of membrane permeation model (see Chapter 13).

9.2.7 Imaging Strategies

The main strategies developed for imaging membrane structure and quantifying molecular fluxes are depicted in Figure 9.10. Experimentally, the primary difference between these methods lies in the relative concentrations of the redox species in the donor and receptor solutions. The choice of imaging method depends on the properties of the membrane as well as the specific goals of the study. In the following descriptions, the SECM tip is assumed to be rastered at a constant absolute height across the membrane surface. However, the distance between the tip and membrane, z_t, may vary due to topographical features on the surface of the membrane.

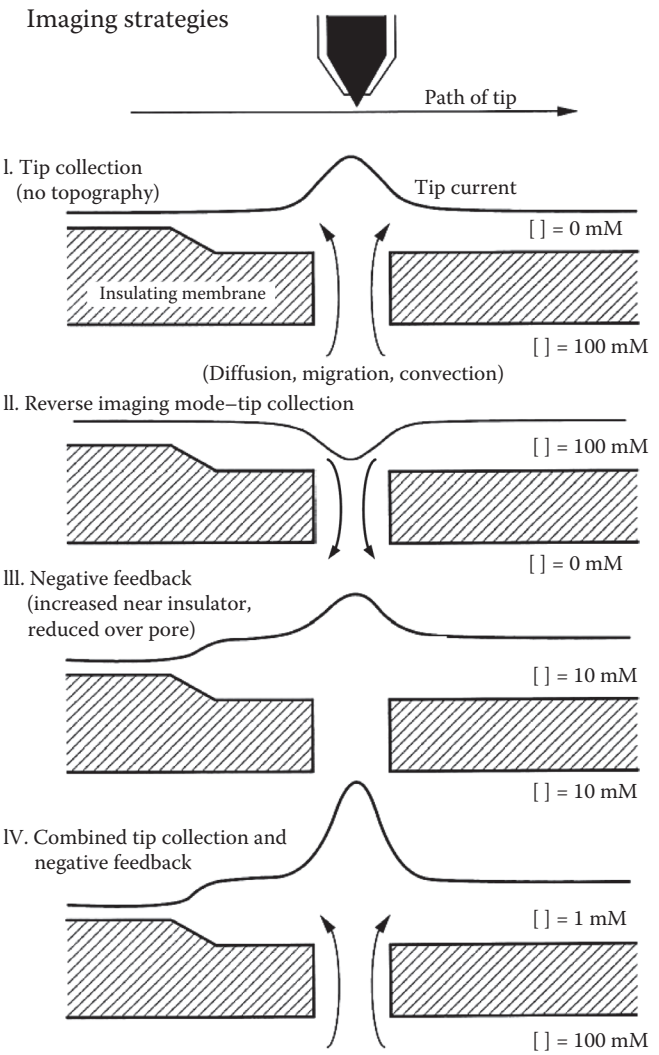


FIGURE 9.10 Imaging modes for SECM analysis of porous membranes. The SECM tip is rastered at constant height from the membrane: (I) Tip collection mode. The electroactive permeant is only present in the donor solution. The tip, held in the receptor solution, senses changes in concentration due to transport through the pore. (II) Reverse imaging mode (opposite to I). The tip, held in the donor solution, senses changes in concentration at the pore opening. (III) Negative feedback mode. The donor and receptor solutions contain equal concentrations of the permeant: there is no driving force for diffusional transport across the pore. Variation in negative feedback due to surface topography and pore openings gives rise to the contrast in the SECM image. (IV) Combined tip collection and negative feedback mode. The SECM image reveals both negative feedback and a net diffusional transport of the permeant across the pore. Migration and convective transport can occur if an electric field gradient or a pressure is applied across the membrane. Then, an increase in mass transport of the permeant is sensed by the tip over the pore.

9.2.7.1 Tip Collection Mode

Tip collection mode is the simplest SECM mode for imaging membranes, and the first to be employed for this purpose.[8,14] The membrane separates a donor solution, which contains a redox species, from a receptor solution in which the redox species is absent. The SECM tip current arises solely from the transport of redox species across the membrane—a large tip current indicates a localized region in which the spatial flux in the membrane is large, often due to a discrete pore. No

information regarding the membrane topography is obtained in this mode. However, as discussed in the preceding sections, the theoretical relationship between the tip current and the flux in the pore is relatively straightforward in this case.

In the absence of an applied field, the redox species is transported across the membrane by diffusion and its diffusive flux may be relatively small, resulting in difficulties in obtaining an SECM image. Higher contrast images are obtained (see Sections 9.2.5 and 9.3) by enhancing the pore transport upon application of an external driving force.

9.2.7.2 Reverse Imaging Mode

For many biological problems such as the transport of a solute into single cell or in vivo, it is convenient to have both the solute and the SECM probe in the same solution and to image the membrane uptake of the solute. This *tip collection* configuration was referred to as RIM,[17,18] as it is the reverse situation of that presented in the preceding section: the tip is scanned on the donor side of the membrane in order to image the solute that *enters* the pore and diffuses toward the receptor phase. In this configuration, the solute is depleted at the pore entrance in the donor solution, resulting in a decrease in the tip current as the tip scans the pore region. In principle, this mode of operation is less sensitive than the tip collection mode because the signal is measured relative to a large background signal. The enhancement of solute transport may circumvent this problem (see Section 9.3.1.2). Pressure-induced and electroosmotic flows can be used to dilute (current decrease) or accumulate (current increase) the solute at the pore entrance. The quantitative analysis of the solute transport in this *RIM* has also been established.[17,18]

9.2.7.3 Negative Feedback Mode

In the negative feedback mode, the concentration of redox species is the same on both sides of the membrane; no concentration gradient exists between the donor and receptor compartments to drive diffusive transport across the pore.[11–13] This mode of imaging can be used to obtain topographical maps of the surface where the variation in the SECM tip current arises from differences in the tip-to-sample separation.[39] When the tip is far from the sample surface, a steady-state current is measured at the tip, $i_{t\infty}$, that is proportional to the concentration of redox species in the receptor compartment (Equation 9.6). When the tip is brought close to the sample surface, diffusion of the redox species to the tip is hindered by the presence of the sample surface. This results in a decrease in tip current relative to $i_{t\infty}$. A three-dimensional image of the surface is obtained by rastering the tip, at a fixed height, across the sample surface. The topography of the surface is obtained from the normalized tip current ($i_t/i_{t,\infty}$) using the expressions for negative feedback (Chapter 5). A decrease in $i_t/i_{t,\infty}$ corresponds to a decrease in the tip-to-sample separation and thus a raised surface. An increase in $i_t/i_{t,\infty}$ indicates that either (i) the tip-to-membrane surface separation is large or (ii) the tip is above a pore. In the latter case, the increase in i_t results from transport of the molecule from the donor-side solution to the tip, via the pore. If an external driving force is used to enhance transmembrane transport, modulation of the force during imaging allows one to decouple the topographical and pore flux components of the SECM tip current.[11–13]

9.2.7.4 Combined Tip Collection and Negative Feedback Mode

Unlike the pure tip collection mode, the concentration of redox species in the receptor compartment has a nonzero value. Thus, the tip current, $i_{t\infty}$, has a nonzero value at large tip-to-sample separations. This tip current is reduced when the tip is brought close to an insulating portion of the sample because of hindered diffusion (*negative feedback* effect). Because there is a concentration gradient present between the donor and receptor solutions, the redox species diffuses through the pores in the sample, resulting in a tip current increase similarly to the response expected in *tip collection mode*. Information on both the surface topography of the membrane and local flux of the redox species across the membrane is obtained in this imaging mode.[9]

9.2.8 Tip Perturbations

Qualitative interpretation of SECM images of a membrane is generally possible without detailed consideration of how the SECM tip influences the diffusion field around a pore opening. However, more quantitative analyses of pore transport generally require that the SECM tip behave as a noninteracting probe. This means that the rate of consumption of electroactive molecules at the SECM tip must be sufficiently small so that the diffusion field around the pore is not significantly altered. A detailed analysis of this problem has not yet been presented; however, as described later, Nugues and Denuault have reported numerical simulations demonstrating how the diffusion field above a membrane can be altered by the SECM tip.[9,40] These simulations demonstrate how the consumption of the electroactive molecules at the tip results in the skewing of the concentration profile above the pore opening. If this interaction is nonnegligible, the theoretical treatment proposed (see Sections 9.2.1 and 9.2.4) cannot be used anymore to depict the concentration profile around the pore opening and the mass transport across the membrane. This interaction can be minimized by using smaller tips or by reducing the tip-to-surface distance. Other interesting situations have been simulated that illustrate the complex nature of probing mass transport across membranes. For instance, when the sample thickness is smaller than the tip radius, the tip may scavenge molecules beyond the membrane, probing the concentration of the redox species in the donor compartment.

9.3 APPLICATIONS

Synthetic membranes, for example, track-etched polycarbonate, have been frequently employed as idealized membrane models in the development of SECM-based methodologies. In these studies, the pore dimensions and spacing, as well as the transport mechanism in the pore, are typically well defined a priori, allowing a rigorous testing of the SECM theory. On the other hand, biological membranes, for example, skin, have a very complex structure with the possibility of parallel transport paths and mechanisms. Even though the analysis of the SECM images and data in these cases is generally less direct, SECM is a very powerful technique for quantifying localized transport across biological membranes.

The following sections present different examples of SECM investigation of transmembrane transport. The first section is dedicated to the experimental quantitative validation of the molecular transport formalism at simple idealized pores. In these examples, the transport of standard redox probes occurs by a variety of mechanisms including simple diffusion, diffusion with migration, pressurized convective flow, and electroosmotic flow. This formalism is then extended to more complex biological membranes or to permeants that require the use of selective SECM tip. The achievement of the ultimate imaging resolution is then discussed by the more recent combination of SECM with scanning force microscopy. The diversity of membrane structures and transport mechanisms that have been investigated indicates a general utility of this scanned probe microscopy for studying membrane transport.

9.3.1 Synthetic Membranes

9.3.1.1 Diffusion and Migration across Porous Mica and Polycarbonate Membranes

9.3.1.1.1 Porous Mica

The initial use of SECM for studying transport across a membrane involved porous mica membranes.[8] The pores in this membrane are produced by a track-etched process in which defect tracks are produced in a thin sheet of mica by exposure to a collimated beam of ^{238}U fission fragments. These tracks are then etched in hydrofluoric acid for a specified time to produce pores. The pores (see Figure 9.4B) have a rhomboidal cross section with 60° and 120° included angles, and with edge lengths ranging from 1.0 to 3.0 μm. These pores are essentially straight with a uniform and large

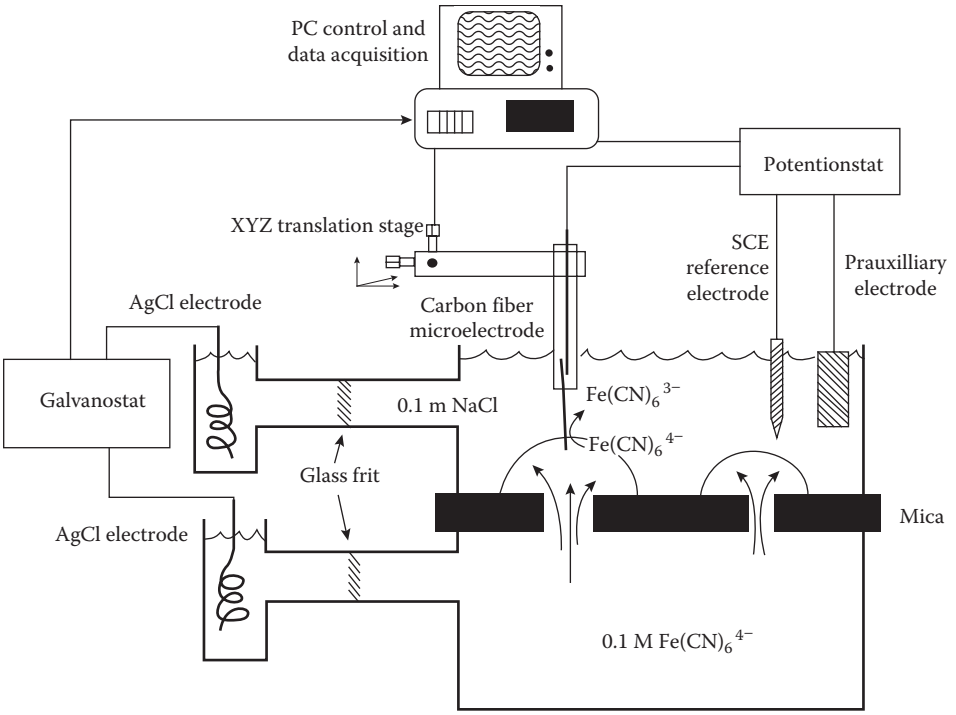


FIGURE 9.11 Schematic drawing of the scanning electrochemical microscope used for imaging molecular transport across a membrane. The membrane separates the donor and receptor solutions. The electroactive species in the donor solution diffuses across the membrane or may be driven across the membrane by an electric current supplied by the galvanostat. The SECM tip detects the electroactive species as it emerges from the membrane. (Reprinted from Scott, E.R. et al., *J. Invest. Derm.*, 104, 142, 1995. With permission.)

cross section throughout the membrane, and are useful as a simple experimental model to validate the principle of quantitative SECM imaging of transport across single pore (see Section 9.2).

Figure 9.11 shows a schematic diagram of the apparatus used to image porous mica. The mica membrane is positioned in a diffusion cell, such that it separates a *donor* solution containing both 0.1 M $K_4Fe(CN)_6$ and 0.1 M NaCl from a *receptor* solution containing only 0.1 M NaCl. $Fe(CN)_6^{4-}$ is transported across the membrane and is detected by the SECM tip as it emerges from the pores into the receptor solution. To detect $Fe(CN)_6^{4-}$ exiting from the pores, the potential of the SECM tip is held at 0.5 V vs. the saturated calomel electrode (SCE), sufficiently positive of the standard electrode potential of the $Fe(CN)_6^{4-/3-}$ redox couple ($E^{o'} = 0.185$ V vs. SCE) to cause the mass-transfer-limited oxidation of $Fe(CN)_6^{4-}$. This experiment corresponds to the "tip collection" mode described in Section 9.2.7. The flux of $Fe(CN)_6^{4-}$ through the pores can be enhanced by driving a current, i_{app}, across the membrane, dramatically improving the signal-to-noise ratio in the SECM images. Experimentally, this is readily accomplished by using the commercial galvanostat and two large Ag/AgCl electrodes as depicted in Figure 9.11. When the cathode (negative terminal) is in the donor compartment, the applied current results in an upward migration of $Fe(CN)_6^{4-}$. The net flux of $Fe(CN)_6^{4-}$ is due to combined diffusion and migration, as described by the Nernst–Planck equation (Equation 9.11).

Figure 9.12 shows an SECM image of a $80 \times 80\,\mu m^2$ region of the mica membrane for $i_{app} = 0$ and 40 μA. The image indicates the magnitude of the current measured at the SECM tip, i_t, as a function of the lateral position of the tip. The two regions of high tip currents are due to an increased concentration of $Fe(CN)_6^{4-}$ above pore openings on the membrane surface. As described in Section 9.2.2, the tip current is directly proportional to the flux of the redox-active permeant inside the pore

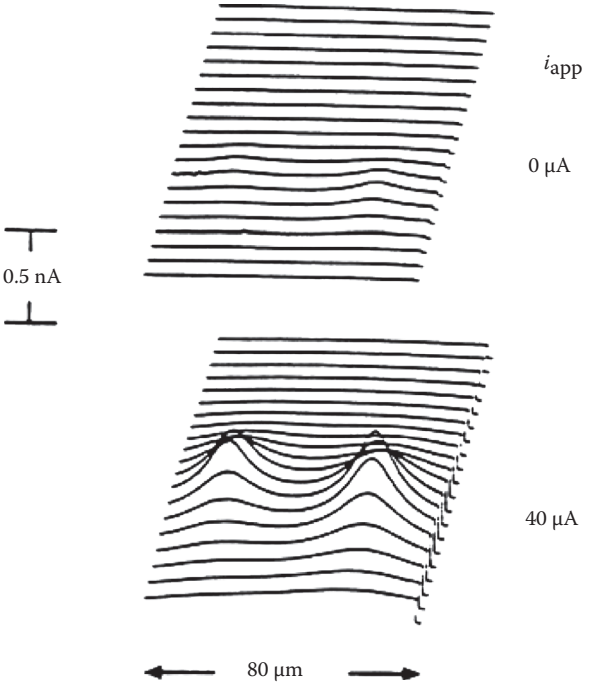


FIGURE 9.12 SECM images of a porous mica membrane as a function of the applied current, i_{app}. The two peaks correspond to the diffusion and migration of $Fe(CN)_6^{4-}$ across the membrane. The donor solution contained 0.1 M $K_4Fe(CN)_6$ and 0.1 M KCl. The receptor solution contained 0.1 M KCl. (From Scott, E.R. et al., *J. Membr. Sci*., 58, 71, 1991. With permission.)

(Equation 9.8). In essence, the SECM images thus provide a means to *visualize* the flux of $Fe(CN)_6^{4-}$ across the membrane. As discussed and illustrated in Section 9.2, the SECM also provides a means to quantify the flux of the permeant across the pore from concentration profiles (see Figures 9.4A and 9.9).

The SECM peaks in Figure 9.12 have apparent widths of ~15 μm (~10 times greater than the average pore dimensions), a result of the SECM tip intercepting the quasi-radial flux of $Fe(CN)_6^{4-}$ from the pores at a nonzero distance from the membrane surface. The SECM-measured density of pores, based on multiple images, is 3×10^3 cm^{-2}, in reasonable agreement with the SEM estimate, 4.5×10^3 cm^{-2}. The density of pores is sufficiently low that the diffusional fields of individual pores do not overlap to any significant extent, corresponding to the ideal type I membrane depicted in Figure 9.9.

The beneficial effect of inducing a migrational flux of the redox species through the pores in mica is also presented in Figure 9.12. The tip current corresponding to the $Fe(CN)_6^{4-}$ flux through the same pores is significantly enhanced by application of iontophoretic current, indicating that the highly charged anion carries a significant fraction of the current, i_{app}, across the membrane. A smaller enhancement in the flux is expected when the transference number of the redox permeant is lowered (e.g., by decreasing its concentration in the donor solution relative to the concentration of the background electrolyte). The use of an applied current to drive the molecular permeant across the membrane at enhanced rates is completely general, and can be used to enhance the quality of SECM images in many instances.

9.3.1.1.2 Porous Polycarbonate

Commercially available porous polycarbonate membranes have a relatively simple structure and have been used by several groups to test SECM methodology. Nugues and Denuault[9] have imaged

a nucleopore membrane (6 μm thickness, 5 μm radius pores, 1.6×10^4 pores/cm^2) in the combined tip collection/negative feedback mode (see Figure 9.11) with a solution of 80 mM $Fe(CN)_6^{4-}$/0.1 M KCl in the donor compartment, and a solution of 0.80 mM $Fe(CN)_6^{4-}$/0.1 M KCl in the receptor compartment. The difference in concentration drives the diffusional transport of $Fe(CN)_6^{4-}$ across the membrane and the density of active pores is obtained from the resolution of regions of higher $Fe(CN)_6^{4-}$ fluxes.

A much more difficult test of the resolution achievable by SECM was obtained from the image of a Poretics polycarbonate membrane (15 μm thickness, 45 nm radius pores, ~10^5 pores/cm^2).[7] Here the pore size is very small and the pore density is large, making it difficult to resolve the molecular flux from individual pores. As a result, the diffusional fields of pores overlap to a large extent (type II membrane, Figure 9.9) resulting in a large background current. Nevertheless, it is possible to visualize molecular fluxes through individual 45 nm radius pores. In principle, this background current can be reduced and images with higher resolution should be obtained by using nanoprobes (see Section 9.3.4).

9.3.1.2 Electroosmosis across Membranes

Electroosmotic flow is a common mechanism of transport occurring in charged channels and therefore in porous ion-exchange membranes. It represents an important practical issue in fuel cells such as in the parasitic crossover of fuel (e.g., methanol) and in the flooding/drying of the fuel cell electrodes.[41,42] In this respect, the improvement of fuel cells efficiency depends on the proton flux that the cation-exchange membrane can sustain. This issue can be addressed by SECM by imaging and quantifying the local flux of H^+ across fuel cells membrane.[43] Since in ion-exchange membranes the pores are too small and too densely packed to be resolved individually, the ion fluxes in such membranes like in biological membranes are interpreted in terms of membrane permeation (see Chapter 13).

9.3.1.2.1 "Mica/Nafion" Membrane

Electroosmotic flows across a single charged pore have first been imaged by SECM by Bath et al.[10] As shown in Figure 9.13, to impart charge and size selectivity to a single pore, a (~50 μm radius) pore has been introduced into a ~200 μm thick mica membrane and has been filled with the perfluorinated cation-selective polymer Nafion. Such model structure may mimic skin, a naturally occurring ion-selective membrane, across which electroosmotic flows may drive transdermal drug delivery, as discussed in Section 9.3.2.2. More recently, electroosmotic flow across

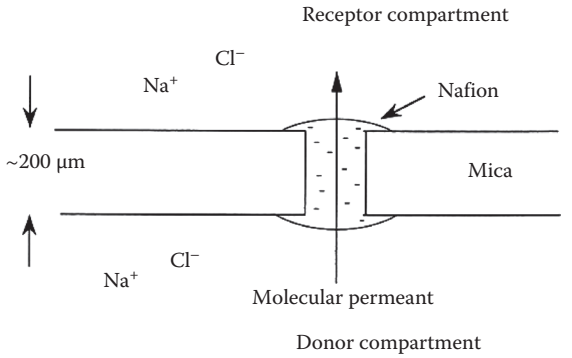


FIGURE 9.13 Schematic diagram of a Nafion-filled pore in mica. Transport of a redox-active permeant through the pore occurs by diffusion, electroosmotic flow, and migration. The membrane separates donor (lower) and receptor (upper) compartments containing equal concentrations of NaCl. The donor solution contains the permeant. (Reprinted from Bath, B.D. et al., *Anal. Chem.*, 70, 1047, 1998. With permission.)

negatively charged nanopores in polycarbonate membrane has been used to capture and detect nanoparticles.

SECM studies of electroosmosis in the persulfonated polymer Nafion have been investigated using the single pore membrane shown in Figure 9.13. Cation transport numbers in Nafion approach unity,[44–47] and electroosmotic flow of water readily occurs in this material. The Nafion-filled, single pore membrane is referred to hereafter as the "mica/Nafion" membrane.

When an *iontophoretic* current is applied across the membrane, transport of a species may occur by diffusion and electroosmotic flow if the species is electrically neutral, and by diffusion, electroosmotic flow, and migration if the molecule is charged. By definition, a positive current is carried across the membrane by the migration of electrolyte cations (Na^+) from the donor compartment to the receptor compartment (the transference number for the electrolyte anions is essentially zero). The experimental arrangement for studying iontophoretic transport is that presented in Figure 9.11. The mica/Nafion membrane separates a donor solution containing a redox-active molecular permeant and electrolyte (e.g., NaCl) from a receptor solution containing only the electrolyte. The SECM tip is used to detect the permeant as it emerges from the pore (tip collection mode).

Figure 9.14 shows voltammograms recorded at the SECM tip, positioned directly above the Nafion-filled pore, for three redox-active permeants having different electric charges (monovalent cation, neutral, and monovalent anion).[48] The voltammograms depict the steady-state transport of the permeants through the pore for different values of the current applied across the membrane, $i_{app} = 50$, 0, and $-50\,\mu A$. The magnitude of the voltammetric limiting current at the tip is directly proportional to the permeant flux in the pore (Equation 9.8, Section 9.2.2); thus, a comparison of the voltammetric response of the SECM tip provides a semiquantitative understanding of the influences of i_{app} and molecular charge on transport behavior in Nafion.

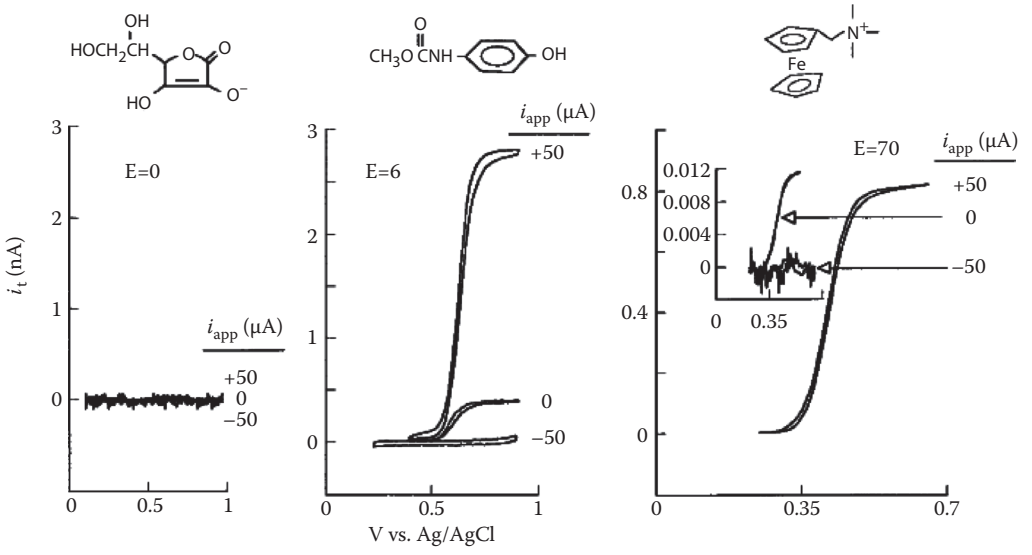


FIGURE 9.14 Voltammetric response at the SECM tip (i_t) above the Nafion-filled pore as a function of the molecular permeant charge and applied current (i_{app}). The magnitude of the SECM tip current is proportional to the rate of transport of the molecules shown in the figure. The voltammetric response at $i_{app} = 0$ corresponds to the diffusional flux through the pore. The voltammograms recorded at $i_{app} = 50\,\mu A$ correspond to iontophoretic transport from the donor solution to the receptor solution. The voltammograms recorded at $i_{app} = -50\,\mu A$ correspond to iontophoretic transport from the receptor solution to the donor solution. E is the enhancement factor due to electroosmosis in the forward direction (equal to the ratio of the flux at $i_{app} = 50\,\mu A$ to that at $i_{app} = 0\,\mu A$). (From Bath, B.D. et al., *Anal. Chem.*, 72, 433, 2000. With permission.)

The SECM data for transport of a monovalent anion (ascorbate) and a monovalent cation ([(trimethylammonio)methyl]ferrocene, FcTMA$^+$) are consistent with the cation-selective properties of Nafion. The absence of electrochemical signal on the left panel of Figure 9.14 shows that ascorbate is not transported through the pore, regardless of the applied current; the ascorbate anion is electrostatically repelled from the negative fixed charges incorporated in the Nafion polymer. For the monovalent cation, FcTMA$^+$ (Figure 9.14, right panel), the response at $i_{app}=0$ corresponds to steady-state diffusive transport of FcTMA$^+$ across the membrane with a diffusional flux (note the change in *y*-axis scale) approximately equal to that of the neutral molecule acetaminophen (Figure 9.14, middle panel). When a positive current $i_{app}=50\,\mu A$ is applied across the membrane, the flux of FcTMA$^+$ is enhanced by a factor of 70, in comparison with an enhancement of ~6 for acetaminophen under the same conditions. The difference is due to the dominant contribution of electric migration to the net flux of FcTMA$^+$. Because acetaminophen is electrically neutral, the observed flux enhancement at $i_{app}=50\,\mu A$ must solely be due to transport of acetaminophen by electroosmotic convective flow, a result of the upward flow of Na^+ in the Nafion-filled pore. When the direction of the current is reversed, that is, $i_{app}=-50\,\mu A$, the flux of acetaminophen (and FcTMA$^+$) is at negligible level, a consequence of electroosmotic flow (and migration–convection flow) occurring from receptor to donor compartment opposing the diffusional flux of the permeants.

Although it is beyond the scope of this chapter, a relatively straightforward analysis of the SECM data, based on Equation 9.12, allows one to fully characterize the transport mode of any solute. The first edition of this chapter detailed the transport of hydroquinone (HQ); the case of acetaminophen is examined here. The complete transport description of a solute across the pore requires the absolute values of pore flux and pore radius, which can be determined (see Section 9.2.4) by measuring the concentration profile along the centerline axis of the pore that extends away from the pore opening into the receptor solution.

Figure 9.15A shows representative examples of experimental acetaminophen concentration profiles, corresponding to diffusive ($i_{app}=0\,\mu A$, squares) and iontophoretic transport ($i_{app}=50\,\mu A$, triangles). The solid lines correspond to theoretical profiles (Equation 9.10) and are based on best fits of the data obtained by varying C_s and a. The excellent fits of Equation 9.10 to the data indicate that (i) diffusion is the predominant mode of transport away from the pore openings, (ii) the pore opening can be approximated as being disk shaped, and (iii) the SECM tip does not significantly alter the concentration profiles. Values of the solute flux across the pore can be computed from Equation 9.3 using a and C_s obtained from these fits. For pure diffusion ($i_{app}=0\,\mu A$) over a pore of 36 μm radius $N_{diff}=4\times10^{-10}$ mol/cm^2/s, increasing by approximately a factor of 7 under iontophoretic conditions ($i_{app}=50\,\mu A$). The convective velocity of the solute, v_{eo}, and the electroosmotic drag coefficient at any specified applied current are then computed from Equation 9.12 ($Q=0$ for neutral solutes). For instance, for $i_{app}=50\,\mu A$, the convective flow velocity of acetaminophen in the Nafion-filled pore is about 1.7 μm/s and approximately one molecule is transported through the pore per 2000 Na^+.[48]

9.3.1.2.2 Reverse Imaging Mode

The SECM is also operated in the RIM (II in Figure 9.10) to visualize the transport of how the solutes are transported at the pore entrance in the donor phase.[17,18] Figure 9.16 shows SECM images in the RIM of the acetaminophen concentration above a mica/Nafion pore at $i_{app}=-100$, 0, and 100 μA. At $i_{app}=0\,\mu A$, the diffusional transport of the solute in the pore is associated with its depletion at the pore entrance.

A negative iontophoretic current, $i_{app}=-100\,\mu A$, corresponds to transport of cations from the receptor to the donor (where the tip is located) solution. This results in a negative (electroosmotic) solvent flow from the receptor to the donor solution, which opposes the passive solute diffusion. As the solution from the receptor solution (free of solute) enters the donor compartment, it forces the donor solution away from the pore opening thereby lowering the local concentration of

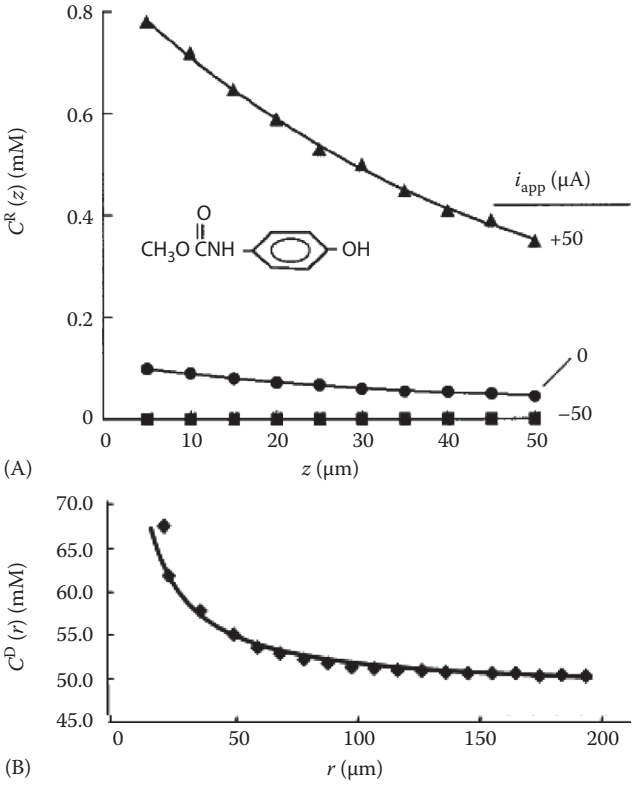


FIGURE 9.15 Concentration profiles of acetaminophen at (A) the exit (tip in the receptor compartment) or (B) at the entrance (tip in the donor compartment, reverse imaging mode) of Nafion-filled pores in mica membranes. The data correspond to passive diffusion and iontophoretic transport; the values of i_{app} are indicated in the figure. The solid lines represent best fits of the data (A) with Equation 9.10 obtained by varying the pore radius, a, and the surface concentration, C_s or (B) obtained by varying the solution velocity v at known flux N_{iont} from values of C_s as estimated in Section 9.2.4. Donor phase: 50 mM acetaminophen + 0.2 M NaCl; receptor phase: 0.2 M NaCl. (Reprinted from (A) Bath, B.D. et al., *Anal. Chem*., 72, 433, 2000 and (B) Uitto, O.D. et al., *Anal. Chem*., 74, 4577, 2002. With permission.)

acetaminophen. Imaged from the receptor compartment, this situation corresponds (see Figure 9.14 and the limiting case $N=0$ in Section 9.2.5) to a featureless image as the solute is not transported across the pore.

The situation of positive solvent is more interesting as the overall transport is affected by the competition between the solvent transfer and the solute transport rates. When solvent transfer is fast ($i_{app} \gg 0$) and solute transport is slow, the solute accumulates above the pore opening. The resulting SECM image for $i_{app} = 100\,\mu A$ in Figure 9.16 displays a peak of solute accumulation above the pore opening. This preferential rejection of the solute at the membrane interface is commonly referred to as ultrafiltration in analytical science.

In the RIM, the concentration profile for the iontophoretic transport ($i_{app} = 50\,\mu A$) of acetaminophen away from the pore opening into a 50 mM donor solution is presented in Figure 9.16 (lower, full symbols). The theoretical profile (solid line) is obtained from the radial expansion of the convective diffusion flux equation (9.13) above a pore of radius r_o:

$$-N(r) = -v(r)C(r) - D\frac{dC(r)}{dr} \tag{9.13}$$

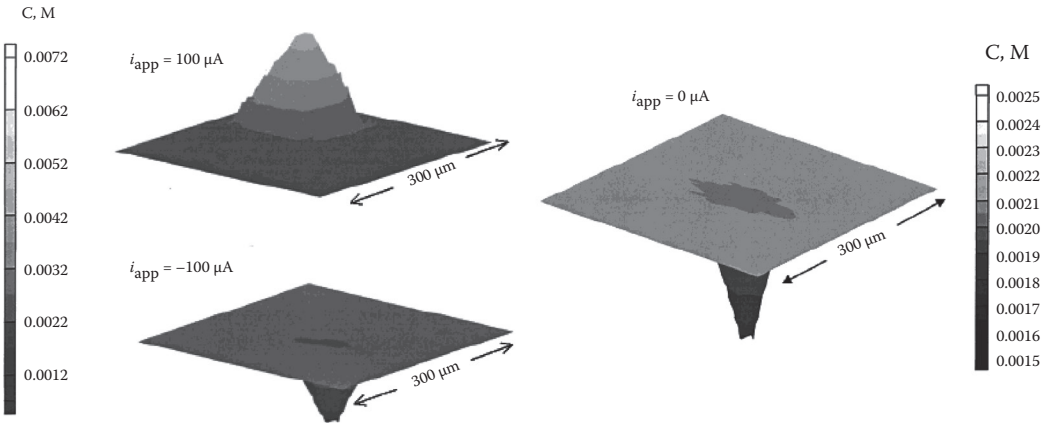


FIGURE 9.16 SECM images (concentration vs. position) in the reverse image mode (RIM) of acetaminophen above a 14.6 µm radius pore filled with Nafion under diffusive (right) or iontophoretic transport (left). The tip was scanned in the donor phase 5 µm above the membrane. The donor compartment contained 2 mM acetaminophen; both donor and receptor compartments contained 0.05 M NaCl. (From Uitto, O.D. and White, H.S., *Anal. Chem.*, 73, 533, 2001. With permission.)

where $N(r)$ and $v(r)$ are, respectively, the flux of solute and the flow velocity at distance r from the pore opening. The minus signs indicate that both the solute and solvent are entering the pore. As in Sections 9.2.1 and 9.2.5, from mass conservation, the concentration profile $C(r)$ is readily obtained as a function of the solute flux N_{iont}, the solvent velocity v at the pore surface, r_o and the solute bulk concentration in the donor phase $C_s^{D^*}$.[39]

Values of N_{iont} and r_o are obtained from the fit of the experimental concentration profile at the pore exit in the receptor solution, like for Figure 9.16 (upper). The fit of the concentration profile at the pore entrance in the RIM gives an estimate of the solution velocity v (2.8×10^{-3} cm/s) in agreement with the estimated velocity of the solvent in the membrane ($\approx 3 \times 10^{-3}$ cm/s).[10,48] It is 15 times higher than the electroosmotic velocity for acetaminophen v_{eo} (2×10^{-4} cm/s) obtained from the flux at the pore exit.[48] This finding indicates that convective transport of the solute in the Nafion phase is impeded relative to convective transport of the solvent, and reflects a higher retention (affinity) of the solute than of the solvent in the Nafion membrane.

9.3.1.3 Access to Transport Dynamics: Detection of Single Nanoparticle Capture

SECM can also be used to measure electroosmotic transport dynamics.[10] As illustrated earlier,[40] the transient response of the SECM tip current $i_t(z=0)$ is measured as the iontophoretic current i_{app} is varied between 50, 0, and −50 µA during HQ transport. The time required to obtain a new steady-state i_t reflects the establishment of new steady-state HQ concentration profiles in the Nafion-filled pore following the change in i_{app}. In a pore of length l, this time can be estimated from the root-mean-square diffusional displacement of HQ given by $l = (2D_p t)^{1/2}$. Using $l \sim 200$ µm and the diffusivity of HQ in Nafion, $D_p = 3.7 \times 10^{-7}$ cm²/s yields a value of $t \sim 9.0$ min, in good agreement with the observed 10 min transient.

This strategy has been extended to the detection of the electrophoretic capture and release of individual nanoparticles at the mouth of a nanopore.[27,28] The schematic description of the strategy used is given in Figure 9.17A. The experimental setup is identical to that presented in Figure 9.11 using a track-etched polycarbonate membrane but the donor phase contains both a redox probe $Fe(CN)_6^{4-}$ and charged polystyrene nanoparticles. The pores of the membrane are conically shaped[49] to facilitate the positioning of the SECM tip above the large-diameter (2.5 µm) opening of the pore, while the small (60 nm diameter) opening of the pore is used to capture a nanoparticle. A typical experiment is presented in Figure 9.17B. When a positive iontophoretic current, $i_{app} = 50$ µA (step (i),

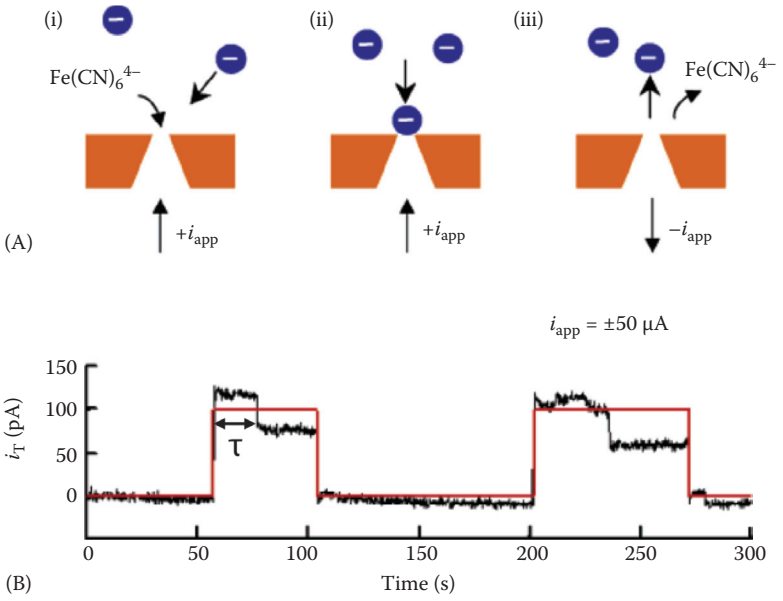


FIGURE 9.17 (A) Schematic description for stochastic nanoparticle detection at a pore mouth from SECM measurement of $Fe(CN)_6^{4-}$ transport across a conical pore under iontophoretic conditions. (i) Application of $i_{app}>0$: enhanced transport of anionic redox probe and particle, (ii) at time t, capture and blocking of a particle at the pore mouth (tip current decrease), and (iii) inversion of iontophoretic transport, $i_{app}<0$, for particle release. (B) Example of iontophoretic current, i_{app}, waveform with associated transient tip current profile for the transport of $Fe(CN)_6^{4-}$ across the pore. (From Lee, S. et al., *Anal. Chem.*, 76, 6108, 2004. With permission.)

Figure 9.17A), is applied between the two sides of the membrane, the tip current increases as a result of electrokinetic transport of $Fe(CN)_6^{4-}$ across the pore. If the nanoparticle is large enough (>60 nm) or has the appropriate charge (negatively charged for a positive iontophoretic current), it may be driven toward the receptor phase and be captured at the pore mouth. The capture of a negatively charged (COOH-terminated polystyrene) nanoparticle is detected, at a time τ after the application of i_{app}, from the change in the flux of the redox probe at the tip. A decrease in tip current indicates that a single nanoparticle capture partially blocks the pore entrance. When the electrophoretic current is reversed, the particle is released and the tip current becomes negligible as a result of counter-diffusion transport of the ionic redox probe. The capture rate of individual nanoparticles, $1/\tau$, can be rationalized by the transport rate of ions into the pore (similar to Equations 9.11 and 9.12).[48] The capture rate decreases when the nanoparticle concentration increases and strongly depends on the electrophoretic current amplitude and waveform.[28] From statistical analysis of the stochastic capture of nanoparticles and the appropriate choice of i_{app} waveform, this Coulter-counting method can analyze nanoparticle solutions in the 10^9–10^{11} particle/mL range.[28]

9.3.2 Biomaterials

9.3.2.1 Diffusion and Convection in Dentine and Laryngeal Cartilage

The SECM has been used to investigate molecular transport in human dentine and laryngeal cartilage. Convective and diffusive transport in these porous biomaterials is of interest in the biomedical and biophysical communities. To study these materials, thin slices (typically ca. 100 μm) of dentine and cartilage are prepared and mounted in a diffusion cell suitable for SECM imaging. Thus, although dentine and cartilage are bulk biomaterials (rather than membranes), the general experimental procedures are basically the same as that described in the previous sections.

9.3.2.1.1 Dentine

Dentine is a calcareous material located between the pulp and enamel in the tooth. Convective fluid flow within the 1–2 µm diameter tubules of this material is associated with dentinal hypersensitivity and the treatment of this condition. Unwin and coworkers have investigated convective flow in individual tubules in SECM experiments in which a fluid is forced through the tubules by pressurized flow.[11,12,50] Images are obtained in negative feedback mode employing a solution of 10 mM $K_4Fe(CN)_6$ and 0.5 M KCl on both sides of the membrane. A hydrostatic pressure gradient across the slice of dentine is introduced by raising the level of solution in the donor compartment relative to the solution in the receptor compartment. The pressure-driven enhanced transport of $Fe(CN)_6^{4-}$ is used to determine the fluid velocity in the tubule. A 1 µm radius tip was used to resolve convective transport of $Fe(CN)_6^{4-}$ through *single* tubules (pores) when a pressure of 2 kPa is applied across the dentine sample. The SECM tip current, i_t, corresponding to flow from a single tubule is given by[11]

$$\frac{i_t}{i_{t\infty}} = 0.94U^{1/2}aD^{-1/3}v^{-1/6}b^{-1/2} \times \left[2.464 - 1.063\frac{d}{b} + 1.5794\frac{d^2}{b}\right] \tag{9.14}$$

where

$i_{t\infty}$ is the current produced at the tip when the tip is far from the sample surface
v is the kinematic viscosity of the solution
b is an empirical constant (~2 µm)
d is the tip-to-sample separation
D is the diffusion coefficient
a is the radius of the pore
U is the average velocity of solution through the pore (estimated to 0.39 cm/s from Equation 9.14)

Unwin and coworkers also investigated the effect of chemical blocking agents on the molecular transport through the tubules in dentine.[12,50] Figure 9.18A shows the normalized tip current, $i_t/i_{t\infty}$, image of a large area (>100 µm^2) over the dentine surface without an applied pressure. The SECM tip current variation simply reflects the topography of the dentine surface.[39] Figure 9.18B shows the same area when 2 kPa of pressure is applied across the sample. Localized regions of increased $Fe(CN)_6^{4-}$ flux reveal convective solution flow through pores from donor to receptor compartments.

SECM images of the same area were then recorded after removing the pressure gradient and introducing either a chemical reagent (calcium oxalate) into the receptor solution that deposits onto the surface and blocks the pores or depositing manually, with a toothbrush under hydrostatic pressure, a thin (~10 µm) film of a toothpaste base containing a chemical blocking reagent (glycerol monooleate) over the dentine surface. The topographical image obtained after treatment with the toothpaste is similar to the image in Figure 9.18A suggesting that the applied paste followed the contour of the underlying dentine surface. Once a pressure is reapplied across the sample, the SECM image recorded is similar to that obtained in the absence of applied pressure, suggesting almost complete retardation of the fluid flow after application of the blocking layer. Calcium oxalate is seemingly the most efficient chemical blocking reagent as it totally inhibits the convective flow.[12,40] The efficiency of the paste-based treatments is quantitatively assigned by converting the $\Delta i_t/i_{t\infty}$ values into local solution velocities through the sample with an empirical equation similar to Equation 9.14.[13] In the absence of retarding treatment, the local fluid velocities under applied pressure are heterogeneously distributed between 0.1 and 8.5 µm/s. The paste-based treatment significantly attenuates the hydraulic permeability as local velocities are more uniform and <0.5 µm/s.

Nugues and Denuault have also used SECM to study *diffusive* transport in the pores of dentine.[9] In these experiments, the concentration of $Fe(CN)_6^{4-}$ was 1 mM in the receptor compartment and 100 mM in the donor compartment, corresponding to the combined tip collection negative feedback imaging mode. With these solution conditions, the SECM image represents a convolution of

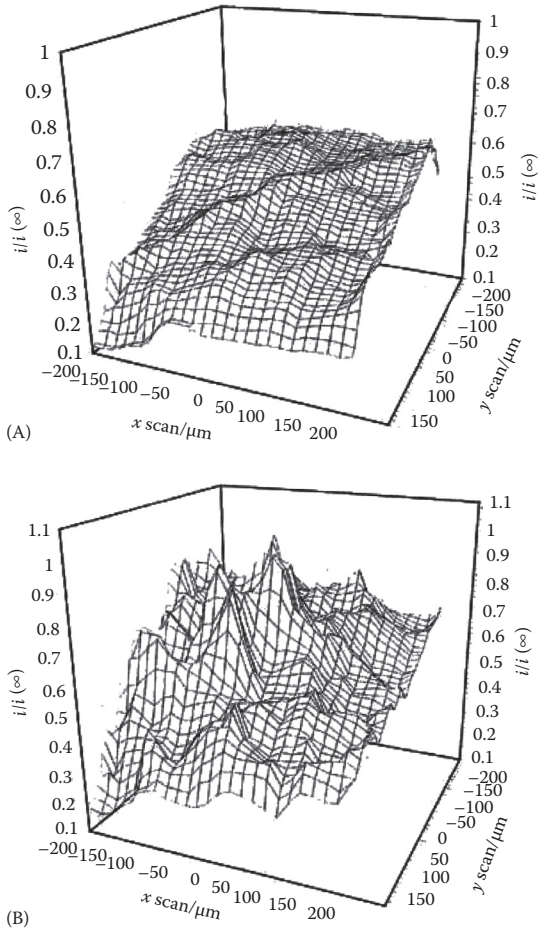


FIGURE 9.18 SECM images recorded over a slice of dentine, resulting from oxidation of $Fe(CN)_6^{4-}$. Images were recorded (A) with no pressure applied across the dentine slice and (B) with a fluid pressure of 2 kPa across the slice. The donor and receptor solutions each contain 10 mM $K_4Fe(CN)_6$ and 0.5 M KCl. (Reprinted from Macpherson, J.V. et al., *Langmuir*, 11, 3959, 1995. With permission.)

the surface topography with the high localized diffusive $Fe(CN)_6^{4-}$ flux associated with pores in the dentine. This study shows regions corresponding to pores that are inactive, possibly because of occlusions inside the tubules. Numerical simulations showed how a blocked pore affected the diffusion of a permeant through neighboring pores. The simulated concentration profile above a blocked pore suggests that the permeant that diffuses across the membrane through a neighboring unblocked tubule can be transported into the blocked pore region. A blocked pore then acts as a sink of the permeant and the tip current is greatly reduced in the surrounding regions of the SECM image where a blocked pore exists.

9.3.2.1.2 Laryngeal Cartilage

Macpherson et al. have used SECM to study molecular transport in laryngeal cartilage. Cartilage acts as a load-bearing material in the human body. Understanding transport mechanisms in this material is of interest for several reasons. First, the rate at which water is redistributed under applied loads determines the viscoelastic properties of the material. Second, the physiological functioning of the material is determined by the diffusive–convective transport of nutrients and metabolites.[13]

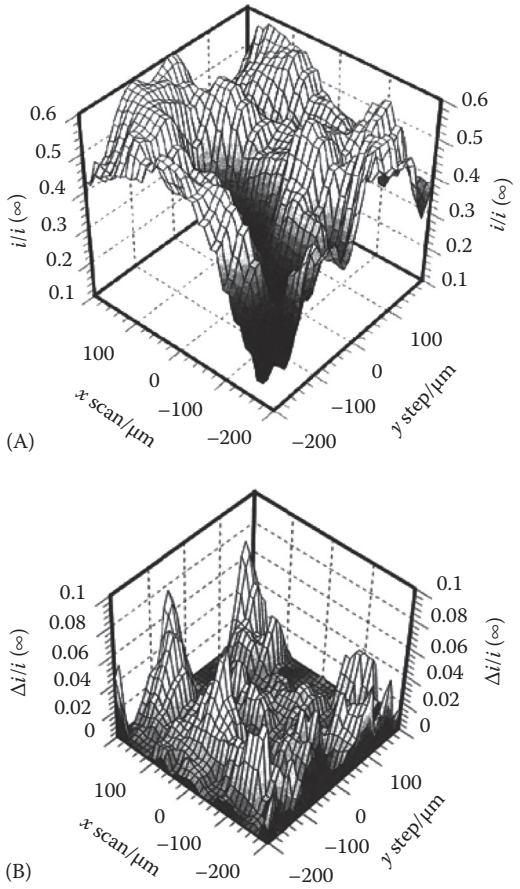


FIGURE 9.19 SECM images of a sample of cartilage (A) in the absence (topographical image) or (B) in the presence of an applied osmotic pressure, $P = 0.75$ atm, across the sample (image of the permeant flux). The image corresponds to the reduction of $Ru(NH_3)_6^{3+}$ at the tip above the cartilage surface. The donor and receptor solutions each contain 10 mM $Ru(NH_3)_6Cl_3 + 0.2$ M KNO_3. (From Macpherson, J.V. et al., *Biophys. J.*, 73, 2771, 1997. With permission.)

Figure 9.19A shows an SECM image of a thin slice of cartilage obtained with the sample mounted in a diffusion cell. The donor and receptor compartments contain identical solutions of the redox mediator $Ru(NH_3)_6^{3+}$. In this *negative feedback mode*, the tip current is purely a function of the tip-to-sample separation[39] and images acquired in this mode reveal the heterogeneous cartilage surface. The current image is transformed into a topographical image using the empirical expression:

$$\frac{d}{a} = 0.984[i_t]^2 + 0.7876[i_t] + 0.0532 \tag{9.15}$$

where

d is the tip-to-sample separation
a is the radius of a pore

An SECM image is then obtained with an osmotic pressure difference equivalent to 0.75 atm applied across the sample by dissolving polyethylene glycol in the receptor compartment. The pressure induced fluid flow across the sample, and SECM images reflect both surface topography and the flux of $Ru(NH_3)_6^{3+}$ across the sample. This image is corrected for the topography of the cartilage

sample by subtracting the current response in the absence of osmotic pressure. The resulting image (Figure 9.19B) is plotted as $\Delta i_t/i_{t\infty}$, where Δi_t is the difference in currents in the presence and absence of the pressure gradient. This image is a visualization of the transport of $Ru(NH_3)_6^{3+}$ away from the cartilage surface due to convective fluid flow. A model is proposed to convert values of $\Delta i_t/i_{t\infty}$ to a flux, *N*. In the cartilage sample surface, the active transport areas in the flux image (high Δi_t in Figure 9.19B) appear to be correlated with recessed areas in the topographical image (low i_t in Figure 9.19A). The results suggest that fluid flow follows paths around the cells at the surface of the cartilage sample.

9.3.2.2 Iontophoresis across Skin

The ability to deliver drugs through the skin at well-defined controlled rates has been a goal in the pharmaceutical community for many years. A promising technique for reaching this goal is iontophoresis. In iontophoresis, a potential difference is applied between two electrodes that are placed in contact with the skin. The drug molecule, which can be either an ion or a neutral molecule, is contained in a solution beneath one of the electrodes. An electric current is driven across the skin tissue, resulting in the transdermal transport of the drug. Ionic molecules are transported across the skin by diffusive-migrational transport. The transport of neutral molecules can also be enhanced by the electric current. The reason for this is that skin tissue has a net negative charge at physiological pH,[51] and behaves as an ion-selective membrane. As with synthetic ion-selective membranes, for example, Nafion, electroosmotic flow occurs in skin when a current is passed through it. However, skin is a very complex membrane, and molecular transport across it is localized to a small number of active sites. This section briefly describes the use of SECM to determine the pathways and mechanisms of molecular transport across skin tissues during iontophoresis.

A section of excised skin tissue is placed in the diffusion cell described in Figure 9.11 and imaged in the *tip collection mode*. The donor compartment contains a redox-active species that is transported across the tissue due to the concentration gradient or an applied current. The two large Ag/AgCl electrodes and a galvanostat are used to drive the iontophoretic current across the skin.

Investigations of molecular transport across skin using SECM were first performed by Scott et al. to identify regions of localized transport.[7] Figure 9.2 shows an SECM image of a 1 mm^2 region of hairless mouse skin (HMS). The tip current corresponds to the oxidation of $Fe(CN)_6^{4-}$ above the skin surface in the receptor compartment and transported from the donor compartment. The bright region in Figure 9.2 shows that iontophoretic transport of $Fe(CN)_6^{4-}$ is highly localized, occurring through discrete pores in skin. These pores have been shown to correspond to individual hair follicles, as determined by optical microscopy[52] or from combined SECM and laser scanning confocal microscopy for human skin.[53] The corresponding isoconcentration contours for $Fe(CN)_6^{4-}$ above a mouse hair follicle are shown in Figure 9.20. Using this data set and the method of analysis discussed in Section 9.2.1, a pore radius of 13 μm and a mass transport rate for $Fe(CN)_6^{4-}$ of 1.6×10^{-13} mol/s were determined for this pore.[7]

Scott et al. also performed experiments examining *competitive* molecular transport through a hair follicle in HMS.[14] In these experiments, both Fe^{2+} and Fe^{3+} are present in the donor compartment, and are simultaneously transported across the skin sample. Figure 9.21 shows a series of one-dimensional SECM line scans (length = 500 μm) across the center of a hair follicle. The line scans are offset on the *x*-axis by the potential at which the SECM tip is held while recording the scan. Fe^{3+} is reduced at the tip at the diffusion-controlled rate when the SECM tip is biased to a value negative of ~0.5 V vs. Ag/AgCl. Thus, the peak heights in this potential region are directly proportional to the flux of Fe^{3+} through the hair follicle. Increasing the tip potential to values positive of 0.5 V results in diffusion-controlled oxidation of Fe^{2+}. The peak heights in this potential region are proportional to the flux of Fe^{2+} in the hair follicle. The envelope of the peak heights for Fe^{3+} and Fe^{2+} transport resembles a conventional voltammetric response. The current envelope suggests that the rate of transport of Fe^{2+} through the hair follicle is about 50% greater than that of Fe^{3+} (the diffusivities of these two species are within 20% of each other in a homogeneous solution). Thus, the

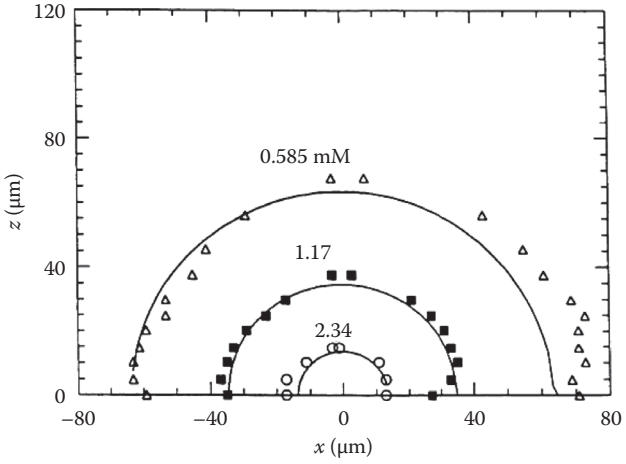


FIGURE 9.20 SECM isoconcentration lines above a pore in skin. The concentration of $Fe(CN)_6^{4-}$ corresponding to each isoconcentration line is given in the figure. The least-squares fits to the data are shown as solid lines. $i_{app} = 40\,\mu A/cm^2$. (From Scott, E.R. et al., *J. Invest. Derm.*, 104, 142, 1995. With permission.)

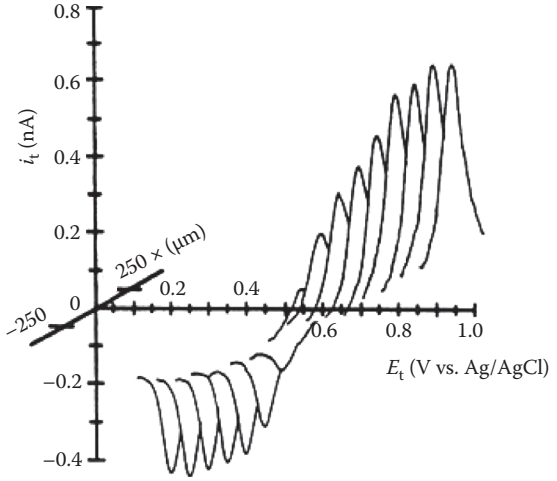


FIGURE 9.21 SECM line profiles above a pore in skin, measured as a function of the tip potential, E_t. Each of the 16 Gaussian-shaped segments is a plot of i_t as a function of the tip position (the x-coordinate). Donor solution: 0.05 M $FeCl_3$ + 0.05 M $FeCl_2$. The anodic currents at $E_t > 0.5$ V vs. Ag/AgCl correspond to detection of Fe^{2+} as it emerges from the pore. The cathodic currents at $E_t < 0.5$ V correspond to detection of Fe^{3+}. (From Scott, E.R. et al., *Solid State Ionics*, 53–56, 176, 1992. With permission.)

difference in the transport rates of these ions in skin suggests that Fe^{2+} and Fe^{3+} interact to different degrees with the pore structures comprising skin. In particular, the ionic mobility of Fe^{3+} in skin may be significantly smaller than that of Fe^{2+}.

In order to define the mechanisms by which molecules traverse the skin, the iontophoretic molecular transport of neutral or charged permeants through hair follicles of HMS[54,55] or through skin tissues of human cadaver[53] has been investigated. For example, Figure 9.22 shows the transient response following changes in the applied iontophoretic current, i_{app}, of the SECM detection of acetaminophen transport above a pore opening in different parts of human skin.[53] A full thickness of human skin is considered in Figure 9.22A while only the excised superficial part (the 200 μm thick stratum corneum) of human skin is considered in Figure 9.22B. In the absence of iontophoresis

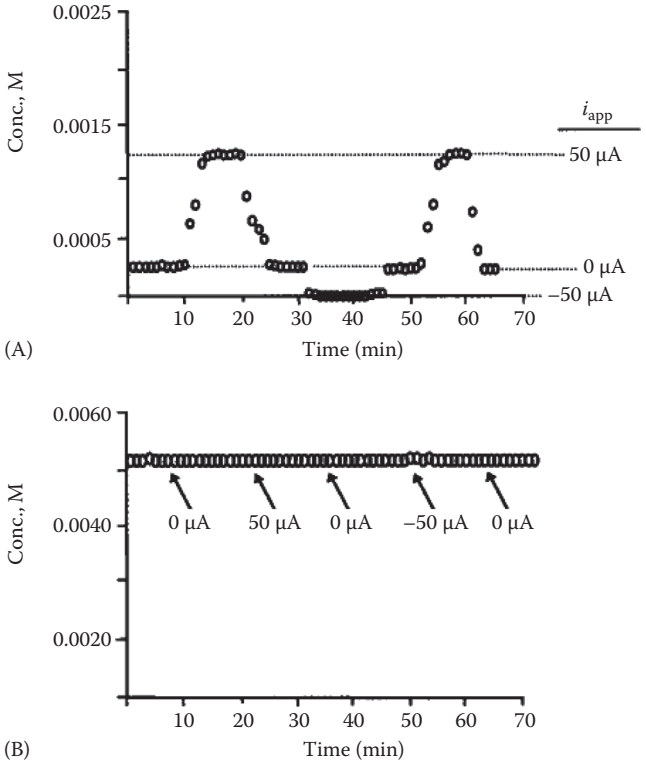


FIGURE 9.22 Plot of acetaminophen concentration directly above a pore opening in (A) full thickness human skin or (B) human stratum corneum while switching i_{app} the iontophoretic current between −50, 0, and 50 μA. Donor solution: 0.2 mM acetaminophen + 0.2 M NaCl, receptor 0.2 M NaCl. Electroosmotic flows can be generated in (A) but not in (B). (From Uitto, O.D. and White, H.S., *Pharm. Res.*, 20, 646, 2003. With permission.)

(i_{app} = 0 μA), acetaminophen is transported by diffusion across the skin. A lower concentration is detected above the full thickness of the skin (Figure 9.22A) suggesting a significant diffusional barrier in the lower dermal region. The application of iontophoretic currents is followed by changes in acetaminophen flux above the full thickness of skin while through the stratum corneum it has no effect. Across the full thickness of skin, as for "mica/Nafion" membrane (Figure 9.22), anodic iontophoresis (i_{app} = 50 μA) yields preferential cation transport from the donor to the receptor compartment. An electroosmotic flow in the direction of diffusion enhances significantly the concentration above the pore opening. Reversing the electroosmotic flow (i_{app} = −50 μA) reduces the neutral solute transport to nearly background levels, as indicated by the small concentration detected by SECM. Measurements across the mouse and human bulk skin tissues have shown a preferential transport of cations. These studies[53–55] suggest that bulk skin is net negatively charged at neutral pH and should exhibit transport behaviors (similar fluxes and electroosmotic velocities) analogous to that of Nafion membranes (see Section 9.3.1.2). The pH-dependent solute transport across HMS was also evidenced, suggesting the pH-dependent permselectivity of HMS is conferred by the charged epithelial cells that decorate the skin pores.[54]

9.3.3 Imaging Transport of Non-Electroactive Species

SECM imaging of the transport of electroinactive species across pores can also be detected by SECM tip selective for a specified target. Different strategies have been developed to extend the

use of potentiometric electrodes, amperometric biosensors, or amperometric micropipettes to the SECM configuration and are reviewed in Chapters 3 and 10. Selective electrodes have been designed to detect specifically the transport of various species across synthetic membranes including protons,[22,56] lead ions, Pb^{2+},[57] nonelectroactive potassium, K^+,[23] or chloride, Cl^-,[24] ions or nonelectroactive species of biological importance such as adenosine-5′-triphosphate, ATP,[25] or glucose.[26] The use of SICM also affords the opportunity to image and quantify local K^+ and Cl^- ionic fluxes transported across a nanoporous membrane.[21]

9.3.3.1 Use of Potentiometric Probes

The use of small ion-selective SECM probes is generally restrained by the substantial effort required in the preparation of submicrometer-sized electrode tips or in the construction of micropipette-based ion-selective electrodes (ISE). Recently, mechanically robust submicrometer-sized ISE have been prepared from cone-shaped glass nanopore electrodes[58,59] and used to map Cl^- ion transport through a microporous Si membrane.[24] A submicrometer cone-shaped nanopore electrode is obtained from the electrochemical etching in 1.2 M $CaCl_2$ solution of the nanometric tip of a conically sharpened Pt wire surface sealed into a sharpened soda-lime glass capillary. Such cone-shaped glass nanopore structure is ideal for containing an ion-selective layer in order to form relatively stable ion-selective nanoelectrodes. When an Ag layer is electroplated on the Pt electrode in the pore and then gently chloridated, an AgCl/Ag-layer-coated nano-ISE probe sensitive to Cl^- ions is obtained. The AgCl/Ag-based nanopore ISE is stable for 3 days and shows a very fast (<3 s) potentiometric response to Cl^-. The nanopore ISE was then rastered 20 μm above a Si membrane to map Cl^- ion flux from a donor compartment (0.1 M KCl) to the receptor one (0.05 M Tris–H_2SO_4, pH = 7.4) through a 5 μm diameter pore. Figure 9.23 shows the SECM potentiometric image of the Cl^- ion distribution over the source of the pore. A pore opening of 15 μm diameter is clearly visible in agreement with hemispherical Cl^- diffusion as it emerges from the pore.

9.3.3.2 Selective Amperometric Probes

The investigation of biological systems requires the detection of weak proton fluxes. A strategy for the measurement of local pH in the range 3–7 has been proposed[22] based on the use of a gold

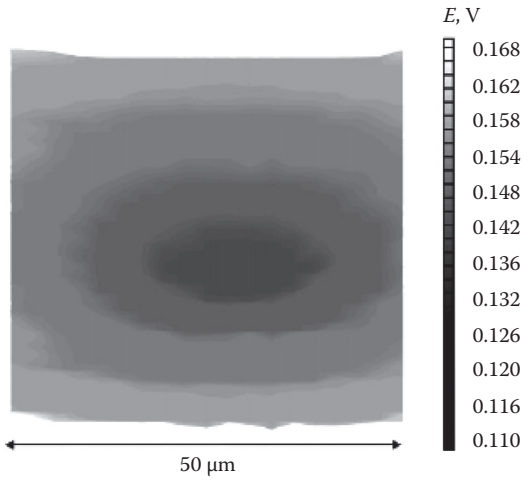


FIGURE 9.23 Potentiometric SECM image at an Ag/AgCl-coated nanopore Pt electrode of Cl^- distribution over a 5 μm diameter hole in a Si membrane. Donor solution: 0.1 M KCl; receptor solution: 0.05 M Tris–H_2SO_4, pH = 7.4. (From Shim, J.H. et al., *Anal. Chem.*, 79, 3568, 2007. With permission.)

ultramicroelectrode (UME) modified with a self-assembled layer (SAM) of HS-$(CH_2)_{10}CO_2H$. The SAM establishes a barrier for the approach of $Fe(CN)_6^{4-}$ to the electrode surface resulting in a pH-dependent blocking of the electron transfer properties (blocking increases with pH).[60,61] Such Au-SAM UME is used to map local pH changes above a track-etched polycarbonate membrane with 8 µm diameter pores held between two solution of the same composition (in electrolyte and $Fe(CN)_6^{4-}$) but different pH; the lower phase has a pH of 8.2 and the upper phase has a pH of 3.3. Imaging is then performed in the negative feedback mode for $Fe(CN)_6^{4-}$, and the contribution of both topographical and local pH changes is obtained by the use of a multiple microelectrodes assembly: an Au-SAM UME detects local pH changes while a bare Pt UME detects the change in $Fe(CN)_6^{4-}$ diffusion hindrance. When the bare Pt UME is rastered across a pore, its current increases as a result of a less hindered region; while the Au-SAM UME senses the same pore region, its current decreases for local H^+ depletion (pH increase). Although this method works in principle, the Au-SAM probe is unstable and more robust systems with more stable and impermeable layers are needed for quantitative analysis.

The imaging of local ATP or glucose fluxes is of particular significance in biological membranes. Dedicated amperometric biosensors are fabricated from the polymer entrapment of a biological recognition element on a tip. The glucose content is obtained from the direct detection of H_2O_2 produced by glucose reaction with immobilized glucose oxidase enzyme:[62]

$$\text{Glucose} + O_2 \xrightarrow{\text{Glucose oxidase}} \text{Gluconic acid} + H_2O_2 \tag{9.16}$$

ATP detection is based on competitive enzymatic reactions of glucose between glucose oxidase (9.16) and hexokinase (9.17), co-immobilized at the tip surface, in the presence of dioxygen and ATP, respectively.[63] At constant glucose concentration, the tip current for the oxidation of H_2O_2 decreases in the presence of ATP due to additional glucose consumption by (9.17). The change in current is then directly proportional to the ATP concentration:

$$\text{Glucose} + \text{ATP} \xrightarrow{\text{Hexokinase}} \text{glucose-6-P} + \text{ADP} \tag{9.17}$$

The ATP or glucose-selective tips are biased at 650 mV vs. Ag/AgCl to detect amperometrically the oxidation of H_2O_2 at diffusion-controlled rate. As the determination of the tip–substrate separation distance is difficult with chemically modified UME, the microbiosensor tip is coupled with an alternative positioning device. The glucose-selective microbiosensor was integrated in an AFM cantilever used for topographical information (see Section 9.3.4.2).[26] The ATP detection was investigated with a dual microelectrode system: the microbiosensor is immobilized on a first UME while the second UME is used to position the electrode assembly at 10 µm from a porous polycarbonate membrane. The ATP-selective tip held in a 3 mM glucose receptor detects the ATP transported across pores from a 1.5 mM ATP donor solution. Figure 9.24 reveals the position of pores as region of lower glucose content. The tip current response suggests hemispherical diffusion of ATP from the pore opening.[25]

Selective amperometric microelectrodes are also obtained from a microinterface between two immiscible electrolyte solutions (ITIES) formed at the tip of a glass micropipette. These micro-ITIES behave as disk UME and allow the quantitative amperometric detection of different ions based on ion-transfer voltammetry. A K^+-selective micro-ITIES successfully imaged the transport of K^+ across a 50 µm diameter pore by SECM.[23]

Even though it is beyond the scope of this book, micropipette electrodes are also used as probes in the SICM to image local ion currents. Recently, the SICM operated with distance-modulated feedback allowed to record simultaneously topographical and local ion current images of ion

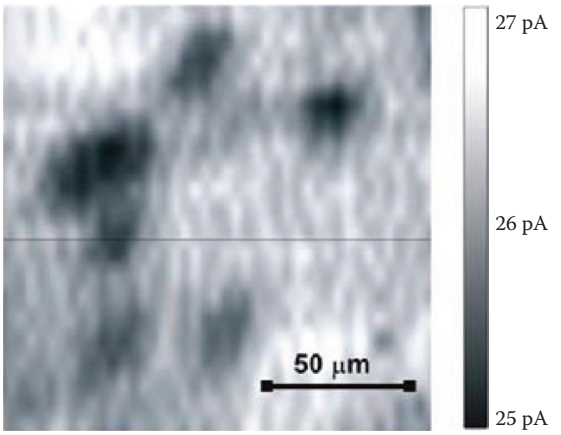


FIGURE 9.24 SECM image of ATP diffusion across a porous polycarbonate membrane (pore size 20 μm). The ATP-selective biosensing tip biased at H_2O_2 oxidation potential (650 mV vs. Ag/AgCl) scanned the membrane at constant height (10 μm) in a receptor solution (3 mM glucose + 5 mM $MgCl_2$ phosphate buffer); donor solution: 5 mM ATP in phosphate buffer. (From Kueng, A. et al., *Biosens. Bioelectron*., 21, 346, 2005. With permission.)

transport across nanoporous membranes with submicrometer resolution. The ion current profiles above single 300 nm diameter nanopores were interpreted quantitatively using formalism similar to that presented in Section 9.2.4 for the expression of ion flux and currents.[21]

9.3.3.3 Alternating Current Impedance Imaging

Images of the transport of nonelectroactive ions across a membrane can also be performed by alternating current impedance using SECM.[64,65] In this configuration, no redox-active species is required and in principle much faster transport dynamics should be accessible. Both advantages are important for measuring transport across biological membranes. The ac impedance SECM is based on the measurement of the variation in the electric impedance as a small tip is scanned over a surface. It has been applied for the SECM imaging of the topographical and electric properties of various surfaces.[66,67] As shown schematically in Figure 9.25, in ac impedance imaging of a pore opening, the SECM tip is placed in a receptor compartment (1 mM KCl) of a diffusion cell and is rastered above a porous membrane. The donor compartment (10 mM KCl) on the opposite side of the membrane contains a large counter electrode. An ac potential, $V_{in} = 10$ mV, is applied between the tip and the counter electrode, and the tip ac current response, i_{ac}, is measured and transformed into ac impedance, R, from Ohm law ($i_{ac} = V_{in}/R$). The pore opening region is associated with tip current increase (Figure 9.26) or an impedance decrease as the tip senses the facilitated ionic path provided by the pore in the membrane. To detect a pore opening, the total impedance between the tip and the counter electrode should change significantly when the tip passes over it. It is then expected that the ac impedance images have higher contrast when the membrane is less resistant to ionic transport, that is, when the membrane contains a larger number of pores. This is confirmed by Figure 9.26A through C that shows the SECM impedance images of the large opening (2.5 μm) of an individual cone-shaped pore in a 6 μm thick membrane containing 2000, 1000, and 1 pore(s). Indeed, when the pore density is decreased, the resolution of a pore opening is decreased (Figure 9.26C). In order to increase the contrast of the ac-SECM image, one can artificially increase the number of pores of the membrane by creating a bypass channel. This is easily accomplished by connecting the solutions in the two opposite sides of the membrane with a salt bridge (a shunt) and as shown in Figure 9.26D a single pore can now be resolved.

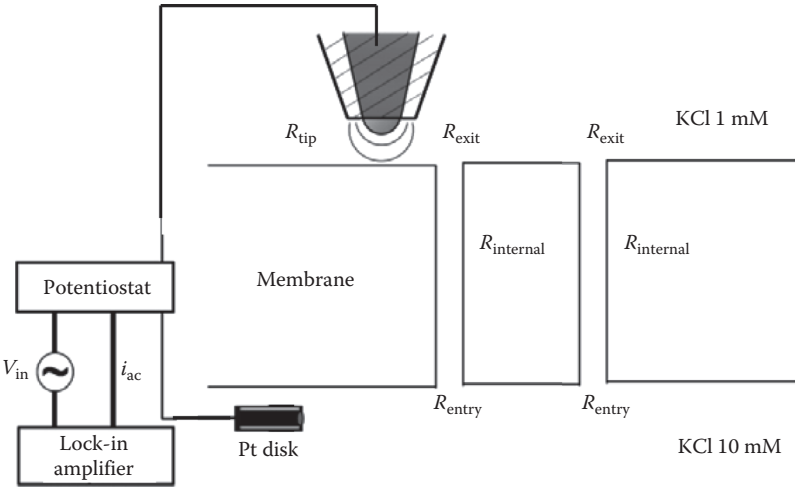


FIGURE 9.25 Schematic description of the experimental setup for ac impedance SECM imaging with the resistances that contribute to the total impedance as the tip is scanned above a porous membrane. (Adapted from Ervin, E.N. et al., *Anal. Chem*., 78, 6535, 2006.)

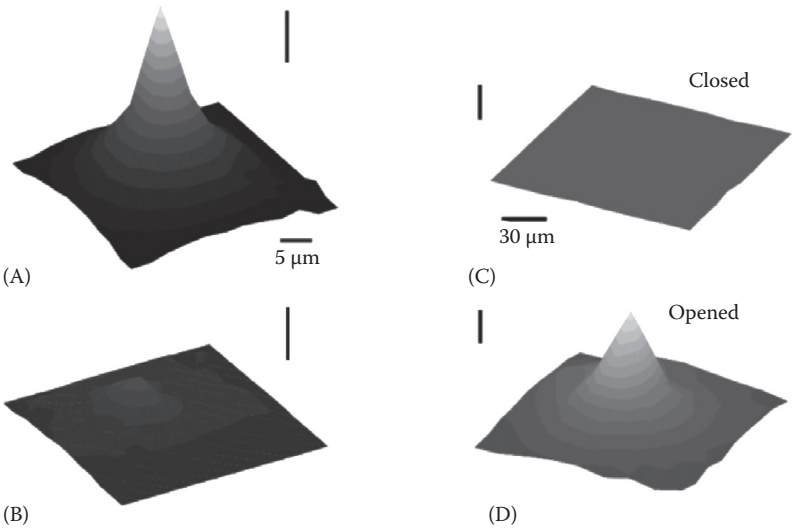


FIGURE 9.26 SECM impedance images of the large opening (2.5 µm) of an individual cone-shaped pore in an ~6 µm thick membrane containing (A) 2000, (B) 10, and (C and D) 1 pores. (C and D) are obtained with a bypass channel, closed or opened, respectively. Pt tip (1 µm) in the receptor phase (1 mM KCl) is biased with an ac input signal $V_{in} = 10$ mV, $f = 1$ kHz; donor phase: 10 mM. The images are normalized to their respective current measured far from the pore opening. Vertical bars 0.1; the absolute value of the current far from the pore: (A) 4.3, (B) 0.1, (C) 0.08, and (D) 5 nA. (Adapted from Ervin, E.N. et al., *Anal. Chem*., 78, 6535, 2006.)

These observations have been explained from a simple electric model of the resistive paths implied (see Figure 9.25) and the total impedance for such a membrane with N identical pores is the impedance of the tip, R_{tip}, in series with N parallel porous ionic pathways, which can be decomposed into a pore exit, internal and entrance resistances in series, respectively, R_{exit}, $R_{internal}$, and R_{entry}. It is then considered that, when the tip rasters a pore region, only the resistances of the tip, R_{tip}, and of the rastered pore exit, R_{exit}, are changed. In order to be observed, a pore needs to induce a significant

change in $R_{tip}+R_{exit}$ compared to the membrane resistance, approximately equal to $R_{internal}/N$. Thus, increasing the pore density, N (e.g., by opening a bypass or imaging membranes with higher pore number) greatly improves the ac-SECM image contrast.[65]

9.3.4 Imaging Single Nanopores

Resolving membrane transport at the nanometer scale is a major requisite for scaling down the investigation of solute transport across many biological membranes and artificial nanoporous structures. As presented in Chapters 3 and 4, electrochemical imaging with submicrometer resolution uses combined SECM and scanning force microscopy (mainly atomic force microscopy [AFM]), where the probe contains an electrode component for the electrochemical imaging and a force sensor for high-resolution topographical imaging. These SECM-AFM combined imaging systems resolved molecular transport across nanoporous membranes (pore radius < 1 μm).[26,68–71] The AFM image, generally recorded in the contact mode, provides the topography of individual nanopores in nanoporous membranes, while the electrochemical imaging, performed either in air or in solution, describes the ion transport rates.

9.3.4.1 Nanopore Images in Air

In the first experiment performed in air, a simple Pt-coated Si AFM tip serving as the SECM-AFM probe is rastered above a membrane whose nanopores are wetted and filled from below by an electrolytic solution containing a redox probe.[68,69] A current is measured when only the apex of the biased probe contacts a nanodomain of solution confined at the exit of the filled nanopores. This confinement of the solution requires imaging under minimal contact force. Figure 9.27 presents the topographical and electrochemical images obtained simultaneously for a nanoporous track-etched polycarbonate membrane. The AFM (Figure 9.27A) clearly identifies 100 nm diameter nanopores in

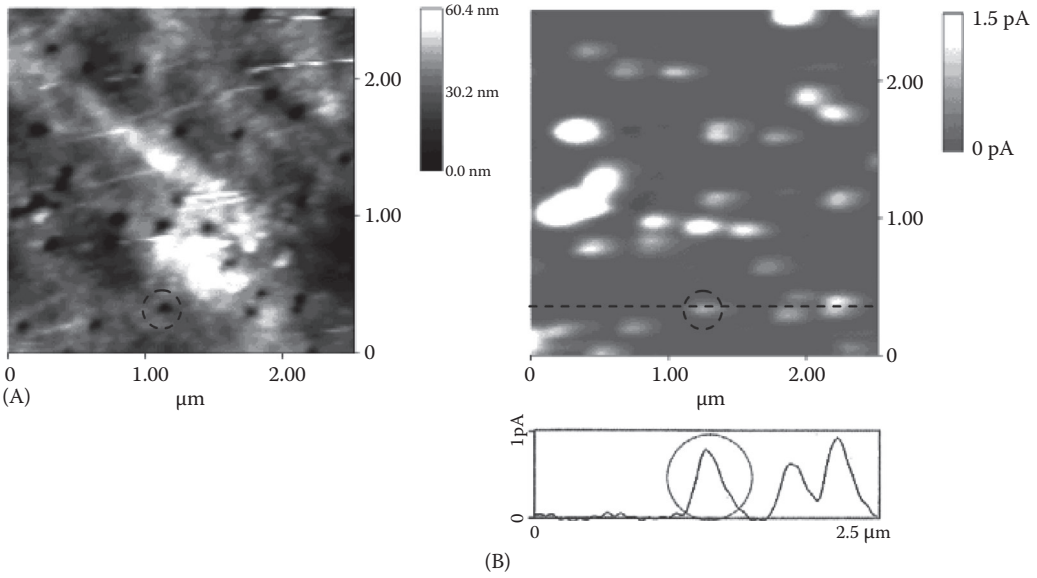


FIGURE 9.27 (A) Height and (B) current images of a wetted tracked etched polycarbonate membrane acquired in air with a Pt-coated Si SECM-AFM tip. The tip is biased at +1 V vs. Ag/AgCl, the wetting solution contained 10 mM $IrCl_6^{3-}$ + 0.5 M KNO_3. Cross-sectional tip current along the dashed line across the center of single (encircled) isolated pores. (From Macpherson, J.V. et al., *Anal. Chem*., 74, 1841, 2002. With permission.)

the membrane. Meanwhile, in Figure 9.27B, these pores correspond to high tip current as a result of the transport of $IrCl_6^{3-}$. Even if the tip movement drags the solution out of the pores and alters the resolution of the electrochemical image, nanopores are addressed individually. The SECM-AFM tip, in air, quantitatively probes the diffusional transport through single nanopores as the maximum tip current detected at a single pore is comparable to the limiting current that the pore can sustain during the diffusion-controlled electrolysis of $IrCl_6^{3-}$. This situation is electrochemically equivalent to the diffusion-limited oxidation of $IrCl_6^{3-}$ at a recessed microdisk electrode of length and radius, the pore length, l, and radius, a, and $i_{lim} = 4\pi nFCD\dfrac{a^2}{4l + \pi a}$.[72]

9.3.4.2 Nanopore Imaging in Solution

When the SECM-AFM experiments are performed in solution,[26,70,71] the electrochemical imaging with submicrometer resolution is more demanding in the tip preparation and insulation steps as a micron- or submicron-sized electrode should be incorporated in the AFM probe. The tips used to image molecular transport across membrane were either hand-fabricated etched, flattened, and insulated Pt microwires[70,71] or a metal-coated rather than insulator-coated conventional AFM tip redesigned by focused ion beam.[26,73]

The first demonstration of SECM-AFM imaging of redox transport across a polycarbonate membrane (pore size 0.6–1.2 μm) from a donor to a receptor solution phases was performed by Macpherson and Unwin.[70] A cone-shaped SECM-AFM tip (radius: 275 nm, height: 550 nm) was used to obtain height and current images of track-etched membrane; the images were simultaneously obtained at the tip–membrane contact either in the negative feedback or the tip collection mode. In the negative feedback mode, a pore is associated with a tip current decrease. Indeed, as the tip scans a pore, it may partially close its entrance resulting in a depletion or hindrance of the redox probe diffusion. In the tip collection mode, the diffusional transport of a redox probe across individual pore is associated with a current increase in qualitative agreement with Section 9.2, while obstructed pores are associated with a current decrease. This study demonstrated the advantage of combining simultaneous topographical image with electrochemical characterization of a porous membrane, for example, to estimate the real density of unobstructed nanopores.

For quantitative electrochemical analysis, the constant height SECM imaging mode[71] should be preferred to the contact one.[70] Figure 9.28 presents the iontophoretic transport of $Fe(CN)_6^{4-}$ across a track-etched PET membrane imaged at a 0.65 μm radius SECM-AFM Pt tip held at a constant

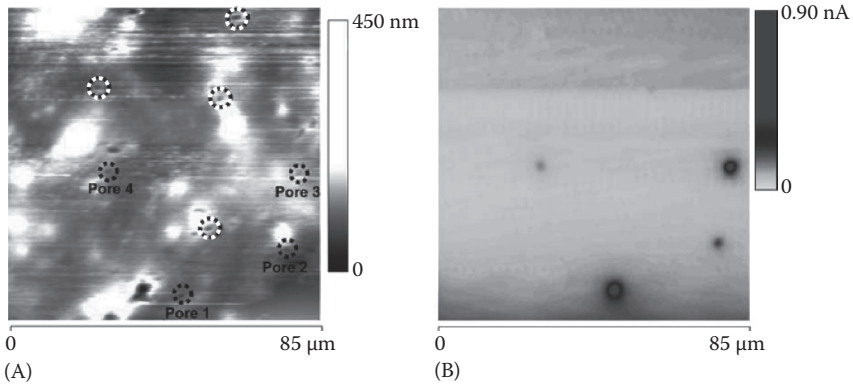


FIGURE 9.28 SECM-AFM topography (A) and constant height (1 μm) current image (B) of the structure and iontophoretic transport of $Fe(CN)_6^{4-}$ across a PET membrane. The SECM-AFM tip is placed in the receptor phase (0.1 M KCl). Donor phase: 0.1 M $Fe(CN)_6^{4-}$ + 0.1 M KCl + 1 μL/mL Triton. The topographical image is acquired in contact mode (tip unbiased). White/dark circles highlight obstructed (inactive)/active pores. (From Gardner, C.E. et al., *Electrochem. Commun.*, 7, 612, 2005. With permission.)

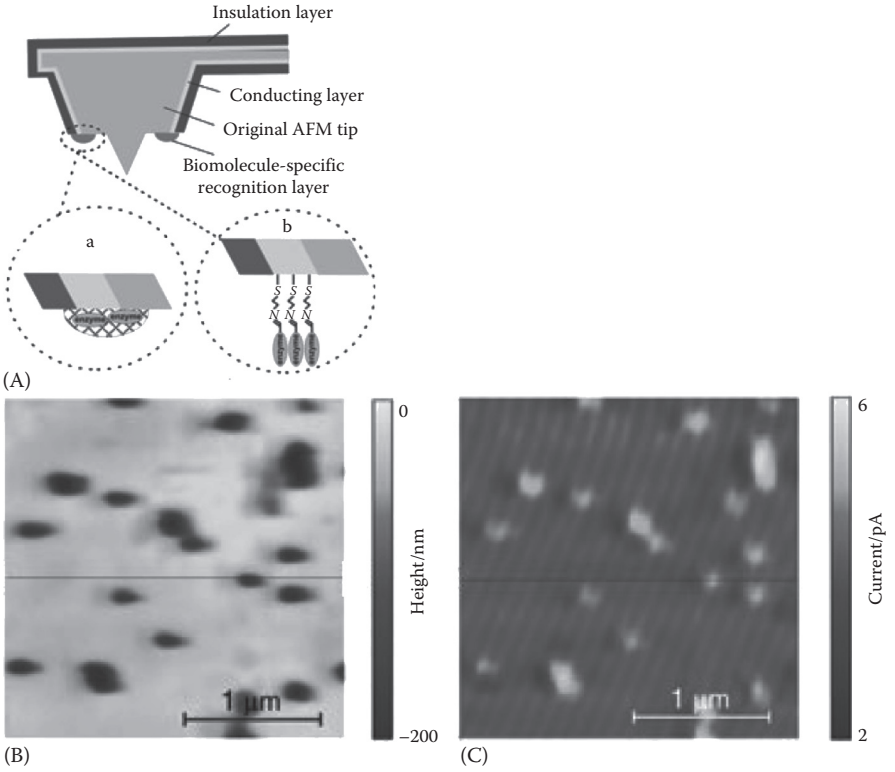


FIGURE 9.29 (A) Schematic cross section of the AFM-tip-integrated glucose-selective biosensor: glucose oxidase is immobilized (a: cast in polymer or b: covalently) at the electrode surface for glucose detection. SECM-AFM topography (B) and current image (C) of glucose diffusion across a porous PC membrane (pore size: 200 nm) with the biosensing AFM tip. Donor solution: 5 mM glucose. (From Kueng, A. et al., *Angew. Chem. Int. Ed*., 44, 3419, 2005. With permission.)

1 μm height above the membrane.[71] Not all the pores identified in the topographical AFM image (Figure 9.28A obtained in the contact mode) are open across the membrane. The SECM-AFM tip allows high-resolution topographical (~100 nm) image of micrometric pores. The resolution of the electrochemical map approaches that of the AFM image with satisfying quantitative information. At the center of the pore, the value of the tip current nicely fits the expected value for migrational transport during iontophoretic solicitation.

High-resolution topographical and electrochemical imaging of the transport of bioactive material such as glucose across a synthetic membrane with 200 nm diameter pores has also been obtained at microfabricated biosensing SECM-AFM probes (Figure 9.29A)[26]. As the AFM tip is imaging the 200 nm diameter pores of the membrane (Figure 9.29B) in the AFM dynamic mode, the enzyme-immobilized biosensing probe (principle in Section 9.3.3.2) images simultaneously the glucose transport in the collection mode. The electrochemical image (Figure 9.29C) clearly shows that the probe current is higher above pores as a result of a local indirect detection of glucose emergence from pores. The current at the pore opening agrees reasonably with the expected concentration or flux of glucose for diffusional transport across the pore.

9.4 FUTURE DIRECTIONS

SECM-based methods provide unique experimental capabilities for imaging and quantifying the transport of molecular and ionic species in porous membranes, including non-electroactive species

in some instances. No other experimental method or technique currently exists that provides a means to visualize localized molecular flux across a membrane or the ability to quantify transport rates at the single pore level. The transport of molecules from individual pores as small as tens of nanometers has been imaged. Further improvements in resolution are anticipated with the development of procedures that allow the routine fabrication of tips of submicrometer dimensions. The detection of very small numbers of molecules, perhaps even single molecules, as they are transported across membranes may eventually be achieved by combining the concepts outlined in this chapter with scanned probe methods that employ fluorescence-based detection instead of amperometric detection.

The future application of SECM in investigations of transmembrane transport appears very promising. Molecular transport across biological materials has been demonstrated and the results are particularly encouraging. With the development of combined SECM-AFM, it is possible to imagine the imaging of ion fluxes across ion channels in cell membranes. The real-time monitoring capabilities of SECM also provide an unprecedented ability to monitor membrane transport dynamics, an area important in designing membrane-based devices for energy conversion (e.g., fuel cells), as well as in biological systems.

REFERENCES

1. Cussler, E. L. *Diffusion: Mass Transfer in Fluid Systems*, Cambridge University Press, New York, 1997.
2. Engstrom, R. C., Weber, M., Wunder, D. J., Burgess, R., Wenquist, S. Measurements within the diffusion layer using a microelectrode probe. *Anal. Chem*. 1986, 58, 844–848.
3. Engstrom, R. C., Meaney, T., Rople, R., Wightman, R. M. Spatiotemporal description of the diffusion layer with a microelectrode probe. *Anal. Chem*. 1989, 59, 2005–2010.
4. Bard, A. J., Fan, F.-R. F., Kwak, J., Lev, O. Scanning electrochemical microscopy. Introduction and principles. *Anal. Chem*. 1989, 61, 132–138.
5. Bard, A. J., Fan, F.-R. F., Mirkin, M. V. Scanning electrochemical microscopy. In *Electroanalytical Chemistry*, Vol. 18, Bard, A. J., Ed., Marcel Dekker, New York, 1994, p. 243.
6. Fan, F.-R. F., Bard, A. J. Electrochemical detection of single molecules. *Science* 1995, 267, 871–874.
7. Scott, E. R., White, H. S., Phipps, J. B. Measurement of iontophoretic transport through porous membranes using scanning electrochemical microscopy: Application to in vitro studies of ion fluxes through skin. *Anal. Chem*. 1993, 65, 1537–1545.
8. Scott, E. R., White, H. S., Phipps, J. B. Scanning electrochemical microscopy of a porous membrane. *J. Membr. Sci*. 1991, 58, 71–87.
9. Nugues, S., Denuault, G. Scanning electrochemical microscopy: Amperometric probing of diffusional ion fluxes through porous membranes and human dentine. *J. Electroanal. Chem*. 1996, 408, 125–140.
10. Bath, B. D., Lee, R. D., White, H. S., Scott, E. R. Imaging molecular transport in porous membranes. Observation and analysis of electroosmotic flow in individual pores using the scanning electrochemical microscope. *Anal. Chem*. 1998, 70, 1047–1058.
11. Macpherson, J. V., Beeston, M. A., Unwin, P. R., Hughes, N. P., Littlewood, D. Scanning electrochemical microscopy as a probe of local fluid flow through porous solids. *J. Chem. Soc. Faraday Trans*. 1995, 91, 1407–1410.
12. Macpherson, J. V., Beeston, M. A., Unwin, P. R., Hughes, N. P., Littlewood, D. Imaging the action of fluid flow blocking agents on dentinal surfaces using a SECM. *Langmuir* 1995, 11, 3959–3963.
13. Macpherson, J. V., O'Hare, D., Unwin, P. R., Winlove, C. P. Quantitative spatially resolved measurements of mass transfer through laryngeal cartilage. *Biophys. J*. 1997, 73, 2771–2781.
14. Scott, E. R., White, H. S., Phipps, J. B. Direct imaging of ionic pathways in stratum corneum using scanning electrochemical microscopy. *Solid State Ionics* 1992, 53–56, 176–183.
15. Scott, E. R., Laplaza, A. I., White, H. S., Phipps, J. B. Transport of ionic species in skin. Contribution of pores to the overall skin conductance. *Pharm. Res*. 1993, 10, 1699–1709.
16. Scott, E. R., Phipps, J. B., White, H. S. Direct imaging of molecular fluxes through skin. *J. Invest. Derm*. 1995, 104, 142–145.
17. Uitto, O. D., White, H. S. Scanning electrochemical microscopy of membrane transport in the reverse imaging mode. *Anal. Chem*. 2001, 73, 533–539.

18. Uitto, O. D., White, H. S., Aoki, K. Diffusive–convective transport into a porous membrane. A comparison of theory and experiment using scanning electrochemical microscopy operated in the reverse imaging mode. *Anal. Chem*. 2002, 74, 4577–4582.
19. Burnette, R. R., Ongpipattanakul, B. Characterization of the pore transport properties and tissue alteration of excised human skin during iontophoresis. *J. Pharm. Sci*. 1988, 77, 132–137.
20. Hansma, P. K., Drake, B., Marti, O., Gould, S. A. C., Prater, C. B. The scanning ion conductance microscopy. *Science* 1989, 243, 641–644.
21. Chen, C. C., Derylo, M. A., Baker, L A. Measurement of ion currents through porous membranes with scanning ion conductance microscopy. *Anal. Chem*. 2009, 81, 4742–4751.
22. Baltes, N., Heinze, J. Imaging local proton fluxes through a polycarbonate membrane by using scanning electrochemical microscopy and functionalized alkanethiols. *ChemPhysChem* 2009, 10, 174–179.
23. Evans, N. J., Gonsalves, M., Gray, N. J., Barker, A. L., Macpherson, J. V., Unwin, P. R. Local amperometric detection of K^+ in aqueous solution using scanning electrochemical microscopy ion-transfer voltammetry. *Electrochem. Commun*. 2000, 2, 201–216.
24. Shim, J. H., Kim, J., Cha, G. S., Nam, H., White, R. J., White, H. S., Brown, R. B. Glass nanopore-based ion-selective electrodes. *Anal. Chem*. 2007, 79, 3568–3574.
25. Kueng, A., Kranz, C., Mizaikoff, B. Imaging of ATP membrane transport with dual micro-disk electrodes and scanning electrochemical microscopy. *Biosens. Bioelectron*. 2005, 21, 346–353.
26. Kueng, A., Kranz, C., Lugstein, A., Bertagnolli, E., Mizaikoff, B. AFM-tip-integrated amperometric microbiosensors: High-resolution imaging of membrane transport. *Angew. Chem. Int. Ed*. 2005, 44, 3419–3422.
27. Lee, S., Zhang, Y., White, H. S., Harrell, C. C., Martin, C. R. Electrophoretic capture and detection at the opening of a membrane pore using scanning electrochemical microscopy. *Anal. Chem*. 2004, 76, 6108–6115.
28. White, R. J., White, H. S. Influence of electrophoresis waveforms in determining stochastic nanoparticle capture rates and detection sensitivity. *Anal. Chem*. 2007, 79, 6334–6340.
29. Breslau, B. R., Miller, I. F. A hydrodynamic model for electroosmosis. *Ind. Eng. Chem. Fundam*. 1971, 10, 554–565.
30. Probstein, R. F. *Physiochemical Hydrodynamics*, Butterworth, New York, 1989.
31. Sims, S. M., Higuchi, W. I., Peck, K. Ionic partition coefficients and electroosmotic flow in cylindrical pores: Comparison of the predictions of the Poisson–Boltzmann equation with experiment. *J. Colloid Interface Sci*. 1993, 155, 210–220.
32. Pikal, M. J. The role of electroosmotic flow in transdermal iontophoresis. *Adv. Drug Deliv. Rev*. 1992, 9, 201–237.
33. Srinivasan, V., Higuchi, W. I. A model for iontophoresis incorporating the effect of convective solvent flow. *Int. J. Pharm*. 1990, 60, 133–138.
34. Crank, J. *The Mathematics of Diffusion*, Oxford University Press Inc., New York, 1956.
35. Bard, A. J., Faulkner, L. R., Eds., *Electrochemical Methods*, John Wiley & Sons, New York, 1980.
36. Saito, Y. Theoretical study on the diffusion current at the stationary electrodes of circular and narrow band types. *Rev. Polarogr*. 1968, 15, 177–187.
37. Guo, J., Amemiya, S. Permeability of the nuclear envelope at isolated *Xenopus* oocyte nuclei studied by scanning electrochemical microscopy. *Anal. Chem*. 2005, 77, 2147–2156.
38. Kim, E., Xiong, H., Striemer, C. C., Fang, D. Z., Fauchet, P. M., McGrath, J. L., Amemiya, S. A structure–permeability relationship of ultrathin nanoporous silicon membrane: A comparison with the nuclear envelope. *J. Am. Chem. Soc*. 2008, 130, 4230–4231.
39. Kwak, J., Bard, A. J. Scanning electrochemical microscopy. Theory of the feedback mode. *Anal. Chem*. 1989, 61, 1221–1227.
40. White, H. S., Bath, B. D., Scott, E. R. Imaging molecular transport across membranes. In *Scanning Electrochemical Microscopy*, 1st edn., Bard, A. J., Mirkin, M. V., Eds., Marcel Dekker, New York, 2001, pp. 343–395.
41. Springer, T. E., Zawodzinski, T. A., Gottesfeld, S. Polymer electrolyte fuel cell model. *J. Electrochem. Soc*. 1991, 138, 2334–2342.
42. Ren, X., Henderson, W., Gottesfeld, S. Electroosmotic drag of water in ionomeric membranes. *J. Electrochem. Soc*. 1997, 144, L267–L270.
43. Barker, A. L., Macpherson, J. V., Slevin, C. J., Unwin, P. R. Scanning electrochemical microscopy (SECM) as a probe of transfer processes in two-phase systems: Theory and experimental applications of SECM-induced transfer with arbitrary partition coefficients, diffusion coefficients, and interfacial kinetics. *J. Phys. Chem. B* 1998, 102, 1586–1598.

44. Pintauro, P. N., Bennion, D. Mass transport of electrolytes in membranes. 2. Determination of sodium chloride equilibrium and transport parameters for Nafion. *Ind. Eng. Chem. Fundam*. 1984, 23, 234–243.
45. Verbrugge, M. W. Methanol diffusion in perfluorinated ion-exchange membranes. *J. Electrochem. Soc*. 1989, 136, 417–423.
46. Verbrugge, M. W. Ion and solvent transport in ion-exchange membranes. *J. Electrochem. Soc*. 1990, 137, 886–893.
47. Lakshminarayaniah, N. Transport phenomena in artificial membranes. *Chem. Rev*. 1965, 65, 491–565.
48. Bath, B. D., White, H. S., Scott, E. R. Electrically facilitated molecular transport analysis of the relative contributions of diffusion, migration, electroosmosis to solute transport in an ion-exchange membrane. *Anal. Chem*. 2000, 72, 433–442.
49. Li, N., Yu, S., Harrell, C. C., Martin, C. R. Conical nanopore membranes. Preparation and transport properties. *Anal. Chem*. 2004, 76, 2025–2030.
50. Macpherson, J. V., Unwin, P. R. Scanning electrochemical microscopy as an in vitro technique for measuring convective flow rates across dentine and the efficacy of surface blocking treatments. *Electroanalysis* 2005, 17, 197–204.
51. Burnette, R. R., Marrero, D. Comparison between the lontophoretic and passive transport of thyrotropin releasing hormone across excised nude mouse skin. *J. Pharm. Sci*. 1986, 75, 738–743.
52. Lee, R. D., White, H. S., Scott, E. R. Visualization of iontophoretic transport paths in synthetic and animal skin models. *J. Pharm. Sci*. 1996, 85, 1186–1190.
53. Uitto, O. D., White, H. S. Electroosmotic pore transport in human skin. *Pharm. Res*. 2003, 20, 646–652.
54. Bath, B. D., White, H. S., Scott, E. R. Visualization and analysis of electroosmotic flow in hairless mouse skin. *Pharm. Res*. 2000, 17, 471–475.
55. Bath, B. D., Scott, E. R., Phipps, J. B., White, H. S. SECM of iontophoretic transport in hairless mouse skin. Analysis of the relative contributions of diffusion, migration, and electroosmosis to transport in hair follicles. *J. Pharm. Sci*. 2000, 89, 1537–1549.
56. Kallio, T., Slevin, C., Sundholm, G., Holmlund, P., Kontturi, K. Proton transport in radiation-grafted membranes for fuel cells as detected by SECM. *Electrochem. Commun*. 2003, 5, 561–565.
57. Gyurcsanyi, R. E., Pergel, E., Nagy, R., Kapui, I., Thu Lan, B. T., Toth, K., Bitter, I., Lindner, E. Direct evidence of ionic fluxes across ion-selective membranes: A scanning electrochemical microscopic and potentiometric study. *Anal. Chem*. 2001, 73, 2104–2111.
58. Zhang, B., Zhang, Y., White, H. S. The nanopore electrode. *Anal. Chem*. 2004, 76, 6229–6238.
59. Zhang, B., Zhang, Y., White, H. S. Steady-state voltammetric response of the nanopore electrode. *Anal. Chem*. 2006, 78, 477–483.
60. Bolt, F. M., Baltes, N., Borgwarth, K., Heinze, J. Investigation of carboxylic-functionalized and *n*-alkanethiol self-assembled monolayers on gold and their application as pH-sensitive probes using scanning electrochemical microscopy. *Surf. Sci*. 2005, 597, 51–64.
61. Wang, Y., Kaifer, A. E. Interfacial molecular recognition. Binding of ferrocene-carboxylate to β-aminocyclodextrin hosts electrostatically immobilized on a thioctic acid monolayer. *J. Phys. Chem. B* 1998, 102, 9922–9927.
62. Kurzawa, C., Hengstenberg, A., Schuhmann, W. Immobilization method for the preparation of biosensors based on pH shift-induced deposition of biomolecule-containing polymer films. *Anal. Chem*. 2002, 74, 355–361.
63. Anicet, A., Bourdillon, C., Moiroux, J., Savéant, J.-M. Step-by-step avidin–biotin construction of bienzyme electrodes. Kinetic analysis of the coupling between the catalytic activities of immobilized monomolecular layers of glucose oxidase and hexokinase. *Langmuir* 1999, 15, 6527–6533.
64. Ervin, E. N., White, H. S., Baker, L. A. Alternating current impedance imaging of membrane pores using SECM. *Anal. Chem*. 2005, 55, 5564–5569.
65. Ervin, E. N., White, H. S., Baker, L. A., Martin, C. R. Alternating current impedance imaging of high-resistance membrane pores using a SECM. Application of membrane electrical shunts to increase measurement sensitivity and image contrast. *Anal. Chem*. 2006, 78, 6535–6541.
66. Katemann, B. B., Inchauspe, C. G., Castro, P. A., Schulte, A., Calvo, E. J., Schuhmann, W. Precursor sites for localised corrosion on lacquered tinplates visualised by means of alternating current scanning electrochemical microscopy. *Electrochim. Acta* 2003, 48, 1115–1121.
67. Gabrielli, C., Huet, F., Keddam, M., Rousseau, P., Vivier, V. Scanning electrochemical microscopy imaging by means of high-frequency impedance measurements in feedback mode. *J. Phys. Chem. B* 2004, 108, 11620–11626.

68. Jones, C. E., Macpherson, J. V., Barbern, Z. H., Somekh, R. E., Unwin, P. R. Simultaneous topographical and amperometric imaging of surfaces in air: Towards a combined scanning force–scanning electrochemical microscope (SF–SECM). *Electrochem. Commun*. 1999, 1, 55–60.
69. Macpherson, J. V., Jones, C. E., Barker, A. L., Unwin, P. R. Electrochemical imaging of diffusion through single nanoscale pores. *Anal. Chem*. 2002, 74, 1841–1848.
70. Macpherson, J. V., Unwin, P. R. Combined scanning electrochemical–atomic force microscopy. *Anal. Chem*. 2000, 72, 276–285.
71. Gardner, C. E., Unwin, P. R., Macpherson, J. V. Correlation of membrane structure and transport activity using combined scanning electrochemical–atomic force microscopy. *Electrochem. Commun*. 2005, 7, 612–618.
72. Bond, A. M., Luscombe, D., Oldham, K. B., Zoski, C. G. A comparison of the chronoamperometric response at inlaid and recessed disc microelectrodes. *J. Electroanal. Chem*. 1988, 249, 1–14.
73. Kranz, C., Friedbacher, G., Mizaikoff, B., Lugstein, A., Smoliner, J., Bertagnolli, E. Integrating an ultramicroelectrode in an AFM cantilever: Combined technology for enhanced information. *Anal. Chem*. 2001, 73, 2491–2500.

10 Potentiometric Probes

Guy Denuault, Geza Nagy, and Klara Toth

CONTENTS

10.1 Introduction 276
10.1.1 Brief History of Ion-Selective Electrodes 276
10.1.2 Technical Approaches Developed to Produce Micro-ISE 278
10.1.2.1 Integrated Circuit Technology 278
10.1.2.2 Glass Microelectrodes 279
10.1.2.3 Metallic Electrodes 280
10.1.2.4 Micropipette Liquid Ion-Selective Microelectrodes 280
10.1.3 Fabrication of Micropipette Ion-Selective Microelectrodes 282
10.1.3.1 Early Preparation Methods 282
10.1.3.2 Typical Fabrication Procedure 286
10.1.3.3 Recent Improvements 287
10.2 Basic Theory: $E = F(ln(activity))$ 288
10.3 Properties and Characteristics of Ion-Selective Microelectrodes 290
10.3.1 Potentiometric Response and Detection Limit 290
10.3.2 Selectivity Coefficients 291
10.3.3 Stability and Reproducibility 292
10.3.4 Response Time 292
10.3.5 Handling and Instrumentation 293
10.4 Potentiometric Measurements in Scanning Probe Microscopies other than SECM 294
10.5 Potentiometric Measurements in SECM 294
10.5.1 Asserting the Tip–Substrate Distance 294
10.5.1.1 Switching from Amperometric to Potentiometric Response 294
10.5.1.2 Conductimetric Approach 295
10.5.1.3 Fit to Theoretical Concentration Profiles 298
10.5.1.4 Double Tip Techniques 299
10.5.1.5 Shear Force Control 300
10.5.2 Considerations Specific to the Potentiometric Mode 301
10.5.2.1 Ohmic Drop Effects 301
10.5.2.2 Mapping and Resolution 302
10.5.3 Applications 303
10.5.3.1 Probing pH 303
10.5.3.2 Probing Cl^- 306
10.5.3.3 Probing K^+ 308
10.5.3.4 Probing NH_4^+ 308
10.5.3.5 Probing Ca^{2+} 308
10.6 Conclusion 309
References 310

10.1 INTRODUCTION

Most scanning electrochemical microscopic (SECM) experiments are conducted in the amperometric mode, yet microelectrodes have long been used as potentiometric devices. Not surprisingly, several SECM investigations have been reported where the tip was operated in the potentiometric mode. In this chapter, we present the background necessary to understand the differences between amperometric and potentiometric SECM applications, we report the progress made in the field of potentiometric microelectrodes, we consider the issues specific to the potentiometric mode of SECM, and we highlight some of the studies involving potentiometric SECM tips. Starting with an historical perspective, we highlight the key discoveries that facilitated the development and applications of micropotentiometric probes and include recent improvements in detection limits. We review fabrication recipes and cover basic theoretical principles, properties, and technical operational details. In the second half of this chapter, we discuss SECM potentiometric applications and emphasize differences with the conventional amperometric mode.

Potentiometric probes constitute the oldest form of electrochemical sensors. They can be used to study many chemical species not accessible to voltammetric techniques. In particular, hydrogen, alkali, and alkaline earth metal ion concentrations of importance in biological systems can be monitored with potentiometric ion-selective electrodes (ISE) but not with voltammetric techniques because these species are mostly not electroactive in aqueous media. This is a key advantage of ion-selective tips besides the high selectivity of their potentiometric signal. Another essential advantage is that potentiometric sensors are passive probes that, in contrast to their amperometric cousins, do not alter the composition of the analyte in the sample. Since the measurement does not involve a faradaic process, the electrode does not alter the redox state of the species of interest, does not consume/produce new species such as protons or hydroxyls, and does not trigger mass transport in the analyte. This is particularly important for biological applications where the sample volume is usually very small.

ISE are typically membrane-based devices with internal filling solution and internal reference electrode. They are often classified according to the nature of the ion-selective membrane or the shape and size of the electrode arrangement. The main types of membrane electrodes are

1. Glass membrane electrodes: for example, H^+-, Na^+-, K^+-, Ag^+-selective glass electrodes
2. Liquid or polymeric ion-selective membrane electrodes:
   a. Classical ion exchangers (with hydrophobic cations and anions providing mobile positively and negatively charged sites, respectively), for example, K^+- and Cl^--selective electrodes
   b. Liquid ion exchanger–based electrodes (with positively or negatively charged sites acting as ion carriers), for example, Ca^{2+}- and NO_3^--selective electrodes
   c. Neutral carrier-based liquid membrane electrodes (with uncharged complex ligands), for example, Na^+-, K^+-, NH_4^+-, Ca^{2+}-, and Cl^--selective electrodes
3. Solid-state electrodes:
   a. Crystalline electrodes, for example, F^--, CN^--, Pb^{2+}-, Cu^{2+}-, and Cd^{2+}-selective electrodes
   b. Sb/Sb oxide, Ir/Ir oxide, and Pd hydride for sensing H^+
   c. Ag/Ag halide based electrodes for sensing Cl^-, I^-, and Br^-

The next section highlights the key discoveries and technological improvements which led to the successful application of ISE.

10.1.1 Brief History of Ion-Selective Electrodes

Cremer's[1] discovery of selective potentiometric probes led the way to the development of many analytical transducers able to provide an electrical signal quantitatively related to the activity

of a species within a complex sample solution. The pH-sensitive glass membrane electrode was introduced soon after[2] and contributed considerably to the development and acceptance of instrumental methods of chemical analysis. The investigation[3] of the reproducible alkaline error of glass electrodes led to the development of glass electrodes sensitive to sodium and potassium ions. Eisenman et al.[4] were the first to report the preparation of a well-behaved sodium ion–selective glass electrode. Several decades passed between the early glass electrodes and the apparition of useful new ISE, but glass membrane electrodes are still popular sodium ion potentiometric sensors.

In 1936, Tendeloo[5] investigated the dependence of the potential response of fluorite, CaF_2 membranes, on calcium ion. A linear relationship was found between the negative logarithm of the calcium ion activity and the electromotive force of the cell. However, the results could not be easily reproduced.[6]

Kolthoff and Sanders[7] almost made the first anion-selective electrode with their study of silver halide disks. Near Nernstian responses were measured for chloride, bromide, and iodide using the corresponding silver halide membranes. They even noticed that the presence of chloride or bromide ions or of a strong oxidizing agent ($KMnO_4$) did not influence the iodide response of the silver iodide disk.

In 1950s, several research groups studied different membrane electrodes prepared from ion-exchanger materials[8]; however, the potentiometric responses were not found to be selective.

Pungor was luckier in this respect since he successfully prepared the first reliable ISE. With his coworkers, he embedded different sparingly soluble inorganic precipitates in hydrophobic membrane materials and managed to develop selective membrane electrodes with near Nernstian response to different ions. The first report[9] of a paraffin membrane loaded with silver iodide appeared in 1961. Later, Pungor-type heterogeneous membrane electrodes were made with a cold vulcanized silicon rubber matrix.[10] Pungor realized the practical importance of his discovery and initiated the fabrication and commercialization of ISE on an industrial scale. Frant and Ross, the founders of the Orion company, followed a similar path with their lanthanum fluoride crystal–based and liquid ion exchanger–based fluoride-selective electrodes.[11]

Ruzicka and Tjell proposed a universal porous graphite rod–based ISE.[12] In the early 1970s, Freiser developed a simple way of preparing ISE by dip-coating the stripped end of a wire with a thin ion-selective membrane. Different anion-sensitive coated wire electrodes were prepared using an ion exchanger, Aliquat 336S (methyltricaprylammonium chloride, General Mill, USA), dissolved in 1-decanol.[13] This so-called coated wire electrode became quite popular despite the heavily disputed stability of the membrane–metal interfacial potential.

Simon's group at ETH Zurich showed first that neutral organic molecules such as the antibiotics nonactin and valinomycin could be used effectively as ionophores in ion-selective membrane electrode preparations.[14] This was an important step forward since liquid ion exchanger–based electrodes tended to exhibit moderate selectivity. This was due to the relatively poor selectivity of the electrostatic interactions at the heart of the ion-exchange process. In contrast, the neutral ionophore is a selective complexing agent capable of transporting a given ion across a membrane by excluding all ionic species except the one fitting its host–guest chemistry. Initially, ionophores were dissolved in diphenyl ether and used mostly in liquid ion-selective films. Later, they were incorporated in plasticized PVC membranes.

Shatkay and coworkers introduced PVC as a membrane matrix into ISE research[15] but it was Thomas's brilliant description of an amazingly simple preparation procedure that helped researchers to make thin plasticized PVC membranes.[16] For more than two decades, electrically charged and neutral ionophore based membranes have been most often made following that recipe.

The first neutral ionophore molecules, valinomycin and nonactin, were borrowed from nature but soon after good success was also achieved with synthetic ionophores. Simon's results initiated intensive research aiming to design, prepare, and test different types of organic molecules in ion-selective potentiometric sensor preparations. This work is still in progress today.[17]

10.1.2 Technical Approaches Developed to Produce Micro-ISE

While electroanalytical chemists were busy looking for new selective ionophores and membrane compositions, biomedical researchers from academia and industry improved the miniaturization of ion-selective devices. Biomedical applications nearly always involve small sample volumes and measurements are difficult. Figure 10.1 illustrates a range of specially shaped miniaturized ISE developed for these conditions. As for amperometric tips, two key dimensions should be considered: the size of the sensing element and the size of the surrounding insulating material. The former will determine the electrical properties of the tip while the latter will determine the range of applications. Currently, the smallest reliable sensors have tip diameters ranging between 0.1 and 1 μm.

10.1.2.1 Integrated Circuit Technology

The technology developed for the semiconductor electronic industry was applied to the manufacture of miniature ion-selective sensors. In the early 1970s, Bergveld[18] was the first to notice that metal oxide field effect transistors (MOSFET) could be sensitized with ion-selective materials (the device was named ISFET) to measure the activity of different ionic species. This was a forerunner of the

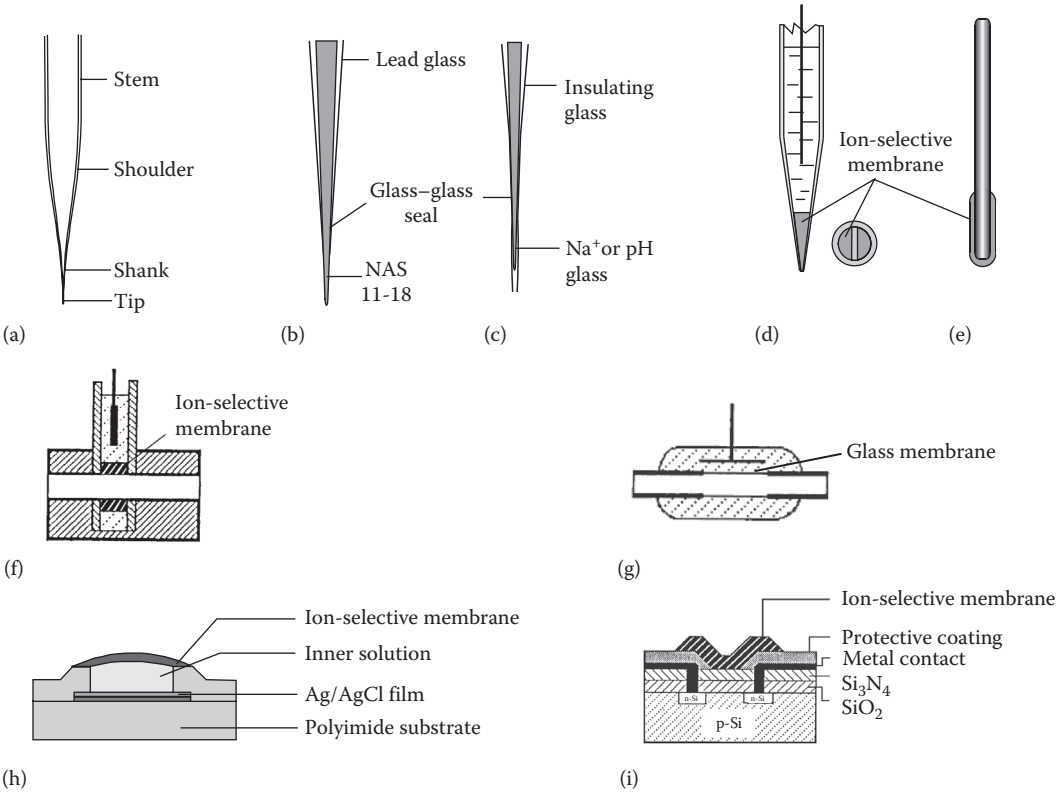


FIGURE 10.1 Schematic cross sections of selected microelectrode configurations. (a) Nomenclature for microelectrode parts, (b) Na^+-sensitive microelectrode, (c) recessed-tip Na^+-sensitive microelectrode, (d) liquid ion-exchanger micropipette electrode, (e) coated wire electrode, (f) flow-through ISE, for example, NOVA 6, Boehringer ISE 2020, (g) tubular flow-through glass electrode, for example, Radelkis OP-266, (h) planar sensor made by microelectronic technology, and (i) ISFET sensor. (b: Taken from Hinke, J.A.M., *Nature*, 184, 1257, 1959; c: Thomas, R.C., *J. Physiology*, 210, 82P, 1970; Thomas, R.C., *J. Physiology*, 238, 159, 1974; d: Walker, J.L., *Anal. Chem.*, 43, 89 A; Thomas R.C., Simon, W., Oehme, M, *Nature*, 258, 754, 1975; e: Coetzee, C.J. and Freiser, H., *Anal. Chem.*, 40, 2071, 1968; h: Neuman, M.R et al., *IEEE Eng. Med. Biol. Mag.*, 13, 409, 1994; i: Bergveld, P., *IEEE Trans. Biomed. Eng.*, BME17, 70, 1970. With permission.)

lab-on-a-chip concept as the original idea was to mass produce with the efficiency and reliability of the high-tech nanofabrication industry, cheap miniaturized sensing elements capable of performing different analytical tasks. The same element could have contained several sensing transistors, measuring electronic circuits, operational amplifiers, etc. The incompatibility of materials used in the fabrication of electronic devices with the conditions found in wet chemical analysis, however, restricted the development of chemically sensitive FET sensors mostly to pH sensing.

Nanofabrication technologies are nevertheless routinely used to produce arrays of potentiometric microelectrode sensors. They may hold either of identical sensors or a range of different sensors on the same substrate. The size of the sensing elements typically ranges between 5 and 200 µm.[21,22] Clinical analyzers routinely use this kind of sensor cartridges. Such planar electrodes have, for example, been employed to image in real time the release of protons from a cation-exchange resin.[23]

10.1.2.2 Glass Microelectrodes

Glass microelectrodes were preceded by microcapillary electrodes where a section of the internal capillary wall consisted of a measuring membrane but these capillaries were too big to perform intracellular measurements. Glass micropipettes often used in biological micromanipulations provided an excellent platform in the preparation of ultramicro-ISE for intracellular applications. Caldwell[24] miniaturized the pH-sensitive glass electrode and successfully measured the intracellular pH of the large size crab muscle fiber. He made the electrode stem from the same glass as the active part, but coated the stem with shellac. In all other aspects, Caldwell's microelectrode had the same structure as the conventional glass electrode, namely a miniature bulb, microcapillary stem, internal filling buffer, and silver/silver chloride internal reference electrode. Hinke[19] prepared needle-type microelectrodes from sodium- or potassium-sensitive glasses and used them for intracellular measurements of these ions. The sealed end of the micropipette was made out of ion-sensitive glass and served as the measuring part. To prepare a microelectrode, a closed ion-sensitive glass micropipette was placed into an open-ended micropipette made of insulating glass. The two glasses were sealed together along the conical sides leaving a 100 µm long protruding sensing tip. This configuration could not give good spatial resolution since intracellular measurements require the whole sensing tip to be positioned inside the cell. Therefore, ordinary cells could not be studied with such microelectrodes. Lev and Buzhinsky[25] managed to decrease the length of the protruding tip to a few micrometers by employing a sealing wax between the two concentric glass cones. This was a considerable improvement but the sampled area was still bigger than the lumen of an average size cell. Thomas[26] tried to solve this problem and produced the so-called recessed-tip glass pipette electrodes. In this case, the pipette made of insulating glass is longer than the active sealed-end measuring pipette. The measuring pipette is sealed inside the lumen of the insulating one and the penetration into biological structures does not need to be so deep. Keeping in mind SECM applications, the use of recessed tips does not bring considerable improvement.

Pucacco and Carter[27] described a method to coat the open end of an insulating glass micropipette with a thin glass film to form a flat micro-pH-sensitive electrode. They blew a very thin-walled bubble from a uranium-containing glass. Under careful heating, the insulating pipette was pushed into the bubble which sealed the open end with a thin glass film. After cooling, the excess glass was broken off from the sides. Levy and Coles[28] using a similar procedure could make a 4 µm double barrel version with appropriate suction inside the pH barrel. While these electrodes look attractive, it is worth stressing that the preparation procedure is very difficult and the success rate is generally low.

Yamaguchi and Stephens[29] proposed to make recessed pH glass microelectrodes by placing a short pH-sensitive glass capillary inside a normal glass capillary, heating the end of this concentric tube assembly (to recess the outer glass to the level of the inner glass while decreasing the diameter of the inner capillary) and pulling the assembly with a conventional pipette puller to produce the microelectrode. The end of the outer capillary remains open while the pH-sensitive capillary is usually sealed and recessed by about 2 µm. First methanol, then distilled water, and finally a

hydrochloric acid or sodium chloride internal filling solution are introduced inside the lumen of the inner glass capillary. In practice, these electrodes function well.

When short response times and short sampling depths are needed, reversed tip glass microelectrodes can be made by introducing the sealed end of a sensing tip into the narrow open end of the electrode body pipette and sealing them together so that the pointed end of the active tip remains inside the insulating glass body.

NAS 11-18 glass is usually chosen to make the sensing tip of ion-selective sodium microelectrodes while the insulating body is made of aluminosilicate glass. To manufacture a protruding sensing tip, an open-ended pipette is first made with the insulating glass. Then another pipette is pulled from the sensing glass. Its end is sealed with a micro-forge and a short section is broken off by scratching. This closed-end conical section is dropped tip down into the end of the insulating glass pipette thus producing a protruding sensing tip. The two pipettes are sealed together above the tip. Recessed sodium-sensitive microelectrodes can be made in a similar manner.

Potassium-selective glass microelectrodes were also used in the early days of potentiometric physiological studies.[30] They were typically made with NAS 27-8 or NAS 27-4 glass by gluing the sealed end of the sensing glass tip inside the insulating glass micropipette with wax. However, the glass-based ion-selective potassium electrodes do not possess the necessary selectivity and are nowadays very seldom used.

10.1.2.3 Metallic Electrodes

In principle, these electrodes can be used for ion activity measurements. Life scientists first tried to take advantage of electrodes of the second kind as early as the 1950s. Mauro[31] measured chloride ion concentrations inside the squid giant axon with a chloride microelectrode that he prepared by cementing a 15 μm diameter silver chloride–coated silver wire into the end of a glass capillary.

A much smaller micropipette silver electrode was prepared for chloride measurements by Kerkut and Meech.[32] They introduced a concentrated ammoniac silver nitrate solution into borosilicate glass micropipettes and kept the micropipettes for 10 h in 20% formaldehyde solution. After diffusing into the narrow opening, formaldehyde reduced the silver and formed a metallic silver plug inside the tip of the micropipette. A silver chloride–coated silver wire was then used as inner reference electrode in a silver nitrate internal filling solution.

Saunders and Brown[20] reported a method to prepare recessed-tip silver/silver chloride microelectrodes. In the first step of this procedure, they electrochemically sharpened the end of a silver wire (diameter 125 μm) by dipping it into basic sodium cyanide solution and anodizing it under voltage control. This was followed by an electrochemical chloride-coating step in 100 mM HCl solution. Denuault et al.[33] prepared Cl^--sensitive microdisk electrodes by electrochemically anodizing 10 μm diameter Ag microdisks to form Ag/AgCl microdisk electrodes.

Palladium has long been known to absorb hydrogen and to form different hydrides depending on its hydrogen content. The α hydride exists for H to Pd ratios below ~0.3 and the β hydride for H to Pd ratios above ~0.5. In both cases, the potential of the material is a function of its composition and of the solution pH. However, in the α/β transition region, the material acquires a potential independent of its composition but linearly dependent on pH. This property is commonly exploited to prepare reliable reversible hydrogen reference electrodes but it can also be used to prepare pH electrodes.[34] This works well for large electrodes but not for microelectrodes because the electroactive area is insufficient to produce a stable potential. To alleviate this problem, Imokawa et al. prepared nanostructured Pd hydride microdisks by templated electrodeposition.[35] The Pd hydride microdisk electrodes were found to have a very reliable Nernstian response over the pH range 2–12. However, the presence of oxygen affected the lifetime of the electrode.

10.1.2.4 Micropipette Liquid Ion-Selective Microelectrodes

Conventional size ion-selective liquid membrane electrodes were well known in the early 1970s.[36] The sensing liquid membrane cocktail was initially held in the pores of a thin porous membrane

(Millipore), the ion-selective liquid consisting of an organic electrolyte or of a neutral ionophore dissolved in a water immiscible, high-molecular-weight organic liquid. These sensors were often commercialized in the form of an electrode preparation kit. The kit contained an electrode body in pieces with washers, O rings, a membrane holding screw cap, small tools to facilitate assembling, a few Millipore membranes, and instruction booklet. The internal filling solution and the organic liquid were also supplied.

Since the glass micropipettes had already been used extensively in micromanipulations and in field measurements, the introduction of the ionophore-containing liquid membrane into the tip of a glass micropipette was an obvious step in ISE miniaturization. Walker[37] pioneered the development of micropipette liquid ion exchanger–based ISE for the measurement of potassium and chloride ions. As expected, the organic ion–selective liquid inside the tip formed a sensing membrane between the internal filling solution and the sample. Submicron size electrodes can be made in this way but the preparation procedure, although universal, necessitates skills (see Section 10.1.3). Stability problems affected the first experiments.[38] The glass is hydrophilic and water rapidly displaces the membrane away from the glass wall. An electrolyte bridge slowly forms between the internal and external solutions on either side of the membrane and the electrode ceases to function. Surface treatment procedures giving a hydrophobic character to the internal glass wall were needed for the ion-selective glass micropipette electrodes to become practically acceptable. Walker treated the readymade micropipettes with organic silicon compounds and the lifetime of the microelectrodes increased dramatically. Different successful procedures have since been proposed for the preparation of these electrodes and are presented in Section 10.1.3.

Natural neutral carriers such as valinomycin and nonactin were first employed in liquid membranes for the selective detection of potassium and ammonium ions. This discovery in Simon's group initiated the design of several synthetic acyclic and macrocyclic compounds such as crown ethers and more recently calixarene derivatives. Their use in liquid membrane technology led to the elaboration of highly selective membrane electrodes. These ionophores have in common a stable conformation with a polar binding "cavity" and lipophilic shell. The first ion-selective microelectrodes based on neutral ionophores were introduced in the mid-1970s[39] and used for physiological measurements of ion activities in living cells.

The invention of liquid membrane microelectrodes and progress in the design and synthesis of neutral ligands opened up new perspectives for the development of ion-selective microelectrodes with excellent selectivity.

The great advantage of the micropipette electrode configuration is that the same procedure can be used to prepare electrodes sensitive to different species, simply by changing the liquid ion-selective cocktail. Different ion-selective cocktails have been elaborated[40] and are commercially available, for instance, from Sigma-Aldrich-Fluka, as organic solutions delivered in a vial ready for electrode preparation. A typical cocktail consists of a low-viscosity organic solvent such as 2-nitrophenyl octyl ether or bis(ethylhexyl)sebacate, in which a few weight percent (5–10 wt%) of the ionophore are dissolved. Most cation-selective ionophore-based cocktails contain lipophilic anionic sites, for example, tetraalkylammonium tetraaryl borate, potassium tetrakis (4-chlorophenyl)borate, or tetradodecylammonium tetrakis(4-chlorophenyl)borate. The role of such additives is to enhance ion selectivity, decrease the response time, and reduce the membrane resistance.[41]

Besides selectivity, a major goal in developing neutral carrier–based membrane solutions is to minimize the resistance of the ion-selective microelectrodes. This requires careful adjustment of the membrane composition typically by altering the membrane solvent, the neutral carrier concentration, the percentage and the nature of the lipophilic salt additives. The amount of salt additives is finely tuned not to compromise ion selectivity.

In the early days of ion-selective micropipette measurements, the cation exchanger, potassium tetra(*p*-chloro)phenylborate commercialized by Corning (K^+ exchanger, type 477317), was very popular for measuring potassium activity.[37] Its limited selectivity allowed only certain applications; however, this electrically charged material advantageously provided low electrode resistance. The

valinomycin based potassium selective cocktail[39] (Fluka No. 60031) showed much better selectivity but at the expense of higher electrode resistance. Bis-crown ether-type neutral ionophores (BME 44), developed by Pungor's group, were also found to work well in potassium ion measuring micropipettes.[42]

Simon's ionophore ETH 227 (Fluka 71176) is now the choice for making Na^+ measuring cocktails. Before this, monensin antibiotic–based sodium-sensitive pipettes were used[43] but suffered poor K^+ selectivity.

Different kinds of ion exchangers were designed for calcium ion measurement. The earlier versions (Orion or Corning calcium cocktails) used charged measuring materials such as the calcium salt of dialkyl phosphoric acid mixed with an organic solvent, for example, di(octylphenyl)phosphonate (DOPP).[44] Brown et al.[45] designed a micropipette calcium electrode using di-*p*-(1,1,3,3-tetramethylbutyl)phenyl phosphoric acid mixed with DOPP. They used a PVC matrix to prepare the measuring membrane. Simon's group synthesized neutral ionophores to improve the selectivity of the calcium measurements. The *N*,*N*′-di[-(11-ethoxycarbonyl)undecyl]*N*,*N*′-tetramethyl 3,6-dioxaoctane diamide (ETH 1001) ionophore was found to work well in calcium micropipette electrodes.[46]

Nonactin-based membrane solutions[47] can be used for the measurement of ammonium ion activity. A great deal of interest arose to design selective lithium electrodes because Li^+ is used clinically to control manic depression. As a result, micropipette Li^+ electrodes have also been reported.[39a]

In terms of selectivity, lifetime, and dynamic range, the glass electrodes are superior to any other tools used for pH measurements; however, the preparation of micrometer-sized glass electrodes is not an easy task, as seen in Section 10.1.2.2. To be able to use the universal and simple micropipette electrode fabrication to pH-sensing, liquid H^+-selective cocktails were also synthesized to produce micro-pH electrodes. These cocktails usually exploit the neutral tridodecylamine as active ionophore.[48] Microelectrodes prepared with this cocktail can be used to monitor pH changes in the physiologically important pH range.

Usually, classical (charged) ion exchangers are employed as active ingredients in potentiometric anion-selective electrodes. Therefore, their selectivity precludes their use in complex matrices containing high concentrations of other anions. The micropipette version of the different anion electrodes can be easily prepared. The commercial Orion 92-07-02 nitrate measuring cocktail contains a tris(substituted 2-phenanthroline) nickel(II) exchanger, while the Corning 477316 cocktail uses tridodecylhexadecylammonium nitrate. If present, chlorate, perchlorate, and iodide will, however, interfere with the nitrate measurement.

The Corning cocktails 477313 and 477315 work well for chloride micropipettes.[20,49] These pipettes were used to measure the concentration of chloride,[50] the major anionic component in biological media.

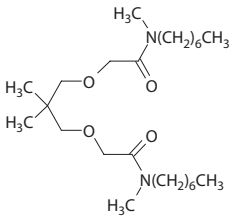
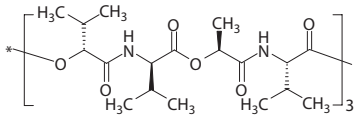
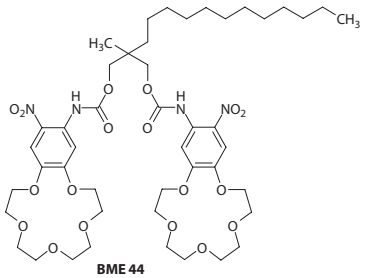
Methyltricaprylammonium chloride, Aliquat 336S, has often been used in anion-selective electrodes as active ion exchanger. Different Aliquat 336S–based micropipette electrodes were prepared and used in life science experiments.[51] Using hydrophobic solvents, the discrimination against chloride ions can be enhanced, leading to an improvement in selectivity. Crystal violet dye was also successfully used as ion exchanger in micropipette anion-measuring electrodes.[52] A survey of ionophores available for ion-selective microelectrodes and membrane solution compositions (ion-selective cocktail) is shown in Table 10.1.

10.1.3 Fabrication of Micropipette Ion-Selective Microelectrodes

10.1.3.1 Early Preparation Methods

According to Walker's method,[37] micropipettes with 0.5–1 μm size tips are made from borosilicate glass tubes previously cleaned in hot ethanol vapor. After pulling, the pipette tip is dipped in a 1% fresh solution of Siliclad (siloxane polymer, Clay Adams) in 1-chloronapthalene. The solution is allowed to rise about 200 μm inside the shank. The pipette, held vertically with the tip up, is baked

TABLE 10.1
Ion-Selective Cocktails for Micropipette Electrode Preparation

Ion	Ionophore	Ion-Selective Liquid (Cocktail)	Reference
Cl^-	$C_{44}H_{28}ClMnN_4$	*Cocktail:* 5.00 wt% chloride ionophore 4.00 wt% 1-decanol 1.00 wt% tetradodecylammonium tetrakis(4-chlorophenyl)borate 90.00 wt% 2-nitrophenyl octyl ether	[53]
		Liquid ion-exchanger microelectrode cocktail: 10.00 wt% trioctylpropylammonium chloride 90.00 wt% 1,2-dimethyl-3-nitrobenzene	[54,55]
H^+	$[CH_3(CH_2)_{11}]_3N$	*Cocktail A*: 10.00 wt% hydrogen ionophore 89.30 wt% 2-nitrophenyl octyl ether 0.70 wt% sodium tetraphenylborate *Cocktail B*: 10.00 wt% hydrogen ionophore 89.30 wt% 2-nitrophenyl octyl ether 0.70 wt% potassium tetrakis(4-chlorophenyl)borate	[48a,b]
Li^+		*Cocktail*: 9.70 wt% lithium ionophore 4.80 wt% sodium tetraphenylborate 85.50 wt% tris(2-ethylhexyl) phosphate	[39a]
K^+	 VALINOMYCIN	*Cocktail A*: 5.00 wt% potassium ionophore (valinomycin) 25.00 wt% 1,2-dimethyl-3-nitrobenzene 68.00 wt% dibutyl sebacate 2.00 wt% potassium tetrakis(4-chlorophenyl)borate	[39b,56]
		Cocktail B: 5.00 wt% potassium ionophore (valinomycin) 93.00 wt% 1,2-dimethyl-3-nitrobenzene 2.00 wt% potassium tetrakis(4-chlorophenyl)borate	[57]
K^+	 BME 44	*Cocktail A*: 5.00 wt% potassium ionophore (BME 44) 80.60 wt% 2-nitrophenyl octyl ether 13.00 wt% poly(vinyl chloride) high molecular weight 1.40 wt% sodium tetraphenylborate *Cocktail B*: 5.00 wt% potassium ionophore (BME 44) 83.20 wt% 2-nitrophenyl octyl ether 10.00 wt% poly(vinyl chloride) high molecular weight 1.80 wt% potassium tetrakis(4-chlorophenyl)borate	[42]

(*continued*)

TABLE 10.1 (continued)
Ion-Selective Cocktails for Micropipette Electrode Preparation

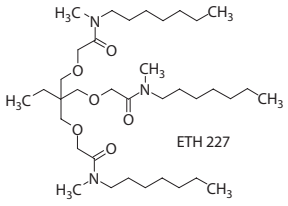
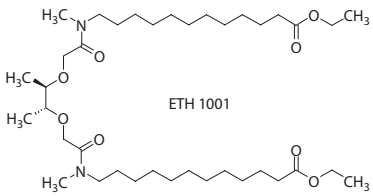
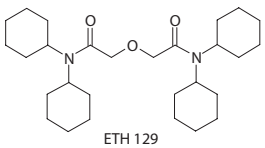
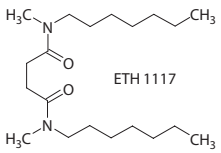
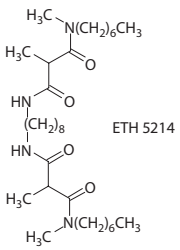
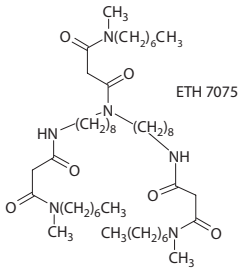
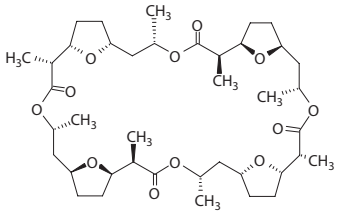
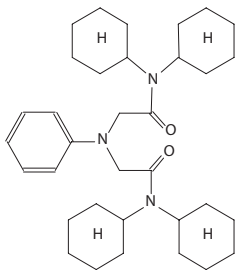
Ion	Ionophore	Ion-Selective Liquid (Cocktail)	Reference
Na^+	 ETH 227	*Cocktail A*: 10.00 wt% sodium ionophore (ETH 227) 89.50 wt% 2-nitrophenyl octyl ether 0.50 wt% sodium tetraphenylborate	[58]
		Liquid ion-exchanger microelectrode cocktail A: 2.10 wt% potassium tetrakis(4-chlorophenyl)borate 12.10 wt% trioctylphosphine oxide 85.80 wt% tris (2-ethylhexyl) phosphate	[59,60]
		Liquid ion-exchanger microelectrode cocktail B: 1.50 wt% potassium tetrakis(4-chlorophenyl)borate 98.50 wt% tris (2-ethylhexyl) phosphate	[61]
		Liquid ion-exchanger microelectrode cocktail C: 2.70 wt% potassium tetrakis(4-chlorophenyl)borate 10.00 wt% monensin 85.80 wt% 1,2-dimethyl-3-nitrobenzene	[62–65]
Ca^{2+}	 ETH 1001	*Cocktail A*: 10.00 wt% calcium ionophore (ETH 1001) 89.00 wt% 2-nitrophenyl octyl ether 1.00 wt% sodium tetraphenylborate *Cocktail B*: 21.50 wt% cocktail A 3.50 wt% poly(vinyl chloride) high molecular weight 75.00 wt% tetrahydrofuran	[66–68]
Ca^{2+}	 ETH 129	*Cocktail A:* 5.00 wt% calcium ionophore (ETH 129) 94.00 wt% 2-nitrophenyl octyl ether 1.00 wt% Sodium tetraphenylborate *Cocktail B*: 21.50 wt% cocktail A 3.50 wt% poly(vinyl chloride) high molecular weight 75.00 wt% tetrahydrofuran	[69–71]
Mg^{2+}	 ETH 1117	*Cocktail*: 20.00 wt% magnesium ionophore I (ETH 1117) 79.00 wt% propylene carbonate 1.00 wt% sodium tetraphenylborate	[72]
Mg^{2+}	 ETH 5214	*Cocktail A*: 10.00 wt% magnesium ionophore (ETH 5214) 87.00 wt% 2-nitrophenyl octyl ether 3.00 wt% potassium tetrakis(4-chlorophenyl)borate	[73–75]
		Cocktail B: 10.00 wt% magnesium ionophore (ETH 5214) 62.00 wt% 2-nitrophenyl octyl ether 25.00 wt% chloroparaffin (60 % chlorine) 3.00 wt% potassium tetrakis(4-chlorophenyl)borate	[76,77]

TABLE 10.1 (continued)
Ion-Selective Cocktails for Micropipette Electrode Preparation

Ion	Ionophore	Ion-Selective Liquid (Cocktail)	Reference
Mg^{2+}	 ETH 7075	*Cocktail*: 2.20 wt% magnesium ionophore (ETH 7075) 18.00 wt% 2-nitrophenyl octyl ether 1.10 wt% Tetradodecylammonium tetrakis(4-chlorophenyl)borate 0.75 wt% potassium tetrakis(4-chlorophenyl)borate 3.00 wt% poly(vinyl chloride) high molecular weight 75.00 wt% cyclohexanone	[78]
NH_4^+	 Nonactin	*Cocktail A*: 6.90 wt% ammonium ionophore (Nonactin) 0.70 wt% potassium tetrakis(4 chlorophenyl)borate 92.40 wt% 2-nitrophenyl octyl ether *Cocktail B*: 3.50 wt% ammonium ionophore (nonactin) 0.35 wt% potassium tetrakis(4 chlorophenyl)borate 0.95 wt% poly(vinyl chloride) high molecular weight 32.95 wt% dibutyl sebacate 62.50 wt% tetrahydrofuran	[79–81] [82]
Zn^{2+}		*Cocktail A*: 5.00 wt% zinc ionophore 3.20 wt% potassium tetrakis(4 chlorophenyl)borate 91.80 wt% 2-nitrophenyl octyl ether *Cocktail B*: 5.00 wt% zinc ionophore 3.20 wt% potassium tetrakis(4 chlorophenyl)borate 81.80 wt% 2-nitrophenyl octyl ether 10.00 wt% poly(vinyl chloride) high molecular weight	[113]

in an oven for an hour at 250°C. It can then be stored for a few days in dry air. Before use, the pipettes are filled with the liquid ion-exchanger cocktail (see Table 10.1) and with the internal filling solution. The cocktail is usually introduced first through the tip with capillary action and light suction. The internal filling solution (e.g., 0.1 M KCl) is often introduced through the back end of the pipette. The smaller the tip, the harder is the filling up procedure. The internal reference electrode most often consists of a 100 µm diameter chloride-coated silver wire. The back end of the electrode is normally sealed with silicone rubber or pasted in some other ways.

Several groups suggested modified versions of the original procedure. Different pipette pulling and glass cleaning procedures were found simpler, easier, or more efficient with less failure rate. Some of the large-scale procedures used for micropipette electrode preparation start with a very effective cleaning of the glass. The glass capillaries to be used for microelectrode preparation are soaked for several hours in a 1:1 mixture of concentrated sulfuric acid and 30% hydrogen peroxide.[83] After intensive washing and drying, the capillaries can be stored before pulling the pipette. Neher and Lux[84] advise to fire polish the pipette, where the broken tips of the freshly made micropipettes are slightly melted then dipped for 1–5 s in 4% dichlorodimethylsilane in carbon tetrachloride

for silanization. Without drying or baking, the pipettes are then immersed in boiling methanol under slight vacuum. When the methanol replaces the air in the lumen of the tubing, the pipette is transferred into distilled water and finally into 0.1 M KCl internal filling solution. The liquid ion-exchanger solution is then introduced through the tip by capillary action.

10.1.3.2 Typical Fabrication Procedure

Micropipettes for liquid membrane microelectrodes can be fabricated from different glass tubes (borosilicate glass, aluminosilicate glass, etc.) with outer and inner diameters typically ranging from 1–3 to 0.6–1.6 mm, respectively. Commercially available glass tubes come in single, double (e.g., theta or double barrel), or multibarrel type. Prior to use, the glass tubes should be soaked in a 1:1 (v/v) mixture of concentrated sulfuric acid and 30% hydrogen peroxide for 24 h, then washed thoroughly with deionized water and dried at 120°C for 30 min. A laser or a heated coil puller (e.g., Stoelting, Sutter Instruments, MicroData Instruments, Narishige, Flaming/Brown, Warner Instruments) is then used to produce the capillary end. The tip diameter should be within the range 1–20 µm and the ratio of tip length to stem radius smaller than 5. For silanization, the single barrel micropipettes are first filled with dimethyldichlorosilane or trimethylsilyldimethylamine vapor by syringe injection and then placed in a covered petri dish, which also contains a few drops of dimethylchlorosilane. The silanization is completed by allowing the glass surface of the micropipette to react with the silanizing reagent vapor for 2 h at 120°C in an oven. Any silanizing reagent remaining in the micropipette is removed by connecting it from the back to a water pump. The internal filling solution containing the ion of interest and potassium chloride is backfilled by applying a slight overpressure with a syringe. The tips are then frontfilled with the corresponding ion-selective cocktail by capillary action and slight suction. Finally, a Ag/AgCl wire is introduced to complete the ion-selective microelectrode.

Double barrel capillaries are silanized by introducing the silanizing vapor into one channel, while continuously flushing the other channel with nitrogen. The channel not silanized is later used for the outer reference electrode. The silanized channel is filled with the ion-selective cocktail as described previously.

Air bubbles trapped between the organic and water phases often break the electrical path. Small tools such as glass filaments, cats' or rabbits' whiskers are combined with skill and great patience to remove the bubble. Submicrometer-sized tips are easily blocked by insoluble plugs when using liquid phase silanization. Thus, very small pipette tips are usually vapor silanized;[85] the same applies to the ion-selective channel of double barrel electrodes but the reference barrel must stay open. Therefore, it must not receive a hydrophobic coating; otherwise, the ion-selective membrane cocktail easily plugs both barrels. Double and multibarrel electrode preparation necessitates an overpressure of nitrogen gas in the reference barrel to prevent silanizing vapors entering into it. The tip diameter of ion-selective micropipette electrodes can be as small as 100–300 nm.[86] However, the preparation and application of such a delicate device is not an everyday routine. Typically, an experienced researcher can easily prepare electrodes with 0.5–3 µm diameter tips with a success rate of 50%–80%.

It is a good practice to prepare several micropipette electrodes before the planned experiment, to check their potentiometric response and to select the best electrode. The following list describes typical tests carried out to check an ISE:

- First check with an optical microscope the integrity of the tip, the interface between the cocktail and the internal filling solution, and the extent of silanization that can be seen by observing the meniscus.
- Insert the electrode in a cell and monitor its potential using a reliable reference electrode.
- Wave your hand over the cell. If the electrode potential is very stable and insensitive to the movement of the hand, then it is very likely that the cocktail is not properly blocking the pipette tip. The electrode should be discarded.

- The potential of a freshly made electrode usually drifts for 20–30 min. It is therefore good practice to soak it in the solution where it will be used.
- Having reached a steady potential, the electrode must be calibrated with standard solutions in the concentration range expected to appear in the measurement cell. This should be done three times by lowering, increasing, and again lowering the concentrations. Washing the electrodes and the salt bridge between solutions is important.
- The potential values for an acceptable electrode should be within 1 mV of the average of three measurements. The slope of ISE pipettes is usually a bit lower than the Nernstian value (~59 mV at 25°C for a monovalent ion, see Equation 10.2). Slopes above 50 mV are acceptable.
- Check the electrode after the SECM experiment. Calibrate it as described earlier; if the potentiometric function differs from that recorded initially, then the data collected during the SECM experiment should be discarded or at the very least analyzed with great care.

10.1.3.3 Recent Improvements

Significant improvements in microelectrode fabrication have been made using solid internal gold contacts. Sundfors et al.[87] produced a robust solid contact ion-selective microelectrode using a recessed microdisk electrode. They chemically etched a 25 µm diameter gold wire sealed in glass to create a cavity of about 50 pL volume. The recessed gold disk was then coated with a conducting polymer, poly(3,4-ethylenedioxythiophene) (PEDOT), doped with poly(4-styrenesulfonate) (PSS) and tetrakis[3,5-bis-(trifluoromethyl)phenyl]borate (TFPB), and electropolymerized from aqueous and organic solvents, respectively, to form the solid contact. The cavity was then filled with the ion-selective liquid membrane. This design ensures that the membrane is mechanically protected by the walls of the pipette. K^+ ion– and Ca^{2+} ion–selective microelectrodes were successfully prepared in this way.

A different approach was reported to improve the response time of ion-selective micropipettes. Conventional ion-selective micropipettes have a rather high resistance and thus suffer large RC time constants. Their response time is therefore poor and the rastering speed is limited when the probe is used for imaging in the potentiometric mode of SECM. If the scanning rate is too high for the probe response time, the potentiometric image shows considerable distortion. In order to lower the electrode resistance while keeping the tip size small, a new fabrication procedure was introduced. The traditional internal filling solution and silver chloride–coated silver wire internal reference electrode were replaced with a solid contact consisting of a carbon fiber inserted into the ion-selective cocktail almost all the way to the opening of the micropipette (see Figure 10.2). The internal contact between the carbon fiber and the cocktail was stabilized by electrochemically coating the carbon fiber with a conducting polymer, doped PEDOT. These structural changes significantly increased the lifetime of the electrode and lowered its resistance. So far, this approach has been successfully employed to prepare solid contact micropipettes for detecting NH_4^+,[88] K^+,[89] and Zn^{2+}.[90]

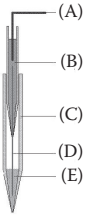


FIGURE 10.2 Schematic design of a solid contact micropipette tip: (A) copper wire, (B) silver epoxy paste or mercury, (C) glass capillary, (D) PEDOT-coated carbon fiber (OD 33 µm), and (E) ion-selective cocktail.

10.2 BASIC THEORY: *E* = *F*(*LN*(*ACTIVITY*))

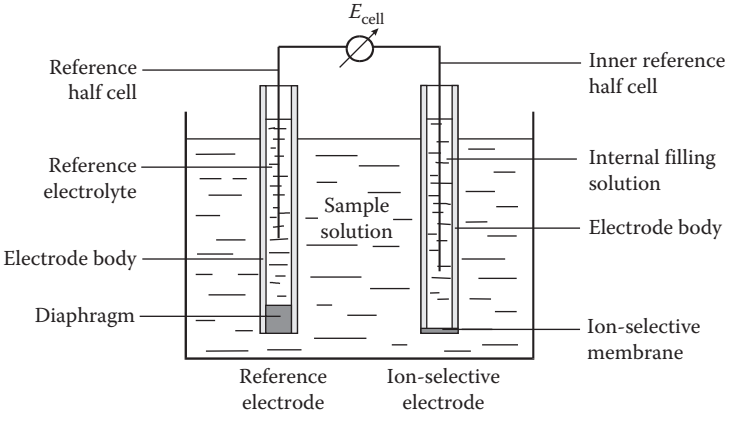
ISE are passive probes whose potentiometric response is linearly dependent on the logarithm of the activity (concentration) of a potential determining ion (primary ion) in the presence of other ions. The schematic layout of a complete potentiometric cell including an ISE is shown in Figure 10.3. The electrochemical notation of the cell assembly is given as

$$\underbrace{\text{Ag}\,|\,\text{AgCl}\,|\,\text{KCl}\,||}_{\text{Reference electrode}}\quad \text{Sample}\,\underbrace{|\,\text{Membrane}\,|\,\text{Internal solution}\,|\,\text{Agc1}\,|\,\text{Ag}}_{\text{Ion-selective eletrode}}$$

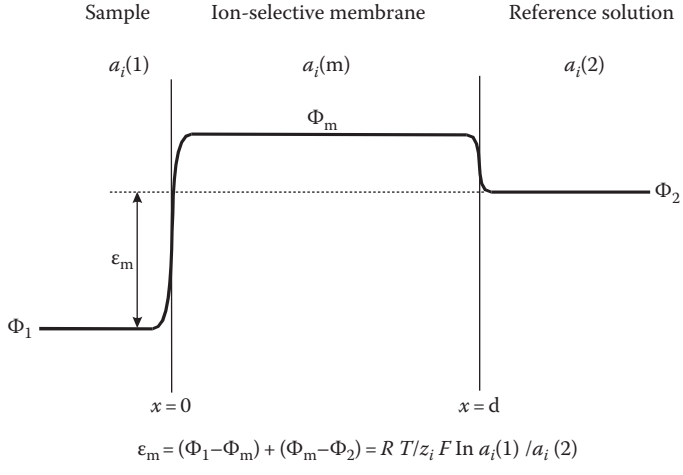
where

Single vertical lines indicate phase boundaries
Double vertical lines indicate a liquid–liquid interface

The cell potential is the sum of a number of local potential differences generated at the solid–solid, solid–liquid, and liquid–liquid interfaces within the cell and measured between the two reference electrodes. Since the device operates at zero current, the cell potential, E_{cell}, is given by



(a)



$$\varepsilon_{\text{m}} = (\Phi_1 - \Phi_{\text{m}}) + (\Phi_{\text{m}} - \Phi_2) = R\,T/z_i\,F\,\text{In}\,a_i(1)\,/a_i\,(2)$$

(b)

FIGURE 10.3 (a) Schematic diagram of a potentiometric measuring circuit and (b) potential profile across an ion-selective membrane of fixed sites, symmetrically bathed with the sample (1) and the reference solution (2).

$$E_{cell} = E_o - E_{jnc} + E_m \tag{10.1}$$

where

E_o is a potential representing terms independent of the primary ion activity
E_m is the membrane potential
E_{jnc} is the liquid junction potential due to the interface between the sample and the reference electrode

In analytical applications, one chooses electrolyte combinations to minimize liquid junction potentials.

In ISE potentiometry, the cell potential reflects the dependence of the membrane potential on the primary ion activity (concentration). According to the Teorell–Meyer–Sievers (TMS) theory,[91] the membrane potential is the sum of three potential contributions namely the phase boundary potentials generated by ion-exchange processes at both interfaces, $(\phi_1 - \phi_{m,1})$ and $(\phi_{m,2} - \phi_2)$, and the inter membrane diffusion potential, $(\phi_{m,1} - \phi_{m,2})$. If the membrane composition is constant and there are no concentration gradients within the membrane, then the membrane diffusion potential is zero and the membrane potential can be described by phase boundary potentials (see Figure 10.3b). This approach is also used to treat the response of ISE made with a range of membranes.

The membrane potential is directly related to the ion-activities in the solutions either side of the membrane and the cell potential can be described by the Nernst equation if the liquid junction potential can be considered to be constant and the composition of the inner filling solution is kept unchanged.

$$E_{cell} = \text{constant} \pm 2.303 \frac{RT}{z_i F} \log(a_i) \tag{10.2}$$

where

a_i refers to the activity of the primary ion i in the sample and inner reference solution
z_i is the charge of the ion
R is the gas constant
T is the absolute temperature
F is the Faraday constant
2.303 (RT/z_iF) is the Nernstian slope, which is equal to $59.16/z_i$ mV at 25°C

In practice, however, deviation from the ideal electrode behavior is common and an additional contribution to the total measured ion activity has to be considered due to the presence of interfering ions j in the sample solution. Under these conditions, the ISE potential can be approximated by the Nikolsky–Eisenman equation:

$$E_{cell} = \text{constant} \pm 2.303 \frac{RT}{z_i F} \log\left(a_i + \sum_{j \neq i} K_{ij}^{pot} (a_j)^{\frac{z_i}{z_j}} \right) \tag{10.3}$$

where

a_j and z_j are the activity and charge of the interfering ions j

The weighting factors K_{ij}^{pot} are the selectivity coefficients of the membrane toward ions j relative to ion i. The smaller the K_{ij}^{pot}, the smaller are the contributions of the interfering ions to the total cell potential. The selectivity coefficients can be determined potentiometrically and are often listed in textbooks. Their value is used as a guideline when designing ISE-based potentiometric experiments.

10.3 PROPERTIES AND CHARACTERISTICS OF ION-SELECTIVE MICROELECTRODES

10.3.1 Potentiometric Response and Detection Limit

The electrode function gives the correlation between the cell potential of the ISE cell assembly and the logarithm of the primary ion activity in the sample solution. ISEs typically exhibit Nernstian electrode functions when the concentration ranges between 10^{-1} and 10^{-5} M. Note that, in practice, micropipette electrodes are calibrated before and after each experiment. If the two calibrations show significant differences, the experiment has to be discarded and repeated.

Different pH-sensitive glass electrodes can show theoretical response over a wide range of pH. Typically, their dynamic range covers 12 orders of magnitude in H^+ activity. Unfortunately, ISE do not have such a broad dynamic range. The range where the electrode potential is linearly dependent on the logarithm of the ion activity is narrower. Therefore, the application of ISE in trace level analysis has been questioned for long times. The theoretical detection limit usually varies with the nature of the ion-selective membrane material and for ionophore-based electrodes it is determined by the stability constant of the ionophore–cation complex. In practice, the detection limit rarely goes below 10^{-6} M and can be determined induced as shown in Figure 10.4. However, following the work of Pretsch and coworkers, it is now understood that the response at low concentrations is due to a nonequilibrium ion-exchange by the graphical method counter diffusion process and that the detection limit is significantly influenced by diffusion gradients across the membrane.[92] His group introduced a new concept for extending the measuring limit of ionosphere-based toward low concentrations.[92a,93] The idea is that the diffusion of the ions of interest from the internal filling solution to the sample solution increases the primary ion concentration in the vicinity of the electrode and leads to an erroneous potential reading. Below ca. 1 μM, the electrode no longer responds to changes in sample concentration. Thus it was obvious that one should try to decrease the ion activity in the internal filling solution in order to extend the lower limit of detection. However, when the ion activity is decreased in the internal filling solution by dilution or by adding

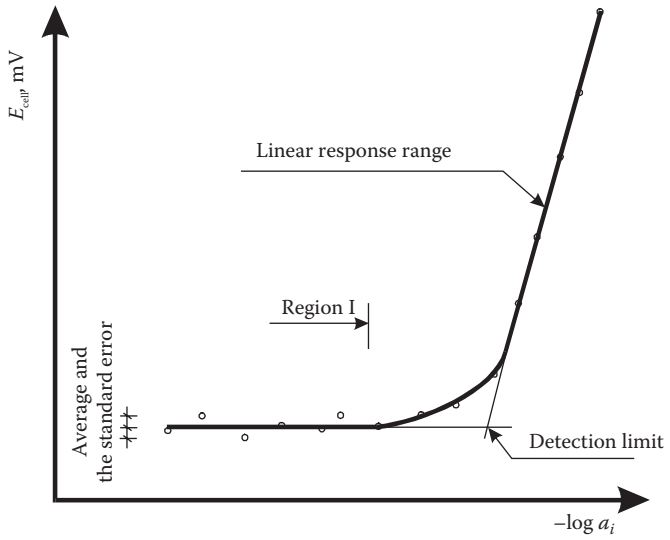


FIGURE 10.4 Schematic diagram of the response function of an ion-selective electrode. a_i denotes the activity of the primary ion, *i* and region I the activity range where the cell potential is independent of the primary ion activity. (Taken from Inczédy, J. et al., *Compendium of Analytical Nomenclature: Definitive Rules 1997*, 3rd ed., Blackwell Science, Oxford, U.K., 1998, p. 288. With permission.)

a chelating agent, a so-called super-Nernstian response is obtained. It results from ion transport across the membrane in the opposite direction, which decreases the interfacial concentration at the sample side.

Intensive research initiated by this concept showed that carefully selecting the composition of the internal filling solution, or using solid internal contacts, could substantially lower the detection limit of ISE. Unfortunately, these approaches did not work over the whole concentration range. Given internal filling solutions provide good response in narrow ranges of small concentrations, but if the electrodes are used in concentrated solutions their response in low concentrations cannot be restored.

The broad pH range of glass electrodes requires further consideration. While pH-sensitive potentiometric electrodes are usually calibrated with buffer solutions, ISE are usually calibrated with aqueous solutions of a salt containing different concentrations of the ion concerned. It was observed by several workers that broader dynamic ranges could be achieved using ionic buffers for calibration. High-capacity buffers can control the ion activity at the interface found in low concentrations.

Most of these range-extending works have been done with conventional size electrodes not applicable as SECM tips. The influence of ion transport through the measuring membrane on the lower limit of detection for ion-selective micropipettes with asymmetric membrane shape was investigated by Sodergard et al.[95] Recently, galvanostatic perturbation of the membrane equilibrium has been used to control the concentrations on either side of the membrane and thus lower the detection limit.[96] Recent advances in potentiometry can be found in the following review article.[97]

10.3.2 Selectivity Coefficients

The selectivity factor, K_{ij}^{pot}, is a measure of the preference of the ion-selective sensor for the interfering ion j relative to the primary ion i to be measured. A selectivity factor below 1 indicates that the preference is for the primary ion i. Two methodologies are used to measure the selectivity factor experimentally:

- The fixed interference method (FIM): The potential of the ISE is measured in solutions of constant activity of interfering ion, a_j and varying activities of the primary ion. The selectivity coefficient, K_{ij}^{pot}, is calculated from the relevant calibration graph plotted for the ion of interest, i. The intersection of the extrapolated linear portions of the response curve indicates the value of a_i^*, which is used to calculate K_{ij}^{pot} from the Nicolsky–Eisenman equation:

$$K_{ij}^{pot} = \frac{a_i^*}{a_j^{z_i/z_j}} \tag{10.4}$$

With the knowledge of the selectivity factor, the experimental error due to poor ion selectivity can be calculated.

- The separate solution method (SSM): The potential of a cell comprising the ISE and a reference electrode is measured in two separate solutions, one containing only the primary ion, i (E_i), and the other containing the interfering ion, j (E_j), at the same activity ($a_i = a_j$). The value of the selectivity coefficient can be calculated on the basis of the Nicolsky–Eisenman equation:

$$\log K_{ij}^{pot} = \frac{E_j - E_i}{2.303(RT/z_iF)} + \left(1 - \frac{z_i}{z_j}\right) \log a_i \tag{10.5}$$

The method is relatively simple and especially suited to compare the selectivity of novel ISE prepared with different membranes. The data thus calculated may not be representative for mixed sample solutions. The above methods are recommended if the electrodes exhibit Nernstian response for both the primary and interfering ions. For further details, see Ref. [98].

10.3.3 Stability and Reproducibility

In ion-selective potentiometry, the stability and reproducibility of E_{cell} depends on the type of ISE used. Carefully optimized liquid membrane electrodes in flow through arrangements for clinical applications yield standard deviations in E_{cell} smaller than 0.1 mV. This corresponds to less than $z_i \times 0.4\%$ error in the determination of activities. Ion-selective microelectrodes have poorer characteristics due to chemical (e.g., silanization) and electrical (high resistance, see section 10.3.5) reasons.

10.3.4 Response Time

The response time is one of the most critical parameters of the potentiometric probe in continuous analyzers and in in situ monitoring; it is usually determined by the activity step method shown in Figure 10.5. The ISE potential-time transient is a complex function of several parameters. It is affected by the properties of the measuring membrane and by the experimental conditions used, such as the method for generating the concentration change, the amount of convection at the electrode surface, and the electronics used for the potential measurements. For conventional size solid-state and most liquid membrane electrodes, the rate-limiting step is the rate of ion transport in the stagnant solution layer adherent to the sensor. However, the response time of microelectrodes with high internal resistance never reflects transport processes toward or within the membrane. Instead, it reflects the *RC* time constant of the measuring circuit or of the ion-selective microelectrode itself:[99]

$$E_{cell}(t) = E_{cell}(\infty) \pm \left[E_{cell}(\infty) - E_{cell}(0)\right] e^{-t/RC} \tag{10.6}$$

where

$E_{cell}(0)$ is the cell potential prior to the change in activity
$E_{cell}(\infty)$ is the cell potential at very long time after the change in activity (i.e., once the potentiometric response has stabilized)
R is the internal resistance of the electrochemical cell
C is the capacitance of the amplifier input

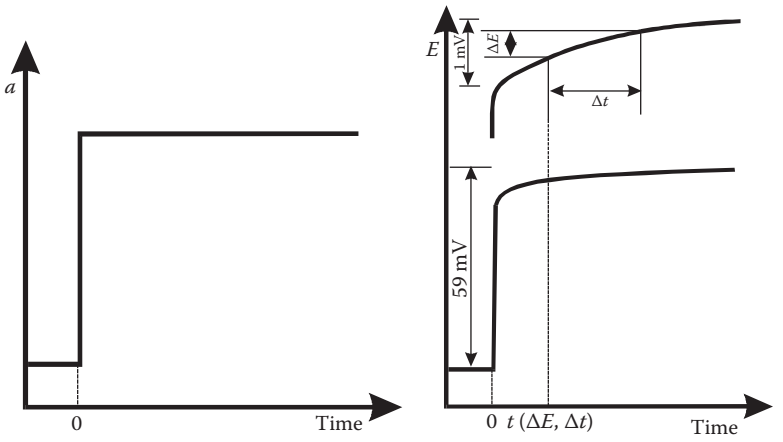


FIGURE 10.5 Schematic diagram of the activity step method used to determine the response time of ISE.

The response time, t_α, is defined as the time taken by the measuring assembly to reach a given percentage α of the final cell voltage following a given change in activity or by the slope $\Delta E/\Delta t$ of the dynamic response curve.[100] For a detailed discussion of the dynamics of ISEs, see Ref. [99].

10.3.5 Handling and Instrumentation

Most ion-selective microelectrodes are very delicate tools; working with them necessitates training and patience. Compared to conventional size ISE, their only advantage is that they can operate in small sample volumes and thus provide higher spatial resolution.

The microelectrodes are sensitive to mechanical stress; their tip can easily break if they touch any hard surface. Some of them are also sensitive to static electrical shocks often generated during handling. Ion-selective micropipettes and glass microelectrodes have a very high resistance. Typically, a submicrometer-sized micropipette prepared with a neutral ionophore-based membrane has an impedance reaching 10^{11} Ω; micropipettes made with charged ion exchangers or glass membrane microelectrodes usually have a lower resistance, ca. 10^8–10^9 Ω. This high resistance has serious effects on the electrode performance. The glass body of the electrode needs to be electrically shielded; otherwise, the internal reference electrode will sense the potential difference across the glass rather than across the membrane. Special instrumentation, arrangements, and shielding are required for the measurements.[101]

The input impedance of the measuring apparatus has to be a few orders of magnitude higher than the electrode impedance; otherwise, the input bias current may produce a significant voltage error. This is important because the impedance of the electrode can change considerably over time. The voltage error, that is, the maximum bias current passing through the electrode multiplied by the largest electrode resistance, should not exceed 0.5 mV. Because of the logarithmic relationship, a 0.5 mV error already corresponds to a 2% (assuming $z_i = 1$, 4% assuming $z_i = 2$) error on the ion activity measured.

With high input impedances and low input currents, FET operational amplifiers make ideal voltage followers when working with high-resistance microelectrodes. Aiming for applications in life sciences, a variety of potentiometric instruments designed for microelectrode measurements are on the market. These commercially available high impedance electrometers usually have several measuring channels. Each measuring channel consists of two inputs respectively for the reference and indicator electrodes. The inputs have high impedance owing to the voltage followers incorporated in the circuitry. This configuration is known as "millivoltmeter with symmetric input". The outputs of the followers are equal to the potential difference between the connected electrode and an auxiliary electrode connected to the virtual earth. The followers' outputs are fed into a differential amplifier stage which measures the potential difference between the indicator and reference electrodes. Additional electronics amplifies the signal if necessary and conveys it for display, recording or further processing. It is important to position the voltage follower very close to the electrodes; the shorter the connecting leads, the less electrical noise they will pick up. For SECM applications, the voltage follower should be located inside a small shielded box attached to the electrode holder. In addition, the whole experimental setup should be placed inside a Faraday cage. The use of battery-powered electrometers inside the cage is highly recommended. Experts in microelectrode potentiometric measurements expect very noisy voltage outputs without appropriate shielding. They check the electrode condition by hand waving close to the cell. An absence of noise spikes indicates an electrode failure.

When properly shielded and connected to the appropriate apparatus, ion-selective microelectrodes should show similar response and selectivity to conventional size electrodes. They should be calibrated in solutions of similar composition to that of the sample solution to be analyzed. The response time of the electrode itself should be comparable to that of conventional electrodes. However, with these electrodes, the diffusion of the ions through the stagnant solution layer adhering to the ion-selective membrane has a smaller effect on the transient response than the time

constant of the measuring circuitry. Measuring instruments often contain a variable capacitor to adjust the delay caused by the capacitance of the input stage.

10.4 POTENTIOMETRIC MEASUREMENTS IN SCANNING PROBE MICROSCOPIES OTHER THAN SECM

The earliest forms of SECM experiments were carried out in the potentiometric mode. Evans[102] reported how he used a traveling reference electrode to map equipotential surfaces in solution and calculate corrosion rates on a water pipeline. Isaacs and coworkers[103] revived the idea in 1972 and coined the acronym SRET for scanning reference electrode technique. Instruments used to be homemade, often with rudimentary traveling devices such as the arm of an X–Y recorder[103a,104] and the spatial resolution was at best submillimeter. A computer-controlled instrument was commercially produced by Uniscan Instruments with a spatial resolution around 20 μm.[105] The SRET has now been superseded by the scanning vibrating electrode technique,[106] known as SVET, which achieves higher spatial resolution[107] and improved sensitivity. A SVET manufactured by Uniscan Instruments is now commercially available from Uniscan Instruments and Princeton Applied Research.

In both SRET and SVET, the potentiometric measurements are carried out with micrometer-sized quasi-reference electrodes, typically platinum cones electrochemically coated with platinum black, held precisely above the sample surface. These commercial instruments have not been designed to accommodate ion-selective microelectrodes. However, some groups have reported the use of homemade instruments to probe the concentration of specific ions (see Section 10.5.2).

10.5 POTENTIOMETRIC MEASUREMENTS IN SECM

10.5.1 Asserting the Tip–Substrate Distance

Potentiometric SCEM requires an independent determination of the absolute distance between the microelectrode and the sample surface. This is motivated by two reasons. First, the probes tend to be very fragile and it is important to restrict their travel to avoid touching the sample, and second, the potentiometric response of the tip does hold the tip–substrate distance dependence found in the amperometric mode. As a result, quantitative information regarding concentration profiles can only be extracted with the knowledge of the tip–substrate distance. The latter is considered in subsequent sections.

Experimentally, the tip position is precisely known but only relative to a reference location in the solution. In the amperometric mode, the tip acts as a kind of electrochemical radar that produces/consumes redox species and the resulting concentration gradients in the tip–substrate gap yield a unique tip current–distance dependence. In the potentiometric mode, however, the tip is passive and does not interfere with the concentration profiles except by shielding the sample surface from the bulk solution. Several procedures have therefore been reported to assess the tip–substrate distance in these conditions. The simplest consists in approaching the tip under visual observation with a microscope until it is seen to barely touch the substrate surface. This position is then defined as the zero on the tip–substrate distance scale. The method is adequate when the user does not require an accurate estimate of the tip–substrate distance. More sophisticated procedures have been reported and are now described in the following sections.

10.5.1.1 Switching from Amperometric to Potentiometric Response

Metal oxide potentiometric devices are advantageous because they can sustain Faradaic reactions and therefore operate in the conventional amperometric mode provided a redox mediator is present in solution. An approach curve is recorded in the conventional positive feedback or hindered diffusion amperometric mode to assess the tip–substrate distance. Subsequently, the tip is electrochemically reconditioned to perform potentiometric measurements. The whole procedure is carried out

in situ to retain precise control of the tip position. Following this approach, Horrocks et al.[108] and Toth et al.[109] recorded the steady-state current for oxygen reduction on an antimony microdisk and showed that the current decreases when moving the electrode close to an inert substrate. This is in agreement with the principle of hindered diffusion and the current–distance curve was exploited to determine the absolute tip–substrate distance. The experiment was conducted as follows. The tip potential was held in the plateau region for oxygen reduction. The approach curve was then recorded from the bulk to the substrate to avoid crashing the tip. After returning to the bulk, the tip potential was held well positive of the oxygen reduction wave to regenerate the antimony oxide and reestablish the pH function. After a few seconds, the tip was switched to the potentiometric mode and used to probe pH profiles and acquire pH maps over the substrate surface.

This approach is only possible with solid-state ISEs and only with those rapidly electrochemically regenerated. Unless removed by purging, oxygen is always present in the solution and alleviates the need for addition of a redox mediator that could alter the rest potential of the antimony electrode and interfere with the pH measurement. Moreover, the normalization of the approach curve with the limiting current in the bulk removes the need for the knowledge of the bulk concentration and diffusion coefficient of oxygen.

Recently, a double function electrode was prepared for imaging copper ion concentration profiles by Csoka and Mekhalif.[110] It was fabricated from a 25 µm platinum disk electrode in a glass capillary and well-polished end plate. The Pt was dissolved to obtain a small cavity by etching in 60 vol% saturated $CaCl_2$, 36 vol% water, and 4 vol% concentrated HCl with a 5 V AC, 50 Hz voltage. The cavity was filled with carbon paste modified with diethyl-thiuram-disulfide ionophore. In the potentiometric mode, the electrode acted as a copper ion–selective microelectrode with 10^{-6}–10^{-3} M linear dynamic range and 16 s response time. In the amperometric feedback mode, using dissolved oxygen as a redox mediator, it could be used to estimate the tip–substrate distance. This approach was used to follow copper dissolution and the dissolution rate could be estimated from tip potential versus tip–substrate distance curves. This tip was quite large compared to micropipette ISE tips, especially when considering the overall diameter of the glass tip.

10.5.1.2 Conductimetric Approach

In absence of a redox mediator, the method described previously is not doable. However, an alternative approach based on conductimetry is possible provided the tip can cope with the passage of current. An AC impedance technique was exploited to determine the absolute tip–substrate distance between an enzyme-coated microelectrode tip and a sample.[111] In the AC mode, a sinusoidal voltage (respectively current) is applied between the tip and the counter electrode normally located in the bulk of the solution. The sinusoidal current (respectively voltage) response is sent to a lock-in amplifier or a frequency response analyzer and the real component of the impedance is recorded as the tip moves closer to the substrate. This component is in fact a measure of the solution resistance between the microelectrode tip and the counter electrode. Several parameters determine the magnitude of this resistance: the conductivity of the solution and of the substrate, the tip–substrate distance, and the geometry of the tip. An equivalent circuit is derived to calculate the dependence of the resistance on the tip–substrate distance and produce a theoretical approach curve. The DC mode offers a somewhat simpler alternative to the AC mode. The instrumentation consists only of a voltage source and a current follower while the procedure is simply to apply a fixed potential between the probe and the counter-reference electrode located in the bulk and measure a small current between the two. The technique, basically analogous to scanning ion-conductance microscopy,[112] was demonstrated with a Ag/AgCl tip and a Ag/AgCl auxiliary electrode[113] (see Figures 10.6 and 10.7).

A constant DC potential difference applied between the two electrodes produces a steady current from two reversible reactions, the formation of silver chloride on the tip and the dissolution of silver chloride on the auxiliary electrode. As the experiment is conducted in the DC mode, the double-layer capacitance of the electrodes is ignored and the tip solution auxiliary electrode

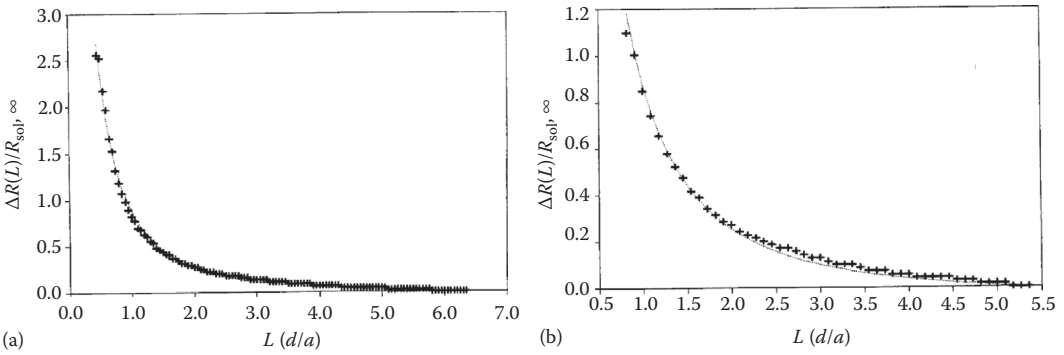


FIGURE 10.6 Solution resistance vs. distance curves recorded between a Ag/AgCl micropipette electrode (20 µm diameter, RG = 10) and a Ag/AgCl auxiliary electrode over (a) Pt and (b) Teflon targets. Solution, 0.1 M KCl; 50 mV applied between the two electrodes. +++, experimental data; …, theoretical curves. (Taken from Wei, C. et al., *Anal. Chem*., 67, 1346, 1995. With permission.)

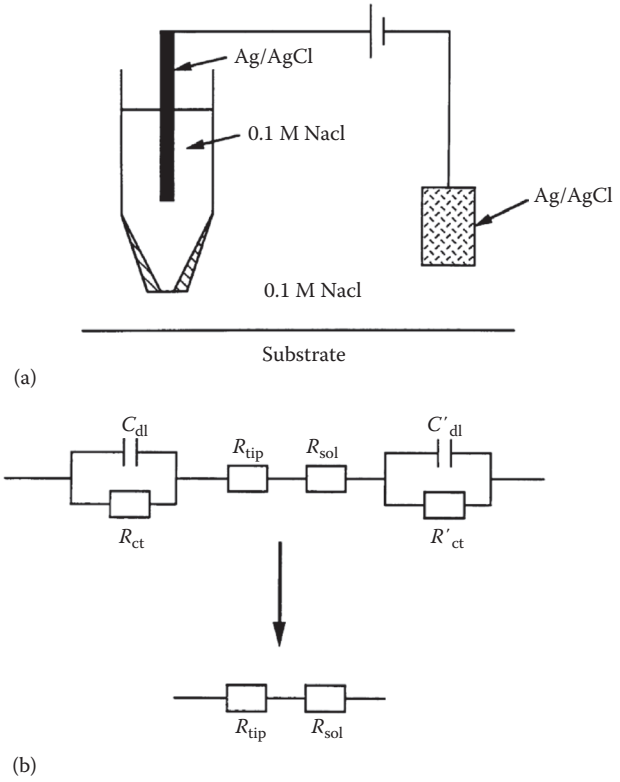


FIGURE 10.7 (a) Setup for distance measurements using a Ag/AgCl micropipette electrode. (b) Equivalent circuits corresponding to the electrode configuration shown in (a). (Taken from Wei, C. et al., *Anal. Chem*., 67, 1346, 1995. With permission.)

system behaves as a purely resistive circuit. Similarly, the charge transfer resistance at the counter electrode–solution interface is neglected because of the large surface area and the rapidity of the reaction. The treatment of the tip impedance depends largely on its geometry. Two kinds of tips are available, the solid microdisk and the micropipette. If the microdisk is very small, then its charge transfer resistance may determine the overall resistance and the dependence on tip–substrate

distance is lost. This is not a problem with the formation and dissolution of silver chloride since the charge transfer is very fast. The overall resistance is therefore made of the charge transfer resistance at the tip in series with the solution resistance. Only the latter varies with the tip–substrate distance. The micropipette on the other hand has a large internal electrode whose charge transfer resistance can be neglected. However, the open micropipette has an internal solution resistance determined by the conductivity of the filling solution, the same electrolyte as in the SECM cell to avoid a liquid junction potential. The internal solution resistance also depends on the pipette geometry, diameter, and shank, but does not depend on the tip–substrate distance. The total resistance is therefore made of the internal tip solution resistance in series with the external solution resistance; again, only the latter depends on the absolute tip–substrate distance. In both cases, the tip–substrate distance is determined by fitting the experimental resistance profile to its theoretical equivalent. In fact, the equation for the potential distribution is analogous to the steady-state diffusion equation and the theoretical dependence of the resistance is very easily derived from the amperometric feedback approach curve to an insulating substrate. The following equations illustrate the analogy and data treatment:

In the steady state, the diffusion equation is written as

$$\nabla^2 c = 0 \tag{10.7}$$

and the current density j is given by

$$j = nFD\nabla c \tag{10.8}$$

where n, F, D, and c have their usual meaning. Far away in the bulk, the steady-state tip current to a microdisk, $i_{T,\infty}$, is

$$i_{T,\infty} = 4nFDc^{b}a \tag{10.9}$$

where

c^{b} is the bulk concentration
a is the tip radius

Similarly, the potential distribution is written as

$$\nabla^2 \phi = 0 \tag{10.10}$$

and the current density, j, is given by

$$j = -\kappa\nabla\phi \tag{10.11}$$

where

ϕ is the potential in solution
κ is the conductivity of the solution

The analogy between Equations 10.7 and 10.10 leads to the following relationship:

$$\frac{R_{sol}(d)}{R_{sol,\infty}} = \frac{i_{T,\infty}}{i_T(d)} \tag{10.12}$$

where $R_{sol}(d)$ and $i_T(d)$ are the solution resistance and tip current, respectively, at a given tip–substrate distance d. The solution resistance between the microdisk and a counter electrode at infinity, $R_{sol,\infty}$, is given by[114]

$$R_{sol,\infty} = \frac{1}{4\kappa a} \tag{10.13}$$

The total resistance between the probe and the secondary electrode, $R_{total}(d)$, is calculated from the applied voltage and the measured current. As discussed previously, this resistance is the sum of two terms:

$$R_{total}(d) = R_{tip} + R_{sol}(d) \tag{10.14}$$

where R_{tip} is a constant equal to the charge transfer resistance for a microdisk or to the internal solution resistance for a micropipette. When the tip is far away in the bulk, the substrate does not interfere with the ionic pathway between the two electrodes and $R_{sol}(\infty)$ is a constant. However, when the tip approaches the substrate, the latter dramatically blocks the ionic pathway and $R_{sol}(d)$ increases. R_{tip} on the other hand is not a function of d and it cancels out when the left-hand side of Equation 10.12 is rewritten as follows:

$$\frac{R_{sol}(d)}{R_{sol,\infty}} = \frac{R_{total}(d) - R_{total}(\infty)}{R_{sol,\infty}} + 1 \tag{10.15}$$

Combining Equations 10.12 and 10.15 leads to

$$\frac{R_{total}(d) - R_{total}(\infty)}{R_{sol,\infty}} = \frac{i_{T,\infty}}{i_T(d)} - 1 \tag{10.16}$$

where

$R_{total}(d)$ and $R_{total}(\infty)$ are measured
$R_{sol,\infty}$ is calculated with Equation 10.13
$i_{T,\infty}/i_T(d)$ is the inverse of the familiar amperometric approach curve for hindered diffusion described by the approximate analytical equations discussed in Chapter 5.

Thus the experimental resistance profile can be compared with the theoretical profile and the absolute tip–substrate distance derived after adjustment of an offset.

It is important to stress one major difference between AC and DC modes. In the AC mode, a conducting substrate participates in the conduction process and reduces the solution resistance observed. On the contrary, an insulating substrate blocks the ionic pathway and increases the solution resistance observed. In the DC mode, both conducting (provided the applied potential is sufficiently small that no Faradaic process occurs on the substrate) and insulating substrates block the conduction pathway and increase the resistance between the tip and the auxiliary electrode (see Figure 10.6).

10.5.1.3 Fit to Theoretical Concentration Profiles

When the electrode resistance is very large, for example, with an ion-selective microelectrode, the method described in Section 10.2 does not work. An alternative approach consists in fitting the experimental concentration profile calculated from the tip potential to the theoretical profile predicted for the substrate geometry and activity. When the system investigated is at steady state, there is a unique relationship between tip potential and tip–substrate distance and an absolute distance scale can be determined. However, the procedure fails when the system is not at steady state because most ISEs are unable to follow rapid changes in concentration.

The experiment is carried out in diffusion-controlled conditions. Theoretical concentration profiles are calculated by solving Fick's second law of diffusion in the steady state with boundary conditions appropriate to the solution domain and to the substrate, taking into account its geometry and the type of reaction occurring on it. Assumption is made that the redox species are stable and not involved in a homogeneous reaction in solution. Two geometries known to produce steady-state concentration profiles have been considered:[108,113] the hemisphere and the microdisk. The former requires only a radial dimension and the diffusion equation can be solved analytically. The latter on the other hand necessitates cylindrical coordinates and the solution becomes much more complex. With the latter, a closed form analytical expression is available for the concentration profile above the center of the disk. The tip potential is determined by the concentration at the tip coordinates when the tip is small relative to the substrate. However, the situation is more complicated when the tip is comparable to or larger than the substrate. In this case, the tip intersects a range of concentration profiles and the tip potential has to be calculated from the average concentration over the tip surface. There again the expression for the average concentration depends on the geometry of the substrate.

Since the concentration profile reflects the concentration in the bulk solution and at the substrate surface (or the flux at the substrate), the nature of the fitting depends on whether the substrate produces or consumes redox species. When the substrate acts as a source, the concentration depends on the distance away from the substrate and on the flux or concentration at the substrate surface. Thus the fitting involves two unknowns, the surface flux or surface concentration (assuming that the substrate radius is known) and the offset needed to turn the relative distance scale into an absolute scale. When the substrate acts as a sink, the bulk concentration is known or measured. In the limiting diffusion-controlled condition where the surface concentration is zero, the offset is the only unknown.

While the theoretical treatment appears simpler than that of the feedback amperometric mode, in practice quantitative agreement between theoretical and experimental concentration profiles is more difficult because the tip travels through the diffusion layer due to the substrate activity. Thus the tip introduces convection within the substrate diffusion layer while shielding the substrate from the bulk. In the amperometric mode, diffusion is mostly confined to the tip–substrate gap and thus shielding and convection are not a problem. In general, the fit between experimental and theoretical concentration profiles works well when the tip is at least one tip radius away from the surface. Shielding dominates at closer tip–substrate distances where the tip significantly affects the concentration profile and the fit becomes poor.

As stated earlier, the theoretical concentration profile is calculated on the assumption that the species of interest is not involved in a homogeneous reaction. With a pH probe such as the antimony–antimony oxide tip, this assumption is not valid because the buffer capacity of the solution significantly affects the concentration profile. For example, protons generated at the substrate react with the base form of the buffer and the concentration profile is no longer solely diffusion controlled. Similarly, hydroxide anions produced by the substrate titrate the acid form of the buffer. A high-capacity buffer reestablishes the bulk conditions very close to the substrate while a low-capacity buffer allows the concentration profile to extend far away from the substrate before returning to the bulk concentration. These effects were quantitatively predicted and theoretical pH profiles were found to agree with experimental profiles.[108] The agreement worsens when the tip–substrate distance is less than three times the target radius. The buffering capacity can be observed on images of the antimony tip potential recorded over a Pt target undergoing water reduction. The pH variations and the region where pH changes are larger in a low buffer concentration than in a high buffer concentration. This approach was successfully used to map, on the micrometer scale, pH changes due to electrochemical reactions, corrosion processes, biocatalytic reactions, and metabolic processes of microorganisms.

10.5.1.4 Double Tip Techniques

Several of the procedures described in the previous sections can be advantageously carried out with double barrel tips. These probes basically consist of two capillaries, see Section 10.1.2.4, where one

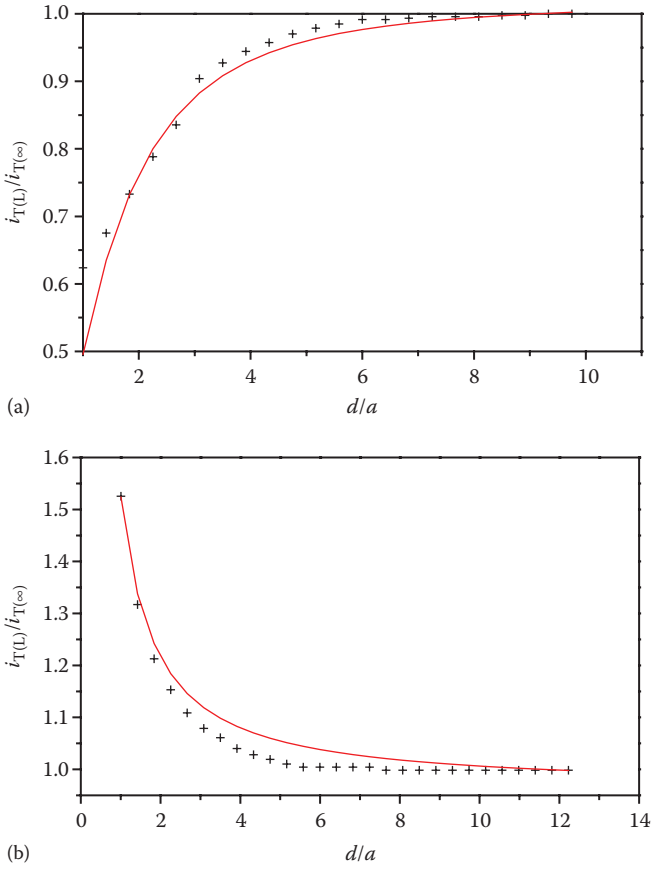


FIGURE 10.8 Feedback current–distance curves for a gallium SECM tip of 22 μm diameter operating in amperometric mode in 0.1 M KCl and 5 mM $Ru(NH_3)_6Cl_3$: (a) Pt surface and (b) Teflon surface. Pluses represent experimental data, while the solid lines are theoretical data. The tip potential was held at −0.6 V vs. Ag/AgCl reference electrode. (Taken from Wei, C. et al., *Anal. Chem*., 1996, 68, 2651, 1996. With permission.)

acts as the potentiometric sensor while the other is used to determine the tip–substrate distance. For example,[115] a gallium microdisk was combined with an ion-selective (K^+) potentiometric probe to image K^+ activity near the aperture of a capillary (see Figure 10.8). Similarly,[113] a double barrel tip with an open channel acting as a Ag/AgCl micropipette to measure solution resistance and the other channel plugged with an ion-selective neutral carrier for potentiometric measurements was successfully used to image concentration distributions for NH_4^+ (Figure 10.9) and Zn^{2+} (Figure 10.10). While dual-channel tips facilitate the approach of the substrate and permit a direct determination of the absolute tip–substrate distance, their difficult fabrication severely limits their use. Reference [116] compares the aforementioned methods.

10.5.1.5 Shear Force Control

Controlling the tip–substrate distance by monitoring the shear force of a vibrating tip was described in Chapter 2. Although originally developed for the amperometric mode of SECM, the approach is very well suited to the potentiometric mode. Monitoring the shear force between the tip and the sample surface provides an independent means to precisely position the tip at a given distance above the sample and to maintain this distance while rastering the tip over the sample. For example, during a line scan the tip *z*-position is continually adjusted to maintain the shear force constant. This method is not influenced by the electrochemical properties of the sample nor does it rely on the electrochemical

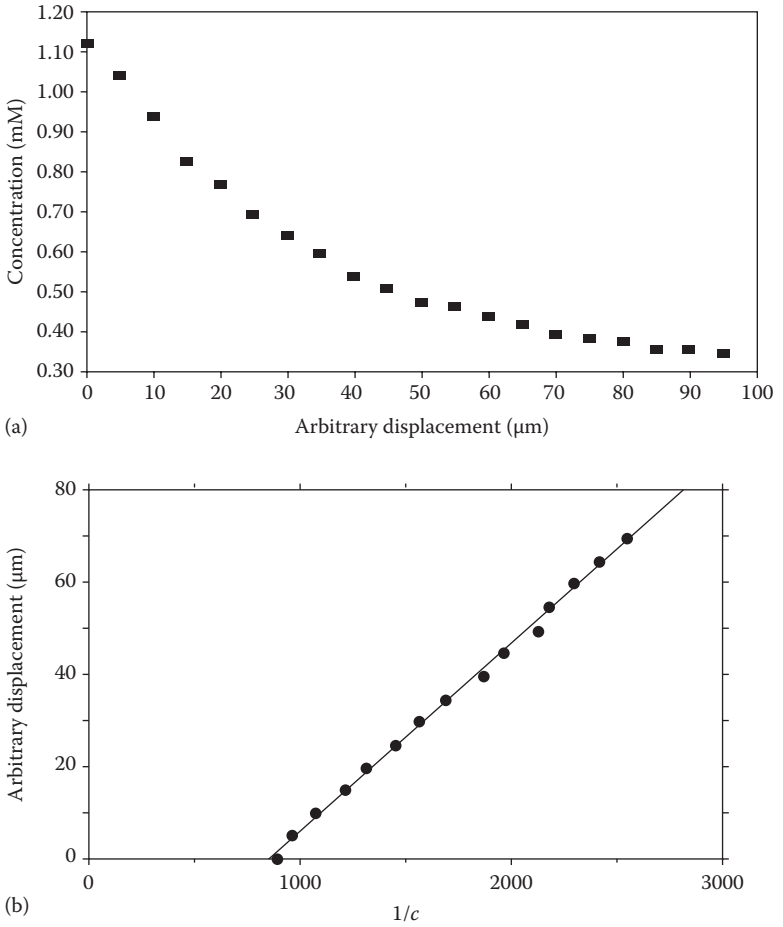


FIGURE 10.9 (a) NH_4^+ concentration profile recorded in the *z*-direction above the center of a 20 μm diameter urease gel target. Tip diameter: 18 μm; bulk concentration, 0.1 M urea, and 0.1 M Tris, pH 7 and (b) plot of arbitrary distance vs. 1/*c* using the data from (a). (Taken from Wei, C. et al., *Anal. Chem*., 67, 1346, 1995. With permission.)

response of the tip. The tip tracks the sample topography and the SECM operates at constant tip–substrate distance irrespective of the sample chemical activity and irrespective of the mode of detection at the tip. This approach is particularly suited to potentiometric probes because it does not depend on their electrical properties, for example, impedance, which can vary significantly between different probes, and because it allows close approaches, ca. 200 nm, without crashing. However, the technical difficulties encountered when implementing the shear force control have limited its application. To our knowledge, only Schuhmann and coworkers have reported studies where the shear force control was successfully used to provide precise positioning of potentiometric SECM tips, namely pH tips for localized corrosion[117] and Ca^{2+}-selective tips to monitor the dissolution of calcium carbonate.[118]

10.5.2 Considerations Specific to the Potentiometric Mode

10.5.2.1 Ohmic Drop Effects

The Ohmic drop should be taken into account when performing potentiometric measurements with a traveling probe. While this effect is the basis of SRET measurements, it becomes a nuisance in potentiometric SECM applications. If the substrate is an electrode involved in a faradaic process,

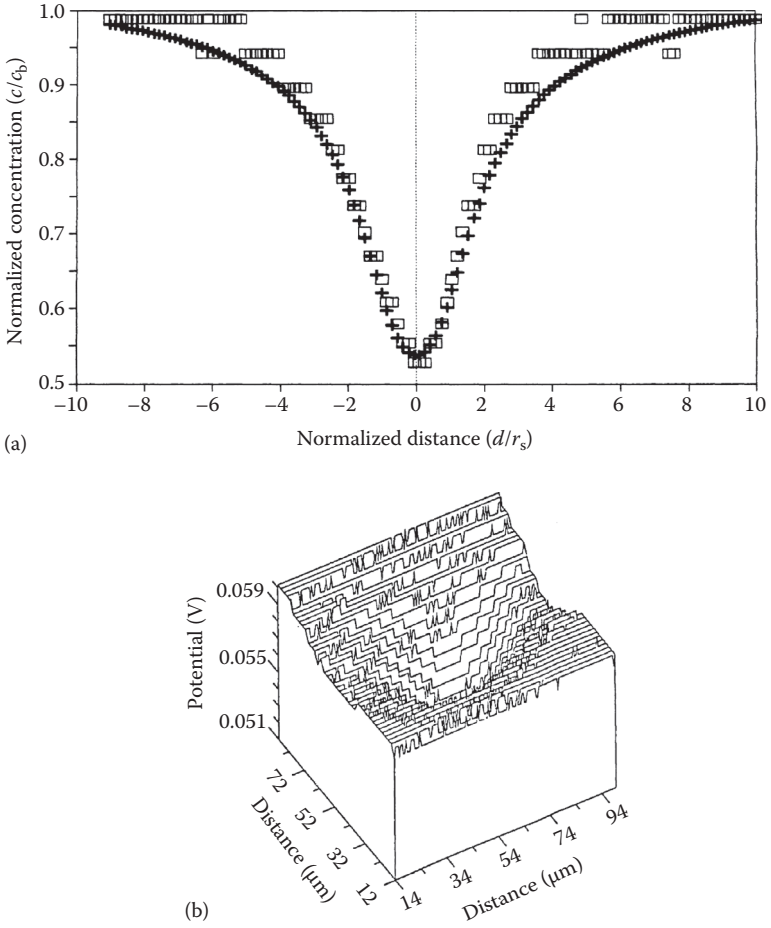


FIGURE 10.10 Map of the Zn^{2+} concentration over a 25 μm diameter Hg-coated Au electrode in 0.84 mM $Zn(NO_3)_2$ + 0.1 M NH_4Cl + 50 mM pH 7 Tris–HCl buffer: (a) radial direction across the center of the electrode at a constant height of 11 μm over the surface. Electrode held at −1.15 V; tip diameter 10 μm; tip scan rate 2 μm/s. c^b bulk concentration, r_s target radius. Empty squares for experimental data and pluses for theoretical data. (b) Corresponding surface plot. (Taken from Toth, K. et al., *Electroanalysis*, 7, 801, 1995. With permission.)

the current flowing between the substrate and its counter electrode leads to potential gradients in the solution. The tip will be sensitive to the potential distribution and this may overcome the signal due to the concentration change for the ion of interest. This is particularly pronounced if the reference electrode associated to the tip is located far away in the bulk and of course if the solution conductivity is low. To remedy this situation, some researchers have used double barrel electrodes where one channel acts as the ion-sensitive element and the other acts as a reference electrode.[119] In the life sciences, intracellular measurements are usually carried out in this way. Alternatively, it is possible to subtract the Ohmic drop from the tip response. This requires an estimate of the solution resistance between the tip and its reference electrode and a measure of the substrate current.[33]

10.5.2.2 Mapping and Resolution

The principles of potentiometric imaging are far simpler than those of amperometric imaging. In the amperometric mode, the tip directly interacts with the concentration profiles of the redox mediator by consuming one redox form and producing the other. Hence, the measurement severely alters

the concentration profiles. In the potentiometric mode, the tip is passive. Its response depends solely on the concentration profiles it encounters. It shields the substrate from the bulk solution but does not consume or produce a species. Unlike the amperometric mode, there is no edge effect and the insulator around the tip plays no role. The tip potential reflects the concentration of the ion of interest, averaged over the sensing region. Thus the tip is only sensitive to the solution in contact with its sensing element. The geometry and dimensions of the sensing element therefore determine the spatial resolution.[120] To improve the spatial resolution, one tries to miniaturize the tip and the insulator around it. The smaller the sensing element, the better the spatial resolution; the smaller the overall tip end, the less shielding there is.

In the potentiometric mode, a single sensor tip can only image the distribution of a specific ion. A multi-barrel tip is needed to follow different species simultaneously. This is in contrast to the amperometric mode where a redox mediator is selected by adjusting the tip potential. Thus by having more than one redox mediator in solution, it is possible to produce several amperometric images simply by changing the tip potential each time. To our knowledge, no one has made use of this idea but in principle it is feasible.

10.5.3 Applications

The following sections consider several potentiometric applications. Some articles do not refer directly to SCEM but are nevertheless closely related to the SECM principles and are therefore included in the present chapter. Applications related to potentiometric probing of biological substrates have not been included since these are covered in Chapter 11.

10.5.3.1 Probing pH

Of all the applications, the use of potentiometric tips to follow pH profiles near electrodes, corroding surfaces, or membranes appears the most common. A short selection of these studies is included later.

Klusmann and Schultze[120] made a comparison between theoretical and experimental pH profiles near planar and microdisk electrodes for constant flux and constant concentration sources. They also investigated the spatial resolution for pH mapping. Horrocks et al.[108] reported the results of SECM experiments where potentiometric pH-selective tips were used to image local pH changes in several model chemical systems. These included platinum microelectrodes during water reduction (Figure 10.11), a corroding disk of silver iodide in aqueous potassium cyanide, a disk of immobilized urease hydrolyzing urea, and a disk of immobilized yeast cells in glucose solution (Figure 10.12). A detailed investigation of proton concentration profiles close to silver iodide–based ion-selective membranes was reported by the same authors.[109] pH measurements were carried out in the vicinity of a semipermeable membrane operating in a chlor-alkali cell.[119b] The tip consisted of two channels, one filled with antimony to form a pH-sensing disk and the other left open to act as a Luggin capillary and eliminate the effect of iR drop. This study showed the extent of penetration and leakage of hydroxides through the membrane. Similarly, pH profiles were recorded near bilayer lipid membranes with an antimony microelectrode.[121] pH measurements were also performed in the vicinity of a cathode evolving hydrogen gas using an antimony microelectrode.[122] The effect of a buffering agent, glycine, was investigated. Tanabe et al.[123] used potentiometric and amperometric SECM techniques to investigate the ionic environment above pits on stainless steel surfaces. They reported the potentiometric detection of Cl^- with Ag/AgCl tips and of protons with 7 μm diameter carbon fibers; the principle of potentiometric detection of protons with a carbon fiber is not clear. Park et al.[119a] fabricated double barrel tips (one filled with a proton-sensitive liquid-exchange resin and the other acting as a local reference electrode) and probed the OH^- buildup generated by cathodic reactions on Al_3Fe in contact with Al 6061 in a galvanic cell. Luo et al.[124] also report the fabrication of potentiometric pH tips to investigate localized corrosion.

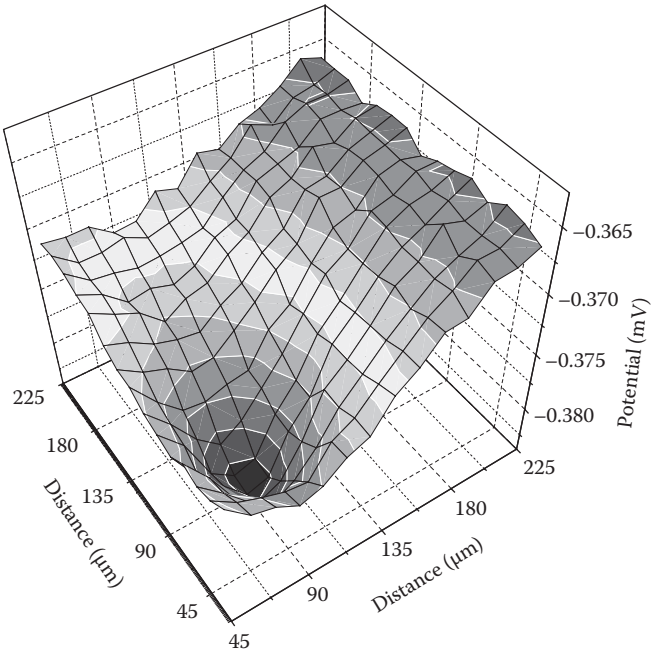


FIGURE 10.11 Image of the pH profile over a 10 μm Pt target reducing water. The potential of the target was –2 V and the current was 0.5 μA. The diameter of the Sb tip was 15 μm, the tip surface distance was 33 μm, and the tip scan rate was 10 μm/s. The solution was 1 mM phosphate buffer (pH = 7).

Micro-pH-sensitive iridium oxide electrodes with <10 μm tip diameter were developed by El-Giar and Wipf.[125] The electrode was fabricated from a glass micropipette having a tip opening of a few micrometers. A sonicated suspension of iridium microparticles in methanol was introduced into the tip. After settling down and evaporation of the methanol, the particles were sintered to form a solid iridium cone inside the tip (see Figure 10.13). Silver epoxy was employed to provide electric contact between iridium and silver-coated copper external connecting wire. Potential cycling in 0.5 M H_2SO_4 at 3.0 V/s was employed to form the pH-sensing oxide film on the iridium disk. The application of these pH -sensitive microelectrodes was demonstrated by imaging the pH changes due to the oxygen reduction reaction at the surface of a cast iron sample.

Mirkin and coworkers[126] used Sb microelectrodes to perform amperometric and potentiometric experiments near living cells. The pH was probed potentiometrically while the topography and redox activity of the cells were probed amperometrically. The topography was determined using hydrophilic mediators as they cannot penetrate the cell membrane; in contrast, the redox activity was determined with hydrophobic mediators that can permeate across the cell membrane. The use of a single tip to probe intracellular redox activity and pH changes provides valuable information when investigating biochemical processes. However, control of the tip–substrate distance was found to be a challenge since biological specimens are soft, not flat, and can be easily damaged by the scanning probe.

In corrosion studies, ISEs have been used to map the local concentration of ions over corroding metals in the liquid phase with high resolution and selectivity. For example, H^+-, Mg^{2+}-, and Zn^{2+}-selective microelectrodes were used in combined applications of the scanning ISE technique (SIET, akin to potentiometric SECM) and of the SVET over corroding alloys.[127] The SIET image showed the local ion activities, while the SVET mapped the local ionic current density. In all cases, their ISE tips were made from single barreled micropipettes with cocktail of ionophores.

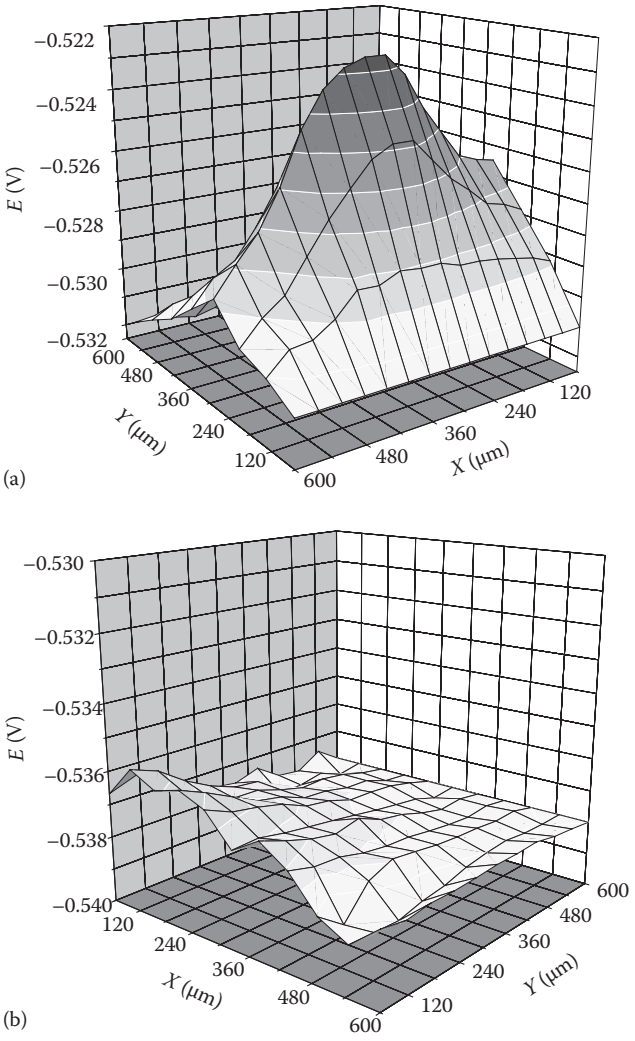


FIGURE 10.12 (a) pH values over a 80 μm diameter yeast/agarose target. The tip diameter was 15 μm, the tip scan rate was 10 μm/s, the solution contained 5 mM glucose in 1 mM phosphate buffer, and the tip target distance was 20 μm; (b) after treatment of the yeast culture with 1 g/dm^3 $NaHSO_3$.

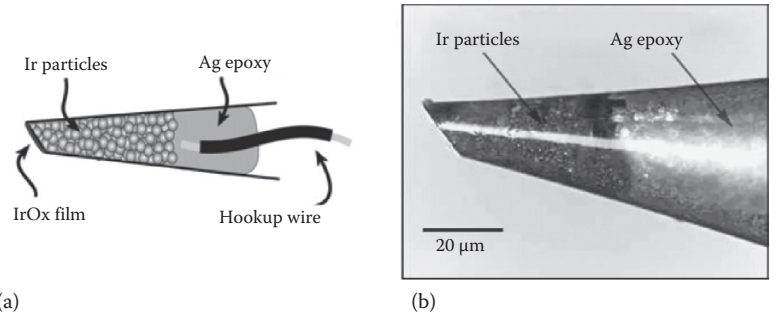


FIGURE 10.13 Iridium oxide microdisk electrodes fabricated by El-Giar and Wipf to map pH profiles in localized corrosion studies. (Taken from El-Giar, E. and Wipf, D.O., *J. Electroanal. Chem*., 609, 147, 2007. With permission.)

10.5.3.2 Probing Cl^-

As in amperometric applications, many experiments can be conducted in the close proximity mode where the tip is moved very close to the substrate surface and a perturbation is applied to the sample. This perturbation may take several forms, typically potentiostatic or galvanostatic excursions if the sample is acting as an electrode, but also optical illumination with a laser beam, change of solution, etc. The tip response is then recorded as a function of time following the application of the perturbation. In these conditions, potentiometric detection offers two advantages over amperometric detection. (i) The range of ions detectable is extended to nonelectroactive species such as alkali metals and (ii) the tip response is selective. There are, however, some drawbacks. Because of the high impedance of the electrometer, the response time is worse in potentiometric applications where the t_{90} is rarely below 30 s. This must be compared to the millisecond timescale available with amperometric responses.[128] Ohmic drop may also affect the tip potential.

Denuault et al.[33] reported the use of potentiometric tips to probe ion fluxes near surfaces. The 10 and 50 µm diameter silver microdisk electrodes were used to probe the concentration profile due to the diffusion of Ag^+ to and from a planar Ag electrode. A similar experiment was carried out with a 50 µm diameter microcylinder substrate electrode. The tip response was recorded at various locations above the substrate while simultaneously applying a potential square wave to the substrate to induce the dissolution and plating of silver. These experiments demonstrated the principle of the technique and confirmed the possibility of obtaining spatially resolved information. Moreover, these experiments clearly showed that the tips response time was in fact very good (t_{90} below 10 ms) (see Figure 10.14). Undoubtedly, this was due to their very low impedance.

In a separate experiment, 10 and 50 µm diameter Ag/AgCl microdisks were used to monitor the flux of Cl^- consumed and generated by a film of polyaniline undergoing redox cycles. The tip potential was recorded while cycling the potential of the polyaniline film. The results obtained (Figure 10.15) provide direct evidence for the ingress and egress of Cl^- ions and support the mechanism previously proposed for the oxidation of polyaniline. Subsequent experiments carried out in the amperometric mode for the reduction of protons were found to be in complete agreement with the potentiometric data.[129]

Horrocks et al.[111] performed similar tip–substrate voltammetric experiments where the potentiometric pH tip response was recorded while scanning the potential of a substrate electrode. Significant pH variations in the vicinity of a gold electrode reducing oxygen were observed with antimony tips.

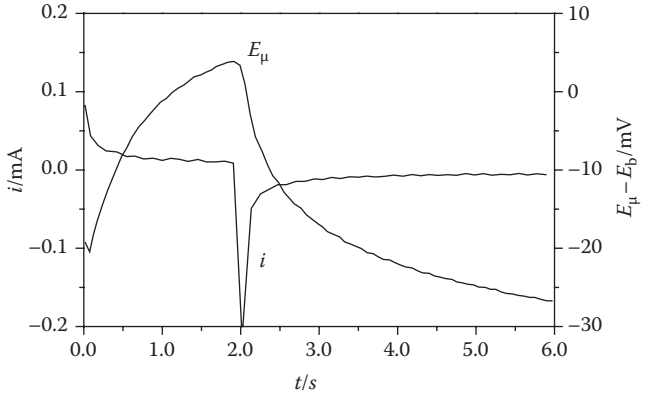


FIGURE 10.14 Potential of a 50 µm diameter Ag disk tip with respect to the bulk electrode potential as a function of time while pulsing the substrate electrode from 0 to 50 mV vs. Ag/Ag^+ for 2 s then to −50 mV for 4 s. The tip–substrate distance is <10 µm. The substrate is a large planar silver electrode. The substrate current is shown on the left-hand scale. (Taken from Denuault, G. et al., *Faraday Discuss.*, 94, 23, 1992. With permission.)

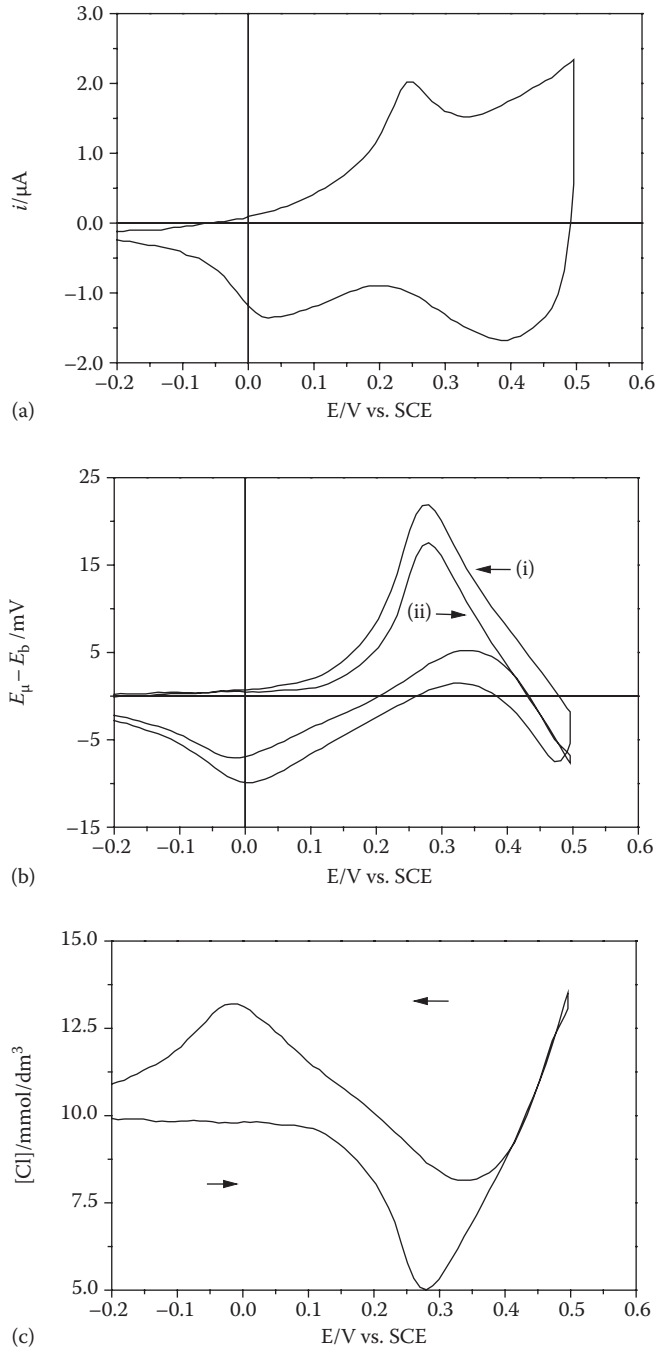


FIGURE 10.15 (a) Cyclic voltammogram of a polyaniline film on Pt (area 9.3×10^{-4} cm^2) recorded at 5 mV/s in 0.01 mol/dm^3 HCl. (b) Microindicator (Ag/AgCl) response recorded as a function of the potential of the Pt electrode supporting the polyaniline film. The probe, a 10 μm diameter Ag/AgCl microdisk with an RG circa 7, is located very close to the polymer film. (i) Uncorrected and (ii) iR corrected. (c) Calculated local Cl^- concentration as a function of the potential of the Pt electrode supporting the polyaniline. (Taken from Denuault, G. et al., *Faraday Discuss*., 94, 23, 1992. With permission.)

Unwin and coworkers[130] used Ag/AgCl microelectrodes to detect chloride concentrations while investigating the hydrolysis rate of triphenylmethyl chloride (TPMCl) at the 1,2-dichloroethane (DCE)–water interface. In their experiments, the ISE was placed in aqueous KNO_3 within 1 mm of a pipette end from where microdroplets of organic solvent (DCE) containing TPMCl in 0.1 M concentration were produced. The rate of interfacial hydrolysis reaction was determined by measuring the local chloride ion concentration potentiometrically at the Ag/AgCl microelectrode in the aqueous phase, as a droplet of DCE containing TPMCl expanded toward the electrode. The expanding sphere transport model was required to derive the kinetic information from the time dependence of the chloride concentration.

Kemp et al.[131] operated in the close proximity mode to study the concentration of chloride ions generated near the surface of UV-irradiated titanium dioxide in the presence of aqueous 2,4-dichlorophenol. The Cl^- concentration was measured potentiometrically with a 50 µm diameter Ag/AgCl microdisk. Experiments were performed at several tip–substrate distances and the concentration of chloride was recorded as a function of time after turning on and turning off the UV irradiation.

10.5.3.3 Probing K^+

A solid contact ion-selective potassium electrode was employed as a potentiometric SECM tip by Gyurcsanyi et al.[132] They made the electrode by electrochemically forming a conductive polymer layer on the surface of a Pt microdisk, fabricated by sealing a 5 µm diameter platinum wire in a glass capillary body, tapering and polishing and coating the tip with a plasticized PVC matrix–based ion-selective membrane. This coating provided a stable interface potential between the ISE membrane and the platinum disk. Potassium concentration profiles resulted by KCl diffusion out from a gel-plugged micropipette were imaged using the electrode. The size of this tip is much bigger than that of conventional micropipettes; however, improved stability and lower resistance compensate for the loss of spatial resolution.

10.5.3.4 Probing NH_4^+

Horrocks and Mirkin[133] used micron-sized ammonium ion–selective micropipettes to image ammonium concentrations in a buffered urea solution over a 50 µm diameter gold disk onto which a Jack Bean urease enzyme (EC 3.5.1.5) had been adsorbed. The flux of ammonium ions could be imaged and the ion-selective microelectrode was found to be a good tool for probing the activity of the enzyme. Interestingly, the ammonium ion concentration profile was changed when scanning the gold potential between 0.0 and 0.4 V vs. Ag/AgCl. The flux decreased when the electrode was polarized at 0.0 V and increased when it was polarized at 0.4 V. The urease is a hydrolase enzyme, not an oxidoreductase. No Faraday current was observed during polarization but the observed dependence of the ammonium flux on electrode potential was explained as a potential-dependent reversible inactivation/reactivation of the enzyme.

The fast solid contact electrode discussed in Section 10.1.3.3. was used to record ammonium activity maps over a disk of urease held in a gel (about 25 µm diameter) in a 0.1 M urea solution buffered at pH 7.2. Figure 10.16 compares two images obtained (a) with a conventional NH_4^+ micropipette and (b) with a solid contact NH_4^+ micropipette. In both cases, the tips were ~3 µm in diameter, the rastering speed was 10 µm/s, and the tip–substrate distance was 70 µm. The equipotential contours obtained with the solid contact electrode are circular as expected for a disk-shaped ammonium ion source, while those recorded with the conventional micropipette are elliptical due to the longer response time of the probe.

10.5.3.5 Probing Ca^{2+}

Berger et al.[134] used ion-selective calcium micropipettes with 2–3 µm tip diameters for real-time detection of calcium ion release from revitalized bovine cortical bone slices. They investigated the applicability of this in vitro technique to the study of osteoclast cell–induced bone resorption (dissolution), which is responsible for osteoporosis. A commercial ion-selective cocktail was used

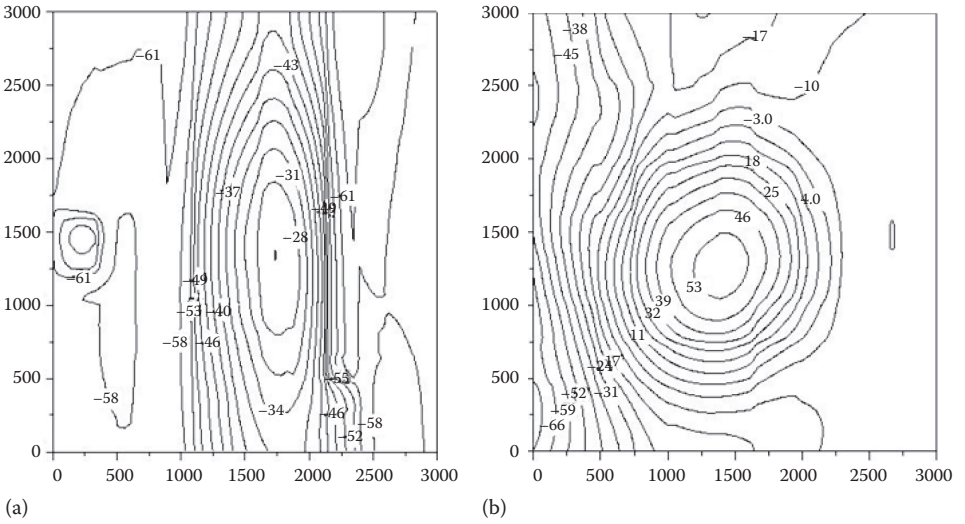


FIGURE 10.16 SECM images of ammonium ion concentration over the same immobilized urease containing disk. Urea concentration 0.1 M and tip travel rate 10 μm/s. Tip–substrate distance, ~70 μm over the enzyme disk. (a) was recorded with a conventional micropipette while (b) was recorded with a solid contact electrode. The *X* and *Y* scales are in micrometers while the contour lines correspond to the tip potential in mV vs. Ag/AgCl.

to prepare the electrodes. The measuring tip was positioned over the bone surface and the local calcium ion activity was followed. Osteoclast cells obtained from sacrificed rats were adsorbed on the bone surface. The experiments showed that treating the bone with dilute ammonium fluoride slowed down significantly osteoclastic resorption of the bone and demonstrated that the potentiometric mode of SECM provides a realistic assay of osteoclast activity.

Similarly, a commercial Ca^{2+} ionophore-based micropipette electrode was used by Etienne et al.[118] to investigate the applicability of the potentiometric mode of SECM to the study of dissolution kinetics at solid–liquid interfaces. Using the shear force technique, they were able to precisely control the tip–substrate distance and perform imaging of the ion activity at constant distance over the substrate. The local dissolution of crystal plates of different orientations, as well as that of different parts of calcium carbonate shells of *Mya arenaria*, was obtained.

10.6 CONCLUSION

One should not see the potentiometric mode as an alternative but as a complement to the amperometric mode. The potentiometric mode offers the possibility of performing measurements on nonredox active species, for example, not detectable amperometrically in aqueous solutions. Another advantage is the increased selectivity of the potentiometric response compared to the Faradaic response. The logarithmic response is also useful when the species of interest is in low concentrations. Since the tip is passive, only substrate generation–tip detection experiments are possible. However, the tip does not alter the concentration profile of the chemically or electrochemically generated species. The potentiometric micropipette tips have very small dimensions, typically 1 μm or less, and the shielding is minimal.

However, one should not forget that the potentiometric mode has several drawbacks. The fabrication of most potentiometric tips is a lot more involved than that of the conventional amperometric tips. It is necessary to have the electrode made by a very skilled technician. Despite this, even when following a proven recipe the success rate is low. The response of potentiometric tips is not always Nernstian and a calibration is required before and after performing the experiment. The behavior typically

varies from one microelectrode to another. Potentiometric tips cannot rely on positive and negative feedback diffusion, thus it is difficult to assess the tip–substrate distance from the tip response. Several approaches are available but most are cumbersome. In the potentiometric mode, the response time depends on several time constants, namely of the measuring circuit, of the other electrode, and of the tip itself. The transient response is typically slower than with amperometric tip but this is not so much a problem for potentiometric probing of one-dimensional (1D) and two-dimensional (2D) concentration distributions; the tip moves slowly and steep concentration gradients are not common. Slow response times can be a limiting factor when performing close proximity experiments.

REFERENCES

1. Cremer, M., Origin of electromotor properties of tissues, and instructional contribution for polyphasic electrolyte chains. *Zeitschrift für Biol* 1906, 47, 562–608.
2. Haber, F., Klemensiewicz, Z., Über elektrische Phasengrenzkräft. *Zeitschrift für Phys Chem* 1909, 67, 383–431 (Vorgetragen in der Sitzung der Karlsruher chemischen Gesellschaft am January 28, 1909).
3. Lengyel, B., Blum, E., The behavior of the glass electrode in connection with its chemical composition. *Trans Faraday Soc* 1934, 30, 461–471.
4. Eisenman, G., Rudin, D. O., Casby, J. U., Glass electrode for measuring sodium ion. *Science* 1957, 126, 831–834.
5. Tendeloo, H. J. C., A new and easy method for the potentiometric determination of calcium concentrations in solutions. *J Biol Chem* 1936, 113, 333–339.
6. Anderson, R. S., The attempted use of crystals as calcium electrodes. *J Biol Chem* 1936, 115, 323–326.
7. Kolthoff, I. M., Sanders, H. L., Electric potentials at crystal surfaces and at silver halide surfaces in particular. *J Am Chem Soc* 1937, 59, 416–420.
8. (a) Sinha, S. K., Ion-activity measurements with resin membrane electrodes. I. Determination of univalent ions. *J Indian Chem Soc* 1953, 30, 529–534; (b) Sinha, S. K., Potentiometric titrations with resin membrane electrodes. *J Indian Chem Soc* 1955, 32, 35–38; (c) Woermann, D., Bonhoeffer, K. F., Helfferich, F., Cation exchanger selective for potassium ions. *Zeitschrift fur Phys Chem* 1956, 8, 265–283; (d) Parsons, J. S., Permselective membrane electrodes. Analytical applications. *Anal Chem* 1958, 30, 1262–1265.
9. Pungor, E., Hollos-Rokosinyi, E., The use of membrane electrodes in the analysis of ionic concentrations. *Acta Chim Acad Sci Hungaricae* 1961, 27, 63–68.
10. Pungor, E., Havas, J., Toth, K., Membrane electrodes in chemical analysis. *Zeitschrift fur Chem* 1965, 5(1), 9–14.
11. (a) Frant, M. S., Ross, J. W., Jr., Electrode for sensing fluoride ion activity in solution. *Science* 1966, 154(3756), 1553–1555; (b) Ross, J. W., Jr., Calcium-selective electrode with liquid ion exchanger. *Science* 1967, 156(3780), 1378–1379.
12. Ruzicka, J., Tjell, J. C., Liquid-state electrode. *Anal Chim Acta* 1970, 49(2), 346–348.
13. Coetzee, C. J., Freiser, H., Anion-responsive electrodes based on ion association extraction systems. *Anal Chem* 1968, 40(13), 2071.
14. (a) Stefanac, Z., Simon, W., A highly selective cation electrode system based on in vitro behavior of macrotetrolides in membranes. *Chimia* 1966, 20(12), 436; (b) Stefanac, Z., Simon, W., Ion-specific electrochemical behavior of macrotetrolides in membranes. *Microchem J* 1967, 12(1), 125–132; (c) Pioda, L. A. R., Stankova, V., Simon, W., Highly selective potassium ion responsive liquid-membrane electrode. *Anal Lett* 1969, 2(12), 665–674.
15. Bloch, R., Shatkay, A., Saroff, H. A., Fabrication and evaluation of membranes as specific electrodes for calcium ions. *Biophys J* 1967, 7(6), 865–877.
16. Craggs, A., Moody, G. J., Thomas, J. D. R., PVC matrix membrane ion-selective electrodes—Construction and laboratory experiments. *J Chem Educ* 1974, 51(8), 541–544.
17. (a) Nakamura, T., Development and application of ion-selective electrodes in nonaqueous solutions. *Anal Sci* 2009, 25(1), 33–40; (b) Dimeski, G., Badrick, T., St. John, A., Ion selective electrodes (ISEs) and interferences—A review. *Clin Chim Acta* 2010, 411(5–6), 309–317; (c) Bühlmann, Ph., Pretsch, E., Bakker, E., Carrier-based ion-selective electrodes. 2. Ionophores for potentiometric and optical sensors. *Chem Rev* 1998, 98(4),1593–1687.
18. Bergveld, P., Development of an ion-sensitive solid-state device for neurophysiological measurements. *IEEE Trans Biomed Eng* 1970, BME17(1), 70–71.

19. Hinke, J. A. M., Glass microelectrodes for measuring intracellular activities of sodium and potassium. *Nature* 1959, 184(Suppl. 16), 1257–1258.
20. Saunders, J. H., Brown, H. M., Liquid and solid-state (Cl^-)-sensitive microelectrodes—Characteristics and application to intracellular Cl^- activity in *Balanus* photoreceptor. *J Gen Physiol* 1977, 70(4), 507–530.
21. Neuman, M. R., Buck, R. P., Cosofret, V. V., Lindner, E., Liu, C. C., Fabricating biomedical sensors with thin-film technology. *IEEE Eng Med Biol Mag* 1994, 13(3), 409–419.
22. Lindner, E., Cosofret, V. V., Ufer, S., Johnson, T. A., Ash, R. B., Nagle, H. T., Neuman, M. R., Buck, R. P., In-vivo and in-vitro testing of microelectronically fabricated planar sensors designed for applications in cardiology. *Fresenius J Anal Chem* 1993, 346(6–9), 584–588.
23. Nomura, S., Nakao, M., Nakanishi, T., Takamatsu, S., Tomita, K., Real time imaging of microscopic pH distribution with a two-dimensional pH-imaging apparatus. *Anal Chem* 1997, 69(5), 977–981.
24. Caldwell, P. C., An investigation of the intracellular pH of crab muscle fibres by means of micro-glass and micro-tungsten electrodes. *J Physiol* 1954, 126(1), 169–180.
25. (a) Lev, A. A., Buzhinsky, E. P., On the technique for determining the activity of potassium ions in muscle fibers with the aid of glass microelectrodes sensitive to potassium ions. *Cytology* (*USSR*) 1961, 3, 614; (b) Lev, A. A., in *Glass Microelectrodes*, Lavalle, M., Schanne, O. F., Hebert, N. C., Eds. John Wiley & Sons, New York, 1969, p. 446.
26. (a) Thomas, R. C., New design for sodium-sensitive glass micro-electrode. *J Physiol* 1970, 210(2), 82P–83P; (b) Thomas, R. C., Intracellular pH of snail neurons measured with a new pH-sensitive glass microelectrode. *J Physiol* (*London*) 1974, 238(1), 159–180.
27. Pucacco, L. R., Carter, N. W., Glass-membrane pH microelectrode. *Anal Biochem* 1976, 73(2), 501–512.
28. Levy, S., Coles, J. A., Intracellular pH of limulus ventral photoreceptor measured with a double-barrelled pH microelectrode. *Experientia* 1977, 33(4), 553–554.
29. Yamaguchi, H., Stephens, N. L., New method of fabricating recessed tip, pH microelectrode. *Federation Proc* 1977, 36(3), 499–499.
30. (a) Armstron, W. M., Lee, C. O., Sodium and potassium activities in normal and sodium-rich frog skeletal muscle. *Science* 1971, 171(3969), 413–415; (b) Lee, C. O., Armstron, W. M., State and distribution of potassium and sodium ions in frog skeletal-muscle. *J Membr Biol* 1974, 15(4), 331–362.
31. Mauro, A., Electrochemical potential difference of chloride ion in the giant axonsea water system. *Federation Proc* 1954, 13, 96.
32. Kerkut, G. A., Meech, R. W., The internal chloride concentration of H and D cells in the snail brain. *Comp Biochem Physiol* 1966, 19(4), 819–832.
33. Denuault, G., Frank, M. H. T., Peter, L. M., Scanning electrochemical microscopy–potentiometric probing of ion fluxes. *Faraday Discuss* 1992, 94, 23–35.
34. Hills, G. J. and Ives, D. J. G., The hydrogen electrode. In Ives, D. J. G.; Janz, G. J., *Reference Electrodes*, Academic Press, New York: 1961.
35. Imokawa, T., Williams, K.-J., Denuault, G., Fabrication and characterization of nanostructured Pd hydride pH microelectrodes. *Anal Chem* 2006, 78, 265–271.
36. Ross, J. W., Jr. *Solid-State and Liquid Membrane Ion-Selective Electrodes*. In *Ion-Selective Electrodes*, RA Durst, Ed. NBS Spec. Pupl. 314, NBS, Washington DC, 1969, pp. 57–88.
37. Walker, J. L., Ion specific liquid ion exchanger microelectrodes. *Anal Chem* 1971, 43(3), A89–A93.
38. Orme, F. W., in *Glass Microelectrodes*, Lavallee, M., Schanne, O. F., Hebert, N. C., Eds. John Wiley & Sons, New York, 1969, pp. 25–31.
39. (a) Thomas, R. C., Simon, W., Oehme, M., Lithium accumulation by snail neurons measured by a new Li^+-sensitive microelectrode. *Nature* 1975, 258(5537), 754–756; (b) Oehme, M., Simon, W., Microelectrode for potassium-ions based on a neutral carrier and comparison of its characteristics with a cation exchanger sensor. *Anal Chim Acta* 1976, 86(October), 21–25.
40. Ammann, D., Neutral carrier based liquid membrane microelectrodes. In Amman, D., *Ion-Selective Microelectrodes: Principles, Design and Application*. Springer-Verlag, Berlin, Germany, 1986, 346pp.
41. Ammann, D., Pretsch, E., Simon, W., Lindner, E., Bezegh, A., Pungor, E., Lipophilic salts as membrane additives and their influence on the properties of macroelectrodes and microelectrodes based on neutral carriers. *Anal Chim Acta* 1985, 171(May), 119–129.
42. Tarcali, J., Nagy, G., Toth, K., Pungor, E., Juhasz, G., Kukorelli, T., In vivo measurements with a potassium ion-selective microelectrode based on a new bis(crown ether). *Anal Chim Acta* 1985, 178(2), 231–237.
43. Kraig, R. P., Nicholson, C., Sodium liquid ion-exchanger microelectrode used to measure large extracellular sodium transients. *Science* 1976, 194(4266), 725–726.

44. (a) Ruzicka, J., Hansen, E. H., Tjell, J. C., Selectrode—Universal ion-selective electrode. 6. Calcium(II) selectrode employing a new ion-exchanger in a nonporous membrane and a solid-state reference system. *Anal Chim Acta* 1973, 67(1), 155–178; (b) Moody, G. J., Nassory, N. S., Thomas, J. D. R., Calcium ion-selective electrodes based on calcium bis[di(*p*-1,1,3,3-tetramethylbutylphenyl)phosphate] sensor and trialkyl phosphate mediators. *Analyst* 1978, 103(1222), 68–71.
45. Brown, H. M., Pemberton, J. P., Owen, J. D., Calcium-sensitive microelectrode suitable for intracellular measurement of calcium(II) activity. *Anal Chim Acta* 1976, 85(2), 261–276.
46. Oehme, M., Kessler, M., Simon, W., Neutral carrier Ca^{2+}-microelectrode. *Chimia* 1976, 30(3), 204–206.
47. Meyerhoff, M. E., Polymer membrane-electrode based potentiometric ammonia gas sensor. *Anal Chem* 1980, 52(9), 1532–1534.
48. (a) Schulthess, P., Shijo, Y., Pham, H. V., Pretsch, E., Ammann, D., Simon, W., A hydrogen ion-selective liquid-membrane electrode based on tri-*N*-dodecylamine as neutral carrier. *Anal Chim Acta* 1981, 131(November), 111–116; (b) Ammann, D., Lanter, F., Steiner, R. A., Schulthess, P., Shijo, Y., Simon, W., Neutral carrier based hydrogen-ion selective microelectrode for extracellular and intracellular studies. *Anal Chem* 1981, 53(14), 2267–2269.
49. Bolton, T. B., Vaughanjones, R. D., Continuous direct measurement of intracellular chloride and pH in frog skeletal-muscle. *J Physiol Lond* 1977, 270(3), 801–833.
50. Chao, A. C., Armstrong, W. M., Cl^--selective microelectrodes—Sensitivity to anionic Cl^- transport inhibitors. *Am J Physiol* 1987, 253(2), C343–C347.
51. Rice, M. E., Gerhardt, G. A., Hierl, P. M., Nagy, G., Adams, R. N., Diffusion-coefficients of neurotransmitters and their metabolites in brain extracellular fluid space. *Neuroscience* 1985, 15(3), 891–902.
52. Nicholson, C., Phillips, J. M., Ion diffusion modified by tortuosity and volume fraction in the extracellular micro-environment of the rat cerebellum. *J Physiol Lond* 1981, 321(December), 225–257.
53. Hauser, M., Morf, W. E., Fluri, K., Seiler, K., Schulthess, P., Simon, W., *Helv Chim Acta* 1990, 73, 1481.
54. Khuri, R. N., Agulian, S. K., Bogharian, K., *Am J Physiol* 1974, 227, 1352.
55. Baumgarten, C. M., *Am J Physiol* 1981, 241, C258.
56. Wuhrmann, P., Ineichen, H., Riesen-Willi, U., Lezzi, M., *Proc Natl Acad Sci* 1979, 76, 806.
57. Amman, D., Chao, P., Simon, W., *Neurosci Lett* 1987, 74, 221.
58. Steiner, R. A., Oehme, M., Amman, D., Simon, W., *Anal Chem* 1979, 51, 351.
59. Cohen, C. J., Fozzard, H. A., Cheu, S. S., *Circ Res* 1982, 50, 651.
60. Palmer, L. G., Civan, M. M., *J Membr Biol* 1977, 33, 41.
61. Century, T. J., Civan, M. M., *J Membr Biol* 1978, 40, 24.
62. Craig, R. P., Nicholson, C., *Science* 1976, 194, 725.
63. Kotera, K., Satake, N., Honda, M., Fujimoto, M., *Membr Biochem* 1979, 2, 323.
64. Fujimoto, M., Honda, M., *Jpn J Physiol* 1980, 30, 859.
65. Fabczak, S., *Acta Protozool* 1987, 26, 129.
66. Lanter, F., Steiner, R. A., Amman, D., Simon, W., *Anal Chim Acta* 1982, 135, 51.
67. Tsien, R. Y., Rink, T. J., *J Neurosci Methods* 1981, 4, 73.
68. Ujec, E., Keller, E. E. O., Kùriùz, N., Pavlik, V., Machek, J., *Bioelectrochem Bioenerg* 1980, 7, 363.
69. Amman, D., Bührer, T., Schefer, U., Müller, M., Simon, W., *Pflügers Arch* 1987, 409, 223.
70. Mack Brown, H., Marron, S. K., *Anal Chem* 1990, 62, 2153.
71. Amman, D., Caroni, P., *Methods Enzymol* 1989, 172, 136.
72. Lanter, F., Erne, D., Amman, D., Simon, W., *Anal Chem* 1980, 52, 2400.
73. Hu, Z., Bührer, T., Müller, M., Rusterholz, B., Rouilly, M., Simon, W., *Anal Chem* 1989, 61, 574.
74. Spichiger, U. E., *Electroanalysis* 1993, 5, 739.
75. Amman, D., Caroni, P., *Methods Enzymol* 1989, 172, 136.
76. Hu, Z., Ye, F., Zhao, P., Qi, D., *Huaxue Xuebao* 1991, 49, 1483.
77. Amman, D., Caroni, P., *Methods Enzymol* 1989, 172, 136.
78. Schaller, U., Spichiger, U. E., Simon, W., *Pflügers Arch* 423.
79. Bührer, T., Peter, H., Simon, W., *Pflügers Arch* 1988, 412, 359.
80. De Beer, D., van den Heuvel, J. C., *Talanta* 1988, 35, 728.
81. Fresser, F., Moser, H., Nair, M., *J Exp Biol* 1991, 147, 227.
82. Henrriksen, G. H., Bloom, A. J., Spanswick, R. M., *Plant Physiol* 1990, 93, 271.
83. Vyskocil, F., Kriz, N., Modifications of single and double-barrel potassium specific microelectrodes for physiological experiments. *Pflugers Arch Eur J Physiol* 1972, 4(3), 265–276.
84. Neher, E., Lux, H. D., Rapid changes of potassium concentration at outer surface of exposed single neurons during membrane current flow. *J Gen Physiol* 1973, 61(3), 385–399.

85. Coles, J. A., Tsacopoulos, M., Method of making fine double-barrelled potassium-sensitive microelectrodes for intracellular-recording. *J Physiol Lond* 1977, 270(1), P12–P14.
86. Brown, K. T., Flaming, D. G., New micro-electrode techniques for intracellular work in small cells. *Neuroscience* 1977, 2(6), 813–827.
87. Sundfors, F., Bereczki, R., Bobacka, J., Toth, K., Ivaska, A., Gyurcsanyi, R. E., Microcavity based solid-contact ion-selective microelectrodes. *Electroanalysis* 2006, 18(13–14), 1372–1378.
88. Gyetvai, G., Sundblom, S., Nagy, L., Ivaska, A., Nagy, G., Solid contact micropipette ion selective electrode for potentiometric SECM. *Electroanalysis* 2007, 19(10), 1116–1122.
89. Gyetvai, G., Nagy, L., Ivaska, A., Hernadi, I., Nagy, G., Solid contact micropipette ion selective electrode II: Potassium electrode for SECM and in vivo applications. *Electroanalysis* 2009, 21(17–18), 1970–1976.
90. Varga, A., Nagy, L., Izquierdo, J., Bitter, I., Souto, R. M., Nagy, G., Development of solid contact micropipette Zn-ion selective electrode for corrosion studies. *Anal Lett* 2011, 44, 2876–2886.
91. (a) Teorell, T., An attempt to formulate a quantitative theory of membrane permeability. *Proc Soc Exp Biol Med* 1935, 33, 282; (b) Teorell, T., Studies on the "diffusion effect" upon ionic distribution. Some theoretical considerations. *PNAS* 1935, 21, 152–161; (c) Meyer, K. H., Sievers, J. F., The permeability of membranes I—The theory of ionic permeability. *Helvet Chim Acta* 1936, 19, 649–677; (d) Teorell, T., Zur quantitativen Behandlung der Membranpermeabilität. *Z Elektrochem* 1951, 65, 460; (e) Teorell, T., Transport processes and electrical phenomena in ionic membranes. *Prog Biophys Biophys Chem* 1953, 3, 305.
92. (a) Sokalski, T., Ceresa, A., Zwickl, T., Pretsch, E., Large improvement of the lower detection limit of ion-selective polymer membrane electrodes. *J Am Chem Soc* 1997, 119(46), 11347–11348; (b) Mathison, S., Bakker, E., Effect of transmembrane electrolyte diffusion on the detection limit of carrier-based potentiometric ion sensors. *Anal Chem* 1998, 70(2), 303–309.
93. Ceresa, A., Sokalski, T., Pretsch, E., Influence of key parameters on the lower detection limit and response function of solvent polymeric membrane ion-selective electrodes. *J Electroanal Chem* 2001, 501(1–2), 70–76.
94. Inczédy, J., Lengyel, T., Ure, A., *Compendium of Analytical Nomenclature: Definitive Rules 1997*, 3rd ed. Blackwell Science, Oxford, U.K., 1998, p. 288.
95. Sodergard, M., Csoka, B., Nagy, G., Ivaska, A., Lowering the detection limit of solvent polymeric ion-selective membrane electrodes. An experimental study with calcium-selective micropipette electrodes. *Anal Lett* 2003, 36(14), 2909–2923.
96. Shvarev, A., Bakker, E., Pulsed galvanostatic control of ionophore-based polymeric ion sensors. *Anal Chem* 2003, 75(17), 4541–4550.
97. Bakker, E., Pretsch, E., Modern potentiometry. *Angew Chem Int Ed* 2007, 46(30), 5660–5668.
98. (a) Umezawa, Y., Umezawa, K., Sato, H., Selectivity coefficients for ion-selective electrodes—Recommended methods for reporting K-A,B(pot) values (technical report). *Pure Appl Chem* 1995, 67(3), 507–518; (b) Bakker, E., Pretsch, E., Bühlmann Ph., Selectivity of potentiometric ion sensors. *Anal Chem* 2000, 72(6), 1172–1173.
99. Lindner, E., Tóth, K., Pungor, E., *Dynamic Characteristics of Ion-Selective Electrodes*. CRC Press, Boca Raton, FL, 1988.
100. Lindner, E., Toth, K., Pungor, E., Definition and determination of response-time of ion-selective electrodes. *Pure Appl Chem* 1986, 58(3), 469–479.
101. Thomas, R. C., *Ion-Sensitive Intracellular Microelectrodes: How to Make and Use Them*. Academic Press, London, U.K., 1978, p. 123.
102. Evans, U. R., *J Iron Steel Inst* 1940, 141, 219–234.
103. (a) Isaacs, H. S., Kissel, G., Surface preparation and pit propagation in stainless-steels. *J Electrochem Soc* 1972, 119(12), 1628–1632; (b) Isaacs, H. S., Vyas, B., Scanning reference electrode techniques in localized corrosion. In *Electrochemical Corrosion Testing*, Florian Mansfeld, U. B., Ed. American Society for Testing and Materials, West Conshohocken, PA, 1981, Vol. ASTM STP 727, pp. 3–33.
104. Tuck, C. D. S., The use of microelectrodes in the study of localized corrosion in aluminum-alloys. *Corros Sci* 1983, 23(4), 379–389.
105. Trethewey, K. R., Sargeant, D. A., Marsh, D. J., Haines, S., New methods of quantitative analysis of localized corrosion using scanning electrochemical probes. In *Modelling Aqueous Corrosion: From Individual Pits to System Management. Proceedings of the NATO Advanced Research Workshop*, Manadon, Plymouth, U.K., September 6–8, 1993, Threthewey, K. R. Roberge, P. R., Eds. NATO Science Series: E: 266, April 1994, 476pp. ISBN 0-7923-2820-5.
106. Isaacs, H. S., The measurement of the galvanic corrosion of soldered copper using the scanning vibrating electrode technique. *Corros Sci* 1988, 28(6), 547–558.

107. Jaffe, L. F., Nuccitelli, R., An ultrasensitive vibrating probe for measuring steady extracellular currents. *J Cell Biol* 1974, 63, 614–628.
108. Horrocks, B. R., Mirkin, M. V., Pierce, D. T., Bard, A. J., Nagy, G., Toth, K., Scanning electrochemical microscopy. 19. Ion-selective potentiometric microscopy. *Anal Chem* 1993, 65(9), 1213–1224.
109. Toth, K., Nagy, G., Horrocks, B. R., Bard, A. J., Investigation of silver iodide-based ion-selective membranes by scanning electrochemical microscopy. *Anal Chim Acta* 1993, 282(2), 239–246.
110. Csoka, B., Mekhalif, Z., Carbon paste-based ion-selective dual function microelectrodes for SECM measurements. *Electrochim Acta* 2009, 54(11), 3225–3232.
111. Horrocks, B. R., Schmidtke, D., Heller, A., Bard, A. J., Scanning electrochemical microscopy. 24. Enzyme ultramicroelectrodes for the measurement of hydrogen-peroxide at surfaces. *Anal Chem* 1993, 65(24), 3605–3614.
112. (a) Hansma, P. K., Drake, B., Marti, O., Gould, S. A. C., Prater, C. B., The scanning ion-conductance microscope. *Science* 1989, 243(4891), 641–643; (b) Prater, C. B., Hansma, P. K., Tortonese, M., Quate, C. F., Improved scanning ion-conductance microscope using microfabricated probes. *Rev Sci Instrum* 1991, 62(11), 2634–2638.
113. Wei, C., Bard, A. J., Nagy, G., Toth, K., Scanning electrochemical microscopy. 28. Ion-selective neutral carrier-based microelectrode potentiometry. *Anal Chem* 1995, 67(8), 1346–1356.
114. Newman, J., Resistance for flow of current to a disk. *J Electrochem Soc* 1966, 113(5), 501–502.
115. Wei, C., Bard, A. J., Kapui, I., Nagy, G., Toth, K., Scanning electrochemical microscopy. 32. Gallium ultramicroelectrodes and their application in ion-selective probes. *Anal Chem* 1996, 68(15), 2651–2655.
116. Toth, K., Nagy, G., Wei, C., Bard, A. J., Novel application of potentiometric microelectrodes—Scanning potentiometric microscopy. *Electroanalysis* 1995, 7(9), 801–810.
117. (a) Schulte, A., Belger, S., Schuhmann, W., Corrosion of NiTi shape-memory alloys: Visualization by means of potentiometric "constant-distance" scanning electrochemical Microscopy. In *Shape Memory Materials and Its Applications*, Chu, Y. Y., Zhao, L. C., Eds. 2001, Materials Science Forum Vol. 394–403, pp. 145–148; *Proceedings of the International Conference On Shape Memory Superelastic Technologies and Shape Memory,* Kunming, China, ISBN: 0878498966. ISBN: 978-0878498963: 2002-05-03. Trans Tech Publications Ltd. (b) Etienne, M., Dierkes, P., Erichsen, T., Schuhmann, W., Fritsch, I., Constant-distance mode scanning potentiometry. High resolution pH measurements in three-dimensions. *Electroanalysis* 2007, 19(2–3), 318–323.
118. Etienne, M., Schulte, A., Mann, S., Jordan, G., Dietzel, L. D., Schuhmann, W., Constant-distance mode scanning potentiometry. 1. Visualization of calcium carbonate dissolution in aqueous solution. *Anal Chem* 2004, 76(13), 3682–3688.
119. (a) Park, J. O., Paik, C. H., Alkire, R. C., Scanning microsensors for measurement of local pH distributions at the microscale. *J Electrochem Soc* 1996, 143(8), L174–L176; (b) Ogata, Y., Uchiyama, S., Hayashi, M., Yasuda, M., Hine, F., Studies of the pH of the membrane-surface in a laboratory chloralkali cell. *J Appl Electrochem* 1990, 20(4), 555–558.
120. Klusmann, E., Schultze, J. W., pH-microscopy—Theoretical and experimental investigations. *Electrochim Acta* 1997, 42(20–22), 3123–3134.
121. Antonenko, Y. N., Bulychev, A. A., Measurements of local pH changes near bilayer lipid-membrane by means of a pH microelectrode and a protonophore-dependent membrane-potential—Comparison of the methods. *Biochim Biophys Acta* 1991, 1070(1), 279–282.
122. Honda, T., Murase, K., Hirato, T., Awakura, Y., pH measurement in the vicinity of a cathode evolving hydrogen gas using an antimony microelectrode. *J Appl Electrochem* 1998, 28(6), 617–622.
123. Tanabe, H., Yamamura, Y., Misawa, T., In situ ionic imaging for pitting corrosion sites on austenitic stainless steels with scanning electrochemical microscopy. In *Passivation of Metals and Semiconductors*, Heusler, K. E., Ed. 1995, *Materials Science Forum*, Vol. 185–188, pp. 991–1000; *Proceedings of the 7th International Symposium on the Passivity of Metals and Semiconductors*, Clausthal, Germany. ISBN 978-0-87849-692-1. Trans Tech Publications Ltd.
124. Luo, J. L., Lu, Y. C., Ives, M. B., Microelectrodes for the study of localized corrosion. *J Electroanal Chem* 1992, 326(1–2), 51–68.
125. El-Giar, E., Wipf, D. O., Microparticle-based iridium oxide ultramicroelectrodes for pH sensing and imaging. *J Electroanal Chem* 2007, 609, 147–154.
126. Liu, B., Cheng, W., Rotenberg, S. A., Mirkin, M. V., Scanning electrochemical microscopy of living cells—Part 2. Imaging redox and acid/basic reactivities. *J Electroanal Chem* 2001, 500(1–2), 590–597.
127. (a) Lamaka, S. V., Karavai, O. V., Bastos, A. C., Zheludkevich, M. L., Ferreira, M. G. S., Monitoring local spatial distribution of Mg^{2+}, pH and ionic currents. *Electrochem Commun* 2008, 10(2), 259–262; (b) Karavai, O. V., Bastos, A. C., Zheludkevich, M. L., Taryba, M. G., Lamaka, S. V., Ferreira, M. G. S.,

Localized electrochemical study of corrosion inhibition in microdefects on coated AZ31 magnesium alloy. *Electrochim Acta* 2010, 55(19), 5401–5406; (c) Bastos, A. C., Taryba, M. G., Karavai, O. V., Zheludkevich, M. L., Lamaka, S. V., Ferreira, M. G. S., Micropotentiometric mapping of local distributions of Zn^{2+} relevant to corrosion studies. *Electrochem Commun* 2010, 12(3), 394–397.

128. Bard, A. J., Denuault, G., Friesner, R. A., Dornblaser, B. C., Tuckerman, L. S., Scanning electrochemical microscopy—Theory and application of the transient (chronoamperometric) SECM response. *Anal Chem* 1991, 63(13), 1282–1288.
129. (a) Frank, M. H. T., Denuault, G., Scanning electrochemical microscopy—Probing the ingress and egress of protons from a polyaniline film. *J Electroanal Chem* 1993, 354(1–2), 331–339; (b) Frank, M. H. T., Denuault, G., Scanning electrochemical microscope (SECM) study of the relationship between proton concentration and electronic charge as a function of ionic-strength during the oxidation of polyaniline. *J Electroanal Chem* 1994, 379(1–2), 399–406.
130. Barker, A. L., Gonsalves, M., Macpherson, J. V., Slevin, C. J., Unwin, P. R., Scanning electrochemical microscopy: Beyond the solid/liquid interface. *Anal Chim Acta* 1999, 385(1–3), 223–240.
131. Kemp, T. J., Unwin, P. R., Vincze, L., Photogenerated chloride-ion concentration near-the-surface of UV-irradiated titanium-dioxide in the presence of aqueous 1,4-dichlorophenol probed using an ultramicroelectrode. *J Chem Soc Faraday Trans* 1995, 91(21), 3893–3896.
132. Gyurcsanyi, R. E., Nyback, A. S., Toth, K., Nagy, G., Ivaska, A., Novel polypyrrole based all-solid-state potassium-selective microelectrodes. *Analyst* 1998, 123(6), 1339–1344.
133. Horrocks, B. R., Mirkin, M. V., Evidence for a potential-dependent reversible inactivation of urease adsorbed on a gold electrode. *J Chem Soc Faraday Trans* 1998, 94(8), 1115–1118.
134. (a) Berger, C. E. M., Horrocks, B. R., Datta, H. K., Application of ion-selective microelectrodes to the detection of calcium release during bone resorption. *Electrochim Acta* 1999, 44(16), 2677–2683; (b) Berger, C. E. M., Rathod, H., Gillespie, J. I., Horrocks, B. R., Datta, H. K., Scanning electrochemical microscopy at the surface of bone-resorbing osteoclasts: Evidence for steady-state disposal and intracellular functional compartmentalization of calcium. *J Bone Miner Res* 2001, 16(11), 2092–2102.

11 Biotechnological Applications

Benjamin R. Horrocks and Gunther Wittstock

CONTENTS

11.1 Approaches to Imaging Biological and Biochemical Systems 318
11.1.1 Nonspecific Imaging in the Feedback Mode 318
11.1.1.1 Negative Feedback Images 318
11.1.1.2 Nonspecific Positive Feedback Imaging 319
11.1.2 Enzyme-Mediated Feedback Imaging 320
11.1.3 Substrate Generation/Tip Collection Mode 321
11.1.3.1 Immobilized Enzymes 322
11.1.3.2 Feedback Effects and Other Artifacts Occurring in the Generation–Collection Mode 323
11.1.3.3 Sensors and Tips 327
11.1.3.4 Distance Calibration and Control of Mass Transport 328
11.1.3.5 Detection Limit 330
11.2 Selected Applications 331
11.2.1 Localization of Enzymatic Reactions in Cells and Tissue 332
11.2.2 Kinetics of Immobilized Enzymes 332
11.2.2.1 Enzyme-Mediated Feedback Mode 332
11.2.2.2 Generation–Collection Mode 333
11.2.2.3 Potentiometric Studies of Enzyme Kinetics in GC Mode 336
11.2.3 Advanced Architectures for Enzyme Electrodes 337
11.2.3.1 Microcompartmentalized Surfaces 337
11.2.3.2 Pattern Formation in Biotechnological Environments 337
11.2.3.3 Overlap of Different Feedback Contributions on Conductive Substrates 338
11.2.3.4 Novel Sensor Architectures Based on Patterned Self-Assembled Monolayers and Patterned Polymer Films 339
11.2.3.5 Screening Procedures for Combinatorial Tests 342
11.2.3.6 Improving the Resolution of the Generation–Collection Mode by Coupling with Solution Chemistry 343
11.2.3.7 Oxygen Reduction in Biotechnology 346
11.2.4 SECM Readout of Biochips 350
11.2.4.1 Using Enzyme Labels 351
11.2.4.2 Small Spot Immunoassays 351
11.2.4.3 Assays Using Magnetic Microbeads 353
11.2.4.4 DNA Arrays with Enzyme Labels 356
11.2.4.5 DNA Arrays with Metal Labels 359
11.2.4.6 Label-Free DNA Arrays 359
11.2.4.7 SECM Studies of Charge Transport at DNA-Modified Electrodes 360
11.2.4.8 Cellular Biosensing Systems 361
11.2.5 Use of SECM Detection Principles in Microanalytical Devices 361
11.2.6 SECM Imaging of Electrophoresis Gels and Fingerprints 363

11.2.7 Applications to Cells and Whole Organisms 363
11.2.8 Imaging Mass Transport in Biological Systems 365
11.3 Conclusion and Outlook 366
11.3.1 Information Content of SECM Measurements and Spatial Resolution 366
11.3.2 Applications in Biotechnology 366
11.3.3 Recording Speed 367
Abbreviations, Acronyms, and Symbols 368
Acknowledgment 369
References 370

From its inception, attempts have been made to apply scanning electrochemical microscopy (SECM) to investigations of biological or biochemically relevant problems [1]. SECM has particular advantages in these studies because measurements can be carried out in buffered solutions with a scanning electrode that does not touch the specimen and that interferes with the sample much less than tips of alternative scanning probe techniques, for example, scanning tunneling microscopy (STM) and atomic force microscopy (AFM). SECM with electrochemical detection of metabolites can be used to map biochemical activity and therefore is complementary to techniques that image only the topography of biological specimens or biomolecules.

This chapter aims to summarize the state of the art in imaging the activity of biochemical species (enzymes, antibodies, and DNA) and to show how to use SECM to investigate biotechnologically relevant surfaces, components, and devices. Many of the imaging principles are applicable to both biomolecule-modified surfaces and living cells or tissues. However, imaging of cells and tissues requires the consideration of additional parameters and owing to the increased importance of this area, a separate chapter (Chapter 12) is devoted to such applications. This chapter will focus on the mechanisms for activity imaging of surface-bound biomolecules and make reference to Chapter 12 where the same mechanisms are important for live cell imaging.

11.1 APPROACHES TO IMAGING BIOLOGICAL AND BIOCHEMICAL SYSTEMS

Layers of immobilized biomolecules and biological specimens can, in principle, be imaged the same way as any other sample (see Chapter 4). The focus of this section will however rest clearly on approaches that exploit specific functional properties of biomolecules or biological systems to generate an image.

11.1.1 Nonspecific Imaging in the Feedback Mode

Nonspecific imaging in the feedback mode is used as part of many complex SECM experiments, to position the probes in a defined distance over the surface, to assess the topography of the sample, or to localize modified regions for subsequent detailed studies.

11.1.1.1 Negative Feedback Images

One of the earliest images using negative feedback was obtained from upper and lower surfaces of leaves immersed in a 0.02 M $K_4[Fe(CN)_6]$ and 0.1 M KCl solution [2]. The highly charged mediator, $K_4[Fe(CN)_6]$, does not easily penetrate the cells and therefore interference with biochemical processes in the leaves was reduced. Where cells protruded from the surface, low currents were recorded. The biochemical function of the specimen was not involved in the image generation mechanism. Therefore, the imaging process does not differ from that at a rough, insulating inorganic surface. Reactive surfaces can be imaged in a nonspecific way, for example, to assess the topography or to determine the working distance, if an irreversible reaction is used at the tip. Often reduction of dissolved dioxygen at a Pt tip in aqueous buffers can be used for that purpose (Section 11.1.3.3). However, care must be taken in samples that may consume oxygen (e.g., living cells) or have a finite permeability for O_2 (e.g., many (bio)polymers).

In addition, these mechanisms may play a role in image generation of other scanning probe techniques. Fan and Bard [3] proposed that imaging of insulating biomolecules on insulating supports such as mica using a STM instrument under ambient humidity may be based on faradaic reactions at the Pt tip and a distant gold contact connected by an ion migration current at a surface water film. The very low currents, typically 1 pA, and high bias voltages of 3–10 V [4], the possibility of electrochemical reactions such as dioxygen reduction, proton reduction, and dioxygen evolution as well as experimental examples showing the importance of relative humidity for such images [5] support this notion even if it may not be straightforward to identify SECM-like mechanisms in STM or conductive AFM experiments. However, when searching literature databases, the reader will find the original work indexed mainly under the keyword "STM" [6]. While the experiments in these studies may approach the ultimate resolution of SECM imaging, this chapter will concentrate on those examples where the electrochemical and biochemical reactions responsible for image generation can be clearly specified.

Another related approach is to use the metallic tip of an electrochemical STM as a potential sensor. The potential difference between the potential applied to a conductive sample and the tip at zero current is used as an input signal for an electronic feedback loop while scanning the tip horizontally. This technique has been termed scanning electrochemical potential microscopy (SECPM) [7]. The tip is brought so close to the surface that it penetrates into the electrochemical double layer of the substrates. It will thus be sensitive to the charge distribution at surfaces and has been successfully applied to image individual enzyme molecules on an HOPG substrate in electrolyte solution [8]. SECPM is distinct from SECM with potentiometric probes as presented in Chapter 10 by the absence of an *ion-specific* interaction at the probe, although it does offer higher resolution.

11.1.1.2 Nonspecific Positive Feedback Imaging

Positive feedback is obtained above electrically conductive samples with reversible redox mediators. If a layer of biomolecules (or a layer of most other organic molecules) is placed onto a conducting sample, electron transfer at the covered areas is inhibited and the positive feedback does not reach the value recorded above the bare surface (Figure 11.1). The decrease of the positive feedback is due to the inhibition of the electron transfer reaction at the sample and may vary depending on the size and packing of the organic layer; the density of defects in the layer and the substrate; the charge, size, and hydrophobicity of the selected mediator; and so on. Such imaging has been used to characterize patterned layers of self-assembled monolayers (SAMs) [9,10]. It can also be used to locate a layer of biomolecules (spots) on sensor surfaces. Often such studies are part of control experiments, where inhibition is first measured. In the second step, inhibition is decreased due to a catalytic reaction at the surface [11–13], or the permeability of a biomolecular layer for a mediator is changed due to a binding event [14].

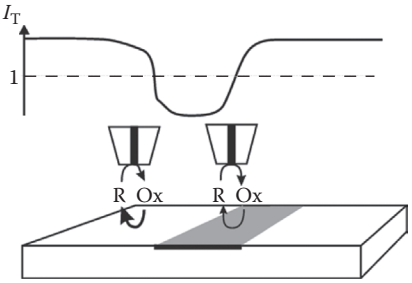


FIGURE 11.1 Schematic representation of the reduced positive feedback over a conductive support locally covered by a layer of biomolecules or other organic blocking layers.

11.1.2 Enzyme-Mediated Feedback Imaging

An imaging mode that contains more information related to the function of the biomolecule is illustrated in Figure 11.2. It may be termed enzyme-mediated positive feedback mode. The SECM mediator is chosen such that one of its redox forms can act as an artificial electron acceptor or electron donor. The enzyme-mediated positive feedback imaging of glucose oxidase (GOx) was reported by Pierce et al. [15]. In this work, GOx was covalently attached to a Nylon® surface. The working solution contained glucose as substrate S and ferrocene monocarboxylic acid (Fc) as mediator and artificial cosubstrate of the enzyme. At the tip, Fc was oxidized to the ferrocenium form (Fc^+). Fc^+ derivatives serve as effective artificial electron acceptors for GOx [16]. The enzymatic reaction commences only if the microelectrode is located above the enzyme-modified surface, because Fc^+ formed at the tip electrode is available only locally as an electron acceptor, while the native electron acceptor O_2 was removed from the solution. During this reaction, Fc is regenerated and becomes available again for oxidation at tip (positive feedback). At glucose concentrations much greater than the Michaelis constant, K_M, the magnitude of the effect depends on the enzyme turnover rate, the kinetics of the reaction between mediator and the reduced GOx, and the flux (mol/cm^2/s) of Fc^+ at the specimen surface (Figure 11.3). As a result, the feedback depends on the bulk mediator concentration (curves a and b). This constitutes an important difference to the diffusion-controlled positive feedback at conducting samples, where plots of normalized current, $i_T/i_{T\infty}$, vs. normalized distance, $L = d/a$, superimpose for different mediator concentrations and electrode radii.

The following conditions must be met for successful imaging of enzymatic activity:

- All solution constituents must be compatible with the diffusion-controlled reaction of the mediator at the tip (no inhibition of the tip electrolysis by the substrate or products of the enzymatic reaction).
- No interference with the enzymatic reaction by dissolved species (no enzyme inhibitors, no alternative cosubstrates for the enzyme besides the oxidized mediator present).
- The enzymatic reaction has to produce a sufficient regeneration rate of the reduced mediator to compete with its mass transport from bulk solution to the tip.

The third requirement has been expressed quantitatively using the results of simulation of enzyme-mediated positive feedback for the GOx-catalyzed reaction as [15]

$$k_{cat}\Gamma_{enz} \geq 10^{-3}(D_{Red}\ c_{Red})/a \tag{11.1}$$

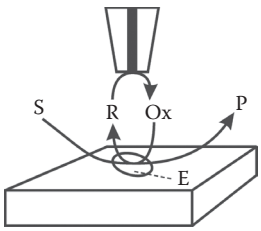


FIGURE 11.2 Schematic of the enzyme-mediated positive feedback for an enzymatic oxidation of the substrate. E, redox enzyme; S and P, substrate and product of the enzymatic reaction; R, SECM mediator added to the working solution; Ox, oxidized form of R generated by a faradaic reaction at the tip electrode. R has to be selected such that Ox is an active cosubstrate of the enzyme to be investigated. As discussed in the text, the following list of compounds provides a working example of this mode: E = glucose oxidase (GOx), S = glucose, P = gluconolactone, R = ferrocene monocarboxylic acid (Fc), and Ox = Fc^+. Of course, the imaging principle can also be used for enzymatic reductions if a suitable mediator Ox is added to the working solution and is reduced at the tip electrode.

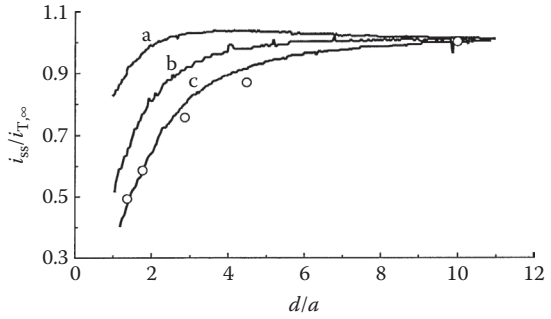


FIGURE 11.3 Normalized current ($i_T/i_{T\infty}$, $i_{SS}=i_T$) vs. normalized distance d/a ($a=4\,\mu m$, RG = 20) over modified Nylon® surfaces in solution of 0.5 mM ferrocene monocarboxylic acid, 0.1 M phosphate/perchlorate buffer pH 7.0. The surface was modified with curve a: maximum glucose oxidase (GOx) coverage, curve b: less than maximum GOx coverage, and curve c: maximum GOx coverage. Curve c was recorded with no glucose in the working solution. For curves a and b, 50 mM D-glucose was added to the working solution. (Reprinted with permission from Pierce, D.T., Unwin, P.R., and Bard, A.J., Scanning electrochemical microscopy. 17. Studies of enzyme–mediator kinetics for membrane- and surface-immobilized glucose oxidase, *Anal. Chem*., 64, 1795–1804, 1992. Copyright 1992 American Chemical Society.)

The left side of Equation 11.1 summarizes the enzyme-dependent terms: the rate constant, k_{cat}, characterizes the catalytic reaction rate under conditions of substrate saturation (at high glucose concentration in the example, reaction of mediator with reduced GOx is the rate-determining step). In general, k_{cat} is characteristic of a particular combination of enzyme, mediator, and substrate. Γ_{enz} is the enzyme surface concentration or, in the case of a film of finite thickness, the product of enzyme concentration in the film and the film thickness. The right side of the expression summarizes the terms related to the mediator. D_{Red} is the diffusion coefficient of the mediator. This criterion is most easily met at low mediator concentration, c_{Red}, and large tip radius, a. On the other hand, decreasing c_{Red} results in small currents that require a more sensitive potentiostat. In work with simple inorganic samples, this limitation is not present and high mediator concentrations may be used to increase the tip current to a level that is convenient to measure.

The procedure described earlier can be refined by using two SECM mediators serving different purposes [15,17]. One of the mediators should be a cosubstrate for the enzyme to be investigated (hydroquinone H_2Q). The other mediator is chosen so as not to interfere with the enzymatic reaction (methyl viologen MV^{2+}) and produces a negative feedback image if a suitable tip potential for this mediator is applied (−0.95 V [AgQRE] for MV^{2+}). At the second working potential of +0.82 V (AgQRE), the electron acceptor for the enzyme is formed from the second mediator H_2Q to map the enzymatic activity while MV^{2+} does not react at the tip electrode.

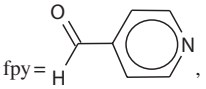
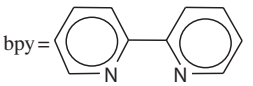
While there is a variety of substances that can act as SECM mediators and that are artificial electron acceptors for GOx (Table 11.1), the extension to different redox enzymes depends on finding suitable mediators and optimization of the imaging conditions.

11.1.3 Substrate Generation/Tip Collection Mode

In the sense used in this chapter, substrate generation/tip collection (GC) mode refers to experiments where the tip is used simply to sense redox-active or electroactive species produced by the specimen under study. This usage is essentially the same as elsewhere in this volume except that the generator is a biochemical reaction or organism rather than another electrode. The tip generation/substrate collection (TG/SC) mode was realized with oxygen-reducing enzymes [25] and is treated in Section 11.2.3.5.

Two cases may be distinguished: one where the tip radius is less than specimen dimensions and another in which the opposite holds. The latter type of experiment has hardly been explored,

TABLE 11.1
Direct Mapping of Enzymatic Activity with the Feedback Mode and Mediators Used

Enzyme Imaged	Enzyme Substrate	Mediator/Reaction Type at the Tip Electrode, the Reaction Product Formed at the Tip Interacts with the Enzyme	References
Glucose oxidase, EC 1.1.3.4	50–100 mM Glucose	0.05–2 mM Ferrocene monocarboxylic acid, dimethylaminomethyl ferrocene/oxidation	[11,15,18] [15]
		0.05–2 mM $K_4[Fe(CN)_6]$/oxidation	[15,17]
		0.02–2 mM Hydroquinone/oxidation	[11]
		0.5 mM [Os fpy $(bpy)_2$Cl]Cl/oxidation	
		fpy =  ,	
		bpy = 	
PQQ-dependent glucose dehydrogenase, EC 1.1.99.17	50 mM Glucose	0.05–2 mM Ferrocene monocarboxylic acid	[19]
		0.05–2 mM Hydroxymethyl ferrocene	[19]
		0.05–2 mM *p*-Aminophenol	[19]
	1 mM Glucose	1 mM $K_4[Fe(CN)_6]$	[20]
Quinohemoprotein alcohol dehydrogenase	1 mM Ethanol	1 mM $K_4[Fe(CN)_6]$	[20]
NADH–cytochrome c reductase, EC 1.6.99.3 within mitochondria	50 mM NADH	0.5 mM *N*,*N*,*N*′,*N*′-Tetramethyl-*p*-phenylenediamine/oxidation	[17]
Diaphorase (NADH acceptor oxidoreductase, EC 1.6.99.-)	5.0 mM NADH	0.5 mM Hydroxymethyl ferrocene/oxidation	[21]
Horseradish peroxidase, EC 1.11.1.7	0.5 mM H_2O_2	1 mM Hydroxymethyl ferrocenium/ reduction	[22]
Nitrate reductase, EC 1.7.99.4	23–65 mM NO_3^-	0.25 mM Methylviologen	[23]
Laccase, EC 1.10.3.2	O_2-saturated solution	0.1 mM $[Fe(CN)_6]^{3-}$	[24]
Bilirubin oxidase, EC 1.3.3.5	O_2-saturated solution	0.1 mM $[Fe(CN)_6]^{3-}$	[24]

although the detection efficiency of species generated at the specimen may be close to 100% and such an experiment can be useful when the analyte is present at low concentration and spatially resolved data are not required [26]. The more common situation is for a small tip to be rastered across the specimen surface to produce a map of the local concentration of a molecule generated or consumed at the specimen. GC mode experiments have some particular advantages and disadvantages compared to feedback mode experiments and these will be discussed in this section with the aim of providing the reader with the information to decide if the technique is appropriate for a particular problem.

11.1.3.1 Immobilized Enzymes

GC mode experiments have been applied to the study of immobilized oxidoreductases such as diaphorase and the GOx system [21,27] which has also been investigated by feedback with ferrocenyl mediators [15]. In the feedback experiment, the catalytic cycle of the enzyme is dependent on ferrocenium species generated at the tip as described in Section 11.1.3. A GC experiment utilizes a bulk solution concentration of the oxidized mediator and the tip is poised at a potential sufficiently positive to detect ferrocene, or another reaction product such as H_2O_2, near the interface (Figure 11.4). The enzymatic reaction therefore occurs wherever there is active enzyme and a supply

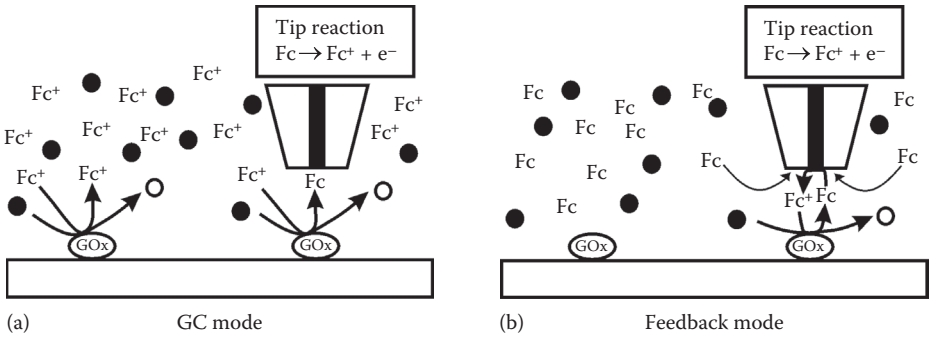


FIGURE 11.4 Schematic illustrating the difference between (a) GC mode and (b) feedback mode detection of immobilized enzyme activity. The example enzyme is glucose oxidase (GOx) with a ferrocenyl redox mediator (Fc) detected at a Pt tip. (a) The bulk solution contains oxidized mediator (Fc^+) and the tip detects the reduced form amperometrically which is generated continually wherever active enzyme is present on the specimen. (b) The bulk solution contains reduced mediator, the tip generates ferrocenium locally and detects the enhanced flux due to feedback when there is active enzyme on the portion of the specimen beneath the tip. ●, Glucose; ○, gluconolactone.

of substrate. In the feedback experiment, the tip current includes the flux of mediator from bulk solution as well as the flux of reduced mediator due to the enzymatic reaction. In contrast, in a GC mode experiment the tip current is entirely due to the enzymatic reaction and the background signal is effectively zero; this gives GC mode a sensitivity advantage over feedback mode [22]. However, since ferrocene may be produced simultaneously across the entire surface wherever enzyme is present, diffusional blurring will tend to result in a loss of image resolution. In the case where there are large areas of active enzyme, a defined steady-state concentration profile will not be established and quantitative measurements will not be possible. For these reasons, imaging experiments in GC mode are only appropriate when there are small, well-separated spots of low enzyme activity on the specimen surface. The experimenter must therefore consider the relative importance of image resolution versus sensitivity in deciding between feedback and generation–collection experiments. One example where GC mode is appropriate owing to the low detection limit is in the development of enzyme-labeled immunosorbent assay (ELISA) sandwich assays using the SECM to address microspots of peroxidase-labeled antibody [22].

11.1.3.2 Feedback Effects and Other Artifacts Occurring in the Generation–Collection Mode

An additional difficulty in GC images with a macroscopic enzymatically active surface as generator consists in the shape of the approach curve (Figure 11.5). The current initially rises on approaching the sample, but then reaches a maximum and falls sharply. The current decrease at small distances L is equivalent to the conventional negative feedback except that here it is the sample reaction whose conversion is limited by hindered diffusion of the reagent from the bulk solution. In contrast to conventional negative feedback, where the approach curve depends only on the tip RG, the ratio between the reagent bulk concentration and the enzymatic activity per unit area of sample is also important. The hindered diffusional transport will still provide enough reagent to saturate the enzyme kinetics (with respect to substrate) if the reagent concentration is high and the immobilized enzymatic activity is low. When looking for low quantities of enzymatic activity (as in immunoassays), this situation is likely to prevail if high reagent concentrations are practicable. A striking example of the artifacts that may result from this effect is shown in Figure 11.6 [28]. The enzyme glucose dehydrogenase oxidizes glucose and can use $[Fe(CN)_6]^{3-}$ as cosubstrate. $[Fe(CN)_6]^{4-}$ can be detected at the tip. At the concentration of 1 mM $[Fe(CN)_6]^{3-}$ in the bulk solution, the enzyme-modified spot consumes more $[Fe(CN)_6]^{3-}$ than can be supplied by diffusion from the bulk to the center of the spot if the

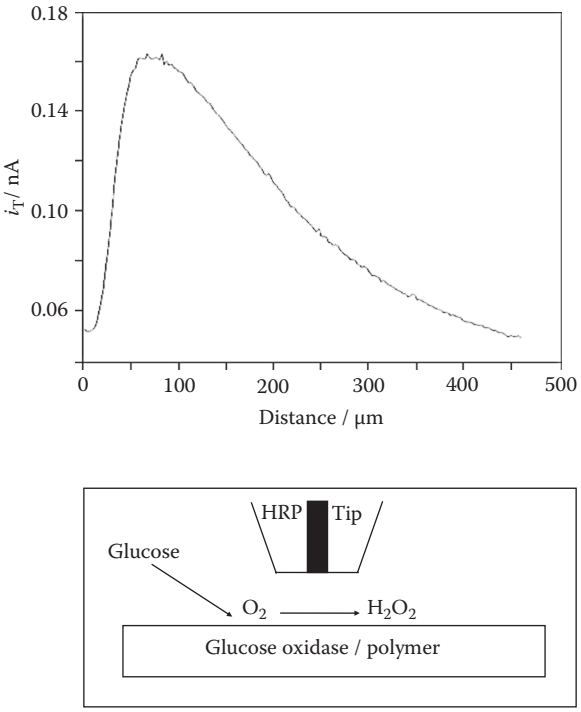


FIGURE 11.5 Approach curve of a H_2O_2-selective amperometric tip electrode toward a polymer layer loaded with GOx. The tip was produced by immobilizing horseradish peroxidase onto the cross section of an insulated carbon fiber of 7 μm diameter. Solution composition: 1 mM glucose in air-saturated 0.2 M phosphate buffer, pH 7. (Reprinted with permission from Horrocks, B.R., Schmidtke, D., Heller, A., and Bard, A.J., Scanning electrochemical microscopy. 24. Enzyme ultramicroelectrodes for the measurement of hydrogen peroxide at surfaces, *Anal. Chem*., 65, 3605–3614, 1993. Copyright 1993 American Chemical Society.)

microelectrode is located over the center of the spot (Figure 11.6b). Therefore, low currents are detected in this location. That this is in fact an artifact could be proved by substantially increasing the concentration of $[Fe(CN)_6]^{3-}$ (Figure 11.6c), increasing d, or decreasing the thickness of the insulation sheath around the tip (smaller RG). Experimenters are advised to prove the absence of such artifacts by checking if changes of these three parameters do not change the qualitative properties of the signal. Oyamatsu et al. [29] demonstrated that probes in the form of a common syringe needle reduce such substrate diffusion shielding by the probe and allow precise positioning with a tuning fork system.

It should also be noted that GC mode experiments with amperometric tips may contain a feedback component to the current if the electrochemical process at the tip is reversible and the tip-to-specimen distance is less than about 5a. However, at greater distances or when employing a potentiometric tip, the tip acts approximately as a passive sensor, that is, one that does not perturb the local concentration save for shielding effects. This situation is quite distinct from feedback mode where the product of the electrolysis at the tip is an essential reactant in the process at the specimen surface. This interdependence of tip and specimen reactions in feedback mode ensures that the biochemical process is confined to an area under the tip defined by the tip radius and diffusional spreading of the various reagents [30]. In contrast, the biochemical process in GC mode is independent of the presence of the tip and may therefore occur simultaneously across the whole surface. In addition, the tip signal often does not directly provide information on the height of the tip above the

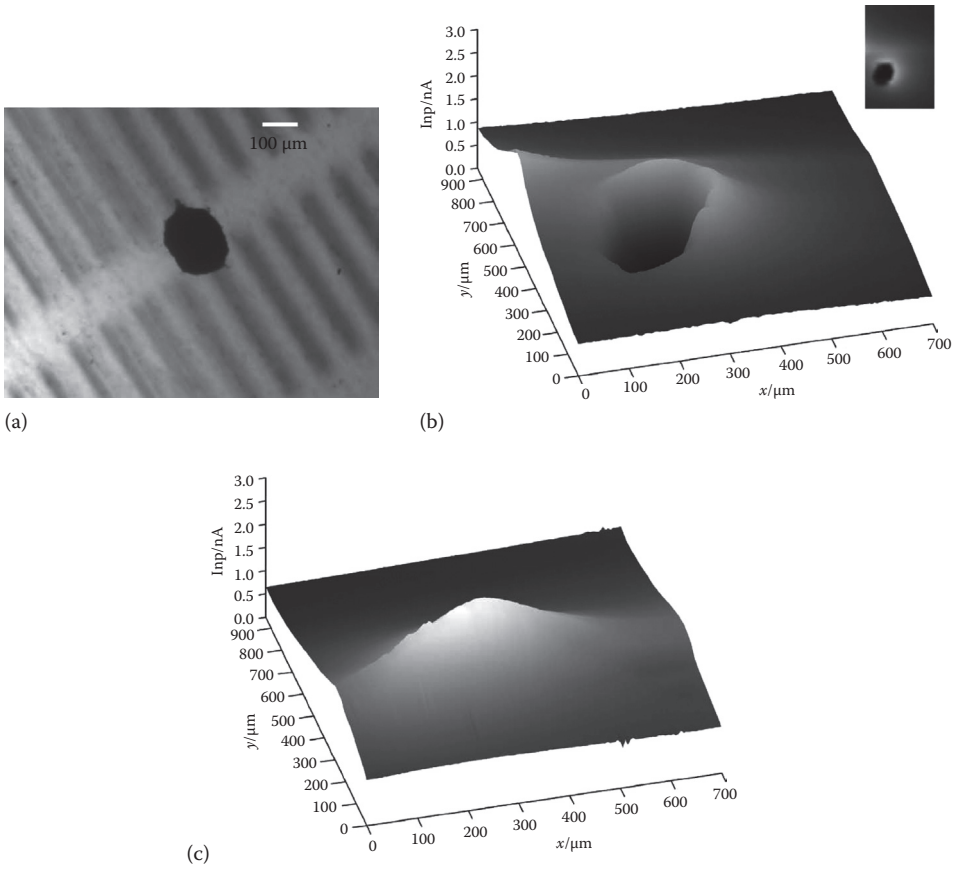


FIGURE 11.6 GC image of a spot of microbeads modified with glucose dehydrogenase. (a) Optical microphotograph, (b) GC image in 1.0 mM $[Fe(CN)_6]^{3-}$ (strong shielding of substrate diffusion to spot) at a working distance of 40 µm, and (c) GC image in 10 mM $[Fe(CN)_6]^{3-}$ and a working distance of 30 µm. (Reprinted from *Biosens. Bioelectron.*, 20, Zhao, C. and Wittstock, G., Scanning electrochemical microscopy for detection of biosensor and biochip surfaces with immobilized pyrroloquinoline quinone (PQQ)-dependent glucose dehydrogenase as enzyme label, 1277–1284, 2005, Copyright 2005, with permission from Elsevier.)

surface and methods to overcome this limitation are described in Section 11.1.3.4. Finally, since the tip process and the biochemical reaction at the specimen are independent, a wide range of microsensors may be employed (Section 11.1.3.3) as the tip, for example, ion-selective microelectrodes, which are not applicable in feedback experiments.

Two practical examples illustrate the possible superposition of GC and feedback contributions to the tip current. Figure 11.7 shows the readout of an array of polypyrrole (PPy) spots (prepared under different deposition conditions) that contain oligonucleotide (ODN) strands [136]. After hybridization with galactosidase-labeled complementary strands, the galactosidase activity was read. The GC image (Figure 11.7b) has a lower lateral resolution than the optical image (Figure 11.7a) due to diffusional spreading of the *p*-aminophenol (PAP) from the spots. For quantitation, line scans at different heights were recorded along the white line in Figure 11.7b. From the line scans in Figure 11.7c, the flux of PAP was extracted using the theory detailed in Section 11.2.2.2. This flux was then used to determine the surface concentration of accessible ODN strands by calibration against a reference system with known enzyme activity. It can be clearly seen in Figure 11.7c that a background component grows as the working distance is reduced. This is shown in more detail in Figure 11.7d. This background component is assumed to result from a feedback contribution

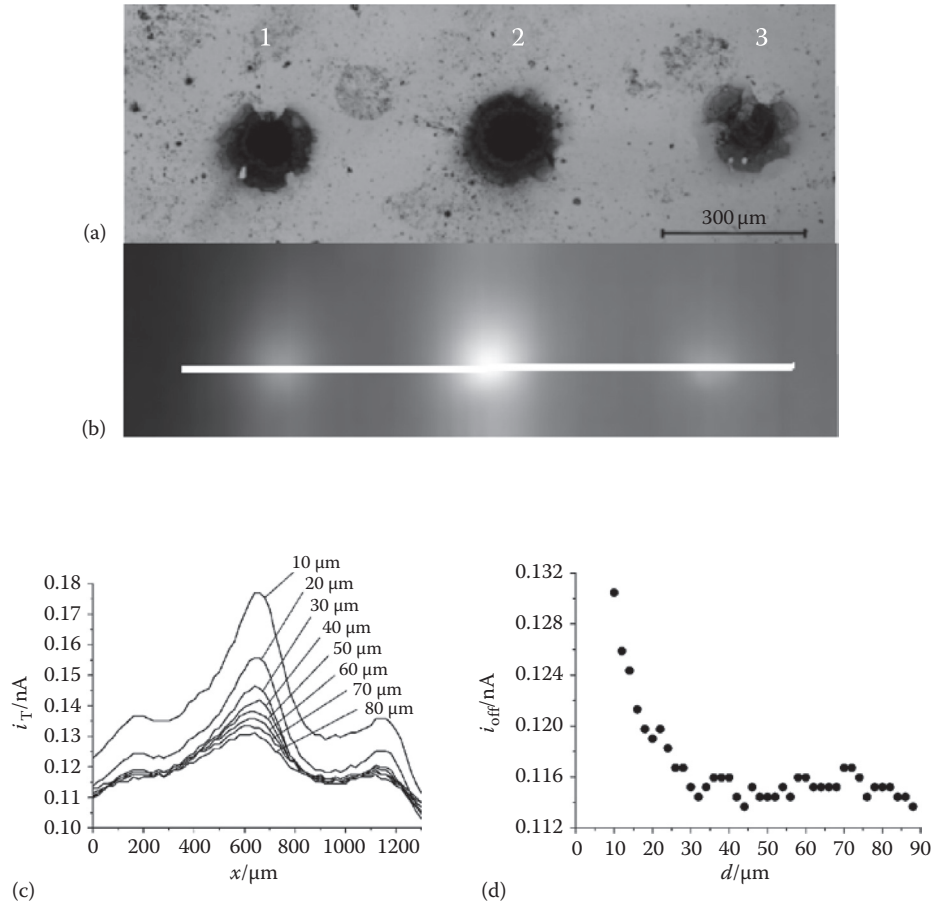


FIGURE 11.7 GC imaging of galactosidase activity used as label for a DNA chip on a gold support. The spots were created by pulsed electropolymerization of pyrrole and oligonucleotide-modified pyrrole. Galactosidase was attached to the complementary DNA stand. (a) Optical microphotograph of spots obtained with different electropolymerization conditions, (b) GC image of galactosidase activity, (c) line scans along the white line in (b) at different working distances, and (d) plot of the offset current as a function of working distance. Other imaging conditions 2 mM *p*-aminophenylgalactose, $v_t = 40\,\mu m/s$, $a = 12.5\,\mu m$, $E_T = 0.35\,V$ (Ag|AgCl|3 M KCl). (From Nunes Kirchner, C., Szunerits, S., Wittstock, G.: Scanning electrochemical microscopy (SECM) based detection of oligonucleotide hybridization and simultaneous determination of the surface concentration of immobilized oligonucleotides on gold. *Electroanalysis*. 2007. 19. 1258–1267. Copyright Wiley-VCH Verlag GmbH & Co. KGaA. Reproduced with permission.)

between the gold support of the chip and the tip and the redox couple PAP/*p*-quinone imine (PQI). This couple is formed during galactose activity imaging. It is also evident that this contribution is negligible at $d > 30\,\mu m$ for a tip with $a = 12.5\,\mu m$ ($L > 2.4$).

Another pitfall is a feedback contribution in GC imaging with very low enzyme activities when no mediator was intentionally added. Small concentrations of mediators may form by chemical decomposition inside the cell or be present as impurities in the biochemicals. An example from the authors' laboratories [31] is shown in Figure 11.8. The enzyme horseradish peroxidase (HRP) was immobilized using layer-by-layer adsorption of oppositely charged polyelectrolyte layers. If H_2O_2 and ferrocene methanol (Fc) is added, HRP reduces H_2O_2 and oxidizes Fc to Fc^+ (Figure 11.8a(1)). Fc^+ is then reduced at the tip. Higher reduction currents (negative sign) in Figure 11.8b seem to confirm the successful lateral patterning of HRP. However, a control experiment in the absence

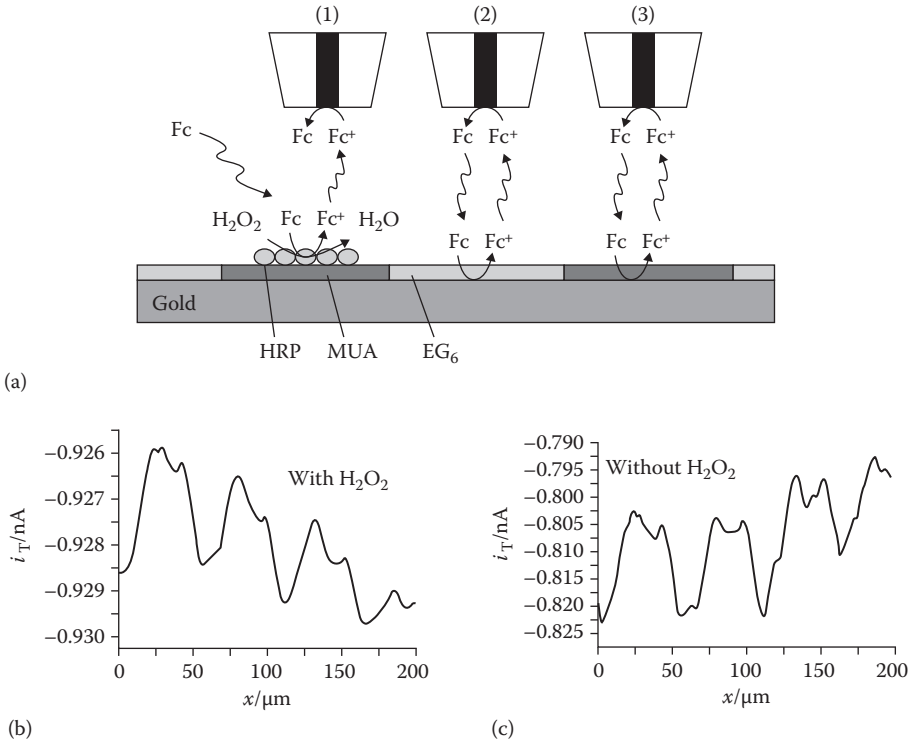


FIGURE 11.8 Experimental example of an unintended feedback imaging. (a) Schematic showing (1) the intended GC imaging of horseradish peroxidase (HRP) activity; (2) hindered diffusion above a densely packed monolayer using the ferrocenium derivative (Fc^+) as mediator. Fc^+ is present in low concentration possibly due to partial chemical oxidation by O_2 or H_2O_2; and (3) the regeneration of Fc^+ at the gold electrode surface under a less-organized monolayer. (b) Experimental line scan in the presence of ferrocene methanol (and traces of Fc^+) and H_2O_2; (c) same as (b) but in the absence of H_2O_2. (Reprinted from *Electrochemical Sensor Analysis*, Vol. 49, Alegret, S. and Merkoci, A., Eds., Wittstock, G., Burchardt, M., Nunes Kirchner, C., Scanning electrochemical microscopy in biosensor research, pp. 907–939, Copyright 2007, with permission from Elsevier.)

of H_2O_2 but otherwise identical conditions produced a qualitatively similar pattern (Figure 11.8b). This pattern may be the feedback image with an unidentified redox mediator (probably traces of air-oxidized Fc). The pattern results from the different permeability of the self-assembled thiol monolayers (SAMs) that were used to prime the surface for the layer-by-layer deposition procedure. Naturally, the layout of the SAM is identical to the intended layout of the enzyme layer. The experiment in Figure 11.8b can be highly misleading if not complemented by control experiments. Their importance for this area cannot be overstressed.

11.1.3.3 Sensors and Tips

GC mode SECM experiments have been used to detect localized activity of a variety of enzymes (see Table 11.2). Since microelectrodes are used in the life sciences to detect neurotransmitters [43], metal cations [44], and free radicals [45], a wide variety of probes may be combined with SECM positioning technology to obtain spatially resolved information. The GC mode experiments may be carried out with potentiometric or amperometric tips depending on the species to be sensed. The tip must be chosen to determine a product or reactant consumed by the enzyme reaction, for example, H^+ for immobilized urease, H_2O_2 for immobilized GOx, or *p*-aminophenolate for alkaline phosphatase (ALP). A list of enzymes and the tips employed is given in Table 11.2. In addition to the enzymes listed, similar strategies have been employed for tissues and cells in order to

TABLE 11.2
Examples of GC Mode Experiments on Biochemical Systems Using a Variety of Tips

Specimen/Enzyme Studied	Analyte	Tip	References
Glucose oxidase, EC 1.1.3.4	H_2O_2	Pt, amperometric	[27]
Glucose oxidase, EC 1.1.3.4	H_2O_2	C/wired enzyme amperometric	[32]
PQQ-dependent glucose dehydrogenase, EC 1.1.99.17	$[Fe(CN)_6]^{4-}$	Pt, amperometric	[19]
Urease, EC 3.5.1.5 and brewers yeast	H^+	Sb, potentiometric	[33]
Urease, EC 3.5.1.5 adsorbed on a gold electrode	NH_4^+	Liquid membrane ISE, potentiometric	[34]
Horseradish peroxidase, EC 1.11.1.7	Ferrocene mediators	Pt, amperometric	[22,35]
Alkaline phosphatase, EC 3.1.3.1	*p*-Aminophenolate	Pt, amperometric	[36]
Galactosidase, EC 3.2.1.93	*p*-Aminophenol	Pt, amperometric	[37,38]
NAD^+-dependent alcohol dehydrogenase, EC 1.1.1.1	H^+	Sb, potentiometric	[39]
Laccase, EC 1.10.3.2	2,2′-Azino-bis(3-ethylbenzothiazoline-6-sulfonate) radical anion ($ABTS^{\cdot-}$)	Pt, amperometric	[40]
Ion diffusion in dentine	$Fe(CN)_6^{4-}$	Pt, amperometric	[41]
Dental materials (alloys)	O_2, metal ions	Pt, amperometric	[42]

detect oxygen production of leaves [46] or algae cells [47]. Detection of neurotransmitters [48], NO [49], and reactive oxygen species released from cells [26] are also a typical example of this class. Neurotransmitter release is not continuous and therefore time-dependent measurements, often concurrent with stimulation of the cells, are performed.

11.1.3.4 Distance Calibration and Control of Mass Transport

The major technical problems with GC mode are the need for an independent distance measurement and the absence of a well-defined mass transport rate in some situations. These are linked in the sense that when mass transport is well defined, the distance dependence of the tip signal can be used to calibrate the tip-to-surface separation as well as to quantify the flux of analyte. One method to overcome these problems is therefore the use of a microfabricated substrate where the enzymatic reaction is confined to a small disk-shaped region. The concentration profile of the products of the enzymatic reaction may then be calculated from the diffusion equation. With such a defined steady-state concentration profile, the tip–substrate distance can be determined by fitting the approach curve of tip response–distance to theory [50,51]. This is described in more detail later in Section 11.2.2.2, where the use of the theory to obtain quantitative kinetic data is covered.

If the enzyme cannot be patterned in this way, or the system under study does not consist of isolated spots of activity, then an independent distance measurement is necessary, even if only to avoid a tip crash. Observation of the tip via optical microscopy is sometimes possible, though it may be difficult and is not usually precise enough for quantitative work. Addition of a reversible redox couple to the system and monitoring the feedback current is possible [21]. The redox couple should be chosen so as not to interfere with the system under study. This method is obviously applicable only to tips that may be used in an amperometric mode, for example, potentiometric antimony pH microelectrodes [33] but not glass or liquid membrane microelectrodes. Irreversible redox processes, for example, oxygen reduction, may also be used for distance calibration. The tip potential should be set sufficiently negative to drive the reduction of oxygen to water. This reaction is totally irreversible and therefore negative feedback will be observed on approaching the surface, unless

oxygen is being generated or consumed at the interface. The product, water, is not likely to interfere with the system under study. It should be noted that it is not essential to measure the oxygen concentration in the solution, all that is required is that oxygen reduction at the tip is diffusion limited, the tip radius is known and that the tip process does not adversely affect either the system under study or the tip response.

For high impedance electrodes, for example, liquid membrane ion-selective tips [50], another method is essential. Using techniques borrowed from electrophysiology, it is possible to construct dual tips from theta glass (Chapter 3). One barrel of the double tip can be used for the liquid membrane and the other may be filled with a low-melting-point metal such as gallium to make a voltammetric sensor [52].

Alternatively, the second barrel can be filled with the electrolyte and used in the same manner as in an ion conductance microscope [50]. It is possible to relate the solution conductance between tip and counter electrode to the normalized tip-to-substrate distance L. If the conductance is measured by a dc technique and the surface is impermeable to ions, a negative feedback effect (decrease of conductance as the tip approaches the surface) is observed. If an ac technique is used and the substrate is metallic, a positive feedback effect can be observed irrespective of whether the substrate is biased or not because the lowest impedance pathway for the current is through the metal via the metal–solution interface. In fact, after normalizing the conductance $G(L)$ by the value with the tip far from the surface G_∞, the distance dependence of the conductance is identical to that for faradaic currents in feedback SECM with a redox mediator:

$$\frac{G(L)}{G_\infty} = \frac{i_T(L)}{i_{T,\infty}} \tag{11.2}$$

This follows from the analogy between Fick's equation and Laplace's equation for the potential [32]. The analogy holds also for metallic tips, but in that case careful analysis of the impedance spectrum is necessary to extract the conductance $G(L)$ from the response of the whole cell, which generally includes capacitive elements and which may be distance-dependent [53,54].

In the case of an electrolyte-filled glass micropipette, the filling solution contributes substantially to the total resistance. This component is distance independent and can be subtracted from the measured value [50], or the full problem can be treated by finite element techniques [55]. A similar technique can be applied with amperometric tips using a small amplitude ac potential perturbation or a bipolar conductance technique [56]. When the electrolyte concentration is low, the contribution of the interfacial impedance is smaller than that of the solution resistance and a simple RC circuit is sufficient to extract $G(L)$ [32]. However, the impedance–distance behavior is sensitive to the electrolyte concentration and more sophisticated models are necessary at higher ionic strength or lower frequencies [53]. There has recently been increased interest in ac-SECM for a variety of applications [54,57–64], but, especially in biological studies, the capability to image without a redox mediator can be very useful [65]. The excellent image quality that can be obtained by combining scanning ion conductance microscopy (contactless topography imaging) and SECM for reactivity imaging is illustrated by a recent work by Takahashi et al. [66] (Figure 11.9).

Other distance calibrations have been proposed which do not depend on the measurement of tip currents. An example is the measurement of the damping of mechanical vibrations of the tip due to hydrodynamic forces that are distance dependent [67,68]. This may have wider application, though some additional equipment is required to produce and detect the oscillation of the tip. A method based on the use of a quartz-tuning fork to sense the surface may also be of use in SECM experiments [69]. In many experiments, a distance measurement is only required before and after the GC mode is employed. However, the "current-independent" distance measurements may provide simultaneous topographic images and are likely to be essential for rough surfaces when a feedback loop can be employed to guide the tip over protrusions in the surface [68].

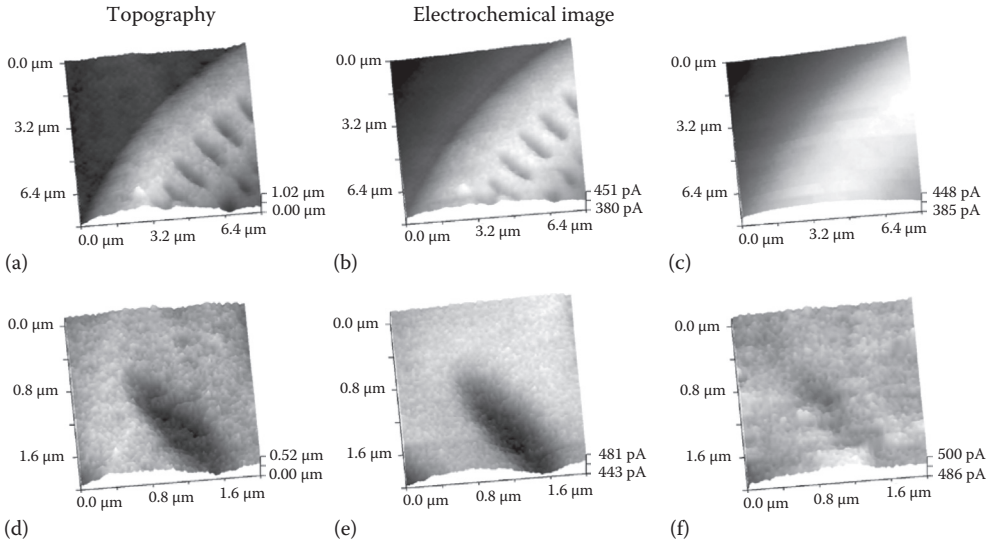


FIGURE 11.9 (a and d) Topographic and (b, c, e, and f) electrochemical images of GOx immobilized substrate adding 20 mM glucose and 0.5 mM ferrocene methanol in 0.1 M KCl. The SECM electrode was held at 500 mV (Ag/AgCl); upper and lower images were captured with 8 μm × 8 μm and 2 μm × 2 μm, respectively. The probe sample distance was held at 100 nm (b and e) and at 600 nm (c and f), respectively. (Reprinted with permission from Takahashi, Y., Shevchuk, A.I., Novak, P., Murakami, Y., Shiku, H., Korchev, Y.E., and Matsue, T., Simultaneous noncontact topography and electrochemical imaging by SECM/SICM featuring ion current feedback regulation, *J. Am. Chem. Soc.*, 132, 10118–10126, 2010. Copyright 2010 American Chemical Society.)

Kranz et al. used integrated AFM-SECM probes to detect products of peroxidase-catalyzed (Figure 11.10) [70] and glucose oxidase-catalyzed reactions [71]. These probes comprise a thorn that establishes the mechanical contact for the AFM imaging and a recessed electrode area for SECM imaging; such microfabricated structures solve the problem of keeping a constant working distance. Biosensors have been successfully constructed as scanning probes based on such electrodes and used for imaging applications [72].

11.1.3.5 Detection Limit

In comparison with feedback methods, generation–collection offers greater sensitivity to low activities of immobilized enzyme. An estimate of the minimum catalytic rate, k_{cat}, of the immobilized enzyme that can still be detected and quantified is made on the basis of the analytical sensitivity of the tip collector. If c' is the detection limit of the tip, then enzyme kinetic data can be obtained if

$$k_{cat}\Gamma_{enz} \geq \frac{c'D}{r_S} \tag{11.3}$$

where Γ_{enz} (mol/cm^2) is the surface coverage of enzyme. From Equation 11.3, it can be seen that sensitivity is increased for large specimen radius, r_S, low c', low D, and high surface coverage of enzyme. Equation 11.3 is similar in form to Equation 11.1 given in Section 11.1.2 for a feedback experiment with a redox enzyme. However, in the feedback case the contribution of the enzymatic flux to the tip signal must be distinguished from a significant background due to diffusion of mediator from the bulk. In the GC experiment, this background signal is absent and the sensitivity of the experiment to kinetics is directly proportional to the detection limit of the tip, c'. Reasonable values of $D = 5 \times 10^{-6}$ cm^2/s, $r_S = 5 \times 10^{-3}$ cm, and $\Gamma_{enz} = 10^{-12}$ mol/cm^2 and a rough estimate of $c' = 10^{-6}$ mol/dm^3 indicate

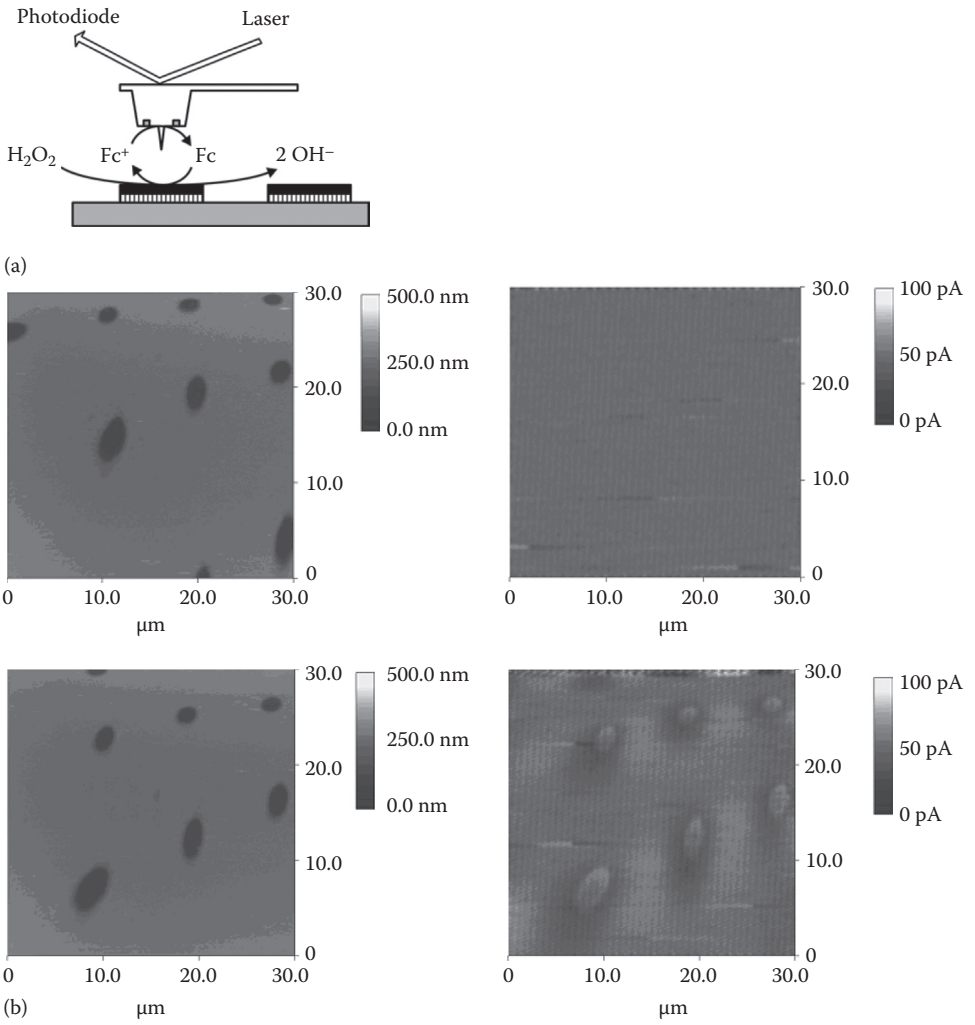


FIGURE 11.10 Images of enzyme spots obtained by an integrated AFM-SECM probe with recessed frame electrode. (a) Schematic representation of the experiment: on patterned SAM (1) immobilized horseradish peroxidase (2) catalyzes the oxidation of ferrocene methanol (Fc) by H_2O_2. The distance between sample and frame electrode is given by the length of the central thorn (410 nm). (b) Simultaneously recorded topography (left) and SECM feedback signals (right) with (bottom) and without (top) enzyme substrate H_2O_2. (Reprinted from *Ultramicroscopy*, 100, Kranz, C., Kueng, A., Lugstein, A., Bertagnolli, E., and Mizaikoff, B., Mapping of enzyme activity by detection of enzymatic products during AFM imaging with integrated SECM-AFM probes, 127–134, Copyright 2004, with permission from Elsevier.)

that enzymes with $k_{cat} > 1\,s^{-1}$ may be studied even at monolayer coverage. A wide range of nonredox enzyme reactions can be studied by generation–collection mode via detection of H^+. However, it should be noted that an exact theory is only available when the reaction product (H^+) does not undergo any solution phase reactions. If the solution is buffered to maintain pH close to the optimum for the enzyme, numerical treatments of the titration of the buffer components may be incorporated [33,51].

11.2 SELECTED APPLICATIONS

This section is a compilation of applications, where biochemical reactions and samples have been investigated with the SECM. Different methodological approaches to the study of similar

samples are presented, wherever possible, to facilitate comparison of different experimental strategies.

11.2.1 Localization of Enzymatic Reactions in Cells and Tissue

The imaging of enzyme activity can be achieved via feedback or generation–collection modes as described in Sections 11.1.2 and 11.1.3. Such studies are best performed on insulating supports because this excludes problems arising from unintentional overlap of different imaging principles. As described in Section 11.1.3.2, substrates such as microscope slides will be the natural choice in most cases anyway, because optical positioning of the microelectrodes greatly facilitates the experiment. Although microscopic techniques, for example, fluorescence microscopy, are commonly used to assay enzyme activity in even subcellular structures, the ability of the SECM to provide quantitative kinetic information may become useful in this context. One early example is the feedback imaging of the NADH–cytochrome c reductase system (EC 1.6.99.3) activity in the outer membrane of rat liver mitochondria using tetramethyl-*p*-phenylene diamine (TMPD) as redox mediator [17]. The images showed a depression (negative feedback) in the absence of NADH, but positive feedback in the presence of substrate. Although this study was successful in detecting the enzyme activity and distinguishing individual mitochondria, which were inactive, the resolution with a tip of 8 µm diameter was not sufficient to observe inhomogeneities in the enzyme distribution over the outer membrane of the mitochondria with diameters of 3–5 µm. The limitation on tip size set by the detection relation (Equation 11.1) makes smaller tips much less sensitive. For this reason, GC schemes may be necessary to achieve the sensitivity needed for the application of smaller tips. The loss of lateral resolution typically encountered in GC experiments may be at least partially compensated by exploiting solution phase chemistry as discussed in Section 11.2.3.3. Tsionsky et al. [73] were able to image O_2 release from individual guard cells in white regions of *Tradescantia fluminensis* with the GC mode. In these regions, only the guard cells contain chloroplasts. Zhou et al. investigated local peroxidase activity within celery tissue [74] and single cell algae protoplasts after mechanical injury of the cell [75].

11.2.2 Kinetics of Immobilized Enzymes

A feature of SECM is the quantitative theory based on reaction–diffusion models that are available (Chapter 5). The SECM may be used for kinetic studies in either the feedback or generation–collection modes. These two possibilities are described in the following from the point of view of an investigation of immobilized enzyme kinetics.

11.2.2.1 Enzyme-Mediated Feedback Mode

When an oxidoreductase enzyme is immobilized at the specimen surface, a redox mediator present in solution may be recycled by the diffusion-limited electrochemical process at the tip and electron exchange with the enzyme active site as described in Section 11.1.2. The mass transport rate is defined by the tip radius and height of the tip above the specimen. The tip current depends on the mass transport rate and the enzyme kinetics. Kinetic information may therefore be obtained from the dependence of tip current on height, that is, an approach curve. When the mediator is fed back from the specimen at a diffusion-controlled rate, the approach curve will be identical to that above a metallic conductor. In the opposite situation, when the flux of mediator fed back from the specimen is much less than the flux of mediator to the tip from bulk solution, the approach curve will correspond to that above an insulating surface, that is, pure negative feedback. In between these two limits, the approach curve will contain information on the steady-state rate of the enzymatic reaction and the shape of the approach curve as a function of substrate and cosubstrate concentrations may be used to investigate the reaction order (Figure 11.3). A detailed study of GOx with several redox mediators and immobilization techniques has been reported [15]. The enzyme reaction kinetics was

modeled with a simple heterogeneous rate law; under the assumption of a thin and highly permeable enzyme layer, the concentrations of glucose and mediator are uniform throughout the enzyme layer. Working curves for zero- and first-order enzyme kinetics (in redox mediator concentration) were computed by a finite difference technique for the case where the glucose concentration was sufficiently large to saturate the enzyme. The data were found to be best fit by zero-order kinetics for several choices of redox mediator and this was interpreted as saturation of the enzyme kinetics with respect to mediator too.

Matsue et al. [21,76] have reported a kinetic study of diaphorase immobilized on glass slides. Ferrocene methanol was oxidized at the tip and reduced at the glass slide by diaphorase in the presence of excess NADH. A slightly different approach to modeling the diffusion problem was taken; although the enzyme kinetics were also assumed to be saturated with respect to substrate, the full Michaelis–Menten expression for the dependence of the rate on the mediator was retained. Working curves of tip current versus active enzyme surface coverage at a given tip–surface distance and mediator concentration were computed using previously obtained values of the kinetic parameters of the immobilized enzyme [77]. At the mediator concentrations employed, 0.5 mM, the kinetics were essentially zero order in this case. Overall, the enhancement over negative feedback due to the enzymatic process is quite small (ca. 10%–20%) and this situation is typical for feedback studies of enzymes. In such cases, the availability of enzyme-modified and bare regions on one surface allows imaging and convenient control experiments.

Zhao and Wittstock [19] conducted a comparative investigation of the kinetics of PQQ-dependent glucose dehydrogenase in the feedback and the generation–collection mode. The experiment was performed under conditions such that zero-order kinetics with respect to glucose and first-order kinetics with respect to the different mediators were maintained. This enzyme showed much faster kinetics than GOx despite some activity loss during immobilization.

Burchardt and Wittstock studied the kinetics of GOx immobilized using the layer-by-layer adsorption of polyelectrolyte technique [78]. This system has the advantage that the amount of immobilized enzyme can be adjusted by changing the number of GOx layers. In addition, the accessibility of the enzyme to mediator and substrate can be varied by cover layers of polyelectrolytes without enzyme. The system was studied under conditions of zero order with respect to glucose. Careful control experiments were performed to limit the mediator (ferrocene methanol) concentration to values under which first-order kinetics with respect to mediator were observed. This was achieved by plotting the difference of the measured tip current and the expected response from a totally inert surface as function of distance [19]. This allowed the available theory [79,80] for first-order processes at the sample to be applied. The extracted normalized rate constants varied with the number of glucose layers and surprisingly showed an odd–even pattern with respect to layer number that correlated with the appearance of the polyelectrolyte film in AFM images.

Recently, the unsatisfying situation that either zero-order kinetics or first-order kinetics must be obeyed in the experiments prompted new simulations that include the transition region from first-order to zero-order kinetics. Burchardt et al. [81] simulated approach curves and provided detailed guidelines for the conditions under which a treatment with first-order kinetics is appropriate. Cornut et al. [82] calculated analytical approximations for the conditions of zero order with respect to the substrate and a mixed regime with respect to the mediator. It is also evident that the reaction order could vary laterally along the sample surface and therefore a special treatment would be required in that case.

11.2.2.2 Generation–Collection Mode

The tip signal in a generation–collection experiment with an enzymatic reaction occurring at the specimen surface depends on the enzyme reaction kinetics and the rate of mass transport of the products to the tip. Quantitative kinetic investigations of immobilized enzymes can be made by GC experiments when this mass transport rate is well defined. In principle, a macroscopic specimen

uniformly coated with enzyme could be used if the enzymatic process was switched on abruptly. This would be analogous to a chronoamperometric generation–collection experiment with electrocatalytic systems [83]; however, such a mechanism is often not available for enzyme-modified surfaces. In practice, measurements have been made where the biochemical reaction is localized at micrometer-scale immobilized enzyme spots of defined geometry so that a steady-state diffusion field is produced [33,34,50]. The simplest experimental realization is a microdisk of immobilized enzyme. If we assume the tip is sufficiently small or distant so as not to perturb the diffusion of enzymatic reaction products, the normalized concentration profile $C(H) = c/c_0$ (c_0 is the concentration at the surface or at the center of the disk) above the center of a disk is related to the normalized flux ($F = r_S f/Dc_0$; f/(mol/cm^2/s)) by established theory [33,51]:

$$C(H) = \int_0^1 \frac{uF(u)}{\sqrt{H^2 + u^2}}\, du \tag{11.4}$$

where $C(H)$ is the concentration of reaction product monitored by the tip at a normalized height $H = d/r_S$ above the center of the specimen disk (r_S, radius of specimen). The flux at the specimen surface, $F(u)$, depends in general on the distance $u = r/r_S$ from the center of the disk

If the enzymatic process is limited by the diffusion of the substrate to the disk surface, then the flux will be nonuniform across the disk in a manner analogous to the current density distribution at a microdisk electrode operating at the diffusion-limited current. However, this situation is not common and does not allow information to be gained on the enzyme kinetics. A more interesting case occurs when the diffusion-limited flux of substrate to the enzyme is greater than the flux of the enzyme-catalyzed reaction. This can often be achieved by increasing the substrate concentration above the K_M to ensure that the enzyme kinetics are saturated. In this case, the flux distribution is determined by the distribution of enzyme. Often it may be assumed to be approximately uniform across the disk-shaped specimen surface. Under these conditions, the flux and concentration profile of an enzymatically created product P can be treated similarly to the diffusion above a disk-shaped pore opening (Chapter 9).

The steady-state UME current can be calculated according to the theory for the diffusion above a disk-shaped pore opening (Chapter 9). When the tip is positioned over the center of the enzyme spot (where the peak current occurs), the lateral distance is $r = 0$; hence, the relation for the tip current above a pore opening simplifies to

$$i_T = gnFDa[P]_S \frac{2}{\pi} \arctan \frac{r_S}{d} \tag{11.5}$$

where

n is the number of transferred electrons per molecule P
F is the Faraday constant
D is the diffusion coefficient of P
a is the tip radius
r_S is the radius of the enzyme-modified spot
$[P]_S$ is the concentration of P at the surface of the enzyme-modified spot
d is the vertical working distance

The factor g is ~4 if a tip with a large insulating sheath is used ($RG = a/r_g \to \infty$). However, in these measurements small RG values are preferable (smaller tips perturb the substrate diffusion field less) and more precise g values are available in the literature [84].

Knowledge of r_S and $[P]_S$ provides the total flux $\Omega = 4Dr_S[P]_S$ and the generation rate [mol/cm²/s] for a circular disk $f = \Omega/\pi r_S^2$. In a steady-state situation, f can also be described by the kinetics of the immobilized enzyme:

$$f = \frac{k_{cat}\Gamma_{enz}[S]_S}{K_M + [S]_S} \tag{11.6}$$

where

f is the heterogeneous reaction rate for the formation of P per unit time and unit area (mol/cm²/s) and characterizes the effective kinetics of the enzymatic reaction
k_{cat} is the turnover number
Γ_{enz} is the enzyme surface concentration (amount of enzyme per unit geometric surface area)
$[S]_S$ is the concentration of substrate at the surface of the spot
K_M is the Michaelis–Menten constant

Taking the description of the flux from Equation 11.6 and the relation $f = 4Dr_S[P]_S/\pi r_S^2$, isolating $[P]_S$, substituting it into Equation 11.5, and assuming $g \approx 4$, the UME current over the center of the spot can be related to the enzyme kinetics [85].

In order to ensure a homogeneous $[S]_S$ over the surface, the most appropriate conditions are $[S] >> K_M$ and a value of d that is large enough to prevent shielding of the substrate flux. Under these conditions, Equation 11.7 forms the basis for quantifying biochips with enzyme labels for SECM detection with horizontal scans:

$$i_{T,peak} = 2nFar_S \arctan\left(\frac{r_S}{d}\right)(k_{cat}\Gamma_{enz}) \tag{11.7}$$

An alternative approach to obtain f (mol/cm²/s) that is also suitable for potentiometric probes converts the $i_T(d)$ data points of an approach curve over the center of the enzyme-modified surface to concentrations as function of normalized distance $C(H)$ and fits Equation 11.8 to this using an independently measured diffusion coefficient D of P and r_S:

$$\frac{C(H)}{F} = \sqrt{H^2 + 1} - H \tag{11.8}$$

Experimentally, the tip may be located over the center of the disk using an optical microscope or by scanning the tip laterally at a constant height till the position of maximum tip response is obtained. As the maximum of the concentration profile is broad in the radial direction, a combination of these approaches is often the best [33,50,51]. Once the tip is centered over the specimen, an approach curve can be recorded using a slow tip speed (typically 1 µm/s) to minimize convective disturbance of the diffusion field. Further, since the theoretical treatment ignores entirely the presence of the tip, a small ratio of tip-to-specimen radii is preferable. Conventional wire-in-glass microelectrodes with RG ~ 10 are not expected to give accurate results for this reason and GC mode kinetic experiments have often employed tips based on finely drawn-out glass capillaries such as liquid membrane ion-selective microelectrodes [50,52].

In principle, the zero tip-to-specimen distance point can be included as a free parameter in the fitting process [34,50]; however, an independent measurement of the absolute tip-to-surface distance is preferable. This has been accomplished via several methods described in Section 11.1.3.4.

11.2.2.3 Potentiometric Studies of Enzyme Kinetics in GC Mode

The enzyme urease produces NH_4^+ by the hydrolytic reaction:

$$(NH_2)_2CO + 3H_2O \rightarrow 2NH_4^+ + HCO_3^- + OH^- \tag{11.9}$$

Urease activity can therefore be detected either by pH-sensitive tips [33] or NH_4^+ [50].

Jack Bean urease adsorbs strongly to soft metals, for example, gold, through interaction with the disulfide links present on the outer surface of the enzyme. The adsorbed urease retained activity for the catalysis of urea when immobilized in this way on a 50-μm radius gold disk microelectrode and provided a useful model system to study the stability of enzymes on metal electrodes. A steady-state diffusion field was observed at a concentration of urea where the enzyme kinetics were saturated. Application of a positive potential bias to the gold surface reduced the enzyme activity, which was observed as a decrease in $[NH_4^+]$ at the tip; this decrease occurred on a timescale comparable to r_S^2/D and the speed of the tip response was therefore limited by diffusion of enzymatic reaction products. However, the recovery of the activity on returning the potential to 0 V was much slower and not masked by diffusion. Double potential step experiments (Figure 11.11) showed that the reduction in activity was reversible and not associated with any faradaic process, ruling out desorption or oxidation of the enzyme as the cause. The kinetics of the modulation of enzyme activity

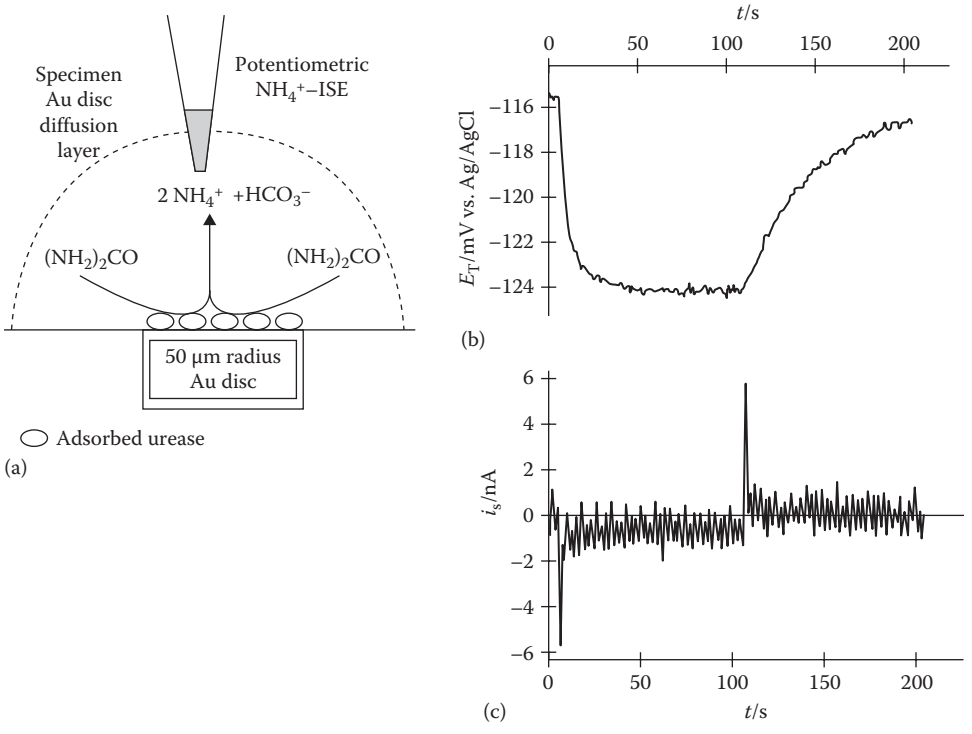


FIGURE 11.11 (a) Schematic diagram of the measurement of the activity of urease adsorbed on a gold microdisk using an ammonium-selective potentiometric SECM tip, (b) tip potential, (c) current at the gold substrate electrode during a potential step of the gold microdisk from 0 to 0.4 V at $t = 0$ and back at $t = 100$ s. The solution contained 0.1 M Tris–HCl buffer adjusted to pH 7.0 and 50 mM urea. The tip potential and current data have been subjected to a 10 point moving average smoothing algorithm. (From Horrocks, B.R. and Mirkin, M.V., Evidence for a potential-dependent reversible inactivation of urease adsorbed on a gold electrode, *J. Chem. Soc. Farad. Trans.* 94, 1115–1118, 1998. Reproduced by permission of The Royal Society of Chemistry.)

during the potential step experiment were analyzed to show that the recovery of enzyme activity obeyed first-order kinetics with an observed rate constant of $0.022\,s^{-1}$ [34].

11.2.3 Advanced Architectures for Enzyme Electrodes

The development of biosensors, especially amperometric enzyme electrodes, is an area where SECM may have an important role. Biosensors find application in the treatment of diabetes mellitus, fermentation control in food processing, and biotechnological production of pharmaceuticals. Such sensing devices consist of a biorecognition layer (e.g., an enzyme layer) and a transducer (e.g., an amperometric electrode). Intensive efforts are currently devoted toward the development of miniaturized biosensors driven by the need to reduce sample volume (e.g., blood drawn from neonates or critically injured patients) or the need to work in confined microenvironments (e.g., in vivo monitoring).

11.2.3.1 Microcompartmentalized Surfaces

Experience with unmodified microelectrodes suggests advantageous characteristics such as short response times and low convection dependence may be obtained with miniaturized sensors. The miniaturization of enzyme electrodes will also allow the construction of multianalyte enzyme electrode arrays. SECM has already been used as a tool to gain a deeper understanding of the cross talk [86], that is, the response of electrodes to the analyte converted at the neighboring electrode or the signal modulation at the sensing electrode by the potential of the adjacent electrode. This is caused by common reactants and products, for example, H_2O_2, diffusing from one electrode to the other. Active shielding was demonstrated by regions consuming the diffusing species by electrochemical or enzymatic reactions [86]. Microcompartmentalization represents another new concept that seems feasible with recent advances in the controlled design of solid–liquid interfaces. In such a device, different components of a sensor are immobilized in separate microscopic domains on one surface, where the environment for each component is optimized, and which are spaced so closely that efficient communication between different domains occurs through diffusing reactants [87]. Nowall et al. [88] obtained microcompartmentalized electrodes by using a laser interference pattern and photobiotin that was incubated with fluorophor-tagged avidin. Segregation observed by fluorescence microscopy corroborated the distribution of the heterogeneous electron transfer rates at the bare and derivatized regions as analyzed by SECM. Besides using SECM as a tool to assess heterogeneous redox kinetics, the potential for imaging biochemical reactivity on the micrometer scale should be very helpful for all of these developments. However, investigations of amperometric biosensors face an additional challenge compared to the examples described so far: above a conducting sensor surface, the SECM feedback signal may be modulated by (i) surface roughness [89], (ii) partial blocking of the specimen surface by the biorecognition layer or other sensor components (feedback mode), (iii) an enzymatic reaction *and* by heterogeneous electron transfer at the specimen surface (feedback mode), and (iv) lateral variation of the enzymatic activity. Typically at least two of these influences are effective simultaneously in any particular application.

11.2.3.2 Pattern Formation in Biotechnological Environments

Although scanning probe techniques are generally not competitive with photolithography or microcontact printing in terms of speed, SECM is particularly useful to explore new concepts of microstructured enzyme electrodes because it can subsequently be used for both microstructuring in aqueous solution and imaging of the obtained structures. Here, only a brief summary is given because a full account of surface modification with SECM is given in Chapter 15.

Biomolecular layers require special structuring techniques that preserve the activity of the biomolecules. Therefore, many established processes involving either the exposure of the specimen to vacuum, elevated temperature, or the use of etchants are not applicable.

In a series of papers, Kranz et al. [68,90,91] developed a technique to electropolymerize pyrrole in two-dimensional and three-dimensional structures using the SECM tip as the auxiliary electrode

and applying a galvanostatic pulse program [92] to the macroscopic specimen. Through the use of N-substituted monomers, the enzyme GOx could be attached to the polymer backbone via a flexible spacer [11]. Fortin et al. used the deposition of PPy substituted with DNA to construct DNA microarrays [13].

Polyelectrolytes as matrices for immobilization of biocomponents can be patterned by tip-induced pH shifts. This has been demonstrated by the deposition of the biopolymer chitosan that is soluble in acetate buffer at pH 5.7, but becomes insoluble at higher pH [93]. Glucose oxidase could be entrapped in the deposit that remained on the surface after the end of the potential pulses and relaxation of the pH in the tip–sample gap. Shifts of pH can also be introduced by electrolysis at microstructured samples to carry out localized deposition of enzymes [94].

Wittstock et al. [9] have demonstrated a route to the formation of patterns of enzymatic activity by desorption of patches of alkanethiol SAMs on gold surfaces. The technique exploits the reductive desorption of alkanethiols and their oxidative decomposition. The technique is particularly effective if used with a square wave potential program in which the high capacitive currents help to focus the modification [95]. The generated bare gold areas can be modified again with ω-functionalized thiols (e.g., cystaminium dihydrochloride). Enzymes or other biomolecules can be anchored to the terminal functional groups and the resulting activity can be imaged [27]. This process can be performed in a one-step operation if the functionalized thiol is present in the desorption solution [102]. The approach is also especially powerful if performed after parallel pattern formation by microcontact printing [96].

A related technique was demonstrated by Shiku et al. [97] who formed alkylsilane monolayers at glass substrates and used electrochemical generation of $OH^{\bullet}$ radicals at the tip via the Fenton reaction to locally destroy the SAM. Diaphorase could then be patterned on the surface by physical adsorption to the undamaged hydrophobic areas. Treatment of the damaged SAM with aminopropyltriethoxysilane produced disk-shaped patches of amino-terminated monolayer at these areas and subsequent covalent attachment of diaphorase. Local generation of Br_2/HOBr can also be used to remove oligoethylene (OEG) units from SAMs. OEG prevents nonspecific protein adsorption and cell adhesion [98]. This mechanism has been used for formation of cell patterns. Wilbur et al. [99] used local reagent generation by the SECM tip in conjunction with biotin/avidin chemistry for microderivatization of carbon surfaces: local derivatization was achieved by activating biotin hydrazine by an unknown electrochemical reaction. Activated biotin bound to the carbon surface and formed a microspot. Alternatively, bound biotin could be removed locally by generation of hydroxide ions at the tip to form a microscopic underivatized region surrounded by the biotin-derivatized surface.

An alternative approach to the patterning of enzymatic activity is to start with a substrate uniformly coated with enzyme and to locally deactivate the enzyme in order to generate the pattern. This can be achieved by the generation of denaturing agents at the tip, for example, Br_2/HOBr [21]. Geometrically well-defined disks and lines of deactivated diaphorase have been produced and imaged. The opposite effect, local activation, has also been demonstrated in an experiment in which the bulk solution was maintained at pH 6 below the optimum (pH 9) for alcohol dehydrogenase immobilized on agarose beads. The tip was used to locally raise the pH by reduction of oxygen and water and the enzymatic activity observed by monitoring the reduced cosubstrate, NADH, via fluorescence microscopy [100].

11.2.3.3 Overlap of Different Feedback Contributions on Conductive Substrates

When working with enzymes on conducting surface, for example, during characterization of amperometric biosensors, overlap of different feedback mechanisms must be expected as exemplified in the work by Kranz et al. who used *N*-(ω-aminoalkyl)pyrrole to form derivatized PPy that provides amino groups for binding periodate-oxidized GOx to the outer polymer surface [11].

Using the enzyme-mediated feedback mode with an artificial electron acceptor for GOx formed at the tip as shown in Figure 11.12 would not give a clear result because of the overlapping effects illustrated in the figure. The overall feedback effect above the GOx-modified conducting polymer has three contributions: (i) mediator regeneration by an electron transfer reaction at the Au–polymer

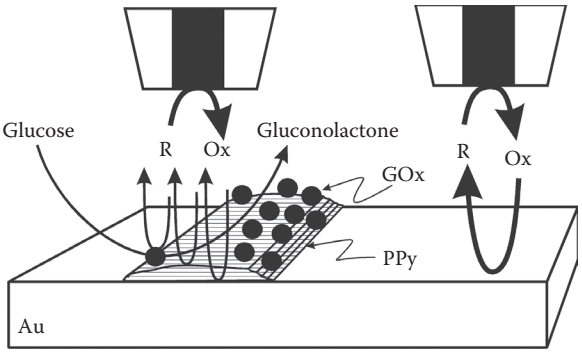


FIGURE 11.12 Illustration of superposition of different contributions to the overall feedback effect above an GOx-modified polymer deposited on a conducting surface as investigated by Kranz et al. [11] (schematic prepared by the chapter authors). The oxidized form of the mediator, Ox, acts as artificial electron acceptor for GOx; PPy, polypyrrole.

interface, (ii) mediator regeneration by an electron transfer reaction at the polymer–solution interface, and (iii) mediator regeneration by the enzymatic reaction at the outer polymer surface. The sum of these contributions has to be compared with the positive feedback above the uncovered Au electrode.

The conductivity of the N-substituted PPy is considerably lower than that of unmodified PPy [101] and the regeneration rate of the mediator at the polymer–solution interface is slow. Since the hydrophobic polymer represents an additional diffusion barrier for highly charged mediator ions, the positive feedback current due to regeneration at the Au–polymer interface is reduced compared to the uncovered Au surface. If a mediator, such as $[Ru(NH_3)_6]^{3+}$, is chosen that does not react with GOx, reduced tip currents indicate the position of the polymer deposit. A qualitatively similar image is obtained if an artificial electron acceptor for GOx is used but the enzyme substrate β-D-glucose is not provided in solution since the enzyme catalytic cycle requires both glucose and an electron acceptor. After addition of glucose to the solution, higher currents were recorded. The combined contributions of the electrochemical positive feedback at the Au–polymer interface and the enzyme-mediated positive feedback at the outer polymer surface almost equal the diffusion-controlled feedback above the bare Au electrode. The contributions of the enzymatic reaction can then be estimated from the difference between the images recorded in the presence of glucose (enzyme-mediated feedback plus conventional feedback) and in the absence of glucose (conventional feedback only).

11.2.3.4 Novel Sensor Architectures Based on Patterned Self-Assembled Monolayers and Patterned Polymer Films

Another approach to microstructured enzymatically active regions makes use of the strong chemisorption of sulfur-containing organic molecules at Au and the tendency of long-chain alkanethiolate adsorbates on Au surfaces to arrange spontaneously into a densely packed SAM. Although such layers provide only monomolecular coverage of the Au surface, electrochemical reactions of solution constituents at the metallic electrode are quite strongly inhibited if the alkyl chains contain more than eight carbon atoms. Among other techniques, SECM can be used for microstructuring of these layers.

To image the localized enzymatic activity in the feedback mode would be even more difficult than in the case of the enzyme-modified PPy lines on electrodes (Section 11.2.3.1). There is negative feedback above the unaffected long-chain SAM and positive feedback above areas from which the long-chain alkanethiolate has been desorbed [9,95,96,102]. The cystaminium-bound enzyme layer is less effective for inhibition of the reaction of ferrocenium derivatives at the Au surface than the densely packed long-chain alkanethiolate layer. Therefore, positive feedback would be observed

above the enzyme-modified region due to the electrochemical feedback at the Au surface although the positive feedback may be reduced to some extent compared with a bare Au surface.

When using an artificial electron acceptor for GOx and adding glucose to the solution, the additional contribution due to the enzymatic regeneration of the mediator would be small and difficult to separate from the contribution of the enzyme layer. This is particularly problematic when the enzymatic activity decreases with time. Furthermore, as enzyme coverage varies the effects of increased electrochemical feedback (due to decreased blocking effects) and diminished enzyme-mediated feedback (due to a decreased amount of bound enzyme) would partly counteract each other.

Under these circumstances, the GC mode represents the better choice [27] (Figure 11.13). Experiments were carried out in an air-saturated solution. In the presence of glucose, the enzymatic reaction commences and gluconolactone and H_2O_2 are formed. The latter is amperometrically detected at the SECM microelectrode. High currents are measured above regions of H_2O_2 production and hence provide a map of GOx activity (Figure 11.14a). Repetition of the experiment in the absence of glucose results in a featureless image of low currents (Figure 11.14b) proving that the signals in Figure 11.14a are due to the oxidation of enzyme-generated H_2O_2.

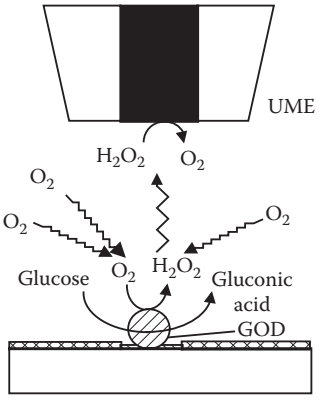


FIGURE 11.13 Detection of GOx activity immobilized on a conductive support in the generation–collection mode; GOx, glucose oxidase; UME, microelectrode tip.

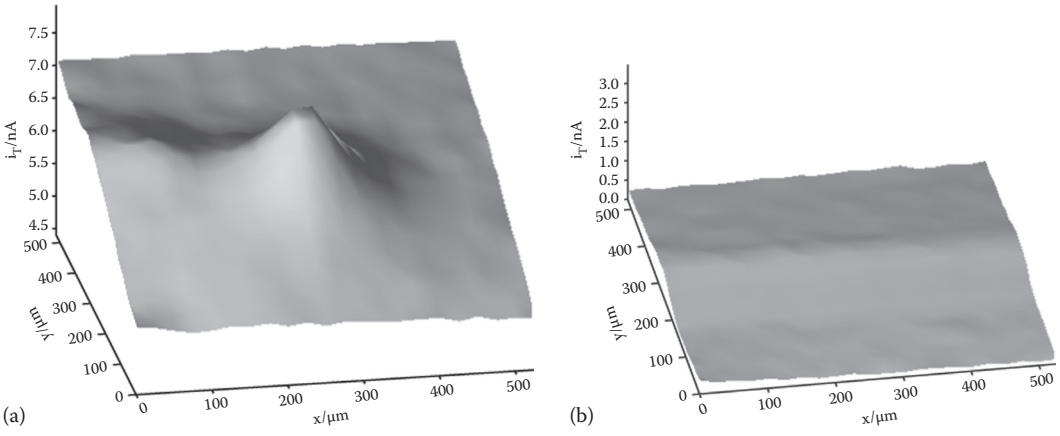


FIGURE 11.14 Generation–collection mode images of GOx bound to a patterned SAM in the presence (a) and absence (b) of 50 mM glucose in air-saturated 0.1 M phosphate buffer (pH 7.4); $E_T = +400$ mV, $v_t = 15$ μm/s. (Reprinted in part with permission from Wittstock, G. and Schuhmann, W., Formation and imaging of microscopic enzymatically active spots on an alkanethiolate-covered gold electrode by scanning electrochemical microscopy, *Anal. Chem*., 69, 5059–5066, 1997. Copyright 1997 American Chemical Society.)

During the experiments, the Au electrode is at the open circuit potential which is established at a macroscopic blank area of Au located several millimeters away from the enzyme-modified regions. From thermodynamic considerations, one might expect H_2O_2 to be oxidized at the Au surface. However, this reaction occurs only at high overpotentials or requires an electrocatalyst. The electrocatalytic properties of noble metal surfaces are deactivated rapidly by the chemisorption of thiolates or other organic molecules; therefore, H_2O_2 diffuses into the solution and can be detected by the microelectrode.

Similar imaging principles were applied to microstructured surfaces obtained by microcontact printing (Figure 11.15) and subsequent modification with HRP and GOx [103]. Wilhelm and Wittstock [96] formed dual enzyme surfaces. HRP was covalently immobilized to a patterned SAM obtained by microcontact printing. The SECM microelectrode was positioned above this surface by monitoring the SECM feedback current due to the underlying gold surface. Due to their higher permeability, the enzyme regions produced a larger feedback. After positioning the tip above a specific feature, local SAM desorption was carried out and the bare gold electrode was back-filled with GOx. Subsequently, the local enzyme activities of GOx and HRP were detected individually and in

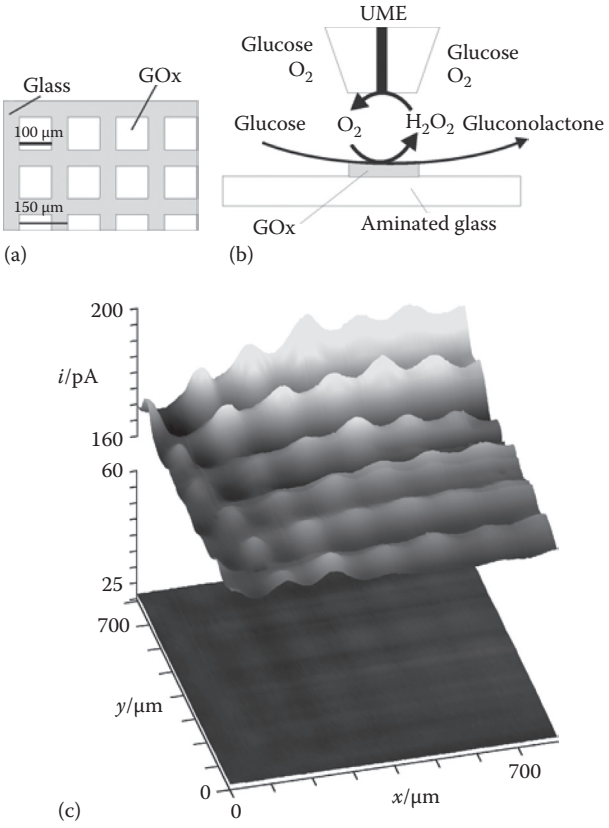


FIGURE 11.15 SECM imaging of localized GOx activity on patterned monolayers on glass. (a) A mixture of GOx and carbodiimide was applied to the stamp and brought into contact with an aminated glass surface on the 100 µm × 100 µm squares, contact time 30 min. (b) Schematic of the SECM GC experiment and (c) top image air-saturated 50 mM glucose + phosphate buffer, pH 7; bottom image air-saturated phosphate buffer without glucose, $r_T = 12.5$ µm, $E_T = 750$ mV. (Reprinted with permission from Wilhelm, T. and Wittstock, G., Generation of periodic enzyme patterns by soft lithography and activity imaging by scanning electrochemical microscopy, *Langmuir*, 18, 9485–9493, 2002. Copyright 2000 American Chemical Society.)

combination. In a solution containing H_2O_2 and ferrocene methanol (Fc), a GC image for the detection of Fc^+ shows a periodic pattern of HRP activity in agreement with the layout of the stamp used for the printing step. No conversion proceeds at GOx. In a solution of glucose and O_2, glucose oxidation and H_2O_2 formation occur at GOx and could be detected in GC mode as in Figure 11.13. HRP is not active in this situation because an electron donor is not present for this enzyme. However, in a solution containing glucose, O_2, and Fc, both enzymes react simultaneously. The GOx spot provides H_2O_2 locally, which is reduced at HRP. In contrast to the imaging in H_2O_2 and Fc solution, only HRP regions in the vicinity of the GOx spot are exposed to H_2O_2 and show a conversion. This conversion is seen in a GC image in which Fc^+ is detected at the tip [96].

Luo et al. [104] stamped a 4 μm diaphorase line on glass and analyzed the resulting structure of protein aggregates using AFM. Localized diaphorase activity was also imaged using the SECM feedback mode. Protein adsorption on surfaces typical for micro total analysis systems has been studied by photoelectron spectroscopy. The amount of protein detected was related to enzyme activity detected by SECM [105]. Diaphorase on glass was also further modified by bleaching using the laser of a confocal scanning laser microscope followed by electrochemical and optical activity imaging [106].

Piezoelectric microdispensing and ink-jet printing systems have been used to form spots of polymer-entrapped enzymes and the resulting structures have been analyzed using SECM [107–109]. Particular attention has been devoted to create dual enzyme structures from GOx and catalaze [108].

11.2.3.5 Screening Procedures for Combinatorial Tests

SECM is well suited to characterize enzyme layers that have been obtained by new nonmanual immobilization techniques such as ink-jet printing [20,109] or site-directed deposition of polyelectrolytes with entrapment of enzymes [94] (Figure 11.16).

Besides analyzing spot homogeneity, spot size, remaining activity after cross-linking, reproducibility and alignment with micropatterned electrode structures, and so on, a particularly interesting field is the study of gradient materials that can be formed with these techniques [110]. An SECM image of such a gradient material can be considered as the response of an array of slightly different sensors for the same analyte on a single support and under identical solution conditions. Instead

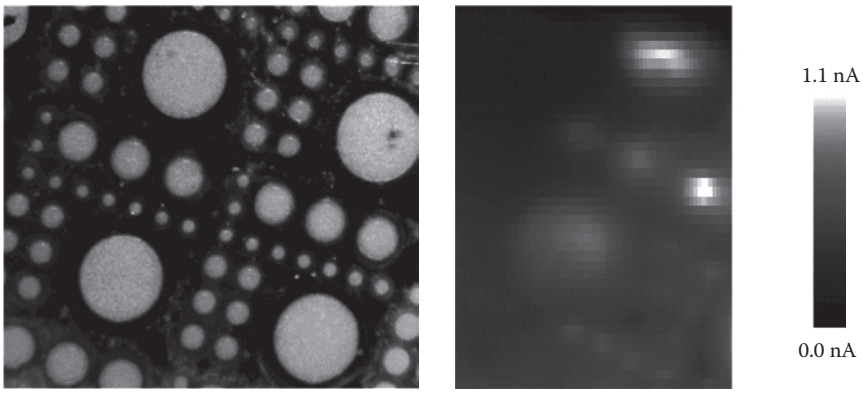


FIGURE 11.16 Au disk microstructure with electrochemically deposited polymer containing GOx. (a) Visualization of the modified Au disks by means of optical microscopy. (b) Localization of immobilized enzyme activity by means of SECM imaging using the generator–collector mode (10 μm Pt disk electrode at 0.6 V to oxidize enzymatically generated H_2O_2). (Reprinted with permission from Kurzawa, C., Hengstenberg, A., and Schuhmann, W., Immobilization method for the preparation of biosensors based on pH shift-induced deposition of biomolecule-containing polymer films, *Anal. Chem.*, 74, 355–361, 2002. Copyright 2002 American Chemical Society.)

of preparing many sensors with slightly varied protocols, one gradient or one spot with different polymer thickness is considered as an ensemble of individual microsensors with specific response characteristics. The location of the highest SECM signal indicates the position, where the recognition layer with optimum characteristics has been deposited. The scope of this approach was subsequently broadened by considering new approaches for interference elimination [111,112]. Polymer spots with entrapped GOx were imaged in the SECM GC mode in different solutions. The data for each grid point and concentration level of the analyte glucose, and the potential interfering species ascorbic acid and 2-deoxy-D(+)-glucose, were subjected to a principal component analysis. From the analysis, an optimum sensor for the analysis of mixtures could be located on the enzyme polymer spot. A similar study was also conducted for PQQ-dependent glucose dehydrogenase in polymer spots with the aim of analyzing glucose in the presence of maltose [113]. Using a similar concept, Kasai et al. [114] prepared spots of GOx and uricase and read the signal at various concentrations by SECM GC mode and scanning chemiluminescence microscopy.

11.2.3.6 Improving the Resolution of the Generation–Collection Mode by Coupling with Solution Chemistry

The tip radius was 25 µm for both electrochemical desorption and mapping of GOx activity in Figure 11.14. The area from which the alkanethiolates were desorbed gave feedback images with a full width at half maximum (FWHM) of about three times the diameter of the microauxiliary electrode (tip) used in the desorption step [9]. The GC image of the enzyme activity shows considerably larger features because it is blurred by the fast diffusion of H_2O_2. In addition, the image does not represent a steady-state situation as the enzymatic reaction produces H_2O_2 continuously leading to a slow increase of the bulk H_2O_2 concentration. This fact is obvious from the background currents in Figure 11.14a which rise steadily from the start of the image at the front left corner to the last recorded point at the far right corner during an image acquisition time of about 40 min. The example illustrates a dilemma when investigating enzymatically active layers on conducting supports: application of the feedback mode is generally problematic and the GC mode is connected with a loss in lateral resolution and difficulties for kinetic analysis owing to the non-steady-state concentration profiles. Even over insulating supports, the feedback mode may not be applicable when no redox-active cosubstrate is involved in the enzymatic reaction. In other cases, its use may be difficult because the enzymatic activity is below the limit of detection (Equation 11.1). As discussed in Sections 11.1.2 and 11.1.3, the GC mode is more sensitive.

Introduction of a homogeneous chemical reaction that competes with the detection reaction at the tip for the species formed at the specimen represents a general approach for resolving these difficulties and has appeared occasionally in the SECM literature. Owing to its significance for biological SECM applications, a systematic discussion is provided here, even if the original applications did not involve a biochemically active specimen [115].

The first systematic study on resolution enhancement for GC mode imaging of biochemically interesting compounds was presented by Engstrom et al. as early as 1992 [116]. A large Pt disk electrode served as model specimen and was used as generator electrode to which a sweep was applied from potentials where no oxidation occurred to a potential causing a diffusion-controlled oxidation of either $[Fe(CN)_6]^{4-}$ or epinephrine. The amperometric microelectrode tip was placed within 2 µm of the specimen and poised at a potential E_T to detect the local concentration of species electrogenerated at the specimen as a function of the specimen potential E_S (Figure 11.17). After movement of the electrode parallel to the specimen surface, a new potential sweep at the specimen was performed.

$[Fe(CN)_6]^{4-}$ undergoes a quasi-reversible reaction at the specimen electrode. The oxidized form $[Fe(CN)_6]^{3-}$ is produced on sweeping to positive potentials. After completing the sweep, the specimen electrode returns to a potential where the generated $[Fe(CN)_6]^{3-}$ is rereduced. By increasing the sweep rate at the specimen electrode, the time available for $[Fe(CN)_6]^{3-}$ generation and diffusion away from the specimen electrode is diminished. Therefore, the distance at which the

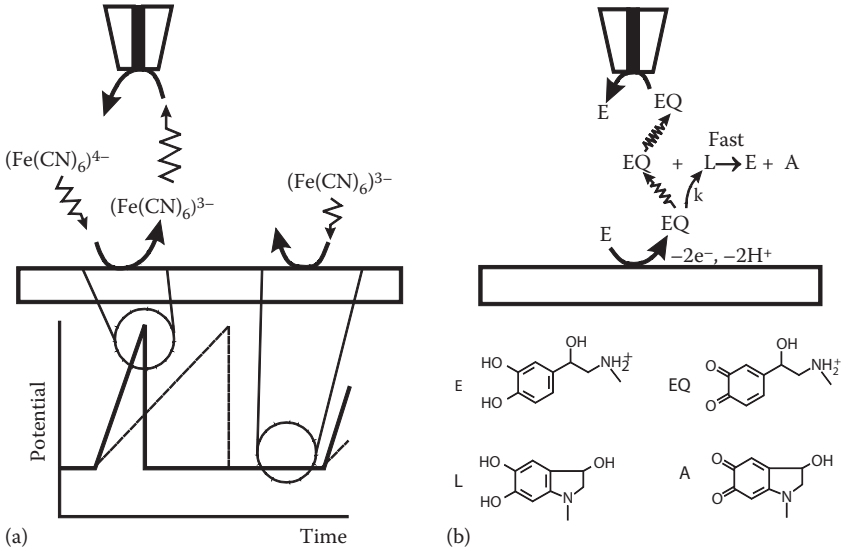


FIGURE 11.17 Image improvement in generation–collection mode imaging as introduced by Engstrom et al. [116] (schematics prepared by the chapter authors).

microelectrode tip can sense the source of $[Fe(CN)_6]^{3-}$ shrinks leading to improved lateral resolution (Figure 11.17a).

However, Engstrom et al. [116] did not find this approach very fruitful because kinetic limitations of the quasi-reversible redox system cause the interfacial concentrations to deviate considerably from Nernstian behavior at high scan rates. However, it is worthwhile to evaluate some possible adaptations of the concept to biological systems. For instance, a discontinuous generation of a redox-active species may be caused by chopped illumination. Light may be the energy source for light-dependent enzymes, enzyme complexes, cells, or organs. Alternatively, light may induce the formation of unstable compounds in solution which are substrates of fast enzymatic reactions. Such reactions are important as natural deactivation pathways for highly toxic radicals like the superoxide anion $O_2^{\cdot-}$, or those formed as result of environmental stress (ozone or UV exposure). The time between light irradiation and the ejection of the product to be detected at the tip may be quite long because of diffusion barriers (membranes) or complicated multienzyme reaction cascades. Tsionsky et al. [73] monitored the oxygen release of single guard cells of an intact plant and found that the time between switching on illumination and reaching a constant oxygen reduction current to be of the order of 6 min. Since a complete on/off cycle of the enzyme activity needs to be performed at each microelectrode tip position, practical constraints for imaging are anticipated for a significant number of biological systems. Periodic addition of the enzyme substrate could also be envisaged in a stopped-flow setup. It remains to be demonstrated that such an arrangement would allow fast and complete solution exchange under the geometric constraints of an SECM cell.

Many enzymes exhibit a pH optimum of their activity. Working in a solution outside that optimum, an electrolysis of solution components involving H^+ or OH^- at the microelectrode can induce a local pH shift toward the pH optimum of the enzyme activity, thereby "switching on" enzyme activity locally. The product of the enzymatic reaction may be collected at the microelectrode tip after applying the detection potential to it. This event would mark the end of the electrolysis causing the local pH shift. The locally changed pH will dissipate rapidly and "switch off" the enzyme activity. This principle has been demonstrated with fluorescence spectroscopic observation of the enzyme activity [100] and may soon find other applications as microelectrode-induced localized pH shifts have also been utilized in SECM microfabrication techniques (see Chapter 15). It remains to be found whether interesting enzyme systems exist which can be manipulated by rather small pH

changes. The trade off for all these discontinuous variations of reaction conditions at the specimen would be increased imaging times.

Engstrom et al. [116] demonstrated the use of a chemically irreversible redox reaction at the specimen as a way to improve resolution in the GC mode (Figure 11.17b). Epinephrine E was oxidized to its quinone EQ at the specimen electrode. EQ is unstable and decomposes to produce adrenochrome A via an intermediate leukoadrenochrome L. EQ is reduced at the tip at potentials negative of +200 mV (SCE) whereas both A and EQ are reduced at potentials negative of −100 mV (SCE). Poising the microelectrode at +100 mV (SCE) allows the detection of EQ molecules that have not yet decomposed to A, decreasing the distance at which the microelectrode tip can sense the source of EQ. The transformation rate EQ → A is pH-dependent providing a tuning mechanism for the lifetime of EQ. Engstrom et al. [116] used a potential sweep for these experiments as they were primarily interested in local concentrations. Using a potential sweep limits the extent of the diffusion layer above the specimen electrode and allows reestablishment of the bulk concentration of oxidizable compounds before initiating a new potential cycle at the next tip position. This scheme is associated with increased imaging time (vide supra). Indeed, when adapting this idea to biological systems, one usually works under conditions of substrate saturation where the enzyme kinetics rather than the mass transport limits the conversion rate at the specimen, thus avoiding the need to reestablish the substrate bulk concentration close to the specimen surface. If the product to be detected at the tip undergoes a homogeneous reaction to a redox-inactive product, an image can be recorded in the usual way, that is, without changing periodically the conditions in the cell at each tip position. On the other hand, tuning the decomposition rates by varying the solution pH may not always be feasible because of the limited pH ranges in which many enzymes are stable and active. The applicability of this mode still depends on finding an enzyme substrate that may be converted to a redox-active product that undergoes a following chemical reaction to a redox-inactive compound within the timescale of the diffusion across the specimen–tip gap. These prerequisites greatly limit the range of biological applications for this imaging scheme.

Instead of creating an unstable redox-active product in the enzymatic reaction, one may use a second enzymatic reaction to decrease the lifetime of the substances generated at the specimen. This approach has already been demonstrated [27] for GOx immobilized on a specimen and catalase dissolved in solution (Figure 11.18a). Under conditions of high glucose concentration, H_2O_2 is continuously formed at the sample. It leads to increasing background currents during image acquisition as discussed in Section 11.2.3.3 and evident from Figure 11.18b and e(1). Adding minute amounts of catalase to the solution phase eliminates the rising background and increases the lateral resolution because the diffusion length of H_2O_2 is limited (Figure 11.18c and e(2)). The peak-to-baseline signal height is still 85% of that in the absence of catalase. One should note that the FWHM is an easily measurable quantity which can be used to follow trends in resolution for similar images of the *same* object. To obtain optimum conditions for imaging, the catalase concentration must be adjusted to make the lifetime of H_2O_2 sufficiently long to diffuse across the specimen–tip gap, but too short to accumulate in the solution phase. The reaction rate does not follow a first-order rate law in this concentration range and adjustment needs to be done empirically. Increasing the catalase concentration leads to a further small improvement of resolution and a considerable decrease of signal (Figure 11.18d and e(3)). A further addition of catalase of up to 0.15 µL suspension per milliliter of working solution quenches the signal for H_2O_2 production [27] (not shown). This is a valuable observation because the high specificity of enzymes shows that the species detected at the microelectrode tip is in fact H_2O_2 and not another redox-active byproduct or solution impurity. Such methods of image verification will gain importance if more complicated biological samples are investigated and the mixture of redox-active compounds released from the specimen is less well understood than in the model system investigated in Figure 11.18. The use of an enzyme microelectrode as the tip electrode, as discussed in Section 11.1.3.3, would be another way to accomplish this task.

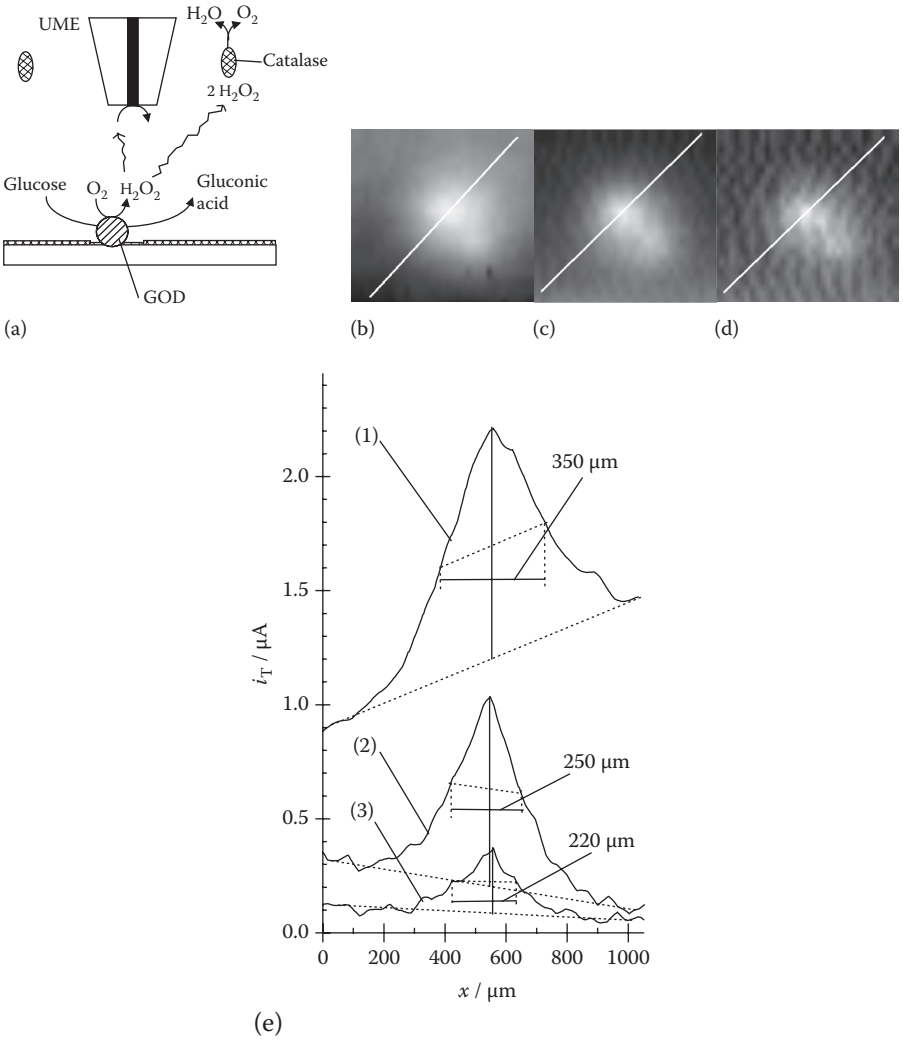


FIGURE 11.18 Improvement of image resolution in the generation–collection mode by providing a catalyst for the solution phase follow-up reaction of the species to be detected at the tip electrode. (a) Schematic; (b)–(d) gray-shaded current images with location of cuts after addition of catalase in microliter suspension (20 mg/mL protein) per milliliter working solution, (b) none, (c) 0.005, (d) 0.03, (e) current profiles (1) for (b), (2) for (c), and (3) for (c). The FWHM is given for each curve; working solution, air-saturated 50 mM glucose + 0.1 M phosphate buffer (pH 7.4); sample was prepared by local desorption of a SAM and subsequent modification with GOx. (Parts (b)–(e): Reprinted with permission from Wittstock, G. and Schuhmann, W., Formation and imaging of microscopic enzymatically active spots on an alkanethiolate-covered gold electrode by scanning electrochemical microscopy, *Anal. Chem*., 69, 5059–5066, 1997. Copyright 1997 American Chemical Society.)

11.2.3.7 Oxygen Reduction in Biotechnology

Recently, SECM has become an important tool in screening catalysts for the oxygen reduction reaction (ORR) in fuel cells, sensors, and oxygen demand electrodes (Chapter 16). Ideally, the product of the irreversible four-electron reduction of dioxygen is water—the solvent in most investigations. Therefore, the study of this technologically important reaction requires new approaches in SECM as SG/TC mode and feedback mode imaging are often not applicable. Besides noble metal and transition metal complexes, some multi-copper enzymes such as laccase (EC 1.10.3.2) and bilirubin oxidase (BOD, EC 1.3.3.5) are able to oxidize numerous organic compounds and to reduce dioxygen

to water without the formation of reactive intermediates. Apart from fundamental interest in ORR, interest in these enzymes arises from possible applications for oxidation of organic compounds and their uses in sensors and the cathodes of enzymatic biofuel cells.

Bard and coworkers used the TG/SC mode (Figure 11.19a) for the analysis of laccase and BOD wired to an Os-containing redox polymer. Micrometer-sized spots of varying compositions were deposited onto glassy carbon plates in order to optimize the composition (Figure 11.20) [25]. In this mode, O_2 is electrogenerated with constant electrolysis current at the UME by water electrolysis. O_2 is reduced at the sample. The sample current i_S is plotted vs. the lateral UME position (x, y) to obtain images of ORR activity on the surface. The experiments are complicated because large sample areas may generate high background currents that make it hard to distinguish small variation of ORR efficiency of catalysts immobilized on the conductive support. Special strategies may be required to overcome this problem [117].

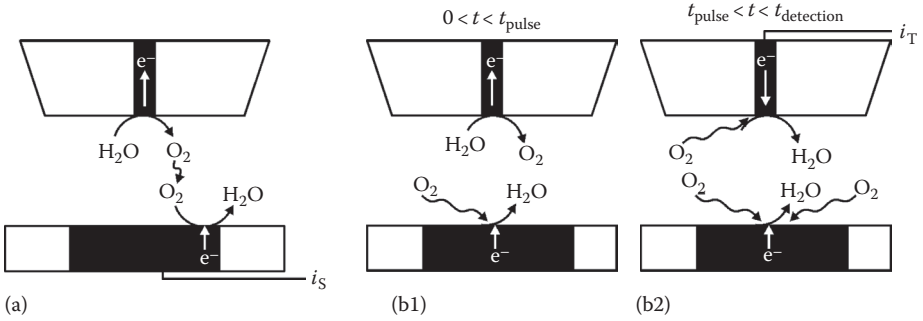


FIGURE 11.19 (a) TG/SC mode experiments for investigation of ORR reaction and (b) pulsed RC mode investigation; (b1) O_2 generation at the UME and (b2) competition for O_2 in the interelectrode space between UME tip and sample.

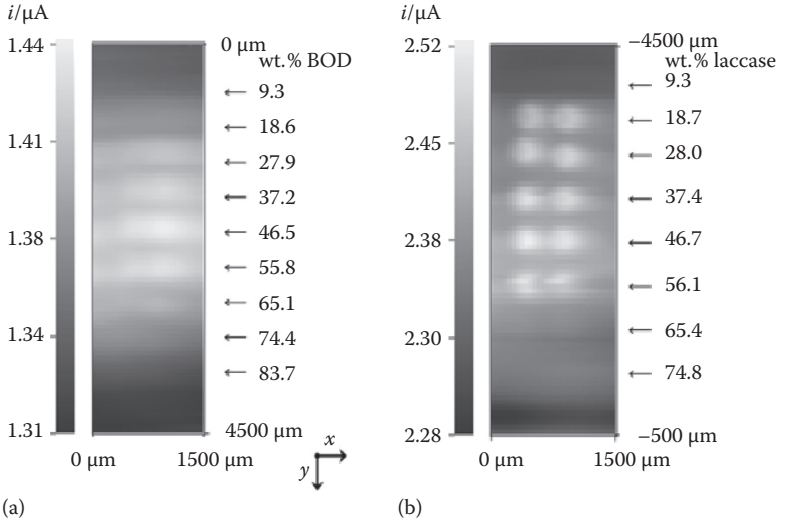


FIGURE 11.20 SECM images of "wired" enzyme arrays containing spots with different polymer/enzyme ratios. (a) BOD (6.9 wt% cross-linker) in pH 7.2 phosphate buffer, $i_T = -161$ nA, $E_S = 0.3$ V versus Ag/AgCl; (b) laccase (6.5 wt% cross-linker) in pH 5.0 citrate buffer, $i_T = -240$ nA, $E_S = 0.4$ V versus Ag/AgCl. (From Fernandez, J.L., Mano, N., Heller, A., and Bard, A. J.: Analytical methods: Optimization of "wired" enzyme O_2-electroreduction catalyst compositions by scanning electrochemical microscopy. *Angew. Chem. Int. Ed.* 2004. 43. 6355–6357. Copyright Wiley-VCH Verlag GmbH & Co. KGaA. Reproduced with permission.)

The problem of high background signals is circumvented in the redox competition (RC) mode introduced by Schuhmann and coworkers [118]. In this case, the potential of the UME is pulsed. In an initial pulse, O_2 is generated at the UME (Figure 11.19b1). In a second pulse, the UME and the catalytically active sample surface compete for the electrogenerated O_2 (Figure 11.19b2). The smaller the UME current in this situation, the more efficient is the ORR catalyst at the sample surface. Among other samples, the RC mode has also been applied to image spots of wired BOD in biofuel cell cathodes [119].

Compared to noble metal ORR catalysts, BOD and laccase show a few special features. They can use a second substrate, that is, the organic compound to be oxidized. The organic compound to be oxidized can be selected as a quasi-reversible redox couple, for example, 2,2′-azino-bis(3-ethylbenzothiazoline-6-sulfonate) ($ABTS^{2-}$) that acts as a one electron donor for the laccase- or BOD-catalyzed reactions and is regenerated electrochemically [120] and thus can be used as mediator in biosensor applications or for SECM imaging:

$$O_2 + 4\,H^+ + 4\,ABTS^{2-} \rightarrow 2\,H_2O + 4\,ABTS^{\bullet -} \tag{11.10}$$

Since $ABTS^{\cdot -}$ or $ABTS^{2-}$ are easily detected amperometrically at Pt UME tips, further working modes can be devised [40]. In an aerated solution containing $ABTS^{2-}$, laccase catalyzes the production of $ABTS^{\cdot -}$ that can be detected in the SG/TC mode at $E_T = -0.1$ V (Figure 11.21b). If the Pt UME tip is set to $E_T = +0.4$ V to oxidize $ABTS^{2-}$, sample and tip compete for $ABTS^{2-}$ (Figure 11.21d). In contrast to Figure 11.19b1 and b2, the electrode potential is kept constant. One may call this experiment continuous RC mode. It can be expected that this mode will be less able to differentiate between active catalysts as the interelectrode space is rapidly depleted of oxygen. In Figure 11.21, the SG/TC and the continuous RC modes were used to investigate segregation phenomena occurring if laccase is embedded in sol-gel processed silicate films. Aggregates are clearly visible in a confocal laser scanning microscopic image (Figure 11.21a). With the help of an optical microscope, the tip could be positioned close to such aggregates and a SG/TC image (Figure 11.21c) showed that the aggregates have a higher ORR activity than the surrounding matrix. The continuous RC mode was used to verify that the features do not result from topographic artifacts (Figure 11.21d). Quantitative analysis of the flux from individual aggregates by SECM measurements combined with size determination by optical microscopy showed that the aggregates had a 38 times higher ORR activity than the average flux of the same silicate–laccase material deposited on conducting glass and using $ABTS^{2-}$ dissolved in solution [40].

Even feedback imaging of BOD and laccase is possible with $[Fe(CN)_6]^{3-}$ as mediator and Au tips (Pt tips are not useful because the ORR would occur at the tip) [24]. The sample should preferably be an insulator to exclude interfering electron transfer reactions between the mediator and the substrate that do not involve the enzymes. This working mode has advantages with respect to lateral resolution and possibilities for quantitation. It has been used for the analysis of spot homogeneity and a comparison of the pH dependence of laccase and BOD (Figure 11.22) [24].

An important difference between the working modes in Figures 11.19 and 11.21 should be emphasized here. The TG/SC and pulsed RC modes require the enzyme to communicate electronically with the substrate. Those modes are thus suitable to probe direct electron transfer to enzymes. Enzymes that are immobilized and active but not in direct electronic communication with the substrate electrodes will not contribute to the signal. The SG/TC, continuous RC, and feedback modes of these enzymes do not require an electrical communication with the substrate electrode. Heterogeneous reactions of the mediators at the conducting substrate can even lead to artifacts as discussed before. These working modes can be performed if the enzyme is deposited onto insulating substrates (e.g., supports for enzyme columns). In sensor research, both modes may be combined to provide complementary information. SG/TC, continuous RC, and feedback mode will show the distribution of immobilized active enzymes; the TG/SC and pulsed RC mode will only show that subpopulation that is in electronic contact with the sample. In any case, it is highly recommended

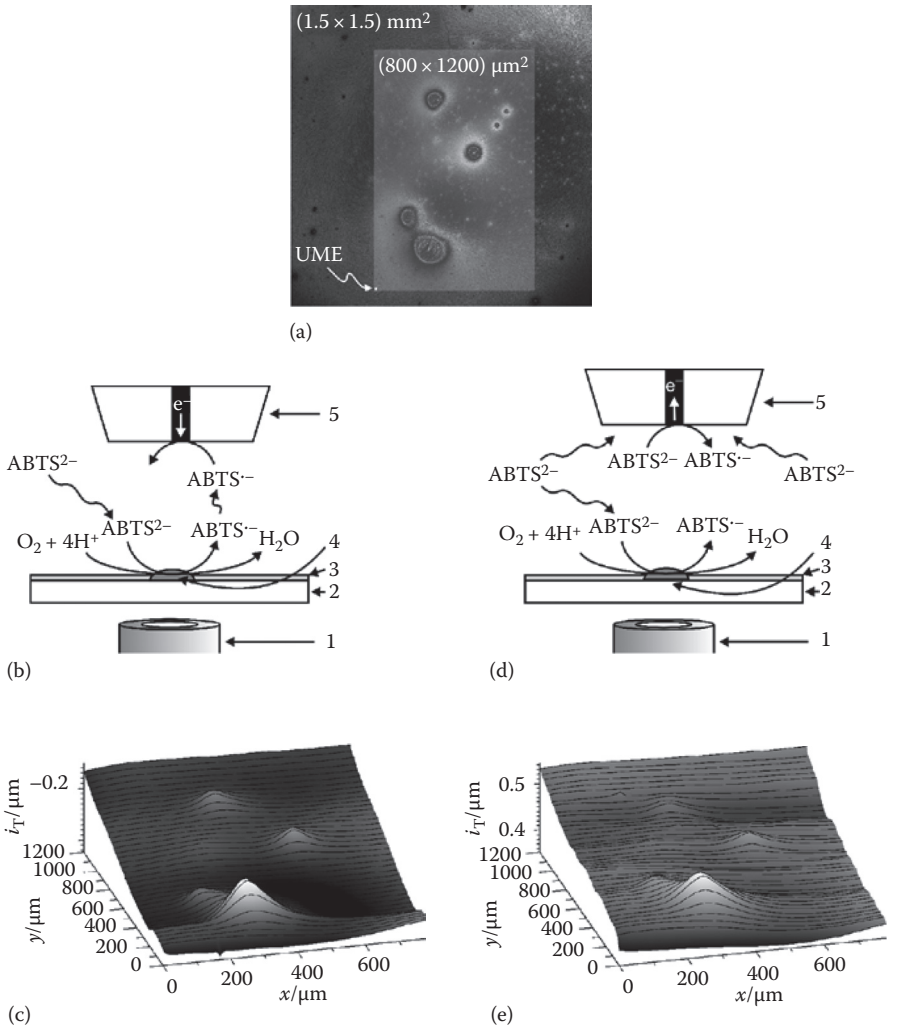


FIGURE 11.21 Combined SECM/confocal laser scanning microscopic mapping of laccase aggregates. (a) Reflection mode CLSM image; (b) schematic of SG/TC mode SECM imaging of laccase activity: (1) microscope objective, (2) glass slide, (3) laccase–silicate film, (4) laccase aggregate, and (5) UME; (c) SG/TC mode SECM image; $E_T = -0.1$ V, $a = 5$ µm, 1 mM $ABTS^{2-} + 0.1$ M phosphate buffer (pH 4.8), $v_t = 7.7$ µm/s; (d) schematic of RC mode SECM imaging of laccase activity; and (e) continuous RC mode SECM image, $E_T = +0.4$ V, other conditions as in (c). Current scales in (c) and (e) are inverted to show high activity as "hills." (Reprinted from *Bioelectrochemistry*, 72, Nogala, W., Burchardt, M., Opallo, M., Rogalski, J., Wittstock, G., Scanning electrochemical microscopy study of laccase within a sol-gel processed silicate film, 174–182, Copyright 2008, with permission from Elsevier.)

to conduct carefully designed control experiments. These may consist of measurements of identical areas in the presence and absence of dissolved O_2, in measurements with an applied sample potential or at OCP (in case of pulsed RC mode), use of specific inhibitors, etc.

SECM has been used as a main tool to optimize laccase and BOD silicate materials for biocathode application. Adsorption of laccase on hydrophilic carbon nanoparticles or carbon nanotubes improved the dispersion and allowed direct communication with the substrate electrode [121]. The mediators can also be co-embedded into the silicate matrix. For such electrodes, mediator leaching is a common problem, but appropriate choice of the embedded mediator ameliorates this problem and produces electrodes that are suitable for reagentless O_2 reduction [122]. Electrodes that are

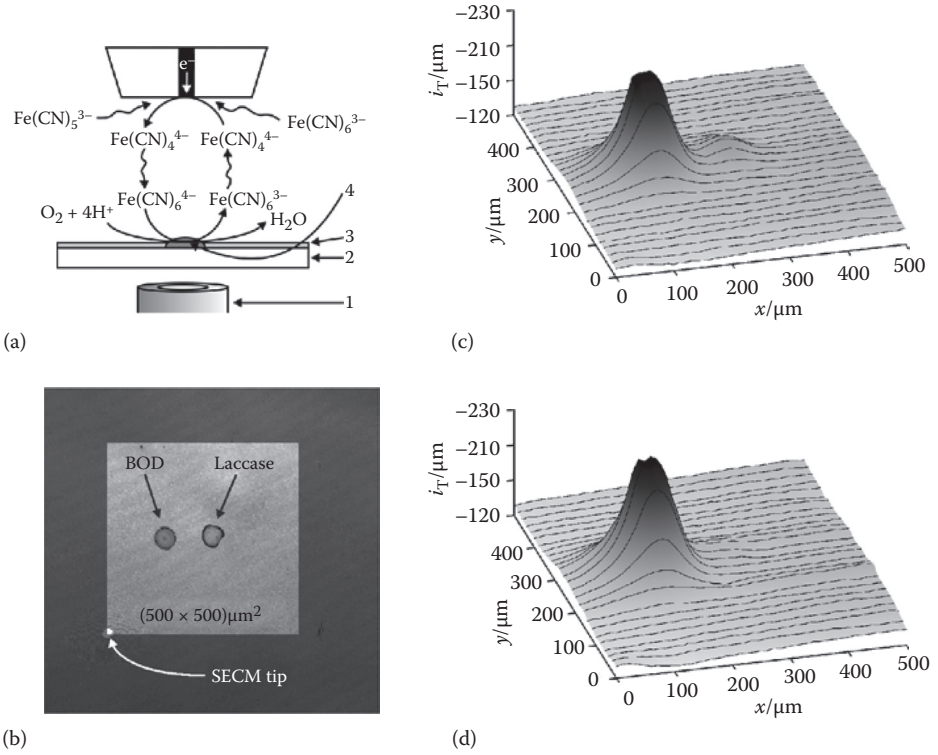


FIGURE 11.22 Combined SECM/CLSM mapping of BOD and laccase immobilized in silicate spots on Plexiglas. (a) Schematic setup of the feedback mode SECM experiments combined with CLSM: (1) CLSM objective, (2) insulating and transparent support, (3) enzyme–silicate film, and (4) enzyme aggregate. (b) Reflection mode CLSM image; (c) SECM feedback image in aerated 0.1 mM $K_3[Fe(CN)_6]$ in 0.1 M phosphate buffer pH 4.8; and (d) SECM feedback image in aerated 0.1 mM $K_3[Fe(CN)_6]$ in 0.1 M phosphate buffer pH 7.0. Other experimental conditions for (c) and (d): $E_T = 0.0$ V, $r_T = 12.5$ μm, RG ≈ 10, $v_T = 10$ μm/s, $d \approx 15$ μm. (From Nogala, W., Szot, K., Burchardt, M., Roelfs, F., Rogalski, J., Opallo, M., Wittstock, G., Feedback mode SECM study of laccase and bilirubin oxidase immobilised in a sol-gel processed silicate film, *Analyst*, 135, 2051–2058, 2010. Reproduced by permission of The Royal Society of Chemistry.)

mixtures of a sol-gel-processed silicate matrix, carbon microparticles for electronic conductivity, and hydrophilic carbon nanoparticles for direct electron transfer to BOD could reduce O_2 without any mediator in solution or in the electrode material as shown by pulsed RC mode [123]. In an air-breathing biocathode, electronic conduction pathways were visualized in the feedback mode with $[Fe(CN)_6]^{3-}$ as mediator. The O_2 diffusion occurred at different locations, that is, through the hydrophobic silicate network and was visualized by detection of O_2 at the tip in the SG/TC mode [124].

Oxygen consumption and oxygen production has also been detected locally for cellular systems as an indicator of viability, to check for the action of cytostatic and toxic chemicals (for diagnostic chips, see Section 11.2.4.8; for single cell experiments, see Chapter 12). Particular attention must be paid to the distinction between larger oxygen consumption and the shielding of mass transport by the protruding cells. Consumption rates are often lower than on catalytic surfaces and the continuous RC mode is often applicable.

11.2.4 SECM Readout of Biochips

Fluorescence-based DNA array technology is now so highly developed that it has enabled rapid sequencing of individual genomes [125]; however, there remains interest in other readout techniques

for gene sensing and protein detection. Electrochemical DNA arrays and sensors are attractive because miniaturization of electronic devices is straightforward and because the performance of electroanalytical methods often improves as the electrodes are scaled down toward the micrometer size regime. Unlike fluorescence microscopy, it does not depend on the optical properties of the specimen surface (transparent or reflective) nor are there any disturbing effects of light absorption by solution components or signal losses at the solution–air interface. In addition, the imaging mechanism can often be modeled numerically and used to extract quantitative kinetic information (see Section 11.2.2.2).

Electrochemical DNA arrays are unlikely ever to compete with existing fluorescence (or mass spectrometric) technologies directly, because those techniques allow fast readout of the arrays and high throughput. Nevertheless, fluorescence microscopes and mass spectrometers are best suited to applications that are carried out in a central laboratory and electrochemical devices (e.g., [126,127]) are potentially more useful for point-of-care diagnostics or as part of portable sensors for detection of bacteria in air, water, or food.

Imaging the activity of antibodies, a large variety of different receptor molecules, DNA, and DNA-binding proteins that are capable of selective interaction with other chemical species is challenging because only a single or a few binding events occur at a given binding site and there is no continuous transformation of a reagent. So far, SECM applications have been considered where enzymes immobilized at a surface catalyze redox reactions of low-molecular-weight compounds. The reaction products are detected at the ultramicroelectrode tip under diffusion-controlled conditions. This approach requires that the biochemically active layer continuously generates or consumes redox-active (for amperometric detection) or charged (for potentiometric detection) species. In the case of biochips, there is no continuous flux of species above the chip. In the absence of a chemical flux, the electrode–electrolyte interface of the microelectrode separated from the specimen surface by a solution layer of finite thickness will be incapable of sensing the modified *state* of the surface. This limitation of SECM can be overcome by a number of labeling techniques; a general approach well-established in the life sciences.

The low throughput, currently the major drawback of all scanning probe techniques, may be increased when SECM detection principles are used with multiple probes [189] or combined with integrated microanalytical devices [128].

11.2.4.1 Using Enzyme Labels

Immobilized antibody (Ab) layers were first imaged using the SECM GC mode by Wittstock et al. [36]. This study provided a new tool for optimization of immobilization protocols in immunoassay development. The approach was demonstrated for an immunoassay of digoxin which is the antigen (Ag) (Figure 11.23). A periodate-oxidized (anti-digoxin) Ab was immobilized covalently at spots onto an amino-functionalized glass surface. During incubation of the layer with an excess of digoxin that was labeled with the enzyme ALP (Ag-E), all accessible and active binding sites formed an Ab–Ag-E complex. The density of the active sites could be imaged by measuring the generation of *p*-aminophenolate (PAP) from *p*-aminophenyl phosphate (PAPP) catalyzed by ALP. The detection was performed amperometrically in the GC mode at a potential where PAP exhibits redox activity but PAPP does not. GC mode is the only option for the enzyme ALP because it is not a redox enzyme. Through applying Ab solutions of different concentration to distinct surface regions, a convenient comparison was possible.

Since nonspecific adsorption is regarded as a major source of systematic error in heterogeneous immunoassays, the adsorptive immobilization of different Ab solutions was studied on clean, nonaminated glass surfaces [36].

11.2.4.2 Small Spot Immunoassays

In a series of papers, Shiku et al. [22,35,129] developed a strategy for small spot heterogeneous enzyme immunoassays using an SECM to read out the signal, thus allowing microscopic sensing regions for the analysis of multiple antigens to be placed in close proximity on one chip. The close

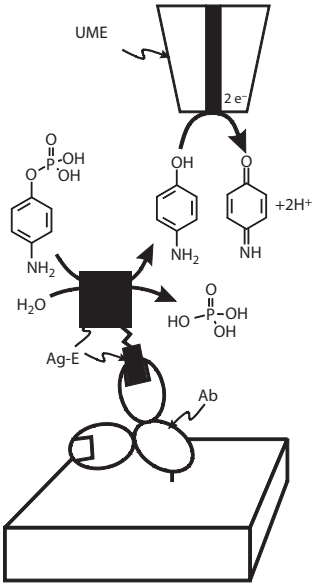


FIGURE 11.23 Schematic of the detection of localized Ab layers via an alkaline phosphatase–labeled Ag and amperometric detection of 4-aminophenol (PAP) at the tip electrode. UME, ultramicroelectrode tip.

proximity of the amperometric tip and the antibody-modified area allows readings to be made without any incubation time to accumulate products of the enzymatic reactions. This feature represents an advantage over conventional ELISA, which usually requires an incubation step prior to detection. The assays were carried out in the sandwich format (Figure 11.24). An antibody Ab against the analyte is immobilized onto glass. After application of the antigen Ag (i.e., the analyte) onto the surface, it is allowed to form an Ab:Ag complex. Subsequently, the surface is exposed to a solution of a second Ab labeled with the enzyme HRP. Microspots are obtained either by micropipetting the Ag [22] or the Ab [35] onto the surface. The continuous reaction used in the SECM detection is the same in each case:

$$2\ FcCH_2OH + H_2O_2 + 2\ H^+ \xrightarrow{[HRP]} 2\ FcCH_2OH^+ + 2\ H_2O \tag{11.11}$$

where

$FcCH_2OH$ is hydroxymethyl ferrocene

$FcCH_2OH^+$ is the corresponding ferrocenium derivative

Detection can conveniently be made in the GC mode. In this case, the working solution contains $FcCH_2OH$. The current at the microelectrode tip results from the reduction of $FcCH_2OH^+$ formed in the HRP-catalyzed reaction at the specimen (Figure 11.24a). One may also work in a solution containing $FcCH_2OH^+$ in the bulk phase using the feedback mode. In this mode, $FcCH_2OH^+$ is also reduced at the microelectrode tip that provides $FcCH_2OH$ for the enzymatic reaction to occur and maintains the feedback (Figure 11.24b). The comparison of both detection schemes [22] supports some general recommendations made in Section 11.1. The GC mode tends to achieve higher sensitivities because the background currents are lower and the current variations within an image frame are larger. On the other hand, the feedback image provides better lateral resolution of fine variations in enzyme activity.

Immunoassays have also been developed for carcinoembryonic antigen (CEA) [22], human chorionic gonadotropin (HCG) [35], and human placental lactogen (HPL) [35]. CEA is a tumor

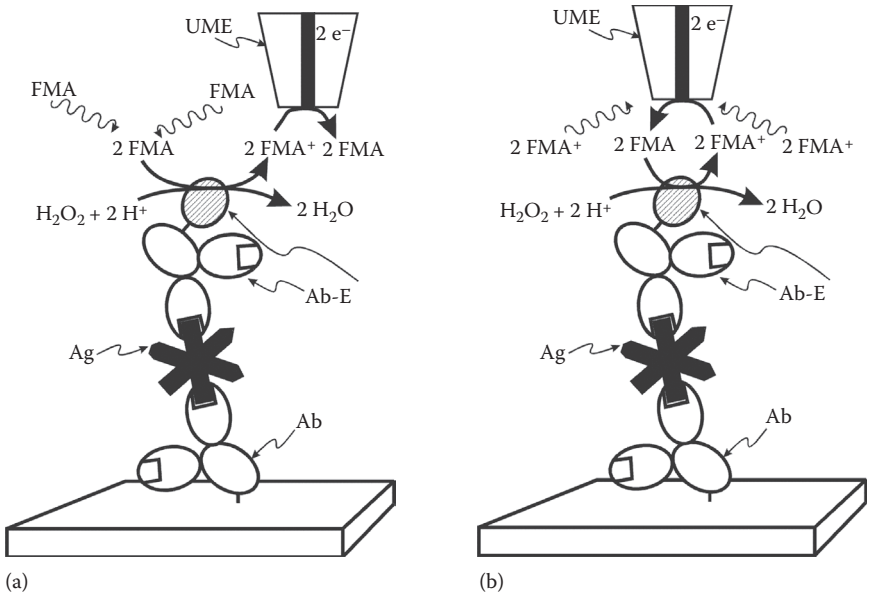


FIGURE 11.24 Schematic representation of the detection scheme in the small spot immunoassays used by Shiku et al. [22] (schematic prepared by the chapter authors). (a) Generation–collection mode and (b) feedback mode. UME, ultramicroelectrode tip; $FcCH_2OH/FcCH_2OH^+$, ferrocene/ferrocenium forms of hydroxymethyl ferrocene; Ab-E, antibody labeled with horseradish peroxidase; wavy lines indicate diffusion; solid lines are reactions.

marker with a molecular weight (MW) of 180,000–200,000; HCG (MW = 38,000) and HPL (MW = 22,000) are peptide hormones that are pregnancy indicators. Yasukawa et al. [130] reported a sandwich immunoassay for pepsinogens (PG) 1 and 2, which are important in the diagnosis of atrophic gastritis and gastric cancer. (Anti-PG1)-Ab and (anti-PG2)-Ab were spotted on glass or poly(dimethylsiloxane) substrates at distinct locations. After capturing the respective antigens, the substrates were exposed to HRP-labeled antibodies forming the sandwich structure. The tip was positioned by recording the hindered diffusion of ferrocene methanol $FcCH_2OH$ oxidation at $E_T = 0.5$ V. All assays were performed in the GC mode using a HRP enzyme label after addition of 0.5 mM H_2O_2 to the working solution and switching the working potential of the tip microelectrode to 0.05 V. At this value, $FcCH_2OH^+$ formed by HRP can be reduced. Thus, the activity and location of the enzyme label HRP bound in the Ab:Ag:Ab–HRP complex could be detected (Figure 11.25). If the analyte solution contained PG1 or PG2, HRP activity was found only above the active region with the corresponding antibody. When both analytes were present, corresponding levels of activity could be detected over both sensing areas. The assays benefit from structuring the substrates for easy relocation of the spots [35] or using more advanced microfabricated cavities on the substrate to obtain sharper images [130].

11.2.4.3 Assays Using Magnetic Microbeads

Wijayawardhana et al. [18] used commercial paramagnetic surface-modified beads (2.8 and 1 μm mean diameter) to assemble biochemically active microspots. The use of the magnetic beads unites the advantages of homogeneous and heterogeneous assays. The bead suspension can be mixed with reagents and dosed as simply as a liquid. Separation of the sensing surface, that is, the bead surface, from excess reagent, rinsing solution, and sample matrix can be made using a magnet to retain the beads against the test tube wall when pouring off the supernatant liquid. The microspots were created from a 1 μL drop extruded from a micropipette mounted to the SECM positioning system. A magnet was placed beneath the receiving, hydrophobic surface. As the pipette is brought

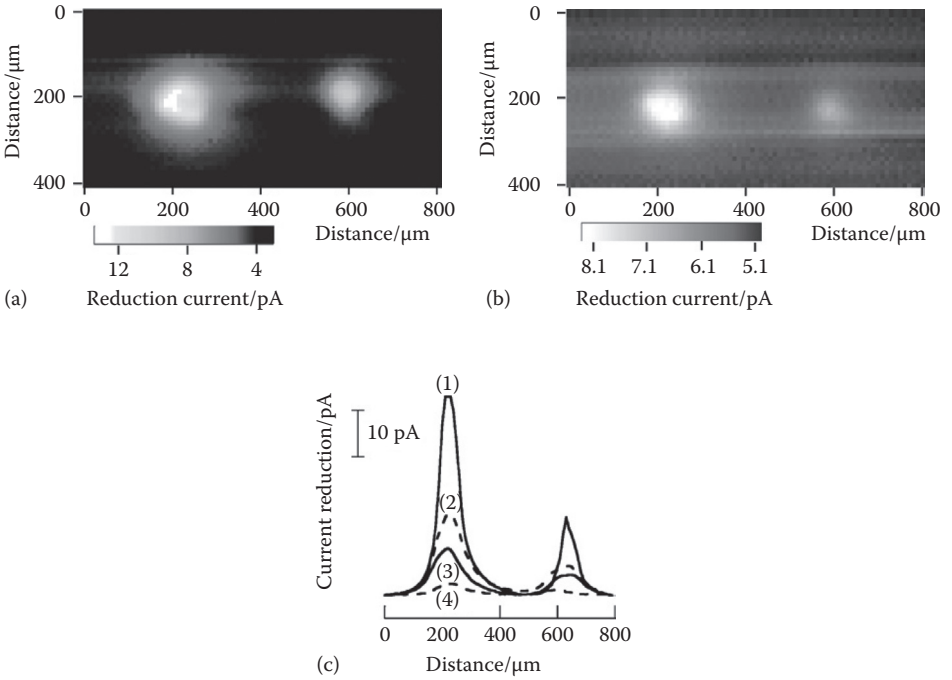


FIGURE 11.25 Dual SECM images for PG1 (left spot) and PG2 (right spot). The PG1:PG2 concentration ratio in the sample solution was 2:1: (a) 20.1 ng/mL PG1 and 10.0 ng/mL PG2 and (b) 6.4 ng/mL PG1 and 3.2 ng/mL PG2. (c) Cross-sectional planes of SECM images across spots exhibiting maximum reduction currents for $FcCH_2OH$ at different concentrations of PG1 and PG2: (1) 60.3 ng/mL PG1 and 30.2 ng/mL PG2, (2) 40.2 ng/mL PG1 and 20.1 ng/mL PG2, (3) 20.1 ng/mL PG1 and 10.0 ng/mL PG2, and (4) 6.4 ng/mL PG1 and 3.2 ng/mL PG2. Working solution, 1.0 mM $FcCH_2OH$ + 0.5 mM H_2O_2 + 0.1 M KCl + 0.1 M phosphate buffer, pH 7.0. The tip was scanned at 48.8 μm/s. $E_T = 0.05$ V (Ag/AgCl), $v_t = 24$ μm/s. (Reprinted from *Biosens. Bioelectron*., 22, Yasukawa, T., Hirano, Y., Motochi, N., Shiku, H., Matsue, T., Enzyme immunosesning of pepsinogens 1 and 2 by scanning electrochemcial microscopy, 3099–3104, Copyright 2007, with permission from Elsevier.)

slowly toward the support surface, the beads collect at the bottom of the drop under the influence of the magnet. After contact of the drop with the surface, the micropipette—with the drop still attached—was retracted leaving the beads behind. The beads assemble in mounds whose size is determined by the number of beads but not by the area wetted by the drop.

If antibodies or other functionalities (e.g., streptavidin) have been immobilized on the beads, the microspots represent a platform on which assays can be performed, for example, an immunoassay has been demonstrated [131]. Furthermore, the bead spots have turned out to be a convenient platform to optimize imaging conditions [19,37] and explore new detection principles [132]. The possibility to prepare a suspension combining differently modified beads offers the possibility to introduce different functionalities in a single spot. This has been used for enhancing the GC detection of galactosidase by enzymatic and enzyme-mediated feedback (Figure 11.26). Galactosidase generated PAP that was detected at the microelectrode tip in the GC mode. The product of the tip reaction is *p*-quinoneimine (PQI). The spot contains a second enzyme, PQQ-dependent glucose dehydrogenase (GDH). In the presence of a high glucose concentration, glucose GDH can oxidize glucose, provided that an artificial electron acceptor is available. O_2 is not a good acceptor for this enzyme, but PQI is. If the microelectrode tip generates PQI, it can be used as cofactor for GDH. During the GDH-catalyzed reaction, PAP is formed from PQI and diffuses back to the tip.

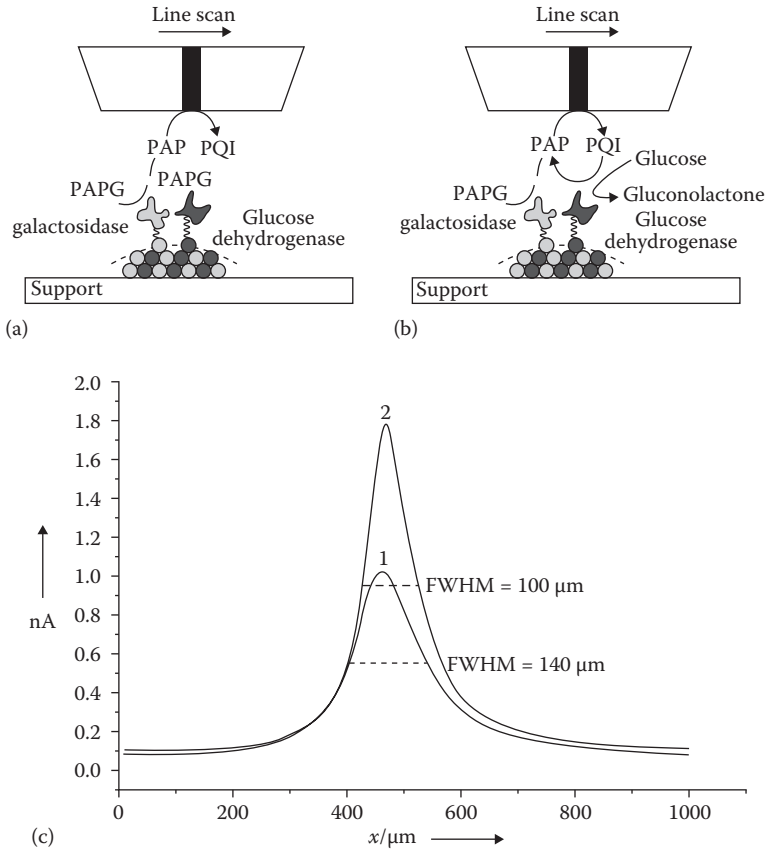


FIGURE 11.26 (a) Schematic of conventional GC mode of Gal in the absence of glucose; (b) schematic of the signal amplification in the presence of glucose. PAPG, *p*-aminophenyl-β-D-galactopyranoside; PAP, *p*-aminophenol; PQI, *p*-quinone imine. (c) SECM line scans across the center of the microspot; (curve 1) conventional GC mode; (curve 2) combined mode. Curve 2 was obtained in the assay solution without glucose and curve 2 was obtained after adding 50 mM glucose to the solution. The schematics are not to scale. (Reprinted with permission from Zhao, C. and Wittstock, G.: An SECM detection scheme with improved sensitivity and lateral resolution: Detection of galactosidase activity with signal amplification by glucose dehydrogenase. *Angew. Chem. Int. Ed.* 2004. 43. 4170–4172. Copyright Wiley-VCH Verlag GmbH & Co. KGaA. Reproduced with permission.)

The enzymatic PQI regeneration can also be replaced by electrochemical regeneration of PAP to enhance the sensitivity of the GC mode for galactosidase and ALP labels [14,128,133].

The system was also used to explore by experiments and simulation how close spots can be placed if the detection is performed in the GC mode [134]. The simulations were performed by the boundary element method in three space coordinates using the external Laplace formulation [135] and simplified boundary conditions for the enzyme kinetics, two independently diffusing species (PAP and PQI), and consideration of shielding effects by the microelectrode tip. It became obvious that it can be very difficult to detect a small enzyme loading (corresponding to small analyte amount in a specific location of a biochip) if this is close to a spot with a very high amount of label (Figure 11.27). Spot sizes of 150 and 236 µm midpoint–midpoint distance allow efficient resolution and detection only if the ratio of labeling between two neighboring spots is between 0.5:1 and 2:1. This interval can be broadened by increasing the midpoint–midpoint distance at the expense of spot density. The same conclusion holds in general for DNA biochips with enzyme labels and GC

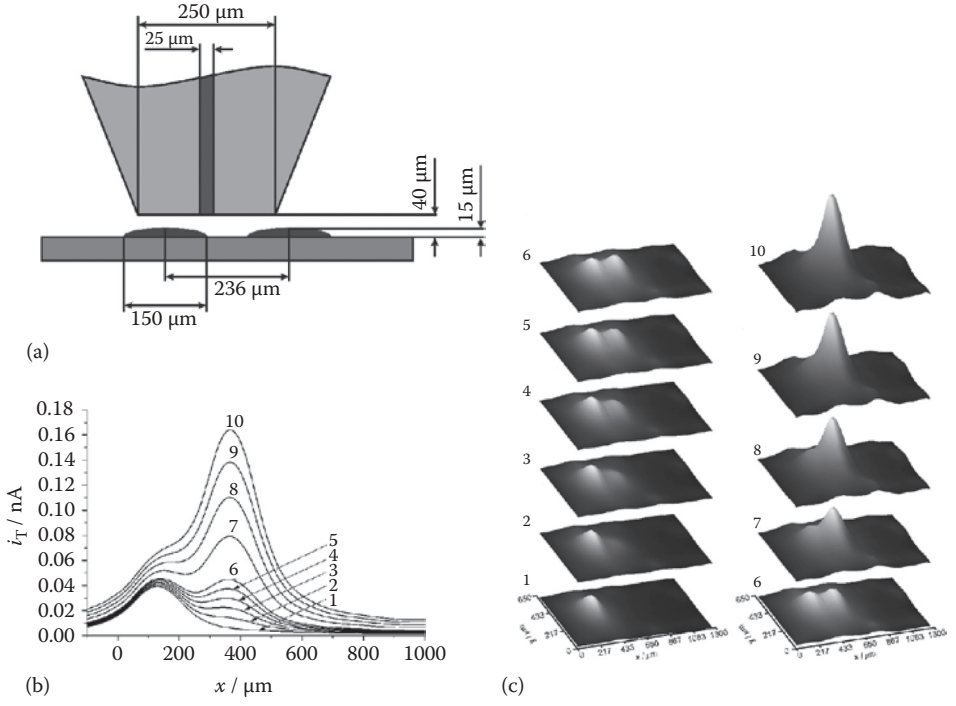


FIGURE 11.27 Simulation of images of two bead mounds of identical shape but with different enzyme loadings. (a) Geometric layout of the simulation. The value for K_M was 1.79×10^{-7} mol/cm^3. The left spot had $(k_{cat}\Gamma_{enz})_{left} = 4.49 \times 10^{-12}$ mol/cm^2/s throughout the series of simulation. The value of $(k_{cat}\Gamma_{enz})_{right}$ for the right spot was in multiples of $(k_{cat}\Gamma_{enz})_{left}$: (1) 0, (2) 0.2, (3) 0.4, (4) 0.6, (5) 0.8, (6) 1, (7) 2, (8) 3, (9) 4, (10) 5. (b) Line scans over the center of the bead spots. The numbers at each trace refer to the simulation setup described earlier. (c) 3D representation of the entire images for the setups (1)–(10). (Reprinted with permission from Sklyar, O., Träuble, M., Zhao, C., and Wittstock, G., Modeling steady-state experiments with a scanning electrochemical microscope involving several independent diffusing species using the boundary element method, *J. Phys. Chem. B*, 110, 15869–15877, 2006. Copyright 2006 American Chemical Society.)

detection as well as other situations with GC detection and individual sources of different fluxes (e.g., porous membranes).

One disadvantage of bead spots is that they are complicated in terms of mass transport because enzyme labels are not uniformly accessible for diffusion of substrates. These effects have been explored under a wide range of conditions by mixing a fixed amount of enzyme-modified beads with bare beads [85] and analyzing the external fluxes resulting above such bead spots. The experiments were performed with galactosidase-modified microbeads and simulations were carried out with the boundary element method implementing truly nonlinear boundary conditions for the description of the Michaelis–Menten kinetics of the enzyme label. It turned out that quantitation of the percentage of label saturation based on calibration can only yield meaningful results if the bead spots show a sufficient uniformity in shape as this greatly influences the internal mass transport.

11.2.4.4 DNA Arrays with Enzyme Labels

11.2.4.4.1 GC Detection of Enzyme Reaction Products

By incorporating an enzyme label, the DNA array can be read out using the techniques developed for electrochemical immunoassay (Section 11.2.4.2). This strategy has been studied in some detail and is therefore discussed separately from the range of other approaches that have been demonstrated.

Nunes Kirchner et al. [136] made a thorough quantitative study of the simplest enzyme-labeling procedure — labeling the target ODN. The direct mode of the SECM (tip acting as an auxiliary electrode to localize the cell current) was used to deposit pyrrole–ODN conjugates on a Au film as PPy spots. This technique has been quite widely employed for electrochemical deposition of ODNs for use in DNA sensing [137] because the extent of deposition is easy to control by coulometry. The radius of the spots formed was confirmed to be about equal to the tip RG by confocal microscopy, but with a ring-disk morphology (confirmed by AFM). The origin of this structure was suggested to be diffusion of monomer from the bulk into the tip/substrate gap. Reasonable agreement between film thickness measured by AFM and estimated by coulometry was shown. The DNA assay comprised a 10 min treatment with bovine serum albumin to reduce nonspecific adsorption, 20 min hybridization with biotinylated complementary ODN, 15 min incubation with streptavidin followed by 30 min exposure to biotin-labeled β-galactosidase as enzyme label. The principle of the assay, illustrated in Figure 11.28, is that the molecule *p*-aminophenyl-β-D-galactopyranoside (PAPG) is electroinactive at +0.35 V, but the enzyme label converts it to the electroactive PAP that is oxidized at the diffusion-controlled rate to the PQI at the tip. SECM line scans across the spot centers were obtained in generation–collection mode at heights in the range $\sim 1 < L < 6$. A detailed quantitative analysis of the SECM data showed that (i) the GC theory of equations (Section 11.2.2.2) is valid when feedback effects are negligible at $L > 3$; (ii) the optimum assay conditions are for saturated enzyme kinetics with respect to PAPG; (iii) by employing β-D-galactosidase-labeled microbeads as a calibration and under the assumption that the turnover number of the enzyme is the same on the DNA array, the SECM data enabled quantitation of the hybridization density in the range $1–2 \times 10^{-13}$

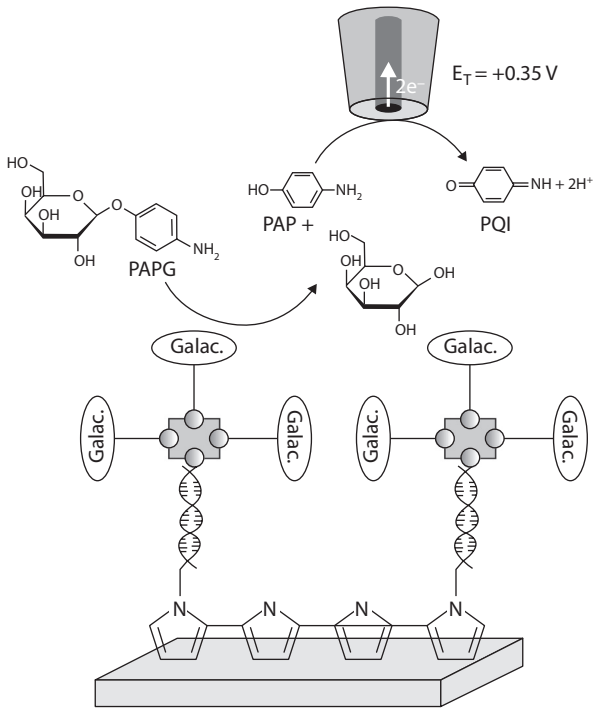


FIGURE 11.28 Schematic representation of the molecular assembly based on oligonucleotide hybridization together with a schematic of the imaging principle (not to scale). (From Nunes Kirchner, C., Szunerits, S., Wittstock, G.: Scanning electrochemical microscopy (SECM) based detection of oligonucleotide hybridization and simultaneous determination of the surface concentration of immobilized oligonucleotides on gold. *Electroanalysis*. 2007. 19. 1258–1267. Copyright Wiley-VCH Verlag GmbH & Co. KGaA. Reproduced with permission.)

mol/cm^2 with statistical uncertainties of about 10%; and (iv) thicker spots provide no advantage in terms of the amount of hybridization.

11.2.4.4.2 Amplification Schemes in GC Mode

Neugebauer et al. [14] employed a related strategy on a 48 element array of 100 µm Au disk electrodes. 3′-Thiolated ODNs were used instead of immobilization by electropolymerization and the biotinylated targets were obtained by a PCR amplification kit that contains a biotinylated nucleotide triphosphate. The enzyme label was an ALP, but this too functions by conversion of electroinactive PAPP to PAP. The LOD for ODNs detected by the oxidation of PAP at the Au substrates was about 100 fM. SECM was also used to image the array and indicated that the activity of the enzyme was uniform. These authors also showed that the assay could be assembled on the SECM tip and that approaching the tip to a bare Au substrate increased the sensitivity 3.6-fold by the feedback of PQI generated at the tip similar to Figure 11.26 for enzymatic PAP regeneration.

11.2.4.4.3 Enzymatic Generation of Blocking Layers for Readout

It is clear that the labeling of the target ODN introduces a significant additional time delay in the assay, it is also inconvenient to have to label the analyte. Alternative strategies are also being explored such as the use of sandwich formats by Palchetti et al. [12]. An unlabeled 255 bp PCR amplicon was detected using an immobilized capture probe and a second, biotinylated signaling probe. GC mode detection could have been employed, but these workers chose instead to use the ALP label on the signaling probe to convert soluble 5-bromo 4-chloro 3-indolylphosphate and nitro blue tetrazolium (BCIP/NBT) to an insoluble product that locally blocked the substrate and was detected as described in Section 11.1.1.2 with ferrocene monocarboxylate as mediator. A similar method was applied by Fortin et al. [13] who used HRP to generate an insoluble BCIOH. In such an experiment, the mediator must be chosen carefully because only neutral or cationic mediator will penetrate the ODN layer [138]. The use of feedback mode permitted relatively high tip scan rates (25 µm/s), but the assay is less sensitive than GC mode.

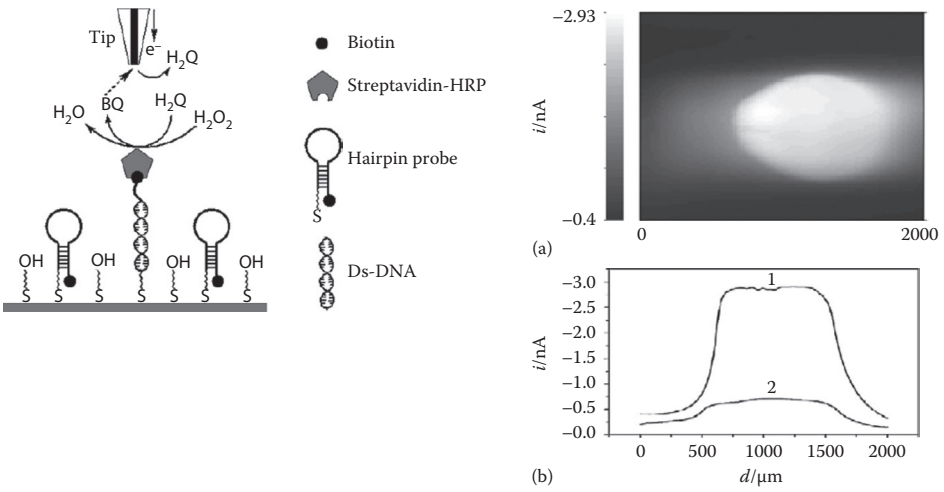


FIGURE 11.29 Left: Schematic representation of the SECM detection methodology for DNA using a hairpin loop capture probe. Right: (a) SECM image of a dsDNA spot fabricated by 450 nM complementary target DNA. $v_t = 50$ µm/s. (b) SECM line scans across the dsDNA spots fabricated with 450 nM complementary DNA (1) and a DNA target with a two base pair mismatch (2). $v_t = 30$ µm/s. (Reprinted from *Biosens. Bioelectron.*, 25, Zhang, Z., Zhou, J., Tang, A., Wu, Z., Shen, G., and Yu, R., Scanning electrochemical microscopy assay of DNA based on hairpin probe and enzymatic amplification biosensor, 1953–1957, Copyright 2010, with permission from Elsevier.)

11.2.4.4.4 Selective Labeling Connected to Conformational Changes of Capture Strand

Another assay strategy has been reported which takes particular advantage of DNA chemistry; the use of hairpin loop capture probes [139] (Figure 11.29). In this case, the probe is partially self-complementary and exists as a loop with the 5′ end anchored to the Au substrate by thiol chemistry and the complementary region at the biotinylated 3′ end is therefore held near the substrate. Two-hour hybridization of a spot of target DNA displaces the self-complementary portion of the capture probe and a large conformational change sends the biotin-labeled end toward the bulk solution where it is available for binding to avidin–HRP. HRP-catalyzed oxidation of hydroquinone by hydrogen peroxide was detected by reduction of benzoquinone at the tip in GC mode. This method neatly avoids the modification of the target strand and was sensitive to a two base pair mismatch, but at the cost of a slow (2 h) hybridization step.

11.2.4.5 DNA Arrays with Metal Labels

Apart from enzyme labels, borrowed from immunoassay technology, SECM DNA arrays have also been designed using metal labels. The concept is to couple metal particles to the hybridization reaction in order to enhance the positive feedback of simple redox mediators at the array elements. This allows readout of the arrays in the feedback mode, which has some advantages in terms of resolution, but because feedback mode always operates with a significant background current due to diffusion from bulk solution into the tip/substrate gap, the sensitivity is usually worse than GC mode. Ferreyra et al. [140] studied the effect of Au nanoparticles on Au substrates modified by electrostatic self-assembly of polyethyleneimine and DNA; they observed that the approach curves for ferrocene methanol and ferrocene monocarboxylate at the AuNP surface were essentially the same as at a bare Au substrate (positive feedback). A sensitive DNA array was made using a similar concept, by combining biotinylated target ODNs and streptavidin–AuNP conjugates [141]. Such conjugates are in fact commercially available because of their use in electron microscopy to enhance contrast. The AuNPs brought to the surface by hybridization served as catalysts for the electroless deposition of Ag to form interconnected metal structures. The metalized regions were imaged in the feedback mode using $[Ru(NH_3)_6]^{3+}$ as the mediator. In combination with temperature control, the array was found to be sensitive (comparable to standard fluorescence techniques) and capable of discriminating against single base mismatches. Metal NPs can also be detected by their dissolution by tip-generated oxidants (Section 11.2.6).

11.2.4.6 Label-Free DNA Arrays

The requirement to employ labels in DNA assays (whether fluorescent or electrochemical) can be a limiting factor in the assay throughput. It also adds to the complexity of the procedure. Significant efforts have therefore been devoted to develop "label-free" approaches to DNA analysis. The study of feedback effects at DNA-coated substrates [138] showed that Donnan exclusion of anions was often a dominant effect on the feedback of anionic mediators such as $[Fe(CN)_6]^{4-}$. Neutral and cationic mediators are able to penetrate ODN films and produce positive feedback, but anionic mediators are blocked and negative feedback is observed. Several groups [142–146] have used this effect to detect hybridization events at electrode surfaces. Hybridization of target ODNs increases the anionic charge density and therefore increases the Donnan exclusion of anions. Schuhmann and coworkers refer to this concept as "repelling mode" SECM and they made a quantitative study of the effects of probe density, mediator concentration, tip/sample separation, and ionic strength on ODNs anchored via Au-thiolate chemistry [142]. Donnan exclusion breakdown was observed at high ionic strength via an increase in the feedback for $[Fe(CN)_6]^{4-}$ mediator and therefore the authors suggest that decreasing the ionic strength as much as is compatible with DNA hybridization will improve the sensitivity of detection of hybridization by this method. Other related approaches include the use of DNA–poly-1,4-benzoquinone films [147].

Diakowski and Kraatz also used $[Fe(CN)_6]^{4-}$ to study mismatches in a 25 base pair ODN hybridization experiment [144]. The negative feedback was greatest for fully matched strands and least for mismatches near the ends of the strands. Their data were reported in terms of the effective rate constant describing the faradaic reaction at the substrate as extracted from feedback approach curves (Chapter 5). Interestingly, a threefold difference between the rate constants at various surfaces with matched/mismatched pairs was observed that was greatly increased to a factor of about 20-fold in the presence of Zn^{2+}. This effect is due to the modulation of the charge density of the DNA by the binding of Zn^{2+} [138] and appears to be a useful means to enhance the performance of such label-free DNA sensors.

Takenaka and coworkers have taken another approach [148,149]. They used a redox-tagged threading intercalator of the ferrocenyl naphthalene diimide type to image DNA arrays in feedback mode. In their first publication [150], the mechanism for the generation of a steady-state current is suggested to be due to direct touching of the tip to the array, but later a second possibility (lateral charge transport between the intercalator species in the DNA layer) is suggested [149]. The method was capable of distinguishing single nucleotide polymorphisms in the tumor-suppressor p53 gene.

11.2.4.7 SECM Studies of Charge Transport at DNA-Modified Electrodes

There have been a few studies of the direct electrochemistry of DNA or nucleosides using SECM. Wang and Zhou [151] were able to detect guanine-rich DNA sequences by feedback imaging with $[Ru(bipy)_3]^{2+/3+}$ because the oxidized form of the mediator is able to oxidize guanine residues. The authors were able to detect hybridization events in a label-free experiment, though it is not clear to what extent this approach can be applied in more general DNA assays. Instead, Wang and Zhou [151] showed that the use of methylene blue as an intercalator facilitated electron transport from the underlying gold substrate and that hybridization of 15 base pair ODNs can be imaged in feedback mode using tip-generated $[Fe(CN)_6]^{3-}$ to collect electrons from the hybridized DNA molecules. A limit of detection of 14 fmol dsDNA/array element was determined and the assay was reported to be easily visualized with solution concentrations of 20 μM DNA. The fundamentals of DNA-mediated charge transport have also been probed by similar experiments [152]. Nile Blue tags were introduced at specific locations in a DNA monolayer and feedback experiments were carried out using $[Fe(CN)_6]^{4-}$ as the mediator. As noted previously [138], this mediator is excluded from sufficiently dense DNA monolayers and therefore positive feedback was used to identify rapid electron transport through the DNA monolayer via electron exchange between the Nile Blue and the $[Fe(CN)_6]^3$ at substrate potentials negative of the Nile Blue formal potential. Feedback was observed only when the Nile Blue was anchored at the DNA–solution interface and could be disrupted by the action of the TATA-binding protein which is known to strongly distort the DNA structure. SECM has also been used to study ODNs synthesized at hydrogen-terminated silicon. Positive feedback using $[Ru(NH_3)_6]^{3+}$ as the mediator was observed at p-Si(111) surfaces at which ODNs had been prepared by standard solid phase synthesis using a bifunctional molecule to prepare the necessary alcohol-terminated monolayer [153,154]. Such Si–C-bonded monolayers are extremely robust chemically and appropriate etching conditions allow preparation of atomically flat Si(111)-H on which the whole process of solid phase synthesis can be carried out and characterized by STM or AFM [155]. Approach curves for a variety of mediators ($[Fe(CN)_6]^{4-}$, $[IrCl_6]^{3-}$, $[Ru(bipy)_3]^{2+}$, $[Co(bipy)_2]^{3+}$, and $[Ru(NH_3)_6]^{3+}$) were analyzed and interpreted in terms of lateral charge transport in the semiconductor or through the DNA monolayer. The use of n-type and p-type substrates allows some discrimination against charge transport through the silicon because, for example, hole injection into n-Si should immediately result in electron–hole recombination and no feedback. The conclusion of this work was that the feedback effects were not due to long range electron transfer, but due mainly to lateral diffusion in the monolayer. It should be noted, however, that these experiments are not directly comparable to those of Gorodetsky et al. [152] because 5′-thiolated ODNs are oriented at about 45° from normal to the Au substrate, but

the oligosynthesis procedure naturally produces 3′-anchored ODNs that are known to lie almost parallel to the Si surface [155].

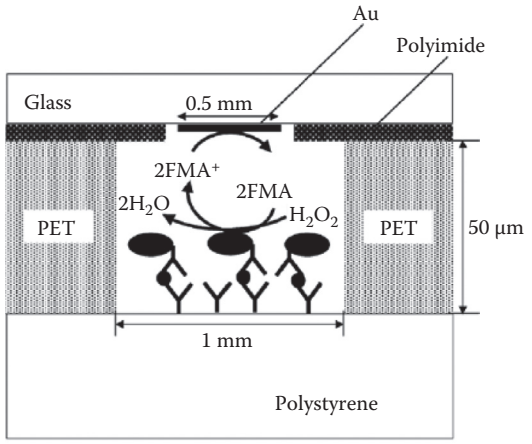
11.2.4.8 Cellular Biosensing Systems

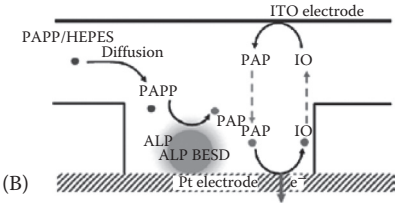
SECM is widely used for monitoring the cellular activity of individual cells (Chapter 12). Here we would like to review briefly another approach in which cells are used as sensors. For instance, cells can respond to environmental stimuli by producing more or less of a particular protein. Monitoring the activity of such reporter proteins, which can also be enzymes listed in Table 11.2 such as β-galactosidase or ALP, allows conclusions to be drawn about the presence of certain analytes in the environment. Genetically modified cells provide specifically large and easily detectable changes in their expression profile. Matsue and coworkers have been active in using SECM detection schemes for such assays [156–158]. Examples include the use of transfected HeLa for sensing of dexamethasone, forskolin, and tumor necrosis factor alpha (TNF-α) that had secreted ALP as reporter protein [156]. One problem of using prokaryotic organisms such as *Escherichia coli* for production of recombinant proteins is the possibility that the proteins are formed as insoluble aggregates. Nagamine et al. [157] developed a screening method for soluble recombinant proteins by coupling them with galactosidase. If the proteins were soluble, galactosidase activity could be detected. Often, it is advantageous to cultivate cells in a collagen or gel matrix because the matrix promotes cell growth and differentiation. If the matrix is placed into a pyramid-shaped cavity on a chip [159], it also eliminates problems of hindered mass transport in the vicinity of protruding cell and variability of spot size. The measurement of oxygen consumption by a collagen spot containing leukemia [160] or breast cancer cells [161] was used to test the sensitivity of these cancer lines against various anticancer drugs. Kasai et al. [158] combined the cultivation of leukemia cells in collagen gel spots on a chip with an SECM immunoassay for the cytokine, interleukin (IL)-1β.

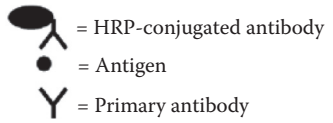
11.2.5 Use of SECM Detection Principles in Microanalytical Devices

In principle, the SECM is a powerful technique to read out electrochemical DNA and protein arrays, because in combination with enzyme labeling and PCR amplification [14] it can achieve the required high sensitivity. However, the SECM is substantially slower than a fluorescence microscope, because of the mechanics of scanning the tip and limitations imposed by the diffusion mass transport rate (typically $v_t < m_0$, where v_t is the tip scan rate and m_0 is the mass transport coefficient of the appropriate SECM mode). The SECM itself may therefore not be the appropriate instrument to carry out the readout of arrays, but the principles of SECM (generation–collection (Figure 11.30a), feedback (Figure 11.30b), tip-generated reagents (Figure 11.30d)) can be implemented in microanalytical devices and the optimization of such devices benefits from the flexibility SECM offers with respect to finding optimum geometries and conditions. Matsue and coworkers made important contributions in this area. They developed miniature electrochemical cells for immunoassay with separated microstructures to hold the analyte and integrated microscopic electrodes for GC detection of galactosidase [162], ALP [163], or HRP [164] activities from enzyme labels or from enzymes used in expression assays (Figure 11.30a). A sensitive coulometric detection of PAP generated from galactosidase in yeast cells was achieved by closing a microwell with the body of a microelectrode of large RG [165]. A further development is the use of addressable microelectrode arrays (Figure 11.30c). Arrays of band electrodes were positioned with orthogonal orientations so that points in the interelectrode space could be addressed by a "row electrode" on the top chip and a "column electrode" at the bottom chip. This device was able to provide GC imaging of ALP-modified spots with electrochemical recycling of PQI [129]. The feedback enhancement of GC signals was also used in simple two electrode setup [133] (Figure 11.30b).

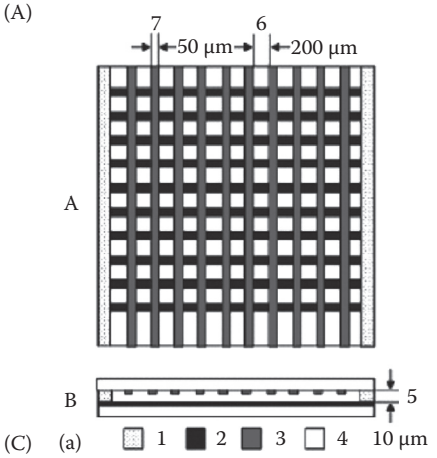
The principles of SECM surface modification have also been integrated into microdevices [166,167]. Surfaces that prevent protein adsorption based on heparin have been activated with electrochemically

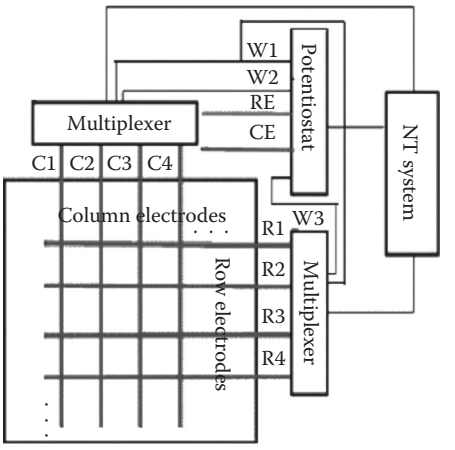

Au
Polyimide
Glass
0.5 mm
2FMA+
2FMA
2H2O
H2O2
PET
PET
50 μm
1 mm
Polystyrene

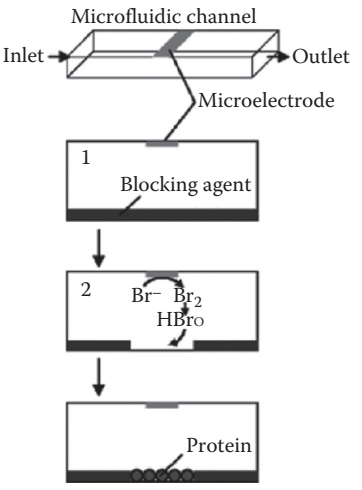

ITO electrode
PAPP/HEPES
Diffusion
PAP
IO
PAPP
PAP
PAP
IO
ALP
ALP BESD
Pt electrode
e-
(B)


= HRP-conjugated antibody
= Antigen
= Primary antibody

(A)


7
6
50 μm
200 μm
A
B
5
(C) (a)
1
2
3
4
10 μm


W1
W2
RE
CE
Potentiostat
NT system
Multiplexer
C1 C2 C3 C4
Column electrodes
W3
R1
R2
R3
R4
Row electrodes
Multiplexer
(b)


Microfluidic channel
Inlet
Outlet
Microelectrode
1
Blocking agent
2
Br−
Br2
HBro
Protein

(D)

generated Br_2/OBr^- at microelectrodes integrated into microfluidic devices. After the modification, protein A could be adsorbed and it captured the primary antibody for a sandwich assay [166]. The activated areas allowed migration of adherent cells and the measurement of cell motility [167]. Further, the integrated microelectrodes allowed the activation of these areas on demand.

11.2.6 SECM Imaging of Electrophoresis Gels and Fingerprints

Silver staining with optical readout is established as a relatively rapid and rather sensitive procedure for visualizing proteins in electrophoresis gels or on blotting foils made of poly(vinylidene difluoride) (PVDF). A number of varying protocols are available although the exact mechanism of the protein-catalyzed silver nucleation is subject to debate. Such procedures result in an array of isolated nanoparticles as shown on the transmission electron microscope image in Figure 11.31a. The silver nanoparticles can be imaged in the SECM feedback mode with a higher sensitivity than possible with optical detection [168]. Positive feedback results if a mediator such as $[IrCl_6]^{3-}$ [168] or $[Os(bipy)_3]^{2+/3+}$ [169] is selected, whose oxidized form is able to oxidize the Ag clusters. During that process, the Ag clusters are consumed (dissolved). Copper staining is also possible and ferrocene methanol is a suitable oxidant in this case [170].

The typical amount of Ag clusters is sufficient to obtain stable imaging if the lateral scan rate is not set too low and mediator concentrations of around 1 mM are chosen. The disadvantage that the Ag clusters are consumed during the imaging was overcome by replacing the Ag staining by a molecular label, *p*-benzoquinone [171]. This molecule reacts in a 1,4-Michael reaction with free thiol groups of cysteines contained in the protein. The benzoquinone label can be detected in the SECM feedback mode with $[Fe(CN)_6]^{3-}$ as mediator. At the tip $[Fe(CN)_6]^{4-}$ is formed and reduces the benzoquinone label. Stable imaging over prolonged time has been achieved by exploiting a chemical reoxidation of protein-bound hydroquinone groups by dioxygen present in the solution [171]. Besides imaging proteins after electrophoretic separation, imaging of latent fingerprints is a very interesting application. Fingerprints contain proteins that can be stained with Ag [172] or tagged with benzoquinone [173]. Figure 11.31b shows a comparison of SECM fingerprint imaging after the silver staining and the benzoquinone tagging.

11.2.7 Applications to Cells and Whole Organisms

The number of reports on the application of SECM to measurements at whole cells, tissues, and organisms has seen a steep increase over the recent years. Many basic imaging modes for detecting

FIGURE 11.30 Integration of SECM working modes into microfluidic devices and analysis systems. (A) GC detection of HRP label by a microelectrode at fixed position. (Reprinted from *Biosens. Bioelectron*., 21, Ogasawara, D., Hirano, Y., Yasukawa, T., Shiku, H., Kobori, K., Ushizawa, K., Kawabata, S., and Matsue, T., Electrochemical microdevice with separable electrode and antibody chips for simultaneous detection of pepsinogens 1 and 2, 1784–1790, Copyright 2006, with permission from Elsevier.) (B) Use of feedback enhancement of GC detection of ALP enzyme label. (From Chang, C.-Y., Takahashi, Y., Murata, T., Shiku, H., Chang, H.-C., and Matsue, T., Entrapment and measurement of a biologically functionalized microbead with a microwell electrode, *Lab Chip*, 9, 1185–1192, 2009. Reproduced with permission of The Royal Society of Chemistry.) (C) Use of row and column band electrode arrays on two opposing chips to address lateral positions. (Reprinted with permission from Lin, Z., Takahashi, Y., Kitagawa, Y., Umemura, T., Shiku, H., and Matsue, T., An addressable microelectrode array for electrochemical detection, *Anal. Chem*., 80, 6830–6833, 2008. Copyright 2008 American Chemical Society.) (D) Local surface modification inside enclosed microchannels by microelectrochemically formed reagents. (Reprinted with permission from Kaji, H., Hashimoto, M., and Nishizawa, M., On-demand patterning of protein matrixes inside a microfluidic device, *Anal. Chem*., 78, 5469–5473, 2006. Copyright 2006 American Chemical Society.)

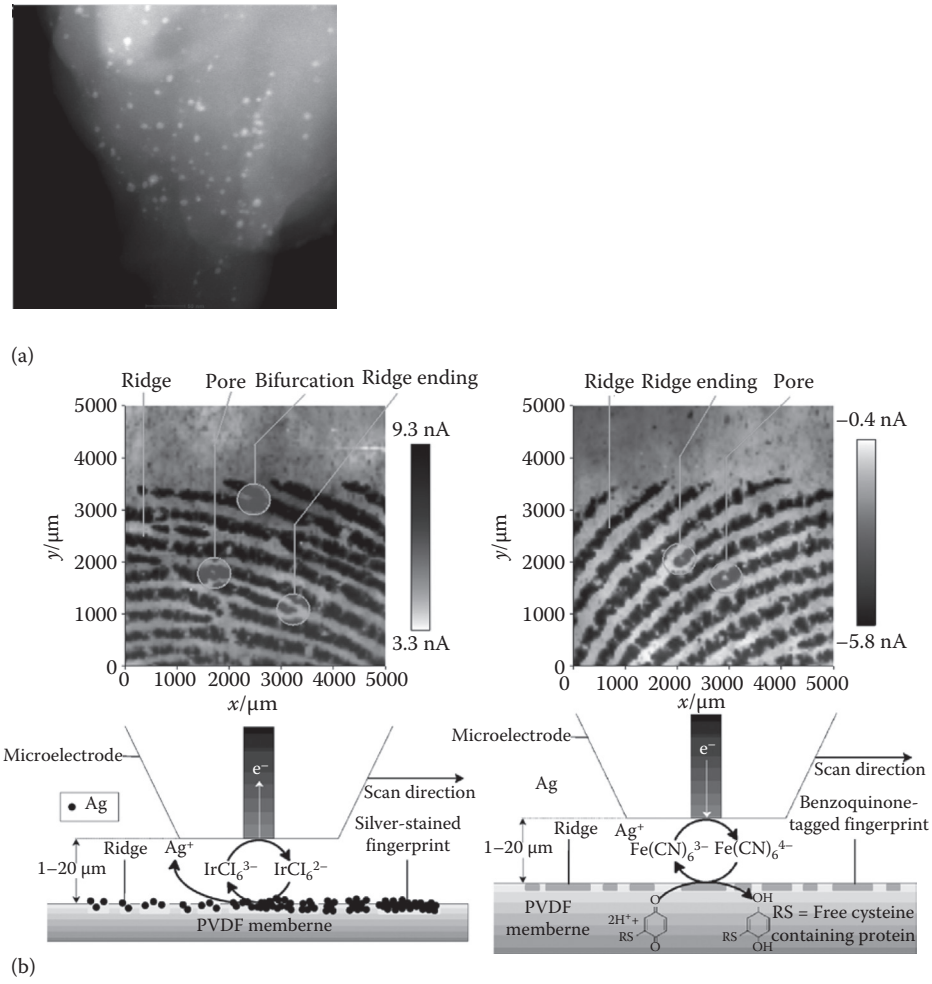


FIGURE 11.31 (a) TEM picture of silver clusters inside a protein spot on PVDF. (Reprinted with permission from Zhang, M., Wittstock, G., Shao, Y., and Girault, H.H., Scanning electrochemical microscopy as a read-out tool for protein electrophoresis, *Anal. Chem*., 79, 4833–4839, 2007. Copyright 2007 American Chemical Society.) (b) SECM images of fingerprints developed by Ag staining (left) or benzoquinone tagging (right). The schematic representations below the images show the detection principles for Ag nanoparticle and benzoquinone labels. (Reprinted from Cortes-Salazar, F. et al., *Chimia*, 63, 580, 2009. With permission. Copyright 2009 Swiss Chemical Society.)

activity of enzymes are similar to those of isolated enzymes. In addition, there are some major conceptual and technical differences in the experiments. Typically, cells are strongly corrugated objects on the size scale of typical microelectrodes. Therefore, independent distance measurements and instrumentation to guide tips at constant distance over cells are of high importance. Biochemical systems can be stimulated by light, mechanical contact and specific chemicals. This can be used to generate on/off experiments analogous to conventional potential step techniques in voltammetry. Mass transport between the tip and reaction sites inside cells is complicated by the requirement to cross several biological membranes. This will delay the response compared to solution systems. However, the permeability of biological membranes varies greatly for different compounds. These considerations make it worthwhile to treat such experiments in Chapter 12 that has been added to this edition.

11.2.8 Imaging Mass Transport in Biological Systems

The tip response in SECM is strongly dependent on local mass transport and this may in fact be utilized to image local mass transport. Examples include the transport of oxygen and electroactive ions in cartilage [174], convective [175], and diffusional [41] transport in dentinal tubules and ionic fluxes through skin [176], which are described in Chapters 9 and 12. In this section, we discuss briefly experiments by Pohl, Antonenko, and coworkers, which, though not SECM, employ microelectrode techniques in a similar manner.

The systems studied by these authors are chemical fluxes at the bilayer lipid membrane, which are of importance in many cellular processes [39]. The experimental system for the study of the reduction of acetaldehyde by alcohol dehydrogenase is shown in Figure 11.32. The pH microelectrodes employed were based on antimony-filled glass capillaries that were pulled to a tip diameter of 5 µm. The pH gradient on the *trans* side due to the enzymatic reaction

$$CH_3CHO + NADH + H^+ \rightarrow CH_3CH_2OH + NAD^+ \tag{11.12}$$

was measured by moving the pH microelectrode normal to the membrane at a speed of 2 µm/s. The zero distance point was determined by touching the membrane with the tip. The pH profile is determined by the kinetics of the enzymatic reaction and the thickness of the diffusion layer in the solution. The combined effects of transmembrane substrate diffusion, enzymatic reaction, and product diffusion were incorporated in a quantitative model based on the Nernst diffusion layer approximation. These workers emphasized that presence of the diffusion layer has a significant effect on the apparent kinetics of important biological phenomena such as membrane permeation, carrier-mediated transport, and the reactions of enzymes immobilized on the membrane surface. Using similar technology, it was possible to observe the dynamics of formation and dissipation of pH gradients in response to a voltage step [177], transmembrane osmotic fluxes [178], and ammonium ion permeation with a micro-ISE [179].

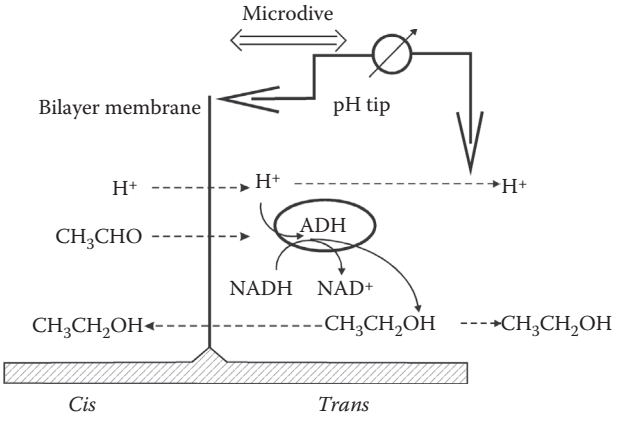


FIGURE 11.32 The reduction of acetaldehyde catalyzed by alcohol dehydrogenase (ADH) in the presence of NADH proceeds at the *trans* side. The enzyme/coenzyme and substrate are added to opposite sides of the membrane. After the addition of acetate, the membrane is highly permeable not only to acetaldehyde and alcohol but to protons as well. pH profiles within the unstirred layer near the planar bilayer lipid membrane are measured with the help of a microelectrode driven by a hydraulic microdrive (schematic redrawn by the chapter authors). (Reprinted from *Arch. Biochem. Biophys*., 333, Antonenko, Y.N., Pohl, P., and Rosenfeld, E., Visualization of the reaction layer in the immediate membrane vicinity, 225–232, Copyright 1996, with permission from Elsevier.)

11.3 CONCLUSION AND OUTLOOK

11.3.1 Information Content of SECM Measurements and Spatial Resolution

SECM images contain information about both local reactivity and the topography of the sample surface. There may be some advantages to the use of SECM feedback imaging for recording the topography of biological samples because there is no physical contact between probe and sample. However, it is our opinion that the greatest utility of SECM in biochemical investigations is its ability to map chemical species and reactivity (i.e., processes) rather than topography for which scanning ion conductance microscopy may be used. Since the theoretical models of SECM are based on established electrochemical principles, the data can often be interpreted in a quantitative manner and kinetic investigations at fixed lateral tip position are possible with a time resolution of milliseconds or better.

Typical SECM tips have radii in the micrometer range; hence, the lateral resolution of the feedback images is in the micrometer scale on a routine basis, and the vertical resolution (sample height variations) is better than 1 μm. Consequently, the majority of investigations have been devoted to systems with spatial heterogeneity on the micrometer scale such as immobilized enzyme layers, immunoassay systems, and DNA chips. Tip fabrication has considerably advanced over the last decade (Chapter 3) and current-independent positioning systems are increasingly used. However, it should be noted that the kinetics of the system also put constraints on the miniaturization of the probe. Therefore, rather large probes may still have to be employed [49,180].

Several proof-of-concept studies have demonstrated how various metabolic processes can be utilized for contrast formation in SECM imaging. The scanning microelectrode may be used to convert a mediator to a redox-active cosubstrate of an enzyme at the specimen surface and to detect the regeneration of the mediator in the course of the enzymatic reaction (feedback mode). Alternatively, the tip can monitor amperometrically or potentiometrically the diffusional flux caused by a metabolic reaction at the specimen in a similar manner to the investigation of localized mass transport phenomena (Chapter 9). The tip may also compete with biochemically active surfaces or cells for the same reagent (RC mode). If one is interested in studying selective binding events at biorecognition layers, enzyme-labeling techniques can be used to enable detection by the SECM. In addition, nonspecific labeling techniques such as Ag staining have opened new interesting applications of SECM detection schemes for proteins and fingerprints. As the biological complexity of the systems increases, strategies for image verification are of very high importance and investigation of complex samples greatly benefits from use of combined instruments such as confocal laser scanning microscopy, scanning force microscopy, or local spectroscopies.

11.3.2 Applications in Biotechnology

Some of the most promising applications of SECM were reported in the area of biotechnology, that is, optimization of immobilized enzyme systems for use in synthesis and analysis and biochip methodologies. The well-established theory of feedback and generation–collection enables extraction of quantitative information and the range of electrochemical probes that are available gives SECM wide application and great flexibility. A particular problem that does remain is the necessity to trade-off image resolution and spatial control of the diffusion fields in the feedback mode against the greater sensitivity of the generation–collection mode. In some cases, spatial confinement of diffusion fields has been achieved by means of microstructured specimens [33,35,50] or by a second solution phase reaction that limits the lifetime of the species detected at the tip [116,181]. Alternately, tip position modulation (TPM) and phase-selective detection [182] may enhance the sensitivity to the feedback flux from the immobilized enzyme.

One application is the use of SECM to make sequential readings from a sensing array. This might be done as demonstrated by Shiku et al. [35] for a dual electrochemical enzyme

immunoassay. Such methods are rapid compared to conventional assays because there is no need to incubate the enzyme-labeled antigens to produce enough products for the detection step. The assay speed might be further enhanced if the SECM detection principle is used in integrated microdevices [128,164].

Recently, SECM detection of nonenzymatic labels such as metal nanoparticles and label-free detection schemes has seen rapid development. These systems have the advantage of a rather generic applicability. However, occasionally they lack the quantitative rigor that is a salient feature of many older SECM applications. In each case, it is worthwhile to evaluate the possibility of a rigorous quantitative description or whether only a simple calibration is possible [141,171,172].

Characterization of enzyme electrodes for synthesis as a clean manufacturing technology, or as electrodes in biofuel cells [183], is another area where SECM may play a role in investigating the factors limiting electrode performance. The characterization of O_2-reducing electrodes requires new imaging modes such as RC [119] or TG/SC mode [25]. Serious issues in the optimization of biosensor manufacturing processes can be addressed by SECM. An incomplete list of examples includes homogeneity analysis of spotted biochemicals [24], aggregation phenomena [40], entrapment of microbubbles above recessed microelectrodes during immersion [184], and the question of whether enzyme immobilization extends beyond the active electrode surface and covers also the support and encapsulation of the sensors [185]. Restricting the enzyme modification to the electrode surface will be one of the crucial prerequisites in miniaturized multianalyte sensors to prevent cross talk between neighboring sensing regions [86]. Further areas of future work may include readout processes for combinatorial libraries [25].

Since the first edition of this book, investigation of single cells, tissues, and organisms has seen a particularly rapid development and is now covered in a separate chapter. This has been driven partly by improvements in current-independent tip-positioning systems and more routine production of submicrometer tips.

Mass transport phenomena in biological systems can be investigated with SECM if the species of interest can be detected by either a potentiometric or amperometric microelectrode. SECM is particularly appropriate in these studies in view of the intimate connection of the imaging mechanism to mass transport effects. The investigation of oxygen and ion transport in various tissues and under a variety of driving forces (concentration gradient, electric field, convection) has been demonstrated with quantitation of the transport process on a micrometer length scale.

11.3.3 Recording Speed

When evaluating ranges of application, the timescale of SECM experiments should be considered. Although SECM allows the investigation of very rapid kinetics under steady-state conditions (microsecond–millisecond time resolution) at laterally fixed microelectrode position, images can be obtained only with a rather limited frequency. It would take about 34 min to record a $100 \times 100\,\mu m^2$ image composed of 100 line scans each 100 µm long with a typical lateral scan rate of 10 µm/s. If the experimenter wishes to follow the activity of biotechnological or biological specimens as a function of time, such frame acquisition rates will turn out to be unacceptably long in many cases. In fact, limited recording speed represents a fundamental problem for all scanning probe techniques, but it is particularly evident for SECM. The upper limit of the lateral scan rate is imposed by the time to establish a steady-state response at each grid point for amperometric tips in the feedback mode, or to attain the equilibrium potential for potentiometric tips. This characteristic time becomes smaller as the *active* tip electrode sizes and tip–sample distances shrink (see Chapter 5). Undesired stirring also sets an upper limit of the lateral scan rate. The problem of stirring will be less severe as the *total* tip diameter is reduced. Distance control mechanisms tend to decrease the recording speed further.

To overcome the limited image acquisition rate, the tip electrode may be positioned above a region of particular interest once a complete image has been recorded. Optical microscopy on transparent samples may greatly facilitate the positioning of the electrode relative to features of interest. Confocal microscopy with resolution in lateral and vertical direction can be particularly valuable [40,106]. Another concept has been demonstrated by Meyer et al. [186]. On one chip of $1 \times 1\,cm^2$, an array of 20×20 individually addressable electrochemical cells were integrated each measuring $500 \times 500\,\mu m^2$ in size. By sequentially reading the current from the working electrodes, images of O_2 and H_2O_2 distributions were obtained within 2 min. After covering the array with a glucose oxidase-containing PPy membrane, glucose distributions could also be measured. Since there is no need for mechanical displacement of the probe array, the restriction imposed by stirring effects or the time to establish a steady-state current at each grid point are circumvented. Matsue's group [128] proposed addressable band electrodes on two opposing chips. By addressing one band of each array, each point can be addressed by "row" and "column." Such devices may potentially allow rather fast readouts and can be tuned for specific application. More recently, Cortes-Salazar et al. introduced soft microelectrodes that operate in contact mode, similar to a giant SFM cantilever [187]. Arrays of such probes could be used to brush surfaces. Such devices may be advantageous when scanning large areas (square centimeter range) as might be required for activity imaging directly on electrophoresis gels or blotting foils or visualization of latent finger prints (see Chapter 18).

Algorithms for imaging sample with different resolution within one image frame have not found wide application although the potential for such does exist [188], in particular, if the measurements are combined with optical microscopy for preselection of different regions.

ABBREVIATIONS, ACRONYMS, AND SYMBOLS

a	Tip radius (active area)
Ab	Antibody
Ab:Ag	Antibody–antigen complex
AFM	Atomic force microscopy/microscope
AC	Alternating current
Ag	Antigen
Ag-E	Enzyme-labeled antigen
ALP	Alkaline phosphatase
ATR-IR	Attenuated total reflectance-infrared (spectroscopy)
c	Concentration, subscript = species
c'	Detection limit of the tip
C	Normalized concentration
cAMP	Cyclic adenosine monophosphate
CEA	Carcinoembryonic antigen
d	Tip–sample distance in micrometers
D	Diffusion coefficient
ELISA	Enzyme-labeled immunosorbent assay
E_S, E_T	Specimen, tip potential
f	Flux
F	Dimensionless flux when concentrations and distances are normalized as in refs. [33,51]; $F = r_S f/DC_0$
$FcCH_2OH$/ $FcCH_2OH^+$	Hydroxymethyl ferrocene/hydroxymethyl ferrocenium
FWHM	Full width at half maximum
G	Conductance between tip and external electrode
G_∞	Conductance between tip and external electrode at quasi-infinite distance

Γ_{enz}	Surface concentration of enzyme
GC	Generation–collection
GDH	PQQ-dependent glucose dehydrogenase
GOx	Glucose oxidase
H	Tip–sample distance normalized by sample radius = distance/sample radius
H_2Q	Hydroquinone
HCG	Human chorionic gonadotropin
HPL	Human placental lactogen
HRP	Horseradish peroxidase
ISE	Ion-selective electrode
i_T	Tip current
$i_{T\infty}$	Tip current at quasi-infinite distance
k_{cat}	Reaction rate constant between SECM mediator and enzyme
K_M	Michaelis–Menten constant
L	Normalized tip–sample distance = distance/tip radius
LOD	Limit of detection
MV^{2+}	Methyl viologen
MW	Molecular weight
NAD^+/NADH	Oxidized/reduced forms of nicotinamide adenine dinucleotide
$NADP^+$/NADPH	Oxidized/reduced forms of nicotinamide adenine dinucleotide phosphate
ODN	Oligo desoxyribonucleic acids
OEG	Oligo ethylene glycol
ORR	Oxygen reduction reaction
PAP	4-Aminophenolate
PAPP	4-Aminophenyl phosphate
PPy	Polypyrrole
PQI	*p*-Quinone imine
PTH	Parathyroid hormone
QRE	"Quasi"-reference electrode (metal wire inserted in solution)
r	Radial coordinate in polar coordinate system
r_S	Sample radius
RC	Redox competition
RG	Ratio between the total tip diameter (active area plus insulator) and the active tip diameter
SAM	Self-assembled monolayer
SECM	Scanning electrochemical microscopy/microscope
SECPM	Scanning electrochemical potential microscopy
STM	Scanning tunneling microscopy/microscope
TEM	Transmission electron microscopy
TMPD	Tetramethyl-*p*-phenylene diamine
u	Normalized radial distance in polar coordinates = r/r_S
v_t	Translation speed of tip vs. sample

ACKNOWLEDGMENT

Benjamin R. Horrocks thanks ONE and RCUK for supporting research in the area of SECM. Gunther Wittstock acknowledges financial support for ongoing research on SECM by Deutsche Forschungsgemeinschaft, Alexander von Humboldt Foundation, Fonds of the Chemical Industries and German Academic Exchange Service. He also thanks Britta Vaske and Heike Hillmer for technical support in preparing the manuscript.

REFERENCES

1. Wang, J., Wu, L.-H., Li, R. Scanning electrochemical microscopic monitoring of biological processes. *J Electroanal Chem* 1989, 272, 285–292.
2. Bard, A. J., Denuault, G., Lee, C., Mandler, D., Wipf, D. O. Scanning electrochemical microscopy: A new technique for the characterization and modification of surfaces. *Acc Chem Res* 1990, 23, 357–363.
3. Fan, F.-R. F., Bard, A. J. STM on wet insulators: Electrochemistry or tunneling. *Science* 1995, 270, 1849–1852.
4. Guckenberger, R., Heim, M., Cevc, G., Knapp, H. F., Wiegräbe, W., Hillebrand, A. Scanning tunneling microscopy of insulators and biological specimens based on lateral conductivity of ultrathin water films. *Science* 1994, 266, 1538–1540.
5. Patel, N., Davies, M. C., Lomas, M., Roberts, C. J., Tendler, S. J. B., Williams, P. M. STM of insulators with the probe in contact with an aqueous layer. *J Phys Chem B* 1997, 101, 5138–5142.
6. Aloisi, G., Bacci, F., Carla, M., Dolci, D. Intermittent contact hydration scanning probe microscopy. *Rev Sci Instrum* 2010, 81, 073707/073701–073707/073704.
7. Woo, D.-H., Yoo, J.-S., Park, S.-M., Jeon, I. C., Kang, H. Direct probing into the electrochemical interface using a novel potential probe: Au(111) electrode/NaBF4 solution interface. *Bull Korean Chem Soc* 2004, 25, 577–580.
8. Baier, C., Stimming, U. Imaging single enzyme molecules under in situ conditions. *Angew Chem Int Ed* 2009, 48, 5542–5544.
9. Wittstock, G., Hesse, R., Schuhmann, W. Patterned self-assembled alkanethiolate monolayers on gold. Patterning and imaging by means of scanning electrochemical microscopy. *Electroanalysis* 1997, 9, 746–750.
10. Liu, B., Bard, A. J., Mirkin, M. V., Creager, S. E. Electron transfer at self-assembled monolayers measured by scanning electrochemical microscopy. *J Am Chem Soc* 2004, 126, 1485–1492.
11. Kranz, C., Wittstock, G., Wohlschläger, H., Schuhmann, W. Imaging of microstructured biochemically active surfaces by means of scanning electrochemical microscopy. *Electrochim Acta* 1997, 42, 3105–3111.
12. Palchetti, I., Laschi, S., Marrazza, G., Mascini, M. Electrochemical imaging of localized sandwich DNA hybridization using scanning electrochemical microscopy. *Anal Chem* 2007, 79, 7206–7213.
13. Fortin, E., Mailley, P., Lacroix, L., Szunerits, S. Imaging of DNA hybridization on microscopic polypyrrole patterns using scanning electrochemical microscopy (SECM): The HRP bio-catalyzed oxidation of 4-chloro-1-naphthol. *Analyst (Cambridge, U.K.)* 2006, 131, 186–193.
14. Neugebauer, S., Zimdars, A., Liepold, P., Gebala, M., Schuhmann, W., Hartwich, G. Optimization of an electrochemical DNA assay by using a 48-electrode array and redox amplification studies by means of scanning electrochemical microscopy. *ChemBioChem* 2009, 10, 1193–1199.
15. Pierce, D. T., Unwin, P. R., Bard, A. J. Scanning electrochemical microscopy. 17. Studies of enzyme–mediator kinetics for membrane- and surface-immobilized glucose oxidase. *Anal Chem* 1992, 64, 1795–1804.
16. Cass, A. E. G., Davis, G., Francis, G. D., Hill, H. A. O., Aston, W. J., Higgings, I. J., Plotkin, E. V., Scott, L. D. L., Turner, A. P. F. Ferrocene-mediated enzyme electrode for amperometric determination of glucose. *Anal Chem* 1984, 56, 667–671.
17. Pierce, D. T., Bard, A. J. Scanning electrochemical microscopy. 23. Reaction localization of artificially patterned and tissue-bound enzymes. *Anal Chem* 1993, 65, 3598–3604.
18. Wijayawardhana, C. A., Wittstock, G., Halsall, H. B., Heineman, W. R. Spatially addressed deposition and imaging of biochemically active bead microstructures by scanning electrochemical microscopy. *Anal Chem* 2000, 72, 333–338.
19. Zhao, C., Wittstock, G. Scanning electrochemical microscopy of quinoprotein glucose dehydrogenase. *Anal Chem* 2004, 76, 3145–3154.
20. Niculescu, M., Gaspar, S., Schulte, A., Csoregi, E., Schuhmann, W. Visualization of micropatterned complex biosensor sensing chemistries by means of scanning electrochemical microscopy. *Biosens Bioelectron* 2004, 19, 1175–1184.
21. Shiku, H., Takeda, T., Yamada, H., Matsue, T., Uchida, I. Microfabrication and characterization of diaphorase-patterned surface by scanning electrochemical microscopy. *Anal Chem* 1995, 67, 312–317.
22. Shiku, H., Matsue, T., Uchida, I. Detection of microspotted carcinoembryonic antigen on a glass substrate by scanning electrochemical microscopy. *Anal Chem* 1996, 68, 1276–1278.

23. Zaumseil, J., Wittstock, G., Bahrs, S., Steinrücke, P. Imaging the activity of nitrate reductase by means of a scanning electrochemical microscope. *Fresenius J Anal Chem* 2000, 367, 352–355.
24. Nogala, W., Szot, K., Burchardt, M., Roelfs, F., Rogalski, J., Opallo, M., Wittstock, G. Feedback mode SECM study of laccase and bilirubin oxidase immobilised in a sol–gel processed silicate film. *Analyst* 2010, 135, 2051–2058.
25. Fernandez, J. L., Mano, N., Heller, A., Bard, A. J. Analytical methods: Optimization of "wired" enzyme O_2-electroreduction catalyst compositions by scanning electrochemical microscopy. *Angew Chem Int Ed* 2004, 43, 6355–6357.
26. Berger, C. E. M., Horrocks, B. R., Datta, H. K. cAMP-dependent inhibition is dominant in regulating superoxide production in the bone-resorbing osteoclasts. *J Endocrinol* 1998, 158, 311–318.
27. Wittstock, G., Schuhmann, W. Formation and imaging of microscopic enzymatically active spots on an alkanethiolate-covered gold electrode by scanning electrochemical microscopy. *Anal Chem* 1997, 69, 5059–5066.
28. Zhao, C., Wittstock, G. Scanning electrochemical microscopy for detection of biosensor and biochip surfaces with immobilized pyrroloquinoline quinone (PQQ)-dependent glucose dehydrogenase as enzyme label. *Biosens Bioelectron* 2005, 20, 1277–1284.
29. Oyamatsu, D., Hirano, Y., Kanaya, N., Mase, Y., Nishizawa, M., Matsue, T. Imaging of enzyme activity by scanning electrochemical microscope equipped with a feedback control for substrate–probe distance. *Bioelectrochemistry* 2003, 60, 115–121.
30. Borgwarth, K., Ricken, C., Ebling, D. G., Heinze, J. Surface analysis by scanning electrochemical microscopy: Resolution studies and application to polymer samples. *Fresenius J Anal Chem* 1996, 356, 288–294.
31. Wittstock, G., Burchardt, M., Nunes Kirchner, C. Scanning electrochemical microscopy in biosensor research, In *Electrochemical Sensor Analysis*, Alegret, S., Merkoci, A., Eds. Elsevier, Amsterdam, the Netherlands, 2007, Vol. 49, pp. 907–939.
32. Horrocks, B. R., Schmidtke, D., Heller, A., Bard, A. J. Scanning electrochemical microscopy. 24. Enzyme ultramicroelectrodes for the measurement of hydrogen peroxide at surfaces. *Anal Chem* 1993, 65, 3605–3614.
33. Horrocks, B. R., Mirkin, M. V., Pierce, D. T., Bard, A. J., Nagy, G., Toth, K. Scanning electrochemical microscopy. 19. Ion selective potentiometric microscopy. *Anal Chem* 1993, 65, 1213–1224.
34. Horrocks, B. R., Mirkin, M. V. Evidence for a potential-dependent reversible inactivation of urease adsorbed on a gold electrode. *J Chem Soc* 1998, 94, 1115–1118.
35. Shiku, H., Hara, Y., Matsue, T., Uchida, I., Yamauchi, T. Dual immunoassay of human chorionic gonadotropin and human placental lactogen at a microfabricated substrate by scanning electrochemical microscopy. *J Electroanal Chem* 1997, 438, 187–190.
36. Wittstock, G., Yu, K.-J., Halsall, H. B., Ridgway, T. H., Heineman, W. R. Imaging of immobilized antibody layers with scanning electrochemical microscopy. *Anal Chem* 1995, 67, 3578–3582.
37. Zhao, C., Sinha, J. K., Wijayawardhana, C. A., Wittstock, G. Monitoring β-galactosidase activity by means of scanning electrochemical microscopy. *J Electroanal Chem* 2004, 561, 83–91.
38. Matsui, N., Kaya, T., Nagamine, K., Yasukawa, T., Shiku, H., Matsue, T. Electrochemical mutagen screening using microbial chip. *Biosens Bioelectron* 2006, 21, 1202–1209.
39. Antonenko, Y. N., Pohl, P., Rosenfeld, E. Visualization of the reaction layer in the immediate membrane vicinity. *Arch Biochem Biophys* 1996, 333, 225–232.
40. Nogala, W., Burchardt, M., Opallo, M., Rogalski, J., Wittstock, G. Scanning electrochemical microscopy study of laccase within a sol–gel processed silicate film. *Bioelectrochemistry* 2008, 72, 174–182.
41. Nugues, S., Denuault, G. Scanning electrochemical microscopy: Amperometric probing of diffusional ion fluxes through porous membranes and human dentine. *J Electroanal Chem* 1996, 408, 125–140.
42. Gilbert, J. L., Smith, S. M., Lautenschlager, E. P. Scanning electrochemical microscopy of metallic biomaterials: Reaction rate and ion release imaging modes. *J Biomed Mater Res* 1993, 27, 1357–1366.
43. Cahill, P. S., Walker, Q. D., Finnegan, J. M., Mickelson, G. E., Travis, E. R., Wightman, R. M. Microelectrodes for the measurement of catecholamines in biological systems. *Anal Chem* 1996, 68, 3180–3186.
44. Ammann, D., Caroni, P. *Methods in Enzymology*, Academic Press, New York, 1989, Vol. 172, pp. 136–155.
45. McNeil, C. J., Smith, K. A., Bellavite, P., Bannister, J. V. Application of the electrochemistry of cytochrome c to the measurement of superoxide radical production. *Free Radical Res Commun* 1989, 7, 89–96.
46. Lee, C., Kwak, J., Bard, A. J. Application of the scanning electrochemical microscopy to biological samples. *Proc Natl Acad Sci USA* 1990, 87, 1740–1743.

47. Yasukawa, T., Kaya, T., Matsue, T. Dual imaging of topography and photosynthetic activity of a single protoplast by scanning electrochemical microscopy. *Anal Chem* 1999, 71, 4637–4641.
48. Hengstenberg, A., Dietzel, I. D., Blöchl, A., Schuhmann, W. Zell-Zell-Kommunikationsprozesse mittels elektrochemischer Rastermikroskopie. *Bioforum* 1999, 22, 595–599.
49. Isik, S., Etienne, M., Oni, J., Blöchl, A., Reiter, S., Schuhmann, W. Dual microelectrodes for distance control and detection of nitric oxide from endothelial cells by means of scanning electrochemical microscope. *Anal Chem* 2004, 76, 6389–6394.
50. Wei, C., Bard, A. J., Nagy, G., Toth, K. Scanning electrochemical microscopy. 28. Ion-selective neutral carrier-based microelectrode potentiometry. *Anal Chem* 1995, 67, 1346–1356.
51. Klusmann, E., Schultze, J. W. pH-microscopy—Theoretical and experimental investigations. *Electrochim Acta* 1997, 42, 3123–3134.
52. Wei, C., Bard, A. J., Kapui, I., Nagy, G., Toth, K. Scanning electrochemical microscopy 32. Gallium ultramicroelectrodes and their application in ion-selective probes. *Anal Chem* 1996, 68, 2651–2655.
53. Diakowski, P. M., Baranski, A. S. Positive and negative AC impedance feedback observed above conductive substrates under SECM conditions. *Electrochim Acta* 2006, 52, 854–862.
54. Eckhard, K., Schuhmann, W. Alternating current techniques in scanning electrochemical microscopy (AC-SECM). *Analyst* 2008, 133, 1486–1497.
55. Edwards, M. A., Williams, C. G., Whitworth, A. L., Unwin, P. R. Scanning ion conductance microscopy: A model for experimentally realistic conditions and image interpretation. *Anal Chem* 2009, 81, 4482–4492.
56. LeSuer, R. J., Fan, F.-R. F., Bard, A. J. Scanning electrochemical microscopy, 52. Bipolar conductance technique at ultramicroelectrodes for resistance measurements. *Anal Chem* 2004, 76, 6894–6901.
57. Mann, S. A., Hoffmann, G., Hengstenberg, A., Schuhmann, W., Dietzel, I. D. Pulse-mode scanning ion conductance microscopy—A method to investigate hippocampal cells. *J Neurosci Methods* 2002, 116, 113–117.
58. Amemiya, S., Guo, J., Xiong, H., Gross, D. A. Biological applications of scanning electrochemical microscopy: Chemical imaging of single living cells and beyond. *Anal Bioanal Chem* 2006, 386, 458–471.
59. Amemiya, S., Bard, A. J., Fan, F.-R. F., Mirkin, M. V., Unwin, P. R. Scanning electrochemical microscopy. *Annu Rev Anal Chem* 2008, 1, 95–131.
60. Eckhard, K., Kranz, C., Shin, H., Mizaikoff, B., Schuhmann, W. Frequency dependence of the electrochemical activity contrast in AC–scanning electrochemical microscopy and atomic force microscopy–AC–scanning electrochemical microscopy imaging. *Anal Chem* 2007, 79, 5435–5438.
61. Ervin, E. N., White, H. S., Baker, L. A. Alternating current impedance imaging of membrane pores using scanning electrochemical microscopy. *Anal Chem* 2005, 77, 5564–5569.
62. Etienne, M., Schulte, A., Schuhmann, W. High resolution constant-distance mode alternating current scanning electrochemical microscopy (AC-SECM). *Electrochem Commun* 2004, 6, 288–293.
63. Gabrielli, C., Huet, F., Keddam, M., Rousseau, P., Vivier, V. Scanning electrochemical microscopy imaging by means of high-frequency impedance measurements in feedback mode. *J Phys Chem B* 2004, 108, 11620–11626.
64. Kashyap, R., Gratzl, M. Adjusting the distance of electrochemical microsensors from secreting cell monolayers on the micrometer scale using impedance. *Anal Chem* 1999, 71, 2814–2820.
65. Kurulugama, R. T., Wipf, D. O., Takacs, S. A., Pongmayteegul, S., Garris, P. A., Baur, J. E. Scanning electrochemical microscopy of model neurons: Constant distance imaging. *Anal Chem* 2005, 77, 1111–1117.
66. Takahashi, Y., Shevchuk, A. I., Novak, P., Murakami, Y., Shiku, H., Korchev, Y. E., Matsue, T. Simultaneous noncontact topography and electrochemical imaging by SECM/SICM featuring ion current feedback regulation. *J Am Chem Soc* 2010, 132, 10118–10126.
67. Ludwig, M., Kranz, C., Schuhmann, W., Gaub, H. E. Topography feedback mechanism for the scanning electrochemical microscope based on hydrodynamic forces between tip and sample. *Rev Sci Instrum* 1995, 66, 2857–2860.
68. Kranz, C., Gaub, H. E., Schuhmann, W. Polypyrrole towers grown with the scanning electrochemical microscope. *Adv Mater* 1996, 8, 634–637.
69. Karrai, K., Grober, R. D. Piezoelectric tip–sample distance control for near optical microscopes. *Appl Phys Lett* 1995, 66, 1842–1844.
70. Kranz, C., Kueng, A., Lugstein, A., Bertagnolli, E., Mizaikoff, B. Mapping of enzyme activity by detection of enzymatic products during AFM imaging with integrated SECM–AFM probes. *Ultramicroscopy* 2004, 100, 127–134.
71. Kueng, A., Kranz, C., Lugstein, A., Bertagnolli, E., Mizaikoff, B. Integrated AFM-SECM in tapping mode: Simultaneous topographical and electrochemical imaging of enzyme activity. *Angew Chem Int Ed* 2003, 42, 3238–3240.

72. Kueng, A., Kranz, C., Lugstein, A., Bertagnolli, E., Mizaikoff, B. AFM-tip-integrated amperometric microbiosensors: High-resolution imaging of membrane transport. *Angew Chem Int Ed* 2005, 44, 3419–3422.
73. Tsionsky, M., Cardon, Z. G., Bard, A. J., Jackson, R. B. Photosynthetic electron transport in single guard cells as measured by scanning electrochemical microscopy. *Plant Physiol* 1997, 113, 895–901.
74. Zhou, H., Shiku, H., Kasai, S., Noda, H., Matsue, T., Ohya-Nishiguchi, H., Kamada, H. Mapping peroxidase in plant tissues by scanning electrochemical microscopy. *Bioelectrochem Bioenerg* 2001, 54, 151–156.
75. Zhou, H., Kasai, S., Noda, H., Ohya-Nishiguchi, H., Shiku, H., Matsue, T. Characterization of peroxide activity of single algae protoplasts by scanning electrochemical microscopy. *Bull Chem Soc Jpn* 2003, 76, 1757–1762.
76. Yamada, H., Shiku, H., Matsue, T., Uchida, I. Microvoltammetric characterization of diaphorase monolayer at glass surfaces. *Bioelectrochem Bioenerg* 1994, 33, 91–93.
77. Sawaguchi, T., Matsue, T., Uchida, I. Catalytic capability of diaphorase bound to a self-assembled thiol monolayer at a gold electrode. *Bioelectrochem Bioenerg* 1992, 29, 127–133.
78. Burchardt, M., Wittstock, G. Kinetic studies of glucose oxidase in polyelectrolyte multilayer films by means of scanning electrochemical microscopy (SECM). *Bioelectrochemistry* 2008, 72, 66–76.
79. Wei, C., Bard, A. J., Mirkin, M. V. Scanning electrochemical microscopy. 31. Application of SECM to the study of charge transfer processes at the liquid/liquid interface. *J Phys Chem* 1995, 99, 16033–16042.
80. Cornut, R., Lefrou, C. New analytical approximation of feedback approach curves with a microdisk SECM tip and irreversible kinetic reaction at the substrate. *J Electroanal Chem* 2008, 621, 178–184.
81. Burchardt, M., Träuble, M., Wittstock, G. Digital simulation of scanning electrochemical microscopy approach curves to enzyme films with Michaelis–Menten kinetics. *Anal Chem* 2009, 81, 4857–4863.
82. Cornut, R., Hapiot, P., Lefrou, C. Enzyme-mediator kinetics studies with SECM: Numerical results and procedures to determine kinetics constants. *J Electroanal Chem* 2009, 633, 221–227.
83. Shen, Y., Träuble, M., Wittstock, G. Detection of hydrogen peroxide produced during electrochemical oxygen reduction using scanning electrochemical microscopy. *Anal Chem* 2008, 80, 750–759.
84. Zoski, C. G., Mirkin, M. V. Steady-state limiting currents at finite conical microelectrodes. *Anal Chem* 2002, 74, 1986–1992.
85. Nunes Kirchner, C., Träuble, M., Wittstock, G. Diffusion and reaction in microbead agglomerates. *Anal Chem* 2010, 82, 2626–2635.
86. Strike, D. J., Hengstenberg, A., Quinto, M., Kurzawa, C., Koudelka-Hep, M., Schuhmann, W. Localized visualization of chemical cross-talk in microsensor arrays by using scanning electrochemical microscopy. *Mikrochim Acta* 1999, 131, 47–55.
87. Ratcliff, B. B., Klancke, J. W., Koppang, M. D., Engstrom, R. C. Microderivatization of anodized glassy carbon. *Anal Chem* 1996, 68, 2010–2014.
88. Nowall, W. B., Dontha, N., Kuhr, W. G. Electron transfer kinetics at a biotin/avidin patterned glassy carbon electrode. *Biosens Bioelectron* 1998, 13, 1237–1244.
89. Wittstock, G., Emons, H., Kummer, M., Kirchhoff, J. R., Heineman, W. R. Application of scanning electrochemical microscopy and scanning electron microscopy for the characterization of carbon-spray modified electrodes. *Fresenius J Anal Chem* 1994, 348, 712–718.
90. Kranz, C., Ludwig, M., Gaub, H. E., Schuhmann, W. Lateral deposition of polypyrrole lines over insulating gaps. Towards the development of polymer-based electronic devices. *Adv Mater* 1995, 7, 568–571.
91. Kranz, C., Ludwig, M., Gaub, H. E., Schuhmann, W. Lateral deposition of polypyrrole lines by means of the scanning electrochemical microscope. *Adv Mater* 1995, 7, 38–40.
92. Schuhmann, W., Kranz, C., Wohlschläger, H., Strohmeier, J. Pulse technique for the electrochemical deposition of polymer films on electrode surfaces. *Biosens Bioelectron* 1997, 12, 1157–1167.
93. Chen, P.-C., Chen, R. L. C., Cheng, T.-J., Wittstock, G. Localized deposition of chitosan as matrix for enzyme immobilization. *Electroanalysis* 2009, 21, 804–810.
94. Kurzawa, C., Hengstenberg, A., Schuhmann, W. Immobilization method for the preparation of biosensors based on pH shift-induced deposition of biomolecule-containing polymer films. *Anal Chem* 2002, 74, 355–361.
95. Wilhelm, T., Wittstock, G. Localised electrochemical desorption of gold alkanethiolate monolayers by means of scanning electrochemical microscopy (SECM). *Mikrochim Acta* 2000, 133, 1–9.
96. Wilhelm, T., Wittstock, G. Patterns of functional proteins formed by local electrochemical desorption of self-assembled monolayers. *Electrochim Acta* 2001, 47, 275–281.

97. Wilhelm, T., Wittstock, G. Analysis of interaction in patterned multienzyme layers by using scanning electrochemical microscopy. *Angew Chem Int Ed* 2003, 42, 2247–2250.
98. Shiku, H., Uchida, I., Matsue, T. Microfabrication of alkylsilanized glass substrate by electrogenerated hydroxyl radical using scanning electrochemical microscopy. *Langmuir* 1997, 13, 7239–7244.
99. Zhao, C., Zawisza, I., Nullmeier, M., Burchardt, M., Träuble, M., Witte, I., Wittstock, G. Microelectrochemical modulation of micropatterned cellular environments. *Langmuir* 2008, 24, 7605–7613.
100. Nowall, W. B., Wipf, D. O., Kuhr, W. G. Localized avidin/biotin derivatization of glassy carbon electrodes using SECM. *Anal Chem* 1998, 70, 2601–2606.
101. O'Brien, J. C., Shumaker-Parry, J., Engstrom, R. C. Microelectrode control of surface-bound enzymatic activity. *Anal Chem* 1998, 70, 1307–1311.
102. Schalkhammer, T., Mann-Buxbaum, E., Pittner, F., Urban, G. Electrochemical glucose sensors on permselective nonconducting substituted pyrrole polymers. *Sens Actuat B* 1991, B4, 273–281.
103. Wilhelm, T., Wittstock, G. Generation of periodic enzyme patterns by soft lithography and activity imaging by scanning electrochemical microscopy. *Langmuir* 2002, 18, 9485–9493.
104. Luo, H. Q., Shiku, H., Kumagai, A., Takahashi, Y., Yasukawa, T., Matsue, T. Microcontact printed diaphorase monolayer on glass characterized by atomic force microscopy and scanning electrochemical microscopy. *Electrochem Commun* 2007, 9, 2703–2708.
105. Glidle, A., Yasukawa, T., Hadyoon, C. S., Anicet, N., Matsue, T., Nomura, M., Cooper, J. M. Analysis of protein adsorption and binding at biosensor polymer interfaces using X-ray photon spectroscopy and scanning electrochemical microscopy. *Anal Chem* 2003, 75, 2559–2570.
106. Oyamatsu, D., Kanaya, N., Shiku, H., Nishizawa, M., Matsue, T. Electrochemical/photochemical formation of enzyme patterns on glass substrates using a scanning electrochemical/confocal microscope. *Sens Actuat B* 2003, B91, 199–204.
107. Mosbach, M., Zimmermann, H., Laurell, T., Nilsson, J., Csöregi, E., Schuhmann, W. Picodroplet-deposition of enzymes on functionalized self-assembled monolayers as a basis for miniaturized multisensor structures. *Biosens Bioelectron* 2001, 16, 827–837.
108. Gaspar, S., Mosbach, M., Wallman, L., Laurell, T., Csöregi, E., Schuhmann, W. A method for the design and study of enzyme microstructures formed by means of a flow-through microdispenser. *Anal Chem* 2001, 73, 4254–4261.
109. Hirano, Y., Oyamatsu, D., Nishizawa, M., Matsue, T. SECM imaging of protein micropatterns prepared by using a conventional ink-jet printer. *Chem Sens* 2002, 18, 121–123.
110. Turcu, F., Hartwich, G., Schaefer, D., Schuhmann, W. Ink-jet microdispensing for the formation of gradients of immobilised enzyme activity. *Macromol Rapid Commun* 2005, 26, 325–330.
111. Maciejewska, M., Schäfer, D., Schuhmann, W. SECM visualization of spatial variability of enzyme–polymer spots. Part 2: Complex interference elimination by means of selection of highest sensitivity sensor substructures and artificial neural networks. *Electroanalysis* 2006, 18, 1916–1928.
112. Schaefer, D., Maciejewska, M., Schuhmann, W. SECM visualization of spatial variability of enzyme–polymer spots. *Biosens Bioelectron* 2007, 22, 1887–1895.
113. Hussien, E. M., Erichsen, T., Schuhmann, W., Maciejewska, M. SECM visualization of the spatial variability of enzyme–polymer spots. 3. Enzymatic feedback mode. *Anal Bioanal Chem* 2008, 391, 1773–1782.
114. Kasai, S., Hirano, Y., Motochi, N., Shiku, H., Nishizawa, M., Matsue, T. Simultaneous detection of uric acid and glucose on a dual-enzyme chip using scanning electrochemical microscopy/scanning chemiluminescence microscopy. *Anal Chim Acta* 2002, 458, 263–270.
115. Tian, Z., Fen, Z., Tian, Z., Zhuo, X., Mu, J., Li, C., Lin, H., Ren, B., Xie, Z., Hu, W. Confined etchant layer technique for two-dimensional lithography at high resolution using electrochemical scanning tunnelling microscopy. *Faraday Discuss* 1992, 94, 37–44.
116. Engstrom, R. C., Small, B., Kattan, L. Observation of microscopically local electron-transfer kinetics with scanning electrochemical microscopy. *Anal Chem* 1992, 64, 241–244.
117. Rodriguez-Lopez, J., Alpuche-Aviles, M. A., Bard, A. J. Selective insulation with poly(tetrafluoroethylene) of substrate electrodes for electrochemical background reduction in scanning electrochemical microscopy. *Anal Chem* 2008, 80, 1813–1818.
118. Eckhard, K., Chen, X., Turcu, F., Schuhmann, W. Redox competition mode of scanning electrochemical microscopy (RC-SECM) for visualisation of local catalytic activity. *Phys Chem Chem Phys* 2006, 8, 5359–5365.
119. Karnicka, K., Eckhard, K., Guschin, D. A., Stoica, L., Kulesza, P. J., Schuhmann, W. Visualisation of the local bio-electrocatalytic activity in biofuel cell cathodes by means of redox competition scanning electrochemical microscopy (RC-SECM). *Electrochem Commun* 2007, 9, 1998–2002.

120. Solomon, E. I., Sundaram, U. M., Machonkin, T. E. Multicopper oxidases and oxygenases. *Chem Rev* 1996, 96, 2563–2603.
121. Szot, K., Nogala, W., Niedziolka-Jonsson, J., Joensson-Niedziolka, M., Marken, F., Rogalski, J., Kirchner, C. N., Wittstock, G., Opallo, M. Hydrophilic carbon nanoparticle-laccase thin film electrode for mediatorless dioxygen reduction. *Electrochim Acta* 2009, 54, 4620–4625.
122. Nogala, W., Szot, K., Burchardt, M., Jonsson-Niedziolka, M., Rogalski, J., Wittstock, G., Opallo, M. Scanning electrochemical microscopy activity mapping of electrodes modified with laccase encapsulated in sol-gel processed matrix. *Bioelectrochemistry* 2010, 79, 101–107.
123. Nogala, W., Celebanska, A., Szot, K., Wittstock, G., Opallo, M. Bioelectrocatalytic mediatorless dioxygen reduction at carbon ceramic electrodes modified with bilirubin oxidase. *Electrochim Acta* 2010, 55, 5719–5724.
124. Nogala, W., Celebanska, A., Wittstock, G., Opallo, M. Bioelectrocatalytic carbon ceramic gas electrode for reduction of dioxygen and its application in a zinc-dioxygen cell. *Fuel Cells* 2010, 10, 1157–1163.
125. Bentley, D. R., Balasubramanian, S., Swerdlow, H. P., Smith, G. P., Milton, J., Brown, C. G., Hall, K. P., Evers, D. J., Barnes, C. L., Bignell, H. R., Boutell, J. M., Bryant, J., Carter, R. J., Cheetham, R. K., Cox, A. J., Ellis, D. J., Flatbush, M. R., Gormley, N. A., Humphray, S. J., Irving, L. J., Karbelashvili, M. S., Kirk, S. M., Li, H., Liu, X. H., Maisinger, K. S., Murray, L. J., Obradovic, B., Ost, T., Parkinson, M. L., Pratt, M. R., Rasolonjatovo, I. M. J., Reed, M. T., Rigatti, R., Rodighiero, C., Ross, M. T., Sabot, A., Sankar, S. V., Scally, A., Schroth, G. P., Smith, M. E., Smith, V. P., Spiridou, A., Torrance, P. E., Tzonev, S. S., Vermaas, E. H., Walter, K., Wu, X. L., Zhang, L., Alam, M. D., Anastasi, C., Aniebo, I. C., Bailey, D. M. D., Bancarz, I. R., Banerjee, S., Barbour, S. G., Baybayan, P. A., Benoit, V. A., Benson, K. F., Bevis, C., Black, P. J., Boodhun, A., Brennan, J. S., Bridgham, J. A., Brown, R. C., Brown, A. A., Buermann, D. H., Bundu, A. A., Burrows, J. C., Carter, N. P., Castillo, N., Catenazzi, M. C. E., Chang, S., Cooley, R. N., Crake, N. R., Dada, O. O., Diakoumakos, K. D., Dominguez-Fernandez, B., Earnshaw, D. J., Egbujor, U. C., Elmore, D. W., Etchin, S. S., Ewan, M. R., Fedurco, M., Fraser, L. J., Fajardo, K. V. F., Furey, W. S., George, D., Gietzen, K. J., Goddard, C. P., Golda, G. S., Granieri, P. A., Green, D. E., Gustafson, D. L., Hansen, N. F., Harnish, K., Haudenschild, C. D., Heyer, N. I., Hims, M. M., Ho, J. T., Horgan, A. M. et al. Accurate whole human genome sequencing using reversible terminator chemistry. *Nature* 2008, 456, 53–59.
126. Nakamura, N., Fukuda, T., Nonen, S., Hashimoto, K., Azuma, J., Gemma, N. Simple and accurate determination of CYP2D6 gene copy number by a loop-mediated isothermal amplification method and an electrochemical DNA chip. *Clin Chim Acta* 2010, 411, 568–573.
127. Jacobs, A. R., Panuganti, S., Babbar, N., Wang, Z., Headley, V., Liu, Y., Argueta, C., Richter, L., Liu, R., Longiaru, M. The eSENSOR (R) XT-8: Platform allows an increased menu to make complex molecular testing simple. *J Mol Diagn* 2009, 11, 670–671.
128. Lin, Z., Takahashi, Y., Kitagawa, Y., Umemura, T., Shiku, H., Matsue, T. An addressable microelectrode array for electrochemical detection. *Anal Chem* 2008, 80, 6830–6833.
129. Shiku, H., Hara, Y., Takeda, T., Matsue, T., Uchida, I. Microfabrication and characterization of solid pattern with enzymes or antigen-antibodies by scanning electrochemical microscopy. In *ACS Symposium Series 656*, Jerkiewicz, G., Soriaga, M. P., Uosaki, K., Wieckowski, A., Eds. American Chemical Society, Washington, DC, 1997.
130. Yasukawa, T., Hirano, Y., Motochi, N., Shiku, H., Matsue, T. Enzyme immunosensing of pepsinogens 1 and 2 by scanning electrochemical microscopy. *Biosens Bioelectron* 2007, 22, 3099–3104.
131. Wijayawardhana, C. A., Wittstock, G., Halsall, H. B., Heineman, W. R. Electrochemical immunoassay with microscopic immunomagnetic bead domains and scanning electrochemical microscopy. *Electroanalysis* 2000, 12, 640–644.
132. Zhao, C., Wittstock, G. An SECM detection scheme with improved sensitivity and lateral resolution: Detection of galactosidase activity with signal amplification by glucose dehydrogenase. *Angew Chem Int Ed* 2004, 43, 4170–4172.
133. Chang, C.-Y., Takahashi, Y., Murata, T., Shiku, H., Chang, H.-C., Matsue, T. Entrapment and measurement of a biologically functionalized microbead with a microwell electrode. *Lab Chip* 2009, 9, 1185–1192.
134. Sklyar, O., Träuble, M., Zhao, C., Wittstock, G. Modeling steady-state experiments with a scanning electrochemical microscope involving several independent diffusing species using the boundary element method. *J Phys Chem B* 2006, 110, 15869–15877.
135. Sklyar, O., Wittstock, G. Numerical simulations of complex nonsymmetrical 3D systems for scanning electrochemical microscopy using the boundary element method. *J Phys Chem B* 2002, 106, 7499–7508.
136. Nunes Kirchner, C., Szunerits, S., Wittstock, G. Scanning electrochemical microscopy (SECM) based detection of oligonucleotide hybridization and simultaneous determination of the surface concentration of immobilized oligonucleotides on gold. *Electroanalysis* 2007, 19, 1258–1267.

137. Szunerits, S., Bouffier, L., Calemczuk, R., Corso, B., Demeunynck, M., Descamps, E., Defontaine, Y., Fiche, J.-B., Fortin, E., Livache, T., Mailley, P., Roget, A., Vieil, E. Comparison of different strategies on DNA chip fabrication and DNA-sensing: Optical and electrochemical approaches. *Electroanalysis* 2005, 17, 2001–2017.
138. Liu, B., Bard, A. J., Li, C.-Z., Kraatz, H.-B. Scanning electrochemical microscopy. 51. Studies of self-assembled monolayers of DNA in the absence and presence of metal ions. *J Phys Chem B* 2005, 109, 5193–5198.
139. Zhang, Z., Zhou, J., Tang, A., Wu, Z., Shen, G., Yu, R. Scanning electrochemical microscopy assay of DNA based on hairpin probe and enzymatic amplification biosensor. *Biosens Bioelectron* 2010, 25, 1953–1957.
140. Ferreyra, N. F., Bollo, S., Rivas, G. A. Self-assembled multilayers of polyethylenimine, DNA and gold nanoparticles. A study of electron transfer reaction. *J Electroanal Chem* 2010, 638, 262–268.
141. Wang, J., Song, F., Zhou, F. Silver-enhanced imaging of DNA hybridization at DNA microarrays with scanning electrochemical microscopy. *Langmuir* 2002, 18, 6653–6658.
142. Turcu, F., Schulte, A., Hartwich, G., Schuhmann, W. Imaging immobilised ssDNA and detecting DNA hybridisation by means of the repelling mode of scanning electrochemical microscopy (SECM). *Biosens Bioelectron* 2004, 20, 925–932.
143. Turcu, F., Schulte, A., Hartwich, G., Schuhmann, W. Label-free electrochemical recognition of DNA hybridization by means of modulation of the feedback current in SECM. *Angew Chem Int Ed* 2004, 43, 3482–3485.
144. Diakowski, P. M., Kraatz, H.-B. Detection of single-nucleotide mismatches using scanning electrochemical microscopy. *Chem Commun* 2009, 1189–1191.
145. Roberts, W. S., Davis, F., Higson, S. P. J. Scanning electrochemical microscopy of genomic DNA microarrays-study of adsorption and subsequent interactions. *Analyst (Cambridge, U.K.)* 2009, 134, 1302–1308.
146. Uetsuka, H., Yang, N., Tokuda, N., Nebel, C. E. Electrochemical microscopy analysis of biofunctionalized diamond surfaces. In *Diamond Electronics—Fundamentals to Applications II*, Nebel, C. E., Jackman, R. B., Nemanich, R. J., Nesladek, M., Eds. Materials Research Society, Warrendale, PA, 2008, Vol. 1039, pp. 195–200.
147. Nakano, K., Nakamura, K., Iwamoto, K., Soh, N., Imato, T. Positive-feedback-mode scanning electrochemical microscopy imaging of redox-active DNA–poly(1,4-benzoquinone) conjugate film deposited on carbon fiber electrode for micrometer-sized hybridization biosensor applications. *J Electroanal Chem* 2009, 628, 113–118.
148. Yamashita, K., Takagi, M., Uchida, K., Kondo, H., Takenaka, S. Visualization of DNA microarrays by scanning electrochemical microscopy (SECM). *Analyst* 2001, 126, 1210–1211.
149. Komatsu, M., Yamashita, K., Uchida, K., Kondo, H., Takenaka, S. Imaging of DNA microarray with scanning electrochemical microscopy. *Electrochim Acta* 2006, 51, 2023–2029.
150. Takenaka, S. Highly sensitive probe for gene analysis by electrochemical approach. *Bull Chem Soc Jpn* 2001, 74, 217–224.
151. Wang, J., Zhou, F. Scanning electrochemical microscopic imaging of surface-confined DNA probes and their hybridization via guanine oxidation. *J Electroanal Chem* 2002, 537, 95–102.
152. Gorodetsky, A. A., Hammond, W. J., Hill, M. G., Slowinski, K., Barton, J. K. Scanning electrochemical microscopy of DNA monolayers modified with Nile Blue. *Langmuir* 2008, 24, 14282–14288.
153. Lie, L. H., Mirkin, M. V., Hakkarainen, S., Houlton, A., Horrocks, B. R. Electrochemical detection of lateral charge transport in metal complex–DNA monolayers synthesized on Si(111) electrodes. *J Electroanal Chem* 2007, 603, 67–80.
154. Lie, L. H., Patole, S. N., Pike, A. R., Ryder, L. C., Connolly, B. A., Ward, A. D., Tuite, E. M., Houlton, A., Horrocks, B. R. Immobilisation and synthesis of DNA on Si(111), nanocrystalline porous silicon and silicon nanoparticles. *Faraday Discuss* 2004, 125, 235–249; discussion 293–309.
155. Patole, S. N., Pike, A. R., Connolly, B. A., Horrocks, B. R., Houlton, A. STM study of DNA films synthesized on Si(111) surfaces. *Langmuir* 2003, 19, 5457–5463.
156. Shiku, H., Takeda, M., Murata, T., Akiba, U., Hamada, F., Matsue, T. Development of electrochemical reporter assay using HeLa cells transfected with vector plasmids encoding various responsive elements. *Anal Chim Acta* 2009, 640, 87–92.
157. Nagamine, K., Onodera, S., Kurihara, A., Yasukawa, T., Shiku, H., Asano, R., Kumagai, I., Matsue, T. Electrochemical screening of recombinant protein solubility in *Escherichia coli* using scanning electrochemical microscopy (SECM). *Biotechnol Bioeng* 2007, 96, 1008–1013.

158. Kasai, S., Shiku, H., Torisawa, Y.-S., Nagamine, K., Yasukawa, T., Watanabe, T., Matsue, T. Cytokine assay on a cellular chip by combining collagen gel embedded culture with scanning electrochemical microscopy. *Anal Chim Acta* 2006, 566, 55–59.
159. Torisawa, Y.-S., Kaya, T., Takii, Y., Oyamatsu, D., Nishizawa, M., Matsue, T. Scanning electrochemical microscopy-based drug sensitivity test for a cell culture integrated in silicon microstructures. *Anal Chem* 2003, 75, 2154–2158.
160. Torisawa, Y.-S., Shiku, H., Kasai, S., Nishizawa, M., Matsue, T. Proliferation assay on a silicon chip applicable for tumors extirpated from mammalians. *Int J Cancer* 2004, 109, 302–308.
161. Torisawa, Y.-S., Shiku, H., Yasukawa, T., Nishizawa, M., Matsue, T. Multi-channel 3-D cell culture device integrated on a silicon chip for anticancer drug sensitivity test. *Biomaterials* 2005, 26, 2165–2172.
162. Kaya, T., Nagamine, K., Matsui, N., Yasukawa, T., Shiku, H., Matsue, T. On-chip electrochemical measurement of β-galactosidase expression using a microbial chip. *Chem Commun* 2004, 248–249.
163. Torisawa, Y.-S., Ohara, N., Nagamine, K., Kasai, S., Yasukawa, T., Shiku, H., Matsue, T. Electrochemical monitoring of cellular signal transduction with a secreted alkaline phosphatase reporter system. *Anal Chem* 2006, 78, 7625–7631.
164. Ogasawara, D., Hirano, Y., Yasukawa, T., Shiku, H., Kobori, K., Ushizawa, K., Kawabata, S., Matsue, T. Electrochemical microdevice with separable electrode and antibody chips for simultaneous detection of pepsinogens 1 and 2. *Biosens Bioelectron* 2006, 21, 1784–1790.
165. Shiku, H., Goto, S., Jung, S., Nagamine, K., Koide, M., Itayama, T., Yasukawa, T., Matsue, T. Electrochemical characterization of enzymatic activity of yeast cells entrapped in a poly(dimethylsiloxane) microwell on the basis of limited diffusion system. *Analyst* 2009, 134, 182–187.
166. Kaji, H., Hashimoto, M., Nishizawa, M. On-demand patterning of protein matrixes inside a microfluidic device. *Anal Chem* 2006, 78, 5469–5473.
167. Kaji, H., Kawashima, T., Nishizawa, M. Patterning cellular motility using an electrochemical technique and a geometrically confined environment. *Langmuir* 2006, 22, 10784–10787.
168. Zhang, M., Wittstock, G., Shao, Y., Girault, H. H. Scanning electrochemical microscopy as a readout tool for protein electrophoresis. *Anal Chem* 2007, 79, 4833–4839.
169. Carano, M., Lion, N., Abid, J.-P., Girault, H. H. Detection of proteins on poly(vinylidene difluoride) membranes by scanning electrochemical microscopy. *Electrochem Commun* 2004, 6, 1217–1221.
170. Carano, M., Lion, N., Girault, H. H. Detection of proteins on membranes and in microchannels using copper staining combined with scanning electrochemical microscopy. *J Electroanal Chem* 2007, 599, 349–355.
171. Cortes-Salazar, F., Busnel, J.-M., Li, F., Girault, H. H. Adsorbed protein detection by scanning electrochemical microscopy. *J Electroanal Chem* 2009, 635, 69–74.
172. Zhang, M., Becue, A., Prudent, M., Champod, C., Girault, H. H. SECM imaging of MMD-enhanced latent fingermarks. *Chem Commun* 2007, 3948–3950.
173. Cortes-Salazar, F., Zhang, M., Becue, A., Busnel, J.-M., Prudent, M., Champod, C., Girault, H. H. Human fingerprint imaging by scanning electrochemical microscopy (SECM). *Chimia* 2009, 63, 580.
174. Macpherson, J. V., O'Hare, D., Unwin, P. R., Winlove, C. P. Quantitative spatially resolved measurements of mass transfer through laryngeal cartilage. *Biophys J* 1997, 73, 2771–2781.
175. Macpherson, J. V., Beeston, M. A., Unwin, P. R., Hughes, N. P., Littlewood, D. Scanning electrochemical microscopy as a probe of local fluid flow through porous solids. *J Chem Soc Faraday Trans 1* 1995, 91, 1407–1410.
176. Scott, E. R., Phipps, J. B., White, H. S. Direct imaging of molecular transport through skin. *J Invest Dermatol* 1995, 104, 142–145.
177. Dzekunov, S. M., Antonenko, Y. N. Dynamics of formation and dissipation of local pH gradients in the unstirred layers near bilayer lipid membranes. *Bioelectrochem Bioenerg* 1996, 41, 187–190.
178. Pohl, P., Saparov, S. M., Antonenko, Y. N. The effect of a transmembrane osmotic flux on the ion concentration distribution in the immediate membrane vicinity measured by microelectrodes. *Biophys J* 1997, 72, 1711–1718.
179. Antonenko, Y. N., Pohl, P., Denisov, G. A. Permeation of ammonia across bilayer lipid membranes studied by ammonium ion selective microelectrodes. *Biophys J* 1997, 72, 2187–2195.
180. Wittstock, G., Burchardt, M., Pust, S. E., Shen, Y., Zhao, C. Scanning electrochemical microscopy for direct imaging of reaction rates. *Angew Chem Int Ed* 2007, 46, 1584–1617.
181. Hess, C., Borgwarth, K., Ricken, C., Ebling, D. G., Heinze, J. Scanning electrochemical microscopy: Study of silver deposition on non-conducting substrates. *Electrochim Acta* 1997, 42, 3065–3073.

182. Wipf, D. O., Bard, A. J. Scanning electrochemical microscopy. 15. Improvements in imaging via tip-position modulation and lock-in detection. *Anal Chem* 1992, 64, 1362–1367.
183. Yu, E. H., Scott, K. Enzymatic biofuel cells—Fabrication of enzyme electrodes. *Energies* 2010, 3, 23–42.
184. Wittstock, G., Gründig, B., Strehlitz, B., Zimmer, K. Evaluation of microelectrode arrays for amperometric detection by scanning electrochemical microscopy. *Electroanalysis* 1998, 10, 526–531.
185. Wilhelm, T., Wittstock, G., Szargan, R. Scanning electrochemical microscopy of enzymes immobilized on structured glass–gold substrates. *Fresenius J Anal Chem* 1999, 365, 163–167.
186. Meyer, H., Drewer, H., Gründig, B., Cammann, K., Kakerow, R., Manioli, Y., Mokwa, W., Rospert, M. Two-dimensional imaging of O_2, H_2O_2, and glucose distributions by an array of 400 individually addressable microelectrodes. *Anal Chem* 1995, 67, 1164–1170.
187. Cortes-Salazar, F., Trauble, M., Li, F., Busnel, J.-M., Gassner, A.-L., Hojeij, M., Wittstock, G., Girault, H. H. Soft stylus probes for scanning electrochemical microscopy. *Anal Chem* 2009, 81, 6889–6896.
188. Kovacs, B., Csoka, B., Nagy, G., Kapui, I., Gyurcsanyi, R. E., Toth, K. Automatic target location strategy-a novel approach in scanning electrochemical microscopy. *Electroanalysis* 1999, 11, 349–355.
189. Cortes-Salazar, F., Momotento, D., Girault, H. H., Lesch, A., Wittstock, G. Seeing big with scanning electrochemical microscopy. *Anal Chem* 2011, 83, 1493–1499.

12 Scanning Electrochemical Microscopy of Living Cells

Janine Mauzeroll and Steen B. Schougaard

CONTENTS

12.1 Electrochemical Methods Used to Study Processes Occurring in Living Systems 379
12.2 SECM in the Realm of the Living 380
12.2.1 SECM Studies in the Bacteria Domain 381
12.2.1.1 SECM Studies of *Staphylococcus aureus* 382
12.2.1.2 SECM Studies of *Rhodobacter sphaeroides* 382
12.2.1.3 SECM Studies of *Paracoccus denitrificans* 383
12.2.1.4 SECM Studies of *Salmonella typhimurium* 383
12.2.1.5 SECM Studies of *Escherichia coli* 384
12.2.2 SECM Studies in the Eukarya Domain 387
12.2.2.1 Intracellular Measurements 388
12.2.2.2 Single Cell Measurements 388
12.2.2.3 Multicell Measurements 404
12.3 SECM Studies in the Future 409
Acknowledgment 411
References 411

12.1 ELECTROCHEMICAL METHODS USED TO STUDY PROCESSES OCCURRING IN LIVING SYSTEMS

In recent years, scanning electrochemical microscopy (SECM) has been applied increasingly to the study of biological systems. In contrast to Chapter 10, which focused on the biotechnological applications of SECM, Chapter 12 describes SECM studies performed on *living* systems.

SECM is by no means the only electrochemical method developed to study processes occurring in biological systems. Amperometric measurements at microelectrodes roughly positioned into, next to, or onto cells have been performed since the mid-1970s.[1] Such measurements enabled in-depth electrochemical studies of neurotransmitter release in the brain, in brain slices, and on adhered neurons, and are still ongoing.[2–4] These studies sparked considerable research interest thereby leading to microelectrodes being increasingly applied to monitoring the dynamic release of molecules, such as catecholamines, insulin, and anticancer drugs, from living cells.[2,3,5–8]

There are several similarities between the classical amperometric and voltammetric measurements performed at microelectrodes and the substrate generation–tip collection modes of SECM, for example, in both cases, a microelectrode in close proximity to a cell membrane is used to oxidize (or reduce) the molecules ejected from the cell to obtain information on cellular functions at the single cell level. However, the use of a SECM provides additional dimensions through the feedback and imaging modes. Such measurements are crucial in establishing SECM as a quantitative bioanalytical microscopy and its ability to perform time-lapse cell response measurements. As such, Chapter 12 focuses exclusively on SECM studies performed on *living* systems.

12.2 SECM IN THE REALM OF THE LIVING

Before embarking on the detailed work on SECM of living systems, it is instructive to first examine how biologists organize the realm of the living. The classification of living systems is described by taxonomy, which strives to organize the profound differences between life forms in terms of hierarchized or interrelated taxa. Although the classification of the periodic table was controversial in its time, chemists must humbly accept that this pales in comparison with the controversy that surrounds the three of life.

To portray the variety and classify living systems, evolution processes must be considered and this has tormented several generations of scientists. In recent years, the development of an evolutionary theory based on molecular phylogenetics has emerged. As it now stands, molecular phylogenetics has transformed taxonomy into a quantitative experimental science, which allows for a new description of living systems brought forth by an enhanced understanding of microbial life (Figure 12.1a).

This implies that classical prokaryote and eukaryote denomination (Figure 12.1b) is slowly being replaced by a universal tree based on a Bacteria, Eukarya, and Archaea classification. The Bacteria domain regroups organisms such as the Thermotogales, flavobacteria and relatives, the cyanobacteria, the purple bacteria, the gram-positive bacteria, and the green non-sulfur bacteria. These organisms represent the more "traditional" bacterial community. The Eukarya domain includes organisms such as the animals, ciliates, green plants, fungi, flagellates, and microsporidia. The Archaea domain defines a "special" group of bacteria that were defined following extensive genetic profiling. They include the kingdom Crenarchaeota, the genus *Pyrodictium*, the genus *Thermoproteus*, the kingdom Euryarchaeota, the Thermococcales, the Methanococcales, the Methanobacteriales, the Methanomicrobiales, and the extreme halophiles.[10]

The reach of SECM studies in the realm of the living only covers a very restricted section. Grossly speaking, SECM studies have looked at a limited number of organisms included in the Eukarya and Bacteria domains (Figure 12.1a), and these are discussed in detail in the following sections. No SECM studies in the Archaea domain have been performed as of yet. This would be a very interesting area for SECM studies to be performed as this domain includes extreme bacteria. For example, the methanogens, because of their use of CO_2 and the halophiles and because of their simple photosynthetic "proton battery", would be well suited for SECM studies. Also, all Archaea organisms possess in their membrane unique lipids composed of either diphytanyl glycerol diethers or tetraethers. SECM would be the technique of choice for the transport studies related to these lipids, due to its ability to evaluate permeability coefficients with good special resolution.

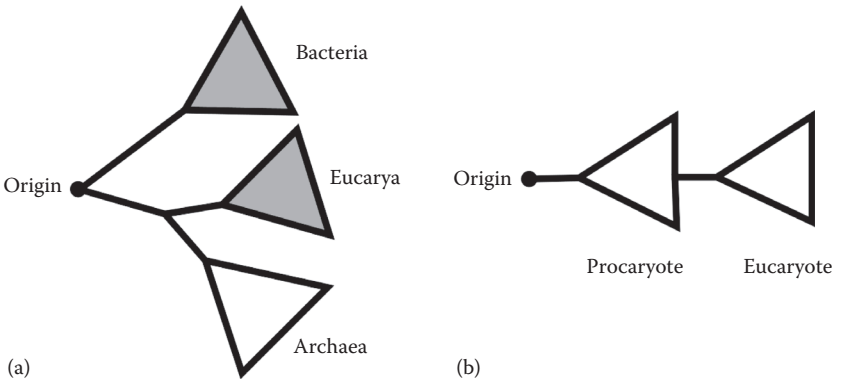


FIGURE 12.1 Two adapted models for the tree of life based on a phylogenetic organization. The wedges represent relatedness groups of organisms based on the work by Norman Pace, "The molecular tree of life changes how we see, teach microbial diversity." (a) three-domain model and (b) procaryote-eucaryote model. (From Pace, N.R., *Microbe*, 3, 15, 2008.) The gray wedges represent areas where SECM studies have been performed.

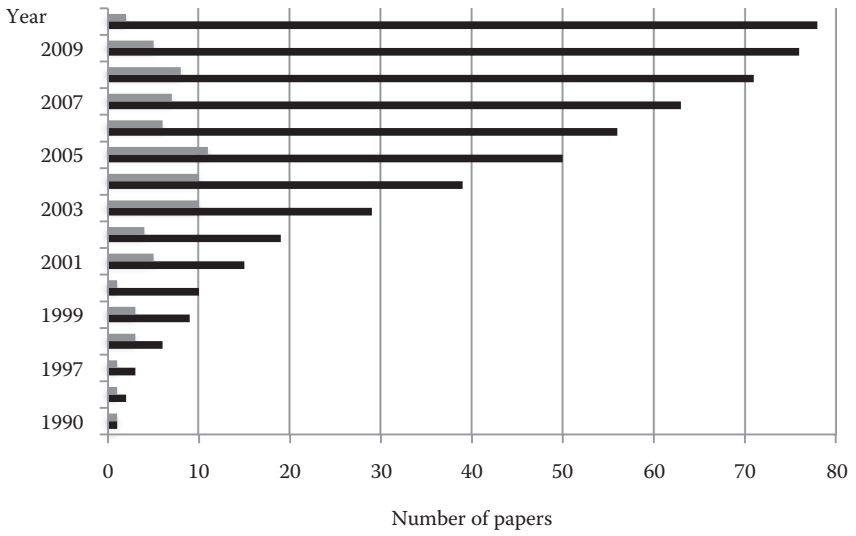


FIGURE 12.2 Cumulative publications (black) and annual publications (gray) of SECM studies of processes occurring in living systems.

In spite of the limited number of domains studied to date, Figure 12.2 demonstrates that application of SECM to living systems is truly an emerging research field.

The earliest report of SECM applied to living systems dates back to 1990. In this work, Lee et al.[11] described how SECM could be used to image the topography and photosynthetic activity of grass leaf with open stomata structures. Progressively, SECM has been used to quantify and image the chemical reactivity of various living systems, which in 2010 roughly amounted to 81 publications directly related to the field, and an annual median number of published manuscripts of 5. There have also been several comprehensive reviews[12–25] and book chapters[26,27] devoted to different aspects of biological SECM.

12.2.1 SECM Studies in the Bacteria Domain

SECM studies in the Bacteria domain represent roughly 10% of the SECM work on living biological systems. These studies (Table 12.1) mainly focus on *Escherichia coli*, a purple sulfur bacteria,

TABLE 12.1
Summary of SECM Studies of Biological Processes Occurring in the Bacteria Domain

References	Domain	Kingdom	Gram	Name
[28]	Bacteria	Firmicutes	+	*Staphylococcus aureus*
[29]	Bacteria	Proteobacteria	n.a.	*Rhodobacter sphaeroides*
[30]	Bacteria	Proteobacteria	–	*Paracoccus denitrificans*
[31]	Bacteria	Proteobacteria	–	*Salmonella typhimurium*
[32–41]	Bacteria	Proteobacteria	–	*Escherichia coli*

Note: Reported works are organized based on the nature of the studied bacteria.

because there is a large knowledge base about this organism, which facilitates the expression of heterogeneous proteins and the development of plasmids. For these same reasons, *E. coli* is an ideal organism for testing new analytical technologies, such as SECM.

Other bacteria studied by SECM include *Staphylococcus aureus*, *Rhodobacter sphaeroides*, and *Paracoccus denitrificans. S. aureus* is a Gram-positive cluster-forming coccus. This bacterium is normally found in the human bacterial flora in the mucous membranes of our noses. The pathogen of humans causes a wide range of infections such as food poisoning. *R. sphaeroides* are purple bacteria (non-sulfur) capable of bacterial photosynthetic activity. Bacterial photosynthesis differs from oxygenic plant-type photosynthesis in several ways. Bacterial photosynthesis does not produce O_2 and only occurs under anaerobic conditions. Bacterial photosynthesis utilizes a type of chlorophyll distinctly different from chlorophyll a, and only one photosystem, photosystem I. The electron donor for bacterial photosynthesis is never H_2O but may be H_2, H_2S, S^o, or specific organic compounds. *P. denitrificans* has the ability to reduce nitrate to dinitrogen under anaerobic growth conditions. Easy to grow, it expresses a respiratory chain very similar to that of the eukaryotic mitochondrion. As such, *P. denitrificans* has been, and continues to be, an interesting subject for fundamental biochemical and bioenergetic studies of the aerobic electron transport chain. In fact, *P. denitrificans* is considered an excellent model for the mitochondrial respiratory chain.

SECM studies of bacterial substrates using *S. aureus*, *P. denitrificans*, *Salmonella typhimurium*, and *E. coli* relied on multicell measurements because the cell diameters of the bacteria range between 500 nm and 1 μm. In general, single bacteria studies are technically challenging because they require the timely use of small diameter probes that have to be precisely positioned over the bacteria using the SECM imaging mode. In comparison, larger diameter bacteria such as *R. sphaeroides* allow for single cell measurements to be performed with relative ease.[29]

12.2.1.1 SECM Studies of *Staphylococcus aureus*

Nagamine et al.[28] used SECM to study *S. aureus* trapped in nanoliter collagen-gel matrixes localized on a chip. In the presence of $Fe(CN)_6^{3-}$, the respiratory chain located within the cytoplasmic membrane of *S. aureus* cells produces $Fe(CN)_6^{4-}$, which can be monitored by the SECM tip. The authors found that the ferricyanide reduction activity in the *S. aureus*, an osmotolerant bacteria, is enhanced in response to high osmotic stress such as the presence of highly concentrated salts.

These results outline the sophisticated survival responses induced by bacteria when they are subjected to deleterious changes of pH, temperature, or osmotic pressure. Under stress, the bacterial defense mechanisms are tightly coupled to the cell's metabolism and homeostatic mechanisms. When stimulating the metabolism of *S. aureus* with D-(+)-glucose in the presence of highly concentrated salts, a significant current response is measured by SECM in spite of the low cytoplasmic membrane permeability to hydrophilic mediators, such as ferricyanide. One explanation for the presence of this current enhancement implies that the bacteria to survive the osmotic stress, changes the cytoplasmic membrane structure or membrane-associated protein profile to promote ferrocyanide production.

12.2.1.2 SECM Studies of *Rhodobacter sphaeroides*

Cai et al.[29] used SECM to probe the redox activity of purple bacteria (*R. sphaeroides*). The objective was to measure kinetic rates of transport and investigate the pathway of transmembrane charge transfer. To this end, the authors used a combination of hydrophilic and hydrophobic redox species to shuttle the electrons between the SECM tip electrode in solution and the redox centers inside the cells (Figure 12.3).

Based on the dependence of the SECM-derived rate constant on the formal potential and concentration of mediator species in solution, the permeability of the outer cell membrane to different ionic species and the intracellular redox properties were studied. For example, hydrophobic mediators, such as quinones, permeate both the outer and cytoplasmic membrane. The authors demonstrated that the effective concentration of intracellular redox centers capable of oxidizing menadiol was on

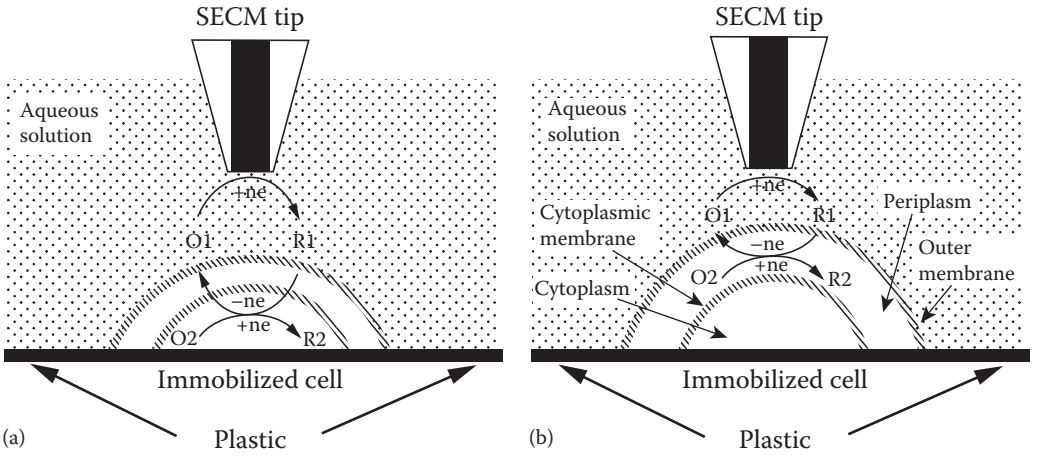


FIGURE 12.3 Schematic diagrams of the feedback mode SECM experiments with purple bacteria. (a) The tip is positioned in the solution close to the cell surface. A hydrophobic redox mediator (O1/R1) can cross both the outer cell membrane and the cytoplasmic membrane. Mediator species are regenerated via bimolecular ET reaction with cell-bound redox moieties (O2/R2). (b) Hydrophilic mediator species can permeate the outer membrane and enter the periplasm. (Reproduced from Cai, C. et al., *Anal. Chem*., 74, 114, 2002. With permission.)

the order of 50–100 μM, while the intracellular potential encountered by hydrophobic redox species was determined to be 90 mV vs. Ag/AgCl. Interestingly, a different behavior is observed for hydrophilic mediators, which are confined to the periplasmic space.

12.2.1.3 SECM Studies of *Paracoccus denitrificans*

Nagamine et al.[30] developed a microbial array chip similar in concept to the SECM studies performed on *S. aureus*. The SECM studies, which also relied on monitoring the ferrocyanide production from the bacteria, demonstrated that this production was dependent on the type of carbon source (glucose or lactate). They also showed and corroborated with enzyme assays that the enzymes affecting glucose catabolic reactions were significantly up-regulated in cultures with a nutrient agar medium containing D-(+)-glucose as a sole carbon source. As such, the electrochemical response of the microbial chip could be used as a vizualization tool that reflects the gene expression control in glucose catabolic pathway enzymes, specifically pyruvate kinase and enzymes of the overall Entner–Doudoroff pathway. The authors suggest that such microbial array chip could be widely applicable for screening bacterial metabolic characteristics that are regulated by environmental variations or imposed stress.

12.2.1.4 SECM Studies of *Salmonella typhimurium*

Matsui et al.[31] reported the development of an electrochemical microbial chip for mutagen screening, also using collagen-imbedded bacterial substrates. The chip was based on the bacteria *S. typhimurium* with a plasmid carrying a fusion gene used for the whole-cell mutagen sensor. The bacteria containing plasmids were submitted to mutagenic conditions in solutions containing 2-(2-furyl)-3-(5-nitro-2-furyl)acrylamido (AF-2), mitomycin C (MMC), or 2-aminoanthracene (2-AA). SECM measurements monitored the (β)-galactosidase expression of the bacteria using *p*-aminophenyl-(β)-D-galactopyranoside (PAPG) as the enzymatic substrate.

Figure 12.4 shows a schematic illustration of electrochemical mutagen screening using the microbial chip. TA1535 is a mutant strain of *S. typhimurium* that lacks a gene encoding for the DNA excision repair system. The *lacZ* gene is fused to *umuC* gene (*umuC*'–'*lacZ*) located downstream of the umu promoter in the plasmid pSK1002.[31] In the presence of mutagenic solutions, the UmuC'–'LacZ

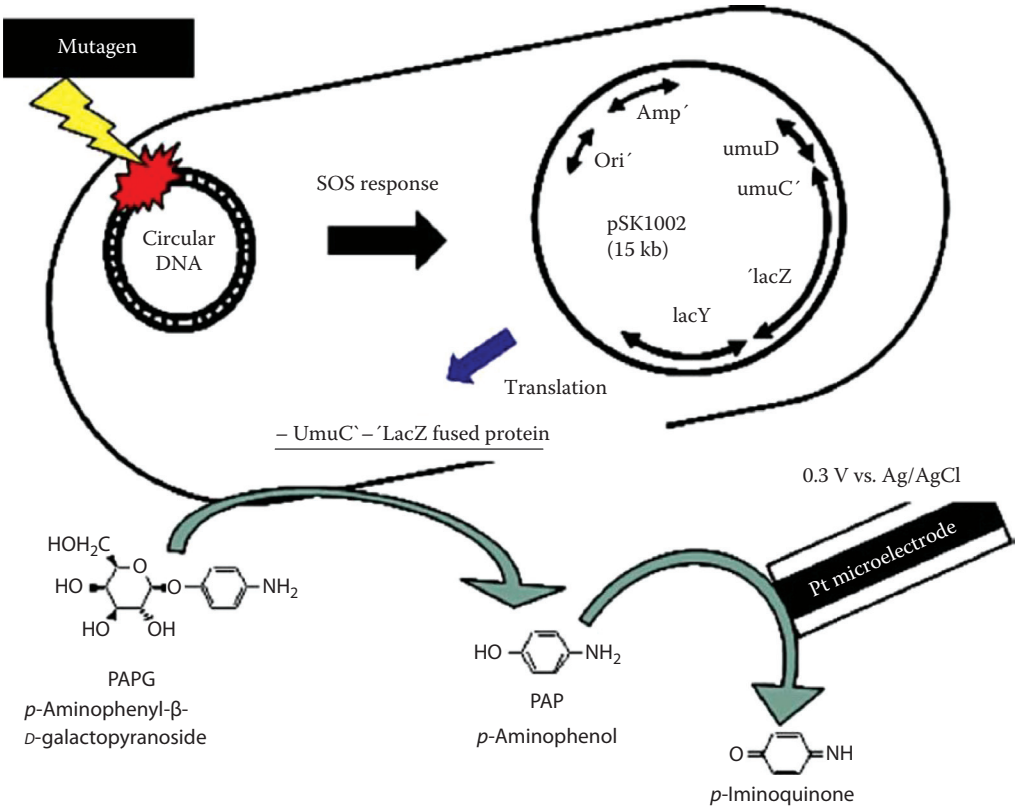


FIGURE 12.4 Schematic view of electrochemical mutagen screening using *S. typhimurium* TA1535/pSK1002. (Reproduced from Matsui, N. et al., *Biosens. Bioelectron*., 21, 1202, 2006. With permission.)

fusion protein is expressed, the (β)-galactosidase activity is electrochemically detected by monitoring the *p*-aminophenol (PAP) production from the PAPG hydrolysis reaction.

The electrochemical mutagen screening was performed on the microbial chip using SECM. In the presence of mutagenic solutions, different SECM responses are imaged as the Pt microelectrode is scanned horizontally across the chip (Figure 12.5).

12.2.1.5 SECM Studies of *Escherichia coli*

SECM measurements performed on *E. coli* containing substrates have targeted bacteria respiration; redox mediator interactions with bacteria or the relationship between SECM measured currents and protein activity.

12.2.1.5.1 Respiration Studies

In 2001, Kaya et al.[32] proposed a microbial chip for SECM bioassays. The chip was composed of *E. coli* spots on a polystyrene substrate. From the oxygen concentration measured by SECM over and around the spot, respiration activity was determined, assuming that the *E. coli* spot height was not dominant. The development of this bacterial microchip was applied to the study of bactericidal effects of antibiotics such as streptomycin and ampicillin.

The respiration activity microbial chip was extended to a similar collagen-imbedded architecture, as was described in the previous bacterial models in 2004.[36] The authors specifically analyzed oxygen (−0.5 V vs. Ag/AgCl) and ferrocyanide (0.6 V vs. Ag/AgCl) concentration profiles around the collagen-imbedded *E. coli* spots to establish the oxygen consumption and

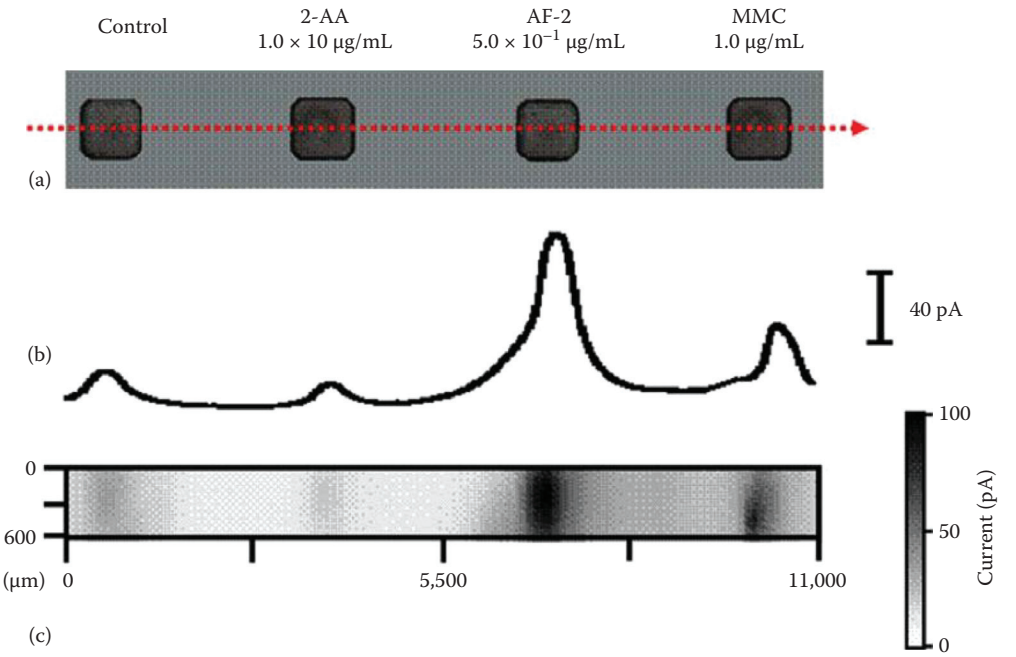


FIGURE 12.5 (a) Optical microscopic image, (b) the current response, and (c) SECM images of four arrayed *S. typhimurium* cell spots unexposed and exposed to 1.0 × 10 μg/mL 2-AA (in the absence of S9-mix), 5.0×10^{-1} μg/mL AF-2, and 1.0 μg/mL MMC. The SECM imaging was performed at 30 min after addition of 15.0 mM PAPG. (Reproduced from Matsui, N. et al., *Biosens. Bioelectron*., 21, 1202, 2006. With permission.)

ferrocyanide production rates. Given the geometrically controlled cone-shaped wells of the microchip, the authors were able to quantify the average ferrocyanide production rate of a single *E. coli* cell.

Oxygen consumption profiles often rely on the use of a Pt microelectrode as a working electrode. However in 2005, Holt and Bard proposed the use of a Clark microelectrode as working electrode in a SECM study investigating the toxicity of silver compounds in *E. coli* deposits.[33] In the Clark microelectrode, the respiration activity is monitored at a 25 μm Pt disk, immobilized behind an oxygen-permeable high-density polyethylene membrane, by measuring the solution oxygen concentration via the oxygen reduction current. The presence of the membrane is reported to increase the Pt microelectrode stability brought forth by reduced biofouling. The authors proceeded to acquire *E. coli* viability curves in the presence of different combinations of $AgNO_3$, glucose, and K^+, which were established based on the measured respiration activity. In this study, ferricyanide was also used as an alternate electron acceptor.

12.2.1.5.2 Redox Mediator Regeneration Studies

Similar to the study on *R. sphaeroides*, SECM is well suited to measure transport and investigate transport pathways in *E. coli*. To do so, a combination of hydrophilic and hydrophobic redox species may be used to shuttle the electrons between the SECM tip electrode noninvasively held in solution and the redox centers outside and inside *E. coli* (Figure 12.6). At present, the studies have often focused on the use of the ferricyanide and ferrocyanide couple.[33,36]

In their 2003 study, Kaya et al.[34] used a collagen-based microbial chip to map the localized concentration of ferrocyanide released from a population of ~100 *E. coli* cells. SECM was further used to acquire microbial growth curves that were corroborated by optical micrographs (Figure 12.7).

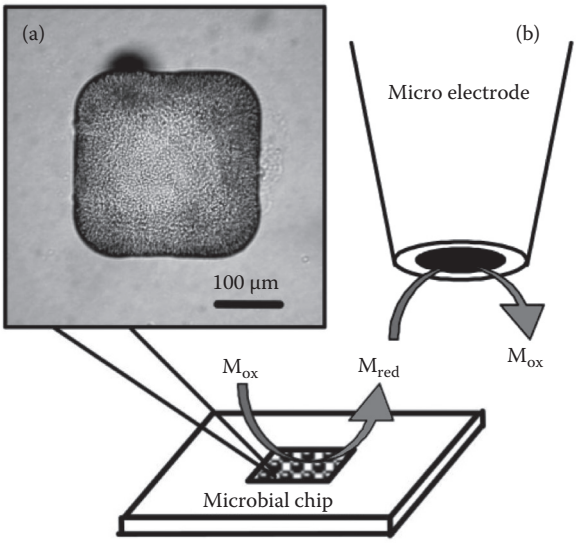


FIGURE 12.6 (a) Optical microscopic image of an *E. coli* collagen-gel microstructure. (b) The principle of SECM measurement using a mediator. M_{ox}: mediator oxidized form, M_{red}: mediator reduced form. (Kaya, T., Nagamine, K., Oyamatsu, D., Shiku, H., Nishizawa, M., Matsue, T. Fabrication of microbial chip using collagen gel microstructure, *Lab Chip*, 3, 313–317, 2003. Reproduced by permission of The Royal Society of Chemistry.)

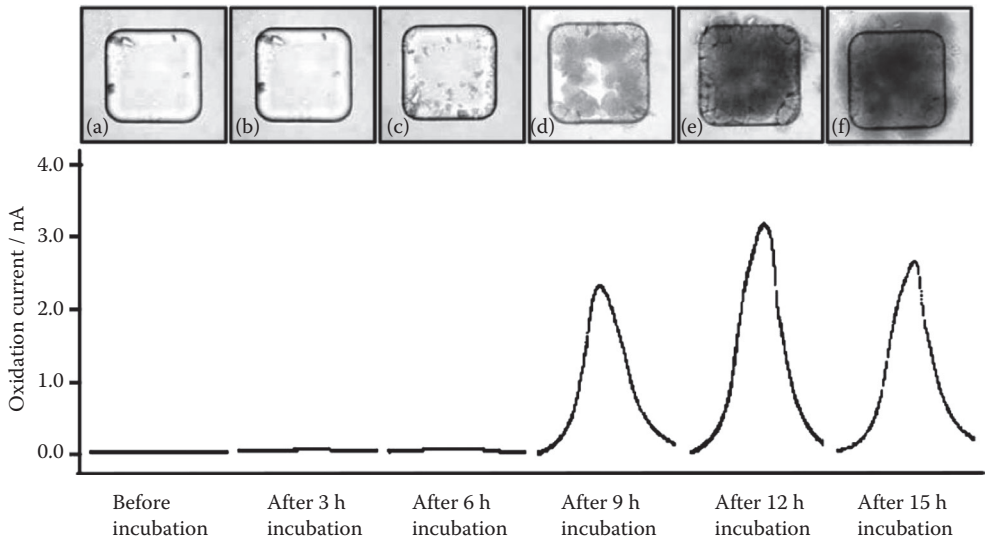


FIGURE 12.7 The current responses in a one-line scan at an *E. coli* microstructure with different times of on-chip incubation. The as-prepared collagen-gel microstructure embedded about 100 *E. coli* cells. The measurement solution was PBS buffer solution containing 5.0 mM ferricyanide and 20.0 mM D-(+)-glucose. (From Kaya, T., Nagamine, K., Oyamatsu, D., Shiku, H., Nishizawa, M., and Matsue, T., Fabrication of microbial chip using collagen gel microstructure, *Lab Chip*, 3, 313–317, 2003. Reproduced by permission of The Royal Society of Chemistry.)

12.2.1.5.3 Protein Activity Studies

With time, the microbial chip fabrication procedures have evolved enabling SECM studies of increasingly complex biological processes. Nagamine et al.[37] reported an on-chip transformation of *E. coli* cells. Their technique was based on soft lithographic processes, which were

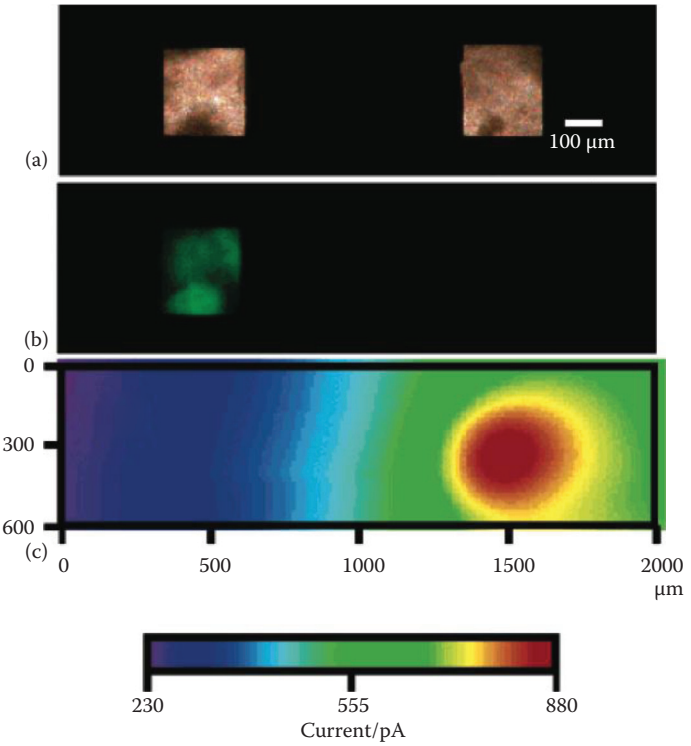


FIGURE 12.8 (a) Micrograph of the microbial array chip with two spots of *E. coli* transformed with pUC19 (right spot) and pUC-GFP (left spot), together with (b) a fluorescence and (c) SECM images of the same areas. (Reproduced from Nagamine, K. et al., *Anal. Chem*., 77, 4278, 2005. With permission.)

used to predeposit a selection of DNA plasmids at predefined locations on a silicon substrate. Subsequently, a PDMS microfluidic device was used to separate *E. coli* cells into segregated compartments, where parallel cell transformation took place. These transformations enabled SECM and fluorescent measurements capable of revealing phenotypic differences between two different DNA plasmids, pUC19 and pUC-GFP (Figure 12.8). Similar to the *Salmonella* study described earlier, the SECM measurement performed at a Pt microdisk relied on the (β)-galactosidase activity, which is electrochemically detected by monitoring the PAP production from the PAPG hydrolysis reaction.

More recently, a SECM study of *E. coli* was used to evaluate the solubility of recombinant proteins, based on the fusion of a β-galactosidase fragment to a maltose-binding protein.[38] The basis of the detection scheme is that if the maltose-binding protein remains in a soluble state, then β-galactosidase fragment is exposed and active. It therefore catalyzes the hydrolysis of PAPG to produce PAP, which is oxidized electrochemically at the microelectrode probe of the SECM. As a validation of the technique, oxidation current increases were linked with increase β-galactosidase activity of the soluble maltose-binding protein using classical Western blotting.

12.2.2 SECM Studies in the Eukarya Domain

SECM studies in the Eukarya domain represent the majority of the work published on living systems. Studies can further be distinguished based on whether the measurements are performed at the intracellular, the single cell, or the multicell level.

12.2.2.1 Intracellular Measurements

It is clear from the recent developments in nanoelectrode fabrication that our ability to perform intracellular SECM measurements should increase as the size of the probes decreases. Yet, this area of SECM research remains virtually unexplored with only a few reported examples.

Early on, Matsue et al. performed intracellular oxygen reduction measurements at an electrode inserted into a single algal protoplast.[42] Through the addition of an electron transport inhibitor (3-(3,4-dichlorophenyl)-1,1-dimethylurea), they observed decreased reduction current following light irradiation.

Twelve years later, Guo and Amemiya[43] studied the local permeability of the nuclear envelope from *Xenopus laevis* oocytes using feedback mode SECM. Based on the approach curves, it was established that the transport of redox molecules across the nuclear envelope membrane was diffusion limited. Chronoamperometry performed inside the nucleus suggested that the concentration and diffusion coefficient of the redox mediator is diminished in the intracellular environment. From fits of the experimental approach curves to theory, it was determined that the nuclear envelope membrane is more permeable than conventional bilayer lipid membranes. This enhancement in permeability is facilitated by the nuclear pore complex, which mediated molecular transport between the cytoplasm and the nucleus. Using a combination of electrochemical and fluorescence techniques, the flux through, the channel dimensions and transport function of the nuclear pore complex were further investigated. Interestingly, this study corroborated existing glass pipette and hourglass techniques that proposed that most nuclear pore complexes on the nucleus are open.

Gao et al.[44] used SECM coupled with an intracellular standard addition sampling method to quantify intracellular enzymatic activity. Based on the hydroquinone conversion by intracellular peroxidase, the produced benzoquinone is detected at a nearby gold microelectrode and imaged with a 2D scan. A standard addition calibration curve based on intracellular microinjections of horseradish peroxidase is then performed by recording the same SECM 2D scan following an injection. Using the peak current from both SECM 2D scans, they determine the enzyme activity. In general, this methodology could be applied to a variety of peroxidase enzymes that have hydrogen peroxide as a substrate.

Sun et al.[45] have used nanoelectrodes to spatially resolve electrochemical experiments in human breast epithelial cells. Using nanoelectrodes, the authors perforated a cell without killing it and were able to navigate the probe in the intracellular space. Using a combination of approach curve and intracellular voltammetric measurements, they measured the rate of transmembrane charge transport and membrane potential. In the future, establishing through electrochemical means the transmembrane potential should be of great interest because alterations in transmembrane potential are responsible for action potentials, which are crucial in neurotransmitter release.

12.2.2.2 Single Cell Measurements

SECM studies performed at the single cell level are the more predominant type of studies within the area of SECM research that focuses on living systems. Up to 2010, there were roughly 45 studies published: 5 used plants as substrate, 25 used human-based cells, and 15 used animal cells other than human. Within the plant studies, most works focus on marine alga *Bryopsis plumosa*. The most predominant human cell lines are breast epithelial (MCF-10A) and cervix carcinoma (HeLa). Rat-based cells, especially PC12 neurons, are the most prevalent nonhuman animal cell lines used as SECM substrate. As detailed in Table 12.2, it is clear that SECM measurements have not yet spread to a large pool of cell lines. Often times, the recurring cells lines are used by a few groups. This can be expected as the development of robust cell culturing and patterning procedures is time intensive and labor intensive. However, it does highlight a growing need in the years to come to cross-validate SECM results, especially within the context of quantitative measurements.

12.2.2.2.1 Single cell Measurements of Plants

SECM studies of plants were carried out early on because of the robustness of the plant substrates. In some of the earliest SECM studies on living systems, Tsionsky et al. performed the first SECM

TABLE 12.2
Summary of SECM Studies of Biological Processes Occurring in the Eukarya Domain

References	Substrate	Domain	Kingdom	Source	Cell Type
[42]	Intracellular	Eukarya	Plant	Algae	Marine alga *Bryopsis plumosa*
[43]	Intracellular	Eukarya	Animal	Frog	*Xenopus laevis* oocytes
[45]	Intracellular	Eukarya	Animal	Human	Breast epithelial (MCF-10A)
[44]	Intracellular	Eukarya	Animal	Human	Neutrophils
[46]	Single cell	Eukarya	Plant	Green plant	*Tradescantia fluminensis* Variegata
[47–49]	Single cell	Eukarya	Plant	Algae	Marine alga *Bryopsis plumosa*
[50]	Single cell	Eukarya	Animal	Leeches	Neurons (PC12)
[51]	Single cell	Eukarya	Animal	Mouse	Fibroblasts (CRL10225)
[52]	Single cell	Eukarya	Animal	Mouse	Leukemic monocyte macrophage
[53]	Single cell	Eukarya	Animal	Hamster	Chinese hamster ovary (CHO)
[54]	Single cell	Eukarya	Animal	Bovine	Chromaffin cells from adrenal glands
[55,56]	Single cell	Eukarya	Animal	Monkey	*Cercopithecus aethiops* kidneys (CV1 & COS-7)
[57]	Single cell	Eukarya	Animal	Rat	Newborn osteoclasts
[40,51,52, 58–62]	Single cell	Eukarya	Animal	Rat	Neurons (PC12) from adrenal medulla
[53]	Single cell	Eukarya	Animal	Human	Epidermoid carcinoma (A431)
[63]	Single cell	Eukarya	Animal	Human	Neutrophils
[64]	Single cell	Eukarya	Animal	Human	Gastric carcinoma (BGC-823)
[65]	Single cell	Eukarya	Animal	Human	Bladder carcinoma (T24)
[66]	Single cell	Eukarya	Animal	Human	Colon adenocarcinoma (SW-480)
[65]	Single cell	Eukarya	Animal	Human	Renal carcinoma (A498)
[67,68]	Single cell	Eukarya	Animal	Human	Human umbilical vein endothelial cells (HUVECs)
[69–71]	Single cell	Eukarya	Animal	Human	Hepatoblastoma (HepG2)
[70–78]	Single cell	Eukarya	Animal	Human	Cervix carcinoma (HeLa)
[51,79–84]	Single cell	Eukarya	Animal	Human	Breast epithelial (MCF-10A)
[85]	Multiple cells	Eukarya	Fungi	Yeast	*Saccharomyces cerevisiae*
[86]	Multiple cells	Eukarya	Plant	Algae	Marine alga *Bryopsis plumosa*
[87]	Multiple cells	Eukarya	Plant	Green plant	Spruce (*Picea abies*)
[88]	Multiple cells	Eukarya	Plant	Green plant	*Brassica juncea*
[89]	Multiple cells	Eukarya	Plant	Green plant	Somatic embryo-derived peanut leaf
[11]	Multiple cells	Eukarya	Plant	Green Plant	*Ligustrum sinensis* leaf
[90]	Multiple cells	Eukarya	Animal	Rat	Basophilic leukemia (RBL-2H3)
[90]	Multiple cells	Eukarya	Animal	Mink	Pulmonary epithelial
[90]	Multiple cells	Eukarya	Animal	Mouse	Leukemic monocyte macrophage
[86,91–95]	Multiple cells	Eukarya	Animal	Bovine	Single bovine embryos
[96]	Multiple cells	Eukarya	Animal	Human	Pancreatic islets
[97]	Multiple cells	Eukarya	Animal	Human	Erythroleukemia cell line (K562)
[98]	Multiple cells	Eukarya	Animal	Human	Promyelocytic leukemia (HL-60)
[39,99]	Multiple cells	Eukarya	Animal	Human	Fibroblast
[100,101]	Multiple cells	Eukarya	Animal	Human	Cervix carcinoma (HeLa)
[86,102,103]	Multiple cells	Eukarya	Animal	Human	Breast carcinoma (MCF-7)
[104–106]	Multiple cells	Eukarya	Animal	Human	Human umbilical vein endothelial cells (HUVECs)

Note: Reported works are organized based on the type of SECM substrate (intracellular, single cell, multiple cells), the source, and type of the studied cells.

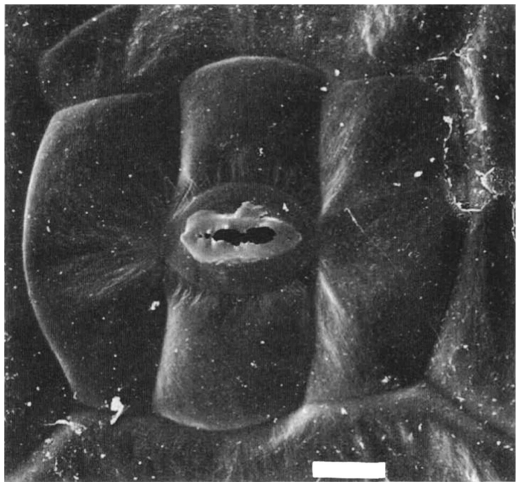


FIGURE 12.9 Scanning electron microscopy image of a stomatal complex of *Tradescantia fluminensis*. Bar = 20 µm. (Reproduced from Tsionsky, M. et al., *Plant Physiol*., 113, 895, 1997. With permission.)

study of an intact plant,[46] by using imaging to examine the topography and oxygen concentration profile of single guard cells (Figure 12.9). The topography of the guard cells is clearly observed in the negative feedback mode SECM images (Figure 12.10), in addition to the photosynthetic activity of guard cells under different light irradiation conditions (Figure 12.11).

Yasukawa et al. examined the permeation of several redox species ($Fe(CN)_6^{4-}$, $Fe(CN)_6^{3-}$, $Co(phen)_3^{2+}$, ferrocenylmethanol, and *p*-hydroquinone) through the cell membrane of a single algal protoplast.[47] The amperometric current was monitored at a Pt microelectrode, so that using approach curves, the permeability coefficients of the protoplast membrane as a function of the nature of the redox mediator could be determined. The same group also reported SECM studies relying on a dual Pt microelectrode to simultaneously study the interaction of two redox mediators with a single algal protoplast.[48] In this manner, the topographic profiles obtained by monitoring the feedback of $Fe(CN)_6^{4-}$ with the protoplast could be determined in parallel with the respiration activity based on the oxygen reduction. The photosynthetic activity of protoplast was further investigated using

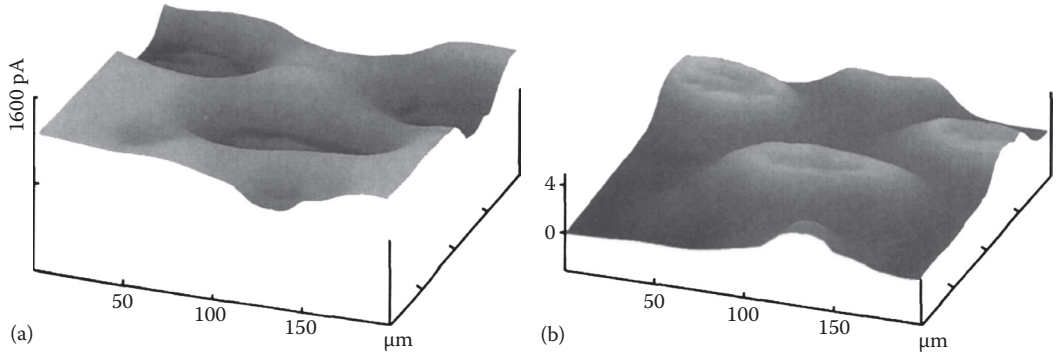


FIGURE 12.10 SECM images of a green portion of the leaf obtained with a 7 µm diameter carbon tip in an air-saturated solution in the dark. (a) i_T across the leaf surface. Because the data were generated in negative feedback mode, the image is inverted (i.e., the dark areas represent bulges on the surface and correspond to low i_T). (b) The image in (a) returned to the proper physical orientation (*y*-axis in µm). The images were obtained 30 min after addition of 0.1 M KCl to the buffer solution to open the stomatas. (Reproduced from Tsionsky, M. et al., *Plant Physiol*., 113, 895, 1997. With permission.)

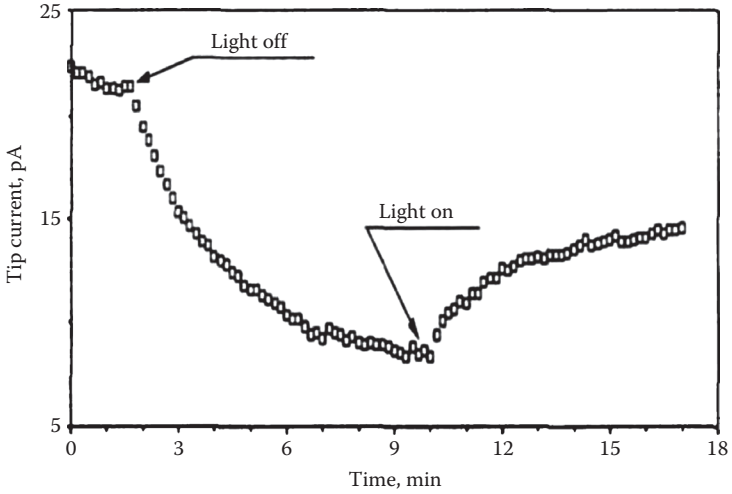


FIGURE 12.11 The response of i_T to step changes in light availability when held over a stomata in a green leaf region. Measured current tracks O_2 diffusion and decreases after the leaf is placed in the dark and increases upon subsequent illumination (800 μE/m²/s). Measurements were made with a 7 μm diameter carbon microelectrode. (Reproduced from Tsionsky, M. et al., *Plant Physiol*., 113, 895, 1997. With permission.)

p-benzoquinone.[49] Amperometric measurements performed in the presence of a single algal protoplast suggested that *p*-benzoquinone was quantitatively reduced to its hydroquinone counterpart following light irradiation. The authors reported that the generation of the hydroquinone increased with light intensity and/or concentration of benzoquinone. Saturation levels for both benzoquinone concentration and light intensity were reported. Finally, the effect of a photosynthetic inhibitor, 3-(3,4-dichlorophenyl)-1,1-dimethylurea, was shown to reduce the generation of hydroquinone. This result suggested that the electron accepted by benzoquinone originated from the photosynthetic electron transport chain of the photosystem II.

12.2.2.2.2 Single Cell Measurements of Nonhuman Cells

All single cell SECM imaging experiments present a current response that is the sum of the cell's topographical and electrochemical contribution. Decoupling of these two contributing factors is an important technical limitation. There are several strategies to efficiently decouple topography from electrochemical data.[25] For example, shear force–controlled SECM is one viable decoupling strategy. It requires the careful design of shear force probes adapted to the soft surface cell interface. Hengstenberg et al.[50] discuss and demonstrate the comparative advantages of using carbon fiber shear force electrodes to image cells rather than the laser-pulled glass electrodes. Regardless of the strategy used, both the morphology and electrochemical activity of the cells can provide information on important biological functions.

Takahashi et al. have studied protein expression level at the surface of living cells using SECM.[53] They have specifically studied the membrane-bound epidermal growth factor protein. This cancer-related protein is important in critical cell function such as proliferation, differentiation, and cell death. Epidermal growth factor protein expression levels can be monitored by SECM through different detection schemes (Figure 12.12). Similar to that discussed in the bacterial studies, alkaline phosphatase can be used as a label. In this case, an alkaline phosphatase antibody-tagged epidermal growth factor can catalyze a reaction generating PAP, which can be oxidized at the SECM tip. A second detection scheme using a biotinylated epidermal growth factor is also possible when combined with ferrocene methanol as the redox mediator. Interestingly, it is possible to track and optimize the expression level through SECM monitoring in different cell lines. In this study, Chinese

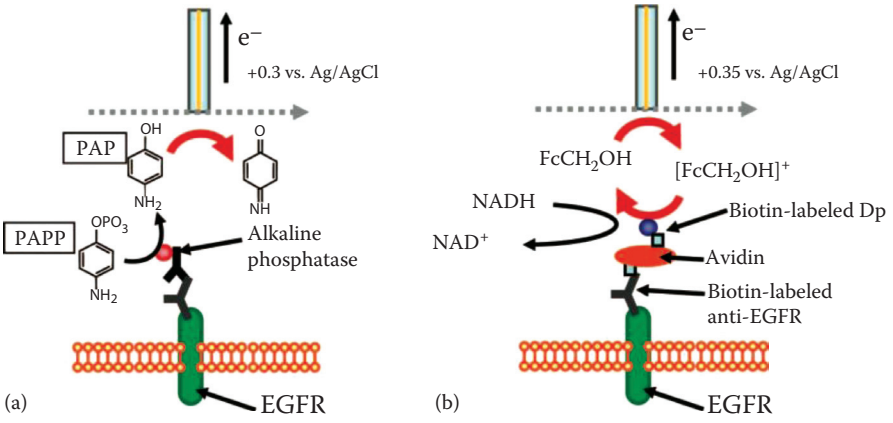


FIGURE 12.12 Optimization of antibody concentration. (a) Schematic representation of standardization of current ΔI. Oxidation current response as a function of the (b) primary antibody concentration (secondary antibody concentration is 1 μg/mL). (Reproduced from Takahashi, Y. et al., *Anal. Chem*., 81, 2785, 2009. With permission.)

hamster ovary (CHO) and human epidermoid carcinomal cells are studied. Finally, the real-time monitoring of the epidermal growth factor using SECM could be well suited to study endocytosis or any other process that alters this protein's surface density.

Pitta Bauermann et al. have applied constant distance shear force–controlled SECM to electrochemically image fibroblasts and adrenal chromaffin cells.[54] In the case of the catecholamine-releasing chromaffin cells, the authors succeeded in amperometrically detecting the release of neurotransmitters from a single secretory vesicle, following chemical stimulation.

Zhao et al. presented the comparative advantages of studying living systems with atomic force microscopy, confocal microscopy, or SECM.[55] With atomic force microscopy, the authors get high-resolution images of the cells. In both contact and noncontact mode, technical difficulties arise from the destruction of the cells by the rigid cantilever or fouling of the cantilever following prolonged contact with the cells. The combined use of confocal microscopy with SECM enabled a detailed study of monkey-based cells (*Cercopithecus aethiops* kidneys [CV1 and COS-7]) in the presence of ferrocene methanol as a redox mediator. Using constant height SECM images, the authors could monitor cell morphology variations in real time. The same group further studied the same cell lines using alternating current SECM. In this mode, SECM functions without the use of a dissolved redox species.[56] The dependence of the AC current measured at the microelectrode was used to monitor real-time changes in cell morphology and in cellular metabolic activity following stimulation by ethanol and phorbol-1,2-myristate acetate-3.

Berger et al.[57] have studied bone-resorbing osteoclasts. In their manuscript, they study the impact of calcium ions in the extracellular environment of osteoclasts. It is believed that high concentration of extracellular calcium ions inhibits the osteoclast resorptive activity. The SECM studies of calcium ions and superoxide anion generation by bone-resorbing osteoclasts were performed on the surface of a bovine cortical bone slice. The detection scheme relied on the use of Ca^{2+}- and O_2^--selective electrodes. Interestingly, the SECM measurements outline the adaptive nature of osteoclasts to even high calcium concentration environments.

Uptake and release of other chemical species by living cells has also been studied at the single cell level using SECM. Ciobanu et al. have monitored oxygen respiration profiles, glucose uptake, and lactate release,[51] through the careful design of biosensor microelectrodes based on glucose oxidase and lactase enzymes. This enabled the authors to monitor nonuniform concentration profiles across the cell surface. For example, nonuniform distribution of oxygen across different living cells is observed, which cannot simply be accounted for by topographical variations. There is a generality to the presented methodology that enables the authors to apply the

same detection scheme to a variety of cell lines (PC12 rat neurons, mouse fibroblast, and human breast epithelial cells).

Takii et al.[60] applied SECM to study the spatial distribution of the respiratory activity in PC12 neurons. Monitoring of the oxygen concentration profiles around the neuron indicated that both the axon and cell body consume oxygen. Oxygen consumption occurs as a result of mitochondrial respiration. Local respiration activity was also observed during axonal growth and was particularly stimulated by the nerve growth factor. Stimulation of PC12 cells by the nerve growth factor is interesting because the cells differentiate into a neuron phenotype by growing a network of narrow (1–2 μm) neurites, which can extend >100 μm from the cell body. Several redox mediators can be used to image both the cell body and neurites: $IrCl_6^{3-}$, $Ru(NH_3)_6^{3+}$, L-ascorbic acid, 1,4-benzoquinone, 4-hydroxy TEMPO. The first three mediators are perfectly benign to cells while the last two lead to budding, a morphological indication of progressive cell death.[62] As such, budding causes significant morphological changes, which can be imaged by SECM. Given that simultaneous detection of different mediators exhibiting a wide range of redox potential could be desirable, it is possible to rely on fast-scan cyclic voltammetry SECM for imaging the distribution of multiple chemical species near a cell surface.[52] In turn, this is interesting because it would expand the amount of electrochemical information acquired through a single measurement. This could be quite beneficial as all mediator response would have been tested on the same living cell exhibiting a given metabolism or phenotypic signature.

Ueda et al. imaged the neurites of PC12 neurons[58] using a combination of near-field optical, atomic force, fluorescent, and scanning electrochemical microscopies. This hybrid microscopy approach enables the authors to image both the distribution of fluorescence near the inner membrane in neurites and the subtle morphological changes. Specifically, the reported images related to the distribution of Ca^{2+} along the neurites and varicosity like structures, which are characteristic in neurons. In line with the development of specialized scanning probe method, the same group also developed specialized optical fiber electrodes capable of simultaneously imaging the neurites of living PC12 cells using the negative feedback mode of SECM.[59] The pencil-shaped optical fiber probes were not only nanometer-sized electrodes but also a scanning light source capable of generating a 300 nm illumination spot. The probes consisted of etched metal-coated fiber optics that are insulated with a polymer-based electrophoretic paint. Optical-based fiber optics probes have also been developed by Takahashi et al.[40] In their study, the electrode probes were fabricated by Ti/Pt sputtering followed by a Parylene C vapor deposition/polymerization insulation step. This method also produced nanometer-sized electrodes and illumination spots, which were used to simultaneously acquire electrochemical and topographical images of the axon and cell body of PC12 neurons (Figure 12.13).

Acquisition of high-resolution images of delicate cells is challenging. Limiting the tip interactions with the cells is important because physical contact of the microelectrode with the cell can stimulate the cell and alter its metabolism. In Figure 12.13, the authors limit this interaction by moving vertically the probe by a few microns to reduce the damage to the cells at each data point. This feedback mode, defined as the standing approach mode, permits extensive imaging of samples exhibiting large height differences or fragile biomaterials including microbeads or living cells. Another alternative is the use of constant impedance mode SECM.[61] The constant impedance mode can function in a solution devoid of redox mediator and can simultaneously measure the topography and faradaic current. The topography of PC12 neuronal cells was readily monitored in this way (Figure 12.14). This work demonstrates that the combination of amperometry and constant impedance SECM has the potential to be a powerful tool for investigating the spatial distribution of neurotransmitter release *in vitro*.

12.2.2.2.3 Single Cell Measurements of Human Cells

As observed in the SECM studies applied to the Bacteria domain and applied to single cell studies of plants and nonhuman animal cells, the respiration activity was used in early SECM studies of human cells. In 1998, Yasukawa et al. monitored the respiration activity of human colon

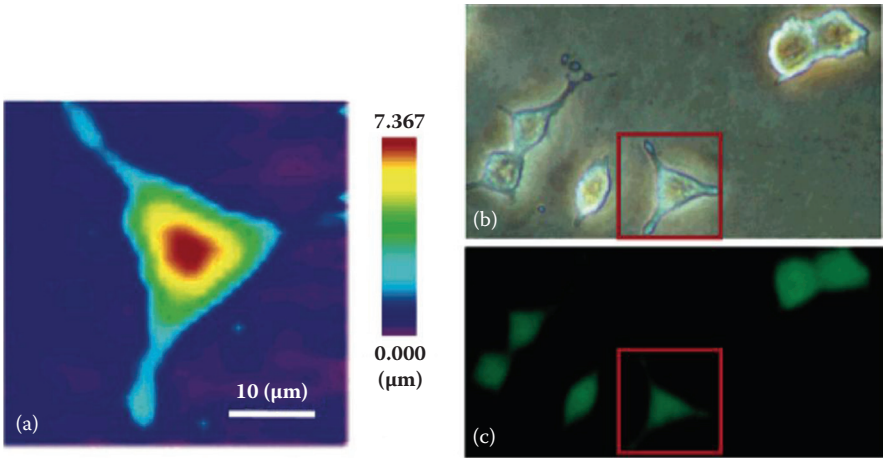


FIGURE 12.13 (a) Topography of a single PC12 cell in culture medium RPMI 1640 in standing approach mode using a capillary probe. The scan range was 40 μm × 40 μm, and the step size was 1.0 μm. (b) Optical and (c) fluorescence images of the sample PC12 cells. Calcein AM was introduced into the culture dish after standing approach-mode scanning and washed three times with PBS before the optical and fluorescence images were obtained. The squares shown in (b) and (c) indicate the exact scanning area. (Reproduced from Takahashi, Y. et al., *Langmuir*, 22, 10299, 2006. With permission.)

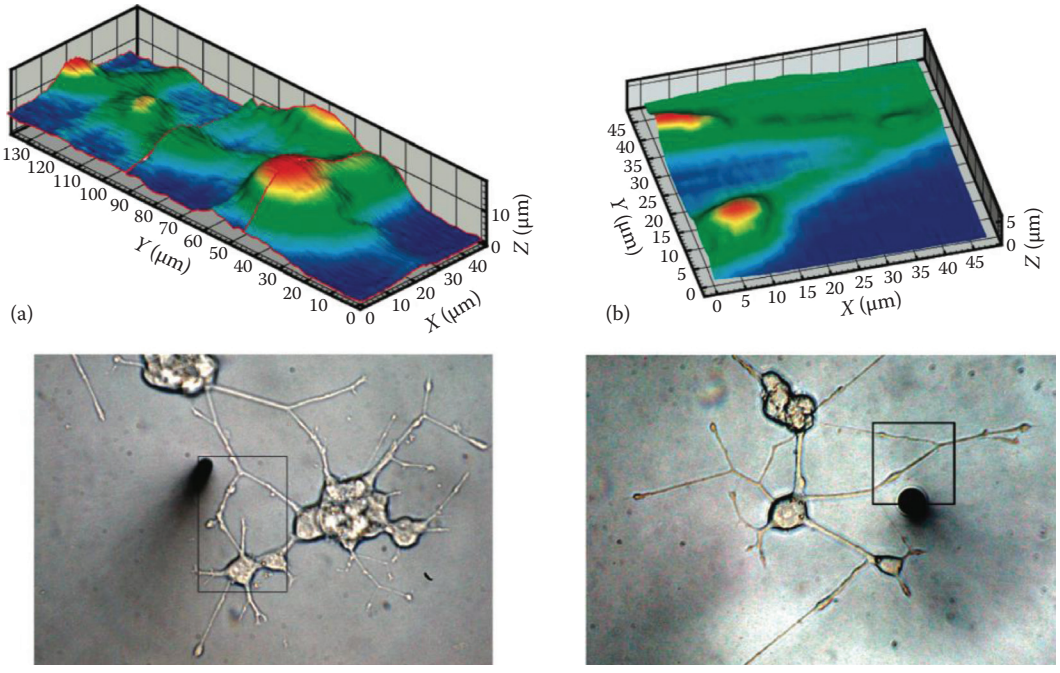


FIGURE 12.14 Topographic images of differentiated PC12 cells acquired using constant impedance imaging. (a) Mosaic image of several cells joined by neurites recorded in supplemented RPMI 1640 growth media; (b) close-up image of a neurite bifurcation recorded in HBSS. Conditions: 5 μm diameter carbon fiber electrode, E_T = +0.75 V, no mediator, and scan rate 7 μm/s. (Reproduced from Kurulugama, R.T. et al., *Anal. Chem.*, 77, 1111, 2005. With permission.)

adenocarcinoma cells in the presence of KCN. Given its cytotoxic properties, a decrease in respiration activity was imaged following KCN exposure.[66]

Zhu et al. also studied the respiration activity but in human neutrophils. They proposed a different method based on a 2D SECM scan to decouple the cell topography from the respiration activity.[63] A first scan across the center of the adhered cells was performed at a Pt microelectrode biased at the oxygen reduction potential. The neutrophil was then killed following incubation in cytotoxic concentration of KCN, and a second scan was performed across the dead cell. The differential of the scan performed on the living cell and that of the dead cell was used as a means of decoupling the cell topography from its respiration activity. This method assumes that swelling as a result of cell death does not contribute significantly to the SECM measurements.

Human gastric carcinoma cells have been studied by Xue et al.[64] The objective of the study was to image different membrane glycan motifs at the single cell level. Once patterned in microwells through a poly(dimethylsiloxane) soft lithography process, the glycans were detectable based on lectin labeling with the horseradish peroxidase enzyme. In the presence of the redox mediator ferrocene methanol and the enzyme substrate hydrogen peroxide, horseradish peroxidase oxidizes the mediator to form the ferrocene methanol cation, which is then reduced at the nearby tip (Figure 12.15).

In turn, the glycan expression levels can be imaged using SECM feedback mode. The authors demonstrate the robustness of the method by statistically demonstrating that up to four different glycans could be imaged on a single cell (Figure 12.16).

Importantly, this expression pattern was corroborated by flow cytometry measurements (Figure 12.17). This is interesting given that several surface-bound glycan molecules play an important role in cell recognition events.

Human bladder and kidney epithelial cells were studied by SECM following an inflammatory stimulation with *E. coli*.[65] Using time-lapse SECM images, the release of reactive oxygen species is linked to the presence of the toll-like receptor based on the differential response of the human bladder and kidney epithelial cells, which, respectively, express and do not express this receptor. This study is generally applicable to several critical biological processes such as cell death, lipid oxidation, and DNA damage.

Single human umbilical vein endothelial cells (HUVECs) were studied by Wang et al.[67] Blood flow is affected by the vasodilatation and vasorelaxation associated with smooth muscle cells. These events imply severe morphological changes in neighboring cells following chemical stimulus. NO is a one of these chemical species that works as an endothelium-derived relaxation factor. As such, the authors investigated the morphological changes that occur at single HUVEC following NO release.

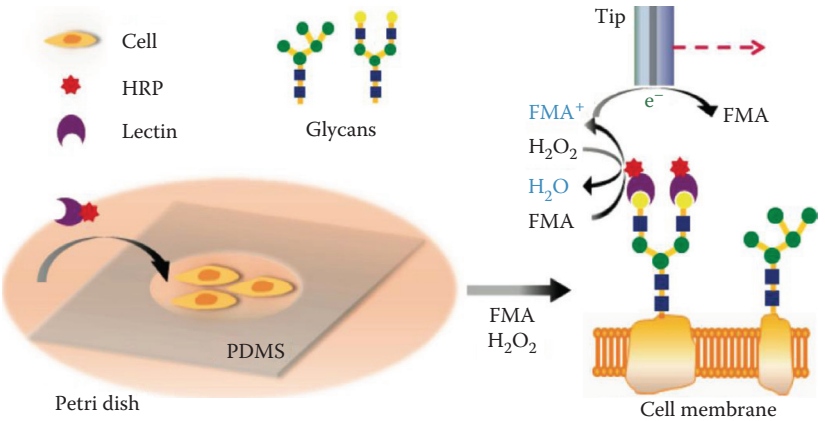


FIGURE 12.15 Scheme of SECM imaging for cell surface glycan expression using SG/TC mode. (Reproduced from Xue, Y. et al., *Anal. Chem.*, 82, 7112, 2010. With permission.)

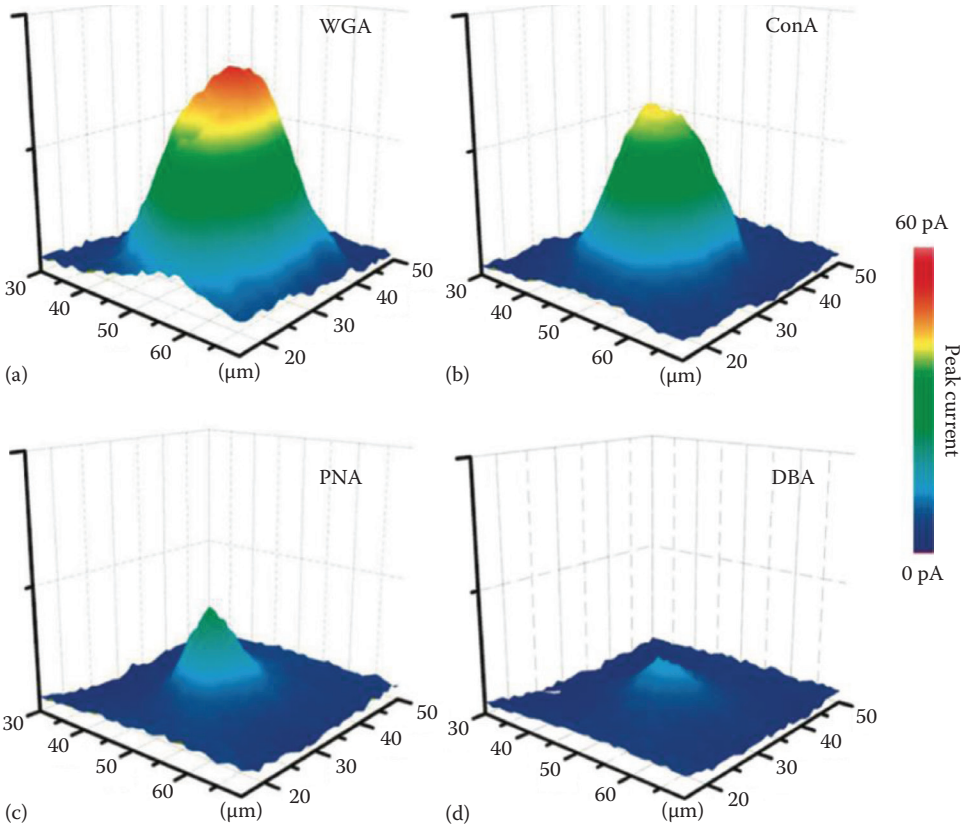


FIGURE 12.16 Single cell SECM images in situ recorded in PBS containing FMA and H_2O_2 for BGC cells after incubation with (a) HRP-WGA, (b) HRP-ConA, (c) HRP-PNA, and (d) HRP-DBA. For facile comparison, the baselines of tip current are corrected as 0. (Reproduced from Xue, Y. et al., *Anal. Chem*., 82, 7112, 2010. With permission.)

Using SECM measurements, they demonstrate that the HUVEC shape before and after NO release changes from a cone-like to plate shape (Figure 12.18). These significant morphological changes were directly related to L-arg, which is used to synthesize NO through the action of nitric oxide synthase. In this study, the NO release was monitored at carbon fiber microdisk electrode but other probes such as platinum-coated and Ni-phthalocyanine-modified carbon fiber microelectrodes are also possible.[68]

Hepatoblastoma were studied by SECM to investigate quinone-imposed oxidative stress.[69] In this study, the authors detected a glutathione metabolite of menadione, which is formed and exported outside the liver cells following an oxidative stress. Time-lapse measurements demonstrated the cytotoxicity of menadione at the single cell level. Hirano et al. also performed time-lapse SECM measurements of hepatoblastoma.[70] In their experiments, the preservation effects of antifreeze proteins are reported. In their fully automated setup, the authors monitor the single cell topography at low temperatures. To perform the measurement (Figure 12.19), the microelectrode is approached in a $K_4[Fe(CN)_6]$ solution until contact with the plastic coverslip using negative feedback. The tip is then retracted to a known distance exceeding the average height of the adhered cells. Using a lateral constant height scan, the apex of the cell is electrochemically located. Following a control negative feedback approach curve performed at the apex of the cell, the morphological changes are monitored through repeated approach curves under hypothermic conditions and in the presence of antifreeze protein from notched-fin eelpout (NfeAFPs).

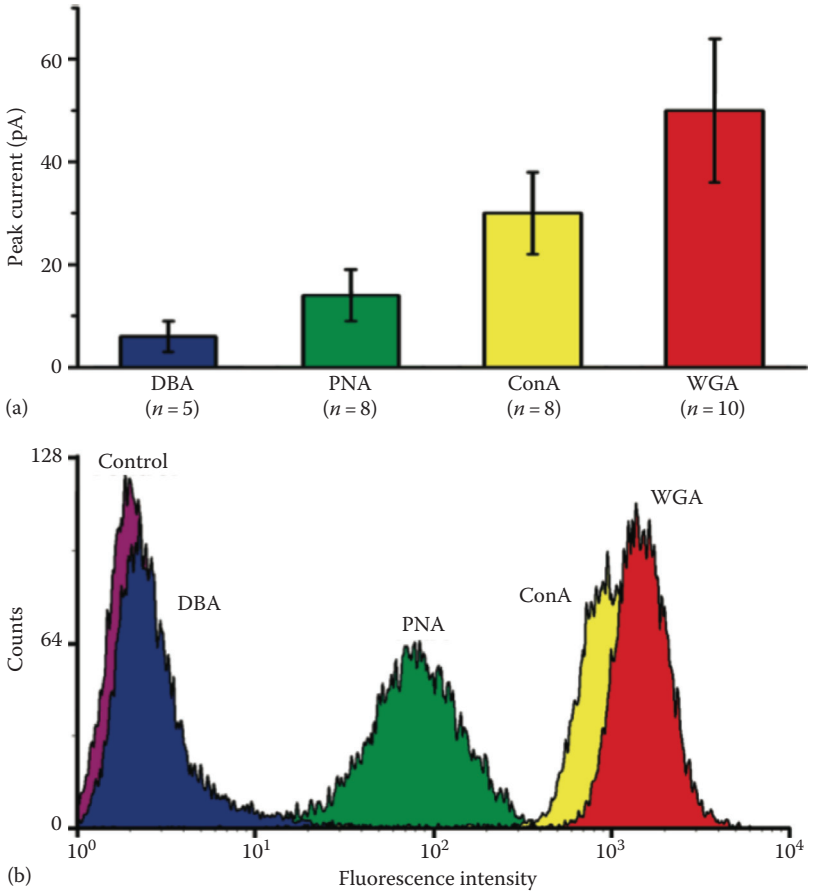


FIGURE 12.17 Relative expression levels of four glycan motifs on an adherent single BGC cell surface measured by (a) SECM in SG/TC mode after background subtraction and (b) flow cytometric fluorescence profiles after treated with FITC lectins. (Reproduced with permission from Xue, Y. et al., *Anal. Chem*., 82, 7112, 2010. With permission.)

In absence of NfeAFPs (Figure 12.20), the hepatoblastoma swelled after 8 h of hypothermic conditions, resulting in a decreased tip-to-substrate distance and lower feedback current. In the presence of NfeAFPs, the hepatoblastoma cells were protected and swelled only after about 18 h of hypothermia. The protective effects of the antifreeze proteins, which stabilize the cellular membrane, can also be monitored through continuous time-lapse SECM imaging (Figure 12.20).

The human cervix carcinoma cell (HeLa) is one of the most widely studied single cells by SECM. Takahashi et al.[71] studied the cellular expression activity of the secreted alkaline phosphatase outside and inside HeLa cells. The cell measurements were performed using a shear force–controlled biological SECM. Shear force regulation was achieved by monitoring the amplitude damping of a tuning fork that was attached to a focused ion-milled fiber nanoelectrode. In this study, the expression level of both secreted alkaline phosphatase and green fluorescent protein were monitored by fiber optic nanoelectrode. The secreted alkaline phosphatase catalyzes the hydrolysis of *p*-aminophenylphosphate. This hydrolysis continuously produces PAP, which was oxidized at the probe electrode (Figure 12.21d). Concomitantly, the green fluorescent protein fluorescence from inside the cells was monitored by a photomultiplier (PMT) detector following stimulation by a 473 nm laser light through the optical fiber electrode.

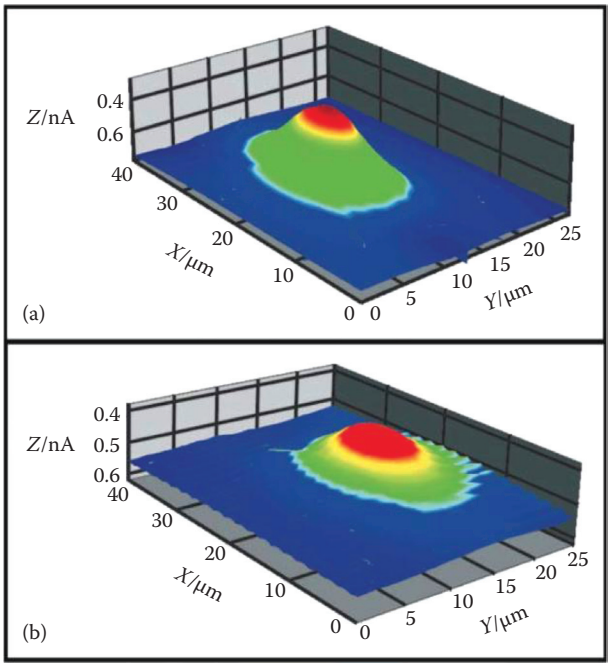


FIGURE 12.18 SECM images of single isolated HUVEC: (a) before NO release and (b) after NO release. Conditions: 1.0 mM $Ru(NH_3)_6Cl_3$ in HBSS with 10 mM HEPES, pH: 7.4; E_T: −400 mV; scan rate: 5 μm/s. (Reproduced from Wang, W. et al., *Analyst*, 132, 515, 2007. With permission.)

The same electrochemical detection scheme was used in a study where the HeLa cells had been individually seeded using positive dielectrophoresis (pDEP, Figure 12.21a through c). This patterning technique involves flowing the cells in a microchannel sandwiched between two ITO electrodes. A patterned microwell array is mounted on the bottom ITO electrode. The application of a pDEP pulse of 3 V pp and 1 MHz between the two ITO electrodes generates an electric field across the microchannel that favors cell seeding and adhesion.[74]

The objective of the study was to monitor cellular signal transduction in HeLa cells through the action of the tumor necrosis factor alpha (TNF-α)–induced activation process of the nuclear factor kappa (NFκB). The SECM measurements demonstrated that HeLa cells constitutively expressing secreted alkaline phosphatase and NFκB generated higher currents in the presence of TNF-α than the same cells measured without TNF-α stimulation (Figure 12.22). This signal enhancement was even more apparent when seeding was performed with the pDEP protocol.

HeLa cell transfection with various plasmid vectors encoding secreted alkaline phosphatase as the reporter protein is a widely applicable strategy. The plasmid vectors can be tailored to contain different responsive elements. For example, glucocorticoid, cAMP, the binding site of NFκB have been used in SECM single HeLa cell studies.[75]

Kaya et al.[72] monitored the respiration activity of HeLa cells. Similar to other cell substrate, a decrease in the respiration activity following chemical stimulus (KCN, ethyl alcohol, and antimycin) was observed. Respiration activity of HeLa cells was also monitored on micropatterns of HeLa cells.[73] The oxygen pattern mapped around the patterns with a Pt electrode demonstrated that fully adhered cells consumed more oxygen than round-shaped cells, which are often dying.

Li and Bard[77] proposed the use of ferrocene methanol as a potential viability indicator. Ferrocene methanol is suitable for this purpose because living HeLa cells generate a positive feedback whereas HeLa cells exposed to cytotoxic concentrations of KCN or UVC radiation present negative feedback response. These results correlated well with the classical oxygen reduction measurements.

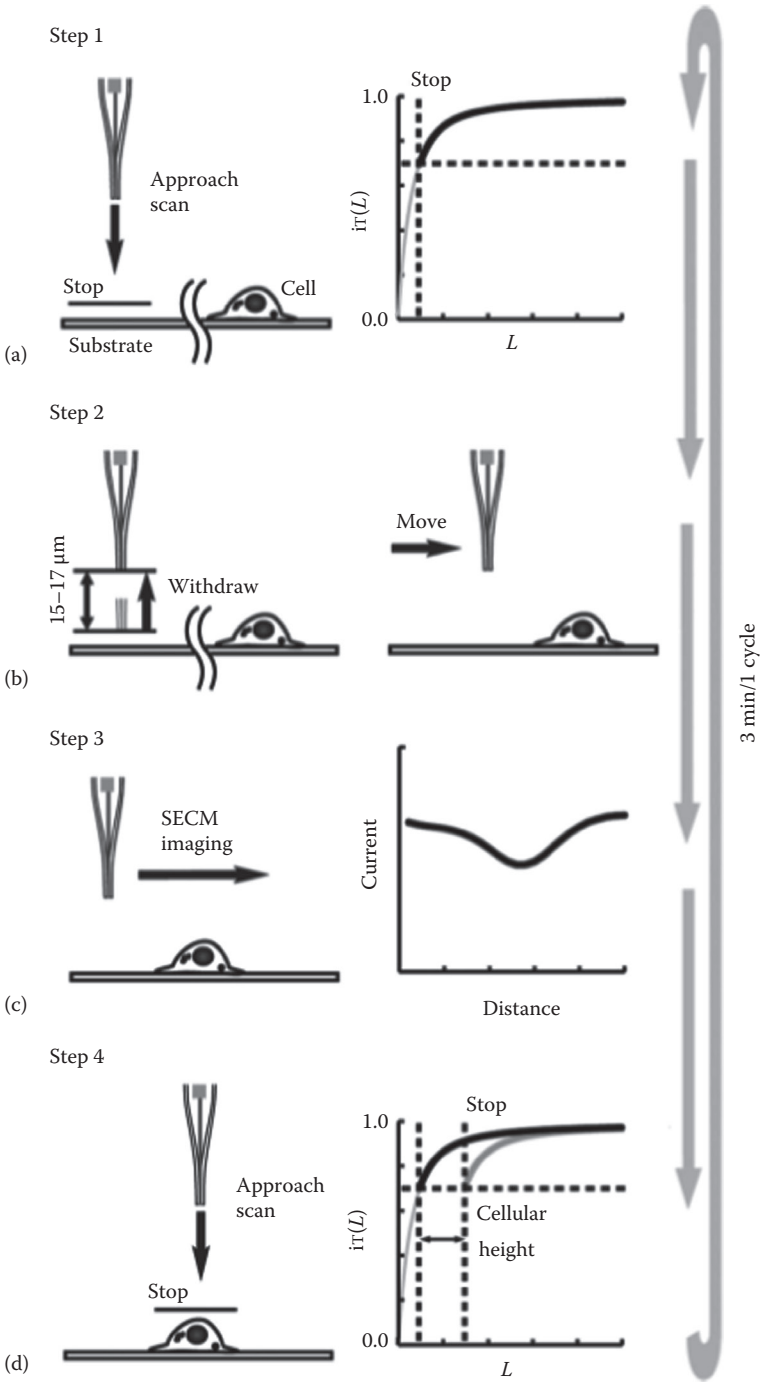


FIGURE 12.19 Schematic procedure of time-lapse SECM for a single cell. (Reproduced from Hirano, Y. et al., *Anal. Chem*., 80, 9349, 2008. With permission.)

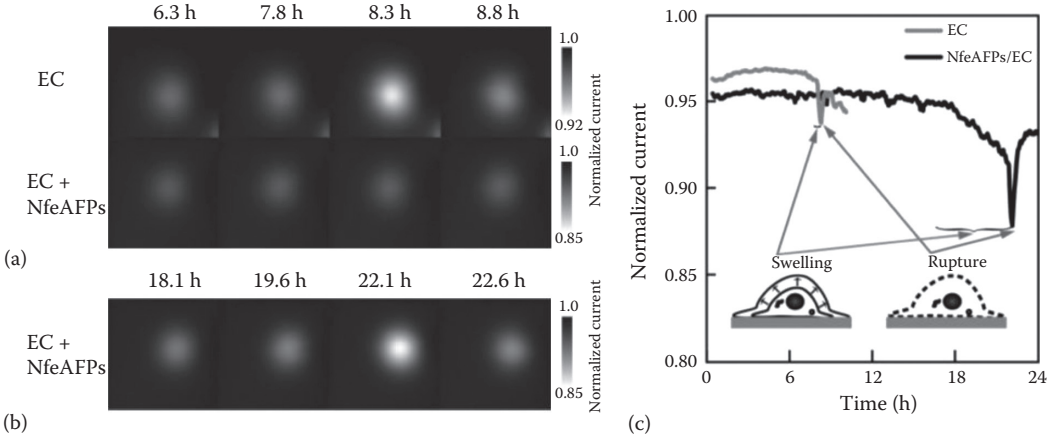


FIGURE 12.20 The time-lapse SECM images of a single HepG2 at low temperature. $E = 0.5$ V vs. Ag/AgCl; tip, Pt 10 µm microelectrode; scanning rate, 20 µm/s; imaging area, 50 µm; resolution, 2 µm. The images were measured in 4 mM $K_4[Fe(CN)_6]$ and Euro–Collins solution with or without 10 mg/mL NfeAFPs. The oxidation currents were normalized with the background current, which was obtained on the dish surface for every image. (a) The images calculated from the current value in the absence or presence of NfeAFPs. (b) The images depict from 18.1 to 22.6 h in the presence of NfeAFPs. (c) The time course of the oxidation current at the top of the cell. Inset: The gray arrows indicate the cellular swelling phase and the cell rupture points. (Reproduced from Hirano, Y. et al., *Anal. Chem*., 80, 9349, 2008. With permission.)

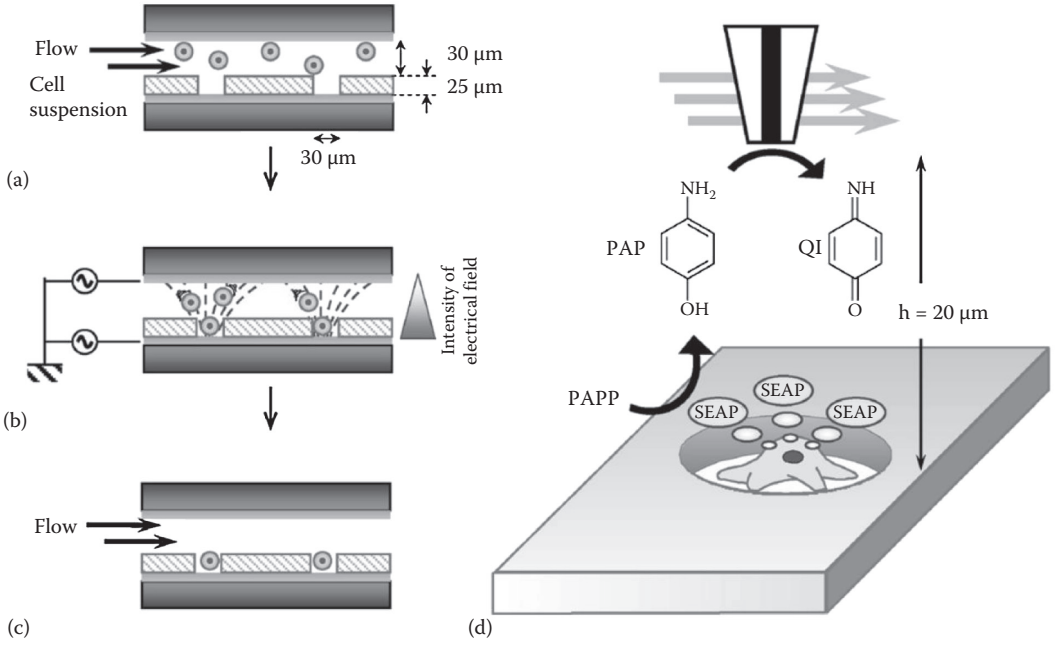


FIGURE 12.21 (a–c) Cell pattern formation based on positive dielectrophoretic pulse method; (d) the expression of the reporter enzyme SEAP is monitored electrochemically. PAPP was enzymatically hydrolyzed to produce PAP, which was oxidized at +0.3 V vs. Ag/AgCl with the probe microelectrode. QI represents the product of electrooxidation. The height (h) of the electrode tip in the constant height mode SECM was set at 20 µm from the top of the SU-8 or PDMS microwells. (Reproduced from Murata, T. et al., *Biosens. Bioelectron*., 25, 913, 2009. With permission.)

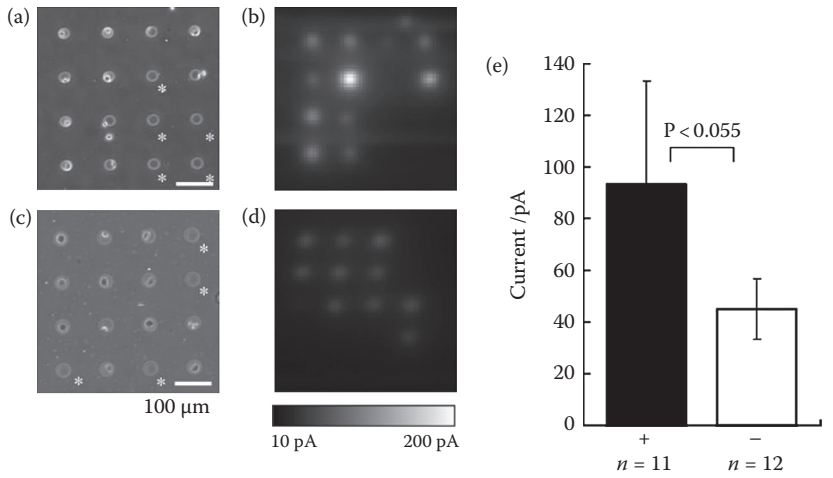


FIGURE 12.22 The optical (a and c) and SECM images (b and d) of the single cell array of HeLa-NFkB-SEAP cells with (a and b) and without (c and d) 100 ng/mL TNF-a stimulation on the PDMS stencil/polystyrene device not subjected to pDEP. The vacant well was marked as (*). The SECM scan area was 600 mm × 600 µm. (e) The average current response of the HeLa-NFkB-SEAP cells with (black bar, $n = 11$) and without TNF-α stimulation (white bar, $n = 12$). (Reproduced from Murata, T. et al., *Biosens. Bioelectron*., 25, 913, 2009. With permission.)

Ferrocene methanol is ideally suited as a viability indicator since incubation for a few hours with mM concentrations does not lead to significant cell death. Also, its uptake by HeLa cells is significantly higher as compared to other agents such as silver ions.

Interestingly, the permeability of the cell membrane can be altered following incubation in nonionic surfactants.[78] In this way, the cell membrane otherwise impermeable to the highly charged hydrophilic molecule ferrocyanide was rendered permeable starting at concentrations of Triton (TX-100) of about 0.17 mM. Below this value, the permeability of HeLa cells remained unaltered. Importantly, this concentration level of TX-100 did not affect cell viability. Based on a simulation model, the membrane permeability for ferrocyanide molecules passing through the live cell membrane was $6.5 \pm 2.0 \times 10^{-6}$ m/s. Cells underwent irreversible permeabilization of the membrane and structural collapse when the TX-100 concentration reached the critical micelle concentration in the range of 0.19–0.20 mM. The impermeability of ferrocyanide molecules in the absence of surfactant was also used to determine the height and diameter of a single living cell with the aid of the approach curve and probe scan methods in SECM.

Finally, SECM studies on single HeLa cells have also focused on their interaction with silver nanoparticles.[76] The detection scheme relied on the interaction of an iridium hexachloride couple with silver nanoparticles. When the microelectrode approached the HeLa cells, two mechanisms competed with $IrCl_6^{3-}$ regeneration from $IrCl_6^{2-}$ by the silver nanoparticles adsorbed on the cell surface: $IrCl_6^{3-}$ diffusing across the intracellular space and $IrCl_6^{2-}$ transported in the intracellular lumen where it could subsequently be reduced by an intracellular redox species or silver nanoparticles segregated in the nucleus (Figure 12.23).

Human breast epithelial (MCF-10A) cells are the last cell type reviewed in this section. As predominant as the HeLa cells, they were used in early studies to probe the redox activity of single living cells using SECM.[79,80] From these early studies, it became clear that there are several ways by which a redox mediator can interact with a live cell (Figure 12.24).

The redox activity of these cells in the presence of different mediators can be expressed in terms of apparent electron transfer rates and mechanistic pathways can thereby be elucidated using SECM. On the basis of feedback approach curves, it is possible to demonstrate significant differences in the redox activities of nontransformed, highly motile, and metastatic human breast epithelial cells

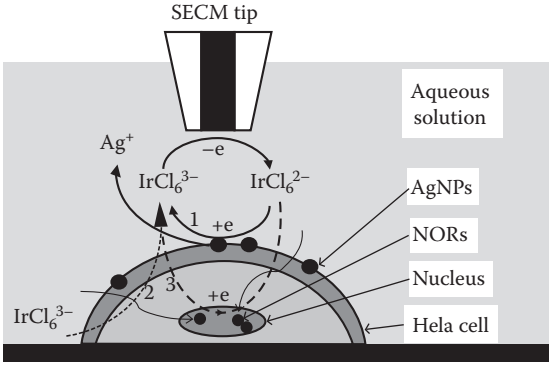


FIGURE 12.23 The operating principle of SECM to detect the interaction between AgNPs and HeLa cells. (From Chen, Z., Xie, S., Shen, L., Du, Y., He, S., Li, Q., Liang, Z., Meng, X., Li, B., Xu, X., Ma, H., Huang, Y., and Shao, Y., Investigation of the interactions between silver nanoparticles and HeLa cells by scanning electrochemical microscopy, *Analyst*, 133, 1221–1228, 2008. Reproduced by permission of The Royal Society of Chemistry.)

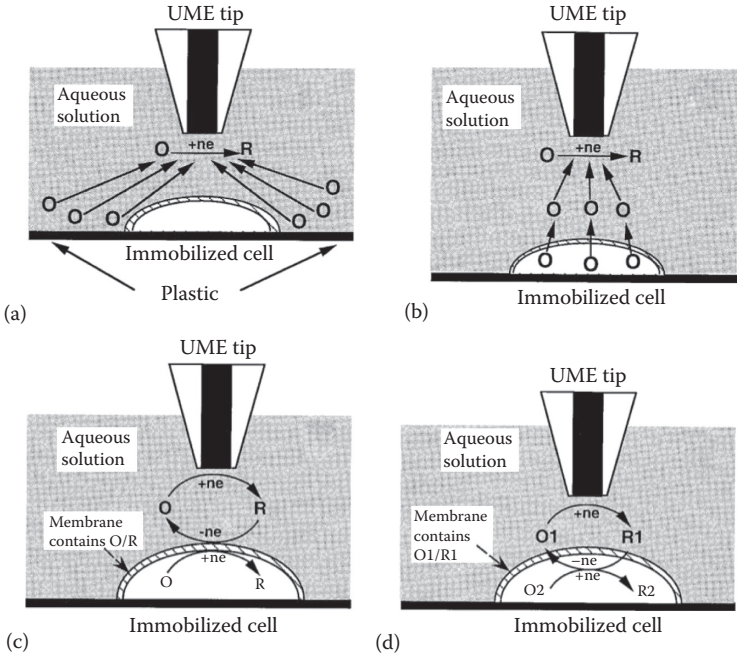


FIGURE 12.24 Schematic diagrams of the SECM experiments with four different types of mediator regeneration. (a) The tip is positioned in the solution close to the cell surface. The lipid cell membrane is impermeable for a hydrophilic redox mediator. Negative feedback is due to the hindered diffusion of redox species to the tip electrode. (b) The UME tip induces the ejection of the redox species, O, from the cell by depleting its concentration near the cell surface via electrolysis. (c) Mediator regeneration proceeds via self-exchange ET reaction. The charge is shuttled across the membrane by the same hydrophobic redox species (O/R). (d) Bimolecular ET between hydrophobic redox mediator (O1/R1) and cell-bound redox moieties (O2/R2). (From Liu, B. et al., *Proc. Natl. Acad. Sci. USA,* 97, 9855, 2000. Copyright 2000 National Academy of Sciences, USA.)

(Figure 12.25). The presence of these differences is dependent on the nature of the redox mediator used. For example, quinone-based mediators resulted in significant differences in the recorded approach curves whereas KI did not (Figure 12.25b and c).

The transport processes and biological response involved in quinone-stimulated human epithelial cells were further studied by Rotenberg and Mirkin.[81] They demonstrated that quinone-based mediators rapidly cross the cell wall to electrochemically react in the intracellular lumen. These events are reported to occur on a microsecond timescale. The apparent electron transfer rates measured for nonmetastatic and metastatic cells demonstrate the modulation effects of protein kinase Cα. Such studies establish the potential for SECM to evolve in an analytical tool capable of discriminating between cancerous and healthy cells. As such, the judicious choice of redox mediator couple will be key in achieving the desired electrochemical contrast.[82]

In fact, there are several critical factors to adjust in just SECM measurements. Liu et al.[83] clearly demonstrated that the mediator species properties (formal potential, ionic charge, and hydrophobicity) as well as biological conditions (intracellular concentration of redox mediator, mixed redox potential inside the cell, rate of membrane permeation by mediator species) are all critical in the overall electrochemical activity measured by SECM. Consequently, detailed kinetic analysis enables one to identify the rate-limiting processes and optimize the resulting electrochemical contrast between cells. Moreover, to perform electrochemical activity studies, the inherent topographical features of the cells must always be considered given their intrinsic coupling.[84]

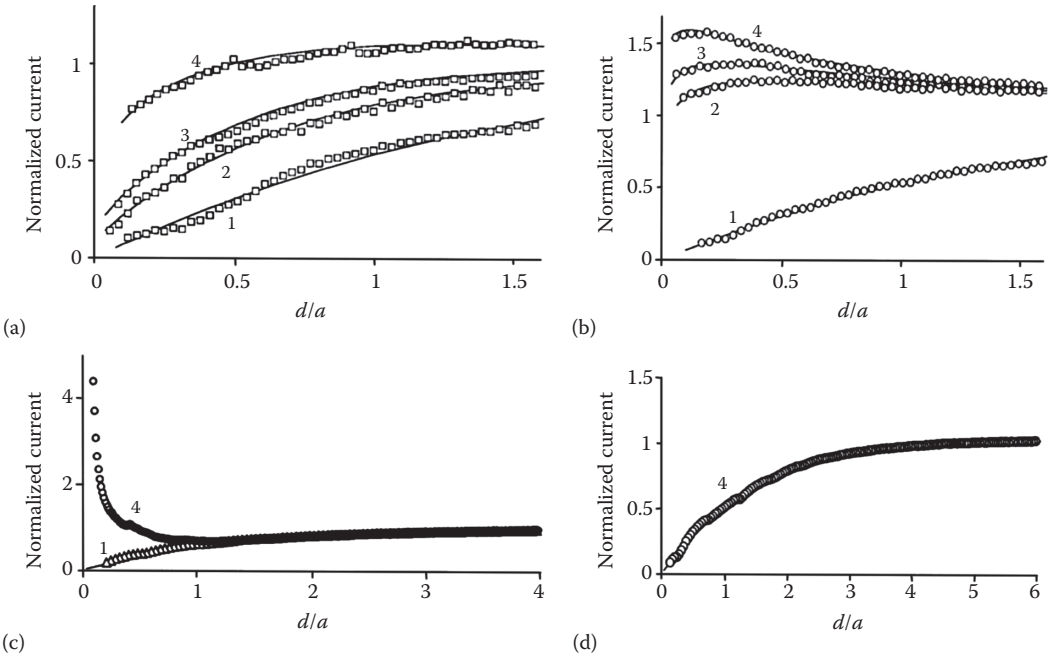


FIGURE 12.25 An UME tip approaches (1) plastic surface, (2) nontransformed, (3) highly motile cell, and (4) metastatic human epithelial breast cell. Solid lines are the theoretical curves for an insulating substrate (1) and finite heterogeneous kinetics (2, 3, 4). Phosphate buffer (pH 7.4) contained (a) 20 μM menadione, (b) 30 μM 1,2-naphthoquinone, (c) 0.1 mM KI, and (d) 0.1 mM KI + 20 μM I_2. (c) Curves for nontransformed and highly motile cells were very similar to curve 4. (d) Curves 1–4 were essentially identical. The tip current is normalized by the i_T value measured in the bulk solution. The tip was a 5.5 μm radius carbon fiber (a and b), and 5 μm radius Pt (c and d). (From Liu, B. et al., *Proc. Natl. Acad. Sci. USA*, 97, 9855, 2000. Copyright 2000 National Academy of Sciences, USA.)

12.2.2.3 Multicell Measurements

SECM studies performed on multiple cells are the second most prominent substrates for SECM studies focusing on living systems. Up to 2010, there were roughly 28 studies published: 1 related to fungi, 5 used plants, 8 used animal cells other than human, and 13 relied on human cells. Fungi can be genetically altered in similar ways as bacteria; they are adaptive to several stressful environments and could be very interesting to further study by SECM. Mauzeroll and Bard studied *Saccharomyces cerevisiae* using SECM. They relied on quinone-based mediators to study detoxification pathways associated with the GS-X pump.[85] Following menadione stimulation, the authors were able to directly detect the efflux of the menadione–glutathione metabolite from aggregates of yeast cells. Based on a quantitative analysis, they demonstrated that the rate-limiting step in the interaction of menadione with yeast was the passive diffusion of the mediator inside the yeast. This in turn suggested that the export of the metabolite through the GS-X pump was an active and rapid process.

12.2.2.3.1 Multiple Cell Measurements of Plant cells

One of the earliest SECM studies was performed on living cell of plant origin.[11] Using the feedback mode, Lee et al. obtained topographical images of the upper surface of a grass leaf and the lower surface of *Ligustrum sinensis* leaf under different illumination conditions.

Leaves from *Brassica juncea* were also studied by Zhu et al.[88] Using SECM images of the oxygen production above stomatal complexes, the authors demonstrated the effect of cadmium-induced chemical stress on stomatal density and size. The presence of cadmium in electrolyte solution resulted in a lower stomatal density and larger stomatal size as compared to control leaves. Also, the oxygen production from cadmium-stressed plants was lower. This decrease in oxygen production was related to a lower photosynthetic yield, as opposed to closed stomatal complexes.

Peanut leaves have also been used to study the stomatal physiology, photosynthetic activity, and chlorophyll distribution.[89] In this work, the authors demonstrate changes in leaf anatomy between somatic embryo and seedling-derived peanut plants grown *in vitro* (in test tubes) and *extra vitrum* (in soil).

In addition to leaves, SECM has been used to study enzyme-modified wood surfaces.[87] Wood surfaces, with their severe topographical changes, were ideal substrate to demonstrate the capabilities of shear force–controlled SECM imaging. In this way, the authors succeeded in decoupling topography enabling them to monitor the distribution of glucose oxidase–labeled amino groups along the annual rings of the three. Interestingly, it was then possible to monitor the nitrogen content in tree rings with higher resolution than that achieved by conventional forestry methods. An advantage of using a detection scheme based on the activity of oxidase-based enzyme is its applicability to other plant substrates such as algal protoplast.[86]

12.2.2.3.2 Multiple Cell Measurements of Nonhuman Animal cells

Single bovine embryos are a multiple cell substrate that has been studied extensively by SECM. The oxygen consumption of the single bovine embryos was monitored at different developmental stages.[92] Of particular interest is the oxygen consumption of the embryos in the morulae development stage. The embryos exhibiting a comparatively larger oxygen consumption in this stage developed into blastocysts of larger size and enhanced respiration activity. This in turn was a strong indication for the successful long-term development of the embryo. These results are promising within the context of bovine artificial insemination and the assessment of optimized culturing conditions. Examples of important parameters would be the culturing solutions[95] and vessels[86,91] as well as the ability to automate the SECM measurements.[93] Interestingly, SECM measurements reflect the quality of the cultured embryo, and is not affected by the sex of the embryo.[94]

12.2.2.3.3 Multiple Cell Measurements of Human Animal cells

Goto et al. evaluated islet potency for clinical transplantation application using SECM.[96] The objective was to monitor the glucose-stimulated respiratory activity of the islet using SECM to

predict the outcome of a transplant. Their results suggest that islet preparation that could cure diabetic rats had a glucose-stimulated respiratory activity greater than those unable to cure diabetic rats.

Multiple human cells have also been used to study the effect of anticancer drugs.[97] In general, such studies correlated well with the results obtained by optical methods and try to establish a dose–response relationship. For example, Torisawa et al.[98] describe an anticancer drug–sensitivity assay for tumors grown in a host mouse (Figure 12.26). Human promyelocytic leukemia (HL-60) cells were inoculated subcutaneously in a mouse and allowed to proliferate for a month. The cells were then removed from the mouse and cultured in a collagen-gel matrix, prior to SECM respiration activity measurements. The proliferation of the extirpated HL-60 cells was consistent with that found in mice and their response to anticancer drugs (cisplatin and etoposide) concurred well with results from conventional colorimetric assays. In general, this strategy is beneficial because

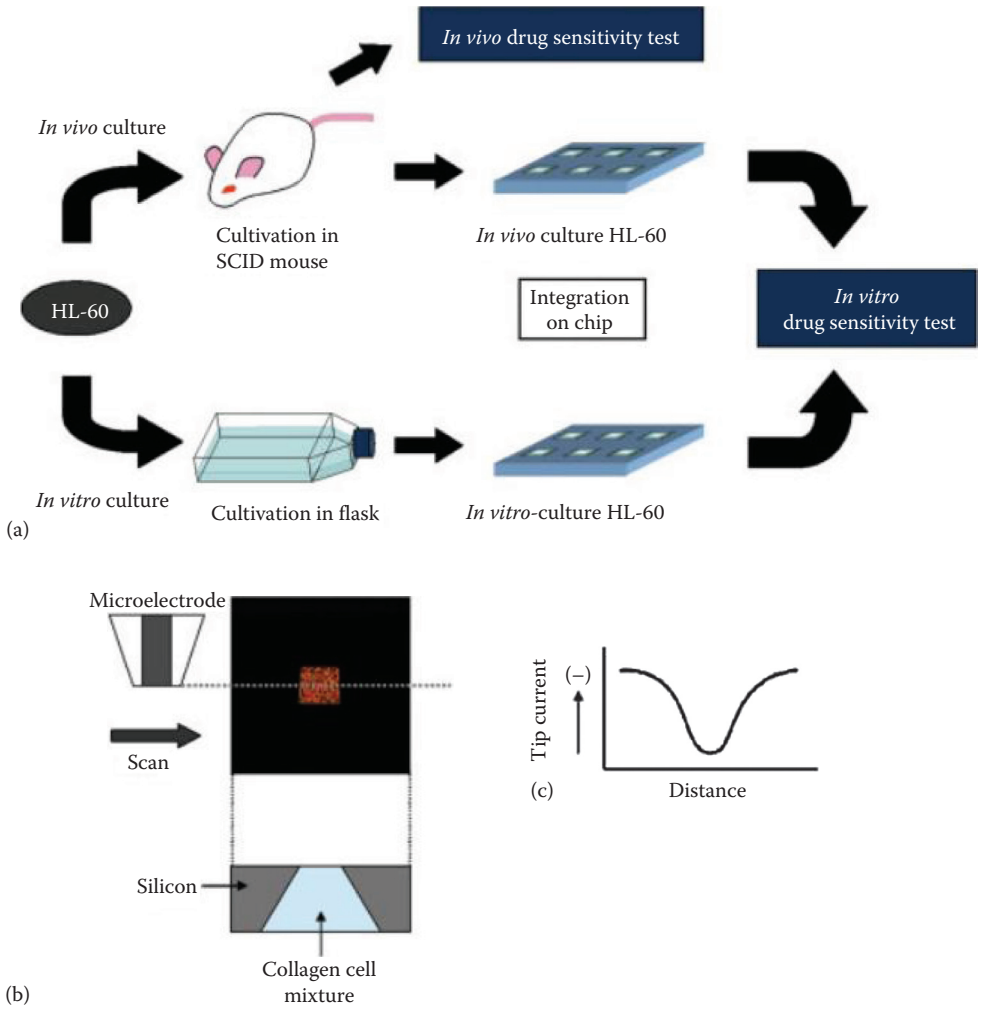


FIGURE 12.26 A flow diagram of the study (a) and principle of the SECM-based assay using cell panels (b). The top side view (upper panel) and the lateral view (bottom panel) of cell panel. The tip scanned over the center of cell panel at a distance of 30 μm from the silicon substrate at the scan rate of 19 μm/s. The oxygen reduction current was monitored by the Pt microelectrode held at −0.5 V vs. Ag/AgCl. The low oxygen reduction current coincides with the location of the cell panel (c). (Reproduced from Torisawa, Y.-S. et al., *Int. J. Cancer*, 109, 302, 2004. With permission.)

it reduces the sample volume to 18 nL and performs the analysis within 4 days rather than 9 days through conventional means.

Multiple cell SECM studies have also been used to study the effect of antimicrobial agents on human fibroblast.[39] Silver ions have well-known antimicrobial properties that are enhanced by the presence of 4-aminopyridine, a voltage-sensitive potassium ion channel blocker. The silver uptake by adhered human fibroblasts was monitored with an amperometric silver ion–selective electrode.[99] The probe consisted of a micropipette supported interface between two immiscible electrolyte solutions. Specifically, a 1,2-dichloroethane solution containing a calixarene-based silver ion ionophore was contained in the glass micropipette, which could monitor micromolar level concentration of silver ions. Interestingly, the uptake and the rate of uptake of silver ions by the fibroblasts were both enhanced in the presence of the ion channel blocker. These SECM results therefore have great potential for the future development of optimized antimicrobial cocktails.

Several multiple cell SECM studies have focused on the preferential patterning of cells on a transparent solid support prior to SECM studies. The collagen-gel-imbedded cell matrix discussed at length in other sections has been applied to multiple human cell studies.[102,103] The use of poly(dimethylsiloxane) soft lithographic processes has also been used because they easily facilitate the acquisition of statistically valid SECM measurements and local delivery of a variety of solutes to the cells.[100] Finally, the use of the microelectrode as a lithographic pencil capable of writing patterns preferentially adhering one cell over another has also been reported.

For example, Kaji et al. have produced HBrO, an oxidizing agent, at the SECM tip through the electrochemical oxidation of Br^-, which is dissolved in the electrolyte solution.[101] The generated HBrO modifies the nature of the albumin-coated substrate to promote cell adhesion. Cells patterns can be generated by using a complete SECM writing procedure (Figure 12.28) or by applying a stepwise writing procedure, which can allow for variable cell conditioning such as fluorescent labeling (Figure 12.27). This approach can pattern single and multiple cells on flat and grooved substrates (Figure 12.27).

Another SECM lithographic strategy involved the localized modification of polystyrene surfaces using electrogenerated reagents (Ag(II), $NO_3^{\bullet}$, and $OH^{\bullet}$), which oxidize the polymer surface

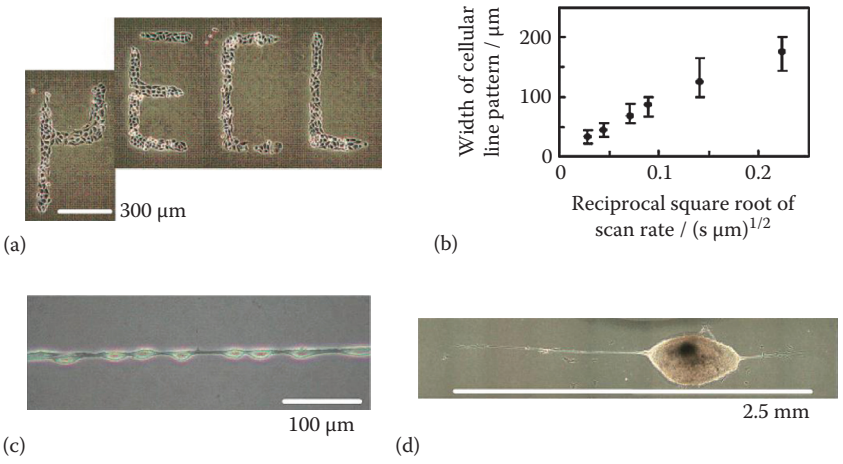


FIGURE 12.27 (a) Optical micrograph of HeLa cells cultured for 24 h on the substrate prepatterned by the microelectrode-based method to produce the letters μ, E, C, and L. The microelectrode was scanned at 500 μm/s, and its potential was kept at 1.7 V vs. Ag/AgCl during "drawing" and at 0 V while not drawing. (b) Plot of the width of cellular (HeLa cells) line patterns versus the reciprocal square root of the scan rate of the electrode probe. Error bars for the plot were calculated from the standard deviation of at least four samples. (c and d) Optical micrographs of bovine aortic endothelial cells and chick embryonic DRG neurons cultured on the substrate prepatterned by scanning the microelectrode at 1250 μm/s. (Reproduced from Kaji, H. et al., *Langmuir*, 20, 16, 2004. With permission.)

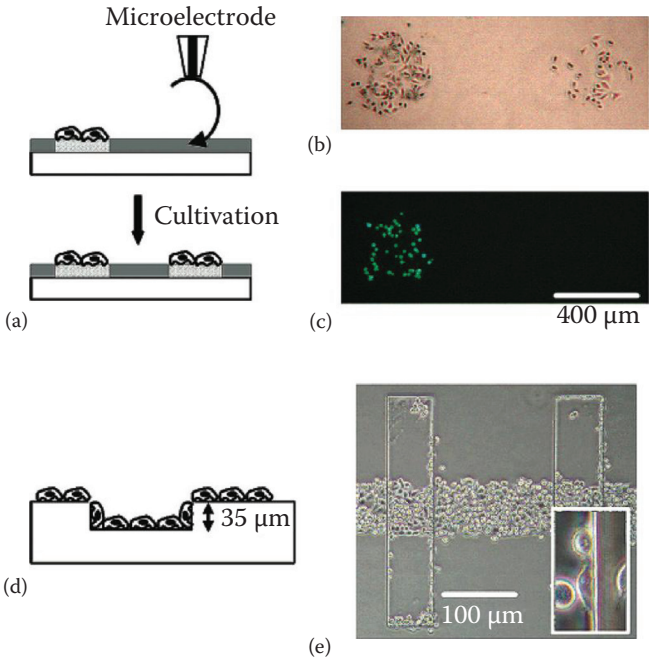


FIGURE 12.28 (a) Schematic diagram of overwriting cell population on a previously cell-patterned substrate using μECL. (b and c) Optical and fluorescence micrographs of a couple of HeLa cell populations patterned in a stepwise fashion. The population on the left side was first cultured for 1 h and stained with calcein, followed by μECL to make the population on the right side. The Br^- oxidation pulse period was 30 s for both patterns. (d) Scheme of cellular patterning on an uneven surface. (e) Optical micrograph of HeLa cells patterned on the quartz substrate with 35 μm deep grooves. The inset shows the cells that adhered on the wall face of the groove. (Reproduced from Kaji, H. et al., *Langmuir*, 20, 16, 2004. With permission.)

(Figure 12.29).[90] Oxidation of the dissolved Ag(I) species in concentrated nitric acid generates a localized source of the strong oxidant Ag(II) that modify the polymer as the SECM tip is rastered across a surface.

This hydrophilization of the surfaces through polymer oxidation favors cell adhesion in a similar fashion as that observed following oxygen plasma conditioning. The process is applicable to several polymers (polystyrene and cyclo-olefin copolymers) and adhering cells (Figure 12.29).

As a final example of SECM studies of multiple human cells, we focus on the detection of nitric oxide, a truly versatile redox-active cell-signaling molecule.

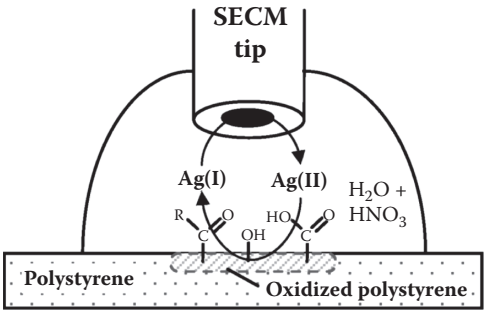


FIGURE 12.29 Principle of oxidative patterning of hydrogenated polymers by silver(II) ions electrogenerated at a UME. (Reproduced from Ktari, N. et al., *Langmuir*, 26, 17348, 2010. With permission.)

As discussed in Section 12.2.2.2.3, HUVECs are ideal models to study NO release. The detection scheme used in SECM studies often relies on NO-selective sensors. The NO sensor consists of a polymerized layer of Ni tetrasulfonate phthalocyanine tetrasodium salt or Ni(4-*N*-tetramethyl)pyridyl porphyrin on a Pt or carbon microelectrode. The selectivity and precise positioning of the NO sensor are key to the successful outcome of SECM NO-releasing measurements. As such, Pailleret et al.[104] used an elaborate positioning and modification scheme (Figure 12.30). In a first step, a Pt microelectrode is approached to a glass coverslip using a negative feedback approach curve. The *z*-position of the microelectrode is then fixed while an underlying *x*–*y* positioning table slides to another glass substrate where a droplet containing 2 mM $[NiTSPc]_4$ in aqueous 0.1 M KOH is used for the electrodeposition of $[NiTSPc]_4$ (step 2). The positioning table slides again to a coverslip containing a rinsing solution that also allows for electrochemical characterization of the NO-sensitive film (step 3). Following further rinsing (step 4), the positioning table moves to a substrate of adhered NO-releasing cells. The chemical stimulation with bradykinin prompts NO release, which is detected at the NO-selective sensor (Figure 12.31).

Amperometric measurements of NO release from HUVECs are acquired at a fix tip-to-substrate distance (Figure 12.32a). The physical change of the cell substrate or use of different NO sensors leads to slight alterations in the maximum recorded current (Figure 12.32b).

In subsequent studies, the same group was able to alter the NO sensor design and vary the control method by which they position the sensor over the cells. For example, to regulate the tip substrate distance using shear force control, vibration needle-type platinized carbon fiber electrodes modified with a polymer layer containing Ni tetrasulfonate phthalocyanine tetrasodium salt were used.[68] As

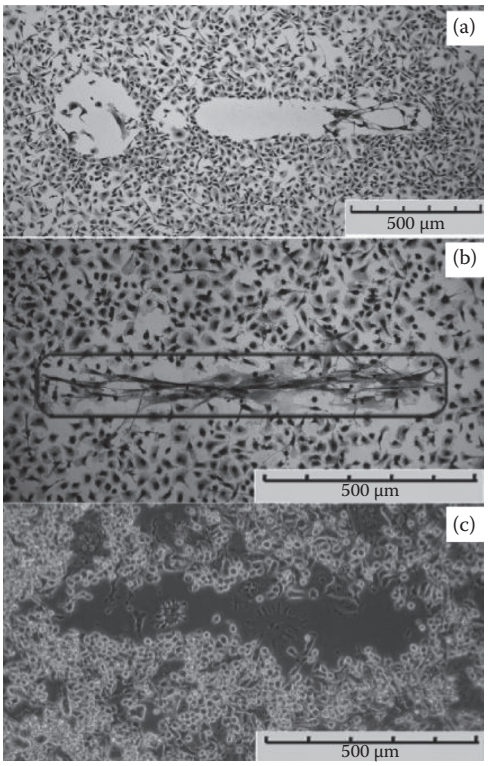


FIGURE 12.30 Cell adhesion discriminative properties of patterned areas: (a) mouse peritoneal cells after 7 days in culture on patterned polystyrene plate (two different experiments, May-Grünwald–Giemsa staining); (b) patterned area (rectangle) where only stretchy cells of myofibroblastic type grew; and (c) RAW macrophage cell line, Day 7. (Reproduced from Ktari, N. et al., *Langmuir*, 26, 17348, 2010. With permission.)

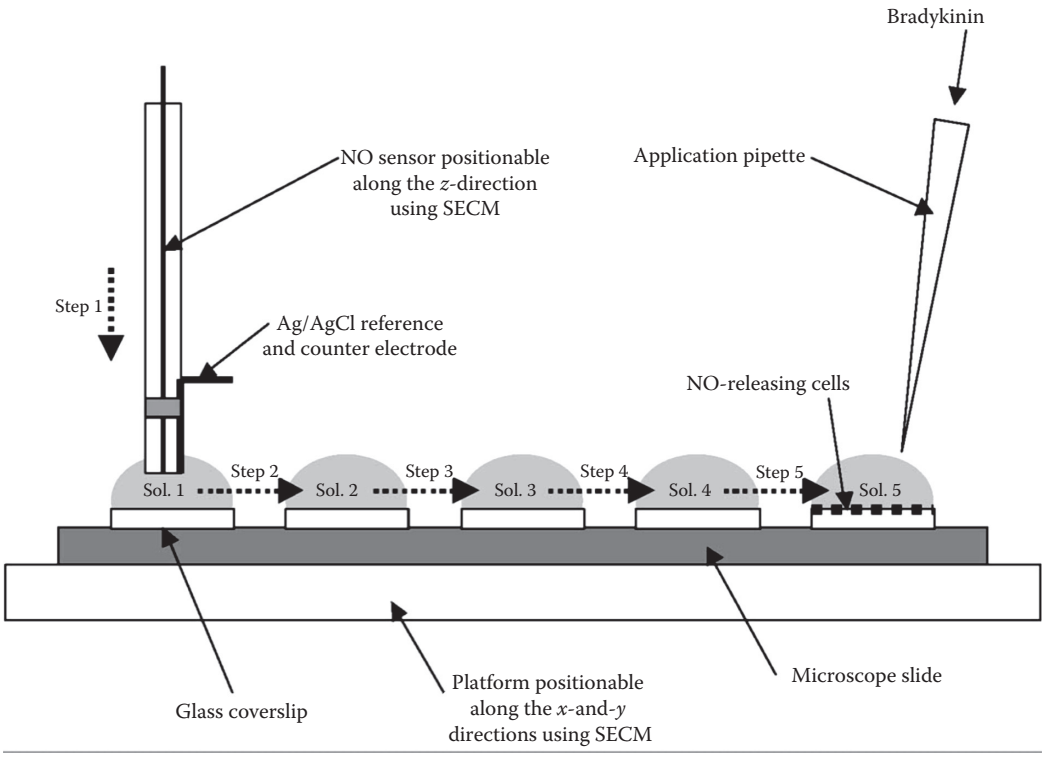


FIGURE 12.31 Schematic representation of the procedure used for the positioning, modification, and the use of an electrochemical NO sensor for the detection of NO release by living cells. (Reproduced from Pailleret, A. et al., *Electrochem. Commun*., 5, 847, 2003. With permission.)

an alternative to shear force tip-to-substrate distance monitoring, a dual electrode sensor was developed, and that allows for simultaneous NO monitoring and approach curve measurements. The dual sensor consisted of a 10 µm diameter Pt distance sensor and a 50 µm diameter porphyrin-based NO sensor enclosed in a polymer matrix. This matrix prevented dissolution of the porphyrin-sensing molecules and aided to circumvent potential interference problems from anions and ascorbate. The sensor's position relative to the cells was recorded by the negative feedback curves of molecular oxygen while the NO sensor captured the NO release from the HUVECs.[106] The dual sensor design was quite successful and enabled a first automation study of NO release from HUVECs.[105] Undoubtedly, the possibility of using an automatic electrochemical robotic system to measure NO release implies the possibility of developing SECM into an online drug screening method.

12.3 SECM STUDIES IN THE FUTURE

SECM is capable of directly and quantitatively detecting electroactive molecules that have been released into solution from living cells. As discussed in Chapter 12, a typical SECM cell experiment involves positioning a very small diameter electrode (microns to nanometer size) noninvasively a few microns above a biological sample immobilized on a solid support. Stimulation of the cells by physical agents, such as heat and light, chemical agents, such as drugs, enzyme co-substrates, or ions can lead to the uptake and/or release of biological metabolites, enzymatic activity, or ion transport—each event being detectable by the probe electrode. Along with the concurrent morphological changes, these transport events can be monitored through the feedback, generation/collection, and imaging modes of SECM.

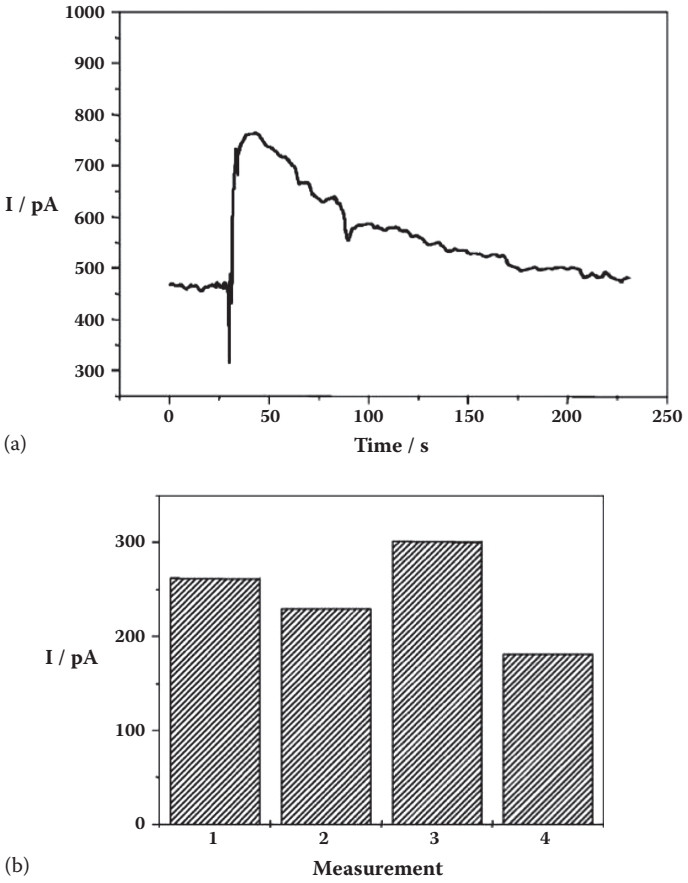


FIGURE 12.32 (a) Current–time plot obtained for the detection of NO released by HUVEC into a microvolume of electrolyte with the detector positioned 15 μm above the cells. (b) Maximum current obtained for four independent measurements of NO release at a tip-to-cell distance of 15 μm. The third bar represents the measurement displayed in (a) in detail. (Reproduced from Pailleret, A. et al., *Electrochem. Commun*., 5, 847, 2003. With permission.)

SECM has the potential to evolve into a multidisciplinary microscopy capable of following specific electroactive metabolites and proteins with high spatial resolution intracellularly, in a single cell and in complex multiple cell substrates. This integrated approach provides a global picture of the effect of stress agents (chemical and physical), on protein expression and activation, on the phenotypic signature of cells, on cell viability, and on cell communication. One major development to this end will be the design of selective nanoelectrodes and/or biochemical detection schemes that can isolate the signal of the molecule of interest from complex mixture of molecules inherent to biological samples. Importantly, SECM can also be used as a tool to pattern cells on solid substrates.

Future developments in this field will likely be directly linked to improvements in microelectrode design, the systematic use of constant distance mode SECM imaging, the development of routine patterning strategies of different cell types, statistical validation of SECM measurements between laboratories and automation of SECM measurements. Finally, to establish SECM as a convincing quantitative bioanalytical tool used for screening, electrochemists must make further use of standard biochemical methods and robotics. All of these improvements will contribute to extending the range of SECM studies to a larger section of the realm of the living.

ACKNOWLEDGMENT

S. Kuss is acknowledged for technical contributions.

REFERENCES

1. Adams, R. N. Probing brain chemistry with electroanalytical techniques. *Anal Chem* 1976, 48, 1126A–1138A.
2. Wightman, R. M., Jankowski, J. A., Kennedy, R. T., Cowage, K. T., Schroeder, T. J., Leszczyszyn, D. J., Near, J. A., Diliberto, E. J., Viveros, O. H. Temporally resolved catecholamine spikes correspond to single vesicle release from individual chromaffin cells. *Proc Natl Acad Sci USA* 1991, 88, 10754–10758.
3. Wightman, R. M., Kennedy, R. T., Wiedemann, D. J., Kawagoe, K. T., Zimmerman, J. B., Leszczyszyn, D. J. Biological systems. In *Microelectrodes: Theory and Applications*. Montenegro, M. I., Queiros, M. A., Daschbach, J. L. (Eds.). Kluwer Academic Publishing, Dordrecht, the Netherlands, 1991, pp. 453–462.
4. Cannon, D. M., Jr., Winograd, N., Ewing, A. G. Quantitative chemical analysis of single cells. *Annu Rev Biophys Biomol Struct* 2000, 29, 239–263.
5. Ewing, A. G., Strein, T. S., Lau, Y. Y. Analytical chemistry in microenvironments: Single nerve cells. *Acc Chem Res* 1992, 25, 440–447.
6. Kennedy, R. T., Huang, L., Atkinson, M. A., Dush, P. Amperometric monitoring of individual exocytosis events in pancreatic beta cells. *Anal Chem* 1993, 65, 1882.
7. Pantano, P., Kuhr, W. G. Enzyme-modified microelectrodes for in vivo neurochemical measurements. *Electroanalysis* 1995, 7, 405–416.
8. Lu, H., Gratzl, M. Monitoring drug efflux from sensitive and multidrug-resistant single cancer cells with microvoltammetry. *Anal Chem* 1999, 71, 2821–2830.
9. Pace, N. R. The molecular tree of life changes how we see, teach microbial diversity. *Microbe* 2008, 3, 15–20.
10. Sapp, J. The new foundations of evolution on the tree of life. New York: Oxford University Press, 2009.
11. Lee, C., Kwak, J., Bard, A. J. Application of scanning electrochemical microscopy to biological samples. *Proc Natl Acad Sci USA* 1990, 87, 1740–1743.
12. Amemiya, S., Bard, A. J., Fan, F.-R. F., Mirkin, M. V., Unwin, P. R. Scanning electrochemical microscopy. *Annu Rev Anal Chem* 2008, 1, 95–131.
13. Bard, A. J., Li, X., Zhan, W. Chemically imaging living cells by scanning electrochemical microscopy. *Biosens Bioelectron* 2006, 22, 461–472.
14. Edwards, M. A., Martin, S., Whitworth, A. L., Macpherson, J. V., Unwin, P. R. Scanning electrochemical microscopy: Principles and applications to biophysical systems. *Physiol Meas* 2006, 27, R63–R108.
15. Schulte, A., Schuhmann, W. Single-cell microelectrochemistry. *Angew Chem Int Ed* 2007, 46, 8760–8777.
16. Wittstock, G., Burchardt, M., Pust, S. E., Shen, Y., Zhao, C. Scanning electrochemical microscopy for direct imaging of reaction rates. *Angew Chem Int Ed* 2007, 46, 1584–1617.
17. Wittstock, G., Wilhelm, T., Bahrs, S., Steinrücke, P. SECM feedback imaging of enzymatic activity on agglomerated microbeads. *Electroanalysis* 2001, 13, 669–675.
18. Amemiya, S., Guo, J., Xiong, H., Gross, D. A. Biological applications of scanning electrochemical microscopy: Chemical imaging of single living cells and beyond. *Anal Bioanal Chem* 2006, 386, 458–471.
19. Sun, P., Laforge, F. O., Mirkin, M. V. Scanning electrochemical microscopy in the 21st century. *PCCP* 2007, 9, 802–823.
20. Schulte, A., Nebel, M., Schuhmann, W. Scanning electrochemical microscopy in neuroscience. *Annu Rev Anal Chem* 2010, 3, 299–318.
21. Yasukawa, T., Kaya, T., Matsue, T. Characterization and imaging of single cells with scanning electrochemical microscopy. *Electroanalysis* 2000, 12, 653–659.
22. Wang, W., Zhang, S.-H., Li, L.-M., Wang, Z.-L., Cheng, J.-K., Huang, W.-H. Monitoring of vesicular exocytosis from single cells using micrometer and nanometer-sized electrochemical sensors. *Anal Bioanal Chem* 2009, 394, 17–32.
23. Roberts, W. S., Lonsdale, D. J., Griffiths, J., Higsona, S. P. J. Advances in the application of scanning electrochemical microscopy to bioanalytical systems. *Biosens Bioelectron* 2007, 23, 301–318.
24. Yotter, R. A., Wilson, D. M. Sensor technologies for monitoring metabolic activity in single cells—Part II: Nonoptical methods and applications. *IEEE Sens J* 2004, 4, 412–429.

25. Beaulieu, I., Kuss, S., Mauzeroll, J., Geissler, M. Biological scanning electrochemical microscopy and its application to live cell studies. *Anal Chem* 2011, 83, 1485–1492.
26. Shiku, H., Ohya, H., Matsue, T. Scanning electrochemical microscopy applied to biological systems. In *Encyclopedia of Electrochemistry*. Bard, A. J., Stratmann, M. (Eds.). Wiley-VCH, Weinheim, Germany, 2001, pp. 257–275.
27. Horrocks, B. R., Wittstock, G. Biological systems. In *Scanning Electrochemical Microscopy*. Bard, A. J., Mirkin, M. V. (Eds.). Marcel Dekker, New York, 2000, pp. 445–519.
28. Nagamine, K., Kaya, T., Yasukawa, T., Shiku, H., Matsue, T. Application of microbial chip for amperometric detection of metabolic alteration in bacteria. *Sens Actuators B Chem* 2005, 108, 676–682.
29. Cai, C., Liu, B., Mirkin, M. V., Frank, H. A., Rusling, J. F. Scanning electrochemical microscopy of living cells. 3. *Rhodobacter sphaeroides. Anal Chem* 2002, 74, 114–119.
30. Nagamine, K., Matsui, N., Kaya, T., Yasukawa, T., Shiku, H., Nakayama, T., Nishino, T., Matsue, T. Amperometric detection of the bacterial metabolic regulation with a microbial array chip. *Biosens Bioelectron* 2005, 21, 145–151.
31. Matsui, N., Kaya, T., Nagamine, K., Yasukawa, T., Shiku, H., Matsue, T. Electrochemical mutagen screening using microbial chip. *Biosens Bioelectron* 2006, 21, 1202–1209.
32. Kaya, T., Nishizawa, M., Yasukawa, T., Nishiguchi, M., Onouchi, T., Matsue, T. A microbial chip combined with scanning electrochemical microscopy. *Biotechnol Bioeng* 2001, 76, 391–394.
33. Holt, K. B., Bard, A. J. Interaction of silver(I) ions with the respiratory chain of *Escherichia coli*: An electrochemical and scanning electrochemical microscopy study of the antimicrobial mechanism of micromolar Ag^+. *Biochemistry* 2005, 44, 13214–13223.
34. Kaya, T., Nagamine, K., Oyamatsu, D., Shiku, H., Nishizawa, M., Matsue, T. Fabrication of microbial chip using collagen gel microstructure. *Lab Chip* 2003, 3, 313–317.
35. Kaya, T., Nagamine, K., Oyamatsu, D., Nishizawa, M., Matsue, T. A microbial chip for glucose sensing studied with scanning electrochemical microscopy (SECM). *Electrochemistry* 2003, 71, 436–438.
36. Kaya, T., Numai, D., Nagamine, K., Aoyagi, S., Shiku, H., Matsue, T. Respiration activity of *Escherichia coli* entrapped in a cone-shaped microwell and cylindrical micropore monitored by scanning electrochemical microscopy (SECM). *Analyst* 2004, 129, 529–534.
37. Nagamine, K., Onodera, S., Torisawa, Y.-S., Yasukawa, T., Shiku, H., Matsue, T. On-chip transformation of bacteria. *Anal Chem* 2005, 77, 4278–4281.
38. Nagamine, K., Onodera, S., Kurihara, A., Yasukawa, T., Shiku, H., Asano, R., Kumagai, I., Matsue, T. Electrochemical screening of recombinant protein solubility in *Escherichia coli* using scanning electrochemical microscopy (SECM). *Biotechnol Bioeng* 2007, 96, 1008–1013.
39. Zhan, D., Fan, F.-R. F., Bard, A. J. The K_v channel blocker 4-aminopyridine enhances Ag^+ uptake: A scanning electrochemical microscopy study of single living cells. *Proc Natl Acad Sci USA* 2008, 105, 12118–12122.
40. Takahashi, Y., Hirano, Y., Yasukawa, T., Shiku, H., Yamada, H., Matsue, T. Topographic, electrochemical, and optical images captured using standing approach mode scanning electrochemical/optical microscopy. *Langmuir* 2006, 22, 10299–10306.
41. Yasukawa, T., Matsue, T. Characterization of single cells using microelectrode systems. *Electrochemistry* 1999, 67, 264–268.
42. Matsue, T., Koike, S., Uchida, I. Microamperometric estimation of photosynthesis inhibition in a single algal protoplast. *Biochem Biophys Res Commun* 1993, 197, 1283–1287.
43. Guo, J., Amemiya, S. Permeability of the nuclear envelope at isolated *Xenopus* oocyte nuclei studied by scanning electrochemical microscopy. *Anal Chem* 2005, 77, 2147–2156.
44. Sun, P., Laforge, F. O., Abeyweera, T. P., Rotenberg, S. A., Carpino, J., Mirkin, M. V. Nanoelectrochemistry of mammalian cells. *Proc Natl Acad Sci USA* 2008, 105, 443–448.
45. Gao, N., Wang, X., Li, L., Zhang, X., Jin, W. Scanning electrochemical microscopy coupled with intracellular standard addition method for quantification of enzyme activity in single intact cells. *Analyst* 2007, 132, 1139–1146.
46. Tsionsky, M., Cardon, Z. G., Bard, A. J., Jackson, R. B. Photosynthetic electron transport in single guard cells as measured by scanning electrochemical microscopy. *Plant Physiol* 1997, 113, 895–901.
47. Yasukawa, T., Uchida, I., Matsue, T. Permeation of redox species through a cell membrane of a single, living algal protoplast studied by microamperometry. *Biochim Biophys Acta Biomembr* 1998, 1369, 152–158.
48. Yasukawa, T., Kaya, T., Matsue, T. Dual imaging of topography and photosynthetic activity of a single protoplast by scanning electrochemical microscopy. *Anal Chem* 1999, 71, 4637–4641.
49. Yasukawa, T., Uchida, I., Matsue, T. Microamperometric measurements of photosynthetic activity in a single algal protoplast. *Biophys J* 1999, 76, 1129–1135.

50. Hengstenberg, A., Blöchl, A., Dietzel, I. D., Schuhmann, W. Spatially resolved detection of neurotransmitter secretion from individual cells by means of scanning electrochemical microscopy. *Angew Chem Int Ed* 2001, 40, 905–908.
51. Ciobanu, M., Taylor, D. E., Jr., Wilburn, J. P., Cliffel, D. E. Glucose and lactate biosensors for scanning electrochemical microscopy imaging of single live cells. *Anal Chem* 2008, 80, 2717–2727.
52. Schrock, D. S., Baur, J. E. Chemical imaging with combined fast-scan cyclic voltammetry–scanning electrochemical microscopy. *Anal Chem* 2007, 79, 7053–7061.
53. Takahashi, Y., Miyamoto, T., Shiku, H., Asano, R., Yasukawa, T., Kumagai, I., Matsue, T. Electrochemical detection of epidermal growth factor receptors on a single living cell surface by scanning electrochemical microscopy. *Anal Chem* 2009, 81, 2785–2790.
54. Pitta Bauermann, L., Schuhmann, W., Schulte, A. An advanced biological scanning electrochemical microscope (Bio-SECM) for studying individual living cells. *PCCP* 2004, 6, 4003–4008.
55. Zhao, X., Petersen, N. O., Ding, Z. Comparison study of live cells by atomic force microscopy, confocal microscopy, and scanning electrochemical microscopy. *Can J Chem* 2007, 85, 175–183.
56. Diakowski, P. M., Ding, Z. Interrogation of living cells using alternating current scanning electrochemical microscopy (AC-SECM). *PCCP* 2007, 9, 5966–5974.
57. Berger, C. E. M., Rathod, H., Gillespie, J. I., Horrocks, B. R., Datta, H. K. Scanning electrochemical microscopy at the surface of bone-resorbing osteoclasts: Evidence for steady-state disposal and intracellular functional compartmentalization of calcium. *J Bone Miner Res* 2001, 16, 2092–2102.
58. Ueda, A., Niwa, O., Maruyama, K., Shindo, Y., Oka, K., Suzuki, K. Neurite imaging of living PC12 cells with scanning electrochemical/near-field optical/atomic force microscopy. *Angew Chem Int Ed* 2007, 46, 8238–8241.
59. Maruyama, K., Ohkawa, H., Ogawa, S., Ueda, A., Niwa, O., Suzuki, K. Fabrication and characterization of a nanometer-sized optical fiber electrode based on selective chemical etching for scanning electrochemical/optical microscopy. *Anal Chem* 2006, 78, 1904–1912.
60. Takii, Y., Takoh, K., Nishizawa, M., Matsue, T. Characterization of local respiratory activity of PC12 neuronal cell by scanning electrochemical microscopy. *Electrochim Acta* 2003, 48, 3381–3385.
61. Kurulugama, R. T., Wipf, D. O., Takacs, S. A., Pongmayteegul, S., Garris, P. A., Baur, J. E. Scanning electrochemical microscopy of model neurons: Constant distance imaging. *Anal Chem* 2005, 77, 1111–1117.
62. Liebetrau, J. M., Miller, H. M., Baur, J. E., Takacs, S. A., Anupunpisit, V., Garris, P. A., Wipf, D. O. Scanning electrochemical microscopy of model neurons: Imaging and real-time detection of morphological changes. *Anal Chem* 2003, 75, 563–571.
63. Zhu, L., Gao, N., Zhang, X., Jin, W. Accurately measuring respiratory activity of single living cells by scanning electrochemical microscopy. *Talanta* 2008, 77, 804–808.
64. Xue, Y., Ding, L., Lei, J., Yan, F., Ju, H. In situ electrochemical imaging of membrane glycan expression on micropatterned adherent single cells. *Anal Chem* 2010, 82, 7112–7118.
65. Zhao, X., Lam, S., Jass, J., Ding, Z. Scanning electrochemical microscopy of single human urinary bladder cells using reactive oxygen species as probe of inflammatory response. *Electrochem Commun* 2010, 12, 773–776.
66. Yasukawa, T., Kondo, Y., Uchida, I., Matsue, T. Imaging of cellular activity of single cultured cells by scanning electrochemical microscopy. *Chem Lett* 1998, 8, 767–768.
67. Wang, W., Xiong, Y., Du, F.-Y., Huang, W.-H., Wu, W.-Z., Wang, Z.-L., Cheng, J.-K., Yang, Y.-F. Imaging and detection of morphological changes of single cells before and after secretion using scanning electrochemical microscopy. *Analyst* 2007, 132, 515–518.
68. Isik, S., Schuhmann, W. Detection of nitric oxide release from single cells by using constant-distance-mode scanning electrochemical microscopy. *Angew Chem Int Ed* 2006, 45, 7451–7454.
69. Mauzeroll, J., Bard, A. J., Owhadian, O., Monks, T. J. Menadione metabolism to thiodione in hepatoblastoma by scanning electrochemical microscopy. *Proc Natl Acad Sci USA* 2004, 101, 17582–17587.
70. Hirano, Y., Nishimiya, Y., Kowata, K., Mizutani, F., Tsuda, S., Komatsu, Y. Construction of time-lapse scanning electrochemical microscopy with temperature control and its application to evaluate the preservation effects of antifreeze proteins on living cells. *Anal Chem* 2008, 80, 9349–9354.
71. Takahashi, Y., Shiku, H., Murata, T., Yasukawa, T., Matsue, T. Transfected single-cell imaging by scanning electrochemical optical microscopy with shear force feedback regulation. *Anal Chem* 2009, 81, 9674–9681.
72. Kaya, T., Torisawa, Y.-S., Oyamatsu, D., Nishizawa, M., Matsue, T. Monitoring the cellular activity of a cultured single cell by scanning electrochemical microscopy (SECM). A comparison with fluorescence viability monitoring. *Biosens Bioelectron* 2003, 18, 1379–1383.
73. Nishizawa, M., Takoh, K., Matsue, T. Micropatterning of HeLa cells on glass substrates and evaluation of respiratory activity using microelectrodes. *Langmuir* 2002, 18, 3645–3649.

74. Murata, T., Yasukawa, T., Shiku, H., Matsue, T. Electrochemical single-cell gene-expression assay combining dielectrophoretic manipulation with secreted alkaline phosphatase reporter system. *Biosens Bioelectron* 2009, 25, 913–919.
75. Shiku, H., Takeda, M., Murata, T., Akiba, U., Hamada, F., Matsue, T. Development of electrochemical reporter assay using HeLa cells transfected with vector plasmids encoding various responsive elements. *Anal Chim Acta* 2009, 640, 87–92.
76. Chen, Z., Xie, S., Shen, L., Du, Y., He, S., Li, Q., Liang, Z., Meng, X., Li, B., Xu, X., Ma, H., Huang, Y., Shao, Y. Investigation of the interactions between silver nanoparticles and HeLa cells by scanning electrochemical microscopy. *Analyst* 2008, 133, 1221–1228.
77. Li, X., Bard, A. J. Scanning electrochemical microscopy of HeLa cells—Effects of ferrocene methanol and silver ion. *J Electroanal Chem* 2009, 628, 35–42.
78. Koley, D., Bard, A. J. Triton X-100 concentration effects on membrane permeability of a single HeLa cell by scanning electrochemical microscopy (SECM). *Proc Natl Acad Sci USA* 2010, 107, 16783–16787.
79. Liu, B., Rotenberg, S. A., Mirkin, M. V. Scanning electrochemical microscopy of living cells: Different redox activities of nonmetastatic and metastatic human breast cells. *Proc Natl Acad Sci USA* 2000, 97, 9855–9860.
80. Mirkin, M. V., Liu, B., Rotenberg, S. A. Probing redox activity of human breast cells by scanning electrochemical microscopy. In *Methods in Enzymology*. Abelson, J. N., Simon, M. I. (Eds.). Academic Press, 2002, pp. 112–122.
81. Rotenberg, S. A., Mirkin, M. V. Scanning electrochemical microscopy: Detection of human breast cancer cells by redox environment. *J Mammary Gland Biol Neoplasia* 2004, 9, 375–382.
82. Feng, W., Rotenberg, S. A., Mirkin, M. V. Scanning electrochemical microscopy of living cells. 5. Imaging of fields of normal and metastatic human breast cells. *Anal Chem* 2003, 75, 4148–4154.
83. Liu, B., Rotenberg, S. A., Mirkin, M. V. Scanning electrochemical microscopy of living cells. 4. Mechanistic study of charge transfer reactions in human breast cells. *Anal Chem* 2002, 74, 6340–6348.
84. Liu, B., Cheng, W., Rotenberg, S. A., Mirkin, M. V. Scanning electrochemical microscopy of living cells: Part 2. Imaging redox and acid/basic reactivities. *J Electroanal Chem* 2001, 500, 590–597.
85. Mauzeroll, J., Bard, A. J. Scanning electrochemical microscopy of menadione–glutathione conjugate export from yeast cells. *Proc Natl Acad Sci USA* 2004, 101, 7862–7867.
86. Shiku, H., Torisawa, Y.-S., Takagi, A., Aoyagi, S., Abe, H., Hoshi, H., Yasukawa, T., Matsue, T. Metabolic and enzymatic activities of individual cells, spheroids and embryos as a function of the sample size. *Sens Actuators B Chem* 2005, 108, 597–602.
87. Garay, M. F., Ufheil, J., Borgwarth, K., Heinze, J. Retrospective chemical analysis of tree rings by means of the scanning electrochemical microscopy with shear force feedback. *PCCP* 2004, 6, 4028–4033.
88. Zhu, R., Macfie, S. M., Ding, Z. Cadmium-induced plant stress investigated by scanning electrochemical microscopy. *J Exp Bot* 2005, 56, 2831–2838.
89. Parthasarathy, M., Singh, S., Hazra, S., Pillai, V. K. Imaging the stomatal physiology of somatic embryo-derived peanut leaves by scanning electrochemical microscopy. *Anal Bioanal Chem* 2008, 391, 2227–2233.
90. Ktari, N., Poncet, P., Snchal, H., Malaquin, L., Kanoufi, F., Combellas, C. Patterning of polystyrene by scanning electrochemical microscopy. Biological applications to cell adhesion. *Langmuir* 2010, 26, 17348–17356.
91. Shiku, H., Shiraishi, T., Aoyagi, S., Utsumi, Y., Matsudaira, M., Abe, H., Hoshi, H., Kasai, S., Ohya, H., Matsue, T. Respiration activity of single bovine embryos entrapped in a cone-shaped microwell monitored by scanning electrochemical microscopy. *Anal Chim Acta* 2004, 522, 51–58.
92. Shiku, H., Shiraishi, T., Ohya, H., Matsue, T., Abe, H., Hoshi, H., Kobayashi, M. Oxygen consumption of single bovine embryos probed by scanning electrochemical microscopy. *Anal Chem* 2001, 73, 3751–3758.
93. Aoyagi, S., Utsumi, Y., Masudaira, M., Yamada, H., Kaachi, M., Shiku, H., Abe, H., Hoshi, H., Matsue, T. Quality Evaluation of in vitro-produced bovine embryos by respiration measurement and development of semi-automatic instrument. *Bunseki Kagaku* 2006, 55, 847–854.
94. Agung, B., Otoi, T., Abe, H., Hoshi, H., Murakami, M., Karja, N. W. K., Murakami, M. K., Wongsrikeao, P., Watari, H., Suzuki, T. Relationship between oxygen consumption and sex of bovine in vitro fertilized embryos. *Reprod Domest Anim* 2005, 40, 51–56.
95. Abe, H., Hoshi, H. Evaluation of bovine embryos produced in high performance serum-free media. *J Reprod Dev* 2003, 49, 193–202.

96. Goto, M., Abe, H., Ito-Sasaki, T., Goto, M., Inagaki, A., Ogawa, N., Fujimori, K., Kurokawa, Y., Matsue, T., Satomi, S. A novel predictive method for assessing the quality of isolated pancreatic islets using scanning electrochemical microscopy. *Transplant Proc* 2009, 41, 311–313.
97. Torisawa, Y.-S., Kaya, T., Takii, Y., Oyamatsu, D., Nishizawa, M., Matsue, T. Scanning electrochemical microscopy-based drug sensitivity test for a cell culture integrated in silicon microstructures. *Anal Chem* 2003, 75, 2154–2158.
98. Torisawa, Y.-S., Shiku, H., Kasai, S., Nishizawa, M., Matsue, T. Proliferation assay on a silicon chip applicable for tumors extirpated from mammalians. *Int J Cancer* 2004, 109, 302–308.
99. Zhan, D., Li, X., Zhan, W., Fan, F.-R. F., Bard, A. J. Scanning electrochemical microscopy. 58. Application of a micropipet-supported ITIES tip to detect Ag^+ and study its effect on fibroblast cells. *Anal Chem* 2007, 79, 5225–5231.
100. Takoh, K., Takahashi, A., Matsue, T., Nishizawa, M. A porous membrane-based microelectroanalytical technique for evaluating locally stimulated culture cells. *Anal Chim Acta* 2004, 522, 45–49.
101. Kaji, H., Kanada, M., Oyamatsu, D., Matsue, T., Nishizawa, M. Microelectrochemical approach to induce local cell adhesion and growth on substrates. *Langmuir* 2004, 20, 16–19.
102. Torisawa, Y.-S., Shiku, H., Yasukawa, T., Nishizawa, M., Matsue, T. Three-dimensional micro-culture system with a silicon-based cell array device for multi-channel drug sensitivity test. *Sens Actuators B Chem* 2005, 108, 654–659.
103. Torisawa, Y.-S., Shiku, H., Yasukawa, T., Nishizawa, M., Matsue, T. Multi-channel 3-D cell culture device integrated on a silicon chip for anticancer drug sensitivity test. *Biomaterials* 2005, 26, 2165–2172.
104. Pailleret, A., Oni, J., Reiter, S., Isik, S., Etienne, M., Bedioui, F., Schuhmann, W. In situ formation and scanning electrochemical microscopy assisted positioning of NO-sensors above human umbilical vein endothelial cells for the detection of nitric oxide release. *Electrochem Commun* 2003, 5, 847–852.
105. Borgmann, S., Radtke, I., Erichsen, T., Blöchl, A., Heumann, R., Schuhmann, W. Electrochemical high-content screening of nitric oxide release from endothelial cells. *ChemBioChem* 2006, 7, 662–668.
106. Isik, S., Etienne, M., Oni, J., Blöchl, A., Reiter, S., Schuhmann, W. Dual microelectrodes for distance control and detection of nitric oxide from endothelial cells by means of scanning electrochemical microscope. *Anal Chem* 2004, 76, 6389–6394.

13 Localized Flux Measurements and Kinetic Imaging at Interfaces

Patrick R. Unwin and Julie V. Macpherson

CONTENTS

13.1 Introduction 417
13.2 Adsorption/Desorption Kinetics 418
13.2.1 Principles and Theoretical Aspects 418
13.2.2 Applications 423
13.3 Two-Dimensional Diffusion 424
13.3.1 Lateral Proton Diffusion 425
13.3.2 Physical Diffusion in Molecular Assemblies 426
13.3.3 Charge Propagation in Ultrathin Films 427
13.4 SECM-Induced Transfer and Related Methods in Two-Phase Systems 428
13.4.1 Permeability Measurements 428
13.4.2 Kinetics of Molecule and Ion Transfer between Fluid Phases 429
13.5 Dissolution Kinetics of Solid Materials 432
13.5.1 Principles and Theoretical Aspects 432
13.5.2 Effect of Surface Structure on Dissolution Characteristics 435
13.5.3 High-Resolution Dissolution Imaging with Integrated Electrochemical–Atomic Force Microscopy 438
13.5.3.1 Potassium Bromide (100) Dissolution 440
13.5.3.2 Potassium Ferrocyanide Trihydrate (010) Surface Dissolution 442
13.5.3.3 Calcite ($10\bar{1}4$) Dissolution 443
13.6 Conclusions and Perspective 446
References 447

13.1 INTRODUCTION

Interfacial physicochemical processes often involve an exchange of material at phase boundaries, such that the boundaries (interfaces) are chemically in flux. Furthermore, such processes typically involve mass transport between bulk solution and the interface, coupled to (a series of) interfacial phenomena. To understand interfacial processes quantitatively, there are two general challenges: (i) to identify the contributions to the overall flux, from the individual events in the sequence, so as to determine the relative importance of mass transport and the interfacial process and (ii) to elucidate the extent to which the various phenomena are spatially heterogeneous across the interface, that is, whether there are distinct sites of activity and, if so, what these are. The extent to which these challenges can be addressed depends on the type of interface and interfacial process.

For electrode (conductor/semiconductor) surfaces, mass transport can be controlled with a variety of experimental protocols and the interfacial flux is measured directly via the current response (measured as a function of potential, time, etc.) [1]. This is not true of other interfaces, such as minerals and many biomimetic surfaces in contact with the solution. In these instances, fluxes have often been deduced in a convoluted time- and space-averaged manner by determining the accumulation/loss of material in a bulk phase as a function of time. This leads to a considerable loss of dynamic resolution. Furthermore, in some systems, mass transport between the bulk and the interface is difficult to estimate, leading to incorrect mechanistic interpretation, with major implications for practical applications, whether this concerns drug transport across cell membranes or the growth of crystals.

The impact of SECM in studying physicochemical processes at electrically insulating interfaces has been the proven ability to measure localized fluxes directly under conditions where mass transport can be calculated and accounted for, so that one obtains interfacial kinetic data [2,3]. Notably, for very close tip/sample distances and small electrode dimensions, high rates of mass transfer can be generated, which is extremely advantageous for studying fast reactions. Coupled with this, the local nature of SECM opens up the possibility of directly monitoring the reactivity of a targeted spot on an interface, enabling surface activity to be directly correlated with structural features. Measurements at higher spatial resolution are possible by combining the local electrochemical capabilities of SECM with the topographical imaging features of the atomic force microscope (AFM) and other methods as highlighted in Chapter 17 and discussed later herein.

This chapter is concerned with the study of interfacial processes and reactions that occur essentially at electrically insulating interfaces, where the role of the SECM tip is often to *induce* and *monitor* the reaction of interest. The work herein is an update of Chapter 12 "Probing reactions at solid/liquid interfaces" of the first edition of *Scanning Electrochemical Microscopy* [4] and highlights how the basic principles of the *SECM-induced transfer (SECMIT) mode* (or *equilibrium perturbation mode*) and related techniques—notably (multi-) potential step transient methods—can be applied to a wide variety of interfaces where flux measurements have traditionally been difficult.

We begin with simple adsorption/desorption measurements and develop the ideas to include transport in two-dimensional (2D) systems, and phase transfer processes such as dissolution and transport in two-phase systems. Some of the work highlighted complements studies described in Chapter 9 on membrane transport where the tip is mainly used as a detector of localized transport phenomena.

13.2 ADSORPTION/DESORPTION KINETICS

13.2.1 Principles and Theoretical Aspects

For the investigation of adsorption/desorption kinetics, SECM is employed to locally perturb adsorption/desorption equilibria and measure the resulting flux of adsorbate from a surface. In this application, the technique is termed SECM-induced desorption (SECMID) [5], but this represents the first use of SECM in an equilibrium perturbation mode of operation. The principles of SECMID are illustrated schematically in Figure 13.1, with specific reference to proton adsorption/desorption at a metal oxide/aqueous interface. For this type of investigation, the tip UME is placed close to the surface of the substrate, such that the tip/substrate separation, d, is of the order of, or less than, the electrode radius, a. The substrate is immersed in a solution of the adsorbate of interest and the adsorption/desorption process is initially at equilibrium.

By stepping the electrode potential from a value where no electrode reactions occur to one where the solution component of the adsorbate (H^+ in Figure 13.1) is removed at a diffusion-controlled rate, H^+ is locally depleted in the solution between the tip and substrate surface. This process perturbs the adsorption/desorption equilibrium, inducing proton desorption from the surface and promoting the diffusion of protons from the surrounding solution into the tip/substrate gap. Additionally, since the desorption process depletes the concentration of adsorbed protons on the part of the substrate

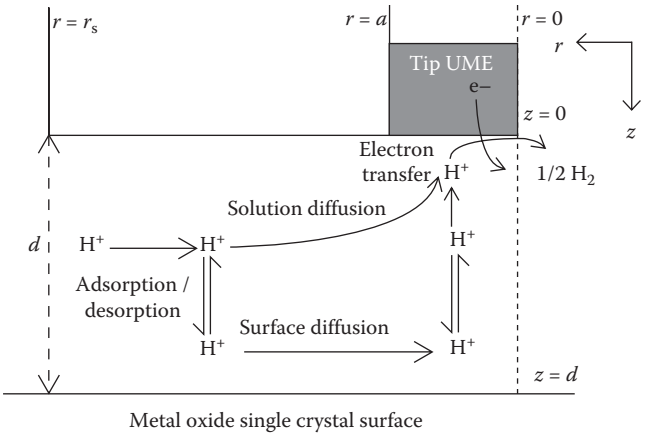


FIGURE 13.1 Principles of SECMID using H^+ as a model adsorbate. Schematic of the transport processes in the tip/substrate domain for a reversible adsorption/desorption process at the substrate, following the application of a potential step to the tip UME where the reduction of H^+ is diffusion controlled. The coordinate system and notation for the axisymmetric cylindrical geometry is also shown. Note that the diagram is not to scale as the tip/substrate separation is typically $\leq 0.01\ r_s$. (Reproduced from Unwin, P.R. and Bard, A.J., *Anal. Chem*., 64, 113, 1992. With permission.)

surface directly under the UME, a radial concentration gradient of adsorbate develops across the surface, promoting—*in principle*—surface diffusion as a pathway for the transport of protons into the gap. This aspect is considered further in Section 13.3.1. The resulting tip current–time behavior provides quantitative information on the rates of adsorption/desorption (and surface diffusion if this operates).

A related potential step approach can be used to investigate adsorption processes, wherein the adsorbate is electrochemically generated at the tip, in a mode termed reactant injection chronoamperometry (RIC). This approach has been used, for example, to study Ag^+ ion binding to phospholipid monolayers at the water–air interface, by electrodissolution of a Ag UME [6]. As the Ag/Ag^+ couple is highly reversible, the current–time characteristics for the potentiostatic electrodissolution reaction provides direct information on mass transport between the UME and interface, from which the binding kinetics can be measured.

A key feature of SECMID (and related methods) is that mass transport and the interfacial processes of interest are well defined so that the tip current response can be calculated readily and compared with experiment to obtain interfacial kinetic data. It is beyond the scope of this chapter to provide a complete overview of the theoretical treatment of SECM problems, but some discussion of the elements involved in the formulation of this particular SECM problem is useful to aid understanding of the method and analysis. Furthermore, the basic theoretical principles and results apply to many of the other modes that are considered subsequently in this chapter and, indeed, in many of the other chapters.

To calculate the tip current response, the diffusion equation for the axisymmetric cylindrical SECM geometry is solved subject to boundary conditions that define the chemical processes occurring at the tip UME and the substrate surface:

$$\frac{\partial C}{\partial \tau} = \frac{\partial^2 C}{\partial R^2} + \frac{1}{\mathrm{R}}\frac{\partial C}{\partial R} + \frac{\partial^2 C}{\partial Z^2} \tag{13.1}$$

Equation 13.1 is the relevant time-dependent diffusion equation expressed in the form of dimensionless variables:

$$C = \frac{c}{c^*} \tag{13.2}$$

$$\tau = \frac{tD_{soln}}{a} \tag{13.3}$$

$$R = \frac{r}{a} \tag{13.4}$$

$$Z = \frac{z}{a} \tag{13.5}$$

where

r and z are the coordinates, respectively, in the directions radial and normal to the electrode surface (Figure 13.1), starting at its center

t is time

c and D_{soln} are the concentration and solution diffusion coefficient of the species (adsorbate) of interest

c^* is the concentration of adsorbate in bulk solution

Prior to the potential step, the concentration of adsorbate in solution is at the bulk value, over all space:

$$\tau = 0, \quad \text{all } R, \quad \text{all } Z: \quad C = 1 \tag{13.6}$$

Following the potential step ($\tau > 0$), the boundary conditions at the surface of the UME are

$$Z = 0, \quad 0 \le R \le 1: \qquad C = 0 \tag{13.7}$$

$$Z = 0, \quad 1 \le R \le \text{RG}: \qquad \partial C/\partial Z = 0 \tag{13.8}$$

$$R = 0, \quad 0 < Z < L: \qquad \partial C/\partial R = 0 \tag{13.9}$$

$$R > \text{RG}, \quad 0 < Z < L: \qquad C = 1 \tag{13.10}$$

where

$$L = \frac{d}{a} \tag{13.11}$$

$$\text{RG} = \frac{r_s}{a} \tag{13.12}$$

r_s is the radial distance from the center of the disk to the edge of the insulating sheath surrounding the electrode (Figure 13.1).

The boundary conditions indicate that electrolysis of the species of interest occurs at a diffusion-controlled rate (Equation 13.7) and the adsorbate is inert on the insulating sheath surrounding the electrode (Equation 13.8). Additional conditions define zero radial flux at the axis of symmetry (Equation 13.9) and the recovery of the bulk concentration of the species beyond the radial edge of the tip/substrate domain (Equation 13.10). This latter assumption is particularly valid for

time-dependent methods, where the process of interest typically occurs on a timescale governed by the tip-to-surface diffusion time. Even for steady-state SECM problems, it is usually reasonable, provided that RG ≥ 10.

The boundary condition at the substrate depends on the nature of the adsorption/desorption process and whether surface diffusion needs to be considered. For the induced desorption (or adsorption) of ions, there is an accompanying change in the local surface charge density, and models taking this into account [5,6], based on the diffuse layer (Gouy–Chapman) surface charge density–potential relationship, have been developed. A simpler limiting case, involving Langmuirian adsorption/desorption, has also been described [5,6] and we consider this here to illustrate the general features of SECMID. For this case, the substrate surface boundary condition is

$$Z = L, \quad 0 < R < \mathrm{RG}: \qquad \partial C/\partial Z = -K_\mathrm{d}\theta + K_\mathrm{a}C(1-\theta) \tag{13.13}$$

where

$$K_\mathrm{a} = \frac{k_\mathrm{a}a}{D_\mathrm{soln}} \tag{13.14}$$

$$K_\mathrm{d} = \frac{k_\mathrm{d}a}{D_\mathrm{soln}c^*} \tag{13.15}$$

k_a (cm/s) and k_d (mol/cm^2/s) are the apparent adsorption and desorption rate constants and θ is the fractional surface coverage.

The time dependence of θ is

$$Z = L, \quad 0 < R < \mathrm{RG}: \qquad \lambda\left(\frac{\partial\theta}{\partial\tau}\right) = -K_\mathrm{d}\theta + K_\mathrm{a}C(1-\theta) \tag{13.16}$$

where

$$\lambda = \frac{N}{c^* a} \tag{13.17}$$

where N is the density of adsorption sites (mol/cm^2). Prior to the potential step, the adsorption/desorption process is at equilibrium and the corresponding initial substrate condition is

$$\tau = 0: \text{substrate}: 0 < R < \mathrm{RG}: \qquad \theta = \left[1 + K_\mathrm{d}/K_\mathrm{a}\right]^{-1} \tag{13.18}$$

The tip current, i, normalized with respect to the steady-state current that flows at an UME in bulk solution, $i(\infty)$, is

$$i/i(\infty) = (\pi/2)\int_0^1 (\delta C/\partial R)_{Z=0}\,dR \tag{13.19}$$

Initially, purpose-written FORTRAN code using the alternating direction implicit finite-difference method (ADIFDM) was employed extensively for the solution of SECMID and related modes [5,7],

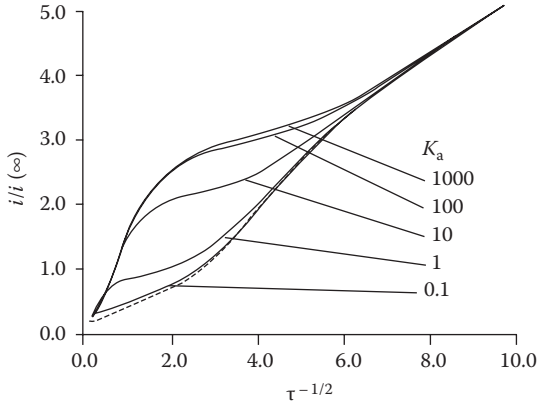


FIGURE 13.2 Theoretical $i/i(\infty)$ versus $\tau^{1/2}$ characteristics for a SECMID adsorption/desorption process characterized by $\lambda = 8$, $K_a/K_d = 1$, $L = 0.32$, and K_a values (solid lines) of 0.1 (lower), 1, 10, 100, and 1000 (upper). The dashed line indicates the behavior for an inert substrate. (Reproduced from Unwin, P.R. and Bard, A.J., *Anal. Chem*., 64, 113, 1992. With permission.)

but a more recent trend in SECM modeling has been toward the use of proprietary software packages, such as Comsol Multiphysics (previously Femlab; Comsol Ab, Sweden). Packages of this type provide several advantages over the direct implementation of numerical algorithms. Primarily, one is able to develop a model rather rapidly, taking advantage of complex algorithms. Graphical user interfaces (GUIs) have facilitated the input and modeling of complicated experimental geometries with relative ease [8,9].

Figure 13.2 illustrates the effect of the adsorption/desorption kinetics on the current–time transient profile, where $K_a/K_d = 1$, that is, half the surface sites are occupied at equilibrium. The results are presented as $i/i(\infty)$ versus $\tau^{-1/2}$ to emphasize the short-time behavior. At very short time, that is, the largest $\tau^{-1/2}$, the UME response is identical for all values of K_a, since under these conditions, the diffusion field adjacent to the electrode is much smaller than the tip/sample separation and so does not sense the presence of the substrate [10]. At times sufficient for the diffusion field to intercept the interface, the resulting chronoamperometric behavior becomes sensitive to the magnitude of K_a and K_d.

When the adsorption/desorption kinetics are slow compared to the rate of diffusional mass transfer through the tip/substrate gap, the current–time characteristics tend toward those predicted for an inert substrate, because desorption is sluggish in response to depletion of the solution component of the adsorbate in the vicinity of the tip and surface. As the kinetics increase, the response to the perturbation of the interfacial equilibrium is more pronounced and, at short to moderate times, the additional source of protons from the induced desorption process increases the current compared to that for an inert surface. This occurs up to a limit where the interfacial kinetics are sufficiently fast that the adsorption/desorption process is essentially always at equilibrium on the timescale of SECM measurements. For the case shown in Figure 13.2, this is effectively reached when $K_a = K_d = 1000$. In the absence of surface diffusion, at times sufficiently long for the system to attain a true steady state, the UME currents for all kinetic cases approach the value for an inert substrate. In this situation, the adsorption/desorption process reaches a new equilibrium (governed by the local solution concentration of the target species adjacent to the substrate–solution interface) and the tip current depends only on the rate of (hindered) diffusion through solution.

The effective adsorbate surface coverage, governed by the occupancy (θ) and density of adsorption sites (λ), has a significant effect on the current–time characteristics. It is particularly interesting to note that much lower surface coverages than considered in Figure 13.2 can readily be detected using SECMID, provided that the kinetics are sufficiently fast. This is demonstrated in Figure 13.3

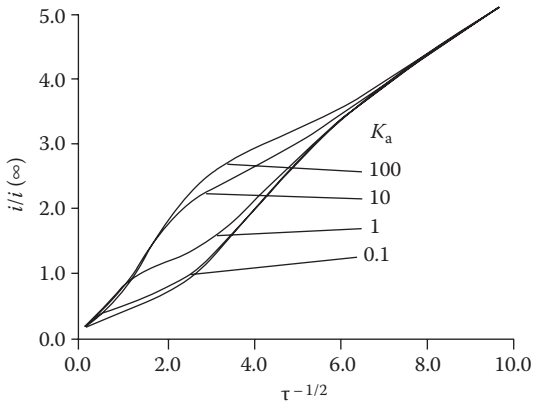


FIGURE 13.3 Theoretical $i/i(\infty)$ versus $\tau^{1/2}$ SECMID characteristics for a substrate adsorption/desorption process characterized by $\lambda = 8$, $K_a/K_d = 0.1$, $L = 0.32$, and K_a values (solid lines) of 0.1 (lower), 1, 10, 100, and 1000 (upper). The dashed line indicates the behavior for an inert substrate. (Reproduced from Unwin, P.R. and Bard, A.J., *Anal. Chem*., 64, 113, 1992. With permission.)

for the case where $K_a/K_d = 0.1$, that is, $\theta = 0.091$. In this particular case, the lower initial surface coverage leads to currents that approach the value for an inert surface more rapidly. However, it is still possible to distinguish the various kinetic cases in the short-time region. Theoretical simulations indicate that kinetic resolution is feasible down to θ values of ca. 0.01, that is, $K_a/K_d = 0.01$ [5]. As with many SECM techniques, the current response becomes increasingly sensitive to the surface process as the tip/substrate separation is decreased, since this serves both to maximize the ratio of effective surface area to solution volume probed by SECMID, and to hinder solution diffusion in the gap. This aspect of SECM sensitivity is covered in more detail in Section 13.5.1 on dissolution kinetics.

13.2.2 Applications

SECMID has been used to investigate the adsorption/desorption kinetics of protons on the (001) face of TiO_2 (rutile) and (010) face of $NaAlSi_3O_8$ (albite) single crystals in dilute acid solutions (2×10^{-4} mol/dm^3 HCl) [5]. The interfacial proton concentration was perturbed locally, and the resulting current–time behavior was measured, using a 25-μm diameter Pt disk electrode positioned close to the crystal surface of interest and stepping the tip potential to a value to reduce protons at a diffusion-controlled rate. At close tip/substrate separations, the short time currents for H^+ reduction above both crystal surfaces were larger than those predicted for an inert surface, as shown in Figures 13.4 and 13.5. This was due to H^+ desorption from the surface providing an additional source of protons, thereby increasing the overall flux at the UME. Using known values of K_a/K_d and λ for rutile and albite [5], it was possible to assign values for the adsorption and desorption rate constants, taking into account surface potential effects for the former system that were found to be important. For rutile, the intrinsic adsorption and desorption rate constants were $k_a = 0.4 \pm 0.1$ cm/s and $k_d = 5.5 \pm 1.4 \times 10^{-8}$ mol/cm^2/s and the initial surface concentration of H^+ was only ca. 8×10^{-11} mol/cm^2, highlighting the surface sensitivity of the technique. For albite, the measured rate constants were much lower: $k_a = 0.003 \pm 0.001$ cm/s and $k_d = 0.84 \pm 0.37 \times 10^{-9}$ mol/cm^2/s, and as a consequence, the measured chronoamperometric responses at close tip/substrate separations in Figure 13.5 are only slightly larger than for an inert surface.

As highlighted earlier, adsorption processes can also be studied directly using RIC, a modification of SECMID, provided that the adsorbate can be electrogenerated and is part of a reversible electrode couple [6]. RIC methodology has been used to determine the influence of surface pressure on the adsorption of Ag^+ ions at a phospholipid (dipalmitoyl phosphatidic acid [DPPA]) Langmuir

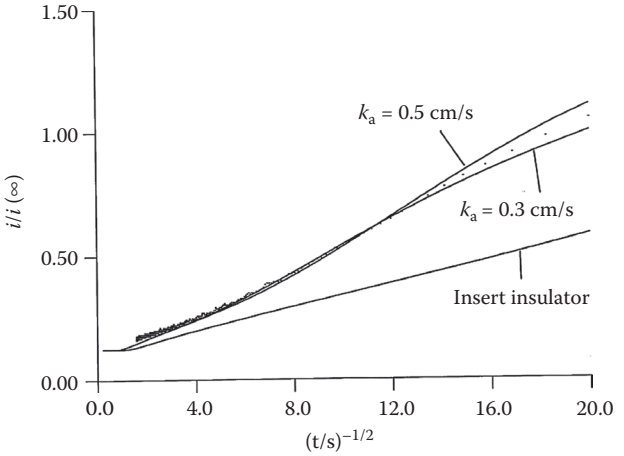


FIGURE 13.4 SECMID chronoamperometric characteristics for H^+ reduction against a rutile (001) surface at a tip/substrate separation of 2.6 μm, with a 12.5 μm radius Pt UME (RG = 10). The solid lines show the behavior for an inert substrate and an adsorption/desorption process characterized by $K_a/K_d = 1.49$, $\lambda = 6.6$, and $k_a = 0.3$ and 0.5 cm/s. The adsorption/desorption fit includes surface potential effects that have not been considered in this chapter. (Reproduced from Unwin, P.R. and Bard, A.J., *Anal. Chem.*, 64, 113, 1992. With permission.)

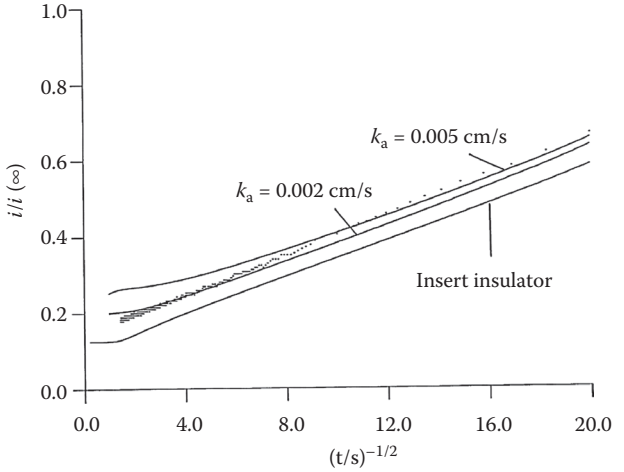


FIGURE 13.5 SECMID chronoamperometric characteristics for H^+ reduction against an albite (010) surface at a tip/substrate separation of 2.8 μm, with a 12.5 μm radius Pt UME (RG = 20). The solid lines show the behavior for an inert substrate and an adsorption/desorption process characterized by $K_a/K_d = 0.86$, $\lambda = 28.4$, and $k_a = 0.002$ and 0.005 cm/s. (Reproduced from Unwin, P.R. and Bard, A.J., *Anal. Chem.*, 64, 113, 1992. With permission.)

monolayer, using a specially designed submarine UME [11] to address the Langmuir monolayer from below. RIC has also been used to investigate the interaction of Ag^+ with the (100) face of pyrite [12], a complex process, involving adsorption (possibly by ion exchange) and Ag^+ reduction.

13.3 TWO-DIMENSIONAL DIFFUSION

As discussed in the previous section, SECM is a local perturbation technique that creates significant radial concentration gradients, both in solution and at interfaces. This effect provides a basis for

studying lateral diffusion processes, as exemplified in studies of lateral proton diffusion [13–15], physical diffusion in ultrathin films [16], lateral electron hopping in thin films [17,18], and surface conductivity [19–26]. In addition to the single potential step transient method discussed earlier, a triple potential step method has been developed [16], which is essentially an electrochemical analog of fluorescence recovery after photobleaching (FRAP) [27]. This allows a wide range of lateral charge propagation rates to be measured, as well as many other important parameters concerning charge propagation in redox-active films.

13.3.1 Lateral Proton Diffusion

The movement of protons between source and sink sites in cell membranes is crucial in cell functioning [13,28]. The rate of the process has been studied quite extensively in model monolayer systems and phospholipid assemblies, but a controversial aspect of prior work was that different techniques provided contradictory results [13,28]. Notably, many early measurements were made over centimeter length scales, where mass transport is much more difficult to control and model, and is undoubtedly affected by natural convection. These studies often found incredibly high lateral (surface) diffusion coefficients. A key advantage of SECM is the ability to make measurements with high spatial and temporal resolution, pertinent to cellular membranes, and—crucially—under well-defined mass transport conditions. As highlighted later, these studies have clearly shown—in a range of systems— that although lateral proton diffusion may occur at model biomembranes, the diffusion coefficient is much less than in bulk solution [13,14].

SECM has been used to investigate lateral proton diffusion at stearic acid [13] assembled at the water–air interface in a Langmuir trough. As for the studies of Ag^+ binding, described earlier, a "submarine" UME was employed [11] which allowed the water–air interface to be approached from below. The UME was held at a potential to reduce protons to hydrogen at a diffusion-controlled rate and the resulting local depletion drove the interfacial acid dissociation reaction, which in turn created a proton diffusion gradient, both in solution and at the interface as shown in Figure 13.6. Under conditions where the majority of stearic acid molecules were initially protonated, the magnitude of the lateral diffusion coefficient measured was found to be critically dependent on surface pressure in the monolayer, but was never >15% of the bulk solution value. This clearly indicates that this acidic surfactant did not provide a support for enhanced proton transport rates.

An SECM proton feedback method has also been developed to investigate lateral proton diffusion at phospholipid assemblies, specifically, Langmuir monolayers at the water–air interface [14].

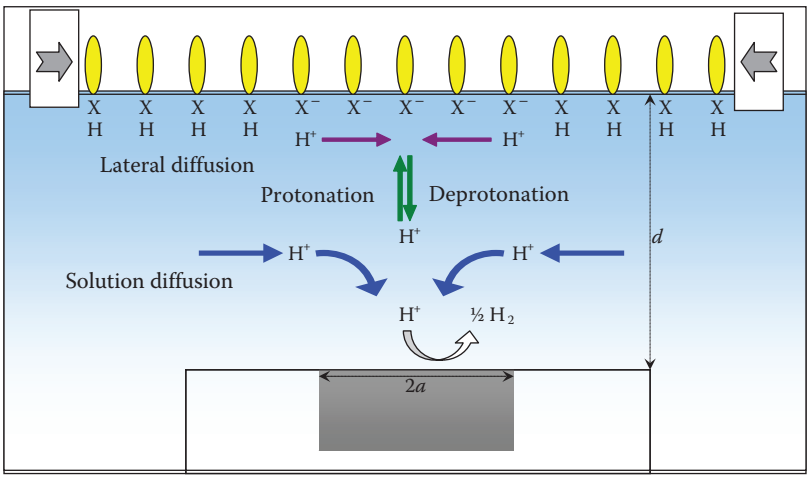


FIGURE 13.6 The use of a submarine UME to investigate lateral proton diffusion at stearic acid assembled at the water–air interface, X^- signifies COO^-.

In this approach, a base (HPO_4^{2-}) was electrogenerated by the reduction of a weak acid ($H_2PO_4^-$) at a submarine UME placed in the aqueous subphase of a Langmuir trough close to a monolayer. The base diffused to the interface and titrated monolayer-bound protons, so that the acid form diffused back to the tip, enhancing the current response at the UME. A comparison was made of monolayers comprising either acidic DL-*R*-phosphatidyl-L-serine, dipalmitoyl (DPPS) or zwitterionic L-*R*-phosphatidylcholine, dipalmitoyl (DPPC) monolayers at a range of surface pressure. An enhanced reduction current (compared to an inert surface) was found for an UME approaching the DPPS monolayer, which was attributed to lateral proton diffusion providing an additional proton source, detected by SECM proton feedback mediated through $H_2PO_4^- / HPO_4^{2-}$. Quantitative analysis of the approach curves showed that as the surface pressure increased from 1 to 20 mN/m, the lateral proton diffusion coefficient increased from ca. 1.5×10^{-6} to 6×10^{-6} cm^2/s, but the maximum value was still only ca. 10% of that in bulk solution. At the higher pressures, where the area per molecule changed only slightly, the lateral diffusion coefficient was reasonably uniform. In contrast, approach curves for both a native water–air interface and a DPPC monolayer showed a current response due only to the hindered diffusion of $H_2PO_4^-$ through solution (negative feedback response).

13.3.2 Physical Diffusion in Molecular Assemblies

An SECM approach for studying the lateral diffusion of redox-active amphiphiles in Langmuir monolayers at a water–air interface has been developed [16]. The approach is general and was subsequently applied to polymer films as highlighted in Section 13.3.3. Analogous to FRAP [27], the electrochemical approach involves an "electrochemical bleaching" step, a "recovery" step, and a final "analysis" step, as illustrated schematically in Figure 13.7, for the case of a redox-active amphiphile at a water–air interface.

In its initial application, a triple potential step was applied at a submarine UME placed in the aqueous subphase of a Langmuir trough, close (1–2 μm) to the monolayer. The technique involves generating an electroactive species (Ox) at the UME by diffusion-controlled electrolysis of a precursor (Red) in an initial potential step. Ox diffuses to, and reacts with, the redox-active amphiphile at the water–air interface resulting in the conversion of the solution redox species to its initial form (Red), which then undergoes diffusional feedback to the UME. In this first step, the rate constant for electron transfer between the solution mediator and the surface-confined species can be measured from the UME current–time transient. In the second period, the potential step is reversed to convert the electrogenerated species (Ox) to its initial form (Red). Lateral diffusion of electroactive amphiphile into the interfacial zone probed by the UME occurs simultaneously in this recovery period.

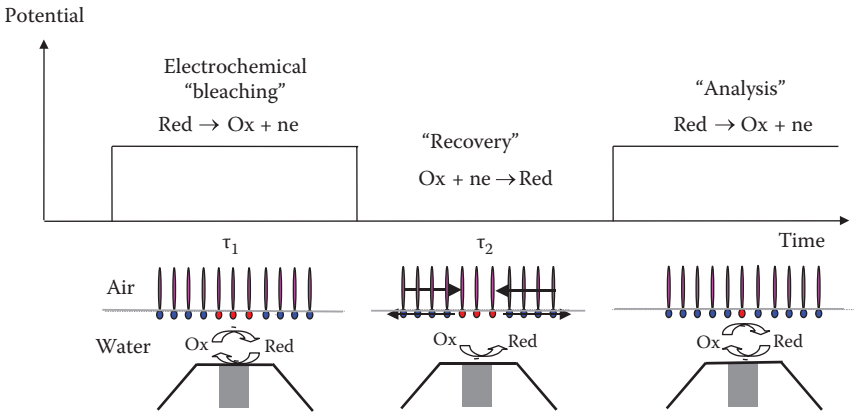


FIGURE 13.7 Schematic (not to scale) of the arrangement for SECM triple potential step measurements of lateral diffusion processes at the water–air interface.

In the third period, the potential step is analogous to the initial potential step. The corresponding UME current–time transient can be used to determine either the distance between the UME tip and the monolayer at the water surface (if an extensive first step and short second step is utilized), or the lateral diffusion coefficient of the amphiphile (if a longer recovery period is set).

This method was demonstrated experimentally with measurements on the lateral diffusion of *N*-octadecyl ferrocene carboxamide in a 1:1 Langmuir monolayer with 1-octadecanol [16], where octadecyl ferrocene carboxamide was oxidized by locally electrogenerated, tris(2,2′-bipyridyl) ruthenium(III), $Ru(bpy)_3^{3+}$. The rate constant for the oxidation of octadecyl ferrocene carboxamide in this environment was found to be 0.016 cm/s/M, which was much lower than would be expected for the reaction in solution, and ascribed to the constrained environment of the Langmuir film. For a mean area/molecule of 50 Å^2, a lateral diffusion coefficient of $1.0 \pm 0.2 \times 10^{-6}$ cm^2/s was measured, whereas for more tightly packed films (higher surface pressures) with areas of 40 and 30 Å^2, lateral diffusion was undetectable. For these investigations, the pulse durations had to be relatively short to avoid natural convection effects, but for solid (polymer) films, much longer measurement times can be employed (Section 13.3.3), which greatly extends the range of diffusion coefficients that can be measured.

13.3.3 Charge Propagation in Ultrathin Films

The triple potential step method has been applied to investigate lateral charge propagation in metallopolymer films, of the type $[Os(bpy)_2(PVP)_nCl]cl$, where bpy is 2,2′-bipyridyl and PVP is poly(4-vinylpyridine) [18]. The complex $Ru(CN)_6^{4-/3-}$ was used to oxidize the film (deposited on a glass surface) and investigate the redox and lateral diffusion processes (see Figure 13.8). $Ru(CN)_6^{3-}$ oxidizes the film locally and recovery involves electron hopping in the film. As this process is relatively slow, the bleaching transient was shown to inform on the kinetics of electron transfer between $Ru(CN)_6^{3-}$ and the concentration of redox moieties in the film (shape of the transient), as well as the

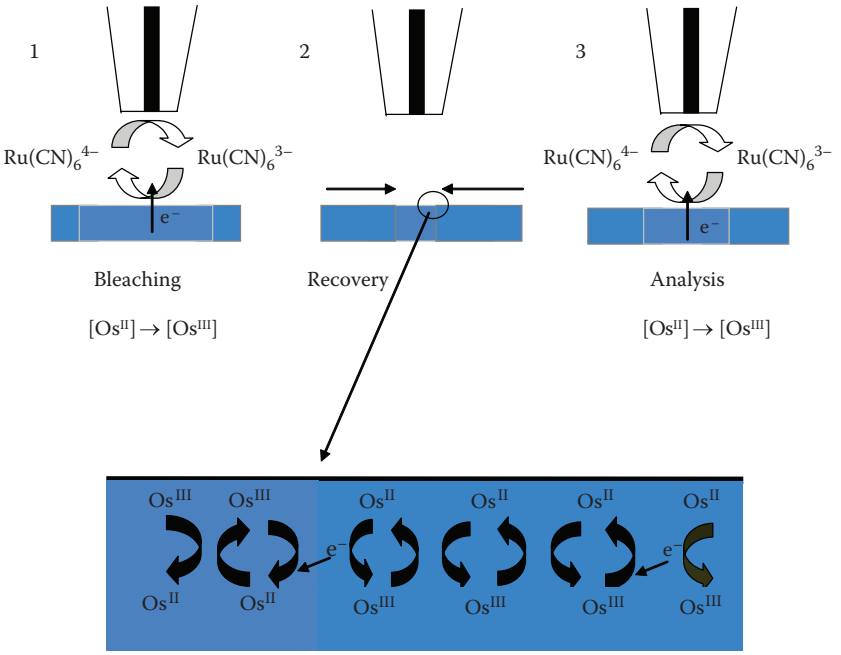


FIGURE 13.8 Schematic showing the use of the triple potential step SECM method to investigate lateral charge propagation in metallopolymer films of the type $[Os(bpy)_2(PVP)_nCl]Cl$, where bpy is 2,2′-bipyridyl and PVP is poly(4-vinylpyridine).

tip/substrate separation. The transient in period 3 then gave information on the extent to which the population of Os(II) recovered in the zone probed by the electrode. This transient could thus be analyzed to reveal the lateral charge transfer coefficient.

If charge propagation in the film is very fast, then this actually sustains the tip current at enhanced values during a single potential step transient, as demonstrated by Mandler and Unwin, who used single potential step SECM to investigate the local oxidation of reduced polyaniline (in its insulating leucoemeraldine base form) to the emeraldine base form [17]. Langmuir Blodgett polyaniline monolayers and multilayers were deposited on glass surfaces and chemically reduced using sodium dithionite. An UME held close to the polyaniline-coated substrate was then used to generate a flux of an oxidant, $Fe(phen)_3^{3+}$ (phen = 1,10-phenanthroline) which diffused to the surface and locally oxidized the reduced polyaniline. By simulating the current–time transients, the kinetics of lateral charge propagation were evaluated.

Following this work, the power of SECM for probing lateral charge propagation has been recognized in several studies, using either steady-state feedback or transient methods. Notably, Hapiot's group have used feedback mode measurements to investigate lateral charge transfer in a number of immobilized molecular assemblies [29,30] and Mirkin and coworkers studied lateral charge transport in monolayers of DNA–metal complexes [31]. Additionally, a novel complementary SECM approach to measure charge transfer across molecular films has also been reported and compared with conventional cyclic voltammetry measurements [32]. In related work, the use of SECM as a probe of the conductivity of ultrathin films and assemblies has also been reported, as exemplified by a number of studies [19–26]. As with many of the applications, described hitherto, a feature of this work is that the experimental methods are underpinned by rigorous theory, enabling the quantitative evaluation of conductance measurements as a function of the film composition and surface pressure, for example [19–26].

13.4 SECM-INDUCED TRANSFER AND RELATED METHODS IN TWO-PHASE SYSTEMS

13.4.1 Permeability Measurements

As an extension to SECMID, SECM-induced transfer (SECMIT), shown schematically in Figure 13.9, can be used to characterize phase transfer processes at a wide variety of interfaces [33].

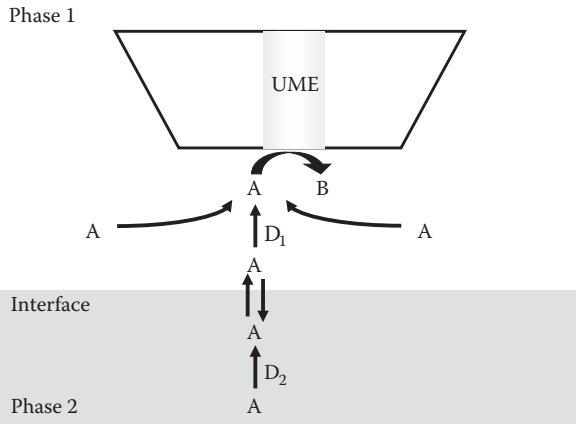


FIGURE 13.9 Schematic illustrating SECMIT: Species A is the common electroactive mediator in the two phases while B denotes the product of the electrode reaction. Electrochemical removal of A in phase 1 induces transfer of A from phase 2 to 1. *D* denotes diffusion coefficient. (Adapted from Gonsalves, M. et al., *Biophys. J.*, 78, 1578, 2000.)

The basic idea is again to perturb the process, initially at equilibrium, through local amperometry at the UME located in one of the phases, close to the interface with the second phase [33,34]. A potential is applied to the tip, sufficient to deplete the species of interest in phase 1 (conversion of A to B in Figure 13.9). This drives the transfer of species A from phase 2 to phase 1, enhancing the current, compared to the situation where there is no net transfer across the target interface and species A diffuses to the tip only by hindered diffusion through phase 1. For a given tip–interface separation, the overall current response is governed by diffusion in the two phases and the interfacial kinetics [33]. This technique has mainly been used in conjunction with metal tips [33], but ion-transfer voltammetric probes can also be used [34].

An attractive feature of SECMIT is the noninvasive measurement of physicochemical quantities in the second phase. It has proved particularly powerful in investigations of solute transfer across interfaces formed between biological tissues and a bathing solution [35,36] where contact of the sample by an UME itself might damage the sample or contaminate the electrode surface. When there are no kinetic limitations to the interfacial transfer process, SECMIT is also an effective analytical technique for determining the permeability, concentration, and diffusive properties of a solute in the target second phase [33]. By operating SECMIT in potential step chronoamperometric mode, it is possible to determine both the partition coefficient of a solute between two phases and its relative diffusion coefficients in the phases.

SECMIT imaging has been used most powerfully to demonstrate that the interterritorial regions, that is, the areas between cells in the surface of cartilage, provide the most facile transport pathways for oxygen transport [35]. These studies employed dual-mediator imaging, in which the redox reaction for one (impermeable) chemical species in the bathing solution, oxidation of $Ru(CN)_6^{4-}$, measured the tip–substrate distance, by way of a hindered diffusion response. Rescanning the same area but detecting oxygen by diffusion-limited reduction provided a permeability response, convoluted by topographical effects. With knowledge of the topography from the $Ru(CN)_6^{4-}$ data, maps of oxygen permeability were obtained.

Current data for the two mediators (normalized by the corresponding bulk current, $i(\infty)$, in each case) and the corresponding topographical and permeability maps that are extracted from the analysis are shown in Figure 13.10. In this figure, permeability is expressed as $K_e\gamma$, where K_e is the partition coefficient of oxygen between cartilage and the aqueous bathing solution and γ is the ratio of the diffusion coefficient of oxygen in cartilage to that in aqueous solution. It can be seen that the value of $K_e\gamma$ varies significantly across the surface. Complementary histochemical and structural analysis revealed that the spots of high $K_e\gamma$ corresponded to pericellular surface regions of cartilage where the collagen content was low. In contrast, regions of high collagen content correlated with diminished $K_e\gamma$ values. Very recently, it has been shown that tip position modulation (TPM)-SECM [36] is particularly effective in the SECMIT mode, allowing permeability measurements to be made with greatly enhanced dynamic resolution [37].

13.4.2 Kinetics of Molecule and Ion Transfer between Fluid Phases

SECMIT and related transient methods can also be used to measure the kinetics of interfacial transfer. Such measurements have proven particularly powerful for the investigation of molecular transfer across molecular monolayers at water–air interfaces and molecular and ion transfer at liquid–liquid interfaces.

For monolayers at water–air interfaces, the deployment of SECM in a Langmuir trough arrangement has allowed investigations of how compression of a monolayer changes molecular transfer kinetics across the interface. The first studies of this type considered oxygen transfer across a water–air interface in the absence and presence of a monolayer of 1-octadecanol [38]. For these investigations, a submarine UME, held at a potential to reduce oxygen at a diffusion-controlled rate, was deployed in the aqueous subphase of a Langmuir trough, close to the water–air interface. The electrochemical process promoted the transfer of O_2 from air to the aqueous solution, with

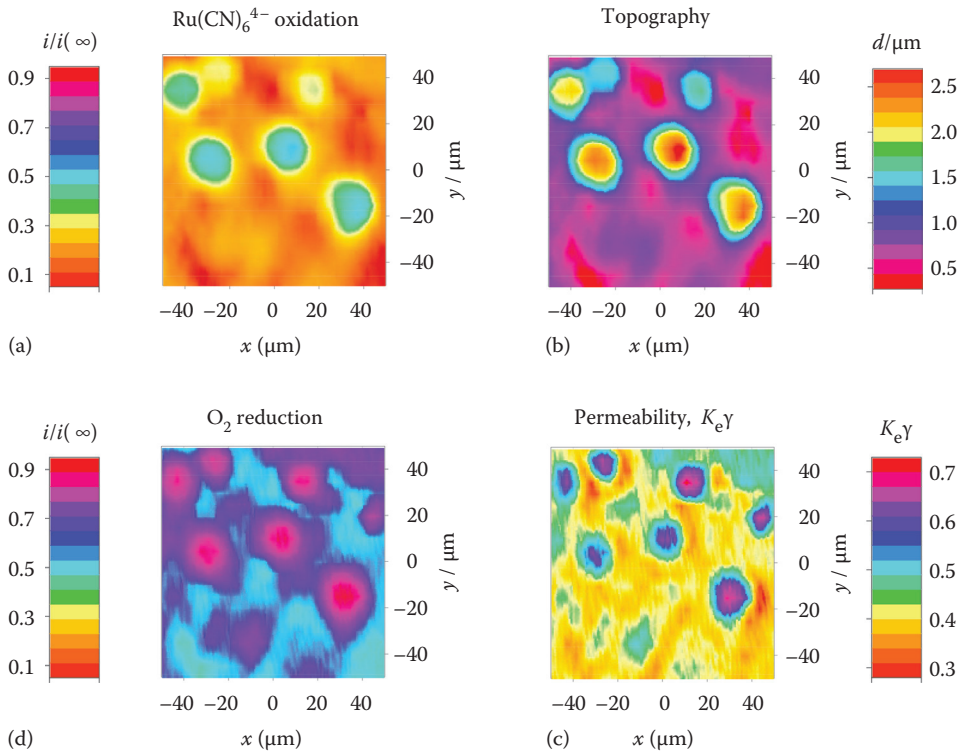


FIGURE 13.10 (a) Contour plot showing the normalized current map for a 100 μm × 100 μm area of cartilage, imaged using the diffusion-controlled oxidation of $Ru(CN)_6^{4-}$ at a 5 μm diameter Pt UME at an initial sample–tip separation of ~2 μm. (b) Contour plot showing the corresponding topography map for the area of cartilage imaged in top left. (c) Contour plot showing the normalized current map for the diffusion-controlled reduction of oxygen at a 5 μm diameter Pt UME in the area of cartilage considered for top left/right. (d) Corresponding oxygen permeability map calculated from the normalized currents measured in the bottom left. (Redrawn from Gonsalves, M. et al., *Biophys. J.*, 78, 1578, 2000.)

subsequent collection of O_2 at the UME (Figure 13.11). These studies demonstrated that the rate of oxygen transfer across a clean water–air interface was diffusion-controlled on the timescale of SECM measurements. The rate of this transfer process was, however, significantly reduced with increasing compression of a 1-octadecanol monolayer assembled at the water–air interface.

This approach was further extended to include monolayers of lipids, 1-octadecanol, and an investigation of the current response during the ultimate deformation of the liquid–air interface by an approaching mercury hemisphere UME probe [39]. Figure 13.12 shows approach curves for O_2 reduction with increasing surface pressure for (a) 1-octadecanol ($C_{18}OH$) and (b) DPPA monolayers, where DPPA is L-α-dipalmitayl phosphatidic acid. It can clearly be seen that by increasing the surface pressure of the monolayers there is a decrease in O_2 flux across the interface, manifested as a decrease in current for O_2 reduction at any normalized tip/interface distance, *d*/*a*.

To examine the effect of permeant size and amphiphile chain length on molecular transfer, studies have been carried out on the diffusion of Br_2 across a water–air interface modified with different chain length fatty alcohols [40]. The principles of these experimental measurements, which employed the SECM-double potential step chronoamperometric (DPSC) mode, are illustrated in Figure 13.13. An initial (forward) potential step was employed to electrogenerate Br_2 by the diffusion-controlled oxidation of Br^- in an aqueous sulfuric acid subphase. Tip-generated Br_2 diffused to and transferred across the fatty alcohol monolayer (Figure 13.13a). Br_2 was then collected back by

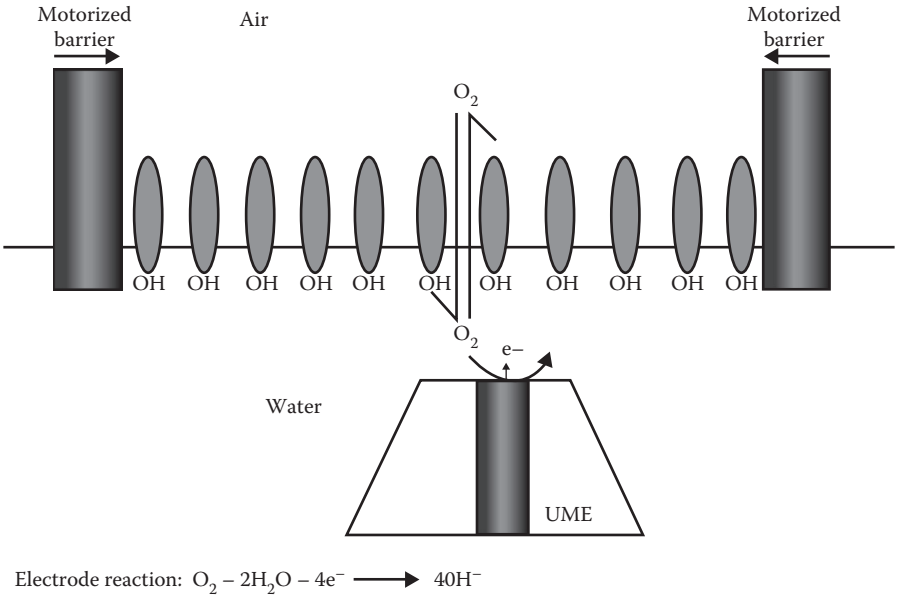


FIGURE 13.11 Schematic illustration (not to scale) of the SECM-induced transfer of oxygen across a long-chain alcohol monolayer at the air–water interface.

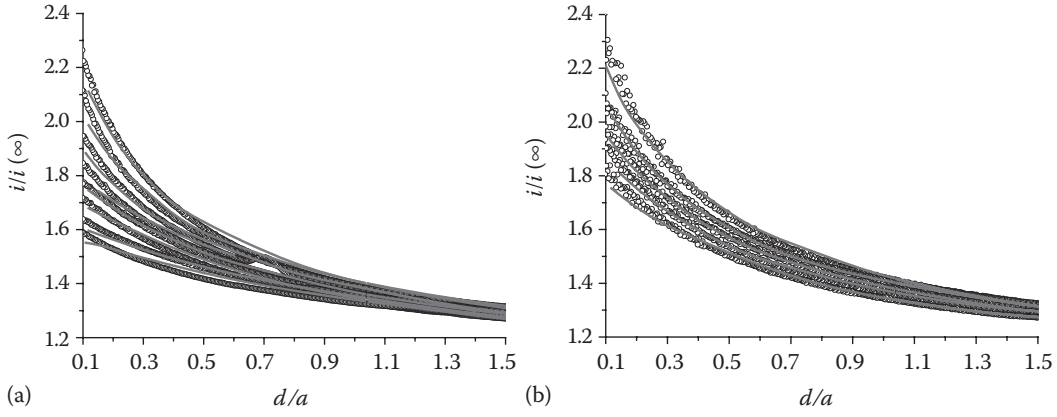


FIGURE 13.12 Normalized experimental approach curves for oxygen reduction at a hemispherical Hg UME approaching a water–air interface for various monolayer pressures. From top to bottom, the curves correspond to uncompressed and surface pressures of 5, 10, 15, 20, 25, 30, and 40 mN/m in (a), which is for 1-octadecanol, and 5, 10, 20, and 30 mN/m in (b), which is for DPPA (b). The solid lines represent the theoretical behavior for a simple kinetic model. (Redrawn from Ciani, I. et al., *J. Phys. Chem. B*, 108, 3801, 2004.)

reversing the potential to effect the diffusion-controlled reduction of Br_2 to Br^- (Figure 13.13b). The current–time behavior provided information on both the tip–interface separation (forward step) and the kinetics of Br_2 transfer (reverse step). A similar approach has examined a range of lipids at the water–air interface [41].

Both single potential step and DPSC methods have been applied in a similar fashion to investigate molecular and ion transfer at immiscible liquid–liquid interfaces [42]. Some of these measurements have considered the effect of molecular monolayers, formed as either a Gibbs film [43] or a Langmuir film in a specially designed Langmuir trough for liquid–liquid interfaces [44], on the kinetics of the transfer process.

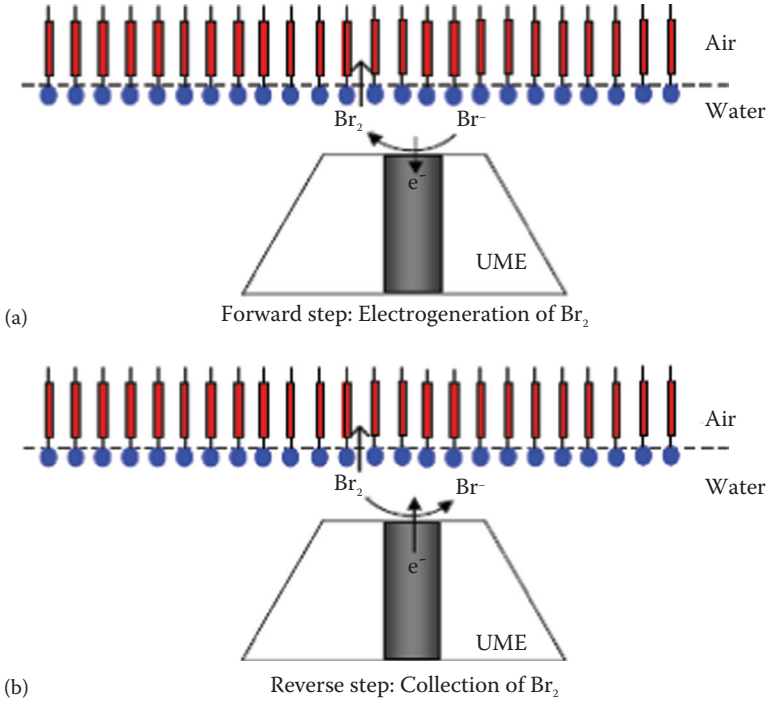


FIGURE 13.13 Schematic (not to scale) of SECM-DPSC measurements. Molecular Br_2 is generated by oxidizing Br^- in the (a) forward potential step and collected when the direction of the potential step is (b) reversed to reduce Br_2 to Br^-.

13.5 DISSOLUTION KINETICS OF SOLID MATERIALS

13.5.1 Principles and Theoretical Aspects

There are broadly three approaches to dissolution studies with SECM. The first (and one of the early uses) is as a fabrication tool to form dissolution channels and other features on materials at the micrometer to submicrometer level. This area is dealt with in greater detail in Chapter 15. The purpose of many of these studies is to create structures in a substrate surface, rather than to measure the rates or nature of the dissolution processes [45]. However, this approach has recently been adapted and made quantitative, by developing a moving boundary model for the etching process. Etch features are then measured as a function of time and matched to the model to obtain quantitative kinetic data [46]. Acid-induced dissolution of dental enamel has been studied in this way, using an SECM tip to generate fluxes of protons galvanostatically just above a sample surface [46]. The resulting etch features in the sample were characterized by white light interferometry. Dissolution was found to be fast, but the high rates of mass transport generated by the SECM approach allowed the surface kinetics of dissolution to be evaluated. The main attributes of SECM for these studies are the ability to deliver high, controllable, and local acid challenges in a defined way and that multiple dissolution measurements can be made on one sample, eliminating intersample variability effects.

A second approach is to use the SECM tip as a "passive" sensor of the concentration boundary layer of a freely reactive crystal. For example, a shear-force constant-distance scanning potentiometric system with a Ca^{2+} ion-selective probe was used to map Ca^{2+} from a calcium carbonate surface under slightly acidic conditions [47]. These studies provide insights into interfacial concentrations, but do not exploit the high mass transport rates that can be generated in SECM to allow quantitative high-resolution kinetic measurements.

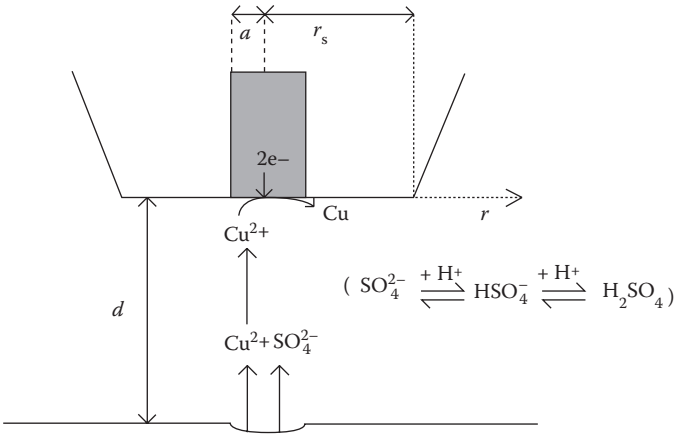


FIGURE 13.14 SECM arrangement for the study of ionic crystal dissolution using copper sulfate pentahydrate as an example substrate in contact with a saturated solution of copper sulfate. (Adapted from Macpherson, J.V. and Unwin, P.R., *J. Phys. Chem*., 98, 1704, 1994.)

The third approach, on which we focus in this section, is to use the equilibrium perturbation mode to initiate, and quantitatively monitor, dissolution reactions, providing unequivocal information on the kinetics and mechanism of the process, under conditions of controlled mass transport and with high spatial resolution. The high spatial resolution attainable with SECM is particularly powerful for dissolution studies, because it opens up the possibility of investigating different regions of a crystal surface to investigate, for example, the effect of dislocations and dislocation density on the dissolution kinetics. Furthermore, different crystal faces of a single crystal or polycrystalline material can readily be investigated.

The SECM arrangement for the study of ionic crystal dissolution is illustrated in Figure 13.14, using copper sulfate pentahydrate as an example substrate. The surrounding solution is saturated with respect to $CuSO_4{\cdot}5H_2O$, so that initially the system is at equilibrium and there is no net dissolution or growth. With the UME positioned close to the substrate, the tip potential is stepped from a value where no electrochemical reactions occur to one where the reduction of Cu^{2+} to Cu occurs at a diffusion-controlled rate. The resulting electrode process depletes the concentration of Cu^{2+} in the tip/substrate gap, creating a local undersaturation at the crystal–solution interface. This perturbs the interfacial equilibrium and provides the thermodynamic force for the dissolution reaction. Dissolving ions diffuse from the crystal across the gap and are detected at the tip UME, thus producing a current flow, the magnitude of which depends on the rate and mechanism of the dissolution process. Using the imaging mode, it is possible to initiate the dissolution reaction over wider areas of the substrate. In this case the UME, which is held at a potential necessary to promote dissolution, is scanned over a selected area of the surface. The current, measured as a function of probe position in the plane of the surface, can be used to provide a map of the dissolution activity.

The key features of this technique are as follows: (i) Mass transfer in the tip/substrate gap is well defined, variable, and calculable enabling the role of interfacial undersaturation in the dissolution process to be quantified. (ii) Extremely high mass transfer rates can be generated using close tip/substrate separations and small radii UMEs facilitating the study of fast reactions. (iii) The extent of dissolution can be controlled by varying the period of electrolysis (down to the millisecond timescale) with a stationary probe, the scan speed for a moving probe in the imaging mode, and/or the UME potential. This enables the study of materials with a very wide range of solubilities. (iv) As the reactivity is probed at a targeted microscopic region of the surface (often a single crystal face), it is possible to establish the relationship between surface structure and dissolution activity. (v) Since

UME measurements can readily be made with and without supporting electrolyte [48], the role of added electrolytes on dissolution processes can be identified.

The theoretical treatment of the UME response for induced dissolution processes is similar to that from SECMID (Section 13.2.1), but the boundary condition on the substrate is the rate law for the dissolution process. Various rate laws and processes for SECM-induced dissolution have been presented and described in detail (see, e.g., Refs. [49–56]). Importantly, the SECM response (e.g., during steady-state approach curve measurements) has been shown to be able to discriminate between different candidate rate laws, providing considerable mechanistic information.

In general, for SECM dissolution, under the conditions outlined earlier, where the solution is initially saturated with respect to the solid material, the UME current approaches that for an inert surface as the rate constant decreases. On the other hand, the flux of material from the crystal surface increases with the dissolution rate constant, increasing up to a point where the UME response is limited by mass transfer between the tip and the substrate, that is, the dissolution process becomes diffusion-controlled. Under these conditions, the kinetics are sufficiently fast to maintain the concentration at the substrate at the saturated solution value and the induced dissolution approach curve resembles that for positive feedback. Under potential step chronoamperometric conditions, the time taken for the current to approach a steady value obviously decreases with increasing rate constant [50–52].

The tip-generated interfacial undersaturation in dissolution studies is governed by the interplay between mass transport in the tip/substrate gap and the dissolution kinetics. This concept is illustrated in Figures 13.15 and 13.16. Figure 13.15a and b shows the radial dependence of the steady-state concentration and flux at the crystal–solution interface for a dissolution process that is first order in interfacial undersaturation, characterized by dimensionless rate constants K_1 (= $k_1 a/D_{soln}$) = 1, 10, and 100, where k_1 is the heterogeneous rate constant for the dissolution process (units cm/s). For rapid kinetics ($K_1 = 100$), the dissolution process is able to maintain the interfacial concentration close to the saturated value and only a small depletion in the concentration adjacent to the crystal is observed over a radial distance of about one electrode dimension. Under these conditions, diffusion in the z-direction dominates over radial diffusion. As the rate constant decreases, diffusion is able to compete with the interfacial kinetics and consequently the undersaturation at the crystal surface increases (surface concentration decreases). The dissolution process provides less material for diffusion toward the UME, as verified by the magnitude of the interfacial flux (Figure 13.15b), and the diffusion field around the UME extends further in the radial direction decreasing the spatial resolution of the technique (Figure 13.15a).

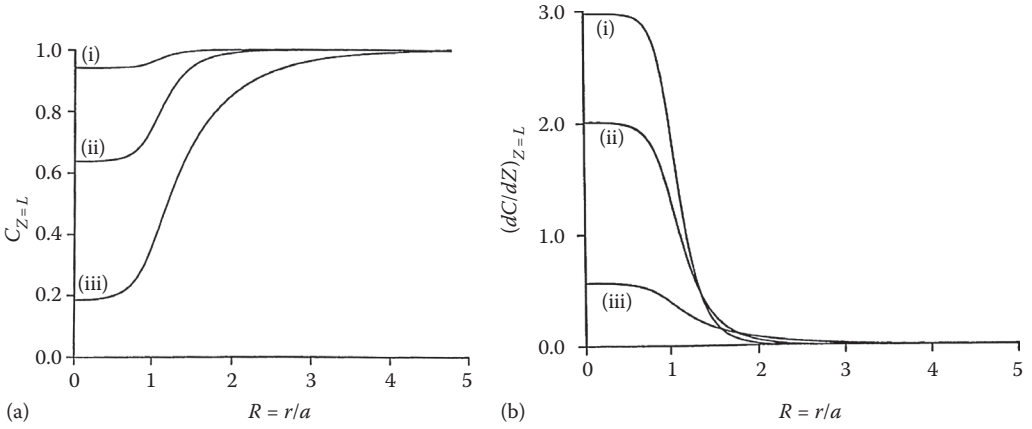


FIGURE 13.15 Calculated normalized profiles of (a) concentration and (b) flux of a target species at a substrate/solution boundary for SECM-induced dissolution with $L = 0.32$ and $K_1 =$ (i) 100, (ii) 10, and (iii) 1. The data relate to a normalized measurement time, τ, of 1.0. (Reproduced from Macpherson, J.V. and Unwin, P.R., *J. Phys. Chem.*, 98, 1704, 1994.)

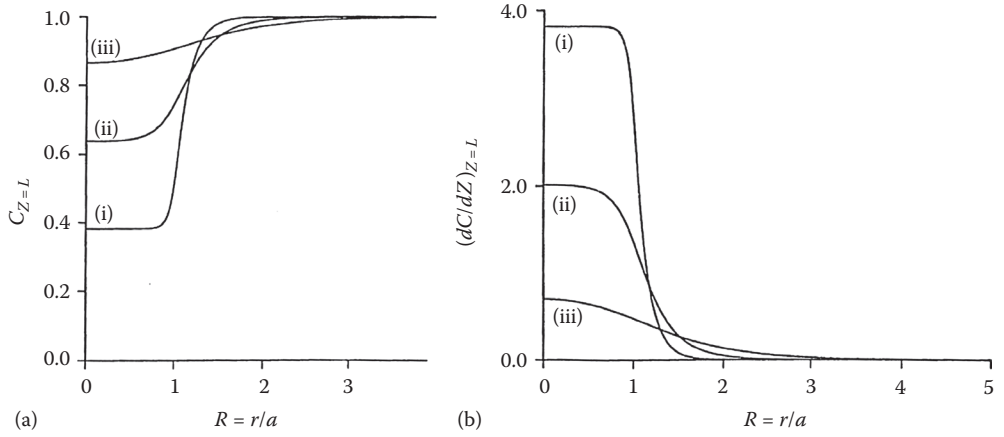


FIGURE 13.16 Calculated normalized profiles of (a) concentration and (b) flux of a target species at a substrate/solution boundary for SECM-induced dissolution with $K_1 = 10$ and $L =$ (i) 0.1, (ii) 0.32, and (iii) 1.0. The data relate to a normalized measurement time, τ, of 1.0. (Reproduced from Macpherson, J.V. and Unwin, P.R., *J. Phys. Chem*., 98, 1704, 1994.)

Figure 13.16a and b shows the effect of L on the radial dependence of the steady-state concentration and flux at the substrate–solution interface for a first-order dissolution process characterized by $K_1 = 10$ and $L = 0.1$, 0.32, and 1.0. As the tip/substrate separation decreases, the effective rate of diffusion between the probe and the surface increases, forcing the crystal–solution interface to become more undersaturated. Conversely, as the UME is retracted from the substrate, the interfacial undersaturation approaches the saturated value, since the solution mass transfer coefficient decreases compared to the first-order dissolution rate constant. Movement of the tip electrode away from the substrate also has the effect of promoting radial diffusion and, consequently the area of the substrate probed by the UME increases.

13.5.2 Effect of Surface Structure on Dissolution Characteristics

SECM-induced dissolution has been applied extensively to a number of systems, including both highly soluble [49–53] and sparingly soluble [54,55] crystalline materials. SECM has also been used to image dissolution kinetics across single crystal surfaces [52]. One of the major achievements has been to elucidate how crystal surface structure and dislocations influence dissolution and we highlight this aspect in this section.

The ability to induce dissolution for brief periods in the chronoamperometric mode facilitates dissolution studies of very soluble materials. This is readily exemplified by comprehensive studies of dissolution from various regions of the (100) face of copper sulfate pentahydrate single crystals, grown from aqueous solution [50,51]. Dissolution was initiated through the chronoamperometric reduction of Cu^{2+} to Cu at a 25 μm diameter Pt disk UME, over selected spots on the crystal surface, as a function of tip/substrate separation. Dissolution was induced for only fractions of a second, in order to prevent the accumulation of Cu at the tip electrode, and to avoid extensive dissolution of the solid, which might otherwise change the geometry of the tip/substrate gap and the integrity of the exposed surface.

In studies of the (100) face, two distinct types of dissolution behavior were observed. In the center of the face, dislocation etching revealed that the average dislocation spacing was considerably less than the size of the UME probe [56], that is, in the SECM configuration the electrode would sit over a constant source of dissolution sites, once the process had been initiated. This was reflected in the shape of experimental SECM chronoamperometric transients [50], such as those depicted in

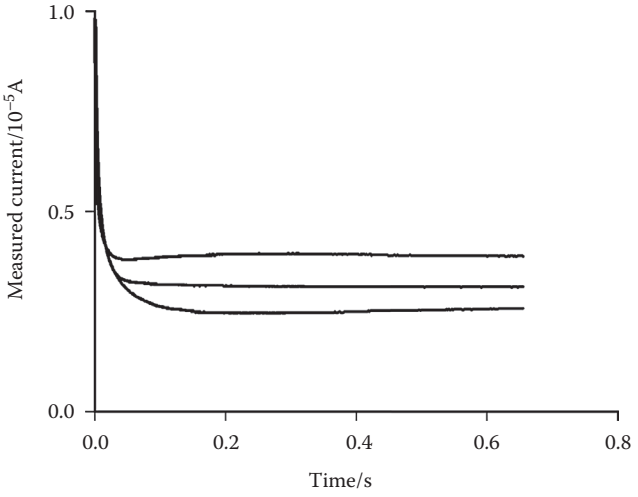


FIGURE 13.17 SECM chronoamperometric transients for the reduction of Cu^{2+} with a 25 μm diameter Pt UME positioned at distances of 2 (upper curve), 5, and 10 μm (lowest curve) from the (100) face of a copper sulfate pentahydrate single crystal. The initial solution conditions were 3.6 mol/dm^3 H_2SO_4 and saturated copper sulfate. In each case, the potential was stepped from −0.2 to −0.65 V versus AgQRE. (Reproduced from Macpherson, J.V. and Unwin, P.R., *J. Phys. Chem*., 98, 1704, 1994.)

Figure 13.17 at different tip/substrate separations. In all cases, the current rapidly attained a steady state, indicative of a uniform, constant rate of dissolution. As the UME was moved closer to the crystal surface, the limiting current increased, consistent with an increase in the flux of Cu^{2+} from the crystal surface to the tip electrode.

Steady-state current–distance approach curves, derived from the long-time portion of transients, are shown in Figure 13.18 for dissolution experiments involving saturated copper sulfate solutions with sulfuric acid at concentrations of 10.2, 7.3, 6.4, 3.6, and 2.8 mol/dm^3. As the concentration of sulfuric acid decreased, the dissolution characteristics moved away from a diffusion-controlled situation (the dashed line in Figure 13.18). This was due to the increase in the activity and diffusion coefficient of Cu^{2+} in solution, which increased mass transfer in the UME/crystal domain and pushed the dissolution reaction toward surface control. An excellent fit to the experimental data was found for a process that was first order in interfacial undersaturation (Figure 13.18).

At the edges of the (100) face of copper sulfate pentahydrate single crystals, etching revealed a mean interdislocation spacing in excess of 100 μm, that is, much greater than the size of the UME employed [56]. This resulted in a high probability of inducing dissolution in an area effectively devoid of dislocation cores, with a UME positioned above this region of the surface. Coupled with the aforementioned studies, this provided an opportunity to compare the dissolution activity in dislocated and dislocation-free areas of the same crystal surface, so allowing an assessment of the role of dislocations in controlling the rate and mechanism of the reaction.

Figure 13.19 shows a typical example of the chronoamperometric response observed when dissolution was initiated in a region toward the edge of the crystal face. In stark contrast to the behavior described earlier (Figure 13.17), SECM-induced dissolution, in the absence of dislocations, occurs via an oscillatory mechanism [51]. After an initial period of high dissolution activity, the rate—reflected by the UME current—rapidly decreases and thereafter proceeds in a series of periodic bursts, each lasting ca. 0.05 s (normalized time intervals ∼0.18).

The initial dissolution activity (at the shortest time) was attributed to dissolution from steps that occur in abundance on the surfaces of crystals grown from solution. Dissolution causes the steps to retreat out of the microscopic zone probed by the SECM. In the absence of dislocation cores in the targeted region, the surface becomes depleted of active sites, as shown schematically

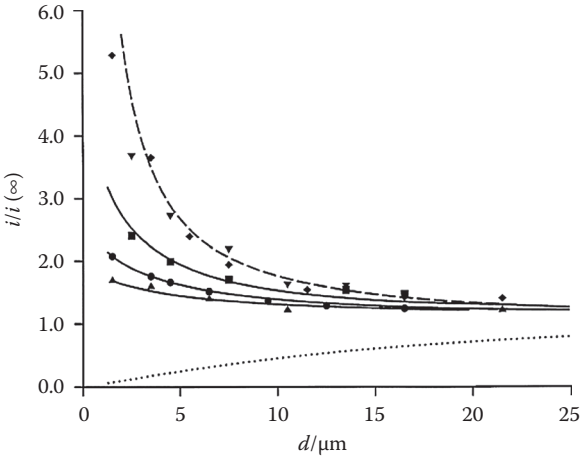


FIGURE 13.18 SECM approach curves (measurement time 0.6 s after a potential step) of normalized current for the reduction of Cu^{2+} versus separation between a 25 μm diameter Pt tip and the (100) face of $CuSO_4{\cdot}5H_2O$. Data are shown for saturated copper sulfate solutions containing 2.3 (▲), 3.6 (●), 6.4 (■), 7.3 (▼), and 10.2 (◆) mol/dm^3 sulfuric acid. The solid lines through each data set represent the best fits for a first-order dissolution process characterized by log $K_1 = 0.46$ (▲), log $K_1 = 0.60$ (●), and log $K_1 = 0.91$ (■). The dashed line shows the theoretical behavior predicted for a diffusion-controlled dissolution process, while the dotted line shows the behavior expected for an inert surface. (Adapted from Macpherson, J.V. and Unwin, P.R., *J. Phys. Chem.*, 98, 1704, 1994; Macpherson, J.V., PhD thesis, University of Warwick, U.K. 1996.)

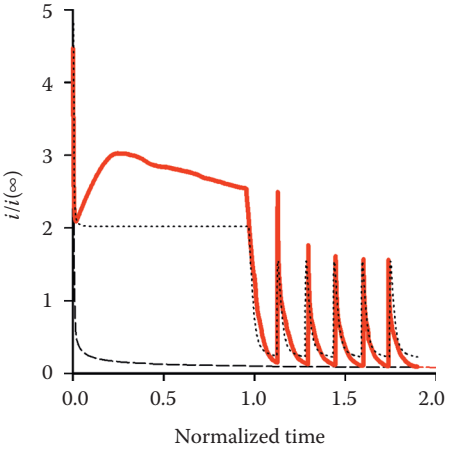


FIGURE 13.19 Experimental current–time characteristics (___) for the reduction of Cu^{2+} at a 25 μm diameter Pt UME located 1.0 μm from a copper sulfate pentahydrate (100) face, in an area of the crystal with a low dislocation density. The experimental characteristics have been normalized using the steady-state current measured at effectively infinite probe/crystal separation, $i(\infty) = 1.88$ μA. $D_{Cu^{2+}} = 4.56 \times 10^{-6}$ cm^2/s and $a = 12.5$ μm. The best fit of a theoretical model (……) is shown alongside the theoretical behavior predicted for an inert surface (- - -). (Adapted from Macpherson, J.V. and Unwin, P.R., *J. Phys. Chem.*, 98, 11764, 1994.)

in Figure 13.20. Consequently, the dissolution rate decreases to a value indicative of close to zero dissolution activity. This is reflected in a drop in the current flowing at the tip electrode, after the initial high values, to a value that corresponds to mass transfer by hindered diffusion only in the tip/substrate gap. The decrease in crystal activity, coupled with strongly hindered diffusion in solution in the SECM configuration, results in a rapid depletion in the local concentration of electroactive material in the tip/substrate gap and crucially at the crystal–solution interface.

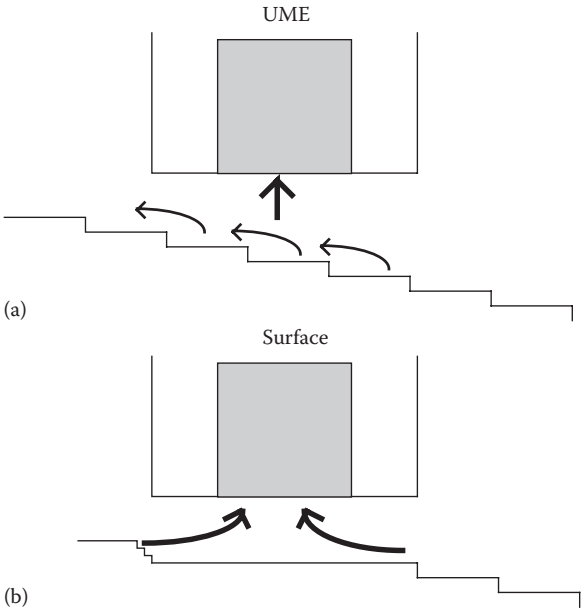


FIGURE 13.20 Schematic illustration of SECM-induced dissolution. Steps initially provide a source of sites for dissolution that is detected at the UME (a). As dissolution proceeds, steps move out of the probe/crystal domain and the activity of the surface decreases. In this case (b), mass transfer tends toward that for an inert surface (hindered diffusion). Note that this diagram is not to scale. The height of and separation between the steps has been significantly exaggerated. The surface is effectively flat on the scale of the probe/crystal geometry: the probe/crystal separation is ~1 μm, the UME diameter is 25 μm, and the overall probe diameter is ~250 μm. (Reproduced from Macpherson, J.V. and Unwin, P.R., *J. Phys. Chem*., 98, 11764, 1994.)

Eventually a value for the interfacial undersaturation is reached which exceeds the threshold required to spontaneously nucleate fresh dissolution sites, from the perfect surface and dissolution is initiated again, reflected in the sudden surge of current. To model this simply, the entire surface was allowed to become active once the undersaturation at any point on the surface exceeded a critical value [51]. As the freshly generated steps, associated with nucleation sites, traverse from the tip/crystal domain, as a consequence of dissolution, the activity of the surface decreases and the current falls accordingly. The process outlined earlier is thus repeated, leading to the observed oscillatory current response shown in Figure 13.19. Evidence for the validity of the proposed dissolution model was revealed through microscopy of the crystal surface in areas of SECM measurements, which revealed a series of ledges inside pits, consistent with the number of current surges. The formation of ledges of this type concurs with dissolution occurring in bursts, in a layer-by-layer fashion, as shown schematically in Figure 13.21.

13.5.3 High-Resolution Dissolution Imaging with Integrated Electrochemical–Atomic Force Microscopy

Chapter 17 describes the various probes and techniques that have been implemented in combined SECM-AFM. For dissolution studies, the very simplest probe can be used, which comprises a Pt-coated AFM tip that is used to measure the topography of a dissolving crystal surface while simultaneously inducing the dissolution process electrochemically, over a wider area, under conditions that essentially mimic those employed for SECM kinetic measurements. This technique is referred to as integrated electrochemical–AFM (IE-AFM) [57] and it has been shown that the electrochemical response of such a probe is well defined and well modeled [58].

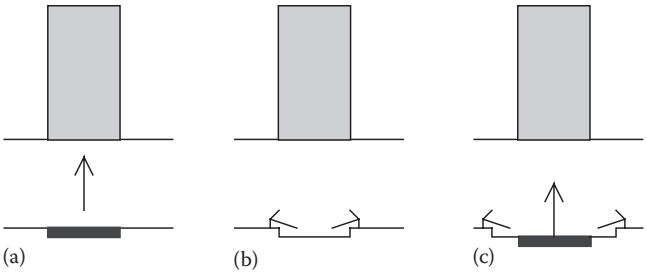


FIGURE 13.21 Schematic illustration of the formation of an SECM-induced dissolution pit with terraced walls. The UME induces dissolution from the area directly under it (a), resulting in a current surge. The flux of material from this area then rapidly declines and slow dissolution occurs from the edge of the resulting pit (b), resulting in expansion. Concurrently, the area directly under the center of the UME becomes increasingly undersaturated, until the critical value for the creation of fresh dissolution sites is attained, when there is a subsequent burst of material from the surface (c), producing a terraced structure within the pit. The overall process may then be repeated. (Reproduced from Macpherson, J.V. and Unwin, P.R., *J. Phys. Chem*., 98, 11764, 1994.)

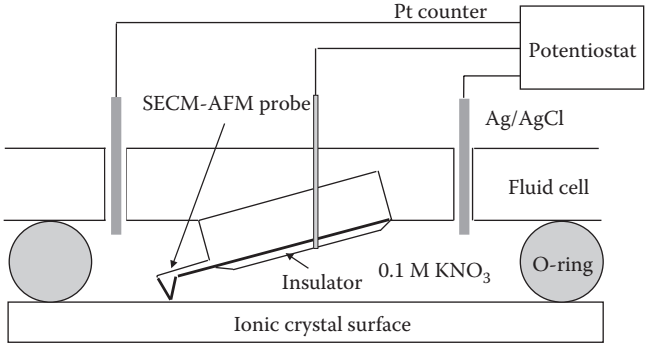


FIGURE 13.22 Schematic of the modified IE-AFM probe employed in a fluid cell. (Redrawn from Macpherson, J.V. et al., *J. Am. Chem. Soc*., 118, 6445, 1996.)

The approach has been illustrated through IE-AFM studies of dissolution from several ionic crystal single crystal surfaces including (i) the (100) cleavage face of potassium bromide single crystals [57] in acetonitrile (MeCN), (ii) the (010) surface of potassium ferrocyanide trihydrate in aqueous solution [59], and (iii) the $(10\bar{1}4)$ surface of calcite in aqueous solution [60]. The experimental arrangement for the IE-AFM-induced dissolution measurements is shown in Figure 13.22. Silicon nitride AFM probes were used that were sputter coated with a 30–60 nm thick layer of Pt and a thin Cr anchor layer. All AFM imaging was carried out in contact mode, although tapping mode is also possible with probes of this type.

After the Pt-coated AFM tip had been secured in the AFM fluid cell, the underside and the part of the tip holder that came into contact with the solution were electrically insulated. Depending on the solvent system employed, different insulating coatings were utilized. In particular, for the MeCN studies, a thin film of polystyrene was employed [57], while in aqueous solution a mixture of nail varnish and super glue was used [59,60], applied with a fine paint brush. This procedure leaves Pt exposed only at the tip, cantilever, and, in some cases, a small fraction of the probe body. To estimate the exposed electroactive areas, cyclic voltammograms were recorded in the presence of an appropriate mediator.

For the IE-AFM studies on the KBr and $K_4Fe(CN)_6$ single crystal surfaces, dissolution was initiated using SECMIT [49] to create a local undersaturation at the crystal–solution interface, akin to

the induced dissolution SECM studies [49–52], described in Sections 13.5.1 and 13.5.2. For KBr, the IE-AFM tip was employed to oxidize Br^- to Br_3^- (or even further to Br_2) while for $K_4Fe(CN)_6$, $Fe(CN)_6^{4-}$ was oxidized to $Fe(CN)_6^{3-}$.

Although the area of the electrode is relatively large compared to a standard SECM tip, dissolution is induced only in areas where the diffusion field has intercepted the substrate. By employing short potential pulses, it is possible to constrain the size of the diffusion field so that an area smaller than the size of the exposed electrode is probed. With the tip in contact with the surface, the separation of the cantilever from the underlying substrate varies from ~3 μm, in the vicinity of the tip, to ~40 μm, where the lever attaches to the main body of the probe. For potential pulse in the subsecond time range, diffusion are typically smaller than the maximum separation between lengths the IE-AFM probe and substrate. Hence, only part of the cantilever electrochemically induces dissolution.

For the calcite dissolution system, the tip was used in tip generation–substrate collection mode. Specifically, the IE-AFM tip was used to generate protons, from the electrooxidation of water, which caused the calcite to dissolve via the following proton-assisted processes:

$$CaCO_3\,(s) + H^+(aq) \rightarrow Ca^{2+}(aq) + HCO_3^-(aq) \tag{13.20}$$

$$HCO_3^-(aq) + H^+(aq) \Leftrightarrow H_2CO_3(aq) \rightarrow CO_2(aq) + H_2O \tag{13.21}$$

By varying the potential applied to the tip, it was also possible to vary the flux of protons generated above the surface of the calcite crystal and thus dose the surface with different amounts of protons.

13.5.3.1 Potassium Bromide (100) Dissolution

Dissolution with the IE-AFM was induced by pulsing the potential at the probe, for 1 s, from a value where no electrode reaction occurred to a series of different driving potentials. Images of the surface topography were recorded in a specific region of the surface in the AFM mode, prior to and after each pulse, as a function of time. A typical sequence of images is shown in Figure 13.23, in which the potential was pulsed to a value of approximately the half-wave potential for the Br^-/Br_3^- couple. Prior to the potential step, Figure 13.23a clearly shows the presence of a dissolution spiral, which was found to slowly rotate (due to dissolution) over a period of several minutes. The wide spacing of the steps is diagnostic of a very slightly undersaturated solution. There were a number of possible explanations as to why, for an initially saturated solution, this might occur: small thermal changes in the sample chamber [61]; local frictional heating effects from the scanning tip; or as a result of the very slight local electrochemical depletion of Br^-, with the potential of the electrode held at the foot of the Br^- to Br_3^- wave.

Previous SECM dissolution measurements carried out on this system showed that even on the fastest timescale accessible, the dissolution process was effectively diffusion controlled, even at a probe/crystal separation as close as 400 nm, with a tip of $a = 2.5$ μm [57]. This was not unexpected given that, under the experimental conditions, K^+ levels in the gap between the SECM tip and the crystal surface increase during dissolution [54], ultimately suppressing the attainment of high undersaturations, and thereby holding the dissolution process in the mass transfer control regime. Thus, for the IE-AFM measurements, dissolution from the KBr surface was also under diffusion-controlled conditions.

Figure 13.23b, recorded immediately after the potential pulse, clearly demonstrates that for diffusion-controlled dissolution, the predominant mechanism is the unwinding of screw dislocations, consistent with the Burton Cabrera Frank (BCF) mechanism for a rapid dissolution process where the interfacial undersaturation is small [62]. These results provided the first in situ experimental

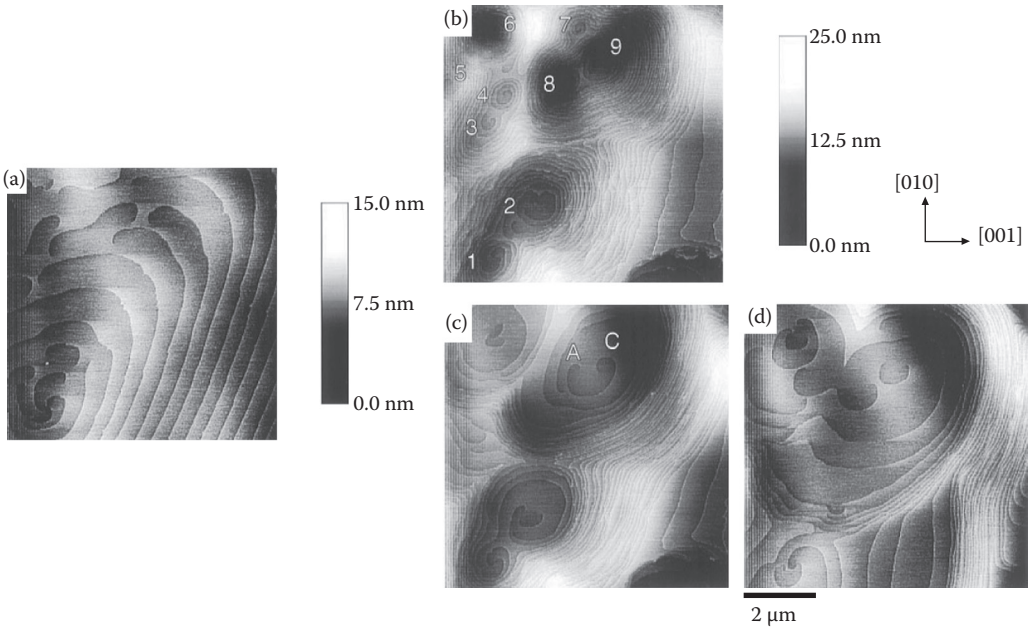


FIGURE 13.23 Height mode AFM images of a 7 μm by 7 μm area of the (100) face of potassium bromide in contact with a saturated KBr solution prior to (a) and (b–d) after the application of a 1 s potential pulse (+0.5 to +1.1 V) to the electrochemically active probe to initiate dissolution. Images (b) to (d) were recorded sequentially at a rate of 21 s/frame. (Adapted from Macpherson, J.V. et al., *J. Am. Chem. Soc.*, 118, 6445, 1996.)

evidence for the applicability of this mechanism in describing fast dissolution processes of ionic single crystal surfaces. The local electrochemically controlled undersaturation provides the driving force that enables many more dislocations to be activated and hence revealed, compared with the situation shown by Figure 13.23a. It is interesting to note that the breaks in the steps in the spiral depicted in Figure 13.23a coincide with the cores of the dislocations that are exposed in Figure 13.23b. Heterogeneities in the shape and depth of the dislocations in Figure 13.23b suggest differences in the associated strain energies of these defects.

After application of the 1 s pulse, the solution in the probe/substrate gap returns to a saturated state via dissolution of the crystal surface. The images in Figure 13.23c and d provide vital information on how steps of unit cell height retreat and interact during dissolution. Further dissolution normal to the surface slows considerably and continued dissolution occurs via the motion of steps away from the dislocation cores, resulting in the step spacing becoming wider toward the center of the spiral and closer at a distance from the core. Spirals with this morphology have been predicted theoretically for dissolution processes close to saturation [63].

Figure 13.23c and d also demonstrate elegantly the interactions between closely spaced spirals at the points where they intercept. It is particularly interesting to note the step pattern that results from the interception of spirals that rotate in opposite directions, labeled A (anticlockwise rotation, moving outward from the center) and C (clockwise rotation) in Figure 13.23c. The steps emerging from dislocations A and C travel toward one another and annihilate when they intersect, leaving a single step connecting the dislocation cores, the morphology of which is very similar to that predicted theoretically for this situation by BCF [63]. After several minutes, the surface was found to reconstruct to a form that was similar to that which prevailed prior to the induction of dissolution.

To increase the driving force exerted on the dissolution process, the potential of the probe was stepped to a value where Br_3^- was oxidized to Br_2 at a diffusion-limited rate. With the tip potential

held in this region, Br^- in the probe/substrate zone was locally depleted by both the direct electrolysis at the IE-AFM probe and titration of Br^- with electrogenerated Br_2. The centers of seven dislocations are observed, which spiral down to hollow cores (cylindrical holes at the center of each dislocation), with radii ranging from 100 to 1000 nm. Such features were absent from Figure 13.23 and all images recorded at lower driving potentials [57]. These results represented the first dynamic and in situ observations of cores at the center of dislocations characterized by small step spacings. The appearance of hollow cores on the dissolving surface is diagnostic of dissolution occurring with a moderate interfacial undersaturation and with the surface kinetics at least partly rate limiting. Hollow cores were not observed for dissolution under diffusion-controlled conditions (Figure 13.23), since the interfacial concentrations of K^+ and Br^- were maintained at a level very close to the saturated value.

13.5.3.2 Potassium Ferrocyanide Trihydrate (010) Surface Dissolution

As with the KBr system, prior SECM studies found the dissolution kinetics of the (010) surface of potassium ferrocyanide trihydrate to be very fast [52], which meant that for the sufficiently large electrode crystal surface separations employed with the IE-AFM, the dissolution images relate to effectively diffusion-controlled conditions.

Figure 13.24 highlights the ability of the IE-AFM probe to electrochemically induce dissolution from the (010) surface of potassium ferrocyanide trihydrate. The top half of the scan was recorded with the tip unbiased, and reflects the structure of the surface in contact with a saturated solution of $Fe(CN)_6^{4-}$ that can be seen to be very flat. In this area, only three widely spaced steps (terrace width $6.0 \pm 0.3\,\mu m$; step height 11 ± 1 Å) are observed. Halfway down the scan, with the tip in contact with the surface, the potential was pulsed from open circuit to 0.42 V (high mass transport rate) for 0.5 s, and back to open circuit, to locally deplete $Fe(CN)_6^{4-}$ adjacent to the crystal surface. As can be seen from the lower half of the scan, the surface reconstructs in response to the electrochemical perturbation. The number of steps increases, with the interstep spacing decreasing (terrace width ca. $2 \pm 0.3\,\mu m$; step height 15 ± 1 Å).

To investigate the effect of the dissolution driving force on the observed topography, in situ IE-AFM images were recorded in the same area as a sequence. For all, the probe potential was pulsed with the tip located in the center of the scan image and retracted 0.11 μm from the crystal

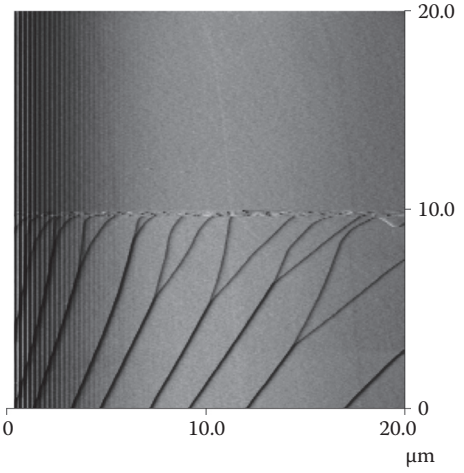


FIGURE 13.24 20 μm × 20 μm IE-AFM deflection image recorded at a scan rate of 6.10 Hz, demonstrating the immediate effect of electrochemically inducing the dissolution of the (010) surface of potassium ferrocyanide trihydrate. The tip was pulsed to 0.42 V for 0.5 s, halfway down the scan, with the tip in contact with the surface. (Reproduced from Jones, C.E. et al., *J. Phys. Chem. B*, 104, 2351, 2000.)

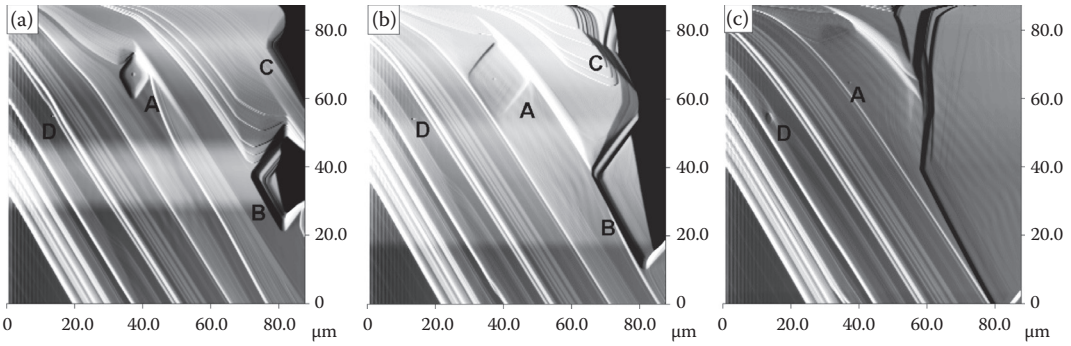


FIGURE 13.25 87.7 μm × 87.7 μm IE-AFM deflection images recorded at a scan rate of 6.1 Hz: (a) 42 s after, (b) 84 s after, and (c) 126 s after electrochemically inducing dissolution by pulsing the probe to 0.33 V for 0.5 s. (Reproduced from Jones, C.E. et al., *J. Phys. Chem. B*, 104, 2351, 2000.)

and the surface imaged as the crystal returned to a state of equilibrium. Initial studies were carried out under low driving force conditions, that is, only slightly depleting the $Fe(CN)_6^{4-}$ concentration in the probe–substrate gap (pulse from open circuit to +0.24 V for 0.5 s). Under these conditions, the dissolution process was observed to proceed mainly by the retreat of preexisting steps aligned in the dominant [102] direction. By increasing the driving force (+0.33 V for 0.5 s), an increased rate of dissolution was noted, with the density of steps aligned in the dominant [102] direction, significantly increasing, as shown in Figure 13.25. However, as this route is unable to maintain the crystal surface close to saturated conditions (for diffusion-controlled dissolution), diamond-shaped etch pits were also revealed on the dissolving crystal surface (labeled A, B, and C in Figure 13.25), which result from the unwinding of steps from screw dislocation sites. The outline morphology of the pit is determined by the [102] and [201] directions. Importantly, the density of etch pits observed on the surface with IE-AFM corresponds closely with the observed density of growth hillocks on the crystal surface, prior to dissolution.

At the highest driving forces employed, IE-AFM shows that etch pit dissolution becomes the dominant mechanism as shown in Figure 13.26, which displays a sequence of AFM images recorded (a) 90 s, (b) 216 s, (c) 258 s, and (d) 400 s after the probe had been used to electrochemically induce dissolution (pulsed from open circuit to +0.34 V for 0.5 s). Dissolution was induced with the tip located over, and in contact with, a preexisting dislocation site. Figure 13.26a shows the presence of a deep etch pit, with a spiral located at the center. Over the subsequent period, the surface continues to slowly dissolve, via the pit opening out as steps associated with the spiral retreat by unwinding. Importantly, the observed surface dynamics made using IE-AFM are consistent with classical dissolution models and earlier SECM kinetic studies [52].

13.5.3.3 Calcite ($10\bar{1}4$) Dissolution

Experiments were made by first identifying a region of interest on the calcite surface using AFM topographical mapping. The electrochemical capabilities of the IE-AFM tip were then utilized to induce dissolution in this area for a series of driving forces, as for the previous two examples. An area of the surface was specifically chosen in which there were no dislocation defects, in order to investigate the role of other surface features, such as point defects and steps, in the dissolution process. In order to observe the earliest stages in the dissolution process, it was necessary to dose the surface with only a very small flux of electrogenerated protons. Dissolution was initially induced by pulsing the potential of the IE-AFM probe from 0.0 to 0.5 V (vs. Ag/AgCl reference electrode) and back again for a period of 0.5 s with the apex of the probe tip about 0.1 μm from the surface. Images were recorded sequentially at a capture rate of one frame every 42 s as the system returned

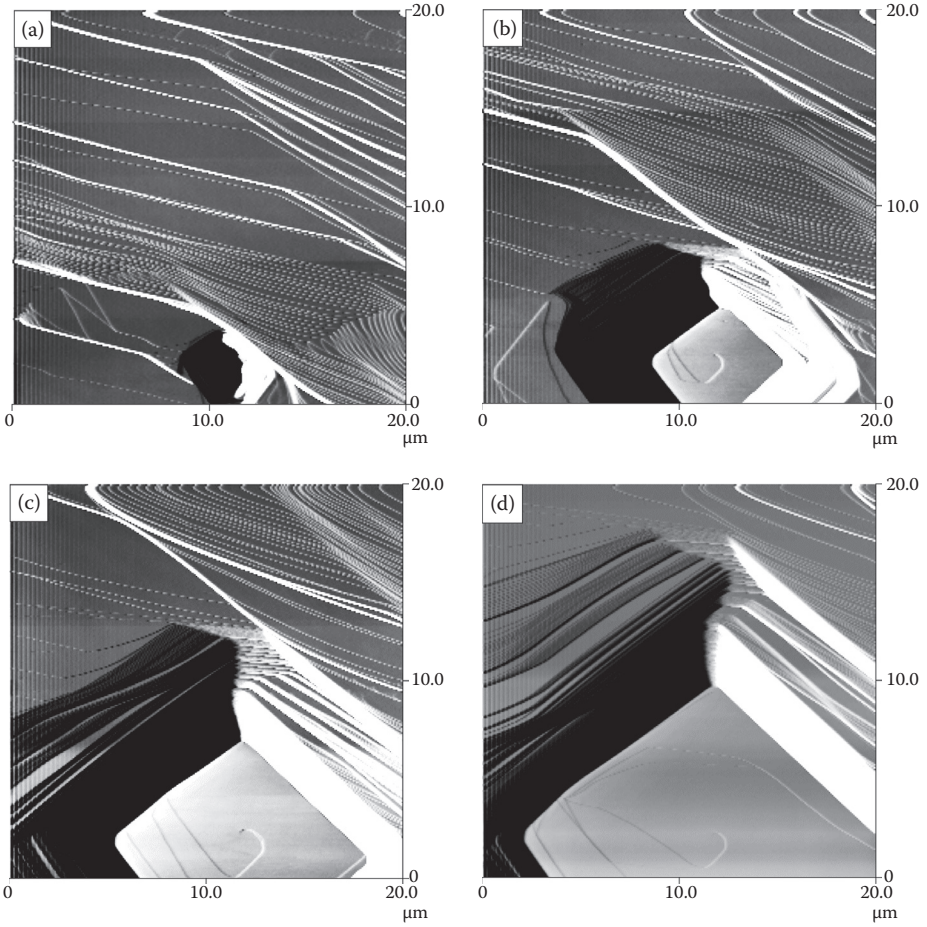


FIGURE 13.26 20 μm × 20 μm IE-AFM deflection images recorded at a scan rate of 6.1 Hz: (a) 90 s after, (b) 216 s after, (c) 258 s after, and (d) 300 s after electrochemically inducing dissolution by pulsing the probe to 0.34 V for 0.5 s, with the tip positioned over a dislocation site. (Reproduced from Jones, C.E. et al., *J. Phys. Chem. B*, 104, 2351, 2000.)

to equilibrium. This potential step corresponded to a proton flux of about 0.6 nmol/cm^2/s, which is less than one proton per carbonate surface site over the period of the pulse.

Initiation of the dissolution process was clearly evident from the immediate formation of discrete nanopits in the calcite surface, as shown in Figure 13.27 (compare (a) recorded before the pulse with (b) recorded immediately after). These small pits were considered to be nucleated at point defects in the surface, since these are the most active sites on a crystal surface and are thus considered to be regions from which dissolution occurs first. The pit number density observed using IE-AFM was, however, orders of magnitude greater than that seen previously using other techniques (e.g., interferometry). This was attributed to the fact that IE-AFM can be performed on a rapid timescale at much higher resolution, so that the number density and size of the pits that form under these conditions were readily quantified.

Figure 13.27 also demonstrates that dissolution on the $(10\bar{1}4)$ surface of calcite occurs by the removal of material from terrace edges and preexisting pits. This can be seen most clearly by observing the expansion of pit A in Figure 13.27b. Moreover, as dissolution of the surface proceeds, as shown in Figure 13.27c and d, the etch pits that nucleated close to pit A also merged with it. The

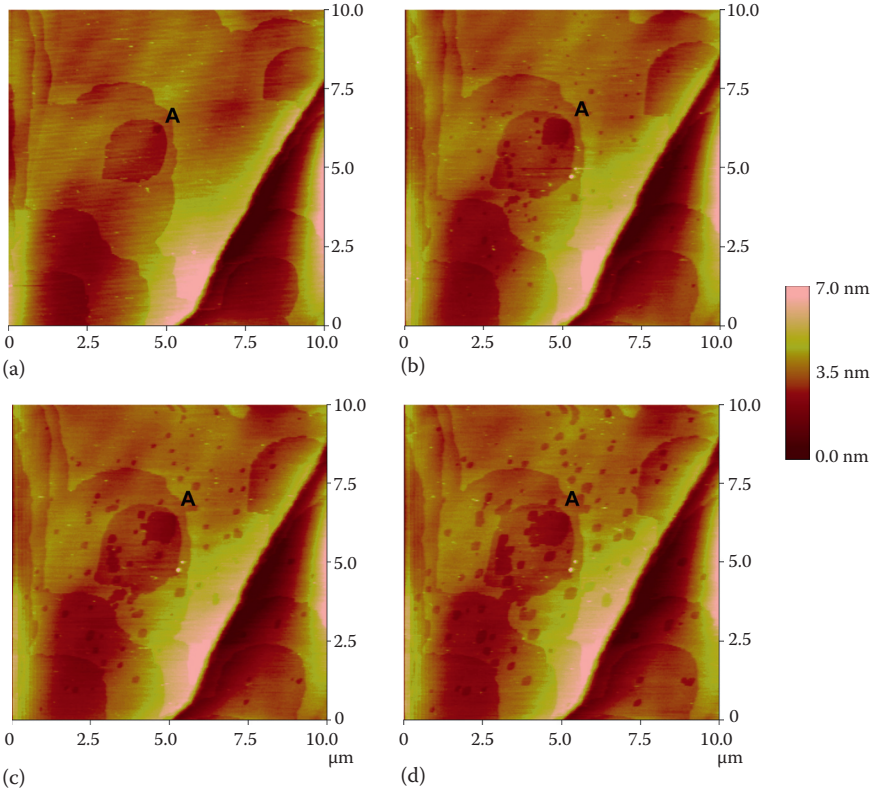


FIGURE 13.27 10 μm × 10 μm IE-AFM height images recorded at a scan rate of 6.1 Hz (a) prior to electrochemically induced dissolution, (b) immediately after, (c) 42 s after, and (d) 84 s after pulsing the potential at the SECM-AFM probe from 0.0 to 0.5 V for a period of 0.5 s. The times relate to the start of the image acquisition on this and all subsequent figures. Additionally, all images were recorded from top to bottom. (Adapted from Jones, C.E. et al., *Chem. Phys. Chem*., 4, 139, 2003.)

expansion of the tiny pits in Figure 13.27b–d allows the corresponding dissolution rates to be calculated as ~1–3 nm/s.

Increasing the flux of protons to the surface by over an order of magnitude (9 nmol/cm^2/s) after the system had returned to an equilibrium state resulted in a significant change in the surface dissolution topography, as shown in Figure 13.28. In particular, extensive dissolution from the step edge reduced this feature in Figure 13.28a to a series of unit cell high steps (Figure 13.28b). The disappearance of the edge was accompanied by the formation of >300 shallow pits in the area imaged. Observation of the dissolution behavior of two pits to the right of position A indicated that the rate of pit expansion remained in the range observed previously (Figure 13.27), ~1–3 nm/s. A few of the pits formed also showed outline morphologies characteristic of the predominant crystallographic directions on the calcite cleavage plane, particularly noticeable at position B in Figure 13.28b. The internal angles approach 78° and 102° of the calcite cleavage rhombohedron.

Finally, increasing the proton flux by a further order of magnitude (~86 nm/cm^2), which produces local proton concentrations, in the gap between the cantilever and crystal surface at the millimolar level, resulted in the dissolution structures displayed in Figure 13.29. Strikingly, the density of etch pits observed on the surface is much smaller than for the lower proton flux cases (Figures 13.27 and 13.28); however, the pit sizes are larger. The pit observed have similar rhombohedron outline morphologies to those observed by ex situ optical microscopy after dissolution under similar acid conditions.

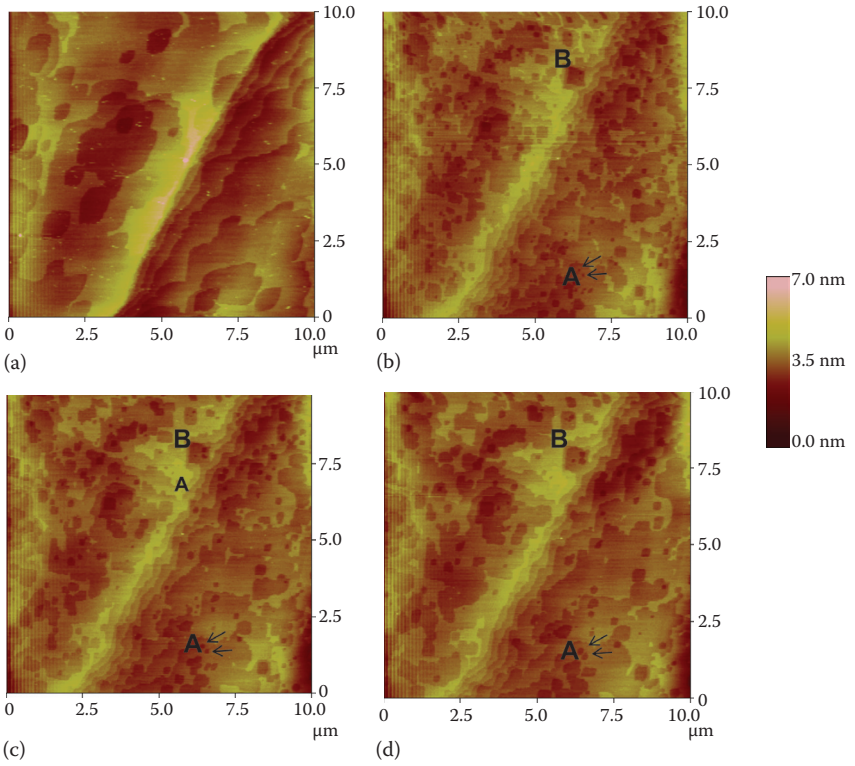


FIGURE 13.28 10 μm × 10 μm IE-AFM height images recorded at a scan rate of 6.1 Hz (a) prior to electrochemically induced dissolution, (b) immediately after, (c) 42 s after, and (d) 84 s after pulsing the potential at the SECM-AFM probe from 0.0 to 1.0 V for a period of 0.5 s. (Adapted from Jones, C.E. et al., *Chem. Phys. Chem*., 4, 139, 2003.)

These data illustrate that using IE-AFM in this way it is possible to elucidate the different dissolution mechanisms of the calcite surface subject to various acid challenges. In particular, proton-assisted dissolution from the surface is initially observed to occur via the formation of tiny pits with mono and dual unit cell layer depths, as well as by the removal of material from step edges. Increasing the acid challenge ultimately results in the formation of micron-sized shallow etch pits.

13.6 CONCLUSIONS AND PERSPECTIVE

This chapter has highlighted numerous and diverse applications of SECM for the study of interfacial physicochemical processes and the measurement of fluxes at interfaces. The simple concept of using SECM to perturb an interfacial process, initially at equilibrium, and to measure the associated kinetics via the current response, has proven particularly versatile in studying adsorption/desorption, dissolution, lateral diffusion, and interphase transfer and kinetics. Many of these processes are ubiquitous in the physical and life sciences, and SECM will continue to have an important role to play in investigating such processes. In many instances, these studies have involved transient techniques, which open up much greater opportunities than can be realized with steady-state techniques, for example, in studying finite quantities of material on surfaces, or applying subtle perturbations to interfacial systems. The latter aspect is particularly well illustrated through studies of dissolution processes in the IE-AFM format, where a wide range of driving forces can be applied briefly to a crystal surface, so as to build up a comprehensive picture of mechanisms and kinetics.

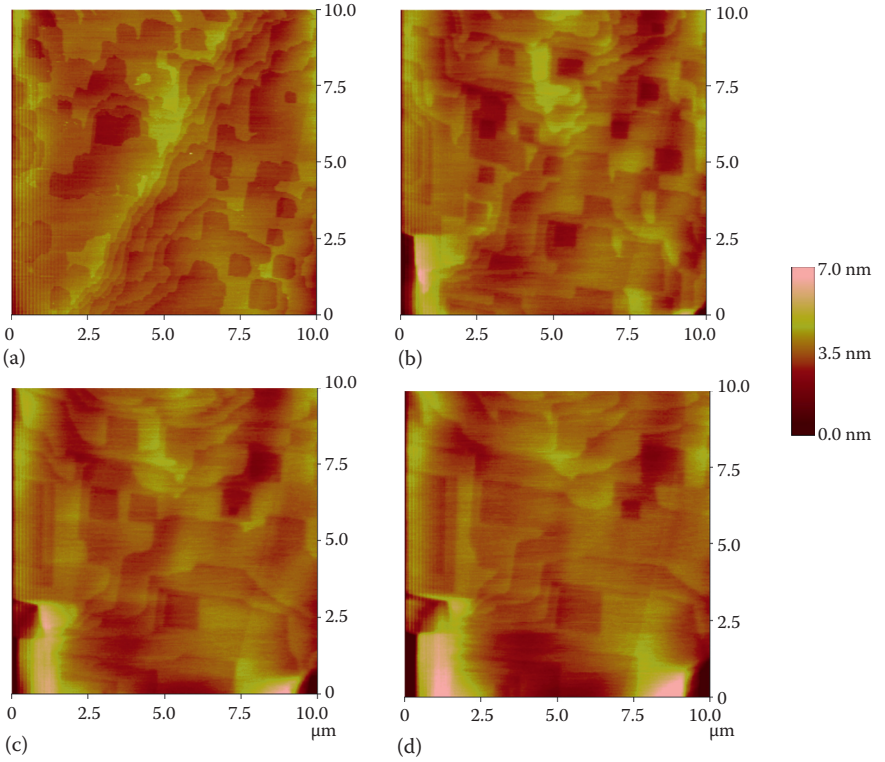


FIGURE 13.29 10 μm × 10 μm IE-AFM height images recorded at a scan rate of 6.1 Hz (a) prior to electrochemically induced dissolution, (b) immediately after, (c) 42 s after, and (d) 84 s after pulsing the potential at the SECM-AFM probe from 0.0 to 1.25 V for a period of 0.5 s. (Adapted from Jones, C.E. et al., *Chem. Phys. Chem*., 4, 139, 2003.)

Opportunities and challenges for SECM flux measurements are closely linked, and center on improving further the spatial and temporal resolution. In this context, newly developed techniques such as intermittent contact (IC)-SECM [64] and scanning electrochemical cell microscopy (SECCM) [65], among other recent developments, described in Chapter 17, should take quantitative electrochemical imaging to the nanoscale and open up the direct measurement of ion and molecular fluxes at the nanoscale. A further trend is the combination of SECM with complementary visualization techniques, such as confocal laser scanning microscopy, which make a powerful combination for flux imaging [66], again as considered in Chapter 17. All of these developments are underpinned by quantitative modeling to ensure rich kinetic and mechanistic views of surface and interfacial processes.

REFERENCES

1. Bard, A. J., Faulkner, L. *Electrochemical Methods: Fundamentals and Applications*, 2nd edn., John Wiley & Sons, New York, 2001.
2. Edwards, M. A., Martin, S., Whitworth, A. L., Macpherson, J. V., Unwin, P. R. Scanning electrochemical microscopy: Principles and applications to biophysical systems. *Physiol. Meas*. 2006, 27, R63.
3. Amemiya, S., Bard, A. J., Fan, F.-R. F., Mirkin, M. V., Unwin, P. R. Scanning electrochemical microscopy. *Ann. Rev. Anal. Chem*. 2008, 1, 95.
4. Macpherson, J. V., Unwin, P. R. Probing reactions at Solid/Liquid Interfaces, In *Scanning Electrochemical Microscopy*, Bard, A. J., Mirkin, M. V. (eds.). Marcel Dekker, New York, 2001, Chap. 12, pp. 521–592.

5. Unwin, P. R., Bard, A. J. Scanning electrochemical microscopy. 14. Scanning electrochemical microscope induced desorption – A new technique for the measurement of adsorption desorption-kinetics and surface diffusion rates at the solid/liquid interface. *J. Phys. Chem*. 1992, 96, 5035.
6. Burt, D. P., Cervera, J., Mandler, D., Macpherson, J. V., Manzanares, J. A., Unwin, P. R. Scanning electrochemical microscopy as a probe of Ag^+ binding kinetics at Langmuir phospholipid monolayers, *Phys. Chem. Chem. Phys*. 2005, 7, 2955.
7. Unwin, P. R., Bard. A. J. Scanning electrochemical microscopy 9. Theory and application of the feedback mode to the measurement of following chemical reaction rates in electrode processes. *J. Phys. Chem*. 1991, 95, 7814.
8. Grime, J. M. A., Edwards, M. A., Rudd, N. C., Unwin, P. R. Quantitative visualization of passive transport across bilayer lipid membranes. *Proc. Natl. Acad. Sci. USA* 2008, 105, 14277.
9. Bitziou, E., Rudd, N. C., Edwards, M. A., Unwin, P. R. Visualisation and modeling of the hydrodynamics of an impinging microjet. *Anal. Chem*. 2006, 78, 1435.
10. Bard, A. J., Denuault, G., Freisner, R. A., Dornblaser, B. C., Tuckerman, L. S. Scanning electrochemical microscopy: Theory and application of the transient (chronoamperometric) SECM response. *Anal. Chem*. 1991, 63, 1282.
11. Slevin, C. J., Macpherson, J. V., Unwin, P. R. Measurement of local reactivity at liquid/solid, liquid/liquid and liquid/gas interfaces with the scanning electrochemical microscope: Principles, theory and applications of the double potential step chronoamperometric mode. *J. Phys. Chem. B* 1997, 101, 10851.
12. Unwin, P. R., Macpherson, J. V., Martin, R. D., McConville, C. F. Scanning electrochemical micros copy as a dynamic probe of metal adsorption, nucleation and growth on surfaces: Silver deposition on pyrite, in *localised In-situ methods for investigating electrochemical interfaces,* In *Electrochemical Society Proceedings*, Vol. 99–28. Taylor, S. R., Hillier, A. C., Seo, M. (eds.). Electrochemical Society, Pennington, NJ, 2000, pp. 104–121.
13. Slevin, C. J., Unwin, P. R. Lateral proton diffusion rates along stearic acid monolayers. *J. Am. Chem. Soc*. 2000, 122, 2597.
14. Zhang, J., Unwin, P. R. Proton diffusion at phospholipid assemblies. *J. Am. Chem. Soc*. 2002, 124, 2379.
15. Zhang, J., Unwin, P. R. Microelectrochemical measurements of electron transfer rates at the interface between two immiscible electrolyte solutions: Potential dependence of the ferro/ferricyanide-7,7,8,8-tetracyanoquinodimethane ($TCNQ/TCNQ^{-}$) system. *Phys. Chem. Chem. Phys*. 2002, 4, 3820.
16. Zhang, J., Slevin, C. J., Morton, C., Scott, P., Walton, D. J., Unwin, P. R. New approach for measuring lateral diffusion in Langmuir monolayers by scanning electrochemical microscopy (SECM): Theory and application. *J. Phys. Chem. B* 2001, 105, 11120.
17. Mandler, D., Unwin, P. R. Measurement of lateral charge propagation in polyaniline layers with the scanning electrochemical microscope. *J. Phys. Chem. B* 2003, 107, 407.
18. O'Mullane, A. P., Macpherson, J. V., Unwin, P. R., Cervera-Montesinos, J., Manzanares, J. A., Frehill, F., Vos, J. G. Measurement of lateral charge propagation in [Os(bpy)(2)(PVP)(*n*)Cl]Cl thin films: A scanning electrochemical microscopy approach. *J. Phys. Chem. B* 2004, 108, 7219.
19. Zhang, J., Barker, A. L., Mandler, D., Unwin, P. R. Effect of surface pressure on the insulator to metal transition of a Langmuir polyaniline monolayer. *J. Am. Chem. Soc*. 2003, 125, 9312.
20. Liljeroth, P., Quinn, B. M., Ruiz, V., Kontturi, K. Charge injection and lateral conductivity in monolayers of metallic nanoparticles. *Chem. Comm*. 2003, 13, 1570.
21. Ruiz, V., Liljeroth, P., Quinn, B. M., Kontturi, K. Probing conductivity of polyelectrolyte/nanoparticle composite films by scanning electrochemical microscopy. *Nano Lett*. 2003, 3, 1459.
22. Liljeroth, P., Vanmaekelbergh, D., Ruiz, V., Kontturi, K., Jiang, H., Kauppinen, E., Quinn, B. M. Electron transport in two-dimensional arrays of gold nanocrystals investigated by scanning electrochemical microscopy. *J. Am. Chem. Soc*. 2004, 126, 7126.
23. Ruiz, V., Nicholson, P. G., Jollands, S., Thomas, P. A., Macpherson, J. V., Unwin, P. R. Molecular ordering and 2D conductivity in ultrathin poly(3-hexylthiophene)/gold nanoparticle composite films. *J. Phys. Chem. B* 2005, 109, 19335.
24. Nicholson, P. G., Ruiz, V., Macpherson, J. V., Unwin, P. R. Effect of composition on the conductivity and morphology of poly(3-hexylthiophene)/gold nanoparticle composite Langmuir–Schaeffer films. *Phys. Chem. Chem. Phys*. 2006, 8, 5096.
25. Whitworth, A. L., Mandler, D., Unwin, P. R. Theory of scanning electrochemical microscopy (SECM) as a probe of surface conductivity. *Phys. Chem. Chem. Phys*. 2005, 7, 356.
26. Zhang, J., Burt, D. P., Whitworth, A. L., Mandler, D., Unwin, P. R. Polyaniline Langmuir–Blodgett films: Formation and properties. *Phys. Chem. Chem. Phys*. 2009, 11, 3490.

27. Axelrod, D., Koppel, D. E., Schlessinger, J., Elson, E., Webb, W. W. Mobility measurement by analysis of fluorescence photobleaching recovery kinetics. *Biophys. J*. 1976, 16, 1055.
28. Teissie, J., Prats, M., Soucaille, P., Tocanne, J. F. Evidence for conduction of protons along the interface between water and a polar lipid monolayer. *Proc. Natl. Acad. Sci. USA* 1985, 82, 3217.
29. Zigah, D., Noel, J. M., Lagrost, C., Hapiot, P. Charge transfer between electroactive species immobilized on carbon surfaces by aryl diazonium reduction. SECM investigations. *J. Phys. Chem. C* 2010, 114, 3075.
30. Wang, A. F., Ornelas, C., Astruc, D., Hapiot, P. Electronic communication between immobilized ferrocenyl-terminated dendrimers. *J. Am. Chem. Soc*. 2009, 131, 6652.
31. Lie, L. H., Mirkin, M. V., Hakkarainen, S., Houlton, A., Horrocks, B. R. Electrochemical detection of lateral charge transport in metal complex–DNA monolayers synthesized on Si(111) electrodes. *J. Electroanal. Chem*. 2007, 603, 67.
32. Bertoncello, P., Ciani, I., Li, F., Unwin, P. R. Measurement of apparent diffusion coefficients within ultrathin Nafion Langmuir–Schaefer films: Comparison of a novel scanning electrochemical microscopy approach with cyclic voltammetry. *Langmuir* 2006, 22, 10380.
33. Barker, A. L., Macpherson, J. V., Slevin, C. J., Unwin, P. R. Scanning electrochemical microscopy (SECM) as a probe of transfer processes in two-phase systems: Theory and experimental applications of SECM-induced transfer with arbitrary partition coefficients, diffusion coefficients and interfacial kinetics. *J. Phys. Chem. B* 1998, 102, 1586.
34. Evans, N. J., Gonsalves, M., Gray, N. J., Barker, A. L., Macpherson, J. V., Unwin, P. R. Local amperometric detection of K^+ in aqueous solution using scanning electrochemical microscopy ion-transfer voltammetry. *Electrochem. Commun*. 2000, 2, 201.
35. Gonsalves, M., Barker, A. L., Macpherson, J. V., Unwin, P. R., O'Hare, D., Winlove, C. P. Scanning electrochemical microscopy as a local probe of oxygen permeability in cartilage. *Biophys. J*. 2000, 78, 1578.
36. Wipf, D. O., Bard, A. J. Scanning electrochemical microscopy. 15. Improvements in imaging via tip-position modulation and lock-in detection. *Anal. Chem*. 1992, 64, 1362.
37. Edwards, M. A., Whitworth, A. L., Unwin, P. R. Quantitative analysis and application of tip position modulation-scanning electrochemical microscopy. *Anal. Chem*. 2011, 83, 1977.
38. Slevin, C. J., Ryley, S., Walton, D. J., Unwin, P. R. A new approach for measuring the effect of a monolayer on molecular transfer across an air/water interface using scanning electrochemical microscopy. *Langmuir* 1998, 14, 5331.
39. Ciani, I., Burt, D. P., Daniele, S., Unwin, P. R. Effect of surface pressure on oxygen transfer across molecular monolayers at the air/water interface: Scanning electrochemical microscopy investigations using a mercury hemispherical microelectrode probe. *J. Phys. Chem. B* 2004, 108, 3801.
40. Zhang, J., Unwin, P. R. Effect of fatty alcohol monolayers on the rate of bromine transfer across the air/water interface: Assessment of candidate models using scanning electrochemical microscopy. *Langmuir* 2002, 18, 1218.
41. Zhang, J., Unwin, P. R. Kinetics of bromine transfer across Langmuir monolayers of phosphatidylethanolamines at the water/air interface. *Phys. Chem. Chem. Phys*. 2003, 5, 3979.
42. Zhang, J., Unwin, P. R. Kinetics of $IrCl62^-$ ion transfer across the water/1,2-dichloroethane interface and the effect of a phospholipid monolayer. *Langmuir* 2002, 18, 2313.
43. Strutwolf, J., Zhang, J., Barker, A. L., Unwin, P. R. Effect of phospholipids on the kinetics of dioxygen transfer across a 1,2-dichloroethane/water interface. *Phys. Chem. Chem. Phys*. 2001, 3, 5553.
44. Zhang, J., Strutwolf, J., Cannan, S., Unwin, P. R. Combined scanning electrochemical microscopy–Langmuir trough technique for investigating phase transfer kinetics across liquid/liquid interfaces modified by a molecular monolayer. *Electrochem. Commun*. 2003, 5, 105.
45. Bragato, C., Daniele, S., Baldo, M. A., Denuault, G. Oxygen as redox mediator in scanning electrochemical microscopy. Application to the study of localised acid attack of marble. *Ann. Chim*. 2002, 92, 153.
46. McGeouch, C. A., Edwards, M. A., Mbogoro, M., Parkinson, C., Unwin, P. R. Scanning electrochemical microscopy as a quantitative probe of acid-induced dissolution: Theory and application to dental enamel. *Anal. Chem*. 2010, 82, 9233.
47. Etienne, M., Schulte, A., Mann, S., Jordan, G., Dietzel, I. D., Schuhmann, W. Constant-distance mode scanning potentiometry. 1. Visualization of calcium carbonate dissolution in aqueous solution. *Anal. Chem*. 2004, 76, 3682.
48. Oldham, K. B. In *Microelectrodes, Theory and Applications*, Vol. 197. Montenegro, M. I., Queirós, M. A., Dashbach, J. L. (eds.). NATO ASI Ser E, Kluwer, Dordrecht, the Netherlands, 1991, pp. 3–16.
49. Macpherson, J. V., Unwin, P. R. A new approach to the study of dissolution kinetics. *J. Chem. Soc. Faraday Trans*. 1993, 89, 1883.

50. Macpherson, J. V., Unwin, P. R. A novel approach to the study of dissolution kinetics using the scanning electrochemical microscope: Theory and application to the dissolution of $CuSO_4 \cdot 5H_2O$ in aqueous sulfuric acid solutions. *J. Phys. Chem*. 1994, 98, 1704.
51. Macpherson, J. V., Unwin, P. R. Oscillatory dissolution of an ionic single crystal surface observed with the scanning electrochemical microscope. *J. Phys. Chem*. 1994, 98, 11764.
52. Macpherson, J. V., Unwin, P. R. Scanning electrochemical microscope induced dissolution: Rate law and reaction rate imaging for the dissolution of the (010) face of potassium ferrocyanide trihydrate in non-stoichiometric aqueous solutions of the lattice ions. *J. Phys. Chem*. 1995, 99, 3338.
53. Unwin, P. R., Macpherson, J. V. New strategies for probing crystal dissolution kinetics at the microscopic level. *Chem. Soc. Rev*. 1995, 24, 109.
54. Macpherson, J. V., Unwin, P. R. Scanning electrochemical microscopy as a probe of silver chloride dissolution kinetics in aqueous solution. *J. Phys. Chem*. 1995, 99, 14824.
55. Macpherson, J. V., Unwin, P. R. Scanning electrochemical microscope induced dissolution: Theory and experiment for silver chloride dissolution in aqueous solution without supporting electrolyte. *J. Phys. Chem*. 1996, 100, 19475.
56. Macpherson, J. V. A New approach to the study of dissolution kinetics, PhD thesis, University of Warwick, Coventry, U.K., 1996.
57. Macpherson, J. V., Unwin, P. R., Hillier, A. C., Bard, A. J. In-situ imaging of ionic crystal dissolution using an integrated electrochemical-AFM probe. *J. Am. Chem. Soc*. 1996, 118, 6445.
58. Holder, M. N., Gardner, C. E., Macpherson, J. V., Unwin, P. R. Combined scanning electrochemical–atomic force microscopy (SECM-AFM): Simulation and experiment for flux-generation at un-insulated metal-coated probes. *J. Electroanal. Chem*. 2005, 585, 8.
59. Jones, C. E., Macpherson, J. V., Unwin, P. R. In-situ observation of the surface processes involved in dissolution from the (010) surface of potassium ferrocyanide trihydrate in aqueous solution using an integrated electrochemical–atomic force microscope. *J. Phys. Chem. B* 2000, 104, 2351.
60. Jones, C. E., Unwin, P. R., Macpherson, J. V. In-situ observation of the surface processes involved in dissolution from the cleavage surface of calcite in aqueous solution using a combined scanning electrochemical-atomic force microscope (SECM-AFM). *Chem. Phys. Chem*. 2003, 4, 139.
61. Kipp, S., Lacmann, R., Schneeweiss, M. A. Problems in temperature control performing in situ investigations with the scanning force microscope. *Ultramicroscopy* 1995, 57, 333.
62. Burton, W. K., Cabrera, N., Frank, F. C. The growth of crystals and the equilibrium structure of their surfaces. *Phil. Trans. R. Soc. Lond*. 1951, A243, 299.
63. Van Der Hoek, B., Van Der Eerden, J. P., Bennema, P., Sunagawa. I. The influence of stress on spiral growth. *J. Cryst. Growth* 1982, 58, 365.
64. McKelvey, K., Edwards, M. A., Unwin, P. R. Intermittent contact–scanning electrochemical microscopy (IC–SECM): A new approach for tip positioning and simultaneous imaging of interfacial topography and activity. *Anal. Chem*. 2010, 82, 6334.
65. Ebejer, N., Schnippering, M., Colburn, A. W., Edwards, M. A., Unwin, P. R. Localized high resolution electrochemistry and multi-functional imaging: Scanning electrochemical cell microscopy (SECCM). *Anal. Chem*. 2010, 82, 9141.
66. Rudd, N. C., Cannan, S., Bitziou, E., Ciani, I., Whitworth, A. L., Unwin, P. R. Fluorescence confocal laser scanning microscopy as a probe of pH gradients in electrode reactions and surface activity. *Anal. Chem*. 2005, 77, 6205.

14 Applications of Scanning Electrochemical Microscopy in Corrosion Research

Dennis E. Tallman and Mark B. Jensen

CONTENTS

14.1 Introduction 452
14.2 Scanning Electrochemical Probe Techniques Used in Corrosion Research 453
14.2.1 Scanning Electrochemical Microscopy 453
14.2.2 Alternating Current SECM 455
14.2.3 Potentiometric SECM 457
14.2.4 Electrochemical Microcell and Scanning Capillary Microscopy 459
14.2.5 Scanning Reference Electrode Technique and Scanning Vibrating Electrode Technique 459
14.2.6 Local Electrochemical Impedance Spectroscopy and Mapping 461
14.3 Applications of Scanning Electrochemical Probe Techniques in Corrosion Research 462
14.3.1 Applications of SECM 462
14.3.1.1 Early Work 462
14.3.1.2 Stainless Steel 463
14.3.1.3 Nonferrous Metals 465
14.3.1.4 Coated Metals 467
14.3.2 Applications of Potentiometric SECM 472
14.3.2.1 pH Mapping 472
14.3.2.2 Mapping of Other Ions 475
14.3.3 Applications of Electrochemical Microcell and Scanning Capillary Microscopy 479
14.3.3.1 Stationary Capillary Techniques 479
14.3.3.2 Scanning Capillary Techniques 479
14.3.4 Applications of SVET and LEIS/LEIM 480
14.3.4.1 SVET 480
14.3.4.2 LEIS/LEIM 482
14.4 Conclusions 482
Acknowledgments 483
References 483

14.1 INTRODUCTION

The corrosion of a pure metal or a metal alloy may be defined as the irreversible reaction of the metal with its environment, resulting in degradation of the metal and/or its properties. For environmental corrosion, the reactions are redox reactions involving the oxidation of one or more of the metals comprising the alloy, driven by reduction of one or more oxidants, such as hydrogen ion, dioxygen, and/or water. Such corrosion reactions have been called "extractive metallurgy in reverse" [1], reflecting the fact that considerable energy must be expended to extract and purify a metal such as Fe or Al from its ore (i.e., its oxide forms). Corrosion is the thermodynamically favored process by which the metal reverts to its oxide form(s). Since it is virtually impossible to completely stop such thermodynamically favorable processes, corrosion control strategies are designed to slow the corrosion rate by retarding the rate of metal oxidation, the rate of oxidant reduction, the rate of ion movement between sites of oxidation and reduction (such ion movement is required for maintaining overall charge balance), or some combination of these approaches.

For a developed country, the annual direct cost of corrosion and its control is estimated to be 3%–4% of the country's gross domestic product (e.g., over $300 billion per year for the United States) [2]. Such direct costs include costs of design, manufacturing, and construction that incorporate strategies to mitigate corrosion, as well as management costs (e.g., maintenance costs such as material replacement, stripping and/or applying coatings, cathodic protection of gas and liquid transmission pipelines, etc.). There are also indirect costs, mostly associated with loss of productivity or product due to outages, delays, failures, and litigation, that are estimated to be nearly as large as the direct costs. Finally, there have been catastrophic failures attributed to corrosion, which have led to loss of life, including airplane crashes [3] and bridge collapses [4]. Such very high cost to society associated with the corrosion of engineering metals provides the major motivation for performing corrosion research, the goal of which is to better understand corrosion mechanisms so that improved methods for corrosion mitigation can be developed.

There are several types of corrosion, including uniform corrosion, galvanic corrosion, pitting corrosion, crevice corrosion, and others (such as hydrogen damage, intergranular corrosion, dealloying, and erosion corrosion) [1]. Uniform corrosion is typically observed for metals that are compositionally and metallurgically uniform and for which a homogeneous corrosive environment has equal access to all areas of the metal surface. Uniform corrosion is characterized by numerous small rapidly interchanging anodic and cathodic sites across the metal surface, leading to a predictable and uniform dissolution of the metal. Uniform corrosion is conveniently studied by "global" electrochemical techniques such as electrochemical impedance spectroscopy (EIS), electrochemical noise methods (ENM), and potentiodynamic techniques, such as the polarization resistance method and the Tafel extrapolation method [1,5]. These global electrochemical techniques provide a surface-averaged response that is appropriate for uniform corrosion. The scanning probe techniques discussed in this chapter provide little additional information about uniform corrosion and, thus, find limited application to this form of corrosion.

Localized forms of corrosion (such as pitting, crevice, and galvanic corrosion) arise when the metal surface is not compositionally uniform and/or when there is not a uniform exposure of the metal surface to the corrosive environment [6]. Such localized forms of corrosion lead to nonuniform current density distribution across the metal surface as well as nonuniform distributions of species concentration (such as metal ions, H^+, and O_2). For these localized forms of corrosion, the scanning probe techniques provide valuable spatial and temporal information not available from the surface-averaging (or global) techniques mentioned earlier. A brief review of scanning probe techniques as applied to localized corrosion studies has recently appeared [7]. We have recently prepared a very extensive review chapter for Volume 24 of *Electroanalytical Chemistry: A Series of Advances* [8], and the reader is referred to that chapter for more in-depth discussion of the application of these techniques in corrosion research. In Section 14.2, we provide an overview of several scanning electrochemical probe techniques used in corrosion research. In Section 14.3, we describe

selected applications of these techniques to corrosion studies, with emphasis on new reports that have appeared since our previous review [8].

14.2 SCANNING ELECTROCHEMICAL PROBE TECHNIQUES USED IN CORROSION RESEARCH

In this chapter, we focus on scanning probe techniques that provide a probe response (a current or a voltage) that originates from some electrochemical phenomenon and that have been applied to corrosion research. This section provides a brief description of each of these techniques. The reader is referred to the cited references and to other chapters in this book for greater detail on the theory and instrumentation. Although each of these techniques may be considered a form of scanning electrochemical microscopy (SECM), we will reserve the use of the acronym SECM to refer to the technique in which a faradaic current at a microelectrode is measured as it is held or moved in a solution in the vicinity of a substrate surface. The term *substrate* will be used to refer to the sample being examined by the scanning probe technique. There are other scanning probe techniques that have found extensive application in corrosion research but for which the probe response does not originate directly from an electrochemical phenomenon, and these techniques will not be considered in this chapter. Examples include scanning Kelvin probe (SKP), scanning tunneling microscopy (STM), atomic force microscopy (AFM) and its various elaborations, and near-field scanning optical microscopy (NSOM). Certain of these techniques have been integrated with SECM and applied to corrosion studies, and a few examples of such combination techniques have been discussed previously [8].

14.2.1 Scanning Electrochemical Microscopy

The instrumentation and theory for the basic SECM experiment are discussed in detail elsewhere in this book, so only a very brief description is provided here. SECM involves the movement of a very small amperometric microelectrode (usually a disk microelectrode of a few micrometers or smaller radius, referred to as the tip or the probe) near the surface of a substrate immersed in an electrolyte containing at least one redox-active species (a mediator). The two most common modes of operation are the *feedback* mode and the *generator–collector* mode.

In the feedback mode, the potential of the tip is maintained constant by a potentiostat and the substrate is usually at the open-circuit potential (OCP), which is dictated by the concentration(s) of redox species in the electrolyte (e.g., according to the Nernst equation). Only the tip current from a reaction such as O → R (where O is an appropriately chosen mediator) is measured. The tip current is perturbed by the presence of the substrate. When the tip is sufficiently far from the substrate, a steady-state current is observed given by the expression:

$$i_{T,\infty} = knFDca \tag{14.1}$$

where

- a is the electrode radius
- c is the mediator concentration
- D is the diffusion coefficient of the mediator
- n is the number of electrons transferred at the tip
- F is the Faraday
- k is a constant that depends on the ratio (RG) of the radius of the tip-insulating material to the radius of the tip electrode ($k \approx 4$ for RG ≥ 10)

When the tip is moved toward the surface of an insulating substrate, the tip current decreases from $i_{T,\infty}$ because the insulating nature of the substrate blocks diffusion of O to the tip from the bulk solution (known as negative feedback). If the substrate is conductive, the species R generated by

the tip can be oxidized back to O (or recycled, since the substrate is poised at a sufficiently positive potential by the bulk redox species), producing an additional flux of O to the tip and, hence, an increase in tip current from $i_{T,\infty}$ (known as positive feedback). It should be noted that the OCP of an active metal substrate such as Fe or Al is controlled by both the thermodynamics and the kinetics of the corrosion reactions as predicted by *mixed potential theory* through the use of Evans diagrams [1,5]. In such cases, the OCP is not an equilibrium potential and may change during the course of the SECM experiment. Thus, it is important to experimentally verify that such change is negligible. For example, our group has used the feedback mode to map the variation of electron transfer activity across the surface of a heterogeneous Al alloy surface [9].

For the generator–collector mode of operation, the tip and substrate potentials are in most cases independently controlled by a bipotentiostat such that a species generated at the tip (e.g., R from the reaction O → R) is collected (detected) at the substrate by forcing the reverse reaction (R → O) at the substrate. This mode is known as the tip generation/substrate collection (TG/SC) mode. Conversely, the substrate may generate R (from the reaction O → R) that is then collected (detected) at the tip, resulting in the complementary mode known as the substrate generation/tip collection (SG/TC) mode. In these generator–collector modes, both tip current and substrate current can be measured. When the tip is rastered in the *x*–*y* plane above the substrate, the tip current variation represents changes in topography and/or changes in the reactivity of the substrate. These two effects can be separated and, thus, SECM permits assessment of the kinetics of heterogeneous electron transfer occurring at the substrate surface as well as the kinetics of homogeneous chemical reactions coupled to electron transfer. The TG/SC mode has been used by our group to study both the passivation of Cu-rich sites and the nucleation of polypyrrole deposition on an Al alloy [10], while the SG/TC mode has been used to examine Cu ion release from Cu-rich sites of the alloy [9,10].

As an example of the latter, Figure 14.1 demonstrates that transient Cu ion release occurs during the passivation of Cu-rich secondary phase particles of AA 2024-T3 in high sulfate concentration [9,10]. The figure shows an SECM image containing a single Cu site. The SECM tip was placed at each of three positions ($y = 30$, 50, 70) and the alloy substrate potential was scanned (200 mV/s) for each tip position. One position ($y = 50$) was directly above the Cu site while the other two were to either side. Both substrate current and tip current (at −0.3 V) were measured. The alloy Cu oxidation peak is clearly observed in the substrate current near 0 V. No significant current was observed at the tip when it was positioned to either side of the Cu site. However, when positioned above the Cu site,

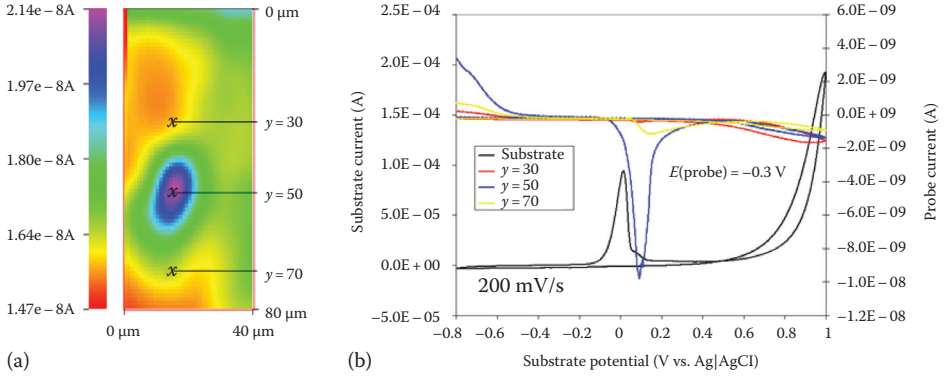


FIGURE 14.1 (a) SECM map showing an active region for reduction on AA 2024-T3 using hydroquinone (HQ) as mediator. Solution contained 0.01 M HQ, 1.0 M Na_2SO_4, 0.005 M H_2SO_4. E(probe) = 1 V, E(substrate) = −0.8 V. (b) Probe/substrate voltammograms showing a substrate metal stripping peak (lower curve) and copper deposition at the microelectrode probe (upper curves) for various positions of the probe along the *y*-scan direction; E(probe) = −0.3 V. (Reprinted from Jensen, M.B. et al., *J. Electrochem. Soc.*, 155, C324 (color online). 2008. Reproduced with permission of The Electrochemical Society.)

a transient reduction current was observed at the tip coincident with the substrate Cu oxidation peak, attributed to the deposition of Cu metal on the tip from Cu ions released from the substrate. To confirm Cu deposition on the SECM tip, a stripping voltammogram obtained at the tip revealed a stripping peak at ca. +0.15 V, matching the position of the Cu stripping peak obtained from the identical experiment performed with pure Cu. Also noted in Figure 14.1 is the detection of H_2 at the tip when positioned above the Cu site (the oxidation current at $y = 50$), generated from reduction of H^+ at the Cu site for substrate potentials less than ca. −0.6 V.

Additional experiments performed with SECM include current–distance measurements, whereby the steady-state tip current is measured as the tip is slowly moved from bulk solution toward the substrate in steps (at a fixed *x*–*y* position above the substrate), yielding a probe approach curve (PAC). Theory can be used to fit the experimentally observed PACs, permitting the extraction of rate constants for irreversible substrate kinetics (see Chapter 5). We are currently using this mode to determine electron transfer rates at Al alloy heterogeneities, using COMSOL Multiphysics to model the PAC for a small active spot (a Cu-rich inclusion at which faster electron transfer occurs) surrounded by a less active area (the Al alloy matrix) at which slower electron transfer occurs [11].

The scanning tip can also be used to detect variations in the concentrations of dissolved species near the substrate surface, such as dioxygen, hydrogen ion, or metal ions (species that are particularly important in corrosion processes), or to locally modify near-surface solution conditions (e.g., pH or Cl^- concentration) by means of a tip redox reaction, often to initiate pit formation. Numerous examples of these approaches were discussed in our previous review [8].

14.2.2 Alternating Current SECM

One of the earliest reports on the use of an AC perturbation in combination with SECM for the study of corrosion was by Tanabe et al. [12]. In what they termed an induced AC current mode, a small amplitude sinusoidal potential perturbation (0.3 mV p–p, 1 kHz) superimposed on a DC potential was applied to a steel substrate, which in turn induced an AC current at the tip (held at 0 V vs. Ag/AgCl, 20 μm above the surface). An increase in induced AC current was shown to correlate with a decrease in local pH and permitted mapping of pitting sites on the steel surface [12].

More recently, Eckhard and Schuhmann have pioneered a technique they refer to as AC-SECM and have applied their approach in corrosion research [13]. In their AC-SECM mode, an alternating potential (usually sinusoidal rather than, or perhaps in addition to, a constant potential) is applied to the tip, and the experiment can often be performed without addition of a mediator. In most cases, the substrate is not connected to a potentiostat and, thus, remains at its OCP. A lock-in amplifier is used to determine both the magnitude of the tip current and its phase angle with respect to the applied AC potential. In this regard, the technique bears some resemblance to impedance spectroscopy and enjoys the signal-to-noise advantage generally associated with frequency selective amplification. The AC current at the tip displays a dependence on the tip-to-substrate distance and can be used for precise positioning of the tip. This distance dependence arises from the influence of the substrate on the local electrolyte conductivity between the tip and the counter electrode in bulk solution. Thus, AC-SECM can be utilized for topographic imaging (of insulating or electrochemically homogeneous substrates) as well as for providing information about the local electrochemical properties of the substrate. The ability to perform experiments in the absence of added mediator is an advantage for systems that might be sensitive to any disturbance caused by such an addition (e.g., the Nernst potential imposed by addition of dissolved redox species). The frequency of the applied AC tip potential may also be varied and has an influence on the electrochemical contrast of AC-SECM. Scanning the frequency at each *x*–*y* tip position leads to a four-dimensional data set (4D AC-SECM) that can be visualized by means of a movie in which the individual AC-SECM images are sequentially displayed with increasing perturbation frequency [13].

Since the AC-SECM signal is sensitive not only to the tip-to-substrate distance but also to the electrochemical nature of the underlying substrate, its applicability as a distance control on

electrochemically heterogeneous samples such as active/passive metal substrates is limited. To overcome this difficulty, Eckhard et al. implemented piezo–piezo shear force detection to maintain constant tip-to-substrate distance and obtain AC-SECM images of electrochemical activity unimpaired by topographic convolution [14]. An example of this approach is shown in Figure 14.2 for a 1 cm^2 piece of 316 Ti stainless steel embedded in PVC. The images were obtained in 1 mM KCl before (left column) and after (right column) induced corrosion. The left column images (before corrosion) show (a) shear force–based topography, (b) false color representation of the AC-SECM current, and (c) the phase shift, all appearing rather featureless (aside from the tilt observed in the topographic image). A pit was then induced (using the substrate as the working electrode and the SECM tip as counter electrode) by positioning the tip near the center of the imaging area (ca. 1 µm above the substrate) and ramping the substrate potential from the OCP to 200 mV positive of the pitting potential, where it was maintained for 15 min to ensure stable pit growth. The area was again scanned by AC-SECM, resulting in the images shown in the right column of Figure 14.2. At the resolution of the shear force measurement, the topographic image remained rather featureless aside from some apparent roughening. However, the AC-SECM current image (Figure 14.2b, right) reveals a hot spot of 5–7 µm dimension at the location where corrosion was induced, while the AC-SECM phase shift image (Figure 14.2c, right) was even more pronounced (the somewhat larger

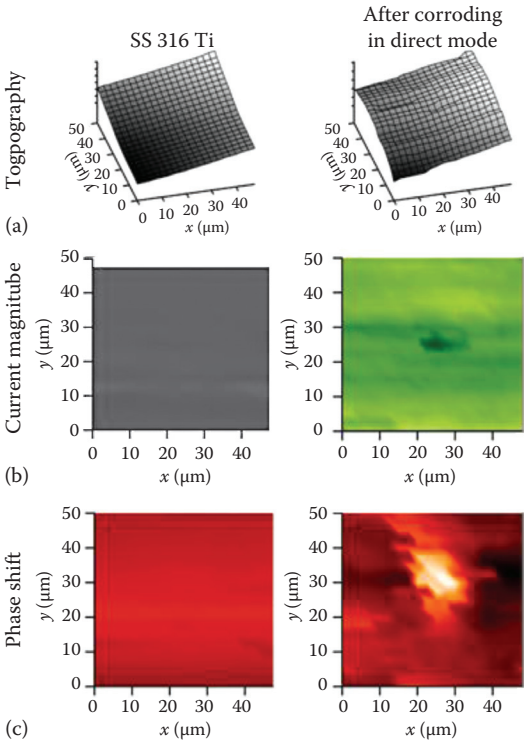


FIGURE 14.2 AC-SECM and simultaneous shear force–based topography measurements. (a) 3D representation of the topography, (b) 2D false color representation of the local current magnitude, and (c) 2D false color representation of the phase shift. (b) and (c) were mathematically corrected for a drift of the background. Left column: initial AC-SECM scan; right column: AC-SECM scan after initiation of localized corrosion in direct mode. Scans were carried out in constant distance with a piezo actuator frequency of 283.5 kHz. Electrochemical imaging was done with an excitation of $f = 1$ kHz, VPP = 250 mV in 1 mM KCl solution. (Reprinted from *Electrochem. Commun.*, 9, Eckhard, K., Etienne, M., Schulte, A., and Schuhmann, W., Constant-distance mode AC-SECM for the visualisation of corrosion pits, 1793–1797 (color online). Copyright 2007, with permission from Elsevier.)

area was attributed to a stronger dependence of the phase shift on the ionic strength of the solution at the chosen frequency of 1 kHz). It was concluded that the induced corroding pit continued to function as an ion point source (i.e., continued to actively corrode, increasing the ion concentration in its vicinity), even after the substrate was returned to the OCP for AC-SECM imaging.

Several other recent applications of AC-SECM to corrosion research have been reported [14–22], though many of these studies are on model systems used to demonstrate proof of concept. These applications have been discussed in considerable detail in our previous review [8].

14.2.3 Potentiometric SECM

Potentiometric SECM, sometimes referred to as the scanning ion electrode technique (SIET) or the local ion concentration technique (LICT) in the corrosion literature, makes use of ion-selective microelectrodes that generate a potential in response to a particular ion concentration (or more specifically, ion activity), as dictated by the Nernst equation. Such electrodes can be used to map temporal and spatial variations in ion concentration near the surface of a corroding substrate. The high selectivity of the potentiometric signal and the ability to detect electrochemically silent ions (such as the alkaline and alkaline earth metals) are the principal advantages of this technique. These measurements must be made rather slowly (approximately 0.5–1 s per point) due to the mechanical disturbance of the concentration gradient by the electrode movement. Otherwise, potentiometric measurements have the advantage over amperometric measurements of not perturbing the target ion concentration. Additionally, the target substrate must generate a steady-state concentration profile of the target ion, or one that changes slowly on the timescale required for a complete potentiometric SECM scan. This, in turn, requires that a steady-state reaction proceeds on the substrate surface, a condition that should be verified for corrosion systems (e.g., from the stability of the OCP and/or by back-to-back potentiometric SECM scans to assess any significant change in concentration).

Another important issue with potentiometric SECM is the measurement and control of tip-to-substrate distance, critical for obtaining exact quantitative information on concentration profiles. Unlike SECM employing active (i.e., amperometric) tips, the passive tip of potentiometric SECM cannot provide distance information from the measured signal (potential). Thus, an alternative means of distance measurement and control is required for exact measurements. If only qualitative information is needed (e.g., an assessment of whether the pH or a metal ion concentration increases or decreases above some substrate surface feature), then distance control is not necessary, although some knowledge of the tip-to-substrate distance is certainly useful. Methods for distance control in potentiometric SECM are discussed elsewhere in this book (see Chapter 10) as well as in our previous review [8].

The most common measurement made by potentiometric SECM is pH, a particularly important measurement in corrosion studies. The high diffusivity of H^+ and OH^- in aqueous solutions can lead to diffusional broadening of pH images, although it is reported that the effect of diffusional broadening can be minimized by choice of an appropriate buffer solution [23]. Our previous review of the corrosion literature found only one report describing the application of potentiometric SECM to an ion other than H^+ or Cl^-, that being for Mg^{2+} [8,24]. The majority of applications involved pH mapping, often in combination with current density measurements obtained by the scanning vibrating electrode technique (SVET, discussed later) to provide supporting evidence for postulated corrosion mechanisms.

A variety of methods have been used to fabricate potentiometric microelectrodes for potentiometric SECM as discussed elsewhere in this book (Chapter 10). In some cases, the electrodes are liquid ion exchange (LIX) electrodes fabricated in drawn capillaries (or micropipettes) for measuring ion concentrations down to picomolar levels [25]. LIX electrodes typically have time constants on the order of tenths of a second. These electrodes can be fabricated with micron or submicron tip diameters and have been used for several decades by life scientists to monitor ion activities in living organisms [26]. Ion exchange liquids for H^+ and for various metal ions are commercially available,

making this approach quite versatile. However, such electrodes are very fragile and are easily damaged if brought into contact with the substrate surface during a potentiometric SECM experiment, and this is particularly troublesome with active metal substrates where corrosion product buildup can occur.

Solid-state microelectrodes tend to be more robust and can be fabricated by a number of approaches. For example, pH microelectrodes for use in corrosion studies have been fabricated based on the reversible Ir/IrO_2 couple [27]:

$$IrO_2 + 4H^+ + 4e^- \leftrightarrow Ir + 2H_2O$$

These iridium oxide electrodes can be prepared by sputtering, as well as by thermal or electrochemical oxidation of iridium wire. Electrochemical oxidation of an iridium substrate is the most common method of preparation, by potential cycling of iridium in sulfuric acid between potentials of −0.25 and +1.25 V vs. SCE.

A general approach to fabricating solid-state ion-selective microelectrodes has been described whereby a conducting electroactive polymer, which is both an electronic and an ionic conductor (e.g., polypyrrole, polythiophene, or polyaniline), is used to mediate charge exchange between an ion-selective membrane (an ion conductor) and a metal substrate (an electronic conductor) [28]. These electrodes are reported to be robust and mechanically flexible while exhibiting good potential stability with no redox sensitivity. While applications to potentiometric SECM have been described [28], these electrodes have yet to find use in corrosion studies.

The use of a single sensing electrode with a remote reference electrode may lead to error in ion concentration measurement due to variation of the local corrosion potential across the substrate surface (indeed, this is the basis for the technique known as scanning reference electrode technique (SRET), discussed later). Combination electrodes fabricated in pulled double-barreled capillaries can circumvent this problem. An example of a Cl^- contour map obtained by Lin et al. [29] using such a double-barreled electrode is shown in Figure 14.3, illustrating pitting corrosion of type 303 stainless steel induced by exposure to 0.5 M $FeCl_3$. The combination electrode consisted of a liquid membrane Cl^- ion–selective microelectrode in one barrel and a Ag/AgCl reference electrode in the other. The Cl^- map revealed higher concentrations of Cl^- ion near sites where pitting corrosion occurred, with higher pitting corrosion activity resulting in higher Cl^- concentration, presumably to

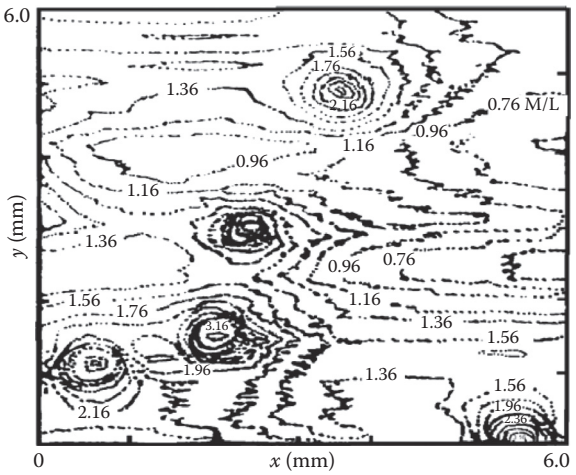


FIGURE 14.3 Cl^- concentration contour map obtained using solid Cl^- ion–selective microelectrode for a type 303 stainless steel surface in 0.5 M $FeCl_3$ solution (pitting corrosion environment). (Reprinted from Lin, C.J. et al., *Corrosion*, 56, 41, 2000. Reproduced with permission from NACE International.)

maintain charge balance. When pitting corrosion ceased, little variation in Cl^- concentration around the metal/solution interface was detected. Such accumulation of Cl^- ions in the anodic regions of crevice and pitting corrosion appears to play an important role in sustaining the propagation of localized corrosion [29].

14.2.4 Electrochemical Microcell and Scanning Capillary Microscopy

Another approach for the study of local electrochemistry involves the use of an electrochemical microcell, a glass microcapillary filled with electrolyte and containing counter and/or reference electrodes. In these experiments, the substrate is not immersed in electrolyte, but rather a very small volume of electrolyte (a droplet) bridges the gap between capillary tip and substrate. The capillary is either stationary (for small area measurements) or scanned above the substrate for spatially resolved measurements. These small area techniques are elegant methods for the study of local phenomena on metal surfaces since they permit polarization of microscopic surface areas, thereby providing a direct correlation between the measured corrosion currents of a local spot and the corresponding corrosion attack [30]. The ability to measure current at the picoampere to femtoampere level with stationary microcells permits study of local processes at length scales in the submicrometer range [30]. The stationary microcell has found application in corrosion studies, especially for probing the effect of microheterogeneities on localized corrosion [31–33].

More relevant to the topic of this book are positionable or scanning microcells for making spatially resolved measurements, often within droplets of electrolyte contacting both the substrate and the capillary [34,35]. These capillary techniques (sometimes referred to as scanning capillary microscopy or the scanning droplet cell) permit all common potentiostatic and galvanostatic measurements, such as cyclic voltammetry, chronoamperometry, impedance spectroscopy, and electrochemical noise measurements [34]. Measurements in subnanoliter solution volumes have been performed by scanning a theta glass capillary containing a carbon fiber microelectrode in one channel and a Ag/AgCl reference electrode in the other channel to different locations within an electrolyte droplet [35]. In another approach, the capillary tip–substrate distance is modulated as in tapping mode AFM, with the amplitude and phase of the modulation providing feedback for control of tip–substrate distance [36]. In some cases, electrolyte flows through the drop by means of a multibarreled capillary, continuously refreshing the solution in the droplet cell [37,38]. A recent review of the many electrochemical configurations using single-barreled and multibarreled capillary cells has been provided by Lohrengel [39], including use of capillary cells for surface modification.

14.2.5 Scanning Reference Electrode Technique and Scanning Vibrating Electrode Technique

Localized corrosion on a metal surface immersed in an electrolyte engenders a flow of ionic current in the electrolyte between local anodic and cathodic sites on the metal surface (due to the requirement for charge balance). This ionic current leads to a potential field and associated potential gradients within the electrolyte, the relationship between the local current density and the potential gradient being given by

$$\bar{i}(x,y,z) = \frac{\nabla \bar{V}(x,y,z)}{\rho} \tag{14.2}$$

where

$\bar{i}(x, y, z)$ is the current density vector having magnitude (A/cm^2) and direction
ρ is the solution resistivity (Ω cm)
$\nabla \bar{V}(x, y, z)$ is the potential gradient (V/cm) at location (x, y, z)

By scanning a small reference electrode near the substrate surface in two dimensions and measuring its potential vs. a remote reference electrode, a map of the potential variation (but not the potential gradient) near the surface can be obtained. One of the earliest examples of this technique was reported in 1940 by Evans [40] for calculating corrosion rates on a water pipeline. Isaacs and Kissel [41] further developed this approach for monitoring pit propagation on stainless steels, using a drawn glass capillary leading from a reference electrode, and first referred to this approach as the scanning reference electrode, later known as SRET.

To measure local current density, the local potential gradient $\nabla\bar{V}(x, y, z)$ must be determined (Equation 14.2). There are two approaches to measuring the local potential gradient. One approach uses a twin-electrode assembly consisting of two microreference (or pseudoreference) electrodes separated from one another along the direction normal to the sample surface (the z-direction) [42]. The second approach (known as the SVET) uses a single microelectrode that is vibrated either in one direction (the z-direction) or in two directions (the x- and z-directions, each at different vibration frequencies) [43,44]. Vibration in two directions permits measurement of the components of current density both normal and parallel to the substrate surface. This second approach (SVET) possesses a signal-to-noise advantage over the single- or dual-electrode SRET measurements since lock-in amplifiers are used to measure the voltage amplitudes at the frequencies of vibration. Thus, SVET with its improved sensitivity and higher spatial resolution has largely replaced SRET.

Originally developed to study ion transport in biology, SVET has found wide application in corrosion research as pioneered by Isaacs and Jackson [45]. The current density vector can be determined from Equation 14.2 provided the electrolyte resistivity is known, typically obtained from a calibration experiment involving the injection of a known current density from a point source. The vibrating probe is scanned just above the surface of the substrate (which is normally at the OCP), producing a map of DC current density distribution. An illustration of the power of this technique is shown in Figure 14.4 for the Al alloy AA 2024-T3 coated with the reduced (n-doped) form of the polymer poly(2,3-dihexylthieno[3,4-*b*]pyrazine). The polymer coating contains a defect (scratch) through the coating to the metal surface. Upon immersion in dilute Harrison's solution (DHS, 0.35 wt% $(NH_4)_2SO_4$ and 0.05 wt% NaCl), the SVET indicated an intense reduction current in the defect area as shown in Figure 14.4, attributed to oxygen reduction at the exposed alloy surface. Oxidation current was distributed more or less uniformly over the polymer surface, attributed to polymer oxidation from the n-doped state to the neutral state. The SVET result strongly suggests that the n-doped polymer cathodically protected the alloy exposed at the defect, a result that was corroborated by galvanic coupling measurements [46].

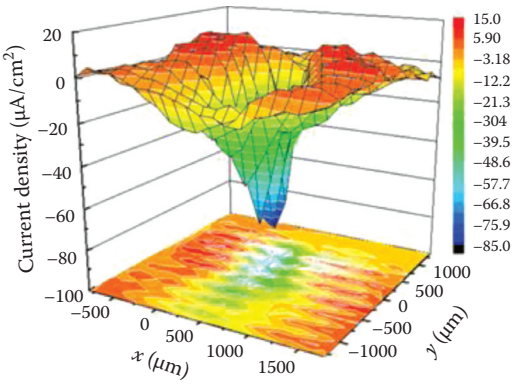


FIGURE 14.4 SVET current density map showing cathodic protection of AA 2024-T3 by a n-doped poly(2,3-dihexylthieno[3,4-*b*]pyrazine) film containing an artificial defect (scratch) after 5 min immersion in 0.35 wt% $(NH_4)_2SO_4$, 0.05 wt% NaCl (reduction current is negative). (Reprinted from Yan, M.C. et al., *J. Electrochem. Soc*., 156, C360 (color online). 2009. Reproduced with permission of The Electrochemical Society.)

14.2.6 Local Electrochemical Impedance Spectroscopy and Mapping

Local EIS (LEIS) and local electrochemical impedance mapping (LEIM) have proven useful in corrosion research, especially for the study of heterogeneous alloys and coated metals. A five-electrode arrangement is usually employed, with reference and counter electrodes used to apply an AC potential perturbation to the substrate (or working electrode, as in global EIS). The local AC current flow through the electrolyte just above the substrate surface is then measured, typically using a twin-electrode probe [47], two examples of which are shown in Figure 14.5. Alternatively, the use of a single vibrating microelectrode for measuring the local current has also been described [48,49]. For the LEIS experiment, the frequency of the AC perturbation applied to the substrate is varied while maintaining a fixed position of the twin-electrode probe above the substrate surface. In the LEIM experiment, the twin-electrode probe is scanned in the x–y plane above the sample surface while holding the AC perturbation frequency constant. The use of higher frequencies of the AC perturbation lowers the impedance of dielectric-type samples, such as coated metals. Thus, LEIS and LEIM can be used for both bare and coated metals. This approach has been used to probe intrinsic and extrinsic defects in organic coatings applied to metals [50].

The power of this technique is nicely illustrated in Figure 14.6, a LEIM scan obtained by Galicia et al. for the Mg alloy AZ91 using the twin-electrode probe technique [51]. The map reveals variations in corrosion rates across the surface that match the alloy microstructure as determined by SEM. The surface of this alloy consists of two phases: the α-phase (containing 96.5% Mg and 3.05% Al) and the β-phase (containing 69.60% Mg and 27.45% Al) [51]. LEIS performed at selected locations above the AZ91 alloy surface revealed that the amplitude of the impedance over the β-phase was about three times higher than that over the α-phase, and the time constant for a high-frequency capacitive loop was 10 times smaller for the α-phase, indicating that the corrosion rate of the β-phase is lower than that of the α-phase, attributed to the increased content of Al in the β-phase [51].

It is important to distinguish between LEIS/LEIM (a five-electrode technique with the AC perturbation applied to the substrate) and AC-SECM (a three-electrode technique with the AC perturbation applied to the probe). Additionally, it should also be noted that LEIS/LEIM as usually implemented does not provide the true local impedance since it is computed from the local current using the global potential, not the local potential. To obtain true local impedance, the local potential must also be measured (or controlled), and some efforts in this direction have been made [52].

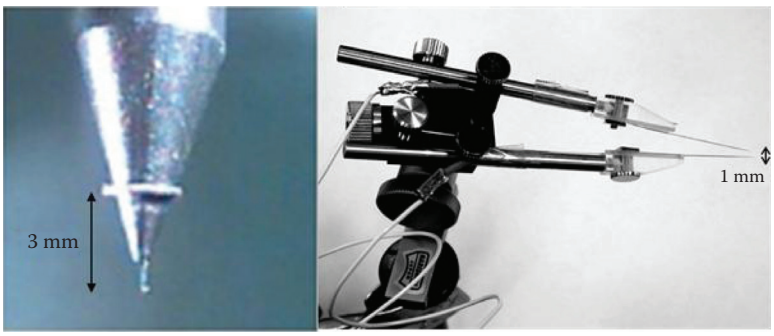


FIGURE 14.5 Twin-electrode probes used for LEIS/LEIM showing spacing between the two electrodes. (a) Probe used with the Princeton Applied Research Model 270/370 LEIS. (b) Probe used with an Applicable Electronics LEIS (two insulated 10 μm Pt–Ir wires exposed at the tips).

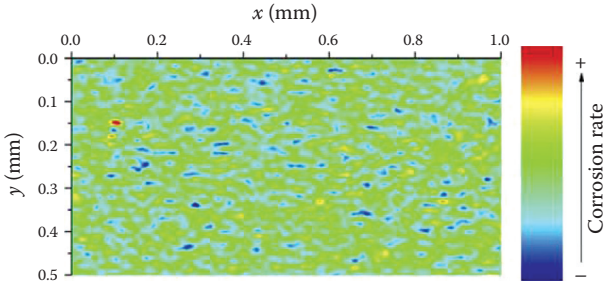


FIGURE 14.6 LEIS image of the AZ91 alloy after 24 h immersion in 1 mM Na_2SO_4 solution at the corrosion potential. The mapping was performed at a fixed frequency (100 Hz) by moving the probe over the alloy surface. (Reprinted from *Corros. Sci*., 51, Galicia, G., Pebere, N., Tribollet, B., and Vivier, V., Local and global electrochemical impedances applied to the corrosion behaviour of an AZ91 magnesium alloy, 1789–1794 (color online), Copyright 2009, with permission from Elsevier.)

14.3 APPLICATIONS OF SCANNING ELECTROCHEMICAL PROBE TECHNIQUES IN CORROSION RESEARCH

Our previous review of this topic covered the literature through the first-half of the year 2009 [8]. In this section, to avoid duplication, the discussion will emphasize examples that have appeared since that time (through October 2010). Approximately 67 publications have appeared since that previous review, attesting to the increasing popularity of these scanning probe techniques for corrosion research. The breakdown of these publications by technique is as follows: SECM, 22; potentiometric SECM (or SIET), 8; the scanning capillary/micropipette technique, 1; SVET, 29; and LEIS/LEIM, 7. Limited space precludes us from discussing all of these applications, so in the following sections we will provide all the references found during the indicated time period, but focus most of our discussion on applications of amperometric and potentiometric SECM. We will limit our discussion of SVET and LEIS/LEIM to example applications that best demonstrate the power of the individual techniques.

14.3.1 Applications of SECM

In this section, we describe corrosion-related applications involving the most common modes of SECM operation (i.e., an amperometric microelectrode in either feedback or generator–collector mode). Traditionally, most of these applications have involved investigations of corrosion on bare metal and metal alloy substrates. But there is also much interest in the further development of coatings for corrosion prevention of metals, and a growing number of reports have appeared describing SECM studies related to these applications.

14.3.1.1 Early Work

The research groups of Smyrl, White, and Wipf appear to be the first to apply SECM to the study of localized corrosion. These early studies focused on two different problems, namely, the identification of precursor sites for pit formation and the monitoring of passive layer breakdown and pit nucleation/growth. The precursor sites for pit formation on the surface of oxide-covered titanium foil were detected by Casillas et al. [53,54]. The feedback mode of SECM was used to visualize a few microscopic domains of intense Faradaic activity from the electrooxidation of bromide at the TiO_2 surface. The tip process was $Br_2 + 2e^- \rightarrow 2Br^-$, and Br_2 was regenerated via the reaction $2Br^- \rightarrow Br_2 + 2e^-$ on the TiO_2 surface. After determining the positions of the active sites, the pits on the surface were nucleated by application of a more positive potential to the substrate. It was found for the first time that pit nucleation occurs preferentially at surface sites of high electrochemical

activity. These electroactive sites have metal-like properties, that is, oxidation reactions occur at these regions of the semiconductor surface at potentials within the bandgap of TiO_2, where the depletion layer structure should inhibit ET [55]. The determined values of the typical active site diameter (ca. 10–50 μm) and density (ca. 20–30 sites/cm^2) showed that active sites represent only a small fraction (~0.04%) of the TiO_2 surface.

A further investigation of pitting precursor sites on titanium was carried out using SPECM, a combination of SECM with photoelectrochemical microscopy [56]. This technique employs an optical fiber/metal ring electrode tip [57]. In contrast to the electrochemical current, the photocurrent produced by illumination of the precursor site was lower than that on the adjacent TiO_2 surface. This was attributed to a more metallic nature of the oxide film at the precursor site [55]. However, no evidence of a chemical basis for the pitting precursor sites was found by EDAX and Auger analysis. In contrast, the active sites on polycrystalline Ti covered with an oxide film have been identified by SPECM and found to be associated with inclusion particles containing Al and Si, on which the oxidation of Br^- can be supported.

Wipf used the SECM to initiate and image active corrosion pits on stainless steel and aluminum samples [58]. Chloride ions were produced at a tip through the reduction of trichloroacetic acid:

$$CCl_3COOH + H_2O + 2e^- \rightarrow CHCl_2COOH + OH^- + Cl^-$$

The electrogenerated Cl^- ions initiated a single corrosion pit at the substrate surface. The recorded substrate current spikes were consistent with initiation, growth, and repassivation of such pits. The probability of successful pit generation was shown to decrease with an increase of the passivating layer growth time [59]. The pitting precursor sites in the passive layer were also detected and ascribed to defects associated with grain boundaries. The presence of pitting precursors was correlated with current fluctuations at the tip observed prior to passive layer breakdown. A similar observation was made by Zhu and Williams for type 304 stainless steel corrosion in dilute chloride solutions [60].

The oxidizable product of iron corrosion (presumably Fe^{2+}) can be collected at the tip [58]. In this way, the spatial distribution of the corrosion current was mapped by scanning the tip over the growing pit. The ability of the SECM to detect small quantities of corrosion products on a millisecond timescale suggests that it can be used for quantitative studies of corrosion processes at single inclusions or defects.

In the remainder of this section, we describe more recent applications of SECM in corrosion research, categorized by the type of substrate investigated.

14.3.1.2 Stainless Steel

As we have previously stated, the small dimensions of the SECM probe make it ideal for investigations of localized corrosion processes occurring on a metal surface, and pitting corrosion has been of primary interest. Pitting corrosion is initiated by a localized breakdown in the passive metal oxide, usually in the presence of chloride ion, and can result in rapid dissolution of the underlying metal (a detailed description and review of this process can be found in Ref. [61]). Therefore, much of the initial work utilizing SECM for corrosion studies on iron and its alloys has focused on using the probe to initiate pitting corrosion, detect the products of pitting, and/or identify sites on the metal that are precursors to pitting [8]. The recent work described in this section continues this trend [62–64].

An example illustrating the efficacy of SECM for detection of pitting products comes from the work of Yin and coworkers in which pitting products generated from stainless steel in chloride solution were detected [62,63]. In this work, anodically polarized type 304 stainless steel was exposed to neutral chloride solution for varying lengths of time. The platinum SECM probe (+0.56 V vs.

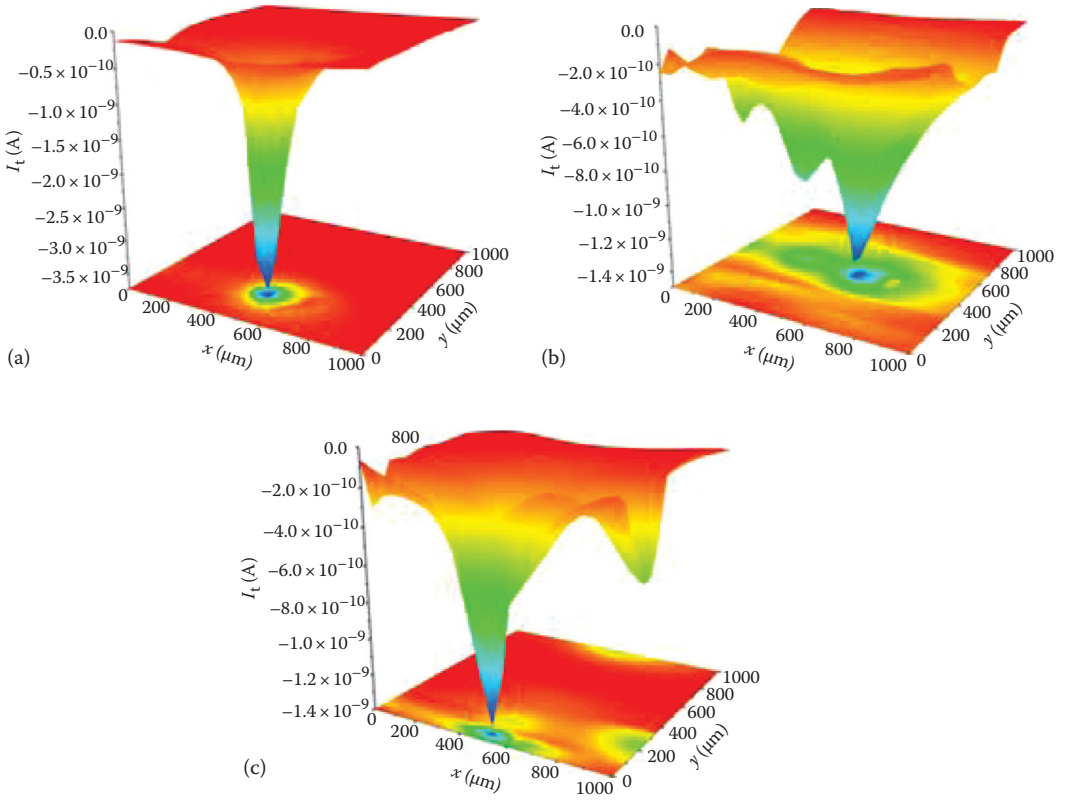


FIGURE 14.7 SECM area scan images of 304 stainless steel in 0.1 M NaCl solution at different immersion times. (a) 2 h, (b) 5 h, and (c) 15 h. $I_s = -80$ mA, $E_t = 0.56$ V. (Reprinted from *Appl. Surf. Sci.*, 255, Yin, Y., Niu, L., Lu, M., Guo, W., and Chen, S., In situ characterization of localized corrosion of stainless steel by scanning electrochemical microscope, 9193 (color online), Copyright 2009, with permission from Elsevier.)

SCE) anodically detected ferrous ions as it was scanned over a 1 mm^2 substrate area. Figure 14.7 shows SECM images resulting from exposure times of 2, 5, and 15 h. A single pit is clearly seen in the first image (Figure 14.7a) corresponding to the shorter exposure time. As exposure time increases (Figure 14.7b and c), previously identified pits appear to passivate, new pits emerge, and the overall pit density increases. The authors demonstrate similar behavior with increasing substrate polarization currents and potentials.

SECM has also proven useful in identifying the corrosion products generated from model galvanic couples in solution. For instance, Terada et al. used SECM, along with EIS and potentiodynamic polarization, to investigate the effects of heat treatments on the corrosion properties of superferritic stainless steel (DIN 1.4575) [64]. This is a chromium-rich steel that is being considered as a potentially less-expensive alternative to titanium for metallic prostheses; therefore, an understanding of its corrosion behavior is of fundamental importance. Extended heat treatment of this material is believed to decrease its corrosion resistance, so a galvanic couple was created consisting of a solution-annealed substrate electrically connected to another solution-annealed substrate that had been subjected to further aging at 475°C for 1080 h. The substrates were anodically polarized in NaCl solution, and the SECM probe was scanned over both substrates to detect Fe^{2+}. As expected, higher probe currents were observed over the aged surface, indicating a higher concentration of Fe^{2+} and confirming the lower corrosion resistance of this substrate. This behavior is believed to result from chromium-rich phases that form with aging and deplete chromium from the protective oxide layer.

14.3.1.3 Nonferrous Metals

While corrosion-related SECM investigations over the past decade have largely focused on the ferrous metals, a number of studies have appeared related to other metals, particularly aluminum and its alloys [8]. Recently reported nonferrous work includes further studies on aluminum alloys [65,66], as well as the first reports of such studies on magnesium [67–69], zirconium [70], and a hyper-stoichiometric uranium oxide [71].

The corrosion behavior of industrially important copper-rich aluminum alloys has received much attention in the literature. While the addition of copper to the aluminum matrix strengthens the material, it also results in intermetallic inclusions that serve as local cathodes for the reduction of O_2 and/or H^+. Corrosion of these alloys can result in redistribution of copper through dealloying of the copper-rich inclusions in the metal, and previous work from our own laboratory (see Figure 14.1) has demonstrated that SECM can be used to detect copper dissolution in these alloys [9]. A recent report by Blanc et al. demonstrated the use of a uniquely designed SECM probe to both localize the dissolution of copper in a model alloy system and detect the products of this dissolution [65]. The probe was an Al–Pt ring-disk microelectrode consisting of a 50 μm diameter Pt wire coated with an insulating layer and sealed in an Al tube, all of which was placed inside a glass capillary of 1 mm diameter. The probe was placed above a copper substrate immersed in sulfate solution to form a thin-layer cell between the probe and the substrate, and electrical connection was made externally between the copper and the aluminum ring creating a galvanic couple. Cyclic voltammetry carried out at the Pt disk during coupling of the Al and Cu detected the presence of Cu^{2+} in the solution. However, no Cu^{2+} was detected when the metals were not connected, or when the distance between the connected metals was large. Postexperiment SEM images showed evidence of corrosion on the copper substrate only in the region of the thin-layer cell created by the probe, indicating that unique chemistry occurs at the Cu–Al interface in this system.

SECM studies on magnesium metal have focused on identifying effective surface pretreatment procedures to increase the corrosion resistance of the metal. These procedures have included immersion in fluoride solution [69] and alternating voltage (AV) treatments [67,68]. AV treatment involves application of a square wave potential waveform through which the passive film is broken down at one limit and reformed at the other, with the intent of creating a high-density passive film with high corrosion resistance. Figure 14.8 shows SECM images obtained in SG/TC mode for three magnesium substrates, each subjected to a different pretreatment method: (a) untreated, (b) immersion in sulfate/hydroxide solution, and (c) AV [68]. Each image was generated following pretreatment by immersing the substrate in ferricyanide solution at its OCP, then using the Pt microelectrode probe to oxidize any $Fe(CN)_6^{4-}$ created at the substrate back to $Fe(CN)_6^{3-}$. Detection of anodic current at the microelectrode (downward direction) is believed to result from breakdown of the passive film to reveal a conductive area, possibly the initiation of pit formation. It can be seen from Figure 14.8 that both the untreated (a) and the immersed (b) samples show high current spikes and a larger background current, indicative of apparent passive film breakdown. The sample subjected to AV treatment (c), however, shows a lower background current and no current spikes, indicating a more corrosion-resistant passive film. These results were consistent with polarization, EIS, and XPS measurements, with XPS identifying a compact MgO film formed by the AV treatment.

Corrosion-related SECM studies on both zirconium and hyperstoichiometric uranium oxide have been reported by Shoesmith and coworkers [70,71]. In both cases, their interest was in identifying areas of high cathodic activity on the substrate and then determining the electron transfer rate constant (k^0) for sites of varying activity. Previously existing models for quantitative kinetic determinations have assumed a substrate of infinite dimensions. In practice, however, the active sites in localized corrosion investigations are often of dimensions similar to the microelectrode probe surface. Therefore, finite element analysis was utilized to generate theoretical PACs that allow for variation in the dimensions of both the active area and the probe, as well as in the level

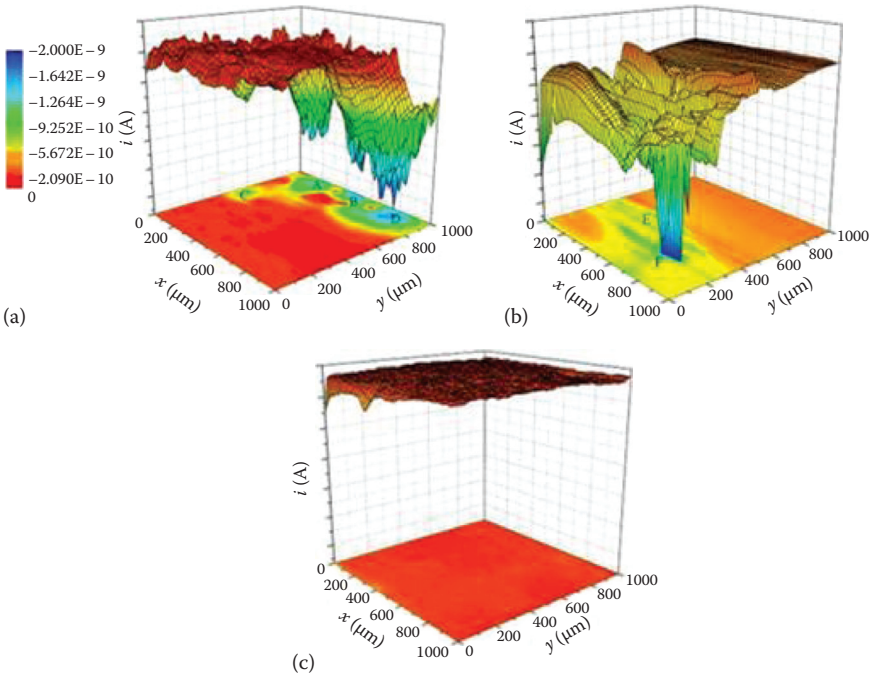


FIGURE 14.8 SECM images of treated and untreated Mg substrates following 10 h immersion in 0.05 M NaCl at pH 12. (a) Untreated sample, (b) sample immersed 30 min in 0.25 M Na_2SO_4 + 0.1 M NaOH, and (c) sample subjected to alternating voltage treatment. Imaging conditions: 0.5 mM $K_3Fe(CN)_6$, E(probe) = +0.40 V_{SCE}, E(substrate) = OCP. (Reprinted from *Corros. Sci*., 51, Liu, X., Zhang, T., Shao, Y., Meng, G., and Wang, F., Effect of alternating voltage treatment on the corrosion resistance of pure magnesium, 1772 (color online), Copyright 2009, with permission from Elsevier.)

of kinetic control. In the case of zirconium, cathodically active areas observed in SECM images acquired in feedback mode using ferrocene methanol as mediator were found to correlate with Fe impurities identified by SEM/EDX [70]. Experimental approach curves were acquired from both the most active and least active sites as a function of cathodic polarization potential, and compared with theoretical curves generated for finite active areas, the sizes of which were determined from the SECM images. Values of k^0 were found to differ by 1–2 orders of magnitude between the most active and least active sites, depending on the polarization potential, and the k^0 values increased by approximately two orders of magnitude at each type of site as the polarization potential was decreased.

Interest in the corrosion behavior of hyperstoichiometric UO_{2+x} stems from concerns about the increased solubility of oxidized forms of UO_2 generated from spent nuclear fuel [71]. Nonstoichiometric ratios have been shown to have a considerable impact on conductivity, yet this ratio is not expected to be distributed uniformly throughout the material, thus leading to localized conductivity variations and a nonhomogeneous distribution of corrosion sites. As in the case of zirconium described earlier, feedback mode SECM images and PACs were obtained with ferrocene methanol, this time however at the OCP (E_{corr}) of the $UO_{2.1}$ substrate. Figure 14.9a shows one of these images, with five highlighted points corresponding to sites where experimental approach curves were obtained. These sites represent regions of high (1), medium (2 and 3), and low (4 and 5) tip feedback currents. The approach curves are shown in Figure 14.9b, along with the simulated curves for selected values of the rate constant corresponding to an active substrate radius of 10 μm and a microelectrode radius of 1 μm. Rate constant values can be seen to range from 1×10^{-3} m/s for spot 1 down to 3×10^{-6} m/s for spot 5. Sites of highest conductivity are believed to represent grain

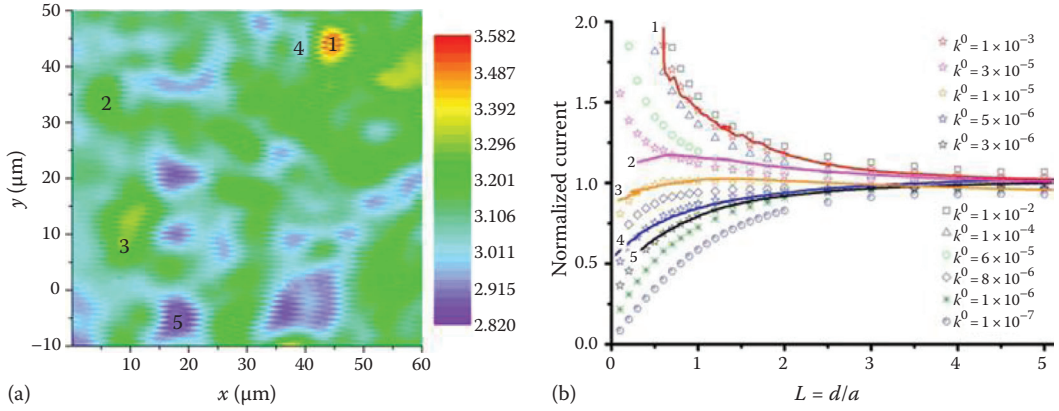


FIGURE 14.9 (a) SECM image recorded in feedback mode at E_{corr} on $UO_{2.1}$ disk electrode in 0.1 M NaCl solution containing 0.9 mM ferrocene methanol. (b) Experimental SECM approach curves (solid lines) obtained in feedback mode at indicated sites from *a*, and corresponding simulated curves (open symbols) for the indicated values of rate constant, k^0. (Reprinted from He, H. et al., *J. Electrochem. Soc.*, 156, C87 (color online), 2009. Reproduced with permission of The Electrochemical Society.)

structures of higher degrees of nonstoichiometry in the substrate, a hypothesis supported by AFM and EDX results [71].

14.3.1.4 Coated Metals

Corrosion protection of metals has traditionally involved complete coating systems that may include organic coatings, metallic coatings, and/or inhibitors (organic and inorganic). While reports of corrosion investigations on metals involving the SECM have appeared in the literature for over 20 years, similar studies involving coated metals have appeared only more recently. Our previous review summarized the literature in this area from 2004 through the beginning of 2009, and described a variety of applications related to formation, degradation, defects, and protection mechanisms of coatings [8]. Several new reports spanning these same themes have appeared in the literature since that time. In this section, we will highlight this most recent work, emphasizing a number of examples that demonstrate the breadth of applications in this area.

14.3.1.4.1 Coating Formation

The early stages of coating or inhibitor interaction with a substrate surface will likely lead to changes in the conductivity of that substrate, making SECM a logical choice for monitoring the growth of these structures in solution. For example, benzotriazole (BTAH) is a commonly used corrosion inhibitor for copper, and Izquierdo et al. used PACs to study BTAH film formation on copper as a function of time and deposition solution electrolyte [72]. Approach curves obtained in feedback mode with ferrocene methanol as mediator were shown to gradually transition from highly positive feedback (conductive) to negative feedback (insulating) with increasing immersion time in the deposition solution, indicating the formation of an insulating BTAH film. These films were found to grow more rapidly in the presence of chloride ions than sulfate ions, and SECM imaging showed that the films grown in chloride provided better protection of the copper in corrosive solution.

SECM has also been recently used to investigate the growth of conducting polymers deposited onto metal surfaces both chemically [73] and electrochemically [10] from solution. Our own interest in conducting polymers stems from their potential as alternatives to chromate conversion coatings for corrosion control of active metals and metal alloys. Specifically, we are investigating the use of hydroxybenzene sulfonates as electrochemical mediators for the electrodeposition of polypyrrole

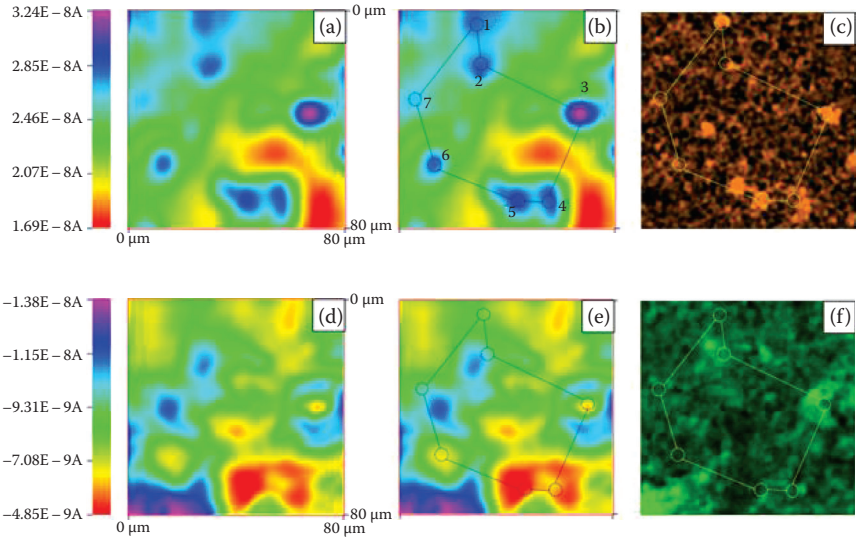


FIGURE 14.10 (a) SECM image of AA2024-T3 obtained with a 10 μm Pt probe electrode in 0.01 M hydroquinone, 1 M Na_2SO_4, and 0.001 M H_2SO_4. E(tip) = +1.2 V; E(substrate) = −0.8 V. (b) Same as *a* but with copper-rich areas indicated for common reference. (c) Copper EDX map of same 80 μm × 80 μm area shown in (a) and (b). (d) SECM image of same 80 μm × 80 μm area after electrodeposition of small amount of polypyrrole. Solution: 0.01 M $K_3Fe(CN)_6$, 1 M Na_2SO_4. E(tip) = 0.0 V, E(substrate) = +0.6 V. (e) Same as *d* but with reference points included from image (b). (f) Carbon EDX map of same 80 μm × 80 μm area shown in other images. (Reprinted from *Electrochim. Acta*, Jensen, M.B., Karels, J.M., Guerard, A.F., and Tallman, D.E., unpublished results (2011). Manuscript in preparation).

on aluminum alloys. These mediators have been shown to decrease the potential required for galvanostatic deposition of polypyrrole by up to 500 mV, thereby minimizing the formation of aluminum oxide and resulting in a more adherent polymer film [74]. Figure 14.10 shows SECM images acquired in TG/SC mode both before and after the potentiostatic deposition of polypyrrole on AA 2024-T3 using 4,5-dihydroxy-1,3-benzenedisulfonic acid (also known as Tiron) as the electrodeposition mediator [10]. Figure 14.10a and b shows cathodically active areas of the alloy before deposition obtained with hydroquinone as the SECM mediator, and the corresponding EDX image in Figure 14.10c identifies these areas as copper-rich secondary phase particles. Figure 14.10d and e shows the same area of the substrate following polymer nucleation. In these images, the SECM mediator was ferricyanide, and areas of high current correspond to polypyrrole nucleation sites where the mediator is anodically regenerated. The EDX image in Figure 14.10f shows these high current regions to be rich in carbon, consistent with areas of high polymer concentration. Comparison of the before- and after-deposition images indicates that polymer nucleation occurs exclusively on the aluminum matrix and not on the copper-rich inclusions. We believe this phenomenon to most likely result from sulfate passivation of the copper particles and/or loss of Tiron mediation due to its complexation with copper ions anodically generated at the particle surface.

14.3.1.4.2 Coating Degradation

Blister formation in a coating is caused by the penetration of water, and is often the first step toward coating failure and subsequent corrosion of the underlying metal. As a blister begins to form, the surface of the coating is expected to rise, and SECM can be used to detect the accompanying changes in surface morphology due to the sensitive dependence of the probe current on probe–substrate separation. Souto and coworkers have utilized this approach to identify early signs of blistering on steel substrates coated with a variety of organic coatings [75–77]. One such example

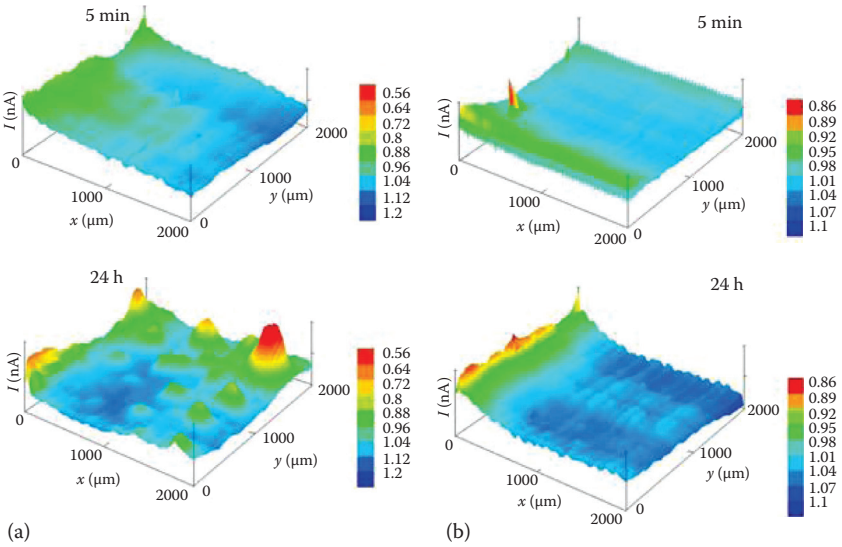


FIGURE 14.11 SECM measurement on a polyurethane-coated carbon steel plate. Tip–substrate distance: 15 μm. Scan rate: 30 μm/s. Tip potential: +0.50 V vs. Ag/AgCl/KCl (saturated) reference electrode. Values of *z*-axis: current, nA. The figures represent an area of 2000 μm × 2000 μm in *x*- and *y*-directions. From top to bottom: 5 min, 24 h immersion in the test solution: (a) 0.1 M KCl + 0.5 mM ferrocene methanol and (b) 0.1 M K_2SO_4 + 0.5 mM ferrocene methanol. (Reprinted from *Corros. Sci.*, 52, Souto, R.M., Gonzalez-Garcia, Y., Izquierdo, J., and Gonzalez, S., Examination of organic coatings on metallic substrates by scanning electrochemical microscopy in feedback mode: Revealing the early stages of coating breakdown in corrosive environments, 748 (color online), Copyright 2010, with permission from Elsevier.)

is demonstrated in Figure 14.11, which shows time-dependent images obtained from polyurethane-coated steel samples immersed in both (a) chloride and (b) sulfate solutions with ferrocene methanol present as the SECM mediator. All images were acquired in feedback mode over the insulating substrate; thus any changes in the probe–substrate separation result in lower (less separation) or higher (greater separation) feedback current. Very little current variation is observed after 5 min immersion in either electrolyte, indicating that the surfaces are flat and featureless. After 24 h, however, the chloride-immersed sample shows many new features attributed to the nucleation and growth of blisters at the metal/coating interface. The authors report that this chloride-induced degradation has been observed in other coating systems as well, and they speculate that this is a general effect driven by the formation of a solid metal chloride phase at the polymer/coating interface [75].

In a related investigation by the same authors, the SECM probe was held in a fixed position above a coated steel substrate immersed in electrolyte solution while the probe feedback current was measured as a function of time [76]. The observed decrease in the feedback current was related to a decrease in the tip–substrate separation distance and indicative of swelling in the coating due to the uptake of water. The authors demonstrated that similar results could be obtained from EIS capacitance measurements of the same system. However, the SECM data showed evidence of swelling on a timescale 200 times shorter than that of EIS, confirming the advantage of the localized nature of the SECM measurements over those that average the behavior over the entire surface.

14.3.1.4.3 Coating Defects

A defect in a coating exposes the underlying metal, resulting in corrosion of the metal and the associated generation of oxidized metal ions and consumption of dissolved oxygen. Both processes can be detected at the SECM probe, and this approach has been used to investigate corrosion processes at defect sites in a number of coating systems [76,78,79]. Gonzalez-Garcia et al. intentionally introduced a large circular hole into a polyurethane-coated steel sample, and then

immersed the sample in chloride solution [76]. Successive SECM lines scans were performed over the defect site, first with the probe potential set to detect Fe^{2+} (+0.60 V vs. Ag/AgCl) followed by a subsequent scan to detect O_2 (−0.70 V). Detection of Fe^{2+} was therefore carried out using SG/TC mode, while O_2 was detected using what the authors refer to as *redox competition* mode (RC-SECM) as dissolved O_2 is reduced both at the SECM probe and at microcathodes in the corrosion cell. The rate of corrosion was seen to initially increase with exposure time, as evidenced by an increase in the anodic Fe^{2+} current and a corresponding decrease in the cathodic O_2 current. At longer immersion times, however, both currents were observed to decrease, most likely resulting from blockage of the defect site by the precipitation of iron corrosion products and a resulting decrease in tip–sample separation.

The effect of immersion solution electrolyte on the corrosion rate at a defect was investigated in a related report from the same authors [78]. Dissolved oxygen was again used as the mediator, in this case to generate SECM images of the defect area on coated steel samples during immersion in tetraborate, sulfate, and chloride solutions. Images acquired in tetraborate showed an increase in the cathodic O_2 current over the defect resulting from positive feedback associated with the enhanced diffusion of O_2 to the microelectrode when positioned over the large hole. No evidence of O_2 consumption was observed over a 24 h immersion period, indicating the steel substrate was effectively passivated by the tetraborate ion. Images generated during immersion in sulfate and chloride solutions, however, did demonstrate O_2 consumption and corrosion of the exposed metal, with a higher corrosion rate observed in the chloride solution over that of the sulfate.

14.3.1.4.4 Mechanism of Protection

There are a number of possible mechanisms through which a coating or coating system may offer corrosion control of a metal. A coating may act as a simple barrier that shields the metal from corrosive agents, it may lower the mobility of ions at the metal surface and thereby increase the electrolyte resistance between local anodes and cathodes, or it may alter the metal through chemical or electrochemical means either before or during corrosion. SECM has proven to be a useful tool in determining the protection mechanism of coatings, as illustrated by recent examples in the literature [80,81]. Dufek and Buttry, for example, have utilized SECM as part of an investigation of the corrosion-inhibiting potential of Zr(IV)-phosphonate thin films on an aluminum alloy [81]. Alkyl phosphonates are known to bind strongly to aluminum oxide and form well-ordered thin films in the presence of Zr(IV). These films may then potentially act as a barrier against the influx of reducible species such as O_2 and H^+. The authors present SECM images of untreated, cathodically polarized AA 2024-T3 obtained in feedback mode using the mediator dimethylaminomethylferrocene as an oxygen surrogate, and strong cathodic activity is evident at sites associated with intermetallic particles in the alloy. This activity disappears, however, when the experiments are repeated using a substrate coated with Zr(IV)-octadecyl-phosphonate (ZOCP), indicating inhibition of O_2 reduction by the thin film.

To determine the possible presence of pinhole defects in these films, SG/TC mode was utilized to detect cathodically generated hydrogen as a function of substrate potential on substrates subjected to various pretreatment methods, with the results shown in Figure 14.12. Significant hydrogen evolution was detected on the untreated substrate with the SECM probe placed either over an intermetallic particle (black) or over the bulk alloy (red). A coated substrate prepared by three immersion cycles (1 cycle = 5 min phosphonate + 1 min Zr(IV) + 30 min methanol) showed reduced hydrogen evolution (blue), and preparation with five immersion cycles (green) showed even greater inhibition, with the H_2 oxidation current dropping by approximately two orders of magnitude over that of the untreated substrate. The results of Figure 14.12 provide further evidence that an effective barrier to O_2 influx is created by the thin film, and that this barrier stays intact under highly reducing conditions. The authors also demonstrate, however, that the films are not stable in more aggressive NaCl solutions.

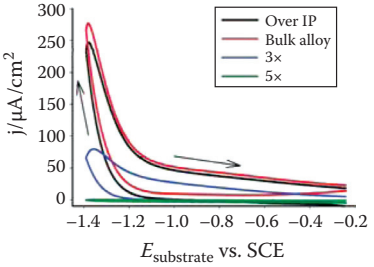


FIGURE 14.12 SG/TC studies of 3× and 5× ZODP-treated and anodized, untreated AA2024-T3 samples. The probe potential was held at −0.15 V, while substrate potential swept from −0.2 to −1.4 V, 10 mV/s. (Reprinted from Dufek, E.J. and Buttry, D.A., *J. Electrochem. Soc.*, 156, C322 (color online), 2009. Reproduced with permission of The Electrochemical Society.)

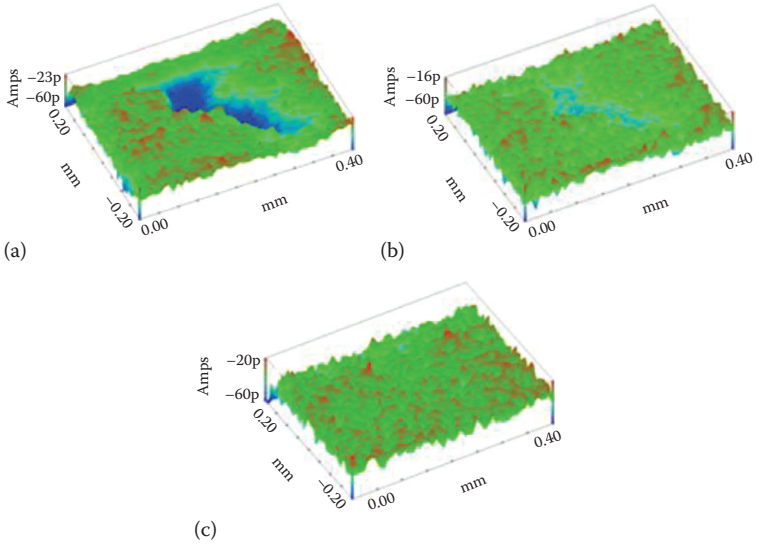


FIGURE 14.13 SECM images of zinc phosphate coating immersed in 3.5% NaCl/0.5 mM $K_4Fe(CN)_6$ solution. (a) Initial stage after making an artificial pore, (b) 36 h after making an artificial pore, and (c) 58 h after making an artificial pore. *E*(probe) = +0.40 V (Ag/AgCl), *E*(substrate) = OCP. (Reprinted from *Corros. Sci*., 51, Shao, Y., Jia, C., Meng, G., Zhang, T., and Wang, F., The role of a zinc phosphate pigment in the corrosion of scratched epoxy-coated steel, 371 (color online), Copyright 2009, with permission from Elsevier.)

Ideally, a coating will not only inhibit corrosion from occurring, but will also stop the corrosion process should the coating become damaged. Shao and coworkers have used SECM to demonstrate the ability of zinc phosphate pigment to repair damage to an epoxy coating on a steel substrate [82,83]. The feedback mode images in Figure 14.13 show the evolution of this repair process following indentation of the coating [82]. Figure 14.13a clearly shows the defect in the coating as an increase in the probe feedback current due to unhindered diffusion of the mediator at the deeper defect site, and Figure 14.13b and c shows the gradual filling in of this defect over time. Similar experiments carried out with an epoxy coating in the absence of zinc phosphate pigment show only a uniform increase in the probe current over the entire image, interpreted as resulting from enhanced corrosion of the exposed metal. X-ray diffraction analysis of the defect area in the repaired coating identified iron hydroxide and iron phosphate salts, leading to the conclusion that repair of the defect site occurs through a barrier created by precipitation of these salts over the exposed metal.

14.3.2 Applications of Potentiometric SECM

Since our previous review, eight applications of potentiometric SECM (or SIET) to corrosion research have appeared [84–91], in most cases to complement SVET measurements of current density [84–89]. The majority of these studies describe the mapping of local pH [84–87,89,91], but descriptions of Zn^{2+} ion [88], Mg^{2+} ion [89], and Cl^- ion [90] mapping have also recently appeared.

14.3.2.1 pH Mapping

The redox reactions associated with corrosion are invariably linked with local changes in pH, with metal oxidation reactions leading to a decrease in pH (since metal ions in aqueous solution are Lewis acids and undergo hydrolysis) and cathodic reactions leading to an increase in pH (e.g., H^+, H_2O, and/or O_2 reduction reactions). Thus, for localized corrosion where anodic and cathodic reactions occur at different sites on a metal surface, measurement of the pH distribution across the surface provides useful details about corrosion mechanisms. Variations in local pH often correlate with the heterogeneous microstructure of a metal alloy surface, since such microstructure influences the location of local anodes and cathodes on the surface.

Ding and coworkers have extended their work on the corrosion behavior of Al-based metal-matrix composites (MMCs), employing SVET for current density mapping and potentiometric SECM for pH mapping [84,85] (see ref. [8] for a discussion of their earlier work). The incorporation of a second phase into a matrix material enhances the physical and mechanical properties of the resulting MMC, but such an addition can also significantly alter its corrosion behavior. The corrosion of particulate 6092-T6 Al MMCs (reinforced with 20 vol% of B_4C, SiC, or Al_2O_3) as well as that of monolithic 6061-T6 Al was investigated in American Society for Testing and Materials (ASTM) synthetic seawater and real seawater and compared with the corrosion behavior observed in either 3.15 wt% NaCl or 0.5 M Na_2SO_4 solutions [84].

Figure 14.14 shows results for an Al 6092-T6 MMC containing 20% B_4C (designated as 6092-T6 Al/B4C/20p MMC) after 1 day immersion in ASTM seawater (prepared using ASTM D-1141-52 sea salt). An intense anodic peak (with a tiny cathodic peak inside the anodic area) is observed in the SVET map (Figure 14.14b), coinciding with the location of a hydrogen bubble observed in the optical micrograph (Figure 14.14a). The SIET map (Figure 14.14c) indicates the pH at this location was ~6.4, lower than the original pH of 8.2, consistent with metal ion hydrolysis. Their pH measurements employed a glass micropipette with a tip diameter of ~5 μm, scanned at ~40 μm above the substrate surface. The pH nearer the surface is likely to be lower than that observed. Upon extended immersion, an anodic–cathodic alternation of local currents accompanied by an acidic–alkaline switching of the local solution pH was observed on all MMCs. It was noted that the local pH fluctuations in ASTM seawater were significantly lower (by up to 2 pH units) than those observed in the NaCl and Na_2SO_4 solutions, attributed to the higher buffer capacity of the seawater due to the CO_2/carbonate equilibrium [84]. The significantly lower corrosion rate of MMCs in seawater than in NaCl and Na_2SO_4 solutions (as determined by weight loss measurements) was attributed, in part, to this buffer capacity.

Lamaka et al. reported the use of SIET (again in combination with SVET) to investigate a new anticorrosion coating system for ZK30 magnesium alloy [86]. The 3.7–7.0 μm thick protective coating was based on a porous anodic oxide layer (produced by spark anodizing) that is loaded with corrosion inhibitors (e.g., Ce^{3+}) and then sealed with a sol–gel hybrid polymer. For SVET and SIET measurements, defects of 100 μm dimension were introduced in the samples prior to immersion in 0.05 M NaCl. The pH-selective glass capillary microelectrode was scanned 30 μm above the substrate surface. Although the SVET map indicated both anode and cathode sites in or near the defects during early stages of immersion, the SIET map indicated only local alkalinization near the defects. The hydrolysis constant of Mg^{2+} ($pK \approx 11.4$) is much smaller than that for Al^{3+} ($pK \approx 5.0$) or Fe^{3+} ($pK \approx 2.2$), so that the lowering of pH normally associated with sites of metal ion production in

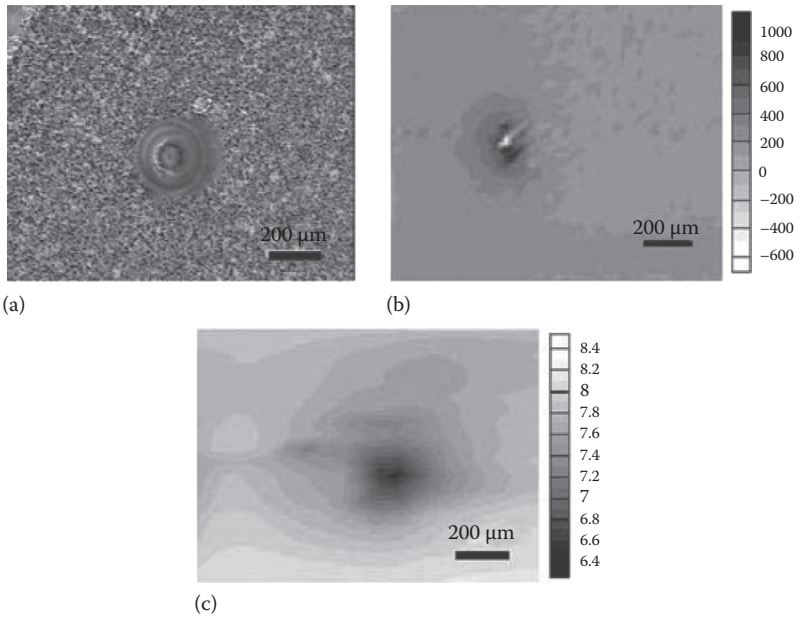


FIGURE 14.14 (a) Optical micrograph of the localized corrosion region on the 6092-T6 Al/B4C/20p MMC after 1 day of immersion in ASTM seawater (note hydrogen bubble at the corrosion site). (b) SVET map of the area shown in (a), units in $\mu A/cm^2$. (c) SIET map of the area shown in (a), units in pH. (Reprinted from Ding, H. et al., *J. Electrochem. Soc.*, 156, C352 (color online), 2009. Reproduced with permission of The Electrochemical Society.)

corrosion reactions may be too subtle to detect in this case, being masked by the alkalinity produced by the nearby cathodic reactions and/or diffusional broadening (see Section 14.2.3). The tip dimension of the pH microelectrode used in this work was not stated, so it was not possible to assess the resolution of their pH map. In any event, complete passivation of the sample was observed by SVET after 24 h of immersion.

Micropotentiometric measurement of pH combined with microamperometric measurement of dissolved oxygen (used as complements to SVET) has been described by Bastos et al. [87] for the investigation of corrosion and inhibition of coated AA 2024-T3 aluminum alloy with artificial defects. The coating was a hybrid organic–inorganic sol–gel film into which two circular defects were introduced. The samples were immersed in 0.05 M NaCl and measurements were performed before and after the addition of a corrosion inhibitor (10 mM cerium nitrate) to the solution, the objective being to simulate the release of an inhibitor from a coating and assess the potential of these techniques to study the kinetics of the corrosion and inhibition processes. The LIX pH electrode was fabricated using a pulled single-barreled glass capillary having a tip diameter of 2 µm, used in combination with a remote Ag/AgCl reference electrode. Dissolved oxygen was measured at a 10 µm diameter Pt disk microelectrode poised at −0.7 V vs. Ag/AgCl. Line scans of current density, pH, and dissolved oxygen were then performed over the two defects before and after the addition of the inhibitor.

Figure 14.15 shows the results of one such experiment. The current density measured by SVET before the addition of inhibitor suggests that the left defect functioned as a cathode while the right defect functioned as an anode. The pH scan seems to corroborate this conclusion since the pH was more alkaline above the left defect, with little or no variation over the right defect. However, the oxygen scan indicated a depletion of oxygen above each defect, with greater depletion above the left defect. Thus, one is led to the conclusion that one defect is predominately anodic (the right defect) and one defect is predominately cathodic (the left defect), but cathodic activity exists in both defects (the OCP of the metal was −0.6 V vs. Ag/AgCl where oxygen can

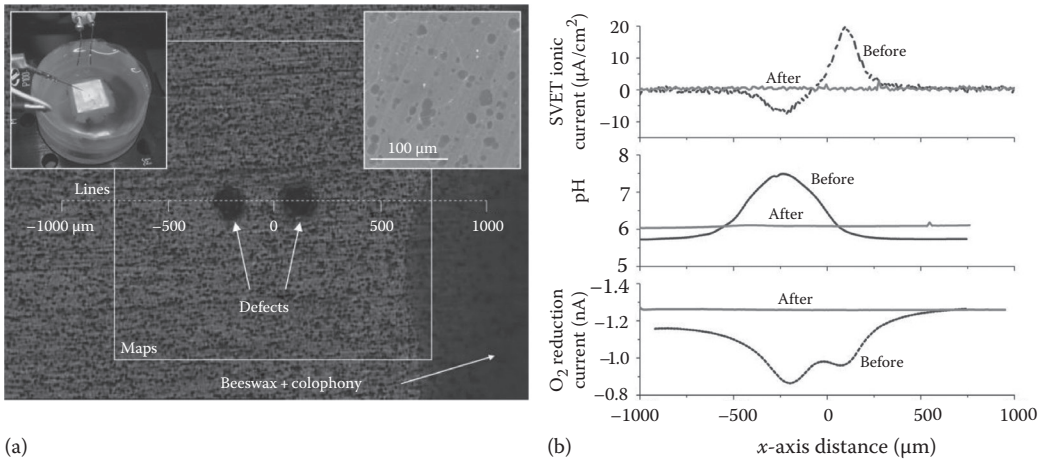


FIGURE 14.15 (a) Sample's surface with indication of the two artificial defects and the position of maps and lines. The myriad of dark spots scattered throughout the surface is a result of the cleaning process that removed the intermetallic precipitates at the surface leaving small holes, later filled by the sol–gel film. Left inset is a sample in the epoxy holder during a SVET measurement. Right inset is a detail of the small holes filled by the sol–gel film. (b) Line scans of (top) ionic currents (SVET), (middle) pH, and (bottom) dissolved oxygen reduction current obtained at 50 µm (100 µm for SVET) above the surface, before and 20 h after addition of cerium nitrate to the solution. Line positions are indicated in left figure. (From Bastos, A.C., Karavai, O.V., Zheludkevich, M.L., Yasakau, K.A., and Ferreira, M.G.S.: Localised measurements of pH and dissolved oxygen as complements to SVET in the investigation of corrosion at defects in coated aluminum alloy. *Electroanalysis.* 2010. 22. 2009. Copyright Wiley-VCH Verlag GmbH & Co. KGaA. Reproduced with permission.)

be reduced). Since SVET measures a net current flow, a small anodic current could also exist in the left defect, masked by the larger cathodic current. The ability to detect Al^{3+} in solution would provide the information needed to address this question, but to date this capability has not yet been achieved. This work illustrates the importance of using complementing scanning probe techniques. Note that after addition of inhibitor, the current density goes to zero and the local pH and oxygen concentration reach their bulk values, confirming that the corrosion process was halted by the inhibitor. PACs for each of the three quantities (current density, pH, O_2 reduction current) were also reported, and supported the conclusions reached from the scanning experiments [87]. The challenges of using a bare Pt microelectrode for measurement of oxygen concentration were also addressed.

We conclude this section with discussion of a paper by Oltra et al. who used a pH microprobe to measure the pH at various locations and as a function of time inside a pure water droplet (5 mm in diameter and 2.15 mm high) deposited on a thermally aged 2011 aluminum alloy [91]. The goal of the work was to assess the relative importance of alkalinization vs. microgalvanic corrosion in the corrosion mechanism of Al alloys. Their pH probe was a W/WO_3 needle sealed in a capillary having a 5 µm tip coupled with a second glass capillary containing a saturated calomel reference electrode. The model alloy contained quite large Al_2Cu phases (10–20 µm in diameter) surrounded by the Al matrix containing ~1% Cu. The secondary phase particles were regularly distributed at the surface of the electrode with the gap between two particles varying from 10 to 100 µm. Additionally, even larger size Al_2Cu phases (a few hundreds of micrometers) were synthesized for use in complementary experiments.

Figure 14.16 shows a pH–time profile near the electrode surface at two locations inside the water droplet, one near the center of the droplet and one near its outer edge. At both locations, there was an initial pH decrease followed by a pH increase to a steady state. The steady-state pH at the droplet center was ~5 while near the edge the steady-state pH was ~8. The same experiment

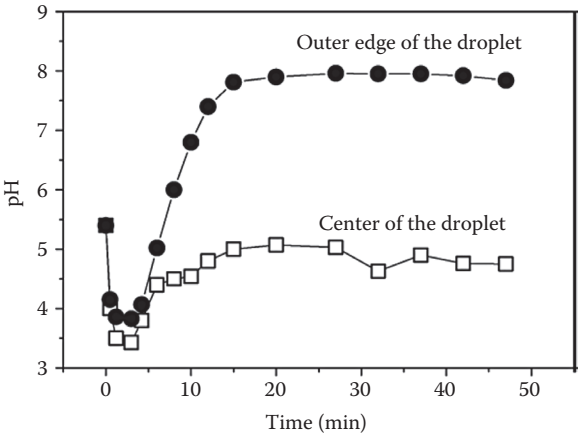


FIGURE 14.16 pH–time profile inside the water droplet near the electrode surface at the center of the droplet and at its outer edge. (Reprinted from *Electrochim. Acta*, 55, Oltra, R., Malki, B., and Rechou, F., Influence of aeration on the localized trenching on aluminium alloys, 4536, Copyright 2010, with permission from Elsevier.)

conducted at a massive Al_2Cu particle produced a profile very similar to that shown in Figure 14.16 for the outer edge position (including a final steady-state pH of ~8). The initial pH decrease is attributed to the dealloying of the Al_2Cu particles, producing Al^{3+} ions that undergo hydrolysis. The resulting Cu-enriched surfaces of the intermetallic particles (as well as some Cu redeposited on the Al matrix) subsequently behave as cathodes for oxygen reduction, leading to the pH increase. Equilibrium is then established between hydrolysis and alkalinization reactions, with differential aeration accounting for the differences in the final steady-state pH (i.e., greater oxygen availability near the outer edge of the droplet). Microscopic examination of the alloy after 1 h 30 min exposure showed very weak attack in the center of the droplet, but marked attack near the droplet edge with copper redistribution around the intermetallic particles. It was concluded that alkalinization is likely to initiate the corrosion process, with galvanic coupling playing the role of a propagation step. Thus, no significant damage was observed in the center of the droplet, not because there was no galvanic driving force, but because alkalinization was not strong enough to initiate localized attacks.

14.3.2.2 Mapping of Other Ions

Only three examples of potentiometric SECM mapping for ions other than H^+ have appeared [89–90] since our previous review [8]. Lin et al. combined in situ imaging of interfacial Cl^- concentration and corrosion potential with ex situ electron microprobe analysis (EMPA) for the study of localized corrosion of reinforcing steel such as that used in concrete (rebar) [90]. For sensing corrosion potential, they used a Pt/Ir wire electrochemically etched to a tip diameter of 5 µm. Their combination Cl^- electrode was fabricated by sealing a Ag wire in one side of a double-barreled pulled glass capillary (2 µm tip diameter) and forming AgCl on the exposed tip. An additional Ag/AgCl electrode connected by an agar salt bridge to the second side of the capillary served as a local reference electrode, eliminating the influence of variations in local corrosion potential on the Cl^- measurement. An interesting aspect of this work was the use of an STM mode for controlling distance between their probes and the substrate surface, accomplished by using a 25 µm Pt wire that had been cut to produce a nanosized tip positioned at the same height as the tips of the other two microelectrodes. Before electrolyte was added to the cell, the probe assembly was brought to the substrate surface until the tunneling current was sensed, indicating approach to within a few nanometers. Then the probe was lifted to 20 µm above the surface and electrolyte was introduced,

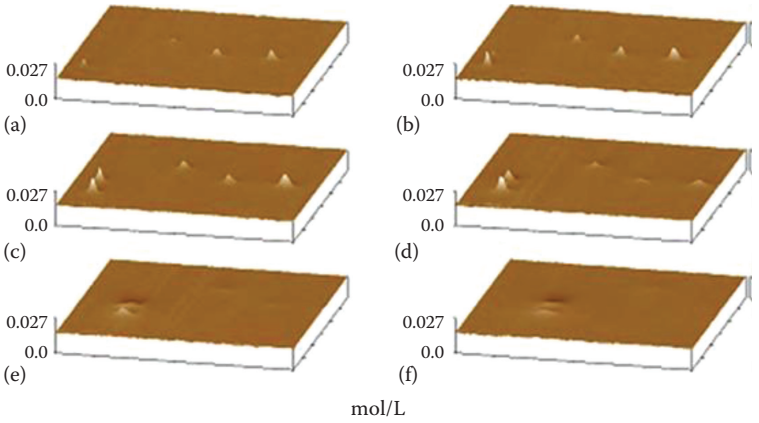


FIGURE 14.17 Chloride concentration distribution (6 mm × 6 mm) on the surface of reinforcing steel immersed in 0.01 mol/L NaCl solution at pH = 10 and open-circuit potential after (a) 0 min, (b) 5 min, (c) 30 min, (d) 60 min, (e) 120 min, and (f) 180 min. (Reprinted from *Electrochim. Acta*, 55, Lin, B., Hu, R., Ye, C., Li, Y., and Lin, C., A study on the initiation of pitting corrosion in carbon steel in chloride-containing media using scanning electrochemical probes, 6542 (color online), Copyright 2010, with permission from Elsevier.)

consisting of 0.01 M NaCl saturated with $Ca(OH)_2$ and adjusted to pH 10 (to simulate the pore solution in carbonated concrete). A control experiment in the absence of Cl^- verified that the combination Cl^- probe did not respond to variations in corrosion potential.

Figure 14.17 shows the distribution of Cl^- concentration across the steel surface at various immersion times. The maps indicate unevenly distributed highly localized enhancement of Cl^- ion concentration, which is thought to induce the initiation of pitting corrosion. Ex situ EMPA mapping in combination with in situ images of corrosion potential and local Cl^- concentration revealed that pitting corrosion initiated and propagated at inclusions of MnS, where Cl^- ions preferentially adsorbed and accumulated [90]. Metastable pitting nuclei either developed into larger corrosion pits or lost their corrosion activity, and this appeared to be closely associated with the local chloride concentration.

A potentiometric Zn^{2+} ion–selective microelectrode has been described by Bastos et al. [88] based on a liquid membrane cocktail containing tetra-*n*-butyl thiuram disulfide ionophore. The electrode was fabricated in a pulled glass capillary having a tip diameter of 2 μm. Calibration curves using $ZnCl_2$ solutions were prepared in either distilled water (linear response from pZn = 5.5 to 1.5) or in 5 mM NaCl (linear response from pZn = 3.5 to 1.5). Thus, Na^+ influences the electrode's response at low Zn^{2+} concentration, with a selectivity coefficient of −1.4. The electrode's 95% response time was reported to be 2.6 s. Figure 14.18 demonstrates an application of this electrode to the corrosion of a coil-coating sample consisting of a carbon steel substrate with a 7.5 μm thick electroplated Zn layer and a 20 μm thick epoxy coating with TiO_2 pigmentation. Two round defects, each 170 μm in diameter, were made manually with a sharp needle (see Figure 14.18a). Maps of current density (from SVET, Figure 14.18b) and of Zn^{2+} distribution (Figure 14.18c) were acquired in two planes, one parallel to and 100 μm from the substrate surface (*x*–*y* plane) and the other normal to the surface exactly above the defects (*x*–*z* plane).

The SVET map of Figure 14.18b indicates that one defect (the left one) is mainly anodic (positive current, red color) while the other is mainly cathodic (negative current, blue color), attributed to the oxidation of Zn and the reduction of oxygen, respectively. The ionic currents are localized near the defects in both planes with the bulk solution remaining undisturbed. The distribution of Zn^{2+} ions in solution (Figure 14.18c) corroborates this interpretation of the SVET data, with higher Zn^{2+} activity near the anodic defect and lower activity near the cathodic defect. In fact, the Zn^{2+} activity in the immediate vicinity of the cathodic defect is lower than that in the surrounding solution, attributed

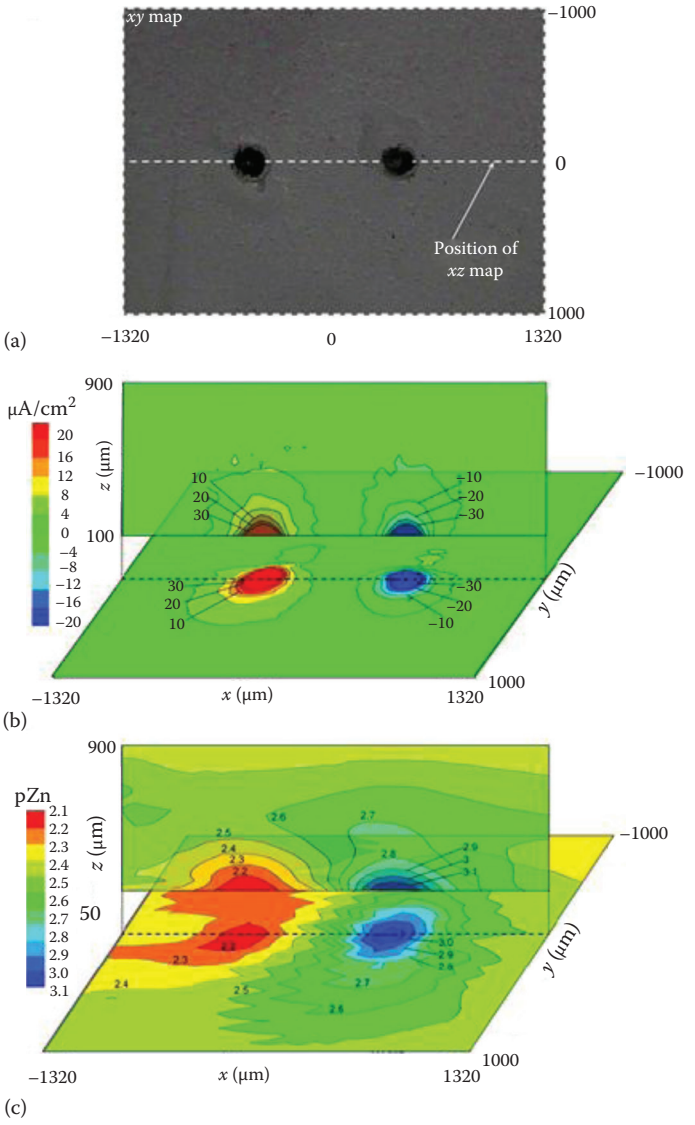


FIGURE 14.18 (a) Picture of painted electrogalvanized steel with two artificial defects after 8 days of exposure to 5 mM NaCl; (b) SVET maps of the ionic currents in solution measured in the *x*–*z* plane, normal to the surface, and in the *x*–*y* plane, parallel to the surface; and (c) distribution of Zn^{2+} in solution obtained in the *x*–*z* and in the *x*–*y* planes. Maps in *x*–*y* plane were taken at 100 μm above the surface and the scanned area corresponded to the area of (a). (Reprinted from *Electrochem. Commun.*, 12, Bastos, A.C., Taryba, M.G., Karavai, O.V., Zheludkevich, M.L., Lamaka, S.V., and Ferreira, M.G.S., Micropotentiometric mapping of local distributions of Zn^{2+} relevant to corrosion studies, 394 (color online), Copyright 2010, with permission from Elsevier.)

to the higher pH near this defect (due to the oxygen reduction reaction) that leads to depletion of solution Zn^{2+} ion by $Zn(OH)_2$ precipitation [88].

As a final example in this section, we consider the work of Karavai et al. who used Mg^{2+} and pH-selective microelectrodes in combination with SVET to study the corrosion inhibition in microdefects on sol-gel-coated AZ31 magnesium alloy immersed in chloride media [89]. The inhibitors investigated were 1,2,4-triazole, F^-, and Ce^{3+}. Both types of ion-selective microelectrodes were

fabricated in pulled microcapillaries using an appropriate (hydrogen or magnesium) ionophore cocktail from Fluka and employed a common remote reference electrode. One distinguishing feature of this work is that both ion sensors were mounted simultaneously on the scanning stage, their tips spaced a few microns apart, so that simultaneous detection of pH and Mg^{2+} activity was possible. The probes were scanned 100 µm above the surface using a 3 s per point acquisition time. As was the case for the Zn^{2+} ion–selective electrode (described by this same group and discussed earlier), the linear response range for the Mg^{2+} electrode was influenced by the presence of Na^+, with pMg limited in 0.05 M NaCl to values from 1.5 to 4.8. The electrodes had reasonably fast response times, the time needed to obtain 95% of the total potential change being 0.3 s for the pH electrode and 1.6 s for the Mg^{2+} electrode.

Figure 14.19 shows an optical micrograph along with pH and pMg maps for a sol-gel-coated AZ31 sample having several circular defects about 200 µm in diameter created with a metallic needle. The sample was immersed in 0.05 M NaCl containing 0.01 M 1,2,4-triazole solution, a corrosion inhibitor. The efficiency of a corrosion inhibitor is influenced by such factors as local pH and electrolyte resistivity within corroding defects. For example, high local pH near a defect can reduce the efficiency of a corrosion inhibitor. Thus, the ion-selective probes were used to understand how conditions (namely pH and Mg^{2+} activity) change during corrosion processes in and near the coating defects both with and without corrosion inhibitor. Figure 14.19b reveals that, in the presence of inhibitor, two defects developed somewhat higher pH while one defect developed lower pH. The dissolution of metal (reflected by lower pMg) is associated with the lower pH zone, while depletion of metal (thus, higher pMg) is observed in regions with higher pH, possibly due to the formation of magnesium complexes. SVET measurements revealed very low current densities, with maximum values of 2–4 µA/cm^2. Thus, the presence of the inhibitor resulted in very low corrosion rates that, in turn, led to pH and pMg conditions close to neutral. A control experiment run in the absence of inhibitor revealed current densities of several hundred µA/cm^2 in some defects and a pH extreme of 11.4. A pMg map was not shown for the control experiment. The authors concluded that 1,2,4-triazole showed the highest inhibition efficiency among the studied inhibitors.

To summarize, the majority of the applications of potentiometric SECM discussed in this section utilized the technique in combination with SVET to provide supporting evidence for the interpretation of current density data and for postulating corrosion mechanisms. The mapping of pH and Cl^- concentration remains the most popular, but examples of metal ion mapping are beginning to appear. Corrosion research could certainly benefit from future developments in metal ion–selective microelectrodes for potentiometric SECM, especially for understanding the corrosion behavior of complex heterogeneous metal alloys.

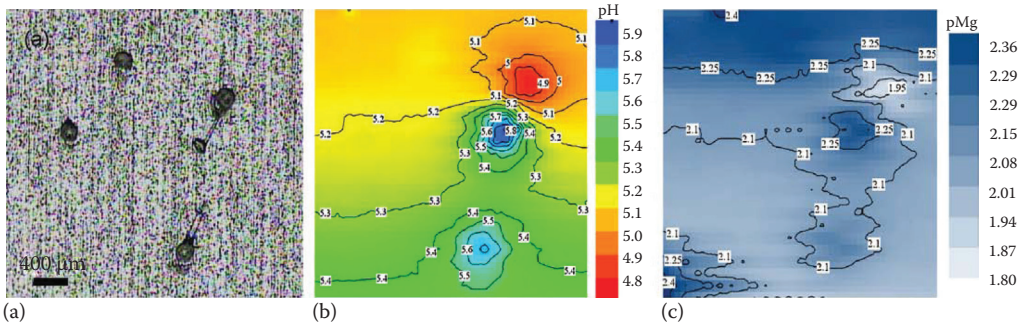


FIGURE 14.19 (a) Optical micrograph, (b) pH, and (c) pMg maps obtained simultaneously after 6.5 h of immersing coated AZ31 in 0.05 M NaCl + 0.01 M 1,2,4-triazole solution. (Reprinted from *Electrochim. Acta*, 55, Karavai, O.V., Bastos, A.C., Zheludkevich, M.L., Taryba, M.G., Lamaka, S.V., and Ferreira, M.G.S., Localized electrochemical study of corrosion inhibition in microdefects on coated AZ31 magnesium alloy, 5401 (color online), Copyright 2010, with permission from Elsevier.)

14.3.3 Applications of Electrochemical Microcell and Scanning Capillary Microscopy

14.3.3.1 Stationary Capillary Techniques

Since our previous review [8], five new reports on the use of stationary capillaries (or electrochemical microcells) in corrosion research have appeared [33,92–95], but only one report on use of a scanning capillary [96]. Since our focus in this chapter is on scanning probe techniques, we will only mention the stationary capillary applications. A stationary capillary has been used to study various types of SAE 1045 steel joints welded by dynamic diffusion bonding [92], to perform electrochemistry on the individual phases of AZ91 magnesium alloy [93], to investigate the influence of applied strain on the microstructural corrosion of AlCu4Mg1 as cast Al alloy [33], to perform localized breakdown measurements on Al alloy AA 5050 in order to assess the effects of recycling and also the role played by trace elements (Pb, Cu, etc.) on electrochemical activation and filiform corrosion susceptibility [94], and to investigate the effect of electrode configuration (a Cu microelectrode vs. an electrochemical microcell approach) on the mass transport process in an EIS study of Cu corrosion in chloride solution [95]. The stationary capillary techniques are powerful tools for studying the electrochemistry of heterogeneous materials such as alloys.

14.3.3.2 Scanning Capillary Techniques

A recent report by the Unwin group describes a scanning capillary (micropipette) method for high-resolution imaging of substrate surface redox activity, a method they term the scanning micropipette contact method (SMCM) [96]. Their approach uses a pulled capillary (300 nm–1 μm in diameter) filled with a redox mediator, such as trimethylammoniomethylferrocene (FA^+), ferrocyanide ($Fe(CN)_6^{4-}$), or ferricyanide ($Fe(CN)_6^{3-}$), in either 0.1 M NaCl or 0.1 M KNO_3 as supporting electrolyte. The capillary also contained a reference–counter electrode, with the substrate connected as the working electrode (i.e., a two-electrode system). The capillary is lowered to the substrate surface so that the liquid meniscus makes contact, signaled by the onset of current flow due to oxidation of FA^+ or $Fe(CN)_6^{4-}$ or reduction of $Fe(CN)_6^{3-}$. Steady-state current or current–voltage curves were then obtained at that position. Rather than pulling the tip across the surface while in contact, the tip was raised (typically 5 μm) and moved to the next position where it was again lowered and the process repeated. This approach makes possible highly localized electrochemical measurements without the substrate being completely immersed in solution. The lateral resolution of this approach should be improved compared to traditional SECM (i.e., employing a microelectrode tip) where convergent diffusion to the tip electrode and/or overlapping diffusion fields of neighboring active sites on the substrate surface (for tip collection experiments) result in loss of resolution.

The SMCM method was used to investigate the influence of heterogeneities on the electroactivity of Al alloys [96]. Figure 14.20 shows (a) an optical image and (b) a SMCM image for a 95% Al–5% Cu alloy. The SMCM image was obtained within the region highlighted by the box in the optical image, using a 1.0 μm diameter capillary containing 2 mM $Fe(CN)_6^{4-}$ and 0.1 M KNO_3. The alloy potential was held at −0.1 V (vs. AgQRE, sufficient to reduce $Fe(CN)_6^{3-}$) and the scan was carried out with a 1 μm separation between points (requiring ~2 h of imaging time). The reduction current over much of the surface was smaller than −2 pA, attributed to low electron transfer activity at oxide-protected Al. A region of higher cathodic activity (to more than −13 pA) was observed in a narrow band that coincides with the location of a Cu intermetallic (inclusion) in the alloy. The dimensions of the inclusion were estimated from the optical image to be ~2.5 μm in width and over 40 μm in length, in good agreement with the dimensions observed with SMCM, illustrating the high spatial resolution achievable using the technique and demonstrating that the solution is confined to the capillary. This observation of higher electron transfer activity on the Cu-rich intermetallics of Al alloys is consistent with what we and others have observed using SECM [9].

A purer Al alloy (AA1050) with much smaller intermetallic features (typically with dimensions between 0.1 and 3 μm) was also imaged using a 300 nm capillary containing the same mediator and electrolyte [96]. The imaged area was 2 μm by 3 μm with 100 nm separation between points (thus,

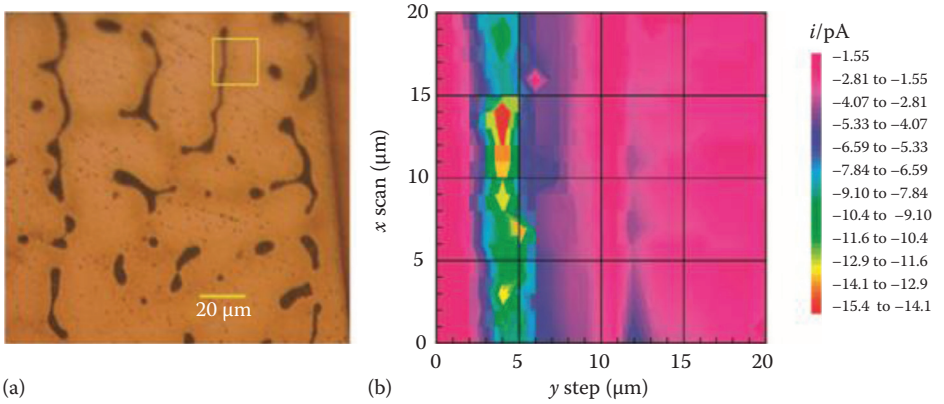


FIGURE 14.20 (a) Optical microscope image of a 95%–5% Al–Cu alloy and (b) an SMCM image of a region of the alloy (marked by small square in panel a), obtained using a 1 μm diameter micropipette containing 2 mM $Fe(CN)_6^{3-}$ and 0.1 M KNO_3. The alloy was held at a potential of −0.10 V vs. AgQRE, corresponding approximately to the half-wave potential for the reduction of $Fe(CN)_6^{3-}$ at noble metal electrodes. (Reprinted from Williams, C.G., Edwards, M.A., Colley, A.L., Macpherson, J.V., and Unwin, P.R., Scanning micropipet contact method for high-resolution imaging of electrode surface redox activity, *Anal. Chem*., 81, 2486, 2009 (color online), Copyright 2009 American Chemical Society.)

some loss of resolution was expected because of the tip size). Within the imaging area, a small oval-shaped region (ca. 0.5 μm by 1 μm) having an enhancement in reduction current (of approximately an order of magnitude compared to the remaining area of the image) was observed. The size of this region was within the size range of individual intermetallic particles observed by field emission scanning electron microscopy.

To summarize, the scanning capillary techniques, such as the one discussed earlier and others discussed in our previous review [8], have certain advantages compared with traditional SECM when applied in corrosion research. The ease of fabrication of capillaries having very small tips of reproducible, well-defined geometry leads to electrochemical measurement with very high spatial resolution that can be supported by detailed simulations (e.g., see [96]). The capillary tip or its content is in contact with the substrate surface, so tip–substrate separation distance is not an issue. Consequently, the spatial resolution is governed only by the dimension of the capillary tip. Finally, it is not necessary to immerse the entire substrate in electrolyte. At any given instant, only the very small area of the surface being imaged is in contact with solution and only for a brief time, so undesirable side reactions (such as corrosion elsewhere on the substrate surface) can be avoided.

14.3.4 Applications of SVET and LEIS/LEIM

Although SVET and LEIS/LEIM are not commonly considered to be SECM, they are important scanning electrochemical probe techniques in the corrosion field, so we provide a brief overview of recent applications here. See our previous review for a more extensive discussion, including historical development, of these techniques [8].

14.3.4.1 SVET

Twenty-nine publications describing the use of SVET in corrosion research have appeared since our previous review, including applications to the study of Al and Al alloys [85,87,97–101], Mg and Mg alloys [86,89,102–104], steel [98,105–113], galvanic corrosion [85,114,115], corrosion inhibitors [86,98,100,101,103,106,111,113,116], and coated metals [86,87,89,98,103,108,110,117–121].

In Section 14.3.2, a few recent examples of the use of SVET in combination with potentiometric SECM were described. Here, we discuss one additional example of SVET that illustrates the power of this technique.

Simoes and Fernandes used SVET (in combination with potentiodynamic polarization and global EIS) to study the effect of sodium phosphate on cut-edge corrosion of electrogalvanized steel [113]. The sample consisted of 800 µm thick steel with 7 µm Zn layers on each side, mounted in resin. Because of the high anode-to-cathode (i.e., steel-to-zinc) area ratio at the cut edge, this type of corrosion leads to accelerated dissolution of zinc and is a major cause of delamination and consequent degradation of coil-coated steel. The narrow dimensions of the zinc and steel surfaces result in the close proximity of anode(s) and cathode(s), which in turn cause large concentration gradients (e.g., of Zn^{2+} and OH^-) and strong chemical interactions that influence the chemistry of the corrosion process. For example, zinc corrosion products can precipitate not only on the zinc (as occurs under self-corrosion conditions), but also on the steel. The spatial resolution of SVET permits the mapping of local anodes and cathodes across the cut edge.

Figure 14.21 shows SVET maps and optical micrographs over the cut edge with and without phosphate addition as a function of time. The maps reveal that the cathodes (attributed to O_2 reduction) are located on the steel, whereas the anodes (attributed to Zn oxidation) are located on the Zn. With phosphate inhibitor, the Zn dissolution was more localized, the lifetime of the local anodes was shorter (note the anodes change position with time), and the peak currents were approximately half to one-third those observed in the absence of phosphate (note differences in current scale). The repassivation of local anodes in the presence of phosphate was attributed to the precipitation of

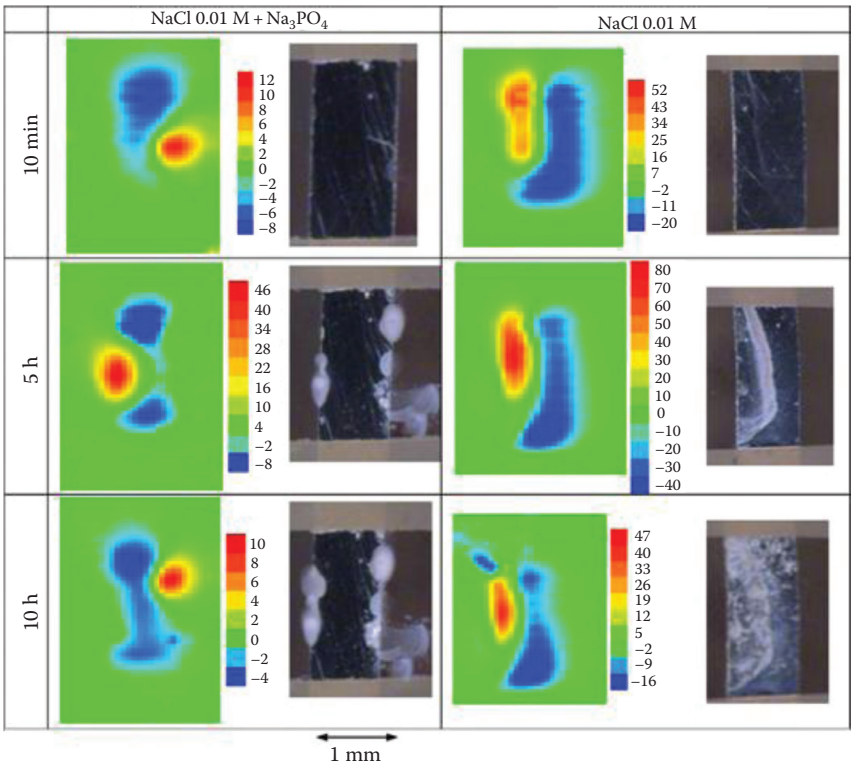


FIGURE 14.21 Ionic current maps over the cut edge, with and without phosphate addition, after various immersion times in NaCl 0.01 M. Current density scale in µA/cm^2. (Reprinted from *Prog. Org. Coat.*, 69, Simoes, A.M. and Fernandes, J.C.S., Studying phosphate corrosion inhibition at the cut edge of coil coated galvanized steel using the SVET and EIS, 219 (color online), Copyright 2010, with permission from Elsevier.)

gel-like zinc phosphate clusters with barrier properties; that is, the phosphate acts locally on the Zn. In contrast, in the blank NaCl solution (without phosphate), the cathode shifts further away from the anode with time as $Zn(OH)_2$ precipitates on the steel cathode, a consequence of Zn^{2+} release at the anode and OH^- generation at the cathode. From this example and others cited earlier, it is clear that SVET is an important tool in the study of localized corrosion, providing details about corrosion mechanisms not available from global electrochemical techniques.

14.3.4.2 LEIS/LEIM

Seven new publications describing the use of LEIS/LEIM in corrosion research have appeared since our previous review [8]. The diverse applications include the study of localized corrosion of 2A12 aluminum alloy in chloride media [122], galvanic coupling in an Al–Mg system [123], sol–gel thin films as a pretreatment prior to organic coating for AZ91 Mg alloy [124], corrosion inhibition of AA 2024 Al alloy by sodium decanoate (considered in more detail later) [125], the pitting corrosion of high strength 7B04 Al alloy subjected to salt spray test [126], the influence of Ni content of galvanostatically deposited Zn–Ni coatings on corrosion resistance in chloride media [127], and the evolution of corrosion products on a carbon steel exposed to a humid atmosphere containing SO_2 [128].

The example discussed in Section 14.2.6 illustrated LEIM for a bare Mg alloy. To further illustrate the utility of this technique, we discuss the recent application described by Boisier et al. for characterizing corrosion inhibition of an aluminum alloy (AA 2024 T351) by decanoate, a long-carbon-chain carboxylate that is known to form hydrophobic films on metal surfaces [125]. Both the alloy and a model system were studied; the model alloy consisting of a 1 cm pure Al disk with a 0.32 cm pure Cu disk at its center, embedded in epoxy resin. Global EIS was used to study the organic film growth on the AA 2024 surface and to characterize corrosion resistance of the alloy, but their LEIS/LEIM spatial resolution was apparently insufficient to study the alloy itself. Thus, LEIS/LEIM was performed only on the model alloy to assess interactions of the decanoate with the (Cu-rich) intermetallic particles. In these experiments, the maps are plotted in terms of admittance (the inverse of impedance) since admittance at low frequencies more directly correlates with corrosion rate.

LEIM performed at 1 kHz (a frequency that permits detection of the presence of the organic film) revealed a strong decrease in admittance modulus on both materials of the model alloy between 2 and 72 h of immersion in pH 6 chloride-free electrolyte, indicating growth of the organic film at the surface of both metals. However, the admittance modulus was higher on the Cu than on the Al after 72 h immersion, attributed to a strengthened passive layer on Al (imposed by galvanic coupling with the Cu) which favored decanoate adsorption. Then a LEIM experiment was performed at 1 Hz (a frequency characteristic of the corrosion process) in the absence and in the presence of 0.05 M sodium decanoate, the results of which are shown in Figure 14.22a and b, respectively, after 2 h immersion. In the absence of inhibitor (Figure 14.22a), the admittance on the Cu was higher (impedance lower) than on the Al, attributed to the facile reduction of O_2 on Cu and the resulting polarization of the Al in the passive state. In the presence of decanoate (Figure 14.22b), the admittance was significantly lower on both metals than observed in the absence of inhibitor. Perhaps, more significant is that the admittance modulus is the same on the Cu and the Al, indicating that galvanic coupling had been eliminated and the organic film protected the entire surface [125]. From these model studies, the authors concluded that the presence of Cu in the intermetallic particles of AA 2024 and the galvanic coupling (primarily responsible for the corrosion of the alloy) do not impede the adsorption of the decanoate over the entire alloy surface [125].

14.4 CONCLUSIONS

The various scanning electrochemical probe techniques discussed in this chapter have contributed greatly to the understanding of localized corrosion mechanisms as well as the role of inhibitors and coatings in reducing corrosion. Techniques such as SECM have also led to an improved

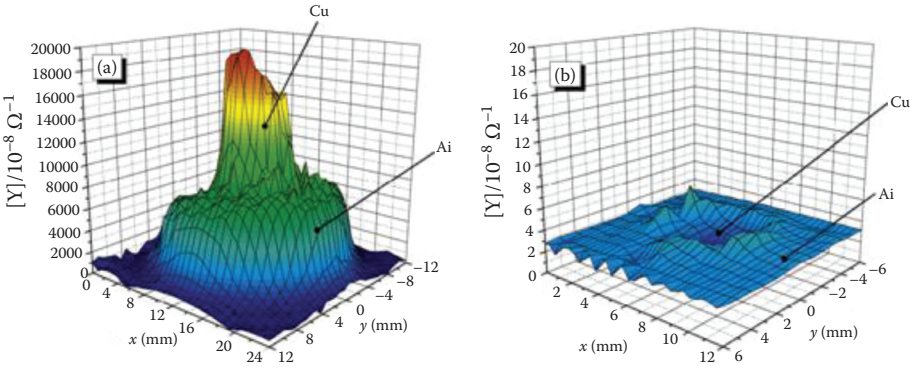


FIGURE 14.22 Local admittance maps on the model couple after 2 h of immersion: (a) without decanoate (0.001 M Na_2SO_4) and (b) in a solution containing 0.05 M sodium decanoate. Frequency = 1 Hz (pH 6, chloride-free electrolyte). (Reprinted from *Electrochim. Acta*, 55, Boisier, G., Portail, N., and Pebere, N., Corrosion inhibition of 2024 aluminum alloy by sodium decanoate, 6182 (color online), Copyright 2010, with permission from Elsevier.)

understanding of electron transfer at complex metal surfaces, such as passive metals and heterogeneous alloys. The traditional corrosion assessment techniques (e.g., EIS, potentiodynamic polarization experiments, and weight loss measurements) will continue to play an important role in corrosion research. However, such global techniques provide a surface-averaged response and do not provide sufficient spatial or temporal information on localized corrosion events. Within the past decade, there has been a rapid increase in application of the scanning electrochemical probe techniques discussed in this chapter to the study of localized corrosion. With continued improvements in commercially available instrumentation, this trend is certain to persist.

ACKNOWLEDGMENTS

We thank our students, postdoctoral associates, and visiting faculty and collaborators, past and present, who have contributed greatly to our efforts to explore corrosion and corrosion control mechanisms through the use of scanning probe techniques. The support of our research by the Air Force Office of Scientific Research and the Concordia Chemistry Research Endowment is gratefully acknowledged.

REFERENCES

1. Jones, D. A., *Principles and Prevention of Corrosion*, 2nd edn., Englewood Cliffs, NJ: Prentice Hall, 1996.
2. Department of Transportation, *Corrosion Costs and Preventative Strategies in the United States*, Tech Brief FHWA-RD-01-157, 2002, 16pp.
3. Miller, D., Corrosion control on aging aircraft: What is being done? *Materials Performance*, 29, 1990, 10.
4. Bennet, J. A. and H. Mindlin, Metallurgical aspects of the failure of the Point Pleasant Bridge, *Journal of Testing and Evaluation*, 1, 1973, 152.
5. Kelly, R. G., J. R. Scully, D. W. Shoesmith, and R. G. Buchheit, *Electrochemical Techniques in Corrosion Science and Engineering*, New York: Marcel Dekker, Inc., 2003.
6. Stratmann, M. and G. S. Frankel, Corrosion and oxide films, in *Encyclopedia of Electrochemistry*, Vol. 4, A. J. Bard and M. Stratmann, eds., Weinheim, Germany: Wiley-VCH, 2003.
7. Niu, L., Y. Yin, W. Guo, M. Lu, R. Qin, and S. Chen, Application of scanning electrochemical microscope in the study of corrosion of metals, *Journal of Materials Science*, 44, 2009, 4511.
8. Jensen, M. B. and D. E. Tallman, Application of SECM to corrosion studies, in *Electroanalytical Chemistry: A Series of Advances: Volume 24*, A. J. Bard and C. Zoski, eds., Boca Raton, FL: Taylor & Francis, 2011.

9. Jensen, M. B., A. Guerard, D. E. Tallman, and G. P. Bierwagen, Studies of electron transfer at aluminum alloy surfaces by scanning electrochemical microscopy, *Journal of the Electrochemical Society*, 155, 2008, C324.
10. Jensen, M. B., J. M. Karels, A. F. Guerard, and D. E. Tallman, Video microscopy and scanning electrochemical microscopy investigations of the mediated electrodeposition of polypyrrole on aluminum alloy AA 2024-T3, *Electrochimica Acta*, 2011 (Unpublished results, manuscript in preparation).
11. Zhou, Q., Y. Wang, D. E. Tallman, and M. B. Jensen, 2010 (Unpublished results, manuscript in preparation).
12. Tanabe, H., Y. Yamamura, and T. Misawa, In situ ionic imaging for pitting corrosion sites on austenitic stainless steels with scanning electrochemical microscopy, *Materials Science Forum*, 185–188, 1995, 991.
13. Eckhard, K. and W. Schuhmann, Alternating current techniques in scanning electrochemical microscopy (AC-SECM), *Analyst*, 133, 2008, 1486.
14. Eckhard, K., M. Etienne, A. Schulte, and W. Schuhmann, Constant-distance mode AC-SECM for the visualisation of corrosion pits, *Electrochemistry Communications*, 9, 2007, 1793.
15. Gabrielli, C., S. Joiret, M. Keddam, H. Perrot, N. Portail, P. Rousseau, and V. Vivier, A SECM assisted EQCM study of iron pitting, *Electrochimica Acta*, 52, 2007, 7706.
16. Belger, S., A. Schulte, C. Hessing, M. Pohl, and W. Schuhmann, Alternating current scanning electrochemical microscopy (AC-SECM) studies on the surface of electrochemically polished NiTi shape memory alloys, *Materialwiss Werkstofftech*, 35, 2004, 276.
17. Katemann, B. B., C. G. Inchauspe, P. A. Castro, A. Schulte, E. J. Calvo, and W. Schuhmann, Precursor sites for localised corrosion on lacquered tinplates visualised by means of alternating current scanning electrochemical microscopy, *Electrochimica Acta*, 48, 2003, 1115.
18. Schulte, A., S. Belger, M. Etienne, and W. Schuhmann, Imaging localised corrosion of NiTi shape memory alloys by means of alternating current scanning electrochemical microscopy (AC-SECM), *Materials Science and Engineering A*, 378, 2004, 523.
19. Ruhlig, D. R. and W. Schuhmann, Spatial imaging of Cu^{2+}-ion release by combining alternating current and underpotential stripping mode scanning electrochemical microscopy, *Electroanalysis*, 19, 2007, 191.
20. Freire, L., X. R. Nóvoa, G. Pena, and V. Vivier, On the corrosion mechanism of AISI 204Cu stainless steel in chlorinated alkaline media, *Corrosion Science*, 50, 2008, 3205.
21. Eckhard, K., T. Erichsen, M. Stratmann, and W. Schuhmann, Frequency-dependent alternating-current scanning electrochemical microscopy (4D AC-SECM) for local visualisation of corrosion sites, *Chemistry—A European Journal*, 14, 2008, 3968.
22. Eckhard, K., W. Schuhmann, and M. Maciejewska, Determination of optimum imaging conditions in AC-SECM using the mathematical distance between approach curves displayed in the impedance domain, *Electrochimica Acta*, 54, 2009, 2125.
23. Schulte, A., S. Belger, and W. Schuhmann, Corrosion of NiTi shape-memory alloys: Visualization by means of potentiometric "constant-distance" scanning electrochemical microscopy, *Materials Science Forum*, 394–395, 2002, 145.
24. Lamaka, S. V., O. V. Karavai, A. C. Bastos, M. L. Zheludkevich, and M. G. S. Ferreira, Monitoring local spatial distribution of Mg^{2+}, pH and ionic currents, *Electrochemistry Communications*, 10, 2008, 259.
25. Ammann, D., *Ion-Selective Microelectrodes: Principles, Design and Application*, Berlin, Germany: Springer-Verlag, 1986.
26. Thomas, R. C., *Ion-Sensitive Intracellular Microelectrodes. How to Make and Use Them*, London, England: Academic Press, 1978.
27. Maile, F. J., T. Schauer, and C. D. Eisenbach, Evaluation of corrosion and protection of coated metals with local ion concentration technique (LICT), *Progress in Organic Coatings*, 38, 2000, 111.
28. Gyurcsanyi, R. E., A.-S. Nyback, A. Ivaska, K. Toth, and G. Nagy, Novel polypyrrole based all-solid-state potassium-selective microelectrodes, *Analyst*, 123, 1998, 1339.
29. Lin, C. J., R. G. Du, and T. Nguyen, In-situ imaging of chloride ions at the metal/solution interface by scanning combination microelectrodes, *Corrosion*, 56, 2000, 41.
30. Suter, T. and H. Bohni, The microcell technique, *Analytical Methods in Corrosion Science and Engineering*, Boca Raton, FL: CRC Press, 2006, p. 649.
31. Suter, T. and H. Bohni, A new microelectrochemical method to study pit initiation on stainless steels, *Electrochimica Acta*, 42, 1997, 3275.
32. Suter, T. and H. Bohni, Microelectrodes for studies of localized corrosion processes, *Electrochimica Acta*, 43, 1998, 2843.

33. Krawiec, H., V. Vignal, and Z. Szklarz, Local electrochemical studies of the microstructural corrosion of AlCu4Mg1 as-cast aluminium alloy and influence of applied strain, *Journal of Solid State Electrochemistry*, 13, 2009, 1181.
34. Lohrengel, M. M., A. Moehring, and M. Pilaski, Electrochemical surface analysis with the scanning droplet cell, *Fresenius Journal of Analytical Chemistry*, 367, 2000, 334.
35. Spaine, T. W. and J. E. Baur, A positionable microcell for electrochemistry and scanning electrochemical microscopy in subnanoliter volumes, *Analytical Chemistry*, 73, 2001, 930.
36. Eng, L., E. Wirth, T. Suter, and H. Bohni, Non-contact feedback for scanning capillary microscopy, *Electrochimica Acta*, 43, 1998, 3029.
37. Lohrengel, M. M., I. Kluppel, C. Rosenkranz, H. Bettermann, and J. W. Schultze, Microscopic investigations of electrochemical machining of Fe in $NaNO_3$, *Electrochimica Acta*, 48, 2003, 3203.
38. Fushimi, K., S. Yamamoto, H. Konno, and H. Habazaki, Limiting current in a flowing-electrolyte-type droplet cell, *ChemPhysChem*, 10, 2009, 420.
39. Lohrengel, M. M., Electrochemical capillary cells, *Corrosion Engineering, Science and Technology*, 39, 2004, 53.
40. Evans, U. R., Report on corrosion research work at Cambridge University interrupted by the outbreak of war, *Journal of the Iron and Steel Institute*, 141, 1940, 219.
41. Isaacs, H. S. and G. Kissel, Surface preparation and pit propagation in stainless steels, *Journal of the Electrochemical Society*, 119, 1972, 1628.
42. Isaacs, H. S. and B. Vyas, Scanning reference electrode techniques in localized corrosion, *ASTM Special Technical Publication*, 727, 1981, 3.
43. Isaacs, H. S., Measurement of the galvanic corrosion of soldered copper using the scanning vibrating electrode technique, *Corrosion Science*, 28, 1988, 547.
44. Sargeant, D. A., Electrochemical scanning probes: Limitations, conflicts and observations. A direct comparison of two variants of the scanning reference electrode technique, *Corrosion Prevention and Control*, 44, 1997, 91.
45. Isaacs, H. S. and R. Jackson, Detection and performance of defects in aluminum coated steels, *Proceedings of the Electrochemical Society*, 84–3, 1984, 339.
46. Yan, M. C., D. E. Tallman, S. C. Rasmussen, and G. P. Bierwagen, Corrosion control coatings for aluminum alloys based on neutral and n-doped conjugated polymers, *Journal of the Electrochemical Society*, 156, 2009, C360.
47. Lillard, R. S., P. J. Moran, and H. S. Isaacs, A novel method for generating quantitative electrochemical impedance spectroscopy, *Journal of the Electrochemical Society*, 139, 1992, 1007.
48. Bayet, E., L. Garrigues, F. Huet, M. Keddam, K. Ogle, N. Stein, and H. Takenouti, Performances and limitations of current probes for LEIS measurements. A comparative study of vibrating (SVET) and double-electrode, *Proceedings of the Electrochemical Society*, 99–28, 2000, 200.
49. Takenouti, H., G. Galicia, M. Keddam, and V. Vivier, Vibrating single probe and stationary bi-probes to measure local electrochemical impedance spectroscopy, *Bulgarian Chemical Communications*, 38, 2006, 165.
50. Wittmann, M. W., R. B. Leggat, and S. R. Taylor, The detection and mapping of defects in organic coatings using local electrochemical impedance methods, *Journal of the Electrochemical Society*, 146, 1999, 4071.
51. Galicia, G., N. Pebere, B. Tribollet, and V. Vivier, Local and global electrochemical impedances applied to the corrosion behaviour of an AZ91 magnesium alloy, *Corrosion Science*, 51, 2009, 1789.
52. Philippe, L. V. S., G. W. Walter, and S. B. Lyon, Investigating localized degradation of organic coatings, *Journal of the Electrochemical Society*, 150, 2003, B111.
53. Casillas, N., S. J. Charlebois, W. H. Smyrl, and H. S. White, Scanning electrochemical microscopy of precursor sites for pitting corrosion on titanium, *Journal of the Electrochemical Society*, 140, 1993, L142.
54. Casillas, N., S. Charlebois, W. H. Smyrl, and H. S. White, Pitting corrosion of titanium, *Journal of the Electrochemical Society*, 141, 1994, 636.
55. Basame, S. B. and H. S. White, Scanning electrochemical microscopy of native titanium oxide films. Mapping the potential dependence of spatially-localized electrochemical reactions, *Journal of Physical Chemistry*, 99, 1995, 16430.
56. James, P., N. Casillas, and W. H. Smyrl, Simultaneous scanning electrochemical and photoelectrochemical microscopy by use of a metallized optical fiber, *Journal of the Electrochemical Society*, 143, 1996, 3853.

57. Casillas, N., P. James, and W. H. Smyrl, A novel approach to combine scanning electrochemical microscopy and scanning photoelectrochemical microscopy, *Journal of the Electrochemical Society*, 142, 1995, L16.
58. Wipf, D. O., Initiation and study of localized corrosion by scanning electrochemical microscopy, *Colloids and Surfaces A: Physicochemical and Engineering Aspects*, 93, 1994, 251.
59. Still, J. W. and D. O. Wipf, Breakdown of the iron passive layer by use of the scanning electrochemical microscope, *Journal of the Electrochemical Society*, 144, 1997, 2657.
60. Zhu, Y. and D. E. Williams, Scanning electrochemical microscopic observation of a precursor state to pitting corrosion of stainless steel, *Journal of the Electrochemical Society*, 144, 1997, L43.
61. Frankel, G. S., Pitting corrosion of metals, *Journal of the Electrochemical Society*, 145, 1998, 2186.
62. Yin, Y., L. Niu, M. Lu, W. Guo, and S. Chen, In situ characterization of localized corrosion of stainless steel by scanning electrochemical microscope, *Applied Surface Science*, 255, 2009, 9193.
63. Qin, R.-J., M. Lu, W.-K. Guo, and L. Niu, Localized electrochemical scanning study on pitting corrosion of stainless steel in acidic chloride solutions, *Fushi Kexue Yu Fanghu Jishu*, 21, 2009, 230.
64. Terada, M., A. F. Padilha, A. M. P. Simoes, H. G. de Melo, and I. Costa, Use of SECM to study the electrochemical behavior of DIN 1.4575 superferritic stainless steel aged at 475°C, *Materials and Corrosion*, 60, 2009, 889.
65. Blanc, C., N. Pebere, B. Tribollet, and V. Vivier, Galvanic coupling between copper and aluminum in a thin-layer cell, *Corrosion Science*, 52, 2010, 991.
66. Zhou, H.-R., J. Ma, X.-G. Li, C.-F. Dong, Q.-K. Lu, and H. Feng, Corrosion study of pure aluminum in 0.6 mol/L NaCl solution by SECM, *Hangkong Cailiao Xuebao*, 29, 2009, 8.
67. Liu, X., G. Wu, Y. Xu, T. Zhang, Y. Shao, G. Meng, and F. Wang, Effect of modulated passivation on corrosion resistance of AZ91D magnesium alloy: I—Effect of modulated passivation on corrosion behavior of AZ91D magnesium alloy, *Zhongguo Fushi Yu Fanghu Xuebao*, 30, 2010, 41.
68. Liu, X., T. Zhang, Y. Shao, G. Meng, and F. Wang, Effect of alternating voltage treatment on the corrosion resistance of pure magnesium, *Corrosion Science*, 51, 2009, 1772.
69. Pereda, M. D., C. Alonso, L. Burgos-Asperilla, J. A. del Valle, O. A. Ruano, P. Perez, and M. A. F. Lorenzo de Mele, Corrosion inhibition of powder metallurgy Mg by fluoride treatments, *Acta Biomaterialia*, 6, 2010, 1772.
70. Nowierski, C., J. J. Noel, D. W. Shoesmith, and Z. Ding, Correlating surface microstructures with reactivity on commercially pure zirconium using scanning electrochemical microscopy and scanning electron microscopy, *Electrochemistry Communication*, 11, 2009, 1234.
71. He, H., R. K. Zhu, Z. Qin, P. Keech, Z. Ding, and D. W. Shoesmith, Determination of local corrosion kinetics on hyper-stoichiometric UO_2+x by scanning electrochemical microscopy, *Journal of the Electrochemical Society*, 156, 2009, C87.
72. Izquierdo, J., J. J. Santana, S. Gonzalez, and R. M. Souto, Uses of scanning electrochemical microscopy for the characterization of thin inhibitor films on reactive metals: The protection of copper surfaces by benzotriazole, *Electrochimica Acta*, 55, 2010, 8791.
73. Huang, H., Y.-W. Shao, T. Zhang, and G.-Z. Meng, Effect of emeraldine base (EB) from of polyaniline on corrosion behavior of carbon steel in 3.5% NaCl solution, *Fushi Kexue Yu Fanghu Jishu*, 21, 2009, 221.
74. Tallman, D. E., C. Vang, G. G. Wallace, and G. P. Bierwagen, Direct electrodeposition of polypyrrole on aluminum and aluminum alloy by electron transfer mediation, *Journal of the Electrochemical Society*, 149, 2002, C173.
75. Souto, R. M., Y. Gonzalez-Garcia, S. Gonzalez, and G. T. Burstein, Imaging the origins of coating degradation and blistering caused by electrolyte immersion assisted by SECM, *Electroanalysis*, 21, 2009, 2569.
76. Gonzalez-Garcia, Y., J. J. Santana, J. Gonzalez-Guzman, J. Izquierdo, S. Gonzalez, and R. M. Souto, Scanning electrochemical microscopy for the investigation of localized degradation processes in coated metals, *Progress in Organic Coatings*, 69, 2010, 110.
77. Souto, R. M., Y. Gonzalez-Garcia, J. Izquierdo, and S. Gonzalez, Examination of organic coatings on metallic substrates by scanning electrochemical microscopy in feedback mode: Revealing the early stages of coating breakdown in corrosive environments, *Corrosion Science*, 52, 2010, 748.
78. Santana, J. J., J. Gonzalez-Guzman, L. Fernandez-Merida, S. Gonzalez, and R. M. Souto, Visualization of local degradation processes in coated metals by means of scanning electrochemical microscopy in the redox competition mode, *Electrochimica Acta*, 55, 2010, 4488.
79. Souto, R. M., L. Fernandez-Merida, and S. Gonzalez, SECM imaging of interfacial processes in defective organic coatings applied on metallic substrates using oxygen as redox mediator, *Electroanalysis*, 21, 2009, 2640.

80. Liu, X.-Y., H.-Y. Ma, S.-H. Chen, and W.-J. Li, Electrochemical characterization of self-assembled monolayers on iron surface by SECM, *Fushi Kexue Yu Fanghu Jishu*, 21, 2009, 239.
81. Dufek, E. J. and D. A. Buttry, Characterization of Zr(IV)-phosphonate thin films which inhibit O_2 reduction on AA2024-T3, *Journal of the Electrochemical Society*, 156, 2009, C322.
82. Shao, Y., C. Jia, G. Meng, T. Zhang, and F. Wang, The role of a zinc phosphate pigment in the corrosion of scratched epoxy-coated steel, *Corrosion Science*, 51, 2009, 371.
83. Cao, J., Y. Shao, T. Zhang, and G. Meng, Roles of zinc phosphate on corrosion of scratched epoxy coating, *Zhongguo Fushi Yu Fanghu Xuebao*, 29, 2009, 437.
84. Ding, H., G. A. Hawthorn, and L. H. Hihara, Inhibitive effect of seawater on the corrosion of particulate-reinforced aluminum-matrix composites and monolithic aluminum alloy, *Journal of the Electrochemical Society*, 156, 2009, C352.
85. Ding, H. and L. H. Hihara, Galvanic corrosion and localized degradation of aluminum-matrix composites reinforced with boron carbide particulates, *ECS Transactions*, 16, 2009, 39.
86. Lamaka, S. V., G. Knoernschild, D. V. Snihirova, M. G. Taryba, M. L. Zheludkevich, and M. G. S. Ferreira, Complex anticorrosion coating for ZK30 magnesium alloy, *Electrochimica Acta*, 55, 2009, 131.
87. Bastos, A. C., O. V. Karavai, M. L. Zheludkevich, K. A. Yasakau, and M. G. S. Ferreira, Localised measurements of pH and dissolved oxygen as complements to SVET in the investigation of corrosion at defects in coated aluminum alloy, *Electroanalysis*, 22, 2010, 2009.
88. Bastos, A. C., M. G. Taryba, O. V. Karavai, M. L. Zheludkevich, S. V. Lamaka, and M. G. S. Ferreira, Micropotentiometric mapping of local distributions of Zn^{2+} relevant to corrosion studies, *Electrochemistry Communication*, 12, 2010, 394.
89. Karavai, O. V., A. C. Bastos, M. L. Zheludkevich, M. G. Taryba, S. V. Lamaka, and M. G. S. Ferreira, Localized electrochemical study of corrosion inhibition in microdefects on coated AZ31 magnesium alloy, *Electrochimica Acta*, 55, 2010, 5401.
90. Lin, B., R. Hu, C. Ye, Y. Li, and C. Lin, A study on the initiation of pitting corrosion in carbon steel in chloride-containing media using scanning electrochemical probes, *Electrochimica Acta*, 55, 2010, 6542.
91. Oltra, R., B. Malki, and F. Rechou, Influence of aeration on the localized trenching on aluminium alloys, *Electrochimica Acta*, 55, 2010, 4536.
92. Andreatta, F., L. Matesanz, A. H. Akita, L. Paussa, L. Fedrizzi, C. S. Fugivara, J. M. Gomez de Salazar, and A. V. Benedetti, SAE 1045 steel/WC–Co/Ni–Cu–Ni/SAE 1045 steel joints prepared by dynamic diffusion bonding: Microelectrochemical studies in 0.6M NaCl solution, *Electrochimica Acta*, 55, 2009, 551.
93. Krawiec, H., S. Stanek, V. Vignal, J. Lelito, and J. S. Suchy, The use of micro-capillary techniques to study the corrosion resistance of AZ91 magnesium alloy at the micro-scale, *Ochr Koroz*, 52, 2009, 458.
94. Premendra, P., H. Terryn, J. M. C. Mol, J. H. W. de Wit, and L. Katgerman, A comparative electrochemical study of commercial and model aluminium alloy (AA5050), *Materials and Corrosion*, 60, 2009, 399.
95. Sanchez, M., J. Gamby, H. Perrot, D. Rose, and V. Vivier, Microelectrochemistry of copper in NaCl solution: Comparison between conventional microelectrode and microelectrochemical cell, *Electrochemistry Communication*, 12, 2010, 1230.
96. Williams, C. G., M. A. Edwards, A. L. Colley, J. V. Macpherson, and P. R. Unwin, Scanning micropipet contact method for high-resolution imaging of electrode surface redox activity, *Analytical Chemistry*, 81, 2009, 2486.
97. Boag, A., R. J. Taylor, T. H. Muster, N. Goodman, D. McCulloch, C. Ryan, B. Rout, D. Jamieson, and A. E. Hughes, Stable pit formation on AA2024-T3 in a NaCl environment, *Corrosion Science*, 52, 2009, 90.
98. Andreeva, D. V., E. V. Skorb, and D. G. Shchukin, Layer-by-layer polyelectrolyte/inhibitor nanostructures for metal corrosion protection, *ACS Applied Materials & Interfaces*, 2, 2010, 1954.
99. Liu, Y. and Y. F. Cheng, Role of second phase particles in pitting corrosion of 3003 Al alloy in NaCl solution, *Materials and Corrosion*, 61, 2010, 211.
100. Williams, G., A. J. Coleman, and H. N. McMurray, Inhibition of aluminum alloy AA2024-T3 pitting corrosion by copper complexing compounds, *Electrochimica Acta*, 55, 2010, 5947.
101. Yan, M., C. A. Vetter, and V. J. Gelling, Electrochemical investigations of polypyrrole aluminum flake coupling, *Electrochimica Acta*, 55, 2010, 5576.
102. Maddela, S., Y.-M. Wang, A. K. Sachdev, and R. Balasubramaniam, The influence of β (Mg17Al12) phase distribution on corrosion behavior of AM50 alloy in NaCl solution, *Proceedings of Magnesium Technology, 2009, Symposium*, 2009, 321.
103. Galio, A. F., S. V. Lamaka, M. L. Zheludkevich, L. F. P. Dick, I. L. Mueller, and M. G. S. Ferreira, Inhibitor-doped sol–gel coatings for corrosion protection of magnesium alloy AZ31, *Surface Coating Technology*, 204, 2010, 1479.

104. Williams, G., H. N. McMurray, and R. Grace, Inhibition of magnesium localised corrosion in chloride containing electrolyte, *Electrochimica Acta*, 55, 2010, 7824.
105. Liu, Z. Y., X. G. Li, and Y. F. Cheng, In-situ characterization of the electrochemistry of grain and grain boundary of an X70 steel in a near-neutral pH solution, *Electrochemistry Communication*, 12, 2010, 936.
106. Motte, C., M. Poelman, M. Jourdier, D. Dispa, and M. G. Olivier, Study of the inhibition mechanism of chrome free inhibitors on the galvanized steel corrosion by classical and local electrochemical techniques, *Chimie Nouveau*, 27, 2009, 1.
107. Tang, X. and Y. F. Cheng, Micro-electrochemical characterization of the effect of applied stress on local anodic dissolution behavior of pipeline steel under near-neutral pH condition, *Electrochimica Acta*, 54, 2009, 1499.
108. Warren, D., H. McMurray, and A. de Vooys, Corrosion behaviour of new PVD coatings on steel, *ECS Transactions*, 16, 2009, 165.
109. Zhang, G. A. and Y. F. Cheng, Micro-electrochemical characterization and Mott-Schottky analysis of corrosion of welded X70 pipeline steel in carbonate/bicarbonate solution, *Electrochimica Acta*, 55, 2009, 316.
110. Olivier, M., A. Lanzutti, C. Motte, and L. Fedrizzi, Influence of oxidizing ability of the medium on the growth of lanthanide layers on galvanized steel, *Corrosion Science*, 52, 2010, 1428.
111. Souto, R. M., B. Normand, H. Takenouti, and M. Keddam, Self-healing processes in coil-coated cladding studied by the scanning vibrating electrode, *Electrochimica Acta*, 55, 2010, 4551.
112. Zhang, C. and Y. F. Cheng, Corrosion of welded X100 pipeline steel in a near-neutral pH solution, *Journal of Materials Engineering and Performance*, 19, 2010, 834.
113. Simoes, A. M. and J. C. S. Fernandes, Studying phosphate corrosion inhibition at the cut edge of coil coated galvanized steel using the SVET and EIS, *Progress in Organic Coatings*, 69, 2010, 219.
114. Deshpande, K. B., Validated numerical modelling of galvanic corrosion for couples: Magnesium alloy (AE44)-mild steel and AE44-aluminium alloy (AA6063) in brine solution, *Corrosion Science*, 52, 2010, 3514.
115. Deshpande, K. B., Experimental investigation of galvanic corrosion: Comparison between SVET and immersion techniques, *Corrosion Science*, 52, 2010, 2819.
116. Kallip, S., A. C. Bastos, M. L. Zheludkevich, and M. G. S. Ferreira, A multi-electrode cell for high-throughput SVET screening of corrosion inhibitors, *Corrosion Science*, 52, 2010, 3146.
117. Luo, H., C. Dong, K. Xiao, X. Li, and D. Wei, Development of microzone electrochemical studies of metallic corrosion (3)–scanning vibrating electrode technique, *Fushi Yu Fanghu*, 30, 2009, 631.
118. Katayama, H., Evaluation of corrosion under the coated film by electrochemical method, *Bosei Kanri*, 54, 2010, 19.
119. Lewis, O. D., D. Greenfield, R. Akid, R. H. Dahm, and G. D. Wilcox, Conversion coatings for zinc electrodeposits from modified molybdate solutions, *Transactions of the Institute of Metal Finishing*, 88, 2010, 107.
120. Yan, M., V. J. Gelling, B. R. Hinderliter, D. Battocchi, D. E. Tallman, and G. P. Bierwagen, SVET method for characterizing anti-corrosion performance of metal-rich coatings, *Corrosion Science*, 52, 2010, 2636.
121. Santana, J. J., J. Gonzalez-Guzman, J. Izquierdo, S. Gonzalez, and R. M. Souto, Sensing electrochemical activity in polymer-coated metals during the early stages of coating degradation by means of the scanning vibrating electrode technique, *Corrosion Science*, 52, 2010, 3924.
122. Dong, C.-F., H. Sheng, Y.-H. An, X.-G. Li, and K. Xiao, Local electrochemical behavior of 2A12 aluminum alloy in the initial stage of atmospheric corrosion under Cl^- conditions, *Beijing Keji Daxue Xuebao*, 31, 2009, 878.
123. Lacroix, L., C. Blanc, N. Pebere, B. Tribollet, and V. Vivier, Localized approach to galvanic coupling in an aluminum–magnesium system, *Journal of the Electrochemical Society*, 156, 2009, C259.
124. Barranco, V., N. Carmona, J. C. Galvan, M. Grobelny, L. Kwiatkowski, and M. A. Villegas, Electrochemical study of tailored sol–gel thin films as pre-treatment prior to organic coating for AZ91 magnesium alloy, *Progress in Organic Coatings*, 68, 2010, 347.
125. Boisier, G., N. Portail, and N. Pebere, Corrosion inhibition of 2024 aluminum alloy by sodium decanoate, *Electrochimica Acta*, 55, 2010, 6182.
126. Cui, J., J. Cai, and C. Jia, Pitting corrosion of high strength aluminum alloys in salt spray test, *Zhongguo Fushi Yu Fanghu Xuebao*, 30, 2010, 197.
127. Kubisztal, J., A. Budniok, E. Lagiewka, and J. Niedbala, Electrochemical scanning techniques in studies of the corrosion resistance of Zn–Ni and Zn–Ni+Ni electroplates, *Ochr Przed Koroz*, 53, 2010, 293.
128. Lin, C., Q. Zhao, Y. E. Liu, and J. Liang, Evolution of corrosion products of 20 carbon steel in atmosphere containing SO_2, *Jinshu Xuebao*, 46, 2010, 358.

15 Micro- and Nanopatterning Using Scanning Electrochemical Microscopy

Daniel Mandler

CONTENTS

15.1 Patterning by the Direct Mode of the SECM 490
15.1.1 Semiconductor Etching 490
15.1.2 Metal Deposition and Etching 491
15.1.3 Deposition of Conducting Polymers 493
15.1.4 Organic and Biomolecule Patterning 496
15.2 Patterning by the Feedback Mode of the SECM 499
15.2.1 Metal Deposition and Etching 499
15.2.2 Semiconductor Etching 504
15.2.3 Inorganic Materials: Deposition and Dissolution 508
15.2.4 Deposition of Conducting Polymers 510
15.2.5 Organics, Self-Assembled Monolayers, Polymers, and Biomolecule Patterning 513
15.2.5.1 Organics and Biomolecules 513
15.2.5.2 Self-Assembled Monolayers 517
15.2.5.3 Polymers 517
15.3 Perspective Approaches 519
15.3.1 Speed of Patterning 519
15.3.2 Resolution 520
15.3.3 Scope of Materials and Approaches 520
References 521

Early in the development of the scanning electrochemical microscopy (SECM), it was recognized that when an ultramicroelectrode (UME) is brought near a conducting surface, electron transfer is confined to a small area on the surface. This realization led to the development of a number of methods for using the SECM as a tool for surface modification. The activity in this field has partially been reviewed[1] and the term microelectrochemistry has been coined to the formation of micropatterns using an electrochemical technique. The range of reactions that have been driven on surfaces spans from metal deposition and etching to patterning of surfaces with polymers, enzymes, and other biomolecules. Moreover, surface reactions other than electron transfer processes were carried out by SECM. Some activity has focused on increasing the resolution of the fabricated patterns, extending the capability of the SECM into the nanoelectrochemistry domain.

The aim of this chapter is to systematically review the different systems and methods, which have been used in conjunction with SECM, for fabricating small patterns on surfaces. We searched the literature until the end of 2010. Most of these can be divided into two main categories based on the mode of operation, that is, the direct and the feedback mode. The two modes differ in respect

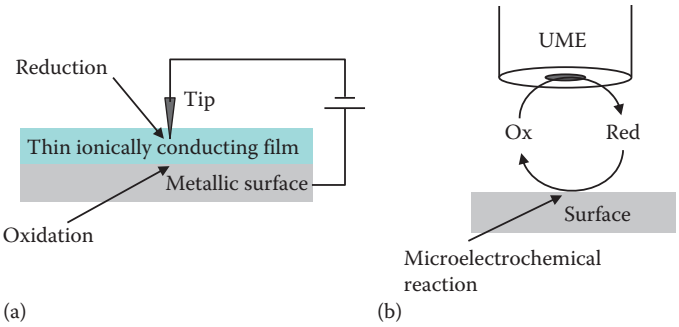


FIGURE 15.1 Schematic representation of the direct (A) and the feedback mode (B) of the SECM.

that in the direct mode the substrate serves as the working electrode and the SECM tip as the auxiliary electrode. On the other hand, in the feedback mode the substrate is quite often unbiased; the UME is used as the working electrode and a mediator, which shuttles between the UME and surface, is added (Figure 15.1). This difference is significant because, as will be shown, it dictates most of the intrinsic parameters, such as the type of reactions that can be carried out, as well as the extrinsic parameters, that is, the resolution and rate of patterning. Since the direct method has been introduced first, it precedes the feedback mode section. The subheading within each section follows the nature of the patterning process or the materials involved, such as conducting polymers. The last section discusses some technological issues that are an integral part of micro- and nanopatterning techniques and presents several approaches that are either being currently undertaken or likely to be demonstrated in the future.

15.1 PATTERNING BY THE DIRECT MODE OF THE SECM

This mode of operation has primarily been developed by Bard and his coworkers in the very beginning of the SECM. In fact, the direct mode started as a direct continuation of attempts to use scanning tunneling microscopy (STM) for patterning and later on changed completely and was utilized differently as will be discussed later. The first studies involving the direct mode were based on approaching a *conducting* substrate with a biased SECM tip that was identical to a conventional STM tip. The configuration of the system was based on two-electrode system where the tip was biased vs. the substrate. This led to two processes: one at the tip, for example, reduction, and another process at the surface, for example, oxidation. The latter is the driving force for the patterning process. Due to the fact that the whole substrate is biased, localization of the process on the substrate is caused by the distribution of the electrical field between the SECM tip and the substrate.[2] Accordingly, the resolution of the patterns is governed mostly by the distance between the tip and the substrate. Therefore, in most cases where the direct mode was applied, special care or approaches were used for minimizing the distance between the tip and the substrate.

15.1.1 Semiconductor Etching

The first and only system that employed the direct mode for semiconductor etching was reported by Lin et al.[2] n-GaAs was photoetched as a result of holding a sharp metallic tip that was insulated in glass in close proximity (<1 μm) above a positively biased (4 V) n-GaAs while illuminating the substrate. The formation of etched patterns with line widths of 0.3–2 μm was attributed to the nonuniform spatial current distribution. Nonetheless, some etching occurred also across the whole surface because there was no attempt to focus the illumination to the area beneath the SECM tip.

15.1.2 Metal Deposition and Etching

One of the critical problems of the previous system was the lack of a mechanism that controlled the distance between the tip and the substrate using a feedback loop. The current measured at the tip was insensitive to the distance and therefore the latter was determined by scanning the tip across the predefined pattern in a STM mode in order to "map the topography" of the path. This problem was resolved by Bard and his colleagues in the following way: An exposed STM-like tip approached a conducting substrate that was coated with a thin film made of an ionically conducting polymer, for example, Nafion. The sample was kept in air and the tip was biased vs. the substrate. As soon as the tip touched the polymeric film, a faradaic current passed across the film. The magnitude of the current was a function of the area of the tip that penetrated the polymer. Therefore, by maintaining the current constant, using an electronic feedback loop, the degree of tip penetration and thus the tip–substrate distance could be controlled.

Local metal deposition in the polymer was accomplished as a result of incorporating metal ions inside the polymer and applying a negative potential to the tip (Figure 15.2). On the other hand, the etching of metals was driven by applying a positive potential to the substrate in the absence of metal ions in the polymer. Specifically, Craston et al.[3] used this approach for the high-resolution deposition of silver in Nafion, while Husser et al.[4,5] reported on the deposition of silver, gold, copper, and palladium in a variety of ionically conducting polymers and high-resolution etching of copper, silver, and gold. For example, Figure 15.3 shows a scanning electron micrograph of a pattern of silver lines deposited in Nafion. The width of the lines was as thin as 0.3 μm. On the other hand, carrying out etching as well as deposition processes on the substrate–polymer interface was less successful and more difficult to detect. The films had to be removed in order to detect the patterns on the substrate and in most cases the resolution was lower as compared with that of patterns formed at the UME–polymer interface. In summary, this approach offered several advantages over the wet

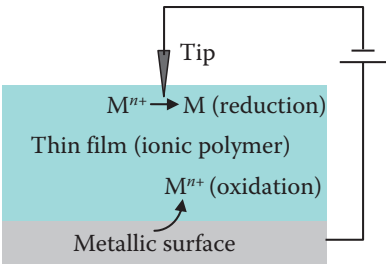


FIGURE 15.2 Schematic representation of the direct mode for deposition of metal in polymeric films.

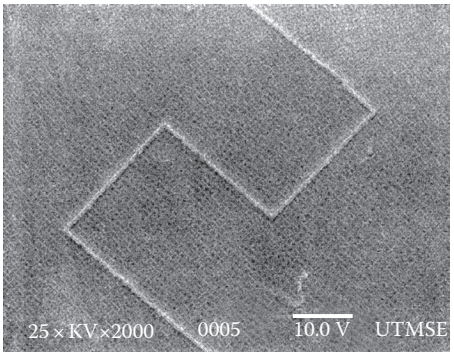


FIGURE 15.3 SEM picture of a pattern of silver lines deposited in a Nafion film. (From Hüsser, O.E. et al., *J. Electrochem. Soc*., 136, 3222, 1989. Reproduced with permission of The Electrochemical Society, Inc.)

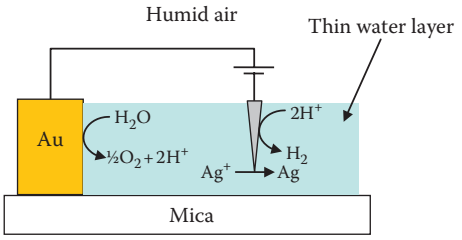


FIGURE 15.4 Schematic representation of high-resolution silver deposition on mica by the STM used in the direct mode of the SECM. (From Forouzan, F. and Bard, A.J., *J. Phys. Chem. B*, 101, 10876, 1997.)

etching of GaAs: the tip/substrate distance could be nicely controlled by the electronic feedback, the tips used were conventional STM tips that did not have to be insulated, and the deposits did not stick to the tip. At the same time, the speed of patterning was relatively low, that is, 0.1 µm/s, because of the movement inside a very thin polymer and the response of the electronic feedback.

A remarkable example of the capabilities of the direct mode of the SECM has been demonstrated by Forouzan and Bard.[6] It basically uses the same concept of controlling the distance between the tip and the substrate by its degree of penetration into an ionically conducting matrix; however, instead of a polyelectrolyte film, a very thin water layer, on the order of 10–15 Å, on an insulator was used (Figure 15.4). The reduction of silver ions and the formation of submicron rectangular patterns were driven by an STM tip that was biased negatively vs. a gold contact on the mica. The thin water layer, which was formed by maintaining the relative humidity of the environment between 80% and 95%, made it possible for a faradaic current to flow between the tip and the gold contact. As long as the applied potential between the tip and the substrate was kept sufficient negative to reduce silver ions and water, the Faradaic current prevented crashing of the tip into the mica.

Thomson and coworkers have substantially extended the application of the direct mode of SECM for metal deposition.[7] Extraordinary copper columns of 25 µm width and up to about 2 mm high were deposited on different substrates (Figure 15.5). The approach involved the application of a voltage between a closely spaced glass insulated Pt disk UME (25 µm diameter) and a substrate, all immersed in a solution of acidified $CuSO_4$. The potential, the concentration of the $CuSO_4$, and the presence of organic additives all affected the microstructure of the deposits and controlled the efficiency of the deposition. They were even successful to grow such an antenna at the end of

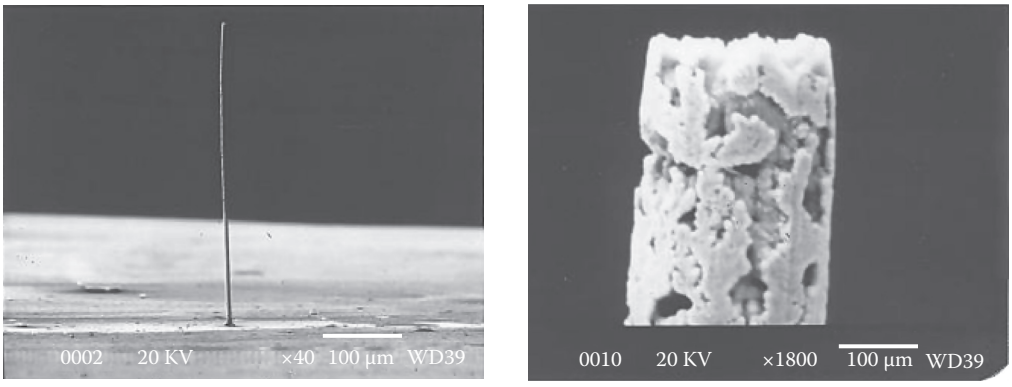


FIGURE 15.5 SEM image of copper column (25 µm diameter and 2 mm long) deposited on a copper substrate using the direct mode of SECM. (From El-Giar, E.M. et al., *J. Electrochem. Soc.*, 147, 586, 2000. Reproduced with permission of The Electrochemical Society, Inc.)

a micromachined cantilever. In a somewhat similar approach, Jansson et al.[8] formed Ni columns using insulated needle-type UMEs. The latter were biased 4–5 V and were slowly withdrawn from the surface. An additional auxiliary coil electrode attached to the Ni substrate gave better results. A 600 µm high column of 3 µm diameter was formed by optimizing the plating bath.

Finally, an interesting approach using a glass capillary filled with metal ions and containing the counter and the reference electrodes for local deposition of copper was demonstrated by Bohni and coworkers.[9] The substrate was not immersed into an electrolyte solution and the tip was brought close by the shear force approach. Hence, only the area between the tip and the substrate was exposed to the electrolyte. This allowed the formation of a row of single submicrometer Cu dots.

Etching of metals by the direct mode has been rather scarce. Schuhmann and coworkers studied the pitting corrosion of steel by combining shear force–based constant-distance mode SECM with the alternating current mode of this technique (AC-SECM).[10] A very small corrosion pit was generated by inducing active corrosion underneath an accurately positioned 5 µm diameter Pt tip that served as counter electrode in the direct mode. Before and after pit initiation, constant-distance mode AC-SECM images were recorded and subsequently used to identify the area of broken passivity.

The local oxidation of glassy carbon was studied by Tenent and Wipf.[11,12] Localized generation of surface oxides was demonstrated using both the microreagent and direct modification modes of the SECM. The microreagent mode was used to perform a chemical oxidation of the surface by generating the strong oxidant Ag(II) at the UME tip while positioned close to the carbon surface. However, this technique had poor reproducibility. Direct mode oxidation was much more versatile toward generating complex patterns of oxides on carbon surfaces. With the tip electrode placed close to a GC electrode, a galvanostat was used to drive a predetermined current between the tip and substrate for a specific amount of time, thereby allowing precise control over the amount of charge "injected" into the carbon surface. During current flow, solvent is reduced at the tip electrode and the carbon electrode is oxidized. Imaging of the oxidized spots was achieved due to differential heterogeneous electron transfer rates for the Fe(II/III) reaction occurring at unoxidized and oxidized glassy carbon electrodes. The reproducibility of the direct mode technique depended heavily on the solution resistance.

15.1.3 Deposition of Conducting Polymers

The fabrication of micro- and nanopatterns of conducting polymers has been the subject of continuous research. Since the best method for depositing thin films of conducting polymers involves electropolymerization, it is only logical that continuous efforts have been made to apply SECM as a tool for driving the local deposition of conducting polymers. The first report by Wuu et al.[13] exploited the direct mode for the deposition of polyaniline. More specifically, anilinium ions were incorporated into a thin Nafion film and the Pt substrate was biased positively, which caused the electropolymerization of aniline. Scanning the negatively biased tip across the film resulted in the simultaneous reduction of protons at the UME and the deposition of submicron width patterns of polyaniline. As before, the resolution of the deposit was controlled by the tip size, its depth of penetration, and the thickness of the Nafion.

Although this approach of the direct mode has not further been used, the lateral deposition of conducting polymers has been the subject of continuous and very successful research in particular by Schuhmann and coworkers.[14–17] The authors realized that in order to deposit a conducting polymer locally, high concentrations of the radical cation of the monomer must be maintained within the volume between the UME and the substrate. Obviously, a constant potential applied to the substrate will cause the depletion of the monomer in the gap between the UME and the substrate and presumably the deposition of the polymer over the entire substrate. The solution was in the form of a series of potentials applied to the gold substrate. The first pulse was of 1.2 V vs. Ag/AgCl for a time interval of 2 s, which caused the oxidation of nearly all the pyrrole monomers in the volume between the substrate and a 10 µm Pt UME. Then a second lower potential of 0.85 V for 1 s was applied in

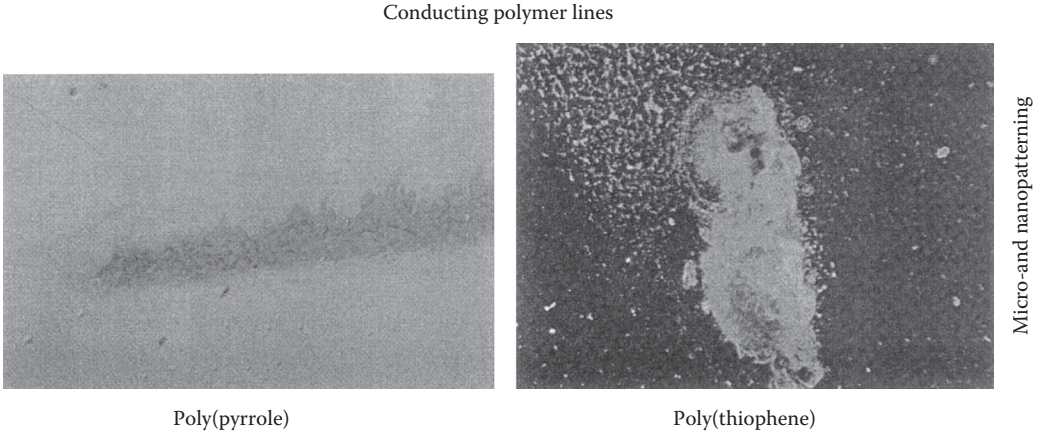


FIGURE 15.6 Scanning electron micrographs of lines of polypyrrole and polythiophene deposited with the direct mode of the SECM. (From Kranz, C. et al., *Adv. Mater.*, 7, 38, 1995.)

order to oxidize the soluble oligomers and finally a third relaxation pulse of 0.35 V for 2 s brought the system back to its initial stage. During this series of pulses, the UME was scanned with a speed of a few μm/s back and forth to obtain a sufficiently thick polypyrrole line of 50–60 μm width. The width of the deposited lines correlated with the total diameter of the UME while no polypyrrole was detected outside the patterns. Other polymers such as polythiophene have been deposited as well (Figure 15.6).

The lateral deposition of polypyrrole lines over insulating gaps has been accomplished by Schuhmann and coworkers using the same approach.[15] The motivation of this work was to develop a polymer-based transistor. Hence, a galvanostatic pulse profile was applied between gold electrodes separated by 100 μm and a 25 μm Pt UME that served as an auxiliary electrode. This three pulse series resulted in the deposition of a continuous spot of polypyrrole in the gap between the two electrodes. As a result, the potential applied to the polypyrrole (the gate) controlled the current between the two gold electrodes, which resembled a source and a drain. Moreover, the combination of this direct mode with the "topography feedback mode" developed by Schuhmann and coworkers[16] enabled the remarkable deposition of polypyrrole towers with height of as high as 400 μm and a diameter of about 80 μm (Figure 15.7).

Schuhmann and coworkers applied the direct mode also for the deposition of poly-*N*-(ω-aminoalkyl)pyrrole.[17] The functionalized patterns were used for covalently attaching periodate-oxidized glucose oxidase (GOx). Instead of applying a series of potential pulses, a series of galvanostatic pulses was used. The SECM was used in this study to verify the formation of the patterns of the functionalized polypyrrole as well as the enzymatic activity. Namely, scanning with an UME across the functionalized polypyrrole, while generating a redox couple resulted in a negative feedback current due to the low conductivity of the polymer as compared with the bare gold surface. On the other hand, the activity of the enzyme was detected with the SECM by comparing the feedback current (obtained over the enzyme patterns) of a mediator, that is, ferrocene carboxylic acid, in the presence and absence of the substrate of the enzyme, β-D-glucose.

Denuault and coworkers extended this approach further.[18] They used the SECM tip as an electrochemical "pen" to drive the deposition of a micrometer-size spot of biotinylated polypyrrole by the direct mode. Subsequent reaction with avidin and a biotinylated enzyme enabled the construction of a "molecular sandwich" capable of producing H_2O_2. The SECM tip was then used to "read" the activity of the microspot in the generation–collection mode.

Szunerits and coworkers have used extensively the direct mode of SECM for local electropolymerization of pyrrole.[19–22] They demonstrated "writing" of polypyrrole and polypyrrole–oligonucleotide



FIGURE 15.7 Scanning electron microscopic image of a polypyrrole tower deposited by the direct mode of the SECM using a 10 μm UME. (From Kranz, C. et al., *Adv. Mater.*, 8, 634, 1996. With permission.)

(ODN) patterns onto thin gold films by the direct mode of SECM, while an optical method, surface plasmon resonance imaging (SPR-i), simultaneously detected the formed micropatterns.[19,20] The combination of these two methods, SECM/SPR-i, had the advantage of not only controlling the patterning process but also providing unique information on the micropattern formation. The influence of the pulsing time and the monomer concentration on the spot size and its characteristics was investigated in detail by SPR-i (Figure 15.8). The same group[21] described the functionalization of oxidized boron-doped diamond (BDD) electrodes with *N*-(3-trimethoxysilylpropyl)pyrrole (TMPP) and its localized polymer formation using the direct mode as well as an electrochemical scanning

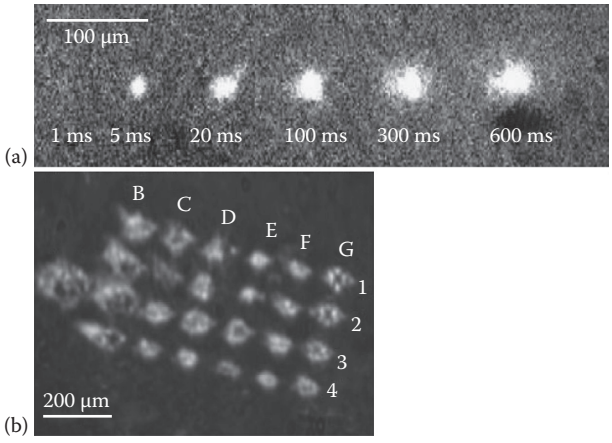


FIGURE 15.8 SPR images of polypyrrole (a) and polypyrrole–oligonucleotide (b) spots deposited by the direct mode of SECM. (From Fortin, E. et al., *Electroanalysis*, 17, 495, 2005. With permission.)

near-field optical microscope. Depending on the method used, polypyrrole dots with diameters in the range of 1–250 μm were electrogenerated.

Additional studies from this group showed the successful combination of the direct and feedback mode of SECM for the writing of ODN patterns on thin gold films alongside the imaging of DNA hybridization.[22] The patterning process was achieved as before using the direct mode to drive the local deposition of micrometer-size polypyrrole spots to which an ODN strand was covalently linked. Imaging of the deposited polypyrrole–ODN was achieved by means of the feedback mode using $Ru(NH_3)_6^{3+}$. The detection of the hybridization reaction of the ODN probes with their biotinylated complementary strands using SECM was possible after subsequent reactions with streptavidin and biotinylated horseradish peroxidase (HRP). The HRP-biocatalyzed oxidation of 4-chloro-1-naphthol in the presence of H_2O_2 and the precipitation of the insoluble product 4-chloro-1-naphthol on the hybridized areas on the gold film caused local alteration of conductivity. This change in conductivity was detected by the SECM tip and allowed imaging of DNA arrays in a fast and straightforward way. A subsequent study where the fabrication part was similar was undertaken by Szunerits and coworkers.[23]

15.1.4 Organic and Biomolecule Patterning

The formation of miniature structures of organic and biological molecules is of particular importance since conventional photolithographic techniques are not applicable for processing these materials. Hence, continuous efforts have been spent to developing novel approaches for micro- and nanopatterning of surfaces with thin films and monolayers of organic and biological molecules.

In this respect, the first report, which took advantage of the direct mode of the SECM, was presented by Masuhara and coworkers.[24] Fluorescent patterns of Rhodamine 6G in an ionically conducting polymer were formed as a result of the local decomposition of the quencher, methyl viologen. The latter was incorporated inside the film with the dye and quenched the fluorescence of the Rhodamine 6G. However, when a tungsten tip biased at −4 V vs. the platinum substrate was scanned at 1 μm/s, the quencher was decomposed, probably due to its reaction with hydroxyl ions that were generated at the tip as well, and the fluorescence of the dye was recovered. The authors concluded that the factors governing the resolution of the patterns were the moisture in the film and the shape of the tip. The mechanism of the fluorescent micropattern formation in the Rhodamine 6G–methyl viologen polymer film was further studied using the direct mode in a three-electrode configuration.[24] An additional reference electrode was constructed on the surface and was covered also by the polymer. This enabled to control the potential of the tip and as a result to correlate between the tip potential and the fluorescent micropattern formation. In essence, the tip had to be biased more negative than a certain threshold potential, which depended on the tip material, in order to form the micropatterns. This potential was substantially more negative than that needed to electrogenerate reduced methyl viologen, indicating that the decomposition of the fluorescence quencher, that is, methyl viologen, was driven by the generation of hydroxyl anions.

Other efforts to pattern surfaces with organic and biomolecules using the direct mode have been carried out by Wittstock and coworkers.[25] The localized desorption of alkanethiol monolayers has been induced by the direct mode of the SECM using again the UME as the auxiliary electrode and applying either negative or positive potentials to a gold substrate coated with dodecanethiol. The reductive and oxidative desorption of alkanethiols has been extensively studied[26–28] and is best carried out in an alkaline solution. Accordingly, Schuhmann found that while the oxidative and the reductive desorption of the thiols in phosphate buffer resulted in only partial desorption, a significant improvement has been achieved using 0.2 M KOH. The width of the patterns was two to three times larger than that of the active UME diameter. In spite of the fact that the resolution of the patterns was not comparable with that obtained by other methods, such as the microcontact printing, the SECM could be used in the feedback mode for imaging the patterns as soon as they were formed.

The success to locally desorb alkanethiols was exploited further by Schuhmann and coworkers for the formation of enzymatic patterns of GOx.[25] Cystamine, $(SCH_2CH_2NH_2)_2$, was adsorbed in the exposed patterns on the gold surface and periodate-oxidized GOx was covalently attached to the amino groups of cystamine. The activity of the enzyme was followed by the generation–collection mode of the SECM. The conventional feedback mode, in which ferrocenium carboxylic acid was generated at the UME, could not be used for detecting the enzymatic activity because the mediator was partially regenerated on unmodified areas. On the other hand, the enzyme patterns could be detected upon introducing oxygen and glucose and applying a positive potential (0.4 V vs. SCE) at the UME that caused the oxidation of hydrogen peroxide. The latter was formed in the modified patterns through a GOx-catalyzed reaction. Improved images were obtained by adding catalase, which decreased the diffusion layer of the H_2O_2. The major advantage of this patterning approach, according to the authors, stems from the possibility of repeating the procedure at different spots, and therefore, by using different enzymes, a route to multienzyme structures was envisaged.

Patterning of self-assembled monolayers (SAMs) was further improved by Wilhelm and Wittstock.[29] The procedures was based on the local electrochemical desorption of an alkanethiolate monolayer by applying a 5 kHz square-wave voltage of 2 V (peak-to-peak) to a two-electrode configuration consisting of a UME of 10 μm diameter placed about 5 μm above a macroscopic SAM-covered gold electrode. Desorption occurred on well-defined regions with a diameter of (12.8 ± 2.8) μm. These regions of bare gold were able to chemisorb a ω-functionalized alkanethiol or disulfide such as cystamine to form patterns of amino-terminated surfaces. Functional proteins were coupled to the amino groups present at the modified regions of the monolayer. A review by Wittstock[30] summarizes these and other approaches.

More recently, Schuhmann and coworkers used the direct mode of SECM for the local reduction of the terminating nitro groups of a *p*-nitrothiophenol SAMs to either hydroxylamine or amino groups.[31] By choosing the appropriate potential and a potential pulse sequence, the reduction of the SAMs end groups to the desired oxidation state was achieved. The local modification of the redox states was "read" by the feedback mode due to the different electron transfer rates governed by the redox state of the SAM end groups. Further biotin attachment to the locally modified end groups followed by complementary binding of an avidin–enzyme conjugate allowed confirming of the "writing process."

Additional studies based on the direct mode where the aim was to attach organic molecules were carried out by Combellas and coworkers. They compared the resolution obtained by the direct and the feedback mode of the local patterning of conductive substrates by polymer brushes through atom transfer radical polymerization (ATRP).[32] Specifically, a gold surface was modified electrochemically by a brominated aryldiazonium, which was then used as ATRP initiator in a following step. The local reduction of the initiator layer, which was achieved by applying −2.6 V to the gold surface vs. the SECM tip, avoided the subsequent polymerization and formed "negative patterns" of polymers. The tip–surface distance was controlled by AC-SECM and calibrated later by the feedback mode.

In another study,[32] they used the direct mode to locally electrograft organic layers by iodonium reduction. A gold substrate was used as the working cathode while the SECM tip was the counter electrode. This enabled writing patterns of a ca. 200–400 μm width. The reduction rate and time controlled the resolution of the writing process. The best results were obtained when using a two-electrode configuration and controlling the charge that flew through the circuit.

The direct mode was also used to induce pH change locally on the surface and cause different reactions. For example, Wittstock and coworkers[33] took advantage of the well-known electrochemical deposition of chitosan that is driven by applying negative potential, which causes water reduction and the elevation of pH. Deprotonation and deposition of chitosan occur at pH > 6.5. Hence, they applied −1.0 V pulses to an Au substrate vs. a Pt tip and caused the local deposition of chitosan. The availability of the amino groups at the surface of the microstructures was visualized after labeling by confocal laser scanning microscopy. The enzyme GOx could be entrapped during the electrochemical deposition and showed activity as seen by SECM images.

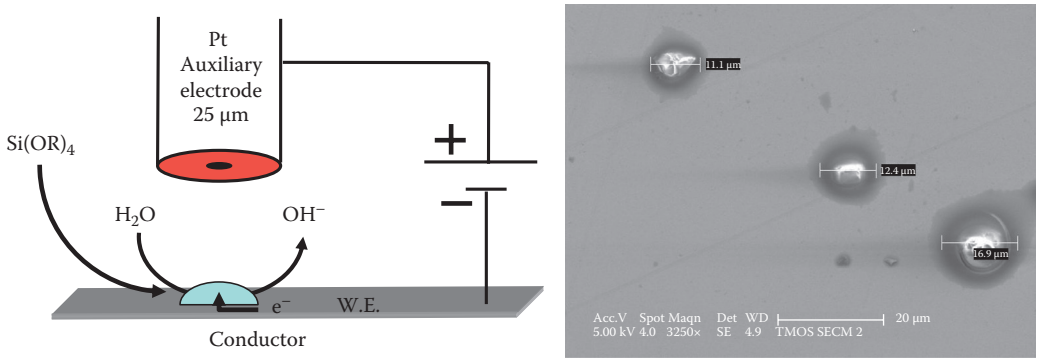


FIGURE 15.9 Schematics of the localized sol–gel deposition by the direct mode of SECM and a SEM image of the sol–gel spots that were deposited (Liu, L., et al., *Chem. Comm,* 47, 6909, 2011. Reproduced with permission of The Royal Society of Chemistry.)

An interesting approach was demonstrated by Han et al.[34] Microscopic spots of GOx were fabricated on platinum substrate electrode with a self-made concave platinum micrometer electrode. First, the concave platinum micrometer electrodes were prepared by means of phenol–allylphenol copolymer insulation and electrochemical etching. Using concave platinum micrometer electrode as reference and counter electrodes and platinum substrate as a working electrode, GOx on the concave platinum electrode was then electrochemically deposited and fixed on a platinum substrate to form microscopic spots with biological activity. The authors claim that the method is based on the local reduction of pH on the electrode surface. The diameter of the microscopic spots fabricated by this method was about 20 μm, and the microscopic spots retained the biological activity.

More recently, the direct mode of SECM was used to enhance the local deposition of sol–gel patterns.[35–37] Applying negative potentials to an indium–tin oxide substrate vs. a Pt tip in the presence of tetramethoxysilane (TMOS) increased the pH on the surface locally and catalyzed the condensation and deposition of TMOS. The growth of the patterns was very rapid and surprisingly the resolution of the deposited sol–gel was higher than the tip, presumably due to "chemical lens" focusing (Figure 15.9).

The main advantage of the direct mode approach originates from the submicron distance that the tip is held close above the substrate. Calculations, as well as experimental results, indicate that the electrical field between the tip and the substrate is relatively focused, which results in submicron resolution of the fabricated patterns. The resolution is also a function of the ionically conducting matrix (in the case where a noninsulated STM tip is used) as well as the shape of the tip and its lateral speed.

On the other hand, the direct mode has a number of significant limitations. The reduction or oxidation at the tip must be accompanied with a reversed reaction at the substrate interface, or vice versa. For example, the deposition of silver was followed by the oxidation of water or substrate etching. This reaction can sometimes, for example, when gas bubbles are formed, deteriorate the pattern formed at the substrate. The resolution is also a function of the tip shape. Very small, preferably needle-like tip electrodes are essential for establishing a focused electrical field that is the key for obtaining high resolution. However, such tips are likely to be damaged as a result of their lateral movement or touches of the substrate. The lateral speed of the tip in the direct mode varies and depends whether the UME scans inside a polymer or in solution. In the former case, the UME speed is of the order of hundreds of Å/s, which makes the formation of large patterns tedious. Nevertheless, possible practical applications of this technique have been suggested, such as the fabrication of lithographic masks and the repair of broken contacts in integrated circuits.

Finally, it must be realized that the SECM in the direct mode is basically an STM probe that is used for microfabrication. Therefore, additional studies, which are usually categorized under STM or scanning probes in general, must not be neglected. Distinguishing between patterning through a

tunneling or a Faradaic mechanism is not evident. Numerous studies on STM-based electrochemical modification of materials have been demonstrated so far. For example, nanostructures with dimensions of 10 nm have been formed on gold surfaces by Schneir et al.[38] Penner and coworkers have fabricated metal pillars with 10–30 nm in diameter on graphite surfaces.[39] Sugimura and coworkers[40–43] fabricated oxide patterns of titanium with a spatial resolution of 20 nm using the STM and in the presence of adsorbed water. Sugimura et al. also used this approach, that is, scanning probe anodization, in order to locally decompose trimethylsilyl monolayers on a Si substrate.[44] Crooks and coworkers termed this mode of operation scanning probe lithography and realized the similarity of their approach to the SECM direct mode.[45,46] A number of reports[45,47–49] have speculated that an electrochemical mechanism could be responsible for STM-induced surface modifications in air. More recently, AFM equipped with conducting tips have been used for driving electrochemical reactions locally on surfaces. This mode of operation was termed by Sagiv and coworkers constructive AFM,[50–53] which involves tip-induced nanoelectrochemical oxidation of mostly silane monolayers on silicon. For example, Sagiv and coworkers showed that it was possible to oxidize the terminal methyl groups of a silane monolayer into carboxylic groups, which were further modified and allowed the construction of a rich variety of patterns such as the particulate cadmium sulfide and other nanoparticles. Cai and Ocko[54] introduced another term electro pen nanolithography (EPN), which is also an AFM-related technique, whereby in a single sweep of an ink-coated, biased conducting AFM probe tip, an underlying thin organic film is oxidized, and the ink molecules are transferred directly to the oxidized regions. This technique provided very fast exceeding 10 μm/s writing speeds with line widths as small as 50 nm. There was no attempt to review here these and many more related contributions. However, there is basically no clear border between the direct mode of the SECM and SPM-based electrochemical mode carried out under nondry conditions.

15.2 PATTERNING BY THE FEEDBACK MODE OF THE SECM

The versatility of this mode of operation has made it extremely powerful for fabrication of microstructures. In the feedback mode, a UME is held close above a substrate in a solution consisting of one form of electroactive species either reduced or oxidized that serves as a mediator (Figure 15.1). The latter is usually utilized both as a means of controlling the distance between the UME and the surface, and to drive the microelectrochemical process on the surface. This poses a number of requirements that must be taken into account while configuring the system. The basic limitation stems from the requirement that the electrochemical reaction be confined only to the surface. This means that the electroactive species generated at the UME will react with the surface or with other species attached onto it. In addition, it is preferable in most cases that the redox couple used exhibit chemical and electrochemical reversibility so that it is effectively regenerated on the surface. The regeneration of the redox couple on the surface is required for controlling the UME–substrate distance. Finally, the thermodynamics and kinetics of the electrochemical process on the surface will dictate the choice of the redox couple introduced.

15.2.1 Metal Deposition and Etching

The first system that was based on the feedback mode aimed to deposit metals (Figure 15.10). Metal ions were incorporated in a polymer layer, for example, protonated polyvinyl pyridine, as a means of attaching them onto the surface. Hexaammineruthenium(III), $Ru(NH_3)_6^{3+}$, was reduced at a UME, diffused to the substrate, and drove the reduction of $AuCl_4^-$ and $PdCl_4^{2-}$ to their respective metals.[55] The different factors that determined the size and pattern of deposited metal were examined. Although this initial system was expected to be simple and straightforward, it concealed complicated chemistry predominantly due to the diffusion of the mediator into the polymer. While gold ions were efficiently reduced by $Ru(NH_3)_6^{2+}$ inside the polymer to form gold patterns, $PdCl_4^{2-}$ ions formed different structures upon reduction. A detailed study of this system revealed that the

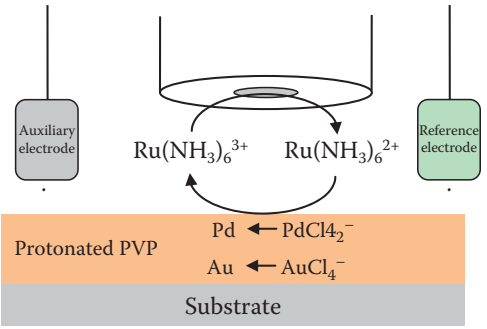


FIGURE 15.10 Schematic representation of the feedback mode for the deposition of metal in polymeric films.

reduction of palladium ions inside the polymer exhibited significantly more sluggish kinetics than in homogeneous solutions and thus required a stronger reductant than $Ru(NH_3)_6^{2+}$.

This system made the investigators change their concept. It was clear that if diffusion inside polymers can be abandoned, the interfacial chemistry involved was likely to be faster and simpler. One possible approach has been the usage of reactive surfaces that react directly with the electrogenerated mediators. The etching of copper[55] as well as a variety of semiconductors, vide infra, represents the implementation of this concept.

The etching of copper using the feedback mode has been driven by electrogenerating a strong oxidant, for example, $Fe(phen)_3^{2+}$ or $Os(bpy)_3^{2+}$ (phen = 1,10-phenanthroline, bpy = 2,2′-bipyridine), at the UME that was held close above a copper surface. The positive feedback current that was observed while approaching a copper surface indicated that the electroactive species were regenerated via electron transfer at the surface. As a result, copper dissolution occurred, which was strictly limited to the diffusion range of the oxidized mediator. Figure 15.11 shows a scanning electron micrograph of three etching spots made by holding a 25 μm Pt UME at a constant distance above a Cu thin layer for various periods of time. The profiles of these spots are also shown.

This system has further been studied by Unwin and coworkers[56] using the SECM in an ingenious configuration, in which two UMEs were made to approach each other. In this configuration, the contribution of the lateral charge transport to the feedback current was totally eliminated. Thus, any deviation from an absolute negative feedback current was due to the chemical regeneration of the mediator on the surface. Accordingly, tris(2,2′-bipyridine)ruthenium(III) and bromine were electrochemically generated at a Pt UME and their feedback currents while approaching an unbiased Cu UME were recorded. Investigations of Cu etching by both strong oxidants revealed that the metal dissolution process is diffusion controlled under all the conditions examined, suggesting that the heterogeneous rate constant controlling the etching process is large. Copper etching by the feedback mode was reinvestigated by Sheffer and Mandler[57] using thin Cu films and different electrochemically generated etchants. The question they raised was why Cu was etched at all by the feedback mode. It is not trivial that dissolution of Cu competes so well with lateral charge propagation. The authors found that etching becomes effective once the lateral contribution cannot dissipate the locally injected charge. This occurred as the concentration of the etchant increases or the film thickness decreased. Measuring the steady-state current above Cu films with different thickness allowed estimating the potential difference across the Cu area underneath the tip. It was concluded that driving local processes, such as etching, depends on creating a mechanism that maintained the injected charge focused.

Etching of iron by the feedback mode of the SECM has been reported by Still and Wipf.[58] They used the SECM as a means of generating localized corrosion at passivating iron surfaces by using the tip to generate chloride ions. This example represents a case in which the metal is covered with an oxide layer that needs to be removed in order to facilitate metal dissolution. Since these experiments are described in great detail in another chapter (Section 12.3) and there

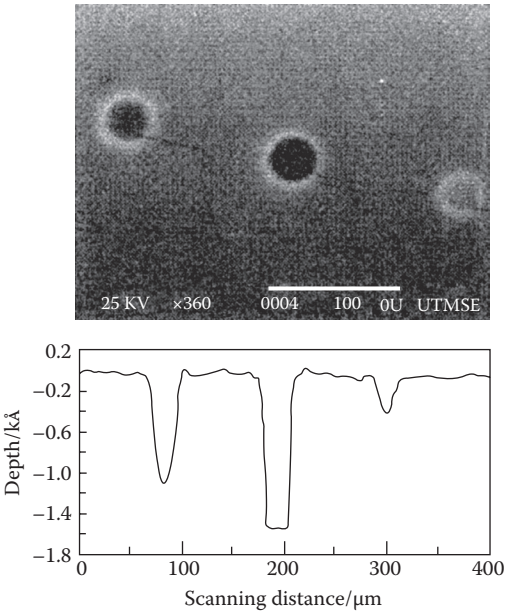


FIGURE 15.11 Scanning electron micrograph and profiles of etching pits on a thin copper layer. The etching pits were formed as a result of leaving a 25 μm diameter Pt UME (biased at 0.7 V vs. SCE) close above (9 μm) the surface for 5, 10, and 20 min. (From Mandler, D. and Bard, A.J., *J. Electrochem. Soc*., 136, 3143, 1989. Reproduced with permission of The Electrochemical Society, Inc.)

was no attempt to use this method for patterning structures on the iron surface, they will not be discussed further.

It is evident that driving the etching of surface by the feedback mode of the SECM is almost straightforward and requires the generation of a strong oxidant that is capable of oxidizing the surface. In addition, the conditions, that is, electrolyte, should be carefully chosen to favor the dissolution of the metal ions. This problem will be discussed in the following section that deals with semiconductor etching. On the other hand, the deposition of metal poses an additional challenge, namely, to attach the metal ions to the surface in order to prevent from the metal to deposit at the UME itself. A few methods have been described that have addressed this challenge.

The local deposition of gold patterns, the so-called microwriting, has been reported by Meltzer and Mandler.[59] The basic idea has been to anodically dissolve a gold UME that was held in close proximity to a negatively biased surface (Figure 15.12). In the presence of bromide ions, the Au UME generated a constant flux of $AuBr_4^-$ ions that diffuse to an indium–tin oxide substrate and were further reduced to form microcrystalline structures of gold. The bromide ions, besides acting as a

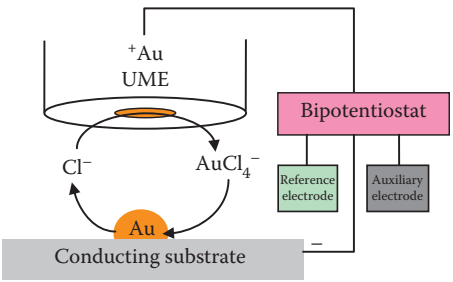
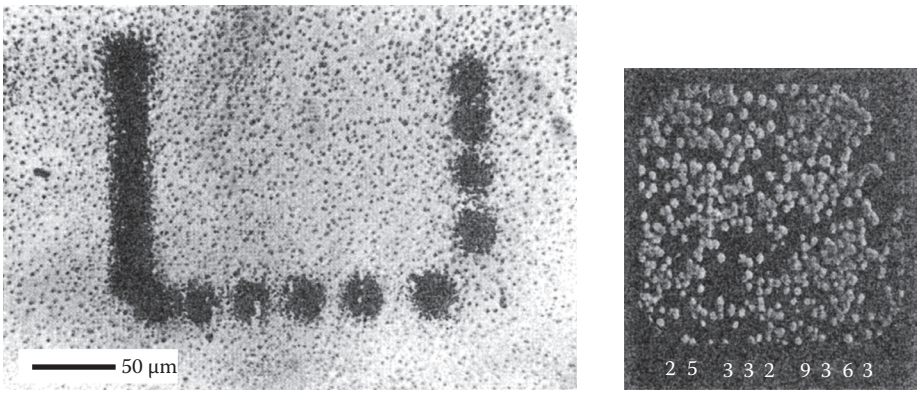


FIGURE 15.12 Schematic representation of the system for "microwriting" of gold patterns with the SECM.



(a) (b)

FIGURE 15.13 (a) Scanning electron micrograph of the gold particles deposited on ITO. (b) A SEM micrograph of the gold particles deposited, the average size of the particles is $1.0 \pm 0.1\,\mu m$. (From Meltzer, S. and Mandler, D., *J. Electrochem. Soc*., 142, L82, 1995. With permission.)

promoter for gold dissolution, were responsible for the positive feedback current that was detected while approaching the surface. This was due to their regeneration on the surface which increased their effective concentration and thus the dissolution of the gold UME. The resolution of the gold patterns, which were made of $1 \pm 0.1\,\mu m$ gold crystals, was determined by the diameter of the UME (Figure 15.13).

This approach of microwriting (also called the "UME pen") has been further used in many studies[59–66] in particular by Mandler's group. The formation of a flux of metallic ions, for example, Ag^+, $AuCl_4^-$, and Co^{2+}, was utilized for the local deposition of the respective metals on different substrates including conducting polymers,[64,65] insulators,[63] and semiconductors.[60,62] For example, de Abril et al.[61] studied the local deposition of Co. The dissolution and uptake of Co on the Au surface was investigated using SECM double potential step chronoamperometry. Danieli et al.[62] studied the reactions between electrogenerated Ag^+ and $AuCl_4^-$ ions with three different CdTe systems: thermally evaporated thin CdTe films, CdTe nanoparticles stabilized by thioglycolic acid, and 20 layers of these CdTe nanoparticles embedded in poly(diallyldimethylammonium) chloride. The flux of $AuCl_4^-$ resulted in the local formation of Au NPs on the CdTe surface, whereas local quenching of the CdTe nanoparticles embedded in thioglycolic acid multilayers was achieved by the flux of Ag^+ ions. More recently, the same approach has been used by Malel and Mandler for the electroless deposition of Au.[63] The concept and an example of deposition are shown in Figure 15.14. It was found that the reduction of $AuCl_4^-$ can be carried out by the addition of hydroquinone. Yet, this reaching although thermodynamically feasible is kinetically sluggish in homogeneous solutions. It is catalyzed by a metallic surface such as Pd nanoparticles. The authors reported that the pH had a significant effect on the nature of the deposited gold and could be correlated with the kinetics of gold ions reduction by hydroquinone. Hence, either nanoparticles or much larger crystals could be formed, depending on the pH of the deposition solution. In a subsequent study, Malel et al.[66] introduced the enzyme cellobiose dehydrogenase as a catalyst for the direct reduction of $AuCl_4^-$.

O'Mullane et al.[67] also used this approach and studied the local galvanic replacement of Cu and Ag by generation of a localized flux of $AuCl_4^-$ ions from a gold UME tip which interacts with the unbiased substrate of interest. The extent of modification with gold could be controlled through the tip–substrate distance and electrolysis time.

Heinze and coworkers[68] developed a method for deposition of silver lines initially on conducting substrates, for example, gold, and later on insulators. The deposition of perfect silver lines was

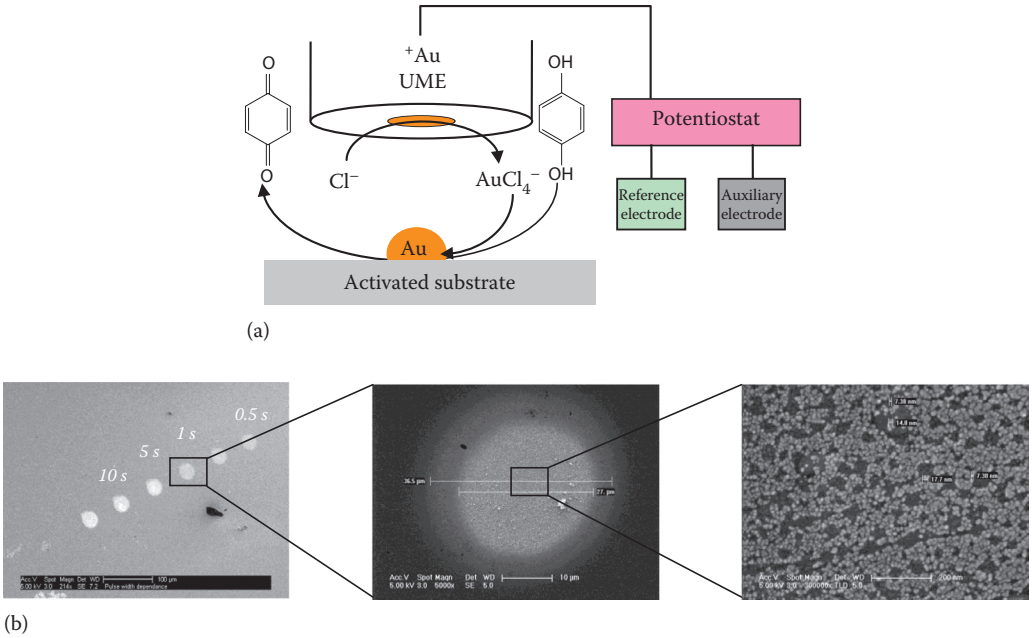


FIGURE 15.14 Electroless deposition of Au nanoparticles by the feedback mode of SECM. (a) Schematic representation of the system. (b) SEM images (different magnifications) of the locally deposited Au micro- and nanostructures. (From Malel, E. and Mandler, D., *J. Electrochem. Soc.*, 155, D459, 2008. With permission.)

accomplished by adopting the method of Shohat and Mandler,[69] vide infra, in which the pH in the volume between the UME and the substrate is altered. Specifically, silver was deposited on a negatively biased gold substrate as a result of shifting the dissociation of a silver complex (Equations 15.1 and 15.2) by decreasing the pH. The latter was caused by oxidizing nitrite ions at the tip (Equation 15.3). The resolution of the deposit was a function of the distance between the UME and the substrate. There was no broadening of the pattern, because ammonia diffused from the solution into the reaction zone and shifted the equilibrium to the silver complex. This latter phenomenon represents the first example of the "chemical lens" that results in focusing the flux of the reactive species to the surface (see Section 15.2.2):

$$[Ag(NH_3)_2]^+ + 2H^+ + e^- \rightarrow Ag^+ + 2NH_4^+ \tag{15.1}$$

$$Ag^+ + e^- \rightarrow Ag \tag{15.2}$$

$$NO_2^- + H_2O \rightarrow NO_3^- + 2H^+ + 2e^- \tag{15.3}$$

Heinze and coworkers[70] studied the local deposition of silver on a nonconducting substrate. Silver lines were formed by the local reduction of a silver chloride thin film using the feedback mode of the SECM (Figure 15.15). AgCl thin films of the thickness of 1–2 μm were vapor deposited on smooth Teflon surfaces. Hydroquinone that was electrochemically generated from benzoquinone in a mixture of ethylene glycol and water diffused to the silver chloride film and caused initially the formation of square-shaped well-ordered silver crystals via "chemical development." After an induction period, these nuclei grew through "physical development" and merged to form fine silver patterns. This caused a two-dimensional propagation of the silver until a limit of lateral extension, which was

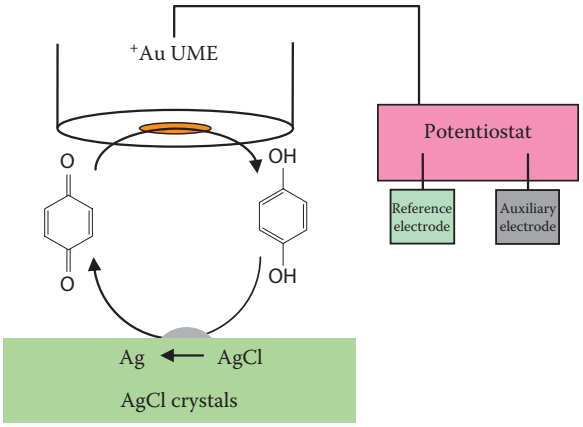


FIGURE 15.15 Schematic representation of the feedback mode for the formation of silver patterns on AgCl. (From Hess, C. et al., *Electrochim. Acta*, 42, 3065, 1997.)

probably controlled by the mixed potential in the periphery of the deposit, was reached. Then, the growth continued in a vertical direction. One of the major accomplishments of this system in respect with patterning is the development of a mechanism that resulted in the formation of patterns with smaller dimensions than the UME. That is, under appropriate conditions, the width of the silver lines was thinner than the metallic diameter of the UME. This "chemical lens," which was further used in other systems, vide infra, and was the result of the reaction of silver ions (that were present in the solution to some extent) with the hydroquinone flux, "focused" the flux of latter that reached the AgCl surface. Accordingly, the minimum line width formed with a 10 μm diameter UME was 7.5 μm. Higher resolution of silver deposition was reported by the same group using nanodes.[71]

The local etching of nickel has also been demonstrated by the same group.[72] The electrochemical reduction of nitrite (Equation 15.3) at a Pt tip close to a thin Ni layer that had been deposited on gold caused the local etching of the nickel and the exposure of the gold underneath. The addition of hydroxyl ions to the solution was successfully used as the "chemical lens" and increased substantially the resolution of the etching patterns.

A different concept for local metal deposition was described by Yatziv et al.[73] and is based on the potential-assisted ion transfer across two immiscible liquids (Figure 15.16). The essence of the method is to replace a solid UME with a micropipette filled with a liquid phase that is polarized vs. an outer phase. The controlled polarization drove the transfer of ions across the liquid–liquid interface. This flux of ions, for example, was electrochemically deposited on a conducting surface such as ITO even without applying an external potential to the surface. An improved approach[74] based on this study took advantage of the nonoptical shear force detection system that was integrated in the SECM, which provided a current-independent tip–surface distance positioning. This allowed positioning of the micropipette in very close proximity to the surface without applying a potential during the approach, and hence, resulted in an improved resolution for metal deposition. Moreover, it allowed the use of potential pulses for a discontinuous delivery of metal ions over the liquid–liquid interface.

15.2.2 Semiconductor Etching

High-resolution etching of semiconductor surfaces is of technological importance in the fabrication of microelectronic devices and is usually carried out by photolithography through several consecutive steps that include coating with photoresist, x-ray, or UV irradiation, etching, and stripping. Since the wet etching of semiconductors is an oxidation process, whereby a reactive surface, namely, the semiconductor, is subjected to strong oxidants, it was only natural to try and exploit the advantages of the SECM for this process.

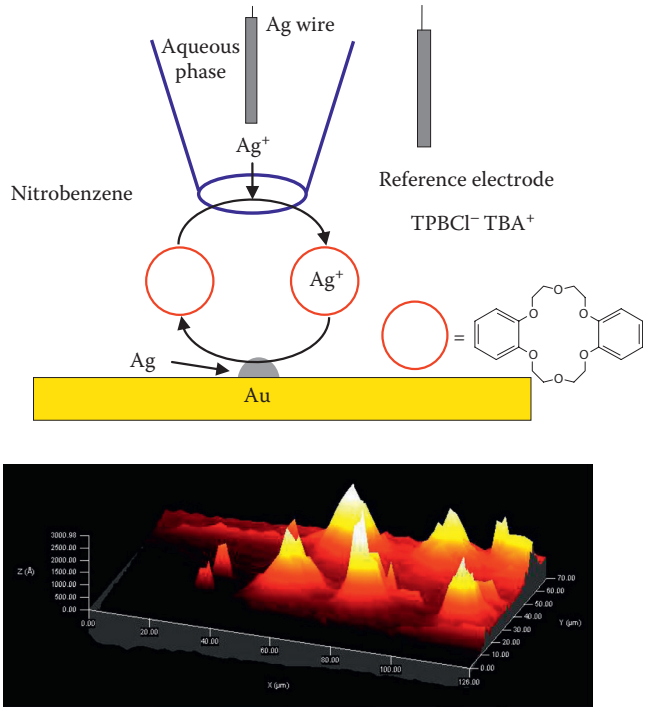


FIGURE 15.16 Schematic representation of the local deposition of Ag using the potential-assisted ion transfer across two immiscible liquids approach and the profile of the deposits (Reprinted from Yatziv, Y. et al., *J. Am. Chem. Soc*., 124, 5618, 2002. With permission. Copyright American Chemical Society 2002.)

Indeed, the few studies in which the SECM was used for etching semiconductors represent one of the most impressive examples of the capabilities of the SECM as a modifying tool. The first system was developed by Mandler and Bard[75] and involved the electrochemical generation of bromine (Figure 15.17). This strong oxidant has been widely applied for etching III–V and II–VI semiconductors. The positive feedback that was observed while approaching a GaAs wafer with an UME generating bromine was followed by the formation of clear and deep etching pits (Figure 15.18). The conditions for continuous etching required to efficiently dissolving the oxide layer that was formed. Oxide layers of GaAs are insoluble in aqueous solutions only at pH of 3–7, which caused the positive feedback current to decrease rapidly while approaching at this range of pH. On the other hand, a continuous and isotropic etching was observed at either acidic or basic media. The parameters that affected the etching size and shape were examined and included the UME size, the distance between the UME and the surface, and the electrolysis time. In a

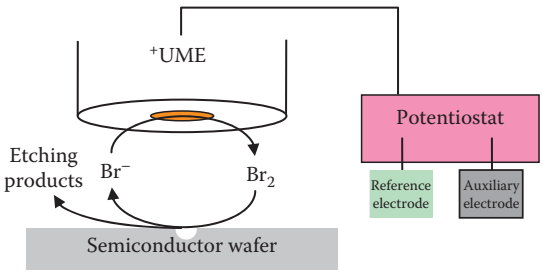


FIGURE 15.17 Overall scheme for the etching of semiconductors using the feedback mode of the SECM.

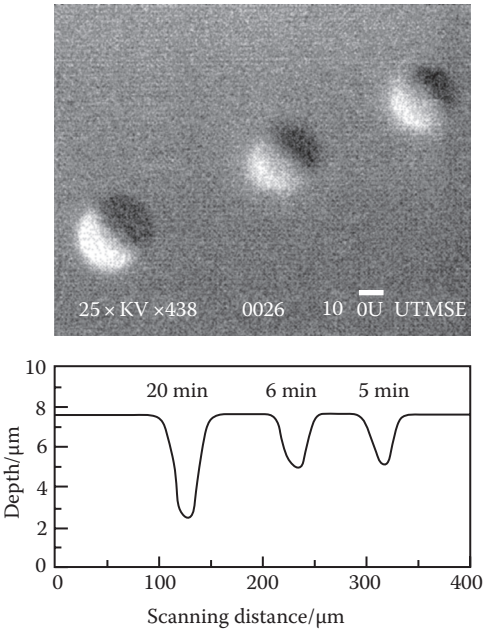


FIGURE 15.18 Scanning electron micrograph and profiles of etching pits made on a GaAs wafer as a result of leaving a 25 μm diameter Pt UME (biased at 1.0 V vs. SCE) above the surface in a 0.02 M HBr/0.1 M HCl solution for different durations. (From Mandler, D. and Bard, A.J., *J. Electrochem. Soc*., 137, 2468, 1990. Reproduced with permission of The Electrochemical Society, Inc.)

succeeding study,[76] the feedback current was carefully studied and used for collecting information about the surface processes involved in the etching of GaAs. Assignment of the energy of the valence band edge of the semiconductor was made by studying the behavior of the feedback current at various pHs and with different redox couples. Changing the pH shifted the band edges of the semiconductor, thus decreasing the overlap between the energy states of the oxidized redox species and the valence band. The feedback current was sensitive to the degree of the overlap, and therefore, could be used for determining the energy of the edge of the valence band. Moreover, the unique characteristics of the SECM to inject charge locally resulted in the selective etching of n-GaAs vs. p-GaAs. That is, n-GaAs was effectively etched by one-electron redox couples, for example, $Fe(phen)_3^{3+}$, while no etching patterns could be detected on p-GaAs even after prolonged generation of such oxidants close to its surface. This behavior was explained by the band bending of the semiconductor, that is, while locally injected holes remained on the surface of an n-GaAs leading to the efficient etching, fast diffusion of injected holes into the bulk of p-GaAs eliminated totally the possibility of its etching. This general phenomenon, which was demonstrated also in the case of silicon etching, vide infra, and had been observed in charge injection into tungsten oxide thin films,[66,67] suggests that in order to drive a local chemical reaction with the feedback mode of the SECM the charge carriers responsible for the reaction ought to be trapped on the surface.

The fast reaction of bromine with GaAs in acidic media was utilized by Sheffer and Mandler[77] who developed the scanning electrochemical imprinting microscopy by which the shape of the conductive part of the UME was imprinted in one step on the substrate. Due to the facile kinetics of GaAs etching, the volume between the entire UME (with the insulating sheath) and the substrate was not filled with reactive species but the latter diffused from the UME to the surface and back and maintained the shape of the flux that was developed at the UME. This resulted in the imprinting the shape of the Pt microelectrode on the GaAs.

Other semiconductors, for example, CdTe, $Hg_{1-x}Cd_xTe$, and GaP, have also been etched using the SECM. Nevertheless, the latter could be etched only with a stronger oxidant such as $Ru(phen)_3^{3+}$. Accordingly, a negative feedback current was detected upon approaching GaP while generating bromine, whereas an increase of the steady-state current followed the approach of GaP using the ruthenium complex.

Silicon that is the major substrate material used in the fabrication of solid-state electronic devices was naturally the next semiconductor to be etched with the SECM. Its etching has been accomplished in acidic fluoride solutions by electrogenerating bromine.[60,78] The different parameters that affected the etching process such as the nature of the oxidant and its concentration, the fluoride concentration, the acidity, and the type of silicon were examined and a detailed mechanism of the overall process based was proposed. The most interesting finding was the fact that only bromine etched silicon (with close to 100% current efficiency), whereas one-electron redox couple had no effect on the silicon surface. The explanation given by the authors is based on the requirement to trap the injected charge on silicon surface in order to result in etching. The formation of Si–Br bonds (when bromine is generated) scavenges the holes on the Si surface. On the other hand, the local injection of holes by one-electron redox couples, for example, $Fe(phen)_3^{3+}$, is insufficient since the holes are not trapped on the surface and therefore diffuse away. Micropatterning was demonstrated as well. Figure 15.19 shows an optical micrograph picture of a pattern which was formed using a 10 μm diameter platinum UME that was scanned laterally at a rate of 0.1 μm/s.

This system has been the subject of a subsequent study[79,80] that aimed at improving the etching resolution using a special focusing technique. The so-called confined etchant layer technique (CELT) involves the introduction of a soluble substance that reacts with the electrogenerated species, thus limiting the diffusion layer of the latter around the UME. The CELT technique is somewhat similar to the previously mentioned "chemical lens" reported by Heinze and coworkers.[70] While these authors used this method to increase the resolution of deposited metal patterns as well as metal etching, Tian applied the approach for increasing the resolution of semiconductor etching. Specifically, etching pits on silicon that matched closely to the UME size were formed by adding H_3AsO_3 into the solution and electrogenerating bromine as in the previous study. The diffusion layer of bromine, μ, could be calculated from the pseudo first-order reaction rate constant, k_s, of the arsenic acid (that was in access) with bromine (Equation 15.4) and the diffusion coefficient:

$$\mu = \left(\frac{D\mathrm{Br}_2}{k_S} \right)^{0.5} \tag{15.4}$$

The same group reported the micromachining of GaAs by a 3D mold using the CELT technique.[81] The etched patterns were found, approximately, to be the negative copy of the 3D molds. The comparison of CELT with the other micromachining techniques, such as 2D projection lithography and electrodischarge machining, was reported and the advantages of CELT were briefly discussed.

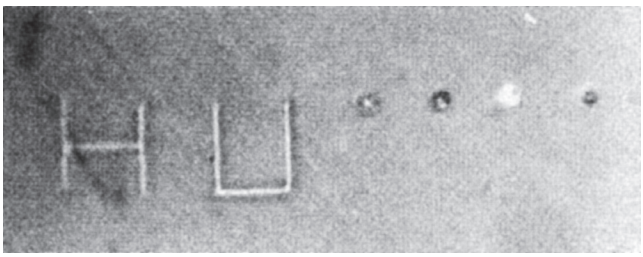


FIGURE 15.19 "HU" etching micropattern formed on silicon <111> surface via the feedback mode of the SECM using a 10 μm diameter Pt UME with a lateral scanning speed of 0.1 μm/s. The total width of the "H" is ~150 μm. (From Meltzer, S. and Mandler, D., *J. Chem. Soc. Faraday Trans.*, 91, 1019, 1995. Reproduced with permission of The Royal Society of Chemistry.)

Nevertheless, it should be noted that there is some significant difference between the "chemical lens" and CELT. That is, in the former approach the additive, hydroxyl ions, is electrochemically inactive and therefore its concentration is not affected by the electrochemical reaction at the tip. This causes the additive to react solely with the electrogenerated species and therefore "focusing" its flux even more than the UME diameter. On the other hand, the reagent added in the CELT is electrochemically active and thus is also consumed at the UME. Obviously, this will limit the "focusing" effect to the size of the UME.

15.2.3 Inorganic Materials: Deposition and Dissolution

Much of SECM work that deals with etching (or dissolution) of inorganic materials has been carried out by Unwin and his colleagues and involved the study of local dissolution kinetics. In a series of excellent papers,[56,82–88] they developed a novel approach and modeling capabilities for studying the kinetics of dissolution of inorganic crystal. These studies are described in detail elsewhere (Chapter 12) and therefore, only the concept will be presented (Figure 15.20). The principle of Unwin and Macpherson's method is to induce the dissolution of an ionic crystal by locally depleting the concentration of one (or more) of the solute ions in the solution zone between the crystal and the UME from an initial saturated value. This has been accomplished by stepping the UME potential from a value where no electrode reaction occurs to a potential at which the ion is electrolyzed at a diffusion-limited rate. This causes the crystal to dissolve and the resulting ion flux from the crystal is detected electrochemically at the UME, providing quantitative information on the kinetics of dissolution. Although no attempts have been made to pattern etching structures on crystals, the etching pits could be studied with atomic resolution as a result of the successful combination of the AFM and the SECM[85,87,88] (see Chapter 14).

They used the same approach for the quantitative study of acid-induced dissolution of enamel.[89] A UME was used to generate a flux of protons galvanostatically just above a sample surface. This produced etch features in the sample, which were characterized by white light interferometry. The technique has been applied to bovine enamel where understanding the kinetics of dissolution is important in the context of acid erosion. Dissolution has been observed as a fast process, but the high rates of mass transport in SECM allowed the surface kinetics of dissolution to be evaluated.

Shohat and Mandler[69] and later Turyan et al.[90,91] have reported additional studies of patterning inorganic materials. The goal of the first report was to develop an approach for driving local acid–base reactions on surfaces. The motivation stem from previous work in which stable metal oxides, for example, nickel hydroxide, served as an anchor for attaching organic and biological molecules onto surfaces in specific patterns.

The basic idea was to utilize an electrochemical reaction on the surface, which would be coupled with proton consumption. This configuration would be characterized by a pH gradient between the surface and the UME. The developed approach is depicted schematically in Figure 15.21.

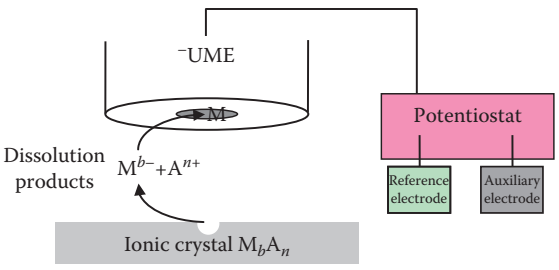


FIGURE 15.20 Schematic representation of the induced dissolution of an ionic crystal by the feedback mode of the SECM.

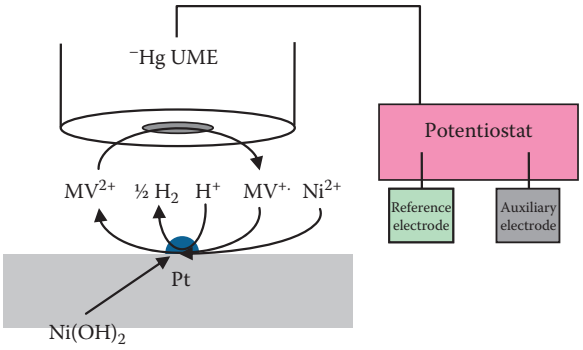


FIGURE 15.21 Schematic representation of the approach for deposition of $Ni(OH)_2$ by the feedback mode of the SECM. (From Shohat, I. and Mandler, D., *J. Electrochem. Soc.*, 141, 995, 1994.)

Specifically, the reduction of protons on the surface was driven by reduced methyl viologen, $MV^{+\cdot}$, a process that is catalyzed by platinum. A mercury UME had to be used to prevent the reduction of protons at the UME surface. As a result of the local increase of the pH on the surface beneath the UME, $Ni(OH)_2$ was irreversibly deposited. The $Ni(OH)_2$ patterns could be imaged by the SECM. Moving the UME across the deposited patterns in a Ni^{2+}-free solution that contained only MV^{2+} showed that the feedback current above the $Ni(OH)_2$ deposits was less positive than over the bare platinum surface. A detailed study suggested that the difference in the feedback current was due to the different conductivities of the Pt vs. $Ni(OH)_2$ and the catalytic effect that regenerated MV^{2+} on the metallic surface. This approach of altering the pH at the electrode surface was used further by Heinze and coworkers for driving the deposition of silver.[70]

The second study involved the local reduction or oxidation of an electrochromic material, tungsten oxide.[90,91] This system has been of particular interest since it has been the first system where the local injection of charge could be followed by an instantaneous change of a color making it possible to follow after the process by an optical microscope. The stable form of tungsten oxide is WO_3, which is colorless and poorly conductive. The reduction of WO_3 (Equation 15.5) results in the formation of deep blue tungsten bronze that is substantially more conducting:

$$WO_3(\text{colorless}) + xe^- + xM^+ \rightarrow M_xWO_3(\text{blue}) \tag{15.5}$$

Two systems were studied using the feedback mode of the SECM: the local reduction of oxidized tungsten oxide by electrochemically generated methyl viologen radical cation and the local oxidation of reduced tungsten oxide by iron(II) generated at the UME (Figure 15.22). The tungsten oxide

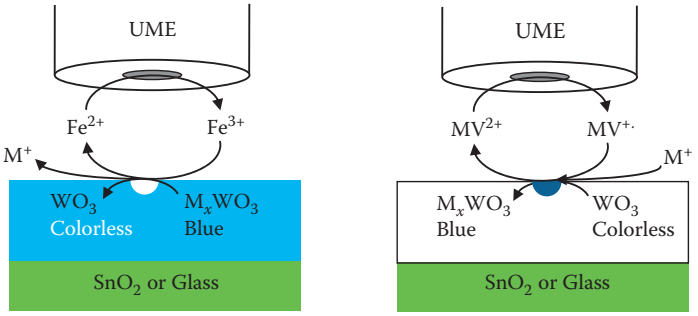


FIGURE 15.22 Schematic representation of the "writing–reading–erasing" system based on tungsten oxide. (From Turyan, I. et al., *Adv. Mater.*, 12, 330, 2000; Turyan, I. et al., *Phys. Chem. Chem. Phys.*, 5, 3212, 2003.)

films were prepared by the sol–gel method that made it possible to control the thickness of the films as well as the substrates on which they were dip-coated. Studying the feedback current while changing the concentration of the mediator, the thickness of the film and the potential of the substrate enabled the authors to conclude whether the feedback current was governed by the diffusion of the mediator or by the kinetics of charge transport inside the film. Moreover, the development of a "writing–reading–erasing" system based on the local change of the color of the tungsten oxide was demonstrated. One of the remarkable characteristics of this system was the fact that the "writing" process was extremely fast and the local injected charge was very stable.

Sauter and Wittstock used the feedback mode of SECM to form local deposits of different Prussian blue analogs on macroscopic surfaces of gold and glassy carbon.[92] Dissolution of Co and Ni sacrificial UMEs generated divalent cations in the gap between the UME and the macroscopic specimen electrode. Co^{2+} or Ni^{2+} precipitated with $Fe(CN)_6^{4-}$ formed by reduction of $Fe(CN)_6^{3-}$ at the macroelectrode. By moving the UME while generating Co^{2+} Ni^{2+}, lines could be "drawn" with a width of 130 μm. The deposited hexacyanoferrate microstructures showed catalytic activity for the reduction of Fe^{3+}, which was imaged in the feedback and generation–collection modes of the SECM.

Li et al. used the same approach[93] for locally depositing and visualizing microarrays of copper hexacyanoferrate and iron hexacyanoferrate on glassy carbon electrode, respectively. Dissolution of a sacrificial Cu UME and stripping of Fe predeposited on a platinum UME generated relevant metal cations in the gap between the UME and the GCE, which precipitated some $Fe(CN)_6^{4-}$ anions that were generated simultaneously by reduction of $Fe(CN)_6^{3-}$ at the GCE. The deposited metal hexacyanoferrate microstructures showed catalytic activity for the oxidation of dopamine and the reduction of hydrogen peroxide, respectively, which were characterized by SECM.

Studies dealing with local etching or oxidation of inorganics include a report by Engstrom and coworkers[94] who oxidized a glassy carbon electrode and then locally restored its activity by generating hydroxyl ions at the SECM tip. Denuault and coworkers[95] reported the localized etching of marble by applying a large positive potential to a UME that was held close to the $CaCO_3$ surface. Pits were produced, and the crater volumes obtained were linearly dependent on the electrolysis time. Unwin and coworkers used a similar approach[88] for studying the surface processes involved in the initial stages of the proton-assisted dissolution of the calcite single crystal. They used a combined SECM-AFM in which a platinum-coated AFM probe functioned as an electrode as well as a high-resolution topographical sensor.

15.2.4 Deposition of Conducting Polymers

The major obstacle that has prevented the much wider application of the feedback mode of the SECM for microfabricating conducting polymer patterns stems from the basic requirement that the monomer must be attached onto the surface. On the other hand, the development of strategies for patterning conducting polymers is very appealing since they are envisioned to eventually replace solid-state devices. Moreover, the SECM could be used for the local doping and undoping of conducting polymers as well. Indeed, Bard, Mirkin, Heinze, and others have used the SECM for studying surface processes at conducting polymers (see Chapter 6). In these investigations, the feedback current was studied while approaching biased surfaces coated with conducting

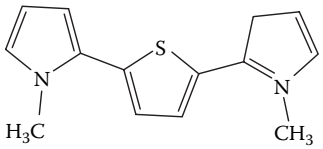


FIGURE 15.23 2,5-Bis(1-methyl-pyrrol-2-yl)-thiophene (NSN).

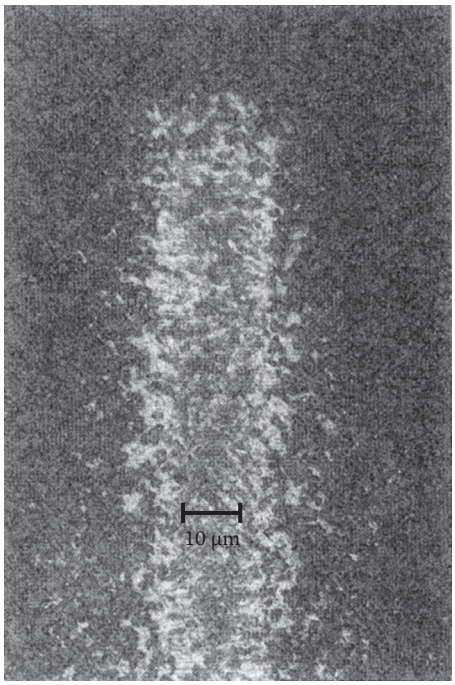


FIGURE 15.24 Pattern of poly-NSN on polymethylmethylmethacrylate. (From Borgwarth, K. et al., *Adv. Mater.*, 11, 1221, 1999.)

polymers. The behavior of the feedback current as a function of the film thickness, the concentration of the mediator in the solution, the potential of the surface, and the nature of the electrolyte provided qualitative and quantitative information about the film and electron transfer processes inside. Only those studies that aimed to microfabricate patterns of conducting polymers will be discussed here.

The first successful attempt to deposit conducting polymers using the feedback mode of the SECM was reported by Heinze and coworkers.[68] The system was further interrogated in Freiburg, Germany.[96] The essence of their method was to take advantage of the different solubility properties of the monomer vs. the polymer in different solvents. The monomer was 2,5-bis(1-methyl-pyrrol-2-yl)-thiophene (NSN) (Figure 15.23) that is very soluble in organic solvents, however, insoluble in aqueous solutions. On the other hand, the respective polymer is insoluble in either aqueous or nonaqueous solutions. A film of the monomer on different substrates was deposited by thermal evaporation and micropatterning was performed in an aqueous solution consisting of a reduced redox couple, that is, Br^-, $Ru(bpy)_3^{2+}$, and $IrCl_6^{3-}$. The oxidant that was electrogenerated at the UME caused the polymerization of the monomer to form patterns of poly-NSN. Then, the unreacted monomer was washed away by an organic solvent that did not remove the polymer. This resulted in the formation of freestanding polymeric structures (Figure 15.24) on either ITO or an insulating substrate such as polymethylmethacrylate. It was found that the mediator as well as the nature of the substrate and its interaction with the monomer and oligomers formed in the course of the polymerization had a significant effect on the polymer.

The group headed by Heinze continued its research in this area and published a few more works.[97,98] For example, micrometric structures of polythiophene were locally deposited as a result of the reaction between the monomer dissolved in the solution and a manganese dioxide surface previously locally activated by tip-generated protons. An increase in resolution by a factor of 5 was reported using the chemical lens. The addition of a scavenger that reacts with the protons produced

a significant focusing effect on the proton's diffusion field. Under these conditions, the resolution was achieved down to 8 μm with a 10 μm Pt electrode.

Zhou and Wipf reported the deposition of polyaniline patterns on gold platinum and carbon surfaces using the feedback mode of the SECM.[99] The essence of their method, termed "microreagent," was to locally increase the pH in the volume between the UME and the surface by the reduction of protons. The increase of alkalinity shifted the oxidation potential of aniline cathodically. Hence, polyaniline was electrodeposited beneath the UME as a result of applying a constant positive potential to the substrate, a potential that caused aniline oxidation under the pH conditions generated by the SECM tip. The different parameters that affected the width and thickness of the deposited films were examined and included the UME dimension and potential, substrate potential, deposition time, and UME–substrate separation. Features as small as 3 μm diameter were formed using a 3 μm diameter Pt UME. The UME and substrate potentials had to be adjusted to cause a large local decrease in proton concentration (required negative potentials at the UME) and polyaniline deposition beneath the UME only (positive potentials at the substrate). Smaller tips required more negative potentials at the UME in order to get good polyaniline deposits. Figure 15.25 shows an optical micrograph image of a structure formed by scanning the SECM tip laterally across the substrate surface. The effects of tip–substrate separation, tip potential, and deposition time were strongly merged. Close separations allowed using shorter deposition times or lower tip potentials. On the other hand, the thickness of the film could be controlled by these parameters. The polyaniline structures could be imaged by the SECM. The fact that positive feedback currents, which were larger than those detected on the bare substrate, were measured over the structures of polyaniline (while the potential of the substrate was held at 0.6 V vs. Ag/

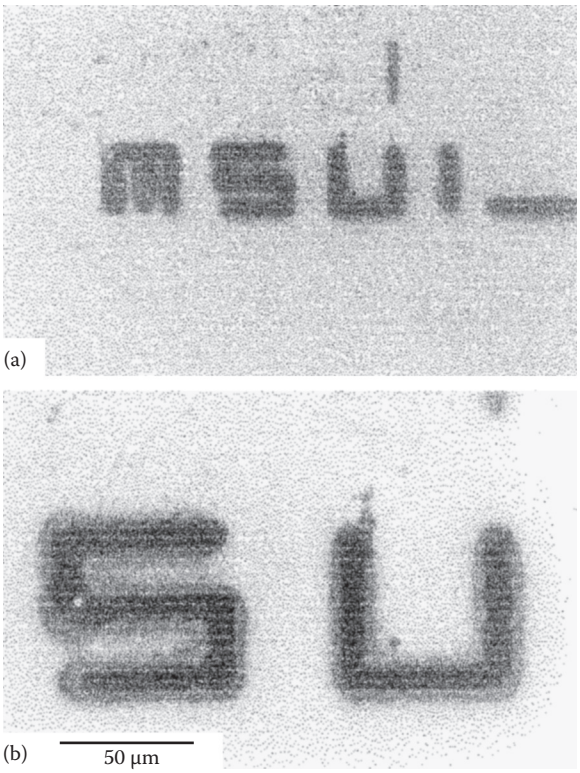


FIGURE 15.25 Optical microscope image (a) of a polyaniline pattern deposited on a gold substrate using a 10 μm Pt UME in the "microreagent" mode. (b) higher magnification (From Zhou, J. and Wipf, D.O., *J. Electrochem. Soc*., 144, 1202, 1997. Reproduced with permission from the Electrochemical Society, Inc.)

AgCl) verified their high conductivity. Finally, measuring the shorting current between the tip and the substrate upon touching the polyaniline provided a rough estimate of the conductivity of ca. 0.18 s/cm.

Microstructuring of conducting polymers by different methods including SECM was discussed by Schultze et al.[100] and Holdcroft.[101]

15.2.5 Organics, Self-Assembled Monolayers, Polymers, and Biomolecule Patterning

The exploitation of the SECM in the feedback mode for microfabrication of organic substances, polymers, and biological structures has been reported much later than its application in the direct mode as described earlier. Presumably, the reasons for this are that most organic and biological molecules do not exhibit simple one-electrode redox behavior, which prevents of using them as the mediators. Moreover, very often oxidation or reduction of these substances leads to their decomposition or deactivation. This means that in order to use the feedback mode of the SECM for micropatterning organic and biomolecules one has to first attach them onto surfaces and then develop approaches for either locally desorb/deactivate or trigger/activate them by an electrochemical reaction driven by the mediator. Although methods for attaching organic and biomolecules onto conducting as well as insulating substrates have been elaborated for many years, the second stage of altering their reactivity by a redox mediator is not straightforward. Accordingly, and as will be described, many contributions to this area have used a similar concept of locally deactivating sites on organic and biological thin film substrates.

15.2.5.1 Organics and Biomolecules

This topic was previously reviewed by Wittstock and Wilhelm.[102] The first study was reported by Matsue and coworkers[103] and aimed at creating micropatterns of diaphorase—a flavin enzyme on a glass substrate. The approach is based on the local electrogeneration of highly reactive species, for example, bromine, which deactivated immobilized enzyme molecules forming nonreactive patterns. The formation of these patterns was verified by the SECM that was used as an imaging tool. Diaphorase catalyzes the oxidation of the reduced nicotinamide cofactor NADH by an artificial mediator such as ferrocenylmethanol. Therefore, the latter was introduced into the solution together with NADH and the diaphorase-nonreactive patterns were detected by the negative feedback current observed while approaching a UME biased at a positive potential that caused the oxidation of the mediator (Figure 15.26). The size of the deactivated zones reflected the diffusion length of the electrogenerated species and therefore, their diameter varied roughly with the square root of the pulse period of deactivation. Smaller patterns were formed as a result of electrogenerating chlorine instead of bromine. The higher resolution could be explained by the "chemical lens" (or CELT), which suggested that the diffusion layer of chlorine was thinner due to its reaction with water.

The SECM has been used by the same group as a means of characterizing enzyme and antigen/antibody patterns[104] of different types. Nonetheless, a glass capillary pen formed the patterns. Later, Matsue and coworkers[105] presented a slightly different approach, in which instead of deactivating an enzyme, silane monolayers attached onto glass surfaces have been modified locally by reactive species, that is, hydroxyl radicals. Three procedures for the preparation of diaphorase micropatterns have been demonstrated (Figure 15.27). Through all these approaches, hydroxyl radicals were electrochemically generated by the Fenton's reaction where Fe^{3+} was reduced at the SECM tip in the presence of H_2O_2 (Equations 15.6 and 15.7):

$$Fe^{3+} + e^- \rightarrow Fe^{2+} \tag{15.6}$$

$$Fe^{2+} + H_2O_2 \rightarrow Fe^{3+} + HO^{\bullet} + HO^- \tag{15.7}$$

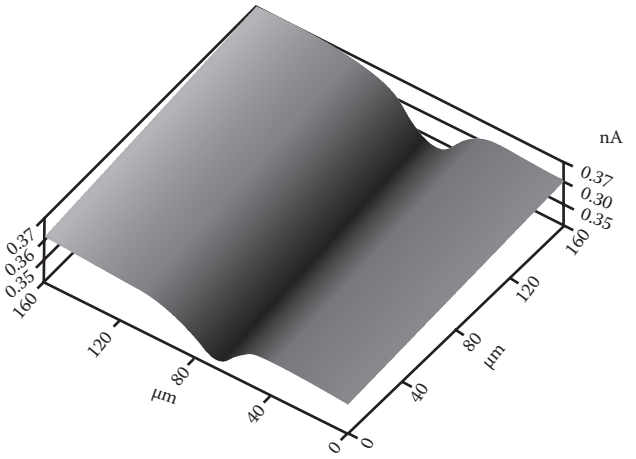


FIGURE 15.26 SECM image of a diaphorase-immobilized substrate with a deactivated line formed by scanning an UME while generating bromine across the surface. (Reprinted with permission from Shiku, H., Takeda, T., Yamada, H., Matsue, T., and Uchida, I., *Anal. Chem*., 67, 312, 1995. Copyright 1995 American Chemical Society.)

The radicals reacted with the end-functional groups of the monolayers altering their chemical and physical properties in terms of their ability to adsorb or covalently attach the enzyme. The SECM itself was used, as previously described, for verifying the presence of attached enzymes. In the first approach (Figure 15.27A), hydroxyl radicals were used to locally degrade octadecylsilyl chains. The hydrophobic chains that are capable of adsorbing diaphorase became significantly more hydrophilic which prevented diaphorase adsorption, hence, creating enzyme-free zones. The second concept (Figure 15.27B) also producing enzyme-free zones involved the degradation of (3-aminopropyl) trimethoxysilane-derived monolayers by hydroxyl radicals. The enzyme was covalently attached through the amino groups of the unaffected molecules using glutardialdehyde as a cross-linker. The resolution of the patterns, which were formed, depended on the different reaction paths that the hydroxyl radicals could follow. The concentration of these highly reactive species depended on the concentration of the oxidized and reduced iron ions as well as on that of hydrogen peroxide. While increasing the concentration of Fe^{3+} increased the levels of the radicals, both Fe^{2+} and H_2O_2 reacted with OH·. In other words, the diffusion layer of the hydroxyl radicals became thinner by the "chemical lens" mechanism.

The third approach (Figure 15.27C) resulted in "positive" patterns, that is, the formation of defined areas where diaphorase was selectively attached. This approach consisted of three steps. Initially, a mercapto-terminated monolayer was locally exposed to hydroxyl radicals, which were formed via the Fenton's reaction. Two simultaneous processes occurred, the monolayer in the areas exposed to the radicals was removed to form hydroxyl-terminated surface. At the same time, the mercapto groups in the remaining area were converted to sulfonate groups in an oxidation process driven by the H_2O_2/Fe^{2+} solution. Diaphorase was immobilized onto the hydroxylated sites through the glutardialdehyde linker and verified by the SECM using the same enzymatic catalyzed reaction as before[105] (Figure 15.28).

Micropatterning of surfaces with organic and biological microstructures by the feedback mode of SECM was described by Mandler and coworkers.[106] The approach was based on the introduction of the spatial resolution by local deposition of gold particles followed by monolayer formation and functionalization. Specifically, gold patterns were deposited locally on silicon wafers with the SECM as a result of the controlled anodic dissolution of a gold UME. The gold patterns were further used as microsubstrates for assembling cystamine monolayers to which either fluorescein isothiocyanate (FIT) or GOx was covalently attached. Characterization of the organic monolayers,

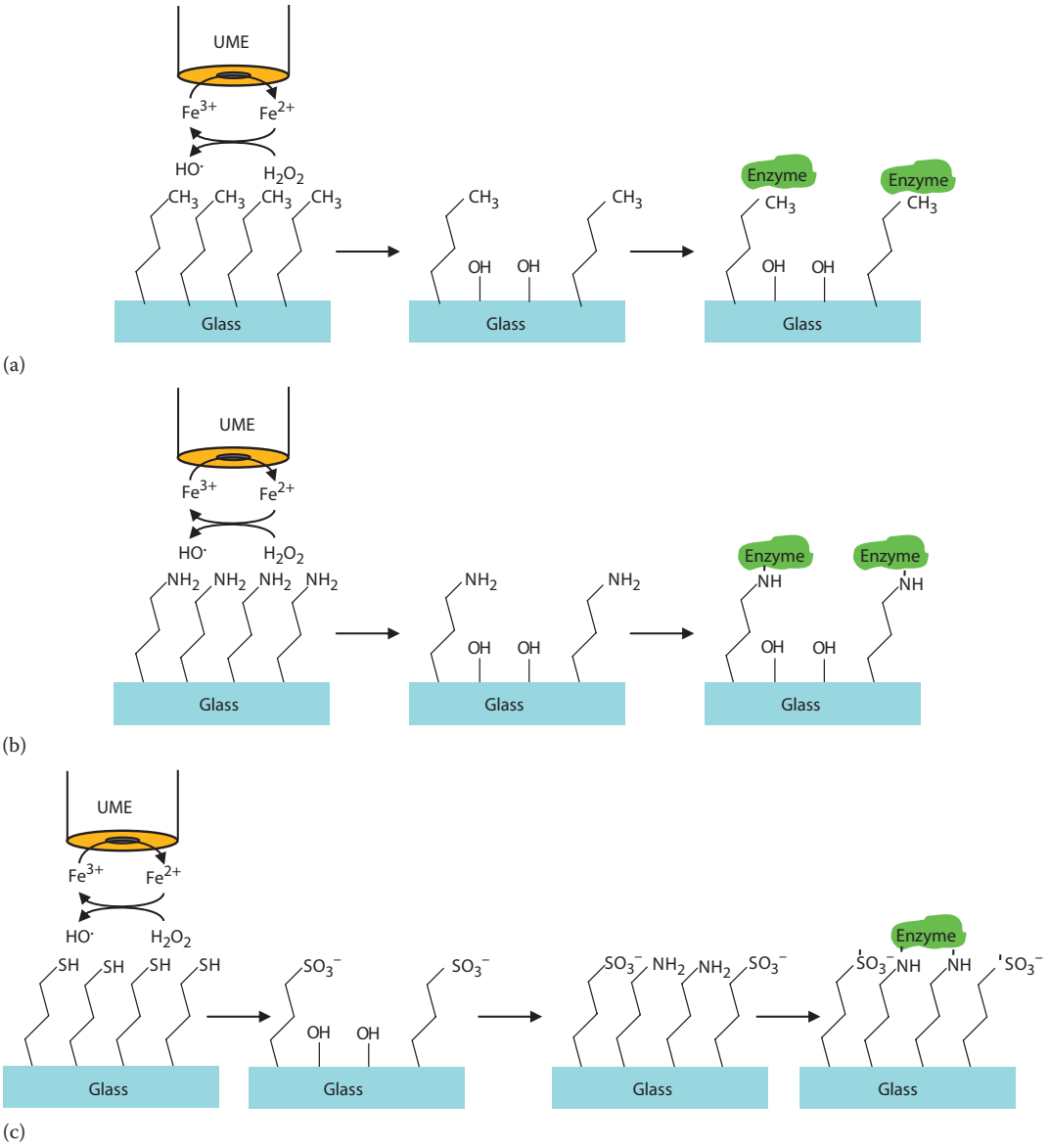


FIGURE 15.27 Schematic representation of the different approaches for micropatterning glass with diaphorase via electrogenerating hydroxyl radicals: (a) diaphorase is physically adsorbed on hydrophobic zones, (b) diaphorase is covalently bound through nonattacked amino groups, and (c) diaphorase is covalently attached to hydroxyl-activated sites.

as well as the biological activity of the enzyme patterns, was carried out by fluorescence microscopy and the SECM, respectively.

Another example of micropatterning surfaces with biological molecules by the feedback mode of the SECM has been demonstrated by Wipf and coworkers[107] and involves the attachment and detachment of biotin on a glassy carbon electrode. Biotin–avidin chemistry has been extensively used as a means of modifying surfaces by protein immobilization. The high specificity of the biotin–avidin interaction allowed to selectively attach any biomolecule containing an avidin label. Two complementary approaches have been developed for either locally attaching biotin hydrazide or locally removing attached biotin. In the former case, an active product was formed at the UME upon

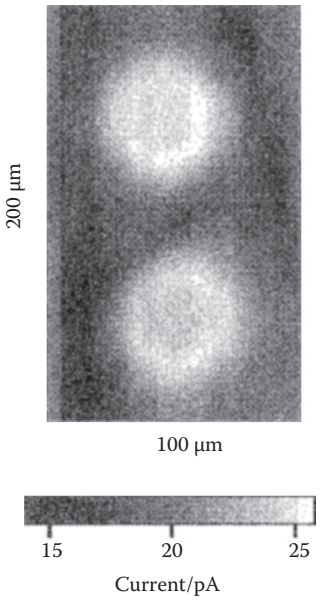


FIGURE 15.28 SECM image of diaphorase attached through the local degradation of a mercapto-terminated monolayer that was subsequently treated with (3-aminopropyl)trimethoxysilane. (Reprinted with permission from Shiku, H., Uchida, I., and Matsue, T., *Langmuir*, 13, 7239, 1997. Copyright 1997 American Chemical Society.)

oxidizing biotin hydrazine that diffused to the glassy carbon electrode and was irreversibly attached through an unknown mechanism. The biotinylated regions were further reacted with a fluorescent avidin in order to form fluorescent spots. A number of parameters affected the formation and resolution of the patterns, namely, the potentials of the UME and the substrate as well as the distance and the speed at which the UME was moved. The potential of the UME had to be sufficiently positive (1.1 V vs. Ag/AgCl) to generate a large but local increase in the activated form of the biotin, while the potential of the surface had to be controlled to avoid generation of active biotin all over the glassy carbon electrode (which occurred at both negative and positive potentials). Moreover, because of the high reactivity of the oxidized biotin, the UME had to be positioned within the thin diffusion layer of the generated species and its scan speed had to be rather slow (between 0.1 and 0.5 μm/s). Optimizing these parameters resulted in reproducible and clear patterns of attached biotin.

On the other hand, the local removal of attached biotin–avidin complex has been accomplished by electrochemically generating hydroxide ions. Investigating the mechanism of the reaction between hydroxide ions and the various constituents of the system led the authors to conclude that the reaction occurring at the electrode was a hydrolysis of all the amide bonds involved in the immobilization reaction.

Matsue and coworkers[108] described a hybrid system consisting of SECM and scanning confocal microscope (SCFM) for micropatterning and imaging of diaphorase immobilized on glass. Simultaneous imaging of the diaphorase spots demonstrated that the SECM can provide information on a localized enzyme reaction, while the SCFM afforded information on the location of the active enzyme. By using this SECM/SCFM system, spatially selective deactivation of diaphorase was performed by inducing a local electrochemical reaction or by irradiating with the focused laser. The resulting patterns of diaphorase were simultaneously imaged with the SECM/SCFM system.

In a following study[109] from the same group, they showed that it was possible to switch the properties of an albumin-coated substrate that blocked protein adsorption and cell adhesion. As a result of locally generating OBr^-, there was a rapid switch to cell adhesive. Wittstock and

coworkers[110] used a similar approach for also switching on the adhesion properties of an organic layer based on oligomers of ethylene glycol. Proteins adsorbed exclusively on the electrochemically treated regions. Jin and coworkers[111] employed the same concept using a newly developed carbon UME for the local deactivation of HRP. More recently, they presented a slightly different approach where instead of generating Br_2 they electrogenerated OH^-.[112] They claimed that the resolution of the deactivated structures was higher due to the slower rate of reaction between this species and HRP.

Bard and coworkers described a novel SECM-based surface patterning of fluorescent molecules onto a solid substrate by forming covalent bonds through a click chemistry reaction.[113] Patterned images could be observed by their fluorescence and the formation of Liesegang rings in the diffusion reaction system was also detected.

15.2.5.2 Self-Assembled Monolayers

There are different examples where the feedback mode of SECM has been used to locally deposit or modify SAMs. A few groups have been involved in this activity. Heinze and coworkers were able to form patterns of SAMs by locally etching a thin Ni film that was deposited on Au, as a result of locally generating nitric acid from nitrous acid.[72] On the exposed Au, SAMs of alkanethiols were assembled onto which fluorescent liposomes containing tetramethylrhodamine-labeled phospholipids were adsorbed. Wittstock and his group demonstrated several approaches for locally modifying SAMs. A combined instrument for electrochemical STM and SECM was constructed and was capable of bringing a combined STM-SECM probe into tunneling contact with a sample and retracted it by defined distances to perform electrochemical experiments outside the tunneling distance but within a separation of 5–30 nm from the sample. The capabilities have been illustrated by the investigation and modification of SAMs of dodecanethiolate on gold. In other studies, they electrogenerated Br_2 at the SECM tip and locally modified PEG-based SAMs.[114] This local treatment changed the properties of the SAMs and allowed the local growth of bacteria.[115]

Additional studies involving mono- and multilayers were carried out by Cougnon and coworkers[116,117] who took advantage of the electrochemical reduction of aryldiazonium or the oxidation of amines (Figure 15.29). Specifically, the in situ generation of aryldiazonium was accomplished by the electrochemical reduction of an aromatic nitro precursor in the presence of $NaNO_2$ and HCl. The aryldiazonium was reduced locally on the surface beneath the SECM tip and formed an organic multilayer. The efficiency of this strategy strongly depended on the kinetics of the diazotization reaction, as the reduction of the diazonium salt also occurred at the SECM tip. Controlling the concentration of $NaNO_2$ in the cell allowed the expansion of the diffusion field of the electrogenerated amine and limited the reduction of the diazonium salt at the tip. To solve this problem of the reaction of the aryl radicals on the tip, they developed an alternative method[117] (Figure 15.29B) whereby amines were electrochemically formed at the tip and oxidized at the surface. The SECM was used to characterize the local deposition of the organic layer.

15.2.5.3 Polymers

The group of Combellas and Kanoufi contributed significantly to patterning of polymers by the feedback mode of SECM.[118–124] Initially, they showed[119] that polytetrafluoroethylene (PTFE) could be electrochemically reduced into a carbon material. This reduced material was stable and allowed further reduction of aryldiazonium, metal ions, or grafting of polymers. For example, they demonstrated[118] the localized metallization, that is, by Au and Cu, of the reduced carbon material by an electroless deposition procedure. PTFE was reduced locally at the contact or in the vicinity of an electrode by SECM. Similarly, they were able to graft polyacrylic acid onto PTFE once the latter was reduced locally by an electrode.[120] Their next stage involved the localized reduction of fluoropolymers by the radical anion of a redox mediator electrogenerated at an UME. Approach curves with different redox mediators were used to investigate the reduction mechanism of the

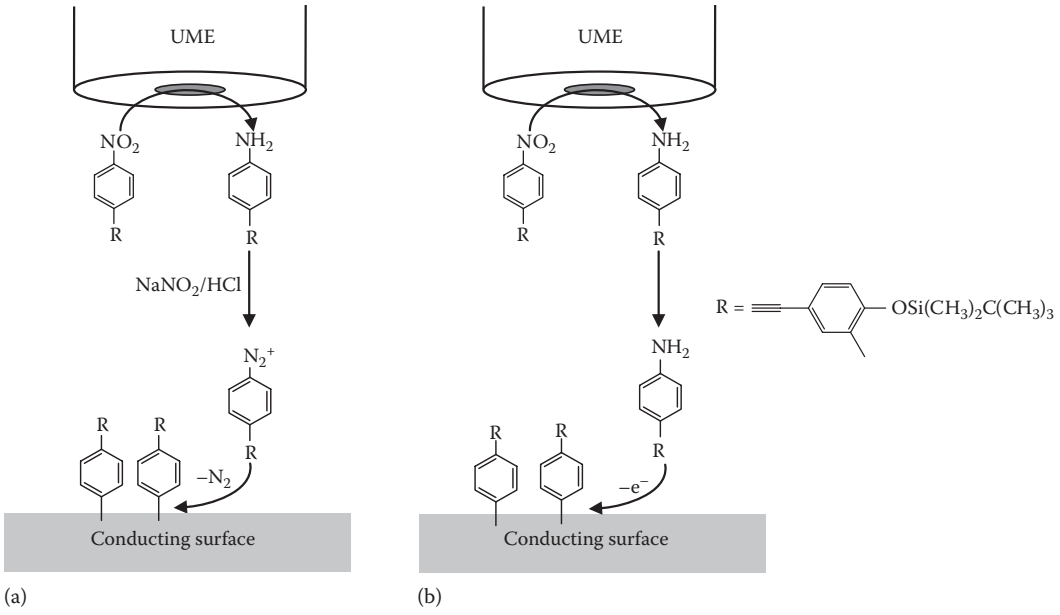


FIGURE 15.29 Two approaches used by Cougnon et al. to locally activate and attach phenyl and aliphatic amino derivatives by the feedback mode of SECM. (a) In-situ formation of diazonium; (b) oxidation of an aromatic amine. (From Cougnon, C. et al., *Angew. Chem. Int. Ed*., 48, 4006, 2009; Cougnon, C. et al., *Angew. Chem. Int. Ed*., 48, 7395, 2009.)

fluoropolymer. Different factors are discussed, such as the monomer reduction mechanism, the kinetic control by the surface modification growth, and the conductivity of the modified surface.

The PTFE reduction process was analyzed quantitatively by the current transients of SECM.[122] In a short time, a nucleation process accounts for the PTFE reduction evolution. The nucleation rate followed a potential dependency similar to that observed for conducting polymer growth or metal deposition. At long time, the expansion of the PTFE carbonization proceeded in a hemi-ellipsoidal fashion, the radial expansion being much easier than the in-depth one. A rough model was proposed in which the reduction along the in-depth direction is mainly controlled by a diffusive process while the material resistivity controls the radial expansion.

Combellas et al. continued to use the same concept and were able to locally reduce PTFE by electrochemically generating a strong reductant such as 2,2′-dipyridyl radical anion.[123] They found that the dimensions of the etched stripes were correlated to the scan rate, the charge passed through the circuit, and the electrode radius. The expansion of the PTFE carbonization was governed by an in-depth diffusive process. In a following contribution,[124] they took advantage of this approach and successfully polymerized vinylic monomers such as 2-dimethylaminoethyl methacrylate. Two approaches were presented: a two-step process where the PTFE was first reduced by a SECM tip and a one-step process whereby polymerization was accomplished by simultaneously generating the strong reductant, for example, 2,2′-dipyridyl radical anion in the presence of the methacrylated monomer.

More recently, the same group applied the SECM in the feedback mode for the debromination of a surface-bound polymerization initiator.[32] This caused that ATRP took place only on the areas, which were not debrominated. They reported that the surface reduction rate, controlled by the UME scan rate and the reducer strength, affected the dimensions of the patterns. The reducer strength allowed tuning the surface density of the initiator layer and then the elongation of the polymer brushes grown in the locally etched regions.

A recent and elegant example by Kanoufi and coworkers aimed at constructing a multiscaled electrochemical probe for SECM experiments.[125] The probe was fabricated by wet chemical etching

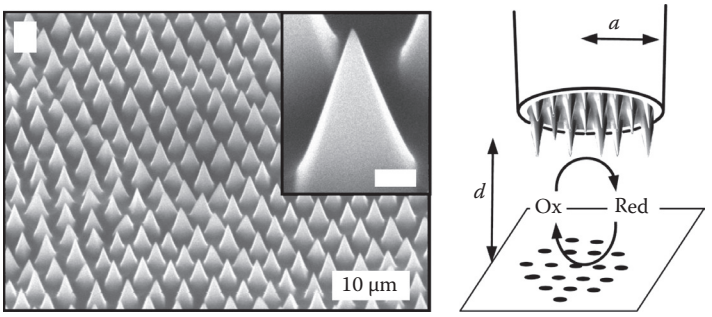


FIGURE 15.30 (a) SEM image of a part of the nanotip electrode array. The inset shows a single nanotip at higher magnification (white bar: 1 μm). (b) Principle of the surface patterning with an etched optical fiber bundle electrode (radius: *a*, electrode/substrate distance. (Reprinted from Deiss, F. et al., *Anal. Chem*., 82, 5169, 2010. With permission. Copyright: American Chemical Society 2010).

of an optical fiber bundle (total diameter: 300 μm) comprising 6000 individually cladded optical cores, which was sputter-coated by a thin gold layer resulting in ~6000 nanotips (Figure 15.30). Numerical simulations and approach curves were used to study the probe properties and the influence of the global shape and of the nanotips. Numerical simulations showed that the approach curves did not depend on the shape of the electrode but rather on the total height of the protuberance of its electroactive part. These new SECM probes were then used to pattern a Teflon surface similarly to the way mentioned earlier. By controlling the timescale of the applied potential pulses, the thickness of the reaction layer was confined at each nanotip, and the nanotip pattern was electrochemically transferred onto the nonconductive surface.

15.3 PERSPECTIVE APPROACHES

In order to evaluate the perspectives of the SECM as a tool for micro- and nanopatterning, its advantages and disadvantages need to be considered. In this last section, we examine the capabilities of the SECM that are essential for a patterning technique, namely, speed, resolution, and scope of materials that can be patterned.

15.3.1 Speed of Patterning

Similar to any other scanning probe microscopic technique, the speed of patterning is limited to the movement of the probe across the substrate as well as to the rate of the patterning reaction. The latter is sometimes diffusion controlled, which suggests that the UME can be scanned relatively fast when it is held very close to the surface. This obviously requires a reliable and fast feedback mechanism in order to assure that the UME does not crash onto the surface. Examples of micropatterning surfaces with speeds exceeding microns per second have been demonstrated in the case of copper etching,[126] tungsten oxide reduction,[90] and deposition of a conducting polymer.[96] At the same time, increasing the speed of the UME causes the steady-state current to increase because of moving faster than the growth of the diffusion layer as has been shown by Borgwarth et al.[127] and termed the picking mode. The picking mode is of particular use when the nature of the surface is not investigated and the importance is to keep the tip at a constant distance above it. Under such conditions, the diffusion layer is substantially smaller than the UME diameter (including the insulating sheath), which results in patterns with the width of that of the conducting part of the UME. Increasing the UME speed will make it possible to apply smaller tips, which will maintain also a reasonable aspect ratio of the patterns that are formed.

On the other hand, there are many cases where the chemical or electrochemical reactions taking place on the surface are the rate-limiting step in the patterning process. This will limit the patterning rate or will require developing other approaches whereby the whole pattern is made at the same time. At present, the common approaches of the SECM, that is, the direct and feedback modes cannot compete with the conventional photolithography methods. Nonetheless, future approaches such as multi-tip configuration might dramatically enhance the SECM capabilities in terms of speed of surface modification. Such an approach has recently been demonstrated by Combellas and coworkers.[125] A different approach, that is, scanning electrochemical imprinting microscopy,[77] whereby the shape of the tip is imprinted on the surface, also opens interesting alternatives to the conventional patterning methods.

In this respect, it should be mentioned that the combined AFM and electrochemistry could provide much faster patterning speeds as the formation of patterns is not limited to solution diffusion. This means that the direct mode of SECM that is not manifested by techniques such as EPN[54] could be used in a programmable approach for making nanometric patterns with speeds of micrometer per second. Yet, the scope of these methods is still somewhat limited and usually involves oxidation of monolayers.

15.3.2 Resolution

While the speed of patterning is probably the major reason that limits the wide application of scanning probe techniques as surface modification tools, their resolution capabilities is the driving force that keeps them as future competitors of nowadays methods. The resolution of the patterns formed by the SECM depends on the size and geometry of the UME as well as on the distance it is held above the surface. At the same time, the resolution of the patterns can easily be controlled (as compared with other SPM techniques) by different approaches such as the "chemical lens." This will enable forming patterns with different widths just by controlling the electrolyte and surface–UME distance rather than by changing the UME.

In the direct mode, the resolution is governed by the electric field distribution which therefore requires that the UME be brought very close to the surface. At the same time, the direct mode does not need that the UME will have a disk shape insulated in an inert matrix but rather that the active part of the UME will be small and close to the surface. As described earlier, high-resolution modification of surfaces by the direct mode of the SECM is basically an STM-driven approach, which enables to carry out in particular nanopatterning. On the other hand, the resolution of the feedback mode is presently governed by the technological abilities of producing micro- and nanoelectrodes with well-defined shapes. The first report of constructing a nanoelectrode was described by Mirkin and coworkers.[128] Since then, numerous methods have been developed for the fabrication of nanoelectrodes.[111,128–146] The latter have been used in combined AFM-SECM systems,[132,135] for imaging different surfaces,[138,142] for studying electron transfer,[139] and for other applications. Nevertheless, such nanoelectrodes are still not in wide use in SECM and their application is by far not trivial in particular due to the deficient control of tip–surface distance, unless another mechanism, for example, shear force mode[134,141] or AFM, is used. If their construction could be popularized, the SECM ability to modify surfaces in the feedback mode with much higher resolution will be substantially increased.

15.3.3 Scope of Materials and Approaches

The major advantage of the SECM as a patterning tool lies in its ability to drive a wide range of chemical and electrochemical surface reactions. As compared with other scanning probe techniques, for example, STM and AFM, in SECM, the mechanism of the surface process is usually known (in the feedback mode) and involves electrochemical and chemical processes. Moreover, the

conditions for patterning are mild, that is, the UME is biased moderately, and, therefore, processes are much easily studied and controlled. This has enabled to exploit the SECM in the feedback mode for driving almost all type of processes including oxidation–reduction, acid–base, and precipitation reactions, which resulted in a variety of surface patterning. These accomplishments stand in contrast with the fact that there are very few straightforward approaches that can be used for patterning surfaces with metals, inorganic materials, as well as organics and biochemicals. The conventional photolithographic methods are capable of depositing metals and inorganic materials, that is, oxides, whereas novel methods such as microcontact printing enables pattern surfaces mostly with organic materials. The fact that the SECM (in the feedback mode) does not require that the surface be conductive makes it an attractive method for the modification (and characterization) of inorganic materials, for example, salt crystals and amorphous materials, such as glass, and in the future of biological membranes and tissues.

Different approaches have been developed based on the feedback mode. Besides driving irreversible electrochemical surface processes such as the dissolution of metals and semiconductors, the SECM has been used for driving acid–base reactions, generating radicals that deactivated biological and organic substances, and shifting precipitation reactions that affected the dissolution of salts.

Finally, the SECM is not limited to electroactive materials as well. Novel approaches based on other modes that are currently being investigated enable to modify surfaces with organic monolayers, polymers, and biological compounds. This might be the major niche where the future of the SECM in terms of nanofabrication lies. For this, generic approaches that will increase the speed of modification will have to be developed.

In conclusion, the SECM was born as a result of the successful combination of UMEs and the scanning probe microscopic techniques. Its extraordinary versatility with the recent advances in our abilities to construct smaller electrodes has turned it into one of the key players for surface nanopatterning.

REFERENCES

1. Mandler, D., Meltzer, S., and Shohat, I., *Israel Journal of Chemistry*, 36, 73, 1996.
2. Lin, C. W., Fan, F. R. F., and Bard, A. J., *Journal of the Electrochemical Society*, 134, 1038, 1987.
3. Craston, D. H., Lin, C. W., and Bard, A. J., *Journal of the Electrochemical Society*, 135, 785, 1988.
4. Husser, O. E., Craston, D. H., and Bard, A. J., *Journal of Vacuum Science & Technology B*, 6, 1873, 1988.
5. Husser, O. E., Craston, D. H., and Bard, A. J., *Journal of the Electrochemical Society*, 136, 3222, 1989.
6. Forouzan, F. and Bard, A. J., *Journal of Physical Chemistry B*, 101, 10876, 1997.
7. El-Giar, E. M., Said, R. A., Bridges, G. E., and Thomson, D. J., *Journal of the Electrochemical Society*, 147, 586, 2000.
8. Jansson, A., Thornell, G., and Johansson, S., *Journal of the Electrochemical Society*, 147, 1810, 2000.
9. Staemmler, L., Suter, T., and Bohni, H., *Electrochemical and Solid State Letters*, 5, C61, 2002.
10. Eckhard, K., Etienne, M., Schulte, A., and Schuhmann, W., *Electrochemistry Communications*, 9, 1793, 2007.
11. Tenent, R. C. and Wipf, D. O., *Journal of the Electrochemical Society*, 150, E131, 2003.
12. Tenent, R. C. and Wipf, D. O., *Journal of Solid State Electrochemistry*, 13, 583, 2009.
13. Wuu, Y. M., Fan, F. R. F., and Bard, A. J., *Journal of the Electrochemical Society*, 136, 885, 1989.
14. Kranz, C., Gaub, H. E., and Schuhmann, W., *Advanced Materials*, 8, 634, 1996.
15. Kranz, C., Ludwig, M., Gaub, H. E., and Schuhmann, W., *Advanced Materials*, 7, 38, 1995.
16. Kranz, C., Ludwig, M., Gaub, H. E., and Schuhmann, W., *Advanced Materials*, 7, 568, 1995.
17. Kranz, C., Wittstock, G., Wohlschlager, H., and Schuhmann, W., *Electrochimica Acta*, 42, 3105, 1997.
18. Evans, S. A. G., Brakha, K., Billon, M., Mailley, P., and Denuault, G., *Electrochemistry Communications*, 7, 135, 2005.
19. Szunerits, S., Knorr, N., Calemczuk, R., and Livache, T., *Langmuir*, 20, 9236, 2004.
20. Fortin, E., Defontaine, Y., Mailley, P., Livache, T., and Szunerits, S., *Electroanalysis*, 17, 495, 2005.
21. Actis, P., Manesse, M., Nunes-Kirchner, C., Wittstock, G., Coffinier, Y., Boukherroub, R., and Szunerits, S., *Physical Chemistry Chemical Physics*, 8, 4924, 2006.

22. Fortin, E., Mailley, P., Lacroix, L., and Szunerits, S., *Analyst*, 131, 186, 2006.
23. Kirchner, C. N., Szunerits, S., and Wittstock, G., *Electroanalysis*, 19, 1258, 2007.
24. Sugimura, H., Uchida, T., Kitamura, N., Shimo, N., and Masuhara, H., *Journal of Electroanalytical Chemistry*, 361, 57, 1993.
25. Wittstock, G., Hesse, R., and Schuhmann, W., *Electroanalysis*, 9, 746, 1997.
26. Widrig, C. A., Chung, C., and Porter, M. D., *Journal of Electroanalytical Chemistry*, 310, 335, 1991.
27. Yang, D. F., Wilde, C. P., and Morin, M., *Langmuir*, 12, 6570, 1996.
28. Yang, D. F., Wilde, C. P., and Morin, M., *Langmuir*, 13, 243, 1997.
29. Wilhelm, T. and Wittstock, G., *Electrochimica Acta*, 47, 275, 2001.
30. Wittstock, G., *Fresenius Journal of Analytical Chemistry*, 370, 303, 2001.
31. Schwamborn, S., Stoica, L., Neugebauer, S., Reda, T., Schmidt, H. L., and Schuhmann, W., *Chem Phys Chem*, 10, 1066, 2009.
32. Hauquier, F., Matrab, T., Kanoufi, F., and Combellas, C., *Electrochimica Acta*, 54, 5127, 2009.
33. Chen, P. C., Chen, R. L. C., Cheng, T. J., and Wittstock, G., *Electroanalysis*, 21, 804, 2009.
34. Han, S. B., Duan, Y. L., and Li, F. F., *Acta Chimica Sinica*, 65, 2750, 2007.
35. Shacham, R., Avnir, D., and Mandler, D., *Advanced Materials*, 11, 384, 1999.
36. Shacham, R., Mandler, D., and Avnir, D., *Chemistry—A European Journal*, 10, 1936, 2004.
37. Toledano, R., Shacham, R., Avnir, D., and Mandler, D., *Chemistry of Materials*, 20, 4276, 2008.
38. Schneir, J., Sonnenfeld, R., Marti, O., Hansma, P. K., Demuth, J. E., and Hamers, R. J., *Journal of Applied Physics*, 63, 717, 1988.
39. Li, W. J., Virtanen, J. A., and Penner, R. M., *Applied Physics Letters*, 60, 1181, 1992.
40. Sugimura, H., Uchida, T., Kitamura, N., and Masuhara, H., *Journal of Physical Chemistry*, 98, 4352, 1994.
41. Sugimura, H. and Nakagiri, N., *Nanotechnology*, 6, 29, 1995.
42. Sugimura, H. and Nakagiri, N., *Thin Solid Films*, 282, 572, 1996.
43. Sugimura, H. and Nakagiri, N., *Journal of Vacuum Science & Technology A—Vacuum Surfaces and Films*, 14, 1223, 1996.
44. Sugimura, H., Okiguchi, K., Nakagiri, N., and Miyashita, M., *Journal of Vacuum Science & Technology B*, 14, 4140, 1996.
45. Corbitt, T. S., Crooks, R. M., Ross, C. B., Hampdensmith, M. J., and Schoer, J. K., *Advanced Materials*, 5, 935, 1993.
46. Schoer, J. K., Zamborini, F. P., and Crooks, R. M., *Journal of Physical Chemistry*, 100, 11086, 1996.
47. McCarley, R. L., Hendricks, S. A., and Bard, A. J., *Journal of Physical Chemistry*, 96, 10089, 1992.
48. Lebreton, C. and Wang, Z. Z., *Scanning Microscopy*, 8, 441, 1994.
49. Lebreton, C. and Wang, Z. Z., *Surface Science*, 382, 193, 1997.
50. Maoz, R., Frydman, E., Cohen, S. R., and Sagiv, J., *Advanced Materials*, 12, 424, 2000.
51. Maoz, R., Frydman, E., Cohen, S. R., and Sagiv, J., *Advanced Materials*, 12, 725, 2000.
52. Hoeppener, S., Maoz, R., and Sagiv, J., *Nano Letters*, 3, 761, 2003.
53. Wouters, D. and Schubert, U. S., *Langmuir*, 19, 9033, 2003.
54. Cai, Y. G. and Ocko, B. M., *Journal of the American Chemical Society*, 127, 16287, 2005.
55. Mandler, D. and Bard, A. J., *Journal of the Electrochemical Society*, 137, 1079, 1990.
56. Macpherson, J. V., Slevin, C. J., and Unwin, P. R., *Journal of the Chemical Society—Faraday Transactions*, 92, 3799, 1996.
57. Sheffer, M. and Mandler, D., *Journal of Electroanalytical Chemistry*, 622, 115, 2008.
58. Still, J. W. and Wipf, D. O., *Journal of the Electrochemical Society*, 144, 2657, 1997.
59. Meltzer, S. and Mandler, D., *Journal of the Electrochemical Society*, 142, L82, 1995.
60. Ammann, E. and Mandler, D., *Journal of the Electrochemical Society*, 148, C533, 2001.
61. de Abril, O., Mandler, D., and Unwin, P. R., *Electrochemical and Solid State Letters*, 7, C71, 2004.
62. Danieli, T., Gaponik, N., Eychmuller, A., and Mandler, D., *Journal of Physical Chemistry C*, 112, 8881, 2008.
63. Malel, E. and Mandler, D., *Journal of the Electrochemical Society*, 155, D459, 2008.
64. Sheffer, M., Martina, V., Seeber, R., and Mandlera, D., *Israel Journal of Chemistry*, 48, 349, 2008.
65. Sheffer, M. and Mandler, D., *Electrochimica Acta*, 54, 2951, 2009.
66. Malel, E., Ludwig, R., Gorton, L., and Mandler, D., *Chemistry—A European Journal*, 16, 11697, 2010.
67. O'Mullane, A. P., Ippolito, S. J., Bond, A. M., and Bhargava, S. K., *Electrochemistry Communications*, 12, 611, 2010.
68. Borgwarth, K., Ricken, C., Ebling, D. G., and Heinze, J., *Berichte Der Bunsen-Gesellschaft-Physical Chemistry Chemical Physics*, 99, 1421, 1995.

69. Shohat, I. and Mandler, D., *Journal of the Electrochemical Society*, 141, 995, 1994.
70. Hess, C., Borgwarth, K., Ricken, C., Ebling, D. G., and Heinze, J., *Electrochimica Acta*, 42, 3065, 1997.
71. Ufheil, J., Hess, C., Borgwarth, K., and Heinze, J., *Physical Chemistry Chemical Physics*, 7, 3185, 2005.
72. Ufheil, J., Boldt, F. M., Borsch, M., Borgwarth, K., and Heinze, J., *Bioelectrochemistry*, 52, 103, 2000.
73. Yatziv, Y., Turyan, I., and Mandler, D., *Journal of the American Chemical Society*, 124, 5618, 2002.
74. Turyan, I., Etienne, M., Mandler, D., and Schuhmann, W., *Electroanalysis*, 17, 538, 2005.
75. Mandler, D. and Bard, A. J., *Journal of the Electrochemical Society*, 137, 2468, 1990.
76. Mandler, D. and Bard, A. J., *Langmuir*, 6, 1489, 1990.
77. Sheffer, M. and Mandler, D., *Journal of the Electrochemical Society*, 155, D203, 2008.
78. Meltzer, S. and Mandler, D., *Journal of the Chemical Society—Faraday Transactions*, 91, 1019, 1995.
79. Zu, Y. B., Xie, L., Tian, Z. W., Xie, Z. X., Mu, J. Q., and Mao, B. W., *Chinese Science Bulletin*, 42, 1318, 1997.
80. Zu, Y. B., Xie, L., Mao, B. W., and Tian, Z. W., *Electrochimica Acta*, 43, 1683, 1998.
81. Sun, J. J., Huang, H. G., Tian, Z. Q., Xie, L., Luo, J., Ye, X. Y., Zhou, Z. Y., Xia, S. H., and Tian, Z. W., *Electrochimica Acta*, 47, 95, 2001.
82. Macpherson, J. V. and Unwin, P. R., *Journal of Physical Chemistry*, 99, 3338, 1995.
83. Macpherson, J. V. and Unwin, P. R., *Journal of Physical Chemistry*, 99, 14824, 1995.
84. Macpherson, J. V. and Unwin, P. R., *Journal of Physical Chemistry*, 100, 19475, 1996.
85. Macpherson, J. V., Unwin, P. R., Hillier, A. C., and Bard, A. J., *Journal of the American Chemical Society*, 118, 6445, 1996.
86. Unwin, P. R., *Journal of the Chemical Society—Faraday Transactions*, 94, 3183, 1998.
87. Jones, C. E., Macpherson, J. V., and Unwin, P. R., *Journal of Physical Chemistry B*, 104, 2351, 2000.
88. Jones, C. E., Unwin, P. R., and Macpherson, J. V., *ChemPhysChem*, 4, 139, 2003.
89. McGeouch, C. A., Edwards, M. A., Mbogoro, M. M., Parkinson, C., and Unwin, P. R., *Analytical Chemistry*, 82, 9322, 2010.
90. Turyan, I., Krasovec, U. O., Orel, B., Saraidorov, T., Reisfeld, R., and Mandler, D., *Advanced Materials*, 12, 330, 2000.
91. Turyan, I., Orel, B., Reisfeld, R., and Mandler, D., *Physical Chemistry Chemical Physics*, 5, 3212, 2003.
92. Sauter, S. and Wittstock, G., *Journal of Solid State Electrochemistry*, 5, 205, 2001.
93. Li, J. P., Fang, C., and Gu, H. N., *Acta Chimica Sinica*, 64, 1812, 2006.
94. Ratcliff, B. B., Klancke, J. W., Koppang, M. D., and Engstrom, R. C., *Analytical Chemistry*, 68, 2010, 1996.
95. Bragato, C., Daniele, S., Baldo, M. A., and Denuault, G., *Annali Di Chimica*, 92, 153, 2002.
96. Borgwarth, K., Rohde, N., Ricken, C., Hallensleben, M. L., Mandler, D., and Heinze, J., *Advanced Materials*, 11, 1221, 1999.
97. Marck, C., Borgwarth, K., and Heinze, J., *Advanced Materials*, 13, 47, 2001.
98. Marck, C., Borgwarth, K., and Heinze, J., *Chemistry of Materials*, 13, 747, 2001.
99. Zhou, J. F. and Wipf, D. O., *Journal of the Electrochemical Society*, 144, 1202, 1997.
100. Schultze, J. W., Morgenstern, T., Schattka, D., and Winkels, S., *Electrochimica Acta*, 44, 1847, 1999.
101. Holdcroft, S., *Advanced Materials*, 13, 1753, 2001.
102. Wittstock, G. and Wilhelm, T., *Analytical Sciences*, 18, 1199, 2002.
103. Shiku, H., Takeda, T., Yamada, H., Matsue, T., and Uchida, I., *Analytical Chemistry*, 67, 312, 1995.
104. Shiku, H., Hara, Y., Takeda, T., Matsue, T., and Uchida, I., in *Solid–Liquid Electrochemical Interfaces*, Vol. 656, G. Jerkiewicz, M. P. Soriaga, K. Uosaki, and A. Wieckowski, Eds., American Chemical Society, ACS Symposium Series 656, 1997, p. 202.
105. Shiku, H., Uchida, I., and Matsue, T., *Langmuir*, 13, 7239, 1997.
106. Turyan, I., Matsue, T., and Mandler, D., *Analytical Chemistry*, 72, 3431, 2000.
107. Nowall, W. B., Wipf, D. O., and Kuhr, W. G., *Analytical Chemistry*, 70, 2601, 1998.
108. Oyamatsu, D., Kanaya, N., Shiku, H., Nishizawa, M., and Matsue, T., *Sensors and Actuators B—Chemical*, 91, 199, 2003.
109. Kaji, H., Kanada, M., Oyamatsu, D., Matsue, T., and Nishizawa, M., *Langmuir*, 20, 16, 2004.
110. Zhao, C., Witte, I., and Wittstock, G., *Angewandte Chemie—International Edition*, 45, 5469, 2006.
111. Li, X. M., Geng, Q. H., Wang, Y. Y., Si, Z. K., Jiang, W., Zhang, X. L., and Jin, W. R., *Electrochimica Acta*, 53, 2016, 2007.
112. Li, X. M., Geng, Q. H., Wang, Y. Y., Si, Z. K., Jiang, W., Zhang, X. L., and Jin, W. R., *Electroanalysis*, 19, 1734, 2007.
113. Ku, S. Y., Wong, K. T., and Bard, A. J., *Journal of the American Chemical Society*, 130, 2392, 2008.

114. Zhao, C., Zawisza, I., Nullmeier, M., Burchardt, M., Taduble, M., Witte, I., and Wittstock, G., *Langmuir*, 24, 7605, 2008.
115. Zhao, C., Burchardt, M., Brinkhoff, T., Beardsley, C., Simon, M., and Wittstock, G., *Langmuir*, 26, 8641, 2010.
116. Cougnon, C., Gohier, F., Belanger, D., and Mauzeroll, J., *Angewandte Chemie—International Edition*, 48, 4006, 2009.
117. Cougnon, C., Mauzeroll, J., and Belanger, D., *Angewandte Chemie—International Edition*, 48, 7395, 2009.
118. Combellas, C., Kanoufi, F., Mazouzi, D., and Thiebault, A., *Journal of Electroanalytical Chemistry*, 556, 43, 2003.
119. Combellas, C., Kanoufi, F., Mazouzi, D., Thiebault, A., Bertrand, P., and Medard, N., *Polymer*, 44, 19, 2003.
120. Combellas, C., Fuchs, A., Kanoufi, F., Mazouzi, D., and Nunige, S., *Polymer*, 45, 4669, 2004.
121. Combellas, C., Ghilane, J., Kanoufi, F., and Mazouzi, D., *Journal of Physical Chemistry B*, 108, 6391, 2004.
122. Combellas, C., Kanoufi, F., and Mazouzi, D., *Journal of Physical Chemistry B*, 108, 19260, 2004.
123. Combellas, C., Kanoufi, F., and Mazouzi, D., *Journal of Electroanalytical Chemistry*, 589, 243, 2006.
124. Combellas, C., Kanoufi, F., and Nunige, S., *Chemistry of Materials*, 19, 3830, 2007.
125. Deiss, F., Combellas, C., Fretigny, C., Sojic, N., and Kanoufi, F., *Analytical Chemistry*, 82, 5169, 2010.
126. Mandler, D. and Bard, A. J., *Journal of the Electrochemical Society*, 136, 3143, 1989.
127. Borgwarth, K., Ebling, D. G., and Heinze, J., *Berichte Der Bunsen—Gesellschaft—Physical Chemistry Chemical Physics*, 98, 1317, 1994.
128. Shao, Y. H., Mirkin, M. V., Fish, G., Kokotov, S., Palanker, D., and Lewis, A., *Analytical Chemistry*, 69, 1627, 1997.
129. Sun, P., Zhang, Z. Q., Guo, J. D., and Shao, Y. H., *Analytical Chemistry*, 73, 5346, 2001.
130. Katemann, B. B. and Schuhmann, T., *Electroanalysis*, 14, 22, 2002.
131. Lugstein, A., Bertagnolli, E., Kranz, C., and Mizaikoff, B., *Surface and Interface Analysis*, 33, 146, 2002.
132. Kueng, A., Kranz, C., Mizaikoff, B., Lugstein, A., and Bertagnolli, E., *Applied Physics Letters*, 82, 1592, 2003.
133. Sklyar, O., Treutler, T. H., Vlachopoulos, N., and Wittstock, G., *Surface Science*, 597, 181, 2005.
134. Etienne, M., Anderson, E. C., Evans, S. R., Schuhmann, W., and Fritsch, I., *Analytical Chemistry*, 78, 7317, 2006.
135. Moon, J. S., Shin, H., Mizaikoff, B., and Kranz, C., *Journal of the Korean Physical Society*, 51, 920, 2007.
136. Sun, P. and Mirkin, M. V., *Analytical Chemistry*, 79, 5809, 2007.
137. Kim, E., Kim, J., and Amemiya, S., *Analytical Chemistry*, 81, 4788, 2009.
138. Laforge, F. O., Velmurugan, J., Wang, Y. X., and Mirkin, M. V., *Analytical Chemistry*, 81, 3143, 2009.
139. Velmurugan, J., Sun, P., and Mirkin, M. V., *Journal of Physical Chemistry C*, 113, 459, 2009.
140. Dumitrescu, I., Dudin, P. V., Edgeworth, J. P., Macpherson, J. V., and Unwin, P. R., *Journal of Physical Chemistry C*, 114, 2633, 2010.
141. Hussien, E. M., Schuhmann, W., and Schulte, A., *Analytical Chemistry*, 82, 5900, 2010.
142. Mezour, M. A., Cornut, R., Hussien, E. M., Morin, M., and Mauzeroll, J., *Langmuir*, 26, 13000, 2010.
143. Velmurugan, J. and Mirkin, M. V., *ChemPhysChem*, 11, 3011, 2010.
144. Walsh, D. A., Lovelock, K. R. J., and Licence, P., *Chemical Society Reviews*, 39, 4185, 2010.
145. Zoski, C. G. and Wijesinghe, M., *Israel Journal of Chemistry*, 50, 347, 2010.
146. Wain, A. J., Cox, D., Zhou, S. Q., and Turnbull, A., *Electrochemistry Communications*, 13, 78, 2011.

16 Application to Electrocatalysis and Photocatalysis and Surface Interrogation

Joaquín Rodríguez-López, Cynthia G. Zoski, and Allen J. Bard

CONTENTS

16.1 Introduction 525
16.2 Electrocatalysis 526
16.2.1 SECM Studies of Electrocatalysts 526
16.2.2 Array Fabrication 527
16.2.3 SECM Array Screening 530
16.2.3.1 Feedback Approach 530
16.2.3.2 Tip Generation/Substrate Collection 533
16.2.3.3 Substrate Generation/Tip Collection 538
16.2.3.4 Shielding 542
16.3 Photocatalysis 542
16.3.1 SECM Studies of Photocatalysts 542
16.3.2 Array Fabrication 543
16.3.3 Array Screening 545
16.4 Surface Interrogation SECM 547
16.4.1 Operation Mode and Experimental Considerations 548
16.4.2 Digital Simulation of the SI-SECM Process 551
16.4.3 Detection and Quantification of Gold Oxides 554
16.4.4 Differential Reactivity of Pt Oxides with Various Mediators 555
16.4.5 SI-SECM of Adsorbed Hydrogen at Pt: An Example of Catalysis 558
16.4.6 SI-SECM of Adsorbed CO on Pt with Br_2, A Catalytic Interrogation 560
16.4.7 Outlook for SI-SECM 561
References 562

16.1 INTRODUCTION

Scanning electrochemical microscopy (SECM) provides an invaluable tool for both the discovery of new materials (electrocatalysts and photocatalysts) and their characterization. The discovery involves the rapid preparation of arrays of small (approximately hundreds of micrometer diameter) spots of different compositions. These can be examined and screened rapidly with an SECM tip producing a visual image, for example, of the current produced at a given spot at a given potential, that can be used to judge the relative efficacy of a given composition. Several different screening schemes are available that are selected by considering the nature of the electrocatalytic reaction of interest. These are described in Section 16.2 along with examples of different electrocatalysts and reactions.

As described in Section 16.2, once good electrocatalytic materials are found, they can be characterized at steady state with the SECM, for example, in a manner analogous to rotating ring-disk electrode (RRDE) voltammetric studies. In this application, the spot or film of the electrocatalyst on the substrate plays the role of the generator (disk) and the tip is the collector (ring) in the SECM substrate generation–tip collection mode. An advantage of SECM over the RRDE is that the diffusion between the substrate and tip, which is fast, even in the absence of convection, is much easier to simulate. Moreover, it is also easier to prepare different materials as spots or films on a substrate than to make different disk materials for the RRDE.

The general approach to screening of photocatalysts, usually semiconductor materials, considered in Section 16.3 is similar, except that in this case the usual UME tip is replaced by an optical fiber that illuminates one spot on the array at a time. Again a visual image of the photocurrents on the array can be used to identify the most efficient compositions. The product of the photoreaction, for example, oxygen in the water oxidation reaction, can be examined electrochemically by a ring electrode surrounding the optical fiber.

The SECM is also useful in a transient mode to examine intermediates generated on an electrode surface as discussed in Section 16.4. Here the tip-generated mediator interrogates the electrocatalyst on a substrate surface, quantifying adsorbed intermediates. Although this surface interrogation technique is still developing, it provides a tool for examining heterogeneous inner sphere reactions that is not readily available by other electrochemical techniques.

16.2 ELECTROCATALYSIS

16.2.1 SECM Studies of Electrocatalysts

SECM has found growing application in the search for electrocatalysts for electrochemical applications (e.g., fuel cells and photoelectrochemical systems) that address the worldwide need for more efficient energy sources.[1] There are two main reasons for the success of SECM in this area. First, SECM has been shown to be excellent for rapid screening of arrays of materials. Second, SECM directly produces electrochemical data that provide quantitative estimates of both rate and activity of the material being studied.

The traditional approach to the electrochemical investigation of an electrocatalyst first involves careful synthesis and characterization, which are followed by testing on a macroscale, usually with a rotating disk or RRDE. This testing is generally accomplished on a one-by-one basis. In contrast, the SECM approach allows a large number of different compositions to be screened rapidly. The screening is performed on arrays that are rapidly prepared to yield small samples of spots or lines that are of reasonably uniform, but varying composition on a substrate that has very low electrocatalytic properties. After an electrocatalyst has been identified through the screening process, SECM can further be used to carry out quantitative analyses similar to those with a rotating disk or RRDE.

Earlier SECM studies of electrocatalytic reactions on model electrode surfaces that preceded the screening of electrocatalysts, the topic of this section, are summarized in Table 16.1. These studies include complex electrode reactions like the oxygen reduction reaction (ORR), formic acid oxidation reaction (FAOR), hydrogen oxidation reaction (HOR), oxygen evolution reaction (OER), and mechanistic pathways involving H_2O_2. Such investigations, involving a tip above a substrate composed of one or two model electrode sites or up to six model catalyst compositions on an inert substrate such as carbon, laid the foundation for the screening of arrays of electrocatalysts to be discussed further in this section. These reactions are of particular interest on promising electrocatalysts in which Pt is either replaced or reduced in proton-exchange membrane fuel cells (PEMFCs), direct methanol fuel cells (DMFCs), direct formic acid fuel cells (DFAFCs), and photoelectrochemical systems (i.e., photocells) which are under investigation as promising power sources. The interest in alternative electrocatalysts to platinum is mainly due to its high cost, limited availability for scale-up, and its rapid loss of activity caused by poisoning species generated during the ORR, FAOR, HOR, and OER.

TABLE 16.1
Electrocatalytic Reactions on Model Substrates of up to Two Active Sites or up to Six Model Catalyst Compositions on an Inert Substrate Such as Carbon

Substrate	Reaction	Solution	References
Pt, Ir, Rh	H_2 oxidation, feedback	$HClO_4$, H_2SO_4	[2–6]
Ir	H_2 oxidation, shielding	$HClO_4$	[7]
Pt	O_2 reduction, feedback	NaOH	[8,9]
Pt, Au, GC, Ru, GC/Pt, GC/Ru, PZT dispenser	O_2 reduction, TG/SC	H_2SO_4	[10–12]
Au/porphyrin monolayer	O_2 reduction, SG/TC	H_2SO_4	[13]
GC/Pt, Au, electrodep.	O_2 reduction, RC	Phosphate buffer	[14,15]
Graphite/Os polymer, electrodep.	O_2 reduction, RC	Phosphate citrate buffer	[16,17]
GC/CNT/Pt, Au, Rh, Au_xPt_y, electrodep.	O_2 reduction, RC	Phosphate buffer	[18]
GC/Prussian blue, electrodep.	H_2O_2 reduction, RC	Phosphate buffer	[19]
Nylon/catalase Glass/colloidal Pt NPs	H_2O_2 decomposition, feedback	Phosphate buffer	[20]
Pt, Pd, Ag, Au, Cu, Hg	H_2O_2 quantification, SG/TC	H_2SO_4	[21,22]
Au, Pt, GC/PdCo, electrodep.	H_2O_2 detection, SG/TC	H_2SO_4	[23]
Pt Microelectrode	Formic acid oxidation, MD/SC	H_2SO_4	[24]
Pt Microelectrode	Methanol oxidation, SG/TC	H_2SO_4, methanol	[4]
Au Microelectrode	Oxygen evolution, SG/TC	H_2SO_4	[25]

Electrodep., electrodeposition; NPs, nanoparticles; MD/SC, micropipette delivery–substrate collection; RC, redox competition; SG/TC, substrate generation/tip collection; TG/SC, tip generation/substrate collection.

16.2.2 Array Fabrication

Table 16.2 summarizes the different array substrates and methods of preparation that have been used in SECM electrocatalyst screening. Practical SECM high-throughput screening requires arrays of samples that can be prepared rapidly, inexpensively, and in an automated way. An array should cover a wide range of compositions with good reproducibility of test spot compositions across the array.

An array substrate that allows control of the potential at each individual electrocatalyst composition site (i.e., individually addressable spots) is preferable due to the small background current that results at each site. That is, only the spot addressed by the tip contributes to the background current, and not the substrate itself or all of the other spots. As an example, an addressable array of 25 Pt spots, 10 μm in diameter and spaced 100 μm apart, was imaged by SECM using ferrocene methanol as the mediator with all of the spots either at the same potential or at open circuit.[26] To make use of the individually addressable feature of the array in a rapid SECM screening mode, the application of the potential at each spot would have to be synchronized with the tip position over a given spot using a form of potentiostat multiplexing, which to date has not been done. Additionally, individually addressable arrays are expensive, limited by the number of conductive sites on the array, and not widely available due to the microfabrication process. They are also not conducive to heating at elevated temperatures. For these reasons, this type of individual addressable array has not been used for SECM screening of electrocatalyst compositions. Another example of an individual addressable array consists of eight individually addressable lines, each 25 mm long, 1 mm wide, and with a 1.5 mm separation.[27] These lines were formed on an indium–tin oxide (ITO) electrode by photolithography and etching. In this study, the individual lines were plated with different compositions of Pt_xRu_y by controlling the potential of one line at a time and changing the electrodeposition solution

TABLE 16.2
Representative Approaches to Forming Sample Arrays, Electrocatalytic Reaction Studied, and SECM Method Used

Substrate	Composition/Deposition Method	Reaction Studied	References
Addressable array, Pt	Pt, proof of concept (5 × 5 array)	FcMeOH, feedback, SG/TC	[26]
Au	Pt, electrodep., proof of concept	H_2 oxidation, feedback	[4]
Patterned ITO	$Pt_xRu_yMo_z$, electrodep. (8 lines)	H_2 oxidation, feedback	[27]
ITO	Pt_xRu_y, gradient, agar, electrodep.	H_2 oxidation, feedback	[28]
ITO	Pt coverage, gradient, electrodep.	H_2 oxidation, feedback	[29]
Si, TiN layer	Pt_xRu_y, sputtering	H_2 oxidation, feedback	[30]
HOPG	Pt colloid, random, drop coating	H^+ reduction, feedback, TG/SC	[31]
GC	Pd_xM_y(M: Co, Ti), PZT dispenser	O_2 reduction, TG/SC	[32–36]
GC	Pd–Co, PZT dispenser	O_2 reduction, MeOH tolerance, TG/SC	[37]
GC	Pt NPs, shape-controlled, colloidal, PZT dispenser	O_2 reduction, TG/SC	[38]
Si, TiN layer	Pt, sputtered	O_2 reduction, TG/SC	[39]
GC	Cu(II) polyhis films, PZT dispenser	O_2 reduction, TG/SC	[40]
GC	Hydrogels, wired laccase	O_2 reduction, TG/SC	[41,42]
GC	Pt_xCe_y, Pd_xCo_y, PZT dispenser	Methanol oxidation, MD/SC	[24]
GC	Pd_xCo_y, PZT dispenser	Formic acid oxidation, TG/SC	[43]
GC	$Pd_{80}Co_{20}$, Au_xCu_y, PZT dispenser	H_2O_2 production, TG/SC	[22]
Ti	IrO_2, $Sn_{1-x}Ir_xO_2$, PZT dispenser	O_2 evolution	[25]

Electrodep., electrodeposition; NPs, nanoparticles; MD/SC, micropipette delivery–substrate collection; SG/TC, substrate generation/tip collection; TG/SC, tip generation/substrate collection.

after each plating. However, as in the previous addressable array example, the SECM screening was performed with all of the lines held at the same potential.

The approach that best meets the requirements of rapid, inexpensive, and automated preparation of a wide range of electrocatalytic compositions involves the use of a single, continuous substrate material that shows poor catalytic properties so that the background current density of the regions between the spots is small. Glassy carbon (GC), Ti, or thin films of either ITO or fluorine-doped tin oxide (FTO) coated on glass are the most commonly used substrates on which an array of spots are prepared. For example, bi- and trimetallic catalyst spots for the ORR on GC substrates were prepared using this approach.[10,32–37] The spots were formed using a piezo dispenser that delivers pL-drops of appropriate solutions of the metal salts and that is computer-controlled to move and dispense at precise locations as shown in Figure 16.1a. After one metal salt is deposited, the solution is drained from the dispenser and a second (and perhaps a third) metal salt solution is used over the same array. The result is an array of drops containing different programmed amounts of each metal salt. The array is then vortexed to mix the metal salts in each spot and treated with H_2 at an elevated temperature to produce alloy catalyst spots. Alternatively, sodium borohydride solution can be used for the reduction by dispensing an appropriate number of drops on each spot of the array, which is then vortexed and heated under argon at an elevated temperature. The formation of reproducible and well-formed electrocatalyst spots (≈200 μm diameter) depends on the pretreatment of the substrate (i.e., careful polishing with alumina and sonication), an exact solution composition (i.e., choice of metal salt and solvent), and vortex mixing prior to heat treatment. Figure 16.1b shows scanning electron micrographs (SEM) of typical arrays of catalyst spots consisting of various amounts of Pd and Co. Figure 16.1b (top) shows a binary mixture of Pd and Co. The rows consist of pure Pd spots (left) and increasing amounts of Co (i.e., 10%, 20%, 30%, etc., where all percentages refer to atomic

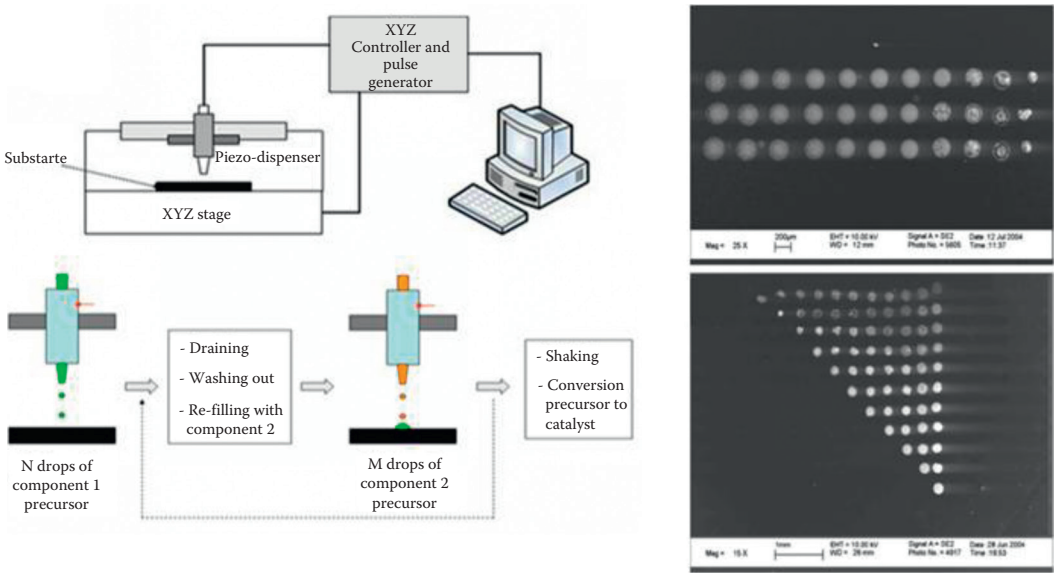


FIGURE 16.1 Catalyst array fabrication. (a) Schematic of the dispenser setup for the preparation of catalyst spots and sequence of steps for the deposition of catalyst precursor solutions. (b) SEM images of typical binary (Pd–Co, top) and ternary (Pd–Au–Co, bottom) catalyst arrays. (Adapted from Fernandez, J.L. et al., *J. Am. Chem. Soc.,* 127, 357, 2005.)

percent) to pure Co spots on the right. Each row is replicated three times in order to examine the intra-array reproducibility of each catalyst spot composition. Figure 16.1b (bottom) shows a ternary array consisting of pure Au (top, right), pure Pd (bottom, right), and pure Co (top, left), with a wide range of mixtures of each metal in the intervening areas. Similarly, pure IrO_2 and $Sn_{1-x}Ir_xO_2$ mixtures were prepared on Ti plates for evaluation as electrocatalysts for the OER.[25] ITO substrates have been used for screening of H_2 oxidation catalysts and FTO substrates are used in the screening of photocatalysts, the topic of the next section.

Arrays of shape-controlled metal nanoparticles (MNPs) on GC can also be made from aqueous suspensions of spherical, cubic, hexagonal, and tetrahedral–octahedral MNPs having equal active surface areas of MNPs.[38] Each MNP suspension is sonicated before use in the picoliter dispenser described earlier, and an equal number of drops of each MNP suspension is used across the array, with time allowed for water evaporation before each new set of MNP drops. The array is not vortexed or heat treated since the MNPs are in a pristine, reduced state.

Arrays of biomimetic[40] and enzyme-type[41,42] spots for the ORR have also been made using a single inert substrate (i.e., GC) and piezo dispensing as described earlier. Ink jet printing devices that are used in combinatorial array preparations with other methods of screening may also be used. To overcome the disadvantage of large background current when using a common conductive substrate, the substrate can be covered with a layer of an insulator such as Teflon, with holes for the spots.[44] This procedure, which is simpler and less expensive than microfabricating an individually addressable array, makes use of the piezo dispenser used in making catalyst spots and is illustrated in Figure 16.2a. In step A1, a GC substrate is mounted and aligned on the SECM stage. The piezo dispenser is then used to dispense a solution of photoresist in an array pattern. In step A2, the substrate is spin-coated with Teflon. The photoresist spots are exposed in A3 by immersing the substrate and acetone where the acetone permeates through the Teflon layer, swells the resin, and breaks away the Teflon on top of each photoresist spot, thus leaving the patterned holes as shown in A4. The Teflon layer is sintered and cooled in step A5, followed by A6 where a catalyst precursor

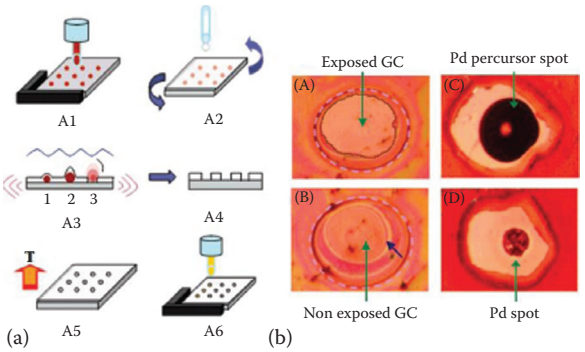


FIGURE 16.2 Steps in selectively insulating a substrate electrode with Teflon. (a) Schematic of the fabrication steps in creating an insulated substrate with an array of holes. A1—microdispensing photoresist in an array pattern, A2—spin coating with Teflon, A3—exposing spots in an acetone bath, A4—side view of the exposed array, A5—sintering of the Teflon layer, and A6—dispensing catalyst precursor over the exposed holes. (b) Optical photographs of holes on Teflon-covered electrodes. (A) Exposed spot. The dashed line indicates the original size of the resin spot; the edge left behind after removing Teflon is shown in brown. (B) Unsuccessful exposure of resin spot. The dashed line indicates the original size of the resin spot; the blue arrow indicates light interference rings that are characteristic of the presence of Teflon layer. (C) Drop of Pd solution in an exposed hole. (D) Pd spot after drying and reduction under H_2. (Adapted from Rodriguez-Lopez, J. et al., *Anal. Chem*., 80, 1813, 2008.)

is dispensed in the exposed spots. Figure 16.2b shows representative micrographs of exposed holes. Panel A shows an exposed hole (e.g., as indicated by clear edge) that was formed after immersion in acetone, whereas panel B shows an unsuccessful spot exposure. Panel C shows an example of a drop of Pd solution that was dispensed in an exposed hole, and Panel D shows the final Pd spot after drying and reduction under H_2. Proof of concept experiments have demonstrated that the presence of metallic spots limits the practical reduction in the background coming from the array, but that background currents can be reduced at least one order of magnitude, in addition to a reduction in background drift across the array during screening. The result is an enhancement in image contrast produced by reducing the impact of both the background size and drift.

Continuous gradients of electrocatalyst compositions have also been prepared as an alternative to the spot or line arrays described earlier. Methods of producing continuous gradients have included electrodeposition across a resistive element,[29] by changing the composition of a thin-layer film (e.g., agar) by controlled solution treatment,[28] or by sputtering.[30,39]

16.2.3 SECM Array Screening

Figure 16.3 illustrates the four different SECM approaches to examining electrocatalyst spots on an electrocatalytically inactive substrate. The reaction to be studied at the substrate and whether the reactant of interest can be generated at the tip are the determining factors in selecting the SECM screening approach. Each of the approaches is discussed later and examples of their use are given.

16.2.3.1 Feedback Approach

The feedback approach can be used if the species to be studied at the substrate can be generated at the tip from a component in the bulk solution. The redox pair of interest then represents a typical SECM mediator where the tip reactant is regenerated at the substrate and feedback occurs. The effect of the substrate potential, E_S, on the tip current, i_T, can be used to determine the activity of the substrate and the heterogeneous rate constant of the reaction at the substrate surface. The H_2 oxidation reaction is an example of a reaction that has been studied at electrocatalysts using SECM, as diagrammed in Figure 16.3a. The tip is held at a potential, E_T, where H^+ is reduced at

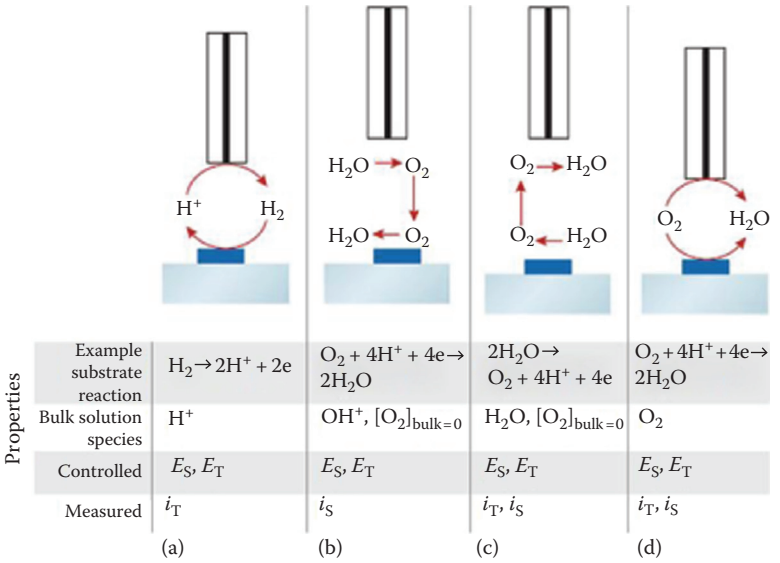


FIGURE 16.3 Schematic representation of the four SECM approaches used in examining electrocatalysts on a substrate. TG; tip generation; SC; substrate collection; E_S; substrate potential; E_T; tip potential; i_S; substrate current; i_T; tip current. (a) Feedback, (b) TG/SC, (c) SG/TC, and (d) shielding or competitive. (From Amemiya, S. et al., *Annu. Rev. Anal. Chem.*, 1, 95, 2008.)

a diffusion-controlled rate in a solution where its concentration is ≈0.01 M. At this concentration, the generated H_2 dissolves in solution and diffuses to the substrate rather than forming bubbles. Similar to other SECM kinetic studies, the heterogeneous rate constant, $k(E)$, can be calculated from approach curves recorded as a function of E_S, as shown in Figure 16.4 for Pt.[2] Figure 16.4A and B show approach curves at seven different substrate potentials, as well as theoretical curves for a diffusion-controlled reaction and no reaction at the substrate. By fitting the approach curves, the variation of the H_2 oxidation rate on Pt with E_S can be observed (Figure 16.4C). For example, H_2 oxidation becomes so rapid at potentials in the region of −0.3 to 0.2 V that the approach curves are indistinguishable from those for a diffusion-controlled reaction and k is constant. At about 0.4 V, oxide formation begins on Pt and the H_2 oxidation rate decreases. Above 0.7 V, the catalytic activity of the Pt surface is very low, with the approach curves being essentially those of surfaces with no regeneration capability. Between −0.3 and −0.5 V, the H_2 oxidation rate decreased with a decrease in E_S. Figure 16.4D is a plot of the H_2 oxidation rate versus substrate overpotential (i.e., equivalent to a Tafel plot). Over this potential range, the Tafel plot is a straight line from which the transfer coefficient, α, can be determined from the slope, and a standard rate constant, k^0, can be determined by extrapolating the line to $E_S = E^0$ (e.g., the standard potential). Similar investigations at Ir and Rh showed that H_2 oxidation on Pt and Ir occurs at a similar rate, but is much slower on Rh.[3]

A substrate can also be scanned at a constant tip–substrate distance, d, to determine relative activities. For example, Figure 16.5 shows a series of line scans measured with an SECM tip scanned over an eight-element Pt_xRu_y band sample for H_2 oxidation on ITO.[27] The band numbers corresponding to the Pt_xRu_y compositions are listed. Each line in the figure represents a scan taken at a fixed tip–sample separation. Decreasing the tip–substrate separation from 60 to 10 μm increases the magnitude of the tip current over bands 1–7. The tip current over the insulating regions between the electrode bands and over band 8 (pure Ru) decreases as the tip–substrate separation is reduced. The increase in tip current over bands 1–7 and the decrease in current over band 8 and the insulating regions are due to the lower magnitude of the rate constant for H_2 oxidation at these substrate locations.

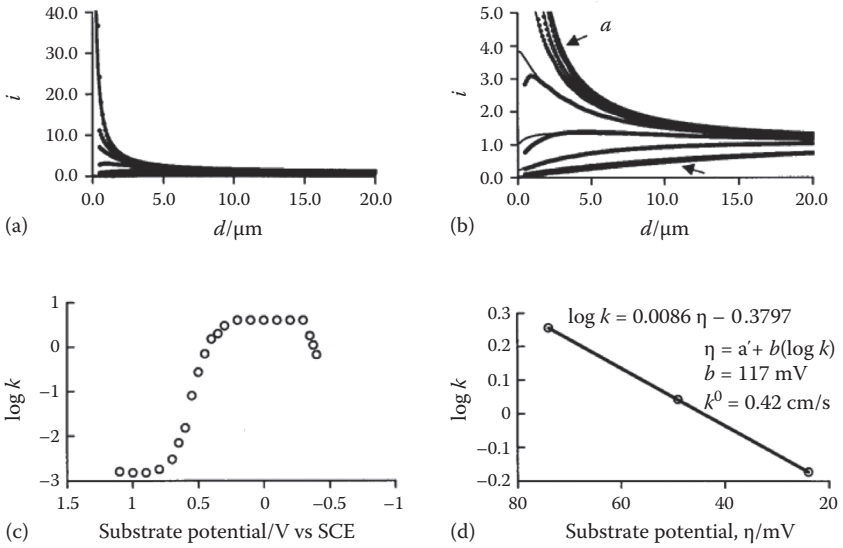


FIGURE 16.4 Determination of the H_2 oxidation heterogeneous rate constant $k(E_S)$ from SECM approach curves. (a) SECM approach curves. (b) Magnification of (a). The solid lines a and b are theoretical approach curves at conducting and insulating substrates, respectively. Experimental approach curves are represented by circle symbols; solid lines are theoretical curves at a Pt substrate with its potential held at, from top to bottom: 0, 0.4, 0.45, 0.5, 0.55, 0.6, and 1 V. (c) Heterogeneous reaction rate constant k of H_2 oxidation at a Pt substrate with different potentials. k was obtained by fitting the experimental approach curves with the theoretical ones shown in (b). (d) Tafel plot of H_2 oxidation. Approach speed: 3 μm/s. Solution: 0.01 M $HClO_4$/0.1 M $NaClO_4$. (From Zhou, J. et al., *J. Electroanal. Chem.,* 491, 22, 2000.)

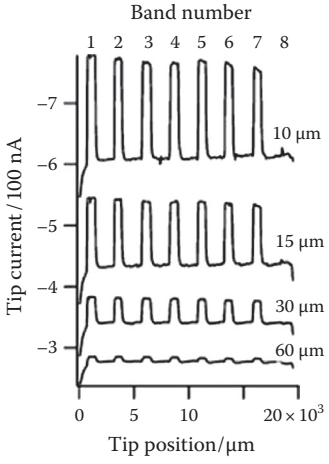


FIGURE 16.5 SECM line images of H_2 oxidation over Pt_xRu_y band electrodes as a function of tip–substrate separation in N_2-purged 0.01 M H_2SO_4/0.1 M Na_2SO_4. $E_T = -1.0$ V vs. RHE; $E_S = 0.1$ V vs. RHE. Each curve is offset for clarity. Band numbers correspond to catalyst composition: 1. Pt_{100}; 2. $Pt_{90}Ru_{10}$; 3. $Pt_{70}Ru_{30}$; 4. $Pt_{40}Ru_{60}$; 5. $Pt_{60}Ru_{40}$; 6. $Pt_{30}Ru_{70}$; 7. $Pt_{10}Ru_{90}$; 8. Ru_{100}. Tip: Au (25 μm diameter). (Adapted from Jayaraman, S. and Hiller, A.C., *J. Phys. Chem. B,* 107, 5221, 2003.)

The effect of other species, such as Br^-,[2] I^-,[2] NO_3^-,[2] and CO,[5,6,27–29] on the HOR can also be studied.

The feedback approach is limited to a small range of H^+ concentration or pH. At much lower concentrations than 0.01 M, the currents become too small to measure above background. At higher concentrations, H_2 bubbles form on the tip surface.[2]

The feedback approach can also be used to study the O_2 reduction reaction at a substrate in alkaline media. Oxygen is generated at a Au tip by oxidation of OH^- and reduced at the substrate. There is a drift in the tip current due to the formation of an anodic film on the tip in the potential range where the oxidation of OH^- occurs. This drift is alleviated by applying a periodic potential program to the Au tip, which resulted in a stable, steady-state tip current. Kinetic parameters can then be determined from SECM approach curves.[8] Similarly, the behavior of the product, $O_2^{\bullet-}$, from O_2 reduction at the tip in O_2-saturated 10 M NaOH solution can be investigated as a function of substrate potential.[9]

16.2.3.2 Tip Generation/Substrate Collection

In the tip generation/substrate collection (TG/SC) mode, there is more flexibility in how the tip generates the substrate reactant than in the feedback approach. Examples of galvanostatic, potentiostatic, and micropipette delivery generation of the substrate reactant are described.

In TG/SC, i_T can be controlled as a constant current that generates a constant flux of reactant, as shown in Figure 16.3b. A scheme for a typical experimental setup is shown in Figure 16.6. When the tip is close to the substrate (i.e., ≈30 μm for a 25 μm diameter tip, RG ≈ 5) and the array spots are sufficiently far apart, only the spot immediately below the tip is addressed during the array screening. The substrate current, i_S, at that spot at a given potential, E_S, is a measure of the activity of the electrocatalyst spot. For example, in the study of the ORR at the substrate, the solution is first deaerated so that the bulk concentration of O_2 is low.[10,11,32–36] O_2 is then generated at the tip and

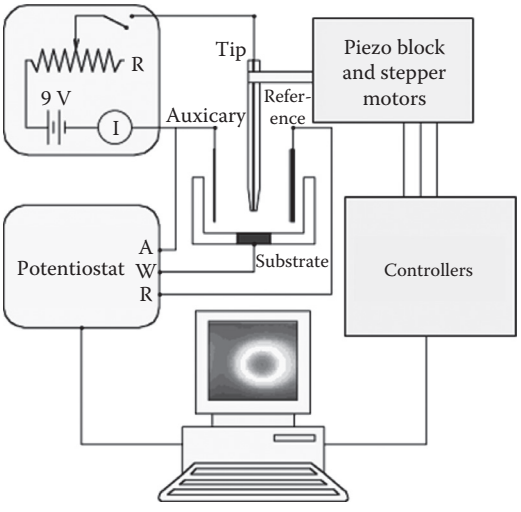


FIGURE 16.6 Electrochemical setup used for TG/SC screening and polarization experiments in investigations of the oxygen reduction reaction (ORR) in acidic solution. A PC-controlled SECM instrument controls tip and stage movement, as well as potentials (e.g., through a bipotentiostat). The tip current is controlled with a battery-powered source (9 V) connected between the tip (positive) and auxiliary electrode. A Au UME tip (25 μm diameter, RG ≈ 5) is used as the O_2 generator. The use of Au as a tip material and as a counter electrode eliminates the possibility of contamination of electrocatalysts by small amounts of Pt. Typical reference electrodes are either Hg/Hg_2SO_4 or reversible hydrogen electrode (RHE). (Adapted from Fernandez, J.L., Bard, A.J., *Anal. Chem.*, 75, 2967, 2003.)

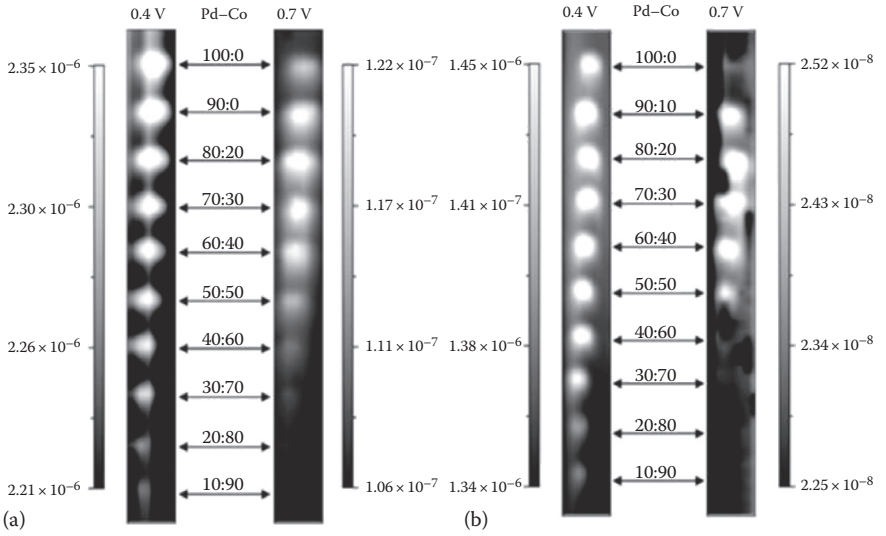


FIGURE 16.7 SECM TG/SC images of ORR activities measured on a Pd–Co array on a GC substrate at 0.4 and 0.7 V in 0.5 M H_2SO_4 solution in (a) the absence or (b) the presence of 0.5 M MeOH in solution. O_2 generation: constant current of −155 nA. Tip–substrate separation: 45 μm. Scan rate: 25 μm/0.2 s. Scale bars correspond to i_S in A. (Adapted from Lin, C.-L. et al., *Electrochem. Solid State Lett.,* 11, B136, 2008.)

reduced at the substrate. The (*x*–*y*) scan shows i_S as a function of position and potential. A typical result for Pd–Co electrocatalysts for the ORR is shown in the SECM TG/SC image of Figure 16.7a, where $Pd_{80}Co_{20}$ (i.e., 80% Pd, 20% Co) showed the highest ORR activity among the different Pd–Co compositions ranging from 70% to 100%,[37] in agreement with previous studies.[32,36] The effect of other species on the ORR reaction, such as methanol, can also be studied. For example, Figure 16.7b shows ORR activities measured on the same Pd–Co array shown in Figure 16.7a in the presence of 0.5 M MeOH in solution.[37] The $Pd_{80}Co_{20}$ electrocatalyst shows slightly lower, but comparable, ORR activity to that in the absence of MeOH in the electrolyte even at a potential as positive as 0.7 V. This is important in direct MeOH fuel cells (DMFC) where it is desirable to operate the ORR cathode electrocatalyst at as positive a potential as possible to increase the overall cell voltage. Therefore, $Pd_{80}Co_{20}$ shows promising ORR activity in the presence of high MeOH concentration. To quantitatively compare MeOH tolerance of the $Pd_{80}Co_{20}$ electrocatalyst to a Pt electrocatalyst, the collection efficiency (CE) of these ORR electrocatalysts at different working potentials in electrolytes with various MeOH concentrations was evaluated by steady-state TG/SC measurements.[10,11,37] The CE is defined as the percentage of O_2 generated at a tip that is reduced by an electrocatalyst and is expressed as

$$\mathrm{CE}(\%) = \left|\frac{i_S}{i_T}\right| \times 100\% \tag{16.1}$$

when the spacing, *d*, between the tip and electrocatalyst spot is small (i.e., ≤10 μm for a 25 μm diameter tip, RG ≈ 5), where i_T is the current applied to the O_2 generator tip and i_S is the corresponding current response of the electrocatalyst substrate. O_2 is generated at an Au UME tip as shown schematically in Figure 16.3b using an experimental setup similar to that diagrammed in Figure 16.6. A typical current–time profile for O_2 generation at the tip and the corresponding ORR current response at a single $Pd_{80}Co_{20}$ spot on a GC plate is shown in Figure 16.8a. Figure 16.8b shows the ORR CE% of the electrocatalysts in electrolytes containing various MeOH concentrations as a function of potential. The $Pd_{80}Co_{20}$ electrocatalyst shows comparable ORR activity to Pt in the

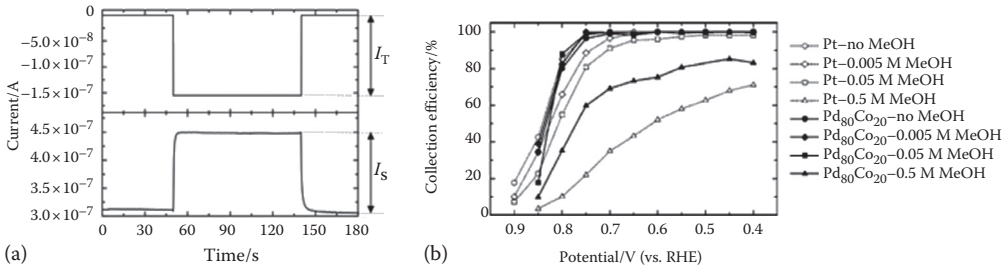


FIGURE 16.8 Steady-state TG/SG measurements. (a) Top panel: Current profile of O_2 generation at the tip (i_T); bottom panel: corresponding ORR current response (i_S) at a $Pd_{80}Co_{20}$ spot below the tip. The distance between the O_2 generator tip and the $Pd_{80}Co_{20}$ spot is 7 μm. The ORR was carried out at 0.4 V in a 0.5 M H_2SO_4 solution containing 0.5 M MeOH. (b) ORR CE of a $Pd_{80}Co_{20}$ spot and a Pt UME (100 μm diameter) as a function of potential in 0.5 M H_2SO_4 solution containing different MeOH concentrations. (Adapted from Lin, C.-L. et al., *Electrochem. Solid State Lett.,* 11, B136, 2008.)

absence of MeOH. With increasing amounts of MeOH in the electrolyte (i.e., from 0.005 to 0.05 M), the CEs of Pt gradually dropped while the CE of $Pd_{80}Co_{20}$ remained essentially constant, with only large amounts of MeOH (i.e., 0.5 M) producing a clear poisoning effect. The CE of $Pd_{80}Co_{20}$ is also significantly higher than that of Pt when 0.5 M MeOH is present in solution. Therefore, based on these types of ORR CE measurements, the $Pd_{80}Co_{20}$ electrocatalyst demonstrates higher MeOH tolerance than Pt during ORR and thus is a good candidate material for the cathode electrocatalyst in both PEMFCs and DMFCs.

The TG/SC scheme for FAOR (e.g., the reaction in DFAFCs) electrocatalyst screening is shown in Figure 16.9a.[43] The tip is a Au UME modified with an electrodeposited Hg thin layer. A constant potential is applied to the tip to generate a constant flux of HCOOH from the reduction of CO_2 dissolved in the $KHCO_3$ electrolyte. HCOOH is then oxidized at the electrocatalyst compositions on the GC substrate. Figure 16.9b shows the SECM images of HCOOH oxidation

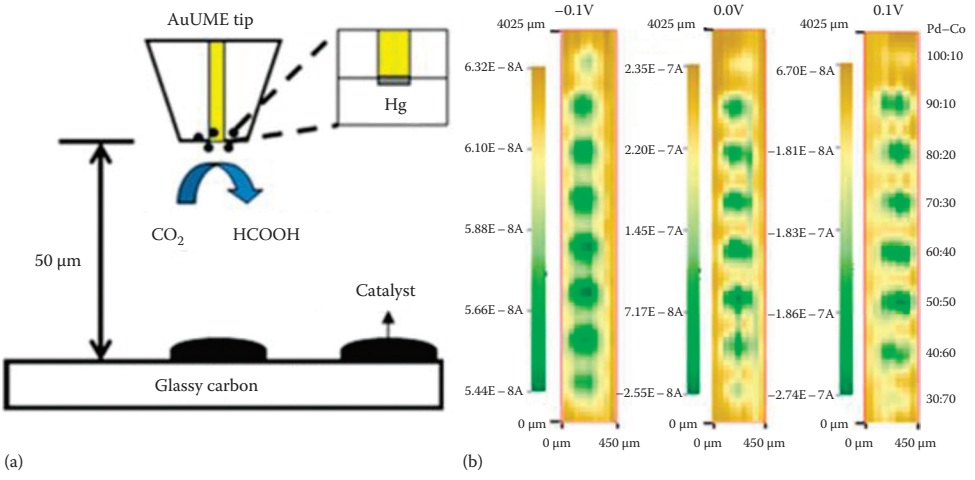


FIGURE 16.9 TG/SC mode of SECM for formic acid oxidation electrocatalyst screening. (a) The Au UME tip (25 μm diameter) is modified with an electrodeposited Hg thin layer. A constant tip potential (i.e., $E_T = -1.6$ to −2.0 V vs. Ag/AgCl) is applied to generate a constant flux of formic acid from the reduction of CO_2 gas dissolved in $KHCO_3$ electrolyte (pH = 8). (b) Formic acid oxidation SECM images of a Pd–Co electrocatalyst array at the indicated potentials. Solution: 0.1 M $KHCO_3$ saturated with CO_2. Tip–substrate distance: 50 μm. Scan rate: 250 μm/s. $E_T = -1.9$ V. (Adapted from Jung, C. et al., *Anal. Chem*., 81, 7003, 2009.)

activity on a Pd–Co electrocatalyst array at different substrate potentials. All three SECM images in Figure 16.9b show a background reduction current due to the contribution of the large GC plate to the overall current. However, either a decrease in the positive background current value (i.e., Figure 16.9b, $E_S = -0.1$ V) or a net oxidation current (i.e., Figure 16.9b, $E_S = 0.0$ and 0.1 V) appears when the tip generator is scanned above an active spot for HCOOH oxidation. Electrocatalytic activity toward HCOOH oxidation is observed at all Pd–Co spots when the substrate was held at −0.1 V in Figure 16.9b, but the current response at the pure Pd spot was smaller than at all of the other spots. When E_S was held at 0.0 or 0.1 V, the magnitude of the HCOOH oxidation currents were greatly increased compared to those at −0.1 V. The highest HCOOH oxidation current was observed at the electrocatalyst spot with the atomic ratio of Pd–Co = 50:50 ($Pd_{50}Co_{50}$), which was distinctly larger than that on the pure Pd spot over the potential range studied. Pt is also an active electrocatalyst for HCOOH, and Figure 16.10a shows the SECM imaging results for a small array with Pt, Pd, and $Pd_{50}Co_{50}$ electrocatalyst spots. The $Pd_{50}Co_{50}$ composition shows better electrocatalytic activity toward HCOOH oxidation than pure Pd or Pt. Because FAOR generally follows a mechanism leading to the formation of CO_2, the CO_2 that is generated at the substrate could diffuse back to the tip and contribute additionally, through positive feedback, to its current, which is always cathodic. For example, Figure 16.10b shows the reduction current recorded at the Hg/Au tip during imaging of Pt, Pd, and $Pd_{50}Co_{50}$ electrocatalyst spots. A tip current enhancement is observed especially when the tip is scanned across the $Pd_{50}Co_{50}$ spot. The result is an enhanced contrast during the imaging of the electrochemical activity of the spots (i.e., a larger current gap is observed between active and nonactive areas of the array in Figure 16.10a). Such a feedback loop will not be established in SECM screening where galvanostatic (i.e., constant current) control of the tip is used. The presence of the feedback loop provides additional information relating to the HCOOH oxidation mechanism and suggests that the main product of the electrocatalytic oxidation of HCOOH at the active spots on the substrate is reducible and is probably CO_2. Further evidence for the CO_2 feedback loop is shown in Figure 16.10c where the cathodic tip and the anodic substrate current responses were recorded simultaneously during a line scan in the *x*-direction over the $Pd_{50}Co_{50}$ electrocatalyst spot at a slow scan rate. This result strongly suggests that the CO_2 generated during HCOOH oxidation at the $Pd_{50}Co_{50}$ electrocatalyst spot forms a supersaturated solution and diffuses to the Hg/Au tip, providing a positive feedback loop and the cathodic current enhancement seen in the corresponding tip image (i.e., Figure 16.10b). The SECM TG/SC screening scheme shown in

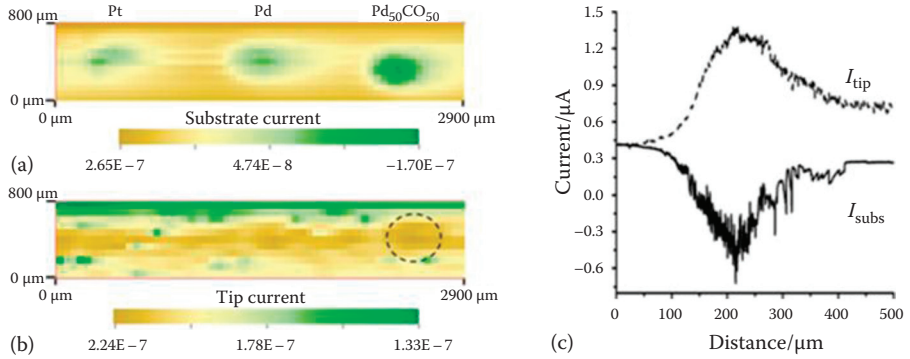


FIGURE 16.10 Formic acid oxidation SECM images and line scans at 0.1 V in 0.1 M $KHCO_3$ saturated with CO_2. Tip–substrate distance: 50 µm. E_T: −1.9 V vs. Ag/AgCl. (a) Substrate current image of Pt, Pd, and $Pd_{50}Co_{50}$ spots. Scan rate: 250 µm/s. (b) Tip current image of Pt, Pd, and $Pd_{50}Co_{50}$ spots. Scan rate: 250 µm/s. (c) Line scan of tip (I_{tip}, dashed line) and substrate (I_{subs}, solid line) current responses during Hg/Au tip CO_2 reduction and scanning in the *x*-direction (parallel to the substrate) over a $Pd_{50}Co_{50}$ electrocatalyst spot. Scan rate: 5 µm/s. (Adapted from Jung, C. et al., *Anal. Chem*., 81, 7003, 2009.)

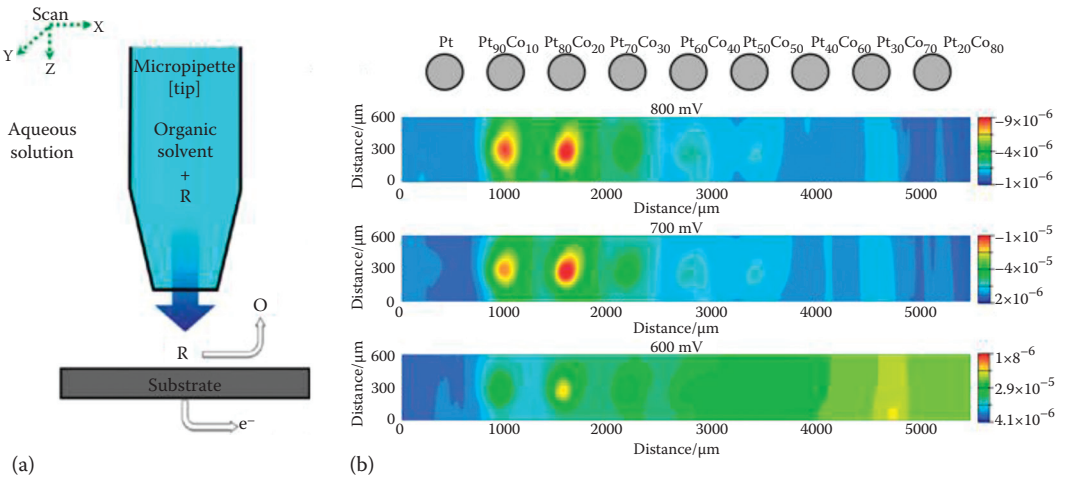


FIGURE 16.11 Micropipette delivery–substrate collection (MD/SC) mode of the SECM. (a) Scheme of the MD/SC operation. (b) MD/SC SECM image of MOR on a Pt–Ce array under different applied potentials. Micropipette opening: 11 μm. Tip–substrate distance: 30 μm. The micropipette tip was loaded with DCE solution with 30% MeOH and 6 mM $BTPPA^+TPBCl^-$. (Adapted from Lin, C.-L. et al., *Anal. Chem.*, 81, 8868, 2009.)

Figure 16.9a is applicable for the screening of new HCOOH oxidation electrocatalysts in slightly basic solution. The technique cannot be used in acidic solutions, however, because the current efficiency for CO_2 reduction is too low.[43]

A micropipette delivery–substrate collection (MD/SC) mode can be used when an electrocatalytic species of interest cannot be generated electrochemically at the tip. This mode allows electrocatalytic reactions of neutral species such as FAOR or methanol oxidation (MOR) to be studied. As shown schematically in Figure 16.11a, a micropipette with an interface between two immiscible electrolyte solutions (ITIES) is used as the tip. The micropipette is filled with a water-immiscible organic solution containing the neutral species of interest, R, that is soluble in both phases. Outside the micropipette, aqueous electrolyte is used. The neutral species spontaneously partitions across the ITIES where the resulting concentration gradient serves as the driving force to move the species into the aqueous bulk solution. Because the organic solvent is immiscible with the aqueous solution, only species R will diffuse from the interior of the micropipette across the ITIES and into the outside aqueous solution. While delivering R, the micropipette is scanned parallel to the electrocatalyst array. R diffuses into the aqueous solution and reaches the substrate where, provided a suitable potential is applied, it will react on the electrocatalyst spots to yield the spatial current response characteristic of a SECM image in a traditional TG/SC mode. To investigate the MOR, for example, the micropipette tip was loaded with methanol (MeOH) in dichloroethane (DCE) solution containing bis(triphenylphosphoranylidene)ammonium tetrakis(4-chlorophenyl)borate ($BTPPA^+TPBCl^-$) and immersed in an aqueous H_2SO_4 solution. Figure 16.11b shows the SECM images of the MOR on a series of Pt–Ce electrocatalyst spots with different metal atomic ratios prepared on a GC substrate by picoliter dispensing followed by high-temperature hydrogen reduction treatment. The $Pt_{80}Ce_{20}$ spot showed the highest MOR activity among all the spots and at all three applied array potentials shown. Similar screenings for the MOR were performed on Pt–Pb and Pt–Ce–Pb electrocatalyst arrays under different applied potentials. The $Pt_{60}Pb_{40}$ electrocatalyst showed superior MOR activity in the former array, while the $Pt_{80}Ce_{20}$ spot showed higher MOR activity than $Pt_{60}Pb_{40}$ by comparing their anodic current responses on the Pt–Ce–Pb array. Carbon-supported $Pt_{80}Ce_{20}$ electrocatalyst was synthesized, and its MOR performance was comparable to the commercial $Pt_{50}Ru_{50}$/C electrocatalyst.

16.2.3.3 Substrate Generation/Tip Collection

When the reactant of interest cannot be generated at the tip, involved in a feedback arrangement, or delivered from a micropipette, then substrate generation/tip collection (SG/TC) can be used. An example is the screening of an array with electrocatalysts for water oxidation, where, as shown in Figure 16.3c, the reactant, water, cannot be generated in an aqueous solution at the tip.[1,25] Instead, in the SG/TC mode, the substrate potential is held at different potentials and O_2 is detected at the tip. For quantitative SG/TC measurements, it is important to reach the highest possible CE, defined in Equation 16.1 as the ratio of the current flowing through one electrocatalyst spot to the current flowing through the tip. Obtaining high CE values in the SG/TC mode is more difficult compared to TG/SC since the electrocatalyst spots typically have larger radii than the tip. However, by using a tip with a sufficiently large radius (i.e., ≈50 µm), so that it still behaves essentially like a UME, and sufficiently large RG (i.e., ≈4), representing a compromise between high CE and ease of positioning, reasonably large CEs can be obtained. Another consideration in the SG/TC approach is that O_2 cannot be present in the bulk solution, and the experimental setup must provide for its removal or another method of preventing interference from O_2 generated at neighboring spots. For example, one could degas the solution or continuously replace it to keep the dissolved O_2 concentration low. However, these methods have the disadvantage of introducing a convective component to the tip current, in addition to technical complications (e.g., the use of a flow cell). Another approach is to shield the tip from the O_2 coming from the neighboring electrocatalyst spots by reducing it at the tip wall, as illustrated in Figure 16.12a.[25] The tip walls are coated with a Au layer that is held at a potential where any O_2 reaching this coating is reduced at diffusion-limiting conditions. Figure 16.12b shows a SG/TC image with the shield "off" and thus at open circuit (Figure 16.12b, A) and with the shield "on" (Figure 16.12b, B), with $E_{shield} = -0.1$ V vs. RHE and $E_S = 1.4$ V vs. RHE; the color scales for both figures have the same upper and lower limits. The array corresponding to these images had $Sn_{1-x}Ir_xO_2$ mixed oxide spots that were 300 µm in diameter and spaced closely at ~500 µm center to center. As shown in (A) of Figure 16.12b, the diffusion layers of the spots overlap, indicating that in the time needed to record the image (around 45 min), the O_2 concentration between spots is relatively high and hampers the image resolution. Additionally, the O_2 that diffuses from the neighboring spots superimposes on the spot under the tip and distorts the screening of electrocatalytic activity so that the CE is considerably higher than expected. This effect is stronger for low-activity

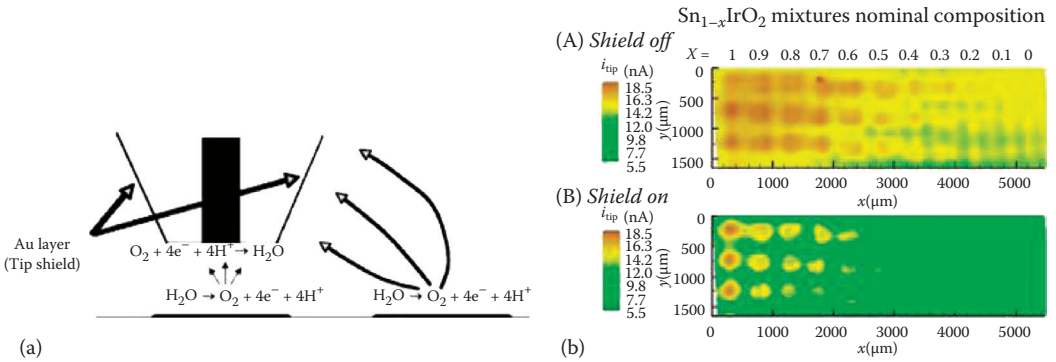


FIGURE 16.12 SG/TC experiment for O_2 evolution (OER) at the substrate and collection at the tip. (a) Tip shield approach. The tip reduces only O_2 coming from the electrocatalyst spot under investigation while O_2 coming from neighboring spots is reduced at the tip shield. (b) SECM images of an array of electrocatalytic spots of $Sn_{1-x}Ir_xO_2$ mixed oxides on Ti, with nominal x varying from 1 to 0 with increments of 0.1. Numbers show the atomic percent of Ir on a metal basis. $E_S = 1.4$ V in 0.5 M H_2SO_4 with a 100 µm diameter Au tip (RG ≈ 4, $E_T = -0.1$ V vs. RHE) with the Au shield "off," at open circuit (A), and "on," applying a potential −0.1 V vs. RHE (B). Tip–substrate distance: 35 µm. Tip scan rate: 200 µm/s. (Adapted from Minguzzi, A. et al., *Anal. Chem.*, 80, 4055, 2008.)

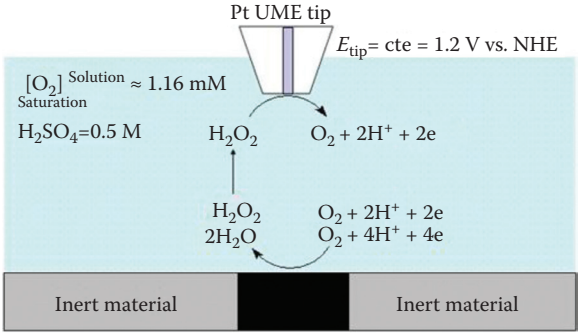


FIGURE 16.13 Substrate generation/tip collection (SG/TC) scheme for determining hydrogen peroxide production during the ORR at a substrate catalyst.

spots since the amount of O_2 produced is comparable with, or even lower than the one coming from surrounding spots. The use of the tip shield prevents this behavior, as shown in (B) of Figure 16.12b. A drawback to using the tip shield is that it reduces a fraction of the O_2 coming from the spot under the tip, thus lowering the CE. Nevertheless, the evaluation of electrocatalytic activity toward the OER on $Sn_{1-x}Ir_xO_2$ composites is straightforward when the tip shield is used during the SECM screening of the array and the images exhibit a direct proportionality between the electrocatalytic activity and the nominal Ir content of the mixed oxide.

Once a good electrocatalyst has been identified through SECM screening, the SG/TC mode coupled with simultaneous linear sweep voltammetry can be used for studies similar to those with rotating disk or RRDEs.[21,22] For example, Figure 16.13 shows a scheme of the experiment for determining H_2O_2 produced during the ORR in acidic solution at a substrate electrocatalyst. The desired overall reaction involves $4e^-$ to produce only H_2O

$$O_2 + 4H^+ + 4e^- \rightarrow 2H_2O \quad E^0 = 1.229 \text{ V} \tag{16.2}$$

and represents the overall thermodynamically favored path. However, it is unlikely that the reaction occurs as one elementary step mechanistically because of the complexity of the reaction involving four electrons, four protons, and O–O bond cleavage. H_2O_2 can be generated during the ORR as the final product (Reaction 16.3) or as an intermediate that undergoes further reduction (Reaction 16.4) and/or disproportionation (Reaction 16.5), depending on the electrocatalytic material where the reaction takes place. This is the so-called peroxide mechanism for the reduction of O_2 to H_2O_2 and H_2O, as shown in the following reactions of interest:

$$O_2 + 2H^+ + 2e^- \rightarrow H_2O_2 \quad E^0 = 0.67 \text{ V} \tag{16.3}$$

$$H_2O_2 + 2H^+ + 2e^- \rightarrow 2H_2O \quad E^0 = 1.77 \text{ V} \tag{16.4}$$

$$2H_2O_2 \rightarrow 2H_2O + O_2 \tag{16.5}$$

Another proposed mechanism for the ORR is the metal oxide route involving initial reaction of O_2 with a metal (as in corrosion reactions) followed by the reduction of the resultant metal oxide:

$$2M + O_2 \rightarrow 2MO \tag{16.6}$$

$$MO + 2H^+ + 2e^- \rightarrow M + H_2O \tag{16.7}$$

Reactions 16.2 through 16.7 can occur in series or in parallel and lead to different overall amounts of H_2O_2 produced and number, n, of electrons transferred. Although the mechanism for the ORR is not known, a combination of the other reaction paths (e.g., reactions 3+4, 3+5, and 6+7) are equivalent to the overall $4e^-$ pathway of Reaction 16.2. As shown in Figure 16.13, the substrate represents the electrocatalyst spot on an inert conductor. The tip–substrate distance is set at a known value (≈10 μm), since the CE for H_2O_2 depends on this distance. The potential of the substrate is then scanned at a low scan rate from a potential where O_2 is not reduced to active potentials for O_2 reduction. At the same time, the tip is held at a constant potential where any H_2O_2 generated at the electrocatalyst spot is oxidized under diffusion-controlled conditions. The substrate and tip currents are compared for any given potential and the maximum CE value, CE^{max}, for the particular tip–substrate distance is obtained from calibration experiments with the same electrode geometry and a stable redox couple (e.g., analogous to calibrations with RRDEs).[21,22] The electrons transferred during the ORR on a particular electrocatalyst and the percentage of H_2O_2 generated are calculated from Equations 16.8 and 16.9, respectively,

$$n = \frac{4i_{subs}}{i_{subs} + \left|\frac{i_{tip}}{CE^{max}/100}\right|} \tag{16.8}$$

$$H_2O_2\% = \left[\frac{4-n}{2}\right] \times 100 \tag{16.9}$$

Using this SG/TC mode of SECM coupled with simultaneous LSV, H_2O_2 formation during the ORR with eight different substrate materials (Hg, Au, Ag, Cu, Pt, Pd, $Pd_{80}Co_{20}$, and $Au_{60}Cu_{40}$) in 0.5 M H_2SO_4 solution was studied.[22] Hg was the only material that showed an n value close to the $n=2$ value for exclusive production of H_2O_2 over the entire potential window of the ORR (e.g., 0.1 to −0.4 V vs. RHE), while for Au, $2.1 < n < 2.5$ (e.g., 0.3–0.05 V vs. RHE), and Cu showed a sharp transition from $n \approx 2$ at potentials close to the corrosion potential (e.g., 0.24 V vs. RHE) to $n \approx 4$ at more negative potentials. The $Au_{60}Cu_{40}$ electrocatalyst showed an n value variation from 3.4 to 3.9 over a potential range (e.g., >0.2 V vs. RHE) more positive than either Au or Cu. Thus, incorporation of Cu into Au increases the overall n value compared to Au and suggests that Cu decreases the amount of H_2O_2 produced. An additional interpretation can be attributed to the synergistic effect of adding Cu to Au according to the metal oxide mechanism (e.g., Equations 16.6 and 16.7), consistent with several previous bimetallic combinations from the TG/SC ORR screening described in the previous section.[10,11,32–37] Although $Au_{60}Cu_{40}$ exhibited much lower H_2O_2 production than Au alone during the ORR, the potential region for oxygen reduction is significantly less positive than that needed for a good electrocatalyst. Figure 16.14a (A–C) show the tip and substrate currents collected using the SG/TC mode of SECM during the ORR at Pt, Pd, and $Pd_{80}Co_{20}$ (e.g., the electrocatalyst composition identified from TG/SC SECM imaging in Figure 16.7) electrodes. As can be seen, the ORR at Pt (A) begins at more positive substrate potentials and shows the lowest H_2O_2 generation–tip collection currents (i.e., I_{tip} scales) compared to either Pd (B) or $Pd_{80}Co_{20}$ (C). The $Pd_{80}Co_{20}$ electrocatalyst shifts the potentials for the ORR to more positive ones compared with pure Pd and also greatly decreases H_2O_2 generation collection currents compared with Pd. Figure 16.14b shows the n value variation as a function of applied potential for Pt, Pd, and $Pd_{80}Co_{20}$. Pt and $Pd_{80}Co_{20}$ exhibit n values much closer to the $n=4$ maximum, with Pd exhibiting a gradual transition from lower ($n=2.8$) to higher ($n=3.6$) n values depending on potential. The improvement in the ORR activity of Pd by incorporation of Co exhibited in $Pd_{80}Co_{20}$ has been attributed to the properties of Co in splitting the oxygen bond, which mainly directs the ORR through the metal oxide pathway (Reactions 16.6 and 16.7).[32,36] However, the results in Figure 16.14a and b shows the production of a small amount of H_2O_2, suggesting a small contribution from the peroxide pathway

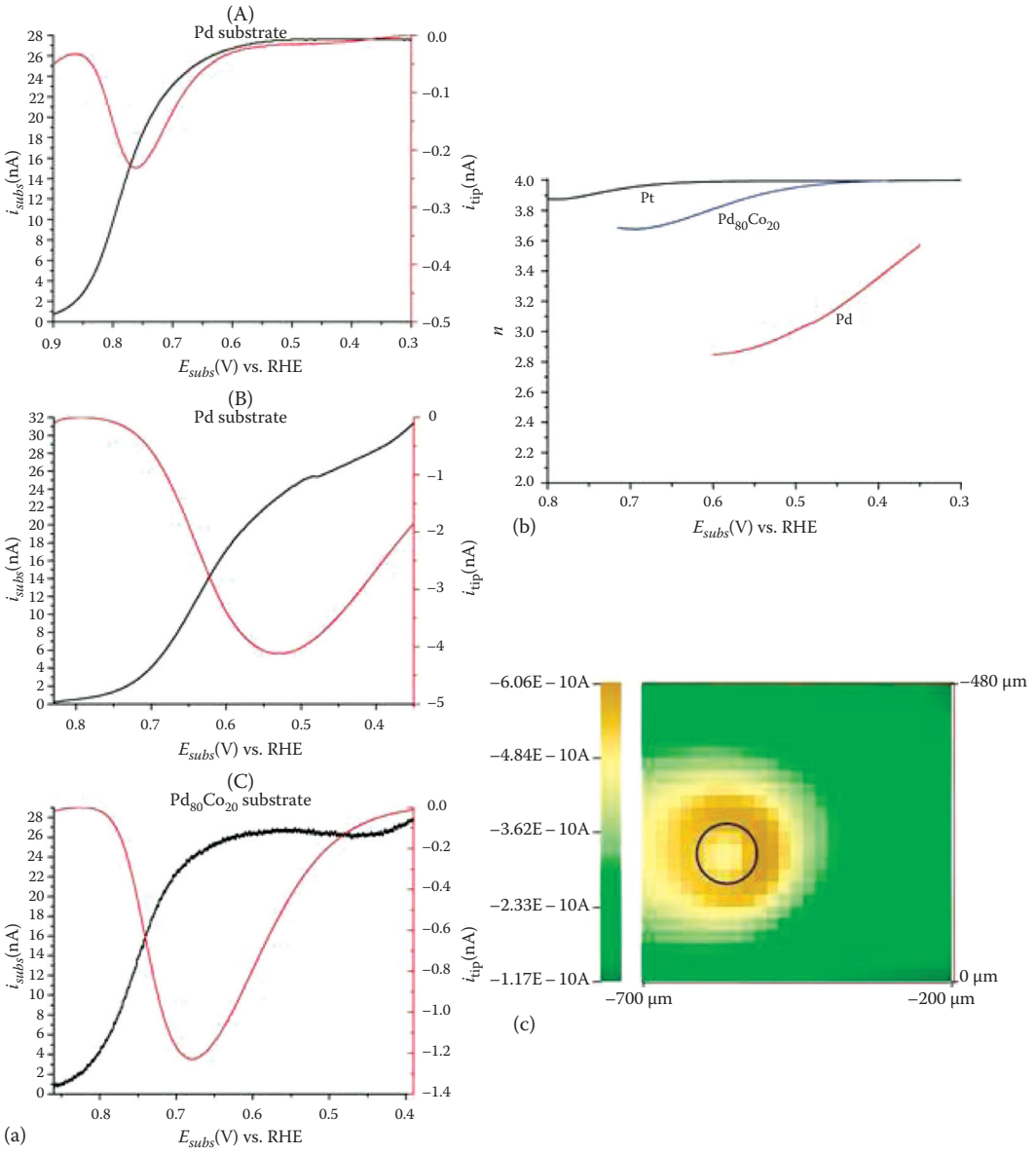


FIGURE 16.14 SG/TC experiments for the ORR in O_2-saturated 0.5 M H_2SO_4 solution at 100 µm diameter Pt, Pd, and $Pd_{80}Co_{20}$ substrates and simultaneous H_2O_2 collection at a Pt tip (25 µm diameter, RG = 6). (a) ORR at Pt, Pd, and $Pd_{80}Co_{20}$ spot substrates (black lines) and simultaneous H_2O_2 quantification at a Pt tip (red lines), d = 10 µm (CE^{max} = 49%) for Pt and Pd and d = 7 µm (CE^{max} = 60%) for $Pd_{80}Co_{20}$. (A) Pt, (B) Pd, and (C) $Pd_{80}Co_{20}$. (b) Number of electrons transferred (n) during ORR at Pt (black line), Pd (red line), and $Pd_{80}Co_{20}$ (blue line) as a function of applied potential. (c) SECM SG/TC image displaying the tip current for H_2O_2 collection above a single $Pd_{80}Co_{20}$ spot supported on GC (circled area), d = 40 µm. E_{tip} = 1.2 V and $Pd_{80}Co_{20}$ substrate held at 0.4 V. Scan rate = 100 µm/s. (Adapted from Sanchez–Sanchez, C.M. and Bard, A.J., *Anal. Chem*., 81, 8094, 2009.)

(Reactions 16.3 through 16.5). Further evidence for this small contribution from the peroxide pathway is shown in the SECM image of Figure 16.14c of H_2O_2 collection current when the tip scans above a $Pd_{80}Co_{20}$ spot held at 0.4 V (where n = 4.0 according to Figure 16.14b). The black circle in this figure marks the substrate spot location. The collection current of the tip when over the electrocatalyst spot is smaller than that in the vicinity around the spot where H_2O_2 can diffuse away in

solution without undergoing any further reaction such as reduction (Equation 16.4) or disproportionation (Equation 16.5). In contrast to the steady-state SG/TC approach to H_2O_2 quantification shown in Figures 16.13 and 16.14, a transient SG/TC SECM mode has also been used to detect the ORR at macroscopic electrodes. This transient approach is based on the calculation of effective rate constants for the different reaction paths involved in the ORR and the determination of the concentration profiles of H_2O_2.[23]

16.2.3.4 Shielding

When the species to be studied cannot be conveniently generated at an electrode and no product of the electrode reaction can be detected, then SECM shielding (Figure 16.3d) can be used to screen an array. In shielding, the same reaction occurs at the tip and the substrate so that the current at the tip is decreased compared to what would be observed with an insulating substrate.[7,45] Thus the tip is shielded by and competes with the substrate for the same reactant. A reactant in bulk solution can be studied by noting how well the substrate competes with the tip for consumption of the reactant. This approach, also called redox competition (RC-SECM), was used to study the ORR on model Pt and Au catalyst spots as an alternative to TG/SC.[14–16,18]

16.3 PHOTOCATALYSIS

Utilization of sunlight to produce chemical energy has led to increased activity in the area of photoelectrochemistry (PEC). There has been growing interest in the use of sunlight to generate fuels like hydrogen, or, combined with CO_2 mitigation, carbonaceous fuels. PEC cells are composed of at least one electrode composed of a semiconductor that is irradiated to generate electron–hole pairs that can be used to produce a current and drive redox reactions.[46–49] In one configuration, an oxidation reaction occurs at an n-type semiconductor and a reduction reaction at the counter electrode. Alternatively, a p-type semiconductor electrode drives a photoreduction with an oxidation at the counter. PEC cells can also employ a pair of semiconductor electrodes. While extensive research over about the last 40 years has led to the elucidation of the general principles for semiconductor electrochemistry and a number of semiconductor materials have been investigated, cells with the efficiencies, costs, and stabilities for a practical, deployable system have not yet been produced. The photocatalyst is the key component of the PEC cell and a lot of effort is now directed toward the discovery of new materials, especially compounds with several metal ions, and, as discussed in the section on electrocatalysts, SECM is also an excellent method for the study of semiconductor photocatalysts and for the systematic screening of their arrays.

16.3.1 SECM Studies of Photocatalysts

The first applications of SECM in PEC were measurements of the rate of electron transfer in the dark to n- and p-WSe_2 electrodes in aqueous electrolytes and at n-Si in acetonitrile and methanol, with the same approach as that described in Chapter 6.[50] For semiconductor electrodes, dark oxidations can be carried out for p-type materials, and dark reductions for n-type ones. SECM has the advantage of making such measurements without difficulties from electrode resistance and capacitance and without perturbation from currents from the corrosion of the semiconductor material itself. In one case, p-WSe_2 with $Ru(NH_3)_6^{3+}$ as a mediator, the results agreed with the expected model for the rate constant as a function of potential (i.e., $\alpha \cong 1$). However, with other mediators or with n-WSe_2 or p-Si this behavior was not seen.

A TiO_2 film on an ITO film in a solution $Fe(CN)_6^{4-}$ was irradiated from above and the Pt tip current from $Fe(CN)_6^{4-}$ oxidation measured as a function of L. By noting the change from negative to positive feedback as a function of irradiation and L, the authors concluded that reduction of $Fe(CN)_6^{3-}$ can occur at sites on the open circuit TiO_2 film under irradiation.[51] Work with an irradiated

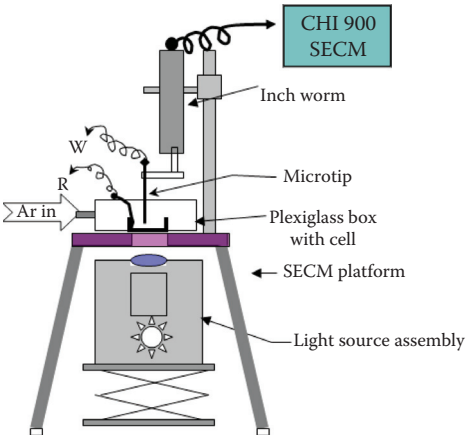


FIGURE 16.15 Setup used for SECM measurements of an n-CdS film on glass that was back-illuminated. It is difficult to illuminate the tip–substrate gap from the top because of the drive assembly. The cell was enclosed in a Plexiglass box filled with Ar to avoid air oxidation of MV^+. (From Haram, S. and Bard, A.J., *J. Phys. Chem. B,* 105, 8192, 2001.)

semiconductor, a film of particles of n-CdS on glass, with methyl viologen ($MV^{2+/+}$) as mediator and triethanol amine (TEA) as sacrificial electron donor, followed.[52] In SECM studies of this type, different approaches to the semiconductor sample irradiation have been used: irradiation through a transparent substrate, irradiation through a fiber optic, or irradiation from a focused beam into the tip–substrate gap. In this study, the CdS film was irradiated from below and always was at open circuit (Figure 16.15). The tip current was employed to find the quantum efficiency of the film reaction. Note that an earlier study of a CdS film was described as an SECM study, but actually was an electrochemical scanning tunneling microscopic investigation.[53] Two studies have dealt and the photochemical decomposition of chlorophenols over a TiO_2 film with detection of Cl^- with a Ag/AgCl UME[54,55] and monitoring the depletion of O_2 at a Pt UME.[56] The tip responses were employed to analyze the kinetics of the processes.

A transient (time-of-flight) approach was used to find the diffusion coefficient of ferrocenium (Fc^+) in a nanostructured TiO_2 film in a dye-sensitized solar cell (DSSC) configuration.[57] By measuring the tip response for Fc^+ reduction (where Fc^+ is produced by the photoreaction) as a function of tip–substrate distance, the *D*-value within the film could be determined. A steady-state measurement was used to measure the rate constant for the oxidation of I^- by the oxidized dye under irradiation with ZnO/eosin Y[58,59] or ZnO/dye D149 DSSCs.[60]

PEC measurements were also carried out with a modified optical fiber in an SECM, sometimes called scanning photoelectrochemical microscopy (SPECM) (Chapter 17). This was used to look at the photogeneration of Br_2 on irradiated TiO_2,[61] with a main interest in studying corrosion films on metals.[62–64] The most recent thrust of SECM in PEC studies has been in comparative studies of the effect of modifications of photocatalysts prepared as arrays and screened with the SECM, which is discussed in the following sections.

16.3.2 Array Fabrication

Generally, array preparation for photocatalysts is similar to that for electrocatalysts, with the use of a robotic dispenser and solution precursors, as discussed in Section 16.2.2. A summary of the arrays discussed in given in Table 16.3.[65–71] Generally, the arrays are prepared on cleaned FTO on glass substrates that can be safely heated to 500°C or somewhat higher without irreversible changes. The solutions used to prepare oxides are typically metal salts, for example, nitrates or chlorides,

TABLE 16.3
Representative Arrays Screened by SECM

Major Component	Additional Metals	Additional Components	PEC Reaction	References
n-Fe_2O_3	Rb, Ni, Pd, Eu		Na_2SO_3 oxidation, 1 M KOH	[65]
n-$BiVO_4$	Zn		OH^- oxidation to O_2, 0.2 M NaOH	[65]
n-Fe_2O_3	Sn, etc.	Be, Al, etc.	OH^- oxidation to O_2, 0.2 M NaOH	[66]
n-Fe_2O_3	Ag	Sn	OH^- oxidation to O_2, 0.2 M NaOH	[67]
n-M_1-M_2-O	M_1 = Cd, Zn, etc.	M_2 = In, Ga, etc.	Na_2SO_3 oxidation, 1 M KOH OH^- oxidation to O_2, 0.2 M NaOH	[68]
n-$BiVO_4$	W		Na_2SO_3 oxidation, 0.1 M Na_2SO_4 H_2O oxidation to O_2, 0.1 M Na_2SO_4	[69]
p-$CuInSe_2$	Ga, Zn, Cd	S	O_2 reduction, 0.1 M Na_2SO_4	[70]
$Zn_xCd_{1-x}S_ySe_{1-y}$			S^{2-} oxidation, 0.1 M Na_2SO_4	[71]

at ~0.1 M concentration, in ethylene glycol or glycerol mixtures with water. The choice of solvent depends on the substrate used and is critical in getting reproducible spot sizes and thicknesses. These are then heated in air by ramping up the temperature to 500°C and holding at this temperature for several hours to convert to the oxide. For other semiconductors, for example, $Zn_xCd_{1-x}S_ySe_{1-y}$,[71] the metal solutions added were 0.1 M $Zn(NO_3)_2$ and $Cd(NO_3)_2$ in a 3:1 solution of water/glycerol. The solutions to produce the anions were 0.2 M thiourea and dimethyl selenourea (containing 0.05 M hydrazine). The arrays were held at 100°C for 12 h under an Ar atmosphere to produce the mixed sulfide–selenide.

The composition of the arrays is often given in terms of the relative amounts of the species dispensed, for example, the number of drops of each solution. The actual compositions of the drops can be determined, for example, by x-ray photoelectron spectroscopy (XPS). The transparent FTO substrate, while not important in the screening, as discussed later, does make it possible to characterize spots spectroscopically, as shown in Figure 16.16, where the absorbance spectra can be used to estimate the band gaps of the spot materials.[71]

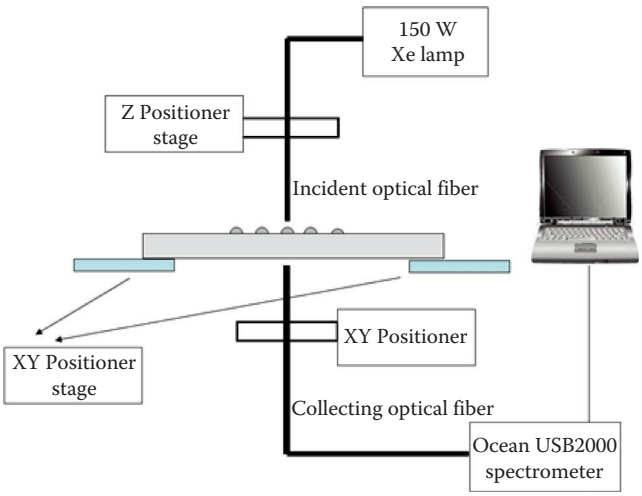


FIGURE 16.16 Setup used for light absorption measurements of the arrays. (From Liu, G. et al., *J. Phys. Chem. C*, 114, 20997, 2010.)

16.3.3 Array Screening

In screening the arrays, the UME tip in the SECM is replaced by an optical fiber (400 μm diameter) connected, via a five-axis fiber aligner, to the Xe lamp. A schematic diagram of the arrangement is shown in Figure 16.17. The fiber is larger than the usual SECM tip and the spots used in these arrays are spaced further apart than the electrocatalyst arrays, so that two spots are not irradiated at the same time. With just a fiber optic, the readout is the substrate photocurrent when a spot is addressed by the Xe lamp. The background current is governed by the dark and photocurrents on the FTO. The optical fiber can also serve as a tip, for example, to detect products produced in the photoreaction or to use SECM approach curves to adjust the distance between the optical fiber surface and the substrate.[65] In this case, a commercial gold-coated optical fiber is used and sealed in borosilicate glass while heating under vacuum, to form a glass insulator around the Au ring. Typical dimensions are shown in Figure 16.18. The smaller fiber (200 μm diameter) decreases the light irradiating the spots compared to the 400 μm one, correspondingly decreasing the photocurrent. Smaller electrodes that incorporate a pulled fiber, a vacuum-deposited Au ring, and electrophoretic paint insulation can be prepared,[72] at the expense of greatly diminished light availability at the array. All of the photocatalyst work carried out so far has employed the larger optical fibers.

Measurements of arrays are basically made by looking at the comparative behavior of spots of different materials. Since the irradiation source is larger than the spots, it is important to maintain the spot sizes the same. Examination of the array by a surface profiler, for example, the Veeco NT-9100 optical profiler, is useful in ensuring uniformity.[71] Often one or more calibration spots of a known material are added to the array for the purpose of calibration and test of reproducibility. When products are examined with the ring electrode, one is operating in the SG/TC mode, however, in a different geometry (large substrate–ring tip) than the usual SECM configuration. The current scale has to be adjusted over a large enough range that observed differences are meaningful and that current densities represent reasonable photoresponses at the given light intensity.

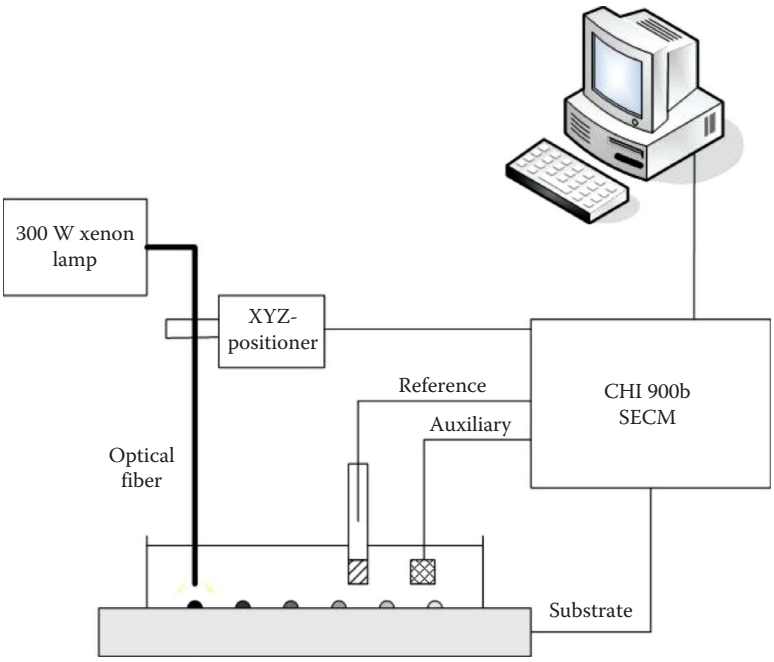


FIGURE 16.17 Setup for using an optical fiber for screening photocatalyst spots on an array. (From Lee, J. et al., *Anal. Chem*., 80, 7445, 2008.)

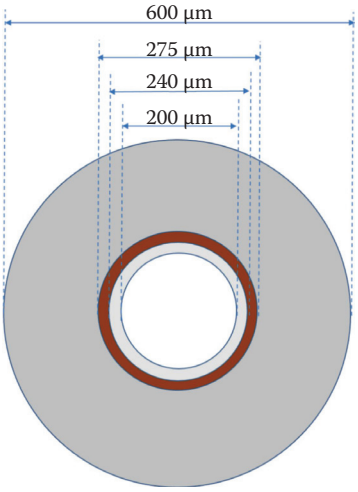


FIGURE 16.18 Bottom of a gold ring optical fiber electrode. (From Lee, J. et al., *Anal. Chem*., 80, 7445, 2008.)

A representative array study is that examining the effect of addition of W to $BiVO_4$ to its PEC behavior.[69] $BiVO_4$ has been of interest in recent years because it has a reasonable band gap and photoresponse and is capable of evolving O_2. However, its solar efficiency as the pure material is not sufficient to be of practical interest. Recent work on many materials has focused on the effect of changing composition and structure to improve performance. This involves changes in band gap and light absorption properties, but also changes in carrier mobility, carrier recombination rates, interfacial charge transfer rates, and other properties that can have a large effect on efficiency. For example, a triangular array of spots on FTO was prepared from solutions of $Bi(NO_3)_3$, VCl_3, and $(NH_4)_{10}W_{12}O_{41}$ as 0.1 M ethylene glycol solutions. A total of 10 drops was dispensed at each location, with the number from the different metals varying between 0 and 10 (Figure 16.19). A scan of this array in a solution of 0.1 M $NaSO_4$ and 10 mM Na_2SO_3 is shown in Figure 16.20. As shown, the spot with the dispensed ratio Bi/V/W of 5:4:1 is significantly more efficient than those lacking the W. After finding a hit by SECM, it is, of course, necessary to characterize the material and test it in larger cells.

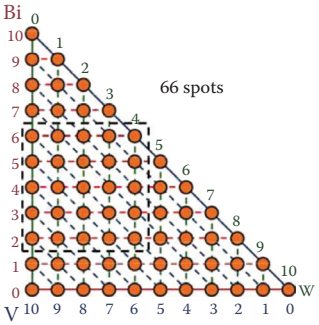


FIGURE 16.19 Bi/V/W/O array. The number of drops of each component is shown outside the triangle and they correspond to those in the corresponding line. The vertical axis represents Bi/V/O mixtures, the horizontal axis, V/W/O mixtures, and the diagonal, Bi/W/O mixtures. The top spot is bismuth oxide, the bottom left spot is vanadium oxide, and the bottom right spot is tungsten oxide. Black dashed box matches the positions of the arrays in the SECM images in the figure. (From Ye, H. et al., *J. Phys. Chem. C,* 114, 13322, 2010.)

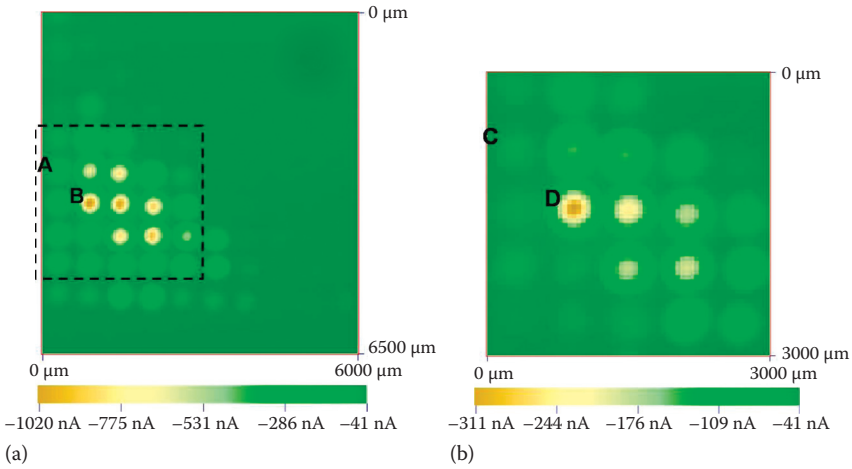


FIGURE 16.20 SECM images of the Bi/V/W oxide array with the distribution shown in Figure 16.19 at 0.2 V under (a) UV–visible and (b) visible (λ > 420 nm) radiation. Spots A and C have the composition Bi/V of 5:5. The highest intensity is shown in the spot (B and D) with the ratio Bi/V/W of 5:4:1. Array scanned at 500 μm/s. (From Ye, H. et al., *J. Phys. Chem. C,* 114, 13322, 2010.)

For example, the above sample, when examined by XPS, showed a composition of 51% Bi, 39% V, and 10% W, within experimental error to the dispensed ratio, with peaks consistent with oxidation states +3, +5, and +6, respectively. The bulk film PEC studies agreed with the array scans and showed improvements in photocurrent in both the UV–visible and visible region by factors of 3–4.

The analogous screening of the four-component $Zn_xCd_{1-x}S_ySe_{1-y}$ system is illustrated in Figure 16.21. The top left spot is ZnS and the bottom right spot is CdSe. The $Zn_{0.3}Cd_{0.7}S_{0.8}Se_{0.2}$ spot showed the highest activity under both UV–visible and visible light. A measure of the reproducibility of size and thickness of a 25-spot array is shown in Figure 16.22, which shows an optical surface profiler scan of the array.

16.4 SURFACE INTERROGATION SECM

In addition to using the feedback and collection modes to quantify the activity of electrocatalysts by measuring or mapping the reactivity of the substrate electrode, SECM can also be used for the in situ study of adsorbed reaction intermediates and products formed on the substrate. Techniques for the characterization of adsorbed species are readily available in high vacuum studies of catalytic systems but many of them are inapplicable to electrocatalytic systems since they feature additional challenges due to the inherent presence of an electrolytic medium. The quantification and characterization of adsorbed species on electrodes is done in the surface interrogation mode of SECM (SI-SECM),[73] which is an application of the feedback mode under transient conditions. In this mode, the SECM tip produces a reactive redox mediator that is used to "microtitrate" the adsorbed species formed at a substrate after it has carried out an electrocatalytic process. The analysis of the resulting time-dependent feedback current can be used to detect and quantify these adsorbates, that is, reaction intermediates and/or products, and can be further analyzed to yield other chemical parameters such as the reaction kinetics of the mediator with the adsorbed species. Selection of a suitable mediator yields information about the type and reactivity of the adsorbed species and can be used to further identify them at the electrode. SI-SECM thus allows the examination of inner sphere electrode processes, for example, electrocatalysis, directly and quantitatively through a simple SECM platform. Transient SECM current measurements have been implemented in other SECM studies, for example, chronoamperometry[74] and cyclic voltammetry.[45,75] The study of the effects of mediator

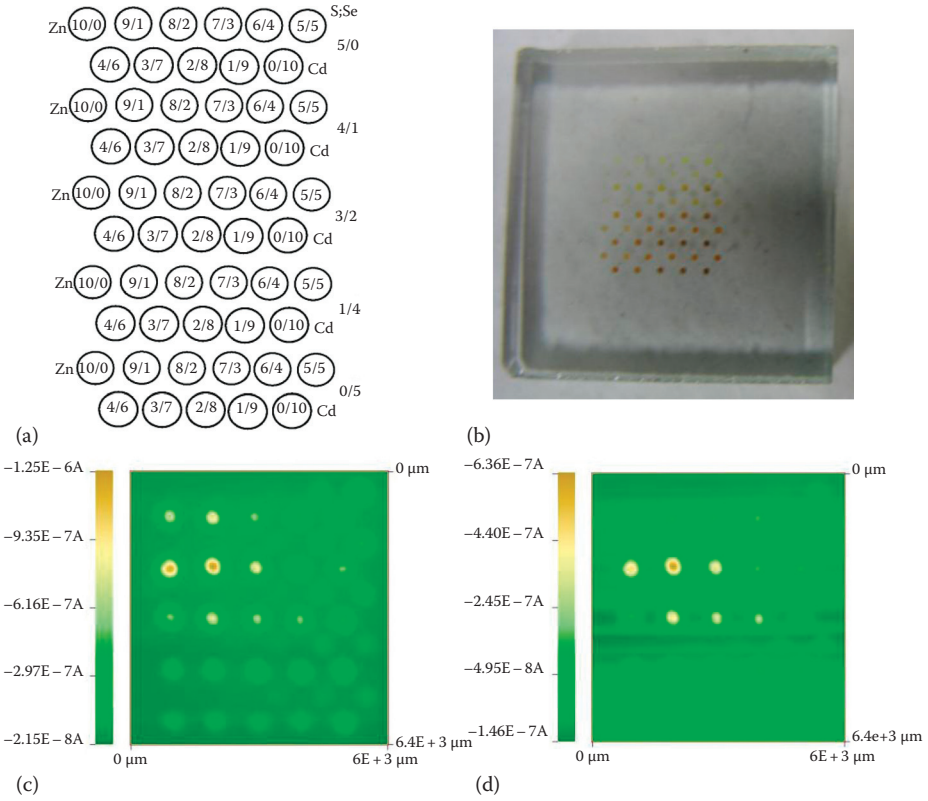


FIGURE 16.21 (a) Dispensed pattern of $Zn_xCd_{1-x}S_ySe_{1-y}$ array, (b) photograph of array sample, (c and d) SECM images of the array photocurrent in a 0.1 M Na_2SO_4/Na_2S solution with the array held at −0.4 V vs. Ag/AgCl with (c) UV–visible and (d) visible light irradiation. The $Zn_{0.3}Cd_{0.7}S_{0.8}Se_{0.2}$ spot shows the largest photocurrent. (From Liu, G. et al., *J. Phys. Chem. C*, 114, 209972, 2010.)

surface diffusion,[76,77] applications to the study of lateral charge propagation in polymer films,[78,79] and diffusion in monolayers,[80] as well as the detection of reactive species in living cells,[81] have been developed through the use of the transient feedback mode. SI-SECM differs mainly in that the chemical species probed are generated in situ at the catalytic substrate and in its selective and quantitative description of these species.

16.4.1 Operation Mode and Experimental Considerations

The SI-SECM mode allows for the quantification of finite amounts of reacting species on a substrate surface at open circuit, that is, left unbiased after treatment. The sensing mechanism is based on allowing the tip-generated member of a redox pair O/R to react chemically with the adsorbed species at the substrate electrode. The tip current reports the amount of adsorbate to the SECM tip through a feedback loop. SI-SECM is unique in that the reactive species generation and the detection scheme based on the feedback mode of SECM are integrated into the same electrochemical tip, which simplifies notably the experimental setup.

In SI-SECM, the tip is approached and concentrically aligned to a substrate electrode (typically a microdisk of the same size as the tip) to at least $L = d/a \leq 0.3$ (e.g., if both microdisk electrodes were 12.5 µm in radius, a, held at a short distance from each other, $d \sim 1$–3 µm) for obtaining a large CE[21] and enhancing the positive to negative feedback contrast. A small substrate size is required to prevent

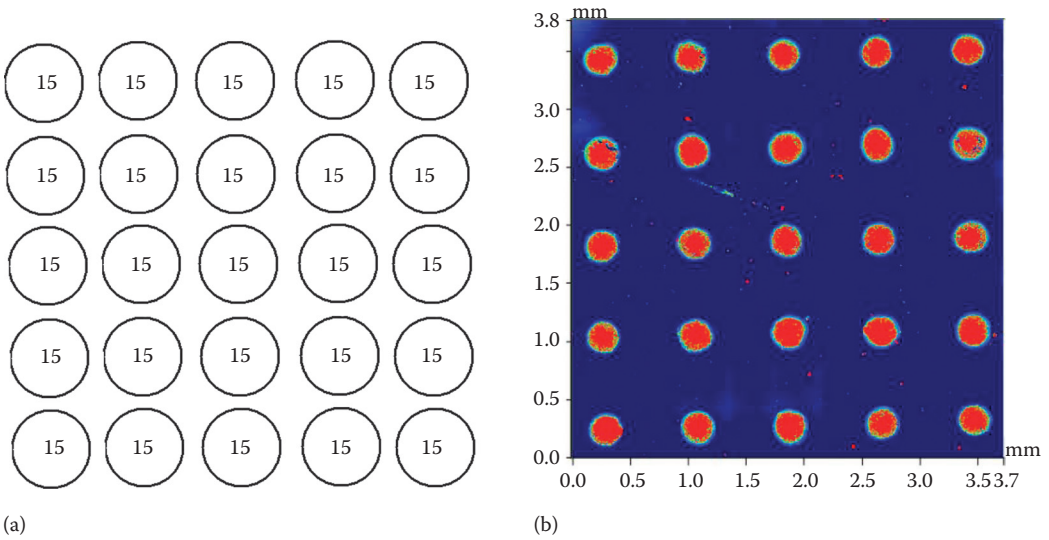


FIGURE 16.22 (a) Dispensed pattern of the 25 spot films. (b) The optical surface profile of the $Zn_{0.3}Cd_{0.7}S_{0.8}Se_{0.2}$ 25 spot array. The color of the spot is a measure of thickness. (From Liu, G. et al., *J. Phys. Chem. C*, 114, 20997, 2010.)

open circuit positive feedback, as well as to provide an easily accessible area for adsorbate quantification. Open circuit positive feedback with a reversible mediator occurs when the substrate electrode is considerably larger than the tip microdisk, and consists in the establishment of a local positive feedback loop at the tip–substrate gap with nonlocal mediator regeneration through lateral charge transfer.[26,82,83] If the substrate is made small, then there is no possibility for lateral charge transfer and mediator regeneration does not occur, *unless a reactive species is adsorbed at the substrate*.

The steps of the SI-SECM process are depicted in Figure 16.23 for a reducible adsorbed species, and a mediator pair O/R where the oxidized species O is present initially in solution. In step (a), the substrate is pulsed or scanned to a potential where oxidation occurs and an adsorbed species, A, is formed; the tip at this time is kept at open circuit. In Figure 16.23 step (b), the substrate electrode is

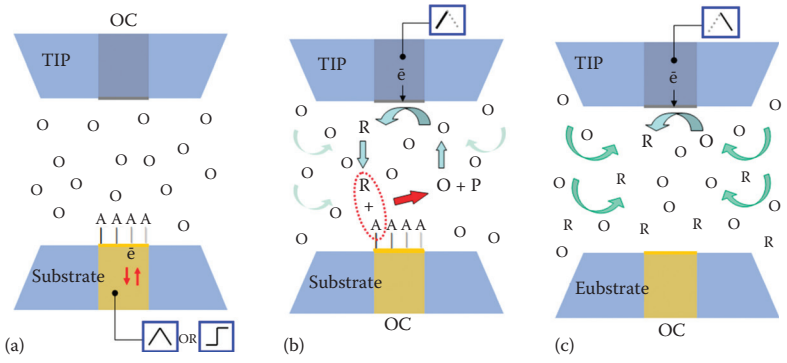


FIGURE 16.23 Schematics of the proposed mechanism for SI-SECM. (a) A reactive species is chemically or electrochemically adsorbed at the substrate upon a potential scan or step while the tip is at open circuit. (b) The substrate is taken to open circuit and the tip generates the titrant that reacts at the surface of the substrate to support positive feedback. (c) After consumption of the adsorbate at the substrate, the tip experiences negative feedback. (Adapted from Rodríguez-López, J. et al., *J. Am. Chem. Soc.*, 130, 16985, 2008.)

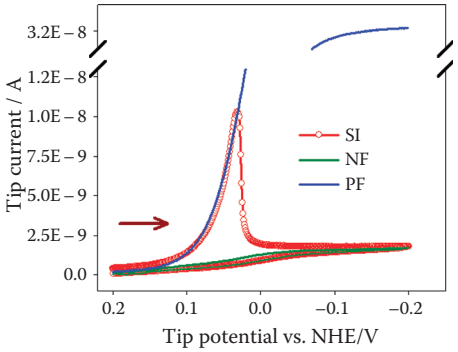


FIGURE 16.24 Representative SI-SECM result of the mediated reduction of Au oxide with hexaammineruthenium(II). Au substrate was oxidized for 30 s in Tris buffer 0.3 M pH = 7 at 1.4 V vs. NHE. The first cycle (SI scan) shows a clear transient feedback that follows the trace of an independent positive feedback experiment under the same alignment. The negative feedback was taken in the absence of substrate oxidation. Both tip and substrate are Au microelectrodes $a = b = 12.5\,\mu m$. Scans ran at $\nu = 50$ mV/s, solution contained 1 mM $Ru(NH_3)_6^{3+}$, electrode gap $L \sim 0.1$. (Adapted from Rodríguez-López, J. et al., *J. Am. Chem. Soc*., 130, 16985, 2008.)

taken to open circuit and the tip is scanned or pulsed to reduce O and generate the reduced species R. After R diffuses across the tip–substrate gap, it reaches the adsorbed species A and reacts chemically with it. A is consumed and transformed into a final product, P, and O will only be regenerated as long as A is available. As shown in Figure 16.23 step (c), the final state of the system shows negative feedback after all A is depleted.

We can take as an example the interrogation of oxides at a gold substrate by the mediator hexaammineruthenium, $Ru(NH_3)_6^{3+/2+}$ which has a standard potential $E^0 = 0.05$ V vs. NHE[84] and whose reduced form can react with these species. At pH = 7, gold shows the onset of oxidation at ~0.9 V vs. NHE, then the reaction with $Ru(NH_3)_6^{2+}$ is allowed thermodynamically by at least $\Delta E^0 \geq 0.85$. Assuming a stoichiometry for the surface oxide, this reaction can be written as shown in Equation 16.10:

$$Au_2O_3 + 6Ru(NH_3)_6^{2+} + 6H^+ \rightarrow 2Au + 6Ru(NH_3)_6^{3+} + 3H_2O \qquad (16.10)$$

Figure 16.24 shows a typical result of SI-SECM run in the CV mode for the reduction by tip-generated $Ru(NH_3)_6^{2+}$ of Au oxides formed at 1.4 V; the tip current shows a transient positive feedback response that follows initially the electrochemical positive feedback curve. The titration of the gold oxide by the reducing agent follows this curve until the consumption of the surface oxide causes a sharp decrease in the feedback current that drops to the level of the expected negative feedback. The amount of oxide formed in this case can be obtained by subtraction of the negative feedback blank and integration of the resulting signal.

The nature of the system under study using SI-SECM will determine the type of mediator to be used. One has to decide if the adsorbed intermediate under study is oxidized or reduced; then one must also consider the availability of mediators that can accomplish the desired transformation (e.g., thermodynamically), their interaction with the electrolyte and with the substrate, as well as the possibility to electrogenerate them with an available tip material. Once these basic conditions are met, other factors, such as the reaction kinetics of the mediator with the adsorbed species or its selectivity toward it, can also be considered. Figure 16.25a shows a good example of the selection process in the interrogation of adsorbed hydrogen on Pt (species formed in the dotted box) in acidic media,[85] for which a good interrogation mediator is *N*,*N*,*N*′,*N*′-tetramethyl-*p*-phenylenediamine (TMPD). The criteria used to determine the goodness of a mediator was largely based on the following characteristics: (1) high to moderate solubility in the medium, (2) stability of both forms of

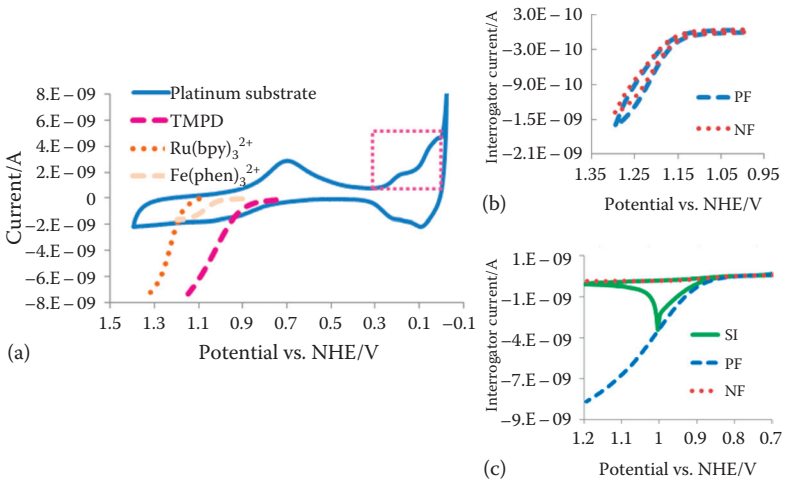


FIGURE 16.25 Experimental considerations for mediator selection. For all, interrogator electrode is Au ($a = 12.5\,\mu m$) approached to $L \approx 0.2$ from a Pt substrate UME ($b = 12.5\,\mu m$); all PF scans taken with E_{sub} at least 0.3 V more negative than $E_{1/2}$. (a) Energetics of mediators with respect to the behavior of Pt in acid media. CV of Pt substrate, $\nu = 50$ mV/s and comparison to positive feedback voltammograms of 0.5 mM mediator (TMPD, $Ru(bpy)_3(ClO_4)_2$ or $Fe(phen)_3(ClO_4)_2$). Solution is 0.5 M H_2SO_4; interrogator electrode $\nu = 50$ mV/s, (b) comparison of positive feedback (PF) and negative feedback (NF) for 0.1 mM $Ru(bpy)_3(ClO_4)_2$ in Ar-purged 0.5 M H_2SO_4; $\nu = 20$ mV/s. (c) SI-SECM of $H_{(ads)}$ on Pt using 0.5 mM TMPD as mediator in 1 M $HClO_4$. Comparison to negative and positive feedback for the same alignment conditions. $H_{(ads)}$ was dosed by taking the Pt substrate through a linear scan from 0.42 to 0.02 V vs. NHE at 50 mV/s. Interrogator electrode scan rate $\nu = 20$ mV/s. (Adapted from Rodríguez-López, J. et al., *J. Am. Chem. Soc.*, 132, 5121, 2010.)

the redox pair, (3) a large difference in E^0 with respect to adsorbed hydrogen ($E^0 = 0$ V vs. NHE for the H^+/H_2 pair, but preferably $E^0 > 0.4$ V for the mediator to be outside the underpotential deposition (UPD) region on Pt), (4) low electrochemical background when performing the SI technique (which reflects lack of interaction with the Pt substrate during the negative feedback acquisition), and (5) quantitative reaction of the oxidized form with $H_{(ads)}$. Figure 16.25a shows the cyclic voltammogram of Pt in 0.5 M H_2SO_4 as well as the position of the oxidation waves for three mediator candidates that comply well with criteria (1), (2), and (3): $Ru(bpy)_3^{2+}$, $Fe(phen)_3^{2+}$ (bpy = bipyridine, phen = phenanthroline), and TMPD. Only TMPD complies well with criteria (4) and (5); in the case of the metal complexes in this example, their high oxidation power causes the background to be high, that is, negative feedback in the absence of adsorbed hydrogen. This could be due to Pt forming small amounts of oxides with concurrent mediator regeneration. Figure 16.25b indeed shows that for $Ru(bpy)_3^{2+}$ there is no room for analysis since the largest expected signal (e.g., positive feedback) and the background (e.g., negative feedback) overlap. Figure 16.25c in contrast shows the successful interrogation of adsorbed hydrogen with TMPD, which exhibits a large contrast between positive and negative feedback, low background, and a well-defined SI curve. One should proceed with caution in choosing the right mediator to avoid triggering undesired surface processes. With Pt, for example, strong reducing agents can cause a steady-state reduction of hydrogen ions at its surface; this difficulty can be overcome by choice of a reasonable pH.[86] Finally, thermodynamics can determine importantly the kinetics of the interrogation process. Full quantitative analysis can only be carried out if the chemical reaction at the substrate is complete and fast.

16.4.2 Digital Simulation of the SI-SECM Process

Recently, the advent of flexible commercial software has allowed an easy implementation of SECM problems. A popular example, software such as COMSOL Multiphysics[87] that uses finite

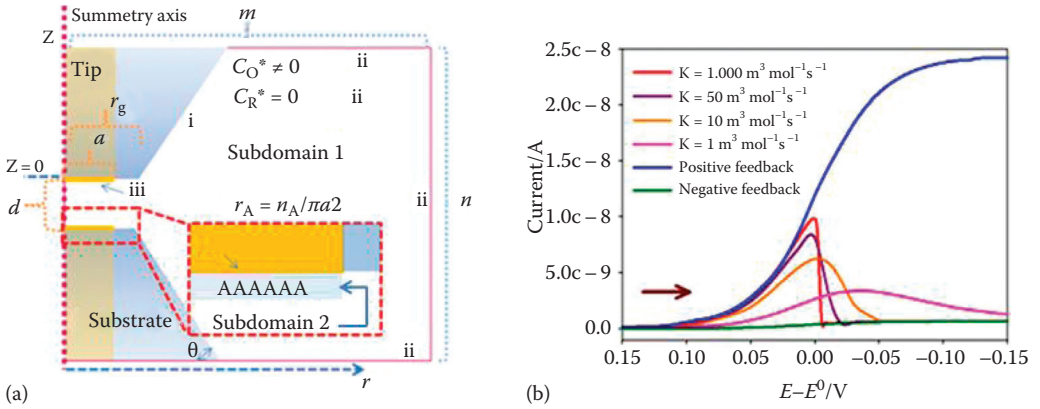


FIGURE 16.26 Simulation of SI-SECM. (a) The three-dimensional geometry in which the tip and substrate are concentrically aligned can be transformed into a two-dimensional geometry with a symmetry axis and described by *z* and *r*. Boundary types: i, insulation; ii, bulk concentration (semi-infinite); iii, flux at the tip; and iv, concentration of A at the substrate; $m=n=20a$ and $\theta>60°$. Other parameters include the interelectrode distance *d*, the size of the microdisk *a*, and the flat end length RG. (b) Representative LSV results of digital simulations for SI-SECM. $\nu=50$ mV/s and $C_O^*=1$ mol/m^3, $O+e\rightarrow R$ at the tip with no kinetic complications. Both tip and substrate $a=12.5$ μm, RG = 2, and $L=0.1$. Curves show the variation of the reaction kinetic constant *k* at a fixed $Q=8$ nC at the substrate electrode. (Adapted from Rodríguez-López, J. et al., *J. Am. Chem. Soc.*, 130, 16985, 2008.)

element methods (FEM) has been useful for treating a variety of SECM problems. Programs such as COMSOL Multiphysics allow the coupling of problems in different geometries and dimensions. Simulation of SI-SECM requires the modeling of diffusion and reaction kinetics in the SECM geometry; these are usually simplified by taking a 2D slice (subdomain 1) of the real 3D problem and using symmetry properties, as depicted in Figure 16.26a. The substrate surface can be represented as a 1D object (subdomain 2) where adsorption of A takes place. In subdomain 1, it is necessary to consider only a diffusion problem in which the reduced species R is generated at the tip from the initially present oxidized species O; thus, for transient conditions following Fick's second law as required for implementing voltammetry, Equations 16.11 and 16.12 apply:

$$\frac{\partial C_O}{\partial t} = D_O \nabla^2 C_O \tag{16.11}$$

$$\frac{\partial C_R}{\partial t} = D_R \nabla^2 C_R \tag{16.12}$$

where

C_O and C_R are the concentrations of oxidized and reduced species, respectively, and are functions of *r*, *z*, and time, *t*

D_O and D_R are the diffusion coefficients of these species

The bulk concentration (C_O^* and C_R^*) of each species is set to the one used during the experiment and the adsorbed species A is not present in this subdomain. At the tip boundary, $z=0$, $0<r<a$, the inward flux condition following Butler–Volmer kinetics (Equations 16.13 and 16.14) is written and in the case of a linear potential sweep, Equation 16.15 is added:

$$-D_O \nabla C_O = -k^o e^{-\alpha f(E-E^{0'})} C_O(0,r) + k^o e^{(1-\alpha) f(E-E^{0'})} C_R(0,r) \tag{16.13}$$

$$-D_R \nabla C_R = k^o e^{-\alpha f(E-E^{0'})} C_O(0,r) - k^o e^{(1-\alpha) f(E-E^{0'})} C_R(0,r) \tag{16.14}$$

$$E = E_{in} - \upsilon t \tag{16.15}$$

where

k^o is the heterogeneous rate constant for the mediator system
α is the transfer coefficient
f is equal to 38.94 V^{-1} at 298 K
$E^{0\Gamma}$ is the formal standard potential of the reaction
E is the potential of the tip and in CV relates the scan to time by means of υ, the scan rate, and the initial potential E_{in}

A simple SI-SECM model can be considered by the reductive interrogation of adsorbed species A. The surface is described by subdomain 2 of Figure 16.26a and the second-order interrogation reaction, with kinetic constant k, is described by Equation 16.16, while Equations 16.17 through 16.19 describe the change of concentrations with time:

$$R + A \xrightarrow{k} O \tag{16.16}$$

$$\frac{\partial C_O}{\partial t} = k C_R C_A \tag{16.17}$$

$$\frac{\partial C_R}{\partial t} = -k C_R C_A \tag{16.18}$$

$$\frac{\partial C_A}{\partial t} = D_A \nabla^2 C_A - k C_R C_A \tag{16.19}$$

It is convenient to refer quantitatively to A in terms of the charge it carries; thus the charge Q is equal to the moles of A, n_A, times Faraday's constant, F, 96,485 C/mol. The surface coverage Γ_A in terms of charge can also be obtained by consideration of the area of the substrate. Figure 16.26b shows representative results for the simulations at different values of the kinetic constant k (for the reaction of titrant R and A) at fixed Q. In Figure 16.26b, the kinetic constant was varied over three orders of magnitude and limiting behavior under these conditions is found when $k \geq 10^2\ m^3\ mol^{-1} s^{-1}$ for this particular setup, as shown by the overlapping of the voltammograms with that of positive feedback before it reaches a maximum and decays as the surface is depleted of A. This limiting behavior establishes that the chemical reaction cannot regenerate O at a rate faster than the diffusion of R to the substrate; this is denoted as a titrant-limited situation. When k drops below this value, there is a shift in the peak and the behavior is kinetically limited. Upon subtraction of the negative feedback curve from these tip responses and integration of the current with time, the CE (defined as the ratio of the recovered charge by the tip to the input charge used in the initial charging of the substrate) was found to be larger than 98% for this simulation in which $a=b$ and $L=0.1$; for slower kinetics, the interrogation may not be complete in one cycle and the experimenter must then change experimental parameters, for example, the scan rate, or use a different mediator. High CEs can only be achieved at very small tip–substrate distances when using a substrate of the same size as the tip, and provide the advantage of obtaining the titrated charge by direct integration of the tip current. If the size of the substrate is larger, for example, $b=2a$, then the CE drops to approximate value of 80% at $L=0.1$, and then this factor has to be taken into account. At larger interelectrode distances not only will the contrast between positive and negative feedback decrease, but also the CE will be

lower. SI-SECM curves obtained by simulation can be fitted to experimental ones to obtain parameters such as k and an example of this will be given in Section 16.4.4.

16.4.3 Detection and Quantification of Gold Oxides

Transition metals tend to form surface oxides upon contact with aqueous electrolytic conditions under electrochemical oxidizing conditions. For the specific case of noble metals such as Pt and Au, these oxides are chemically reversible, that is, they can be formed through anodization and then reduced by switching the potential to an appropriate cathodic value[88]; while other changes may accompany this process such as metal dissolution or roughening of the surface, the initial conditions of the surface are largely restored.[89] The exact stoichiometry of the surface oxides of Au and Pt is still a matter of debate due to the coexistence of different species[90,91]; however, to a first approximation, one can talk about the formation of a few (or sub-) monolayers of Au_2O_3 or PtO.

A powerful feature of SI-SECM is that it allows the open circuit study of the adsorbed species formed at different potentials of operation of the substrate. Figure 16.27a shows the cyclic voltammograms of gold at selected reversal potentials; the amount of oxide is quantifiable above 1.0 V by integration of the surface reduction wave present between 0.8 and 0.5 V in the cathodic scan. With CV, the oxidation of the substrate below 0.9 V shows no presence of the surface reduction wave when reversing the scan, and presumably only double layer charging occurs. This is consistent with previous observations of gold oxidation in phosphate buffer at pH = 7 reported by Oesch

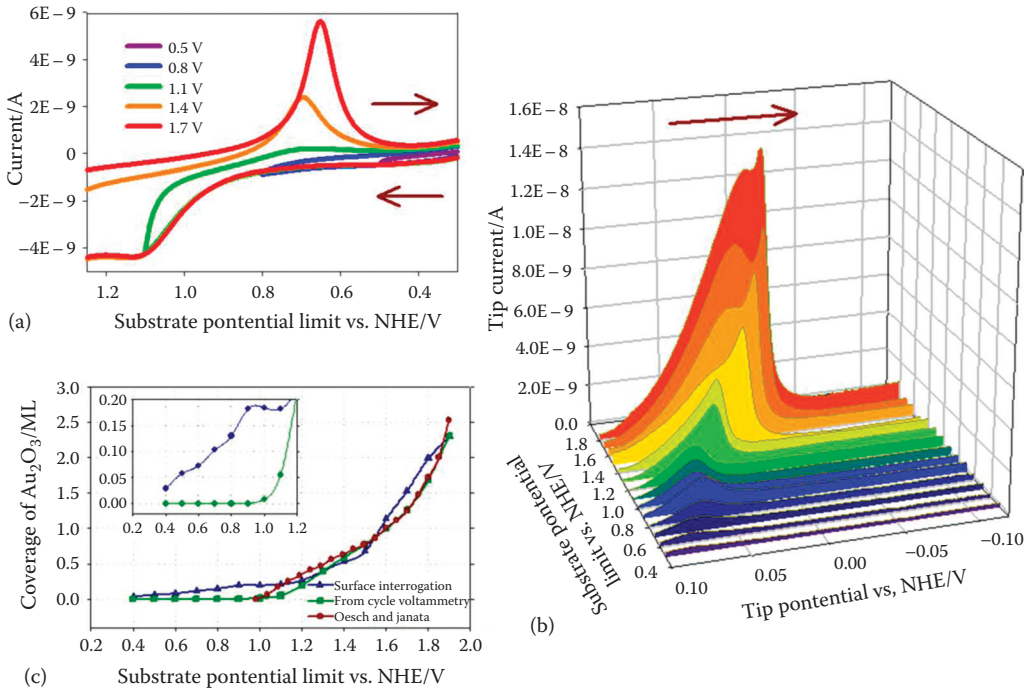


FIGURE 16.27 Reactivity of Au oxides by CV and by SI-SECM with $Ru(NH_3)_6^{2+}$ in phosphate buffer 0.3 M pH = 7 with 1 mM $Ru(NH_3)_6^{3+}$. (a) Voltammetry of the Au substrate, $\nu = 50$ mV/s, showing curves at different reversal potentials. (b) Spectrum of SI-SECM tip scans where Au oxides were formed by taking the Au substrate to different substrate potential limits through a potential scan at $\nu = 50$ mV/s. Both tip and substrate were Au microelectrodes $a = b = 12.5$ µm. Scans ran at $\nu = 50$ mV/s, electrode gap $L \sim 0.1$. (c) Comparative isotherm obtained by CV and SI-SECM. Inset shows blowup of the early potential region. Data for Oesch and Janata, as well as coverage determination procedure obtained from Ref. [92]. (Adapted from Rodríguez-López, J. et al., *J. Am. Chem. Soc.*, 130, 16985, 2008.)

and Janata.[92] Figure 16.27b shows the spectrum of tip voltammograms obtained by SI-SECM for increasingly positive potential limits to which the substrate was brought. The total surface coverage on the substrate can then be obtained by integrating these tip reduction currents and Figure 16.27c shows the isotherm for oxide coverage on the substrate versus the substrate oxidation potential limit. The comparison presented in Figure 16.27c shows very clearly that the SECM-based technique senses a reactive species adsorbed at less positive substrate potentials where the CV of the substrate electrode does not, in both the results obtained here or those previously reported.[92] This was suggested as evidence for the formation of the so-called incipient oxides or a singly oxygenated species such as Au-OH or Au-O. The observed coverage for the incipient oxide is about 20% of a monolayer, which is consistent with very early observations done by capacitance measurements[93] (≈15%), electroreflection techniques[94] (10%–20%), and more recent studies using contact electroresistance[95] (≈15%); indirect evidence is provided in photoelectrochemical[96] and SERS[97] studies, by the enhanced adsorption of radioactively labeled alkaline earth cations[98] and by AC voltammetry.[99] An inherent feature of SI-SECM is its ability to measure directly the charge that corresponds to such an adsorption feature, thus avoiding more complex treatments to estimate coverage. Figure 16.27b also shows a transition between 1.4 and 1.5 V from a single-peaked tip response to a double-peaked one. This transition corresponds to the coverage reaching more than half of a monolayer. The finding of a change in behavior upon reaching discrete coverage values has been treated in the literature as an indicator of the presence or transformation of different oxygen species (e.g., surface hydroxyl species and/or place exchanged oxides).[88,90,91] The impact of species with differential reactivity in the shape of SI-SECM CV scans will be shown in the next section.

16.4.4 Differential Reactivity of Pt Oxides with Various Mediators

SI-SECM gives unprecedented access to experimental quantities that describe the reactivity of electrogenerated adsorbates and that may help explain long-standing issues in electrocatalysis; in specific, SI-SECM allows one to take a closer look into the interplay of the electrochemical reactivity of the electrode and contrast it to the chemical reactivity of the species that are formed at it. SI-SECM was used to study systematically the reaction of different mediators with Pt oxides.[100] Studies of the electrochemical reactivity of Pt oxides formed at different stages of anodization have observed the loss of reversibility of these species when they are formed at higher potentials.[88,101] This irreversibility has been ascribed to the formation of a "place-exchanged" oxygen species, that is, oxygen buried into the surface layers of Pt.[90,102] The characterization of the structure of surface Pt oxides however is challenging and still not well understood, even at single crystal electrodes.[103] In fact, there is no general agreement on the type of species of which Pt oxide consists; early CV studies suggested that PtOH and place-exchanged OHPt were the relevant species in the initial stages of oxide formation.[101] Other measurements done ex situ such as XPS and Auger spectroscopy suggest the formation of anhydrous PtO in varying amounts.[104,105] Experiments here focus on the <2 ML PtO, that is, equivalent to <880 μC/cm^2, or to roughly four times an adsorbed hydrogen ML, Q_H (210 μC/cm^2). Thus, it is assigned $\theta_{OX} = 1$ (1 ML) at $Q_{OX} = 2Q_H$ (formally PtO).[102]

The reduction of different amounts of Pt oxide at open circuit, obtained after bringing the Pt substrate to different potentials, was studied by performing SI-SECM with different mediators, methyl viologen (+/2+) (MV), $Ru(NH_3)_6^{3+/2+}$ (Ruhex), iron(II/III) EDTA (FeEDTA), and $Fe(CN)_6^{3-/4-}$ (ferricyanide), and fitting the corresponding scans to the simulation model. The model presented previously in Section 16.4.2 was modified to account for the possibility of forming more than one type of oxide species with defined reaction kinetics. In this case, the system could be well described by two sequentially formed reactive species with reaction constants k_1 and k_2.

The effects of the energetics of reaction of the mediator with the surface oxide on its kinetics can be explored by choosing different reducing agents and conditions. Figure 16.28a shows the SI-SECM scans with Ruhex in acidic media (pH = 4, $E^0 = 0.05$ V vs. NHE) for the reduction of Pt oxides formed at different potentials; these reveal very sharp curves that denote fast interrogation

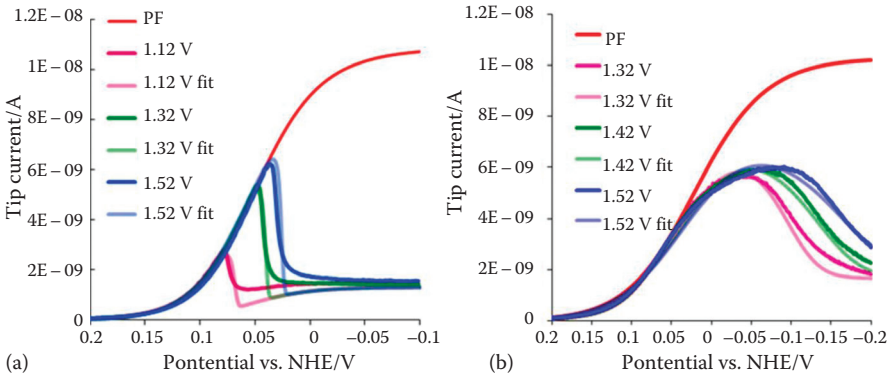


FIGURE 16.28 SI-SECM of Pt oxide using different mediators, Au tip ($a = 12.5\,\mu m$) and Pt substrate ($b = 25\,\mu m$), were used. (a) Curves for Ruhex. pH = 4, 0.6 mM $Ru(NH_3)_6(ClO_4)_3$ in 0.15 M acetate buffer. Substrate oxidation done by holding for 70 s at the indicated potential vs. RHE. Tip scan rate $\nu = 10\,mV/s$, $d = 2.3\,\mu m$; fitted rate constants: $k_1 = 100\,m^3\,mol^{-1}s^{-1}$, $k_2 = 100\,m^3\,mol^{-1}s^{-1}$ as shown in light curves. (b) Curves for FeEDTA. pH = 6.8, 0.89 mM in Fe(III)$[EDTA]^-$ in 0.1 M phosphate buffer. Substrate oxidation done by holding for 70 s at the indicated potential vs. RHE: tip scan rate $\nu = 50\,mV/s$. $d = 2.3\,\mu m$; fitted rate constants: $k_1 = 10\,m^3\,(mol^{-1}s^{-1}$, $k_2 = 6\,m^3)\,mol^{-1}s^{-1}$ as shown in light curves. (Adapted from Rodríguez-López, J. et al., *J. Phys. Chem. C*, 114, 18645, 2010.)

kinetics. A decrease in the value of the rate parameters, specifically k_2, was observed when performing SI-SECM with less reducing mediators. When the mediator was FeEDTA (pH = 6.8, $E^0 = 0.12$ V vs. NHE), the SI-SECM curves shown in Figure 16.28b exhibited clear deviations from the ideal positive feedback curve, which can be well accounted in our model by a reduction in k_2 as shown by the fitted curves. When even less reducing mediators were used, as in the case of ferricyanide ($E^0 = 0.4$ V vs. NHE), the rate of oxide reduction was so slow that one might consider the system as unreactive.

Provided the E^0 of the mediator is not pH sensitive, the energetic gap between the mediator and the oxide can also be modified by changing the pH of the solution since the oxide reduction process is linearly dependent on pH (ca. −59 mV per pH unit). For instance, this energetic gap will decrease as the solution is made more basic, such that the same SI-SECM curves run with Ruhex at pH = 6.8 will show kinetic deviations compared to the ones at pH = 4; another example is that, although Ruhex and methyl viologen ($E^0 = -0.45$ V vs. NHE) have different reduction potentials, their reducing power toward Pt oxides are almost leveled by choosing pH = 4 for Ruhex and pH = 11.3 for MV.

The free energy of reaction between the mediator and the oxide can be represented by the parameter ΔE, which equals the potential separation between the E^0 of the mediator and the peak potential of the electrochemical oxide reduction wave at $\theta_{OX} \approx 0.5$ at a given pH. Figure 16.29 shows a plot of $\ln k_2$ vs. ΔE. Homogeneous outer sphere reactions are often modeled by parabolic relationships with respect to the free energy of activation of the process in the context of Marcus and related electron transfer theories,[106–109] where the free energy of activation, ΔG^*, is expressed in terms of the driving force of the process ΔG^0 (in our case proportional to ΔE) and the reorganization energy, λ, the energy required to transform the nuclear configurations in the reactant and the solvent to those of the product state; Equations 16.20 and 16.21 are relevant[108]:

$$k_{et} = \frac{2\pi}{\hbar}\left|H_{DA}\right|\frac{1}{\sqrt{4\pi\lambda RT}}\exp\left(\frac{-\Delta G^*}{RT}\right) \tag{16.20}$$

$$\Delta G^* = \frac{F\left(\lambda + \Delta E\right)^2}{4\lambda} \tag{16.21}$$

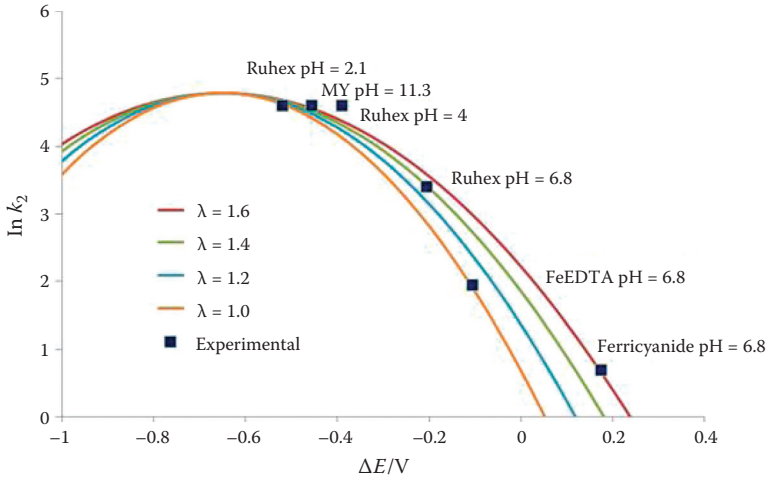


FIGURE 16.29 Dependence of the Pt oxide reduction rate constant on reducing power of mediator. ΔE stands for the difference between the E^0 of the mediator and the peak potential for electrochemical reduction of the oxide at the indicated pH. Values for k_2 as obtained from digital simulations in $m^3 mol^{-1} s^{-1}$. The graph also shows the parabolic curves obtained by the use of Equations 16.20 and 16.21 with different values of λ and adjusted to overlay on the data. (Adapted from Rodríguez-López, J. et al., *J. Phys. Chem. C*, 114, 18645, 2010.)

where

k_{et} is the rate constant for electron transfer
$\hbar$ is Planck's constant
H_{DA} is the electronic coupling matrix element between the donor and acceptor states
R is the gas constant
T is the temperature[108]
λ in this case is expressed in eV

It is tempting to plot the data for the heterogeneous (inner sphere) reaction studied here to this formalism, and locate the calculated rate constants in the context of the parabolic relationship to obtain an estimate of λ.[109] Such parabolas are shown in Figure 16.29 for values of λ; our data would fall into the range $1.6\,eV > \lambda > 1.0\,eV$ so an average value of $\lambda = 1.3 \pm 0.3\,eV$ matches the rate constants fairly well. This value of λ suggests that the reduction of the oxide, possibly the place-exchanged oxide, is accompanied by a significant rearrangement of the products compared to the reactants. This is consistent with the model proposed by Nagy and You in which considerable interactions, that is, induced local fields, need to be overcome in order to reduce the place-exchanged oxide[110] and is also consistent with observations of loss of reversibility in cyclic voltammetry upon formation of the place-exchanged oxide.

SI-SECM is useful in this case to obtain kinetic information that is unavailable by other techniques, and that might be helpful for understanding the reactivity of metal oxides formed at different potentials. In an extension of SI-SECM measurements, the positive feedback of the FeEDTA system on a biased Pt substrate at potentials where oxides are present was studied, and is shown in Figure 16.30. In this case, it was found experimentally that at a coverage roughly equivalent to half a monolayer of PtO, the feedback current of FeEDTA on the substrate decreased in a way that cannot be accounted for by electron transfer theories across thin insulating barriers.[108,109] However, the shape and feedback currents of this steady-state experiment could be well explained by using the rate constants and coverage values obtained from SI-SECM (simulated curve). In this case, the chemical reactivity of PtO could be the main driving force to oxidize FeEDTA, instead of the direct electron transfer at the Pt electrode. These oxide effects are relevant to inner sphere electrocatalytic processes that may be

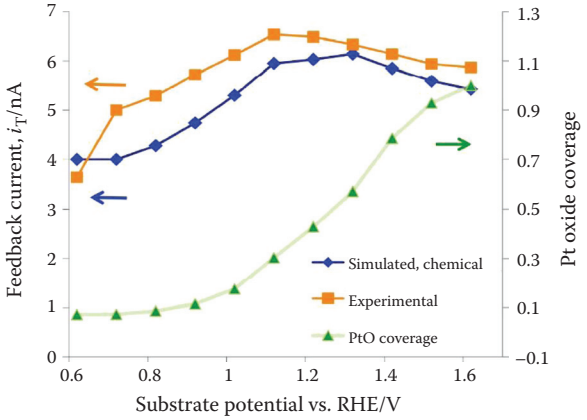


FIGURE 16.30 FeEDTA feedback on Pt at anodizing substrate potentials. Comparison of experimental feedback to simulated positive feedback for the Fe(III/II)EDTA system assuming only oxides are reactive (chemical route) at the Pt substrate and using the PtO coverage values and reaction rates determined by SI-SECM. $E_{tip} = -0.2$ V vs. NHE; $d = 2.6$ μm in 0.89 mM Fe(III)[EDTA]$^-$ in pH = 6.8, 0.1 M Phosphate buffer. E^0 (Fe(III/II)EDTA) = 0.12 V vs. NHE. E_{sub} as indicated vs. RHE. All points recorded after first holding at the indicated substrate potential for 70 s and then maintaining the potential. (Adapted from Rodríguez-López, J. et al., *J. Phys. Chem. C*, 114, 18645, 2010.)

affected by coverage of oxide, for example, when nonadsorbed reaction intermediates are reactive with the oxide, for example, H_2O_2[22] in the reduction of O_2 and organics in the oxidation of alcohols.[111]

16.4.5 SI-SECM of Adsorbed Hydrogen at Pt: An Example of Catalysis

We now turn to the use of SI-SECM for the analysis of oxidizable species at electrodes, in specific for adsorbed hydrogen at Pt[85,89] through the use of oxidizing mediators. As a model application of this mode to catalysis, the decomposition of dissolved formic acid (HCOOH) on an unbiased Pt surface to produce $H_{(ads)}$ was studied. SI-SECM allows a simple and direct route to determine in situ the surface coverage of reaction intermediates that would otherwise remain obscured in more conventional electrochemical techniques.

The redox pair formed by the aromatic amine TMPD and its radical cation were found to be suitable for quantitative interrogation of $H_{(ads)}$. In addition to the results presented in Section 16.4.1, the quantitative surface interrogation of $H_{(ads)}$ on Pt by $TMPD^+$ in acidic media was studied with different amounts of $H_{(ads)}$ dosed on the substrate electrode. Figure 16.31a shows a typical progression of SI scans performed with a 200 μm diameter GC interrogator electrode on a 100 μm diameter Pt substrate dosed with $H_{(ads)}$; the amount of $H_{(ads)}$ was adjusted by scanning the substrate to different potentials within the UPD region for hydrogen. A common feature exhibited by these SI scans was a displacement of the peak signal with respect to the dosage. This displacement is possibly related to the pH sensitive nature of TMPD that may be affected by the discharge of protons after the interrogation process. Figure 16.31b shows a comparison of the charge obtained by SI-SECM experiments to that obtained by CV upon dosing. There is quantitative agreement to ~0.2 V more positive than the onset of hydrogen evolution, with an average standard deviation of 5% of a monolayer for five independent experiments. The small disagreement observed for more positive potentials in Figure 16.31b, which accounts roughly for 10% of a monolayer of $H_{(ads)}$, was found to be caused by traces of oxygen in the cell and could possibly indicate the presence of additional adsorbed species at the electrode.

SI-SECM was used for the study of the decomposition of formic acid at Pt to yield $H_{(ads)}$. The electrochemical oxidation of formic acid has been widely studied in noble metals because of the potential use of HCOOH in fuel cells.[112] One of the limiting factors for the efficient electrochemical

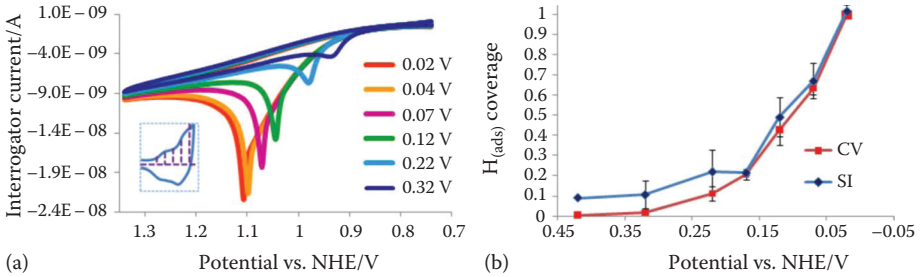


FIGURE 16.31 $H_{(ads)}$ on Pt at different dosing in Ar-purged 0.5 mM TMPD in 1 M $HClO_4$. (a) Different doses of $H_{(ads)}$ delivered to the Pt substrate by a linear sweep at $\nu = 50$ mV/s from 0.42 V to the potential limit indicated for each curve. Interrogator glassy carbon electrode ($a = 100$ μm), Pt substrate ($b = 50$ μm), $L = 0.2$. Interrogator electrode scan rate $\nu = 5$ mV/s. (b) Comparison of the normalized charge from SI and substrate CV. Normalization is done with respect to the hydrogen UPD integrated charge to a potential limit of 0.02 V on the sweep experiment at the substrate, which is assigned the value of 1 ML. (Adapted from Rodríguez-López, J. et al., *J. Am. Chem. Soc.*, 132, 5121, 2010.)

conversion of HCOOH to CO_2 and H^+ at Pt in acidic media is the poisoning and blocking effect of adsorbed intermediates,[113,114] such as $CO_{(ads)}$, $HCOO_{(ads)}$ (sometimes called "formate"), $COOH_{(ads)}$, $COH_{(ads)}$, or $HCO_{(ads)}$.[115–119] Since early studies,[120–122] a route termed the "direct pathway,"[116,123] that is, direct oxidation to CO_2 and H^+, was identified as beneficial in terms of avoiding poisoning species. Early discussions on HCOOH oxidation point to the formation of $H_{(ads)}$ by the catalytic decomposition of HCOOH at the Pt surface. An indication of this was the observation that the open circuit potential (OCP) of a Pt electrode in contact with HCOOH would exhibit a transient that reached potentials where $H_{(ads)}$ UPD is possible,[120–122,124–128] but the quantification of the species was not fully described.[127] Recent computational studies have discussed the formation of $H_{(ads)}$ on Pt from HCOOH,[129] so the quantification of this species by SI-SECM is clearly of interest.

The SI-SECM technique showed that the amount of the quantified adsorbate in the Pt–formic acid system is related to the OCP of the substrate at the time of interrogation. In the absence of formic acid, the OCP of the Pt substrate in acid solution was typically close to the foot of the TMPD oxidation wave (≈0.7 V vs. NHE); upon injection of HCOOH into the solution, the OCP of the platinum substrate drops to a limiting potential of ≈0.22 V vs. NHE. Figure 16.32a shows a set of SI-SECM scans where the substrate was interrogated after reaching different OCP values in the presence of formic acid. There is a qualitative similarity to the SI scans done for the interrogation of $H_{(ads)}$ from the UPD of hydrogen shown in Figure 16.31a, for example, in the shift of the peak intensity with respect to the interrogator potential at growing signal intensity. Interrogation at different potentials could be carried out numerous times during an experiment, which suggests that the adsorbate forms reversibly on the Pt surface.

Figure 16.32b shows the quantification of the adsorbate (normalized to 1 ML of UPD $H_{(ads)}$) for three series of experiments and corrected for transient effects during the interrogation process;[85] the most relevant experimental finding is the dependence of the adsorbate coverage with respect to the OCP of the Pt substrate at the time of interrogation and that the limiting coverage corresponds to the limiting amount of charge used in forming 1 ML of UPD $H_{(ads)}$. The quantification of the adsorbate strongly suggests that it can be identified as $H_{(ads)}$ although the presence of some other intermediates cannot be completely discarded. The possibility that oxidized TMPD reacts with adsorbed carbon monoxide, $CO_{(ads)}$, a possible product or intermediate of the decomposition of HCOOH, was also assessed but no reactivity was observed. Over extended periods of experimentation time, ~2–3 h, quantifications dropped by up to 10%, which may be indicative of a loss in the activity of the Pt substrate due to formation of $CO_{(ads)}$. In these experiments, SI-SECM yielded information about an adsorbate that is challenging to identify spectroscopically. It also showed the possibility of detecting species at a catalytic surface without activating it electrochemically in a direct manner.

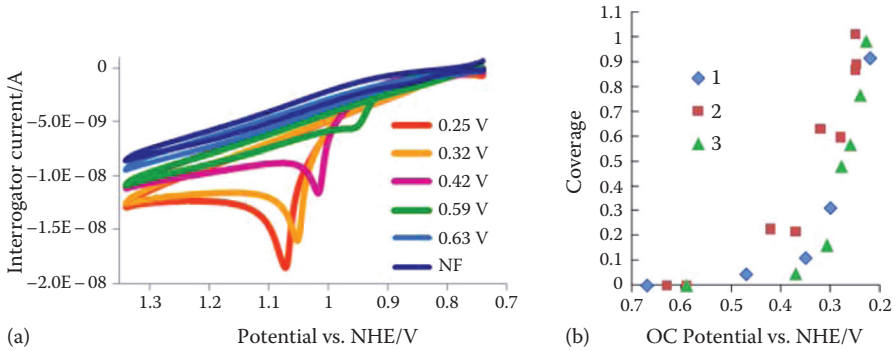


FIGURE 16.32 Catalytic decomposition of formic acid (HCOOH) studied by SI-SECM. (a) SI-SECM scans run at different values of the open circuit potential at the time where the scan began. Solution: 1 M $HClO_4$ + 0.5 mM TMPD + 12.5 mM HCOOH and Ar-purged to traces of O_2. Interrogator glassy carbon electrode (a = 100 μm), Pt substrate (b = 50 μm), L = 0.2. Interrogator electrode scan rate ν = 5 mV/s. (b) Plot of $H_{(ads)}$ coverage vs. open circuit potential limit at the time of interrogation for the decomposition of formic acid at Pt. Coverage values have been corrected for time uncertainties. Shown are three independent SI-SECM experiments. Unit coverage of $H_{(ads)}$ was determined from integration of the UPD region at the substrate on a linear potential scan previous to the addition of HCOOH. (Adapted from Rodríguez-López, J. et al., *J. Am. Chem. Soc*., 132, 5121, 2010.)

16.4.6 SI-SECM of Adsorbed CO on Pt with Br_2, A Catalytic Interrogation

The reaction of bromine, Br_2, with adsorbed carbon monoxide, $CO_{(ads)}$, on polycrystalline platinum in aqueous 0.5 M H_2SO_4 to yield CO_2 and Br^-, a previously unreported reaction, was studied by SI-SECM.[130] In this case, Pt not only acts as a support for $CO_{(ads)}$ but also as a heterogeneous catalyst that promotes the oxidation process. The adsorption and electrochemical oxidation of CO on Pt, both on single crystal and polycrystalline surfaces, have been widely studied[131,132] by electrochemical techniques[133–135] and their combination with Raman and IR spectroscopy.[136–138] A part of the interest in these studies is driven by the identification of $CO_{(ads)}$ as an important blocking intermediate (i.e., a poison) in the oxidation of short chain alcohols and organic acids,[114,115,139–141] at the anode of fuel cells.[112,131,132] Studies of the electrochemical oxidation of $CO_{(ads)}$ on Pt have traditionally been carried out by scanning or stepping an electrode into the oxidizing potential regime where oxides (e.g., $OH_{(ads)}$ or $O_{(ads)}$) are proposed to oxidize $CO_{(ads)}$ to CO_2.[134,137,142] For SI-SECM to be implemented, a suitable mediator had to be found. The use of halogens (X_2) is a good starting point since they are good oxidizing agents and their dissociated products, that is, $X^{\cdot}$ radicals, can react with organic species. The chemical transformation is shown in Equation 16.22:

$$Br_2 + CO_{(ads)} + H_2O \xrightarrow{Pt} 2Br^- + CO_2 + 2H^+ \qquad (16.22)$$

Reaction 16.22 regenerates Br^-, which produces a transient positive feedback loop at the interrogator tip as long as there is $CO_{(ads)}$ to react with. The Br^-/Br_2 system showed a high gain on positive feedback and low background on negative feedback. Figure 16.33 shows a SI-SECM interrogation with Br^-/Br_2 of a platinum electrode dosed with $CO_{(ads)}$ and its comparison to the negative and positive feedback CV scans. The SI scans revealed a response that consisted of two peaks, often merging into a single peak with a shoulder when slower scan rates were used.

Independent of shape, the quantification of the amount of adsorbate was consistent in all runs. The charge of adsorbed carbon monoxide, Q_{CO}, to that of adsorbed hydrogen, Q_H was found to be $Q_{CO}/Q_H = 0.94(\pm 6\%)$. Lopez-Cudero has reported a typical value of 291 ± 3 μC/cm^2 for the saturation coverage of CO in the presence of chlorides on polycrystalline Pt, which leads to $Q_{CO}/Q_H = 1.38(\pm 1\%)$.[148]

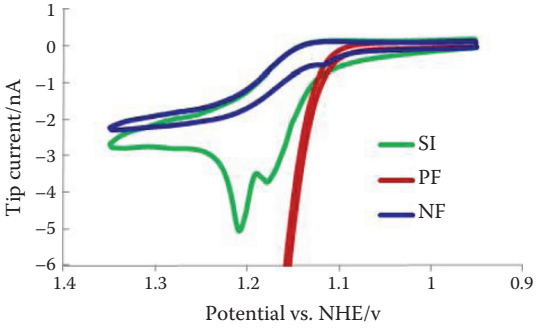


FIGURE 16.33 SI-SECM of adsorbed carbon monoxide at Pt using the Br^-/Br_2 mediator couple and comparison of NF and PF. Solution is 0.5 M H_2SO_4 + 1 mM KBr, $d \sim 2\,\mu m$; both tip and substrate are Pt with $a = 12.5\,\mu m$ and RG ~ 2. Tip $\nu = 20$ mV/s. NF, substrate at open circuit; PF, substrate at 0.95 V vs. NHE. Substrate in SI scan was predosed with CO saturated 0.5 M H_2SO_4 solution (KBr-free) at a potential of 0.3 V vs. NHE for 5 min. (Adapted from Wang, Q. et al., *J. Am. Chem. Soc.*, 131, 17046, 2009.)

Our result is reasonable, but low. Mechanistic insight into the reaction may explain some of the losses in quantification since it is possible to form species that do not decompose immediately to yield the necessary Br^- to establish the complete positive feedback cycle. A possible route for the oxidation of $CO_{(ads)}$ by Br_2 is shown in Equations 16.23 through 16.25:

$$Br_2 \xrightarrow{\text{Pt substrate}} 2Br\cdot_{(ads)} \tag{16.23}$$

$$2Br\cdot_{(ads)} + CO_{(ads)} \xrightarrow{\text{Pt substrate}} OCBr_2 \tag{16.24}$$

$$OCBr_2 + H_2O \longrightarrow 2Br^- + CO_2 + 2H^+ \tag{16.25}$$

The product of Reaction 16.24, $OCBr_2$ or "bromophosgene" (an analog of phosgene, $OCCl_2$), has been reported[143–145] (but also debated)[146] to be the product of a photosensitized low yield reaction of Br_2 and CO in the gas phase in the absence of catalyst, where the radical-forming reaction (16.23) proceeds through photochemical excitation. In our experiment, the Pt substrate provides a catalytic surface where Reaction 16.23 occurs more readily. The hydrolysis reaction (Equation 16.25) is thermodynamically allowed and proposed to occur at high altitude in the atmosphere[147] and provides the Br^- necessary for the transient positive feedback as well as a source of oxygen for the production of CO_2. The SI-SECM signal was proved to be partially inhibited when sites for CO adsorption were blocked by the cyanide ion, proving the surface nature of the process. Bulk experiments, where Pt black was added to a reaction mixture of bromine in acidic conditions with CO bubbling, revealed the formation of CO_2 as end product.

16.4.7 Outlook for SI-SECM

There are opportunities for considerable growth in the SI-SECM technique. For example, the identification of sensitive and selective chemical systems for specific adsorbate recognition will expand the types of reactions that SI-SECM can be used to study. It would also be desirable to find mediators that are able to resolve the reactivity of a same chemical species on different adsorption sites or crystallographic planes. The differences in reactivity observed in the case of the titration of Pt oxides formed at different stages of oxidation with different mediators also suggest the possibility of applying similar schemes to solve long-standing issues in electrocatalysis, for example, the participation of adsorbed oxygen during the OER, or the participation of differently adsorbed hydrogen on the hydrogen evolution reaction.

REFERENCES

1. Amemiya, S., Bard, A.J., Fan, F.-R.F., Mirkin, M.V., Unwin, P.R. Scanning electrochemical microscopy. *Annu. Rev. Anal. Chem*. 2008, 1, 95–131.
2. Zhou, J., Zu, Y., Bard, A.J. Scanning electrochemical microscopy. Part 39. The proton/hydrogen mediator system and its application to the study of the electrocatalysis of hydrogen oxidation. *J. Electroanal. Chem*. 2000, 491, 22–29.
3. Zoski, C.G. Scanning electrochemical microscopy: Investigation of hydrogen oxidation at polycrystalline noble metal electrodes. *J. Phys. Chem. B* 2003, 107, 6401–6405.
4. Shah, B.C., Hillier, A.C. Imaging the reactivity of electro-oxidation catalysts with the scanning electrochemical microscope. *J. Electrochem. Soc*. 2000, 147, 3043–3048.
5. Jambunathan, K., Shah, B.C., Hillier, A.C. Scanning electrochemical microscopy of hydrogen electrooxidation. Rate constant measurements and carbon monoxide poisoning on platinum. *J. Electroanal. Chem*. 2001, 500, 279–289.
6. Jambunathan, K., Hillier, A.C. Scanning electrochemical microscopy of hydrogen electro-oxidation. Part II. Coverage and potential dependence of platinum deactivation by carbon monoxide. *J. Electroanal. Chem*. 2002, 524–525, 144–156.
7. Zoski, C.G., Aguilar, J.C., Bard, A.J. Scanning electrochemical microscopy. 46. Shielding effects on reversible and quasireversible reactions. *Anal. Chem*. 2003, 75, 2959–2966.
8. Liu, B., Bard, A.J. Scanning electrochemical microscopy. 45. Study of the kinetics of oxygen reduction on platinum with potential programming of the tip. *J. Phys. Chem. B* 2002, 106, 12801–12806.
9. Zhang, C., Fan, F.-R.F., Bard, A.J. Electrochemistry of oxygen in concentrated NaOH solutions: Solubility, diffusion coefficients, and superoxide formation. *J. Am. Chem. Soc*. 2009, 131, 177–181.
10. Fernandez, J.L., Bard, A.J. Scanning electrochemical microscopy. 47. Imaging electrocatalytic activity for oxygen reduction in an acidic medium by the tip generation–substrate collection mode. *Anal. Chem*. 2003, 75, 2967–2974.
11. Fernandez, J.L., Bard, A.J. Scanning electrochemical microscopy. 50. Kinetic study of electrode reactions by the tip generation-substrate collection mode. *Anal. Chem*. 2004, 76, 2281–2289.
12. Liu, H., Fernandez, J.L., Zoski, C.G. A gas-diffusion gold-ring-tip: Fabrication, characterization, and application in electrocatalysis. *Electrochem. Commun*. 2009, 11, 1554; 2009, 11, 885–888.
13. Mezour, M.A., Cornut, R., Hussien, E.M., Morin, M., Mauzeroll, J. Detection of hydrogen peroxide produced the oxygen reduction reaction at self-assembled thiol-porphyrin monolayers on gold using SECM and nanoelectrodes. *Langmuir* 2010, 26, 13000–13006.
14. Eckhard, K., Chen, X., Turcu, F., Schuhmann, W. Redox competition mode of scanning electrochemical microscopy (RC-SECM) for visualization of local catalytic activity. *Phys. Chem. Chem. Phys*. 2006, 8, 5359–5365.
15. Eckhard, K., Schuhmann, W. Localized visualization of O_2 consumption and H_2O_2 formation by means of SECM for the characterization of fuel cell catalyst activity. *Electrochim. Acta* 2007, 53, 1164–1169.
16. Karnicka, K., Eckhard, K., Guschin, D.A., Stoica, L., Kulesza, P.J., Schuhmann, W. Visualisation of the local bio-electrocatalytic activity in biofuel cell cathodes by means of redox competition scanning electrochemical microscopy (RC-SECM). *Electrochem. Commun*. 2007, 9, 1998–2002.
17. Ackermann, Y., Guschin, D.A., Eckhard, K., Shleev, S., Schuhmann, W. Design of a bioelectrocatalytic electrode interface for oxygen reduction in biofuel cells based on a specifically adapted Os-complex containing redox polymer with entrapped *Trametes hirsuta* laccase. *Electrochem. Commun*. 2010, 12, 640–643.
18. Chen, X., Eckhard, K., Zhou, M., Bron, M., Schuhmann, W. Electrocatalytic activity of spots of electrodeposited noble-metal catalysts on carbon nanotubes modified glassy carbon. *Anal. Chem*. 2009, 81, 7597–7603.
19. Guadagnini, L., Maljusch, A., Chen, X., Neugebauer, S., Tonelli, D., Schuhmann, W. Visualization of electrocatalytic activity of microstructured metal hexacyanoferrates by means of redox competition mode of scanning electrochemical microscopy (RC-SECM). *Electrochim. Acta* 2009, 54, 3753–3758.
20. Fernandez, J.L., Hurth, C., Bard, A.J. Scanning electrochemical microscopy. 54. Application to the study of heterogeneous catalytic reactions—Hydrogen peroxide decomposition. *J. Phys. Chem. B* 2005, 109, 9532–9539.
21. Sanchez-Sanchez, C.M., Rodriguez-Lopez, J., Bard, A.J. Scanning electrochemical microscopy. 60. Quantitative calibration of the SECM substrate generation/tip collection mode and its use for the study of the oxygen reduction mechanism. *Anal. Chem*. 2008, 80, 3254–3260.
22. Sánchez-Sánchez, C.M., Bard, A.J. Hydrogen peroxide production in the oxygen reduction reaction at different electrocatalysts as quantified by scanning electrochemical microscopy. *Anal. Chem*. 2009, 81, 8094–8100.

23. Shen, Y., Trauble, M., Wittstock, G. Detection of hydrogen peroxide produced during electrochemical oxygen reduction using scanning electrochemical microscopy. *Anal. Chem*. 2008, 80, 750–759.
24. Lin, C.-L., Rodriguez-Lopez, J., Bard, A.J. Micropipet delivery-substrate collection mode of scanning electrochemical microscopy for the imaging of electrochemical reactions and the screening of methanol oxidation electrocatalysts. *Anal. Chem*. 2009, 81, 8868–8877.
25. Minguzzi, A., Alpuche-Aviles, M.A., Rodriguez-Lopez, J., Rondinini, S., Bard, A.J. Screening of oxygen evolution electrocatalysts by scanning electrochemical microscopy using a shielded tip approach. *Anal. Chem*. 2008, 80, 4055–4064.
26. Zoski, C.G., Simjee, N., Guenat, O., Bard, A.J. Addressable microelectrode arrays: Characterization by imaging with scanning electrochemical microscopy. *Anal. Chem*. 2004, 76, 62–72.
27. Jayaraman, S., Hillier, A.C. Screening the reactivity of Pt_xRu_y and $Pt_xRu_yMo_z$ catalysts toward the hydrogen oxidation reaction with the scanning electrochemical microscope. *J. Phys. Chem. B* 2003, 107, 5221–5230.
28. Jayaraman, S., Hillier, A.C. Construction and reactivity screening of a surface composition gradient for combinatorial discovery of electro-oxidation catalysts. *J. Comb. Chem*. 2004, 6, 27–31.
29. Jayaraman, S., Hillier, A.C. Construction and reactivity mapping of a platinum catalyst gradient using the scanning electrochemical microscope. *Langmuir* 2001, 17, 7857–7864.
30. Black, M., Cooper, J., McGinn, P. Scanning electrochemical microscope characterization of thin film combinatorial libraries for fuel cell electrode applications. *Meas. Sci. Technol*. 2005, 16, 174–182.
31. Kucernak, A.R., Chowdhury, P.B., Wilde, C.P., Kelsall, G.H., Zhu, Y.Y., Williams, D.E. Scanning electrochemical microscopy of a fuel-cell electrocatalyst deposited onto highly oriented pyrolytic graphite. *Electrochim. Acta* 2000, 45, 4483–4491.
32. Fernandez, J.L., Walsh, D.A., Bard, A.J. Thermodynamic guidelines for the design of bimetallic catalysts for oxygen electroreduction and rapid screening by scanning electrochemical microscopy. M-Co(M: Pd, Ag, Au). *J. Am. Chem. Soc*. 2005, 127, 357–365.
33. Fernandez, J.L., Raghuveer, V., Manthiram, A., Bard, A.J. Pd–Ti and Pd–Co–Au electrocatalysts as a replacement for platinum for oxygen reduction in proton exchange membrane fuel cells. *J. Am. Chem. Soc*. 2005, 127, 13100–13101.
34. Raghuveer, V., Manthiram, A., Bard, A.J. Pd–Co–Mo electrocatalyst for the oxygen reduction reaction in proton exchange membrane fuel cells. *J. Phys. Chem. B* 2005, 109, 22909–22912.
35. Walsh, D.A., Fernandez, J.L., Bard, A.J. Rapid screening of bimetallic electrocatalysts for oxygen reduction in acidic media by scanning electrochemical microscopy. *J. Electrochem. Soc*. 2006, 153, E99–E103.
36. Fernandez, J.L., White, J.M., Sun, Y., Tang, W., Henkelman, G., Bard, A.J. Characterization and theory of electrocatalysts based on scanning electrochemical microscopy screening methods. *Langmuir* 2006, 22, 10426–10431.
37. Lin, C.-L., Sanchez-Sanchez, C.M., Bard, A.J. Methanol tolerance of Pd–Co oxygen reduction reaction electrocatalysts using scanning electrochemical microscopy. *Electrochem. Solid State Lett*. 2008, 11, B136–B139.
38. Sanchez-Sanchez, C.M., Solla-Gullon, J., Vidal-Iglesias, F.J., Aldaz, A., Montiel, V., Herrero, E. Imaging structure sensitive catalysis on different shape-controlled platinum nanoparticles. *J. Am. Chem. Soc*. 2010, 132, 5622–5624.
39. Lu, G., Cooper, J.S., McGinn, P.J. SECM imaging of electrocatalytic activity for oxygen reduction reaction on thin film materials. *Electrochim. Acta* 2007, 52, 5172–5181.
40. Weng, Y.C., Fan, F.-R.F., Bard, A.J. Combinatorial biomimetics. Optimization of a composition of copper (II) poly-L-histidine complex as an electrocatalyst for O_2 reduction by scanning electrochemical microscopy. *J. Am. Chem. Soc*. 2005, 127, 17576–17577.
41. Mano, N., Fernandez, J.L., Kim, Y., Shin, W., Bard, A.J., Heller, A. Oxygen is electroreduced to water on a "wired" enzyme electrode at a lesser overpotential than on platinum. *J. Am. Chem. Soc*. 2003, 125, 15290–15291.
42. Fernandez, J.L., Mano, N., Heller, A., Bard, A.J. Optimization of "wired" enzyme O_2-electroreduction catalyst compositions by scanning electrochemical microscopy. *Angew. Chem. Int. Ed*. 2004, 43, 6355–6357.
43. Jung, C., Sanchez-Sanchez, C.M., Lin, C.L., Rodriguez-Lopez, J., Bard, A.J. Electrocatalytic activity of Pd–Co bimetallic mixtures for formic acid oxidation studied by scanning electrochemical microscopy. *Anal. Chem*. 2009, 81, 7003–7008.
44. Rodriguez-Lopez, J., Alpuche-Aviles, M.A., Bard, A.J. Selective insulation with poly(tetrafluoroethylene) of substrate electrodes for electrochemical background reduction in scanning electrochemical microscopy. *Anal. Chem*. 2008, 80, 1813–1818.

45. Zoski, C.G., Luman, C.R., Fernandez, J.L., Bard, A.J. Scanning electrochemical microscopy. 57. SECM tip voltammetry at different substrate potentials under quasi-steady-state and steady-state conditions. *Anal. Chem*. 2007, 79, 4957–4966.
46. Bard A.J. Photoelectrochemistry, *Science* 1980, 207, 139–144.
47. Nozik, A.J., Memming, R. Physical chemistry of semiconductor–liquid interfaces. *J. Phys. Chem*. 1996, 100, 13061–13078.
48. Kudo, A., Miseki, Y. Heterogeneous photocatalyst materials for water splitting. *Chem. Soc. Rev*. 2009, 38, 253–278.
49. Archer, M.D., Nozik, A.J., Eds., *Nanostructured and Photoelectrochemical Systems for Solar Photon Conversion*, Imperial College Press, London, U.K., 2008.
50. Horrocks, B., Mirkin, M., Bard, A.J. Scanning electrochemical microscopy. 25. Application to the kinetics of heterogeneous electron transfer at semiconductor (WSe_2 and Si) electrodes. *J. Phys. Chem*. 1994, 98, 9106–9114.
51. Maeda, H., Ikeda, K., Hashimoto, K., Ajito, K., Morita, M., Fujishima, A. Microscopic observation of TiO_2 photocatalysis using scanning electrochemical microscopy. *J. Phys. Chem. B* 1999, 103, 3213.
52. Haram, S., Bard, A.J. Scanning electrochemical microscopy. 42. Studies of the kinetics and photoelectrochemistry of thin film CdS/electrolyte interfaces. *J. Phys. Chem. B* 2001, 105, 8192–8195.
53. Zhao, X.K., McCormick, L., Fendler, J.H. Electrical and photoelectrochemical characterization of CdS particulate films by scanning electrochemical microscopy, scanning tunneling microscopy, and scanning tunneling spectroscopy. *Chem. Mater*. 1991, 3, 922–935.
54. Kemp, T.J., Unwin, P.R., Vincze, L. Photogenerated chloride ion concentration near the surface of UV-irradiated titanium dioxide in the presence of aqueous 2,4-dichlorophenol probed using an ultramicroelectrode. *J. Chem. Soc. Faraday Trans*. 1995, 91, 3893–3896.
55. Fonseca, S., Barker, A., Ahmed, S., Kemp, T., Unwin, P. Scanning electrochemical microscopy investigation of the photodegradation kinetics of 4-chlorophenol sensitized by TiO_2 films. *Phys. Chem. Chem. Phys*. 2004, 6, 5218–5224.
56. Fonseca, S., Barker, A., Ahmed, S., Kemp, T., Unwin, P. Direct observation of oxygen depletion and product formation during photocatalysis at a TiO_2 surface using scanning electrochemical microscopy. *Chem. Commun*. 2003, 1002–1003.
57. Bozic, B., Figgemeier, E. Scanning electrochemical microscopy under illumination: An elegant tool to directly determine the mobility of charge carriers within dye-sensitized nanostructured semiconductors. *Chem. Commun*. 2006, 2268–2270.
58. Shen, Y., Nonomura, K., Schlettwein, D., Zhao, C., Wittstock, G. Photoelectrochemical kinetics of eosin Y-sensitized zinc oxide films investigated by scanning electrochemical microscopy. *Chem. Eur. J*. 2006, 12, 5832–5839.
59. Shen, Y., Tefashe, U.M., Nonomura, K., Loewenstein, T., Schlettwein, D., Wittstock, G. Photoelectrochemical kinetics of eosin Y-sensitized zinc oxide films investigated by scanning electrochemical microscopy under illumination with different LED, *Electrochim. Acta* 2009, 55, 458–464.
60. Tefashe, U.M., Loewenstein, T., Miura, H., Schlettwein, D., Wittstock, G. Scanning electrochemical microscope studies of dye regeneration in indoline (D149)-sensitized ZnO photoelectrochemical cells. *J. Electroanal. Chem*. 2010, 650, 24–30.
61. Casillas, N., James, P., Smyrl, W.H. A novel approach to combine scanning electrochemical microscopy and scanning photoelectrochemical microscopy. *J. Electrochem. Soc*. 1995, 142, L16–L18.
62. James, P., Casillas, N., Smyrl, W.H. Simultaneous scanning electrochemical and photoelectrochemical microscopy by use of a metallized optical fiber. *J. Electrochem. Soc*. 1996, 143, 3853–3865.
63. Shi, G., Garfias-Mesias, L.F., Smyrl, W.H. Preparation of a gold-sputtered optical fiber as a microelectrode for electrochemical microscopy. *J. Electrochem. Soc*. 1998, 145, 2011–2016.
64. Sosa, E., Cabrera-Sierra, R., Oropeza, M.T., Hernandez, F., Casillas, N., Tremont, R., Cabrera, C., Gonzaleza, I. Chemical characterization of corrosion films electrochemically grown on carbon steel in alkaline sour environment. *J. Electrochem. Soc*. 2003, 150, B530–B535.
65. Lee, J., Ye, H., Pan, S., Bard, A.J. Screening of photocatalysts by scanning electrochemical microscopy. *Anal. Chem*. 2008, 80, 7445–7450.
66. Jang, J.S., Lee, J., Ye, H., Fan, F.-R.F., Bard, A.J. Rapid screening of effective dopants for Fe_2O_3 photocatalysts with scanning electrochemical microscopy and investigation of their photoelectrochemical properties. *J. Phys. Chem. C* 2009, 113(16), 6719–6724.
67. Jang, J.S., Yoon, K.Y., Xiao, X., Fan, F.-R.F., Bard, A.J. Development of a potential Fe_2O_3-based photocatalyst thin film for water oxidation by scanning electrochemical microscopy: Effects of Ag–Fe_2O_3 nanocomposite and Sn doping. *Chem. Mater*. 2009, 21(20), 4803–4810.

68. Liu, W., Ye, H., Bard, A.J. Screening of novel metal oxide photocatalysts by scanning electrochemical microscopy and research of their photoelectrochemical properties. *J. Phys. Chem. C* 2010, 114(2), 1201–1207.
69. Ye, H., Lee, J., Jang, J.S., Bard, A.J. Rapid screening of $BiVO_4$-based photocatalysts by scanning electrochemical microscopy (SECM) and studies of their photoelectrochemical properties. *J. Phys. Chem. C* 2010, 114, 13322–13328.
70. Liu, G., Bard, A.J. Rapid preparation and photoelectrochemical screening of $CuInSe_2$ and $CuInMSe_2$ arrays by scanning electrochemical microscopy. *J. Phys. Chem. C* 2010, 114, 17509–17513.
71. Liu, G., Liu, C., Bard, A.J. Rapid synthesis and screening of $Zn_xCd_{1-x}S_ySe_{1-y}$ photocatalysts by scanning electrochemical microscopy. *J. Phys. Chem. C* 2010, 114, 20997–21002.
72. Lee, Y., Bard, A.J. Fabrication and characterization of probes for combined scanning electrochemical/optical microscopy experiments. *Anal. Chem*. 2002, 74, 3626–3633.
73. Rodríguez-López, J., Alpuche-Avilés, M.A., Bard, A.J. Interrogation of surfaces for the quantification of adsorbed species on electrodes: Oxygen on gold and platinum in neutral media. *J. Am. Chem. Soc*. 2008, 130, 16985–16995.
74. Unwin, P.R., Bard A.J. Scanning electrochemical microscopy. 9. Theory and application of the feedback mode to the measurement of following chemical reaction rates in electrode processes. *J. Phys. Chem*. 1991, 95, 7814–7824.
75. Diaz-Ballote, L.F., Alpuche-Aviles, M., Wipf, D.O. Fast-scan cyclic voltammetry–scanning electrochemical microscopy. *J. Electroanal. Chem*. 2007, 604, 17–25.
76. Unwin, P.R., Bard, A.J. Scanning electrochemical microscopy. 14. Scanning electrochemical microscope induced desorption: A new technique for the measurement of adsorption/desorption kinetics and surface diffusion rates at the solid/liquid interface. *J. Phys. Chem*. 1992, 96, 5035–5045.
77. Slevin, C.J., Unwin, P.R. Lateral proton diffusion rates along stearic acid monolayers. *J. Am. Chem. Soc*. 2000, 122, 2597–2602.
78. Mandler, D., Unwin, P.R. Measurement of lateral charge propagation in polyaniline layers with the scanning electrochemical microscope. *J. Phys. Chem. B* 2003, 107, 407–410.
79. O'Mullane, A.P., Macpherson, J.V., Unwin, P.R., Cervera-Montesinos, J., Manzanares, J.A., Frehill, F., Vos, J.G. Measurement of lateral charge propagation in $[Os(bpy)_2(PVP)_nCl]Cl$ thin films: A scanning electrochemical microscopy approach. *J. Phys. Chem. B* 2004, 108, 7219–7227.
80. Zhang, J., Slevin, C.J., Morton, C., Scott, P., Walton, D.J., Unwin, P.R. New approach for measuring lateral diffusion in Langmuir monolayers by scanning electrochemical microscopy (SECM): Theory and application. *J. Phys. Chem. B* 2001, 105, 11120–11130.
81. Liu, B., Rotenberg, S.A., Mirkin, M.V. Scanning electrochemical microscopy of living cell. 4. Mechanistic study of charge transfer reactions in human breast cells. *Anal. Chem*. 2002, 74, 6340–6348.
82. Xiong, H., Guo, J., Amemiya, S. Probing heterogeneous electron transfer at an unbiased conductor by scanning electrochemical microscopy in the feedback mode. *Anal. Chem*. 2007, 79, 2735–2744.
83. Macpherson, J.V., Slevin, C.J., Unwin, P.R. Probing the oxidative etching kinetics of metals with the feedback mode of the scanning electrochemical microscope. *J. Chem. Soc. Faraday Trans*. 1996, 92, 3799–3805.
84. Bard, A.J., Fan, F.-R. F., Mirkin, M.V. Scanning electrochemical microscopy. In *Electroanalytical Chemistry*, Bard, A.J., Ed., Marcel Dekker, New York, 1994, pp. 243–373.
85. Rodríguez-López, J., Bard, A.J. Scanning electrochemical microscopy: Surface interrogation of adsorbed hydrogen and the open circuit catalytic decomposition of formic acid at platinum. *J. Am. Chem. Soc*. 2010, 132, 5121–5129.
86. Selzer, Y., Turyan, I., Mandler, D. Studying heterogeneous catalysis by the scanning electrochemical microscope (SECM): The reduction of protons by methyl viologen catalyzed by a platinum surface. *J. Phys. Chem. B* 1999, 103, 1509–1517.
87. COMSOL Multiphysics v.3.2 software, COMSOL, Inc., Burlington, MA.
88. Angerstein-Kozlowska, H., Conway, B.E., Barnett, B., Mozota, J. The role of ion adsorption in surface oxide formation and reduction at noble metals: General features of the surface process. *J. Electroanal. Chem*. 1979, 100, 417–446.
89. Woods, R. Chemisorption at electrodes. In *Electroanalytical Chemistry*, Bard, A.J., Ed., Marcel Dekker, New York, 1976, pp. 1–162.
90. Conway, B.E., Angerstein-Kozlowska, H. The electrochemical study of multiple-state adsorption in monolayers. *Acc. Chem. Res*. 1981, 14, 49–56.
91. Pletcher, D., Sotiropoulos, S. Hydrogen adsorption–desorption and oxide formation–reduction on polycrystalline platinum in unbuffered aqueous solutions. *J. Chem. Soc. Faraday Trans*. 1994, 90, 3663–3668.

92. Oesch, U., Janata, J. Electrochemical study of gold electrodes with anodic oxide films. I. Formation and reduction behavior of anodic oxides on gold. *J. Electrochim. Acta* 1983, 28, 1237–1246.
93. Schmid, G.M., O'Brien, R.N. Oxygen adsorption and double layer capacities; gold in perchloric acid. *J. Electrochem. Soc*. 1964, 111, 832–837.
94. Nguyen Van Huong, C., Hinnen, C., Lecoeur, J. Spectroscopic study of single crystal gold electrodes. Part II. The incipient oxidation of gold electrode. *J. Electroanal. Chem*. 1980, 106, 185–191.
95. Marichev, V.A. Contact electroresistance method for in situ studies of metal surfaces in electrolytes: Adsorption of hydroxyl ions and submonolayer electrooxidation of gold. *Russ. J. Electrochem*. 1999, 35, 434–440.
96. Watanabe, T., Gerischer, J. Photoelectrochemical studies on gold electrodes with surface oxide layers. Part. I. Photocurrent measurement in the visible region. *J. Electroanal. Chem*. 1981, 117, 185–200.
97. DeSilvestro, J., Weaver, M.J. Surface structural changes during oxidation of gold electrodes in aqueous media as detected using surface-enhanced Raman spectroscopy. *J. Electroanal. Chem*. 1986, 209, 377–386.
98. Horányi, G. Induced cation adsorption on platinum and modified platinum electrodes. *Electrochim. Acta* 1991, 36, 1453–1463.
99. Lertanantawong, B., O'Mullane, A.P., Surareungchai, W., Somasundrum, M., Burke, L.D., Bond, A.M. Study of the underlying electrochemistry of polycrystalline gold electrodes in aqueous solution and electrocatalysis by large amplitude Fourier transformed alternating current voltammetry. *Langmuir* 2008, 24, 2856–2868.
100. Rodríguez-López, J., Minguzzi, A., Bard, A.J. The reaction of various reductants with oxide films on Pt electrodes as studied by the surface interrogation mode of scanning electrochemical microscopy (SI-SECM). Possible validity of a Marcus relationship. *J. Phys. Chem. C* 2010, 114, 18645–18655.
101. Angerstein-Kozlowska, H., Conway, B.E. Real condition of electrochemically oxidized platinum surfaces. I. Resolution of component processes. *J. Electroanal. Chem*. 1973, 43, 9–36.
102. Tremilosi-Filho, G., Jerkiewicz, G., Conway, B.E. Characterization and significance of the sequence of stages of oxide film formation at platinum generated by strong anodic polarization. *Langmuir* 1992, 8, 658–667.
103. Markovic, N.M., Ross, P.N., Jr. Surface science studies of model fuel cell electrocatalysts. *Surf. Sci. Rep*. 2002, 45, 117–229.
104. Dickinson, T., Povey, A.F., Sherwood, P.M.A. X-ray photoelectron spectroscopic studies of oxide films on platinum and gold electrodes. *J. Chem. Soc. Faraday Trans*. 1975, 71, 298–311.
105. Wagner, F.T., Ross, P.N., Jr. AES and TDS studies of electrochemically oxidized platinum(100). *Appl. Surf. Sci*. 1985, 24, 87–107.
106. Andrieux, C.P., Savéant, J.-M., Su, K.B. Kinetics of dissociative electron transfer. Direct and mediated electrochemical reductive cleavage of the carbon–halogen bond. *J. Phys. Chem*. 1986, 90, 3815–3823.
107. Saveant, J.-M. *Elements of Molecular and Biomolecular Electrochemistry*, Wiley-Interscience, Hoboken, NJ, 2006.
108. Fletcher, S. The theory of electron transfer. *J. Solid State Electrochem*. 2010, 14, 705–739.
109. Miller, C.J. Heterogeneous electron transfer kinetics at metallic electrodes. In *Physical Electrochemistry, Principles, Methods and Applications*, Rubinstein, I., Ed., Marcel Dekker, New York, 1995, pp. 27–79.
110. Nagy, Z., You, H. Applications of surface x-ray scattering to electrochemistry problems. *Electrochim. Acta* 2002, 47, 3037–3055.
111. Leiva, E., Sánchez, C. Theoretical aspects of some prototypical fuel cell reactions. In *Handbook of Fuel Cells*, Vol. 2, Vielstich, W., Lamm, A., Gasteiger, H., Eds., Wiley, Chichester, England, 2003, pp. 93–131.
112. Rice, C., Ha, S., Masel, R.I., Wieckowski, A. Catalysts for direct formic acid fuel cells. *J. Power Sour*. 2003, 115, 229–235.
113. Rodríguez, J.L., Pastor, E. Consecutive adsorption as studied by electrochemical mass spectrometry: Coadsorption, desorption and displacement reactions on platinum. *Electrochim. Acta* 1998, 44, 1173–1179.
114. Lu, G.-Q., Crown, A., Wieckowski, A. Formic acid decomposition on polycrystalline platinum and palladized platinum electrodes. *J. Phys. Chem. B* 1999, 103, 9700–9711.
115. Chen, Y.-X., Shen, Y., Heinen, M., Jusys, Z., Osawa, M., Behm, R.J. Application of in-situ attenuated total reflection–Fourier transform infrared spectroscopy for the understanding of complex reaction mechanisms and kinetics: Formic acid oxidation on a Pt film electrode at elevated temperatures. *J. Phys. Chem. B* 2006, 110, 9534–9544.
116. Chen, Y.-X., Heinen, M., Jusys, Z., Behm, R.J. Bridge-bonded formate: Active intermediate or spectator species in formic acid oxidation on a Pt film electrode. *Langmuir* 2006, 22, 10399–10408.

117. Chen, Y.-X., Heinen, M., Jusys, Z., Behm, R.J. Kinetic isotope effects in complex reaction networks: Formic acid electro-oxidation. *Chem. Phys. Chem*. 2007, 8, 380–385.
118. Miki, A., Ye, S., Senzaki, T., Osawa, M. Surface-enhanced infrared study of catalytic electrooxidation of formaldehyde, methyl formate, and dimethoxymethane on platinum electrodes in acidic solution. *J. Electroanal. Chem*. 2004, 563, 23–31.
119. Samjeske, G., Miki, S., Ye, A., Yamakata, Y., Mukouyama, H., Okamoto, H., Osawa, M. Potential oscillations in galvanostatic electrooxidation of formic acid on platinum: A time-resolved surface-enhanced infrared study. *J. Phys. Chem. B* 2005, 109, 23509–23516.
120. Breiter, M.W. Oxidation mechanism of formic acid on platinum at low potentials in acidic solutions. *J. Electrochem. Soc*. 1964, 111, 1298–1299.
121. Gottlieb, M.H. Anodic oxidation of formic acid at platinum electrodes. *J. Electrochem. Soc*. 1964, 111, 465–472.
122. Munson, R.A. Constant current transition time investigations of the electrochemical oxidation of formate–formic acid at a smooth platinum electrode. *J. Electrochem. Soc*. 1964, 111, 372–376.
123. Parsons, R., VanderNoot, T. The oxidation of small organic molecules. A survey of recent fuel cell related research. *J. Electroanal. Chem*. 1988, 257, 9–45.
124. Oxley, J.E., Johnson, G.K., Buzalski, B.T. The anodic oxidation of methanol: Open-circuit transient reactions. *Electrochim. Acta* 1964, 9, 897–910.
125. Schwabe, K. Potential measurements on metal catalysis in aqueous solution. *Z. Elektrochem*. 1957, 61, 744–752.
126. Breiter, M.W. Anodic oxidation of formic acid on platinum. I. Adsorption of formic acid, oxygen and hydrogen in perchloric acid solutions. *Electrochim. Acta* 1963, 8, 447–456 and 457–470.
127. Fleischmann, C.W., Johnson, G.K., Kuhn, A.T. Electrochemical oxidation of formic acid on platinum. *J. Electrochem. Soc*. 1964, 111, 602–605.
128. Eckert, J. Electrochemical behavior of formic acid on platinum electrodes in acidic solutions. *Electrochim. Acta* 1967, 12, 307–328.
129. Yue, C.M.Y., Lim, K.W. Adsorption of formic acid and its decomposed intermediates on (100) surfaces of Pt and Pd: A density functional study. *Catal. Lett*. 2009, 128, 221–226.
130. Wang, Q., Rodríguez-López, J., Bard, A.J. The reaction of Br_2 with adsorbed CO on Pt studied by the surface interrogation mode of scanning electrochemical microscopy. *J. Am. Chem. Soc*. 2009, 131, 17046–17047.
131. Vielstich, W. CO, formic acid, and methanol oxidation in acid electrolytes—Mechanisms and electrocatalysis. In *Encyclopedia of Electrochemistry*, Vol. 2, Bard, A.J., Stratmann, M., Eds., Wiley-VCH, Weinheim, Germany, 2003, pp. 466–511.
132. Iwasita, T.; Ciapina, E. G., Mechanistic aspects of carbon monoxide oxidation. In *Handbook of Fuel Cells*, Vol. 2, Vielstich, W., Lamm, A., Gasteiger, H.A., Eds., Wiley & Sons Ltd., Chichester, England, 2003, pp. 224–239.
133. Siwek, H., Lukaszewski, M., Czerwinski, A. Electrochemical study on the adsorption of carbon oxides and oxidation of their adsorption products on platinum group metals and alloys. *Phys. Chem. Chem. Phys*. 2008, 10, 3752–3765.
134. Inkaew, P., Korzeniewski, C. Kinetic studies of adsorbed CO electrochemical oxidation on Pt(335) at full and sub-saturation coverages. *Phys. Chem. Chem. Phys*. 2008, 10, 3655–3661.
135. Czerwinski, A., Sobkowski, J. The adsorption of carbon monoxide on a platinum electrode. *J. Electroanal. Chem*. 1978, 91, 47–53.
136. Cuesta, A., Couto, A., Rincón, A., Pérez, M.C., López-Cudero, A., Gutiérrez, C. Potential dependence of the saturation CO coverage of Pt electrodes: The origin of the pre-peak in CO-stripping voltammograms. Part 3: Pt(poly). *J. Electroanal. Chem*. 2006, 586, 184–195.
137. Batista, E.A., Iwasita, T., Vielstich, W. Mechanism of stationary bulk CO oxidation on Pt(111) electrodes. *J. Phys. Chem. B* 2004, 108, 14216–14222.
138. Samjeske, G., Komatsu, K.-I., Osawa, M. Dynamics of CO oxidation on a polycrystalline platinum electrode: A time-resolved infrared study. *J. Phys. Chem. C* 2009, 113, 10222–10228.
139. Lu, G.-Q., Chrzanowski, W., Wieckowski, A. Catalytic methanol decomposition pathways on a platinum electrode. *J. Phys. Chem. B* 2000, 104, 5566–5572.
140. Lai, S.C.S., Kleyn, S.E.F., Rosca, V., Koper, M.T.M. Mechanism of the dissociation and electrooxidation of ethanol and acetaldehyde on platinum as studied by SERS. *J. Phys. Chem. C* 2008, 112, 19080–19087.
141. Cao, D., Lu, G.-Q., Wiekcowski, A., Wasileski, S.A., Neurock, M. Mechanisms of methanol decomposition on platinum: A combined experimental and ab initio approach. *J. Phys. Chem. B* 2005, 109, 11622–11633.

142. Koper, M.T.M., Jansen, A.P.J., van Santen, R.A., Lukkien, J.J., Hilbers, P.A.J. Monte Carlo simulations of a simple model for the electrocatalytic CO oxidation on platinum. *J. Chem. Phys*. 1998, 109, 6051–6062.
143. Lissi, E., Simonaitis, R., Heicklen, J. Bromine atom catalyzed oxidation of carbon monoxide. *J. Phys. Chem*. 1972, 76, 1416–1419.
144. Piva, A. The action of bromine on carbon monoxide. *Gazz. Chim. Ital*. 1915, 45(1), 219–237.
145. (a) Lenher, S., Schumacher, H.-J. Bromophosgene. I. Thermal decomposition—A first order wall reaction. *Z. Physik. Chem*. 1928, 135, 85–101; (b) Schumacher, H.-J., Lenher, S. Bromophosgene. II. Its preparation and properties. *Berichte der Deutschen Chemischen Gesellschaft [Abteilung] B: Abhandlungen* 1928, 61B, 1671–1675.
146. Livingston, R. The halogen sensitized oxidation of carbon monoxide. *J. Phys. Chem*. 1930, 34, 2121–2122.
147. Francisco, J.S. Energetics for the reaction of CBr_2O with water. *Chem. Phys. Lett*. 2002, 363, 275–282.
148. López-Cudero, A., Cuesta, A., Gutiérrez, C. The effect of chloride on the electrooxidation of adsorbed Co on polycrystalline platinum electrodes, *J. Electroanal. Chem.* 2003, 548, 109–119.

17 Hybrid Scanning Electrochemical Techniques
Methods and Applications

Julie V. Macpherson and Christophe Demaille

CONTENTS

17.1 Combined Scanning Electrochemical Microscopy: Atomic Force Microscopy 570
17.1.1 Introduction 570
17.1.2 Hand-Fabricated SECM-AFM Probes 571
17.1.3 Use of Commercially Available AFM Probes for SECM-AFM Probe Development 572
17.1.4 Wafer Scale Batch Fabrication of SECM-AFM Probes 574
17.1.5 Other SECM-AFM Fabrication Methodologies 577
17.1.6 Modeling of SECM-AFM Probe Responses 578
17.1.7 Application Areas of SECM-AFM 578
17.1.7.1 Imaging Reactive Sites on a Surface 578
17.1.7.2 Imaging Membrane Transport Processes 581
17.1.7.3 Biosensor Activity 581
17.1.7.4 Substrate Patterning 582
17.1.7.5 Probing Surface-Attached Redox Macromolecules: Mt/SECM-AFM 583
17.1.7.6 Attaching a Redox SECM Mediator to an SECM-AFM Probe: Tarm/SECM-AFM 586
17.2 Combined Scanning Electrochemical Microscopy–Scanning Tunneling Microscopy 587
17.3 Distance Control in SECM 590
17.3.1 Shear Force Scanning Electrochemical Microscopy 590
17.3.1.1 Shear Force SECM with Vibrating Needle UMEs 590
17.3.1.2 Using Quartz Crystal Resonators as Shear Force Transducers for SECM 595
17.3.2 Intermittent Contact–Scanning Electrochemical Microscopy 599
17.3.3 Alternating Current–Scanning Electrochemical Microscopy 599
17.4 Capillary-Based Electrochemical Imaging Probes 602
17.4.1 Combined Scanning Electrochemical Microscopy–Scanning Ion Conductance Microscopy 602
17.4.1.1 Scanning Ion Conductance 602
17.4.1.2 Different Methods of SECM-SICM Tip Fabrication 604
17.4.1.3 Imaging Applications of SECM-SICM 605
17.4.2 Scanning Micropipette Contact Method 607
17.4.3 Scanning Electrochemical Cell Microscopy 607
17.5 Combination of SECM with Optical and Spectroscopic Techniques 609
17.5.1 Scanning Electrochemical Microscopy–Photoelectrochemical Microscopy 609
17.5.2 Scanning Electrochemical Microscopy–Scanning Optical Microscopy 611

17.5.3 Scanning Electrochemical Microscopy–Electrogenerated Chemiluminescence 615
17.5.3.1 Using the SECM Tip as a Light Source for Scanning Optical Microscopy 615
17.5.3.2 Detection of Enzyme Activity by SECM-ECL 617
17.5.4 Scanning Electrochemical Microscopy–Fluorescence Microscopy 617
17.5.4.1 Solution Studies 618
17.5.4.2 Surface Measurements 620
17.5.5 Scanning Electrochemical Microscopy–Surface Plasmon Resonance 621
17.5.6 Scanning Electrochemical Microscopy–Attenuated Total Reflection Spectroscopy 623
17.6 Scanning Electrochemical Microscopy–Quartz Crystal Microbalance 624
17.7 Fast Scan Cyclic Voltammetry–Scanning Electrochemical Microscopy 624
References 625

Since the writing of the first version of this book, scanning electrochemical microscopy (SECM) has advanced significantly. With the excitement and promise of the technique validated, researchers looked for ways to enhance its capabilities. One of the key issues with SECM is that in order to extract quantitative information on surface processes, knowledge of the tip–substrate separation is essential; obtaining this parameter using electrochemical principles can be a difficult and tiresome process. Many of the hybrid techniques discussed in this chapter have been developed with this limitation in mind. The research was further pushed forward by the fact that in order to go to higher resolution, smaller electrodes are required, which makes positioning and imaging even more challenging. This was especially true on rougher surfaces, where fixed height imaging with a small electrode invariably results in tip crash. Hence the combination of SECM with techniques such as AFM, STM, shear force, and SICM, as described in Sections 17.1 through 17.4, began to flourish. The concept of hybrid SECM techniques became more popular and imaging tips were designed that could measure more than one property, such as the combined optical–SECM–shear force probes described in Section 17.5. Taking this concept one step further, researchers looked to mount the SECM platform onto a variety of different microscopes in order to enable complementary fluorescence, confocal laser scanning microscopy (CLSM), surface plasmon resonance (SPR), and attenuated IR measurements. Looking back over the past 10 years, the wealth and diversity of hybrid SECM techniques and methodologies that have emerged is astonishing. One wonders what the next 10 years will bring.

17.1 COMBINED SCANNING ELECTROCHEMICAL MICROSCOPY: ATOMIC FORCE MICROSCOPY

17.1.1 Introduction

The combination of SECM with atomic force microscopy (AFM) is perhaps one of the most well-known and well-documented hybrid SECM technologies. Its development arose from the need to have a robust method of distance determination in SECM measurement. Traditionally, in amperometric SECM measurements the current that flows at the tip, when the tip is placed close to a surface, is due to the diffusional flux of a specific electroactive moiety to the electrode, which is dependent on both surface reactivity and tip–substrate separation, d. If d is not known accurately, then the (electro) chemical process under investigation cannot be correctly interpreted. Descriptions of SECM-AFM methodology and applications have featured in reviews, notably [1] by Macpherson in 2002; [2,3] by Kranz and coworkers in 2003 and 2008, respectively; and [4] by Wittstock et al. in 2007.

AFM, introduced in 1986 by Binnig et al. [5], is one of the most versatile scanned probe microscopes available to date. In AFM, the probe is a very sharp tip attached to a force-sensing cantilever, typically beam shaped, and fabricated from silicon or silicon nitride. During imaging, the tip scans

across the sample, and a physical property of the cantilever varies in response to force interactions between the tip and substrate, for example, deflection when the AFM is operated in contact mode or amplitude when the AFM is employed in tapping mode. These changes are monitored in conjunction with a feedback loop, which continually adjusts the tip–substrate separation in order to maintain a constant force (constant cantilever deflection or amplitude of vibration). In this way, a topographical map of the sample surface is built up with a z-resolution of sub-Å and (x, y) resolution of approximate nanometers. The latter is controlled primarily by the radius of curvature of the sharp tip.

Given that AFM can measure x, y, and z surface topography with very high spatial resolution, and control of the position of the tip in the z-direction is possible with sub-Å resolution over many microns from the surface, combining AFM with SECM significantly extends the capability of SECM. More importantly, SECM-AFM provides an accurate, electrochemical signal–independent measurement of tip position in all three axial directions.

However, implementation of the technology requires integration of an electrode into the AFM probe, in order to confer dual functionality. The cantilever functions as the force sensor, which in conjunction with a sharp tip provides high-resolution (nanometer-level) topography measurements, and *precise* control of the tip–substrate separation. The current response of the electrode, which can be located at various positions on the probe, serves as a quantitative measure of the (electro)chemical properties of the interface, akin to SECM. SECM-AFM probes are extremely powerful as they enable structural information to be correlated directly with chemical surface activity, and the effect of local changes in solution composition, initiated electrochemically, to be interrogated structurally. The various different SECM-AFM probe designs in operation to-date are discussed in detail below with applications of the technology described.

17.1.2 Hand-Fabricated SECM-AFM Probes

The first documented SECM-AFM probe is described in [6], fabricated from a 50 µm diameter Pt wire. In the arena of nanoscopic electrode fabrication [7] and the production of tips for electrochemical STM [8], procedures are well established for the electrochemical etching and insulation of microwires, to produce sharpened and insulated, except at the very apex of the tip, nanoelectrodes. In the AFM field, solid metal AFM probes, for the measurement of the electrical, frictional, and topographical properties of a substrate, have been fabricated previously, by hand, from metal microwires [9]. Thus, by combining the two methodologies together, it was possible to fabricate SECM-AFM probes.

Simply, the wire is etched, to form the sharp imaging tip, and bent and flattened, to form the force-sensing cantilever. An insulating film is applied to the probe, in the form of an electrodeposited paint, which retracts from the apex during curing, so that only the very end of the tip is exposed, leaving a submicron "cone-shaped" electrode at the tip apex. As with conventional SECM measurements, the cone geometry is especially attractive for noninvasive, quantitative imaging of concentration profiles at reactive surfaces. An image of a typical SECM-AFM probe produced this way is shown in Figure 17.1. A crucial requirement of all SECM-AFM probe development is that the only exposed metallic area on the probe is that of the electrode itself; thus, it is essential that no pinholes are present in the insulating coating, which can be challenging.

SECM-AFM probes of this design format, that is, where the electrode is also in the same location as the apex of the imaging tip, can also be used in conductive AFM mode (C-AFM), that is, to directly measure the current that flows through a substrate when a voltage is applied between the tip and the substrate [6,10]. In this way, the electrical properties of the substrate, if (semi)conducting, can also be spatially quantified and correlated with the electrochemical response [11]. Due to the low resonant frequencies of these hand-fabricated SECM-AFM probes, topographical imaging is often carried out in contact mode. As, electrochemical imaging is typically carried out with the tip maintained at a "constant distance" from the substrate of interest, the tip scans each line twice. In the first pass, sample topography is recorded, while in the second pass this information is used to hold

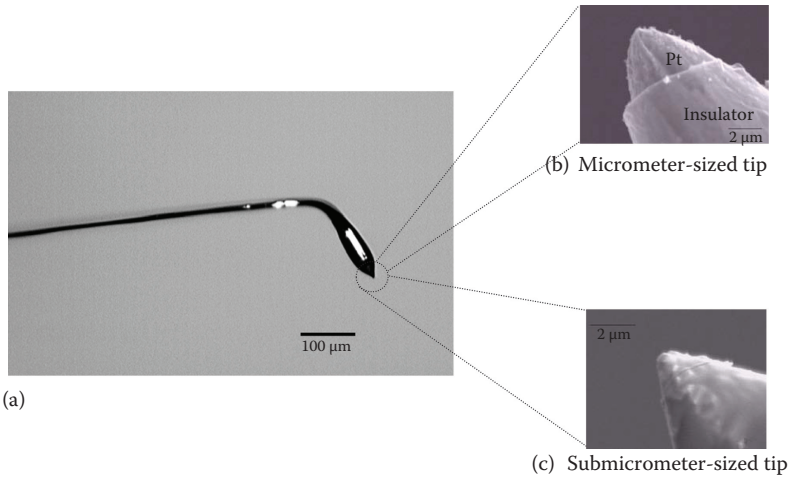


FIGURE 17.1 (a) Micrograph of a coated SECM-AFM probe. Scanning electron micrographs of the end of (b) micrometer- and (c) submicrometer-sized SECM-AFM tips. (Adapted from Macpherson, J.V. and Unwin, P.R., *Anal. Chem*., 72, 276, 1999.)

the tip at a constant, defined distance from the surface while electrochemical data is acquired [12]. This methodology is also used for magnetic- and electrostatic AFM imaging. In this way, the tip–substrate separation is always known, which is not possible with conventional SECM imaging.

This fabrication technique has been adapted for the production of submicrometer-sized gold SECM-AFM electrodes of well-defined conical or spherical geometry [13]. Here the apex of etched gold microwire is molded into a defined spherical or conical structure by local melting using a controlled arc discharge. The whole structure is then coated in an electrodeposited insulating paint and the very end of the tip exposed by applying a high voltage pulse to the gold wire.

An image of a typical tip structure is shown in Figure 17.2. These types of SECM-AFM probes have been employed to (i) probe the structure and dynamics of redox-labeled end-grafted polymer chains and short DNA strands [14–16]; (ii) monitor enzyme-catalyzed incorporation of a redox nucleotide to end-grafted DNA strands [17]; (iii) image the distribution of end-grafted polymer chains on composite surfaces [18]; (iv) probe the reactivity of nanometer-sized surface sites independent of their turnover rate, using tip attached redox mediator (Tarm)/SECM-AFM [19,20]; and (v) locally electrograft polyacrylic acid patterns on a conducting substrate [21]. All are described in more detail in Section 17.1.7.4.

17.1.3 Use of Commercially Available AFM Probes for SECM-AFM Probe Development

For more widespread application of SECM-AFM, there is a need for probes with reproducible and defined characteristics, and microfabrication technologies represent an attractive way forward. Two approaches currently exist: (1) modification of an existing commercial AFM probe in order to build in electrochemical functionality and (2) bottom-up fabrication, where the probe structure is built from first principles. This section will deal with the former, while Section 17.1.4 discusses the latter.

In this area, Kranz et al. [22] were the first to make significant progress. In their initial work, conventional silicon nitride AFM probes were coated with a 100–300 nm thick layer of Au (the electrode material), followed by ~800 nm thick layer of silicon nitride (insulator). Successive millings, using a focused ion beam (FIB), sharpened and redefined the geometry of the AFM tip, so that a gold square-shaped microframe electrode was positioned around the base of the AFM tip. Here, each tip was individually fabricated. The FIB milling process can be adapted to produce ring electrodes [23] and electrodes of submicron dimensions [24] and different insulating materials have

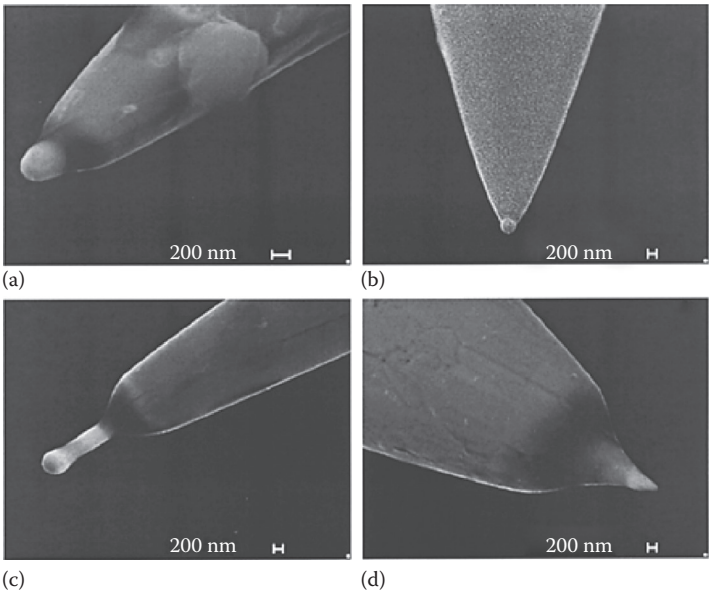


FIGURE 17.2 SEM micrographs of submicroelectrodes. The electrodes are made from gold wires bearing submicrometer-sized structures formed as a result of the controlled arc discharge technique. The body of the wire is insulated by a layer of electrophoretic paint; only the preformed tip end is bare gold. (a)–(d) represent the different structures formed by varying the settings of the spark generator used to make the submicroelectrodes shown. (Reproduced from Abbou, J. et al., *Anal. Chem*., 74, 6355, 2002.)

been employed, for example, Parylene [25], plasma-deposited fluorocarbon films [26]. A typical image of an SECM-AFM probe produced this way is shown in Figure 17.3.

In the Kranz tip design, the distance between the electrode and the surface is kept constant, governed by the height of the tip. Thus with the tip imaging in contact mode, the electrode is maintained at a constant distance from the surface and is protected from potential fouling issues associated with the electrode making intimate contact with the surface. As with SECM, the spatial resolution of this type of electrochemical probe will depend on the electrode size and its distance from the surface. This probe design contrasts significantly with that described in Section 17.1.2. The probe can also be operated in tapping mode [27], acting to minimize frictional forces associated with contact mode imaging. Given the very small oscillation amplitudes employed during tapping, the current flowing at the electrode is very similar to that obtained with the tip operated in contact mode. These probes

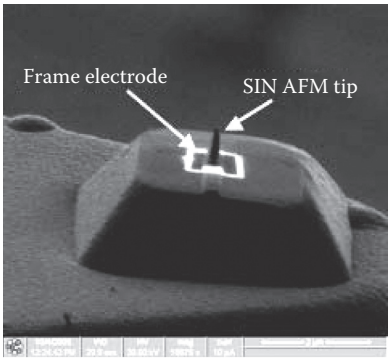


FIGURE 17.3 Focused ion beam image of an integrated frame submicroelectrode with an edge length of 800 nm and a tip height of 300 nm. (Unpublished data.)

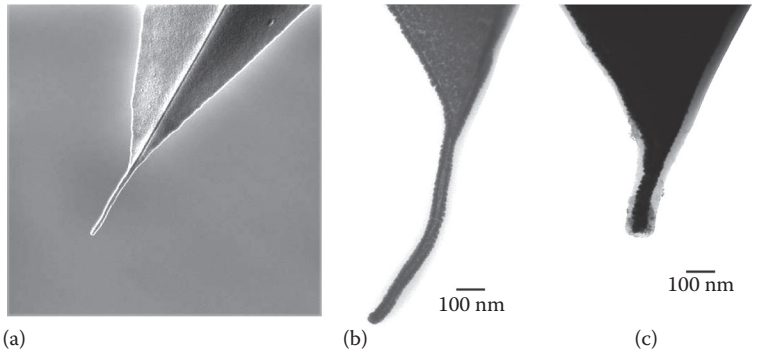


FIGURE 17.4 Various stages of SECM-AFM tip production. (a) A CNT-AFM tip is coated in a thick film of metal to produce a nanowire tip. (b) The tip is insulated with an electrodeposited polymer. (c) The end of the tip is removed using a focused ion beam to reveal a disk-shaped electrode. (Unpublished data.)

have been used predominantly for mapping biosensor activity [3,28,29] as described in Section 17.1.7.3.

Other researches have used less sophisticated techniques than FIB to reveal and define the electrode. For example, metal-coated commercially available probes are insulated with either Parylene C [30] or a photoresist layer [31] and then the apex of the tip exposed using either mechanical grinding [30] or UV light, exposed through a mask [31]. However, the drawback of using these approaches is the inability to produce electrodes of reproducible dimensions and the difficulty in characterizing electron dimensions, using, for example, electron microscopy.

Finally, in a novel approach using single-walled carbon nanotubes (SWNTs) attached to AFM tips [32] as a template for metal nanowire formation [33], SECM-AFM probes have been fabricated [34]. Here, SWNTs are attached to commercial AFM tips using the "pickup" method of attachment [32] and used as a template for subsequent deposition of metal to create metallic nanowires on the apex of the AFM tip [33]. The probe is then fully insulated with an electrodeposited polymer and the end of the probe removed using FIB to reveal a nanosized disk-shaped electrode (metal with a SWNT core) embedded in an insulating sheath, as shown in Figure 17.4. The advantages of this approach are (1) the size of the metallic electrode can be exquisitely controlled by controlling the amount of metal deposited in the sputter process—this means disk electrodes down to ~10 nm can be reliably produced, although there is scope for having just a single SWNT as the electrode; (2) the electrode never makes intimate contact with the surface, it is the edge of the insulator that forms the imaging tip; and (3) the dimensions of the tip can be accurately characterized in a transmission electron microscope.

17.1.4 Wafer Scale Batch Fabrication of SECM-AFM Probes

In the history of AFM development, microfabrication and lithographic techniques were introduced early on to facilitate the production of multiple probes at a time with a high reproducibility. Today, more advanced microfabricated probe designs are increasingly commonplace, as the applications of AFM become more adventurous. For example, electron beam lithography can be used to write submicron and nanoscale metal patterns on the end of an AFM tip for magnetic and thermal imaging applications [35]. Gerber and colleagues at the IBM research laboratories in Zurich, in collaboration with Güntherodt in Basel, have produced arrays of cantilevers for "electronic nose" type applications [36]. To this end, it is no surprise that researchers have turned to microfabrication technologies as a way forward for the batch production of SECM-AFM probes.

Several research groups have been active in this area and include Kranz and colleagues [37,38], Staufer and coworkers [39–43], Fasching and coworkers [44,45], Macpherson and coworkers

[46,47], and Wittstock and coworkers [48,49]. Kranz and colleagues introduced batch fabrication processes to produce ring microelectrodes, 2–3 μm in diameter at the base of a silicon carbide tip [37,38], similar to their design employed previously where they revealed a ring electrode in a metal-coated commercial AFM probe, using FIB [23]. Briefly, silicon pillars on cantilever structures were coated in Pt, followed by silicon carbide. Preferential, etching of the surface left a silicon carbide tip on the top of the pillar, surrounded by a ring of Pt (the electrode), at the base of the tip. Typical yields were quoted at 60% [38].

The majority of all other approaches have the electrode located in the vicinity of the AFM tip. For example, Frederix et al. opened up pyramidal etch pits in Si(100), which were then coated with a film of silicon nitride. These were used as the template for electrode and tip formation. The electrode (tip) was formed by depositing a film of polycrystalline silicon, restructured by ion etching, followed by a layer of platinum. Finally, a layer of silicon nitride was deposited to encapsulate the metal, and the surface was subject to etching to reveal the cantilever shape, resulting in a cantilever and tip totally insulated, except for the Pt_xSi_y apex, as shown in Figure 17.5 [39,41,43]. Although the probes are formed in a batch process, variation was found in the electrode base radii, between 40 and 400 nm, and ratio of electrode height to base radii from 2 to 2.5. Tips with apex radii, as small as 10 nm, were formed. The motivation for this probe development was to perform C-AFM in solution, targeted at biological applications, for example, measuring and manipulating the function of membrane proteins [39].

Prinz and coworkers came up with several approaches to the formation of SECM-AFM tips. The earliest [44] involved the production of sharpened high aspect ratio silicon (HARS) tips, with base diameters as small as 600 nm and tip radii smaller than 50 nm, using isotropic and anisotropic deep-reactive etch processes. Deposition of silicon nitride followed by a back etch step enabled the silicon tips to protrude through the silicon nitride layer. Layers of platinum, followed by silicon nitride, were then deposited on the tips. Finally, using a mask in combination with FIB, the underlying metallic layer was exposed to reveal the Pt electrode sitting atop the HARS tip. However, only cyclic voltammetric analysis was carried out with no demonstration of combined SECM-AFM imaging.

Further work, building on the above fabrication processes, involved the fabrication of planar- and needle-shaped probes, the latter enabling AFM imaging, with either single or dual (encompassing two tips) electrode systems built in [45]. In brief, metal is deposited on the tip (which is angled with respect to the cantilever as shown in Figure 17.6) and FIB is used to precisely define the shape of the tip, giving radii as small as 50 nm. After encapsulating with an insulating material (silicon nitride), FIB is employed again to remove the insulator in the vicinity of the apex and define the electrode

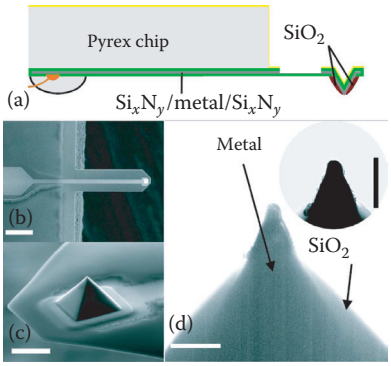


FIGURE 17.5 (a) Schematic representation of the conductive probe. The metal was embedded between two Si_xN_y thin films and the tip was insulated with SiO_2. (b and c) Scanning electron micrographs of the fabricated probes; the total height of the tip is 5 μm. (d) TEM image of the Pt_xSi_y tip apex. The scale bars are (b) 50 μm, (c) 5 μm, and (d) 100 nm (scale bar in the inset is also 100 nm). (Reproduced from Frederix, P.L.T.M. et al., *Nanotechnology*, 16, 997, 2005.)

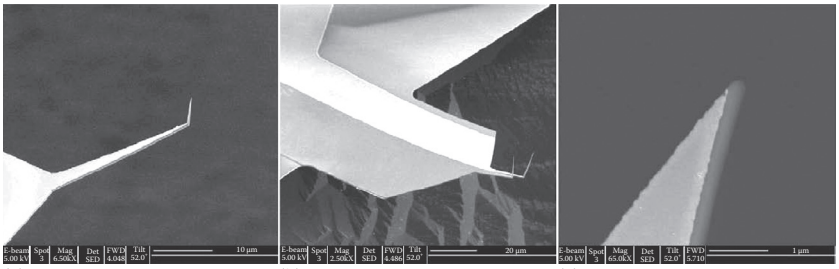


FIGURE 17.6 (a) Single and (b) dual probes with bended nanoprobes for combined electrochemical and AFM analyses. (c) Tip of the single probe. (Reproduced from Bai, S.-J. et al., *Sens. Actuators*, 130, 249, 2008.)

geometry (as shown in Figure 17.6c). The probes were found to have an average electrode area of 0.1 μm^2 and both Pt and Ag/AgCl (formed from Ag and then chloridized) submicrometer electrodes were formed on the AFM tips.

A similar design to the one used by Fasching et al. in 2008 [45] had been adopted earlier in 2005 by Macpherson and Weaver [46,47], except in this study electron beam lithography was used as opposed to FIB, as a means of exposing the defined electrode area. Figure 17.7 shows a typical image of the final SECM-AFM probe fabricated using this methodology; here triangular-shaped electrodes, base width ca. 1 μm, defined at the apex of the tip in gold are revealed at the tip apex. Yields of ~80% were reported.

Finally, Wittstock and colleagues proposed a hollow fourfold silicon dioxide pyramid [50] as the tip (with an integrated electrode) [48,49]. The probes were completely coated with an Au layer from the top side, in order to fill the inside of the pyramid with a conductive material. Initially, insulation of the sensor was achieved by depositing a 1 μm thin layer of Parylene C. However, it was found that this was not sufficient to completely insulate all the deposited Au areas. To rectify the situation, the amount of Au on the surface (e.g., on the probe body, cantilever) was reduced using lithographic processes, especially in the vicinity of edges, and the insulator was changed to silicon nitride. The electrode was revealed by slicing off the apex of the silicon dioxide tip using FIB, as shown in Figure 17.8. As can be seen, the electrode is slightly offset from the imaging tip, which must be taken into account when interpreting the electrochemical images. Electrodes as small as ~10 nm radius were fabricated using this approach [49]. It was noted that with this type of SECM-AFM design

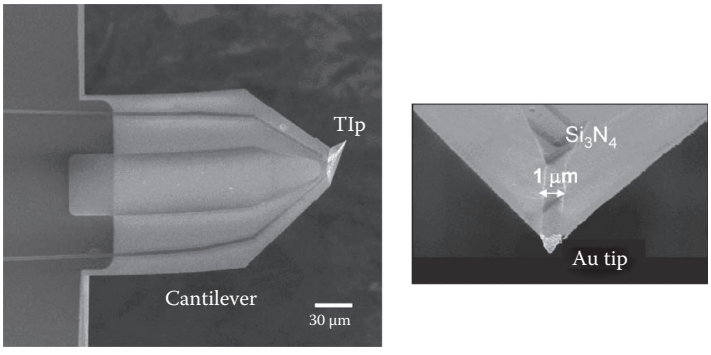


FIGURE 17.7 (a) Low- and (b) high-resolution FE-SEM images of the tip and cantilever geometry of a typical SECM-AFM probe fabricated using microfabrication and electron beam lithography. (Adapted from Dobson, P.S. et al., *Anal. Chem*., 77, 424, 2004.)

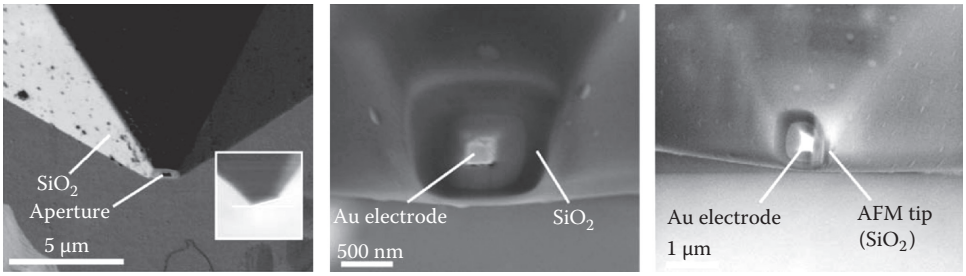


FIGURE 17.8 (a) Slice of the pyramidal tip yielding a small square electrode (inset shows the same tip at the same magnification but at a different angle in order to visualize the sloped cut of ~15°). (b) Electrode at the apex of the pyramid achieved by removing SiO_2 at the very tip. (c) Ion beam milling was performed so that one half of the top SiO_2 layer was left as distance holder in SECM and as AFM tip. (Reproduced from Salomo, M. et al., *Microelectron. Eng*., 87, 1537, 2010.)

topographical features on the surface of a certain size (dependent on probe–electrode geometry) led to artifacts in the SECM current image [49].

17.1.5 Other SECM-AFM Fabrication Methodologies

Davoodi et al. described two alternative SECM-AFM probe designs in their work. The first involved pulling and embedding Pt microwire in an insulating epoxy to produce an insulated ultramicroelectrode (UME) of 1–5 μm in diameter. The probe was L-shaped with the shoulder flattened, to act as the cantilever, and coated with gold to aid laser deflection. The insulated end was cut with FIB to reveal a small tip next to the Pt disk electrode, as shown in Figure 17.9 [51]. This design is similar to that adopted by Kranz et al. [22], where the electrode is recessed from the imaging tip by a defined distance.

The second involved embedding and pulling Pt microwire in quartz glass to ~10 μm diameter and then polishing the end at an angle of 15°–25°. In this way, the end point of the quartz glass could be used as the imaging tip, and the Pt wire as the sensing electrode [52]. In both cases, and in contrast to all of the probes discussed earlier, the AFM shoulder for laser deflection was not immersed in the electrolyte solution. This was achieved by using a long bending arm about 2–3 mm in length. These probes were used for investigating structure–activity problems related to corrosion at high resolution [52–56], as discussed in Section 17.1.7.1.

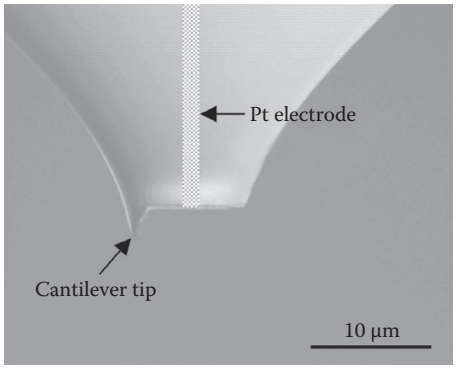


FIGURE 17.9 Micrograph of the SECM-AFM tip end formed by embedding Pt wire in insulating epoxy. (Reproduced from Davoodi, A. et al., *Electrochem. Solid State Lett*., 8, B21, 2005.)

17.1.6 Modeling of SECM-AFM Probe Responses

Of the probe designs discussed earlier, several authors have used numerical simulations to quantify the electrochemical response of the integrated electrode and compare this to the values measured experimentally. Modeling the response of an SECM-AFM tip is more complicated than for the traditional disk-shaped UME, employed in SECM, due to the lack of axial symmetry and the need to move to 3D. Skylar et al. [57] used the boundary element method (BEM) to model the electrode response of the submicrometer frame electrodes, introduced by Kranz et al. [22]. They showed that theoretically the presence of the tip did not alter the current–distance response, compared to the case of no tip present, when approaching infinite surfaces with associated, zero, finite and diffusion-limited electron transfer rate constants. The tip was also found to have no effect on the current response when recording the feedback current as the tip scanned over gold islands, >10 times larger the dimensions of the integrated frame electrode. Experimental currents were found to agree well with those simulated numerically.

Finite element method (FEM) simulations were used to predict the current response of the triangular-shaped electrodes defined by electron beam lithography at the apex of the AFM tip [46,47] and the diffusion-limited current response of the tip approaching insulating and conducting surfaces. With probes of this design, it was shown that the tip does not significantly perturb the diffusion field of a reactive site on the surface and thus could be used most effectively in substrate generation–tip collection (SG-TC) mode. SG-TC images of the tip current response recorded at a defined distance over a 10 μm diameter Pt disk electrode, generating electroactive species under diffusion-controlled conditions, were found to agree well with those predicted by FEM simulations. Further experimental and theoretical studies showed that this tip design, compared to a conventional V-shaped silicon nitride contact mode AFM probe and a single beam silicon AFM probe [58], was the least physically invasive for measuring reactive site diffusion profiles.

The BEM numerical simulation method was also used by Wittstock and coworkers to predict useful SECM-AFM tip and electrode geometries before time, effort, and cost were invested in microfabrication [49]. They simulated approach curves and tip feedback images for SECM-AFM tips where the electrode was recessed, by polishing the tip at an angle or using FIB to expose the probe end [48,51,59], with respect to the imaging tip.

17.1.7 Application Areas of SECM-AFM

17.1.7.1 Imaging Reactive Sites on a Surface

One of the most popular choice of model substrates for examining the performance of SECM-AFM probes is patterned conducting–insulating regions, with the sample typically comprising conducting microbands or micrometer-sized electrodes. Imaging is either carried out in feedback mode or SG-TC mode. For example, Figure 17.10 shows SG-TC SECM-AFM tapping mode images of (a) surface height and (b) tip-collection current [34]. The latter equates to a diffusional concentration profile generated at a substrate electrode, ~2 μm in diameter, and biased at a potential to generate a flux of electroactive species for collection at the tip electrode. In this case, the SECM-AFM probe was formed from a metal nanowire (templated from a SWNT) [34] as described in Section 17.1.3.

There have been many applications described where SECM-AFM has been used to investigate structure–activity relationships important in the materials science area. Macpherson et al. described the use of hand-fabricated probes [6] to investigate the electrochemical and electrical properties of an industrially important dimensionally stable electrode, $Ti/TiO_2/Pt$ [10,11]. The electrode was prepared by the galvanostatic oxidation of titanium to form a porous, micrometer-thick layer, followed by the galvanostatic deposition of Pt. The surface was first interrogated with C-AFM, as the apex of the tip was conducting, and it was found that not all the exposed spherically shaped Pt deposits were ohmically contacted to the underlying titanium. Some of the Pt structures were contacted via

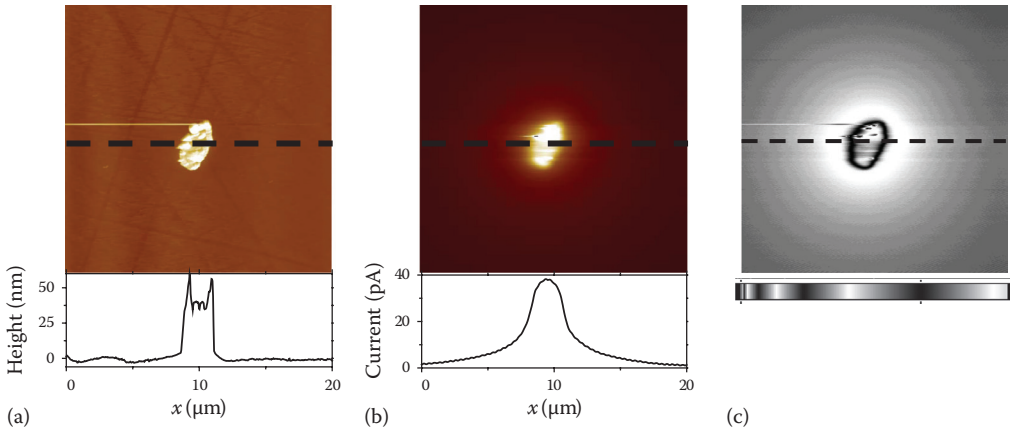


FIGURE 17.10 (a) Tapping mode AFM height and (b and c) electrochemical current images of a 2 μm diameter Pt substrate recorded using a nanowire SECM-AFM probe at a scan rate of 0.5 Hz. The electrochemical data in (b) is replotted in (c), using a multibanded color scheme to emphasize the emergence of pure radial diffusion at larger distances from the electrode, even though the electrode itself is clearly not circular. The images are 20 μm square. (Reproduced from Burt, D.P. et al., *Nano Lett*., 5, 639, 2005.)

titanium dioxide to produce a Schottky contact, as verified by FIB cross sectioning of the sample. The corresponding SECM-AFM maps of surface structures and electroactivity (in SG-TC mode) also confirmed this.

Wittstock and coworkers used their SECM-AFM probes to map the topography and electrochemical activity of the biphasic alloy Ti-6Al-4V (used in load-bearing implants) in feedback mode [49]. They found a comparable topographical resolution compared with conventional AFM probes, although it was not possible to image the substructure of the phases which was possible with a standard AFM tip [60]. Subtle variations in the SECM current were recorded, simultaneously with surface topography measurements. Current variations were recorded at phase change boundaries in the alloy which were also associated with changes in surface height. Given the low heterogeneous electron transfer rate constants associated with the two phases in the alloy, the current variations were associated with changes in the separation between the tip and the substrate only. Their study [49] highlighted a drawback of using very small electrodes for the measurement of slow electron transfer kinetics. When the electrode is too small and flux of species to the surface is very high, it is difficult to quantify small differences in slow electron transfer rates, especially when the current signals are low themselves.

Davoodi et al. have predominantly used their SECM-AFM probes to investigate localized corrosion processes [51–56]. Initial studies focused on the aluminum alloy AA1050. Dissolution was initiated by anodically polarizing the sample in a solution containing chloride ions (10 mM NaCl) and the redox mediator, I_3^- [51]. I_3^- was turned over to I^- at sites where the aluminum alloy started to corrode and the SECM-AFM tip was biased at a potential to detect I^-. In this way, it was possible to correlate images of the corroding surface with redox activity, as shown in Figure 17.11. Preliminary results indicated that enhanced local dissolution may occur well below the breakdown potential, but only for a small fraction of the surface area.

Further work saw the use of SECM-AFM in conjunction with in situ AFM and Kelvin probe microscopy to examine and interpret the localized corrosion behavior of two aluminum alloys, EN AW-3003 and Al–Mn–Sr–Zr, which are commonly used as heat exchangers [55]. It was found that the Al–Mn–Sr–Zr alloy contained a smaller number of intermetallics with larger Volta differences, compared to the EN AW-3003 alloy. This correlated well with the SECM-AFM images that showed that the EN AW-3003 alloy was significantly more corrosion active, resulting in higher material loss during dissolution.

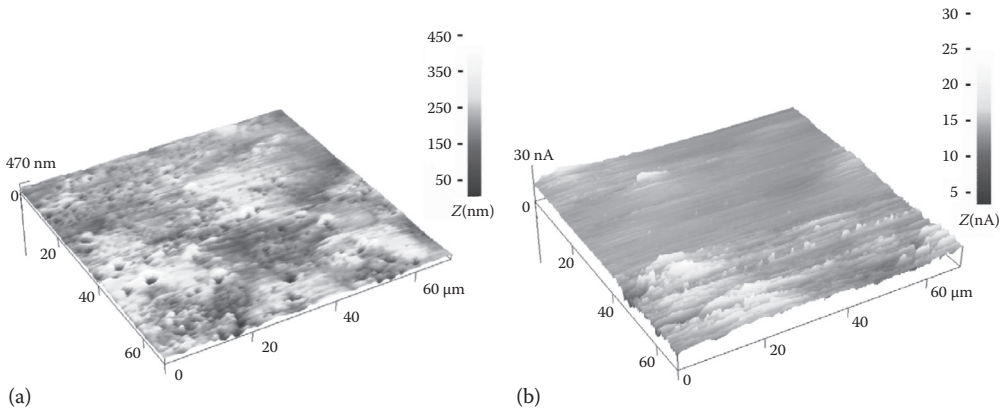


FIGURE 17.11 EC-AFM/SECM images of AA1050 in 10 mM NaCl + 5 mM KI at 300 mV anodic polarization (near breakdown potential) and tip at +750 mV vs. Ag/AgCl. (a) Topography and (b) electrochemical activity map. (Reproduced from Davoodi, A. et al., *Electrochem. Solid State Lett*., 8, B21, 2005.)

More detailed work on the EN AW-3003 alloy was carried out with the sample held under both cathodic and anodic controls [53,54]. For the former, the redox mediator $Fe(CN)_6^{3-}$ was added to allow electrochemical visualization of cathodically active sites. Importantly, SECM-AFM measurements at cathodic and anodic polarizations revealed both enhanced cathodic *and* anodic activities, on the surface, and in the vicinity of some of the large intermetallics.

Frederix et al. used their SECM-AFM probe design to investigate the electrochemical activity of highly orientated pyrolytic graphite (HOPG) [43]. Feedback experiments, in the presence of the redox mediator $Ru(NH_3)_6^{3+}$, were recorded as the tip approached a biased HOPG substrate (base of the tip 150 ± 20 nm). A positive feedback response was observed, which was not consistent with time due to possible time-dependent fouling of the surface. Taking the size of the tip into account, the electron transfer rate for the HOPG surface could be estimated as $2–3 \times 10^{-2}$ cm/s, which was at least three orders of magnitude higher than that estimated from cyclic voltammetry alone; a technique that averages over the whole surface.

SECM-AFM simultaneous height and feedback currents of the surface, as shown in Figure 17.12, indicate that over some step edges the electron transfer rate is higher than that associated with the basal plane. The authors comment that as the electron transfer rate is high for both basal and step edges, discrimination of electrochemically activity would not have been possible with larger sized

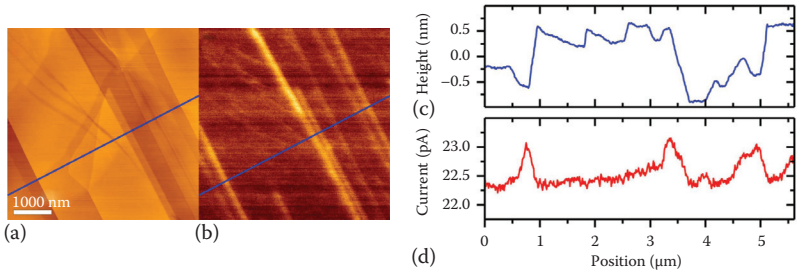


FIGURE 17.12 (a) Topography and (b) current response of a simultaneous AFM-SECM recording of HOPG. The topography was line-by-line corrected for background, whereas the current image was only scaled. This results in line-to-line variations in the current, likely caused by contaminants temporarily blocking the tip during scanning (scale bar: 1000 nm, height range: 10 nm, current range: 21.5–24.5 pA). (c) Topography profile and (d) current profile. Reproduced from (a) and (b), respectively, at the position denoted by the diagonal lines. (Reproduced from Frederix, P.L.T.M. et al., *Nanotechnology*, 19, 384004, 2008.)

electrodes [43]. Interestingly, although with this design the apex of the tip is exposed metal, no short circuit current was observed upon scanning the conducting HOPG surface in contact mode. This was attributed to tip contamination.

17.1.7.2 Imaging Membrane Transport Processes

In this section, applications in the imaging of membrane transport processes are highlighted. The transport of chemical species across synthetic and biological membranes is of great interest in many areas, ranging from, for example, separation, membrane-supported reactions, and gas permeation, to life science applications, such as transdermal drug delivery. For other techniques, in many cases, transport measurements are averaged over the whole (or a large section of the) membrane and if correlation is made between the rate of transport and the structure of the membrane, the latter is often inferred from ex situ microscopy.

SECM-AFM is thus ideally suited to measurements of this kind, as pores in the substrate can be identified topographically with high spatial resolution while transport through an individual pore can be mapped simultaneously by measuring the current signal. Through simulation, this signal can then be converted into a quantifiable rate of mass transfer. The only requirement for the measurement is that the molecule transporting through the membrane has an associated electrochemical signature, for example, is redox active or can be detected indirectly via electrochemical means. Up to now, measurements have been made on predominantly model systems but it should only be a matter of time before the move is made to real systems.

Work in this area has focused on the use of polymer-based porous membranes that are used for a variety of separation processes. In the transport studies described herein, the membrane functions as a separator between a donor (containing the species of interest) and a receptor compartment. Transport across the membrane can occur via diffusion, migration, or convection, although using SECM-AFM only the first two transport modes have been studied.

Using $Fe(CN)_6^{4-}$ as the redox-active probe, $Fe(CN)_6^{4-}$ was driven across a low pore density, track-etched polyethylene terephthalate membrane, containing pores of diameter 0.5–1.5 μm, using iontophoresis, for detection at the hand-fabricated SECM-AFM tip electrode (Figure 17.1) [61]. The tip current thus has contributions from diffusion and migration under the experimental conditions employed. Experimentally, the SECM-AFM tip currents were found to vary significantly between different pores, but were found to correlate with pore diameter, which could be accurately characterized using the AFM component of the probe, as shown in Figure 17.13a. Thus, it was possible to assess the transport properties of the membrane on a pore-by-pore basis.

Kranz et al. investigated the diffusion-controlled transport of glucose through a porous polycarbonate membrane, containing pores of size ~200 nm [29]. Tips similar to those shown in Figure 17.3 were employed. For these experiments, in order to make the SECM-AFM tip electrode sensitive to glucose, the redox-active enzyme glucose oxidase was immobilized at the surface of the integrated frame electrode by electrochemically induced, localized precipitation of the enzyme-containing solution. Turnover of glucose at the enzyme results in the production of hydrogen peroxide, which is electrochemically detected at the tip electrode, in much the same way a commercial glucose biosensor functions. Figure 17.13c and d shows simultaneously recorded images of AFM membrane topography and glucose diffusion through the pores. The current measured could be accurately quantified in terms of a local glucose concentration and was found to be in good agreement with that predicted for radial diffusion of glucose away from the pore opening.

17.1.7.3 Biosensor Activity

Much work in the area of mapping the bioactivity of surfaces has been carried out by Kranz et al. using the integrated frame electrode SECM-AFM probe, which sits back from the tip of the AFM probe [22] (Figure 17.3). To date, the tip electrode has been modified accordingly to make it sensitive to glucose (discussed in Section 17.1.7.2) [29], hydrogen peroxide [2,29], and ATP [3].

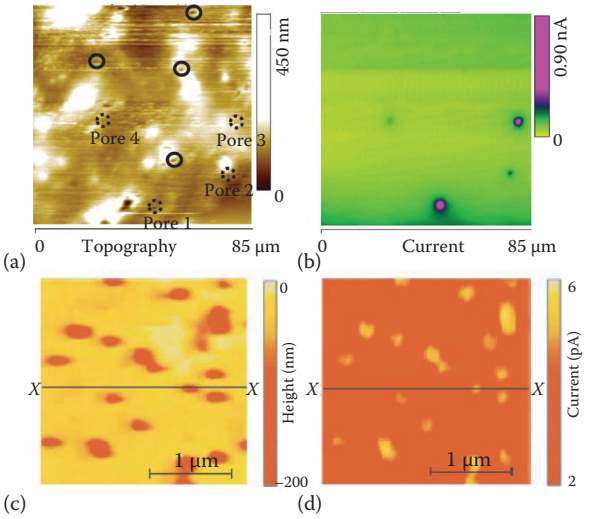


FIGURE 17.13 (a) SECM-AFM topography and (b) fixed height current images of the structure and iontophoretic transport activity of a porous membrane. For topographical imaging, the tip was held in contact with the surface, while electrochemical data was acquired with the tip imaging at a fixed height of 1 μm. In (a), the solid black circles highlight some of the potential candidates for open pores. The dotted black circles show the pores that are active to transport. (Reproduced from Gardner, C.E. et al., *Electrochem. Commun.*, 7, 612, 2005.) Simultaneously recorded (c) height and (d) current images of glucose diffusion, detected via tip immobilized glucose oxidase, through a porous polycarbonate membrane (pore size: 200 nm); images recorded in AFM dynamic mode. (Reproduced from Kueng, A. et al., *Angew. Chem. Int. Ed.*, 44, 3419, 2005.)

However, this concept can be reversed and an unmodified tip electrode employed to map the electrochemical activity of a redox-active enzyme. For example, in separate experiments, the pores of a periodic microstructure were filled with polymer matrix containing either glucose oxidase or horseradish peroxidase (HRP) [25]. In the former, in the presence of glucose, the SECM-AFM tip electrode detected electrogenerated hydrogen peroxide while in the latter, in the presence of hydrogen peroxide and hydroxyl methyl ferrocene (FMA), peroxidase catalysis resulted in the formation of water and FMA^+. The latter was electrochemically detected at the SECM-AFM tip electrode. In this way, it was possible to spatially visualize redox enzyme activity and correlate with substrate topography, as shown in Figure 17.14.

Hirata et al. used a similar approach to map the topography and redox activity of glucose oxidase immobilized on poly-L-lysine and poly(4-styrenesulfonate). HOPG was the support substrate and the SECM-AFM tip employed [31] is as described in Section 17.1.3. In the absence of glucose, no current was recorded for the production of hydrogen peroxide; however, in the presence of glucose, variation in current activity was seen over the enzymatic film. When the HOPG was biased at a potential to collect hydrogen peroxide, the current detected at the SECM-AFM electrode was significantly reduced.

17.1.7.4 Substrate Patterning

The use of an SECM-AFM tip to electrochemically pattern substrates was demonstrated by Nishizawa and colleagues [30]. Here the tip electrode (~500 nm), situated at the apex of the AFM tip, was biased at a potential to locally generate the oxidizing agent, hypobromous (HBrO) acid, in order to render a heparin-coated surface protein adhesive toward fluorescently labeled fibronectin. Compared to conventional SECM, the use of SECM-AFM enabled an increase in the resolution of the pattern size generated and the ability to topographically image the electrochemically treated

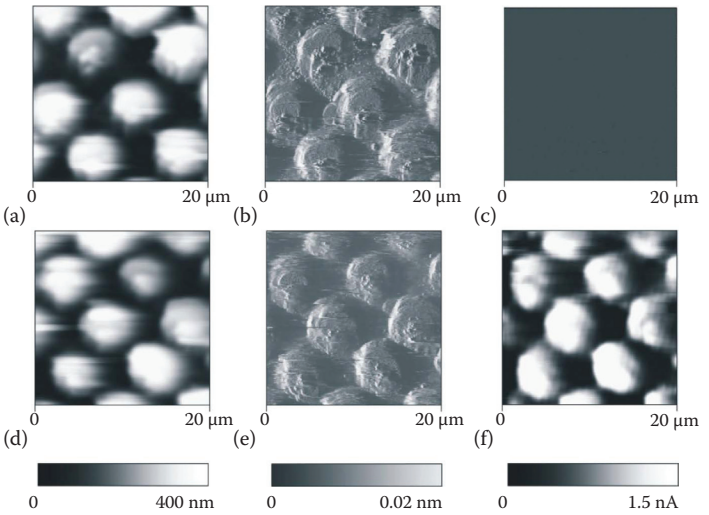


FIGURE 17.14 Simultaneously recorded topography of the enzyme-containing periodic polymer structure (height image) and current image of GOD activity in AFM tapping mode with free drive amplitude of 5 V and drive frequency of 32.4 kHz. Height (a and d), corresponding amplitude (b and e), and simultaneously recorded Faraday current (c and f) images recorded in air-saturated phosphate buffer (0.1 mol/L, pH 7.4) in the absence (a–c) and in the presence (d–f; 50 mmol/L) of glucose. The tip was held at a potential of 0.75 V (vs. Ag/AgCl quasi-reference electrode). Electrode edge length: 770 nm; tip height: 700 nm; scan rate: 3 Hz. (Reproduced from Kueng, A. et al., *Angew. Chem. Int. Ed*., 42, 3238, 2003.)

surface in situ. The resulting size of the drawn fibronectin patterns was found to be ~2 μm, which was an order of magnitude smaller than that obtained using a 10 μm disk UME operating in SECM mode [62].

Charlier and coworkers used hand-fabricated SECM-AFM probes to electrochemically locally induce grafting of a nonconductive polyacrylic film onto gold surfaces [21]. Grafting of vinyl monomers was carried out from an aqueous solution containing acrylic acid monomers and nitrobenzene diazonium tetrafluoroborate (NBD). The gold substrate was biased cathodically in order to produce nitrophenylen radicals, by reduction of NBD, which assembled onto the surface and served as an initiator for the radical polymerization of vinylic monomers. The SECM-AFM probe was used as a counter electrode and positioned close (~5 μm) to the substrate surface, to ensure polymerization occurred locally. Spatial movement of the probe resulted in nanopatterning of the surface with polymer lines ~200 nm wide and 35 nm thick. Imaging of the deposited polymer pattern was realized ex situ using conventional AFM probes in tapping mode.

17.1.7.5 Probing Surface-Attached Redox Macromolecules: Mt/SECM-AFM

Demaille and coworkers used hand-fabricated SECM-AFM gold probes (described in Section 17.1.2) to directly electrochemically address nanometer-sized redox-tagged chains, either DNA (oligonucleotide) or polyethylene glycol (PEG) chains, end-grafted onto electrode surfaces [14–16]. With the SECM-AFM probe in contact with the chains, it was possible to oxidize or reduce their redox heads, as shown in Figure 17.15. This particular mode of SECM-AFM, where the tip actually "touches" surface-grafted molecules (no mediator in solution), is labeled "molecule touching" SECM-AFM (Mt/SECM-AFM) [18]. The force-sensing capabilities of the combined SECM-AFM probe allowed the interactions between the polymer chains and the probe to be finely controlled. Using an AFM-based setup was also indispensable in order to position the tip with subnanometer precision within the end-grafted layers. SECM-AFM probes with spherical microelectrode tips

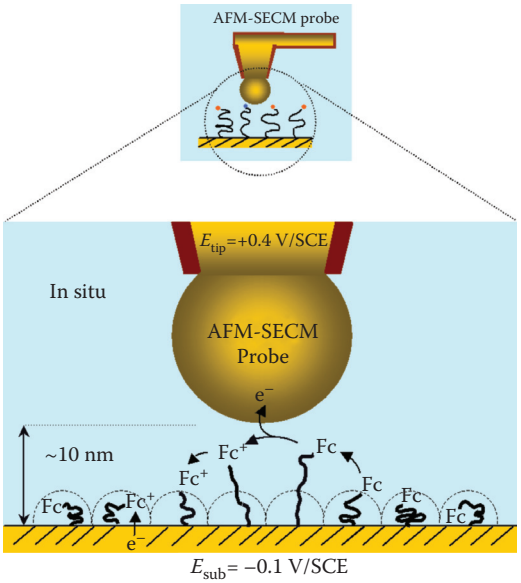


FIGURE 17.15 Direct electrochemical contact between an incoming AFM-SECM probe and the redox Fc heads of nanometer-sized, flexible chains (such as PEG or DNA), end-grafted onto an electrode substrate. The Fc heads are alternatively oxidized at the tip and reduced back at the substrate. For clarity, the tip is not drawn to scale. The chains are pictured in the mushroom conformation. (Adapted with permission from Abbou, J., Anne, A., and Demaille, C., Probing the structure and dynamics of end-grafted flexible polymer chain layers by combined atomic force—Electrochemical microscopy. Cyclic voltammetry within nanometer-thick macromolecular poly(ethylene glycol) layers, *J. Am. Chem. Soc.*, 126,10095–10108, 2004. Copyright 2004 American Chemical Society.)

were preferred since this particular tip geometry was expected to yield more current than conical tips due to the larger contact area.

The first system studied by Mt/SECM-AFM consisted of flexible linear PEG_{3400} chains, grafted onto a gold substrate, with the free end bearing a redox ferrocene (Fc) label [14,15]. Low-density monolayers of Fc-PEG chains were assembled, within which the PEG chains formed an array of coils (mushrooms) ~5 nm in size. The free Fc-labeled chain ends were able to explore a large hemispherical volume limited by the fully elongated chain length (~30 nm) (Figure 17.15).

Contact and compression of the SECM-AFM probe with the Fc-PEG layer was monitored simultaneously using the deflection (force) and current approach curve (Figure 17.16). The current signal corresponded to positive feedback redox cycling of the Fc heads, which were alternatively oxidized at the tip and reduced back at the conducting substrate. The current approach curve was quantitatively analyzed using a model that described motion of the Fc head as a diffusion process retarded by the restoring force exerted by the PEG chain. This model allowed the dynamics of the end-grafted chain to be quantified in terms of an effective chain-end diffusion coefficient.

At very close tip–substrate separation, an unpredicted peak was observed in the current response. Analysis of the force curve and random walk simulations of the chain conformation enabled this peak to be attributed to compression-induced conformational change of the end-grafted chains; overcompressed chains elongate to escape confinement. These results illustrate the power of SECM-AFM in being able to characterize, in situ, the dynamics of end-grafted polymer chains. Moreover, as SECM-AFM allows the force and current responses associated with chain compression to be simultaneously measured, the interplay between chain conformation and dynamics and their modulation upon confinement can be explored. Additionally, as SECM-AFM is a local probe

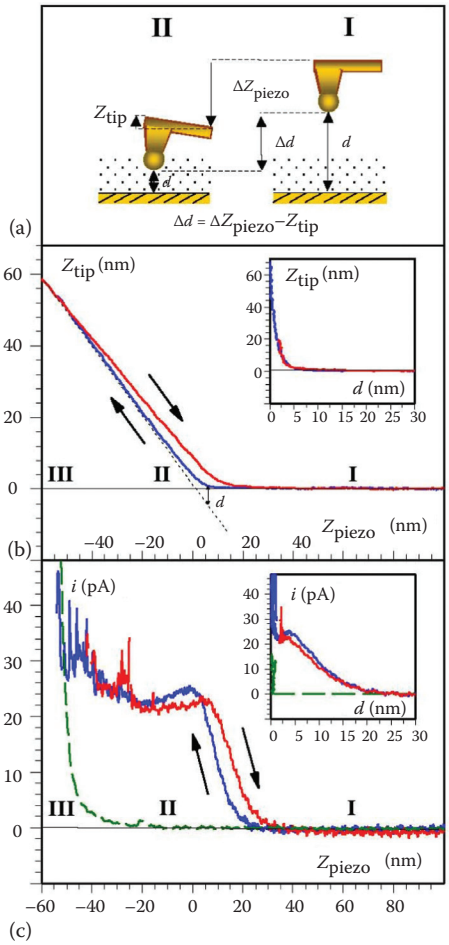


FIGURE 17.16 (a) Representative deflection behavior of a combined AFM-SECM probe partially penetrating a substrate-grafted PEG layer (represented as a dotted area). (I) The gold tip is in solution far away from the substrate and thus not deflected. (II) Upon further approach by an increment ΔZ_{piezo}, the tip is brought in contact with the layer and starts to compress it. As a result, the flexible cantilever-arm bends upward by an amount Z_{tip}. When in region III, the tip has made hard contact with the substrate. Simultaneously recorded tip deflection (b) and tip current (c) vs. piezo elongation Z_{piezo} curves for a gold substrate bearing redox Fc-PEG_{3400} chains (continuous lines) or biotin-PEG_{3400} chains (dashed line in (c), the retraction curve is not represented). The dotted line in (b) is used to show graphically how the tip-to-substrate distance d is determined and how the $Z_{piezo}=0$ point is defined. The insets in (b) and (c) show the respective replots of the curves as a function of d as derived as explained in the text. $E_{sub}=-0.1$ V/SCE; $E_{tip}=+0.4$ V/SCE. 1 M $NaClO_4$ supporting electrolyte. (Adapted with permission from Abbou, J., Anne, A., and Demaille, C., Probing the structure and dynamics of end-grafted flexible polymer chain layers by combined atomic force—Electrochemical microscopy. Cyclic voltammetry within nanometer-thick macromolecular poly(ethylene glycol) layers, *J. Am. Chem. Soc.*, 126, 10095–10108, 2004. Copyright 2004 American Chemical Society.)

technique only a small number of chains are addressed by the tip (~100–200 in [14,15]). Finally, since redox cycling of the Fc head is an efficient amplification mechanism, achieving single molecule sensitivity is conceivable.

Mt/SECM-AFM was also used to explore the conformation and motional dynamics of end-grafted DNA oligonucleotides [16]. Force and current approach curves were recorded at a gold surface bearing a layer of thiol-end grafted Fc-labeled $(dT)_{20}$ chains, both before and after hybridization

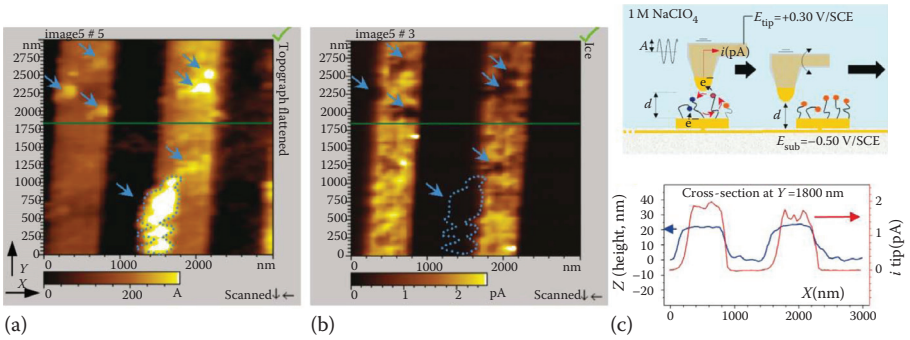


FIGURE 17.17 Tapping mode Mt/AFM-SECM imaging of a patterned substrate consisting of 500 nm wide, 20 nm high gold band electrodes deposited on an insulating SiO_2 surface and functionalized by a grafted layer of Fc-labeled PEG chains. (a) and (b) are the simultaneously acquired topography and the tip current (i_{tip}) images, for which the correlated cross sections along the horizontal green line at $X = 1800$ nm are shown in (c). Upper right is a schematic description of the tip scanning the patterned grafted substrate. $E_{tip} = +0.30$ V/SCE, $E_{sub} = -0.05$ V/SCE. The lateral scan rate is 0.5 line/s. The blue arrows indicate the locations of prominent contamination particles observed in the topography image (a), which corresponds to the dark "holes" seen in the tip current image (b). As small as ~100 nm sized particles/current depleted regions are resolved. (Adapted with permission from Anne, A., Cambril, E., Chovin, A., and Demaille, C., Touching surface-attached molecules with a microelectrode: Mapping the distribution of redox-labeled macromolecules by electrochemical-atomic force microscopy, *Anal. Chem.*, 82, 6353–6362, 2010. Copyright 2010 American Chemical Society.)

with complementary $(dA)_{20}$ strands. The force curves recorded before and after hybridization were similar, while an approximately fourfold decrease in the intensity of the current approach curve was observed after hybridization. It was concluded that the dominant motional mode of both single- and double-stranded oligonucleotides was hinge motion around the relatively long C_6-thiol anchoring spacer of the chains.

Mt/SECM-AFM was also used by Anne et al. for the in situ monitoring of enzymatic incorporation of a Fc-labeled nucleotide at the free end of oligonucleotides grafted on a gold surface [17]. Force curves were used to demonstrate grafting of unlabeled $(dT)_{20}$–SH chains onto the gold surface. The onset of a current approach curve after the DNA layer had been exposed to the enzyme terminal transferase in the presence of the Fc-nucleotide revealed the efficient single base extension of the end-grafted DNA strands.

Very recently, Demaille and coworkers further expanded the use of Mt/SECM-AFM to image the distribution of redox-labeled macromolecules grafted onto surfaces [18]. Here, direct electrochemical detection of the redox (Fc) head of end-grafted Fc-PEG chains could be carried out with an oscillating probe (tapping mode). The compatibility of Mt/SECM-AFM with tapping mode also made it possible to map simultaneously sample topography and Fc-PEG chain distribution. Using composite-patterned surfaces, a sub-100 nm resolution was demonstrated (Figure 17.17). Importantly, for these studies the typical SECM configuration, employing the use of a soluble mediator, could not have been used since direct electron transfer between the gold substrate and the soluble redox mediator would have interfered with chain detection. Mt/SECM-AFM imaging is expected to be a very useful technique for the imaging of advanced biosensor surfaces that use redox-tagged linear flexible chains as transducers.

17.1.7.6 Attaching a Redox SECM Mediator to an SECM-AFM Probe: Tarm/SECM-AFM

As discussed in Section 17.1.7.1, SECM can only probe surface reactivity if the turnover of the surface reaction is fast enough with respect to the diffusion rate of the soluble redox mediator; otherwise, the system tends to negative feedback. Therefore, increasing the lateral resolution of SECM by simply decreasing the UME size leads to the following paradox: resolving small reactive sites on

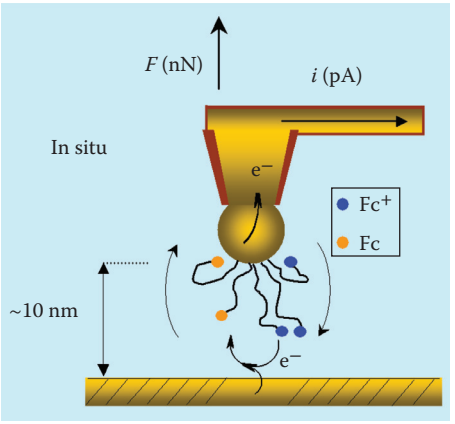


FIGURE 17.18 Working principle of Tarm/AFM-SECM microscopy. The SECM mediator, ferrocene (Fc), is attached to the AFM-SECM probe via a nanometer-sized, linear, and flexible polymer chain (PEG). The AFM-SECM configuration allows the tip separation to be set close to the chain length (below ~10 nm), so that the Fc heads of the chains can electrochemically probe the surface reactivity with nanometric resolution. For clarity the tip is not drawn to scale. (Adapted with permission from Anne, A., Demaille, C., and Goyer, C., Electrochemical atomic-force microscopy using a tip-attached redox mediator. Proof-of-concept and perspectives for functional probing of nanosystems, *Nano*, 3, 819–827, 2009. Copyright 2009 American Chemical Society.)

a surface requires small probes, but decreasing the probe size increases the rate of diffusion up to a point where comparatively "slow" reacting sites become undetectable by SECM.

This problem is particularly acute for the functional probing of surface-confined enzymes; since the rate of enzymatic reactions is typically low (~1 ms), probing enzymatic activity at a tip–substrate separation smaller than ~1 μm (distance over which a small redox mediator would diffuse in ~1 ms) is not possible using "regular" SECM or SECM-AFM. As an original strategy to solve this problem, Demaille and coworkers attached a redox mediator, Fc, to the tip of a hand-fabricated gold SECM-AFM probe via nanometer-sized flexible PEG chains (Figure 17.18) [19]. In such a configuration, diffusional loss of the mediator is avoided; the tip-generated redox-active form of the mediator can be held indefinitely in the vicinity of a reactive site, "waiting" for the reaction to occur.

It was shown that using an PEGylated SECM-AFM probe in tapping mode allowed a small enough tip–substrate distance to be set and held (10 nm or below) so that the Fc-PEG chains could efficiently shuttle electrons between the tip and substrate. In this constant distance mode, scanning the PEGylated probe over a substrate allows both topography and surface reactivity to be mapped. This new type of SECM-AFM microscopy, which was labeled Tarm/SECM-AFM, was used to image a HOPG substrate, a naturally nanostructured surface [20]. Not only was the topography of HOPG clearly mapped, with a vertical resolution below 1 nm, but the enhanced electrochemical reactivity of step edges vs. basal planes of HOPG could be visualized in the current image (Figure 17.19). This result demonstrated the ability of Tarm/SECM-AFM to probe the reactivity of nanometer-sized active sites on surfaces. Beyond reactivity imaging, attaching the mediator to the tip also has the advantage of potentially increasing the lateral resolution of SECM-AFM, which is now ultimately limited by the length of the anchoring tether (chain).

17.2 COMBINED SCANNING ELECTROCHEMICAL MICROSCOPY–SCANNING TUNNELING MICROSCOPY

Electrochemical scanning tunneling microscopy (ECSTM) is a very useful technique for investigating electrochemical processes at the solid–liquid interface at extremely high (~sub-Å to ~nm level)

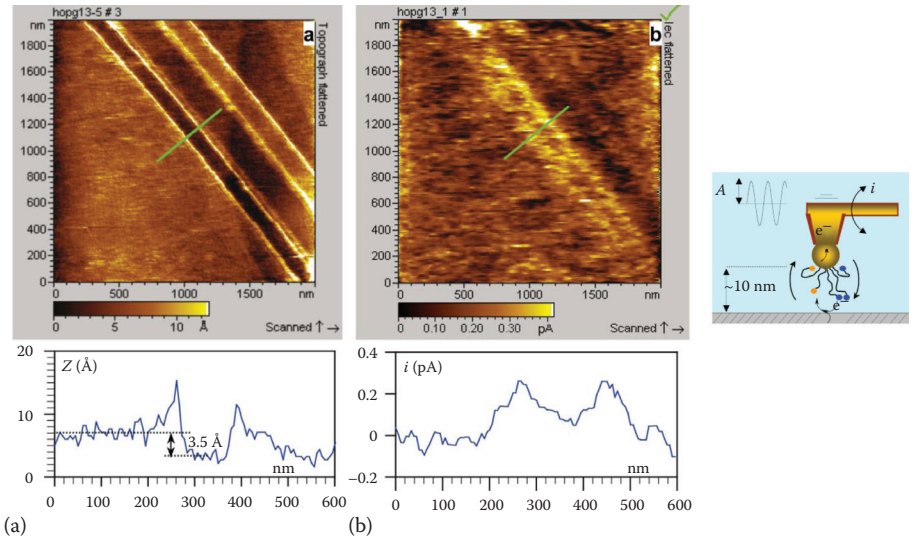


FIGURE 17.19 Tapping mode Tarm/AFM-SECM imaging of a HOPG substrate: discriminating the electron transfer rate at edge sites and at the basal planes of the HOPG surface. The simultaneously acquired topography (Z) and tip current (i_{tip}) are presented in images (a) and (b). The cross sections of the images, along the short green line shown, are represented in the lower part of the figure, below each corresponding image. $E_{tip} = +0.30$ V/SCE, $E_{sub} = +0.20$ V/SCE. At this potential, reduction of the oxidized Fc heads at the substrate is slow. The edge sites are clearly resolved in the topography image and for some of them also in the current image. Drive frequency = 8.66 kHz, tip oscillation amplitude A ~4 nm. 1 M $NaClO_4$ supporting aqueous electrolyte. Image scan rate 1 line/s. The topography image was second-order flattened, the current image was first-order flattened. (Adapted with permission from Anne, A., Cambril, E., Chovin, A., Demaille, C., and Goyer, C., Electrochemical atomic force microscopy using a tip-attached redox mediator for topographic and functional imaging of nanosystems, *Nano*, 3, 2927–2940, 2010. Copyright 2010 American Chemical Society.)

x-, y-, and z-resolution [8]. In ECSTM, the tip consists of a conventional sharpened STM tip, coated in insulator, at all but the tip apex to minimize unwanted electrochemical processes contributing to the tunneling current, during topographical imaging of the substrate. Given that this tip design has also been used by many for the fabrication of nanoelectrodes in electrochemical studies [7,8,63], it is no surprise that researchers have investigated ways forward to perform ECSTM and SECM together, with the same probe. In fact, there has been some debate in the literature as to whether the current that flows when STM is carried out in a humid environment on low conductivity substrates is actually due to electrochemistry or tunneling [64,65].

Initial studies in this area were carried out by Williams and coworkers who employed a Pt–Ir wire electrolytically sharpened and insulated, in ECSTM tunneling mode, to determine the point of contact with the substrate of interest, that is, tip–sample separation = 0. The tip was then retracted a set distance (100–500 nm) and SECM SG-TC imaging carried out in a fixed plane above the sample surface [66,67]. However given that the tip is not tracing sample topography in SECM mode, significant variations in sample topographically can result in tip crash.

This approach was employed to investigate pitting corrosion activity on stainless steel surfaces. In particular, current spikes were observed in the SECM images that were thought to be linked to pitting precursor events and the formation of metastable pits. In most cases, the local environment was unable to support continued propagation of the pits and the spiked current signal indicated re-passivation. Where pit growth was possible, it was postulated that this was due to the presence of manganese sulfide inclusions in the surface [66,67].

In an interesting approach, Stimming and researchers used the ECSTM tip to directly transfer a single Pd nanoparticle, deposited electrochemically, from the tip to a conducting substrate [68] and

then the same tip was employed to probe the electrocatalytic activity of the particle. Once transferred, the ECSTM imaging mode was used to first locate the Pd particle and then with the feedback control disabled the tip was retracted ~10 nm from the surface of the nanoparticle. Finally, in a solution containing 0.1 M sulfuric acid, the substrate potential was pulsed to a potential sufficient to enable proton reduction at the surface of the Pd nanoparticle (~2–5 nm radius), while the tip was held constant at a potential sufficient to detect any electrogenerated hydrogen. Current densities for the electrooxidation of hydrogen, at the Pd nanoparticles investigated in this study, were found to be two orders of magnitude greater than for a 200 nm sized particle.

Treutler and Wittstock [69] employed Pt-etched tips coated with an electrophoretic paint, of an optimized geometry, for combined ECSTM and SECM measurements. After the probe was brought into tunneling contact, an ECSTM image of the substrate topography was recorded in constant current mode. The tip was then retracted a set distance (here ~20 nm) and an SECM feedback map of the sample recorded (with tip and substrate held under appropriate potential control) at constant distance, that is, tracing the substrate topography. In this way, it was possible to record SECM maps at tip–substrate separations that were smaller than the surface roughness. This methodology was applied to a flame-annealed gold substrate covered with an insulating self-assembled monolayer (SAM). The tip was used to mechanically remove zones of the SAM in selected areas, in order to pattern the sample.

Figure 17.20 shows an ECSTM topography map of the substrate and the corresponding SECM feedback map of the surface recorded in a solution containing the redox mediator, $Ru(NH_3)_6^{3+}$ [69]. The substrate was biased at a potential to reduce $Ru(NH_3)_6^{3+}$ while the tip was poised at a potential to detect electrogenerated $Ru(NH_3)_6^{3+}$. Figure 17.20a shows although the ECSTM tip was able to

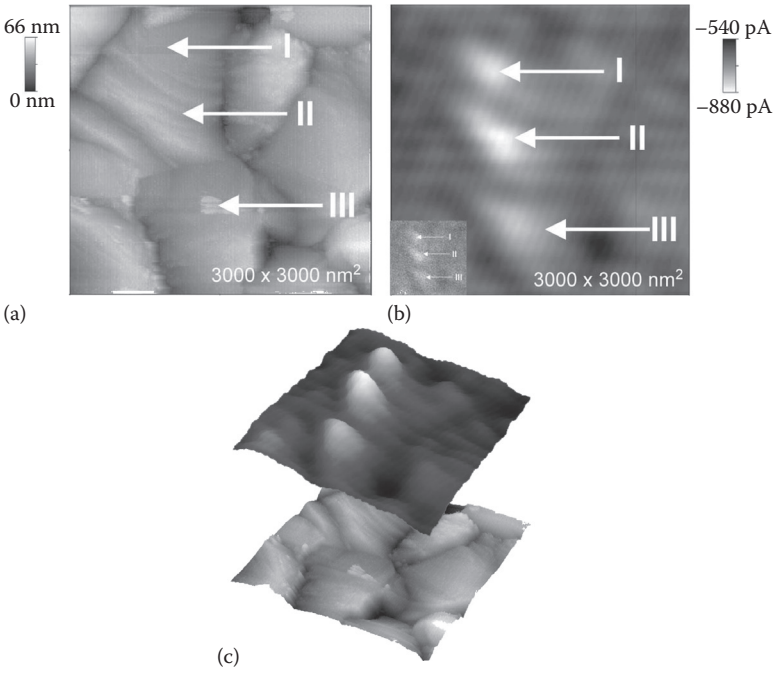


FIGURE 17.20 (a) ECSTM scan of a dodecanethiolate-covered gold electrode, $E_T = -50$ mV, $E_S = 0$ mV, tunneling current = 0.8 nA, after tip-induced removal of the dodecanethiolate film and (b) quasi-simultaneous SECM scan of the same area, image frame 3000 × 3000 nm², 2D FFT filtered, $E_T = -250$ mV, $E_S = 10$ mV, radius of tip electrode = 69 nm, imaging distance = 20 nm; inset shows SECM data without filtering. (c) Pseudo-3D representation of the measurements: top, SECM data from (b); bottom, ECSTM data from (a). (Reproduced from Treutler, T.H. and Wittstock, G., *Electrochim. Acta*, 48, 2923, 2003.)

resolve the structure of the underlying Au substrate, at high resolution, revealing height differences of ca. 70 nm, it was not possible to reveal the areas where the insulating SAM had been mechanically removed. However, these appear to have been revealed in the SECM feedback map (Figure 17.20b), where zones of increased current are clearly evident.

In a novel application, Siegenthaler and coworkers integrated a pH electrode into the STM tip design so that it was possible to simultaneously combine in situ STM studies with the ability to electrochemically generate or scavenge protons and hydroxide ions [70]. The STM tip protruded ~50 μm from a cylinder structure that incorporated a microring iridium oxide (pH) electrode. The distance between the STM tip and the pH electrode was ~80 μm. This structure was similar to the integrated frame electrode AFM tips introduced by Kranz and colleagues (discussed in Section 17.1.3). The concept was demonstrated by investigating the pH-dependent properties of an electropolymerized polyaniline film. In particular, it was shown that decreasing the pH resulted in the thickness of the film increasing while increasing the pH resulted in a decrease in film conductivity.

Although a useful technique, STM-SECM has not shown as much promise or been used as widely as SECM-AFM, most likely due to the fact that the substrate topography can only be obtained using ECSTM if the sample is sufficiently conducting, given that a tunneling current must be recorded. Moreover, AFM typically can be used on much rougher surfaces than STM and obviously can be employed independent of substrate conductivity.

17.3 DISTANCE CONTROL IN SECM

There have been many different approaches employed to control and measure the tip–substrate distance of "conventional" glass-coated UME disk probes during SECM imaging. Perhaps the most utilized at the time of writing is shear force SECM, pioneered by Schuhmann and colleagues, although here specialized glass-coated electrodes are required. However, other methodologies such as AC-SECM have been implemented with glass-insulated UMEs and recent developments have seen the introduction of intermittent contact–SECM (IC-SECM) by Unwin and coworkers. These techniques are described in this section.

17.3.1 Shear Force Scanning Electrochemical Microscopy

The idea of using the detection of hydrodynamic forces—shear forces—occurring when a vibrating local probe tip is approached toward a planar substrate, as a way of measuring and controlling the tip–substrate distance, was initially developed for near-field scanning optical microscopy (NSOM) [71]. It was found that when an optical fiber (the tip) was vibrated horizontally, the amplitude of the vibration was damped as the tip approached within a few tens of nanometers from the surface. It was thus possible to use the strong distance dependence of damping to set a desired tip–substrate distance and offer a convenient way of controlling the tip approach, avoiding crash.

This methodology was adopted by the SECM community as a means of developing constant distance mode SECM. Two experimental strategies have been proposed and are described in detail later: (1) specially designed flexible needle-type UMEs that can be easily vibrated upon mechanical excitation and (2) attaching SECM electrodes to an oscillating device, such as a quartz oscillator.

17.3.1.1 Shear Force SECM with Vibrating Needle UMEs

The first attempt to adapt shear force detection to SECM was reported by Schuhmann's group [72]. In the original configuration, a long and flexible needle-type glass-insulated disk UME, fabricated by sealing 25 μm diameter platinum wire in a pulled-glass capillary (1–1.5 cm long, 100 μm outer diameter), was vibrated using an excitation piezo. The vibrational motion of the tip was monitored by focusing a laser onto the lower part of the tip and detecting the resulting diffraction pattern on a spilt photodiode (Figure 17.21).

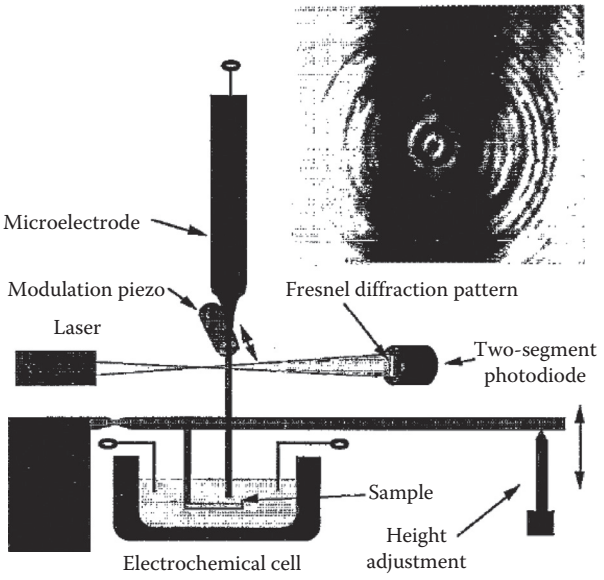


FIGURE 17.21 Instrumental setup for shear force–based constant distance SECM. The SECM tip is a needle-type microelectrode vibrated using a piezo. The tip vibration is monitored optically by diffracting a laser on the electrode body. The diffraction pattern formed on a two-segment photodiode (upper right) is used to monitor shear force–induced damping of the tip vibration. (Adapted with permission from Ludwig, M., Kranz, C., Schuhmann, W., and Gaub, H.E., Topography feedback mechanism for the scanning electrochemical microscope based on hydrodynamic forces between tip and sample, *Rev. Sci. Instrum.*, 66, 2857–2860, 1995. Copyright 1995 American Institute of Physics.)

The tip excitation amplitude spectrum of the vibrating UME submerged into buffer solution, displayed numerous peaks in the 0–20 kHz region, corresponding to various modes of tip vibration. Only the lowest mode, corresponding to a frequency around 1 kHz, was sensitive to the tip–substrate sample distance. The excitation amplitude of the tip vibration was varied from 1 nm up to a few microns. The effect of vibrating the UME on the tip current recorded in an SECM configuration was investigated. It was shown that the tip current displayed a linear dependence on amplitude for large excitation amplitudes. However, by employing a low enough amplitude (<1 μm) conditions could be found so that the tip current was not affected by the vibration.

Upon approaching the vibrating tip toward a conducting (gold) surface, the expected decay in tip amplitude, resulting from shear forces, was recorded concomitantly with an increase in tip current as a result of SECM positive feedback. However, it was observed that the decay length of the vibration approach curve was highly dependent on the stiffness of the underlying substrate material. On hard surfaces, this length was ~1 μm, whereas on softer surfaces, for example, gold on mica, it was several tens of microns. These results indicated the non-negligible magnitude of the tip–substrate interaction forces involved, estimated to be ~150 μN, high enough to even bend a mica substrate. However, this initial work established the compatibility of SECM with shear force.

In a following paper, Schuhmann and coworkers [73] demonstrated that by employing a feedback loop that relied on the detection of shear forces between the vibrating UME and sample, it was possible to keep the tip–substrate distance constant (constant damping amplitude) during SECM imaging. Hence it was possible to implement constant distance SECM imaging, a mode free of artifacts due to sample tilt and roughness. Moreover, it was demonstrated that shear force damping of the needle-like UMEs occurred within a distance of 100 nm from the surface, meaning it was possible to hold the UME extremely close to the surface during imaging. This resulted in a much better lateral resolution compared to fixed height imaging (Figure 17.22). Additionally, an image of the substrate topography could be reconstructed from the known adjustments of the vertical tip

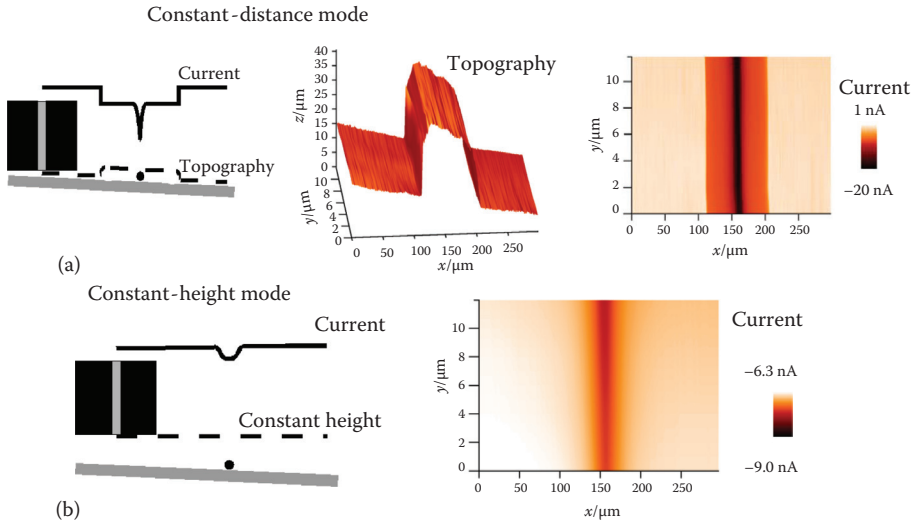


FIGURE 17.22 Comparison of constant height and constant distance imaging of a 10 μm diameter Pt wire glued onto a glass slide. (a) Representation of the shear force–based constant distance mode leading simultaneously to topographical and current images of the sample. (b) Representation of the constant height mode and the obtained current image. (5 mM $[Ru(NH_3)_6]^{3+}$ in 100 mM KCl electrolyte; UME at –300 mV/Ag/AgCl, UME: 10 mm diameter). (From Hengstenberg, A., Kranz, C., and Schuhmann, W.: Facilitated tip-positioning and applications of non-electrode tips in scanning electrochemical microscopy using shear force based constant-distance mode. *Chem. Eur. J.* 2000. 6. 1547–1554. Copyright Wiley-VCH Verlag GmbH. Adapted with permission.)

position imposed by the feedback loop in order to maintain a constant distance at each position of the scanned area. Hence in constant distance SECM imaging, topography and SECM current images could be simultaneously acquired.

Shear force can be used to bring any tip close to a surface and this approach has been successfully employed with non-amperometric pipette-based tips, such as miniaturized enzyme sensors or potentiometric probes [73]. Initially, work saw the use of an enzyme-filled glass capillary tip to image a 50 μm Pt modified disk in shear force feedback mode [73]. In one application, a glucose dehydrogenase (GLDH)-filled micropipette tip was used to map the production of NAD^+, the natural cofactor of GLDH, resulting from the catalytic oxidation of NADH at the surface of the Pt-modified UME [73] (Figure 17.23).

Shear force constant distance scanning potentiometry has been employed to map the dissolution of calcite crystals and shells [74] and to map spatial variations in pH at high resolution over complex microcavity-patterned substrates [75]. The ability to approach capillaries very close to a surface, using shear force feedback, was also used for the local deposition of silver microstructures on conducting surfaces using potential-assisted ion transfer at the tip of a micropipette [76].

Using shear force–based constant distance SECM imaging to characterize the activity of single live cells was demonstrated by Schumann and colleagues [77]. Here glass needle-type SECM tips could not be used, since the significant tip surface interactions occurring during shear force feedback caused irreversible damage to the cells. For this work, a special type of needle electrode consisting of ~10 μm diameter carbon fibers protruding by ~0.5 mm from a supporting glass capillary was employed. The walls of the carbon fiber were insulated by deposition of an electrophoretic paint. The extremity of the fiber was cut with a scalpel to expose a disk-shaped electrode. The resulting carbon fiber UME was flexible enough for the interaction forces between the tip and the cell to be sufficiently small to allow shear force mode to be applied to visualize the topography of individual living cells without damaging them (Figure 17.24). The carbon fiber

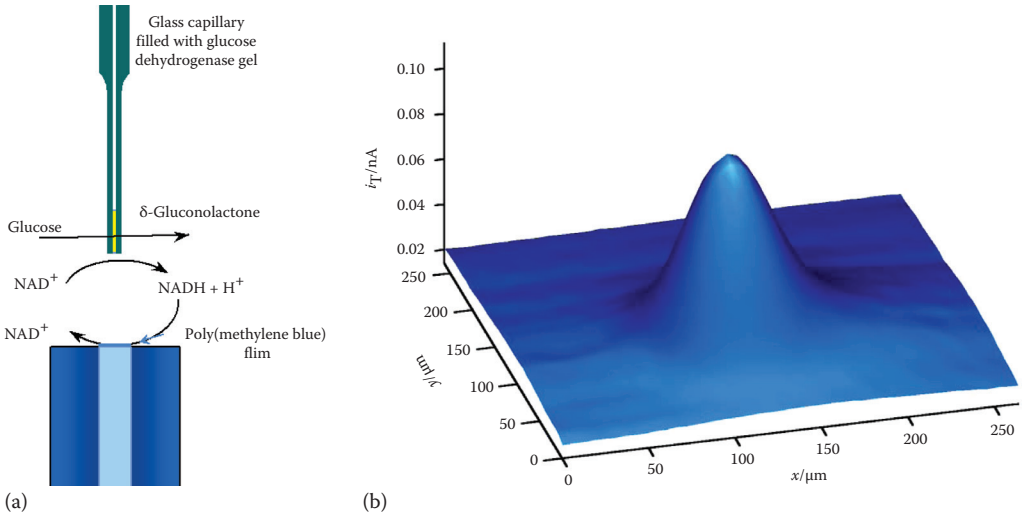


FIGURE 17.23 (a) Principle of generation/collection experiment with enzyme-filled glass capillaries used as tips in shear force–based constant distance SECM. The enzyme glucose dehydrogenase, in the presence of glucose, reduces NAD^+ to NADH, which then diffuses to the substrate electrode at which it is converted back to NAD^+. (b) The current through the substrate electrode (50 μm poly(methylene blue)-modified Pt disk) is used to visualize the local chemical activity with respect to the (x, y) position of the enzyme tip. (From Hengstenberg, A., Kranz, C., and Schuhmann, W.: Facilitated tip-positioning and applications of non-electrode tips in scanning electrochemical microscopy using shear force based constant-distance mode. *Chem. Eur. J.* 2000. 6. 1547–1554. Copyright Wiley-VCH Verlag GmbH. Adapted with permission.)

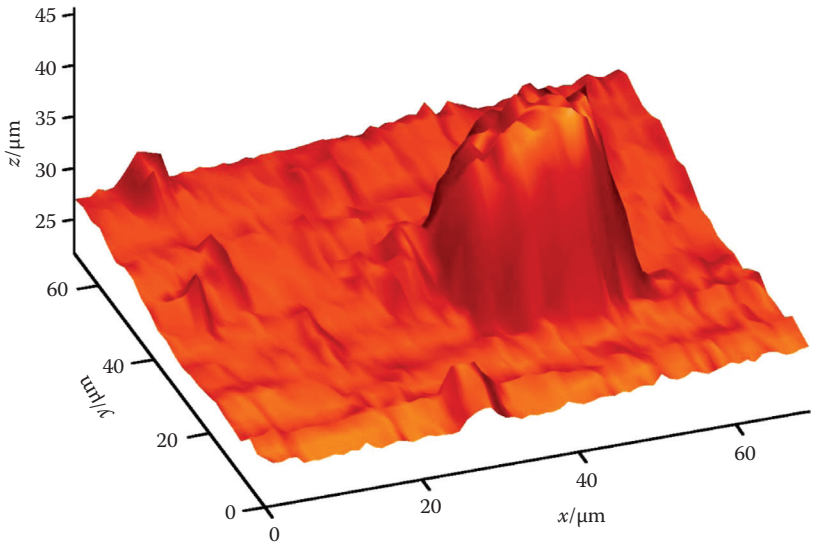


FIGURE 17.24 Shear force–based imaging of biological samples with carbon fiber electrodes with optimal stiffness (carbon fiber microelectrode of diameter ~10 μm). Topographic image of an individual PC12 cell. (From Hengstenberg, A., Blöchl, A., Dietzel, I.D., and Schuhmann, W.: Spatially resolved detection of neurotransmitter secretion from individual cells by means of scanning electrochemical microscopy. *Angew. Chem. Int. Ed.* 2001. 40. 905–908. Copyright Wiley-VCH Verlag GmbH. Adapted with permission.)

tip could thus be positioned above a single cell and the secretion of redox-active neurotransmitters amperometrically detected at the tip. The very short gap between the cell membrane and the UME, made possible by shear force positioning, insured a 100% collection efficiency of the neurotransmitter.

The shear force constant distance mode SECM was later mounted onto an inverted optical microscope, in a so-called "Bio-SECM" configuration, in order to study individual living cells. The Bio-SECM instrument was notably used to detect nitric oxide released from single cells [78]. In parallel, the shear force setup was modified by replacing the optical detection system, used to monitor the tip vibrating motion, by a piezoelectric element [79]. Electrical detection of the tip vibration was shown to be much easier and more convenient than optical detection, partly because the delicate laser alignment on the tip was made unnecessary. Further developments to shear force SECM have seen the implementation of high-resolution constant distance mode AC-SECM, which was used for the visualization of corrosion pits on stainless steel samples [80,81].

The aforementioned work has focused on needle-type SECM tips, having a diameter of the order of a few to tens of microns, positioned very close to a surface. Bringing such relatively "large" electrodes very close to a surface may be advantageous in the case where the tip is used as a collector. However for SECM imaging the "electrochemical" resolution is not only governed by the tip–substrate distance, which can be made very small using shear force, but also by the size of the disk-shaped UME. Moreover, the lateral resolution of the topography image, acquired simultaneously with the current image, is, in theory, limited by the overall size of the imaging tip, which includes the glass sheath surrounding the disk-shaped electrode.

Hence, reduction in tip size is necessary for better control of the imaging conditions and to improve both the topographical and electrochemical resolution of constant distance mode SECM imaging. To this end, needle-type nanoelectrodes were fabricated by pulling Pt wires in glass capillaries. This method, described in detail in Chapter 3, results in submicron-sized disk-shaped Pt electrodes encased in long, thin glass capillaries [82].

It was found that, upon mechanical excitation, these nanoneedles displayed several resonance frequencies in the 150–300 kHz range; although only some were sensitive to the presence of the substrate and were thus suitable for use to control the tip–substrate approach and distance. By holding the submicron-sized probes some ~100–200 nm away from a surface using shear force feedback, very high-resolution topography and constant distance current images could be acquired (Figure 17.25) [79].

In order to further improve the topographical resolution of constant distance mode SECM, a new generation of platinum nanoelectrodes was produced. Instead of the classical inlaid disk format, these pulled-glass Pt electrodes were conically polished so that the Pt disk electrode was located hundreds of nanometers above the conical extremity of the tip. Due to the geometric shape, the probe did not exhibit SECM feedback while approaching a sample. Thus these probes are best suited for concentration gradient profiling at active submicron-sized sites on a surface without interference from SECM feedback. As a proof-of-concept, these electrodes were successfully used for imaging the diffusion layer of a redox mediator $[Ru(NH_3)_6]^{2+}$ generated at a complex test structure consisting of microcavities incorporating disk (cavity bottom) and ring (cavity walls) electrodes [83].

Even though shear force feedback has been successfully used for constant distance mode SECM imaging in many instances, it nevertheless has several shortcomings. One of the problems is that the imaging scan rate has to be low in order for the electronic feedback loop to reestablish the set-point value (hence distance) every time the tip is moved to a new position, otherwise tip crash occurs. Another problem is that the range of the shear force interaction is very small (a few hundreds of nanometers) and shear force–based feedback can thus only position tips at this distance or closer to the substrate. For very small tip–substrate separations, the presence of the tip will block diffusion of species toward/away from the surface thus potentially interfering with the

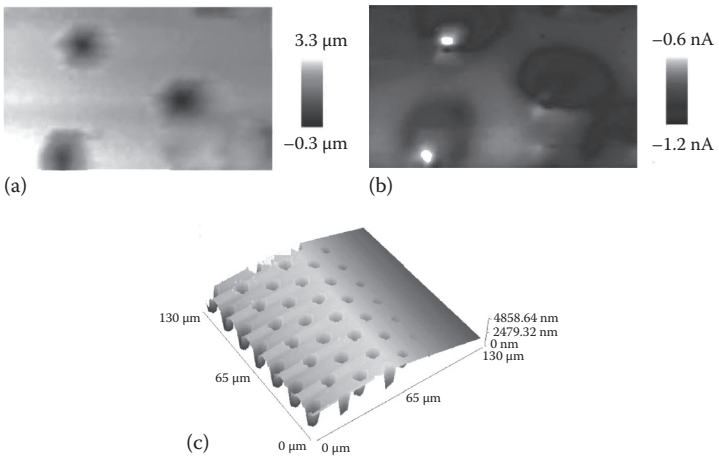


FIGURE 17.25 Constant distance SECM imaging using shear force feedback. Topographic (a) and amperometric feedback (b) images of a 23 µm × 38 µm portion of a honeycomb microstructure (LIGA). An AFM image of the structure is shown in (c) for comparison. The SECM images (a) and (b) were acquired all at once by constant distance mode SECM carried out in a solution of 5 mM $[Ru(NH3)_6]^{3+}$ containing 0.5 M KCl using a 450 nm diameter Pt disk nanoelectrode as the scanning probe (vibrating at resonance and kept at a constant potential of 300 mV vs. Ag/AgCl). (From Ballesteros Katemann, B., Schulte, A., and Schuhmann, W.: Constant-distance mode scanning electrochemical microscopy (SECM)–Part I: Adaptation of a non-optical shear force-based positioning mode for SECM tips. *Chem. Eur. J.* 2003. 9. 2025–2033. Copyright Wiley-VCH Verlag GmbH. Adapted with permission.)

phenomenon to be probed; for example, this is problematic when probing the activity of surface-attached enzymes.

Very recently, Schuhmann and coworkers [84] proposed a new imaging mode to address many of the aforementioned issues: 4D shear force–based constant distance SECM. Here, the tip is first approached under shear force control very close to the substrate. The tip current and vertical tip position are then recorded, allowing current and topography images to be reconstituted as usual. The tip is then retracted from the surface by small user-defined increments and the tip current at each distance is recorded. When the tip is retracted to its final position, it is laterally moved to a new (x, y) position above the sample and approached again at this new location. This procedure minimizes both the risk of crashing the tip and tip–substrate interactions occurring during lateral tip motion. Ultimately, a 4D data set (x, y, z tip current) is acquired from which topography and SECM images at different but constant tip–sample distances can be built. The feasibility of 4D imaging was demonstrated using amperometric feedback mode imaging of a Pt band electrode array and mapping of the diffusion profile of a redox-active species above a microelectrode in the generator/collector arrangement.

The work described earlier has demonstrated that monitoring shear force interactions between a vibrating needle SECM tip and a substrate is a robust approach for implementing constant distance SECM. Recently, work by Mauzeroll and colleagues demonstrated that monitoring the phase change of the tip vibration associated with the onset of shear forces, instead of the amplitude change, could further improve the sensitivity of distance regulation [85].

17.3.1.2 Using Quartz Crystal Resonators as Shear Force Transducers for SECM

In 1995, a paper from the NSOM community introduced the use of a small oscillating piezoelectric component, a crystal oscillator in the shape of a millimeter-sized tuning fork, as a transducer for detecting shear force damping of an oscillating optical fiber approaching a surface [86]. Typically, the fiber was glued onto one of the arms of the tuning fork which was mechanically excited by a

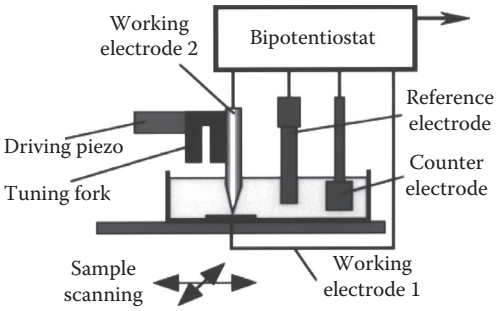


FIGURE 17.26 Schematic representation of a SECM setup using a tuning fork as a shear force–transducing element. The SECM tip (here a conically etched microelectrode, working electrode 2) is glued to one of the prongs of the tuning fork. Only the last ~1 mm of the tip is immersed into solution; the tuning fork itself is kept above the thin film of solution. (Adapted from Büchler, M. et al., *Electrochem. Solid State Lett*., 3, 35, 2000. With permission. Copyright 2000 Electrochemical Society.)

dithering piezo. The tuning fork was oriented toward the substrate and hence the fiber was vibrated parallel to the sample surface. Here the excitation frequency was perfectly defined: it had to exactly match the resonance frequency of the tuning fork (e.g., 32 kHz). The oscillation of the fork/fiber assembly was electrically monitored by measuring the voltage between electrical contacts on the prongs of the fork and analyzed using lock-in detection.

This shear force monitoring technique was later adapted to SECM by Smyrl et al. [87] who replaced the optical fiber with an etched tungsten wire (~2 μm apex), insulated by dip coating, and acting as an SECM tip. The conical tungsten tip was glued onto one of the prongs of the tuning fork so that a few millimeters of the probe extremity was protruding from the fork (Figure 17.26). In order to avoid complete damping of the tuning fork (and tip) motion, only the very end of the probe was immersed into the solution, that is, the tuning fork was in air. Thus, measurements were made in a thin film of solution (a few millimeters deep) bathing the substrate.

The tuning fork/tip assembly was mounted on the head of a commercial NSOM microscope and the tuning fork oscillation amplitude used as a feedback signal to regulate the tip–substrate separation. With this setup, an extremely small tip–substrate separation of the order of 10–30 nm was maintained by the feedback loop. Constant distance SECM imaging in SG-TC mode of a 50 μm platinum disk UME was carried out. Topography and SECM images were simultaneously acquired validating the use of the tuning fork for shear force–based constant distance SECM imaging. Later, feedback mode constant distance imaging of 5 μm gold wires aligned onto a substrate, using a gold-coated pulled optical fiber as an SECM tip, was successfully carried out with the same tuning fork–based setup [88]. This approach has also been used to observe defects in hexadecanethiol monolayers at submicron resolution [89].

A similar configuration was later used by Bard and coworkers [90,91] to develop a combined scanning electrochemical–optical microscope (see also Section 17.5.2). Here the SECM tip, a conically etched platinum wire insulated with electrophoretic paint, was used to generate light in situ via an electrogenerated chemiluminescence (ECL) reaction. Due to the small effective size of the conical microelectrode tip (down to 155 nm), shear force monitoring had to be used to control the tip-to-substrate approach and distance. The tip was thus attached to one of the prongs of a tuning fork. Here again, and this is pertinent to all tuning fork–based systems used in solution, immersion of the tuning fork itself had to be avoided. Hence, only the last ~0.5 mm of the probe, protruding from the end of the tuning fork, was in contact with solution.

The tip was first brought into very close proximity to the surface by shear force feedback: the approach was stopped when a 3%–5% damping of the fork oscillation was recorded. The tip was then withdrawn by 24 nm, before the ECL light intensity transmitted to the substrate was monitored. This "tapping mode–like" procedure was repeated for every imaging position of the substrate. The

tip was thus not scanned above the surface, but rather approached and then withdrawn, and only then translated laterally between measurements. This process minimized the chances of crashing the tip. Due to the small size of the tip, and the very close tip–substrate separation enabled by shear force distance control, submicrometer-resolution ECL near-field images were acquired.

The same shear force–based SECM setup was later employed using, this time as the tip, a pulled optical fiber bearing a ring-shaped electrode at its apex. Shear force detection using the tuning fork signal set a constant tip–substrate distance while simultaneous topography, current, and optical images of test substrates were acquired. Interdigitated band electrodes, consisting of 30 μm wide gold bands spaced by 25 μm glass, were imaged. Even though the "tapping mode–like" scanning procedure was utilized, it was observed that some samples were destroyed by the tip, for example, diatoms immobilized on glass [91]. This was a result of potentially destructive tip–substrate interactions that occur when a tuning fork is used as a shear force–sensing element.

The recurring problem of imaging fragile biological material using a tuning fork–based shear force distance control was addressed by Matsue and Yamada [92–94] by judicious choice of the imaging conditions in combination with the standard approach (STA) imaging mode, which is similar to the "tapping mode–like" mode introduced by Bard [91]. Yamada et al. imaged a glass surface bearing co-immobilized diaphorase and albumin with an SECM equipped with a tuning fork [92]. Disk-shaped platinum UMEs (2–10 μm) were used as the imaging tip that were cut to 4 mm length and glued onto the tuning fork. Only the last 0.5–1.5 mm of the tip was immersed in solution. Experimental conditions minimizing tip–substrate interactions were chosen, in particular a low set point that was 2% damping of the tip oscillation and the amplitude of the shear fork excitation signal was kept at a minimum. Under these conditions, STA mode imaging allowed the enzyme layer to be preserved.

Later, Yamada and coworkers showed that the STA mode could also safely be used for constant distance SECM imaging of living cells provided the shear force excitation signal was kept low enough [93]. Here, a combined optical fiber/UME having an effective electrode radius ~35 nm was used for imaging oxygen consumption by single PC12 cells in a culture medium. The local oxygen level was monitored amperometrically by the tip. Electrochemical images, reflecting the localized oxygen consumption by cell respiration, and topography images of the single cell were acquired simultaneously with micron-level resolution (Figure 17.27).

In a related work, Matsue et al. investigated systematically the influence of the amplitude of the vibration of the tuning fork on cell imaging [94]. They showed that if too large amplitudes were used the cells were damaged, whereas if too low amplitudes were employed the hydrodynamic forces caused by solution viscosity interfered with shear force detection and increased the noise level. Hence, an optimal amplitude has to be found. It was emphasized that this value actually depends on the shape of the probe and the depth of immersion of the probe into solution. Under optimal condition, well-resolved topography images of living cells could be obtained (Figure 17.28). These images were acquired in STA mode using fast electronic circuitry to shorten the scanning time acquisition. Moreover, in this particular work, with the probe acting both as a UME and an optical fiber, topography, fluorescent, and current images of single cells could be obtained in constant distance mode SECM–optical microscopy.

Other improvements to shear force–based SECM systems using tuning fork transducers have been reported [95,96]. Heinze et al. [95] showed that by using high-frequency (1 MHz) crystal oscillators, instead of the commonly used tuning fork (32 kHz) quartz, the dependence of the quartz resonance on the tip immersion depth could be minimized. Moreover, by using the phase shift of the quartz oscillation, as a feedback signal rather than the amplitude, the system achieved a greater stability. Matsue et al. reported the use of beveled disk-in-glass Pt UMEs glued to a tuning fork as a local probe for constant distance SECM shear force feedback imaging of enzyme activity [96], adopting a similar approach to Schuhmann et al. [83], discussed earlier in Section 17.3.1.2.

Using quartz crystal resonators as shear force transducers for distance control in SECM is seemingly universal, since it simply requires the gluing of a low mass probe to a crystal resonator to

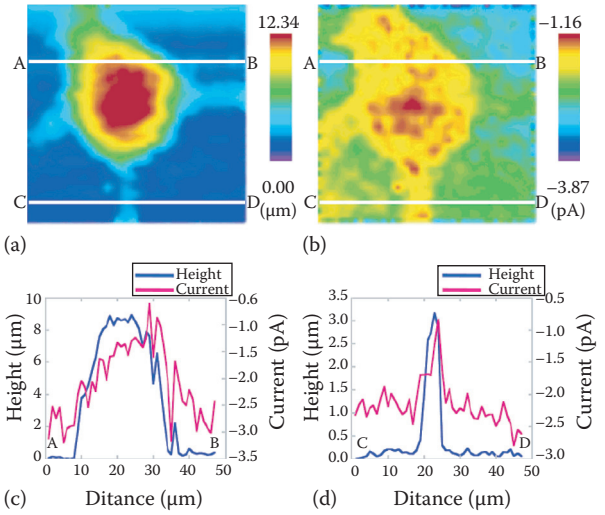


FIGURE 17.27 Constant distance SECM imaging using shear force feedback in the STA mode of model neurons (PC12 cells). (a) Topography and (b) electrochemical images of PC12 in a PBS solution using a capillary electrode probe. The tip was biased at −0.50 V (vs. Ag/AgCl) so as to reduce oxygen. Hence, the contrast of the electrochemical image (b) reflects the local oxygen level. Oxygen depletion due to cell respiration is visualized as orange–red regions. The scan range was 47 μm × 47 μm, and the step size was 1.0 μm. The white lines in (a) and (b) indicate the position of the cross section. (Adapted with permission from Takahashi, Y., Hirano, Y., Yasukawa, T., Shiku, H., Yamada, H., and Matsue, T., Topographic, electrochemical, and optical images captured using standing approach mode scanning electrochemical/optical microscopy, *Langmuir*, 22, 10299–10306, 2006. Copyright 2006 American Chemical Society.)

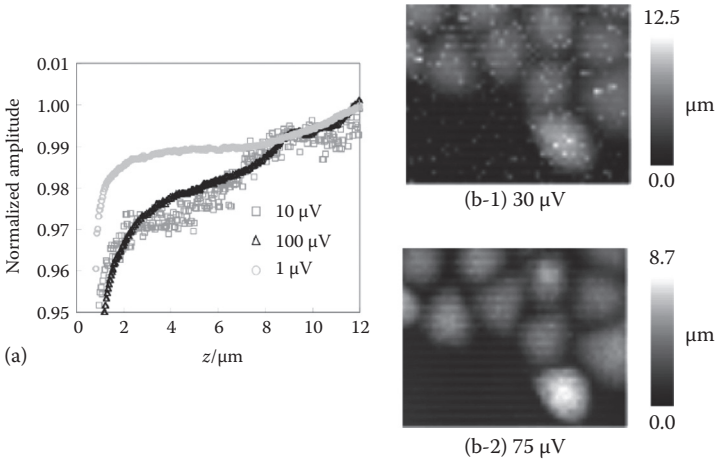


FIGURE 17.28 Imaging live HeLa cells using shear force feedback with a tuning fork transducer. Optimization of tuning fork amplitude for living cell topography imaging. (a) Tuning for amplitude–distance profiles of a living cell. The cells are not detected in the approach curve (the tip probably impales the cells) if the tuning fork amplitude is too high (>100 mV). (b) Topography images of HeLa cells at tuning fork amplitudes of 30 and 75 μV. Noise (white dots in image b-1) appears if a too low tuning fork amplitude is used. The scan range was 100 μm × 80 μm, and the step size was 2.0 μm. (Adapted with permission from Takahashi, Y., Shiku, H., Murata, T., Yasukawa, T., and Matsue, T., Transfected single-cell imaging by scanning electrochemical optical microscopy with shear force feedback regulation, *Anal. Chem*., 81, 9674–9681, 2009. Copyright 2009 American Chemical Society.)

obtain a shear force–sensing device. Sensing is straightforward as it can be performed simply by measuring the voltage at the electrical pins of the tuning fork. However, many parameters, including the immersion depth of the probe and even the amount of glue used to attach the tip, can modify the crystal response, hence care is advised. Moreover, as the shear force signal is only obtained for extremely short tip–substrate distances, of the order of a few tens of nanometers, this translates to very intense tip–substrate interactions. However, researchers, as reviewed earlier, have proposed many alternative strategies to alleviate, if not to solve, these problems.

17.3.2 Intermittent Contact–Scanning Electrochemical Microscopy

One of the most common modes of AFM imaging is tapping mode. Here the probe is oscillated close to resonance, A_o, and then brought into intermittent contact (IC) with the sample resulting in damping of the oscillation amplitude to a value, A [97]. The level of damping (A/A_o) is kept constant and used as the feedback signal to monitor the topography of the surface. The value of A/A_o denotes the hardness of the tap on the surface, with a light tap close to 1 and a hard tap much less than 1. By monitoring the phase, it is also possible to extract information on the material properties of the sample such as elasticity, adhesion, etc.

This general concept has very recently been applied to SECM by Unwin and coworkers to control the tip–substrate separation during imaging [98]. Here, a small AC positional perturbation is made to the piezoelectric positioner controlling the tip position normal to the surface of interest (z-axis). This is especially attractive as it requires minimal additional hardware and is easily implemented. Typically, much lower oscillation frequencies (<100 Hz with the system documented in [98]) are employed than in conventional tapping mode AFM (typically > two orders of magnitude higher). The amplitude of the oscillation is damped as the tip touches the surface. This damping is detected and used to provide information on the point of tip–substrate contact and hence can be used to quantify tip surface separation (e.g., for approach curve measurements). The damping can also be used as a set point to determine the tip–substrate contact point at all (x, y) positions during a scan. IC-SECM differs from the early tip position modulation (TPM) studies of Wipf and Bard [99] in that here a non-electrochemical signal is used to provide the feedback and positioning sensitivity.

Key advantages over shear force are (1) the experimental setup is much simpler, existing traditional glass-coated SECM probes can be utilized, (2) the level of immersion into the fluid of interest does not need to be controlled, and (3) the tip can be operated for imaging at any user-defined tip–substrate separation. During imaging, the tip typically scans across the surface in "tapping mode" recording the topography of the surface. At the same time, it is possible to record the tip current (both mean current and AC current information). Here, it is advantageous if the tip is polished at a slight angle or fortuitously the tip–substrate alignment is not exactly parallel so that direct contact is avoided between the substrate and electrode. This is especially problematic for conducting substrates. The tip can then retrace the topographical line scan for electrochemical imaging at any distance the user so chooses.

Figure 17.29a shows typical approach curves recorded with a 2 μm diameter Pt disk UME toward an insulating and conducting surface. Also, simultaneously recorded is the oscillation amplitude (typically ~40 nm as used in this study). For the studies herein, contact was assumed when there was a greater than 15% sustained decrease in the Z-piezoelectric positioner strain gauge sensor oscillation amplitude, as compared to that in the bulk solution. Figure 17.29b shows a constant distance feedback SECM image (1 μm tip–substrate separation) recorded with a 1 μm radius Pt UME of Au bands 25 μm wide on glass, separated by 20 μm. Future developments will see the use of higher frequency piezoelectric positioners to enable faster imaging and softer tapping.

17.3.3 Alternating Current–Scanning Electrochemical Microscopy

AC-SECM is a specific mode of SECM, which can also be used as an alternative to hybrid SECM techniques to set a constant tip–substrate distance during SECM imaging. The use of AC-SECM as

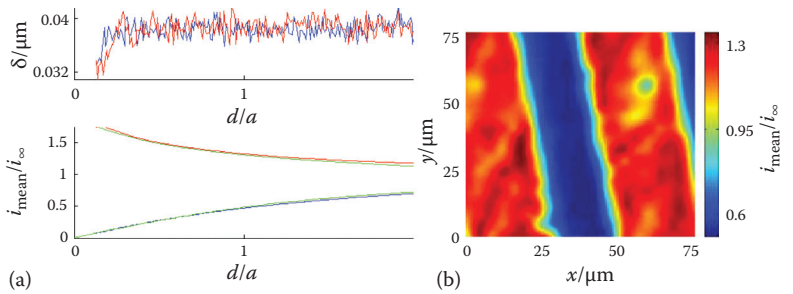


FIGURE 17.29 (a) Feedback approach curves to conducting, gold (red), and nonconducting, glass (blue), substrates. One micrometer radius Pt disk electrode oscillated at 70 Hz, oscillation amplitude 39 nm in 2 mM $FcTMA^+$. Top: SECM tip oscillation amplitude as a function of the tip–substrate separation. Bottom: Mean SECM tip current, i_{mean}, as a function of the tip–substrate separation. The mean SECM current for the analytical approximation for the feedback response is shown in green. There is excellent agreement between the theory and mean experiment at SECM current, for both positive and negative feedback. i_{mean} was normalized by the bulk steady-state SECM tip current. The distance from the substrate, d, was normalized by the SECM tip radius, a. (b) IC-SECM imaging of gold bands on glass obtained using a 1 μm radius Pt disk electrode (70 Hz, oscillation amplitude is 39 nm in 2 mM $FcTMA^+$). Average tip current in IC forward scan. (Adapted from McKelvey, K. et al., *Anal. Chem*., 82, 6334, 2010. With permission.)

a tip-positioning technique was initially introduced by Horrocks et al. [100]. The various applications of this technique were recently reviewed, and are therefore only briefly presented here [101]. In AC-SECM, a low amplitude (~10 mV) alternating potential is superimposed on the tip bias while the ensuing modulation of the tip current is recorded. The current signal is then analyzed in terms of the AC-current magnitude and phase offset with respect to the tip potential excitation signal. Interestingly, no redox mediator is required in solution since it is the local impedance of the tip–sample system which is probed.

In low supporting electrolyte solution (1–10 mM ionic strength), the impedance is dominated by the solution resistance. Both the current and phase have been shown to display a smooth tip–sample distance dependence. For insulating substrates, this dependence originates from hindered ion movement in the tip–substrate gap, which results in a decrease of the AC tip current amplitude as the tip–substrate distance is made smaller, closely following negative feedback behavior. Importantly, it was shown that, if a redox mediator is introduced in solution, the contribution of the faradaic process appears as a DC amperometric signal which can be electronically separated from the high-frequency component of the full impedance signal. Hence for insulating substrates, the AC impedance signal can be used to hold the tip at a constant tip–substrate separation while the DC current, relates to local faradaic processes that can be independently and simultaneously measured [102].

The simplicity of AC-SECM is that it can be implemented using regular disk-in-glass SECM tips, that is, no specific sophisticated tips have to be fabricated. However, a limitation of using AC-SECM as a vertical positioning technique is that it can only be confidently used if the substrate is *homogeneously* insulating. The reason is that the AC signal is also modulated by the local conductivity of the sample surface: a higher AC current is recorded over a conducting surface than over an insulating surface. Hence over conductive surfaces information regarding the topography and the local conductivity of the substrate cannot be separated from simply recording the AC current signal.

However, a notable exception is when the conductive substrate is unbiased: it has been reported that, in such cases, provided a low AC frequency and low supporting electrolyte concentration are used, an AC-SECM feedback signal, similar to the one recorded at insulating surfaces, that is, negative feedback, is obtained [103]. In this particular case, AC-current-based constant distance amperometric SECM imaging can be implemented.

AC-SECM has notably been used for single-cell studies. The specific advantage of AC-SECM for imaging cells is that, as mentioned earlier, no potentially toxic redox mediator has to be added to

the solution. Hence, AC-SECM imaging can be carried out directly in the cell growth media. Baur and Wipf et al. [104] have shown that AC-based feedback can be used for constant impedance (i.e., distance) topography imaging of model neurons PC12 cells (Figure 17.30). The resolution obtained was slightly lower in this AC mode than in amperometric constant current DC mode imaging.

The ability to amperometrically record vesicular release at the tip while using AC-current-based distance feedback was also demonstrated [104]. It was observed that vesicular release did not significantly alter the local impedance (albeit ions were released) meaning constant distance imaging/positioning was unaffected. However, it was observed that the injection of a K^+-containing solution, used to depolarize the cell and trigger vesicular release, did cause a large decrease of the background impedance, thus prohibiting the use of AC-current-based distance regulation *during* application of this stimulus.

It was therefore determined that provided the tip is initially positioned next to a cell, and at such a distance so that it cannot collide with the cell, the distance feedback loop can be disabled, the stimulus applied, and the tip rastered at fixed height above the cell. In such a case, the AC current probes the tip position with respect to the cell, while the amperometric current reveals individual release events (Figure 17.31). Impedance feedback control of the sample–probe separation was also used to position an SECM tip above single cells and monitor amperometrically metabolic cellular consumption [105].

So far, only the use of AC current measurements as a distance regulation mechanism have been considered; however, AC-SECM can also be used in the fixed height mode to image the topography

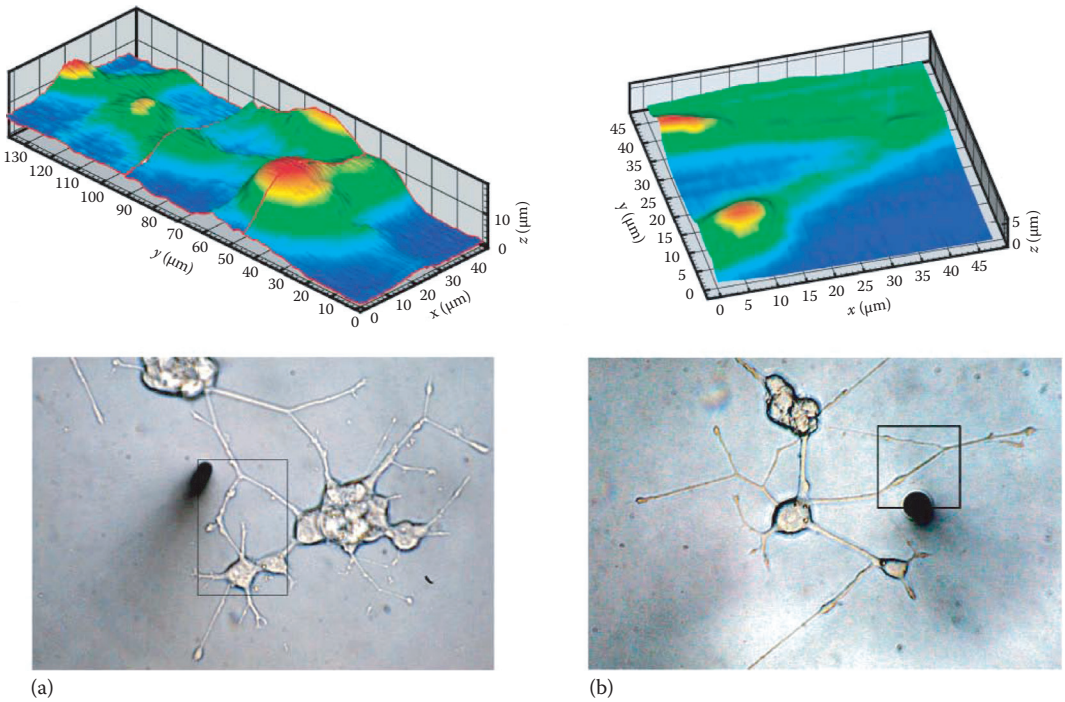


FIGURE 17.30 Topographic images of differentiated PC12 cells (model neurons) acquired using constant impedance imaging (AC-SECM). (a) Mosaic image of several cells joined by neurites recorded in supplemented RPMI 1640 growth media and (b) close-up image of a neurite bifurcation recorded in HBSS (buffer). Conditions: 5 μm diameter carbon fiber electrode, no mediator, and scan rate 7 μm/s. AC signal: 90 kHz and 10 mVpp superimposed onto a 0.75 V (vs. 3 M NaCl Ag/AgCl) DC bias applied to the tip. (Adapted with permission from Kurulugama, R.T., Wipf, D.O., Takacs, S.A., Pongmayteegul, S., Garris, P.A., and Baur, J.E., Scanning electrochemical microscopy of model neurons: constant distance imaging, *Anal. Chem*., 77, 1111–1117, 2005. Copyright 2005 American Chemical Society.)

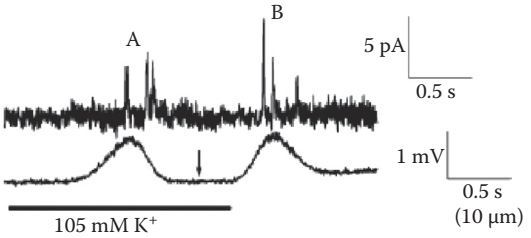


FIGURE 17.31 AC-SECM study of isolated cells. Simultaneous recordings of release by amperometry (upper trace) and cell morphology by tip impedance (lower trace) during a 6-s K^+ stimulus at an undifferentiated PC12 cell. The data were recorded during repeated line scans in the *x*-direction at a constant *y*-location. Arrows denote changes in direction (i.e., forward/reverse) of the *x*-line scan. Conditions: HBSS buffer (no mediator), 5 μm diameter carbon fiber electrode, and scan rate 20 μm/s. AC signal: 90 kHz and 10 mVpp superimposed onto a 0.75 V (vs. 3 M NaCl Ag/AgCl) DC bias applied to the tip. (Adapted with permission from Kurulugama, R.T., Wipf, D.O., Takacs, S.A., Pongmayteegul, S., Garris, P.A., and Baur, J.E., Scanning electrochemical microscopy of model neurons: constant distance imaging, *Anal. Chem*., 77, 1111–1117, 2005. Copyright 2005 American Chemical Society.)

(*or* conductivity) of a sample. For example, it was recently shown that fixed height AC-SECM imaging reveals not only cell topography but also local variations in impedance linked to cell activity, for example, cell wall oscillation or release of metabolites [106]. Fixed height AC-SECM imaging was also used to image the reactivity of composite substrates such as model Pt-microband electrode arrays (25 μm width) [107] and recessed Pt UMEs (cavity electrodes, 60 μm in diameter) [102]. In this latter case, amperometric feedback and AC impedance (electrolyte resistance) images were acquired simultaneously and displayed similar resolution of a few microns.

Further improvements in the resolution of AC-SECM imaging is possible either by varying (increasing) the frequency of the AC voltage applied to the tip [108] or by implementing constant distance mode AC-SECM. This requires coupling AC-SECM with an external distance regulation mechanism such as shear force detection [80,81] or AFM; the latter is illustrated in Figure 17.32 [109,110].

17.4 CAPILLARY-BASED ELECTROCHEMICAL IMAGING PROBES

In addition to SECM-AFM and SECM-STM, researchers have tried to merge other scanned probe techniques with SECM with a view to providing the SECM probe with an independent distance control. Although SECM-AFM is by far the most popular approach, recent work has seen significant research progress on the combination of scanning ion conductance microscopy (SICM) with SECM using glass capillaries as the initial probe structure. Others have employed a solution-filled capillary, scanning micropipette contact method (SMCM), as the electrochemical probe for work on conducting surfaces in air; here, the resolution of the technique is governed primarily by the inner diameter of the capillary. In order to add in a height control mechanism to the capillary, SMCM has been very recently developed further—scanning electrochemical cell microscopy (SECCM)—and is described in detail in Section 17.4.3.

17.4.1 Combined Scanning Electrochemical Microscopy–Scanning Ion Conductance Microscopy

17.4.1.1 Scanning Ion Conductance

The SICM was introduced by Hansma et al. in 1989 [111]. In general, the probe is typically a glass capillary pulled to a fine point, typically with a submicrometer capillary opening, filled with electrolyte solution and into which is placed an Ag/AgCl reference electrode. The probe sits in an

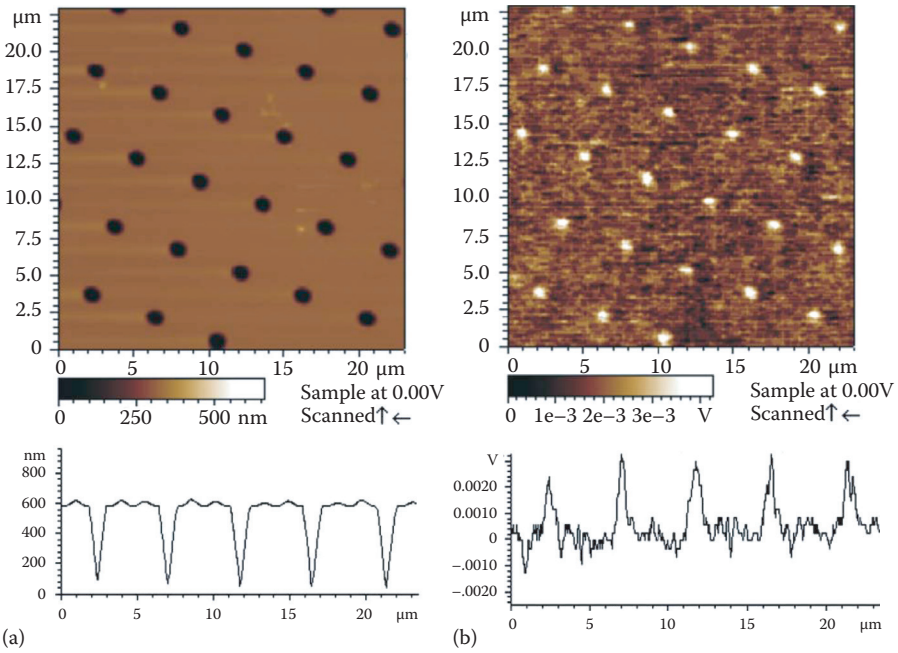


FIGURE 17.32 AC-SECM coupled with AFM. Images of periodically microstructured silicon nitride/gold structure with recessed 1 µm gold spots. (a) topography recorded in contact mode; scanned area: 25×25 µm; scan speed: 0.1 line/s. (b) simultaneously recorded AC-SECM image at 14.92 kHz and 110 mVpp superimposed onto a 100 mV DC bias applied to the tip-integrated WE in 1 mM KCl. (Adapted from *Electrochem. Commun*., 9, Eckhard, K., Shin, H., Mizaikoff, B., Schuhmann, W., and Kranz, C. Alternating current (AC) impedance imaging with combined atomic force scanning electrochemical microscopy (AFM-SECM), 1311–1315, Copyright 2007, with permission from Elsevier B.V.)

electrolyte solution, which contains a second Ag/AgCl reference electrode, close to the substrate of interest. Upon application of a potential bias between the two electrodes, an ion current flows that is incredibly sensitive to the tip–substrate separation, especially at distances less than the radius of the capillary opening [112]. A typical ion current and tip–substrate separation approach curve is shown in Figure 17.33. In this way, by keeping the ion current fixed, that is, constant tip–substrate separation, it is possible to track the topography of the surface, by monitoring the displacement of the piezoelectric positioner as the tip images over the surface. The resolution of the technique is governed by the size of the capillary opening.

Improvement to the imaging capabilities of the technique has been made by using distance-modulated feedback protocols whereby the capillary is vertically oscillated as it approaches the surface [113]. An AC current signal is thus recorded which enables more reliable control over rapid responses to changes in substrate topography. In hopping mode SICM [116], continuous feedback is no longer employed. Instead, the pipette approaches the sample from a starting position above any surface feature. A reference current is recorded in this position with the tip far from the surface and then tip approached until the current is reduced by a predefined amount, ca. 0.25%–1%. This is defined as the height of the sample and the position is recorded from the Z_{piezo}. The tip is then withdrawn and moved laterally to the next imaging point. By continuously updating the reference current with the tip far from the surface, the technique self-adjusts for any drifts in SICM current.

The majority of applications of SICM are based around high-resolution imaging of the topography of soft biological samples in physiological buffers, for example, SICM has been used to image living cell surfaces, such as beating cardiac myocytes [113,115], neurons [116], rat oligodendrocytes

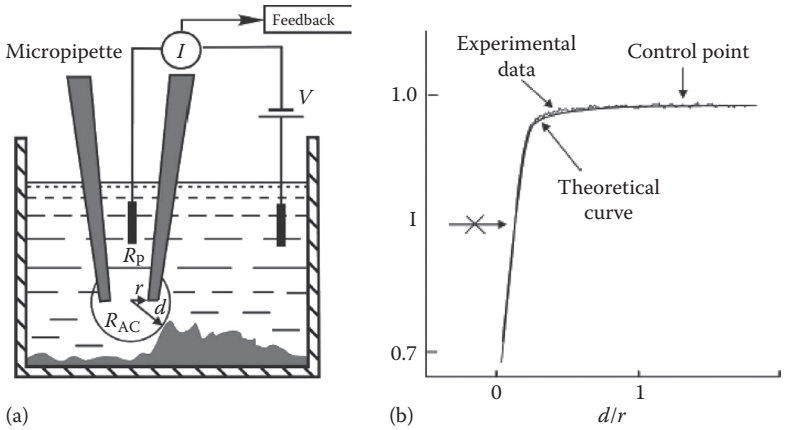


FIGURE 17.33 Diagram of sensing mechanism of the scanning ion conductance microscope. (a) The micropipette tip–surface interaction. The position of the micropipette tip relative to the sample surface strongly influences the access resistance (R_{AC}) and, consequently, the ion current (I) flowing through the pipette. The current value at a distance that exceeds the radius (r) can be used to control the vertical position of the tip to sense neighboring structures that are higher than the vertical sample/probe separation. During the scan, the tip of the pipette, with its "spherical current sensor" of radius, d, "rolls" over surface irregularities of the specimen without damaging it. (b) Comparison of expected and actual values of tip current (I) as a function of the tip–substrate separation. The theoretical curve was calculated for a simplified model of a frustum (truncated cone)-shaped tip of known geometry approaching a flat, nonconductive surface. The experimental data show the approach characteristic of a tip of similar geometry. The vertical arrow indicates the value of current (control point) used for the scanning protocol in the feedback control circuit. (Reproduced from Korchev, Y.E. et al., *Biophys. J.*, 73, 653, 1997.)

[117,118], renal tubular cells [119], stem cells [120], and image proteins in the membranes of living cells [121]. To obtain further information on the system under study, SICM has been combined with scanning confocal microscopy [113,122] and patch clamp technology [115,123].

However, SICM remains insensitive to the electrochemical properties of a surface, as the total ion flow is recorded; thus the technique is not ion specific. SICM is also insensitive to neutral species in solution. By combining the power of SICM with SECM and integrating an electrode component into the SICM probe, it is possible to have a redox signal–independent measure of the surface topography, while recording local substrate electrochemical activity. This is in much the same way the AFM probe provides an independent measure of substrate structure in SECM-AFM. However unlike AFM, the SICM tip never makes contact with the surface so there is no risk of sample mechanical deformation.

17.4.1.2 Different Methods of SECM-SICM Tip Fabrication

To date, at the time of writing this chapter, there have been only two fabrication approaches for the preparation of SICM-SECM tips for dual imaging [124,125]. Both approaches use a traditional SICM glass capillary as the starting structure. In the first, nanopipettes were pulled to produce capillaries with ~100 nm diameter openings and then coated on *one side* with a layer of Au. The pipette was then insulated using a 70–100 nm layer coating of aluminum oxide. Finally to reveal the gold electrode and expose an open nanopipette, the end of the capillary was milled using FIB. An example of an SECM-SICM nanopipette produced this way is shown in Figure 17.34a; here the electrode is a half ring. In the second methodology, the pulled pipette was fully coated with a layer of Au and then insulated using an anodic electrophoretic paint. To expose the aperture and reveal the electrode, FIB was again employed. Figure 17.34b shows the SECM-SICM probe produced; here the electrode is a full ring. For both approaches for the insulators employed, it was not possible to produce a defect-free coating.

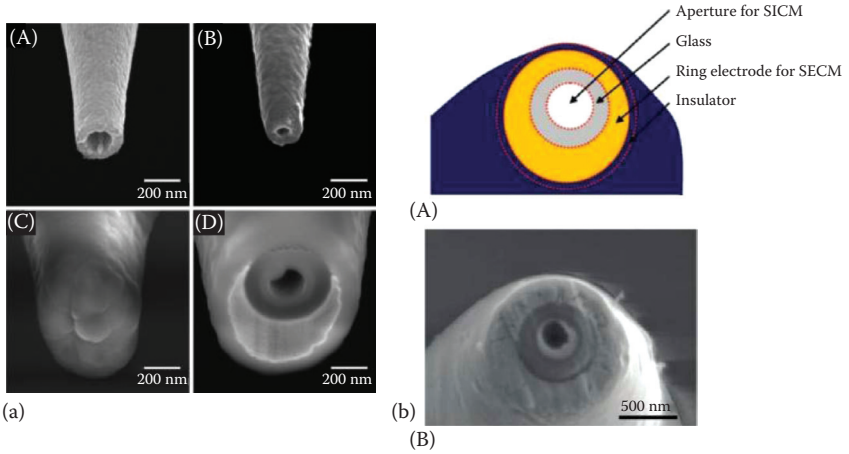


FIGURE 17.34 (a) SEM images of the SECM-SICM nanopipette throughout the fabrication process: (A) as-pulled borosilicate nanopipette with 30 nm AuPd film to minimize charging, (B) after evaporation of the gold electrode film with titanium adhesion layer, (C) after ALD of 100 nm thick Al_2O_3 with occluded nanopipette tip, and (D) after FIB milling to expose the gold and open the nanopipette tip. (Reproduced from Comstock, D.J. et al., *Anal. Chem*., 82, 1270, 2010.) (b) (A) SEM micrographs of the SECM-SICM probe. (B) Schematic illustration of probe structure. (Reproduced from Takahashi, Y. et al., *J. Am. Chem. Soc*., 132, 10118, 2010.)

17.4.1.3 Imaging Applications of SECM-SICM

With the first approach, the performance of the combined SECM-SICM was evaluated by imaging the topography, acquired using the SICM component of the SECM-SICM probe in AC mode (50 nm rms and 570 Hz oscillation frequency) and redox activity, acquired using the SECM electrode, of 400 nm wide trenches milled into a thin gold film on glass [124]. Due to the asymmetric nature of the probe (i.e., the electrode is on one side only), the topography images were offset by a defined distance from the images of redox activity. Typical feedback mode SECM-SICM images of the gold–glass structures are shown in Figure 17.35a.

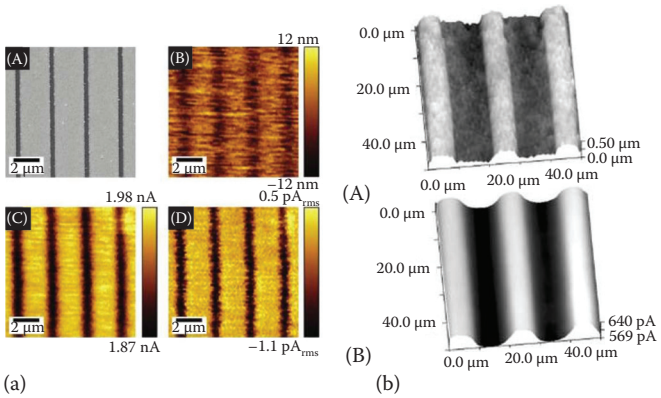


FIGURE 17.35 (a) SEM and feedback mode SECM-SICM images of 400 nm wide trenches FIB-milled into a gold film on a glass substrate; SECM-SICM images were acquired in 10 mM $Ru(NH_3)_6CI_3$, 100 mM KNO_3 solution: (A) SEM, (B) SECM-SICM topography, (C) SECM-SICM DC redox current, and (D) SECM-SICM AC redox current. (Reproduced from Comstock, D.J. et al., *Anal. Chem*., 82, 1270, 2010.) (b) (A) Topographic and (B) electrochemical images of a Pt band microarray in 0.50 mM $FcCH_2OH$ + 0.1 M KCl. The SECM nanoring and SICM nanopipette electrodes were held at 500 and 300 mV vs. Ag/AgCl, respectively. (Reproduced from Takahashi, Y. et al., *J. Am. Chem. Soc*., 132, 10118, 2010.)

Full ring electrode SECM-SICM probes were employed to image the topography and electrochemical activity of a Pt-interdigitated array (IDA) electrode as shown in Figure 17.35b [125]. Using the SICM response, recorded in hopping mode, the tip was maintained at a separation of 300 nm from the surface at all times while the electrochemical feedback current was recorded. With the probe dimensions employed, it was possible to measure the height of the Pt band ~100 nm.

These probes were used in further application studies. The redox enzymatic activity of enzyme spots was interrogated. Enzyme spotting is popular in protein microarray technologies but can produce an inhomogeneous distribution of the enzyme across the surface. Using the SECM-SICM probe, it was possible to visualize these heterogeneities. In particular, both glucose oxidase (GOx) and horse radius peroxidase redox-active enzymes were employed in the presence of glucose and H_2O_2, respectively. For GOD, glucose is turned over at the GOD leaving the GOD in a reduced state. $FcCH_2OH^+$ generated from $FcCH_2OH$, at the SECM component of the SECM-SICM electrode, is converted back to $FcCH_2OH$ in regions of the surface where the GOD is present. Thus high regions of SECM current are associated with high enzyme activity areas.

The tip–substrate separation was maintained fixed using hopping mode SICM; in this way, it was also possible to monitor the topography of the image simultaneously. Topography and electrochemical activity images of immobilized GOD are shown in Figure 17.36. At the edges of the drop, the immobilized enzyme shows a ring-like structure due to enzyme accumulation; this correlates with the images of electroactivity [125]. As expected, increasing the tip–substrate separation during imaging resulted in a decrease in the sensitivity of the redox tip current to the enzymatic surface reaction.

SECM-SICM has also been used to explore the permeation property of a cell membrane, in particular that of a cardiac myocyte [125]. Using hopping mode SICM, it was possible to record the topography of an individual heart cell, which was revealed to exceed 20 μm in height. Current profiles were recorded for oxygen, $Fe(CN)_6^{4-}$, and $FcCH_2OH$ as the SECM-SICM probe approached the cell surface. The probe was then moved laterally to the next position in the line scan and the

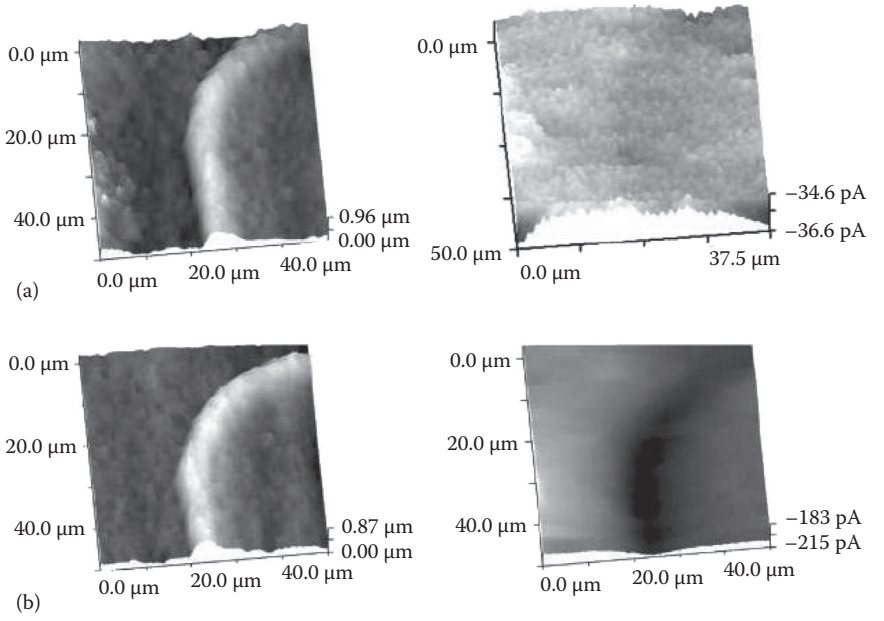


FIGURE 17.36 Topographic (left) and electrochemical (right) images of a portion of the HRP spot immobilized on a glass substrate (a) before and (b) after adding 0.50 mM H_2O_2 in 0.50 mM $FcCH_2OH$ and PBS. The SECM nanoring and SICM nanopipette electrodes were held at 50 and 300 mV vs. Ag/AgCl, respectively. Scan ranges were 50 μm × 50 μm. (Reproduced from Takahashi, Y. et al., *J. Am. Chem. Soc.*, 132, 10118, 2010.)

approach curve measurement repeated until the probe had moved across the surface of the cell. Both oxygen and $FcCH_2OH$ were shown to be permeable to the cell membrane.

17.4.2 Scanning Micropipette Contact Method

In the scanning micropipette contact method (SMCM), a fine capillary is used as the imaging probe; however, unlike SICM, it is only the capillary that is filled with solution, the sample remains in air. For this technique, it is essential that the sample is conducting or semiconducting. A reference electrode is placed into the capillary and a potential is applied between this and the working electrode, the substrate. The applied potential is sufficient such that a measurable current will flow upon contact of the meniscus which forms at the end of the capillary with the electrode surface. Once contact has been made, the probe is held in position for a defined period of time to enable the appropriate electrochemical measurement to be carried out. The probe is then retracted from the surface and moved to a new position and approached again, in the *z*-direction, until meniscus contact is made. In this way, an electrochemical image of the surface can be produced, with a resolution governed by the size of the capillary, typically here between 300 nm and 1 μm [126].

This work significantly advances on initial work in this area, using capillaries 1–1000 μm in diameter [127–129], which focused on making individual measurements at specific surface locations, in particular, for applications in corrosion science. In these studies, the end of the capillary in contact with the working electrode was typically sealed in silicon rubber, to prevent leaking of electrolyte. The technique was subsequently developed by the introduction of a method to regulate the tip–substrate separation [130]. Here the substrate was oscillated and changes in the resonant frequency shift or amplitude of oscillation as the tip approaches the surface were measured. Thus by maintaining a constant amplitude damping or resonant frequency phase shift, it was possible to control the distance of the tip from the surface. However, no imaging applications were presented.

Typically with the SMCM, imaging measurements are carried out in a controlled humidity environment to prevent evaporation from the capillary meniscus. A typical image of a pulled capillary in contact with an electrode surface is shown in Figure 17.37a. The technique was employed to address two scientific issues: the redox activity of the basal plane of HOPG and the corrosion activity of the surface of an aluminum alloy (AA1050). In the former, for the HOPG samples employed, no apparent variations in the electroactivity of the surface were observed. Given the size of the capillary employed, which was smaller than the step separation on the surface of HOPG, the data implied that basal plane areas on the surface were not as inactive as earlier, although differently sourced HOPG samples were employed compared with earlier studies. Both electrochemical images and point-by-point CV measurements were recorded.

Figure 17.37b shows a typical field emission–scanning electron micrograph (FE-SEM) of an AA1050 alloy and the SMCM image of that alloy using the redox mediator $Fe(CN)_6^{3-}$ to identify sites that are cathodically active. In the SMCM scan, one distinctive region of electroactivity is observed which is on the correct length scale for the intermetallic features observed in the FE-SEM image.

17.4.3 Scanning Electrochemical Cell Microscopy

SECCM significantly advances SMCM by building in a feedback control into the capillary design such that it is possible to much more accurately control the point of tip–substrate contact in addition to enhancing the capabilities of the technique [131]. The probe consists of a tapered theta pipette, at present ~1 μm inner diameter, filled with the electrolyte solution of interest. Into each channel of the pipette is placed a Ag/AgCl wire reference electrode, as shown schematically in Figure 17.38a. A meniscus protrudes from the end of the capillary. The probe is subject to a gentle oscillation (~50 nm amplitude at 70 Hz) and the AC and DC currents flowing between the two channels are measured. Both currents remain constant with the tip away from the surface. However, upon contact of the meniscus with the substrate, the meniscus deforms, which is reflected in a change in both

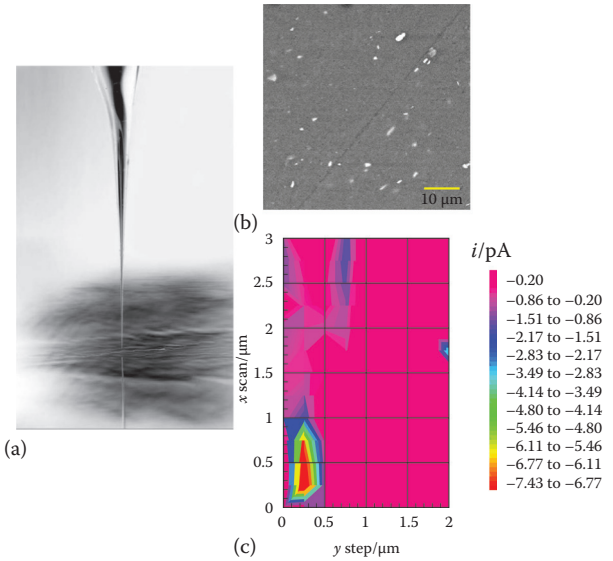


FIGURE 17.37 (a) Optical image of a 300 nm (i.d.) micropipette approaching an HOPG surface. (b) FE-SEM image of an AA1050 alloy surface and (c) a SMCM image of the alloy, obtained using a 300 nm diameter micropipette containing 2 mM $Fe(CN_6)^{3-}$ and 0.1 M KNO_3. The substrate potential was held at a value to effect the diffusion-limited reduction of ferricyanide. (Reproduced from Williams, C.G. et al., *Anal. Chem*., 81, 2486, 2009.)

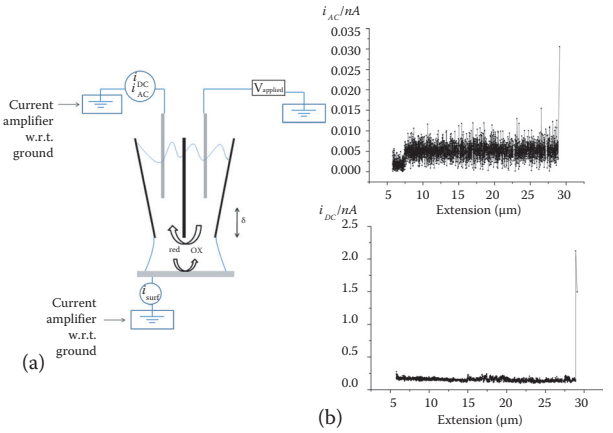


FIGURE 17.38 (a) Schematic (not to scale) of the theta pipette system that serves as a localized conductivity cell (measurement of i_{DC} and i_{AC}) and for conducting/semiconducting surfaces as a local dynamic electrochemical cell (i_{surf}). (b) Typical pipette approach data showing i_{AC} (top) and i_{AC} (bottom) as a theta pipette was translated toward a glass surface, until surface contact was made. A bias of 500 mV was applied with 20 mM KCl in the pipette. (Reproduced from Ebejer, N. et al., *Anal. Chem*., 82, 9141, 2010.)

DC, i_{DC}, and AC, i_{AC}, current, as shown in Figure 17.38b. Thus in this technique, the i_{AC} is utilized as a set point to determine contact with the surface while i_{DC} can provide information on substrate properties. In this way, the technique can be employed to image nonconducting surfaces, which is a limitation of SMCM. The feedback control also enables information on substrate topography to be elucidated.

In variations of the technique, i_{DC} can be measured between one of the channels of the capillary and the substrate itself thus providing information on the local conductance properties of the

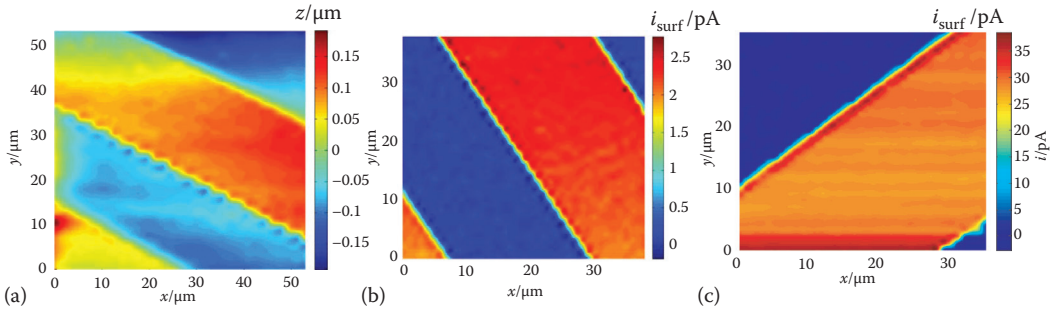


FIGURE 17.39 (a) SECCM images of gold bands on glass, plane fitted topographical data. (b) Surface current maps of the gold band structure. (b) 20 mM KCl and (c) 2 mM $FcTMA^+$, 20 mM KCl. The substrate was at an electrode potential of +500 mV with respect to the Ag/AgCl quasi-reference electrode. (Reproduced from Ebejer, N. et al., *Anal. Chem*., 82, 9141, 2010.)

substrate such as double-layer charging. By adding a redox species to solution, it is also possible to probe the redox activity of a substrate as with conventional SECM. Importantly, the feedback control of the system enables significantly faster imaging and far superior control over tip–substrate interaction thus providing a more stable imaging system.

Figure 17.39 shows SECCM maps of a surface containing Au bands (25 μm wide) separated by 20 μm, on glass. In the first image (Figure 17.39a), the topography of the sample is obtained. It is clear that the sample is sloping by ca. 2°. However, even with this tilt gold bands 200 nm high are revealed. Figure 17.39b shows the same Au band structure but this time recording the current that flows when a bias is applied between the substrate and one of the reference electrodes in the theta capillary (containing 20 mM KCl only). Obviously in the region of the glass no current flows. Finally, Figure 17.39c is recorded in the presence of redox mediator ($FcTMA^+$) in the pipette. Here a potential was applied sufficient to turn over $FcTMA^+$ at the gold band surface.

At the time of writing, there is only one paper related to this new imaging technique [131]. However, given the versatility of the methodology and applicability to many different sample substrates both conducting and insulating, coupled with the ability to examine surface conductivity, substrate redox activity, challenge the surface locally with different electrolyte compositions, for example, to probe dissolution/growth processes, many more are expected. Finally, the use of probes such as SECCM and SMCM has one significant advantage over SECM measurement carried out in solution; provided the correct sized capillary is employed, closely spaced reactive sites can be resolved readily due to diffusional overlap no longer being an issue.

17.5 COMBINATION OF SECM WITH OPTICAL AND SPECTROSCOPIC TECHNIQUES

17.5.1 Scanning Electrochemical Microscopy–Photoelectrochemical Microscopy

Coupling of SECM with photoelectrochemical microscopy (PECM) was originally described by Smyrl et al. [132,133] and given the abbreviation SPECM. Scanning PEM is a surface characterization technique that involves rastering a small spot of light across a surface while recording the total electrochemical current from the entire sample. The light spot, which is the effective local probe, is either focused laser light or light passed down an optical fiber. PEM is typically used to characterize semiconducting surfaces; the light spot produces a photocurrent by driving locally an electro-assisted reaction at the surface. The photocurrent is plotted as a function of spot position to create a map of the electronic properties of the semiconducting surface.

To combine PEM with SECM, a combined probe needs to be fabricated, which can serve as both a SECM tip electrode and a light source. This is typically achieved by coating an optical fiber with a

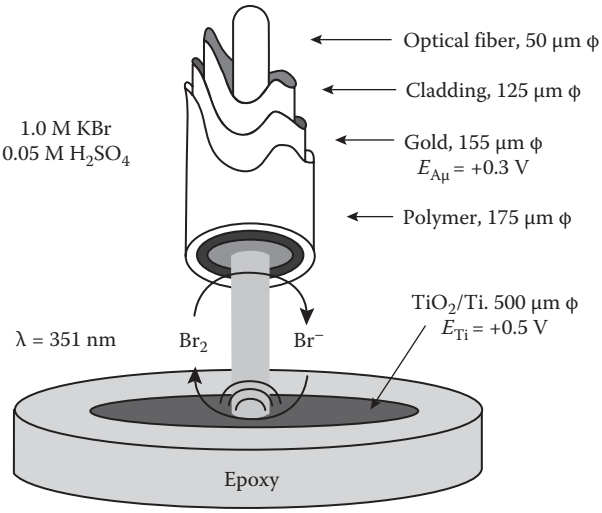


FIGURE 17.40 Working principle of SPECM. A combined optical fiber/microelectrode probe excites photoreactions on a substrate (here oxidation of Br^-) and also detects photoproducts amperometrically (hereby reducing the photogenerated Br_2). (Adapted from Casillas, N. et al., *J. Electrochem. Soc*., 142, L16, 1995. With permission. Copyright 1995 Electrochemical Society.)

gold layer which is subsequently insulated. Exposing the end of the modified fiber yields a gold ring electrode surrounding the fiber core. By recording the tip current (SECM), additional information regarding the local light-triggered photoelectrochemical reactions at the substrate can be obtained. For example, the tip can be used as a collector to detect and identify products from the local surface reaction (Figure 17.40).

In the original paper from Smyrl's group [132,133], a combined SECM-PEM tip probe was fabricated from a standard 50 μm diameter quartz optical fiber (125 μm cladding), which was coated with 15 μm gold and insulated by a 10 μm thick polyimide layer. The fiber was cleaved and polished. The outer diameter of the overall cylindrical combined probe was thus quite large (175 μm); the external and internal diameters of the ring microelectrode were 155 and 140 μm, respectively. The probe was positioned ~40 μm above a Ti/TiO_2 substrate surface and rastered in constant height mode in a Br^--containing solution. Illumination of the TiO_2/Ti substrate by a 351 nm laser light guided through the fiber microelectrode initiated the local photooxidation of Br^- at the surface. The produced Br_2 was collected at the gold ring electrode and reduced back to Br^- (Figure 17.40). Simultaneously acquired tip current (SECM) and substrate current (PEM) images allowed pitting precursor sites, a few tens of microns in size, to be identified on the Ti/TiO_2 surface.

In order to increase the resolution of SPECM, Smyrl's group reported a technique to prepare micron-sized SPECM probes [134]. This involved chemically etching the optical fiber in dilute HF solutions to form a cone-shaped apex ~1 μm in size. The etched fiber was sputter-coated with a ~1 μm thick layer of gold and insulated with varnish. The disk-shaped gold ring electrode surrounding the fiber core was exposed by polishing. The final tip diameter of the gold probe, 3–5 μm, was very substantially reduced compared to previous work. Even though electrochemical characterization of the probes revealed imperfect insulation, these probes were successfully used for PEM and SECM imaging of a titanium surface. Since these initial reports SPECM has been used by several groups to gain insights into the mechanism of corrosion of metals and alloys [67,135].

More recently, Bard's group reported the use of SPECM for rapid screening of photocatalysts [136,137] (Chapter 16). Here, photocatalysts with different compositions were deposited as ~300 μm spots on a conducting glass substrate. Typically, these spots consisted of iron oxide doped with

various metals (Ag, Pd, Eu, Rb). Under illumination, the anodically biased spots catalyzed the oxidation of water (1 M OH^-). In PEM mode, a fiber optic was scanned over the substrate and the performance of the spots could be evaluated by measuring the photocurrent at the substrate. In a SPECM configuration, the product of water photooxidation (O_2) was also detected at the combined optical fiber/ring electrode probe. For both configurations, fixed height mode was used (~50 μm) and the combined probes were unsharpened optical fibers. Due to the large number of spots that could be deposited and analyzed, this methodology constitutes an effective way to quickly identify metallic combinations that yield high photocatalytic effects.

17.5.2 Scanning Electrochemical Microscopy–Scanning Optical Microscopy

The idea behind combining SECM with scanning optical microscopy (OM) is to be able to simultaneously probe the local electrochemical and the optical properties of interfaces at high spatial resolution. To accomplish SECM-OM, a combined probe that can serve as a light source and as a microelectrode is required. To build an optical image, light transmitted through the substrate has to be detected, using, for example, a photomultiplier tube (PMT) placed under the substrate (Figure 17.41a). Optical fiber/ring microelectrode combined probes, initially designed for SPECM [132] (Section 17.5.1), are also suitable for SECM-OM, as shown in Figure 17.41b.

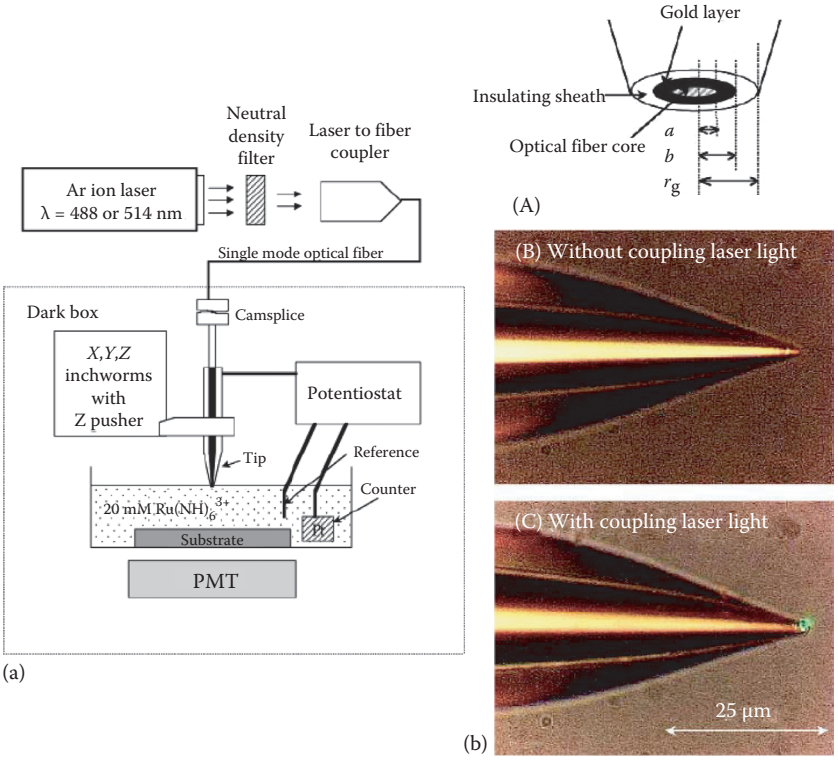


FIGURE 17.41 (a) Block diagram of an experimental setup for combined scanning electrochemical and optical microscopy (SECM-OM). A photomultiplier tube (PMT) is positioned below the (partly transparent) substrate. (b) (A) Schematic diagram of an ideal optical fiber/microelectrode tip for SECM-OM. A sharpened optical fiber bearing a ring-shaped microelectrode at its apex. Optical microscopy images of an anodic paint insulated combined SECM-OM tip (B) without and (C) with coupling of Ar ion laser light at 514 nm. (Reproduced with permission from Lee, Y. and Bard, A.J., Fabrication and characterization of probes for combined scanning electrochemical/optical microscopy experiments, *Anal. Chem.*, 74, 3626–3633, 2002. Copyright 2002 American Chemical Society.)

In developing SECM-OM, the aim is to achieve <100 nm resolution (as with NSOM) and thus ultrasmall SECM-OM probes are required. Lee and Bard reported the fabrication of a combined probe with ring electrodes <1 μm in diameter (Figure 17.41b and c) [138]. The procedure involved (1) heating and pulling optical fibers using a laser puller, so that pulled fibers with a sharp conical apex were produced. (2) Vacuum evaporating a thin gold film on the pulled fiber (~50–100 nm gold). (3) Insulating the whole coated fiber body by electrophoretic deposition of an anodic paint, followed by heat curing at 150°C. The insulating layer shrinks during this last heating step so that the sharp gold-coated extremity of the tip is selectively exposed, while the rest of the tip surface remains insulated. These combined probes were thoroughly characterized by CV and by recording SECM approach curves at both conducting and insulating surfaces. The voltammetric response of these probes was shown to be ideal, while SECM approach curves confirmed the ring shape of the gold microelectrode and allowed the outer and inner radii of the ring to be measured.

The imaging capability of the SECM-OM probes was tested using an IDA electrode that contained 30 μm gold bands spaced by 25 μm glass gaps. The solution contained 20 mM $Ru(NH_3)_6^{3+}$ as redox mediator in 0.1 M aqueous KCl. The SECM-OM fiber probe was approached toward the IDA substrate until an SECM feedback current was recorded corresponding to a tip–substrate separation of ~1 μm. Imaging was carried out in the fixed height mode.

An SECM electrochemical image and an optical image, obtained by plotting the intensity of the light transmitted through the IDA as a function of the probe position, were simultaneously recorded (Figure 17.42). As expected, positive and negative SECM feedback responses were recorded, respectively, when the tip was above a gold band or the glass interband spacing. The optical image correlated well with the SECM feedback image, showing dark and white areas, respectively, for the gold (opaque) and glass (transparent) bands. Hence, the principle of acquiring SECM-OM images of microstructures was validated. Even though the width of the gold bands and glass spacing measured from the optical image matched relatively well with the actual IDA dimensions, the achieved spatial resolution was limited by the use of fixed height imaging.

In order to increase the imaging resolution, Bard and coworkers later modified their SECM-OM setup to add a shear force–based distance-regulating mechanism, enabling constant distance imaging [91], as discussed in Section 17.3.1.2. Three images were simultaneously obtained by plotting

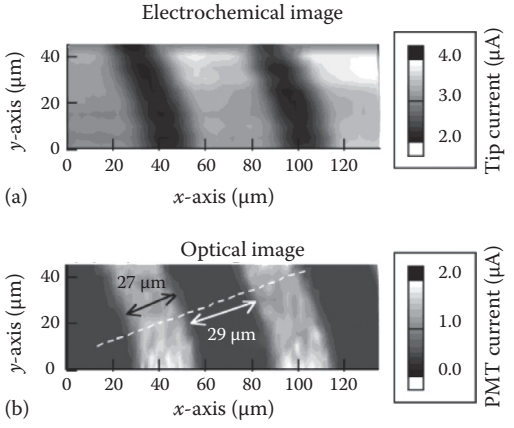


FIGURE 17.42 SECM–optical microscopy images of band microelectrodes (IDA electrode) acquired using an optical fiber/microelectrode tip in the fixed height mode. Simultaneously obtained (a) electrochemical and (b) optical images ($d = 1$ μm over the bands). Scan speed was 1 μm/s. Fiber apex (r_g) = 1.75 μm. (Reproduced with permission from Lee, Y. and Bard, A.J., Fabrication and characterization of probes for combined scanning electrochemical/optical microscopy experiments, *Anal. Chem.*, 74, 3626–3633, 2002. Copyright 2002 American Chemical Society.)

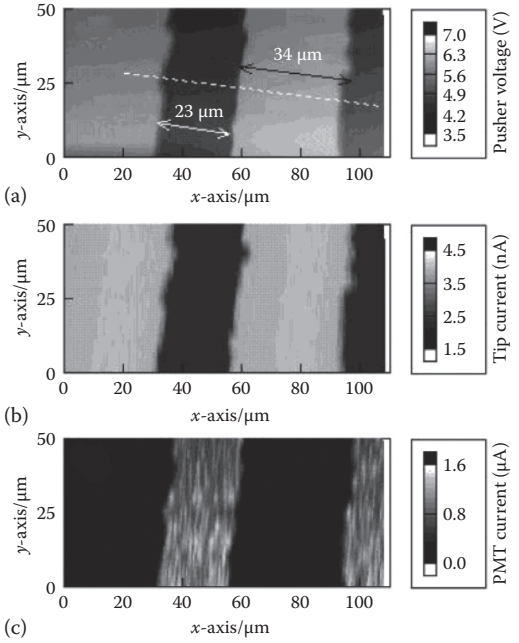


FIGURE 17.43 SECM–optical microscopy images of band microelectrodes (IDA electrode) acquired using an optical fiber/microelectrode tip in the constant distance mode. Constant distance was maintained using shear force feedback. Simultaneously obtained (a) topographic, (b) electrochemical, and (c) optical images over an IDA electrode: 30 μm gold bands spaced by 25 μm glass. Fiber apex (r_g) = 1.75 μm. Scan speed was 1 μm/s; 5 mV pusher voltage corresponds to 8 nm of distance change. (Reproduced with permission from Lee, Y., Ding, Z., and Bard, A.J., Combined electrochemical/optical microscopy with shear force and current feedback, *Anal. Chem*., 74, 3634–3643, 2002. Copyright 2002 American Chemical Society.)

the following recorded data as a function of tip position, as shown in Figure 17.43: (1) The voltage applied to the piezoelectric pusher to bring the tip in "contact" with the surface, that is, enabling a topography image to be constructed. (2) The tip SECM current image, providing a map of the electrochemical reactivity of the substrate, free from any topography artifacts. (3) Light intensity data providing a map of the optical properties of the substrate.

This SECM-OM imaging technique was validated by acquiring simultaneously high-resolution topography, electrochemical, and optical images of an IDA structure (30 μm wide gold bands separated by 25 μm wide glass gaps). It was observed that softer samples, such as diatoms immobilized on glass, could not be imaged using the reported tapping mode–like scanning mode, attributed to the strong interaction forces occurring between the vibrating tip and the diatoms. As an alternative to the tuning fork signal, the SECM feedback current was used to regulate the tip–sample separation, that is, imaging was carried out in constant current mode. Since SECM is a noncontact mode of imaging, deformation of the cell by the tip was fully avoided and simultaneous topography and optical images of live diatoms could be obtained.

An SECM-OM setup specifically designed to allow imaging of biological material was later developed in Matsue's group [93]. The combined optical fiber–microelectrode probes were based on laser-pulled fibers, coated with Ti/Pt by sputtering and subsequently insulated with a 900 nm thick layer of vapor-deposited Parylene C. The electroactive area of the probe was created by blowing hot air (450°C) vertically toward the probe apex using a heat gun. The radius of curvature of the probe including the insulator was ca. 250 nm. The precise shape of the electroactive area of the probe could not be determined, but an electrochemical apparent radius of ~35 nm was determined from recording CVs at the probe. Combined SECM-OM constant distance images were acquired using shear force distance feedback.

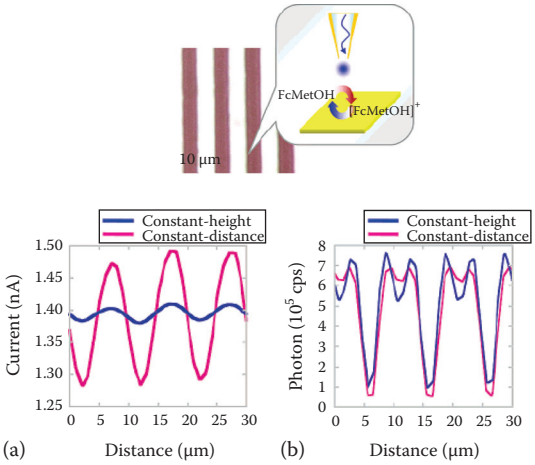


FIGURE 17.44 Comparison of the resolution achieved in constant height vs. constant distance SECM-OM imaging of an Au band array. (a) Current and (b) optical line scans recorded in constant height (blue traces) or constant distance (STA) mode (pink traces). The approximate size of the optical fiber microelectrode probe was 6.5 µm. Probe potential of +0.50 V (vs. Ag/AgCl) in 0.5 mM FcMetOH, 0.1 M KCl. (Adapted with permission from Takahashi, Y., Hirano, Y., Yasukawa, T., Shiku, H., Yamada, H., and Matsue, T., Topographic, electrochemical, and optical images captured using standing approach mode scanning electrochemical/optical microscopy, *Langmuir*, 22, 10299–10306, 2006. Copyright 2006 American Chemical Society.)

Similar to Bard and coworkers approach [90], the probe was initially brought in close "contact" with the substrate, using damping of the shear force oscillation to sense the surface, and retracted before electrochemical or optical data were acquired. This mode was labeled STA for standing approach mode, as discussed in Section 17.3.1.2. The possibility of acquiring topography images of live cells in STA mode using a glass fiber was also demonstrated, indicating that with the reported shear force–based step up destructive tip–cell surface interactions were minimal. Finally, in a fully integrated configuration, simultaneous topography, electrochemical, and optical images of an IDA structure composed of alternating gold bands and glass gaps each 5 µm wide were acquired (Figure 17.44).

More recently, Matsue's group described an improved SECM-OM setup allowing the simultaneous capture of electrochemical, fluorescent, and topography images of immobilized cells [94]. The authors improved their probe fabrication technique by using an ion beam to mill the apex of the probe to expose a better-defined submicron-sized electroactive ring-shaped area. This also had the effect of giving the tip apex a flat disk-like shape, thus increasing the SECM feedback sensitivity of the probe. The shear force distance regulation was also optimized. In particular, the effect of the tuning fork–free excitation amplitude on the tip–cell wall interaction was studied. It was shown that, provided a low enough tuning fork amplitude was used, shear force regulation could be safely employed to image living cells (Figure 17.28). Constant distance imaging was carried out in STA mode [92].

Simultaneous topography and fluorescent images of cells expressing the green fluorescent protein (GFP) were demonstrated. Simultaneous detection of topography, fluorescence, and electrochemical activity was also demonstrated by imaging cells expressing both GFP and secreting alkaline phosphatase (Figure 17.45). The enzyme substrate, *p*-aminophenol phosphate (PAPP), was added into the medium. Phosphatase liberated by the cell catalyzed the conversion of PAPP into *p*-aminophenol, which was detected amperometrically (oxidized) at the tip. Hence, in this work, two proteins reporting gene cellular expression were simultaneously detected at the single-cell level using SECM-OM.

Further improvement in SECM-OM includes optimizing the combined probe fabrication technique to yield probes of nanometer dimensions. This would improve the spatial resolution of SECM-OM and ultimately lead to NSOM-SECM. In this respect, it is noted that the fabrication

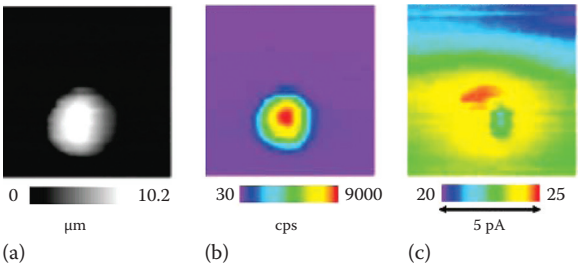


FIGURE 17.45 (a) Simultaneous topographic, (b) fluorescent, and (c) electrochemical images of a GFP (green fluorescent protein)—and SEAP (secreted alkaline phosphatase)—transfected single HeLa cell obtained in the constant distance mode. The cell both expresses GFP and excretes the enzyme alkaline phosphatase. The combined SECM-OM tip, an optical fiber bearing a ring-shaped microelectrode at its apex, excites the fluorescence of GFP and collects the electroactive enzymatic product (*p*-aminophenol). A tuning fork is used as a shear force transducer. The scan rate was 3 μm/s. The scan range was 40 μm × 40 μm, and the step size was 1.0 μm. (Adapted with permission from Takahashi, Y., Shiku, H., Murata, T., Yasukawa, T., and Matsue, T., Transfected single-cell imaging by scanning electrochemical optical microscopy with shear force feedback regulation, *Anal. Chem*., 81, 9674–9681, 2009. Copyright 2009 American Chemical Society.)

of nanometer-sized optical fiber electrode based on selective etching of fibers has already been reported [139].

17.5.3 Scanning Electrochemical Microscopy–Electrogenerated Chemiluminescence

17.5.3.1 Using the SECM Tip as a Light Source for Scanning Optical Microscopy

One motivation for coupling SECM with ECL is to be able to use the SECM tip as a controllable light source that locally illuminates the sample surface. To achieve this, the tip is biased so as to trigger an electrochemical reaction that produces light by chemiluminescence. The sample surface has to be at least partly transparent and the emitted light is collected by a PMT tube located below the substrate. The ECL intensity measured by the PMT can then be plotted as a function of the tip position to form an image that reflects the local optical properties of the substrate, for example, its absorbance. The setup is similar to the one used for SECM-OM described earlier in Section 17.5.2.

One of the interests of using an SECM tip instead of a metal-coated fiber-optic probe as a light source is that preparation of the SECM tip is comparatively easier. Additionally, no laser is needed to illuminate the tip apex which avoids heating of the sample or tip. Moreover, the SECM tip current can provide feedback for positioning the light source in close proximity to the substrate surface. The first description of SECM-ECL in a scanning optical microscopy configuration was reported by Bard et al. [140]. In this pioneering work, the choice of the tip-triggered ECL reaction was discussed together with the effect of tip–substrate distance on light emission.

Two kinds of ECL-generating reactions were considered. The first one involved the annihilation of $Ru(bpy)_3^{3+}$ and $Ru(bpy)_3^{+}$ sequentially generated at the tip from the solution species $Ru(bpy)_3^{2+}$, by applying potential pulses (between +1.6 and −1.4 V vs. SCE). The tip-generated $Ru(bpy)_3^{3+}$ and $Ru(bpy)_3^{+}$ species encounter in a reaction zone located close to the surface of the tip electrode. A high-energy electron transfer process takes place between these species, generating the excited species $Ru(bpy)_3^{2+*}$, which emits light upon deactivation. Due to the large tip potentials applied, a nonaqueous solvent, such as acetonitrile, is required.

When the tip was approached toward an insulator, the ECL intensity was observed to be steady until the tip was within a few tenths of the tip radius away. A sharp drop of the ECL intensity was recorded upon closer approach due to hindered diffusion of the ruthenium species in the tip–substrate gap. When the tip was approached toward a conducting substrate, the ECL intensity was

shown to again remain nearly steady until the tip–substrate separation distance was ~0.3 times the tip radius. For such a close tip–substrate separation, electron transfer at the conducting substrate competes with the annihilation reaction and limits the ECL intensity. However, the tip could be brought close enough to a test IDA substrate for a scanning optical image to be acquired. The resolution was limited to the micron range due to the relatively large tip size and tip–substrate spacing; ~5 μm disk-in-glass tip held at a constant height of 25 μm over the substrate.

The possibility of generating ECL from the co-oxidation of $Ru(bpy)_3^{2+}$ and tri-*n*-propylamine (TPrA) for combined SECM-ECL was also investigated. In this coreactant ECL scheme, the tip potential is set at a sufficiently anodic potential to oxidize both $Ru(bpy)_3^{2+}$ and TPrA. The ensuing reduction of the $Ru(bpy)_3^{2+/3+}$ species by the highly reductive radical species produced by TPrA oxidation ultimately results in the formation of the light-emitting $Ru(bpy)_2^{2+*}$ species [141]. Compared to the annihilation reaction [140], this ECL reaction has the advantage of not requiring pulsing of the tip potential. Moreover, the ECL reaction takes place in a very thin reaction layer around the tip surface and is not broadened by diffusion of the reactants away from the tip. This also allows for very close tip–sample separations without interference from SECM feedback, that is, the presence of the substrate.

The use of the $Ru(bpy)_3^{2+}$ coreactant scheme for generating ECL in acetonitrile was shown to result in rapid tip fouling, which is problematic. However, in a following paper [90], Bard et al. demonstrated that very stable ECL signals, enabling SECM-ECL imaging, could be obtained using the $Ru(bpy)_3^{2+}$–TrPA system in an aqueous medium. Using conically etched submicron-sized Pt UMEs as tips, the authors also considerably improved the resolution of SECM-ECL, reaching a resolution close to that achieved with NSOM, that is, of the order of ~100 nm (Figure 17.46). As it was necessary to place the tip very close to the substrate, a shear force–based feedback had to be used to control the tip–substrate distance with submicrometer resolution. The cone shape of the Pt tip limited the effect of hindered diffusion of the ECL reagents to the tip surface which, in the case of disk-in-glass electrodes, decreased ECL intensity for insulating substrates at close tip–substrate separation.

At about the same time, Maus and Wightman described an alternative ECL system for OM [142]. In this work, 9,10-diphenylanthracene (DPA) and benzonitrile (BN) were, respectively, oxidized and reduced at a microelectrode that was alternatively biased at anodic and cathodic potentials. Electron transfer between the tip-generated $BN^{\cdot-}$ and $DPA^{+\cdot}$ radicals generated an emissive excited state of DPA which gave out light. Radical ions generated an emissive excited state of DPA that gave out hight. BN was not only a reactant but was also used as the solvent.

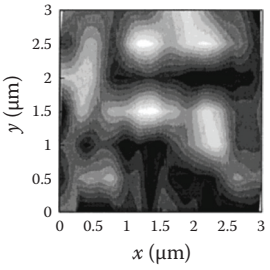


FIGURE 17.46 SECM-ECL near-field image of a test sample containing submicrometer holes. The tip was a conically etched Pt wire, insulated by an electrophoretic paint, and displaying a 172 nm effective diameter. ECL emission at the tip was triggered by biasing the tip at 1.2 V in a $Ru(bpy)_3^{2+}$–TPrA containing aqueous phosphate buffer solution (pH 7.5). A tuning fork–based shear force detection scheme is used to hold a constant tip–substrate distance during imaging. Data acquisition time, 8 min. (Adapted with permission from Zu, Y., Ding, Z., Zhou, J., Lee, Y., and Bard, A.J., Scanning optical microscopy with an electrogenerated chemiluminescent light source at a nanometer tip, *Anal. Chem*., 73, 2153–2156, 2001. Copyright 2001 American Chemical Society.)

A conically shaped carbon fiber, with a high aspect ratio, functioned as the microelectrode for these studies. Interestingly, the electrode was not insulated to its very apex as it was demonstrated that ECL emission could be forced to occur selectively at the tip apex by using high-frequency (20 kHz) tip potential modulation. With this ECL scheme as one of the reactants was the solvent, the reaction layer, where light is emitted, is located very close to the tip electrode surface. Thus the presence of the substrate interferes much less with light generation, that is, there is no SECM feedback effect on the ECL intensity. The tip was placed at fixed height above the sample and the substrate was rastered in the *x*- and *y*-dimensions. The absence of a feedback mechanism enabled fast scan rates. The resolution attained was of the order of 600 nm.

Finally, it is worth noting that SECM-ECL has been used to investigate the mechanism of ECL emission for the $Ru(bpy)_3^{2+}$–TrPA and $Ru(bpy)_3^{2+}$–oxalate systems [141,143].

17.5.3.2 Detection of Enzyme Activity by SECM-ECL

The SECM-ECL configuration was also used to image the activity of enzymes immobilized on a surface [144,145]. In particular, the chemiluminescence and topography of a glass surface bearing immobilized enzyme HRP were simultaneously imaged [144]. The SECM tip was scanned over the enzyme-bearing surface in a luminol-containing solution. The tip was biased so as to generate the enzyme substrate (H_2O_2) by reduction of dissolved oxygen. When the tip passed over an enzyme-containing region, the tip-generated H_2O_2 diffused to the immobilized HRP-catalyzed and reacted with luminol to emit light. The distribution of active enzyme "spots" on the surface was thus mapped by plotting the collected light intensity as a function of the tip position. Since the tip current was not affected by the presence or the absence of the enzyme, but solely controlled by oxygen diffusion, the variation of the current during the (fixed height) scan could be translated into surface topography. Hence, dual chemiluminescent and tip current SECM images could be acquired simultaneously without interference.

More recently, a similar experimental configuration was used to image the biocatalytic activity of localized GOx-containing surface structures [145]. The oxidized form of luminol was generated at the SECM tip. When the tip was scanned over active GOx spots, light was emitted due to the reaction of oxidized luminol with H_2O_2 produced by the glucose oxidase–catalyzed oxidation of glucose (Figure 17.47). Large Pt disk electrodes, 250 μm in diameter, had to be employed due to the limited amount of H_2O_2 generated by the enzyme-catalyzed reaction. To increase sensitivity, the ECL emission was modulated by oscillating the tip potential and using a phase-sensitive lock-in amplifier for light detection.

17.5.4 Scanning Electrochemical Microscopy–Fluorescence Microscopy

In Sections 17.5.1 through 17.5.3, the tip was primarily used as the light source, providing the same probe with both spatial optical and electrochemical information. However, there is still much to be gained by mounting an SECM on an optical microscope. At the simplest level, an optical microscope can be used to aid positioning of an SECM tip over a feature of interest, for example, a single cell, provided it is within the resolution limit of the microscope. By using a fluorescent microscope, it is possible to spatially locate fluorescently active zones on the surface. Hence, fluorescent labeling is often employed to aid identification of areas of interest on a substrate.

Taking this approach one step further by using a CLSM, it is possible to obtain higher resolution than any other conventional microscope, especially in the depth (*z*) direction, due to the reduction of out-of-focus blur [146]. This enables direct, noninvasive serial optical sectioning of objects or profiling of multilayer structures. The ultimate sensitivity is provided by *single molecule* fluorescence spectroscopy (SMFS) that requires both the optical detection volume to be confined to femtoliters and concentration of the analyte of interest to be at the nanomolar and lower level. This can be achieved in two ways: (1) for surfaces, the use of total internal reflection fluorescent microscopy enables single molecules immobilized on a surface to be detected and (2) in solution, a laser beam is focused to a diffraction-limited spot size. When the fluorescent molecules traverse the detection

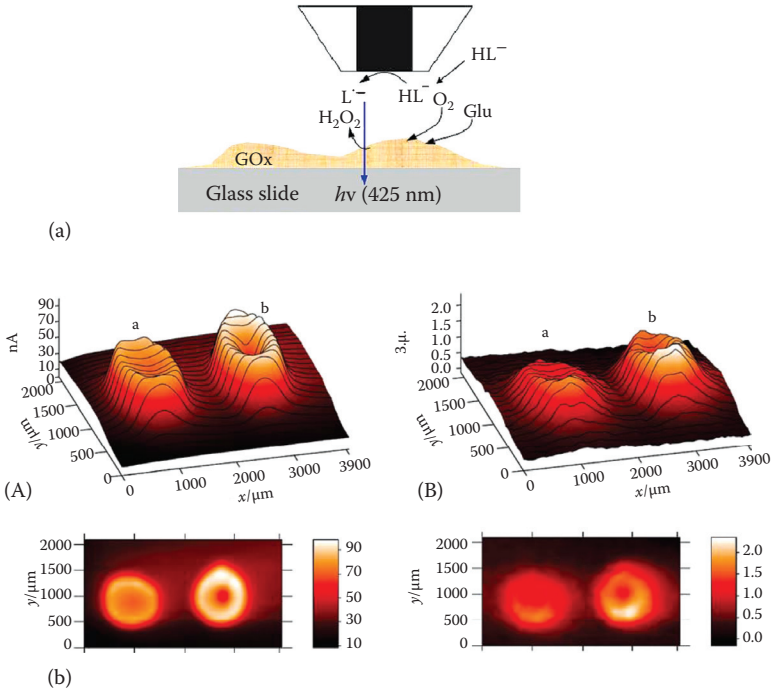


FIGURE 17.47 SECM-ECL for studying local biocatalytic activity of enzyme–polymer spots. (a) Working principle. The oxidized form of luminol (L^{-}) is generated at the SECM tip. When the tip is scanned over active glucose oxidase (GOx) spots, light is emitted due to the reaction of oxidized luminol with H_2O_2 produced by the GOx-catalyzed oxidation of glucose. (b) (A) GC-SECM image of GOx polymer spots in 100 mM glucose and 0.20 M phosphate buffer (pH 6.8) and (B) ECL image of the same spots as SECM in 100 mM glucose, 1 mM luminol, and 0.20 M Tris–HCl buffer (pH 8.5) using a 250 μm Pt disk as tip electrode (r_g = 2.2 mm). (Adapted with permission from Lei, R., Stratmann, L., Schäfer, D., Erichsen, T., Neugebauer, S., Li, N., and Schuhmann, W., Imaging biocatalytic activity of enzyme-polymer spots by means of combined scanning electrochemical microscopy/electrogenerated chemiluminescence, *Anal. Chem*., 81, 5070–5074, 2009. Copyright 2009 American Chemical Society.)

volume, a burst of photons is generated. To date, there have been many interesting applications of SECM combined with fluorescent microscopy.

17.5.4.1 Solution Studies

Unwin and coworkers used CLSM to quantify 3D pH diffusion gradients generated at UMEs in solution [147,148]. Two reactions were (i) the reduction of 1,4-benzoquinone (BQ) in an unbuffered solution of fluorescein; fluorescein exhibits a pH-sensitive fluorescence signal. As this process involves the addition of two protons and two electrons, the local consumption of protons causes the pH to increase locally at the surface of the electrode, which in turn causes the fluorescein to fluoresce with greater intensity. (ii) The reduction of oxygen at Pt UMEs and the reduction of water at both Pt and Au UMEs, in unbuffered electrolyte solutions containing fluorescein. Both processes result in the production of hydroxide ions that again causes fluorescein to fluoresce with greater intensity.

Figure 17.48 shows CLSM profiles for the reduction of BQ as a function of driving potential [148]. As the reaction is driven to more negative potentials, the size of the pH-dependent diffusion field can be seen, by CLSM, to increase in size, as expected. Taking advantage of the CLSM's ability to cross section in the *z*-direction, it was also possible to map the diffusion profile in 3D. Figure 17.48 displays (*x*, *z*) profiles recorded in different zones of the 3D pH diffusion profile. Using FEM modeling, the experimental observations were found to be in very good agreement with the theoretical predictions [148].

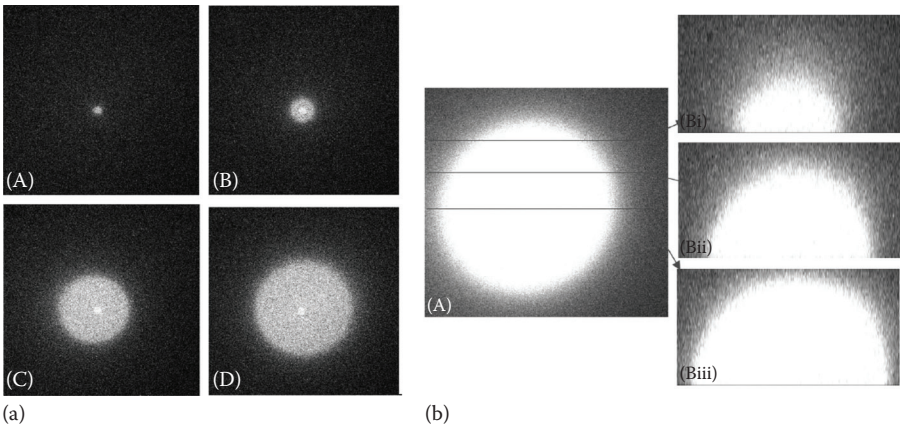


FIGURE 17.48 (a) CLSM images of fluorescence profiles for the reduction of 1 mM benzoquinone in disodium fluorescein solution, at the surface of a 25 μm Pt disk electrode (clearly seen in the center of the image). Potential held at (A) −0.10 V, (B) −0.15 V, (C) −0.20 V, and (D) −0.25 V. Image size, 650 μm × 650 μm. (b) Fluorescence images of an electrode surface at −0.25 V. (A) Two-dimensional (*x*–*y*) image at a distance 2 μm above the electrode. (Bi–Biii) Cross sections through the *x*-axis in the *z*-direction (normal to the electrode surface) of the image (A) at marked distances. This series of (*x*–*z*) axis scans was taken over a distance of 200 μm in the *z*-direction, which is the height scale on these images. (Reproduced from Cannan, S. et al., *Electrochem. Commun*., 4, 886, 2002.)

Using CLSM, it was also possible to map the pH diffusion profile of an electrode only 80 nm in diameter [147] given that the size of the diffusion field is significantly larger than the size of the active site, thus illustrating the power of the technique for identifying submicroscopic sites on a surface. For the reduction of oxygen at a Pt UME, FEM modeling showed that the size of the resulting pH-dependent diffusion field correlated with the number of electrons, *n*, transferred in the process. In this way, it was possible to determine *n* for oxygen reduction at a Pt UME [147].

Finally by coupling SECM with CLSM, it was possible to quantitatively measure the permeation of a weak acid through a bilayer lipid membrane (BLM) [149]. Here, an UME placed close to a BLM was used to deliver weak acids in a well-defined manner by the electrogeneration of protons in the presence of weak acid anions and fluorescein (Figure 17.49). The resulting steady-state pH distribution in the vicinity of the UME and on either side of the BLM, visualized using CLSM, was found to be, from FEM simulation, highly dependent on the distribution of the weak acid and the BLM permeation coefficient. Hence by matching experiment to theory, it was possible to determine permeation coefficients for a series of aliphatic weak acids. Significantly, the data obtained cast doubt on the applicability of a well-known existing model that had been previously employed to extract permeation values.

In an exciting development, Heinze and coworkers combined SECM with single molecule fluorescence spectroscopy to generate space- and time-controlled pH gradients in solution, in a similar way to that discussed earlier. However, here fluorescence detection was possible at the single molecule level and information was also provided on the real-time behavior of systems in response to pH gradients [150]. The pH-dependent fluorophore used in these studies was SNARF-1-dextran. For solution work, the optical detection volume was positioned inside the proton or hydroxide-generated diffusion field, whilst for pH profiling of fluorophores immobilized on a surface, total internal reflection excitation was employed.

Initial studies focused on generating pH gradients at UMEs of sizes over the wide range 2 nm–5 μm and mapping the resulting fluorescent intensity either in solution or at a fluorescently labeled surface; for the latter, a UME positioned in close proximity provides a local pH gradient. Both the oxidation of nitrite to nitrate (generates protons) and the reduction of BQ (consumes protons) were employed to generate pH diffusion profiles. To demonstrate a biological application,

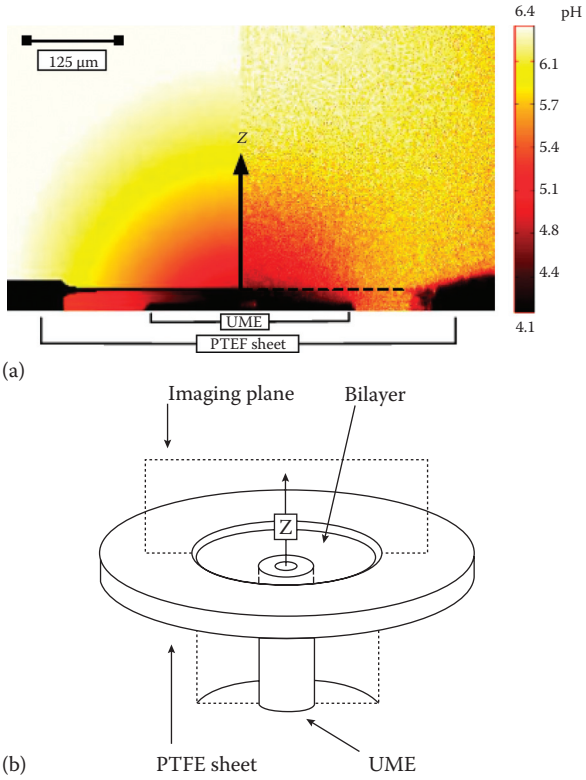


FIGURE 17.49 Image and imaging plane for the visualization of electrochemically induced passive transport. (a) Simulated pH profile (left) and experimental pH profile (right) for the permeation of hexanoic acid. Bilayer position is marked by a solid line in the simulated profile and a dashed line in the experimental profile. (b) Illustration of the LCSM scan plane with respect to the experimental bilayer. (Reproduced from Grime, J.M.A. et al., *Proc. Natl. Acad. Sci. USA*, 105, 14277, 2008.)

the researchers studied the enzyme ATP synthase embedded in a liposome. In response to a proton gradient, the ATP synthase is stimulated to produce ATP. When ATP is synthesized, the head unit of the enzyme rotates in one direction; conversely, when ATP is hydrolyzed, the head unit rotates in the opposite direction. Fluorophores were added to two of the ATP synthase subunits so that rotation of the two units relative to one another during ATP synthesis and hydrolysis could be studied using single molecule fluorescence resonance energy transfer (FRET). The SECM tip was used to create a pH gradient. When the liposome carrying the enzyme diffused into this gradient, the enzyme responded to the changing pH. Although there was no direct evidence for ATP synthesis, the resulting FRET patterns observed indicated that the system was likely to be rotating in the correct direction for ATP production [151].

17.5.4.2 Surface Measurements

Combined SECM-CLSM was employed by Matsue and colleagues to both identify fluorescently active spots of the enzyme diaphorase supported on a substrate surface (CLSM) and provide information on the activity of the enzyme toward turnover of NADH (SECM) [152]. It was also shown that by using both CLSM and SECM it was possible to locally pattern the enzyme. This was achieved by using an enzyme-covered substrate and then selectively deactivating the enzyme in defined zones. With CLSM, this was undertaken by irradiating the sample with very strong light from a focused laser beam (to photodegrade the enzyme). By scanning the beam over the surface, the enzyme could be deactivated in selected regions. Using electrochemistry, the tip UME was used to electrogenerate

Br_2 from Br^-, which when coupled with water formed HOBr, a strong oxidant. Diffusion of HOBR to the substrate surface resulted in degradation of the enzyme in the zones where the SECM tip scanned. The regions of deactivated enzyme could then be visualized using CLSM, as photodegradation caused the fluorescent intensity of the enzyme to greatly reduce [152].

Bard and coworkers used an SECM tip to selectively pattern redox-inactive fluorescent-labeled molecules onto an azido-functionalized glass substrate using "click" chemistry [153]. The tip UME was utilized to produce Cu^+ from Cu^{2+} salen oxidation in DMF (to stabilize the Cu^+) in the small gap between the Au UME and the underlying substrate. The Cu^+ served as a catalyst to "click" the fluorescently labeled alkyne on to the glass-supported azide molecules. The size of the patterned zones could then be visualized using fluorescence microscopy. They were found to be bigger than the size of the UME employed, which was thought to result from the reaction rate of the click process and the thick insulating layer around the Au UME.

17.5.5 Scanning Electrochemical Microscopy–Surface Plasmon Resonance

A surface plasmon is an electromagnetic wave that propagates along the surface of a metal in contact with a dielectric. Surface plasmons can thus be generated at the surface of metal electrodes in contact with an electrolyte. A configuration coupling SPR with electrochemistry typically uses a thin layer of gold (~50 nm) deposited on a glass prism, as the working electrode (Figure 17.50). A polarized laser beam is directed through the prism in order to illuminate the back side of the

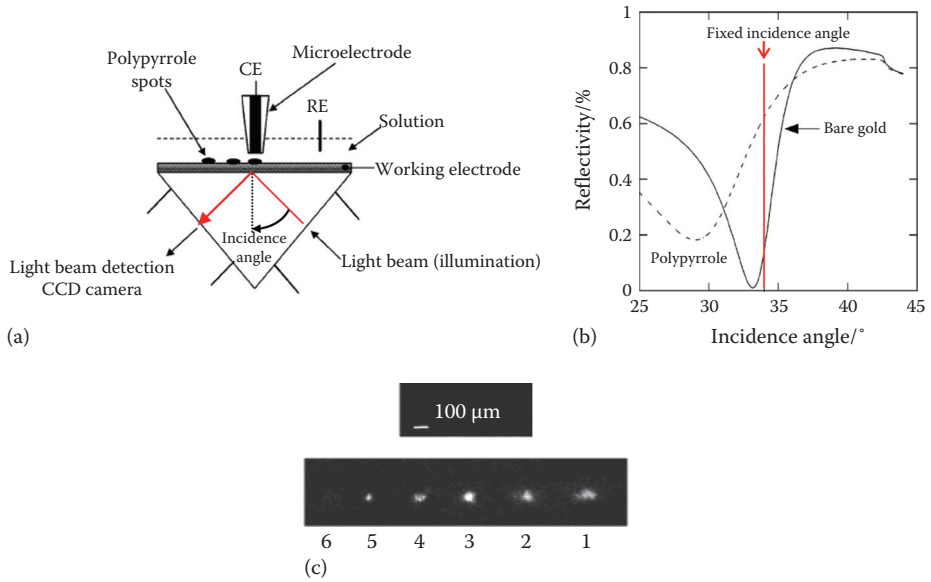


FIGURE 17.50 Combining SECM with surface plasmon resonance imaging (SPR-i). (a) Principle for simultaneously writing and imaging micropatterns on a surface in SECM/SPR-i. (b) Reflectivity vs. incident angle curves recorded at a gold substrate, either bare (solid line) or coated with a polypyrrole ultrathin film (dashed line). The vertical red line shows the fixed incidence angle used for SPR-i. One can see that for the angle chosen the presence of the polypyrrole film translates into a higher substrate reflectivity. (c) SPR-i of polypyrrole dots locally deposited onto the substrate using the SECM tip as the counter electrode. Tip–substrate distance during deposition ~10 μm. Spots of varying sizes and thicknesses were deposited by decreasing the deposition time from 600 ms (spot 1) down to 1 ms (spot 6). The last visible spot (spot 5) was only ~3 nm thick. (Adapted with permission from Szunerits, S., Knorr, N., Calemczuk, R., and Livache, T., New Approach to writing and simultaneous reading of micropatterns: combining surface plasmon resonance imaging with scanning electrochemical microscopy (SECM), *Langmuir*, 20, 9236–9241, 2004. Copyright 2004 American Chemical Society.)

gold–solution interface, under total reflection conditions. The intensity of the reflected light is monitored as a function of the incident angle of the laser with respect to the gold surface. At a defined angle, there is coupling of the incident light with the surface plasmon modes and consequently the intensity of the reflected light decreases. Hence the reflected intensity vs. illumination angle curve presents a very distinct minimum, whose position on the incident angle axis is extremely dependent on the local optical properties of the electrode–solution interface (Figure 17.50).

Deposition of minute amounts of material onto the gold electrode surface, for example, polymer or macromolecular ultrathin films, modifies these optical properties (optical index) resulting in detectable shifts of the angular position of the SPR minimum. The magnitude of this shift allows the thickness of even nanometer-thick films to be quantified. SPR can thus be used to probe interfacial phenomena at a fixed location, corresponding to the position of a focused laser spot on the surface (approximately tens of micrometers), but can also be used to map film deposition over a larger illuminated surface area (few millimeters) in SPR-imaging mode (SPR-i). Here the incidence angle of the laser is kept constant and an image of the illuminated area is acquired using a CCD camera. The presence of the deposited layer results in a shift of the reflectivity curve so that more light is reflected from areas where the film is deposited, as shown in Figure 17.50b. Hence, areas covered with film appear as bright zones in SPR-i.

Coupling of SECM with SPR-i was originally described in the seminal work by Szunerits et al. [154,155]. In the proposed configuration, SECM was used to locally deposit polypyrrole and polypyrrole–oligonucleotide microspots onto the gold surface of a SPR gold sensor. A 10 μm diameter SECM disk-in-glass tip was initially positioned ~5–10 μm from the gold SPR substrate using the positive feedback response of a redox mediator. The SECM cell was then flushed, rinsed, and filled with a pyrrole-containing solution. For polypyrrole deposition, short duration pulses were applied to the gold substrate while the SECM tip was used as a counter electrode. As a result, polypyrrole spots were specifically deposited below the tip (Figure 17.50c).

In this configuration, the thickness and lateral dimensions of the deposited polypyrrole spots could be monitored (read) from the SPR-i during in situ deposition by SECM (writing). Using only SECM to deposit and subsequently image the spots would have been possible in principle, but would have required significantly more time. Moreover, the exquisite sensitivity of SPR-i allowed very thin (~3 nm thick) polypyrrole spots to be clearly visualized. The respective influence of the pyrrole monomer concentration and of the potential pulse time on the dimensions of the polypyrrole and polypyrrole–oligonucleotides was quantified.

Combination of SPR with SECM was also reported by Zhou et al. [156]. In these studies, the backside of the gold SPR surface was illuminated using a ~100 μm diameter focused laser and the angular position of the SPR minimum was monitored using a photodetector. In the first set of experiments, molecular layers of 6-ferrocenyl-1-hexanethiol were assembled onto the gold surface and a redox mediator (Ce^{3+}) was introduced in solution. A 10 μm diameter SECM tip was then positioned 10 μm above the illuminated portion of the gold substrate. The SECM tip was biased so as to generate the oxidizing Ce^{4+} species which, upon reaching the gold surface, locally oxidized the surface containing Fc moieties.

It was observed that this oxidation was accompanied by a marked shift of the SPR minimum, which was attributed to a local change of the thickness of the film due to the repulsion between adjacent ferrocenium ions. Based on this model system, it was thus demonstrated that SECM-SPR was viable for determining local variations in thin film thickness induced by redox reactions. Here, redox conversion of surface-bound species was achieved using SECM tip-generated species and not by biasing the substrate. Hence, the interfering effect of an applied substrate potential on the SPR signal was eliminated.

This approach was further extended to the determination of redox-induced conformational changes of cytochrome c molecules electrostatically attached to the gold surface. Conversion of cytochrome c from its oxidized to its reduced state by tip-generated methyl viologen monocations was found to result in a ~0.27 Å increase in protein size. More recently, the same SECM-SPR

approach was used for real-time detection of Cu^{2+} sequestration and release by an immobilized metalloprotein, metallothionein-2 (MT) [157]. Copper ions were stripped from a Cu-coated SECM tip positioned close to a gold SPR surface bearing MT molecules. Stepwise changes in the time-resolved SPR minimum shifts were observed and ascribed to conversion of MT between three stable structures sequestrating 5, 9, and 12 copper ions. Conversely, metal release by MT was triggered by locally acidifying the solution with protons generated from hydroquinone oxidation at the SECM tip. The simultaneously recorded time-resolved SPR shifts showed that metal release also proceeded through the three conformations identified.

The advantage of using an SECM-based configuration is that the fast mass transfer achieved at the local scale avoids the mass transfer limitation on kinetic measurements commonly encountered in flow injection SPR systems. This work evidenced that SECM-SPR is amenable for studies of rapid functional and dynamic conformational changes of protein at the solid–liquid interface.

17.5.6 Scanning Electrochemical Microscopy–Attenuated Total Reflection Spectroscopy

A novel combination of SECM with mid-infrared (IR) (3–25 μm wavelength region) spectroscopy was reported by Kranz et al. [158,159]. Here, the SECM substrate is the flat top of a hemispherical ZnSe attenuated total reflection (ATR) single bounce crystal. IR radiation is directed through the crystal and focused onto a small spot at the ATR crystal–solution interface. The locally created evanescent field penetrates a few microns into solution and the radiation reflected at the interface (internally reflected) is directed toward a photodetector. Hence, IR-adsorbing molecules present in the close vicinity of the interface can be spectroscopically probed, that is, an evanescent field adsorption spectrum is acquired.

One of the interests of combining IR-ATR spectroscopy with SECM is that this configuration affords a current-independent way of determining tip–substrate distance [158]. Indeed when the SECM tip is approached toward the IR-irradiated spot of the ATR crystal, so that it enters the evanescent field, IR spectra corresponding to the IR adsorption of the borosilicate glass sheath of SECM tips can be detected. Since the IR-evanescent field decays exponentially away from the surface, the closer the tip is approached the more intense the absorbance of the IR radiation by the tip. Hence, the absolute tip–substrate distance can be quantitatively determined from the magnitude of the IR adsorption bands of the glass spectrum (Si–O stretching and bending mode). Alternatively, provided an aqueous solvent is used, the O–H bending mode of water can also be recorded and used for distance calibration. A narrowing tip–substrate gap translates into a decreasing OH band due to water being expelled from the gap upon the approach.

A major interest of ATR-SECM is that this combined technique allows for the specific spectroscopic probing of species either located in the narrow tip–substrate gap or locally adsorbed at the ATR surface. Moreover, since the "fingerprint" regime of the IR spectrum is used (10–25 μm wavelength), almost any organic molecule can be unambiguously identified from the distinct adsorption pattern acquired. In that respect, it should be noted that using IR-ATR spectroscopy provides a high surface sensitivity, and alleviates the usual problem of the strong IR adsorption of water, which otherwise limits the use of in situ IR spectroscopy.

The possibility of using ATR-SECM for in situ studies of an electrochemically induced process has been demonstrated by spectroscopically monitoring the deposition of polymer microspots induced by SECM in feedback mode [159]. In this work, Kranz et al. coated the surface of an ATR crystal with a ~300-nm thick water-insoluble layer of 2,5-di-(2-thienyl)-pyrrole (SNS) monomer. Local polymerization of SNS was then triggered by approaching a 25 μm Pt tip, generating the oxidizing species $Ru(bpy)_3^{3+}$, toward the surface. Polymerization of SNS was simultaneously monitored by recording evanescent field absorption intensity changes of SNS-specific bands, providing information on the polymerization mechanism.

So far, only insulating ATR-SECM substrates (ATR crystals) have been used. However, ATR-SECM conducting substrates could, in principle, be fabricated by coating ATR crystals with mid-IR transparent conducting thin films (such as diamond-like films). Combining ATR-SECM with AFM for simultaneous in situ studies on topography, IR spectroscopy, and electrochemical processes is also contemplated [159].

17.6 SCANNING ELECTROCHEMICAL MICROSCOPY–QUARTZ CRYSTAL MICROBALANCE

The quartz crystal microbalance (QCM) consists of a quartz crystal that is electrically driven into oscillation. The resonance frequency of the crystal is monitored. This frequency is highly dependent on any mass added to the crystal surface. Hence the mass dependence of the QCM resonance frequency can be, in air, used to "weigh" minute amounts of material with a sensitivity of the order of 1 ng/cm. QCM can also be coupled with electrochemistry; here, the quartz crystal surface is coated with an appropriate electrode material, for example, thin film gold. This electrochemical QCM (EQCM) configuration can be used to monitor electrochemically triggered surface processes associated with the deposition (or loss) of material at the working electrode surface. However, in liquid medium the frequency shift of the QCM crystal is not solely sensitive to added mass but is also influenced by changes in the local property of the medium associated with the surface electrochemical process of interest. For example, density or viscosity variation of the medium in the electrode vicinity, in addition to variation in the viscoelastic properties of the deposited layer, can cause shifts in the resonant frequency of QCM.

The main interest in coupling QCM with SECM is that the SECM tip can *specifically* monitor the flux of electroactive species associated with the surface electrochemical process. This additional information can help to quantify the actual contribution of electroactive flux to the apparent total mass change derived from the QCM frequency shift. The combination of SECM with EQCM was initially described by Hillier and Ward [160]. The authors used an SECM tip to trigger the electrodeposition of a small amount of copper on predefined locations of the QCM surface. By monitoring the ensuing frequency shift of the QCM, the radial sensitivity of the QCM crystal was mapped.

The first use of SECM-QCM in a SG-TC configuration was later reported by Bard et al. [161,162]. The tip was used to detect C_{60}^- ions released during the potential cycling of the quartz substrate surface bearing either an insoluble C_{60} film or C_{60} caged in *tert*-butylcalix[8]arene, cast as a particle film. In the first of these studies, the effect of the lateral and vertical motion of the SECM tip on the QCM response was investigated [161]. It was shown that both motions resulted in a frequency shift of the QCM, which led to the conclusion that SECM-QCM measurements should be performed with a stationary tip in order to avoid tip motion–induced frequency shifts. Further studies by Bartlett et al. [163] and Heinze et al. [164] confirmed these effects and showed that they could be minimized by using small tips (with small r_g) or tips with high aspect ratio cone-shaped glass sheath. However, the tip–substrate distance dependence of the QCM frequency shift can also be used to set the tip–substrate distance in SECM-QCM in a current-independent way [165].

More recently, SECM-QCM has been employed to monitor localized corrosion processes [166], the electrochemical growth of poly(*o*-phenylenediamine) thin films [167], and ion exchange at the poly(butyl viologen)–electrolyte interface [168].

17.7 FAST SCAN CYCLIC VOLTAMMETRY–SCANNING ELECTROCHEMICAL MICROSCOPY

The coupling of fast scan cyclic voltammetry (FSCV) with SECM to resolve the distribution of chemical species generated at a substrate surface was first introduced by Wipf's group [169,170]. In FSCV-SECM, CV is carried out at an SECM tip using rapid scan rates, typically between 10 and

1000 V/s. The vertical and lateral positions of the SECM tip over the substrate have to be recorded concomitantly with the transient tip CV. Unlike "classical" amperometric SECM, where the tip potential is typically held constant, in FSCV-SECM the tip potential is scanned so that several species of interest giving rise to differing CV peaks can be simultaneously detected, that is, images of multiple analytes can be recorded in a single surface scan.

The species are probed over a distance corresponding to the transient diffusion layer created at the tip which, at high enough scan rates, can be made much smaller than the tip–substrate distance. Hence, no diffusional feedback interaction occurs and the recorded signal (and hence images) is free from perturbations due to substrate topography. Interestingly, images of the concentration profile of non-electroactive species can also be acquired in FSCV-SECM since the only requirement for detection is that the surface-released species modifies in some way the fast scan CV. For example, the localized concentration of chloride ions was mapped by collecting the chloride at a mercury SECM tip [169]. The Hg tip was first scanned anodically to form a calomel layer (Hg_2Cl_2) on the tip surface. The cathodic (return) CV scan then showed a characteristic chloride-dependent peak corresponding to the stripping of the Hg_2Cl_2 layer. FSCV-SECM has also been notably employed to map simultaneously oxygen and hydrogen peroxide released during the oxidative bursts of stimulated macrophage cells [171].

FSCV-SECM combines the spatial resolution of SECM with the specificity of CV. A theoretical description of the CV response of a disk UME facing an insulating substrate, that is, in a negative feedback FSCV-SECM configuration, can be found in literature [172]. Further development of FSCV-SECM would include coupling the methodology with another technique to allow the tip–substrate distance to be set independently from the current measurement.

REFERENCES

1. Gardner, C. E., Macpherson, J. V., Atomic force microscopy probes go electrochemical. *Anal. Chem*. 2002, 74, 576A.
2. Kueng, A., Kranz, C., Mizaikoff, B., Scanning probe microscopy with integrated biosensors. *Sens. Lett*. 2003, 1, 2.
3. Kranz, C., Wiedemair, J., Scanning force microscopy based amperometric biosensors. *Anal. Bioanal. Chem*. 2008, 390, 239.
4. Wittstock, G., Burchardt, M., Pust, S. E., Shen, Y., Zhao, C., Scanning electrochemical microscopy for direct imaging of reaction rates. *Angew. Chem. Int. Ed*. 2007, 46, 1584.
5. Binnig, G., Quate, C. F., Gerber, C., Atomic force microscope. *Phys. Rev. Lett*. 1986, 56, 930.
6. Macpherson, J. V., Unwin, P. R., Combined scanning electrochemical–atomic force microscopy. *Anal. Chem*. 1999, 72, 276.
7. Penner, R. M., Heben, M. J., Longin, T. L., Lewis, N. S., Fabrication and use of nanometer-sized electrodes in electrochemistry. *Science* 1990, 250, 1118.
8. Nagahara, L. A., Thundat, T., Lindsay, S. M., Preparation and characterization of STM tips for electrochemical studies. *Rev. Sci. Instrum*. 1989, 60, 3128.
9. Stern, J. E., Terris, B. D., Mamin, H. J., Rugar, D., Deposition and imaging of localized charge on insulator surfaces using a force microscope. *Appl. Phys. Lett*. 1988, 53, 2717.
10. Macpherson, J. V., de Mussy, J.-P. G., Delplancke, J.-L., Conducting-atomic force microscopy investigation of the local electrical characteristics of a Ti/TiO_2/Pt anode. *Electrochem. Solid State Lett*. 2001, 4, E33.
11. Macpherson, J. V., de Mussy, J.-P. G., Delplancke, J.-L., High-resolution electrochemical, electrical, and structural characterization of a dimensionally stable Ti/TiO_2/Pt electrode. *J. Electrochem. Soc*. 2002, 149, B306.
12. Macpherson, J. V., Unwin, P. R., Noncontact electrochemical imaging with combined scanning electrochemical atomic force microscopy. *Anal. Chem*. 2001, 73, 550.
13. Abbou, J., Demaille, C., Druet, M., Moiroux, J., Fabrication of submicrometer-sized gold electrodes of controlled geometry for scanning electrochemical–atomic force microscopy. *Anal. Chem*. 2002, 74, 6355.
14. Abbou, J., Anne, A., Demaille, C., Probing the structure and dynamics of end-grafted flexible polymer chain layers by combined atomic force–electrochemical microscopy. Cyclic voltammetry within nanometer-thick macromolecular poly(ethylene glycol) layers. *J. Am. Chem. Soc*. 2004, 126, 10095–10108.

15. Abbou, J., Anne, A., Demaille, D. Accessing the dynamics of end grafter polymer chains by atomic force electrochemical microscopy. Theoretical modeling of the approach curves by the elastic bounded diffusion model and Monte Carlo simulations. Evidence for compression induced lateral chain escape. *J. Phys. Chem. B* 2006, 110, 22664–22675.
16. Wang, K., Goyer, C., Anne, A., Demaille, C. Exploring the motional dynamics of end grafted DNA oligonucleotides by in situ electrochemical atomic force microscopy. *J. Phys. Chem. B* 2007, 111, 6051–6058.
17. Anne, A., Bonnaudat, C., Demaille, C., Wang, K. Enzymatic redox 3′-end-labeling of DNA oligonucleotide monolayers on gold surfaces using terminal deoxynucleotidyl transferase (TdT)-mediated single base extension. *J. Am. Chem. Soc*. 2007, 129, 2734–2735.
18. Anne, A., Cambril, E., Chovin, A., Demaille, C., Touching surface-attached molecules with a microelectrode: Mapping the distribution of redox-labeled macromolecules by electrochemical–atomic force microscopy. *Anal. Chem*. 2010, 82, 6353–6362.
19. Anne, A., Demaille, C., Goyer, C., Electrochemical atomic-force microscopy using a tip-attached redox mediator. Proof-of-concept and perspectives for functional probing of nanosystems. *Nano* 2009, 3, 819–827.
20. Anne, A., Cambril, E., Chovin, A., Demaille, C., Goyer, C., Electrochemical atomic force microscopy using a tip-attached redox mediator for topographic and functional imaging of nanosystems. *Nano* 2010, 3, 2927–2940.
21. Ghorbal, A., Grisotto, F., Charlier, J., Palacin, S., Demaille, C., Localized electrografting of vinylic monomers on a conducting substrate by means of an integrated electrochemical AFM probe. *ChemPhysChem* 2009, 10, 1053–1057.
22. Kranz, C., Friedbacher, G., Mizaikoff, B., Lugstein, A., Smoliner, J., Bertagnolli, E., Integrating an ultramicroelectrode in an AFM cantilever: Combined technology for enhanced information. *Anal. Chem*. 2001, 73, 2491.
23. Lugstein, A., Bertagnolli, E., Kranz, C., Mizaikoff, B., Fabrication of a ring nanoelectrode in an AFM tip: Novel approach towards simultaneous electrochemical and topographical imaging. *Surf. Interface Anal*. 2002, 33, 146.
24. Lugstein, A., Bertagnolli, E., Kranz, C., Kueng, A., Mizaikoff, B., Integrating micro- and nanoelectrodes into atomic force microscopy cantilevers using focused ion beam techniques. *Appl. Phys. Lett*. 2002, 81, 349.
25. Kueng, A., Kranz, C., Lugstein, A., Bertagnolli, E., Mizaikoff, B., Integrated AFM–SECM in tapping mode: Simultaneous topographical and electrochemical imaging of enzyme activity. *Angew. Chem. Int. Ed*. 2003, 42, 3238–3240.
26. Wiedemair, J., Balu, B., Moon, J.-S., Hess, D. W., Mizaikoff, B., Kranz, C., Plasma-deposited fluorocarbon films: Insulation material for microelectrodes and combined atomic force microscopy–scanning electrochemical microscopy probes. *Anal. Chem*. 2008, 80, 5260.
27. Kueng, A., Kranz, C., Mizaikoff, B., Lugstein, A., Bertagnolli, E., Combined scanning electrochemical atomic force microscopy for tapping mode imaging. *Appl. Phys. Lett*. 2003, 82, 1592.
28. Kranz, C., Kueng, A., Lugstein, A., Bertagnolli, E., Mizaikoff, B., Mapping of enzyme activity by detection of enzymatic products during AFM imaging with integrated SECM-AFM probes. *Ultramicroscopy* 2004, 100, 127.
29. Kueng, A., Kranz, C., Lugstein, A., Bertagnolli, E., Mizaikoff, B., AFM-tip-integrated amperometric microbiosensors: High-resolution imaging of membrane transport. *Angew. Chem. Int. Ed*. 2005, 44, 3419.
30. Sekine, S., Kaji, H., Nishizawa, M., Integration of an electrochemical-based biolithography technique into an AFM system. *Anal. Bioanal. Chem*. 2008, 391, 2711.
31. Hirata, Y., Yabuki, S., Mizutani, F., Application of integrated SECM ultra-micro-electrode and AFM force probe to biosensor surfaces. *Bioelectrochemistry* 2004, 63, 217.
32. Wilson, N. R., Macpherson, J. V., Carbon nanotube tips for atomic force microscopy. *Nat. Nano*. 2009, 4, 483.
33. Wilson, N. R., Macpherson, J. V., Single-walled carbon nanotubes as templates for nanowire conducting probes. *Nano Lett*. 2003, 3, 1365.
34. Burt, D. P., Wilson, N. R., Weaver, J. M. R., Dobson, P. S., Macpherson, J. V., Nanowire probes for high resolution combined scanning electrochemical microscopy–atomic force microscopy. *Nano Lett*. 2005, 5, 639.
35. Zhou, H., Mills, G., Chong, B. K., Midha, A., Donaldson, L., Weaver, J. M. R., Recent progress in the functionalization of atomic force microscope probes using electron-beam nanolithography. *J. Vac. Sci. Technol. A* 1999, 17, 2233.

36. Baller, M. K., Lang, H. P., Fritz, J., Gerber, C., Gimzewski, J. K., Drechsler, U., Rothuizen, H., Despont, M., Vettiger, P., Battiston, F. M., Ramseyer, J. P., Fornaro, P., Meyer, E., Güntherodt, H. J., A cantilever array-based artificial nose. *Ultramicroscopy* 2000, 82, 1.
37. Shin, H., Hesketh, P. J., Mizaikoff, B., Kranz, C., Batch fabrication of atomic force microscopy probes with recessed integrated ring microelectrodes at a wafer level. *Anal. Chem*. 2007, 79, 4769.
38. Shin, H., Hesketh, P. J., Mizaikoff, B., Kranz, C., Development of wafer-level batch fabrication for combined atomic force-scanning electrochemical microscopy (AFM-SECM) probes. *Sens. Actuators* 2008, 134, 488.
39. Akiyama, T., Gullo, M. R., de Rooij, N. F., Tonin, A., Hidber, H.-R., Frederix, P. L. T. M., Engel, A., Staufer, U., Development of insulated conductive probes with platinum silicide tips for atomic force microscopy in cell biology. *Jpn. J. Appl. Phys*. 2004, 43, 3865.
40. Frederix, P. L. T. M., Gullo, M. R., Akiyama, T., Tonin, A., de Rooj, N. F., Staufer, U., Engel, A., Assessment of insulated conductive cantilevers for biology and electrochemistry. *Nanotechnology* 2005, 16, 997.
41. Gullo, M. R., Frederix, P. L. T. M., Akiyama, T., Engel, A., de Rooj, N. F., Staufer, U., Characterization of microfabricated probes for combined atomic force and high-resolution scanning electrochemical microscopy. *Anal. Chem*. 2006, 78, 5436.
42. Frederix, P. L. T. M., Bosshart, P. D., Engel, A., Akiyama, T., De Rooij, N. F., Staufer, U., Comparison of two redox couples for AFM-SECM. *IEEE Sens*. 2007, 703.
43. Frederix, P. L. T. M., Bosshart, P. D., Akiyama, T., Chami, M., Gullo, M. R., Blackstock, J. J., Dooleweerdt, K. de Rooj, N. F., Staufer, U., Engel, A., Conductive supports for combined AFM–SECM on biological membranes. *Nanotechnology* 2008, 19, 384004.
44. Fasching, R. J., Tao, Y., Prinz, F. B., Cantilever tip probe arrays for simultaneous SECM and AFM analysis. *Sens. Actuators* 2005, 108, 964.
45. Bai, S.-J., Fabian, T., Prinz, F. B., Fasching, R. J., Nanoscale probe system for cell-organelle analysis. *Sens. Actuators* 2008, 130, 249.
46. Dobson, P. S., Weaver, J. M. R., Holder, M. N., Unwin, P. R., Macpherson, J. V., Characterization of batch-microfabricated scanning electrochemical–atomic force microscopy probes. *Anal. Chem*. 2004, 77, 424.
47. Dobson, P. S., Weaver, J. M. R., Burt, D. P., Holder, M. N., Wilson, N. R., Unwin, P. R., Macpherson, J. V., Electron beam lithographically-defined scanning electrochemical–atomic force microscopy probes: Fabrication method and application to high resolution imaging on heterogeneously active surfaces. *Phys. Chem. Chem. Phys*. 2006, 8, 3909.
48. Salomo, M., Pust, S. E., Wittstock, G., Oesterschulze, E., Integrated cantilever probes for SECM/AFM characterization of surfaces. *Microelectron. Eng*. 2010, 87, 1537.
49. Pust, S. E., Salomo, M., Oesterschulze, E., Wittstock, G., Influence of electrode size and geometry on electrochemical experiments with combined SECM–SFM probes. *Nanotechnology* 2010, 21, 105709.
50. Vollkopf, A., Rudow, O., Leinhos, T., Mihalcea, C., Oesterschulze, E., Modified fabrication process for aperture probe cantilevers. *J. Microscopy* 1999, 194, 344.
51. Davoodi, A., Pan, J., Leygraf, C., Norgren, S., In situ investigation of localized corrosion of aluminum alloys in chloride solution using integrated EC-AFM/SECM techniques. *Electrochem. Solid State Lett*. 2005, 8, B21.
52. Davoodi, A., Farzadi, A., Pan, J., Leygraf, C., Zhu, Y., Developing an AFM-based SECM system; Instrumental setup, SECM simulation, characterization, and calibration. *J. Electrochem. Soc*. 2008, 155, C474.
53. Davoodi, A., Pan, J., Leygraf, C., Norgren, S., The role of intermetallic particles in localized corrosion of an aluminum alloy studied by SKPFM and integrated AFM/SECM. *J. Electrochem. Soc*. 2008, 155, C211.
54. Davoodi, A., Pan, J., Leygraf, C., Norgren, S., Multianalytical and in situ studies of localized corrosion of EN AW-3003 alloy—Influence of intermetallic particles. *J. Electrochem. Soc*. 2008, 155, C138.
55. Davoodi, A., Pan, J., Leygraf, C., Norgren, S., Integrated AFM and SECM for in situ studies of localized corrosion of Al alloys. *Electrochim. Acta* 2007, 52, 7697.
56. Davoodi, A., Pan, J., Leygraf, C., Norgren, S., Probing of local dissolution of Al-alloys in chloride solutions by AFM and SECM. *Appl. Surf. Sci*. 2006, 252, 5499.
57. Sklyar, O., Kueng, A., Kranz, C., Mizaikoff, B., Lugstein, A., Bertagnolli, E., Wittstock, G., Numerical simulation of scanning electrochemical microscopy experiments with frame-shaped integrated atomic force microscopy–SECM probes using the boundary element method. *Anal. Chem*. 2004, 77, 764–771.

58. Burt, D. P., Wilson, N. R., Janus, U., Macpherson, J. V., Unwin, P. R., In-situ atomic force microscopy (AFM) imaging: Influence of AFM probe geometry on diffusion to microscopic surfaces. *Langmuir* 2008, 24, 12867.
59. Ueda, A., Niwa, O., Maruyama, K., Shindo, Y., Oka, K., Suzuki, K., Neurite imaging of living PC12 cells with scanning electrochemical/near-field optical/atomic force microscopy. *Angew. Chem. Int. Ed*. 2007, 46, 8238.
60. Pust, S. E., Scharnweber, D., Nunes Kirchner, C., Wittstock, G., Heterogeneous distribution of reactivity on metallic biomaterials: Scanning probe microscopy studies of the biphasic Ti alloy Ti_6Al_4V. *Adv. Mater*. 2007, 19, 878.
61. Gardner, C. E., Unwin, P. R., Macpherson, J. V., Correlation of membrane structure and transport activity using combined scanning electrochemical–atomic force microscopy. *Electrochem. Commun*. 2005, 7, 612.
62. Kaji, H., Tsukidate, K., Matsue, T., Nishizawa, M., In situ control of cellular growth and migration on substrates using microelectrodes. *J. Am. Chem. Soc*. 2004, 126, 15026.
63. Slevin, C. J., Gray, N. J., Macpherson, J. V., Webb, M. A., Unwin, P. R. Fabrication and characterisation of nanometre-sized platinum electrodes for voltammetric analysis and imaging. *Electrochem. Commun*. 1999, 1, 282288.
64. Fan, F.-R. F., Bard, A. J., STM on wet insulators: Electrochemistry or tunneling? *Science* 1995, 270, 1849–1851.
65. Guckenberger, R., Heim, M., Cevc, G., Knapp, H. F., Wiegrabe, W., Hillebrand, A., Scanning tunneling microscopy of insulators and biological specimens based on lateral conductivity of ultrathin water films. *Science* 1994, 266, 1538–1540.
66. Zhu, Y., Williams, D. E., Scanning electrochemical microscopic observation of a precursor state to pitting corrosion of stainless steels. *J. Electrochem. Soc*. 1997, 144, L43–L45.
67. Williams, D. E., Mohiuddin, T. F., Zhu, Y. Y., Elucidation of a trigger mechanism for pitting corrosion of stainless steels using submicron resolution scanning electrochemical and photoelectrochemical microscopy. *J. Electrochem. Soc*. 1998, 145, 2664–2672.
68. Meier, J., Freidrich, K. A., Stimming, U., Novel method for the investigation of single nanoparticle reactivity. *Faraday Discuss*. 2002, 121, 365–372.
69. Treutler, T. H., Wittstock, G., Combination of an electrochemical tunneling microscope (ECSTM) and a scanning electrochemical microscope (SECM): Application for tip-induced modification of self assembled monolayer. *Electrochim. Acta* 2003, 48, 2923–2932.
70. Ammann, E., Beuret, C., Indermühle, P.-F., Kötz, R., de Rooj, N. F., Siegenthaler, H., Local pH-controlled reactivity investigations by thin-layer scanning tunneling microscopy. *Electrochim. Acta* 2001, 47, 327–334.
71. Betzig, E., Finn, P. L., Weiner, J. S., Combined shear force and near-field scanning optical microscopy. *Appl. Phys. Lett*. 1992, 60, 2484–2486.
72. Ludwig, M., Kranz, C., Schuhmann, W., Gaub, H. E., Topography feedback mechanism for the scanning electrochemical microscope based on hydrodynamic forces between tip and sample. *Rev. Sci. Instrum*. 1995, 66, 2857–2860.
73. Hengstenberg, A., Kranz, C., Schuhmann, W., Facilitated tip-positioning and applications of non-electrode tips in scanning electrochemical microscopy using shear force based constant-distance mode. *Chem. Eur. J*. 2000, 6, 1547–1554.
74. Etienne, M., Schulte, A., Mann, S., Jordan, G., Dietzel, I. D., Schuhmann, W., Constant-distance mode scanning potentiometry. 1. Visualization of calcium carbonate dissolution in aqueous solution. *Anal. Chem*. 2004, 76, 3682–3688.
75. Etienne, M., Dierkes, P., Erichsen, T., Schuhmann, W., Fritsch, I., Constant-distance mode scanning potentiometry. High resolution pH measurements in three-dimensions. *Electroanalysis* 2007, 19, 318–323.
76. Turyan, I., Etienne, M., Mandler, D., Schuhmann, W., Improved resolution of local metal deposition by means of constant distance mode scanning electrochemical microscopy. *Electroanalysis* 2005, 17, 538–542.
77. Hengstenberg, A., Blöchl, A., Dietzel, I. D., Schuhmann, W., Spatially resolved detection of neurotransmitter secretion from individual cells by means of scanning electrochemical microscopy. *Angew. Chem. Int. Ed*. 2001, 40, 905–908.
78. Isik, S., Schuhmann, W., Detection of nitric oxide release from single cells by using constant-distance-mode scanning electrochemical microscopy. *Angew. Chem. Int. Ed*. 2006, 45, 7451–7454.
79. Ballesteros Katemann, B., Schulte, A., Schuhmann, W., Constant-distance mode scanning electrochemical microscopy (SECM)–Part I: Adaptation of a non-optical shear force-based positioning mode for SECM tips. *Chem. Eur. J*. 2003, 9, 2025–2033.

80. Etienne, M., Schulte, A., Schuhmann, W., High resolution constant-distance mode alternating current scanning electrochemical microscopy (AC-SECM). *Electrochem. Commun*. 2004, 6, 288–293.
81. Eckhard, K., Etienne, M., Schulte, A., Schuhmann, W., Constant-distance mode AC-SECM for the visualisation of corrosion pits. *Electrochem. Commun*. 2007, 9, 1793–1797.
82. Katemann, B. B., Schulte, A., Schuhmann, W., Constant-distance mode scanning electrochemical microscopy. Part II: High-resolution SECM imaging employing Pt nanoelectrodes as miniaturized scanning probes. *Electroanalysis* 2004, 16, 60–65.
83. Etienne, M., Anderson, E. C., Evans, S. R., Schuhmann, W., Fritsch, I., Feedback-independent Pt nanoelectrodes for shear force-based constant-distance mode scanning electrochemical microscopy. *Anal. Chem*. 2006, 78, 7317–7324.
84. Nebel, M., Eckhard, K., Erichsen, T., Schulte, A., Schuhmann, W., 4D Shearforce-based constant-distance mode scanning electrochemical microscopy. *Anal. Chem*. 2010, 82, 7842–7848.
85. Cougnon, C., Bauer-Espindola, K., Fabre, D. S., Mauzeroll, J., Development of a phase-controlled constant-distance scanning electrochemical microscope. *Anal. Chem*. 2009, 81, 3654–3659.
86. Karraia, K., Grober, R. D., Piezoelectric tip–sample distance control for near field optical microscopes. *Appl. Phys. Lett*. 1995, 66, 1842–1844.
87. James, P. I., Garfias-Mesias, L. F., Moyer, P. J., Smyrl, W. H., Scanning electrochemical microscopy with simultaneous independent topography. *J. Electrochem. Soc*. 1998, 4, L64–L66.
88. Büchler, M., Kellye, S. C., Smyrl, W. H., Scanning electrochemical microscopy with shear force feedback. Investigation of the lateral resolution of different experimental configurations. *Electrochem. Solid State Lett*. 2000, 3, 35–38.
89. Yamada, H., Ogata, M., Koike, T., Scanning electrochemical microscope observation of defects in a hexadecanethiol monolayer on gold with shear force-based tip–substrate positioning. *Langmuir* 2006, 22, 7923–7927.
90. Zu, Y., Ding, Z., Zhou, J., Lee, Y., Bard, A. J., Scanning optical microscopy with an electrogenerated chemiluminescent light source at a nanometer tip. *Anal. Chem*. 2001, 73, 2153–2156.
91. Lee, Y., Ding, Z., Bard, A. J., Combined electrochemical/optical microscopy with shear force and current feedback. *Anal. Chem*. 2002, 74, 3634–3643.
92. Yamada, H., Fukumoto, H., Yokoyama, T., Koike, T., Immobilized diaphorase surfaces observed by scanning electrochemical microscope with shear force based tip–substrate positioning. *Anal. Chem*. 2005, 77, 1785–1790.
93. Takahashi, Y., Hirano, Y., Yasukawa, T., Shiku, H., Yamada, H., Matsue, T., Topographic, electrochemical, and optical images captured using standing approach mode scanning electrochemical/optical microscopy. *Langmuir* 2006, 22, 10299–10306.
94. Takahashi, Y., Shiku, H., Murata, T., Yasukawa, T., Matsue, T., Transfected single-cell imaging by scanning electrochemical optical microscopy with shear force feedback regulation. *Anal. Chem*. 2009, 81, 9674–9681.
95. Garay, M. F., Ufheil, J., Borgwarth, K., Heinze, J., Retrospective chemical analysis of tree rings by means of the scanning electrochemical microscopy with shear force feedback. *Phys. Chem. Chem. Phys*. 2004, 6, 4028–4033.
96. Oyamatsu, D., Hirano, Y., Kanaya, N., Mase, Y., Nishizawa, M., Matsue, T., Imaging of enzyme activity by scanning electrochemical microscope equipped with a feedback control for substrate–probe distance. *Bioelectrochemistry* 2003, 60, 115–121.
97. Hansma, P. K., Cleveland, J. P., Radmacher, M., Walters, D. A., Hillner, P., Bezanilla, M., Fritz, M., Vie, D., Hansma, H. G., Prater, C. B., Massie, J., Fukunaga, L., Gurley, J., Elings, V., Tapping mode atomic force microscopy in liquids. *Appl. Phys. Lett*. 1994, 64, 1738.
98. McKelvey, K., Edwards, M. A., Unwin, P. R., Intermittent contact–scanning electrochemical microscopy (IC–SECM): A new approach for tip positioning and simultaneous imaging of interfacial topography and activity. *Anal. Chem*. 2010, 82, 6334.
99. Wipf, D. O., Bard, A. J., Scanning electrochemical microscopy. 15. Improvements in imaging via tip-position modulation and lock-in detection. *Anal. Chem*. 1992, 64, 1632.
100. Horrocks, B. R., Schmidtke, D., Heller, A., Bard, A. J., Scanning electrochemical microscopy. 24. Enzyme ultramicroelectrodes for the measurement of hydrogen peroxide at surfaces. *Anal. Chem*. 1995, 65, 3605–3614.
101. Eckhard, K., Schuhmann, W., Alternating current techniques in scanning electrochemical microscopy (AC-SECM). *Analyst* 2008, 133, 1486–1497.
102. Gabrielli, C., Huet, F., Keddam, M., Rousseau, P., Vivier, V., Scanning electrochemical microscopy imaging by means of high-frequency impedance measurements in feedback mode. *J. Phys. Chem. B* 2004, 108, 11620–11626.

103. Diakowski, P. M., Ding, Z., Novel strategy for constant-distance imaging using alternating current scanning electrochemical microscopy. *Electrochem. Commun*. 2007, 9, 2617–2621.
104. Kurulugama, R. T., Wipf, D. O., Takacs, S. A., Pongmayteegul, S., Garris, P. A., Baur, J. E., Scanning electrochemical microscopy of model neurons: Constant distance imaging. *Anal. Chem*. 2005, 77, 1111–1117.
105. Osbourn, D. M., Sanger, R. H., Smith, P. J. S., Determination of single-cell oxygen consumption with impedance feedback for control of sample–probe separation. *Anal. Chem*. 2005, 77, 6999–7004.
106. Diakowski, P. M., Ding, Z., Interrogation of living cells using alternating current scanning electrochemical microscopy (AC-SECM). *Phys. Chem. Chem. Phys*. 2007, 9, 5966–5974.
107. Katemann, B. B., Schulte, A., Calvo, E. J., Koudelka-Hep, M., Schuhmann, W., Localised electrochemical impedance spectroscopy with high lateral resolution by means of alternating current scanning electrochemical microscopy. *Electrochem. Commun*. 2002, 4, 134–138.
108. Eckhard, K., Erichsen, T., Stratmann, M., Schuhmann, W., Frequency-dependent alternating-current scanning electrochemical microscopy (4D AC-SECM) for local visualisation of corrosion sites. *Chem. Eur. J*. 2008, 14, 3968–3976.
109. Eckhard, K., Shin, H., Mizaikoff, B., Schuhmann, W., Kranz, C., Alternating current (AC) impedance imaging with combined atomic force scanning electrochemical microscopy (AFM-SECM). *Electrochem. Commun*. 2007, 9, 1311–1315.
110. Eckhard, K., Kranz, C., Shin, H., Mizaikoff, B., Schuhmann, W., Frequency dependence of the electrochemical activity contrast in AC-scanning electrochemical microscopy and atomic force microscopy-AC-scanning electrochemical microscopy imaging. *Anal. Chem*. 2007, 79, 5435–5438.
111. Hansma, P. K., Drake, B., Marti, O., Gould, S. A., Prater, C. B., The scanning ion conductance microscope. *Science* 1989, 243, 641.
112. Korchev, Y. E., Bashford, C. L., Milovanovic, M., Vodyanoy, I., Lab, M. J., Scanning ion conductance microscopy of living cells. *Biophys. J*. 1997, 73, 653.
113. Shevchuk, A. I., Gorelik, J., Harding, S. E., Lab, M. J., Klenerman, D., Korchev, Y. E., Simultaneous measurement of Ca^{2+} and cellular dynamics: Combined scanning ion conductance and optical microscopy to study contracting cardiac myocytes. *Biophys. J*. 2001, 81, 1759.
114. Novak, P., Li, C., Shevchuk, A. I., Stepanyan, R., Caldwell, M., Hughes, S., Smart, T. G., Gorelik, J., Ostanin, V. P., Lab, M. J., Moss, G. W. J., Frolenkov, G. I., Klenerman, D., Korchev, Y. E., Nanoscale live-cell imaging using hopping probe ion conductance microscopy. *Nat. Methods* 2009, 6, 279.
115. Korchev, Y. E., Negulyaev, Y. A., Edwards, C. R., Vodyanoy, I., Lab, M. J., Functional localization of single active ion channels on the surface of a living cell. *Nat. Cell Biol*. 2000, 2, 616.
116. Mann, S. A., Hoffmann, G., Hengstenberg, A., Schuhmann, W., Dietzel, I. D., Pulse-mode scanning ion conductance microscopy—A method to investigate cultured hippocampal cells. *J. Neurosci. Methods* 2002, 116, 113.
117. Happel, P., Hoffmann, G., Mann, S. A., Dietzel, I. D., Monitoring cell movements and volume changes with pulse-mode scanning ion conductance microscopy. *J. Microscopy* 2003, 212, 144.
118. Mann, S. A., Meyer, J. W., Dietzel, I. D., Integration of a scanning ion conductance microscope into phase contrast optics and its application to the quantification of morphological parameters of selected cells. *J. Microscopy* 2006, 224, 152.
119. Gorelik, J., Zhang, Y., Shevchuk, A. I., Frolenkov, G. I., Sánchez, D., Lab, M. J., Vodyanoy, I., Edwards, C. R. W., Klenermann, D., Korchev, Y. E., The use of scanning ion conductance microscopy to image A6 cells. *Mol. Cell. Endocrinol*. 2004, 217, 101.
120. Gorelik, J., Ali, N. N., Sheikh Abdul Kadir, S. H., Lab, M., Stojkovic, P., Armstrong, L., Sviderskaya, E. V., Negulyaev, Y. A., Klenerman, D., Bennett, D. C., Lako, M., Harding, S. E., Stojkovic, M., Korchev, Y. E., Non-invasive imaging of stem cells by scanning ion conductance microscopy: Future perspective. *Tissue Eng*. 2008, 14, 311.
121. Shevchuk, A. I., Frolenkov, G. I., Sánchez, D., James, P. S., Freedman, N., Lab, M. J., Jones, R., Klenerman, D., Korchev, Y. E., Imaging proteins in membranes of living cells by high-resolution scanning ion conductance microscopy. *Angew. Chem. Int. Ed*. 2006, 45, 2212.
122. Korchev, Y. E., Gorelik, J., Lab, M. J., Sviderskaya, E. V., Johnston, C. L., Coombes, C. R., Vodyanoy, I., Edwards, C. R. W., Cell volume measurement using scanning ion conductance microscopy. *Biophys. J*. 2000, 78, 45.
123. Gorelik, J., Gu, Y., Spohr, H. A., Shevchuk, A. I., Lab, M. J., Harding, S. E., Edwards, C. R. W., Whitaker, M., Moss, G. W. J., Benton, D. C. H., Sánchez, D., Darszon, A., Vodyanoy, I., Klenerman, D., Korchev, Y. E., Ion channels in small cells and subcellular structures can be studied with a smart patch-clamp system. *Biophys. J*. 2002, 83, 3296.

124. Comstock, D. J., Elam, J. W., Pellin, M. J., Hersam, M. C., Integrated ultramicroelectrode-nanopipet probe for concurrent scanning electrochemical microscopy and scanning ion conductance microscopy. *Anal. Chem*. 2010, 82, 1270.
125. Takahashi, Y., Shevchuk, A. I., Novak, P., Murakami, Y., Shiku, H., Korchev, Y. E., Matuse, T., Simultaneous noncontact topography and electrochemical imaging by SECM/SICM featuring ion current feedback regulation. *J. Am. Chem. Soc*. 2010, 132, 10118.
126. Williams, C. G., Edwards, M. A., Colley, A. L., Macpherson, J. V., Unwin, P. R., Scanning micropipet contact method for high-resolution imaging of electrode surface redox activity. *Anal. Chem*. 2009, 81, 2486.
127. Bohni, H., Suter, T., Schreyer, A., Micro- and nanotechniques to study localised corrosion. *Electrochim. Acta* 1995, 40, 1361.
128. Suter, T., Bohni, H., Microelectrodes for studies of localized corrosion processes. *Electrochim. Acta* 1998, 43, 2843.
129. Suter, T., Bohni, H., A new microelectrochemical method to study pit initiation on stainless steels. *Electrochim. Acta* 1997, 42, 327.
130. Eng, L., Wirth, E., Suter, T., Bohni, H., Non-contact feedback for scanning capillary microscopy. *Electrochim. Acta* 1998, 43, 3029.
131. Ebejer, N., Schnippering, M., Colburn, A. W., Edwards, M. A., Unwin, P. R., Localized high resolution electrochemistry and multi-functional imaging: Scanning electrochemical cell microscopy (SECCM). *Anal. Chem*. 2010, 82, 9141–9154.
132. Casillas, N., James, P., Smyrl, W. H., A novel approach to combine scanning electrochemical microscopy and scanning photoelectrochemical microscopy. *J. Electrochem. Soc*. 1995, 142, L16–L18.
133. James, P., Casillas, N., Smyrl, W. H., Simultaneous scanning electrochemical and photoelectrochemical microscopy by use of a metallized optical fiber. *J. Electrochem. Soc*. 1996, 143, 3853–3865.
134. Shi, G., Garfias-Mesias, L. F., Smyrl, W. H., Preparation of a gold-sputtered optical fiber as a microelectrode for electrochemical microscopy. *J. Electrochem. Soc*. 1998, 145, 2011–2016.
135. Sosa, E., Cabrera-Sierra, R., Oropeza, M. T., Hernandez, F., Casillas, N., Tremont, R., Cabrera, C., Gonzaleza, I., Chemical characterization of corrosion films electrochemically grown on carbon steel in alkaline sour environment. *J. Electrochem. Soc*. 2003, 150, B530–B535.
136. Lee, J., Ye, H., Pan, S., Bard, A. J., Screening of photocatalysts by scanning electrochemical microscopy. *Anal. Chem*. 2008, 80, 7445–7450.
137. Jang, J. S., Yoon, K. Y., Xiao, X., Fan, F.-R. F., Bard, A. J., Development of a potential Fe_2O_3-based photocatalyst thin film for water oxidation by scanning electrochemical microscopy: Effects of Ag–Fe_2O_3 nanocomposite and Sn doping. *Chem. Mater*. 2009, 21, 4803–4810.
138. Lee, Y., Bard, A. J., Fabrication and characterization of probes for combined scanning electrochemical/optical microscopy experiments. *Anal. Chem*. 2002, 74, 3626–3633.
139. Maruyama, K., Ohkawa, H., Ogawa, S., Ueda, A., Niwa, O., Suzuki, K., Fabrication and characterization of a nanometer-sized optical fiber electrode based on selective chemical etching for scanning electrochemical/optical microscopy. *Anal. Chem*. 2006, 78, 1904–1912.
140. Fan, F.-R. F., Cliffel, D. E., Bard, A. J., Scanning electrochemical microscopy. 37. Light emission by electrogenerated chemiluminescence at SECM tips and their application to scanning optical microscopy. *Anal. Chem*. 1998, 70, 2941–2948.
141. Miao, W., Choi, J.-P., Bard., A. J., Electrogenerated chemiluminescence. 69: The tris(2,2′-bipyridine) ruthenium(II), ($Ru(bpy)_3^{2+}$)/tri-*n*-propylamine (TPrA) system revisited—A new route involving $TprA^+$ cation radicals. *J. Am. Chem. Soc*. 2002, 124, 14479–14486.
142. Maus, R. G., Wightman, R. M., Microscopic imaging with electrogenerated chemiluminescence. *Anal. Chem*. 2001, 73, 3993–3998.
143. Kanoufi, F., Cannes, C., Zu, Y., Bard, A. J., Scanning electrochemical microscopy. 43. Investigation of oxalate oxidation and electrogenerated chemiluminescence across the liquid–liquid interface. *J. Phys. Chem. B* 2001, 105, 8951–8962.
144. Zhou, H., Kasai, S., Matsue, T., Imaging localized horseradish peroxidase on a glass surface with scanning electrochemical/ chemiluminescence microscopy. *Anal. Biochem*. 2001, 290, 83–88.
145. Lei, R., Stratmann, L., Schäfer, D., Erichsen, T., Neugebauer, S., Li, N., Schuhmann, W., Imaging biocatalytic activity of enzyme–polymer spots by means of combined scanning electrochemical microscopy/ electrogenerated chemiluminescence. *Anal. Chem*. 2009, 81, 5070–5074.
146. Sheppard, C. J. R., Shotton, D. M., *Confocal Laser Scanning Microscopy*, BIOS Scientific Publishers Ltd., Oxford, U.K., 1997.

147. Rudd, N. C., Cannan, S., Bitziou, E., Ciani, I., Whitworth, A. L., Unwin, P. R., Fluorescence confocal laser scanning microscopy as a probe of pH gradients in electrode reactions and surface activity. *Anal. Chem*. 2005, 77, 6205–6271.
148. Cannan, S., Macklam, I. D., Unwin, P. R., Three dimensional imaging of proton gradients at microelectrode surfaces using confocal laser scanning microscopy. *Electrochem. Commun*. 2002, 4, 886–892.
149. Grime, J. M. A., Edwards, M. A., Rudd, N. C., Unwin, P. R., Quantitative visualization of passive transport across bilayer lipid membranes. *Proc. Natl. Acad. Sci. USA* 2008, 105, 14277–14282.
150. Boldt, F.-M., Heinze, J., Diez, M., Petersen, J., Börsch, M., Real-time pH microscopy down to the molecular level by combined scanning electrochemical microscopy/single molecule fluorescence spectroscopy. *Anal. Chem*. 2004, 76, 3473–3481.
151. Mukhopadhay, R., SECM meets fluorescence microscopy. *Anal. Chem*. 2004, 76, 224A.
152. Oyamatsu, D., Kanaya, N., Shiku, H., Nishizawa, M., Matsue, T., Electrochemical/photochemical formation of enzyme patterns on glass substrates using a scanning electrochemical/confocal microscope. *Sens. Actuators B* 2003, 91, 199–204.
153. Ku, S.-Y., Wong, K.-T., Bard. A. J., Surface patterning with fluorescent molecules using click chemistry directed by scanning electrochemical microscopy. *J. Am. Chem. Soc*. 2008, 130, 2392–2393.
154. Szunerits, S., Knorr, N., Calemczuk, R., Livache, T., New approach to writing and simultaneous reading of micropatterns: Combining surface plasmon resonance imaging with scanning electrochemical microscopy (SECM). *Langmuir* 2004, 20, 9236–9241.
155. Fortin, E., Defontaine, Y., Mailley, P., Livache, T., Szunerits, S., Micro-imprinting of oligonucleotides and oligonucleotide gradients on gold surfaces: A new approach based on the combination of scanning electrochemical microscopy and surface plasmon resonance imaging (SECM/SPR-i). *Electroanalysis* 2005, 17(5), 495–503.
156. Xiang, J., Guo, J., Zhou, F., Scanning electrochemical microscopy combined with surface plasmon resonance: Studies of localized film thickness variations and molecular conformation changes. *Anal. Chem*. 2006, 78, 1418–1424.
157. Xina, Y., Gaoa, Y., Guoa, J., Chena, Q., Xianga, J., Zhoua, F., Real-time detection of Cu^{2+} sequestration and release by immobilized apo-metallothioneins using SECM combined with SPR. *Biosens. Bioelectron*. 2008, 24, 369–375.
158. Wang, L., Kranz, C., Mizaikoff, B., Monitoring scanning electrochemical microscopy approach curves with mid-infrared spectroscopy: Toward a novel current-independent positioning mode. *Anal. Chem*. 2010, 82, 3132–3138.
159. Wang, L., Kowalik, J., Mizaikoff, B., Kranz, C., Combining scanning electrochemical microscopy with infrared attenuated total reflection spectroscopy for in situ studies of electrochemically induced processes. *Anal. Chem*. 2010, 82, 3139–3145.
160. Hillier, A. C., Ward, M. D., Scanning electrochemical mass sensitivity mapping of the quartz crystal microbalance in liquid media. *Anal. Chem*. 1992, 64, 2539–2554.
161. Cliffel, D. E., Bard, A. J., Scanning electrochemical microscopy. 36. A combined scanning electrochemical microscope-quartz crystal microbalance instrument for studying thin films. *Anal. Chem*. 1998, 70, 1993–1998.
162. Cliffel, D. E., Bard, A. J., Shinkai, S., Electrochemistry of *tert*-butylcalix[8]arene-C_{60} films using a scanning electrochemical microscope–quartz crystal microbalance. *Anal. Chem*. 1998, 70, 4146–4151.
163. Gollas, B., Bartlett, P. N., Denuault, G., An instrument for simultaneous EQCM impedance and SECM measurements. *Anal. Chem*. 2000, 72, 349–356.
164. Hess, C., Borgwarth, K., Heinze, J., Integration of an electrochemical quartz crystal microbalance into a scanning electrochemical microscope for mechanistic studies of surface patterning reactions. *Electrochim. Acta* 2002, 45, 3725–3736.
165. Shin, M., Jeon, I. C., Frequency–distance responses in SECM-EQCM—A novel method for calibration of the tip–sample distance. *Bull. Kor. Chem. Soc*. 1998, 19, 1227–1232.
166. Gabrielli, C., Joiret, S., Keddam, M., Perrot, H., Portail, N., Rousseau, P., Vivier, V., Development of a coupled SECM-EQCM technique for the study of pitting corrosion on iron. *J. Electrochem. Soc*. 2006, 153, B68–B74.
167. Tu, X., Xie, Q., Xiang, C., Zhang, Y., Yao, S., Scanning electrochemical microscopy in combination with piezoelectric quartz crystal impedance analysis for studying the growth and electrochemistry as well as microetching of poly(*o*-phenylenediamine) thin films. *J. Phys. Chem. B* 2005, 109, 4053–4063.
168. Hsua, C.-Y., Vasanthaa, V. S., Kuo-Chuan Ho, K.-C., A study of ion exchange at the poly(butyl viologen)-electrolyte interface by SECM. *Electrochim. Acta* 2008, 53, 6244–6251.

169. Díaz-Ballote, L., Alpuche-Aviles, M., Wipf, D. O., Fast-scan cyclic voltammetry–scanning electrochemical microscopy. *J. Electroanal. Chem*. 2007, 604, 17–25.
170. Schrock, D. S., Wipf, D. O., Baur, J. E., Feedback effects in combined fast-scan cyclic voltammetry–scanning electrochemical microscopy. *Anal. Chem*. 2007, 79, 4931–4941.
171. Schrock, D. S., Baur, J. E., Chemical imaging with combined fast-scan cyclic voltammetry–scanning electrochemical microscopy. *Anal. Chem*. 2007, 79, 7053–7061.
172. Mahé, E., Electrochemistry in confined microsystems. Part 1. CV-SECM of reversible system at a confined disk ultramicroelectrode. *Electrochim. Acta* 2007, 52, 5018–5029.

18 Additional Recent Applications and Prospects

Allen J. Bard, Fernando Cortés Salazar, and Hubert H. Girault

CONTENTS

18.1 New SECM Probes and New Fabrication Methods 636
18.2 New SECM Tip Operation Modes 639
18.3 Additional Hybrid Techniques 640
18.3.1 SECM-MS 640
18.3.2 SKP-SECM 641
18.3.3 SECM-ECL 642
18.3.4 SECM-PEC 642
18.4 Novel Interfaces and Nonstandard Conditions 642
18.5 Concluding Remarks 643
Acknowledgments 644
References 644

As shown in the previous chapters, scanning electrochemical microscopy (SECM) has become a popular and mature technique for the spatial characterization of surface reactivity and mass fluxes at solid–liquid, liquid–liquid, and liquid–gas interfaces.[1–3] A wide range of applications, extending from imaging-patterned sensor surfaces,[4] measuring substance uptake and release from biological cells (see Chapter 12),[5] investigating very fast electrochemical reactions,[6] studying local corrosion (see Chapter 14),[7] screening electrocatalysts and photocatalysts (see Chapter 16),[8] forensic sciences,[9] and surface modification (see Chapter 15), demonstrate the versatility of the technique. Additionally, SECM has been successfully applied to samples with a spatial resolution ranging from nanometer to micrometer and to the study of a wide range of kinetic processes, made possible by using different electrode sizes and tip–substrate spacings.[10–12] Finally, SECM has been coupled with different techniques to complement and confirm the information extracted by SECM.[13] These applications have been discussed in detail in this book, and in the present chapter we would like to explore new applications and prospects.

The widespread use of SECM has attracted not only the interest of researchers, but also of enterprises that see in the manufacturing of SECM equipment an economic opportunity. Commercial SECM instrumentation is discussed in Chapter 2 and its availability has permitted wider SECM usage in both academia and industry, by researchers who are not specialists in this technique.

Although SECM is a mature technique, there is still room for further developments in different directions, such as new SECM probes and new fabrication methods, new SECM operation modes, combination of SECM with other techniques, and the application of SECM to novel interfaces and systems under extreme conditions. These are discussed in the following sections.

18.1 NEW SECM PROBES AND NEW FABRICATION METHODS

There has been continued progress in the fabrication of tips with nanometer radii as described in Chapter 3 and their utilization in SECM. Such tips can be very fragile and difficult to renew by polishing without significantly increasing their radii. This difficulty with polishing has also led to techniques using a hydrofluoric acid (HF) treatment for the final exposure.[14] Moreover, there are few approach curves or quantitative studies with nanometer tips. This is clearly an area where significant advances can be made, with important application, for example, in studies of electrode surfaces and in biological systems.

There has also been the fabrication of probes on flexible substrates, called soft stylus probes, which allow scanning in a contact mode that is especially useful in the SECM imaging of large area samples. Soft stylus probes are fabricated in flexible materials such as polyethylene terephthalate (PET) films where a carbon track is prepared, for example, by machining a microchannel with a UV laser and subsequent filling with carbon ink. After a curing process (i.e., 80°C for 1 h), the microchannel is closed by a thin Parylene coating. Finally, the probe is cut in a "V" shape and a carbon microelectrode is obtained by exposing the tip of the probe by laser ablation, mechanical polishing, or blade cutting (see Figure 18.1).[15–17]

Soft stylus probes provide steady-state currents as classical microdisk electrodes. When performing approach curves over both insulating and conductive surfaces, typical behavior for negative and positive feedback, respectively, has been observed (see Figure 18.2a). Notice that a new probe–substrate coordinate "h_P" has been introduced to differentiate sample penetration ($d \leq 0$) and probe bending ($h_P \leq 0$), when the probe is in physical contact with the substrate. For more details, see Ref. [17]. Moreover, after contacting the substrate ($h_P \leq 0$), the probe–substrate distance and the probe response are determined by the degree of probe bending and the thickness of the polymer film enclosing the carbon track. As a consequence, the recorded current remains constant upon contact between the probe and the substrate as well as the current contrast obtained between conductive and insulating regions. Indeed, by scanning over a substrate with an angle of 70° and over the very thin Parylene coating film, the direction and degree of the probe bending can be controlled and a very close probe–substrate position achieved (see Figure 18.1).

A specific characteristic of soft stylus probes is operation at an almost constant probe–substrate distance, as the flexible probe can accommodate to the topography of the substrate.[16,17] Moreover, if the probe is sufficiently flexible, it is not damaged by the sample roughness, and if the probe is softer

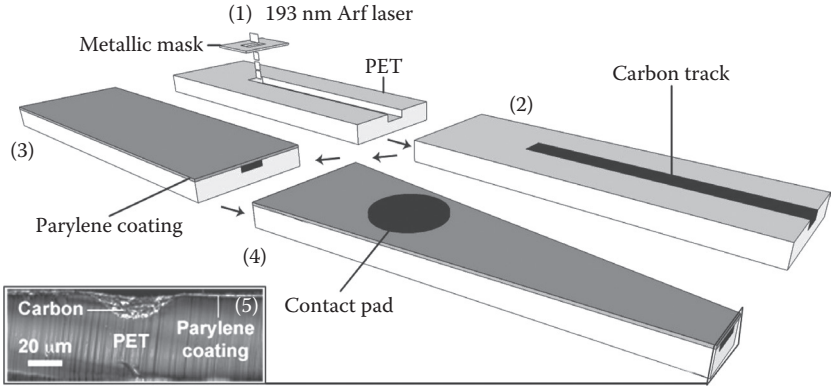


FIGURE 18.1 Schematic representation of a microfabrication process of soft stylus probes. (1) Microchannel drilling by laser ablation, (2) microchannel filling with carbon ink and ink curing at 80°C for 1 h, (3) Parylene coating, (4) electrical contact formation and final shaping of the probe, and (5) optical picture of the carbon microelectrode obtained after blade cutting. Polyethylene terephthalate (PET). (Inset No. 5 was taken from Cortés-Salazar, F. et al., *Anal. Chem.*, 82, 10037, 2010. With permission.)

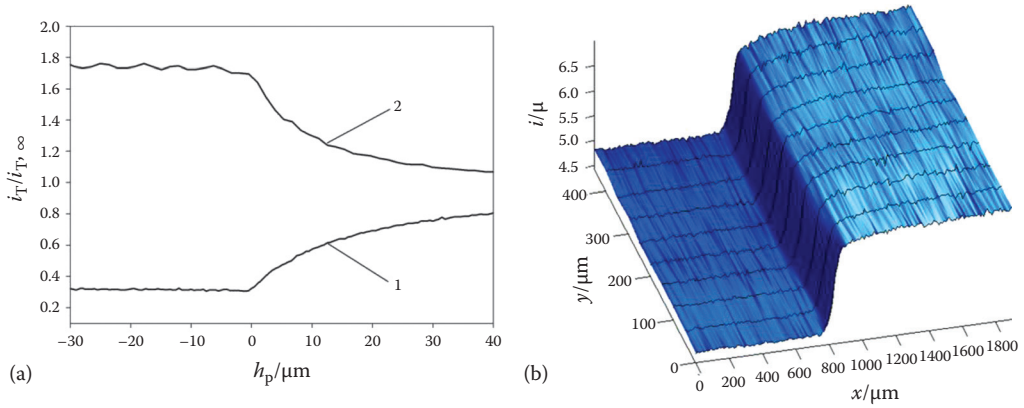


FIGURE 18.2 (a) Experimental approach curves with a soft stylus probe over insulating glass (1) and unbiased gold electrode (2) in 2 mM $FcCH_2OH$ and 0.1 M KNO_3. $E_T = 0.35$ V, translation rate $v_T = 0.5$ μm/s. (b) SECM image in a contact regime of a partially gold-covered glass surface obtained by using a soft stylus probe. Imaging conditions: 2.1 mM $FcCH_2OH$, 0.1 M KNO_3. Working electrode potential $E_T = 0.3$ V, step sizes in x- and y- directions were 10 and 50 μm, respectively. Translation rate $v_T = 10$ μm/s. (From Cortés-Salazar, F. et al., *Anal. Chem*., 83, 1493, 2011. With permission.)

than the sample, the latter is not damaged by the contact scanning mode. As shown in Figure 18.2b, surface reactivity imaging of a gold-covered glass border is possible when scanning in the contact mode. Experiments are under development to prove the capability to image soft samples in contact mode without modifying physically the substrate, such as the protective properties of self-assembled monolayers (SAMs) deposited over gold films. Rough and tilted samples can be scanned in the contact mode avoiding topographic artifacts.

For situations where the sample cannot be imaged immersed in an electrolyte, the fountain pen probe has been suggested.[15] The fountain pen probe is a soft stylus in which an additional open microchannel is placed parallel to the carbon track but on the opposite side on the PET film (Figure 18.3). The open microchannel is employed for flowing a redox mediator solution from a reservoir to the tip of the probe allowing SECM experiments in microenvironments or over surfaces that were previously dry (see Figure 18.3).

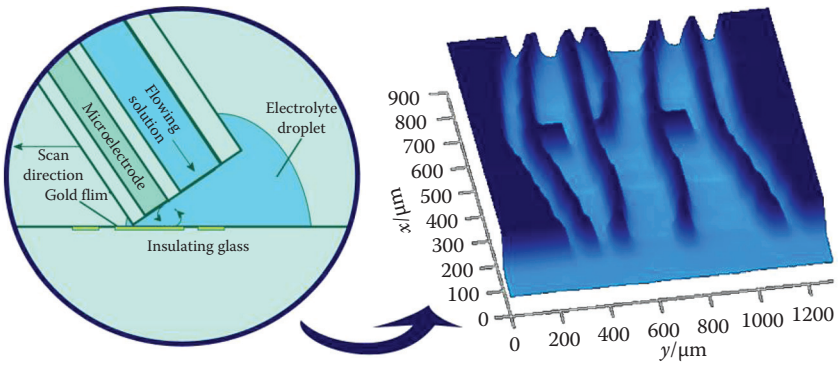


FIGURE 18.3 Schematic representation of the fountain pen probe principle for surface reactivity imaging and SECM in contact mode of a gold-on-glass EPFL logo. The fountain pen was lifted off after each forward scan by a stroke height of 200 μm and placed back at the original vertical position of the scanning but shifted by 20 μm in y-direction. $h_P = -30$ μm, $E_T = 0.4$ V, flow rate = 20 mL/h, step size = 20 μm, and translation rate $v_T = 20$ μm/s. 2.6 mM $FcCH_2OH$ with 0.1 M KNO_3. (From Cortés-Salazar, F. et al., *Anal. Chem*., 83, 1493, 2011. With permission.)

The fountain pen probe is a microfluidic device that integrates a two-electrode cell where a counter-reference electrode is placed inside the open microchannel, and the electrical connection is completed by the electrolyte solution. By using the fountain pen probe in contact mode, it is then possible to perform SECM imaging of heterogeneous surfaces, as the one shown in Figure 18.3. This image was obtained over a gold-on-glass EPFL logo by simply flowing a solution of a redox mediator to the tip of the probe. The total time for taking this image was 2 h 15 min, without problems from solvent evaporation. The major drawback of the fountain pen was the deposition of electrolyte material over the sample after scanning, which represents a potential source of sample contamination. To address this factor, a push–pull probe has been developed in which a second open microchannel is employed for aspirating the solution that is delivered to the substrate.[18] This new push–pull probe is designed to allow the coupling of SECM with complementary analytical techniques.

Flexible probes might also be useful in multiplexing the SECM measurements with multitip arrays; this could decrease the times required for imaging, especially of large samples.[16] Similar approaches have been reported previously by Meyer et al.[19] and Barker et al.[20] for fast SECM imaging with two- and one-dimensional array of microelectrodes, respectively. So far, there have been few applications reported with multitip arrays (similarly with scanning tunneling microscopy), probably because of the difficulty of making arrays where the distance of each individual tip is either constant or adjustable and the considerable instrumental requirements for their utilization. Also, there can be complications related to the assembling and alignment of the whole-sample electrochemical cell setup, diffusion layer overlapping among the neighboring electrodes in the planar array, and difficulties in the regeneration of the electrodes. The fabrication of the linear array of microelectrodes on a flexible array is based on the same procedure developed for preparing the soft stylus probe, but with the difference that instead of one microelectrode, 8 or 32 independent microelectrodes can be prepared. Similar to soft stylus probes, linear arrays of microelectrodes yield stable steady-state currents. However, differences between the steady-state currents recorded among all the electrodes were observed most likely due to the different electrode areas produced during the microfabrication and the electrode exposure processes.[16]

A linear array of microelectrodes allows one to image large sample areas in less time, such as a full human fingerprint shown in Figure 18.4a.[21] This image was taken based on a SECM protein detection method,[22] where a fingerprint is wetted with a protein solution and then transferred to a polyvinylidene difluoride (PVDF) membrane. Afterward, the protein-printed fingerprint is tagged with benzoquinone molecules and is detected by the mediated reduction of benzoquinone adducts with ferrocyanide (see Figure 18.4b). This image was taken in a total time of 5 h; this shows the possibility of SECM as a versatile surface characterization tool for not only rough and tilted, but also large, samples.[21]

It should be possible to modify or functionalize the material of the electrode, for example, as ion-selective electrodes or dual electrodes, for simultaneous potentiometric or amperometric monitoring of chemical or electrochemical reaction processes. Figure 18.5 shows the calibration curve of a soft stylus that has been functionalized to detect amperometrically H_2O_2. The functionalization of this soft stylus is based on the modification of screen-printed electrodes reported by Turkusic et al.[23] where the carbon paste employed for electrode preparation was mixed with MnO_2 nanoparticles that react chemically with H_2O_2 present in the media. H_2O_2 can be thus spatially quantified by recording the current produced during the electrochemical regeneration of MnO_2 nanoparticles.[24]

For the batch preparation of multitip arrays, photolithography techniques, which have been used in the preparation of microprobes for atomic force microscopy (AFM) and SECM-AFM,[25] are under development (Figure 18.6).[26] The advantages of photolithography techniques are the high reproducibility and the opportunity of preparing several probes in the same run, thus reducing costs and preparation time.

The use of new SECM probes with geometries that differ from microdisk electrodes is not a limitation in terms of quantitative studies, since one can employ numerical methods to treat such cases (Chapter 5).

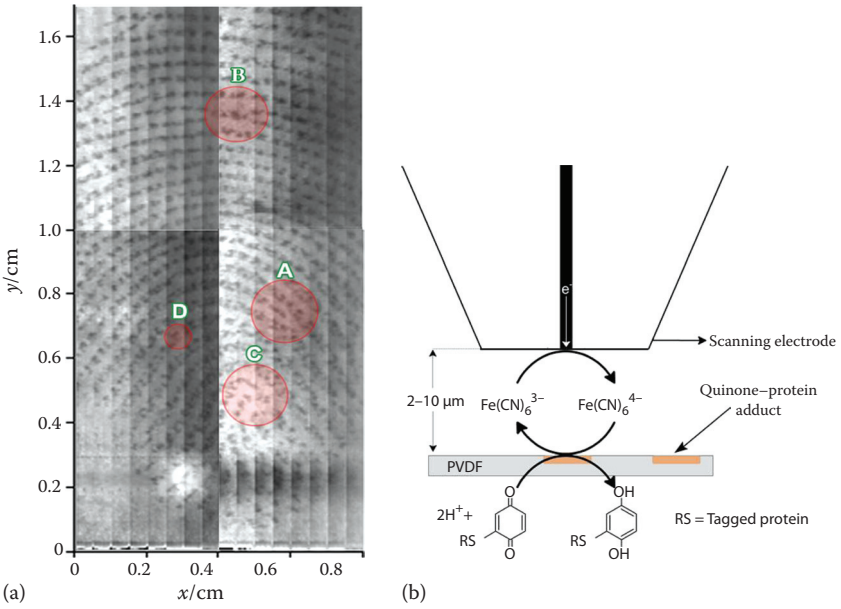


FIGURE 18.4 (a) SECM feedback image of a human fingerprint developed by benzoquinone tagging with an array of eight microelectrodes of 500 µm interelectrode spacing. $E_T = -0.35$ V, step size = 50 µm, and translation rate $v_T = 50$ µm/s (acquisition time = 5 h 12 min) in 2 mM $K_3[Fe(CN)_6]$ with 0.1 M KCl. (b) Schematic representation of the human fingerprint detection principle by the mediated reduction of protein–quinone adducts. (From Cortés-Salazar, F. et al., *Anal. Chem.*, 83, 1493, 2011. With permission.)

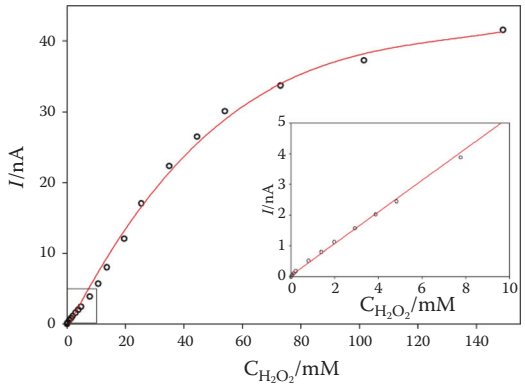


FIGURE 18.5 Amperometric detection curve of H_2O_2 at different concentrations with a functionalized soft stylus probe. (From Pei Yu, G. et al., 2011, In preparation.)

18.2 NEW SECM TIP OPERATION MODES

In most SECM experiments, the tip is held at a constant potential in an amperometric mode or scanned in the cyclic voltammetry (CV) mode.[27] The substrate can also be subjected to various potential treatments. Studies involving transients or time-dependent signals are especially useful in obtaining information about adsorbed intermediates or products, as discussed in Chapter 16. Another time-dependent technique involves an AC signal applied to the tip, a form of electrochemical spectroscopy impedance (EIS).[28] Examples of this approach have been discussed in Chapter 14 as applied to studies of the mechanism of corrosion processes. For example, in the

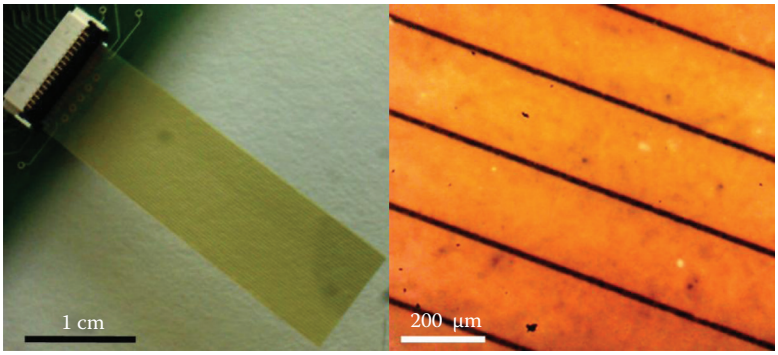


FIGURE 18.6 Optical pictures of (a) a linear array of 32 microelectrodes and (b) Pt microelectrodes prepared by photolithography and coated with Parylene coating. (From Momotenko, D. et al., 2011, In preparation.)

work of Eckhard et al.,[28] visualization of local protective coating defects and pitting corrosion on 304 stainless steel was possible. Although the AC mode of SECM dates back to the earliest work,[29] its utilization in SECM has been more limited. Growth in this field is expected.

An important issue in SECM, and in UME techniques in general, is the sensitivity of the technique and its application for detecting small concentrations (e.g., in the μM range). This is often an important consideration in studies of biological systems, like living cells. At these concentrations, techniques like CV are less useful, and detection by differential pulse voltammetry (DPV) or square wave voltammetry (SWV) may be useful. So far, little has been done in SECM with these approaches, which are particularly good for decreasing the contribution of charging current.

Most SECM imaging is carried out at a constant height mode, or less frequently, constant current mode, where neither the tip material nor the insulator makes contact with the sample. Recently, there have been studies where the tip is made to contact the sample surface. In the intermittent contact mode (IC-SECM), the tip is oscillated in the *z*-direction, as in tip-position modulation (Chapter 2), except that it makes periodic contact with the surface (as in tapping mode AFM).[30] The oscillation is damped when the tip encounters the surface and this assists in determining the tip–substrate distance. With tips made with soft polymeric materials, as described earlier, it is possible to maintain an almost constant probe–substrate distance by scanning in an insulator contact mode. The probe–substrate distance is defined by the polymeric film thickness that covers the carbon track and by the contact angle established when the probe is pressed against the substrate. A concern with scanning in the contact mode is possible damage to the sample, especially for soft materials such as biological samples.

18.3 ADDITIONAL HYBRID TECHNIQUES

18.3.1 SECM-MS

In Chapter 17, the combination of SECM with other techniques has been presented. Hybrid systems, like SECM-AFM, are useful for obtaining more information about processes at an interface. In addition to these techniques, SECM can be combined with other methodologies that allow further sample analysis and afford the extraction of sample structural information, for instance, by coupling SECM with mass spectrometry (MS). Several approaches for scanning mass spectrometry have been reported for the spatial detection of different species at solid–liquid,[31] liquid–liquid,[32] or air–solid[33] interface. Both chemical[33,34] and electrochemical[31] reactions have been characterized by these means. These approaches are based on the use of concentric capillaries that allow the flux of carrier gas or redox components to the substrate (i.e., through the outer capillary) and the extraction

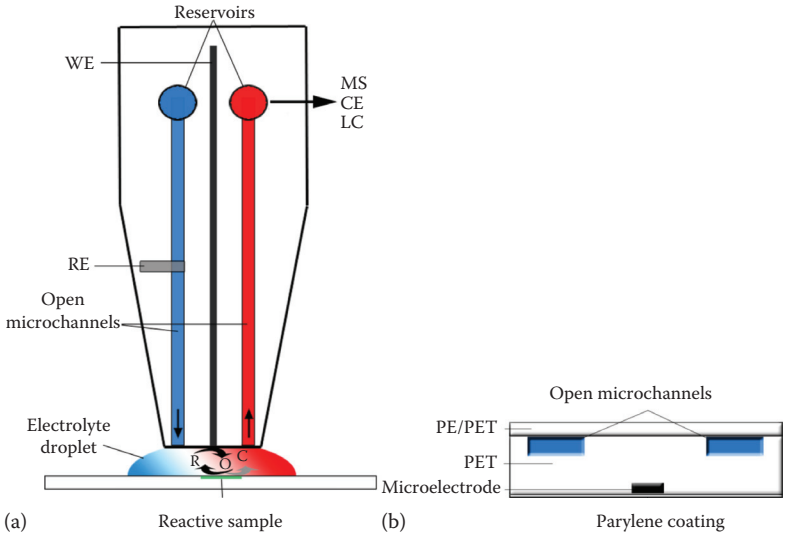


FIGURE 18.7 (a) Schematic representation of a push–pull probe for SECM, where the solution is connected with a secondary analytical technique such as mass spectrometry (MS), capillary electrophoresis (CE), or liquid chromatography (LC). (b) Front view of a push–pull probe. Polyethylene/polyethylene terephthalate (PE/PET). Working electrode (WE) and reference/counter electrode (RE). (From Momotenko, D. et al., *Anal Chem*., 83, 5275, 2011. With permission.)

of localized species over the sample surface or the product of a chemical reaction (i.e., through the inner capillary). However, scanning mass spectrometry probes can neither control nor survey in situ electrochemical reactions over the sampled surface because of the lack of an integrated electrode. As a consequence, no electrochemical information is collected to complement the MS data. To couple SECM and MS, new microfluidic probes have to be developed such as the push–pull probe,[18] which contains a microelectrode and two open microchannels for flowing and aspiration of redox mediator solution to and from the tip of the probe. Moreover, such a push–pull system might also be useful for surface patterning by reacting (electro)chemically one or two different components at the tip of the probe, similar to the capillary-based droplet-cell concept reported recently by Chen et al.[35] The advantages of using the push–pull probe are the feasibility for introducing more chemicals into the reaction and the lower possibilities of capillary or substrate destruction when physical contact between them is established.

In addition, one can envisage the coupling of SECM with other analytical techniques such as liquid chromatography (LC) or capillary electrophoresis (CE). Therefore, relevant analytes detected in a complex sample by SECM can be extracted and separated by a secondary analytical technique. As a consequence, online monitoring of electrochemical and chemical surface information can be imagined (see Figure 18.7).

18.3.2 SKP-SECM

Another interesting coupling of SECM is with a scanning Kelvin probe (SKP).[36] The SKP method allows the simultaneous determination of topography and potential distribution (i.e., contact potential difference and working function, if calibrated) of a surface. The latter is an important parameter in corrosion science, for instance, where the surface potential distribution might be more important than the surface composition since the former will determine the most probable locations for corrosion.[37] In addition to corrosion studies,[38,39] SKP has been applied to semiconductor dopant profiles,[40] biological surface potential,[41] and forensic science.[42] Therefore, the coupling of SKP and SECM

provides more information not only about electrochemical surface reactivity, but also about surface topography to achieve a constant working distance. Recently, Maljusch et al.[36] used SKP-SECM for studying the contact potential difference of Cu-rich intermetallic compounds on aluminum alloys and their catalytic activity for oxygen reduction.

18.3.3 SECM-ECL

Electrogenerated chemiluminescence (ECL) involves the production of an emitting species by radical ion annihilation (electron transfer) in a nonaqueous solvent, or reaction of an electrogenerated species with an appropriate coreactant.[43] While probing the details of the interesting ECL reactions seems like a natural application of SECM, few studies have appeared. Experiments with coreactants, for example, of the reaction of oxidized Ru complexes in benzonitrile with oxalate in an aqueous phase to generate light[44] are straightforward, since these are not susceptible to side reactions with water or oxygen, but radical annihilation reactions need to be carried out in an inert atmosphere (Ar) glove box. This involves not only placing the SECM scanning stage in the glove box, but also the ECL radiation measuring device. One motivation for such studies is the possibility of measuring the rate of the homogeneous reaction by generating one reactant, for example, R^+, at one tip and the counter reactant, R^-, at a facing tip so the reaction is carried out in a pL volume, as described in Chapter 7.[45] While measurements of the currents in such an arrangement are insensitive to the kinetics, simultaneous measurements of the emitted light are more informative. Recently, such measurements were carried out for rubrene and $Ru(bpy)_3^{2+}$ and a simulation of the system with generation of one reactant at the tip and the other at the substrate.[46] ECL approach curves (emission vs. distance), in addition to the usual current vs. distance curves, can provide information about the kinetics of the reaction in the interelectrode gap.

18.3.4 SECM-PEC

Current interest in solar energy and searches for new materials for photoelectrochemical (PEC) applications suggests that SECM will find wider use in this field. Earlier work in this area has been discussed in Chapter 16, where rapid fabrication of arrays of materials and their screening in a modified SECM is described. In addition to these studies, SECM should be useful in examination of intermediates in the PEC reaction, that is, at a semiconductor material under irradiation, by using the surface interrogation (SI) approach, used for electrocatalysts (Chapter 16) for PEC as well. In a first study of this kind,[47] a TiO_2 layer under irradiation (the substrate) was examined by generating $IrCl_6^{3-}$ at the tip and studying the transient feedback as a result of reaction with photogenerated hydroxyl radicals. Measurements of the rate constants of the reaction of hydroxyl radical in a dimerization and with added methanol were also reported.

In addition to the previously mentioned synergetic combinations of SECM, additional hybrid SECM versions will be developed and applied in the coming years. Such techniques provide complementary information to that extracted by SECM. Not only will this allow imaging in more than one mode but also a more complete quantitative understanding of phenomena taking place at an interface.

18.4 NOVEL INTERFACES AND NONSTANDARD CONDITIONS

Chapters 8 and 13 reviewed the application of SECM to the study of charge and electron transfer at the liquid–liquid and solid–liquid interfaces, respectively. Most studies have used molecular mediators (Chapter 1). However, there is a continued interest in nanoparticles, for example, of metals and semiconductors. These can also be studied by SECM. For example, SECM was used to determine the rate of electron transfer for gold monolayer-protected clusters (MPCs) as a function of the surface thiol group chain length.[48] Such studies are more difficult than with molecular mediators because

of the smaller diffusion coefficients and concentrations involved with nanoparticles. However, by using electrocatalytic amplification techniques, even single nanoparticle collisions with the UME tip can be seen,[49] and studies with IrO_2 nanoparticles showing collision frequency (rather than current) as a function of *d* have produced analogous negative feedback approach curves.[50]

New systems composed of nonconventional phases such as water or organic solvents can be explored as well. As shown in Chapter 6, SECM studies at the solid–ionic liquid interfaces have been performed, since ionic liquids can be used in electrochemical experiments as both media and supporting electrolyte. Additionally, depending on the ionic liquid composition, properties like hydrophobicity and chemical lability can be tuned. The major drawback that ionic liquids present to electrochemistry is their high viscosity, which slows down the diffusional mass transport; the charge transfer process itself takes place at a liquid–liquid interface (Chapter 6). Thanks to the fact that microelectrodes provide a faster mass transport than macroelectrodes, the viscosity effects in ionic liquids can be overcome, as shown by Lovelock et al.[51] By employing ionic liquids as media and supporting electrolyte, new SECM experiments can be explored, for example, the study of heterogeneous electron transfer reactions at liquid–ionic liquid interfaces.

Parameters such as pressure and temperature have not usually been considered as significant variables in SECM experiments. However, as recently pointed out by Gründler et al.[52] and others, thermoelectrochemistry is a branch of electrochemistry that has not received too much attention despite the special benefits that high temperatures could bring to mass transport processes and slow kinetic reactions. Schuhmann et al.[53] also highlighted that temperature plays an important role on many properties studied by SECM that present a strong influence of the temperature, such as enzymatic activity. By varying the temperature in a controlled way, Arrhenius type plots can be obtained showing the influence of the temperature on the local activity of catalysts, for example.[53] However, for controlled temperature experiments in SECM, one must consider the material properties (e.g., chemical stability and thermal expansion coefficient) in designing the electrochemical cell and positioning system to avoid contamination or material mismatch.[54,55] Moreover, a special design is needed to precisely control and measure the temperature in the electrochemical cell.[53] It is more challenging to work at temperatures and pressures above the critical point of the liquid of interest, where the fluid properties resembles both liquid and gas phases. Supercritical fluids have been extensively applied for liquid–liquid extraction processes, since they can replace organic solvents. Electrode reactions taking place in near- and supercritical fluids have been explored, showing the feasibility of electrochemical reduction or oxidation of nonpolar organic compounds that dissolve better in near-critical water,[56] or the feasibility to study electrochemical processes over a wider potential window.[57] By applying SECM to such systems, a better understanding of electron and charge transfer reactions taking place at high temperatures and pressures might be achieved. However, SECM experiments in supercritical fluids will require careful consideration of the material properties of the UME and the cell materials to avoid destruction under these extreme conditions.[54,55,58] Moreover, controlling the motion of the UME tip within a practical supercritical liquid cell will not be simple.

18.5 CONCLUDING REMARKS

During the 10 years since the first edition of this book, we have witnessed significant evolution of SECM for qualitative and quantitative surface reactivity characterization and patterning. It has also become an indispensible tool in electrochemistry. Evidence of this assertion is the increase in the number of chapters of the present book in comparison to the first edition. The new chapters contain further developments of previous SECM research areas that because of their relevance and progress merit an additional chapter. Other new areas have been opened recently thanks to extensions in instrumentation and new applications. One can expect in the next 10 years to see a continued growth of the SECM applications presented in this book and the emergence of new ones that will broaden even further the scope of this technique.

ACKNOWLEDGMENTS

Fernando Cortés Salazar and Hubert H. Girault thank PeiYu Ge and Dmitry Momotenko for providing the results shown in Figures 18.5 and 18.6, respectively, as well as the Fonds National Suisse pour la Recherche Scientifique (Grant No. 20PA21_121570/1) for the financial support provided to the project "High-throughput SECM imaging." The support of the National Science Foundation (CHE-0808927) to Allen J. Bard for our work in the area of SECM was vital in the development of this technique.

REFERENCES

1. Engstrom, R. C., Weber, M., Wunder, D. J., Burgess, R., Winquist, S. Measurements within the diffusion layer using a microelectrode probe. *Analytical Chemistry* 1986, 58, 844–848.
2. Liu, H. Y., Fan, F. R. F., Lin, C. W., Bard, A. J. Scanning electrochemical and tunneling ultramicroelectrode microscope for high-resolution examination of electrode surfaces in solution. *Journal of the American Chemical Society* 1986, 108, 3838–3839.
3. Barker, A. L., Gonsalves, M., MacPherson, J. V., Slevin, C. J., Unwin, P. R. Scanning electrochemical microscopy: Beyond the solid/liquid interface. *Analytica Chimica Acta* 1999, 385, 223–240.
4. Wittstock, G., Hesse, R., Schuhmann, W. Patterned self-assembled alkanethiolate monolayers on gold. Patterning and imaging by means of scanning electrochemical microscopy. *Electroanalysis* 1997, 9, 746–750.
5. Yasukawa, T., Kaya, T., Matsue, T. Characterization and imaging of single cell with scanning electrochemical microscopy. *Electroanalysis* 2000, 12, 653–659.
6. Sun, P., Mirkin, M. V. Kinetics of electron-transfer reactions at nanoelectrodes. *Analytical Chemistry* 2006, 78, 6526–6534.
7. Fushimi, K., Seo, M. Trial for evaluation of heterogeneity of passive film on iron by a scanning electrochemical microscope. *Zairyo to Kankyo* 1997, 46, 797–803.
8. Walsh, D. A., Fernandez, J. L., Bard, A. J. Rapid screening of bimetallic electrocatalysts for oxygen reduction in acidic media by scanning electrochemical microscopy. *Journal of the Electrochemical Society* 2006, 153, E99–E103.
9. Zhang, M., Girault, H. H. SECM for imaging and detection of latent fingerprints. *Analyst* 2009, 134, 25–30.
10. Macpherson, J. V., Unwin, P. R. Combined scanning electrochemical–atomic force microscopy. *Analytical Chemistry* 2000, 72, 276–285.
11. Pust, S. E., Salomo, M., Oesterschulze, E., Wittstock, G. Influence of electrode size and geometry on electrochemical experiments with combined SECM-SFM probes. *Nanotechnology* 2010, 21, 105709.
12. Fernandez, J. L., Walsh, D. A., Bard, A. J. Thermodynamic guidelines for the design of bimetallic catalysts for oxygen electroreduction and rapid screening by scanning electrochemical microscopy. M-Co (M: Pd, Ag, Au). *Journal of the American Chemical Society* 2005, 127, 357–365.
13. Zhao, X., Petersen, N. O., Ding, Z. Comparison study of live cells by atomic force microscopy, confocal microscopy, and scanning electrochemical microscopy. *Canadian Journal of Chemistry* 2007, 85, 175–183.
14. Aoki, K., Zhang, C., Chen, J., Nishiumi, T. Fabrication of glass-coated electrodes with nano- and micrometer size by means of dissolution with HF. *Electrochimica Acta* 2010, 55, 7328–7333.
15. Cortés-Salazar, F., Lesch, A., Momotenko, D., Busnel, J.-M., Wittstock, G., Girault, H. H. Fountain pen for SECM. *Analytical Methods* 2010, 2, 817–823.
16. Cortés-Salazar, F., Momotenko, D., Lesch, A., Wittstock, G., Girault, H. H. Soft microelectrode linear array for SECM. *Analytical Chemistry* 2010, 82, 10037–10044.
17. Cortés-Salazar, F., Traeuble, M., Li, F., Busnel, J.-M., Gassner, A., Hojeij, M., Wittstock, G., Girault, H. H. Soft stylus probes for scanning electrochemical microscopy. *Analytical Chemistry* 2009, 81, 6889–6896.
18. Momotenko, D., Cortés-Salazar, F., Lesch, A., Wittstock, G., Girault, H. H. Microfluidic push–pull probe for scanning electrochemical microscopy. *Analytical Chemistry* 2011, 83, 5275–5282.
19. Meyer, H., Drewer, H., Gründig, B., Cammann, K., Kakerow, R., Manoli, Y., Mokwa, W., Rospert, M. Two-dimensional imaging of O_2, H_2O_2, and glucose distributions by an array of 400 individually addressable microelectrodes. *Analytical Chemistry* 1995, 67, 1164–1170.

20. Barker, A. L., Unwin, P. R., Gardner, J. W., Rieley, H. A multi-electrode probe for parallel imaging in scanning electrochemical microscopy. *Electrochemistry Communications* 2004, 6, 91–97.
21. Cortés-Salazar, F., Momotenko, D., Girault, H. H., Lesch, A., Wittstock, G. Seeing big with scanning electrochemical microscopy. *Analytical Chemistry* 2011, 83, 1493–1499.
22. Cortés-Salazar, F., Busnel, J.-M., Li, F., Girault, H. H. Adsorbed protein detection by scanning electrochemical microscopy. *Journal of Electroanalytical Chemistry* 2009, 635, 69–74.
23. Turkusic, E., Kalcher, J., Kahrovic, E., Beyene, N. W., Moderegger, H., Sofic, E., Begic, S., Kalcher, K. Amperometric determination of bonded glucose with an MnO_2 and glucose oxidase bulk-modified screen-printed electrode using flow-injection analysis. *Talanta* 2005, 65, 559–564.
24. Pei Yu, G., Cortés-Salazar, F., Girault, H. H. Spatially hydrogen peroxide detection with a functionalized soft stylus probe. 2011, In preparation.
25. Shin, H., Hesketh, P. J., Mizaikoff, B., Kranz, C. Development of wafer-level batch fabrication for combined atomic force-scanning electrochemical microscopy (AFM-SECM) probes. *Sensors and Actuators, B: Chemical* 2008, 134, 488–495.
26. Momotenko, D., Cortés-Salazar, F., Lesch, A., Wittstock, G., Girault, H. H. High-throughput SECM imaging with photolithography fabricated probes. 2011, In preparation.
27. Diaz-Ballote, L., Alpuche-Aviles, M., Wipf, D. O. Fast-scan cyclic voltammetry-scanning electrochemical microscopy. *Journal of Electroanalytical Chemistry* 2007, 604, 17–25.
28. Eckhard, K., Erichsen, T., Stratmann, M., Schuhmann, W. Frequency-dependent alternating-current scanning electrochemical microscopy (4D AC-SECM) for local visualisation of corrosion sites. *Chemistry—A European Journal* 2008, 14, 3968–3976.
29. Bard, A. J., Fan, F. R. F., Kwak, J., Lev, O. Scanning electrochemical microscopy. Introduction and principles. *Analytical Chemistry* 1989, 61, 132–138.
30. McKelvey, K., Edwards, M. A., Unwin, P. R. Intermittent contact-scanning electrochemical microscopy (IC-SECM): A new approach for tip positioning and simultaneous imaging of interfacial topography and activity. *Analytical Chemistry* 2010, 82, 6334–6337.
31. Modestov, A. D., Srebnik, S., Lev, O., Gun, J. Scanning capillary microscopy/mass spectrometry for mapping spatial electrochemical activity of electrodes. *Analytical Chemistry* 2001, 73, 4229–4240.
32. Kottke, P. A., Degertekin, F. L., Fedorov, A. G. Scanning mass spectrometry probe: A scanning probe electrospray ion source for imaging mass spectrometry of submerged interfaces and transient events in solution. *Analytical Chemistry* 2010, 82, 19–22.
33. Li, N., Eckhard, K., Assmann, J., Hagen, V., Otto, H., Chen, X., Schuhmann, W., Muhler, M. Scanning mass spectrometry with integrated constant distance positioning. *Review of Scientific Instruments* 2006, 77, 084102.
34. Modestov, A. D., Gun, J., Savotine, I., Lev, O. On-line electrochemical-mass spectrometry study of the mechanism of oxidation of *N*,*N*-dimethyl-*p*-phenylenediamine in aqueous electrolytes. *Journal of Electroanalytical Chemistry* 2004, 565, 7–19.
35. Chen, X., Eckhard, K., Zhou, M., Bron, M., Schuhmann, W. Electrocatalytic activity of spots of electrodeposited noble-metal catalysts on carbon nanotubes modified glassy carbon. *Analytical Chemistry* 2009, 81, 7597–7603.
36. Maljusch, A., Schönberger, B., Lindner, A., Stratmann, M., Rohwerder, M., Schuhmann, W. Integrated scanning kelvin probe-scanning electrochemical microscope system: Development and first applications. *Analytical Chemistry* 2011, 83, 6114–6120.
37. Guillaumin, V., Schmutz, P., Frankel, G. S. Characterization of corrosion interfaces by the scanning Kelvin probe force microscopy technique. *Journal of the Electrochemical Society* 2001, 148, B163–B173.
38. Stratmann, M., Leng, A., Fürbeth, W., Streckel, H., Gehmecker, H., Grosse-Brinkhaus, K. H. The scanning Kelvin probe; a new technique for the in situ analysis of the delamination of organic coatings. *Progress in Organic Coatings* 1996, 27, 261–267.
39. Hochstrasser-Kurz, S., Reiss, D., Suter, T., Latkoczy, C., Gunther, D., Virtanen, S., Uggowitzer, P. J., Schmutz, P. ICP-MS, SKPFM, XPS, and microcapillary investigation of the local corrosion mechanisms of WC-Co hard metal. *Journal of the Electrochemical Society* 2008, 155, C415–C426.
40. Henning, A. K., Hochwitz, T., Slinkman, J., Never, J., Hoffmann, S., Kaszuba, P., Daghlian, C. Two-dimensional surface dopant profiling in silicon using scanning Kelvin probe microscopy. *Journal of Applied Physics* 1995, 77, 1888–1896.
41. Baikie, I. D., Smith, P. J. S., Porterfield, D. M., Estrup, P. J. Multitip scanning bio-Kelvin probe. *Review of Scientific Instruments* 1999, 70, 1842–1850.

42. Williams, G., McMurray, N. Latent fingermark visualisation using a scanning Kelvin probe. *Forensic Science International* 2007, 167, 102–109.
43. Bard, A. J. *Electrogenerated Chemiluminescence*. Marcel Dekker, New York, 2004.
44. Kanoufi, F., Cannes, C., Zu, Y., Bard, A. J. Scanning electrochemical microscopy. 43. Investigation of oxalate oxidation and ECL across the liquid–liquid interface. *Journal of Physical Chemistry B* 2001, 105, 8951–8962.
45. Wang, Q. A., Rodríguez-López, J., Bard, A. J. Evaluation of the chemical reactions from two electrogenerated species in picoliter volumes by scanning electrochemical microscopy. *ChemPhysChem* 2010, 11, 2969.
46. Rodríguez-López, J., Shen, M., Nepomnyaschii, A., Bard, A. J. Study of the electrogenerated chemiluminiscence in the radical annihilation mode of rubrene by scanning electrochemical microscopy. 2011, In preparation.
47. Zigah, D., Rodríguez-López, J., Bard, A. J. Quantification of photoelectrogenerated hydroxyl radical on TiO_2 by surface interrogation scanning electrochemical microscopy (SI-SECM). 2011, In preparation.
48. Peterson, R. R., Cliffel, D. E. Scanning electrochemical microscopy determination of organic soluble MPC electron-transfer rates. *Langmuir* 2006, 22, 10307–10314.
49. Bard, A. J., Zhou, H., Kwon, S. J. Electrochemistry of single nanoparticles via electrocatalytic amplification. *Israel Journal of Chemistry* 2010, 50, 267–276.
50. Kwon, S. J., Zou, H., Fan, F.-R., Vorobyev, V., Zhang, B., Bard, A. J. Stochastic electrochemistry with electrocatalytic nanoparticles at inert ultramicroelectrodes-Theory and experiments. *Physical Chemistry Chemical Physics*, 2011, 13, 5394–5402.
51. Lovelock, K. R. J., Cowling, F. N., Taylor, A. W., Licence, P., Walsh, D. A. Effect of viscosity on steady-state voltammetry and scanning electrochemical microscopy in room temperature ionic liquids. *Journal of Physical Chemistry B* 2010, 114, 4442–4450.
52. Gründler, P., Kirbs, A., Dunsch, L. Modern thermoelectrochemistry. *ChemPhysChem* 2009, 10, 1722–1746.
53. Schäfer, D., Puschhof, A., Stoica, L., Finger, J., Chen, X., Schuhmann, W. SECM at variable temperatures. System development and visualization of local catalyst activity, in *Sixth SECM Workshop*. Frejus, France, 2010.
54. Gründler, P., Degenring, D. The limits of aqueous hot-wire electrochemistry: Near-critical and supercritical fluids in electrochemical sensors? *Electroanalysis* 2001, 13, 755–759.
55. Liu, C. Y., Snyder, S. R., Bard, A. J. Electrochemistry in near-critical and supercritical fluids. 9. Improved apparatus for water systems (23–385°C). The oxidation of hydroquinone and iodide. *Journal of Physical Chemistry B* 1997, 101, 1180–1185.
56. Flarsheim, W. M., Tsou, Y. M., Trachtenberg, I., Johnston, K. P., Bard, A. J. Electrochemistry in near-critical and supercritical fluids. 3. Studies of Br^-, I^-, and hydroquinone in aqueous solutions. *Journal of Physical Chemistry* 1986, 90, 3857–3862.
57. Cabrera, C. R., Garcia, E., Bard, A. J. Electrochemistry in near-critical and supercritical fluids. Part 7. SO_2. *Journal of Electroanalytical Chemistry* 1989, 260, 457–460.
58. Giovanelli, D., Lawrence, N. S., Compton, R. G. Electrochemistry at high pressures: A review. *Electroanalysis* 2004, 16, 789–810.

Chemistry

Scanning Electrochemical Microscopy Second Edition

Because of its simplicity of use and quantitative results, Scanning Electrochemical Microscopy (SECM) has become an indispensable tool for the study of surface reactivity. The fast expansion of the SECM field during the last several years has been fueled by the introduction of new probes, commercially available instrumentation, and new practical applications. **Scanning Electrochemical Microscopy, Second Edition** offers essential background and in-depth overviews of specific applications in self-contained chapters.

Recent methodological advances have greatly increased the capacity of SECM to characterize interfaces at the nanoscale and to obtain molecular-level chemical information. This thoroughly updated edition retains original chapters describing the principles of SECM measurements, instrumentation, preparation of SECM probes, imaging methodologies, and theory and offers:

- New chapters on studies of single biological cells, corrosion, electrocatalysis, and hybrid techniques
- Descriptions of recent advances of SECM in several areas of current interest: biotechnological applications, nanofabrication and surface patterning, and molecular transport across films and membranes
- Discussion of the ongoing shift from micrometer-scale experiments to the nanoscale

Useful for a broad range of interdisciplinary research—from biological systems to probing reactions at the liquid–liquid interface—this book is invaluable to all interested in learning and applying SECM.

K11523

CRC Press
Taylor & Francis Group
an informa business
www.crcpress.com

6000 Broken Sound Parkway, NW
Suite 300, Boca Raton, FL 33487
711 Third Avenue
New York, NY 10017
2 Park Square, Milton Park
Abingdon, Oxon OX14 4RN, UK

ISBN: 978-1-4398-3112-0
90000
9 781439 831120